Applied Mechanics and Materials Vol. 164 (2012)

Applied Mechanics, Materials, Industry and Manufacturing Engineering

Edited by
Helen Zhang and David Jin

TRANS TECH PUBLICATIONS

Applied Mechanics, Materials, Industry and Manufacturing Engineering

Edited by
Helen Zhang
David Jin

Applied Mechanics, Materials, Industry and Manufacturing Engineering

Selected, peer reviewed papers from the
2012 2nd International Conference on
Mechanical Engineering, Industry and Manufacturing Engineering
(MEIME2012),
June 23-24, 2012, Hefei, China

Edited by

Helen Zhang and David Jin



Copyright © 2012 Trans Tech Publications Ltd, Switzerland

All rights reserved. No part of the contents of this publication may be reproduced or transmitted in any form or by any means without the written permission of the publisher.

Trans Tech Publications Ltd
Kreuzstrasse 10
CH-8635 Durnten-Zurich
Switzerland
http://www.ttp.net

Volume 164 of
Applied Mechanics and Materials
ISSN 1662-7490

Full text available online at *http://www.scientific.net*

***Distributed** worldwide by*

Trans Tech Publications Ltd
Kreuzstrasse 10
CH-8635 Durnten-Zurich
Switzerland

Fax: +41 (44) 922 10 33
e-mail: sales@ttp.net

and in the Americas by

Trans Tech Publications Inc.
PO Box 699, May Street
Enfield, NH 03748
USA

Phone: +1 (603) 632-7377
Fax: +1 (603) 632-5611
e-mail: sales-usa@ttp.net

Preface

MEIME2012 is a comprehensive conference,and it is an integrated conference concentrating its focus upon Applied Mechanics and Materials in Mechanical Engineering,Industry and Manufacturing Engineering. In the proceeding, you can learn much more knowledge about Applied Mechanics and Materials in Mechanical Engineering,Industry and Manufacturing Engineering of researchers all around the world. The main role of the proceeding is to be used as an exchange pillar for researchers who are working in the mentioned field. In order to meet high standard of *Applied Mechanics and Materials*,the organization committee has made their efforts to do the following things. Firstly, poor quality paper has been refused after reviewing course by anonymous referee experts. Secondly, periodically review meetings have been held around the reviewers about five times for exchanging reviewing suggestions. Finally, the conference organization had several preliminary sessions before the conference. Through efforts of different people and departments, the conference will be successful and fruitful.

MEIME2012 is co-sponsored by ISER Association, Beijing Gireida Education Research Center and VIP-Information Conference Center,China. The goal of the conference is to provide researchers from Applied Mechanics and Materials in Mechanical Engineering,Industry and Manufacturing Engineering fields with a free exchanging forum to share the new ideas, new innovation and solutions with each other. In addition, the conference organizer will invite some famous keynote speaker to deliver their speech in the conference. All participants will have chance to discuss with the speakers face to face, which is very helpful for participants.

During the organization course, we have got help from different people, different departments, different institutions. Here, we would like to show our first sincere thanks to Mr. Thomas Wohlbier,Anne and Trans Tech Publications for their kind and enthusiastic help and support for our conference. Secondly, the authors should be thanked too for their enthusiastic writing attitudes toward their papers. Thirdly, all members of program chairs, reviewers and program committees should also be appreciated for their hard work.

In a word, it is the different team efforts that they make our conference be successful on June 23-24, Hefei, China. We hope that all of participants can give us good suggestions to improve our working efficiency and service in the future. And we also hope to get your supporting all the way. Next year, In 2013, we look forward to seeing all of you at MEIME 2013.

March, 2012

MEIME committee

Committee

Honor Chairs
Prof. Chen Bin, Beijing Normal University,China
Prof. Hu Chen, Peking University,China
Chunhua Tan, Beijing Normal University,China
Helen Zhang, University of Munich,China

Program Committee Chairs
Xiong Huang, International Science& Education Researcher Association,China
LiDing, International Science& Education Researcher Association,China
Zhihua Xu, International Science& Education Researcher Association,China

Organizing Chair
ZongMing Tu, Beijing Gireida Education Co.Ltd,China
Jijun Wang, Beijing Spon Technology Research Institution,China
Quanxiang, Beijing Prophet Science and Education Research Center,China

Publication Chair
Zhihua Xu, International Science& Education Researcher Association,China
Sally Wang, Beijing Normal University,China

Committee
Sally Wang, Beijing normal university,China
LiLi, Dongguan University of Technology,China
BingXiao, Anhui university,China
Z. L. Wang, Wuhan university,China
Moon Seho,Hoseo University,Korea
Kongel Arearak,Suranaree University of Technology,Thailand
Zhihua Xu, International Science& Education Researcher Association,China
Xiangrong Jiang, Wuhan University of Technology,China
LiHu, Linguistic and Linguidtic Education Association,China
Moon Hyan,Sungkyunkwan University, Korea
Guangwen, South China University of Technology,China
Jack.H. Li, George Mason University, USA
Marry. Y. Feng, University of Technology Sydney, Australia
Li Hu, Wuhan University of Science and Technology, China,
ZhongYan, Wuhan University of Science and Technology, China
Haiquan Huang, Hubei University of Technology,China
Xiao Bing, WUhan University, China
Brown Wu, Sun Yat-Sen University, China

Co-sponsored by
International Science& Education Researcher Association, China
Beijing Gireida Education Research Center
VIP-Information Conference Center,China

Table of Contents

Preface and Committees

Chapter 1: Material Research in Mechanical Engineering, Industry and Manufacturing Engineering

Research on Propagation Characteristics of Stress Waves in Laser Shock Processing for DD6 Single Crystal Alloy Materials
Y.W. Fang, Y.H. Li and H. Wang 3

Predicting the End Temperature of Molten Steel Using CBR
D.H. Liu, H.B. Wang and A.J. Xu 7

Influence of Surface Modification on Si_3N_4 Powder Fluidity
J. Chen and X.G. Wang 12

Peparation and Magnetic Propriety of Carbon-Coated Iron Magnetic Nanoparticles by Starch Coating Method
J. Chen and H.Y. Zhang 17

The Reaction Kinetics of Aluminum and Isopropanol
X.H. Wang, H.H. Ni, Y. Cao, G. Li, H. Gao and J.L. Yang 21

Study on Critical Load Position and Cracking in Asphalt Layer of Continuously Reinforced Concrete Composite Asphalt Pavement
S. Li, Z.H. Liu, Y.Z. Li and Y.X. Zhang 26

Py-GC-MS Analysis on Biomass Energy Components from Wood Extractives of *Eucalyptus urophydis* under High Temperature
L.S. Wang and W.X. Peng 30

Study on Corrosion Inhibition Performance of PASP Composite on A3 Carbon Steel in Seawater
X. Wang, Z. Liu and Z.F. Liu 33

Affection of Manufacture Parameters and Mixture Material on Plastic Alloy Bearings
C.Y. Yang and J.M. Peng 37

Thermal Study on the Grinding Special-Shaped Surface of Granite Material
Y.B. Shi, B. Huang and D.B. Liu 42

Ferroelectric and Optical Properties of BST/BZT/BST Sandwich Structure Thin Films Prepared by RF Sputtering
C.B. Ma, X.G. Tang, D.P. Xiong, Y.P. Jiang and Q.X. Liu 47

Effection of Wood Extractives on Burning Time of Fuel for Add-On Bioenergy
W.X. Peng and L. Cui 52

Orthogonal Analysis on Hardness of Nickel/Graphite Sealing Coating
S.P. Song, C. Li and Z.H. Ji 55

Effect of Laser Processing on Electroless Copper Deposition on Modified Plastic
X. Peng and K.Y. Jiang 59

Influences of Process Parameters on the Forming of YAG Phase
X.H. Wang, J.T. Dong, Y. Cao, G.Q. Zhao, H. Gao and J.L. Yang 65

Preparation and ESR Properties of Silicon Nitride Nanowires
J. Chen, X.G. Wang and H.Y. Zhang 69

Gearbox Non-Ferrous Metal Bearing Wear Condition Monitoring Based on Oil Analysis
X.F. Jiang, F. Liu and P.C. Zhao 73

Solar Shading Performance of Different Louver Shading Materials in Hot Summer and Cold Winter Zone
Z.K. Li and J. Yao 77

Research on Material Selection Standard of Graded Crushed Stone Base Course for Municipal Road
K. Liu, F. Wang, W.H. Zhang and Y.R. Wang 81

A Comparative Study on Building Energy Performance between Movable and Fixed Shading Materials
X.C. Yang and J. Yao 85

Evaluation on Safety of Internal Bambooen and Wooden Biomaterials for Food
H.Y. Guo and Z.Z. Zheng 89

Effect of same Insulation Materials on Energy-Saving Potential of Different Buildings
C. Guo and J. Yao 93

Application of Fluorescent Aerosols to Verifying the Leakage of Protective Clothing by Image Processing
C.H. Luo, H.Z. Chen, Y.C. Huang, S.H. Yang and S.H. Wang 97

Healing of Cracked Concrete by *Sporosarcina pasteurii* Mediated Carbonate Deposition
P.H. Li and B. Jin 103

Modelling of Chloride Diffusion into Surface-Biodeposited Concrete
P.H. Li and B. Jin 107

Treatment of the Lead Waste Water with Electrochemical Process
J.J. Song 111

Low-Temperature Synthesis and Characterization of Single-Phase $BiFeO_3$ Nano-Crystallites
H.F. Guo, S.X. Guo and L.B. Li 115

Electron Transport of Boron Nitride Nanoribbons Materials
D.M. Zhang, D.Q. Wang, H.Q. Yang, Z.G. Bao and Y.S. Zhang 120

The Structure and Fluid Flow Analysis for a New SXSH Static Mixer
Q. Wu, Q.L. Li and B.A. Han 124

The Application Research of Biological Materials in Meniscus Injuries
P.F. Huo 128

Preparation Process of Antioxidation Coating of Prebaked Carbon Anode Steel Claw
Z.X. Liu, Z.S. Qiu, J.K. Yan, G.Y. Gan, R.J. Jia, Y.Q. Zhou and J.H. Yi 132

Study on Pile-Soil Interaction during Pile Sinking and Drivability of Pile in Offshore Platform
Y.P. Song, Y.F. Sun, C.L. Cao and S.L. Li 137

Mechanical and Thermal Properties of Kaolin/Natural Rubber Nanocomposites Prepared by the Conventional Two-Roll Mill Method
Q. Zhang, Y.D. Zhang and Y. Wang 142

Study on Aggregation Behaviour of Mixture of Alkylbenzene Sulfonate Gemini Surfactant Ib and Nonionic Surfactant Triton X-100
X.G. Du, C.S. Zhang, J. Zhang, X.M. Guo, W.W. Lu and Z.Y. Yang 146

Synthesis and Properties of a Novel Material Chemistry Unsymmetrical Material, Diarylethene with Cyano
W.W. Geng, C.B. Fan and S.Z. Pu 150

Enhanced Adsorption Properties of Poly(2-Acrylamido-2-Methyl-1-Propansulfonic Acid)/Silica Composite Materials for Heavy Metal Ion Removal
J.J. Wang and X.N. Li 154

Effect of Interface States on the Properties of a-Si:H/c-Si Heterojunction Solar Cells Based on Solar Materials
C.L. Zhong, L.E. Luo and Y.Q. Xia 158

Preparation and Charactorization of Superfine YAG Powder Materials via the Co-Precipitation Methods
J.G. Song, A.X. Chen, Q. Li, Z.W. Qiu, J.F. Zhou, Y.F. Xiong, T. Xu, W. Wei and W.T. Li 162

Synthesis of a Photochromic Diarylethene Material Bearing Fluorine Atoms for Rewritable Holographic Optical Storage
S.H. He, W.J. Liu and G. Liu 166

Sintering Temperature Establishment of Quartz Sand Heat Insulating Porous Materials
J.G. Song, F. Wang, W.B. Li, Z.W. Wang, X.D. Ma, G.H. Cao, Q. Li, W. Li, J. Zhang and Y.H. Liu 170

Wear Morphology and Mechanism Analysis of Plasma Spraying Nanometer Al_2O_3-13%wtTiO_2 Coating Material
Z.F. Cheng, F.C. Wang and Z. Ma 174

Synthesis and Properties of a New Photochromic Material Based on Isoxazole Unit for Optical Storage Recording
T.F. Wang, Y.H. Yang, S.Q. Cui and G. Liu 178

Transport of a Thermophilic *Geobacillus* sp. in Sandpack Core as an Enhanced Oil Recovery Material
X.P. Kong 182

Effect of Placement Pattern and Quantity of Iron Shavings in Reactor on Biological Nutrient Removal from Domestic Wastewater
Z. Wang, Z. Chen, H.W. Wang and L.M. Ma 186

Study of Rapid Synthesis on $LiFePO_{4B}$ and $LiFePO_{4B}$/C by Molten Salt Method and its Electrochemical Properties as Cathode Material
N.Y. Gu, X.H. He and C. Li 190

Synthesis and Properties of the ESA/AMPS Copolymer
Z. Liu, X. Wang and Z.F. Liu 194

Advanced Landfill Leachate Treatment Using the Tubular Membrane Bio-Electro Reactor
E.H. Liu, L. Yang and H.Y. Xu 199

Effects of Organic Solvent Treated on the Performance and Structure of Polysulfone Tubular Ultrafiltration Membrane
E.H. Liu, H.Y. Xu and X.C. Zhao 203

Germanium Doping and Impurities Analysis on Industrial Scale Mc-Silicon Ingot
S.A. Li, P. Wu, B.T. Zhao and W.X. Gao 207

Research on the Mathematical Model of the Plastic Profile Cooling Analysis
X.S. Huang and L.D. Chen 214

The Technology Analysis and Development Trend of Biological Materials Energy
S.D. Zhou, L.M. Hu and X.D. Ouyang 218

Effect of Preparation Conditions on the Performance of Anodic Aluminum Oxide Films
X.Z. Liu, J.H. Yang, G. Wang, L.L. Song and G.S. Zhuang 223

Noise Reduction of Elastic Structure Paste Viscoelastic Material Based on Complex Radius Vector of Virtual Source
Y.M. Wang, Y.A. He and D.J. Shang 227

Transport of Bacteria in Natural Core as Enhanced Oil Recovery Material
X.P. Kong 231

Properties and Application of a Novel Diarylethene Photochromism Material with a Naphthyl Ring
L.Q. Wang, S.Z. Pu and L.S. Yan 235

Photochromism Material of New Unsymmetrical Isomeric Diarylethenes Bearing a Thiophene and Pyridine Unit
M. Liu, G. Liu and S.Q. Cui 239

Synthesis a New Function Materials and Photochromic Properties of Diarylethene Bearing a Naphthalene and Isoxazole Moiety
R.J. Wang, S.Q. Cui and S.Z. Pu 243

Synthesis and Properties of a Novel Photochromic Diarylethene Material Bearing Two Five-Membered Aryl Unit
X.T. Li, H. Li and S.Z. Pu 247

Photochromism and Fluorescence of a Novel Unsymmetrical Diarylethene Material Bearing Benzene and Thiophene Ring
S.H. Jing, S.Z. Pu and H. Li 251

Photochromic Properties of 1-[2-Methyl-5-(4-Chlorophenyl)-3-Thienyl]-2-[2-Methyl-5-(Phenanthren-10-Yl)-3-Thienyl]Perfluorocyclopentene
X. Li, C.B. Fan and G. Liu 255

Properties and Synthesis of a Novel Unsymmetrical Photochromic Diarylethene Functional Material
H.C. Ding, C.H. Zheng and S.Z. Pu 259

Recovery of Precious Metal Material Ni from Nickel Containing Wastewater Using Electrolysis
R.J. Jin, C.S. Peng, A. Abou-Shady and K.D. Zhang 263

Preparation and Performance of Si/Al/C Composites Anode Material Prepared by Glucose-Modified
X. Ma, L.L. Kong, Y.L. Liu, Y.H. Ding, J. Zhao, L. Li and N. Xu 268

Toxic Effect of Cadmium Material on *Eisenia fetida*
M.Y. Huang, R.Y. Duan, R.J. Hao and L.P. Ren 272

The Effects of the Sputter-Etching Power on the Formation of Conical Protrusions on the Surface of SUS304 Stainless Steel
T. Bai and Q.L. Zhang 276

Efficient Synthesis and Properties of a Novel Unsymmetrical Photochromic Diarylethene Material Based on Pyrazolyl Group
W.J. Liu, W.P. Wang, D.H. Jiang and G. Liu 280

The Effects of the Self-Assembly Time on the Preparation of Lanthanum-Based Thin Films on Sulfonated 3-Mercaptopropyl Trimethoxysilane
T. Bai and X.H. Cheng 284

Feasibility of Reutilizing Municipal Solid Waste Incineration Residues as Construction Materials
R.J. Zhang and Y.J. Hu 289

Preparation and Electrochemical Performance of $Li_4Ti_5O_{12}$ as Anode Material for Li-Ion Battery by Solid State Method
F. Gu 293

Application of Carbonaceous Materials to Phenol Removal from Aqueous Solution by Adsorption
W.F. Dong, L.H. Zang, Q.C. Gong, C.C. Chen, C.H. Zheng, X.S. Meng and T.T. Liu 297

The Study on Carbon Emission Influencing Factors of Industrial Energy Consumption of Changchun City
Z. Ma, X.G. He, X.Z. Tong, H.Y. Duan, X.E. Wang and D.M. Dong 302

Anti-Corrosion Materials and Spray Technology in the Coastal Wind Generating Set
H.M. Sun and X.G. Feng 306

Chapter 2: Mechanics Study in Mechanical Engineering, Industry and Manufacturing Engineering

Mechanics Analysis of Protective Casing and Splicing Sleeve
J. Qin and Y.P. Qiu 313

CAD/CAE on the Mould Plates of Horizontal Type High-Pressure Grouting Machine
Z.C. Huang 317

Analysis of Jib Strength and Broken Jib Accident of High Pedestal Jib Crane from the Perspective of Mechanics
Q.D. Zeng and F. Liu 322

Analysis of Flanges Mechanics and Sealing on Horizontal Pipes Connector in Deep Sea
Z. Wang, Y.J. Li, B. Zhang, W. Zhang and F.K. Liu 326

Research on the Virtual Prototype of Grinding System for Wafer Precision Grinding Machine Based on Mechanical System Mechanics
Z.H. Sha, Z.N. Zhang and S.F. Zhang 330

Faults Monitoring and Diagnosis of Air Compressor from Vibration Mechanics
Y.J. Jia, G.Z. Cheng and Y.Y. Han 334

Coupling Analysis of Vibration and Fatigue Crack Propagation for a Breathing Cracked Beam
W. Cui and J.J. Wang 338

Rotating Clamping Device of the Hydraulic Prop Disassemble Machine Based on Hydromechanics
Y.J. Jia, D.Y. Zhang, G.Z. Cheng and Y.J. Dai 344

Research on Energy Saving Mechanism of Optimal Regulation Voltage for Overhead or Gantry Crane Based on Mechanics Analysis
B. Zhong and W.M. Cheng 348

Hoist Lubricating Oil Pressure and Liquid Level Detection
G.Z. Cheng and J. Lin 352

Study on Mechanics of Special Materials against Oil Volatility Risk
T. Li 356

Research on Constant Pressure of Air Supplying and Energy Saving for the Air Conditioning System
G.Z. Cheng, Z.Q. Liu and H.F. Lin 362

Calculating Method of Assembly Clearance Magnitude of Centrifugal Pump Impeller with Mechanics Analysis
L.H. Li and Q.J. Guo 366

Pumping Underground Extended-Range Application Practice and Process Analysis with Mechanics
L.J. Qiu and J. Yang 371

Fit Clearance of Impeller to Turbocharger Performance Influence with Mechanics Properties
S.Y. Xu and L.J. Qiu 375

Finite Element Modeling and Stress Analysis for Planetary Gear with Thin Rim
J.F. Huo, J. Zhang and Y.M. Song 379

Research on Pre-Slip Gait Mechanical Contributions and Gait Self-Balancing Mechanics during Walking
H.L. Su and D.W. Zhang 383

Oscillatory Behavior in a Nonlinear Gyroscopic System with Mechanics
C.H. Feng and Y.H. Lin 387

Hydraulic Cylinder Cold Pulling Processing and Mechanics Analysis
X.X. Zhang, Y.J. Jia and G.Z. Cheng 392

Calculating the Quasi-Static Pressures of Confined Explosions Considering Chemical Reactions under the Constant Entropy Assumption
W. Zhong and Z. Tian 396

Failure Analysis of Rolling Bearing Based on Oil Monitoring Techniques with Mechanics Basis
X.F. Jiang, F. Liu and P.C. Zhao 401

Study of Thermodynamics of Alkali-Free Glass Reaction
S. Liu, Y.C. Yao, Y.L. Liu and Y.N. Dai 405

Research on Magnetic Fluid Based Optical Deformable Mirrors with Fluid Mechanics
Z.Z. Wu and M. Liu 409

Mechanics Analysis of Grade V Surrounding Rock Primary Support in Maanziliang Tunnel
J.M. Han 414

Chapter 3: Industry, Mechanical Engineering, Manufacturing Engineering Based on Dynamic Systems

Research of Hydraulic Cylinders Dynamic Characteristic and Synchrocontrol on Horizontal Pipes Connector in Deep Sea
Z. Wang, Y.J. Li, B. Zhang, W. Zhang and Y.Z. Zhang 421

Analysis of 3D Dynamic Response for TC4 Blades by the FEM
Y.W. Fang, Y.H. Li and W.F. He 425

Engine Valve Motion Simulated with Mechanical Dynamics
Z.Z. Ma and X.L. Wang 429

Power Spectral Density Model of Torsional Dynamic Wind Loads on Tall Buildings
T.Y. Xiao 433

Structure and Motion Analysis of a Tire Building Drum Based on Parallel Mechanism
X.H. Pan 437

Research on Energy Harvesting Behaviors of Different Shapes of Piezoelectric Vibrator
W.D. Chen, H.S. Hu, S.X. Qian and D.K. Zhu 441

Research on Improving the Test Effectiveness of Rock Dynamic Fracture Toughness
S. Zhang, X.W. Li and X.H. Yang 446

Design and Analysis on the Dynamic System of an Oil-Well Pump Lifting Test System
B. Li 451

Modal Finite Element Analysis of Reconstructive Structure for Gantry Crane on the Basis of ANSYS and Dynamic Stiffness
Q.D. Zeng and B.H. Guan 456

Analysis on the Characteristics of Scale Wave Energy Dynamic System during Extended Period of the Massive Drought in Southwestern Region
T.G. Xiao, Y. Wu and R.H. Jin 460

Dynamic Modeling for a Non-Linear System Based on the MOESP Algorithm
Q. Teng, J.B. Zhang and P. An 467

Dynamic Model of the Knife Rollers in the Spiral Cutting Machines
L.S. Wang, J.L. Cheng, D.A. Wang, H.N. Ni and Y.C. Han 473

Photochromism, Fluorescence and Dynamic System of a Novel Unsymmetrical Diarylethene Material Based on Naphthyl Rings
P.P. Ren, M. Deng, S.Q. Cui and G. Liu 478

Study on Optimal Circulation Dynamic System and Feasibility Analysis for a Solar Biogas Digester
Y. Zhang, C.S. Peng and F.M. Li 482

Helicid-Loaded Zein Microparticles Prepared Using Electrohydrodynamic Atomization
D.G. Yu, X. Wang, Y.Z. Liao, Y. Li, W. Qian and X.Y. Li 487

Research on Mechanical Properties of Geopolymer Concrete under early Stage Curing System
Q. Wang, K. Ran, Z.Y. Ding and L.G. Qiu 492

Water Storage Bucket Chain Convey-Cleaning Machine for Cleaning Up Coal Mine Water Storage
Y.J. Jia, D.Y. Zhang, G.Z. Cheng and Y.J. Dai 497

Features of Jianshanchong Klippe and its Control to Gas Geology at Qingshan Coal Mine, Jiangxi Province
Z.G. Zhao, J. Chen and J.P. Yan 501

Effect of Anode Size, Membrane and Membrane Size on Power Generation and Wastewater Treatment in Microbial Fuel Cells
G.Y. Zhou, Y. Yoshino, T. Yamashita, T. Sato and Y. Kawagoshi 506

Research on the Characteristics of Gas Geology in Yongshanqiao Mining Area, Jiangxi Province
Z.G. Zhao, M.M. Zhang and J.P. Yan 511

Enhancing Biological Nutrient Removal from Real Domestic Wastewater by Using Iron Shavings
Z. Wang, Z. Chen, H.W. Wang and L.M. Ma 517

CHAPTER 1:

Material Research in Mechanical Engineering, Industry and Manufacturing Engineering

© (2012) Trans Tech Publications, Switzerland
doi:10.4028/www.scientific.net/AMM.164.3

Research on propagation characteristics of stress waves in laser shock processing for DD6 single crystal alloy materials

YingWu Fang[1,a], YingHong Li[2,b] and Hui Wang[1,c]

[1]Telecommunication Engineering Institute, Air Force Engineering University, Xi'an China

[2]College of Engineering, Air Force Engineering University, Xi'an China

[a]fangyw72@126.com, [b]yinghli@126.com, [c]wanghui77@163.com

Corresponding author: Yingwu Fang, Email: fangyw72@126.com, fywwy123@yahoo.com.cn

Address: 1st East Fenghao Road No.117, Xi'an 710077, Shaanxi, China

Keywords: Laser shock processing; ANSYS/LS-DYNA; DD6; Propagation characteristics

Abstract. The finite element ANSYS/LS-DYNA was applied to simulate the propagation characteristics of stress waves in laser shock processing (LSP) for DD6 single crystal alloy materials. The constitutive model of dynamic response and computational modeling of LSP was built in this paper. Results of numerical simulation indicates that the change of stress waves was mainly appeared to the first wave, and the time with fluctuation was expanded slowly with the spread depth of stress wave was increased. The results can be used as theoretical basis for optimizing the process parameters in laser shock processing.

Introduction

DD6 single crystal alloy materials have very excellent performances on high temperature fatigue resistance and creep resistance, and it is important materials for manufacturing hot-end parts of aero engine[1]. Fatigue is one of the main fail ways for these materials during attended time. How to improve fatigue strength, extend life and task reliability, which is discussed widely[2]. In order to meet the requirement of high performance aero engine, it is very important fields for using laser shock technology to process aerial materials now[3].

The domestic and foreign research shows that laser shock can raise metal fatigue performance effectively, and the main reason is that high residual compressive stress has been produced on the surface of metal after metal was processed[4,5]. But the stress waves by shocking how to spread in the DD6 single crystal alloy materials, which has little attention. So, the propagation and fading characteristics of stress waves will be simulated based on the DD6 materials by laser shock processing, and the corresponding theoretical basic can be given for optimizing laser shock parameter.

Materials constitutive model of dynamic response

As a new surface strengthening technology, laser shock processing (LSP) uses intense pulse laser to produce shock waves on metal surface, which induce strain hardening in the surface of metal. Plasma moving and dynamic mechanism have very crucial roles for coupling of laser and target materials. The basic principle is shown in Fig.1[6].

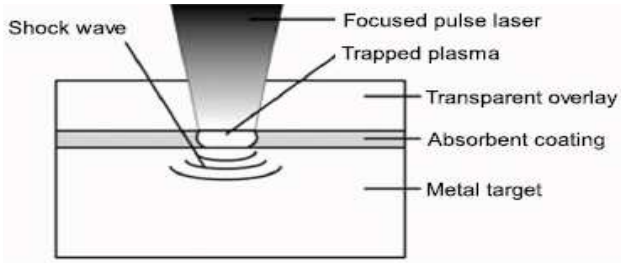


Fig.1 Schematic representation of laser shock processing

According to Fig.1, the character of LSP is dynamic interaction process of shock waves and materials. LSP is based on the application of a high intensity pulsed laser beam (I>1GW/cm2, t <50ns) at the interface between the metallic target and the surrounding medium (a transparent confining material, normally water) forcing a sudden vaporization of the metallic surface into a high temperature and density plasma that immediately develops inducing a shock wave propagating into the material. Owing to the press of shock waves belongs to middle shock load, elastic-plastic model was elected to analyzing the press. At present, kinds of constitutive relations of describing materials dynamic performances were given by scholars, and the common models have Elastic Perfectly Plastic(EPP), Cowper-Symonds(C-S), Johnson-Cook(J-C), Zerilli- Armstrong(Z-A), et al[5]. Considering to J-C model has simple form and clear physics explanation, the model was used to analyzing the dynamic response, and the corresponding expression by experiment method is shown:

$$\sigma_y = \left(A + B\varepsilon^n\right)\left(1 + C\ln\dot{\varepsilon}^*\right)\left[1 - \left(T^*\right)^m\right]. \quad (1)$$

Where ε is the anelastic strain, $\varepsilon^*=\varepsilon/\varepsilon_0$ is the nondimensional strain ratio, T_0 is the room-temperature, T_m is the materials melting point, which m is the softening effect of temperature, A, B and n denotes the materials character of strain hardening, C denotes the influence of rate of straining for materials performance.

Computational modeling of LSP

Owing to shock waves has short action time in the process of laser shock, with most in the range of 15 to 25 ns, LSP can generate strain-rate exceeding $10^7 s^{-1}$ within the target material. At such rates, metals behave in a significantly different manner than under quasi-static conditions. ANSYS/LS-DYNA is an explicit dynamic analysis program, which is used to simulate laser high speed shock process, and the software will be used to analyze the simulating process.

FEM modeling. The model size of DD6 materials is 5mm×5mm×3mm. In order to improve computed efficiency, different elements are used to the whole model. The size of 0.04mm is used to the shock area interior, and the size of 03mm is used to the shock area exterior. At last, the FEM model is shown as Fig.2.

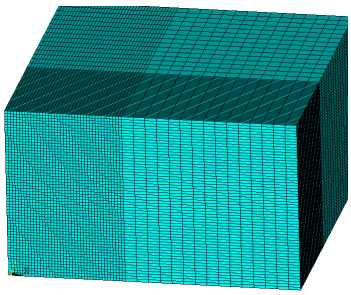


Fig.2 FEM model of DD6 material

Shock pressure loading and solution controlling. The shock mechanism by laser inducing is very complicated, and it is difficult to simulate the shock waves by ANSYS/LS-DYNA. In this study, the peak value pressure P_{max} of shock wave can be estimated by the following equation[6]:

$$P_{\max} = 0.8\rho^{0.5} I^{0.5}. \quad (2)$$

Where $2/\rho=1/\rho_1+1/\rho_2$, I is the laser power density, ρ_1, ρ_2 is the density of restraint layer target materials, respectively.

For the problem of solution controlling, the setting of solution time and whole damp are main, and the rest control items can adopt the default setting of ANSYS. According to the theoretical handbook of LS-DYNA, the optimal damp value should be given the two times of the first natural frequency for DD6 model, which can be gotten by analyzing modal shapes of ANSYS implicit program.

Numerical simulating and discussion

Simulation analysis for spread process of stress waves. The spread process of stress waves is very complicated. The change of stress waves is mainly appeared to the first wave, and the subsequent propagation characteristics can be seen the simplified form of the first wave path.

A case of laser shock I=3.2GW/cm^2 was analyzed, 11 nodes were selected along the depth direction of material in the center of spot size. The velocity of Z direction V_z was given in Fig.3 and Fig.4.

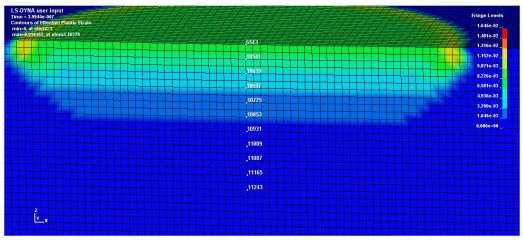


Fig.3 Selected nodes along the depth direction of target material

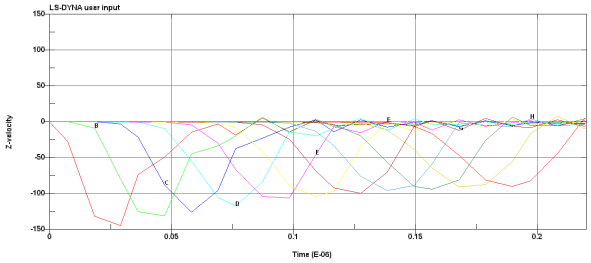


Fig.4 Every node V_z along the depth direction of target material

The peak value V_z of every node was seen as the arrived time of elastic-plasticity wave. The average plasticity wave speed C_p from surface to the depth of 0.5mm was 6250m/s by simulating analysis, and the average elastic wave speed C_e from the depth of 0.6mm to 1.0mm was 6305m/s by the formula of stress wave theory. The results agree with the theoretical calculated results by the above discussion.

The following will use the post processor of ANSYS/LS-DYNA to dynamic simulation propagation characteristics of stress wave for the first wave path in target materials. The stress of Z direction within every time and plasticity strain was intercepted, respectively, and the two aspects can influence spread state of stress wave. At last, when t=10ns, 20ns, 50ns, 500ns, 510ns and 590ns, respectively, the propagation process of stress wave and plasticity strain were gotten in Fig.5.

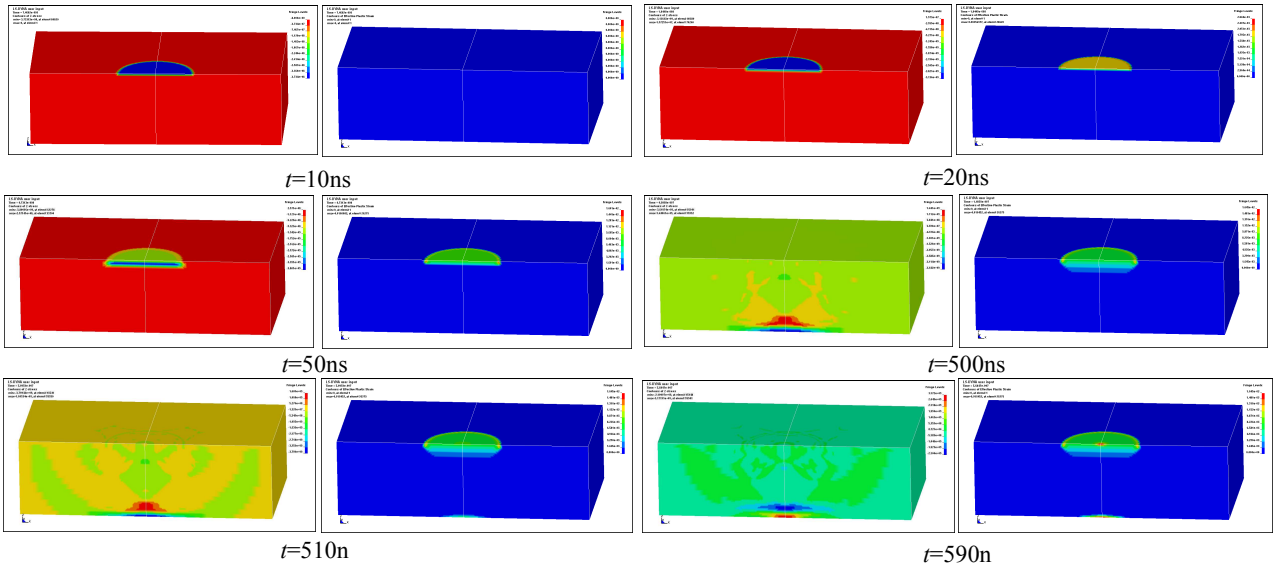


Fig.5 The propagation process of stress wave and plasticity strain different time

According to Fig.5, the shock wave was introduced target material at 10ns, the pressure at 10ns hadn't arrived to HEL, the plasticity strain hadn't been appeared at 10ns, and the stress wave appears the character of elastic wave. When shock wave was loaded to 20ns, the shock pressure exceed the limit of HEL, the plasticity strain been appeared in target materials. With the stress wave was spread to inner, the area which appear plasticity strain was grown at 50ns. When stress wave was spread at 500ns, the wave was spread to bottom of target materials. At 510ns, the wave was reflected on the bottom of target materials, and the corresponding plasticity strain was appeared. At 590ns, the plasticity and elastic waves were spread to top of target materials after reflected. Although the

superposition of reflection pressure makes the shock pressure super exceed HEL, the plasticity strain was happened for bottom materials. When completing the reflection of stress wave, the effect of nestification could be disappeared, the strength of stress wave would be fad down HEL again, and the results of shock was that the plasticity strain was developed a little depth on the bottom of materials.

Simulation analysis for fading process of stress waves. On the condition of I=3.2GW/cm^2, the value of facular area center along Z axis depth direction is 0.1mm, 0.3 mm, 0.5 mm, 0.8 mm, 1.2mm and 1.6mm, respectively, the corresponding variable relation of stress along z direction can be gotten, the stress of Z axis at 320ns was given in Fig.6.

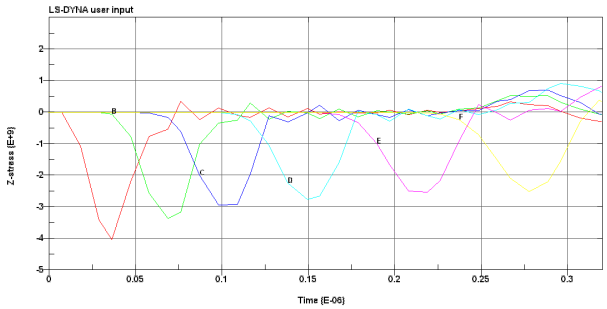


Fig.6 The stress along Z axis depth direction when I=3.2GW/cm^2

According to Fig.6, the value of stress wave was being reduced continuously with the stress wave was spread to material inner. The fading speed of stress wave was fast firstly, then, it was slow. In the process of spreading stress wave from the depth of 0.1mm to 0.5mm, the wave had being faded fast, and the average fading ratio was 0.172Pa/s. In the process of spreading stress wave from the depth of 0.5mm to 1.6mm, the fading speed of stress wave was slow obviously, and the average fading ratio was 0.035Pa/s. With the spread depth of stress wave was increased, the time with fluctuation was expanded slowly. Namely, the time of loading and unloading stress wave could be extended slowly.

Conclusions

LSP is a conceptually advanced emerging application for the improvement of surface characteristics of metallic high performance components. Numerical simulation is an effective way to predict the dynamic propagation characteristics induced by LSP and study the effects of laser shock parameters on the target materials . This paper main investigates the spread and fading process of stress waves by simulating for DD6 materials. On the basis of analyzing the generation, structure and fading of the stress wave, dynamic propagation characteristics of stress wave was simulated by ANSYS/LS-DYNA.

Acknowledgements

Work partly supported by natural science foundation of shaanxi province, China (No.2010JM6012), China postdoctor (No. 20100471835) and the national defence key project of AATR program.

References

[1] S.L. Han, S.X. Li and D.J. Smith: Comparison of phenomenological and crystallographicmodelsfor single crystal nickel base superalloys: Analytical identification. Mechanics of Materials Vol. 33 (2001), p. 251-266.

[2] Z.Y. Yin, X.M. Cheng, Z.G. Yang, et al. Study on strength and life of anisotropic single crystal blade part 1: Crystallographic Constitutive Models and Applications. Chinese Journal of Aeronautics Vol. 14 (2001), p. 18-23.

[3] D.J. Kong, Y.K. Zhang, J.Z. Lu, et al: Mechanical properties of Ni-based superalloy by laser shock processing. Chinese J. of Mater. Research Vol. 20 (2006), p. 492-495.

[4] W. Li, Y.H. Li, W.F He, et al: Effects study of laser shock processing on the fatigue life of nickel-based superalloy. New Technique & New Technology Vol. 8 (2008), p. 70-72.

[5] M. Morales, J.A. Porro and M. Blasco: Numerical simulation of plasma dynamics in laser shock processing experiments. Applied Surface Science Vol. 255 (2009), p. 5181-5185.

[6] Y.K Zhang, L.C. Zhou, X.D. Ren: Experiment and finite element analysis on residual stress field in laser shock processing TC4 titanium alloy. J. of Jiangsu University Vol. 30 (2009), p. 10-13.

© (2012) Trans Tech Publications, Switzerland
doi:10.4028/www.scientific.net/AMM.164.7

Predicting the End Temperature of Molten Steel using CBR

Dehua Liu[1, a], Hongbing Wang[2,b] and Anjun Xu[1,c]

[1]School of Metallurgical and Ecological Engineering, Uni. of Sci.&Tech. Beijing, 100083, China

[2]School of Computer and Communication Engineering, Uni. of Sci.&Tech. Beijing, 100083, China

[a]ak_agent@126.com, [b]wanghongbing0816@163.com, [c]ak_agent@163.com

Corresponding author: Hongbing Wang, wanghongbing0816@163.com

Keywords: molten steel; case based reasoning; analytic hierarchy process; temperature

Abstract. Steel is a kind of important material. The accurate control about the end temperature of molten steel has significant impact on the quality of steel material. Case Based Reasoning (CBR) is used to predict the end temperature of molten steel in Argon Oxygen Decarburization (AOD). Grey Relational Degree (GRD) with different weights of attributes is adopted to calculate the similarity between cases. Analytic Hierarchy Process (AHP) is taken to determine the weights of attributes. Multiple Linear Regression (MLR) is applied to compute the relative weight of two different attributes for AHP. Two methods, CBR using AHP with Equal Weights (CBR_AHP_EW) and CBR using AHP with Different Weights (CBR_AHP_DW), are employed to for a comparison. The results show that CBR_AHP_DW is effective in predicting the end temperature of molten steel in AOD and CBR_AHP_DW outperforms CBR_AHP_EW.

Introduction

Argon Oxygen Decarburization (AOD) is a key unit for stainless steel production. With the development of fine production in steel plants, the temperature of molten steel requires more and more strict control. To obtain the temperature of molten steel accurately and promptly is an urgent need. The traditional thermocouple measuring method fails to be fit for the high efficient, compact and modern production because it can not be fit for the requirement of continuous measurement, and more importantly, the delay of data feedback. Therefore, predicting the end temperature of molten steel is becoming more and more important in metallurgy.

The research about predicting the end temperature of molten steel in AOD, Basic Oxygen Furnace (BOF) and Ladle Furnace (LF) has attracted much attention in the past. These researches can be arranged in physical models and intelligent models [1]. Most of physical models are based on the conservation of mass and energy. There are just some works in AOD [2,3,4], which are almost based on physical models. The model based on physical energy during the steel production process was proposed [5] and thermodynamics was presented for molten steel [6]. A new mathematical model used for forecasting molten steel temperature during LF refining process was established on the basis of heat transfer principle with theoretical analysis [7]. These physical models were useful thermal analysis tools and were very accurate. However, these models can not be used efficiently for on-line prediction as the required parameters were hard to obtain.

Another kind of model is the intelligent model that uses artificial intelligence technology for predicting the end temperature of molten steel, such as Artificial Neural Network (ANN) and Case Based Reasoning (CBR). ANN was developed for predicting the change of the liquid steel temperature during a BOF operation [8]. An inverse neural model was proposed in order to adjust end-blow oxygen to match with the targets of end temperature in BOF [9]. A model was constructed by using neural networks as classifier to return a predicted temperature in Electric Arc Furnace (EAF) [10]. An improved AdaBoost RT using BP network as a learning machine is presented to modify the parameters of the physical model, which is used to predict the temperature of molten steel [11].

ANN requires a lot of training time and is not fit for online application. Furthermore, the weak generalization ability of ANN goes against predicting the end temperature of molten steel for the big production volatility in the metallurgical process. The most easily understandable and potential

methodology in prediction is the family of CBR, such as financial prediction [12,13], fault prediction [14] and cost prediction [15]. CBR with the weights derived by AHP is proposed for bankruptcy prediction and cost estimation [15]. But the relative weight of attributes in these CBR models is determined by domain experts. This study proposes a CBR method with the weights derived by AHP and the relative weight of attributes in AHP is determined using Multiple Linear Regression (MLR).

AHP

Factors Influencing the End Temperature of Molten Steel in AOD. The factors influencing the end temperature of molten steel in AOD consist of 20 attributes: smelting time, charge weight of molten steel, tapping weight of molten steel, amount of Oxygen usage, amount of Argon usage, amount of Nitrogen usage, the time interval between the time to sense the temperature and the end time of smelting, amount of caustic-burned dolomite usage, amount of fluorite usage, amount of metallurgical lime usage, amount of scrap usage, amount of ferrosilicon usage, amount of high carbon ferro-chrome, amount of nickel usage, amount of silicon manganese alloy usage, amount of micro-carbon ferro chrome usage, initial carbon content in molten steel, initial silicon content in molten steel, initial chrome content in molten steel and starting temperature of molten steel.

Role of AHP in CBR. AHP is adopted to determine the relative importance of attributes for the end temperature of molten steel in AOD through pairwise comparison of these attributes.

AHP with the Relative Weights derived by MLR. The relative weights of attributes for the end temperature of molten steel in AOD can be determined by some domain experts. Thus, human-caused disturbance can not be avoided. Here, MLR is used to determine the relative weights of any two different attributes. MLR attempts to model the relationship between two or more explanatory variables and a response variable by fitting a linear equation to observed data. The process is: to obtain the coefficients for the attributes using MLR on many production data; to divide pairwise using the coefficients to get the relative weight between any two different attributes; to determine the relative weights of attributes in AHP. Suppose the coefficients for two attributes A1 and A2 be c1=0.30195 and c2=0.00032. The relative weight of A1 to A2 is the result of 0.30195/0.00032, i.e., 943.59375. Then, the relative weight of A1 to A2 in AHP is 9.

CBR with AHP and MLR

Framework of CBR with AHP and MLR. The framework of CBR with AHP and MLR is shown in Fig. 1. AHP is used to compute the weights of attributes, which is applied for the computation of similarity between the new problem and the stored case. The pairwise comparison matrix is built according to the weight coefficients of attributes, which is derived by MLR.

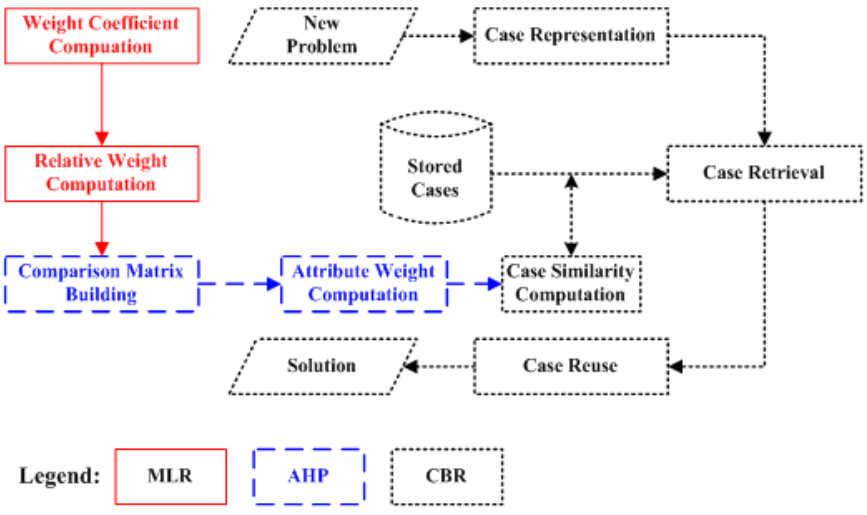


Fig.1 Framework of CBR with AHP and MLR

Case Similarity based on Grey Relational Degree. Let the problem to be solved s_0, the stored cases $\{s_i \mid i = 1...m\}$, and m the number of stored cases. The case similarity between s_0 and s_i is defined as follows:

$$G_{SIM}(s_0, s_i) = \frac{1}{1 + \sqrt{\sum_{k=1}^{n} G_d^2(s_0(k), s_i(k))}}. \quad (1)$$

The grey distance of the k-th attribute between s_0 and s_i is defined as follows:

$$G_d(s_0(k), s_i(k)) = {}^{1}\!/_{G_s(s_0(k), s_i(k))} - 1. \quad (2)$$

The Grey Relational Degree (GRD) of the k-th attribute between s_0 and s_i is defined as follows:

$$G_s(s_0(k), s_i(k)) = [\min_i \min_k (w_k |s_0(k) - s_i(k)|) + \varsigma \max_i \max_k (w_k |s_0(k) - s_i(k)|)] / [w_k |s_0(k) - s_i(k)| + \varsigma \max_i \max_k (w_k |s_0(k) - s_i(k)|)]. \quad (3)$$

Here, $\varsigma \in [0,1]$ is identification coefficient, w_k is the weight of the k-th attribute, which is computed by AHP and MLR.

Case Retrieval. A large amount of production data can be stored in the case library. So, the decrease of search time must be considered when retrieving similar cases. The two-step case retrieval, composed of rough search and delicate search, is provided for the purpose.

Case Reuse. Case reuse is to determine the solution for the new problem, i.e., the predicted end temperature of molten steel. One or several cases may be obtained by delicate search. The predicted end temperature of molten steel can be computed as follows:

$$T = {}^{\sum (G_i * T_i)}\!/_{\sum G_i}, \quad G_i \geq G_0. \quad (4)$$

Here, G_0 is the threshold of similarity for cases to be reused, G_i is the similarity between the new problem and the i-th case, T_i is the real temperature in the i-th stored case.

Experiments and Results

Experiments Design. The number of stored cases is 500 and the number of new problems is 80. The stored cases and problems are all from the real production data. Let G_0 be 0.8. Two methods are compared on the same stored cases and the same problems. One is the CBR method using AHP with equal weights, which is called CBR_AHP_EW. The other is the CBR method using AHP with different weights, which is called CBR_AHP_DW. For CBR_AHP_DW, the different weights of attributes are derived using AHP and MLR.

Results and Analysis. MLR is firstly used to get the coefficients of attributes from A1 to A20. Then, the relative importance in AHP according to the result of pairwise division is shown in Table 1. The effectiveness of AHP and MLR for determining the weights of the attributes in the CBR method was evaluated by comparing CBR_AHP_EW and CBR_AHP_DW. The result using CBR_AHP_EW is shown in Fig. 2, and the result using CBR_AHP_DW is shown in Fig. 3.

CBR_AHP_EW has the 31.25% percentage of predicted temperature hits in the error scope [-5℃,+5℃], but CBR_AHP_DW has the 41.25% percentage of hits. CBR_AHP_EW has the 61.25% percentage of predicted temperature hits in the error scope [-10℃,+10℃], but CBR_AHP_DW has the 72.5% percentage of hits. CBR_AHP_EW has the 86.25% percentage of predicted temperature hits in the error scope [-15℃,+15℃], but CBR_AHP_DW has the 92.5% percentage of hits. The results show that CBR_AHP_DW outperforms CBR_AHP_EW for predicting the end temperature of molten steel in AOD.

Table 1 Relative Importance in AHP according to the Result of Pairwise Division

		A1	A2	A3	A4	A5	A6	A7	……
		0.30195081	0.000324	9.29E-05	0.010421	0.000827	0.003344	3.817735	……
A1	0.301951	1	9	9	9	9	9	1/9	……
A2	0.000324		1	3	1/9	1/3	1/9	1/9	……
A3	9.29E-05			1	1/9	1/9	1/9	1/9	……
A4	0.010421				1	9	3	1/9	……
A5	0.000827					1	1/4	1/9	……
A6	0.003344						1	1/9	……
A7	3.817735							1	……
……	……								……

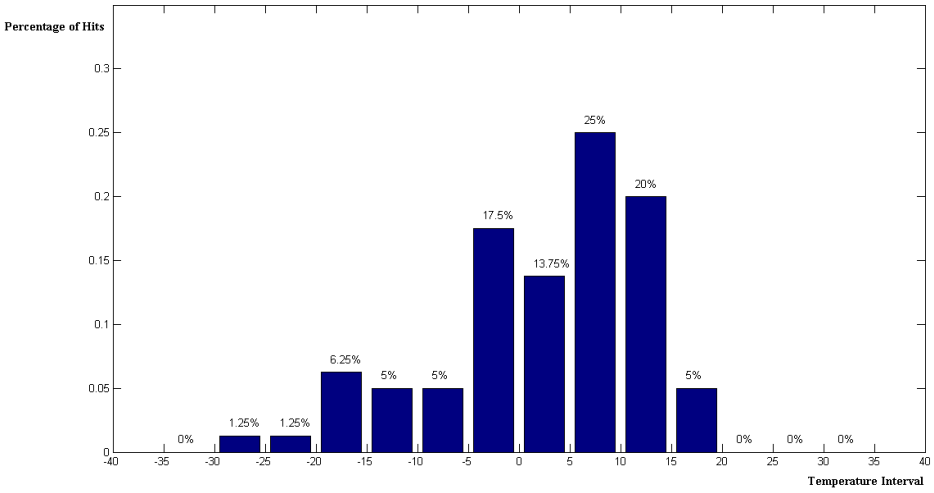


Fig.2 Percentage of Predicted Temperature Hits using CBR_AHP_EW

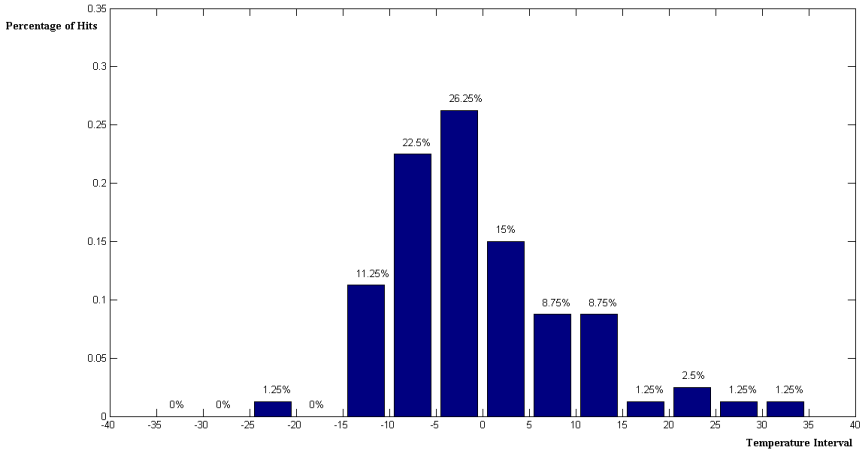


Fig.3 Percentage of Predicted Temperature Hits using CBR_AHP_DW

Summary

CBR is an effective method that reuses the real production data to predict the end temperature of molten steel in AOD. However, it is difficult to determine the weight of attributes applied in the computation of case similarity based on GRD. AHP is used to compute the weight of attributes. The pairwise comparison matrix in AHP is built according to the coefficients of attributes, which is

obtained by MLR. The results show that CBR_AHP_DW outperforms CBR_AHP_EW. CBR_AHP_DW uses different weights of attributes derived by AHP and MLR, but CBR_AHP_EW uses equal weights of attributes.

References

[1] Huixin Tian, Zhizhong Mao and Anna Wang. Hybrid Modeling for Soft Sensing of Molten Steel Temperature in LF. Journal of Iron and Steel Research International. Vol.16, No.4 (2009), p.1.

[2] Hantao Hu, Hebing Chi, Zongze Huang. Simulation of Burden Material During Stainless Refining With Hot Metal in AOD. Journal of Iron and Steel Research. Vol.20, No.10 (2008), p.6.

[3] Shiqi Li, Guoli Jiang and Junping Lu. A Study on Model of Steelmaking Process for Stainless Steel by AOD. Special Steel. Vol.30, No.1 (2009), p.29.

[4] Jihe Wei, Jiehui Shu and Hongli Zhu. Preliminary investigation on mathematical modeling of the side and top combined blowing refining process of stainless steel in an AOD converter. Journal of Baotou University of Iron and Steel Technology. Vol.25, No.2 (2006), p.106.

[5] Unal Camdali, Murat Tunc. Steady State Heat Transfer of Ladle Furnace During Steel Production Process. Journal of Iron and Steel Research International. Vol.13, No.3 (2006), p.18.

[6] Unal Camdali, Murat Tunc. Energy and Energy Analysis of a Ladle Furnace. Canadian Metallurgical Quarterly. Vol.42, No.4 (2003), p.439.

[7] Yongjun Wu, Zhouhua Jiang, Maofa Jiang. Temperature Prediction Model of Molten Steel in LF. Journal of Iron and Steel Research. Vol.14, No.2 (2002), p.9.

[8] Kitisak Ngamjaruskochakorn, Chatchai Somsiri and Ittipon Diewwanit. Modeling of Temperature Change of Liquid Steel in BOF by Neural Network. Journal of Metals, Materials and Minerals. Vol.7, No.2 (1998), p.17.

[9] A.M. Frattini Fileti, T.A. Pacianotto, and A. Pitasse Cunha. Neural modeling helps the BOS process to achieve aimed end-point conditions in liquid steel. Engineering Applications of Artificial Intelligence. Vol.19, No.1 (2006), p.9.

[10] Jose Manuel Mesa Fernandez, Valeriano Alvarez Cabal, Vicente Rodriguez Montequin and Joaquin Villanueva Balsera. Online estimation of electric arc furnace tap temperature by using fuzzy neural networks. Engineering Applications of Artificial Intelligence. Vol.21, No.7 (2008), p.1001.

[11] Zhizhong Mao, Huixin Tian and Yan Wang. Molten steel end temperature soft sensing in LF based on hybrid model using AdaBoost. Chinese Journal of Scientific Instrument. Vol.29, No.3 (2008), p.662.

[12] Hui Li and Jie Sun. Ranking-order case-based reasoning for financial distress prediction. Knowledge-Based Systems. Vol.21, No.8 (2008), p.868.

[13] Hui Li, Jie Sun and Boliang Sun. Financial distress prediction based on OR-CBR in the principle of k-nearest neighbors. Experts Systems with Applications. Vol.36, No.1 (2009), p.643.

[14] Xiaosheng Si, Changhua Hu and Jianbo Yang. On the dynamic evidential reasoning algorithm for fault prediction. Experts Systems with Applications. Vol.38, No.5 (2011), p.5061.

[15] Sung-Hoon An, Gwang-Hee Kim and Kyung-In Kang. A case-based reasoning cost estimating model using experience by analytic hierarchy process. Building and Environment. Vol.42, No.7 (2007), p.2573.

© (2012) Trans Tech Publications, Switzerland
doi:10.4028/www.scientific.net/AMM.164.12

Influence of surface modification on Si_3N_4 powder fluidity

Jin Chen *, Xiaogang Wang

Faculty of Materials science, Xi'an University of Science and Technology, Xi'an, 710070,

Key words: Silicon nitride; surface modification; organic coating modification;

Abstract: The effect of organic modification on the surface of silicon nitride powders has been investigated. The Si_3N_4 powder modified by tartaric acid and PEI was characterized by using granulometer, X-ray diffraction, thermogravimetric analysis, diffuse reflectance infrared Fourier transform spectroscopy, SEM. The results show that modifier on Si_3N_4 powder surface is chemical adsorption coating. The addition of modifier dose not change phase, but modified particles have spherical tendency. Modifier coating occurred oxidative decomposition in 200-400^{o}C. surface modification can improve the fluidity of powder and density of green bodies. As the amount of modifier increased, the angle of repose and compression degree firstly decreases and then increases. The angle of repose of artaric acid and PEI modified powder decrease 9 º and 12º, compression degree decline 15% and 20% respectively.

1. Introduction

As a covalent material, silicon nitride (Si_3N_4) is recognized as an important candidate in a wide range of industrial applications due to its special set of physical and chemical properties such as high hardness and strength retention at elevated temperature, good thermal stress resistance and excellent wear, erosion, and oxidation resistance[1]. All these superior characters has arouse a lot of interest by materials researchers[2]. This material can be used in many field, for example it can serve as catalyst support[3]. Silicon nitride are also used as special class of electronic devices which require extreme process conditions such as high temperatures and oxidizing environment[4].

In order to improve the subsequent sintering and performance of final ceramics attainment of a well mixed, uniform green body with a high density, minimum density variation and homogenous pore size distribution is the most important aspect in its production[5]. For now, it seems that the powder surface modification is one of the most effective ways to obtain a uniformly consolidated compact and components with complex shape [6].

However, it is well known that the surface charge properties of different ceramic powders vary with the type of powder and in some cases even with the producer[7,8] ,so a number of studies on powder surface modification processing have been carried out. They main include : surface adsorption coating method [9].

In this work, we use Polyethylene imine (PEI) and Tartaric acid as dispersant, and study the performance of organic surface coating, and its mechanism with Si_3N_4 micro-powder.

2. Experimental

Weigh a certain amount of Si_3N_4 powder with 10% hydrochloric acid, then react 30 min, washed with deionized water 2-3 times to remove free Fe, Mg of samples. The after washing powders was prepared into 20% Si_3N_4 suspension, under high-speed disperser conduction adding a certain percentage of modifier solution, after 4h stirring reaction, the suspension filtered, and drying oven at 80 ℃ to form a modified block. Using ball mill smash it and sift. The modified Si_3N_4 powders was prepared.

3.Results and discussion

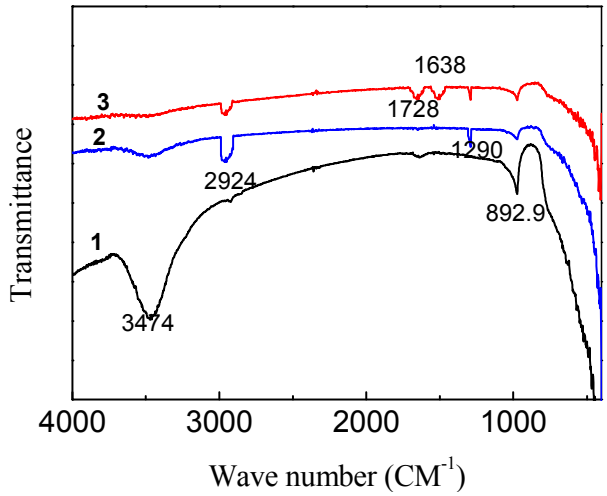


Fig.1. FTIR spectra of Si_3N_4 powder(a, original Si_3N_4 powder; b, tartaric acid Si_3N_4 powder; c,PEI Si_3N_4 powder)

To determine the bonding of Modifier coating and powder. The FTIR spectra of origin silicon nitride powder, tartaric acid silicon nitride powder and PEI silicon nitride powder are presented in Fig.1. Curve 1 is the spectrum of origin powder, the peak in the wave number 892.9 cm-1 is Si-N bond stretching vibration, while the 3474 cm-1 peak related with the O-H stretching vibration, due to hydrolysis of silicon in the air, which results of the O-H bond. Curve 2 and 3 are tartaric acid Si_3N_4 powder and PEI Si_3N_4 powder respectively. Obviously, there are still Si-N and OH vibration peak in the modified powder, but the intensity is weaker, There are a few new stretching vibration emerged in the modified powder. The 1290 cm-1 peak is Si-O vibration of functional group in tartaric acid and PEI. 2949 cm−1 is related to the C-H stretching bond.

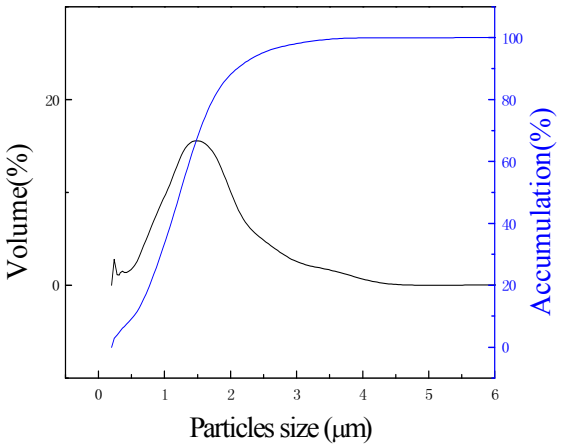


Fig.2.（a） Particle size distribution of origin Si_3N_4 powder

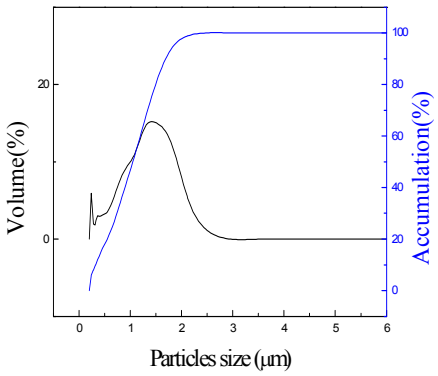


Fig.2. (b) Particle size distribution of tartaric acid Si3N4 powder

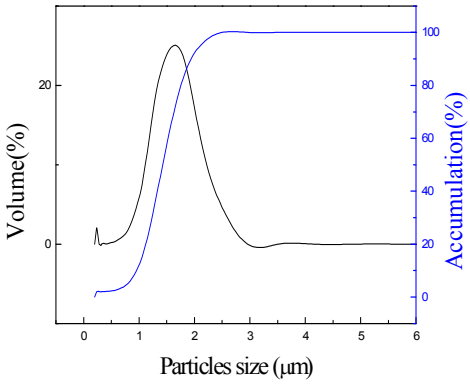


Fig.2. (c) Particle size distribution of PEI Si3N4 powder

In order to determine whether the surface modifier layer coated on the surface of the particle, and modified the original powder particle size was tested. Figure 2 are the particle size chart of original and modified Si_3N_4 powders. We can see that the d(0.1),d(0.5) and d(0.9) of original powder are 0.54μm,1.23μm and 2.55μm, Curve (b) shows the particle size of using tartaric acid modified powder .the d(0.5) increase to 1.32μm. The PEI Si_3N_4 particle size increased more significantly, d0.5 can reach 1.42μm. At the same time, we can see that the Particle size distribution of PEI Si_3N_4 powder becomes narrower. Particle size distribution chart adequately describes modifier formed coating layer on the surface of powders, which made the particle size increased.

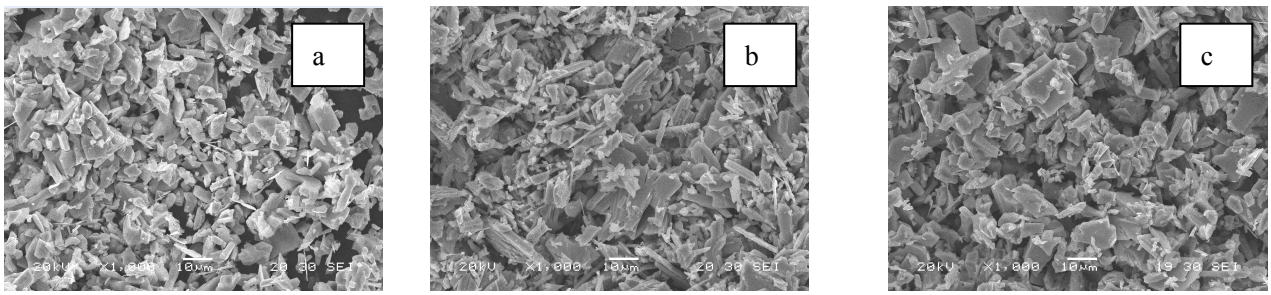


Fig.3（a） The SEM of original Si_3N_4 powder

Fig. 3 shows the morphology and grain size of Si3N4 powder without modifier and powders modified by tartaric acid and PEI. It can be seen that the original powder is diamond-like, flakes and other irregular shapes, reunion between particles is very serious, fine particle aggregate and finally Small particles together to form large clumps. While the powder modified by tartaric acid, dispersion of particles achieve a clear improvement,aggregation reduced Significantly, But still a small amount of aggregates. Obvious, the powder after adding PEI modifier was greatly enhanced on segregation, with little reunion, more uniform particle dispersion. At the same time we can see the powder modified with PEI are spherical trend, diamond, flaky particles significantly reduced the number of spherical particles increased significantly.

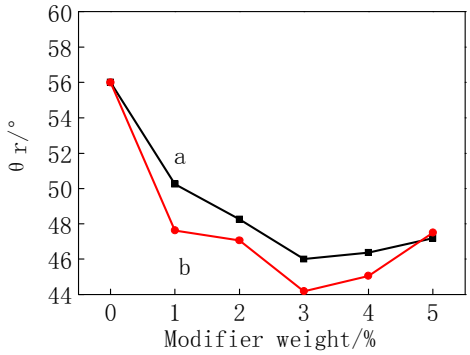


Fig. 4.（a）θr of the Modified powder

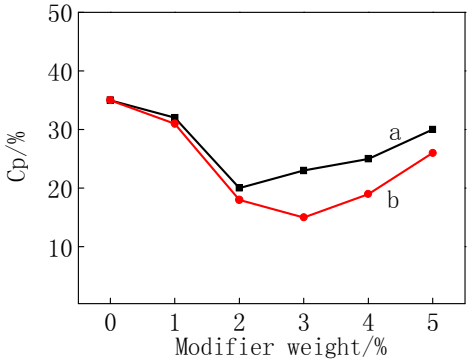


Fig.4.（b）Compression degree of the modified powder

（a, tartaric acid Si_3N_4 powder; b, PEI Si_3N_4 powder）

General, the fluidity of powder can be measured through the angle of repose and compression degree. The angle of repose is the minimum angle made by the inclined plane with the horizontal surface such that the body lying on the inclined plane is just at the verge of sliding down along the inclined plane. When bulk granular materials are poured onto a horizontal surface, a conical pile will form. The internal angle between the surface of the pile and the horizontal surface is known as the angle of repose. The smaller angle of repose, the smaller the friction, the better the fluidity. Compression degree of the powder is the ratio of tap density and bulk density. Therefore, the lower bulk density the better the flow of powder. Figure 4 (a) (b) are the angle of repose and compressibility degree of the modified powder respectively . 3% tartaric acid modifier can reduce the powder angle of repose 9º. the same dose of PEI modifier can reduce the angle of repose of 12º. The change of compression degree is first increased and then decreased with the increase of modifier. 2% tartaric acid can reduce 15%, at the same time 3% PEI reduce powder compression degree 20%.

4.Conclusion

The surface modification of silicon nitride powder was characterized physical and chemical testing methods. Modifier can form surface coating layer on powder surface. Large molecular weight modifier can significantly increase particle size and narrow size distribution. Modification reaction can change the morphology of powders, but will not change its phase. At the same time, modifier can be oxidation and decomposition at a high temperature. Both the fluidity and density increase of modified powder, and PEI modifier is superior to tartaric acid. This is because on the one hand modified reactions make the particles spherically, on the other hand due to organic coating layer reduce surface friction of particles.

Acknowledgments

This work was supported by the Scientific Research Program Funded by Shaanxi Provincial Education Commission（Program NO. 2010JK676）

References

[1] Zweben, C., Advances in composite materials for thermal management in electronic packaging. JOM 1998, 6, 47–51.

[2] Sun, J. and Gao, L., Dispersing SiC powder and improving its rheological behaviour. J. Eur. Ceram. Soc. 2001, 21, 2447–2451.

[3] Millán, A.J., Nieto, M. I. and Moreno, R., Near-net shaping of aqueous alumina slurries using carragreenan. J. Eur. Ceram. Soc. 2002, 22, 297–303.

[4] Sigmund, M., Bell, N. S. and Bergström, L., Novel powder-processing methods for advanced ceramics. J. Am. Ceram. Soc. 2000, 83(7), 1557–1574.

[5] Gutiérrez, C.A. and Moreno, R., Interparticle potentials in nonaqueous silicon nitride suspension. J. Am. Ceram. Sci. 2003, 86(1), 59–64.

[6] Tartaj, P., Reece, M. and Moya, J. S., Electrokinetic behaviour and stacility of silicon nitride nanoparticulate dispersions. J. Am. Ceram Sci. 2008, 81(2), 389–403.

[7] Wei Li, Ping Chen, Mingyuan Gu, Yanping Jin. Effect of TMAH on rheological behavior of Si_3N_4 aqueous suspension. Journal of the European Ceramic Society.2004:3479-3484.

[8] Huang, Q., Chen, P., Gu, M. Y., Jin, Y. P. and Sun, K., Effect of surface modification on the rheological behavior of concentrated, aqueous SiC suspensions. Mater. Lett. 2002, 56, 546–553.

[9] Yang, C. Y., Shih, W. Y. and Shih, W. H., Gelation, consolidation, and rheological properties of bohemite-coated silicon carbide Suspensions. J. Am. Ceram. Soc. 2000, 83(8), 1879–1884.

© (2012) Trans Tech Publications, Switzerland
doi:10.4028/www.scientific.net/AMM.164.17

Peparation and magnetic propriety of carbon-coated iron magnetic nanoparticles by starch coating method

Jin Chen [1]*, Haiyan Zhang[2]

[1,]Faculty of Materials science, Xi'an University of Science and Technology, Xi'an, 710070,China
[2,]Guangdong University of Technology, Guangzhou,510006, China
E-mail address: chenjin85056@163.com (chen jin)

Keywords：Carbon；Carbon coated nanoparticles；magnetic propriety

Abstract: We synthesized carbon-coated iron magnetic nanoparticles by a low cost method using Ferric nitrate as the iron precursor and starch as both reductive agent and carbon source under H_2 atmosphere. The structure, size distribution, phase composition, magnetic properties and oxidation resistance of the particles were investigated by transmission electron microscopy, X-ray diffraction, vibrating sample magnetometry and differential scanning calorimetry. The results show that the carbon-coated iron nanoparticles are spherical particles with a diameter of 20-40 nm. They are particles of core-shell structure with an iron core inside and an onion skin carbon layer outside, carbon layer can protect inner iron core from been oxidized, the hysteresis curves show that they are super paramagnetic materials. At the same time the annealing can change the magnetic properties of carbon coated iron nanoparticles.

1. INTRODUCTION

Magnetic nanoparticles such as iron oxides have been applied to magnetic fluids [1], magnetic recording media [2]and magnetic beads [3].Though Fe, Co, Fe based alloys show superior magnetic properties with high saturation magnetization[4], their fine particles are easy to be oxidized in air[5]. This prevents them from wide variety of practical applications.Therefore, many studies on coating them with inorganic layers have been devoted to overcome this problem[6].Fe and Fe–Co nanoparticles encapsulation in C formed by an arc discharge method have been proposed [7].The particles are uniformly encapsulated with a total C layer less than 10-nm thickness [8].However, this method is regarded as a gas phase reaction and not supposed to be suitable for mass production[9,10].

In this paper, We have developed a new technique to synthesize Fe nanoparticles coated with C nanolayers by means of starch coating method,

2. EXPERIMENTAL

Fe $(NO_3)_3 \cdot 9H_2O$, starch powders and ammonia were used as starting materials. Dissolved starch in ammonia solution, mixed it with Fe $(NO_3)_3 \cdot 9H_2O$ in ethanol solution under agitation. Then yellow brown viscous solution was obtained, and dried it at 100 ^oC for 24h, ferric nitrate starch gel was prepared. Then the gel was placed in the tube furnace for coal carbonization. The carbonization process was under the atmosphere of hydrogen, hydrogen flow rate 35mL / min. Carbonization temperature curve: 10 ^oC / min, from room temperature to 300 ^oC. Then to 800 ^oC with the increase rate of 5 ^oC / min, and keep in 800 ^oC for 4 h. Natural cooled to room temperature. A black powder-like substance was obtained, these powder are the final products.

B Characterization

A X-ray diffraction(XRD) with Cu（Kα） radiation was used at room temperature to identify the phase and the crystal structure .The micro-structure of carbon-coated iron nanoparticles was observed by using transmission electron microscope (TEM)(JEM-2010 HR) operating at 200Kv. Magnetic properties at room temperature of the products were characterized by a vibrating sample magnetometer (VSM), at magnetic field of -12-+12KOe. Q600 DSC / TGA simultaneous, TA companies in the United States was employed to test DSC / TGA .Test conduction: weight between 1.5-2.0 mg, carrier gas is air, heating rate 20 ^{o}C / min, from room temperature to 800 ^{o}C.

3. RESULTS AND DISCUSSION

A Structural and morphology of carbon-coated iron nanoparticles

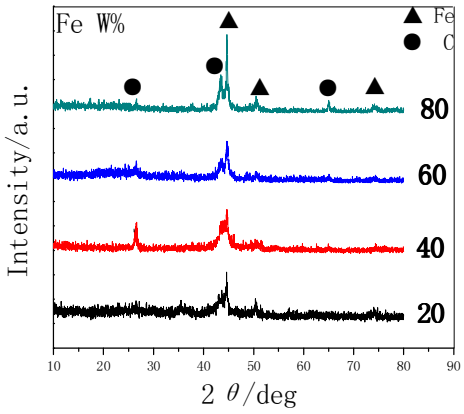


Fig.1. XRD patterns of different content iron carbon-coated iron nanoparticles

Fig.1 is XRD patterns of different content iron carbon-coated iron nanoparticles, (iron content in the sample are 20%, 40%, 60%, 80% respectively) what can be seen from the diagram, the products only have carbon and iron peaks do not find iron carbide and oxide diffraction peaks, indicating carbon-coated iron nanoparticles did not contain iron oxides and carbides. We found there are not obvious diffraction peaks in the sample of 20% iron content (carbon content 80%)

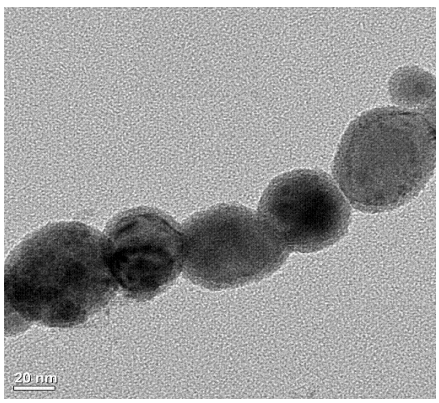


Fig.2. TEM images of carbon coated iron nanoparticles

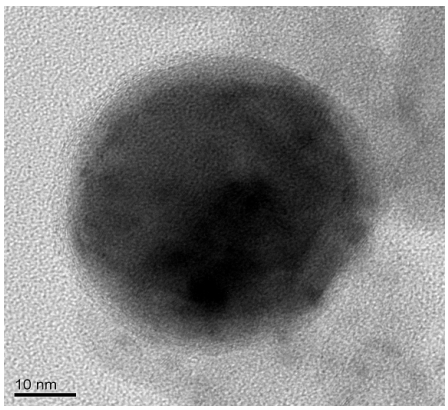


Fig.3. HRTEM image of carbon coated iron nanoparticles

carbon-coated iron anoparticles, this is due to amorphous carbon in the samples. It is obviously that all the samples have the diffraction peak of iron. and with the increase of iron content the diffraction intensity increased, the sample of 80% iron content with the strongest (110), (200), (211) diffraction peak (PDF card 06-0696). At the same time we can see that the carbon-coated iron nanoparticles of carbon content of 40% of with a strong carbon peaks, which shows that the sample contains crystalline carbon[11].

Fig.2 shows TEM image of carbon-coated iron nanoparticles, which reveal the general morphology, a typical core-shell structure of the nanocapsule materials, nanoparticles are spherical particles with a diameter of 20-40 nm, particle size is fairly uniform. The core (dark part) is metal iron, outside (light part) is carbon layers, except carbon-coated iron nanoparticles in the specimen, there is a small amount of amorphous carbon particles(the arrows in Figure 2a, 2b). These amorphous carbon particles, also explained why there is not a strong diffraction peak of carbon in the XRD pattern of the sample which the iron content is 20% (carbon content 80%).

HRTEM image of carbon-coated iron nanoparticles, as shown in fig.3, reveals fine structure of these nanocapsules, the thickness of outside carbon layer is 5-10 nm, the iron core is about 25 nm in diameter. Carbon layers that close to iron core are regular stripes structure, carbon layers that away from the iron core are relatively disordered stripes, this is because in the carbonation process iron nanoparticles could promote carbon around them be graphite structure, due to the lack of the presence of iron catalyst, carbon layers away from iron core formed amorphous structure.

B Magnetic property of carbon-coated iron nanoparticles

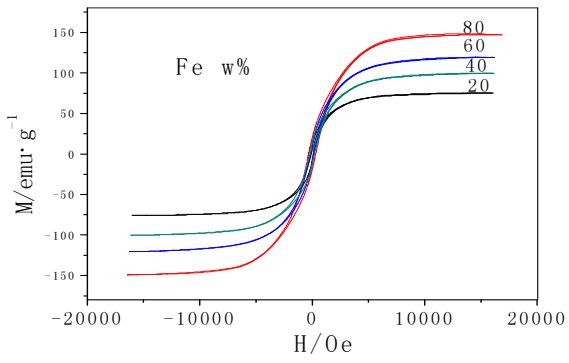


Fig.4. Magnetic field dependence of magnetization of carbon coated iron nanoparticles

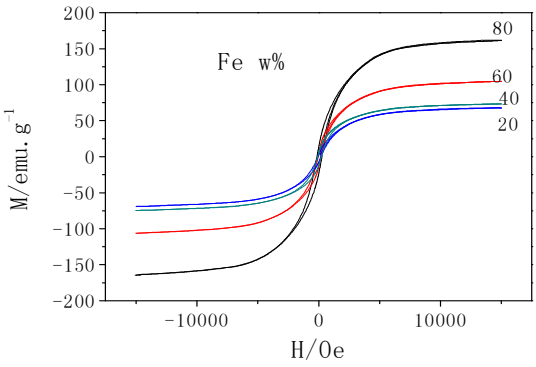


Fig.5. Magnetic field dependence of magnetization carbon coated iron nanoparticles annealed at 500°C

Carbon-coated iron nanoparticles as a means of potential applications of magnetic record materials. It is useful to study the magnetic properties of the products. The hysteresis loops at room temperature of carbon coated iron nanoparticles (Fig.4) show the saturation magnetization of samples increase with the increasing of iron content, at the same time remanent magnetization and intrinsic coercivity also increase with the iron content increase. Sample of 20% Fe, the saturation magnetization is 75.46 emu/g, remanent magnetization is 8.48emu/g, intrinsic coercive force is 95 Oe, while the saturation magnetization, remanent magnetization and intrinsic coercive force of iron content 80% sample is 146.8emu/g, 19.35 emu/g, 307.3 Oe respectively.

Fig.5 is the Magnetic field dependence of magnetization carbon coated iron nanoparticles annealed at 500°C. It can be seen from the figure, a high iron content(80% iron content),the annealing treatment can improve its magnetic properties, while when the iron content is low, annealing treatment will decrease the magnetic properties.

4. Summary

Carbon-coated iron nanoparticles can be synthesized by the starch coating method, they are spherical particles with the size of particles 20-40nm in diameter. It is believed that the nanoparticles have a typical core-shell structure with carbon layer outside and iron core inside. Hysteresis loops show as-made materials have good superparamagnetic properties, with the increase of iron content their magnetic properties enhance. Annealing can change the magnetic properties of carbon coated iron nanoparticles. a high iron content, the annealing treatment can improve its magnetic properties, while when the iron content is low, annealing treatment will decrease the magnetic properties.

Acknowledgments

This work was supported by the Scientific Research Program Funded by Shaanxi Provincial Education Commission（Program NO. 2010JK676）

This work was supported by the Natural Science Foundation of Shaanxi Provincial Department of Education (2010JK676)

References

[1] Ruoff R S , LORENTS D C , CHAN B . Single crystal metals encapsulated in carbon nanoparticles[J] . Science, 1993 ,259 : 3462348.

[2] Gadd GE, Collela M., Blackford M, A. Dixon, PJ, Evans, et al. The encapsulation of Ni in graphitic layers using C60 as a precursor. Carbon, 2001, 39 (12) : 1 769-1787.

[3] Lei ZX, Li Xuan K, Wang HZ. Magnetic properties of carbon nanotubes encapsulating nanosized nickel particles. New Carbon Materials, 2002, 17 (4): 672-680.

[4] Tsai JY, Chao JH , Lin CH. Low temperature carbon monoxide oxidation over gold nanoparticles supported on sodium titanate nanotubes. J Mol Catal-Chem, 2009, 298: 115-124

[5] Qiu JS, Li YF, Wang YP. Preparation of carbon-coated magnetic iron nanoparticles from composite rods made from coal and iron powders. Fuel Process Technol, 2004, 86 (3): 2672-2674.

[6] Hayashi T, Hirono S, Tomita M. Magnetic thin film of cobalt nanocrystals encapsulated in graphite like carbon. Nature,1996, 381: 772-774.

[7] Chen J, Zhang HY, Li LP. The targeting magnetic induction heating of nano-carbon iron composite. Mat Sci Forum. 2009, 610: 1284-1289

[8] Tsang SC, Qiu J, Harris P J F . Synthesis of fullerenic nano-capsules from biomolecule carbonization. Chem Phys Lett , 2000, 322: 553-560.

[9] Sano N, Akazawa H, Kikuchi T. Separated synthesis of iron included carbon nanocapsules and nanotubes by pyrolysis of ferrocene in pure hydrogen. Carbon, 2003, 41 (11) : 2159-2179.

[10] Ping ZS , Zhi DZ, Diany G. Synthesis and characteristics of carbon-coated iron and nickel nanocapsules produced by arc discharge in ethanol vapor. Carbon, 2003,41:247-251.

[11] Revesz A , Lendvai J . Thermal properties of ball-milled nano crystalline Fe , Co and Cr powders . Nan Mat, 1998,10(1):13-24

© (2012) Trans Tech Publications, Switzerland
doi:10.4028/www.scientific.net/AMM.164.21

The Reaction Kinetics of Aluminum and Isopropanol

XiuHui Wang[1,a], HuanHuan Ni[1,b], Ye Cao[1,c] , Gang Li[1,d], Hong Gao[1,e], JinLong Yang[2,f]

[1]Liaoning Key Laboratory for fabrication and Application of Super-fine Inorganic Powders, Dalian Jiaotong University, Dalian, Liaoning, 116028, China

[2]Department of Materials Science and Engineering, State Key Lab of New Ceramics and Fine Processing, Tsinghua University, Beijing 100084, China

[a]dl_wangxh@ditu.edu.cn, [b]nihuanhuan04112006@126.com, [c]xuanerxuanerne@gmail.com, [d]leegemo@163.com, [e]taoci@djtu.edu.cn, [f]jlyang@mail.tsinghua.edu.cn

Keywords: Aluminum isopropoxide, catalytic mechanism, reaction kinetics, reaction rate constant

Abstract: $AlCl_3$ was used as catalyst in the reaction. The reaction kinetics of aluminum and isopropanol was investigated in this paper. Metallograph showed that the surface of the aluminum bar had corrosive pitting. The reaction was zero order reaction when aluminum was overdosed. Reaction order was 0.75 when isopropanol was overdosed. Finally, catalytic mechanism of $AlCl_3$ was investigated and the reaction of corrosive pitting was the same as that in microbattery.

1. Introduction

Wislicenus and Kaufman synthesized aluminum alkoxide from aluminum amalgam in overdosed refluxing alcohol in 1893. Hillyer synthesized aluminum alkoxide from aluminum and alcohol by using $SnCl_4$ as catalyst in 1897[1]. Aluminum isopropoxide has already been the important precursor of high-tech materials and functional nanomaterials, and it also has new application in the markets of new luminescent materials and high purity ultrafine Al_2O_3 powders[2] , etc. Aluminum isopropoxide is also used as catalyst of the reaction for expoxy compounds polymerize, ester exchange and dehydrating agent, waterproofing agent[3], pharmaceutical raw materials[4], etc. So it has important industrial significance to study the reaction kinetics. However, few papers were introduced to explain the reaction kinetics of aluminum and isopropanol.

In this study, the reaction kinetics of aluminum and isopropanol was studied. Kinetic mechanism was studied from the hydrogen that generated from the reaction, meanwhile the catalytic mechanism of $AlCl_3$ was also studied.

2. Experimental

Aluminum (Al, 99.996%, from Xinjiang Joinworld), isoproponal (Pr^iOH, AR, from Tianjin Kermel Chemical Reagent) were used as raw materials. $AlCl_3$ (AR, from Tianjin Kermel Chemical Reagent) was used as catalyst. The facilities were self-assembled reflux condenser and gas drainage collection devices. Aluminum was first shaped into bars and polished by No.2 sandpaper to remove the alumina layer in isopropanol. The mixture of the starting materials went through heating, refluxing, evaporating of the dissolvent, and finally aluminum isopropoxide was obtained.

The hydrogen was collected and the volume was measured to calculate the reaction rate. The following formula was introduced to calculate the instantaneous rate of generating hydrogen.

$$v_{H_2} = \frac{V}{t} \tag{1}$$

Where, v_{H2} is the instantaneous rate of generating hydrogen, V the instantaneous volume of collecting hydrogen, t the time of generating hydrogen.

3. Results and Discussion

3.1 Experimental phenomenon of aluminum and isopropanol

Metallographs are shown in Fig. 1. From Fig. 1 (a), the surface of aluminum bar became rough and many corrosive holes appeared. Most of the holes were round and did not spread uniformly. The areas of different colors ascribed to the grains that arranged by different directions, and corrosive holes were on the grain boundaries. From Fig. 1 (b), the reaction progressed in the manner of parallel to some crystal face to the internal parts, and this phenomenon indicated that the reaction was related to the grain arrange of aluminum and the defects of the grain boundaries in aluminum bars.

Hydrogen appeared until the isopropyl alcohol refluxed for 30 min, and this indicated that the reaction had induction period. The reacting system was vibrated by using ultrasonic wave for 5 min, hydrogen did not appear after 30 min and the reaction stopped. This probably contributed to the active layer that existed in the surface of aluminum. The induction period was the time forming active layer. Later active layer was destroyed, so reaction stopped.

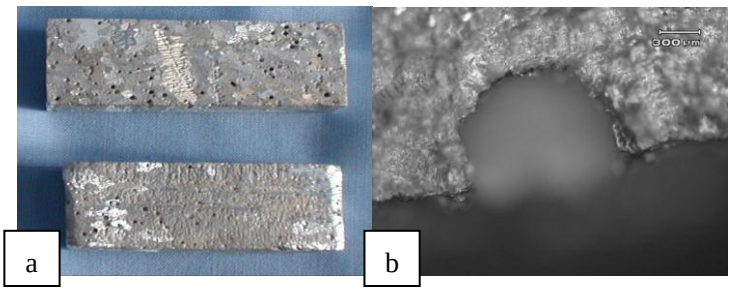


Figure 1 Micrograms of aluminium in isopropanol

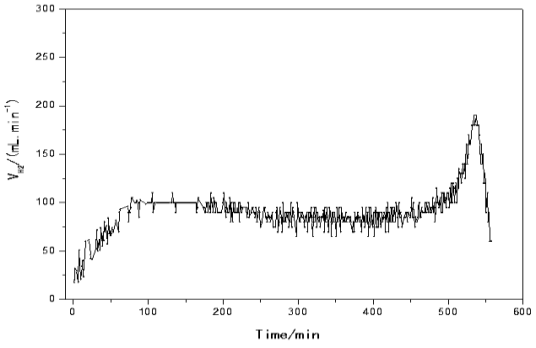


Figure 2 The curve of H_2 generation of the reaction

3.2 Reaction kinetics of aluminum and isopropanol

3.2.1 Dependence of H_2 generation about the reaction of aluminum in isopropanol

The curve is illustrated about the rate of H_2 generation at different time in Fig. 2. The reaction rate of aluminum (overdosed) in isopropanol was calculated. The rate of H_2 generation was delegated as the reaction rate. The curve could divide into four stages: (1) Stage of surface acting, the time when the active layer formed was the induction period. With the areas of the active layer became larger, reaction rate became quicker.(2) Stage of reaction balance, the active layer and the rate of H_2 generation became steady, and there were no changes in temperature.(3) Stage of reaction rate high-speed rising, the temperature of the system sharply went up, reaction rate increased

quickly until reached the highest value.(4) Stage of reaction rate rapidly descending, the content of aluminum isopropoxide approached to 100% meanwhile the content of alcohol to zero, reaction rate sharply descended from the highest value to zero.

3.2.2 Determination of the order of reaction and the reaction equation

(a) When aluminum was overdosed, the concentration of the alcohol was zero after the reaction. There were pure aluminum isopropoxide left. The concentration of the surface area remained unchanged; there was no need to consider aluminum, so the reaction rate equation is:

$$\upsilon = k\left[C_a\right]^n \tag{2}$$

Calculating the reaction with half-life method, as the half-life equation of n-order reaction is:

$$t_{0.5} = \frac{2^{n-1}-1}{(n-1)k_A[C_a]_0^{n-1}} \qquad (n \neq 1) \tag{3}$$

The following equation could be got:

$$\log t_{0.5} = \log\frac{2^{n-1}-1}{(n-1)k_A} - (n-1)\log[C_a]_0 \tag{4}$$

The curve of $\log t_{0.5}$ on different values of $\log[C_a]_0$ was drawn, so the slope of the line is(1-n). According to formula (5) and (6):

$$[C_a] = [C_a]_0 - \frac{2\sum V_{H_2}}{22.4} \times \frac{P}{P_0} \tag{5}$$

$$[C_d] = [C_d]_0 + \frac{[C_a]}{3} \tag{6}$$

The concentration of the alcohol and isopropoxide could be calculated at different time. The half-life time $t_{0.5}$ of different starting concentration $[C_a]_0$ could be checked from the statistics of the calculation. The statistics of $\log t_{0.5}$ at different values of $\log[C_a]_0$ are shown in Table 1. The curve according to the statistics of Table 1 is shown in Fig. 3.

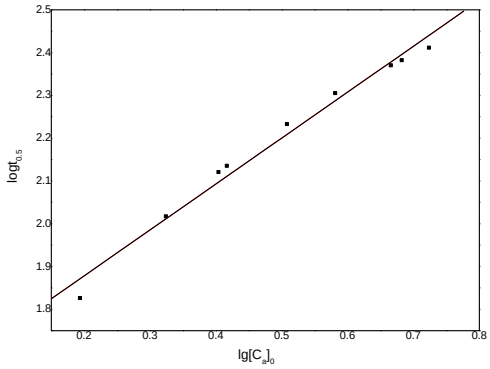
Table 1 Half-life time of the concentration of Isopropyl alcohol

Starting concentration $[C_a]_0$	$[C_a]_0/2$	Half-life time	$\log[C_a]_0$	$\log t_{0.5}$
5.292503	2.646252	258	0.723661	2.41162
4.80946	2.40473	241	0.682096	2.382017
4.630968	2.315484	234.5	0.665672	2.370143
3.81158	1.90579	202	0.581105	2.305351
3.21921	1.609605	171	0.507749	2.232996
2.609326	1.304663	136.5	0.416528	2.135133
2.535141	1.26757	132	0.404002	2.120574
2.108992	1.054496	104	0.324075	2.017033
1.561245	0.780623	67	0.193471	1.826075

The slope of the curve is 1.07335, so the order of the reaction n≈0. The reaction is no relationship with the concentration of alcohol, but the state of the surface of aluminum. This was similar as the surface catalysis reaction. So the reaction rate equation is:

$$\upsilon = k[Pr^i OH]^0 = k \tag{7}$$

Where k is reaction rate constant which is a function related to temperature, pressure, catalyst and the state of the surface of the aluminum bars.



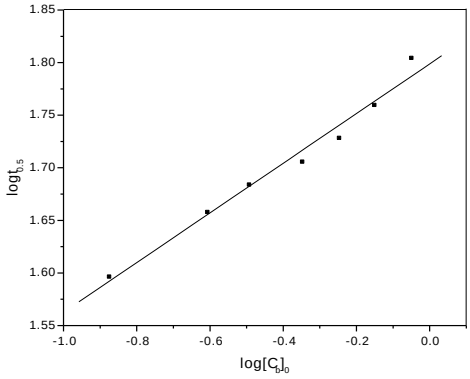


Figure 3 The curve of $logt_{0.5}$-$log[C_a]_0$ Figure 4 The curve of $logt_{0.5}$-$lg[B]_0$

(b) The former (a) was a reaction rate equation in the ideal situation. In practical situation, alcohol was always overdosed; the concentration of aluminum became lower. As there was no relationship between the reaction rate and the concentration of alcohol, and isolated method could be used. Assuming that only the surface area of the aluminum changed, so the equation is:

$$\upsilon = k\left[C_a\right]^n [C_b]^m = k'[C_b]^m \tag{8}$$

$$k' = k\left[C_a\right]^n \tag{9}$$

$[C_b]$ is the concentration of the surface of aluminum in unit volume. Half-life method was used to calculate m. The statistics of $logt_{0.5}$ at different values of $log[C_b]_0$ are shown in Table 2. The curve according to the statistics of Table 2 is shown in Fig. 4.

Table 2 Half-life time of the concentration of aluminium alkoxide

Starting concentration $[C_b]_0$	$[C_b]_0/2$	Reaction time (min)	Half-life time	$log[C_b]_0$	$Logt_{0.5}$
0.89149702	0.445749	128.85	192.6	-0.04988	1.80448
0.706423218	0.353212	153.1	210.6	-0.15094	1.759668
0.565801088	0.282901	173.1	226.6	-0.24734	1.728354
0.448508444	0.224254	192.1	242.9	-0.34823	1.705864
0.321232002	0.160616	217.6	265.9	-0.49318	1.683947
0.247066648	0.123533	236.4	281.9	-0.60719	1.658011
0.133203812	0.066602	277.9	317.4	-0.87548	1.596597

From Fig.4, 1-m=0.23616, so m ≈0.75=3/4, finally the reaction equation of aluminum and isopropyl alcohol is:

$$\upsilon = k[C_b]^{\frac{3}{4}} \tag{10}$$

3.3 Catalytic mechanism of $AlCl_3$

Because of its Lewis acidity, $AlCl_3$ is often used as catalyst in organic synthesization[5]. Whereas, it is rarely used as catalyst to synthesize metal alkoxides. $AlCl_3$ is the molecule lacked electrons.It can help to synthesize aluminum alkoxides because it could combine with oxygen atom in the hydroxyl of the alcohol and formed coordination bond. So that the electronic clouds in the alkali of the alcohol would incline to oxygen atom and the hydrogen atom would be isolate. H^+ would be easily got and the acidity of the alcohol would increase.It could react with active aluminum more easily meanwhile H_2 and Al^{3+} generate, the chemistry equation is:

$$R\text{-}OH + AlCl_3 \rightarrow [R\text{-}OAlCl_3]^- + H^+ \quad (11)$$

$$Al + H^+ \rightarrow Al^{3+} + H_2 \uparrow \quad (12)$$

A unit of negatrons in $[R\text{-}OAlCl_3]^-$ are mainly spreaded over O^{2-}. If there are more kations which would combine with O^{2-}, the bond of aluminum and oxygen would break. Besides, Al^{3+} also has empty orbit and Lewis acidity, so it has the tendency to atract electrons. When it combines with O^{2-} in $[R\text{-}OAlCl_3]^-$, the coordination bond would break meanwhile $AlCl_3$ and $Al(OR)_3$ produce:

$$[RO - AlCl_3]^- + Al^{3+} \rightarrow Al(OR)_3 + AlCl_3 \quad (13)$$

The catalytic mechanism of aluminum and isopropanol is shown in Fig. 5. The reaction of corrosive pitting was the same as that in microbattery. Aluminum lost electrons and became Al^{3+}, this was the positive pole of the battery. Simultaneously, the electrons were neutralized by H^+ in the inert impurity surface of aluminum which attaching solution, and this was the negative pole of the battery. The phenomenon of corrosive pitting is shown in Fig. 6.

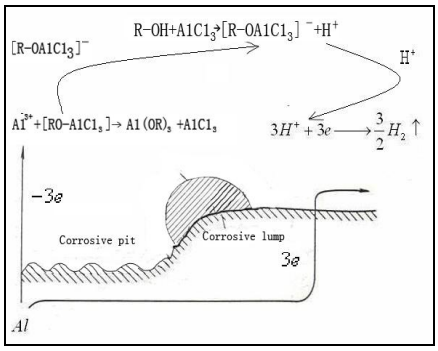


Figure 5 Micrograms of aluminum in the isopropanol

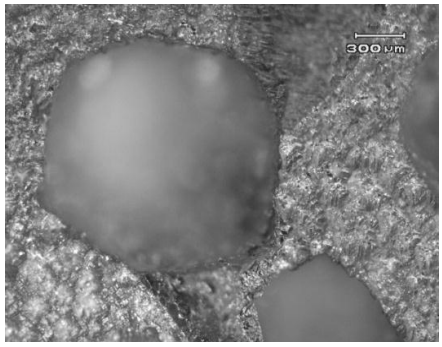


Figure 6 Corrosive pit on the surface of aluminum

4. Conclusion

The catalytic mechanism and reaction kinetics were studied between aluminum and isoproponal. Their reaction was zero order reaction and was not related to the concentration of alcohol when aluminum was overdosed. Reaction order was 0.75 when isopropanol was overdosed. The catalytic mechanism of $AlCl_3$ was also investigated which mainly relied on its Lewis acidity, combining with the hydroxyl oxygen of alcohol and forming coordination bonds. The phenomenon of corrosive pitting toke place in the reaction and it was microbattery reaction.

References:

[1] Pan Dong-hui, Fu Guang-hui, Du Jia-feng. Metal alkoxide synthesis and application J. Chemistry. 11(1989)

[2] Yang Yun-xia, Xu Zhi-zhen, Yuan Shuang-long, etc. The study of nano-Al_2O_3 with the light-emitting J. Journal of Rare Earth, 6:20(2002)

[3] Shanghai Chemical research and technological achievements, Application technology. (2007).

[4] Wilds A. Reduction with Aluminum Alkoxides, Organic Reactions, 2d.New York John Wiley & Sons Inc, p.178 (1953)

[5] Inorganic Chemistry (Volume 2), Beijing Normal University, China Central Normal University, Inorganic Chemistry Department of Nanjing Normal University M. Beijing Higher Education Press, second edition, (1986) p.844-860

© (2012) Trans Tech Publications, Switzerland
doi:10.4028/www.scientific.net/AMM.164.26

Study on Critical load position and Cracking in asphalt layer of Continuously Reinforced Concrete Composite Asphalt Pavement

Sheng Li, Zhaohui Liu, Yuzhi Li, Yingxue Zhang

Key Laboratory of Special Environment Road Engineering of Hunan Province,Changsha University of Science and Technology, Changsha 410004, China, E-mail: lishengttt@163.com

Keywords: Road engineering; Continuously reinforced concrete; Composite Asphalt pavement; Critical load position; Cracking Analysis.

Abstract. This paper is mainly focused on the structure characteristics and the flaws of existing studies of CRC+AC composite pavement, mechanics theory and finite element method are applied to establish CRC+AC composite pavement finite element models based on crack pattern, the critical load position of CRC+AC composite pavement is found out under different crack spacing, and cracks on the AC layer extended mechanisms have been studied. The results show that: critical load position may appear in the horizontal cracks in the middle of the edge and vertical of the central free edge; in the long-term effect of traffic load, AC layer surface because of traffic loads, temperature effects, quality of construction, materials, aging and other factors produce longitudinal and transverse cracking. CRC layer transverse cracks in the bottom layers of the corresponding region AC will also have cracks, and finally forms reflective crack on the AC layer surface.The results can provide a basis for rational design of CRC+AC composite pavement.

Introduction

Continuously Reinforced Concrete Composite Asphalt Pavement have the advantages of the whole structure, high strength, good ride comfort, long life, maintenance costs and small, It is heavy traffic highway long-life asphalt pavement structure development[1].The traditional road engineering analysis program can not be solved with joint state CRC- layer composite mechanical response of the pavement structure.

Based on the theory of mechanics theory and the elastic layered theoretical system, using ABAQUS finite element software, established based on crack patterns CRC+AC Composite Pavement finite element model, determining the under the different crack spacing CRC+AC composite pavement critical load position, calculating and analyzing the stress state of AC layer, analyzing the cracking mechanism of AC layer. The results provide reference for the CRC+AC rational design of composite pavement.

1 Parameter determination and modeling

1.1 Basic assumption

This will be reinforced layer modeled by solid elements, simplified equivalent orthotropic thin-layer element model of multi-layer composite structure. To improve the calculation accuracy, concrete is an 8-node hexahedral linear space or first-order unit, using linear interpolation in each direction, using linear reduced integration elements, that C3D8R, and with sufficient mesh refinement to minimize the hourglass problems.

Basic assumptions of the model following:

Full bond between steel and concrete, and regularly arranged, fully into line; where the non-reinforced concrete layer regarded as isotropic, homogeneous; completely continuous layer; ignoring the role of transverse reinforcement. Taking multi-slabs to compute, Transverse crack spacing is considered by the same; Transverse cracks throughout the entire width of the road, load transfer function are not considered embedded in the concrete aggregate lock. Only considering the continuous reinforcement; Considering only parallel to the plane strain, paralleling to the surface of

the plane during the deformation process mutually squeeze; Plate deflection is much smaller than its thickness, which are small deflection bending problem; Using Elastic half-space foundation, finite element analysis fetch a limited size.

1.2 Calculation model and parameter

Researching that in order to reduce flaking, the maximum distance between adjacent transverse cracks should not exceed 2.4m,;In order to reduce thrust damage, the ideal minimum distance is 1.1m; Literature[2][3] that the optimal spacing of cracks 1.5m ~ 2.0m. Accordingly, research results, we collected from 0.5m, 1.0m, 1.5m, 2.0m, 2.5m, 3.0m six calculation and analysis of crack spacing, crack width of 0.7mm to take. 3-D prismatic quarter point 20-node isoperimetric degenerate paradoxical elements are used for the region near the crack tip[4-6].

Calculation parameters are as follows:

The AC layer is with the thickness h=8cm, elastic modulus E=1200MPa, and v_e=0.3.The CRC layer is with the thickness h =20cm.When the ϕ16mm deformed steel bar is used as the longitudinal bar, the reinforcement ratio ρ_1=0.6%.When the ϕ10mm deformed steel bar is used as the transverse bar, the reinforcement ratio ρ=0.1%. And, the steel bar is set as the 1/2 place of the CRC layer, which is with the concrete modulus E=2.9×10^{4}MPa, v_e=0.167, and coefficient of linear expansion of 1.0×10^{-5}℃$^{-1}$. The steel bar is with the modulus E=2.0×10^{5}MPa, v_e=0.28, and coefficient of linear expansion of 9.5×10^{-6}℃$^{-1}$.The base material is the cement-stabilized macadam, which is with the thickness h=20cm, elastic modulus E=1.0×10^{3}MPa, and Poisson's ratio of 0.25. The subgrade modulus is 50MPa, and v_e=0.4.

1.3 Definition of vehicle load

Mechanical analysis under the vehicle on the road, when the traffic load calculation standard dual axle load 100kN, tire pressure 0.707MPa.Since each tire approximate the actual shape of the ground area, may be composed of a rectangle and two semi-circular, Assuming uniform distribution of axle load of vehicles in the area on the ground, ground contact pressure area about the size of the contact with the road wheel tracks can be simplified, the wheels in contact with the road surface is equivalent to a rectangular shape.

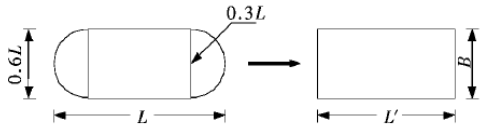


Fig.1 Tire in contact with the road shape and roughly equivalent to the shape

Assuming the vehicle tire and road contact area is A, then,

$$A = \pi(0.3L)^2 + 0.4L \times 0.6L = 0.5227L^2$$

$$A = L' \times B$$

$$L' = 0.87L = 0.87 \times \frac{0.157}{0.6} = 0.23m$$

According to the literature research, the tire and road contact area is equivalent to the following figure shows the shape and size.

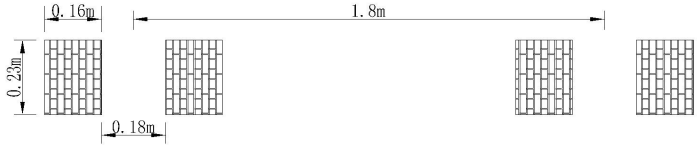


Fig.2 Tire and road contact area equivalent diagram

2 Analysis and Determination of critical load position

Experience and research shows that[7] there are cracks in the concrete pavement, the critical load position is generally in the crack edge. Therefore, the analysis assumed critical load position, respectively, in the following two paths.

Path 1: from the horizontal edge of the vertical cracks in the edge of the junction with the board horizontal cracks along the horizontal movement of the plate;

Path 2: In the middle of the edge from board to board in the longitudinal horizontal movement.

2.1 calculation of critical load position

Calculation of different transverse crack spacing, the load moves along the path 1 of a CRC layer of maximum principal stress, the results are as follows:

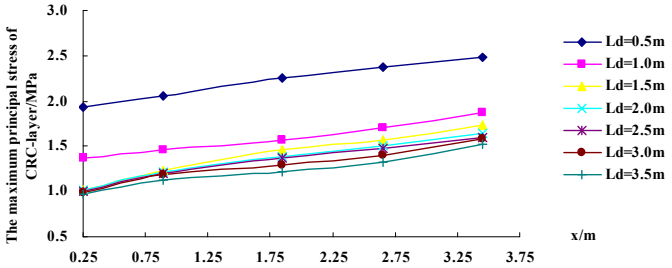


Fig.3 When the load moves along the path of a CRC-layer variation of the maximum principal stress

The results show that the load moves along the path of a process, CRC layer of maximum principal stress with transverse crack spacing decreases; CRC layer of the maximum principal stress during the move was an increasing trend.

Calculation of different transverse crack spacing, the load moves along the path 2, and the CRC layer always the maximum principal stress and the results are as follows:

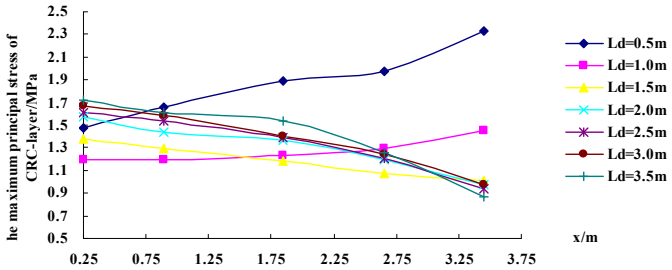


Fig. 4 When the load moves along the path 2 the CRC layer variation of the maximum principal stress

The results show that the load moves along the path 2 in the process, when the crack spacing is less than or equal to 1.0m, the CRC layer of maximum principal stress with transverse crack spacing will decreases, and with the horizontal movement of the load was increased big trend. When the crack spacing is greater than or equal to 1.5m, CRC layer of maximum principal stress with transverse crack spacing will increases, and as the load tends to decrease the level of movement.

2.2 Determination of the critical load position

From the above analysis, the law shows that Critical load position possible location for the central edge of transverse cracks, longitudinal free edge of the middle of the center plate.

Based on the above calculations shows: When the transverse crack spacing L_d is less than or equal to 2m, the critical load position for the lateral edge of the central crack; When the transverse crack spacing L_d is greater than or equal to 3m, the critical load position to the central longitudinal free edges. When the transverse crack spacing L_d is in between 2m and 3m, the above two critical load position are likely to load position, to be calculated to determine the actual situation.

3 Cracking of AC Layer

CRC+AC composite pavement layer itself has transverse cracks, some studies show[3] that The best crack spacing is1.5m~2.0m, width of cracks in the appropriate is 0.7mm~1.0mm, visible, CRC+AC composite pavement structure are in a state with initial imperfection.

In general, cracks in asphalt pavement is divided into two categories, namely, load and non-load-type cracks, load-type cracks mainly open-and shear cracking mode, non-load-type fatigue cracks mainly temperature and low temperature cracking shrinkage cracking, mainly reflected in the tension-type cracking mode. Tearing mode in the asphalt layer is infrequently.

Because of the AC surface layer has vertical and horizontal of level tensile stress, with the temperature effect, the quality of construction, materials, aging and other factors, long-term effect of traffic load in the AC layer under the surface to produce vertical and horizontal cracking; In the role of standard axle load. CRC layer of transverse cracks in the bottom AC layers of the corresponding region will be very small tensile stress, and it is unlikely that there appear the cracks. However, in the long-term overload and the combined effect of temperature, with material aging and other factors, this area will still be cracking in the role of external factors; the cracks continue to move upwards, the final surface of the asphalt surface layer manifested in the form of reflective cracking.

On under of the positive load (when the wheel is located just above the crack), AC layer surface, the bottom surface of the crack transverse cracks mainly has pressure, I-mode crack intensity factor K_I is negative, cracks is be in the closed state, it is no contribution to the crack propagation, Unlikely occurrence of unstable growth. Therefore, below only consider the partial load (cracks in the wheel at the side) layer under the action of AC crack propagation.

4 Conclusion

Main conclusions are as follows:

1) When the transverse crack spacing $L_d \leq 2m$, the critical load position is lateral edge of the central crack;

2) When $L_d \geq 3m$, the critical load position is the central longitudinal free edges; when $2m < Ld < 3m$, the above two load position are likely to be critical load position, to be calculated to determine the actual situation;

3) long-term effect of traffic load, AC surface layer due to traffic loads, temperature effects, quality of construction, materials, aging and other factors, resulting in longitudinal and transverse cracking;

4) CRC layer of transverse cracks in the bottom layers of the corresponding region AC will also have cracks, and finally to the AC surface layer of reflective crack forms.

Acknowledgements

This work is financially supported by the National Natural Science Foundation of China under Grant No.51178062, 51008038 and 51038002, the Ph. D. Programs Foundation of Ministry of Education of China under Grant No. 20114316110001, the Open Fund of Key Laboratory of Special Environment Road Engineering of Hunan Province under Grant No. kfj110401, and the Open Fund of the Key Laboratory of Highway Engineering (Changsha University of Science & Technology),Ministry of Education under Grant No. kfj080104.

References

[1] Seong-Min Kim, MoonC.Won, B.Frank McCullough.Mechanistic Analysis of Continuously Reinforced Concrete Pavements[J].the University of Texas at Austin, October, 2001.

[2] NICOLASM,TED Belytschko.Extended Finite Element Method Forcohesive Crack Growth [J].Engineering Fracture Mechanics,2002,69:813-833.

[3] LIU Zhaohui.The Research on Rigid-flexible Continuously Reinforced Concrete Composite Asphalt Pavement [D]. Changsha:Changsha University of Science and Technology,2007.

[4] LIAO Gongyun, HUANG Xiaoming.Application of ABAQUS Finite Element Software in Highway Engineering [M].Nanjing: Southeast University Press, 2008.

[5] ABAQUS/Standard User's Manual Version 6.0[M].Hibbitt,Karlsson & Sorensen, Inc.,2002.

[6] WANG Bing.Effects of Vehicle Dynamic Loading on CRCP by 3D Finite Element Method [J].Journal of Southeast University (Natural Science Edition),2008,38(5):851-853.

[7] CHEN Fengfeng.Research on the Mechanism and Structural Design Method of CRC-AC Composite Pavement [D].Nanjing: Southeast University, 2007.

© (2012) Trans Tech Publications, Switzerland
doi:10.4028/www.scientific.net/AMM.164.30

Py-GC-MS Analysis on Biomass Energy Components from Wood Extractives of *Eucalyptus urophydis* under High Temperature

WANG Lan-sheng, PENG Wan-xi[a]

School of Materials Science and Engineering, Central South University of Forestry and Technology, City Changsha 410004, P.R. China

[a]correspondent author's email: pengwanxi@163.com

Keywords: Biomass energy; Wood; *Eucalyptus urophydis;* Ether/acetone Extractives

Abstract. In order to widely use *Eucalyptus urophydis* wood, its ether/acetone extractives were identified by Py-GC/MS. The main and abundant constituents of 750°C pyrolysis products were 1,3-butadiene, 2-methyl-(5.9%), benzofuran, 2,3-dihydro-(4.11%), 1,3-butadiene(3.69%), stigmastan-3,5-diene (3.66%),.gamma.-sitosterol(2.13%), 2-butene, 2,3-dimethyl-(2.03%), toluene (1.92%), 1,4- cyclohexadiene,1-methyl-(1.76%), 1h-indene, 5-butyl-6-hexyloctahydro-(1.73%), 1,3-cyclohexadiene(1.66%), phenol(1.58%), 1-hexene(1.54%), sulfide, bis(2-cyano-3,4- dihydro-2,3,3-trimethyl-2h-pyrrol-5-yl)- (1.46%), benzene(1.38%), phenol, 4-methyl-(1.35%), cholest-8(14)-ene-3,15-dione(1.23%), acetic acid(1.21%), benzene, 1,2,4-trimethyl-(1.2%), stigmast-4-en-3-one (1.12%), 1-decene(1.1%), 1-heptene(1.08%),etc. So the ether/acetone extractives of *Eucalyptus urophydis* biomass were used as biomass energy.

Introduction

With the deficient of petroleum resources, the biomass energy had been put on the agenda. And Eucalyptus has been the most important plantation resources in south China. Eucalyptus biomass would be the application of tree species for biomass energy. Thereby, the ether/acetone extractives of Eucalyptus urophydis wood were identified by Py-GC/MS to find out products with high additional value.

Materials and Methods

Materials. A 5-year-old Eucalyptus urophydis with the diameter of about 12cm at breast height was collected from Zengcheng Forest Farm, Guangdong province, P.R. China. The sample chips were processed from fresh material. Ether and acetone (chromatographic grade) were prepared for the subsequent experiments.

Experiment methods. The experiment methods were as same as the literature[1].

Py-GC/MS analysis. The two 1.0 mg ether/acetone extractives of *Eucalyptus urophydis* wood was pyrolyzed in helium atmosphere at 750°C. Other analysis conditions were as same as the literature[1].

Results and discussions

Based on the designed above experiments, the ether/acetone extractives of *Eucalyptus urophydis* wood were determined, and the total ion chromatogram of the ether/acetone extractives by MS are shown in Figure1. Combined with Figure1, the area of every peak and the relative content could be calculated. The chemical components of the ether/acetone extractives could be identified according to the MS data, contrasting the NIST standard map by computer.

It was shown that 192 peaks were obtained from 750°C pyrolysis compounds of the ether/acetone extractives of *Eucalyptus urophydis* biomass by GC/MS (seen in Fig.1) and 178 compounds were identified. The main components were carbon dioxide(6.87%), 1,3-butadiene, 2-methyl-(5.9%), benzofuran, 2,3-dihydro-(4.11%), 1,3-butadiene(3.69%), stigmastan- 3,5- diene (3.66%),.gamma.-sitosterol(2.13%), 2-butene, 2,3-dimethyl-(2.03%), toluene(1.92%), 1,4-cyclohexadiene,1-methyl-(1.76%), 1h-indene, 5-butyl-6-hexyloctahydro-(1.73%),

1,3-cyclohexadiene(1.66%), phenol(1.58%), 1-hexene(1.54%), sulfide, bis(2-cyano-3,4-dihydro-2,3,3-trimethyl-2h-pyrrol-5-yl)- (1.46%), benzene(1.38%), phenol, 4-methyl-(1.35%), cholest-8(14)-ene-3,15-dione(1.23%), acetic acid(1.21%), benzene, 1,2,4-trimethyl-(1.2%), stigmast-4-en-3-one(1.12%), 1-decene(1.1%), 1-heptene(1.08%), and so on.

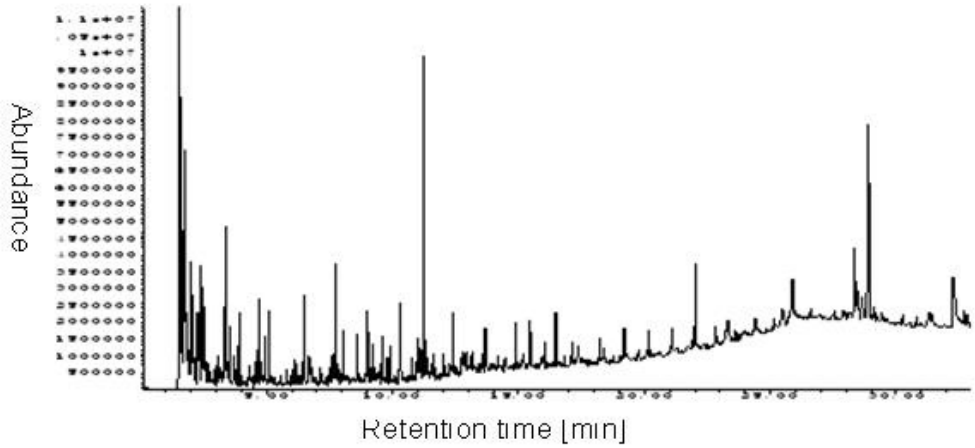


Figure1 Total ion chromatogram of 750°C pyrolysis of the ether/acetone extractives of *Eucalyptus urophydis* wood by GC/MS

The others were Phenol, 4-ethyl-, 2-Naphthalenamine, N-phenyl-, Cedrol, p-Xylene, o-Xylene, 1,4-Benzenedicarboxaldehyde, 2,3,4-Trimethoxyphenylacetonitrile, Phenanthren-9(4aH)-one, 4a-dibromo methyl-1,2,3,4-tetrahydro-, 1-Tetradecene, E-15-Heptadecenal, Cyclotrisiloxane, hexamethyl-, 2-Pentene, 4-methyl-, (Z) -, 1-Dodecanol, 3,7,11-trimethyl-, 9-Tricosene, (Z)-, Phenol, 4-ethyl-3-methyl-, 1-Nonene, (4-Methoxyphenyl)[4-methoxy-6-(2,2,2-trifluoro-1-trifluoromethylethoxy)-[1,3,5]triazin-2-yl]amine, 1,4-Hexadiene, 2,3-dimethyl-, Phenol, 2-methyl-, 1-Pentadecene, Cyclopropane,1,1-dimethyl-, Naphthalene, 2,6-dimethyl-, 1-Octene, 2-Naphthyl carbamate, 2-Methyl-7-phenylindole, Ethylbenzene, 2-Heptene, (E)-, 2,4-Hexadiene, (E,E)-, 1-Nonadecene, 2-Methyl-3-[(1S,2S)-2-ethyl-1,3,3- trimethylcyclohexyl]tetrahydrofura, 1-Undecene, 13-Methyl-Z-14-nonacosene, 1-Tridecene, Hexacosanoic acid, Benzene,(1-methyl-2- cyclopropen-1-yl)-, 15-Crown-5, [2-(benzo-1,3,2-dioxab orol-2-yl)phenyl]-, 1-Hexadecene, Phenol, 2,4-dimethyl-, Benzene, 1-ethyl-3-methyl-, Naphthalene, 1-methyl-, 2,4,6-Octatriene, 2,6-dimethyl-, 1-Dodecene, Indene, 9,12,15,18,21,24-Hexaoxa(2,16)[30] paracyclophane, Cyclopentene,3-ethylidene-1-methyl-, 4-Methyl-3-(3-nitrophenyl)-6-pheny l-5,6-dihydro-4H-[1,2,4,5]oxatriaz ine, 1,4,6,7-Tetramethyl1,2,3,4-tetrahy dronaphthalene, 4H-Pyrane-3-carboxamide, 5-cyano-6-ethoxy-2-methyl- 4-(4-pyridyl)-, Carbonic acid, methyl 3,4-xylyl ester, 3-Buten-2-one, 4-phenyl-, 1H-3a,7-Methanoazulene, 2,3,4,7,8, 8a-hexahydro-3,6,8,8-tetramethyl-, Cholest-7-en-3-ol, 4,4-dimethyl-, (3.beta.,5.alpha.)-, Naphthalene, Triacontanoic acid, methyl ester, Stibine, trimethyl-, 2-Allylphenol, 2,4-Hexadiene, 3-methyl-, Stannane, triethyl(1-methylethyl)-, Phthalan, Phenol, 2-propyl-, Naphthalene, 2-methyl-, Naphthalene, 1,4-dimethyl-, Ascorbyl Palmitate, 1H-Indenol, Hexadecane, 4-Cycloocten-1-one, 1-Heptadecene, Benzene, 1,3,5-trimethyl-, Benzene, (1-methyl-2-cyclopropen-1-yl)-, Bicyclo[2.2.2]oct-2-ene-1-carboxyl icacid, 3-Methylpenta-1,3-diene-5-ol, (E)-, Tricyclo [4.1.1.0(7,8)] oct-3-ene, Naphthalene,2,7-bis(1,1-dimethyle thyl)-, Benzaldehyde, 2-hydroxy-, 1,4-Benzenediol, 2,6-dimethyl-, 1,2,5,5,8a-Pentamethyl-1,2,3,5,6,7,8,8a-octahydronaphthalen-1-ol, Thiocarbamic acid, N,N-dimethyl, -1,3-diphenyl-2-butenyl ester, 1-Octadecene, 9,19-Cyclo-27-norlanostan-25-one, 3-(acetyloxy)-24-methyl-, (3.beta. ,24R)-, 5,8,11,14-Eicosatetraynoic acid, 1,4-Heptadiene, Cyclopentadiene, 2,5,5-trimethyl-, Cyclohexene,3-propyl-, Benzene,1-methyl-4-(1-methylethyl)-, 1,4-Methanonaphthalene,1,4-dihydro-9-((1-methylethylidene)-, Naphthalene, 1,2-dihydro-6-methyl-, Benzene, propyl-, Methanol, 6,8,9-trimethyl-4-(2-phe nylethyl)-3-oxabicyclo [3.3.1]non-6-en-1-yl)-, 1,3,5-Hexatriene,3-methyl-,(E)-, Silicic acid, diethyl bis(trimethy lsilyl) ester, Phenylacetamide, N-(3,5-dimethylph enyl)-, Phenanthrene, 9,10-dihydro-1-methyl-, Cinnamyl carbanilate, Benzenemethanol, .alpha.-ethyl-, 4-Adamantan-1-yl-benzoic acid isop ropyl ester, 3-

Cyclohexylthiolane,S,S-dioxide, 1-Bromo-11-iodoundecane, [1,1'-Bicyclopentyl]-2-one, 5H-Dibenzo [a,d]cyclohepten-5-one, 2,6-Octadienal, 3,7-dimethyl-, (Z), 2,4-Hexadiene, 2,5-dimethyl-, Lathodoratin, 1-Cyclohexyl-2-buten-1-ol (c,t), Thiocarbamic acid, N,N-dimethyl, S -1,3-diphenyl-2-butenyl ester, Phenanthrene, 9,10-dihydro-, Cyclopentasiloxane, decamethyl-, Cyclohexane, 1,1-dimethyl-2,4-bis(1-methylethenyl)-, cis-, Cyclohexane, (1-octylnonyl)-, 1,5-Heptadiyne, 1,4-Dihydronaphthalene, (1-Methylpenta-1,3-dienyl)benzene, Naphthalene, Cyclopentene, 3-ethenyl-, Benzothiazole, Benzene, 4-fluoro-1-methyl-2-nitro, Benzene, 1-methyl-4-(1-methylethen yl)-, 9-Octadecenamide, (Z)-, 2-Cyclohexen-1-one semicarbazone, 1-Phenanthrenecarboxylic acid, 1,2 ,3,4,4a,9,10,10a-octahydro-1,4a-dimethyl-7-(1-methylethyl)-, Cyclohexane, 1,2,4-tris(methylene), Bicyclo[2.1.0]pentane, 5-(4,5-Dihydro-3H-pyrrol-2-ylmethy lene)-4,4-dimethylpyrrolidin-2-one, 1,4-Dihydronaphthalene, 1,4-Benzenediol, 2,3,5-trimethyl-, Methanone, [1,4-dimethyl-7-(1-meth ylethyl)-2-azulenyl]phenyl-, 3(4H)-Dibenzofuranone, 4a,9b-dihyd ro-8,9b-dimethyl-, 1H-Indene, 1,3-dimethyl-, Phthalic acid, benzyl isobutyl ester, Cyclohexene, 1,6-dimethyl-, Benzene, 1-ethenyl-3-methyl-, 1-Naphthalenol, 5,8-dihydro-, 1-Naphthalenol, 2-methyl-, Phthalic anhydride, Cyclodecene, (Z)-, 5H-3,5a-Epoxynaphth[2,1-c]oxepin, dodecahydro-3,8,8,11a-tetramethyl-, 2-Cyclopenten-1-one, 2,3-dimethyl-, 2(1H)-Benzocyclooctenone, decahydr o-10a-methyl-, trans-, Spiro[4.5]decane, Phenanthrene, 3,6-dimethyl-, N-carbobenzyloxy-l-tyrosyl-l-valin, Benzene, 1-ethenyl-2-methyl-, Benzene, 1-butenyl-, (E)-, 2-Spirocyclohexyl-4,8-dimethyl-6-n itro-3,4-dihydro-2H-quinoline- 1-carbaldehyde, Phenanthrene, 1-methyl-, 2-Propenoic acid, 3-[3-(trifluoromethyl)phenyl]-, (E)-, Fluorene, 4-[1,2-dihydroxyethyl]-, Naphthalene, 2-(1-cyclopenten-1-yl)-, Isoquinolinium diethoxycarbonyl-methylide, Benzenacetic amide, .alpha.,.alpha.-dimethyl-2-methoxy-6-nitro-, 2-Cyclohexen-1-one, 3-(3-hydroxybu tyl)-2,4,4-trimethyl-, 2,3-Dimethylanisole, 1H-Indene, 1-ethenyl-2,3-dihydro-, Dehydroabietylamine, Benzamide, N-(3-methylphenyl)-4-et hyl-, 1,3-Xylyl-15-crown-4, 2,3-.pinaned ioxyboryl-, 1-(3,5-Bis-trifluoromethylphenyl)e thanol.

Conclusions

There were many bioenergy components in the pyrolysis products from the ether/acetone extractives of *Eucalyptus urophydis* wood. What's more, the pyrolysis byproducts also contain many components of biomedicine. It presented a scientific foundation for refinery use of *Eucalyptus urophydis* wood.

Acknowledgements

This work was financially supported by the Project Supported by National Natural Science Foundation of China (No. 31070497), Program for New Century Excellent Talents in University(No. NCET-10-0170), A Project Supported by Scientific Research Fund of Hunan Provincial Education Department(No.10A131), the Key Project of Chinese Ministry of Education.(No. 211128).

References

[1] Q. Hong-chen, P. Wan-xi, W. Yi-qiang, ZH. Ming-long. Advanced Materials Research Vols. 129-131 (2010), p.1055

© (2012) Trans Tech Publications, Switzerland
doi:10.4028/www.scientific.net/AMM.164.33

Study on corrosion inhibition performance of PASP composite on A3 carbon steel in seawater

Xin Wang[1,2,a] , Zhan Liu[1,2,b] , Zhenfa Liu[2,c]

[1]College of Chemical Engineering ,Hebei University of Technology,Tianjin , China

[2]Hebei Engineering Research Center for Water Saving in Industry,Institute of Energy Resources,Hebei Academy of Science,Shijiazhuang, China

[a]hbsjzwx06@163.com , [b]liuzhan1216@126.com , [c]lzf63@sohu.com

Keywords: steady polarization , carbon steel , PASP ,corrsion inhibition ,seawater .

Abstract . The polyaspartic acid (PASP) composite was prepared from PASP , sodium gluconate , zinc sulfate , sodium tungstate and phosphate .The corrosion inhibition performance of PASP composite on A3 carbon steel in seawater was studied by using steady polarization. The results showed that PASP composite had good corrosion inhibition performance in seawater . When the concentration of PASP composite was 300 mg/L , the corrosion inhibition rate reached 79.25% .

Introduction

Corrosion was a serious problem when seawater was used in cooling recirculating water system . Electrochemical corrosion was the primary corrosion of A3 carbon steel in seawater[1] . The anodic reaction of metal in seawater could be described as follows:

$$Fe=Fe^{2+}+2e$$

The cathodic corrosion reaction in seawater was

$$1/2O_2+H_2O+2e=2OH^-$$

Ping Gong etc [2] developed a composite of OTCA , phosphate, calcium gluconate,and zinc sulfate and studied its corrosion inhibition performance in seawater . Liqun Zhu etc[3]composited sodium gluconate with other three kinds of corrosion inhibitors and studied the corrosion inhibition performance of the composite in seawater . PASP was biodegradable and was used as corrosion inhibitor and scale inhibitor in colling recirculating water[4,5].When PASP was used in seawater , the corrosion inhibition performance was not satisfactory .

In this paper , PASP composite was prepared and its corrosion inhibition performance on A3 carbon steel in seawater was studied by using steady polarization.

Electrode Materials and Experiment Methods

Electrode Materials. A3 carbon steel electrode , platinum electrode , aturated calomel electrodes(SCE) , CHI660B electrochemical workstation (Chenhua Instrument,Inc., Shanghai ,China) .

Preparation of PASP composite. The PASP composite was prepared by mixing PASP , sodium gluconate , zinc sulfate , sodium tungstate and phosphate in beaker according to mass ratio .

Test Methods. The Experiment water was seawater of Huanghua area and the polyaspartic acid (PASP) was purchased from Taihe Company .The electrochemical measurements were perfomed in a typical three-compartment glass cell consisting of the A3 carbon steel specimen as a working electrode (WE) , platinum mesh as a counter electrode (CE) , and a saturated calomel electrode (SCE) as the reference electrode . Measurements were carried out on A3 carben steel electrode molded in polyester leaving an exposed area of 1.5 cm^2 . The electrode surface was polished with abrasive paper from 1200 to 800 grade and washed with alcohol cotton , then making it dry naturally . The electrodes were placed in the test solution for 30 min prior to each experiment . Potentiostatic polarization measurements were carried out using CHI660B electrochemical workstation . The polarization curves were obtained from the corrosion potential (E_{corr}) up to $\pm$300 m at a potential scan rate of 1.0 mV/s . The specific method see literature[6] .

Results and discussion

The corrosion inhibition performance of single PASP on A3 carbon steel in seawater

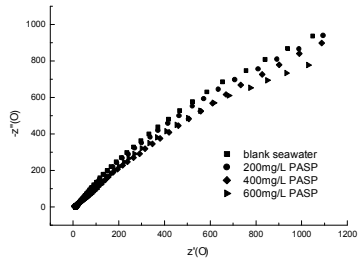


Fig.1 Nyquist curves of A3 carbon steel in seawater at different concentration of PASP

Fig.1 was the nyquist curves of A3 carbon steel in seawater at different concentration of PASP . It showed that PASP could change the nyquist curves' size . The distribution of the pots showed that the curves' size decreased slightly with the PASP concentration increased . That meant that the corrosion inhibition efficiency increased not obviously with the PASP concentration increased .

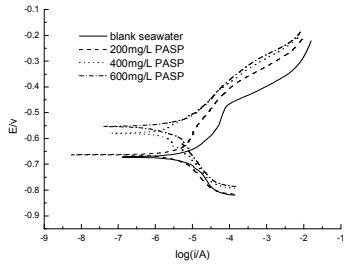


Fig.2 Potentiodynamic polarization curves of A3 carbon steel in the seawater at different concentration of PASP

Tabel 1 The electrochemical parameters of A3 carbon steel in the seawater at different concentration of PASP

Concentration[mg/L]	I_{corr}[A]	η [%]
0	1.144×10^{-5}	~
100	8.775×10^{-6}	23.30%
200	8.022×10^{-6}	29.88%
300	5.116×10^{-6}	55.40%
400	2.736×10^{-6}	76.15%
500	9.614×10^{-7}	89.30%
600	1.579×10^{-8}	99.82%

Fig.2 was the potentiodynamic polarization curves of A3 carbon steel in the seawater at different concentration of PASP . It showed that the corrosion potential shifted towards more anodic values in the presence of PASP . This meant that PASP was an anodic inhibitor in seawater . As shown in Tabel 1 , the anodic current decreased and corrosion inhibition rate increased when the PASP concentration increased . The corrosion inhibition rate was calculated by Eq. 1

$$\eta = \frac{i_0 - i_{corr}}{i_0} \quad (1)$$

Where icorr and io represented the corrosion current of the blank seawater and the seawater with the PASP .

The corrosion inhibition performance of PASP composite on A3 carbon steel in seawater

In order to improve the corrosion inhibition performance of PASP , the PASP composite was prepared . The corrosion inhibition performance of the PASP composite on A3 carbon steel in seawater was studied .

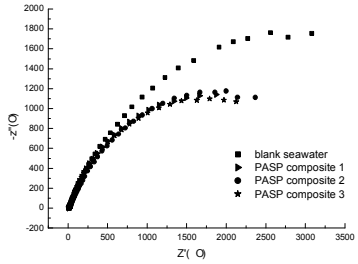


Fig.3 Nyquist curves of A3 carbon steel in seawater with PASP composite

Fig.3 was the nyquist curves of A3 carbon steel in seawater with PASP composite . The presence of PASP composite led to changes of the impedance plots in both shape and size . The size of the curves reduced meant that the resistance increased and corrosion decreased .

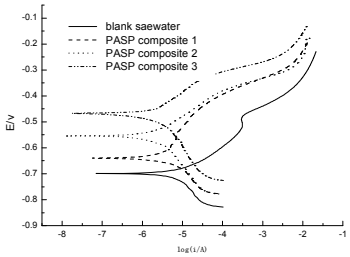


Fig.4 Potentiodynamic polarization curves of A3 carbon steel in the seawater with PASP composite

The PASP composite 1 was consisted of 40 mg/L sodium gluconate , 20 mg/L zinc sulfate , 20 mg/L PBTCA and 60 mg/L PASP ； the PASP composite 2 was consisted of 40 mg/L sodium gluconate , 20 mg/L zinc sulfate , 20 mg/L PBTCA and 200 mg/L PASP ； the PASP composite 3 was consisted of 50 mg/L sodium tungstate , 50 mg/L sodium hexametaphosphate and 200 mg/L PASP .

Fig.4 was the potentiodynamic polarization curves of A3 carbon steel in the seawater with PASP composite . The corrosion potentials shifted to more anodic values in presence of PASP composite indicating that the composite inhibitors had a stronger influence on the A3 carbon steel oxidation reaction than the oxygen cathodic reduction . This meant that the PASP composite was anodic inhibitor .The icorr decreased meant that the corrosion inhibition rates increased when the PASP composite was used .

Tabel 2 The electrochemical parameters of A3 carbon steel in the seawater with PASP composite

Concentration[mg/L]	I_{corr}[A]	η [%]
0	1.144×10^{-5}	~
200 mg/L PASP	8.022×10^{-6}	29.88%
PASP composite 1	4.184×10^{-6}	63.43%
PASP composite 2	2.857×10^{-6}	75.03%
PASP composite 3	2.374×10^{-6}	79.25%

As shown in Tabel 2 , the corrosion inhibition rate of PASP composite was higher than PASP alone . When PASP composited with sodium gluconate , zinc sulfate and PBTCA , the corrosion inhibition rate reached 75.03 % . When PASP composited with sodium tungstate and sodium hexametaphosphate , the corrosion inhibition rate was 79.25% .

Conclusion

The PASP composite was prepared . The experiment showed that the PASP composite was anodic inhibitor in seawater . The corrosion inhibition performance of PASP composite on A3 carbon steel in seawater was good . The corrosion inhibition rate was 79.25 % when the concentration of PASP composite was 300 mg/L .

Acknowledgements

This work was financially supported by the Natural Science Foundation (B2011302001) and Science and Technology Research and Development Projects (11276711D) of Hebei Province .

References

[1]Ma QG, Wei YL, Zhang XL, et al . The research development of green corrosion inhibition for carbon steel in seawater . Enviroment Science & Technology , 2010 , 33(5) : 631-635 .

[2]Gong P, Du M, Wang QZ . Reseach on enviriment friendly corrosion inhibition of carbon steel in seawater . 2002 ,10 : 406-410 .

[3] Zhu LQ, Shan DD, Zhao B , et al . Study of the inhibitors of the carbon steel in dynamic hot seawater . Materails Science & Technology , 2007 , 15(5) : 631-635 .

[4]Robert , J.R;Kim , C.J.Materials Performance , 1997 , 2 : 53 .

[5]Roweton,S.;Huang,S.J.J.Environmental Polymer Degradation,1997,5:175 .

[6]Song YS, Zhang K, Zuo P . Choice of Electrode Material for Detecting Low Frequecy ElECTRIC Field in Sea Water . Advanced Materials Reseacher , 2011 , 1 : 137-140 .

© (2012) Trans Tech Publications, Switzerland
doi:10.4028/www.scientific.net/AMM.164.37

Affection of Manufacture Parameters and Mixture Material on Plastic Alloy Bearings

Chengyun Yang[1,a] , Jinmin Peng[2,b]

[1]Mechanical Engineering College, Chongqing University, Shapingba District, Chongqing, P.R. China, 400030

[2].Department of Electromechanical and Automation Engineering, Fujian University of Technology, Fuzhou 350108,

[a]ycycqu@sina.com, [b]pjm@sina.com

Keywords: Water Lubricated, Molding technology, Mechanic Performance

Abstract. Manufacture process parameters will be obtained from experiments in research. Molding technology determines the mechanical properties and performance of the product. The influence of molding temperature and time are significant on the performance of water lubricated bearing, the plastic alloy is based on latex material, synthesized with different fillings, accelerators and other matters, and displays great mechanical and friction properties. The main performance included peel strength, tensile strength and wearing capacity. Optimization of manufacture process parameters and the orthogonal experiments on them were carried out by integrating the results of experiments and finally the optimal manufacture process was achieved. In the experiment, three-leveled orthogonal tests were conducted for the three systems to test the tensile strength, tearing strength, stress at definite elongation, hardness and tensile rate. The impacts of the respective systems were analyzed and the content of each component are determined to get the optimal formula.

0 Introduction

The difference in material between water lubricated bearings and traditional bearings stems from the change in working medium. In detail, traditional bearings are lubricated by oil, which has less caustic impact on mental material. An oil film more easily formed means a wider pick of material. For the water lubricated bearing however, in material choice we must also consider antifriction, abrasion and corrosion resistance.

The adoption of plastic alloy saves a considerable amount of oil and valuable non-ferrous metal and simplifies the shafting construction to prevent water pollution caused by oil leakage. The replacement of mineral oil with water as the working medium for machine driven systems and hydrodynamic system has become a cutting-edge topic in the realm of energy-efficient and environmentally friendly scientific research of machine driven system that attracts great attention from industrial countries in the world [1,2].

1 Experiment Method and Conditions

The mechanical property plastic alloy lies closely with its formula: The kind and dosage of mixture material picked will lead to plastic alloy of different properties[1]. Bearing vulcanization technology is essentially different from that of other materials and is also closely related to the size of the bearing. If not further explained, all the subjects in this experiment are sampled from 1-1/2″×2″×6″ bearings, vulcanization pressure 0.39Mpa. Experiment conditions and standards are shown in Tab.1. Wear loss is tested by MPV-20B for two hours at 2000N.

Tab.1 Experiment application and standard

Test Item	Test Standards	Equipment Model
Mixed material		X-1500K
(300%)definite elongation MPa	GB528-92	DXLL-5000
Tensile strength MPa	GB528-92	DXLL-5000
Tensile rate %	GB528-92	DXLL-5000
hardness Shore A	GB/T531-88	XY-1

2 Experiment Results and Analysis

2.1 Impact of Vulcanization Temperature on Bearing Performance

The test duration for vulcanization to examine the correlation between temperature and plastic alloy performance is set to be 20min. Test results are shown in Fig.1, 2 and 3.

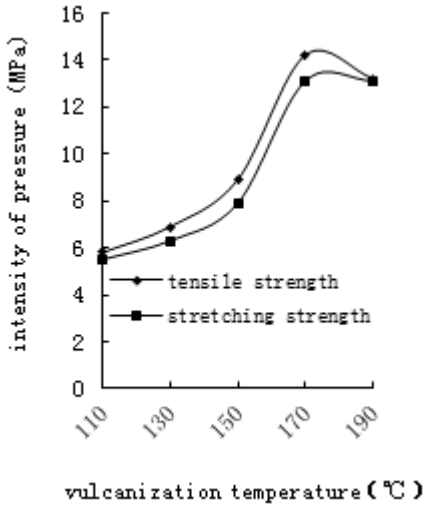


Fig.1 Relationship between mechanic performance and vulcanization Tem.

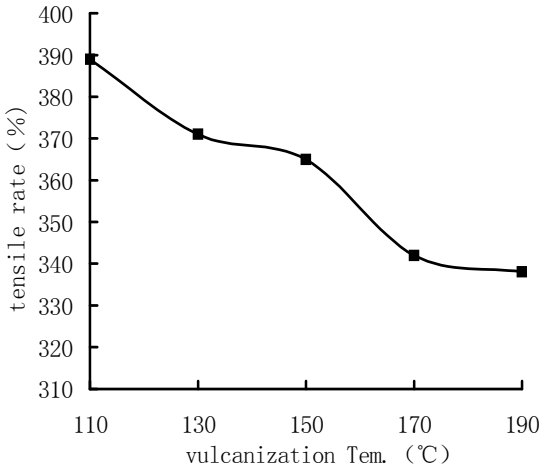


Fig.2 Relationship between tensile rate and vulcanization Tem.

It is illustrated that, as the vulcanization temperature rises, the tensile strength, stretching strength and abradability of the material increase too, However there is a slight decrease when temperature hit 170℃.

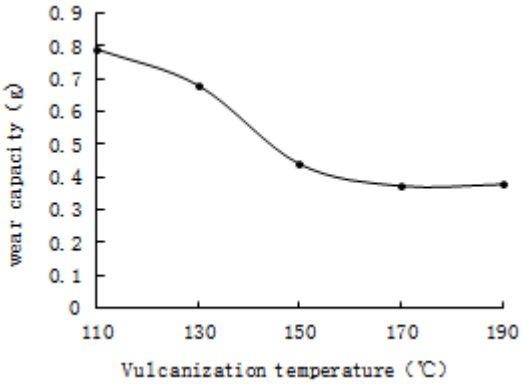


Fig. 3 Relationship between wear capacity and Tem.

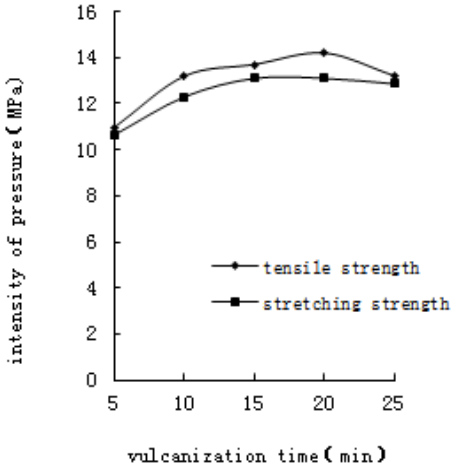


Fig. 4 Relationship between mechanic performance and vulcanization time

Vulcanization temperature is the primary condition for the bearing material to vulcanize and cast a direct impact on the speed of vulcanization and product quality. The higher the temperature is, the faster the vulcanization, the higher the efficiency; otherwise, the slower the vulcanization speed, the lower the efficiency. The vulcanization temperature depends on the component of the material of bearing, the most important ones are the primary base and vulcanization system. However, it is worth the caution that in a high-temp situation, molecule chains are prone to break, causing vulcanization reversion. Therefore, it is not wise to set the vulcanization temperature too high [3].

However in Fig.2 we observe a slump in tensile rate with the increased vulcanization temperature. When we are seeking a material with a high tensile rate, we should opt for those that are 'under cure' which have a more desirable tensile strength and a high tensile rate.

2.2 Vulcanization Time Impact on Bearing Performance

The temperature environment of the time-performance test was set at 170℃. The results of the experiment are shown in Fig.7, 8.

Tensile strength, stretching strength and attrition change with time in accordance in principle with the change of temperature, the reason for which being either 'under cure' or 'over cure'. However, vulcanization time has a less strong impact than vulcanization temperature.

Vulcanization time is requisite in the process of vulcanization, determined by the ingredients of the material, vulcanization temperature and pressure. For a given material, under the circumstances of a certain vulcanization temperature and pressure, there appears a time that is optimal for vulcanization (positive vulcanization). Vulcanization that goes on for too long will lead to over vulcanization, too short, to under cure. Over cure and under cure are both reasons for a decline in overall product performance [5].

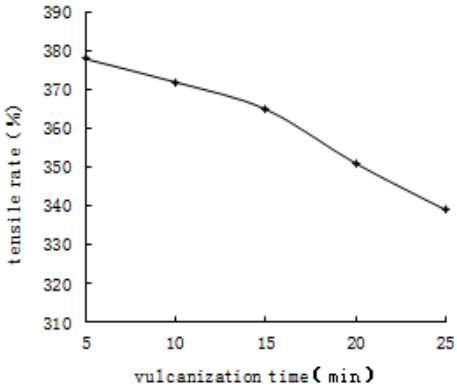


Fig.7 Relationship between tensile rate and time

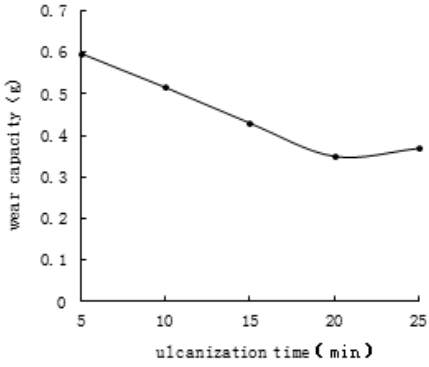


Fig.8 Relationship between wear capacity and vulcanization time

3. Affection of mixture material formula

The mechanical property plastic alloy lies closely with its formula: The kind and dosage of mixture material picked will lead to plastic alloy of different properties[1]. This essay stresses on the analysis of the impact each system of the formula, such as vulcanization, reinforced filling, preservation and softened plastification system, brings to the property and performance of the plastic alloy.

3.1 Tensile Strength

Tab. 1 Experimental gene and level

LEVEL / GENE	1	2	3
A（Vulcanization）	0.4	0.8	1.2
B（Softening Agent）	0.1	0.15	0.2
C（Reinforcing Agent）	0.2	0.3	0.4

We examine the impact reinforcing agent, softening agent and vulcanizing agent have on the tensile strength, the genes and levels need assessing are shown in Tab. 2.

C peaks at level 3, A at level 2, B at level 1. In the situation of C3A2B1, the elongation test ends on a tensile strength of 12.16Mpa.

3.2 Stress at definite elongation and hardness

Stress at definite elongation and hardness are both important indexes for plastic alloy rigidity, indicating the amount of force needed to incur a change in shape. Stress at definite elongation is associated with stretched deformation, which causes a comparatively bigger change; rigidity is associated with the relatively less influential compressed deformation. For the relevance of both elements and the general accordance of reaction to all genes, these two elements are both discussed in this part of the essay.

Tab. 2 Experimental gene and level

LEVEL / GENE	1	2	3
A（HAF）	15	30	45
B（TDAE）	20	40	60
C（Hard Clay）	25	50	75

A peaks at level 3, B at level 1, C at level 3. In the situation of A3B1C3, the stretching test ends on the strength of 11.01Mpa, hardness of 79 degree Shore A.

3.3 Tensile rate

Tensile rate is relevant to some mechanical properties, especially to the tensile strength.

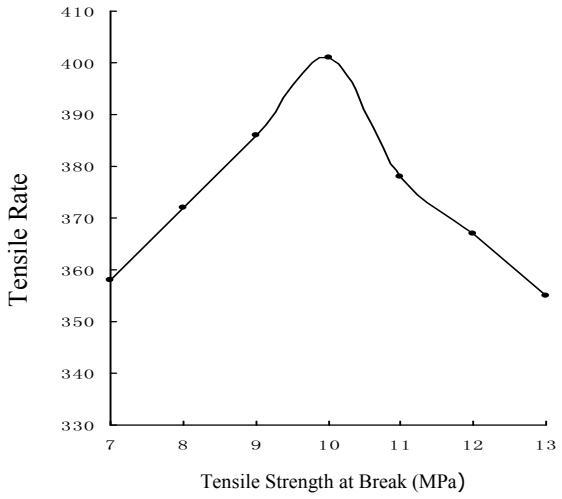


Fig. 5 Relationship between tensile strength and tensile rate

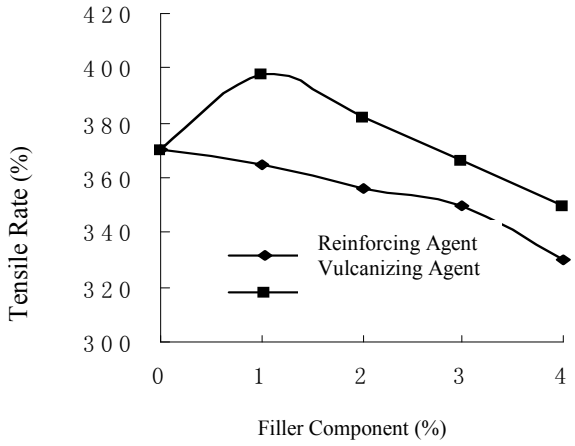


Fig. 6 Relationship between tensile rate and filling

Only with a relatively high tensile strength can there be guarantee a comparatively high tensile rate, hence it is a prerequisite condition that the material enjoys an adequate tensile strength[4]. However as we can see in the experiment, an enhanced tensile strength does not necessarily enhance its tensile rate (see Fig.5).

The reason for this phenomenon is that there usually are reinforcing agents added and the vulcanization is often intensified in the process of increasing tensile strength – factors that decrease the tensile rate (see Fig. 6). Therefore, in order to attain a material that has a comparatively high tensile rate, we can adopt a less vulcanized plastic alloy and lower the dosage of vulcanizing agent to increase the tensile rate.

4 Conclusion

（1）The mechanical properties of water lubricated bearings are closely related to their vulcanization temperature and time. From the vulcanization time we can deduce how the tensile strength, stretching strength and attrition react to temperature and time to better instruct production.

（2）A comparatively high tensile strength is the prerequisite for a higher tensile rate, however an enhanced tensile strength does not categorically lead to a high tensile rate.

(3) After the modification, the mechanical properties of the plastic alloy are significantly enhanced, the tensile strength and hardness reached: 12.16Mp and 79 degree SHORE A

References

[1] WANG, Xian Feng, LIN, Qing, HU, Mao Heng, TANG, Yu Min, HAI, Peng Zhou, Property study on water lubricated rubber tail piece bearing. Vessel Engineering. 1993(4):45~49. (in Chinese)

[2] Ei-TayebNS, GadelrabRM. *Friction and wear properties of E-glassfiber reinforced epoxy composites under different sliding contact conditions*[J].Wear,1996,192:112~117

[3] Fukahori Y and Yamazaki. Mechanism of rubber abrasion. Part Ⅲ:How is friction linked to fracture in rubber abrasion?, Wear,1995:19~28

[4] Liu Dahua, Manuals about Compound Rubber Industry in Chinese. 1st press. Chemical industry Press. 1991 29~35

[5] Wang Jiaxu, Translate. USA. MIL-B-17901B(Marine) Military Standard. Technical report of the State Key Lab. Of Mechanic Transmission, Chongqing university. 1995 57~59

© (2012) Trans Tech Publications, Switzerland
doi:10.4028/www.scientific.net/AMM.164.42

Thermal Study on the Grinding Special-shaped Surface of Granite Material

Yanbin Shi[1,a], Bo Huang[2,b1] and Debao Liu [2,c]

[1] School of Mechanical & Automotive Engineering, Shandong Polytechnic University, Jinan, China

[2] School of mechanical engineering, Shandong University, Jinan, China

[a]shiyanbin79@163.com, [b]huangbo@sdu.edu.cn, [c]debao.liu@126.com

Corresponding author: Bo Huang, Email address: huangbo@sdu.edu.cn.

Keywords: Granite materials, Special- shaped surface, grinding, Temperature field, Infrared imaging

Abstract. The heat released from grinding process plays a very important role for the machining quality, so studying the temperature distributions on the machined surfaces of granite is necessary. For grasping the influencing factors of temperature, the experimental analysis basing on the infrared imaging method were carried out. The grinding temperatures for two kinds of granite materials (Qilu Red and Jinan Green) are measured. In the results, there are obvious variations of the highest temperatures with different grinding depths, spindle speeds and feed velocities on the machined surfaces. Then, it is suggested that the degree of difficulty is affected by property of granite material to a great extent.

Introduction

The heat is to be released with the temperature changes in material removal machining, which affects the machining quality and tool life. Facing to the metal and ceramic materials removal, the heat generation has been researched with different methods deeply [1-3]. Then the heat researches on the hard and brittle stone materials, such as granite, are known unclearly. As well known, the heat released when grinding or sawing the stone surfaces always brings some harmful effects on the tool and machining quality. For example, when the temperature rising to 800℃ and above, the diamond grit would be graphitized highly to decrease the cutting ability of diamond tool. So the cutting heat is important factor in the process of machining special-shaped surface of granite.

At present, two approaches are used commonly to get the temperature in grinding process, namely theoretical analysis and experimental measurement. To be specific, both theoretical derivation and empirical formula method are belong to theoretical analysis, and based on the heat transfer theory to build/solve differential equations between tool and workpiece. However, the temperature measurement is the better direct approach in grinding process, but the measurement method must be developed further to study the rules of temperature change on the special-shaped surfaces with different machining conditions in detail.

Experimental Method and Conditions

The direct measuring methods to study the temperature of grinding zone of granite are thermocouple temperature measurement, optical fiber temperature measurement and infrared temperature measurement commonly. However, all the above methods don't derive the complete temperature field on the cutting surfaces. Using the thermocouple and optical fiber is more suitable to study the inner heat transfer between tool and stone workpiece [3], but the electrical non-conductivity of the hard and brittle granite make it difficult to measure. In addition, the response speed of thermocouple is slow correspondingly to receive the temperature change, especially used for the high-speed rotating

tool. Simultaneously, considering other factors such as dynamic thermosensitive, measurement area, measurement precision, the effect of cutting fluid, measurement costs and whether or not is easy to collect and process data and so on, the infrared temperature measurement is more advanced than other two methods to obtain the surface temperature in wider area, so an infrared thermal imager is used to analyze the temperature field of tool-workpiece interface in this work. The infrared thermal imager could receive the infrared radiation energy of any point of the object to show the temperature distribution images, which is non-contact detector, avoiding the adverse effects of high temperature for operation. In addition, the advantages of this method lie in the higher response speed, wider measurement area, and easier operation [4-6]. In this work, for obtaining the temperature field of special-shaped surface of granite in grinding process, the assembly of infrared measuring system is used.

Here, the infrared thermal detector QH5104R produced by NEC is used in experiments to monitor the grinding operation on the machining center SPEED Y2000 produced by CMS. The maximum scale speed of machining center is 15000r/min, and the maximum feed velocity of whose X axis, Y axis, Z axis: 54m/min, 36m/min, 30m/min. The cutting tool ASS10105 produced by You-oriented Company is selected to finish the grinding process. The above assembly is suitable for machining hard and brittle materials, being able to shape, grinding, polishing, carve the special-shaped surfaces or geometry, which provides the favorable efficient machining conditions for this work.

Granite products are always complex in shape, which could be machined through several operations of simple surface cutting. As a typical arc unit, the quarter-circle surface is easy to be measured in cutting operations, so which is used in following experiments, as illustrated in Fig. 1. The other special-shaped surfaces could be deduced from this experimental result. Otherwise, for receiving the cutting heat more exactly, the grinding fluid or cooling fluid are not considered in experiments.

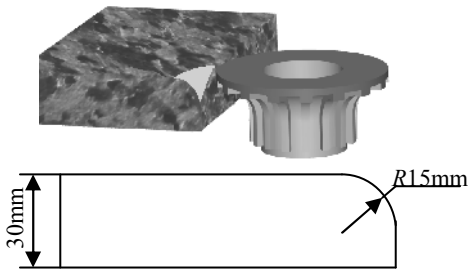


Fig. 1 The surface grinded in experiments

The local granite materials named Qilu Red (G3754) and Jinan Green (G3701) are selected as the research object in experiments, which are different in their intrinsic physical properties, such as hardness, brittleness, toughness and so on.

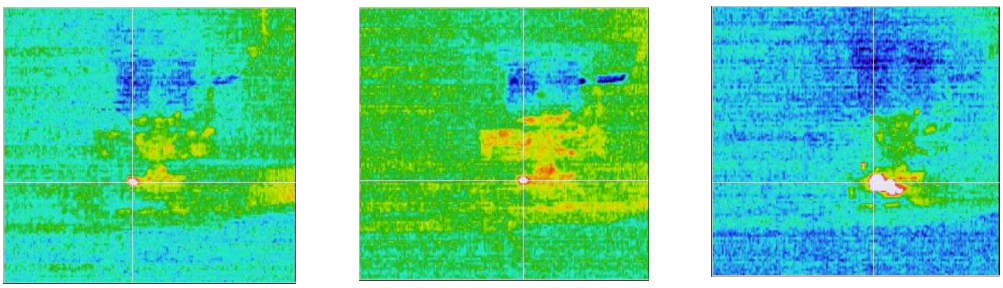


Fig. 2 The temperature distribution images for v_f=600mm/min, v_s=20/40/60m/s when Qilu Red grinded

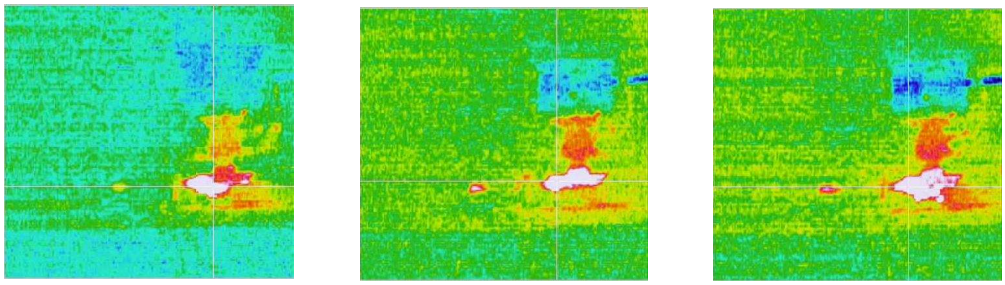


Fig. 3 The temperature distribution images for v_f=600mm/min, v_s=20/40/60m/s when Jinan Green grinded

Analysis and Discussion

The high efficient grinding experiments with the two kinds of granites in several operating conditions (feed velocity of the tool: v_f, circumferential velocity of the tool: v_s) were executed, being detected with the above infrared thermal system. The temperature distribution images around the tool-workpiece interface were captured with the infrared thermal imager, as shown in Fig. 2 and Fig. 3, the temperature peak points being marked with cross lines. As seen, the peak points are about on the center of the interfaces usually.

When the special-shaped surface of specific material granite is grinded with specific tool, the grinding temperature is mainly affected by the processing parameters and conditions, such as grinding depth, rotational speed of tool, feed velocity and so on. Then, certain of simple factor experiments in different operation conditions were developed to capture the grinding temperature under different processing parameters and study the change law of grinding temperature on the special-shaped surface of granite.

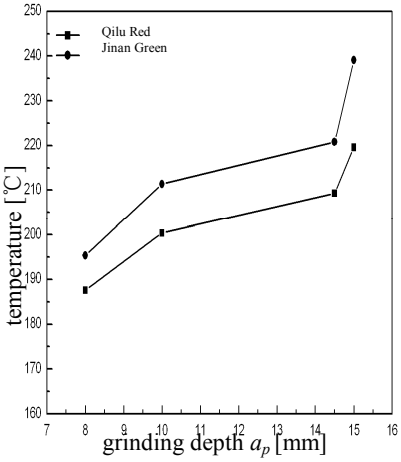


Fig. 4 The peak temperatures of grinding zone for different a_p

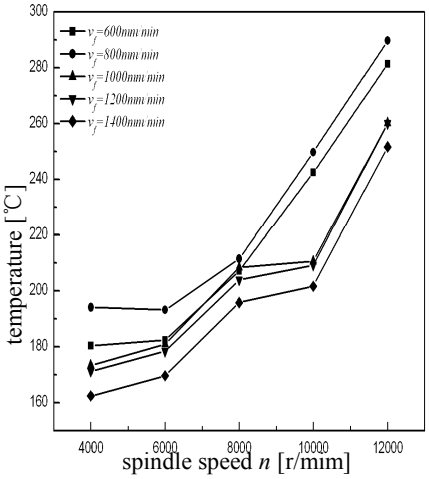


Fig. 5 The peak temperatures of Jinan Green grinding zone for different n

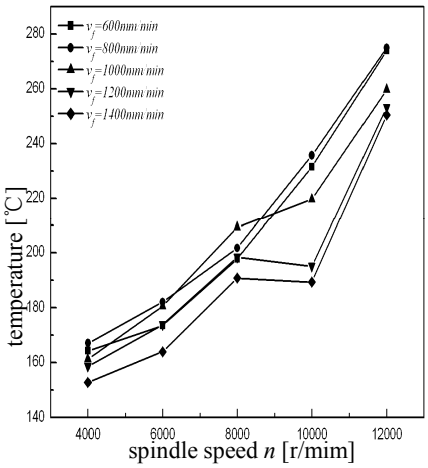


Fig. 6 The peak temperatures of Qilu Red grinding zone for different n

Temperatures response to different grinding depth (a_p). The peak temperatures of grinding zone (quarter-circle surface) are captured with the infrared thermal detector and marked in Fig. 4, which shows the temperature change law with different grinding depths under the specific processing condition. Here, specific condition: feed velocity v_f=1000mm/min, circumferential velocity v_s=40m/s, and dry machining.

As shown in Fig. 4, the temperatures in grinding zone of the two kinds of granites increases visibly with the increase of a_p, and the temperature rises increase for certain range of grinding depths. Under the same conditions, the peak temperature of grinding zone of Jinan Green is higher than that of Qilu Red.

It suggests by complicated analysis that the increase of the a_p makes the removal volume of granite bigger, the cutting power more; then the heat from grinding integrates into the grinding zone, making the temperature higher. The temperature presents a close relation with a_p.

As above mentioned, the degrees of temperature rise are different between grinded Qilu Red and Jinan Green. According to the components of granites, the quartz content of Qilu Red is more than that of Jinan Green, which make the granite harder. So, the abrasive particles finishing the breaking work during grinding process depends on the impact action. However, the less quartz content of Jinan Green makes the granite softer and tougher. So, the abrasive particles finishing the breaking work during grinding process depends on the shearing action and squeezing action. Consequently, most parts of the Qilu Red are removed in brittle fracture format, and most parts of the Jinan Green is removed in ductile fracture format. Based on the breakup theory of grinding, the ductile particles on

the stone surface consume more energy, and contact with more abrasive particles of tool than the brittle particles. It is means that the Qilu Red would consume more energy to overcome friction, bring more heat and higher temperature from that process.

On the other side, all the temperatures of points in grinding zone don't exceed 350℃, the peak temperatures are always below 800℃ during the above experiments. Therefore, the temperature rise from the tool-workpiece interface couldn't make the diamond abrasive particles graphitized to lose the ability of cutting.

Temperatures response to different spindle speeds (*n*). When the grinding depth ap keeps at 14.5mm, the heat from the grinding process with different spindle speed n is detected by thermal imager. With 5 certain feed velocities of tool to grinding two kinds of granites, the corresponding peak temperatures are shown in Fig. 5 and Fig. 6. As the figures shown, under a certain feed velocity, the temperatures of grinded quarter-circle surface uprise with the increase of n. The increasing n would lead the more clear temperature rise beyond the speed of 10000r/min.

Moreover, at a certain feed velocity, the cutting rate of the abrasive particles doesn't change with the increasing n, but the tool would consume more energy in unit time. Meanwhile, the more proportions of stone are removed in ductile fracture format, and the more heat released from that doesn't diffuse quickly to make it accumulate there. The great heat transferred into the workpiece caused the higher temperature rise in grinding zone. The proportion of the heat transferred into workpiece increase with the increasing of n to a higher temperature rise.

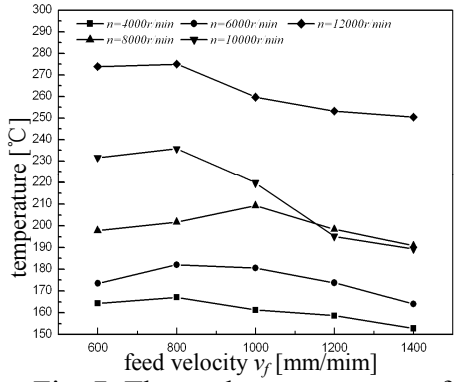


Fig. 7 The peak temperatures of Qilu Red grinding zone for different v_f

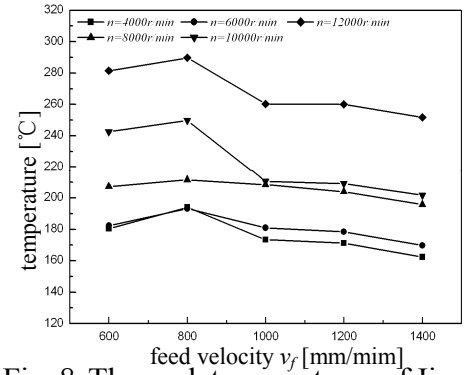


Fig. 8 The peak temperatures of Jinan Green grinding zone for different v_f

Temperatures response to different feed velocities (v_f) . With 5 certain spindle speeds to grinding two kinds of granites, the corresponding peak temperatures are shown in Fig. 7 and Fig. 8. As the figures shown, under a certain n, the temperatures of grinded quarter-circle surface uprise first, then descend with the increase of spindle speed. It is analyzed that the descent is due to the increasing of moving speed of tool along the arc surface with the increasing of v_f, which make the heat diffused more quickly despite the higher v_f make the friction stronger. So, the quick diffusion of heat from the grinding zone affects the whole temperature rise directly. Because the rate of heat diffusion for the moving tool is less than the rate of heat production for the friction, the curves uprise at first in the figures.

Results

Using the infrared measurement, the temperature filed of quarter-circle surface on the granite and its influencing factors during grinding process are studied from different views. The research results would provide important basis for the parameter selection, optimal tool design and cooling mode. Based on the data detected by the infrared thermal imager, the peak temperatures on the grinding zone are analyzed to the following conclusions. Using the diamond formed milling cutter to grind the special-shaped surface of granite, the temperature of grinding zone would rise with the increasing of grinding depth or spindle speed, showing certain linear rule; the temperature of grinding zone would

rise first and then descend with the increasing of feed velocity, because the quick movement of heat source. In addition, the temperature fields of two granites show some differences, indicating the distinct machining difficulty.

Acknowledgements

The authors thank the Science & Technology Plan Project of Shandong Province (BS2011ZZ015), and the Science & Technology Plan Project of Jinan City (201102024).

References

[1] M.R. Miller, G. Mulhooland and C. Anderson: Journal of Manufacturing Science and Engineering, Vol. 125 (2003) No.11, p. 667.
[2] H.T. Young: Wear, Vol. 201 (1996), p. 117.
[3] X.P. Xu: Tribology International, Vol. 34 (2001), p. 419.
[4] R. Fu, H.X. Shen and L. Guo: Precise Manufacturing & Automation, (2011) No.2, p. 5.(In Chinese)
[5] Z.X. Zhou, C. Mao and D.W. Zhou: Mechanical Engineering of China, Vol. 19 (2008) No.8, p. 980.
[6] Z.Y. Dong: Microcomputer Applications, Vol. 24 (2008) No.9, p.54.

© (2012) Trans Tech Publications, Switzerland
doi:10.4028/www.scientific.net/AMM.164.47

Ferroelectric and Optical Properties of BST/BZT/BST Sandwich Structure Thin Films Prepared by RF Sputtering

C.B. Ma [a], X.G. Tang [b,*], D.P. Xiong [c], Y.P. Jiang [d] and Q.X. Liu [e]

School of Physics & Optoelectric Engineering, Guangdong University of Technology, Guangzhou Higher Education Mega Centre, Guangzhou 510006, People's Republic of China

[a]email: ma_caibin@163.com, [b]email: xgtang@gdut.edu.cn (corresponding author), [c]email: depingxiong@gdut.edu.cn, [d]email:ypjiang@gdut.edu.cn, [e]email:liuqx@gdut.edu.cn

Keywords: BST; BZT; Thin films; Sandwich Structure; Ferroelectric properties; Dielectric properties; Optical properties.

Abstract. In this work, $(Ba_{0.65}Sr_{0.35})TiO_3$ (BST) and $Ba(Zr_{0.20}Ti_{0.80})O_3$ (BZT) ceramic targets were prepared using the traditional solid-state reaction technique, which were sintered at 1200 °C for 2 h. The thin films of BST, BZT and sandwich structure BST/BZT/BST were grown on $Pt/Ti/SiO_2/Si(100)$ and Si(100) substrates by rf-sputtering at 500 °C, respectively. And all samples crystallied at temperatures 650 °C for 30 min in oxygen atmosphere. The cross-sectional images of the thin films were characterized by scanning electron microscope (SEM). The dielectric constant and dissipation factor tanδ of the BZT, BST and BST/BZT/BST thin films are 680 and 0.030, 240 and 0.021, 85 and 0.018, respectively at 100 kHz. Compared with BST and BZT films, the BST/BZT/BST film has lower dielectric constant and lower dissipation. The remanent polarization (P_r) of the sandwich structure BST/BZT/BST thin film is up to 9.57 μC/cm^2, the P_r value is larger than that BST (0.25μC/cm^2) film and BZT (8.45μC/cm^2) film. The optical properties (refractive index *n* and extinction coefficient *k*) of the BST/BZT/BST film on Si(100) substrate were measured by *n & k* analyzer 2000.

Introduction

Barium strontium titanate $(Ba_{1-x}Sr_x)TiO_3$ (BST) has attracted considerable attention in recent years because of good dielectric properties and ferroelectric, such as high dielectric constant, high dielectric loss, low leakage current and large dielectric breakdown strength [1-3]. The materials with large electrical field-dependent dielectric constant can be widely used in tunable oscillators, filters and phase for instance shifters and so on. In such devices, a high dielectric tenability is desirable in a certain electric field range and low dielectric loss [4]. However, the large dielectric loss and high leakage current have limited the application. Barium zirconium titana $Ba(Zr_xTi_{1-x})O_3$ (BZT) has good dielectric properties, high tunability and higher dielctric constant and has shown great potential for the application in tunable microwave devices [5-8]. Because Zr^{4+} is chemically more stable than Ti^{4+}, with increasing Zr content, phase transition peak shifts to lower temperature, the dielectric constant of $Ba(Zr_{0.20}Ti_{0.80})O_3$ at room temperature is as high as ~2200 at 1M Hz [6].

In recent years, the dielectric properties and high tunability of the $(Ba,Sr)(Zr,Ti)O_3$ ceramics and thin films have been reported [7,8]. The dielectric constants in BST/BZT heterostructures and sandwich structure BST/BZT/BST thin films were investigated [9,10]. However, there is no corresponding studies about enhance ferroelectric property were reported. In this work, combining BST with BZT, and BST/BZT/BST thin films were prepared on $Pt/Ti/SiO_2/Si(100)$ and Si(100) substrates, and the dielectric, ferroelectric and optical properties were studied.

Experimental procedure

The $(Ba_{0.65}Sr_{0.35})TiO_3$ (BST) and $Ba(Zr_{0.20}Ti_{0.80})O_3$ (BZT) ceramic targets were prepared by the traditional solid-state reaction technique, and the targets were calcined at 1200 °C for 2 h. The BST, BZT and ferroelectric sandwich structure BST/BZT/BST thin films were grown on $Pt/Ti/SiO_2/Si(100)$ and Si(100) substrates kept at 500 ^oC by rf-sputtering, respectively. Then the all of

samples were crystallized at 650 °C in by a tube furnace under oxygen atmosphere for 30 min.The more details for the preparation conditions of the thin films are shown in the Table 1. The BST, BZT and BST/BZT/BST thin films were achieved. For electrical measurements of metal/insulator/metal (MIM) structure, top gold (Au) electrodes of 0.2 mm diameter were deposited through a shadow mask onto the BST, BZT and BST/BZT/BST thin films by a vacuum evaporation. The surface and cross-sectional morphologies were measured by scanning electron microscope (SEM, S-3700N, Hitachi). The dielectric properties of Au/BST/Pt, Au/BZT/Pt and Au/BST/BZT/BST/Pt capacitors were measured by using an Agilent E4980A impedance analyzers at room temperature. All measurements were performed as cycle sweeps (zero voltage to positive voltage back to zero voltage, zero voltage to negative voltage back to zero voltage) to check for any possible hysteretic behaviour. Ferroelectric properties were measured using Radiant Technolies' Precision premier II (USA). The optical properties (refractive index *n* and extinction coefficient *k*) of the BST/BZT/BST films on Si(100) substrates were measured by *n & k* analyzer 2000.

Table 1 Deposition conditions of BST, BZT and BST/BZT/BST thin films by sputtering

Targets	$Ba(Zr_{0.20}Ti_{0.80})O_3$, $(Ba_{0.65}Sr_{0.35})O_3$
Substrates	Si(100), $Pt/Ti/SiO_2/Si(100)$
Base Vacuum	1.0×10^{-4} Pa
Ar/O_2 ratio	40:8
Deposition rate	30 ~ 50 nm/h
Deposition time	3~5 h
Working pressure	1.0 ~ 1.5 Pa
Substrate temperature	500~550 °C
Annealing temperature	650 °C
Thickness	180~600 nm

Results and discussion

Figure 1 shows the SEM cross-sectional image of the sandwich structure BST/BZT/BST thin films on $Pt/Ti/SiO_2/Si$ substrate. The thickness of the Pt and BST/BZT/BST were 130 and 515 nm, respectively. From the SEM images, it is seen that the sandwich structure thin films is smooth and dense. The thickness of BST and BZT thin films are measured by stylus profiler (Ambios, USA), are 180 and 155 nm, respectively.

The dielectric constant and dielectric loss (tanδ) were measured by applying a small ac signal of 0.05 V amplitude and as a function of frequency in the ranging of 100 Hz to 1 MHz at room temperature. Fig.2 shows the dielectric constant and loss tanδ of the BST, BZT and BST/BZT/BST thin films on $Pt/Ti/SiO_2/Si$ substrates, respectively. From the Fig.2, it is seen that for BST and BZT films, the dielectric constants decreased from 289 to 224 and from 810 to 651 with increasing frequency from 100 Hz to 1 MHz, respectively. But for BST/BZT/BST film, the dielectric constant decreased slightly from 96 to 80 with increasing frequency from 100 Hz to 1 MHz. At 100 kHz, the dielectric constants of the BST, BZT and BST/BZT/BST thin films on $Pt/Ti/SiO_2/Si$ substrates, are 250, 686 and 85, respectively.

The dielectric constant value of BST/BZT/BST thin film was lower than that of BST and BZT thin films. This reason is that sandwich type structure BST/BZT/BST was composed of three capacitors in series, include of top BST, BZT and bottom BST capacitors. In general, the equivalent capacitor of multilayer structure thin films may be expressed by a series capacitors. The equivalent

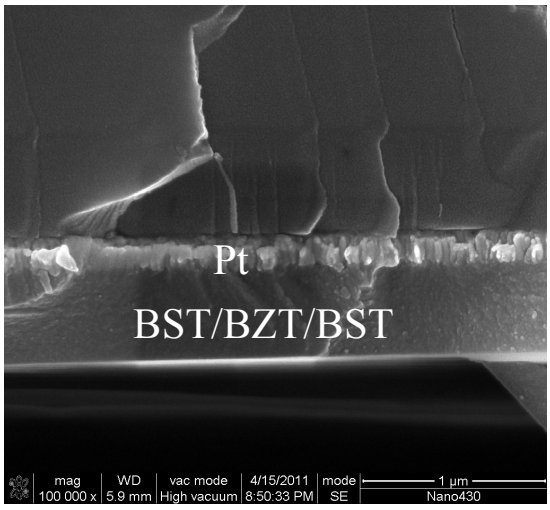


Fig. 1 The SEM picture of cross-section BST/BZT/BST thin films.

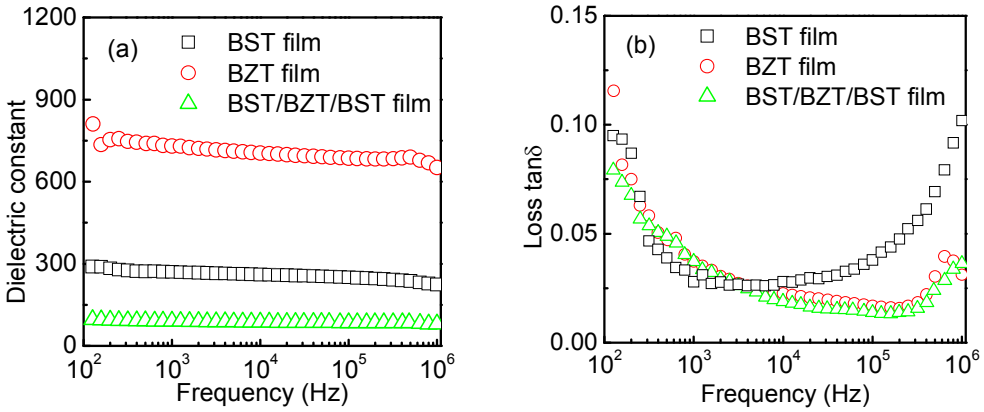


Fig.2 The dielectric constant and dielectric loss of BST, BZT and ST/BZT/BST sandwich type structure at roomtemperature.

calculation formula of the BST/BZT/BST sandwich type structure thin film is as followed:

$$\frac{1}{C_s}=\frac{1}{C_{dBST}}+\frac{1}{C_{BZT}}+\frac{1}{C_{tBST}}+\frac{1}{C_b} \tag{1}$$

Where the C_s is total capacitor, the C_{tBST}, C_{BZT} and C_{dBST} are the capacitors of top BST, BZT and bottom BST thin films, respectively. And C_b is the capacitor of the interface. The contribution of capacitor of boundary surface may be from the interface of BST and BZT thin films, top electrode bottom and BST, and BST thin film and down electrode bottom. Because the $\varepsilon \sim C$, it is similar to C, the equivalent dielectric constant ε_s shows the same pattern as the following:

$$\frac{1}{\varepsilon_S}=\frac{1}{\varepsilon_{dBST}}+\frac{1}{\varepsilon_{BZT}}+\frac{1}{\varepsilon_{tBST}}+\frac{1}{\varepsilon_b} \tag{2}$$

Where ε_s is the total dielectric constant, ε_{tBST}, ε_{BZT} and ε_{dBST} are dielectric constants of top BST, BZT, bottom BST thin films, respectively. And the ε_b is the dielectric constant of the interface. To calculate the ε_s, if the $1/\varepsilon_b \sim 0$, take the dielectric constant of the BZT thin film (230) and BST thin film (675) at 100 kHz in to the algebraic Eq. (2), we can get the result value is about 136. Apparently, the calculated value is higher than measured value 85. Under this conditions, we can get the value

of ε_b is about 224. We think that it owed to amounts of oxyen holes and space charge appeared in thin films, Garcia-Barriocanal *et al* reported that the oxyen holes and space charge could decrease the resistance [11], and the capacitor of boundary surface also lead to decreasing dielectric constant [12].

From the Fig.2, we find the dielectric loss of the sandwiched BST/BZT/BST is 0.015 at 100 kHz, while it is lower than that of BST thin film. Because Zr^{4+} is chemically more stable than Ti^{4+} [5,6], the free charges in BST films pass through the BST/BZT/BST film need higher energy, and the amounts of oxyen holes and space charge turn up in thin films, leading to increasing the leakage current [11]. Under two kinds of mechanism affected, the dielectric loss of the BST/BZT/BST sandwich type structure is comparable to the BZT thin film.

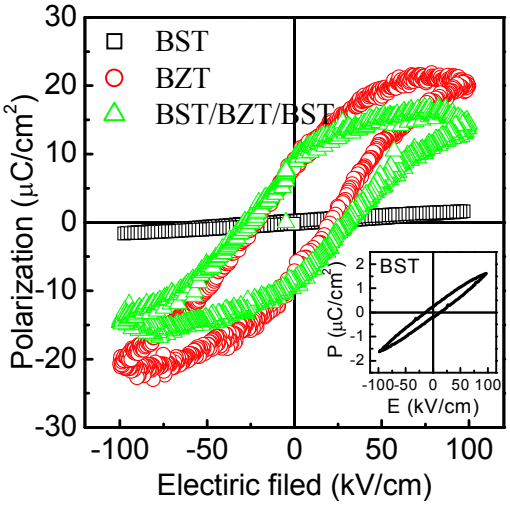


Fig. 3 The P-E hysteresis loops of the BST, BZT thin films and BST/BZT/BST sandwich type structure at room temperature and 250 Hz. Inset is the P-E loop for BST film.

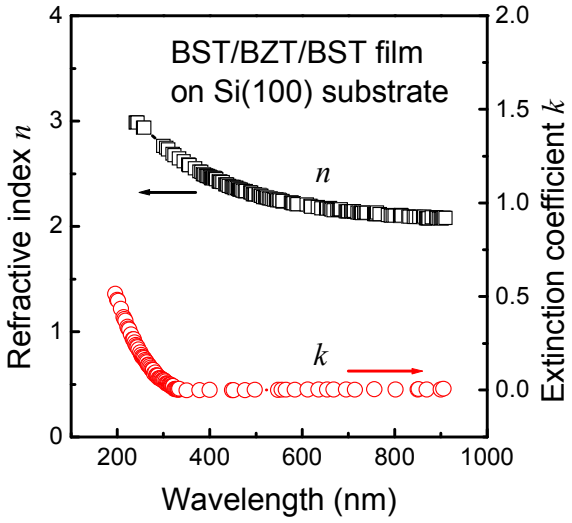


Fig. 4 Calculated dispersions of the refractive index n and extinction coefficient k for a BST/BZT/BST sandwich type structure thin film on Si(100).

Figure 3 shows the *P-E* hysteresis loops of the BST, BZT and sandwiched BST/BZT/BST thin film at room temperature and 250 Hz. For the BST and BZT thin films, the remanent polarization (P_r) and the coercive electric field (E_c) are 0.25μC/cm^2 and 13.9 kV/cm, 8.45μC/cm^2 and 24.1 kV/cm, respectively. But for the BST/BZT/BST thin film, the P_r and E_c are 9.57μC/cm^2 and 33.5 kV/cm, respectively. The P_r value of BST/BZT/BST is larger than that of the BST and BZT films. The polarization is proportional to the charge density under fixed electric field. Because the charges collected together between the top electrode and bottom electrode, and a large amounts of oxygen

holes and space charge appeared in thin films, so the P_r value of BST/BZT/BST thin film is higher than that of BZT film. The coercive electric field value of the BST/BZT/BST film is higher than that in BZT thin film, and the leakage current behavior of the sandwich type structure has no obvious improvement [13].

The optical constants including the refractive index n and extinction coefficient k were modeled using a Cauchy dispersion with an Urbach absorption model [14]. The calculated optical parameters curve was shown in Fig. 4. As can be seen that the n and k of the sandwich type structure BST/BZT/BST thin films are 2.58 and 0, respectively at the 350 nm. The refractive index value of the BST/BZT/BST thin film is higher than that of BST film (2.197) [15] and BZT film (2.33) [16].

Conclusion

In summary, a sandwich type structure of BST/BZT/BST thin film was successfully grown on Pt/Ti/SiO_2/Si(100) substrate by rf-sputtering. Compared with BST and BZT thin films, the BST/BZT/BST sandwich type structure thin film has a lower dielectric constant. The remanent polarization (P_r) and the coercive electric field (E_r) of the sandwich type structure BST/BZT/BST film are 9.57 μC/cm^2 and 33.5 kV/cm, respectively. The P_r value of BST/BZT/BST film was larger than that of BZT (Pr=8.02 μC/cm^2) thin film and BST (Pr=0.25 μC/cm^2) thin film. The good properties from the cumulated interface charges together with space charge and oxygen holes, include those between the top and BST film, BST and BZT films, BST and bottom electrodes. The BZT/BST/BZT grown on Si(100) have a good refractive index $n\sim2.58$ and extinction coefficient k~0, respectively.

Acknowledgements

This work was supported by the National Natural Science Foundation of China (Grant No. 10774030 and 11032010), and the Guangdong Provincial Natural Science Foundation of China (Grant No. 8151009001000003 and 10151009001000050).

References

[1] J. M. Lee, S. Y. Kang, J. C. Shin, W. J. Kim,C. S. Hwang, and H. J. Kim, Appl. Phys. Lett., 74(1997)151-742.
[2] S. Zafar, R. E. Jones, B. Jiang, B. White, P. Chu, D. Taylor, and S. Gillespie, Appl. Phys. Lett. 73(1998) 175-177.
[3] O. Jim, O. Auciello, P. K. Baumann, S.K. Streiffer, D. Y. Kaufman, and A. R. Krauss, Appl. Phys. Lett. 10(2000)761-763.
[4] W.J. Kim, W. Chang, S. B. Qadri, J. M. Pond, S.W. Kirchoefer, D. B. Chrisey, and J.S. Horwitz, Appl. Phys. Lett., 70 (2000)313-316.
[5] J. Y. Wang, J. J. Zhang, and X. Yao, J. Alloy. Compd. 505(2010)783–786.
[6] X.G. Tang, K.H. Chew, and H.L.W. Chan, Acta Mater. 52(2004)517-523.
[7] X.G. Tang, J. Wang, and H.L.W. Chan, J. Crystal Growth, 276(2005)453-457.
[8] X. G. Tang, X. X. Wang, and H. L.W Chan, Solid State Commun. 136(2005)89-93.
[9] N. Y. Chan, G. Y. Gao, Y. Wang and H. L.W. Chan, Thin Solid Films, 518(2010)e82-e84.
[10] W.F. Qin, J. Xiong, J. Zhu, J.L. Tang, W.J. Jie, and Y.R. Li, J. Mater. Sci. 43(2008)409-412.
[11] J. Garcia-Barriocanal, Rivera-Calzada A, M. Varela, Z. Sefrioui, E. Iborra, C. Leon, and S. J. Pennycook, J.Santamaria, Science, 321(2008)676-680.
[12] S.U. Adikary, AL. Ding, and H.L.W. Chan, Appl. Phys. A. **75**, (2002) 597-600.
[13] S. Sheng and C. K. Ong, Appl. Phys. Lett. 44(2011)165-170.
[14] X. G. Tang, Q. X. Liu, L. L. Jiang, and A. L. Ding, Mater. Chem. Phys., 103 (2007)329-333.
[15] S.Z. Li, Y.Q. Yang, L. Liu, W.C. Liu, S.B. Wang, Physica B 403 (2008) 2618–2623.
[16] J.Z. Xin, C.W. Leung, H.L.W. Chan, Thin Solid Films 519 (2011) 6313–6318.

© (2012) Trans Tech Publications, Switzerland
doi:10.4028/www.scientific.net/AMM.164.52

Effection of Wood Extractives on Burning Time of Fuel for Add-on Bioenergy

PENG Wan-xi[a], CUI Le

School of Materials Science and Engineering, Central South University of Forestry and Technology, City Changsha 410004, P.R. China

[a]correspondent author's email: pengwanxi@163.com

Key words: Wood extractives; Burning time; Add-on bioenergy; Fuel

Abstract. In order to explore the application prospects of wood extractives in the biomass energy, the several wood extractives were isolated by organic solvent. The results of functional analysis suggested that these wood extractives could accelerate benzene-alcohol's burning, but played a certain role in inhibiting ether's burning. This reslut revealed that the wood extractives had huge potential applications in the field of add-on bioenergy.

Introduction

With the rapid development of population and economy, the demands for energy were quick enhanced increasingly, especially for fuel energy [1]. However, the resources of traditional fuel energy was become dwindled quickly, and the pollution to the environment by burning traditional fuel energy was more and more serious [2]. Wood was the most environment friendly materials to human, accompanied with the features of natural appearance, beautiful pattern, inexpensive, abundant and low energy consumption, and so on. Basing on the availability and regeneration, lots of scientists, politicians and economists gave a high evaluation to wood resources again [3]. Initially, wood was mainly used for burning, furniture and architecture. As a natural-growed organic, wood had the primary group of cellulose, hemi-cellulose and lignin, moreover, wood also contained a certein amount of components, which were generally referred to extractives, extraction material, leaching composition, inclusion, non-cell wall components [4]. Therefore, the influence of wood extractives on burning time of organic solvents were anlyzed, presenting a new research direction for new energy.

Materials and methods

Test materials. The wood of China fir(*Cunninghamia lanceolata*), Masson pine(*Pinus massoniana*), bamboo(*Phyllostachys pubescens*), poplars from Italy were collected from Central South University of Forestry and Technology. Then these wood samples were smashed into powders by using FZ102 Disintegrator suitable for plant (Tanjing Taisite Ins. Corp., China), and 40-60 mesh powders were sieved out using AS200 Sieving Instrument (Made in America). Benzene, ether and ethanol in chromatographic grade were chosen for the present experiment.

Test Methods. Taking eight powder samples from each species wood, each weight 20g. Five wood powder samples were treated by ether extraction, and the other three samples were extracted treated by benzene/alcohol extraction. The benzene/ethanol extractives was obtained from 20 g above-mentioned powders in 150ml benzene/ethanol solution under the condition: temperature

80°C, time 1 hour, 2 hours, 3 hours, respectively. The benzene/ethanol solution was mixed according to ratil: $V_{ethanol}$ /$V_{benzene}$ =2. The ether extractives was obtained from 20 g above-mentioned powders in 150ml ether solution under the condition: temperature 20°C, time 3 hours, 7 hours, 9 hours, 20 hours, 24 hours. Then took 20ml for each extractives in the bowl, direct ignition, and record the burning time.

Results and analysis

The results. After direct burning test, the burning time was observed (shown in Table 1 and Table 2, respectively).

Table 1 Burning time of wood benzene/alcohol extractives [s]

species of wood	1h of Extraction time	2h of Extraction time	3h of Extraction time
China fir	246.62	234.07	232.58
Masson pine	230.73	205.04	202.51
Bamboo	234.32	210.95	207.14
Poplars from Italy	280.45	247.39	228.04

Table 2 Burning time of wood ether extractives [s]

species of wood	3h of Extraction time	7h of Extraction time	9h of Extraction time	20h of Extraction time	24h of Extraction time
China fir	225.06	200.26	204.50	201.33	216.68
Masson pine	348.74	314.41	365.27	229.51	231.62
Bamboo	362.31	381.98	307.87	265.70	368.76
Poplars from Italy	327.10	384.58	370.95	343.67	426.89

Results and Analysis. It was deduced from Table 2, at 80 °C, as the extraction time become longer, the burning time of wood benzene/alcohol extractives from China fir, Masson pine, bamboo and poplars from Italy are getting shorter. This result suggested that wood benzene/alcohol extractives from China fir, Masson pine, bamboo and poplars from Italy can promote burning.

It was observed from Table 1, at room temperature, accopanied with the longer extraction time, the burning time of poplars from Italy wood ether extractives was longer, suggesting that poplars from Italy wood ether extractives can play a significant role in inhibiting burning. The burning time of China fir wood ether extractives have a shorten trend, suggesting it plays a role in promoting burning. When extraction treatment for 9h, the burning time of Masson pine wood ether extractives reaches the longest, suggesting that when the extraction time was less than 9 hours, the Masson pine wood ether extractives can inhibit burning, when the extraction time was more than 20 hours, the Masson pine wood ether extractives can promote burning. When extraction treatment for 7h, the burning time of bamboo ether extractives reaches the longest, suggesting that bamboo ether extractives plays a role in inhibiting burning at that time.

By Comparing Table 1 and Table 2, It was deduced that the longest burning time condition is 24h extraction treatment for poplars from Italy wood extracives, whose burning time is 426.89 s. As the extraction time becomes longer, the overall burning time also become longer than others.

Conclusions

The analysis result revealed that as the extraction time become longer, the burning time of wood benzene/alcohol extractives become shorter; and in some species, the wood ether extractives become longer accompanied with longer extraction time. It can be deduced that benzene/alcohol extractives can play a role in promoting burning, and ether extractives can play a role in inhibiting burning. Further researches should be carried out to find out what kind of ingredients in the extractives can promote or inhibit the burning.

Acknowledgements

This work was financially supported by the Project Supported by National Natural Science Foundation of China (No.31170532), Program for New Century Excellent Talents in University (No.NCET-10-0170), A Project Supported by Scientific Research Fund of Hunan Provincial Education Department (No.10A131), the Key Project of Chinese Ministry of Education (No. 211128).

References

[1] http://baike.baidu.com/view/1383160.htm

[2] http://baike.baidu.com/view/25178.htm

[3] Roger Lowell. Beijing: China Forestry Publishing House, 1998

[4] P Wanxi, ZH Tonglin, ZH Zhenzhen, F Zhicai, L Kaifu, L Niancun. Forestry Science and Technology, Vol.18 (2004), p.6

© (2012) Trans Tech Publications, Switzerland
doi:10.4028/www.scientific.net/AMM.164.55

Orthogonal Analysis on Hardness of Nickel/graphite Sealing Coating

ShuPing Song [1,a], Chao Li [2,b], ZhaoHui Ji [3,c]

[1]Airport College, Civil Aviation University of China, Tianjin 300300, China

[2]Huludao Special Equipment Supervision and Testing Institute, Huludao 125001, China

[3]Tianjin Key Lab for Aircraft Airworthiness and maintenance, Civil Aviation University of China, Tianjin 300300, China

[a]spsong@cauc.edu.cn, [b]hldlc@yahoo.com.cn, [c]zhji@cauc.edu.cn

Keywords: HVOF; sealing coating; orthogonal analysis; hardness.

Abstract. Ni/Graphite seal coating was fabricated by flame spraying technology and the effect of oxygen pressure, the powder feeding rate and spraying distance on the coating hardness was investigated base on the orthogonal regression experimental design method. Analysis of orthogonal calculation results suggest that powder feeding rate is the key spraying influential factor valuing 140.884 which affects coating hardness; both oxygen pressure and spraying distance can be considered as secondary factors; the analysis of cross-sectional microstructure shows that the coating hardness value increases with the increase of graphite content; during coating deposition process, the content of graphite in the coating will change when adjusting the flame spraying parameters, which furthermore leads to that the coating hardness changes with variation of flame spraying parameters.

Introduction

Sealing coating is also called clearance controlled coating, which is used for gas path seal, thus reducing the gas leakage, reducing fuel consumption, increasing the surge margin, elevating the efficiency of compressor and turbine. Sealing coating is one of the most widely used and most important coatings in aircraft engines[1-3]. Nickel/graphite seal coating is widely applied in dynamic seal of aero-engine compressor, for the fabricating technology is simple and the safe in usage[4-6].

Hardness is one of the most important technical indicators of the nickel/graphite seal coating. As for flame spraying, spraying power, powder feeding rate, spraying distance, the cooling gas flow, the oxidation of spray flame flow are the main factors affecting the nickel/graphite coating hardness. Therefore, it is imperative to investigate the effect of spraying technology parameters on the coating harness comprehensively. Our investigations concerning both orthogonal experimental design and corresponding spraying technology are focused on the effect of flame spraying technology on coating hardness. Meanwhile, orthogonal method was employed to calculate the influencing factor of each spraying parameters on coating hardness. The corresponding investigation conclusions can be considered as guidance in industrial production.

Test material and method

Sparing materials and equipments. 45# steel was selected as the coating substrate. The surface of the specimen was cleared by acetone prior to spraying, then grit blasting with 36# white corundum sand was applied for rough treatment on the surface of the substrate. Bond coat layer is composed of nickel-clad aluminum composite powder, with nominal composition Ni_5Al and powder particle diameter range is 45-90μm. The thickness of bond coat layer was controlled within 0.05-0.17mm. Nickel/graphite coat layer is composed of nickel-clad graphite composite powder, with nominal composition $Ni_{15}C$ and powder particle diameter range is 30-90μm. The thickness of Nickel/graphite coat was controlled within 1.5-2.0mm. In order to get rid of the moisture, spraying powder was treated in the oven drying for 2h in the environment of 100℃. Spraying parameters can be seen in

Table 1. The fabrication equipments consisits of 6P flame spraying gun, a 6C control cabinet, a 2214 powder feeder produced by Praxair&Tafa company. Six-axis robot produced by ABB company was employed to control the movement of spraying gun, in order to ensure the accuracy of the spraying parameters.

Orthogonal Experimental Design. Various factors affects the flame spraying coatings, including the gas pressure/flow rate, combustion gas pressure/flow, feeding gas pressure/flow, the cooling gas pressure/flow, spraying distance, powder feeding rate and so on. Based on our preliminary investigation experience, three major factors were chosen to continue our research: oxygen pressure, powder feeding rate and spraying distance. In the investigation of the effects of these three factors on coating hardness, three levels of each factor were selected to establish the orthogonal test, that is, L9 (33) three factors and three levels orthogonal arrangement test, as can be seen in Table 1 and Table 2.

Table 1 Factor level table

Factor level	A powder feeding rate R/r.m.p.	B spraying distance D/mm	C oxygen pressure P/psi
1	10	170	30
2	14	220	40
3	18	250	50

Table 2 L9(33) orthogonal test

serial number	1	2	3	4	5	6	7	8	9
A	1	1	1	2	2	2	3	3	3
B	1	2	3	1	2	3	1	2	3
C	1	2	3	3	1	2	2	3	1

Coating performance test. Prior to the tests, coating surface was polished smooth by grinder machine(processing thickness no less than 0.30mm) in order to eliminate the effect of nickel/graphite coating surface roughness on coating hardness. TH320 whole Rockwell hardness tester produced by Time company was employed to test the coating hardness. HR15y was selected for hardness scale indenter(The indenter is a hardened steel ball with diameter 12.7mm, weight load 15kg), the pressure was maintained for 5s. The hardness tests repeated for five times for each sample and the average hardness of five values was considered to be the coating hardness value. The coating microstructure was analyzed by vertical smart materials microscope, which typed Axio Imager. A1m and is produced by CARL ZEISS, Germany. The binary method in the Chinese image analysis system was employed to calculate the graphite volume fraction in the coating. While preparing for the testing samples, graphite may peel off from the coating, which may lead to test results distortion. In order to avoid this, vacuum impregnation process was employed to inlay nickel/graphite coating and the inlay material was 12-hour- curing cold mounting epoxy resin.

Test results and discussion

Hardness test results and data analysis. The nickel/graphite coating hardness test results can be seen in table 3, from which we can come to the conclusion that the hardness value of NO.2 ranks the first, valuing 81.7HR15y; the corresponding powder feeding rate is 10 r.m.p.， spraying distance is 220mm，oxygen pressure is 40psi.While the hardness value of NO.9 is the minimum, valuing 12.1HR15y; the corresponding powder feeding rate is 18 r.m.p.，spraying distance is 250mm，oxygen pressure is 30psi. The orthogonal analysis results can be seen in table 4, considering the construct statistic F in which we can come to the conclusion that the value of the A ranks the first valuing 140.884, as a result, it is considered as the main influencing factor; on the other hand, the values of B and C were 2.462 and3.820 respectively, both of which can be considered as negligible secondary factors. All the data above well explains that the most important factor which affects the coating hardness is the powder feeding rate, while the influencing factors of spraying distance and oxygen pressure are rather limited, just affecting the economy of fabrication and coating quality. All these above also confirm that esting result that when the powder feeding rate is the minimum value,

the coating hardness value is the highest value; when powder feeding rate is the maximum value, the coating hardness value of the lowest; all the hardness values tends to descending values with the increase of powder feed rate.

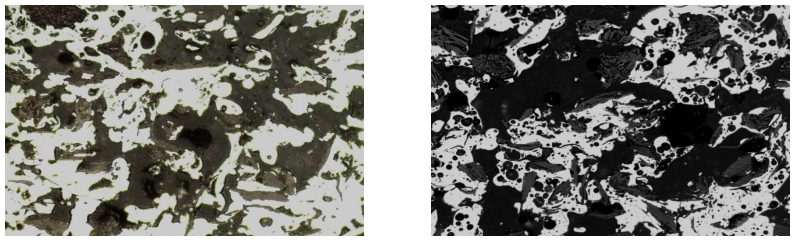
Table 3 Hardness test results

serial number	Hardness （HR15Y）					Average value
1	66.4	68.2	67.9	69.4	67.5	67.9
2	79.6	78.4	83.2	84.4	82.9	81.7
3	72.4	73	72.4	73.3	74.8	73.2
4	69.4	71.8	68.8	72.4	67.6	70.0
5	58.6	57.1	54.7	57.1	55.9	56.76
6	58	58.9	59.2	57.1	64	59.4
7	48.4	56.8	51.7	55	54.1	53.2
8	23.2	27.4	28.3	28.6	25.6	26.6
9	11.9	12.9	12.5	13.4	10.4	12.1

Table 4 Orthogonal analysis results

Source	I square	df	Mean Square	F	Sig.
Model	31822.669	7.0	4546.096	62.174	0.016
A	30903.986	3.0	10301.329	140.884	0.007
B	360.077	2.0	180.039	2.462	0.289
C	558.606	2.0	279.303	3.820	0.207
error	146.238	2.0	73.119		
totalling	31968.907	9.0			

Coating microstructure analysis. Through observing the microstructure of coatings fabricated by technology 2 and technology 9, as can be seen in Fig.1(a) and Fig.1(b), a conclusion can be drawn that the metallic nickel forms the coating skeleton which ensures the bonding strength of the coating system. While the gray part distributing within nickel skeleton are graphite particles is with low hardness value, low shear strength and low friction coefficient, which ensures the abrasive resistance of the coating. The black part is the porosity of the coating. The significant difference in the cross-section microstructure of coatings fabricated by technology 2 and technology 9 lies in the graphite content. Two-value method was employed to calculate the volume content of graphite in nickel/graphite coating and the corresponding result shows that graphite volume contents of coatings fabricated by technology 2 and technology 9 technology are 50% and 62% respectively.



（a）Technology 2 （b）Technology 9

Fig.1 Cross-section microstructure of nickel/graphite coatings（200X）

Graphite loss in nickel/graphite coating is mainly that graphite particles are oxidized and burned into gas during spraying powder being heated, as well as graphite loss with the splashing of the spray powder during deposition process. However, the graphite loss with the splashing of the spray powder will not cause changes of the graphite content in the coating, so what affects the graphite content is the oxidation and combustion. The leading conditions of graphite oxidation and combustion are temperature and oxygen. Nickel/graphite particle is a composite particle with core/shell structure, one of the major role of the shell is to protect the coated particles. Although the temperature of spraying flame is about 2600℃, it is still hard for the nickel-coated graphite particles to rise to a extremely high temperature in such short period of time. However, the temperature can still make thin nickel layer,

on the surface of graphite, semi-melt or even entirely melt. Part of oxygen comes from the remaining oxygen in the spraying flame stream, another part comes from atmosphere oxygen which contacts the external flame stream. Thus, part of graphite will be consumed because of oxidation and combustion in such short period of time, which well explains that the combustion loss of graphite occurs in the overall flame stream during flame spraying[7].

The flight speed of particles during flame spraying is generally 30-45 m/s, so Ni/graphite particles travel through the spraying gun in 3 to 8×10^{-3}s during flame spraying process. The time is so short that the changes of spraying technology has a very limited effect on the oxidation and combustion of graphite, thus, changes of spraying technology has a very limited effect on coating hardness. During flame sparing, the amount of graphite oxidation and combustion loss is certain in each unit of time, so the coating hardness can be degraded through elevating the powder feeding rate. Therefore, powder feeding rate is the main factor which affects the coating hardness.

Summary

Orthogonal experiment results show that the oxygen pressure, powder feeding rate, spraying distance are the three spraying parameters which affect the fabrication of nickel/graphite seal coating by flame spraying. Analysis of orthogonal calculation results suggest that powder feeding rate is the key spraying influential factor valuing 140.884 which affects coating hardness. In the industrial production, nickel/graphite seal coating with different hardness can be achieved through adjusting powder feeding rate. However, the influential factors of oxygen pressure and spraying distance are 2.462 and 3.820 respectively, both of which can be considered as secondary factors, which just affect the economy of fabrication and coating quality in the industrial production.

The analysis of cross-sectional microstructure of the coating shows that the coating hardness is closely related to the graphite content, the higher the content of graphite, the higher value of coating hardness. Through analysis of the flame spraying technology characteristics, a conclusion can be drawn that, by elevating powder feeding rate, the proportion of graphite burning loss can be reduced, thereby increasing the graphite content of the coating powder coating deposition process, reducing the hardness of the coating. Therefore, powder feeding rate is the main factor affecting the coating hardness.

References

[1] S.M. Laio,Thermal Sprayed Sealing Coating for the Control of Running Clearance between Rotor and Stator in Aero engine[J]. Air plasma process technology, S1, (1995), p. 53-55.

[2] B. Hao, C.G. Li, Application of Surface Coating Technologies to Aeroengines[J]. Aeroengines, 30(4), (2004), p. 38-40.

[3] H.G. Wang, Criteria for Analysis of Abradable Coatings[J]. Surface and Coatings technology, 79(1-3), (1996), p. 71-75.

[4] P. Dowson, M.S. Walker, A.P. Watson, Development of Abradable and Rub-tolerant Seal Materials for Application in Centrifugal Compressors and Steam Turbines[J]. Sealing Technology, 12, (2004), p.5-10.

[5] J.L. Wu, A Novel Ni/C Composite Powder and Its Derived Thermal Sprayed Coating[J]. The Chinese Journal of Process Engineering, 7(6), (2007), p.1221-1228.

[6] Q.Y. Hou, L.X. Guo, Research on Process of Nickel-Graphite Coating with Flame Sparing[J]. Manufacturing Technology & Machine Tool, 8, (2010), p.97-99.

[7] Y.G. Yu, Graphite Content Change of Powders for Abradable Seal Coatings during Flame or Plasma Process[J].Thermal Spray Technology，1(1)2009, p.20-23.

© (2012) Trans Tech Publications, Switzerland
doi:10.4028/www.scientific.net/AMM.164.59

Effect of laser processing on electroless copper deposition on modified plastic

Xiao Peng[1, a], Kaiyong Jiang[2,b]

College of Mechanical Engineering and Automation, Huaqiao University,Xiamen,China

[a]peng_xiao_001@163.com, [b]jiangky@hqu.edu.com

Corresponding author: Email address: jiangky@hqu.edu.cn.

Keywords: Laser processing; Electroless copper deposition; Modified plastic

Abstract. Copper was selectively deposited on modified plastic without the palladium-catalyzed process. Laser direct writing was used to create the selective seeds.The effect of laser processing on the electroless copper deposition was investigated. Thus the morphologies and compositions of the sample before and after laser processing were investigated by means of sanning electron microscopy(SEM) equipped with an energy dispersive X-ray spectrometer(EDX) and X-ray photoelectron spectroscopy(XPS). The relationship between laser pulse frequency , scanning velocity and the topography of the deposited copper lines were also discussed.

Introduction

The conventional electroless copper deposition procedure involves pretreatment, activation or seeding,and plating.The important step in electroless deposition process is the activation or seeding of the dielectric substrate prior to metal plating. The traditional seeding process consists of either a two-step method using successively solution of $SnCl_2$ and then activation solution of $PdCl_2$ or a one-step method using a colloidal mixture of $SnCl_2$ and $PdCl_2$[1]. However,those methods are expensive and could cause environmental problems. So lots of efforts have been tried to find new activation method[2-4]. In these paper, laser induced activation was used to produce the circuit pattern on polymer substrates and then deposit the copper selectively via the electroless copper plating without the palladium-catalyzed process. Laser-assisted activation is a noncontact, maskless, low-temperature, selective, and relatively simple process.Technology process as follow: graphic design → laser surface treatment → electroless copper deposition. Laser surface treatment plays a key role in this process. The morphologies and microstructures and compositions of the sample before and after laser processing were investigated by means of sanning electron microscopy(SEM) and X-ray photoelectron spectroscopy(XPS). The influences of laser pulse frequency on the topography of the deposited copper lines were discussed. The action of laser processing in the activation-free electroless plating of copper were studied.

Experimental methods

The fiber laser with wavelength 1064nm was used to treat the sample, and the spot size of laser beam was 80μm. After laser irradiation, the sample was dipped into the 5%NaOH solution and cleaned with ultrasonic washer for 10 minutes,and then washing it with running water. Finally, the irradiated sample was immersed in an electroless copper plating bath containing formaldehyde as the reducing agent for 2h at 60℃, the PH value was 12.5. The morphologies and microstructures

and compositions of the sample before and after laser processing were investigated by means of sanning electron microscopy(SEM) and X-ray photoelectron spectroscopy(XPS). The surface roughness of the sample was measured by Roughness Measuring Instrument.

Results and discussion

Effect of laser treatment on plastic surface morphology. SEM graph of before and after laser irradiation were showed in Fig. 1. On the rignt,the surface of sample was smooth originally(Ra=0.514); the left of the sample which was treated by the laser with numerous cavities and protrusions (Ra=3.236). The most reasonable cause may be explained that laser irradiation induce the breaking of the molecular chain and the cross-linking of the polymers. At the same time,the high temperature lead to the surface melting and rapid solidification. Fig.2 shows the surface roughness of the sample which was treated by different laser power. It was found that with the increase of laser power, surface roughness also increased. This is due to the greater laser power, the more energy reaching the surface, high-energy increases the surface roughness.It is just the rough surface which ensure the excellent adhesion between the copper deposit and substrate.

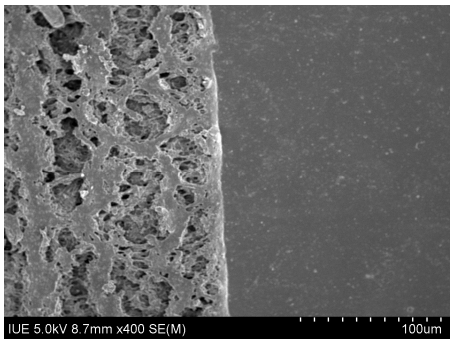


Fig.1 SEM graph of plastic

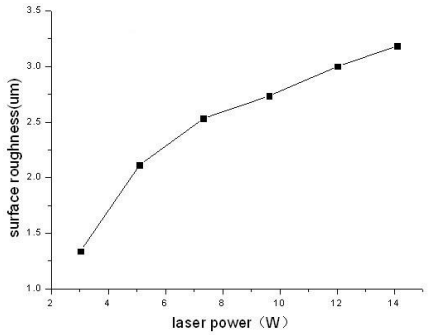
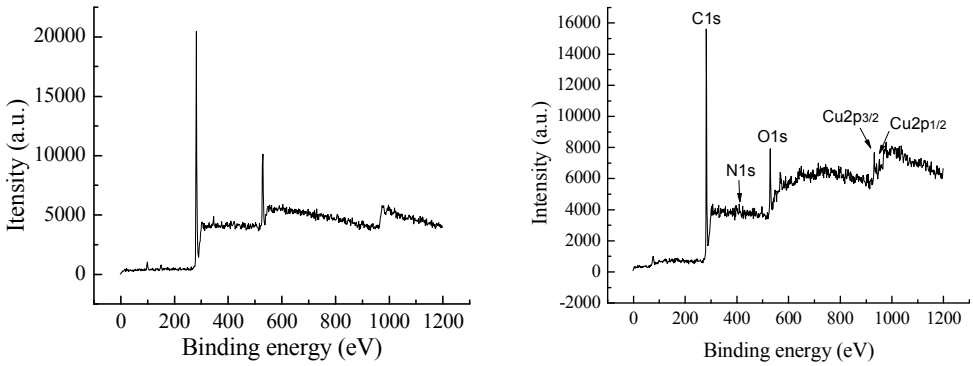


Fig.2 Laser power vs. the surface roughness

XPS analysis of the sample before and after laser processing. We used XPS to analyzed elements on the surface of the untreated and treated sample. Fig.3 gives XPS spectrum on the surface before and after laser processing. It was clearly showed that the characteristic peaks of Cu appeared in Fig3(b). It indicate that laser irradiation result copper or copper oxide on the substrate surface.Fig .4 shows the main and the satellite peaks of Cu $2p_{3/2}$ and Cu $2p_{1/2}$ of the sample. These spectra are normalized based on intensity of main peak of Cu $2p_{3/2}$ .The peak of Cu $2p_{3/2}$ is related to Cu_2O or Cu. Cu_2O and Cu connot be resolved by this deconvolution because their binding energies are very close and are different by only 0.1Ev. One can distinguish them from the position of their LMM-2 auger transition in XPS spectra which are 568eV and 570eV for Cu and Cu_2O respectively[5]. There is a peak at about 570eV in the XPS spectra of our samples. According to above mentioned fact,one can conclude that peak in the Fig .4 is related to Cu_2O.



(a) (b)

Fig.3 Full XPS spectra of the sample: (a) before laser treated; (b) after laser treated

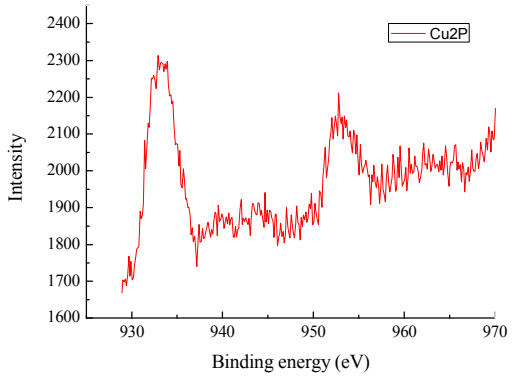


Fig.4 Main and satellite peak of Cu $2p_{3/2}$ and Cu $2p_{1/2}$

From the XPS spectra, the concenrtration of carbon, nitrogen,oxygen can also be calculated ,and the results are listed in Table 1.After laser processing, the concentrationi of C increased while other element concentration decreased ,indicating that a carbon-rich surface was generated after laser processing.It was worthwhile to note that after the laser processing the concentration of Cu change from 0 to 0.98. This may be explained that before the laser irradiation, the copper content of the substrate surface was few, and the analytical depth of XPS measurements is on the order of 50nm. With the decline of N, O, Si and Ca content, the copper content of the sample surface was correspondingly increased.

Laser irradiation results in Cu_2O occurring on the surface. The answer is that laser irradiation induce the organometallic compound which contained in the modified plastic decoposition due to the weak bond between the metal ioin and the organical of the compound. In the process, because of the thermal effect of the laser, copper was oxidized into Cu_2O at high temperature which would act as catalysts for subsequent electroless metal deposition.

Table 1 Atomic concenrtration before and after laser treated

sample	C%	N%	O%	Si%	Ca%	Cu%
Before laser treated	81.09	1.44	15.18	2.00	0.29	0.00
After laser treated	86.58	0.72	11.22	0.50	0.01	0.98

The influence of laser pulse frequency on the topography of the deposited copper lines. Fig.5 shows the OM images of the deposited copper lines obtained at different laser pulse frequency.It is clear that the lines were more uniform and compact with high pulse frequency. When the pulse frequency equal to 25KHZ, the plated line was disconnected; When the pulse frequency is 50KHZ, the edges of the plating line was jagged, not uniform; When the pulse frequency is 100KHZ, we can get a smooth, uniform plating line.

The laser pulse frequency affected the topography of the deposited copper lines. Parameter β in Eq.1 was used to describe the continuity of copper lines,where s is the distance between the two adjacent copper points, D is the spot size of laser beam which is demonstrated in Fig. 5.

$$\beta = \frac{D_d - S}{D_d} \times 100\% \tag{1}$$

When β is less than 0, the line was point arrangement and disconnected； when β is equal to 0, tangency circle connected into a line； when β is more than 0, there were covered area between adjacent points. The relationship between the S and the pulse frequency can be writtern as

$$s = \frac{v}{f} \tag{2}$$

The deposition line to be continuous, β needs to be less than 0, so $\frac{v}{f} < D_d$. To get a smooth, uniform line, β need more than 50%.

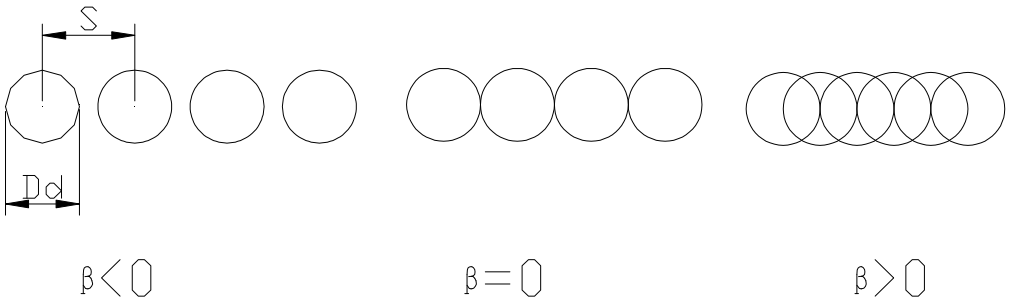


Fig.5 Parameter β was used to describe the continuity of copper lines(a)β<0 ; (b) β=0; (c) β>0.

The scanning velocity in the Fig.6 was 3.5m/s. From the above equation it can be calculated that only when the pulse frequency f is greater than 45KHZ, the continuous line can be achieved. So When the pulse frequency equal to 25KHZ, the plated line was disconnected; When the pulse frequency is 50KHZ,and S approximately is equal to D, the edges of the plating line was jagged; when β more than 50%,we can get continuous and smooth line as in the Fig.6(c).This equation may be helpful in choosing the laser pulse frequency when knowing the scanning velocity and the spot size of laser beam.



(a) (b) (c)

Fig.6 The copper lines with different laser pulse frequency: (a)25KHZ; (b)50KHZ; (c)100KHZ

Fig.7(a) shows the optical image of the copper patterns made by this method which shows good selectivity. The width and the distance between the lined were 80um and 100um,respectively. The EDX analysis results in the Fig.7(b) demonstrate that the line consists of metallic copper, free of impurities.The appearance of gold peaks is because of the need of the SEM operation.

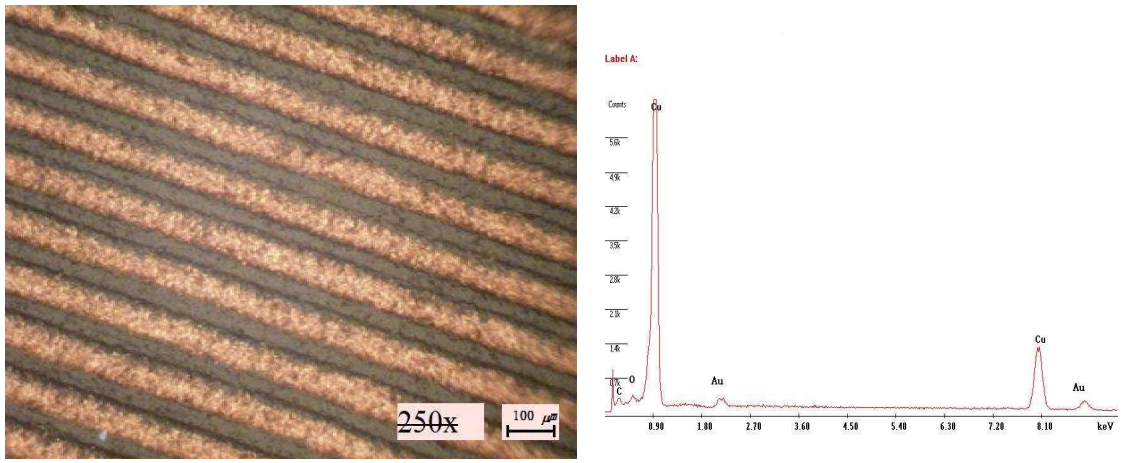


Fig.7 (a) optical photograph of copper patterns; (b) EDX result of the copper pattern

Conclusions

The laser irradiation increased the surface roughness of plastic substrate which enhanced the mechanical meshing between the Cu plating and substrate to improve the adhesive strength. XPS analysis results showed that after laser irradiation, the surface of the modified plastic substrate containing copper oxide due to organometellic compound decoposition, which will serve as the catalytic center of the subsequent electroless copper plating. The topography of the deposited copper lines greatly depend on the choice of laser processing parameters, such as laser pulse frequency, scanning velocity and laser spot size. So the accurate match among those paraments should be calculated before the procedure.

Acknowledgments

This work is supported by the national natural science foundation of China (NSFC) (Grant No.50975100)

References

[1]. WANG Sen Lin:Chinese Journal Applied Chemistry,Vol.20(2003).No.5,p.491

[2]. G. Zhao, H.M.P.H: Proceedings of SPIE, Vol. 3933(2000)505-510.

[3]. Su, W:Applied Surface Science, Vol.257(2011)No 18, p. 8067-8071.

[4]. Chen, D: Applied Surface Science, Vol.246(2005)No.1-3,p. 167-173.

[5]. T.Ghodselahi, M.A. Vesaghi:Applied Surface Science, Vol.255(2008), p. 2730-2734.

© (2012) Trans Tech Publications, Switzerland
doi:10.4028/www.scientific.net/AMM.164.65

Influences of Process Parameters on the Forming of YAG Phase

XiuHui Wang[1,a], JiaTai Dong[1,b], Ye Cao[1,c], GuoQuan Zhao[1,d], Hong Gao[1,e] and JinLong Yang[2,f]

[1]Liaoning Key Laboratory for fabrication and Application of Super-fine Inorganic Powders, Dalian Jiaotong University, Dalian, Liaoning, 116028, China

[2]Department of Materials Science and Engineering, State Key Lab of New Ceramics and Fine Processing, Tsinghua University, Beijing 100084, China

[a]dl_wangxh@ditu.edu.cn, [b]jiatai_3102@163.com, [c]xuanerxuanerne@gmail.com, [d]reddevils.utd@gmail.com, [e]taoci@djtu.edu.cn, [f]jlyang@mail.tsinghua.edu.cn

Keywords: yttrium aluminum garnet; ball milling; mineralizer; solid-state reaction; powders

Abstract: Submicron single-phase yttrium aluminum garnet ($Y_3Al_5O_{12}$, YAG) powders were fabricated by solid-state reactive heat-treating a mixture of pyrolysis product, heat-treating isopropyl aluminum at 500℃, and yttria (Y_2O_3) powders. The powders were mixed by ball milling for 2~3 h doped with 5wt% aluminium fluoride (AlF_3), and then heat-treated at 1200℃ for 2~5 h. Characterized by XRD, mixing the powders by ball milling and doped with AlF_3 lowered the heat-treating temperature and made the forming of YAG phase be single.

1. Introduction

The yttrium aluminum garnet (YAG) has been widely applied in various fields as laser crystal material, for its stable chemical feature, excellent optical and high-temperature mechanical performance. In 1995, A. Ikesue et al demonstrated the feasibility of fabricating polycrystalline Nd:YAG transparent ceramics with optical quality and lasing efficiency parallel to Nd:YAG single-crystal [1]. Owing to the great potential application of YAG ceramics, the heat-treating of YAG transparent ceramics become a heat-issue, and it is necessary to study the synthesis of YAG powders. The general synthesis method mainly includes high-temperature solid-state method, co-precipitation method, hydrothermal method, sol-gel method, spray pyrolysis, solvothermal method, etc.

YAG powders were obtained by direct reaction of Al_2O_3 and Y_2O_3, by conventional solid-state method. Single-phase YAG could be obtained at the temperature of 1500℃ or even higher [2]. In this work, AlF_3, used as mineralizer, was introduced as one of the starting material to be mixed with AlOOH. AlOOH is also an active intermediate product created during the transformation from $Al(OH)_3$ to stable α-Al_2O_3. An amorphous mixture of fine particle size by ball-milling of certain amount of AlF_3 and AlOOH was substituted for conventional α-Al_2O_3 as the starting materials. After the heat-treatment of precursor, the powders were characterized by XRD analysis to detect the phase composition, from which we determined the ideal dispersant volume, ball milling time and amount of mineralizer. Based on the analysis of XRD, the effect of each process can be concluded and a proper way to synthesize single phase YAG powders is determined finally.

2 Experimental

Starting materials include yttria (Y_2O_3) (99.99%, Zibo Jiahua New Materials Resource Co.) , AlOOH (99.999%, prepared) and AlF_3 (AR, Shanghai Sss Reagent Co.) .

Focusing on the influences of dispersing medium, ball milling time and mineralizer amount on YAG phase formation, the experiment was conducted by weighing starting materials at $n(Al^{3+})$: $n(Y^{3+})$ ratio of 5:3, ball milling for mixing, preparing different precursors according to different ball milling dispersant volume, ball milling time and mineralizer amount, heating-treat at 1200℃, characterizing the product.

3 Results and discussion

3.1 Influence of dispersant volume on particle distribution of powders

2.5, 5, 7.5, 10 and 12.5 mL of anhydrous ethanol were added into 50 g of starting materials respectively and then ball-milled for 60 min to find the optimum dispersant usage. The results are shown in Fig. 1.

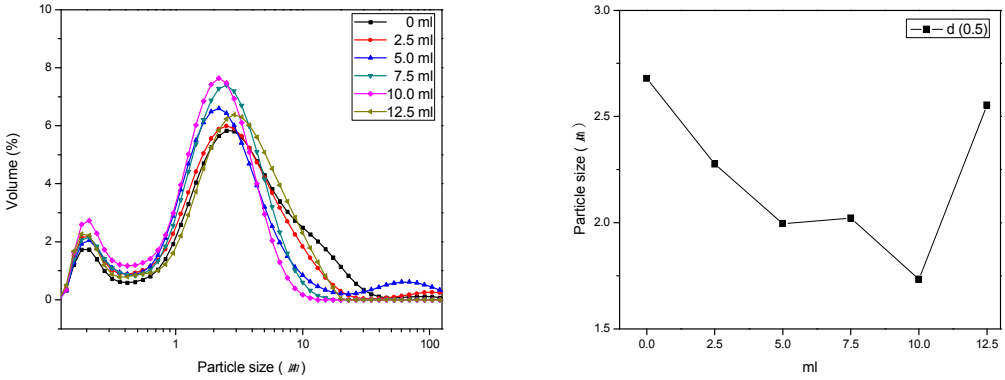


Figure 1 The particle distribution of the powders with different volume of EtOH

Sample obtained without dispersant had average particle size of about 2.7 μm. The average particle size was gradually reduced with the increase of additional volume of ethanol. When ethanol volume was 10 mL, the average particle size could be decreased to about 1.7 μm. The optimum ethanol volume was 10 mL. If higher, part of powders could be wetted during ball milling to agglomerate or even be adhered to tank walls, which would severely interrupt the ball milling effect.

3.2 Influence of ball milling time on the forming of product phase.

Figure 2 shows the phase transformation of the powders (6wt% AlF_3 composition), ball-milled for 30 min, 1, 2, 3 and 4h, respectively, and 10 mL of anhydrous ethanol added, after heat-treating for 5 h at 1200℃.

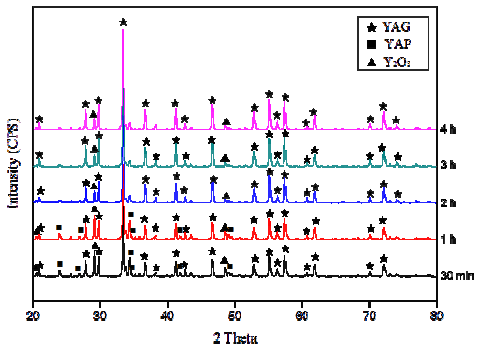


Figure 2 The XRD pattern of the samples calcined at 1200℃ for 5 h by grinding at different times

Others peak number is reduced while YAG characteristic peak becomes stronger gradually, along with the increase of ball milling time. When the powder ball-milled for 2 h before heat-treating, diffraction peak intensity of yttria is gradually decreased. YAP diffraction characteristic peak disappears and YAG phase proportion is increased and reaches the highest value when the powder ball-milled for 3 h before heat-treating.

In the early stage of solid-state reaction, the powder was composed of Y_2O_3 and AlOOH, but as the temperature rise, diffusion of Y^{3+} and Al^{3+} occurred owing to concentration gradient, and they further reacted with each other to produce YAG finally. Since Y^{3+} and Al^{3+} are all trivalent ions, each region always kept electric neutrality during the diffusion process and there was no electron transfer, the solid-state reaction velocity was then mainly dependent on diffusion velocity of Y^{3+} and Al^{3+} [3]. In the ball milling process, the powder activity was improved to be benefit to diffusion. Meanwhile, the ball milling introduced a great deal of crystal defects such as vacancy and dislocation, all of which could accelerate the diffusion of Y^{3+} and Al^{3+} under low heat-treating temperature, to further increase reaction velocity [4]. In addition, after ball milling, the powder generated multiple fresh surfaces, the particle size was decreased and the specific surface was increased which contributed to improving the surface energy of crystal grains and reducing the heat-treating activation energy. As a result, the solid-state reaction can be carried out at low temperature.

After that, the forming of product phase was basically not changed. That is to say, when the powder was ball-milled to a certain extent, particle size and mixing uniformity of the starting material powder were no longer the dominant factors influencing solid-state reaction.

3.3 Influence of mineralizer AlF_3 on the forming of product phase.

The phase formation of the ball-milled powders with 4, 5, 6 and 8 wt% AlF_3 after heat-treating at 1200℃ for 4 h is shown in Fig. 3.

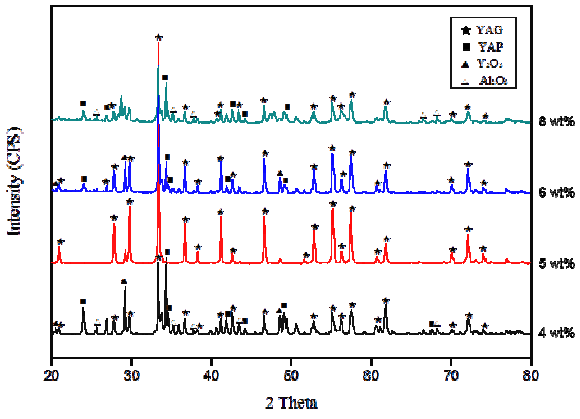


Fig. 3 The XRD pattern of the samples by different amount of AlF_3

It is illustrated that when the amount of AlF_3 is gradually increased from 4 wt%, diffraction peak intensity of YAG phase is obviously enhanced and there are few impurity peaks. When 5 wt% AlF_3 doped, single-phase YAG powder is generated after heat-treating at 1200℃ for 4 h. But the impurity phase is increased and diffraction peak intensity of YAG phase is reduced gradually if more AlF_3 doped. This demonstrates that single-phase YAG can only be obtained with an appropriate amount of AlF_3.

During heat-treating process, along with temperature rise, AlF_3 started to transform into vapor when approaching its sublimation temperature (1291℃). Aluminum molecules diffused to the solid powder surfaces and then collision occurred, which could lead to the fact that the molecules were either adsorbed by the surfaces or reflected to space directly. AlF_3 molecules produced gaseous intermediate compound through chemical reaction and the compound was adsorbed on Al_2O_3 surfaces to release AlF_3 molecules. The whole process could be summarized as γ-Al_2O_3 +AlF_3→{ intermediate compound }→α-Al_2O_3 + AlF_3 [5] . The gaseous intermediate compound greatly increased diffusion speed of Y^{3+} and Al^{3+} in solid-state reaction. The volatile gaseous intermediate compound could not escape rapidly as the reaction was carried out in a sealed crucible, which ensured the continuous reaction. Meanwhile, a large number of high energy defects could be introduced in the crystals in the process. When they were eliminated thoroughly, energy would be released, which helped to overcome nucleation potential barrier and thereby reduced the formation temperature of YAG phase [6]. In a word, the addition of AlF_3 accelerated diffusion of reactants, making it possible that single-phase YAG could be achieved via the reaction at low temperature.

4 Conclusions

By adopting AlOOH, Y_2O_3 and AlF_3 instead of conventional Al_2O_3 and Y_2O_3 powders as starting materials, the influence of the time of ball milling and mineralizer on the forming of YAG phase was explored. Submicron single-phase yttrium aluminum garnet powders were obtained by solid-state reactive heat-treating a mixture of the powders, mixed by ball milling for 2-3 h, doped with 5wt% AlF_3, and heat-treated at 1200℃ for 2-5 h.

Reference:

[1] A. Ikesue , K Kinoshita, K Kamata: Fabrication and Optical Properties of High Performance Polycrystalline Nd:YAG Ceramics for Solid-state Lasers. J. Am. Ceram. Soc. 78(4) (1995), p. 1033-1040

[2] A. E. Siegman: Lasers. University Science Books, Mill Valley, CA, (1986).

[3] Wu Jianpeng, Wang Xinzhen, Huang Jianfeng, etc.: XRD Research of YAG Crystallites powders Prepared by Solid-phase Reaction Method. Journal of Synthetic Crystals. 38(5) (2009), p. 3-4

[4] Li Changqing, ZuoHongbo, Zhang Mingfu, etc.: Fabrication of Transparent YAG Ceramics by Solid-state Method. Journal of the Chinese Ceramic Society. 34(8) (2006), p. 979-984

[5] Li Suoping , Jia Xiaolin, Shang Xuejun, etc.: Reaction Mechanism of Mineralizers in the Preparation of α-alumina Nanopowder. Inorganic Chemicals Industry. 41(5) (2009), p. 19-20

[6] Sang-Ho Lee, Sujarinee Kochawattana: Solid-State Reactive Heat-treating of Transparent Polycrystalline Nd: YAG Ceramics. J. Am. Ceram. Soc, 8(6) (2006), p. 1945-1950

© (2012) Trans Tech Publications, Switzerland
doi:10.4028/www.scientific.net/AMM.164.69

Preparation and ESR properties of silicon nitride nanowires

Jin Chen [1], Xiaogang Wang [1] Haiyan Zhang [2]

[1] Faculty of Materials, Xi'an University of Science and Technology, xi'an, 710054,China
[2] Faculty of Materials, Guangdong University of technology, Guangzhou,510006, China

Keywords: Silicon nitride nanowires; Carbon nanotubes; ESR

Abstract: We prepared Solid silicon nitride nanowires using carbon nanotubes as precursors., Si and SiO_2 were used as raw materials,the reaction was carried out in ammonia atmosphere The structure, phase composition, ESR properties and oxidation resistance of the sample were investigated. The results showed that the sizes of the nanorods are 60–80 nm in diameter and up to several microns in length. In the products α-Si_3N_4 is the main component; the FTIR spectra of the silicon nitride nanowires have blue shift phenomena;The ESR properties show that the as made materials contains a large number of unpaired electrons

1. INTRODUCTION

Silicon nitride and its derivative sialon ceramics continue to be subjected to the sustained attention of ceramics research groups worldwide[1]. Although earlier hopes of utilizing the excellent thermomechanical properties of these materials in such demanding applications as gas turbines were not realized[2,3], the advancements of the last decade have led to implementation of silicon nitride materials in cutting tools[4], bearings[5], turbochargers[6], engine valves[7] and other wear-resistant components[8].

Compared with nanopowders(0 dimensional nanomaterials), the synthesis of one dimensional structure nanomaterials still remain a challenge. Since the discovery of carbon nanotube[,9], efforts have been made on synthesis of one dimensional nanoscale materials by using carbon nanotubes as the precursors. L.T. Sun [10] who prepared the diamond nanowires use CNTs-templated method and proposed a model for growth mechanism of nanorods. Han[11] reported that they synthesized SiC nanorods in a two-step process involving the generation of SiO followed by reacting with carbon nanotubes under N_2 atmosphere. In this paper, we developed a method fabricate Si_3N_4 nanowires using carbon nanotubes as the precursor and ammonia as a reaction gas. This method can prepare Si_3N_4 nanowires at low temperature, which make the production low cost.

2. EXPERIMENTAL

A Synthesis of silicon nitride nanowires

In the first step, the MWCNTs were purified by concentrated sulfuric acid, the CNTs (1.5 g) were boiled for 24 h in 100 ml 95 wt% H_2SO_4 under fluxing; Then they were washed with water and dried at 80 ^oC for 24 h. The mixture of silicon and silicon dioxide powder were spread on the Al_2O_3 boat, and covered with as treaded carbon nanotubes to react. The reaction was carried out at 1500 K for 1 h, at the same time ammonia gas was fed into the tube at a flow rate of 50 sccm to maintain the reactant pressure. After reaction for several hours, the specimens were cooled down in nitrogen. Finally a white woollike material formed at the original nanotube bed.

B Characterization

A X-Ray Diffraction(XRD) with Cu Kα radiation was used at room temperature to identify the phase and the crystal structure. The micro-structure of carbon coated iron nanoparticles was observed by using transmission electron microscope (TEM)(JEM-2010 HR) operating at 200Kv. Q600 DSC / TGA simultaneous, TA companies in the United States was employed to test DSC /

TGA .Test conduction: weight between 1.5-2.0 mg, carrier gas is air, heating rate 20 ^{o}C / min, from room temperature to 800 ^{o}C. A Fourier transform infrared spectroscope was used to examine the surface bond of the nanowires. The dielectric constant of the products was measured using multi-frequency meter (HP-4294A).

3. RESULTS AND DISCUSSION

A Phase analysis

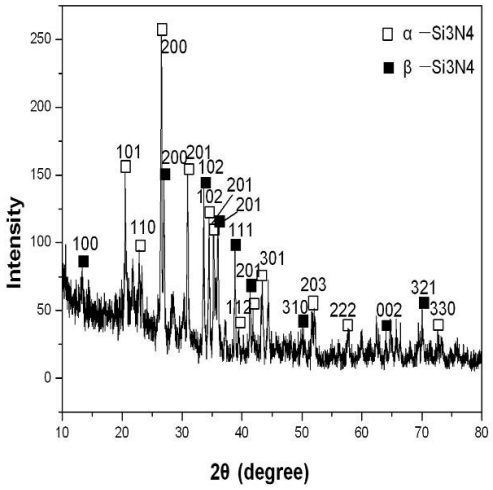


Fig. 1. X-ray diffraction spectrum of silicon nitride nanowries

Figure 1 is an XRD pattern of the products, we can see that only α-Si_3N_4 phase and β-Si_3N_4 phase are detected by X-ray. As can be seen from Fig. 1, the peaks assigned to α-Si_3N_4 (20.5° , 26.6°and 30.9°)are stronger than that of β-Si_3N_4, which indicate the products are mainly α-Si_3N_4. At the same time we can see that there is no peak associated with silicon carbide, graphite, or other crystalline in the XRD pattern.

B Structural and morphology of silicon nitride nanowires

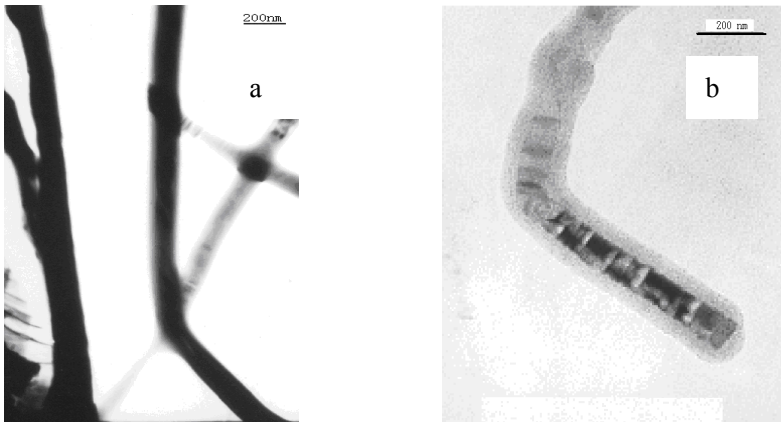


Fig. 2. TEM micrographs of silicon nitride nanowires(a, silicon nitride nanowires; b, growth of silicon nitride nanowire)

Fig.2(a,) are the TEM micrographs of the products-silicon nitride nanowires. They are solid other than the hollow core structure of nanotubes. The diameters of the produced nitride nanowires(about 60-80nm) are significantly larger than the carbon precursors. Fig.2(b) shows the growth of nitride nanowires in the carbon nanotube(40-60nm), it can be seen that nitride start grow at the outlet of the carbon nanotubes. This phenomenon can be expressed simply as follows:

3.3 FTIR spectra of silicon nitride nanowires

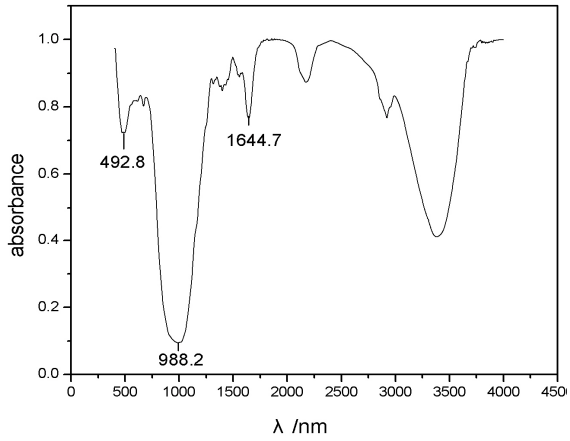


Fig.3. FTIR spectra of the silicon nitride nanowires

The FTIR spectra of the silicon nitride nanowires are shown in Fig. 3, the sample have three main peaks., the peak at 492.8cm-1 is stretching motion of N-Si bonds, the peak at 1644.7cm-1 is flexural vibration of the N-Si bonds, the Si=O stretching bond is observed near 998cm-1. Comparison with block nitride peaks at 481.3 cm-1，989cm-1 and 1599 cm-1 [16]. The infrared spectrum of nano-structure materials has a blue shift phenomena. The reason is that the nano-material's quantum size effects lead to blue shift. Nano-materials have great surface area, surface atoms will have defects and lattice distortion, the bond length of surface atoms different to the body atoms, which makes the nanowire's blue shift of infrared absorption spectrum.

C ESR propriety of silicon nitride nanowires

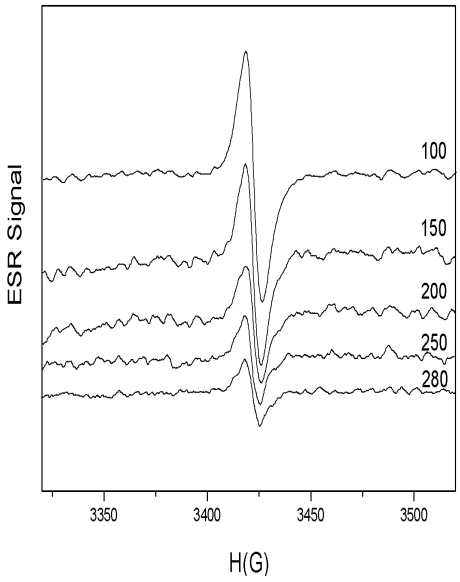


Fig.4 ESR curves of silicon nitride nanowires at different temperature

Fif.4 is the ESR curves of silicon nitride nanowires from 100K-280K, as we can see that at all the temperature range , the ESR spectrum showed obvious symmetrical shape, and the at low temperature(100K) the ESR curves show Higher spectral intensity, this means that at low temperatures, silicon nitride nanowires contains more unpaired electrons.

4. CONCLUSIONS

Silicon nitride nanowires are fabricated using carbon nanotubes as precursors, and the samples mainly are α-Si_3N_4 and β-Si_3N_4. α-Si_3N_4 ; different from the nanotubes, the silicon nitride nanowires are solid materials, at the same time the diameter of nitride is larger than the nanotubes; the sample shows good oxidation resistance, only a little of the nitride can be oxidized in high temperature; The ESR proprieties low temperatures, silicon nitride nanowires contains more unpaired electrons than that of high temperature.

Acknowledgments

This work was supported by the Scientific Research Program Funded by Shaanxi Provincial Education Commission（Program NO. 2010JK676）

References

[1] Frank L. Riley. J Am Ceram Soc.83(2) (2009): 245-265
[2] Guang-Quan Mo, Jian-Shan Ye ,Wei De Zhang. Electrochimica Acta 55 (2009):511–515.
[3] P. Bhandhubanyong, T. Akhadejdamrong. Journal of Materials Processing Technology 63 (1997) : 277-280.
[4] Fei Teng, Shuhui Liang, Buergen Gaugeu, Ruilong Zong, Wenqing Yao. Catalysis Communications 8 (2007) : 1748–1754.
[5] Weiqiang Han , Shoushan Fan, Qunqing Li, Binglin Gu. Appl. Phys. Lett. 71 (1997) : 2271-2273.
[6] She J H, Yang J F, Danel D J, et al. J Am Ceram Soc 86(4)(2003): 738-740.
[7] Zhang Y, Chen Y B, Srinvasarao L, et al. J Am Ceram Soc, 88(1) (2005): 114-120.
[8] A. Diaz, S. Hampshire. J. Eur. Ceram. Soc. 24 (2004) : 413-419.
[9] J.F. Yang, S.Y. Shan, R. Janssen, G. Schneider, T. Ohji, S. Kanzaki. Acta Mater. 53 (10) (2005) 2981-2990.
[10] W. Han, S. Fan, Q. Li, W. Liang, B. Gu, and D. Yu, Chem. Phys. Lett.265(1997), 374-377
[11] L.T. SunT, J.L. Gong, Z.Y. Zhu, D.Z. Zhu, Z.X. Wang, W. Zhang et al. Diamond & Related Materials. 14 (2005): 749-752.
[12] S Ze, S. M, Bell .J Appl Phys. 38 (7) (2009): 2951-295

© (2012) Trans Tech Publications, Switzerland
doi:10.4028/www.scientific.net/AMM.164.73

Gearbox Non-ferrous Metal Bearing Wear Condition Monitoring Based on Oil Analysis

Xufeng Jiang[1, a], Fang Liu[2, b], Pengcheng Zhao[1, c]

[1]Air Force Servece College of PLA, Xuzhou, Jiangsu, 221000, China

[2]Air Force Shanghai Logistics Training Base, Shanghai, 200120, China

[a]jiangziya@163.com (corresponding author), [b]15162167853@163.com, [c]jiangziya70@163.com

Keywords: gearbox, oil analysis, condition monitoring

Abstract. Oil comprehensive analysis technologies, which included oil routine physical and chemical analysis, atomic spectroscopic analysis, ferrographic analysis and filtergram analysis, were used to analyse gear oil samples. The results of atomic emission spectrometry and ferrography showed that the quality of the gear oil were normal. But, the result of filtergram particle analysis showed that the gear oil contained many large-size non-ferrous metal wear particles. So this gear box was likely abnormal or not completed. Thus, The organic synthesis of several particle analysis technology is an effective way to improve machine wear condition monitoring reliability.

Introduction

In one factory, a few using gear oil samples were taken from an important gearbox after which had completed a running-in test. Maintenance staff would like to analyze these samples by oil comprehensive analysis technologies to determine whether the gear oil can continue to use and whether the gearbox wear normally after running-in test.

Oil Analysis Technology

Machinery oil analysis technology mainly covers two major technology areas [1, 2] of oil analysis and wear particle analysis. The former monitors machinery lubricating status and identifies faults caused by insufficient lubrication by monitoring physical and chemical property indexes of oil products; the latter realizes effective monitoring and diagnosis of the friction state by observing size, shape, color, and concentration, etc of wear particles carried in the oil. So far, one mature and perfect oil monitoring system is basically composed of six major technologies [3, 4] of the oil routine physical and chemical analysis, particle counter, atomic emission spectroscopic analysis, infrared spectroscopic analysis, ferrographic analysis and filtergram analysis.

The atomic emission spectroscopic analysis can determine concentration level of wear metal elements, additives and containments in lubricating oil and decide equipment wear degree and position, additive consumption and lubricating oil contamination. It is the core of the oil monitoring and is also routine monitoring means [5-7] of the laboratory. The ferrographic analysis finds out wear and failure mechanism of equipments and parts and analyzes failure causes [8] through micro-observation of size, shape and color, etc of wear particles, containments and metamorphic substances separated from lubricating oil sample. Filtergram analysis, which was developed and improved by the condition examination center of Australia Monash University in the 80's, is a kind

of particle analytical technique. This technique separated all solid particles larger than 3μm, including ferrous metal, non-ferrous metal particles as well as various contaminants and oil metamorphic substances, from gear oil by the acetic acid fiber filter with pore size of 3μm, not by the magnetic field.

Monitoring Result and Analysis

Like most of the gear oil samples, the gear oil samples only slightly darker color, there is no bottom sediments and turbidity. The experimental results show that the physical and chemical indexes of gear oil (viscosity, acid number, etc.) are within satisfied range. And the concentration of metallic elements determined by atomic spectroscopic analysis is the important data to detect machine wear. The data in Table 1 clearly shows that the parts wear metal elements, such as very low concentrations of iron, chromium, tin, copper, lead, nickel, etc., almost not be detected.

Table 1. Metal element concentration

Element	Concentration /ppm	Element	Concentration /ppm	Element	Concentration /ppm
Mo	0	B	0	Cu	0
P	10.4	Si	0.34	Ag	0
Zn	0.16	Mn	0	Ti	0
Pb	0	Cr	0	Al	0
Cd	0	Sn	0	Na	0.1
Ni	0	Mg	0	Li	0
Ba	0	V	0	K	0
Fe	0.54	Ca	0.09		

Routine monitoring data show that the lubricating oil in the gear box can be reused, and the wear state of the gear box seems to be quite normal. The oil sample cleanliness measured by particle counting method was ISO 19/17/16. Although the solid particle pollution level of the oil beyond the required cleanliness (ISO l8/16/13) of the initiative lubricating maintenance, but because of the gear box work in the high pollution environment, therefore, the cleanliness level does not seem to mean any unusual or even failure. But two last numbers 17 and 16 of oil sample cleanliness was little high. This show the number and proportion of large particles in the samples of this oil is a little abnormal. Because atomic spectroscopic analysis can only detect metal wear particles less than 6-8 μm, the particles in the oil samples are greater than 10-20μm of wear particles which was likely undetectable by atomic spectroscopic analysis, and so on oil samples continue to be detected by ferrographic analysis.

The detection results of ferrographic analysis show that there were no large-size wear particles which amount corresponding to its cleanliness values in the gear oil, as shown in Figure 1-2, on the contrary, amount of the wear particles was a little, size was no more than 20-30μm. Seemingly the wear state of the gear box is normal, but the detection of ferrographic analysis showed that there were a small number of non-ferrous metal wear particles in the gear oil (Fig. 2).

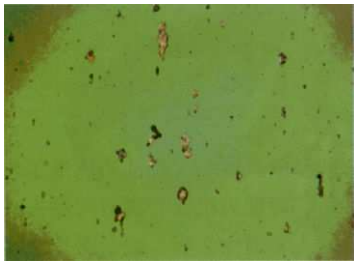


Fig. 1 A small amount of metal wear particles are enlarged by 200 times



Fig. 2 Part of metal wear particles are enlarged by 500 times

Therefore, oil samples continued to be tested by using filtergram analysis techniques. Figure 3-8 showed the result was completely different from which of ferrographic analysis. Depositing on the filter, a large number of large-size non-ferrous metals were mainly copper alloy babbitt wear metal particles. Some particles showed the existence of significant thermal oxidation. These results indicated that the non-ferrous metal bearing in the gearbox had occurred very serious adhesion and cutting wear. Therefore, this gearbox running -in test was likely not normal or not yet completed.

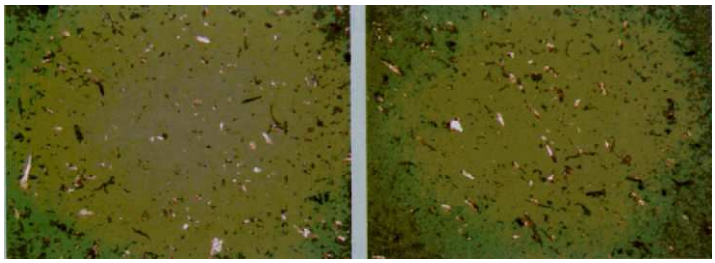


Fig.3-4 A large number of wear particles which deposite on the filter are enlarged by l00 times

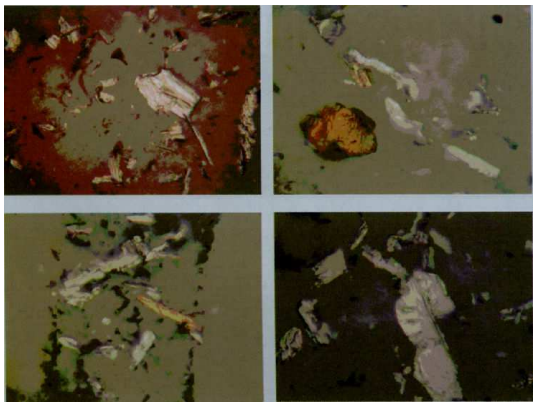


Fig.5 to 8 Abnormal no-ferrous large-size alloy wear particles are enlarged by 500 times

Based on results of filtergram analysis, maintenance staff should immediately check the quality of the installation of the gearbox, and co-operation procedures of running-in test, and cleanness of the gearbox, also check the wear state of the ferrous alloy bearing of the gearbox and other non-ferrous alloy parts. In addition, because the physical and chemical indexes of gear oil were qualified, the gear oil was required be filtered only. After filtered by high-efficiency filters, if its cleanliness standard index would achieve the ISO 16/14/12, the gear oil could continue to be used.

Summary

Several oil wear particle detection techniques have their own characteristics and limitations. Atomic spectroscopic analysis can detect up to 20 kinds of metal elements, so it is useful for monitoring wear and corrosion of the metal friction parts, contamination of the coolant, solvents and suspended dust, as well as identification of lubricant additive component, but not suitable for detecting greater than 6-8 microns of wear particles; ferrographic analysis mainly monitors ferrous wear particles; filtergram analysis can detect ferrous, non-ferrous wear particles and solid contaminants. Therefore, the organic synthesis of above analysis techniques is an effective way to improve the reliability of the wear condition monitoring of machinery and equipment.

References

[1] Li Qiongwei, Mao Meijuan and Chen Yong: China Mechanical Engineering Vol.15 (2004), pp. 272-275.

[2] Zhang Yingtang and Ren Guoquan: Lubrication Engineering No.2 (2000), pp. 65-66.

[3] Li Zhuguo: *Oil Analysis diagnostic techniques* (Shanghai Science and Technology Press Shanghai, 1997).

[4] Xu Bin and Yu Xuejun: Lubricating Oil Vol.21 (2006), pp. 61-64.

[5] Wei Haijun, Yu Hongliang and Guan Delin: Spectroscopy and Spectral Analysis. 4 (2006), pp. 738-740.

[6] Huang Zongping: Metallurgical Analysis No.2 (2006), pp. 43-46.

[7] Zhao Jinwei, Cheng Wei and Feng Yahui: Spectroscopy and Spectral Analysis No.6 (2004), pp. 733-736.

[8] Xiao Hanliang: *Ferrography and its application in machine monitoring and diagnosis* (Beijing People Communication Press Beijing, 1993).

© (2012) Trans Tech Publications, Switzerland
doi:10.4028/www.scientific.net/AMM.164.77

Solar shading performance of different louver shading materials in hot summer and cold winter zone

Zhangkai Li, Jian Yao*

Faculty of Architectural, Civil Engineering and Environment, Ningbo University, Ningbo, China

email: yaojian@nbu.edu.cn

Keywords: Louver shading materials; solar shading performance; building energy.

Abstract. The aim of this paper is to investigate the solar shading performance of louver shading materials. Regression analysis is used to compare the potential performance of horizontal and vertical louver shading materials. Results show that louver shading is not suitable for north facing windows and has little improvement of shading performance in south orientation. For east windows in the west orientation, horizontal louver shading performs well only in summer. Horizontal and vertical shading materials have similar shading performance in summer and winter.

I. INTRODUCTION

Buildings are currently using more and more energy than before. Saving building energy, improving indoor built thermal conditions and reducing carbon emissions are recognized as major challenges for the whole world. The reduction of building energy use and abatement of green gas emissions by various measures are important and have been detailed discussed by different researchers [1-10]. However, the solar shading performance of different louver shading materials has rarely been investigated. This paper tried to give an insight into the solar shading performance of horizontal and vertical louver shading by regression of calculated results.

II. METHODOLOGY

Solar shading coefficient for different louver shading materials can be determined by：

$Sc = ax^2 + bx + 1$

Where Sc ——solar shading coefficient；

$x = A / B$;

a , b ——coefficient，see table 1；

A , B ——louver dimensions, see Fig. 1.

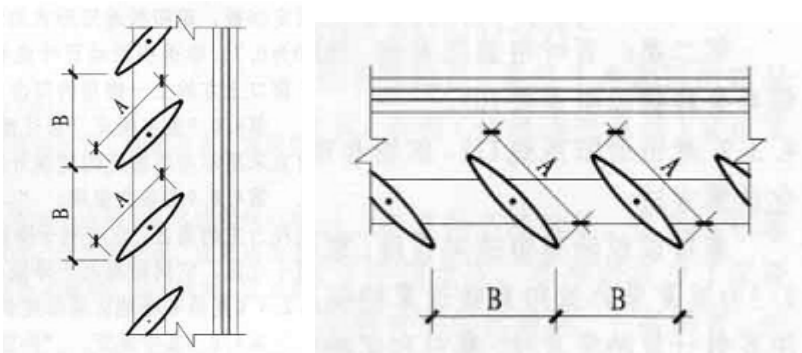


Fig. 1 Typical horizontal and vertical louver shading materials

To calculate most kinds of louver shading, x ranges from 0.05, 0.1, 0.2, 0.3, 0.4, 0.5, 0.6, 0.7, 0.8, 0.9 to 1.

Table 1 Coefficient of horizontal and vertical louver shading for different orientations

Structure		coefficient	East	South	West	North
Horizontal	winter	*a*	0.23	0.03	0.23	0.2
		b	-0.66	-0.47	-0.69	-0.62
	summer	*a*	0.54	0.56	0.56	0.56
		b	-1.28	-1.32	-1.32	-1.22
Vertical	winter	*a*	0.17	0.11	0.29	0.19
		b	-0.61	-0.6	-0.73	-0.61
	summer	*a*	0.16	0.45	0.13	0.73
		b	-0.76	-1	-0.73	-1.3

III. RESULTS AND DISCUSSION

The shading performance of horizontal louver shading materials in summer is illustrated in Fig. 2. It can be seen that the SC values of east and west facing windows decrease as x increases, while the opposite variation is observed for south and north facing windows. This means that the width of horizontal shading materials should be as short as possible when used in south and north facing windows and on the contrary it is as long as possible for east and west facing windows.

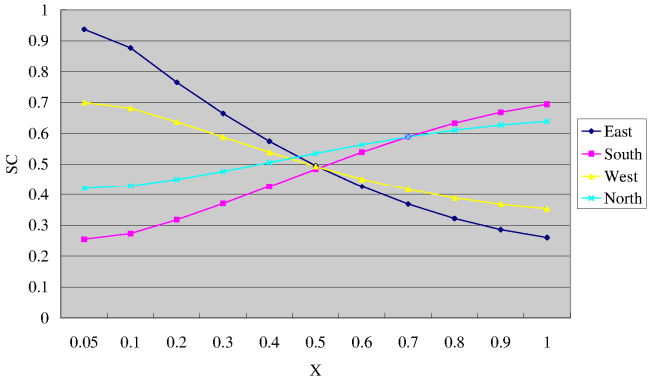


Fig. 2 Shading performance of horizontal louver shading materials in summer

Fig. 3 shows the shading performance of horizontal louver shading materials in winter. We can see that the dimension variation of horizontal louver shading materials has little impact on the SC values of south, west and north facing windows, and these values mainly range from 0.6-0.7. With the increase of x, the SC value of east facing windows drops significantly. Therefore, horizontal louver shading materials is effective in winter and the x value should be as small as possible.

From Fig. 4 we can see that the shading performance of vertical louver shading materials in summer keeps almost constant for west and north facing windows as x changes, indicating a poor modification of solar gains. The dimension variation of vertical louver shading materials in summer for east and south facing windows has a relatively significant influence on SC values. For east facing windows, x is as large as possible. On the other hand, it is as small as possible for south facing windows.

The shading performance of vertical louver shading materials in winter demonstrated in Fig. 5 is similar to that in Fig. 4. SC values of vertical louver shading materials in winter keep almost constant for west and north facing windows as x changes. Both east and south shading has a more significant variation and their trends are similar to Fig. 4. This indicates that x for east shading is as small as good while the opposite result is for south facing windows.

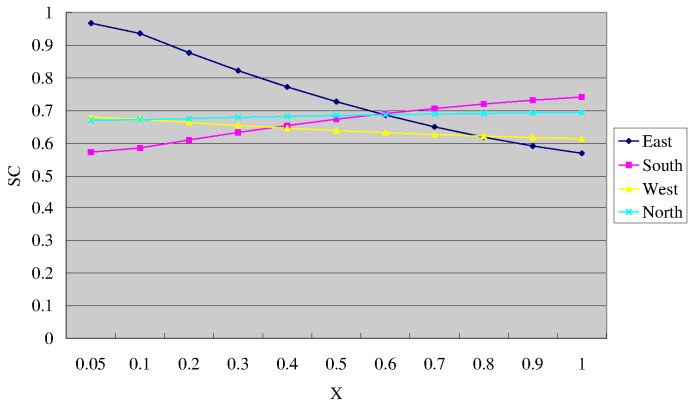


Fig. 3 Shading performance of horizontal louver shading materials in winter

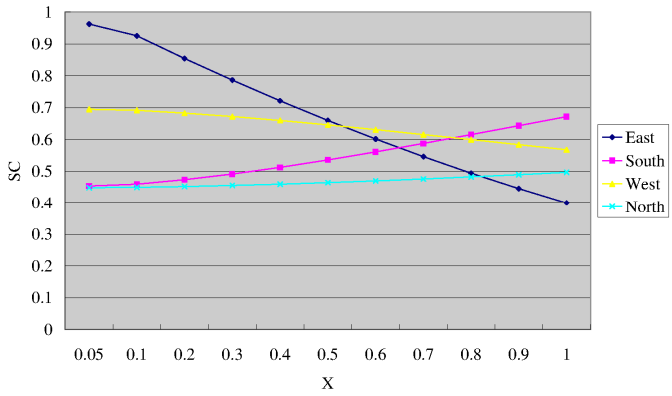


Fig. 4 Shading performance of vertical louver shading materials in summer

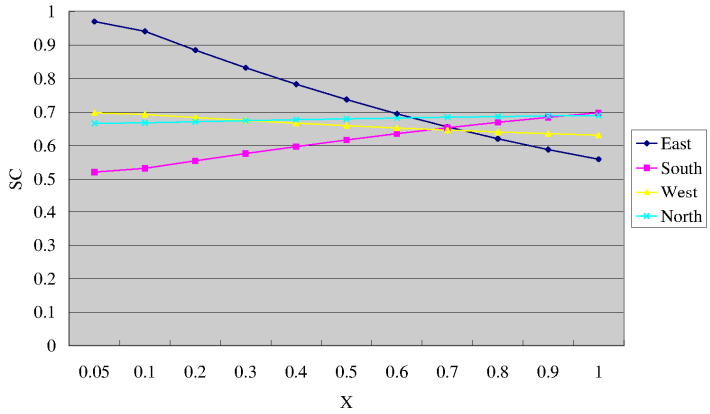


Fig. 5 Shading performance of vertical louver shading materials in winter

IV. CONCLUSION

Louver shading is not suitable for north facing windows and has little improvement of shading performance in south orientation. For east windows in the west, horizontal louver shading performs well only in summer. Horizontal and vertical shading materials have similar shading performance in summer and winter. This means that the dimension of shading should be optimized with building simulations to obtain a balance between cooling and heating performance.

V. ACKNOWLEDGEMENT

This work was supported by Scientific Research Fund of Zhejiang Provincial Education Department (Y201120006) and by Foundation of Ningbo University (XYL11004, XKL11D2073 and XKL09080).

REFERENCES

[1] Koo, S.Y., M.S. Yeo and K.W. Kim, "Automated blind control to maximize the benefits of daylight in buildings." Building and Environment, vol. 45, pp. 1508-1520, 2010.

[2] DAI Lei, CAI Li, "Analysis on the Characteristics of Modern Urban Residence in Ningbo: A Case Study of the Residence at Daici Alley and Deji Alley in Jiangbei District," Journal of Ningbo University (Natural science & engineering edition), vol.24, pp.128-132, 2011.

[3] J. Yao and Z. Yuan, "Study on Residential Buildings with Energy Saving by 65% in Ningbo," Journal of Ningbo University (Natural science & engineering edition).vol. 23, pp. 84-87, 2010.

[4] Yao, J. and N. Zhu, "Evaluation of indoor thermal environmental, energy and daylighting performance of thermotropic windows." Building and Environment, vol.49, pp. 283-290, 2012.

[5] HU Xing-yun, XU Jin and ZHANG Jin-quan, "Study on the Modern Rural Residence Planning with Regional Features of Fanshidu Village," Journal of Ningbo University (Natural science & engineering edition), vol. 24, pp. 110-114, 2011.

[6] Yao, J. and C. Yan, "Evaluation of The Energy Performance of Shading Devices based on Incremental Costs," Proceedings of World Academy of Science, Engineering and Technology, vol.77, pp. 450-452, 2011.

[7] Yao, J. and C. Yan, "Effects of Solar Absorption Coefficient of External Wall on Building Energy Consumption," Proceedings of World Academy of Science, Engineering and Technology, vol.76, pp. 758-760, 2011.

[8] GAO Hua-sheng, YANG Xiao-xian and CHEN Yu –hui et al., "Water Pollution Control in Rural Villages: Case Study," Journal of Ningbo University (Natural science & engineering edition), vol.23, pp.74-78, 2010.

[9] J. Yao and N. Zhu, "Enhanced Supervision Strategies for Effective Reduction of Building Energy Consumption-A Case Study of Ningbo," Energy and Buildings, vol. 43, pp. 2197-2202, 2011.

[10] J. Yao, "Energy optimization of building design for different housing units in apartment buildings," Applied Energy, vol. 94, pp. 330-337, 2012.

© (2012) Trans Tech Publications, Switzerland
doi:10.4028/www.scientific.net/AMM.164.81

Research on Material Selection Standard of Graded Crushed Stone Base Course for Municipal Road

Kai Liu[1,2,a], Fang Wang[3,b], Weihua Zhang[2], Yuanrong Wang[4]

[1]Civil Engineering Center for Post-doctoral Studies, Hefei University of Technology, Hefei, Anhui, 230009, China

[2]School of Transportation Engineering, Hefei University of Technology, Hefei 230009, Anhui, China

[3]School of Civil Engineering, Anhui University of Architecture, Hefei 230601, Anhui, China

[4]Hefei Key Project Construction Administration, Hefei 230001, Anhui, China

[a]ronaldo_1@163.com, [b]wf7110807@163.com

Keywords: municipal road, material, material selection standard, graded crushed stone

Abstract. For reasonably selecting graded crushed stone materials, material selection standard is proposed for each traffic level of municipal roads according to the local common material properties in Anhui province, and referring to technical index provision and research results about graded crushed stone material at home and abroad. The selection standard of coarse aggregate takes crushing value, abrasion value, needle and plate particle content and robustness as index. The selection standard of fine aggregate takes robustness, sand equivalent, liquid limit and plasticity index as index. The research results promote the popularization and application of graded crushed stone base course on municipal road engineering in Anhui province.

Introduction

Graded crushed stone is the mixture that's composed of pre-screening gravel with different size and stone chips through strictly gradation design. Many countries commonly used graded crushed stone base course flexible pavement such as United States, France, Germany, Canada, Japan, South Africa, etc. They had relatively mature pavement design methods and design specifications, as well as more rich research experience about structure and material composition and construction experience [1]. Chinese scholars conducted research on graded crushed stone material properties [2-3], mix design [4-5], construction technology [6] and so on, and paved a certain number of graded crushed stone base course asphalt pavement [7], also obtained abundant research results.

The strength of graded crushed stone mainly is attributed to the strength of gravel itself and inlay squeezing effect between particles. Therefore, reasonable selection standard of raw material is the premise and base of ensuring road performance of graded crushed stone base course. While the related specifications at home and abroad have given certain requirements about technical indexes of raw materials, the requirements are selected according to the average level of various materials' properties. The research on raw material of graded crushed stone mainly focused on highway construction, and referencing to related specifications for selecting material. This paper will propose material selection standard applying to graded crushed stone base course on municipal roads in Anhui province, according to physical and mechanical properties of local common road materials in Anhui province and combining with related specifications. The results provide a technical basis for application and dissemination of graded crushed stone base course in Anhui province.

Organization of the Text

Section Headings. The section headings are in boldface capital and lowercase letters. Second level headings are typed as part of the succeeding paragraph (like the subsection heading of this paragraph).

Technical Indexes Selection of Graded Crushed Stone Material

Selected technical indexes of graded crushed stone base course in China's current specification are shown in Table 1.

Table 1. **Selected technical indexes of graded crushed stone in China's current specification**

Specification name	Technical indexes of coarse aggregate	Technical indexes of fine aggregate
Technical Specifications for Construction of Highway Roadbases (JTJ 034-2000)	crushing value, needle and plate particle content	liquid limit, plasticity index, plasticity Index times fine soil content with particle size below 0.5mm
Code for Construction and Quality Acceptance of Road Works in City and Town (CJJ 1-2008)	crushing value, needle and plate particle content , soft particle content, flat elongated gravel content	liquid limit, plasticity index
Specifications for Design of Highway Asphalt Pavement(JTG D50-2006)	crushing value	liquid limit, plasticity index
Technical Specification for Construction of Highway Asphalt Pavements(JTJ F40-2004)	crushing value, Los Angeles abrasion loss, needle and plate particle content, soft stone content, apparent relative density, water absorption, robustness	washing method <0.075mm particle content, apparent relative density, water absorption, robustness, sand equivalent

The main indexes used in Table 1 are crushing value, needle and plate particle content, robustness, abrasion value, liquid limit, plasticity index and sand equivalent. These indexes can adequately reflect the basic physical and mechanical properties, deformation characteristics, durability and volume stability of materials. Therefore, the above seven indexes are used to control selection of graded crushed stone material in the paper.

Material Selection Standard of Coarse Aggregate

Crushing Value and Abrasion Value. Crushing value is used to measure anti-crushing ability under gradually increased load and is strength index. Crushing value is tested according to crushing value test of coarse aggregate (T0316-2005) in test methods of aggregate for highway engineering (JTG E42-2005). In technical specification for construction of highway asphalt pavements, crushing value is not more than 28% for city express way and city thoroughfare and is not more than 30% for sub arterial road and branch road. In other specifications, crushing value is not more than 28% for city express way and city thoroughfare, is not more than 30% for sub arterial road, and is not more than 35% for branch road. Abrasion value reflects anti-friction and anti-crash ability of coarse aggregate, and is tested by Los Angeles abrasion test of coarse aggregate (T0317-2005). The standard of abrasion value is 40% ~ 50% in America, less than 35% in Britain, 25%~40% in France, less than 30% in Ireland. Commonly used materials in Anhui province mainly contain andesite, Dang mine slag, Anshan rock, granite, limestone and so on. Because the differences of these materials' strength are large, the strength standard can not be too high, but not be too low. We recommend that the strength index of aggregate of graded crushed stone use crushing value and abrasion value. For city express way and city thoroughfare, crushing value is not more than 26% and abrasion value is not more than 30%. For sub arterial road and branch road, crushing value is not more than 30% and abrasion value is not more than 35%.

Needle and Plate Particle Content. It is used to assess shape and anti-crushing ability of aggregate, and is tested by needle and plate particle content test of coarse aggregate (vernier caliper method, T0312-2005). The European standard EN 13242-2008 demands needle and plate particle content less than 20% for graded crushed stone. In French, needle and plate particle content is not more than 25% for heavy traffic roads and medium traffic roads, is not more than 35% for light traffic roads. Needle and plate particle content is not more than 35% in Ireland. Both technical specifications for construction of highway roadbases and code for construction and quality acceptance of road works in city and town require needle and plate particle content not more than 20%. While in technical specification for construction of highway asphalt pavements, needle and plate particle content is not more than 18% for city express way and city thoroughfare, and is not more than 20% for sub arterial

road and branch road. According to local materials in Anhui province, it is easier to achieve the requirement of less than 20%, so we suggest that needle and plate particle content of graded crushed stone is not more than 20%.

Robustness. It reflects the durability of coarse aggregate and fine aggregate. Robustness of coarse and fine aggregate is tested by ruggedness test of coarse aggregate (T0314-2000) and ruggedness test of fine aggregate (T0340-2005), respectively. The horizon of graded crushed stone is relatively low, and graded crushed stone has permeability and there is no binder wrapped in graded crushed stone. Meanwhile corrosion effect on graded crushed stone is large by water and salt. Therefore should pay attention to the robustness of aggregate. Based on local materials, recommended robustness index is mass loss after sodium sulfate 5 cycles and it is not more than 12% for city express way and city thoroughfare. For sub arterial road and branch road, there is no requirement for robustness.

Material Selection Standard of Fine Aggregate

Liquid Limit and Plasticity Index. Liquid limit and plasticity index mainly control the quality of fine aggregate under 0.5mm sieve, while sand equivalent control the quality of fine aggregate under 4.75mm sieve. Liquid limit and plasticity index is tested by liquid- plastic limit combined test method (T0118-2007). The greater the plasticity index and liquid limit, the worse water stability is, CBR value decreases, the plastic deformation increases. Fine aggregate with high plasticity index easily expands with water. It reduces the water permeability and water stability of aggregate and increases freezing sensibility. In technical specifications for construction of highway roadbases and code for construction and quality acceptance of road works in city and town, requirement of liquid limit is less than 28%, and plasticity index is less than 6% in moist and rainfall areas, less than 9% in other areas. In specifications for design of highway asphalt pavement, liquid limit is less than 25% and plasticity index is less than 8%. According to investigation of liquid limit and plasticity index of fine aggregate on municipal roads in Anhui province, all liquid limit is less than 28% and plasticity index is less than 6%. Anhui province belongs to humid region and moderate humid region, so it is suggested that liquid limit is less than 25% and plasticity index is less than 6% for municipal roads.

Sand Equivalent. Sand equivalent is used to assess clean class of aggregate, and is tested by sand equivalent test of fine aggregate (T0334-2005). From the sand equivalent of limestone, granite, andesite on municipal roads in Anhui province, most of sand equivalent are more than 50%~60%. Therefore, the proposed sand equivalent is not less than 60% for city express way and city thoroughfare. For sub arterial road and branch road, sand equivalent is not less than 50%.

According to the above analysis and material characteristics in Anhui province, the recommended material selection standard of graded crushed stone base course is shown in Table 2.

Table 2. Material selection standard of graded crushed stone

Aggregate type	Technical indexes	City express way and city thoroughfare	sub arterial road and branch road
Coarse aggregate	crushing value(%)	≤26	≤30
	Los Angeles abrasion value (%)	≤30	≤35
	needle and plate particle content (%)	≤20	
Coarse and fine aggregate	robustness (%)	≤12	—
Fine aggregate	sand equivalent (%)	≥60	≥50
	liquid limit (%)	＜25	
	plasticity index (%)	＜6	

Laboratory Test of Graded Crushed Stone Base Course Material

According to related test methods in test methods of aggregate for highway engineering (JTG E42-2005), the value of various technical indexes of coarse and fine aggregate is tested. The laboratory uses limestone gravel from Hanshan county Anhui province. Gravels are divided into four groups of 0~4.75mm, 4.75~9.5mm, 9.5~19mm, 19~31.5mm grain size. Test results are shown in Table 3.

Table 3. Test results of raw material

Test items	Test results of aggregate				Test method
	0~4.75mm	4.75~9.5mm	9.5~19mm	19~31.5mm	
Crushing value (%)	—	—	17.75	18.14	T0316-2005
Los Angeles abrasion value (%)	—	—	24.9	29.7	T0317-2005
Needle and plate particle content (%)	—	0.5	3.6	1.1	T0312-2005
Sand equivalent (%)	74	—	—	—	T0334-2005
Liquid limit (%)	19	—	—	—	T0118-2007
Plasticity index (%)	3.3	—	—	—	T0118-2007
Silt content (%)	0.462	0.376	0.281	0.438	T0310-2005
Water absorption (%)	0.3	0.8	0.7	0.4	T0304-2005 T0330-2005
Apparent density(g/cm^3)	2.804	2.795	2.743	2.697	
Bulk density(g/cm^3)	2.726	2.738	2.653	2.638	

The results meet standard requirement in Table 2. These materials can be used for various grades of municipal roads.

Conclusions

(1) Based on China's current specifications, technical index system is proposed. Crushing value, abrasion value, needle and plate particle content and robustness represent technical quality of coarse aggregate. Robustness, sand equivalent, liquid limit and plasticity index represent technical quality of fine aggregate.

(2)According to local common material properties in Anhui Province and the related technical index provision at home and abroad, the paper proposes material selection standard of coarse and fine aggregate applying to graded crushed stone base course on each traffic level of municipal roads.

Acknowledge

This work was supported by the National Natural Science Foundation of China (Grant No. 51108150), Scientific and Technological Project of Hefei Key Project Construction Administration (Grant No.2011CGAZ1153), the Fundamental Research Funds for the Central Universities (Grant No.2010HGBZ0558, 2011HGQC1017), the China Postdoctoral Science Foundation (Grant No.2011M501377).

References

[1] JTJ034-2000, Technical Specifications for Construction of Highway Roadbases[S].

[2] Jiang Yingjun, Ren Jiaolong,Xu Yinshan,Li Di. Simulation Method of Mechanical Properties of Graded Broken Stone Based on Particle Flow Code [J]. Journal of Tongji University (Naturel Science), 2011, 39(5):699-704

[3] Wang Long, Xie Xiaoguang, Feng Decheng. Characteristics of the Modulus and Distortion of the Graded Aggregate Material [J]. Journal of Harbin Institute of Technology, 2007, 39(6):944-947

[4] Tian Lin. Research on Anti-cracking Characteristics of Frame-densed Cement Stabilized Graded Crushed Stone [D]. Doctoral Dissertation of Harbin Institute of Technology,2010.

[5] Ma Biao, Wang Binggang. Graded and Broken Stone Composing Design Method based on Deformation Resistance [J]. Journal of Chang'an University (Natural Science Edition), 2007, 27(5):1-5.

[6] LüWenjiang, Han Junliang, Guo Ping,etal. Construction Key Technique of Graded Broken Stone Basement [J].Highway, 2011,(7):21-25.

[7] Xie Xianggeng, Wu Shanxzhou, Huang Kaiyu. Application Research on Graded Crushed Stone Base Course on Expressway [J]. Journal of China & Foreign Highway, 2010, 30(2):208-212.

© (2012) Trans Tech Publications, Switzerland
doi:10.4028/www.scientific.net/AMM.164.85

A Comparative Study on Building Energy Performance between Movable and Fixed Shading Materials

Xiaochang Yang, Jian Yao*

Faculty of Architectural, Civil Engineering and Environment, Ningbo University, Ningbo, China

email: yaojian@nbu.edu.cn

Keywords: Building shading materials; energy consumption; energy efficiency.

Abstract. The purpose of this paper is to investigate the effect of movable shading on building energy demands. A public building and a residential building with movable shading and fixed shading were modeled by the building energy use simulation software DOE-2. Cooling and heating energy demands were calculated. The results showed that movable shading is better than fixed shading.

I. INTRODUCTION

In hot summer areas, building shading can reduce building energy consumption and it can significantly improve the indoor living comfort. Its main functions include avoiding thermal cooling, preventing glare, green, environmental protection and architecture decoration and so on. In China most of buildings use added clothe or louvers within the sunshade. Although it can block direct sunlight, most of the heat stays indoors. So it had little effect in reducing the load of air-conditioning. On one hand, in many offices with glass curtain wall where they use the opaque curtains to block sunlight, on another hand they rely on artificial lighting to hold acceptable illumination indoor. Air-conditioning and lighting of the annual energy consumption are often amazing; the fixed shading of many buildings is simply starting from the form, or too little scale, or choosing the shape with incorrect manner, and thus not have proper effects. Numerous studies have been conducted to analyze the energy saving potential of building envelope improvement measures such as shading devices [1-5]. In this paper, we take Ningbo as an example to study the effect of shading on building energy performance. We use the U.S. building energy simulation software DOE-2 to set up two models. Based on the comparison of activities shading and fixed shading outside the buildings, and we found advantages and disadvantages of they in the energy saving potential of architecture. We focused on studying the effect of energy saving of activities shading outside from comprehensive analysis.

II. METHODOLOGY

A. Typical Buildings

Integrating the common characters of the current situation of residential buildings in Ningbo, we designed a typical residential building model (baseline) for dynamic simulation. The total building area is about 3150 m^2 and building shape coefficient is 0.30, which is shown in Fig. 1. The thermal properties of the building are set according to the "Design standard for energy efficiency of residential buildings in hot summer and cold winter zone". DOE-2 was used to carry out building simulation for building energy consumption with fixed and movable shading. The typical movable and fixed shading are illustrated in Fig.2-3.

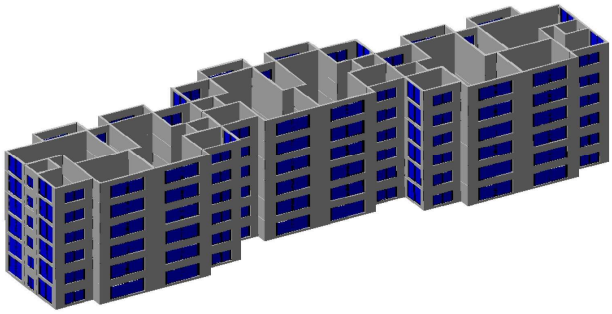


Fig. 1 Typical building



Fig. 2 Movable shading-screen



Fig. 3 Picture of ixed shading-overhang

III. RESULTS AND DISCUSSION

Figs. 4-6 present the cooling, heating and total energy consumption for the baseline building, fixed shading and movable shading. Obviously, movable shading has the best performance in terms of cooling, heating and total energy consumption, followed by the fixed one.

Fixed shading has good performance in the low cost, easy to install and operate. In addition, fixed shading make shading coefficient ranging from about 0.56 to 0.84, which is very valuable. Fixed shading also increased energy-saving rate from about 50.0% to 53.6%. But it may cause negative effects. For example, it increases heating energy consumption which is shown in Fig. 5, and reduces natural ventilation rate, making ventilation rate weakens about 22% ~ 47%. And solar energy and light is reduced by fixed shading in winter or cloudy circumstances which will leads to a negative impact.

Besides building energy consumption, energy efficiency is another important index when designing buildings. Therefore, the energy efficiency of baseline, fixed shading and movable shading is calculated according to the design standard.

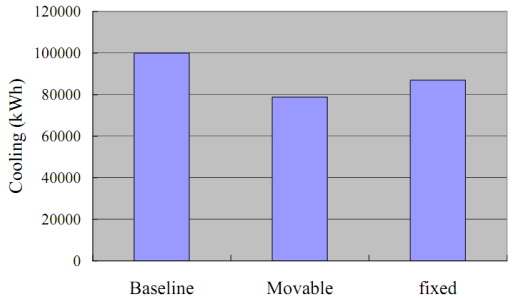


Fig. 4 Energy consumption for cooling

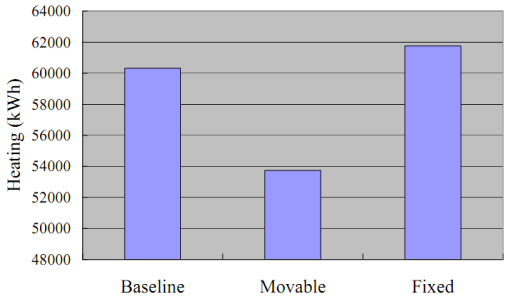


Fig. 5 Energy consumption for heating

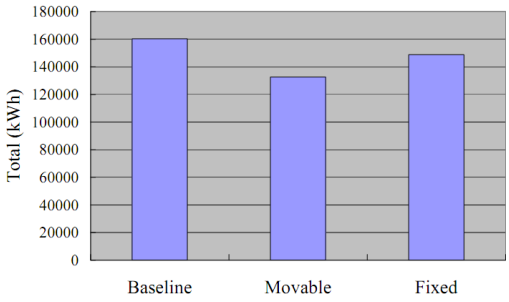


Fig. 6 Energy consumption for the total building

According to the calculation, the baseline building gets a 50% energy saving rate since it is designed according to the design standard. Baseline building with fixed shading achieves better energy efficiency performance (53.6%) than without shading. Of course, movable shading has the high energy efficiency of 58.6%. Therefore, movable shading has considerable energy saving potential and should be considered in designing buildings.

IV. Conclusion

Based on the analysis of the energy consumption of buildings with fixed and movable shading, fixed shading has cooling energy saving potential but increases heating energy consumption. However, movable shading saves both cooling and heating energy consumption, and achieves the highest energy efficiency.

V. Acknowledgement

This work was supported by Scientific Research Fund of Zhejiang Provincial Education Department (Y201120006) and by Foundation of Ningbo University (XYL11004, XKL11D2073 and XKL09080).

REFERENCES

[1] Koo, S.Y., M.S. Yeo and K.W. Kim, "Automated blind control to maximize the benefits of daylight in buildings." Building and Environment, vol. 45, pp. 1508-1520, 2010.

[2] DAI Lei, CAI Li, "Analysis on the Characteristics of Modern Urban Residence in Ningbo: A Case Study of the Residence at Daici Alley and Deji Alley in Jiangbei District," Journal of Ningbo University (Natural science & engineering edition), vol.24, pp.128-132, 2011.

[3] J. Yao and Z. Yuan, "Study on Residential Buildings with Energy Saving by 65% in Ningbo," Journal of Ningbo University (Natural science & engineering edition).vol. 23, pp. 84-87, 2010.

[4] Yao, J. and N. Zhu, "Evaluation of indoor thermal environmental, energy and daylighting performance of thermotropic windows." Building and Environment, vol.49, pp. 283-290, 2012.

[5] HU Xing-yun, XU Jin and ZHANG Jin-quan, "Study on the Modern Rural Residence Planning with Regional Features of Fanshidu Village," Journal of Ningbo University (Natural science & engineering edition), vol. 24, pp. 110-114, 2011.

[6] Yao, J. and C. Yan, "Evaluation of The Energy Performance of Shading Devices based on Incremental Costs," Proceedings of World Academy of Science, Engineering and Technology, vol.77, pp. 450-452, 2011.

[7] Yao, J. and C. Yan, "Effects of Solar Absorption Coefficient of External Wall on Building Energy Consumption," Proceedings of World Academy of Science, Engineering and Technology, vol.76, pp. 758-760, 2011.

[8] GAO Hua-sheng, YANG Xiao-xian and CHEN Yu –hui et al., "Water Pollution Control in Rural Villages: Case Study," Journal of Ningbo University (Natural science & engineering edition), vol.23, pp.74-78, 2010.

[9] J. Yao and N. Zhu, "Enhanced Supervision Strategies for Effective Reduction of Building Energy Consumption-A Case Study of Ningbo," Energy and Buildings, vol. 43, pp. 2197-2202, 2011.

© (2012) Trans Tech Publications, Switzerland
doi:10.4028/www.scientific.net/AMM.164.89

Evaluation on Safety of Internal Bambooen and Wooden Biomaterials for Food

GUO HaiYan[a], ZHENG ZhenZhen

Hunan Prouince Product Commodity Quality Supervision Tesiting Institute, Changsha City in Hunan 410007, P.R. China

[a]e-mail: 17612017@qq.com

Keywords: Bamboo products; Wood products; Food; Quality; Safety indexes

Abstract. China is the biggest country in producing and using of bamboo and wood products for food in the world. The quality status of the bamboo and wood products for food concerns the safety of everybody. Samples were taken for safety indexes testing from the provinces of the main production, and marketing of the bamboo and wood products for food at home. A preliminary conclusion of quality and safety status of the bamboo and wood products for food was drawn via the analysis for testing results, and some foundation work has been done for the quality control of the bamboo and wood products for food.

Introduction

China is rich in bamboo, timber resources. Bamboo species, distribution and bamboo forest area ranks first in the world. The forest stock volume occupies world front row, the plantation area ranks first in the world. The bamboo and wood products for food use bamboo and wood as raw materials ,which are used for food contact after a course of proper material processing and physical mechanical processing, which are renewable, biodegradable and of natural materials, which are in line with the current international theme of low carbon, environmental protection, and sustainable development. Our country is rich in bamboo, timber resources. Being deeply influenced by the tradition culture, our country is the biggest country in producing and using bamboo and wood products for food in the world.

The raw materials of the bamboo and wood products for food are the best source for environmental protection, but during processing--especially during the material processing. The addition of kinds of processing reagents brings the quality and safety hazards to the products. In order to know current situation of safety and quality of the bamboo and wood products for food at home. We took samples for safety indexes testing from the provinces of the main production, and marketing of the bamboo and wood products for food at home, and do preliminary analysis on the quality and safety status according to inspection results, on the chance that do some preparatory work for the quality control of the bamboo and wood products for food.

Situation of testing samples

Sample size and sample varieties. Sample size and sample varieties in this inspection are as follows: Sample capacity of bamboo products is 123, including the following 11 kinds of products: Agglutination bamboo chopping block, other bamboo chopping block, disposable chopsticks, non-disposable chopsticks, Sticks (fork) for food, bamboo toothpicks, bamboo tube (tank), bamboo garlic can(including tamping rod), bamboo bowl, bamboo cage drawer, bamboo spoon; Sample capacity of wood products is 109, including the following 11 kinds of products: Agglutination wood chopping block, other wood chopping block, disposable wooden chopsticks, non-disposable wooden chopsticks, wooden string (fork) for food, wood toothpicks, wooden bowl, wood spiked, wood garlic can(including tamping rod), wooden spoon, cork. total sample size is 232, sample varieties is 22.

Territorial sampling. Samples in this test were bought from supermarket, farmer's market, or bought directly from the manufacturer. Territorial sampling covers 16 provinces: Hunan, Zhejiang, Guangdong, Fujian, Guangxi Autonomous Region, Jiangxi, Anhui, Guizhou, Heilongjiang, Jilin, Liaoning, Hebei, Henan, Shandong, Shaanxi.

Inspection items settings

Basis of setting inspection items. The following aspects should be mainly considered when establish inspection items:

(1) Safety performance hidden troubles brought by production cycle: Bamboo and wood products in raw material selection, sample handling, production processing, transportation and storage, each link is likely to bring safety performance hidden troubles. We need to fully consider the effect of each link, treat the possible existence of safety problems as the emphases of this safety evaluation monitoring.

(2) The latent safety troubles in applications: There are latent safety troubles in applications. Though some of the projects are not chemical indexes, they concerns security issue. We will also consider putting this kind of projects in the scope of inspection.

(3) Product reference standards: Safety indexes are fixed in the product standards of some products. These indicators are also very good reference to similar products.

(4) Safety requirements for food products oversea: Many bamboo and wood packaging container products for food in our country are exported abroad. The foreign instructions and regulations have demands on safety performance of the products for food contact. In order to make this assessment issues have a higher level, we will also be reference with inspection items conducted by enterprises when they make export trade.

Confirm inspection items.After a series of investigation and data collection, according to the production status of bamboo and wood products for food in our country, the following projects were determined as the inspection items in this inspection:

There were 10 inspection items of bamboo products: Sulfur dioxide extraction volume, antioxidant residues, heavy metal (lead, cadmium, chromium, mercury), mildew preventive (thiabendazole, orthophenylphenol, diphenyl, imazalil), microbial indicator (coliform, pathogenic bacterium, molds), formaldehyde emission, melamine, pentachlorophenol, handle soundness, burr and sharp edge.

There were 10 inspection items of wood products: Sulfur dioxide extraction volume, antioxidant residues, heavy metal (lead, cadmium, chromium, mercury), microbial indicator (coliform, pathogenic bacterium, molds), formaldehyde emission, melamine, pentachlorophenol, total volatile organic carbon content, handle soundness, burr and sharp edge. The corresponding inspection items details of the products were listed in Table 1.

Table 1 The corresponding inspection items list of the products

No.	Product category	Interventions Requested
1	Agglutination bamboo chopping block	Formaldehyde emission, sulfur dioxide extraction volume, melamine, pentachlorophenol, handle soundness
2	Other bamboo chopping block	Sulfur dioxide extraction volume, melamine, pentachlorophenol, handle soundness
3	Disposable Chopsticks	Sulfur dioxide extraction volume, thiabendazole, orthophenylphenol, diphenyl, imazalil, microbial indicator (coliform, pathogenic bacterium, molds), antioxidant residues, burr and sharp edge.
4	Non-disposable chopsticks	Paint chopsticks: Heavy metal, sulfur dioxide extraction volume Ecru chopsticks: Sulfur dioxide extraction volume, burr and sharp edge
5	Sticks (fork)	Sulfur dioxide extraction volume, microbial indicator(coliform, pathogenic bacterium, molds), antioxidant residues, burr and sharp edge
6	Bamboo toothpicks	Sulfur dioxide extraction volume, microbial indicator(coliform, pathogenic bacterium, molds), antioxidant residues, burr and sharp edge
7	Bamboo tube (tank)	Sulfur dioxide extraction volume

No.	Product category	Interventions Requested
8	Bamboo Bowl	Sulfur dioxide extraction volume, burr and sharp edge
9	Bamboo garlic can	Sulfur dioxide extraction volume
10	Bamboo cage drawer	Sulfur dioxide extraction volume
11	Bamboo spoon	Sulfur dioxide extraction volume, burr and sharp edge
12	Agglutination wood chopping block	Formaldehyde emission, sulfur dioxide extraction volume, extraction volume, melamine, pentachlorophenol, handle soundness
13	Other wood chopping block	Sulfur dioxide extraction volume, extraction volume, melamine, pentachlorophenol, handle soundness
14	Disposable wooden chopsticks	Sulfur dioxide extraction volume, microbial indicator(coliform, pathogenic bacterium, molds), antioxidant residues, burr and sharp edge
15	Non-disposable wooden chopsticks	Paint chopsticks: heavy metal, sulfur dioxide extraction volume
16	Wooden string (fork) for food	Sulfur dioxide extraction volume, microbial indicator(coliform, pathogenic bacterium, molds), antioxidant residues, burr and sharp edge
17	Wood Toothpicks	Sulfur dioxide extraction volume, microbial indicator(coliform, pathogenic bacterium, molds), antioxidant residues, burr and sharp edge
18	Wooden bowl	Sulfur dioxide extraction volume, burr and sharp edge
19	Wood spiked	Sulfur dioxide extraction volume
20	Wood garlic can	Sulfur dioxide extraction volume
21	Wooden spoon	Sulfur dioxide extraction volume, burr and sharp edge
22	Cork	Sulfur dioxide extraction volume, antioxidant residues

Test results and Comprehensive analysis

Owing to space constraints, test results were not listed in this paper, qualified rate was listed according to the inspection items, see Table 2.

Table 2 Qualified rate statistical table of inspection findings

No.	Item	Sample size	Qualification rate	Main unqualified products
1	Sulfur dioxide extraction volume	232	99.1%	Bamboo chopsticks
2	Antioxidant residues	92	93.5%	Bamboo Toothpicks ,bamboo fruit fork
3	Heavy metal lead	18	77.8%	Paint chopsticks
4	Heavy metal cadmium	18	100%	
5	Heavy metal chromium	18	77.8%	Paint chopsticks
6	Heavy metal mercury	18	100%	
7	Coliform	84	100%	
8	Pathogenic bacterium	84	100%	
9	Molds	84	94%	Bamboo chopsticks
10	Mildew preventive	9	100%	
11	Formaldehyde emission	23	39.1%	Bamboo chopping block, wood

				chopping block
12	Pentachlorophenol	25	100%	
13	Melamine	25	100%	
14	Burr and sharp edge	70	99.1%	Bamboo chopsticks
15	Handle soundness	13	92.3%	Bamboo chopping block

In several respects such as quantify sample volume, sample varieties, sampling region, inspection items, this test has large sample volume, complete variety, wide controlling area, inspection items are relatively able to response the safety performance of the product. Combined with test results, we make the following analysis on the quality conditions of the domestic bamboo and wood products for food:

(1) Antioxidant residues of toothpick, fruit fork which are made of bamboo and the like exceed the standard. The production process of toothpick, fruit fork and food sign which are made of bamboo is similar. In order to bleach and be anticorrosive, enterprises always use hydrogen peroxide, but the super scale of the antioxidant residues didn't appear to bamboo food sign. According to our analysis, that's because appearance of toothpick, fruit fork which are made of bamboo affects sales, but bamboo food sign would not affect sales. This makes the enterprise use excessive bleach, causing the unqualified antioxidant residues of the products.

(2) Finishing chopsticks especially paint chopsticks have great quality problems. Qualified rate of the indexes such as the amounts of lead, chromium was low, and amounts of lead and chromium in individual products exceeded badly.

(3) Microbial index of the disposable products--Mold is easy to appear not qualified. Through the test, we found that the disposable products in the packaging and storage link were easy to bring secondary pollution, causing microbiowoody indicators of the mold to exceed the standard.

(4) Qualified rate of formaldehyde emission values of chopping block was very low. In this detection, the qualified rate was 39.1%, mainly because at present during the chopping block production, enterprises use adhesives containing aldehydes, which are basically used in the wood based panel production, the surface of wood-based panel usually has finish coat, the surface of chopping block is directly exposed, free formaldehyde is more easily released, causing the formaldehyde emission values of chopping block to exceed the standard.

(5) As a whole, wood products quality is better than bamboo products, because bamboo becomes mildewed and decomposed more easily than wood, the material processing technology of bamboo is complex which makes more pollution; Secondly, the aperture in bamboo is so wide, material is porous, at the same treatment conditions, bamboo would adsorb more processing reagents than wood, making pests residues increase.

Conclusions

Through this test we can see, the quality status of China's bamboo and wood products for food still has some problems. These quality problems are caused by many factors, Such as lack of product standards, it is difficult for related department to police the industry effectively; The industry threshold and practitioner quality are low, product quality issues bring harmfulness to society etc can’t be recognized profoundly. Solving these problems will require relevant national authorities to unite, to adopt multi-facetted approach, source from the production, to put the production process into effective supervision, to help enterprises to improve the manufacturing technology level, to improve consciousness of product quality and safety, and to make the whole industry to develop in order to benefit the society.

© (2012) Trans Tech Publications, Switzerland
doi:10.4028/www.scientific.net/AMM.164.93

Effect of Same Insulation Materials on Energy-Saving Potential of Different Buildings

Chang Guo, Jian Yao*

Faculty of Architectural, Civil Engineering and Environment, Ningbo University, Ningbo, China

email: yaojian@nbu.edu.cn

Keywords: Energy-saving materials；energy-saving rate；building shape coefficient.

Abstract. This paper analyzed the effect of same insulation materials on energy-saving potential of three different buildings by using the energy simulation program DOE-2. The results show that the heating energy saving rate of the building decreases when the building shape coefficient increases, while cooling energy saving rate of the building rises and the total energy saving rate of the buildings will reduce.

I. INTRODUCTION

There is a large quantity of buildings in China at present. The amount of construction is as high as 1600 to 2000 millions square meters, which is more than the total number of all the developed countries. At the same time, 97 percent of the construction is high energy consumption buildings. To reduce building energy consumption, China has issued several building energy-saving standards [1-2]. Meanwhile, a variety of studies were carried out to identify the possible energy efficiency measures for building envelope [3-9]. However, different buildings shape may have different energy saving potential even with the same design options. Therefore, this paper carried out a simulation-based study on the energy-saving potentials of different buildings with the same design measures.

II. METHODOLOGY

A. Typical Buildings

Three typical residential buildings in Ningbo are adopted in this paper and the properties of these buildings are illustrated in table 1.

Table 1 Three Typical Residential Buildings

Building	Style	Storey	Building Area (㎡)	Building Shape Coefficient
158#	residential	16above ground, 1under ground	17008.5	0.32
162#	residential	24above ground, 1under ground	20529.94	0.31
170#	residential	24above ground, 1under ground	14589.9	0.27

The elevations for these buildings are illustrated in Fig.1-3.

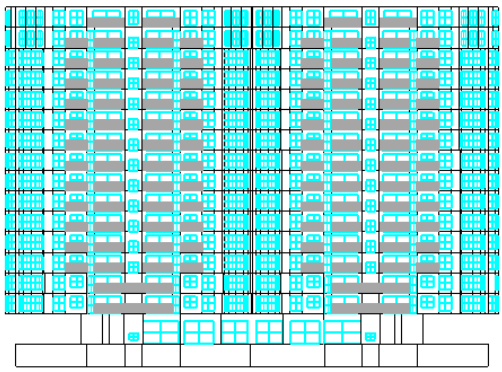


Fig. 1 Elevation of the building 158

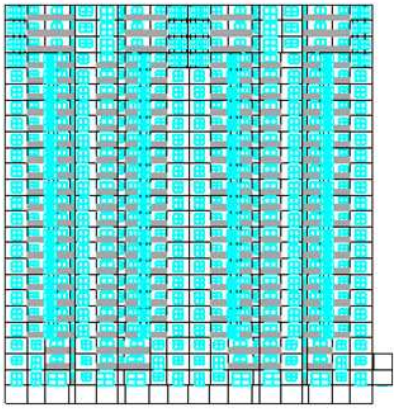


Fig. 2 Elevation of the building 162

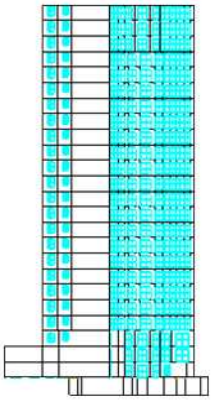


Fig. 3 Elevation of the building 170

B. Simulation Setting

This paper analyzed the energy-saving potential of the buildings by using the energy simulation program DOE-2. These three selected buildings have the same design measures. Regular building insulations are used and the heat transfer coefficient of wall is 0.97W/(㎡.K), the heat transfer coefficient of roof is 0.51W/(㎡.K) and the heat transfer coefficient of door is 2.47 W/(㎡.K). These three buildings have the same orientation of 30 degrees south by west. The area ratio of window to wall is 0.47 for south and 0.42 for north, while 0.16 for east and west. The heat transfer coefficient of exterior window is 2.85W/(㎡.K),while the shading coefficient is 0.84.

According to the building simulation, the design values and reference values of energy consumption can be output. And then the building energy saving rate can be calculated by the following equation.

Energy saving rate=（2×reference value-design value）/（2×reference value）×100％.

III. Results and Discussion

The energy indicator of the selected buildings with the energy-saving measures above is presented in Figs. 4-6.

For the building 158, it has the highest energy consumption of 53.12, while the building 162 has a less energy consumption of 47.24 and the building 170 has the lowest energy consumption of 37.26. Although these energy values vary largely, the energy efficiency does not differ greatly. The following section discusses the energy efficiency of these buildings.

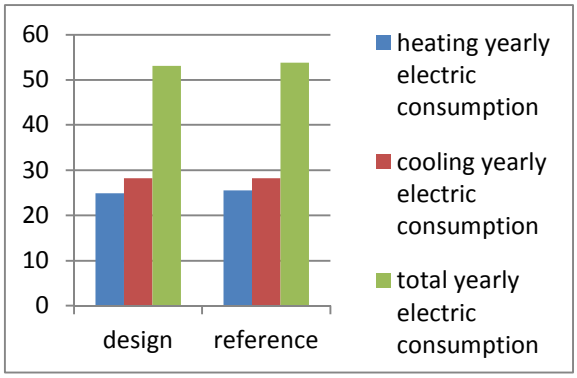


Fig. 4 Energy consumption for the building 158

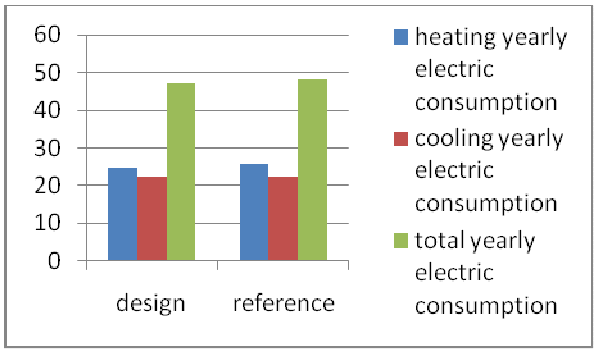


Fig. 5 Energy consumption for the building 162

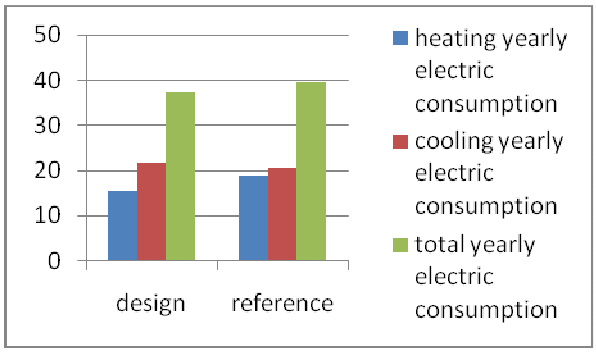


Fig. 6 Energy consumption for the building 170

The relationship between building shape coefficient and heating energy consumption is presented as follows. The heating energy saving rate of building 158,162 and 170 increases by 51.29%, 51.59% and 58.62%, when the building shape coefficient decreases by 0.32,0.31 and 0.27. It is clear that the less building shape coefficient, the better heating energy saving rate.

IV. Conclusion

Building shape coefficient has an important influence on energy-saving potential. Therefore, to reduce building energy consumption, lowering building shape coefficient is a very useful measure in the design stage and should always be considered as a prior passive design option.

V. ACKNOWLEDGEMENT

This work was supported by Scientific Research Fund of Zhejiang Provincial Education Department (Y201120006) and by Foundation of Ningbo University (XYL11004, XKL11D2073 and XKL09080).

REFERENCES

[1] Koo, S.Y., M.S. Yeo and K.W. Kim, "Automated blind control to maximize the benefits of daylight in buildings." Building and Environment, vol. 45, pp. 1508-1520, 2010.

[2] DAI Lei, CAI Li, "Analysis on the Characteristics of Modern Urban Residence in Ningbo: A Case Study of the Residence at Daici Alley and Deji Alley in Jiangbei District," Journal of Ningbo University (Natural science & engineering edition), vol.24, pp.128-132, 2011.

[3] J. Yao and Z. Yuan, "Study on Residential Buildings with Energy Saving by 65% in Ningbo," Journal of Ningbo University (Natural science & engineering edition).vol. 23, pp. 84-87, 2010.

[4] Yao, J. and N. Zhu, "Evaluation of indoor thermal environmental, energy and daylighting performance of thermotropic windows." Building and Environment, vol.49, pp. 283-290, 2012.

[5] HU Xing-yun, XU Jin and ZHANG Jin-quan, "Study on the Modern Rural Residence Planning with Regional Features of Fanshidu Village," Journal of Ningbo University (Natural science & engineering edition), vol. 24, pp. 110-114, 2011.

[6] Yao, J. and C. Yan, "Evaluation of The Energy Performance of Shading Devices based on Incremental Costs," Proceedings of World Academy of Science, Engineering and Technology, vol.77, pp. 450-452, 2011.

[7] Yao, J. and C. Yan, "Effects of Solar Absorption Coefficient of External Wall on Building Energy Consumption," Proceedings of World Academy of Science, Engineering and Technology, vol.76, pp. 758-760, 2011.

[8] GAO Hua-sheng, YANG Xiao-xian and CHEN Yu –hui et al., "Water Pollution Control in Rural Villages: Case Study," Journal of Ningbo University (Natural science & engineering edition), vol.23, pp.74-78, 2010.

[9] J. Yao and N. Zhu, "Enhanced Supervision Strategies for Effective Reduction of Building Energy Consumption-A Case Study of Ningbo," Energy and Buildings, vol. 43, pp. 2197-2202, 2011.

© (2012) Trans Tech Publications, Switzerland
doi:10.4028/www.scientific.net/AMM.164.97

Application of fluorescent aerosols to verifying the leakage of protective clothing by image processing

Chin-Hsiang Luo[1,a], Hong-Zhou Chen[2,b], Yi-Chin Huang[1,c], and Shinhao Yang[3,d,*], Sz-Han Wang[1,e]

[1]Institute of Occupational Safety and Hazard Prevention, Hungkuang University, Taichung, Taiwan, ROC

[2]Department of Animation and Game Design, Toko University, Chiayi, Taiwan, ROC

[3]Department of Environmental and Occupational Health, Toko University, Chiayi , Taiwan, ROC

[a]andyluo@sunrise.hk.edu.tw, [b]stephen@mail.toko.edu.tw, [c]f87541110@ntu.edu.tw, [d]shinhaoyang@ntu.edu.tw, [e]is_han@msn.com

Keywords: Fluorescent, Protective clothing, Image processor, Leakage ratio

Abstract. This work aims to measure the leakage of the personal protective equipment by using the fluorescent aerosol tracer. The fluorescent aerosols were employed as airborne particulates in a controlled chamber with ultraviolet (UV) light-detectable stickers. After an exposure and leakage test, the protective equipment was removed and photographed with UV-scanning to evaluate areas and color depth ratio of the areas where fluorescent aerosols had adhered to the body through the protective equipment. An image processor installed with an entropy-based algorithm was developed to segment the fluorescent area and calculate its relative leakage ratio (Lr) in real time. This study shows that the total leakage rate of the K brand protective clothing is 2.04×10^{-4} in two repetitions, and its 10- repetition total leakage rate is about 3.15×10^{-3}. The two-repetition total leakage rate of the P brand protective clothing is about 2.47×10^{-4}, and its 10 repetition total leakage rate is about 4.79×10^{-3}. The two-repetition total leakage rate of the W brand protective clothing is about 1.04×10^{-4}, and its 10-repetition total leakage rate is about 4.68×10^{-3}.

Introduction

Personal protective clothing is designed to protect workers against hazardous substances that might come into contact with the skin. The leakage of protective clothing is an important issue in the occupational health field. Several widely accepted test methods are available to measure barrier properties of protective clothing against liquid and vapor assaults.[1-3] Previous, the measurement of the protective clothing is according to the standard method, which is used to measure the hazard material penetration through the protective clothing surface. Similarly, the researchers always investigate the aerosol penetration through the protective mask surface. There is no quantitative method for measuring the leakage of personal protective equipment.

Industrial processes can produce and suspend various hazardous aerosols. Recently, bioaerosol propagation has become an issue for medical hygiene and occupational health. Infectious and contagious bioaerosols, such as Tuberculosis, SARS and H1N1 virus, are transmitted by suspended droplet nuclei with diameter of 1-20 μm [4-5] through coughing, laughing, talking, and singing. In factory manufacturing, erosive dust, particles of heavy metals, organic aggregates of polymers and dyes, bituminous coal, and epoxy resin are concerns. Protective clothing, gloves, and masks are used to insulate related staff from contact transmission between skin and hazardous particles when operations and first aid are processed. The pumping effect[6], mentioned above, affects protective clothing rather than gloves and masks, because the boundary between the body and clothing is the most difficult to make airtight. Several studies have simulated or estimated the pumping effect on thermal insulation loss of workwear and cold-weather clothing in wind conditions.[6-9] However, there has been little research into the pumping effect on leakage of aerosols.

Furthermore, there is no officially accepted test method for leakage ratio of protective clothing, probably due to leakage of aerosols data. For any given situation, equipment and clothing should be selected that provide an adequate and appropriate level of protection. Overprotection as well as underprotection can become hazardous and should be avoided. Accordingly, the ultimate goal of this study is to determine if particulate leakage into protective clothing worn by volunteer simulated workers would happen after a series of designed exercises. The image processor installed with an entropy-based algorithm was used to quantify the segmented images of boundary leakage areas adhered to by fluorochrome aerosols. Moreover, leakage ratio was introduced to assess the pumping effect on protective clothing in various conditions, such as exposure time and body parts.

Experimental Methods

Designed Action Sets. For simulating the intensity and range of activities in hospitals and factories, simplified and disciplined exercises were taught to volunteers wearing protective clothing before exposure-and-leakage tests. For understanding the pumping effect on the leakage of protective clothing, the boundaries between protective clothing and subject were not sealed. The designed exercises included squatting, standing, raising elbows, turning left and right, holding arms across the chest, and stooping. All action sets were performed and finished successively in one minute, and repeated for the next minute if necessary. Therefore, the ten-repetitions of designed exercises lasted ten minutes. Volunteers wearing protective clothing performed designed exercises in a stabilized chamber, described below, for two- and ten-repetitions. [10]

Functional requirements of protective clothing. Three types of protective clothing were chosen for the testing. The Protective clothing was a one-piece coverall of high-density polyethylene fibers. The functional requirements of protective clothing include breaking strength (vertical orientation≧50N, horizontal orientation≧40N), water vapor transmission rate (≧1500 g cm^{-2} day^{-1}), bursting strength (≧200 kPa), sewn seam strength (≧40N), hydrostatic pressure (140 cmH_2O), tearing strength (vertical and horizontal orientations≧20N), and impact penetration (≦0.5 g).[10]

Exposure And Leakage Test. According to our previous work, the testing process was addressing as the following.[10] For controlling the physical conditions, a closed chamber 360 cm (length)×213 cm (width)×180 cm (height), was fanned with a wind velocity of 1.3 m/s to simulate an indoor environment. The temperature was set at 21(±3)^{o}C by an air conditioner, and relative humidity was controlled at 50(±3)% by a dehumidifier. The aerosol solution was prepared by a mixture of SiO_2 powders, an ethanol solution of 20% (v/v), and the Hoechst 33258 fluorescent dye ($C_{25}H_{24}N_6O \cdot 3HCl$, Aldrich Inc.), a non-toxin used in flow cytometry. The fluorescent aerosols with a count median diameter of 0.30 μm (shown in Fig 1.) were dispersed into the chamber through a nozzle (model 8012/1010L, Natural Fog®, Taiwan) with a caliber of 0.80 mm. The concentration detected by a portable aerosol spectrometer (model 1.109, Grimm Aerosol Technik GmbH & Co., Germany) was 10^5-10^6 particles/cm^3. Figure 2 depicts the experimental setups.

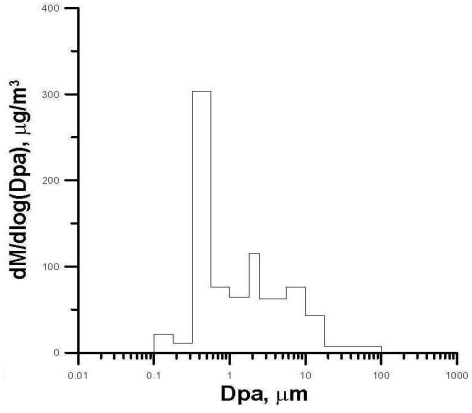


Figure 1. Size distribution of the testing aerosol

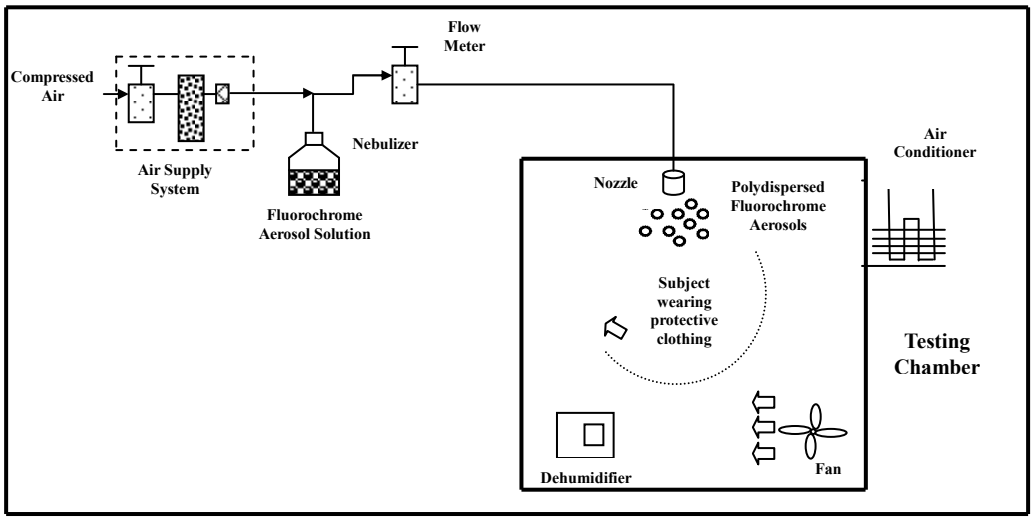


Figure 2. Exposure-and-leakage test setups

Image Processor. The following steps were according to the previous study.[10] After a series of designed exercises, volunteers left the chamber, removed protective clothing, and stood in a darkroom. If boundary leakage of protective clothing happened, the selected boundary parts deposited by challenged aerosols presented fluorescent in a UV scanner of 365 nm. Fluorescent pictures were taken with a digital camera (Nikon D3000) equipped with a manual and automatic focusing lense (Nikon AF NIKKOR 50mm 1.8D, Japan). Its charge-couple device's (CCD) picture quality is 3872×2592 pixels. The camera shutter was set to 1/60, and the camera's diaphragm and ISO value was F2.0 and 800, respectively. Before photographing, the response of the CCD was checked with a standard multicolor chart (a digital image file). In an enclosed environment, the camera took a picture of the standard chart lit by an electric bulb with a color temperature of 5000K. A digital comparison of the photograph of the chart and the chart confirmed the constancy of CCD quality. Finally, fluorescent areas were segmented and analyzed for their fluorescent gray levels (or brightness) by an image processor developed using an entropy-based algorithm described below.

The entropy (E) of an event is:

$$E = P \times I(P). \quad (1)$$

P and $I(P)$ which is equal to $\log(1/P)$ denote the probability and quantity of the event, respectively. For a $H \times W$ fluorescent image, each pixel is represented as a gray-level, g, and $g \in N$ ranging from 0 to 255. C_1 and C_2 denote two regions of the image, and their size ratios with respect to $H \times W$ are W_1 and W_2. P_g is the probability of picking a pixel of gray-level (g) from the image. The event is defined as picking a pixel of g from the C_1 region. The probability of this event is P_g/W_1, and its entropy is:

$$\frac{P_g}{W_1} \cdot \log \frac{W_1}{P_g} = -\frac{P_g}{W_1} \cdot \log \frac{P_g}{W_1}. \quad (2)$$

Since C_1 region contains the pixels whose gray-level is ranged from 0 to T, the entropy of the C_1 region is:

$$E(C_1) = -\sum_{g=0}^{T} \left(\frac{P_g}{W_1} \cdot \log \frac{P_g}{W_1}\right), \quad (3)$$

where $W_1 = \sum_{g=0}^{T} P_g$ denotes the summation from P_0 to P_T. Similarly, the entropy of the C_2 region whose values of g are ranged from T+1 to 255 is:

$$E(C_2) = -\sum_{g=T+1}^{255} \left(\frac{P_g}{W_2} \cdot \log \frac{P_g}{W_2}\right), \quad (4)$$

where $W_2 = \sum_{g=T+1}^{255} P_g$ denotes the summation from P_{T+1} to P_{255}. Obviously, the sum of W_1 and W_2 should be equal to one.

According to the entropy theorem[11-12], an optimal threshold can be found to separate the two regions. The optimal threshold, T^*, is defined as:

$$T^* = \max[E(C_1)+E(C_2)]. \quad (5)$$

The T^* can be found when all possible values of T (0-255) are used to repeat the calculation from Eqs. (3) to (5). The fluorescent areas where the pumping effect occurs can segment the background from the body image.

Leakage Ratio Measurements.[10] The fluorescent area mathematically divided by body surface area of volunteers is defined as the leakage ratio (L_r) which is dimensionless. For a volunteer, his body surface area (BSA, m^2) is statistically derived from a relationship between individual height (h, cm) and weight (w, kg):[12]

$$\mathrm{BSA} = \sqrt{\frac{\mathrm{h} \times \mathrm{w}}{3600}}. \quad (6)$$

In this study, the five boundary parts included were wrists, neck, chest (anterior arms included), back (posterior arms included), and belly. Two steps were used to describe how to calculate L_r. First, a proportional scale (R) between physical size (A, m^2) and pixel number (p) on the sampled image was established.

$$\mathrm{R} = \frac{\mathrm{A}}{\mathrm{p}}. \quad (7)$$

The R value (m^2/pixel) needs to be recalculated if the camera's focus changes. Second, the L_r of protective clothing can be calculated as:

$$\mathrm{L_r} = \frac{\mathrm{p_f} \times \mathrm{R}}{\mathrm{BSA}}, \quad (8)$$

where p_f denotes the pixel number that segmented by the image processor developed by an entropy-based algorithm, and R is used to convert the pixel number into its physical size (m^2).

Results and Discussion

Preliminary Test. Aerosol leakage of protective clothing usually is quantified by measuring the area challenged aerosols deposited. For understanding the major aerosol-deposited area, the preliminary testing was applying to measure the hot spots around the whole subject's body. Under ten-repetition of designed exercises, it is finding that the major aerosol-deposited areas were neck, chest, back, belly, and wrists. There are no fluorescent aerosols deposited on the lower part of the body. Thus, the following experiments in this work chose the five areas of neck, chest, back, belly, and wrists as the testing areas.

Two-Repctitions Testing. The leakage ratio (L_r) can be used to represent the pumping effect level on protective clothing due to movements of the body. Figure 3 shows the leakage ratios for five body parts after two- repetitions of designed exercises. Six duplicates for each leakage measurements were conducted. Experimental results show that the major leakage areas of the subject A were chest, belly, and wrists. For subject B, chest and wrists were the major leakage areas. According to the data, the wrists have the highest leakage ratio. Therefore, the wrist was affected by pumping effects under the two-repetitions testing. The finding also indicated that the two-repetition total leakage rate of the K, P, and W brand protective clothing were about 2.04×10^{-4}, 2.47×10^{-4}, and 1.04×10^{-4}. The total leakage ration of the W type protective clothing was highest.

Furthermore, a paired t-test revealed a significant difference ($p < 0.05$) between two-repetitions leakage ratios of five test parts obtained with two testing subjects suggesting that the leakage ratios of the different subject was quite distinct. It is due to that the operating strength of the designed exercises for each testing subject is different. Thus, pumping effecting for each subject is not the same. An

F-test revealed a significant difference ($p < 0.05$) between two- repetitions leakage ratios of five test parts obtained with three testing protective clothing suggesting that the leakage ratios of the different protective clothing was quite distinct. It is due to that the boundaries between protective clothing and subject were different for each clothings.

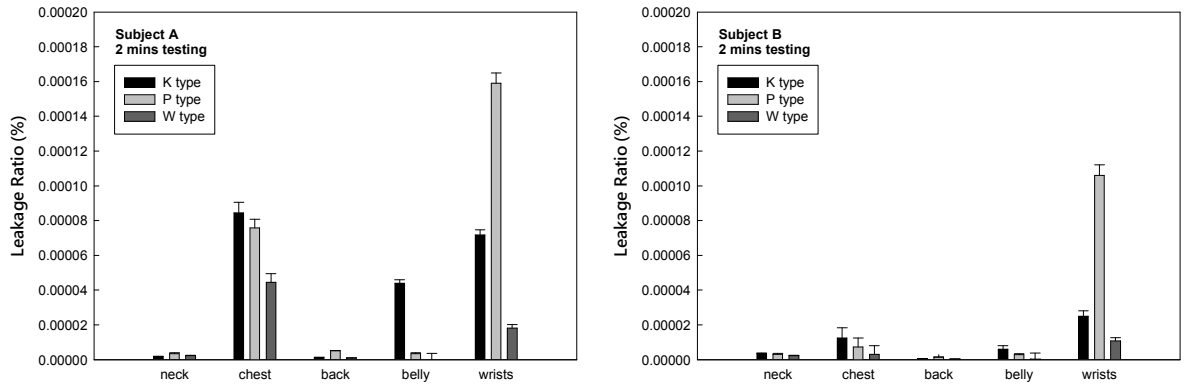


Figure 3. Leakage ratio of the testing subjects in two repetitions

Ten-Repctitions Testing. The leakage ratio (L_r) can be used to represent the pumping effect level on protective clothing due to movements of the body. Figure 4 shows the leakage ratios for five body parts after ten- repetitions of designed exercises. Six duplicates for each leakage measurements were conducted. Experimental results show that the major leakage areas of the subject A were chest, and neck. For subject B, chest and neck were the major leakage areas. According to the data, the neck have the highest leakage ratio. Therefore, the wrist was affected by pumping effects under the two-repetitions testing. The finding also indicated that the two-repetition total leakage rate of the K, P, and W brand protective clothing were about 3.15×10^{-3}, 4.79×10^{-3}, and 4.68×10^{-3}. The total leakage ration of the W type protective clothing was highest. The ten-repetition leakage area was quite different to two-repetition one. The major reason is that after ten-repetitions of designed exercises the boundary between neck and the protective clothing was getting loosed.

Furthermore, a paired t-test revealed a significant difference ($p < 0.05$) between ten-repetitions leakage ratios of five test parts obtained with two testing subjects suggesting that the leakage ratios of the different subject was quite distinct. It is due to that the operating strength of the designed exercises for each testing subject is different. Thus, pumping effecting for each subject is not the same. An F-test revealed a significant difference ($p < 0.05$) between ten- repetitions leakage ratios of five test parts obtained with three testing protective clothing suggesting that the leakage ratios of the different protective clothing was quite distinct. It is due to that the boundaries between protective clothing and subject were different for each clothing.

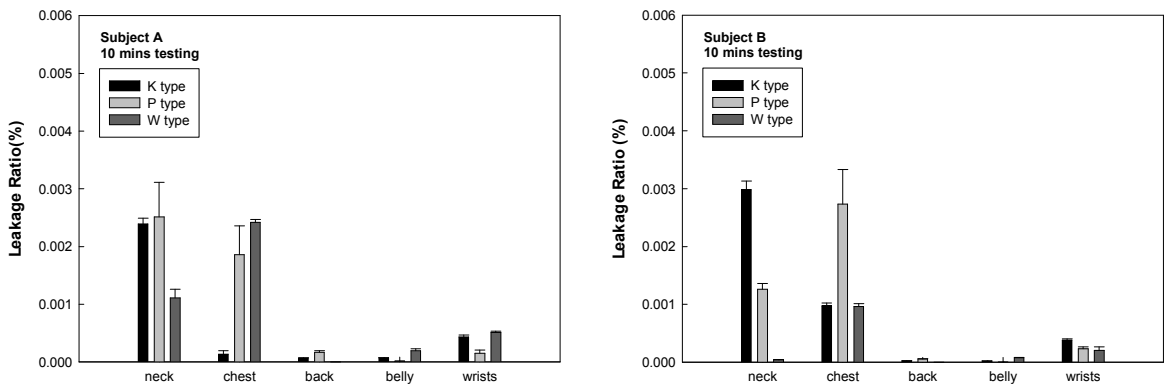


Figure 4. Leakage ratio of the testing subjects in ten repetitions

Summary

An image processor installed with an entropy-based algorithm has been addressed for assessing the pumping effects on protective clothing worn by workers in real time. The results imply the exposure time was a major factor for evaluating leakage of protective clothing. The leakage ratio (L_r) was used to quantify the level of the pumping effect on five body parts by programming calculations. The total leakage rate of the K brand protective clothing is 2.04×10^{-4} in two repetitions, and its 10- repetition total leakage rate is about 3.15×10^{-3}. The two-repetition total leakage rate of the P brand protective clothing is about 2.47×10^{-4}, and its 10 repetition total leakage rate is about 4.79×10^{-3}. The two-repetition total leakage rate of the W brand protective clothing is about 1.04×10^{-4}, and its 10-repetition total leakage rate is about 4.68×10^{-3}. The results of this study can be applied to devise safe and optimal procedures for donning and removal of protective clothing and decontamination after specific clinical and industrial situations.

Acknowledgements

This work was financially supported by the National Science Council, Taiwan, under Contract No. NSC-100-2221-E464-001-MY2.

References

[1] J.O. Stull and D.F. White: Am. Ind. Hyg. Assoc. j. Vol. 53 (1992), 455-462.

[2] NFPA 1999: Standard on Protective Clothing for Emergency Medical Operations, National Fire and Protective Association: US (2003).

[3] CNS 14798: The performance requirements for disposable medical protective clothing, Bureau of Standards, Metrology and Inspection: Taiwan (2004).

[4] S. Yang, G.W.M. Lee, C.M. Chen, C.C. Wu and K.P. Yu: J. Aerosol Med. Vol. 20 (2007), 484-494.

[5] C.Y.H. Chao, M.P. Wan, L. Morawska, G.R. Johnson, Z.D. Ristovski, M. Hargreaves, K. Mengersen, S. Corbett, Y. Li, X. Xie and D. Katoshevski: J. Aerosol Sci. Vol. 40 (2009), 122-133.

[6] G. Havenith and H.O. Nilsson: Eur J Appl Physiol DNLM. Vol. 92 (2004), 636-640.

[7] Y. Aoyagi, T.M. McLellan and R.J. Shephard: Eur. J. Appl. Physiol. Occup. Physiol. Vol. 68 (1994), 234-245.

[8] G. Havenith, R. Heus and W.A. Lotens: Ergonomics. Vol. 33 (1990), 89-1005.

[9] C.H. Luo, S. Yang, C.Y. Wen, M.Y. Syu, K.H. Lin, S.H. Chiu and C.P. Chang: J. Aerosol Sci. Vol. 42 (2011), 491-496.

[10] J.N. Kapur, P.K. Sahoo and A.K.C. Wong: Computer Vision, Graphics and Image Processing. Vol. 29 (1985), 273-285.

[11] C.H. Chen, Y.T. Lin, C.Y. Wen, L.C. Wang, K.H. Lin, S.H. Chiu, Y.H. Yang, J.H. Lee and B.L. Chiang: J. Allergy Clin. Immunol. Vol. 123 (2003), 665-671.

© (2012) Trans Tech Publications, Switzerland
doi:10.4028/www.scientific.net/AMM.164.103

Healing of Cracked Concrete by *Sporosarcina pasteurii* Mediated Carbonate Deposition

Peihao Li [1, 2, a], Bo JIN [1, b]

[1] School of Aerospace Engineering and Applied Mechanics, Tongji University, Shanghai, China

[2] College of Civil Engineering and Architecture, Zhejiang University of Technology, Hangzhou, China

[a] pumalph@163.com, [b] jinliuyk@online.sh.cn

Keywords: Bacterial, *Sporosarcina pasteurii*,Cracked concrete, Bio-deposition, healing.

Abstract. A remediation technique of cracked concrete by bacterial mediated carbronate deposition i.e. bio-deposition is discussed. Bio-deposition is a technique that comes from a broader category of biomineralization. The aim of this study was to investigate the plugging of artificially cracked concrete using bacteria *Sporosarcina pasteurii* and combined with sand as a filling material in artificially made cuts in concrete specimens which was cured in urea and Ca^{2+} medium and to research the effects on the compressive strength and flexural load of healing of concrete specimens by bio-deposition. The remediation efficacy of cracks in concrete was studied through compressive strength test and flexural failure test. Experimental results show that bio-deposition is able to make the improvement in concrete compressive strength and flexural load. The technique can be used to improve the compressive strength and flexural load of cracked concrete specimens and the remediation of cracks.

Introduction

Cementitious materials have been used extensively as worldwide construction materials. They have been typically characterized by a high-compressive strength and a relative low-tensile strength. The latter can be offseted by the application of steel or other material reinforcements taking over tensile forces. High tensile stresses may be result from external loads, imposed deformations (due to confined shrinkage, temperature gradients or differential settlement), plastic settlement, plastic shrinkage, and expansive reactions (e.g. due to alkali silica reaction, reinforcement corrosion or sulphate attack). Micro crack formation is a commonly phenomenon in concrete structures due to various natural or human activities, execrably affects concrete structural properties, increases permeability, and substantially reduce the durability of concrete structures ingress of detrimental components in moist environments. Once micro cracks form a continuous network, they may provide an easy path for the transport of potentially contain detrimental substances and substantially contribute to the permeability of cementitious materials, thereby reducing the resistance against attack of detrimental substances. If micro-cracks grow further and reach the reinforcement, not only the concrete itself may be attacked, but also the reinforcement will be corroded when it is exposed to water and oxygen, and possibly carbon dioxide and chlorides. Micro cracks may reduce or impair the durability of concrete structures and are therefore precursors to structural failure. [1, 2]

Some important measures were taken to diminish the permeability of detrimental components or to slow down or even to eliminate concrete degradation. Many of techniques are available but traditional repair systems have a number of disadvantageous aspects such as different thermal expansion coefficient compared to concrete and environmental and health hazards and so on. Bio-deposition plays an important role in limiting the infiltration of detrimental components into concrete and lead to the exploration of remediation technique in the field of cementitious materials. Cracks were plugged and healed with a mixture of bacteria, nutrients and a filler material. Among the different materials that were mixed with S. pasteurii, the silica fume and sand mixture lead to the highest compressive strength and lowest permeability. [3-5] Different microorganisms have been used to increase the

compressive strength of cement mortar and for the remediation of cracks in concrete [6–7]. Ghosh et al. demonstrated the positive effect of the addition of Shewanella on the compressive strength of mortar specimens. An increase of 25% of the 28 days compressive strength was obtained for a cell concentration of about 10^5 cellsmL^{-1} [8]. Microbial cells also prevent ingress of water effectively in different concentrations of fly ash-amended concrete. It is therefore more advisable and economical to restrict the development of early age small cracks the moment they appear, than to repair them after they have developed to large cracks [9, 10].

Therefore, Bio-deposition has been proposed as an alternative and environmental friendly crack repair technique. The aim of this study was to investigate the plugging of artificially cracked concrete using bacteria *Sporosarcina pasteurii* and combined with sand as a filling material in artificially made cuts in concrete specimens which was cured in urea and Ca^{2+} medium and to research the effects on the compressive strength and flexural load of healing of concrete specimens by bio-deposition. The remediation efficacy of cracks in concrete was studied through compressive strength test and flexural failure test. Experimental results show that bio-deposition is able to make the improvement in concrete compressive strength and flexural load. The technique can be used to improve the compressive strength and flexural load of cracked concrete specimens and the remediation of cracks.

Materials and methods

Bacterial strain and culture media. The microorganism used throughout the study was *Sporosarcina pasteurii* (strain number 11859 provided by American Type Culture Collection). For inoculum preparation, *Sporosarcina pasteurii* was precultured in liquid medium NH_4-YE (ATCC Medium 1376 broth: Tris±HCl, 130 mM (pH 9.0); $(NH_4)_2SO_4$, 10.0 g; yeast extract, 20.0 g; and distilled water, 1 L.). Individual ingredients were autoclaved separately and mixed afterward to avoid precipitation. The pH of the medium was adjusted to 8.6. Precipitation experiments were carried out in liquid medium (Urea＋Ca^{2+}) containing the following L^{-1} of glass distilled water: nutrient broth (Bacto), 3.00 g; urea, 20.00 g; NH_4Cl, 10.00 g; and $NaHCO_3$, 2.12 g. The pH of the medium was adjusted to 6.0 with 6 mol/L HCl prior to autoclaving for 20 min at 121℃. 10 ml of filter-sterilized solution containing 5.60 g $CaCl_2$ or 7.96 g $Ca(CH_3COO)_2$ was added afterward to yield 50.4 mM Ca^{2+}. The final pH of the medium was measured to be 8.0.

Concrete specimens and bio-deposition experiments. Concrete specimens were made by using ordinary Portland cement. The composition of the concrete mix: cement, 442Kg; sand, 473Kg; aggregates, 1280Kg; and water, 221Kg. Moulds with dimensions of 70 mm×70 mm×70 mm, 50 mm×100 mm×300 mm and 40 mm× 40 mm× 160 mm were used. After casting, all moulds were placed in an air-conditioned room with a temperature of 20 ±2℃ and a relative humidity of more than 90% for a period of 24h. After demoulding, the specimens were cured for more than 28 days. Some specimens with dimensions of 70 mm×70 mm×70 mm and 50 mm×100 mm×300 mm were used for compressive strength test and flexural failure test, respectively.

Bio-deposition experiments were conducted in liquid media. The culture was incubated on a shaker with constant shaking 160 rpm for 24 h at 30℃, which is the optimal duration for *Sporosarcina pasteurii* to reach a density of 2.8×10^7 cfu/mL during the exponential growth. Cell concentrations were determined by viable cell counting on NH_4-YE plates. Specimens were placed in Urea±Ca^{2+} culture media and inoculated with *Sporosarcina pasteurii*. A minimum of three specimens were run in each experiment. Bio-deposition concrete specimens were immersed for 24 h (10±5 mm depth) in a precultured 24 h old stock culture of *Sporosarcina pasteurii*. After this inoculation, specimens were wiped with a paper towel to remove excess liquid. Following this wiping, specimens were immersed (10±5 mm depth) in precipitation medium. The specimens were removed from the medium in 72 hours, and left to dry for a week at room temperature. Control experiments identical to those indicated above were carried out without bacterial inoculation. The same procedure was used to check contamination of inoculated specimens.

Artificial cracks were made on the completely cured specimens using a saw with a special arrangement. The width of cut was maintained constant and was 3.0 mm, while the depth of cut varied. The crack was cut to the depths of 10.0 mm, 20.0 mm and 30.0 mm. The cracks were filled with bacteria and sand in standard quantities and cured in Urea＋Ca^{2+} medium. Control specimens without bacterial inoculation in the cracks were also prepared. Specimens were cured in the nutrient medium for 14 days. The medium was replaced after 7 days. The beams were tested for their stiffness after 28 days using a three point loading test/ flexural failure test with a span of 270 mm. The concrete cubes were cured for 7 and 28 days and tested for compressive strength.

Results and discussion

The results from table 1 show the evident increase in compressive strength of the cube specimens with bacteria and sand in their cracks over the control ones with no filler material in their cracks. The compressive strength of the cubes with deeper cracks is lower than that with shallower ones. The increase in the compressive strength of specimens with bacteria and sand in their cracks is evident for all the depths of cracks. The compressive strength of specimens increases by 0.87%, 7.60% and 14.67% with 10 mm, 20 mm and 30 mm cracks respectively, which show more effective remediation in deeper cracks than shallower ones.

Table 1 Cube samples with cracks remedied by bacteria

cracks	cube samples with cracks				cracks remedied by bacteria for 7 days in Urea-$Ca(CH_3COO)_2$ medium			
Depth/mm	Compressive strength/MPa				Compressive strength/MPa			
	Cracks with no filling		Sand + water		Sand + dead bacteria		Sand + bacteria	
	average	Standard deviation	average	Standard deviation	average	Standard deviation	average	Standard deviation
10	35.64	1.25	35.71	1.08	35.74	1.27	35.95	1.32
20	30.54	1.33	30.78	1.89	31.53	1.24	32.86	1.97
30	27.82	1.12	28.50	1.01	29.22	1.28	31.90	1.08

The results from table 2 show the evident increase in compressive strength of the cube specimens with bacteria and sand in their cracks over the control ones with no filler material in their cracks. Cube samples with cracks remedied by bacteria for 14 days in Urea-$CaCl_2$ and Urea-$Ca(CH_3COO)_2$ medium. The increase in the compressive strength of specimens with bacteria and sand in their cracks is evident for all the depths of cracks. The compressive strength of specimens increases by 1.35%, 9.36% and 15.17% with 10 mm, 20 mm and 30 mm cracks respectively in Urea-$CaCl_2$ medium, and the compressive strength of specimens increases by 1.54%, 9.59% and 15.28% with 10 mm, 20 mm and 30 mm cracks respectively in Urea-$Ca(CH_3COO)_2$ medium. The increase in the compressive strength is most significant in the cubes prepared with the deepest crack (30 mm.) whose bacterial remediation increase the compressive strength by approximately 15.28% to that of control in the strength regain.

Table 2 Cube samples with cracks remedied by bacteria for 14 days

cracks	remedied by bacteria in Urea-$CaCl_2$ medium				remedied by bacteria in Urea-$Ca(CH_3COO)_2$ medium			
Depth/mm	Compressive strength/MPa				Compressive strength/MPa			
	Sand + dead bacteria		Sand + bacteria		Sand + dead bacteria		Sand + bacteria	
	average	Standard deviation	average	Standard deviation	average	Standard deviation	average	Standard deviation
10	35.95	1.90	36.12	1.24	35.99	1.53	36.19	1.58
20	32.51	1.43	33.40	1.23	32.93	1.12	33.47	1.62
30	28.91	1.76	32.04	1.67	28.47	1.97	32.07	1.46

The results from table 3 show the evident increase in the ultimate concentrated load of the beams with all the depth of cracks. The load values of beams filled with sand and bacteria are found to be more than the load values of the control specimens. It is observed during the course of loading of the specimens that almost all the specimens fail at the surface of the artificial crack where it is exposed

to the sand and bacteria. Even after failure of the beam, the sand particles remain together. This show bio-deposition of carbonate in the voids between the sand particles has stuck the sand particles together, which can heal the crack. Bio-deposition in the crack show more effective remediation in shallower cracks than deeper ones, the load values of beams increases by 8.46%, 6.86% and 4.87% with 10 mm, 20 mm and 30 mm cracks respectively. The increase in load values is most significant in the cubes with the shallowest crack (10 mm).

Table 3 Concrete beams with cracks remedied by by bacteria for 14 days in Urea-$Ca(CH_3COO)_2$ medium

Depth / mm	Ultimate concentrated load / kN					
	Cracks with no filling		Sand + dead bacteria		Sand + bacteria	
	average	Standard deviation	average	Standard deviation	average	Standard deviation
10	3.90	0.17	3.90	0.10	4.23	0.15
20	3.06	0.12	3.13	0.15	3.27	0.15
30	2.67	0.21	2.73	0.23	2.80	0.10

Conclusions

1. The research project demonstrated that biodeposition can be as a remediation method for cementitious materials. The increase in the compressive strength of specimens with bacteria and sand in their cracks is evident for all the depths of cracks. The increase in the compressive strength is most significant in the cubes prepared with the deepest crack (30 mm.) whose bacterial remediation increase the compressive strength by approximately 15.28% to that of control in the strength regain.
2. For the load values of beams, the results show more effective remediation in shallower cracks than deeper ones, the increase in load values of beams filled with sand and bacteria are found to be more than the load values of the control specimens. The increase in load values is most significant in the cubes with the shallowest crack (10 mm) whose bacterial remediation increase by approximately 8.46%.
3. Bio-deposition is able to make the improvement in concrete compressive strength and the remediation of cracks. Biodeposition might be as an ecological and novel alternative for the remediation of cracks.

Acknowledgements

Financial supports from Natural Science Foundation of China (No.51008281) and National Basic Research Program of China (973 Program)(No.2009CB623200) are gratefully appreciated.

References

[1] V. Wiktor, H. M. Jonkers: Cem. Concr. Comp. Vol. 33 (2011), p.763.

[2] K. V. Tittelboom, N. De Belie, W. De Muynck: Cem. Concr. Res. Vol. 40 (2010), p.157.

[3] W.De Muynck, N.De Belie, W.Verstraete: Ecol. Eng. Vol. 36 (2010), p. 118.

[4] S.K. Ramachandran, V. Ramakrishnan, S.S. Bang: ACI Mater. J. Vol. 98 (2001), pp. 3.

[5] W. De Muynck, D. Debrouwer, N. De Belie: Cem. Concr. Res. Vol. 38 (2008a), p.1005.

[6] W. De Muynck, K.Cox, N.De Belie: Build. Mater. Vol. 22 (2008a), p. 875.

[7] C. Qian, J.Wang, R.Wang: Mater. Sci. Eng. Vol. 29 (2009), p. 1273.

[8] P. Ghosh, S. Mandal, B.D. Chattopadhyay, S. Pal.: Cem. Concr. Res. Vol. 35 (2005), p. 1980.

[9] V. Achala, X. Pan, N. Ozyurt: Ecol. Eng. Vol.37 (2011), p. 554.

[10] J. Wang, K. V. Tittelboom, N. De Belie, W.Verstraete: Build. Mater. Vol. 26 (2012), p. 532.

© (2012) Trans Tech Publications, Switzerland
doi:10.4028/www.scientific.net/AMM.164.107

Modelling of Chloride Diffusion into Surface-biodeposited concrete

Peihao Li [1, a], Bo JIN [2, b]

[1] College of Civil Engineering and Architecture, Zhejiang University of Technology, Hangzhou, China

[2] School of Aerospace Engineering and Applied Mechanics, Tongji University, Shanghai, China

[a] pumalph@163.com, [b] jinliuyk@online.sh.cn

Keywords: Biodeposition, Chloride diffusion, Concrete, Modeling, Finite difference analysis.

Abstract. Chloride diffusuion is regarded as the dominant chloride transport process in concrete and the main cause of the corrosion of steel in concrete structures exposed to chloride-rich environments. Surface biodeposition can be applied to both new and existing concrete structures to restrain this deterioration. To gain comprehensive overview to the protective mechanism of surface biodeposition, a theoretical study of chloride diffusion through surface-biodeposited concrete is required. This paper proposes a physical model for surface biodeposited concrete, and develops a theoretical model to predict chloride diffusion of surface-biodeposited concrete structures. The model describes movement and retention of moisture and chloride by means of balance equations and diffusion laws. The influences of biodeposition and substrate properties on chloride diffusion are studied by a finite difference model. Results indicate that chloride diffusion is controlled by both the biodeposition and the substrate.

Introduction

Strong and relatively inexpensive concrete has been used extensively as worldwide construction materials. However, the formation of cracks may reduce the durability of concrete structures. Once micro cracks form a continuous network, they may substantially contribute to the permeability of cementitious materials, thereby reducing the resistance against ingress of aggressive substances [1]. Reinforcement corrosion can be initiated when the chloride at the surface of rebars reaches a threshold level. Damage to reinforced concrete structures exposed to chloride-rich environments is often caused by corrosion of steel on account of chloride penetration. Surface treatments play a key role in limiting the diffusion of detrimental components into concrete. Conventional treatment products of protection show, however, beside advantageous influences also many of disadvantageous aspects. To overcome disadvantages, biodeposition has been proposed as environmentally friendly strategy to improve the durability of cementitious materials [2, 3]. The method relies on the bacterially induced carbonate precipitate on the surface of these materials. This technique has been explored for its potential to improve the durability of construction materials [4-5]. Micro cracks are an almost unavoidable for ordinary concrete. Micro cracks were plugged and healed with a mixture of bacteria, nutrients and a filler material. Among the different materials that were mixed with S. pasteurii, the silica fume and sand mixture lead to the highest compressive strength and lowest permeability [6, 8]. The promising results have drawn the attention of different research groups and encouraged them to evaluate alternative approaches [7, 8].

However, knowledge of how a biodeposition reduces chloride diffusion is limited and the relationship between chloride diffusion resistance and surface biodeposition parameters, such as thickness, porosity and diffusion coefficient, has not been quantitatively identified. This paper proposes a physical model for the concept of water-percolated porosity and surface biodeposition, and develops a theoretical model to predict chloride diffusion of surface-biodeposited concrete structures. The model describes movement and retention of moisture and chloride by means of balance equations and diffusion laws. The influences of biodeposition and substrate properties on chloride diffusion are studied by an efficient numerical method using a finite difference model.

Physical model

Surface treatments play a key role in the protection of construction materials from immerging of water and other deleterious components. Because of the negative side-effects of the conventional methods, biodeposition has been proposed as a novel and environmental friendly strategy for the protection of construction. Surface-biodeposited treatment results in precipitation of carbonate crystals on the surface of concrete. Additional surface treatments can be classified into three sorts as shown in Fig. 1: (a) coatings, (b) penetrants and (c) sealers.

Bio-deposition relies on the bacterially induced formation of a compatible carbonate precipitate on the surface of cementitious materials. It can be seen as an additional physical layer on the concrete. Some of carbonate crystals penetrates the concrete, lining or blocking pores with leaving a surface layer. The carbonate layer acts as both a coating and a penetrant. For penetrants or sealers, the concrete layer impregnated by the surface treatment material can be regarded as the same as a coating on the underlying untreated substrate concrete. Hence bio-deposition can be regarded as surface treatment layers as shown in Fig. 1 (d).

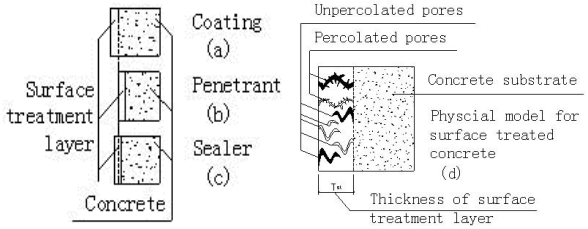


Fig. 1. Physical model of surface-biodeposited concrete

Defects of deposition layers such as pinholes and cracks are possible water paths. Neither all the pores can be occupied by water and nor do all the water-filled paths contribute to chloride diffusion. As shown in Fig. 1 (d), only the water-percolated paths contribute. Therefore, it is necessary to define the volume fraction of water-percolated paths (based on the whole volume of bio-deposited layer) as the water-percolated porosity, P_{st}, of bio-deposited layer. Similarly, the water-percolated porosity of the substrate, P_{su} is defined. The value of P_{st} is related to the external environment, e.g. water pressure or relative humidity. In the context of this study, other important characteristics are its chloride diffusion coefficient, D_{st}, and thickness, T_{st}. These two parameters together with P_{st} will be used to characterise a biodeposition layer. The values of P_{st}, D_{St} and Tst may be interdependent. However, for simplicity of interpretation, the parameters are considered independently.

Governing equations and finite difference schemes

Governing equations. Surface-biodeposited concrete can be modelled mathematically as a thin layer in contact with a semi-infinite medium (concrete substrate). Chloride diffusion profiles are expressed as chloride concentration (mol L-l) of the pore solution. Fick's law is used to describe diffusion:

$$\begin{cases} \dfrac{\partial C}{\partial t} = P_{st} D_{st} \dfrac{\partial^2 C}{\partial x^2} - \upsilon_{st} \dfrac{\partial C}{\partial x}, 0 \le x \le T_{st} \\ \dfrac{\partial C}{\partial t} = P_{su} D_{su} \dfrac{\partial^2 C}{\partial x^2} - \upsilon_{su} \dfrac{\partial C}{\partial x}, x \ge T_{st} \end{cases} \tag{1}$$

where C is the concentration of chlorides, Dst is the diffusion coefficient, $\upsilon_{st}, \upsilon_{su}$ is the average velocity in pore water in concrete and biodeposition layer, L is the concrete cover thickness of the rebar, x is space, and t is time.

With initial and boundary conditions:

$$C(x,0) = C_i \text{ and } C(0,t) = C_s,\ C(L,t) = C_f \tag{2}$$

To model chloride transfer across the surface bio-deposited layer/concrete interface, the following conditions are applied at $x = T_{st}$:

$$P_{st}D_{st}\left.\frac{\partial C}{\partial x}\right|_{st} = P_{su}D_{su}\left.\frac{\partial C}{\partial x}\right|_{su}, C_{st} = C_{su} \tag{3}$$

where C_i, C_s and C_f are the initial concentration of chlorides in concrete, on the surface of the concrete structures, and at the interface between the concrete and rebar, respectively.

Finite difference schemes. The schemes adopt mesh of $(x,t) \in Q^T := [0,0.01]m \times (0,T]$, with a step $\Delta x = 1/M$, $\eta = \frac{\Delta t}{\Delta x}$, $\sigma = \frac{\Delta t}{\Delta x^2}$. $\Delta t = T/N$, $t_n = n\Delta t$, and set $u(t) = (u_1(t) \cdots\cdots u_m(t))^T$, a smooth function such that $u_m(t_n) = u_m^n$, $u^n = (u_m^n)_{1 \le m \le M}$ denotes the approximation of u at the time tn.

Then discretize equation of (1) and simplify as follows:

$$\begin{cases} C_m^{n+1} = (1-2P_{st}D_{st}\sigma)C_m^n + \left(P_{st}D_{st}\sigma - \frac{1}{2}\upsilon_{st}\eta\right)C_{m+1}^n + \left(P_{st}D_{st}\sigma + \frac{1}{2}\upsilon_{st}\eta\right)C_{m-1}^n, 0 \le x \le T_{st} \\ C_m^{n+1} = (1-2P_{su}D_{su}\sigma)C_m^n + \left(P_{su}D_{su}\sigma - \frac{1}{2}\upsilon_{su}\eta\right)C_{m+1}^n + \left(P_{su}D_{su}\sigma + \frac{1}{2}\upsilon_{su}\eta\right)C_{m-1}^n, x \ge T_{st} \end{cases} \tag{4}$$

The initial, boundary and interface conditions:

$$C_m^0 = C_i, 1 \le m \le M, \quad \begin{cases} C_0^n = C_s \\ C_{M+1}^n = C_f \end{cases} n \ge 0 \quad \text{and} \quad \begin{cases} P_{st}D_{st}\left(C_{j+2}^n - C_j^n\right) = P_{su}D_{su}\left(C_{j+1}^n - C_{j-1}^n\right) \\ C_{j+1}^n = C_j^n \end{cases}, \left(j = \left[\frac{T_{st}}{\Delta x}\right] + 1\right) \tag{5}$$

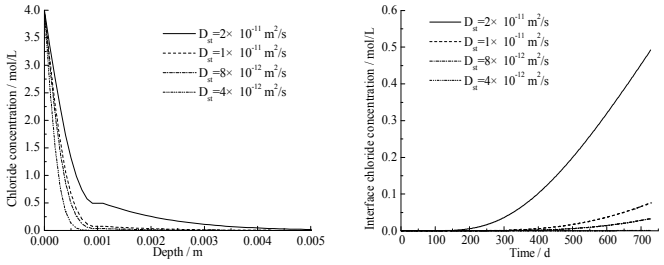
Stability is defined by the criterion:

$$\Delta t \le Min\left(\frac{2\Delta x^2}{4P_{st}D_{st} + \upsilon_{st}\eta}, \frac{2\Delta x^2}{4P_{su}D_{su} + \upsilon_{su}\eta}\right) \tag{6}$$

Results and discussion

This section is devoted to some numerical experiments. The data are as follows:

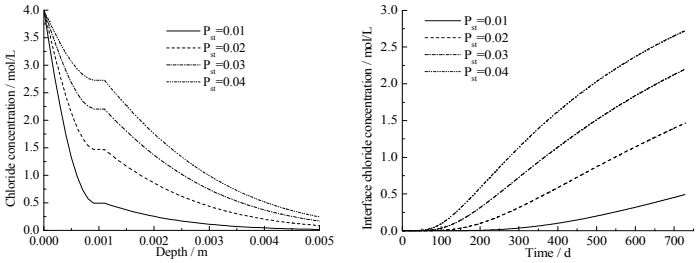
$T_{st} = 0.001\ m$, $x \in [0,0.05]\ m$, $\Delta x = 0.0001\ m$, $D_{st} = 2\times10^{-11}\ m^2/s$, $P_{st} = 0.01$, $D_{su} = 4\times10^{-11}\ m^2/s$, $P_{st} = 0.2$, $\upsilon_{st} = 1\times10^{-12}\ m/s$, $\upsilon_{su} = 1\times10^{-11}\ m/s$, $C_i = 0\ g/m^3$, $C_s = 4.0\ g/m^3$, $C_f = 0\ g/m^3$, $\Delta t = 2.88\times10^2\ s$.



(a) Concentration vs depth relationships (b) Interface concentration vs diffusion time relationships

Fig.2. Effect for D_{st}, $T_{st} = 0.001\ m$.

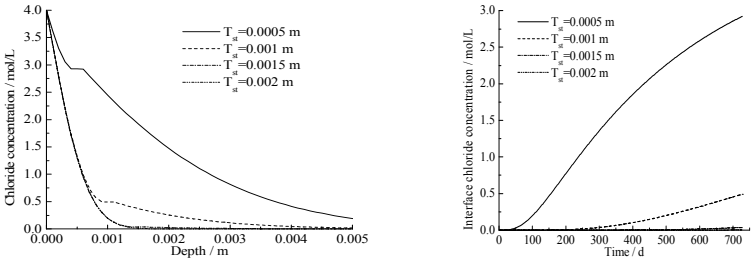
Here only numerical results are given to demonstrate the effects of surface bio-deposited concrete parameters on D_{st}, P_{st} and D_{st}. Fig. 2 show that C_i increases with increases in D_{st}, and interface concentration, C_i, increases with increases in the diffusion coefficient of the bio-deposition layer, D_{st}.



(a) Concentration vs depth relationships (b)Interface concentration vs diffusion time relationships

Fig.3. Effect for P_{st}.

Fig. 3- Fig. 4 show that C_i increases with increases in P_{st} and with a decrease in T_{st}, and interface concentration, C_i, increases with increases in P_{st} and with a decrease in T_{st}. Therefore, it can be concluded that the more effective a surface bio-deposition is, the lower D_{st} is.



(a) Concentration vs depth relationships (b) Interface concentration vs diffusion time relationships

Fig.4. Effect for T_{st}

Fig. 2- Fig. 4 show the dependence of D_{st} on the surface bio-deposited parameters. D_{st} decreases with an increase in T_{st} and with decreases in P_{st}.

It is interesting to note that P_{st} has a pronounced effect on C_i to D_{st}, implying that water-percolated porosity is an important parameter in controlling chloride diffusion. Decreasing P_{st} can reduce chloride diffusion as effectively as reducing D_{st} or increasing Tst. Any methods which reduce Pst and D_{st} will be evidently effective at increasing resistance to chloride diffusion.

Conclusions

A physical model and finite difference model have been established which can be used to investigate theoretically the influences of different parameters on chloride diffusion into surface bio-deposited concrete.

Chloride diffusion into surface bio-deposited concrete is controlled by both the surface bio-deposition and the substrate. Interface concentration, C_i, decreases with increases in the thickness of the bio-deposition layer, Tst, and increases with increases in the diffusion coefficient of the bio-deposition layer, D_{st}, water-percolated porosity, P_{st}, and time.

The water-percolated porosity, P_{st} is an important factor in controlling chloride into a surface bio-deposited concrete. Any methods which reduce P_{st} will be evidently effective at increasing resistance to chloride diffusion and reduce chloride diffusion as effectively as reducing D_{st} or increasing T_{st}.

Acknowledgment

This work was financially supported by Natural Science Foundation of China (No.51008281), the National Key Technology R&D Program of China during the 11th Five-Year Plan Period (No.2006BAJ03A07-04) and National Basic Research Program of China (973 Program) (No2009CB 623200).

References

[1] V. Wiktor, H. M.Jonkers: Cem. Concr. Comp. Vol. 33 (2011), p.763.

[2] W. De Muynck, K.Cox, N.De Belie: Constr. Build. Mater. Vol. 22 (2008a), p. 875.

[3] W. De Muynck, D. Debrouwer, N. De Belie: Cem. Concr. Res. Vol. 38 (2008b), p.1005.

[4] C.X.Qian, J.Y.Wang, R.X.Wang: Mater. Sci. Eng. Vol. 29 (2009), p. 1273.

[5] V. Achala, X. Pan, N. Ozyurt: Ecol. Eng. Vol. 37 (2011), p. 554.

[6] Ramachandran, S.K., Ramakrishnan, V., Bang, S.S: ACI Mater. J Vol. 98 (2001), p. 3.

[7] H. M.Jonkers, A.Thijssen: Ecol. Eng. Vol. 36 (2010), p. 230.

[8] W.De Muynck, N.De Belie, W.Verstraete: Ecol. Eng. Vol. 36 (2010), p. 118.

© (2012) Trans Tech Publications, Switzerland
doi:10.4028/www.scientific.net/AMM.164.111

Treatment Of The Lead Waste Water With Electrochemical Process

Juanjuan SONG [1, a,*]

[1]School of Chemical and Environmental Engineering,Hunan City University, Yiyang,Hunan,413000,China

[a]songdajuanjuan@163.com

Keywords: Lead recycling,Power generation method,Conditional experiment.

Abstract. Industrial waste water with high levels of lead has serious threat to human health and other organisms. Power generation methods were used for recycling of lead. Some factors such as temperature,power generation time,the anode material, type and concentration of anode area solution on the power generation process were studied to find the optimal process parameters.The experimental results show that:in the optimum conditions,the recovery rate of lead was more than 90% and the lead concentration in waste water has reached the discharge standard. This method does not produce by-products of environmental pollution in the power generation process and needn't external supply of energy but produce certain energy. So it is a green chemistry technology.

1. Introduction

In recent years, wastewater, waste gas and waste residue make the soil, lakes and oceans have suffered varying degrees of lead pollution. Lead-containing waste water have serious hazards to human health and crops.So elimination of lead in waste water is very important to protect the environment.

In this study, we recycled lead from waste water using the method of generating electricity,and we investigated the influence of five factors （temperature,power generation, the anode material,the type of solution of the anode region, the concentration of solution）on the power generation process, in order to find the optimal parameters.

2. Experiment

2.1 Preparation of leaded solution

Leaded solution is simulatiing leaded wastewater,it is prepared from KNO_3,$CuCl_2$,$FeCl_3$,$ZnCl_2$, $Cr(NO_3)_3$ and deionized water.

2.2 Composition of leaded wastewater

First, have a qualitative detection on the cation in the solution,then removal the ion of Cu^{2+} , Cr^{2+}, Fe^{3+}, determinate of the concentration of lead ions in the solution, as follows:Concentrate the leaded wastewater, the volume of wastewater is reduced to 1/10, Then take three 25ml solution into the beaker,add 1mol·l-1 of NaOH solution, until no longer generate precipitate.

Had a titration on the three solution. Added 1-2 drops of xylenol orange indicator, then added hexamethylene tetramine solution, after the solution appeared stable purple, added 5ml hexamethylene tetramine solution, the pH value of the solution is about 5-6.Had a titration with EDTA standard solution, when the solution changed from purple to yellow, this is the end of the titration.

Table 1. Content of Lead

	Calibrated with EDTA concentration (mol·L^{-1})	V $_{(EDTA)}$ Titration of lead (mL)	Concentration of Pb Ions (mg·L^{-1})
1	0.1056	25.0	0.50328
2	0.1042	23.5	0.50068
3	0.1105	26.0	0.50516
Average	0.1068	24.6	0.50304

Calculate the content of Pb^{2+} in the mixed solution according to the titration results, the results are shown in Table 1. By calculating the concentration of lead ions is 0.50304g·L^{-1}

2.3 Design of the experimental device

The generating device is made of plexiglass, Two power generation interval dimensions are 4cm× 4cm×6.5cm. Two intervals are separated by a layer of anion exchange membrane. The wire is copper, the anode solution is deionized water.

2.4 Data processing

The data need to be recorded is the value of the voltmeter and ammeter. Power Q is the product of current and time, When the current is a constant value, power Q is the current ,it is the integral of time.When the unit of current is ampere and the unit of time is second, the integrated area of the value S is the power.

So from Z=2, F=96500C·mol^{-1}, we can get:$n=S/1.93\times10^{5}$ (2-1)

$m_{Pb}=207.2\times n=1.0736\times10^{-3}\times S_{(g)}=1.0736\times S_{(mg)}$ (2-2)

3. Results and discussion

3.1 Temperature conditional experiment

Do experiments in the condition of: the experimental time is 4 hours, the anode solution is concentration of 0.1mol·l^{-1} KCl, the anode is iron, the temperature separately are 30℃,35℃,40℃, the result is shown in Figure 1. Determinate the concentration of lead ions and the volume volume of the solution after the experiment, calculate the content of lead according to equation 2-2.It is shown in table 2:

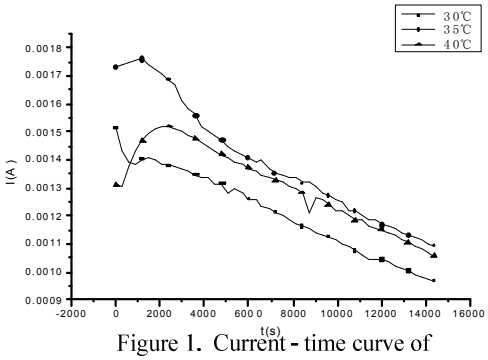


Figure 1. Current - time curve of Temperature Conditional Experiment

Table 2. Lead recovery rate of Temperature Conditional Experiment

Factor	30℃	35℃	40℃
Integration area	41.3543	44.3061	42.2224
quality of lead（mg）	44.398	47.567	45.33
Rate of recovery	88.26%	94.56%	90.12%

Table 2 shows, the recovery rate of 35 ℃ is better than the recovery rate of 30 ℃ and 40 ℃.

3.2 Time conditional experiment

Do experiments in the condition of: the experimental time is 6 hours, the anode solution is concentration of 0.1mol·l^{-1} KCl, the anode is iron, the temperature is 35℃, the result is shown in Figure 2.Integral with 0-7200s,0-14400s and 0-21600s in Figure 2, calculate the content of lead according to equation 2-2.

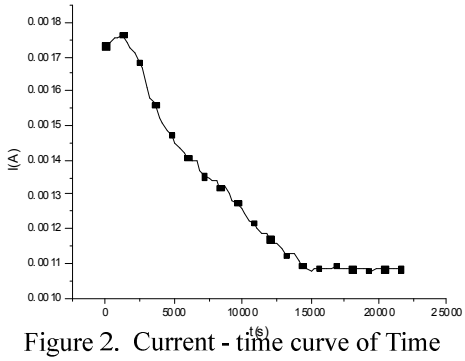


Figure 2. Current - time curve of Time Conditional Experiment

Table 3. Lead recovery rate of Time Conditional Experiment

Factor	2h	4h	6h
Integration area	27.4963	44.3648	44.9981
quality of lead（mg）	29.52	47.63	48.31
Rate of recovery	58.68%	94.69%	96.03%

Table 3 shows that when the power generation time is 2 hours, the recovery rate is 58.68%, if you add two hours, the recovery rate increased 36.01%, add two hours more, while the recovery rate only increased 1.34%.So 4 hours is the best time.

3.3 Concentration of the anode solution conditional experiment

Do experiments in the condition of: the experimental time is 4 hours, the anode solution are concentration of 0.05 mol • l^{-1},0.1 mol • l^{-1} and 0.15mol • l^{-1} KCl, the anode is iron, the temperature is 35℃ ， the result is shown in Figure 3. Figure 3 shows under the conditions of the same time, the current of 0.1M KCl is higher than one of 0.2M and 0.05M.Integral with the curve in Figure 3, calculate the content of lead according to equation 2-2. Calculate the recovery of lead.

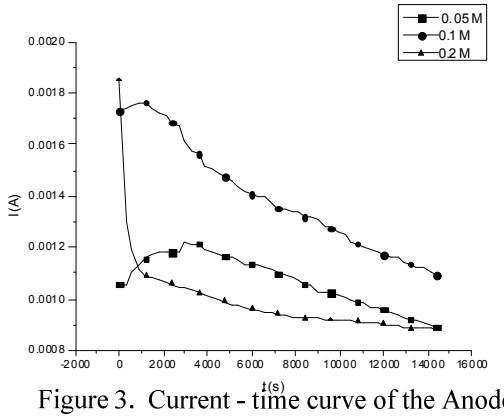


Figure 3. Current - time curve of the Anode Solution Conditional Experiment

Table 4. Lead recovery rate of Concentration of the Anode Solution Conditional Experiment

Factor	0.05M	0.1M	0.2M
Integration area	34.0415	44.3461	31.1196
quality of lead（mg）	36.547	47.61	33.41
Rate of recovery	72.64%	94.62%	66.39%

Table 4 shows that 0.1M is the optimal anode concentration ,we can get the highest recovery rate.

3.4 Anode conditional experiment

Do experiments in the condition of: the experimental time is 4 hours, the anode solution is concentration of 0.1mol·l^{-1} KCl, the anodes separately are iron, aluminum and zinc, the temperature is 35℃, the result is shown in Figure 4. Integral with the curve in Figure 4, calculate the content of lead according to equation 2-2. Calculate the recovery of lead.

Table 5 shows that when we use the aluminum electrode as the anode, the recovery rate is the highest, while the surface of aluminum electrode is easily passivated,and it prevents the reaction.From the analysis of economic value and the difficulty of the operation, Aluminum electrodes is not practical.The zinc electrode has the same problem, and the zinc price is relatively high.Using scrap metal as the electrode, the waste resources can be reused, and it can produce current.

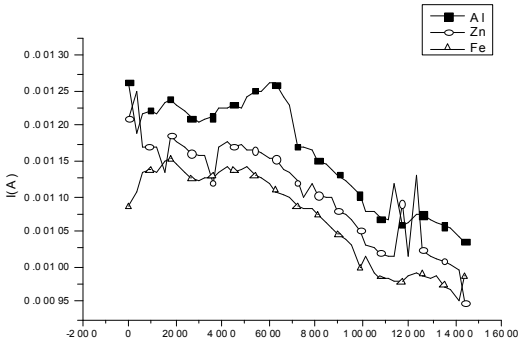


Figure 4. Current - time curve of the Anode Conditional Experiment

Table 5. Lead recovery rate of the Anode Conditional Experiment

Factor	Al	Zn	Fe
Integration area	45.1285	43.0523	40.7945
quality of lead（mg）	48.45	46.221	43.797
Rate of recovery	94.29%	89.96%	85.24%

3.5 Anode solution conditional experiment

Do experiments in the condition of: the experimental time is 4 hours, the temperature is 35℃, the anode solution is concentration of 0.1mol·l^{-1} KCl, KNO_3,Na_2SO_4, the anodes is iron, the result is shown in Figure 5. Integral with the curve in Figure 5, calculate the recovery of lead.

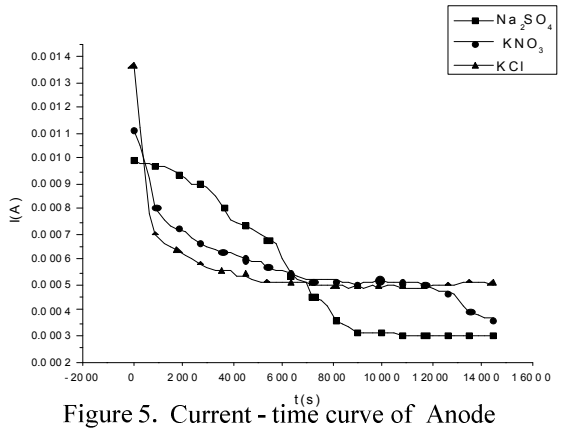


Figure 5. Current - time curve of Anode Solution Conditional Experiment

Table 6. Lead recovery rate of Anode solution Conditional Experiment

Factor	Na_2SO_4	KNO_3	KCl
Integration area	40.2395	41.5186	43.2709
quality of lead（mg）	43.201	44.574	46.456
Rate of recovery	85.88%	88.61%	92.35%

Table 8 shows that when the anode solution is KCl, we can get the highest recovery rate.

4. Conclusion

The method of generating electricity is a green chemical technology, it does not require energy. applied generation technologies to the recovery of lead,from conditional experiments, we can get the optimization parameters of lead recycling: The optimum temperature is 35 ℃, the optimum time is 4h, anode electrode material is iron, the anode solution is concentration of 0.1 mol • l^{-1} KCl solution.

References

[1] Huang Y,BatchelorB,Koseoglu S S.Crossflow surfactant-based ultrafiltration of heavymetals from waste streams[J].*Sep Sci and Tech*,1994,29 (15):1979-1998.

[2] CheryanM.Ultrafiltration andmicrofiltration handbook[M].*New Holland Avenue:USA,Technomic Publishing Company Inc*,1998.

[3] Scamehorn J F,Christian S D,E12Sayed D A,et al. Removal of divalentmetal cations and theirmixture from aqueous streams usingmicellar-enhanced ultrafiltration[J].*Sep Sci and Tech*, 1994,29 (7):809-830.

© (2012) Trans Tech Publications, Switzerland
doi:10.4028/www.scientific.net/AMM.164.115

Low-temperature synthesis and characterization of single-phase $BiFeO_3$ nano-crystallites

Huifen Guo[1,a], Shuxia Guo[2,b], and Liben Li[1,c]

[1]School of Physics and Engineering, Luoyang Key Laboratory of Photoelectric Functional Materials, Henan University of Science and Technology, Luoyang 471003, China

[2] School of Physics and Electronic Engineering, Jiaozuo Teachers College, Jiaozuo 454000, China

[a]E-mail:jyguohuifen@126.com, [b]E-mail: gsx0391@eyou.com, [c]E-mail:liliben2001@sina.com

Keywords: $BiFeO_3$, nano-crystallites, single-phase, synthesis

Abstract. Single-phase $BiFeO_3$ (BFO) nano-crystallites were successfully synthesized in the temperature range of 500 – 750 ^oC by a simple diluted HNO_3 sol method. During the crystallization process no intermediate phases were observed. As an example, we studied the electronic structure and thermodynamic stability of the BFO nano-crystallites calcined at 750 ^oC by X-ray photoelectron spectroscopy (XPS) and differential scanning calorimetry (DSC). The XPS showed that the oxidation state of Fe is Fe^{3+}. The DSC indicated a novel exothermic peak at about 769 ^oC during cooling, which might be due to $Bi_2Fe_4O_9$ or some other phases produced in the decomposition of BFO at high temperature.

Introduction

Multiferroic materials, which have coupled electric, magnetic, and structural order parameters that result in simultaneous ferroelectricity, ferromagnetism, and ferroelasticity [1], are of great interest due to their potential applications for novel multifunctional devices and for exploring fundamental science in the coupling mechanism between electronic and magnetic order parameters [2-4]. As one of several rare single-phase multiferroic materials at room-temperature, bismuth ferrite ($BiFeO_3$, BFO) with a coexistence of ferroelectric (T_C~850 ^oC) and antiferromagnetic (T_N~370^oC) order parameters has attracted much attention for many decades[5-7].

However, potential applications of bulk BFO were greatly limited due to its leakage current problems, which is usually caused by defects and nonstoichiometry [8,9]. In order to overcome these disadvantages, several attempts were done to obtain single-phase BFO powders, such as sol–gel method [10], precipitation/coprecipitation [11], hydrothermal synthesis [12], high energy ball milling [13] and the liquid phase sintering with a high heating rate (100^oC/s) [8]. Among these methods, the sol–gel route is attractive for the advantage of easy control of chemical composition. Up to now, in the sol–gel synthesis of single-phase BFO powders, the sol is usually prepared based on carboxylic acid [14], acetic acid [10,15], ethylenediamine-tetraacetic acid route [16], etc, by which BFO nanopowders were usually synthesized not from amorphous structure but from some undesirable impurities produced at the lower temperature.

In this letter, we report a simple approach to synthesize pure BFO nano-crystallites through a diluted HNO_3 complexing sol–gel process at low temperature. Single-phase BFO nano-crystallites were crystallized from amorphous structure at a temperature as low as 500 ^oC, not having undergone other intermediate phase. This process is simple, energy saving and cost effective. The structure and thermodynamic stability of as-prepared BFO nanocrystallites were characterized by X-ray diffraction (XRD), X-ray photoelectron spectroscopy (XPS) and differential scanning calorimetry (DSC). A novel exothermic peak was observed at about 769 ^oC by DSC during cooling, which may be due to the $Bi_2Fe_4O_9$ or some other phases produced in the decomposition of BFO at high temperature.

Experiment

Synthesis of BFO nano-crystallites. The BFO nano-crystallites were synthesized by chemistry solution methods without and with the addition of diluted HNO_3, respectively. According to the atomic ratio of Bi/Fe = 1, the analytical reagents $Bi(NO_3)_3 \cdot 5H_2O$ (99% pure) and $Fe(NO_3)_3 \cdot 9H_2O$ (98.5% pure) were dissolved in ethylene glycol. The parent solution was stirred for hours at room temperature until the $BiFeO_3$ concentration reached 0.3 M, and then divided into two parts. One part was added with diluted 2mol/L HNO_3 in the volume proportion of 1.5ml per 10ml parent solution. Here, the diluted HNO_3 was used as the chelating agent to complex the cations. After stirring for half an hour, a stable transparent, blackish red, and clear sol was obtained. The other part of the parent solution and the sol with diluted HNO_3 were dried at 60°C for about 48 h. The obtained dried samples were grounded into fine powders in the agate crucible, and calcined in air at temperatures of 350, 450, 500, 550, 600, 680, and 750 °C for 0.5 h, respectively. After quenching to room temperature, the BFO nano-crystallites were obtained and re-grounded into powders for measurements.

Characterization. The as-prepared samples were characterized by XRD on an X'Pert Philips X-ray diffractometer with Cu Kα radiation (λ=1.5406 Å) with the scanning step size and scanning rate of 0.02° and 0.3°/min. The XRD was carried out at 40KV and 40 mA. The crystallite sizes were calculated by Scherrer's equation. XPS (Kratos Axis Ultr) was used to characterize the valence of the elements in the samples. DSC (Exstar 6000 thermal system) were conducted with a heating rate of 10°C/min and in nitrogen ambience.

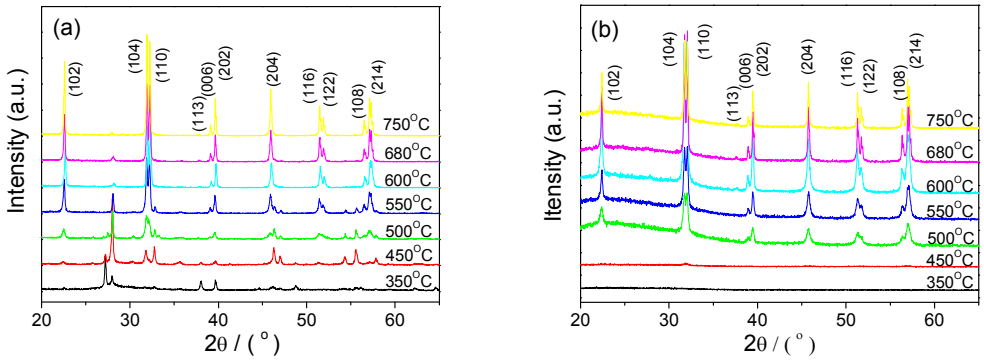


Fig. 1 XRD patterns of BFO powders synthesized (a) without and (b) with the addition of the diluted HNO_3 at various sintering temperatures.

Results and discussion

XRD patterns of BFO powders synthesized without and with the addition of the diluted HNO_3 are shown in Figs. 1(a) and 1(b), respectively, in which the corresponding sintering temperatures were labeled. After calcined at 350 °C, the powders synthesized by the diluted HNO_3 sol displayed completely amorphous XRD patterns, while XRD of the other showed some unidentified Bragg reflections. The relative diffraction intensity of all these unidentified reflections decreased with the increasing of sintering temperature above 500 °C, while the phase BFO emerged out abundantly and became stronger. After calcined at 750 °C, single-phase BFO was achieved, the XRD pattern of which is well consistent with the power data of JCPDS Card No. 86-1518. However, the XRD analyse of the samples synthesized by the diluted HNO_3 sol indicates that single-phase BFO was crystallized from amorphous structure at a lower sintering temperature 500 °C, not having undergone other intermediate phases. With the increasing of sintering temperature, the relative diffraction intensity of BFO became stronger. The samples calcined between 500 °C to 750 °C exhibit the same rhombohedrally distorted perovskite structure and no impurity phases were detected. The crystal size of the powders calcined at 750 °C was calculated about 83 nm using Scherrer's formula.

To determine the oxidation state of Fe, XPS was carried out on BFO sample calcined at 750°C by the diluted HNO_3 sol method. Figs. 2(a) and 2(b) show the XPS of Fe 2p and O1s, respectively. The 3/2 and 1/2 spin-orbit doublet component of the Fe 2p photoemission were located at 710.3 and 723.7eV, respectively, which were identified as Fe^{3+}. While no peak due to $Fe2^{+}$ can be found. It indicated that the oxidation state of Fe was Fe^{3+}, which was advantageous for producing BFO nanopowders with low leakage. In Fig. 2(b), the asymmetric broad bond at 529.3eV can be divided into three subbands at 529.3, 530.7, 531.4eV using Gaussian fitting, which correspond to the O1s binding energy of the lattice, hydroxy oxygen and adsorbent oxygen in the sample.

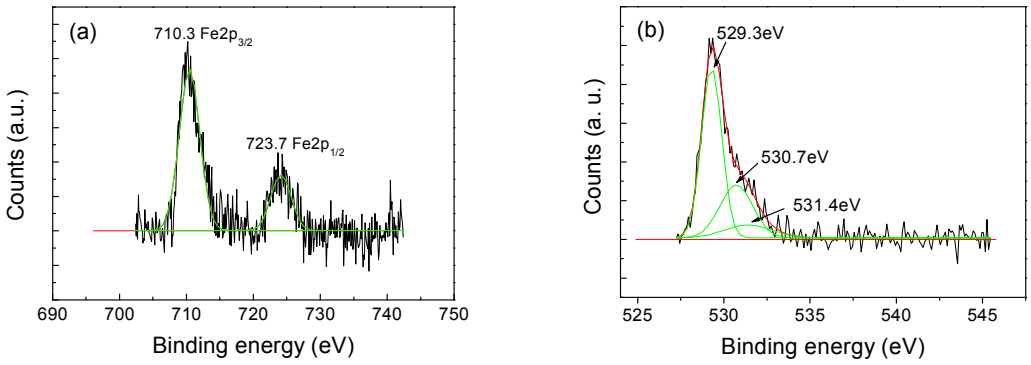


Fig. 2 X-ray photoelectron spectrum of the single-phase BFO calcined at 750°C. (a) the Fe2p line and (b) the O1s line.

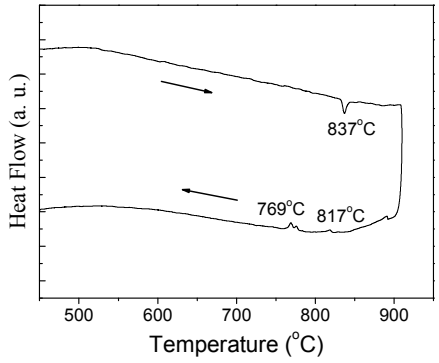


Fig. 3 Dependence of heat flow with temperature for single-phase BFO calcined at 750°C.

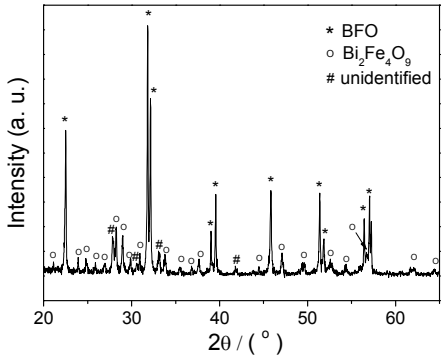


Fig. 4 The XRD pattern of the BFO sample which were sintered again at 850 °C for 0.5h after calcined at 750 °C.

Thermodynamic stability of the pure BFO powders calcined at 750 °C has been investigated by DSC while heating and cooling in the temperature range of 450 °C ~ 900 °C with heating/cooling rate of 10 °C/min in N_2 atmosphere (Fig. 3). A stronger endothermic and a weaker exothermic peaks are observed, respectively, at about 837 °C during heating and about 817 °C during cooling. The positions of the two peaks are consistent with those observed on BFO ceramic with grain size 1~3μm by Kumar et al [17], which indicates one reversible ferroelectric phase transformation at about 837 °C. But the relative intensities of them were inverted in the BFO ceramic synthesized by Kumar et al., in which the peak at about 817 °C was greatly stronger than that at about 837 °C. Besides, a novel exothermic peak was also observed at about 769 °C during cooling in Fig. 3. From these phenomena, it was suggested that the BFO nano-crystallites were metastable and were partly decomposed into some other phases at 850 °C. The decomposition caused the reduction of BFO phase in the samples, resulting in the decrease of the total heat from phase transformation at about

817 °C. The products of BFO thermal decomposition underwent a phase transformation at about 769°C during the cooling, in which some heat was released. So, the greatly weaken and the novel exothermic peaks are observed, respectively, at 817 °C and 769 °C during the cooling.

In order to confirm the suggestion above, the BFO powders calcined at 750 °C were sintered again at 850 °C for 0.5h. The corresponding XRD results are shown in Fig.5. After sintering at 850°C for 0.5h, the sample shows the presence of $Bi_2Fe_4O_9$ phase, in accord with the data of JCPDS card No. 72-1832. The majority of the sample is still the rhombohedrally distorted perovskite phase BFO. Besides, some unidentified Bragg reflections are also observed. It indicates that the BFO nano-crystallites were metastable with respect to $Bi_2Fe_4O_9$, and partly decomposed into $Bi_2Fe_4O_9$ and some other phases at 850 °C, which supports our suggestion above.

Conclusions

In summary, conditions for synthesizing single-phase BFO nano-crystallites using the diluted HNO_3 sol method were established. XRD indicates that the moderate addition of the diluted HNO_3 can inhibit impurities produced by chemistry solution method and reduce the temperature of synthesizing single-phase BFO nano-crystallites. By the moderate addition of the diluted HNO_3, single-phase BFO nano-crystallites were successfully crystallized at a temperature as low as 500°C from amorphous structure, not having undergone other intermediate phases. And all samples calcined between 500 °C to 750 °C exhibited the same rhombohedrally distorted perovskite structure of BFO without other impurities. The oxidation state of Fe was Fe^{3+} in the sample calcined at 750°C. However, the BFO nano-crystallites are metastable with respect to $Bi_2Fe_4O_9$, and partly decomposed into $Bi_2Fe_4O_9$ and some other phases after calcined at 850 °C.

References

[1] J. Wang, J.B. Neaton, H. Zheng, V. Nagarajan, S.B. Ogale, B. Liu, D. Viehland, V.Vaithyanathan, D.G. Schlom, U.V. Waghmare, N.A. Spaldin, K.M. Rabe, M. Wuttig and R. Ramesh, Epitaxial $BiFeO_3$ multiferroic thin film heterostructures, Science 299 (2003) 1719-1722.

[2] N. Hur, S. Park, P.A. Sharma, J.S. Ahn, S. Guha and S-W. Cheong, Electric polarization reversal and memory in a multiferroic material induced by magnetic fields, Nature 429 (2004) 392-395.

[3] T. Kimura, T. Goto, H. Shintani, K. Ishizaka, T. Arima and Y. Tokura, Magnetic control of ferroelectric polarization, Nature 426 (2003) 55-58.

[4] J.F. Scott, Applications of Modern Ferroelectrics, Science 315 (2007) 954-959.

[5] P. Fischer, M. Polomska, I. Sosnowska and M. Szymanski, Temperature dependence of the crystal and magnetic structures of $BiFeO_3$, J. Phys. C 13 (1980) 1931-1940.

[6] W. Eerenstein, N.D. Mathur and J.F. Scott, Multiferroic and magnetoelectric materials, Nature 442 (2006) 759-765.

[7] G. Catalan and J.F. Scott, Physics and Applications of Bismuth Ferrite, Adv. Mater. 21 (2009) 2463-2485.

[8] Y.P. Wang, L. Zhou, M.F. Zhang, X.Y. Chen, J.-M. Liu and Z.G. Liu, Room-temperature saturated ferroelectric polarization in $BiFeO_3$ ceramics synthesized by rapid liquid phase sintering, Appl. Phys. Lett. 84 (2004) 1731-1733.

[9] X.D. Qi, J. Dho, R. Tomov, M.G. Blamire and J.L. MacManus-Dirscoll, Greatly reduced leakage current and conduction mechanism in aliovalent-ion-doped $BiFeO_3$, Appl. Phys. Lett. 86 (2005) 062903-1-3.

[10] J.K. Kim, S.S. Kim and W.-J. Kim, Sol–gel synthesis and properties of multiferroic $BiFeO_3$, Mater. Lett. 59 (2005) 4006-4009.

[11] J.-C. Chen and J.-M. Wua, Dielectric properties and ac conductivities of dense single-phased $BiFeO_3$ ceramics, Appl. Phys. Lett. 91 (2007) 182903-1-3.

[12] C. Chen, J.R. Cheng, S.G. Yu, L.J. Che and Z.Y. Meng, Hydrothermal synthesis of perovskite bismuth ferrite crystallites, J. Crystal Growth 291 (2007) 135-139.

[13] V.F. Freitas, H.L.C. Grande, S.N.D. Medeiros, I.A. Santos, L.F. Cótica and A.A. Coelho, Structural, microstructural and magnetic investigations in high-energy ball milled $BiFeO_3$ and $Bi_{0.95}Eu_{0.05}FeO_3$ powders, J. Alloys Compd. 461 (2008) 48-52.

[14] S.M. Selbach, M.-A. Einarsrud, T. Tybell and T. Grande, Synthesis of $BiFeO_3$ by Wet Chemical Methods, J. Am. Ceram. Soc. 90 (2007) 3430-3434.

[15] J. H. Xu, H. Ke, D. C. Jia, W. Wang and Y. Zhou, Low-temperature synthesis of $BiFeO_3$ nanopowders via a sol–gel method, J. Alloys Compd. 472 (2009) 473-477.

[16] T. Xian, H. Yang, X. Shen, J.L. Jiang, Z.Q. Wei and W.J. Feng, Preparation of high-quality $BiFeO_3$ nanopowders via a polyacrylamide gel route, J. Alloys Compd. 480 (2009) 889-892.

[17] M.M. Kumar and V.R. Palkar, Ferroelectricity in a pure $BiFeO_3$ ceramic, Appl. Phys. Lett. 76 (2000) 2764-2766.

© (2012) Trans Tech Publications, Switzerland
doi:10.4028/www.scientific.net/AMM.164.120

Electron transport of Boron Nitride nanoribbons materials

Dongmei Zhang, Dequan Wang, Huiqin Yang, Zhigang Bao,

Yongsheng Zhang*

Department of mathematics and Physics, Luoyang institute of science and technology, Luoyang 471023, China

*email: yszhang@lit.edu.cn

Keywords: electron transport properties; hexagonal boron nitride nanoribbons; Green's function

Abstract: The transport properties of hexagonal Boron Nitride nanoribbons (BNNRs) are investigated by the Green's function method. The effect of triangle vacancy on the electron transport of BNNRs is different from that of perfect BNNRs. In particular, the features of the conductance steps are significantly changed in compared to perfect BNNRs. The conductance and density of state of zigzag Boron Nitride nanoribbons are calculated and analyzed in detail to explain these characteristic.

1. Introduction

With the single-layer of hexagonal boron nitride (h-BN) [1-3] can be obtained from the experiment, people pay more and more attention to h-BN which has similar structure type of new graphite nanometer material [4]. Compared with the graphite, boron nitride has not only excellent electronic properties due to the unique hexagonal structure of graphite, such as high quantum transport properties, and ionization effects due to nitrogen atoms and boron atoms in the hexagonal structure. In addition, boron nitride also has many excellent properties different from those on the graphite. For example, the wide band gap, the higher thermal stability and chemical stability. The rapid development of science and technology makes cutting-edge field of higher and higher requirements for integrated. Therefore, the one-dimensional nanoribbons are more competitive than single-layer atoms nanosheets.

Recent studies show that both vacancy defects on the boundary and internal defects will have a significant effect on the electronic structure and transport properties of graphene nanoribbons [5-9]. The presence of triangle vacancy is found to can change the distribution of charge density in the h-BN sheets. As for the quasi-one-dimensional BNNRs, it is shown that the vacancy could lead to an electron localized state and spontaneous magnetization. In the preparation of boron nitride nanoribbons, the triangular vacancy defects were inevitable introduced. And that recent studies show that the triangular defects on the electronic properties of boron nitride nanoribbons have a great impact - resulting in boron nitride nanoribbons with a spontaneous polarization. It is well-known that the role of defects on the transport properties of graphene nanoribbons is very significant. Nevertheless, by comparing the graphene nanoribbons, to the best of our knowledge, research on the vacancy on the electron transport through BNNRs has not received deserved attention until now. Therefore, what happens when the triangle vacancy impacts on the electron transport of BNNRs is interesting and also important in the design of electron devices. In this paper, we investigate electron transport properties of boron nitride nanoribbons (BNNRs) with a triangle vacancy.

2. Model and method

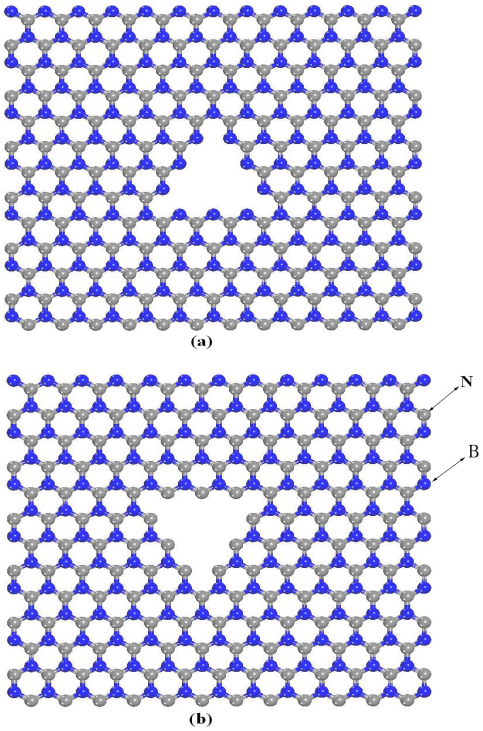


Fig. 1 Two types of triangle vacancy of BNNRs (a) edge atom for boron atoms, (b) edge atom for nitrogen atoms.

The geometries of BNNRs with a triangle vacancy are respectively shown in Fig. 1(a) and (b). The different colors represent two different types of atom. To investigate the electron transport properties, we employ the tight-binding model and the Green's function [10] for BNNRs, Hamiltonian is expressed as

$$H = \varepsilon_B \sum_i a_i^+ a_i + \varepsilon_N \sum_j b_j^+ b_j + V \sum_{<i,j>} (a_i^+ b_j + H.c) \quad (1)$$

where $\varepsilon_B = 0eV$ and $\varepsilon_N = 4.632eV$ separately denote the lattice-site energies of B and N atoms. a_i^+ (b_j^+) is creation operator at site i (j) of B (N) atom. V = 2.4 eV expresses the on-site energies of nearest neighbor between two atoms. The sums in <i,j> are all the nearest-neighbor atoms. According to the Green's function equation, one can show the Green's function of BNNRs:

$$G_s = (E - H_0 - \Sigma_L - \Sigma_R)^{-1} \quad (2)$$

where H_0 is the Hamiltonian of the central region and $\Sigma_{L/R} = H_1^+ g_{L/R} H_1$ represents the self-energy term of left or right lead, respectively, H_1 denotes the interaction matrix between lead and central region. $g_{L/R}$ represents the Green's function of left or right lead, which could be obtained base on the recursive Green's function method (RGF) [11]. Once the total Green's function is calculated, the conductance *G* of BNNRs can be obtained:

$$G = \frac{2e^2}{h} Tr\left(\Gamma_L G_s^+ \Gamma_R G_s\right) \quad (3)$$

where $\Gamma_{L,R} = i\left(\Sigma_{L,R} - \Sigma_{L,R}^*\right)$ is the coupling function of left or right lead.

3. Results and discussion

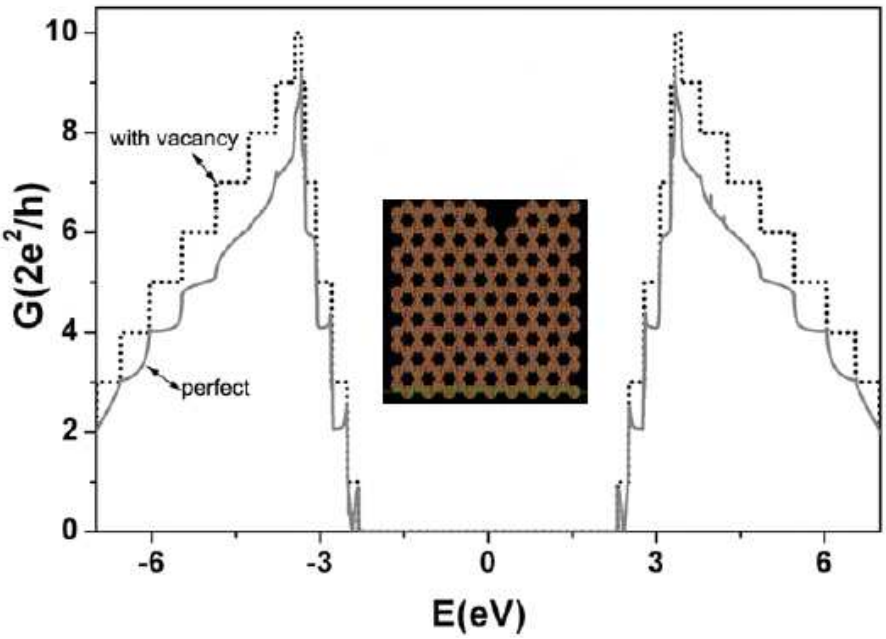


Fig.2 The conductances as a function of electron energy for defects and perfect BNNRs with W=10

In Fig. 2 the transport properties of the nanoribbons with W=10 were calculated , at the edge of the missing four atoms of the triangle-shaped vacancy (shown in the illustration). Where the solid line represents the conductances of perfect boron nitride nanoribbons, dashed line denotes the conductances of nanoribbons with triangle-shaped vacancy. We can see the conductance steps of perfect zigzag boron nitride nanoribbons show first increasing and then decreasing trend with increasing electron energy. It is found that the conductance exhibits a perfect stepwise profile and a wide-band-gap exists around the Fermi energy. The maximum value of conductance is $10G_0$ ($G_0=2e^2/h$), that reflects the number of transmission channels in nanoribbons. From the conductance spectrum of nanoribbons with triangle-shaped vacancy, we can find that low valleys with zero-conductance appear in the conductance steps of the low energy region. The other steps of the low-energy region relative to perfect nanoribbons steps have reduced, and the unobvious valley structure appear. Meanwhile, steps disappear on the highest point of conductance step, and the trend with rise linear emerges. The highest conductance value also decreased compared with the value of perfect nanobobons. These results indicate that the transport properties of BNNRs are very sensitive to triangle-shaped vacancy on the structure.

To further characterize the nature of the transport properties of nanoribbons with triangle-shaped vacancy, we calculated the state density [DOS] for perfect nanoribbons and defects nanoribbons. The results are shown in Fig. 3. Where the solid line represents the density of states of perfect boron nitride nanoribbons, dashed line denotes the density of states of defective boron nitride nanoribbons. We can see that the first step of the corresponding conductance in the low energy region responses to Van Hove in the same electron energy for DOS of the perfect and defects nanoribbons. However, a very high peak between Van Hoves before low-energy area appears for the nanoribbons with vacancy.

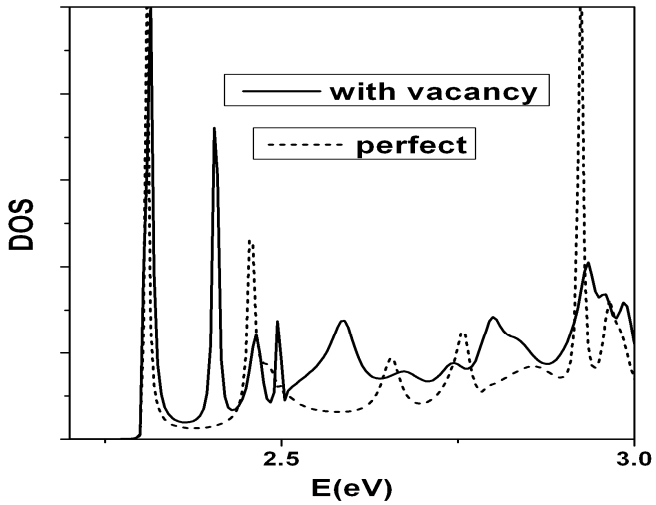


Fig.3 The density of state as a function of electron energy for defects and perfect BNNR with W=10

And this peak value of the electronic energy just corresponds to the electronic energy value of the low valley with zero-conductance in conductance steps. Thus, we speculate that the low valley with zero-conductance is caused by electrons localized in conductance steps.

4. Conclusions

In conclusion, we have studied the electron transport properties of BNNRs with a triangle vacancy by using the Green's function method. It is shown that the transport properties are sensitive to the triangle vacancy.

Acknowledgements

The authors wish to acknowledge financial support from the NSF of China (Grant no. 60876014), and the NSF of Henan Province (Grant nos. 072300410180 and 2010B140009). The project was also sponsored by Program for Science and Technology Innovation Talents in the Universities of Henan Province (Grant no. 2008HASTIT029), and the Innovation Scientists and Technicians Troop Construction Projects of Henan Province (No.104100510018).).

References

[1] K. S. Novoselov, D. Jiang, F. Schedin, T. J. Booth, V. V. Khotkevich, S. V. Morozov and A. K. Geim Proc. Natl. Acad. Sci. 102 (2005) 10451.
[2] W. Q. Han, L. J. Wu, Y. M. Zhu, K. Watanabe and T. Taniguchi, Appl. Phys. Lett. 93 (2008) 223103.
[3] Pacilé D, Meyer J C, Girit Ç Ö and Zettl A Appl. Phys. Lett. 92 (2008) 133107.
[4] Arnaud B, Lebegue S, Rabiller P and Alouani M, Phys. Rev. Lett. 96 (2006) 26402.
[5] L.C. Yin, H.M. Cheng, R. Saito, Phys. Rev. B 81 (2010) 153407.
[6] M.S. Si, D.S. Xue, Phys. Rev. B 75 (2007) 193409.
[7] A. Du, Y. Chen, Z. Zhu, R. Amal, G.Q. Lu, S.C. Smith, J. Am. Chem. Soc. 131 (2009) 17354.
[8] S. Tang, Z. Cao, Comput. Mater. Sci. 48 (2010) 648.
[9] M. Topsakal, E. Aktürk, S. Ciraci, Phys. Rev. B 79 (2009) 115442.
[10] Chen Y P, Xie Y E and Yan X H J. Appl. Phys. 103 (2008) 063711.
[11] Sols F, Macucci M, Ravaioli U and Hess K, J. Appl. Phys. 66 (1989) 3892.

© (2012) Trans Tech Publications, Switzerland
doi:10.4028/www.scientific.net/AMM.164.124

The Structure and Fluid Flow Analysis for a New SXSH Static Mixer

Qing Wu,QuanLai Li, BaoAn Han

School of Material and Mechanical Engineering, Beijing Technology and Business University, Beijing 100048, China

Email: wuqing@th.btbu.edu.cn;liquanlai@th.btbu.edu.cn;646333407@qq.com

Keywords: static mixer, new structure, fluid flow analysis

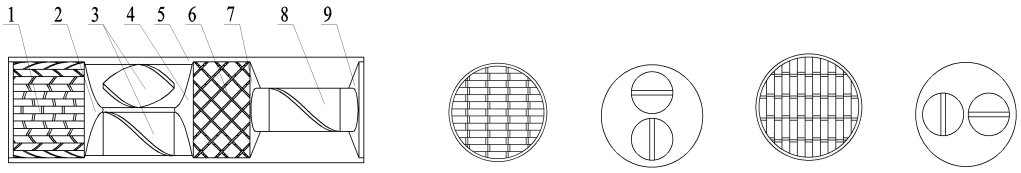
Abstract. In this paper, the new SXSH static mixer structure is described by the author firstly. Then the working flow field is analyzed. The fluid flow is impinged, separated, flowed around and merged by the SX and SH static mixer. The mixture effect is strengthened. The application field of the mixer is expanded and the mixer efficiency is improved. Meanwhile the static mixer structure dimension is reduced. Under the considerations of the relationships of real structure flowage parameters and the influence factors comprehensive analysis, the turbulent flow pattern is derived and analyzed. The results can be used for the further structure improvement, as well as the parameters effectively selection and optimization, of the SXSH static mixer.

Introduction

Static mixer is an ideal absorption and mixer device, with the advantages of small volume, simple structure and none applied force. At present, there are many types of static mixer. However since the structure of the inner mixer unit is singleness, the application field is limited. In order to expand the application, enhance the mixture efficiency, as well as reducing the static mixer structure dimension, various mixers are analysis by the author. Then the new SXSH static mixer is developed combined the characteristics of the existing mixer. The mixer structure is introduced firstly. Then the preliminary theoretical analysis of the fluid flow is carried out, under the consideration of turbulent flow pattern in practical working condition of the inner static mixer structure and combined with the relevant turbulent flow model.

Structure characteristics of SXSH static mixer

The SX and SH static combined mixer units are fixed in the outer pipe of the new SXSH mixer in ordered, which is shown in figure 1. There is a fluid transition area between the mixer units. The static mixer unit structure is shown in figure 2.



1, 6. SX static mixer unit 2, 7. fluid transition area 1 3, 8. fixed spiral blade
4, 9. fluid transition area 2 5. outer pipe

Fig.1 The structure of SXSH mixer

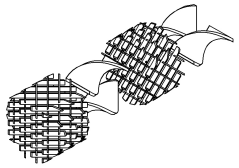


Fig.2 Static mixer unit structure

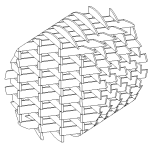


Fig.3 SX static mixer unit structure

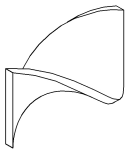


Fig.4 SH static mixer unit structure

The inside of the outer pipe is separated into different sectors. The SX static mixer unit is fixed in the area of hollow straight cylinder sector, while the SH static mixer unit is fixed in the area of bimodal pore sector. The fluid transition area is formed by the curved surface at the two extremities of the bimodal pore.

The SX type static mixer is composed of the stitch welded multi-layer reciprocal chiasmata stainless steel thin crossbands. In the single level, the crossbands are paralleled with the same spacing, and the angle between the orientations of crossband and the pipe axis is 45°, meanwhile the angle between the orientations of adjacent crossbands is 90° which shown in figure 3.

The SH type static mixer is composed of double blades which are fixed into the two paralleled pore respectively. The chiasmata stainless steel spiral blade is twisted 180° from one side to the other side of the pore(figure 4). The angle between the blades of two paralleled pores is 90°. The angle between the orientations of adjacent site of pores is 90°.

The flow pattern in the channel of SXSH static mixer

The fluid, which flows into the SX mixer unit along the outer pipe axis, impinges onto the blade of the unit structure, and then it is divided into two streams. One stream flows into the channel formed by the adjacent crossband, and the flow direction is changed about 45°. Then the non-barrier concurrent is formed, which is main stream. The other stream, the flow direction is changed about 45° in the reverse direction, bypassing the crossband. The circumferential flow which is vertical to the flat plate is formed. Since the upper and lower section of the channel is expanded suddenly, the fluid mixed with the adjacent fluid by the vertical impingement when it flows bypassing the crossband. Then the channel space of adjacent crossband is narrowing. Therefore, the channel space of circumferential flow is narrowing which lead to the vertical impingement of adjacent fluid. Then the channel space is expanded, therefore the wave current is formed. Both of the concurrent and the circumferential flow are blocked and change the flow direction when they are forced to flow through the channel along this direction. Due to the special reciprocal chiasmata structure of static mixer unit, the two-phase flow impingement and agitating along different direction, and the intensity eddy mixing is formed.

The fluid flow from the SX mixer unit, through the fluid transition area, and is forced into the bimodal pore of the SH mixer unit. Then the fluid is divided into two sections by the spiral blade fixed at the middle of the pore. The fluid flows and revolves along the spiral pore. Hence the intense rotational agitation is formed. As for a semicircular cross-sectioned channel, the flow near the edge of the channel is not axisymmetrical. There is a curved vortex at the core. The circulation flow (spin) is formed along the channel normal center, meanwhile the fluid revolves along the channel spiral blade. The fluid flow revolution is completed from the inlet to the outlet. The average angular velocity is small when the fluid flows into the channel. As the inlet distance increases, the average angular velocity becomes larger. The average angular velocity is the largest and the agitating is the most intense at the outlet position. The fluid flows out from the bimodal pore and through the fluid transition area, leading to the intense mixture. Then it flows into the next SX mixer unit. The fluid mixed uniformly after flowing through many units in such way.

The space change will lead to the fluid flow pressure and velocity rather large change. The velocity of inlet fluid from the SX unit will increase due to the space reduction. The fluid flow out from the SH unit, the space enlarge and the flow velocity is reduced, which is benefit for the mixture.

The fluid flow analysis of SHSX mixer

The fluid flow of SHSX mixer is the complicate three-dimensional turbulent flow. In order to develop the fluid flow model, it is necessary to make some simple in the theoretical analysis.

The fluid flow analysis of SX mixer

The fluid can be divided into two streams of concurrent with different directions and one stream of rotation flow with expanding and narrowing continuously.

The fluid flows into the static mixer unit along the outer pipe axis and impinges onto the crossband with the inclination angle of 45°. Then it is divided into concurrent and circumferential flows. It is assumed that the distribution of the flow velocity is uniformly with a distance far away from the impingement surface. The cross point of outer pipe axis and the crossband surface is the initial point of the Cartesian coordinate, the x axis is vertical to the crossband surface, y axis is parallel to the corssband surface, the angle between the out pipe axis and the x axis is α. The momentum transport equation is $\oiint_{\Sigma} \rho u_1(u_1 \cdot n)dA = \iint_{1,2} \rho u_1(u_1 \cdot n)dA + \iint_{2,3+6,1} \rho u_1(u_1 \cdot n)dA + \iint_{3,4} \rho u_2(u_2 \cdot n)dA + \iint_{5,6} \rho u_3(u_3 \cdot n)dA$

The circumferential flow in the SX mixer unit

The flow area is expanded suddenly and then narrowed when fluid is forced to flow through the space between the adjacent crossband, while the flow area is narrowed and then expanded successively when the flow is forced to bypass the crossband. As a result, the streams of flow impinge mutually and the spiral vortex is formed.

The flow pattern analysis of the fluid flow along the crossband

The complex potential can be described as $W(z) = A(r^n \cos n\alpha + ir^n \sin n\alpha)$.The circumferential flow pattern can be described in a power function as $W = Az^n$.The velocity field can be described as $\overline{U} = \frac{dW}{dz} = nAz^{n-1}$.The flow impinges on crossband with a angle and bypasses the crossband, $n = 1/2$, then $W = A\sqrt{z} = A[\sqrt{r}\cos(\alpha/2) + i\sqrt{r}\sin(\alpha/2)]$.The fluid flow bypass the crossband with the angle of 2π, and the $W(z)$ can be described as $W = -A\sqrt{r}$.

The flow pattern analysis of the fluid flows through the expanded channel

When the channel expanded suddenly, the centerline part of the fluid flow direction is not changed, while the direction of marginal streamlines is changed, the outermost streamlines flow along the vertical direction. The Cartesian coordinate is built with the x_1 axis of centerline and y_1 axis direction is radial. The continuity equation can be described as $\frac{\partial u_{11}}{\partial x_1} + \frac{\partial \upsilon_{11}}{\partial y_1} = 0$. As for the Reynolds average motion equation of y_1 direction can be described as $(u_m + u_{11})\frac{\partial \upsilon_{11}}{\partial x_1} + \upsilon_{11}\frac{\partial \upsilon_{11}}{\partial y_1} = -\frac{1}{\rho}\frac{\partial p}{\partial y_1} - \frac{\partial}{\partial x_1}\overline{\upsilon_{11}'u_{11}'} - \frac{\partial}{\partial y_1}\overline{\upsilon_{11}'^2}$. The fluid boundary layer is formed and then separated. The boundary layer momentum thickness δ can be expressed by $\delta(y_1) = l\left(\frac{u_{12}}{u_{10}}\right)^{-3}\left[c_1 + \left(\frac{c_2}{2}\right)^{1+\frac{1}{n}}\int_{\frac{y_c}{l}}^{\frac{y}{l}}\left(\frac{u_{12}}{u_{10}}\right)^{3+\frac{2}{n}} d\left(\frac{y_1}{l}\right)\right]^{\frac{n}{n+1}}$. c_1, c_2 ,n are determined by the experiments. As for the separation of the boundary layer $\frac{\partial u_{y_1}}{\partial z_1} = \frac{u_{12}(1-\eta)^2}{\delta}\left[4\eta\ (1-\frac{B}{6}) + (2+\frac{B}{6})\right]$, $\eta = \frac{z_1}{\delta\ (y_1)}$.

The flow pattern analysis at the final position of the channel

The inverse eddy flow is formed with the equivalent radius of r_0 and angular velocity of ω_1 when the fluid flow from the channel to the pipe wall. As for $r \le r_0$, the flow field is $u_\theta = r\omega$, the eddy flow velocity circulation is $\Gamma = \int_0^{2\pi} r u_\theta d\theta = 2\pi r^2 \omega$;vorticity is $\Omega_z = 2\omega$. As for $r > r_0$, the velocity field is $u_\theta = \frac{r_0^2 \omega}{r}$; the circumference velocity circulation of potential vorticity is $\Gamma = 2\pi r_0^2 \omega$.

The fluid, which impinges on the pipe inner wall with angle of 45°, is separated and the flow direction is changed, the velocity distribution of potential flow can be described as $U = ax_1, V = ay_1$.

Fluid flow analysis in the channel of SH mixer unit

The fluid flows through the fluid transition area and is forced into the spiral channel of SH mixer. The initial point of the Cartesian coordinate is the spiral blade endpoint, the x axis is along the pipe wall, while the y axis is along the exterior normal of the pipe wall. The N-S equation can be described in a simple form as $\frac{\partial u}{\partial x} + \frac{\partial \upsilon}{\partial y} = 0$, $\frac{\partial u}{\partial t} + u\frac{\partial u}{\partial x} + \upsilon\frac{\partial u}{\partial y} + \frac{u\upsilon}{R} = -\frac{1}{\rho}\frac{\partial p}{\partial x} + \nu\left[\frac{\partial^2 u}{\partial y^2} - \frac{\partial^2 \upsilon}{\partial x \partial y} + \frac{1}{R}\left(\frac{\partial u}{\partial y} + \frac{\partial \upsilon}{\partial x}\right) - \frac{u}{R^2}\right]$, $\frac{\partial \upsilon}{\partial t} + u\frac{\partial \upsilon}{\partial x} + \upsilon\frac{\partial \upsilon}{\partial y} - \frac{u^2}{R} = -\frac{1}{\rho}\frac{\partial p}{\partial y} + \nu\left[\frac{\partial^2 \upsilon}{\partial x^2} - \frac{\partial^2 u}{\partial x \partial y} - \frac{1}{R}\frac{\partial u}{\partial x} + \frac{u}{R^2}\frac{dR}{dx}\right]$.

Conclusion

The new SXSH mixer designed by the author combines the advantages of SX and SH static mixer. Therefore, the application field of the static mixer is expanded and the mixer efficiency is enhanced, meanwhile the dimension of the static mixer is reduced. According to the analysis and study of the SXSH mixer, considering the comprehensive influencing factor, applying the numerical solution, the results are useful for the structure parameters effectively selection and the characteristic optimization.

Acknowledgements

Supported by the Beijing College Students Research and Career-creation Program

REFERENCES

[1] Wu Qing,Wang Xiaobei,Li Quanlai,Yang Yanxiang: Advanced Materials Research, Vol. 422 (2012) pp 486-489.

[2] Zhang Zhixiong，Dong Zengnan: Viscous Fluid Mechanics.TSINGHUA UNIVERSITY PRESS, BEIJING.1998 (In Chinese).

[3] Wu Qing, Study of Two-Phase Flow in SH Type High-Efficiency Static Mixer,Proceedings of the First International Conference on Mechanical Engineering(ICME2000), Compendex pp97-98, Shanghai,China.2000.

[4] Zhang Zhaoshun，Cui Guixiang: Fluid Mechanics(The Second Edition).TSINGHUA UNIVERSITY PRESS, BEIJING.2006 (In Chinese).

[5] Lin Jianzhong,Ruan Xiaodong,Chen Bangguo et al:Fluid Mechanics. TSINGHUA UNIVERSITY PRESS, BEIJING. 2005 (In Chinese).

[6] MENG Huibo,YU Yanfang,WU Jianhua:Journal of Machinery Design & Manufacture, September (2007),pp173-175 (In Chinese).

© (2012) Trans Tech Publications, Switzerland
doi:10.4028/www.scientific.net/AMM.164.128

The application research of biological materials in meniscus injuries

Peng feng Huo

Environmental Management College of China, China

email: tyxzhanghuan@163.com

Keywords: Biological materials; meniscus; injuries; application

Abstract. The intervention means for rehabilitation of meniscus injury using artificial biomaterials were increasingly sophisticated, which provide brand new research directions for rehabilitation of meniscus injuries. However, it is difficult to select the desired implant due to existent a series of problems, including the biocompatibility, shape matching, adhesion, toughness, strength of artificial biological materials to human body in the process of specific practical application. Nowadays, main biological materials for meniscus injuries including hyaluronic acid, collagen, gelatin, poly hydroxyl acid, lactic acid, calcium Polyphosphate-accumulating, Polytetrafluoroethylene, carbon fiber reinforced polymer that is not absorbed, and so on. The stem cells were induced redirect directionally or gene modified by transforming growth factor beta 1. Make bone marrow mesenchymal stem cells differentiate into cartilage cells by adjusting the number of cell growth and differentiation, and being inoculated for biomaterial scaffold, which provides new research directions for meniscus injury rehabilitation.

Introduction

The knee joint is the main body weight-bearing exercise joint; it is central parts of human body to promote motion, and the sudden and complexity for stress and weighted were substantial clause of Knee joint injuries. Human articular cartilage is more prone to acute injury and chronic fatigue in daily life physical exercise due to its structural weakness, and the extrusion, grinding and pulling of various forces, especially, the injury about fibers of cartilage tissue in the knee joint is more common. It is very difficult to restoration in cartilage injury owing to less Blood supply, and its Nutritional supphes were mainly from tissues and joints around it. With the continuous progress of modern medicine and the rapid development of sports medicine, tissue engineering techniques have application in the field of sports medicine for the treatment of sports injuries.

The physiological anatomy damage mechanisms of meniscus

The majority of knee joint injuries were the injuries about ligament, tendon, joint capsule and other organizations around the knee joint. Those injuries reasons were mainly directly or indirectly force, and twisted pinch injuries are most common. Knee joint cartilage injury is often divided into acute exercise-induced injury and chronic strain injury. Acute sport injury owing to frequently attack of external force, Thereby causing joint in extension, flexion with rotary motion, resulting in cartilage fracture of fiber connection to the surrounding tissue, cartilage breakdown in internal structure of the cartilage damage, loss of normal physiological functions, and articular cavity appears "joint mice", namely the cartilage fragment. With the passage of time, whether acute or chronic strain, if it do not receive effective treatment in time, the injuries severity gradually deepens, lesions range gradually expanded, which will eventually lead to joint activities restricted movement ability decreases. Meniscal cartilage is a crescent-shaped fiber; it fills in the clearance between the femur and tibia joint, which is divided into the medial meniscus and the lateral meniscus. Its edge with thick tissue, and it was close connections with the joint capsule, and with the center of thin, free state. The medial meniscus is "c" shape, the hook angle attached to the point of attachment before anterior cruciate ligament, back angle to the intercondylar eminence of the tibia, and posterior cruciate ligament attachment points between its outer edge and closely linked to the medial collateral ligament in the

middle. The back angle attached to the point of attachment between intercondylar process of tibia and posterior cruciate ligament of knee, its outer edge was closely linked to the medial collateral ligament in the middle. The lateral meniscus is "O" shape, its hook angle attached to the reattachment point before anterior cruciate ligament, and its postcornu attached to the point before medial meniscus, the outer edge was not attached to the lateral collateral ligament, and their activities were greater than the medial meniscus. Meniscus is a fibrocartilage, which themselves without a blood supply, their nutrition primarily from synovial fluid, and it only connected to the articular capsule of the synovial level part for get some blood supply and it limiting the meniscus in the meniscus of edge width in 15%~20% region, Therefore, the meniscus rupture is difficult to repair itself, in addition to outside edge can repair itself after injury. The used traditional therapies for meniscus injury include the closure conservative treatment, meniscus suture, excision of meniscus, meniscal transplants. Allograft tissue transplantation materials with low cost and draw materials easy, plastic is convenient and easy to save, therefore, there is a potential for development, but there are bio-compatibility and many other issues in its development.

Meniscus injury and biomaterials repair engineering

At present, the synthetic material making frequently with artificial meniscus of acetic acid, polylactic acid, PTFE, carbon fiber reinforced polymer, but the softness, creep and its physiological function for this artificial meniscus is difficult to meet the requirement of the body's own meniscus, it only play a supporting role to fill, long-term effects of inaccurate. With the development of tissue engineering and the mature of tissue engineering materials, many iatrotechniques of tissue engineering have application in the field of sports medicine for the treatment of meniscus injury. The application of artificial biological material as medicinal materials: Hyaluronic acid is unique linear macromolecules, Mucopolysaccharide from glucuronic acid and n-acetyl-Glucosamine disaccharide formed by an iterative process connection. Hyaluronic acid is widely present in animals and humans in the interstitial connective tissue cells, vitreous, skin, umbilical cord, cartilage and synovial fluid in the higher levels, lowest content of serum.

Table 1 The type and experimental results of support material for Meniscus tissue engineering

Material type	Examples of materials	experimental results
Natural biological material	Collagen type I	Type I collagen meniscus support cells has good compatibility, but poorer mechanical properties
Synthetic materials	L-polylactic acid	It has a good compatibility，and can be as carrier to undertake people fibrochondrocytes
Nano-materials	RGD-modified nano-structure polycaprolactone	Nano-structured materials conducive to cell adhesion, proliferation and metabolism

In recent years, the hyaluronic acid as a biodegradable bio-absorbable material and because of its high level of viscoelasticity, plasticity, permeability and good biocompatibility, therefore, it as medicinal materials in applications in the field of medicine has made remarkable progress. Hyaluronic acid constitutes a major component of articular cartilage and synovial fluid, event of osteoarthritis, rheumatoid arthritis, and other infectious and noninfectious joint disease, intra-articular hyaluronic acid production and metabolism is an exception occurs, the synovial fluid of concentration and molecular weight hyaluronic acid significantly reduced, cartilage degradation and destruction, articular physiological dysfunction. Research has proven that Cu2+ and hydrogen peroxide reaction simulation Fenton reaction, called Fenton-like reactions, further validation of osteoarthritis, rheumatoid arthritis is associated with the degradation of hyaluronic acid. Visco-elastic replacement therapy has emerged, which aimed at make recovery of synovial fluid lubrication function through

supplementation with exogenous hyaluronic acid to promote cartilage repair and improve joint function. So far, large number results of clinical application shown that the effect of hyaluronic acid on osteoarthritis, rheumatoid arthritis and other joint diseases treatment is clear, safe, and very good prospects. For example, Arthroscopy micro-fractures technique for treatment of articular cartilage injury can promote the growth of bone marrow stem cells, stimulating cartilage regeneration.

Selection and development of artificial biomaterial scaffold: Collagen is main protein of connective tissue of cartilage, bone, skin, which constitute the main part of the animal extra cellular matrix, but because of the antigenicity of animal origin, and collagen hydrolysate--its thermal denaturation of antigens can be eliminated, and composed of gelatin containing 18 amino acids in proteins, Which 7 amino acids were the necessary to human being. Gelatin's biggest advantage is the extensive source of it, biocompatibility, and it can be absorbed completely in the body, no antigens and nontoxic on human body, environmentally safe, easy molding, so the gelatin is an ideal materials for tissue engineering. However, the gelatin cannot be directly used as a tissue engineering materials due to the low strength of gelatin, brittle, easily absorb water after swelling and swelling very low strength and modulus. Currently, the performance of gelatin porous scaffold materials usually were improved by a modification of physical and chemical cross linking approach. Some research displayed poly calcium phosphate/out rubber organization engineering bracket composite pore rate is in 60%~80%, It basically meet tissue engineering composite materials rate of gap requirements, compression modulus of tissue engineering composite materials with Cross linking agent and increased with the increase of the concentration, degradation rate of degradation with time extension increases, as the cross linker concentration increase and decrease, degradation of liquid remained at pH values between 5~7. For example, in 1991, the scientists are cartilage cells vaccination on the biodegradable poly hydroxy acid, regeneration of new tissue, confirmed as new cartilage. By experimental used fiber cartilage cell-collagen composite real construction regeneration "half months Board sample" Organization, research pointed out that, will half months Board fiber cartilage cell planting to collagen bracket Shang formed cell-bracket composite real, then will cell-collagen composite species plant Yu nude rat skin Xia and not transplantation into joint cavity within, after a time generated has similar Yu half months Board of organization block. Again, periosteal mesenchymal stem cells in the germinal layer, experiments confirm periosteal mesenchymal stem cells play an important role in the fracture healing. Scientists periosteal mesenchymal stem cells found in cultivation, when the cell concentration 2x109 L-1 is reached, its underlying cells to differentiate into chondrocytes, study confirms periosteum has the ability to regenerate cartilage, can be used to repair articular cartilage defect

Prefabrication and regeneration of the meniscus cartilage tissue: stem cells cultured in vitro after amplification, vaccinated up to a scaffold, cell complexes of biological material, and cell biological materials plant biology under the skin, gradually absorbed by the organism in biological materials by process, 's own secretion of extra cellular matrix on the formation of new organizations.

Discussion

Articular cartilage in general non-vascular, its nutrition mainly provided through the surrounding tissue and synovial fluid in the joint, so the repair of the damage is very difficult, poor healing. To select appropriate rehabilitation treatments should according to the torn meniscus injury location, characteristics and severity. Meniscus injury should be as minimally invasive surgery, and take a partial or conservative treatment, if appropriate to take a stitch or transplant, reducing the impact on joints after the meniscus is missing. From a large number of research reports, current cartilage injury healing using artificial biomaterials intervention and rehabilitation methods are becoming increasingly sophisticated and diverse. With the rise of tissue engineering, bio-mechanics, genetic engineering, and materials science and other disciplines, it provides a new ways for treatment of meniscus injury. But in the course of application of artificial biomaterials in practice, because of the need to take into account its biocompatibility with human, shape matching, adhesion, toughness, strength, select the desired implant is more difficult. Currently, stem cells induced by transforming

growth factor beta 1 gene-modified, by adjusting the number of cell growth and differentiation and induced differentiation of bone marrow mesenchymal stem cells into chondrocytes, meniscal sports injury rehabilitation provides new research directions.

References

[1] A.M. Bhosale, P. Myint, S. Roberts, J. Menage, P. Harrison, B. Ashton, T. Smith, I. McCall, J.B. Richardson. Combined autologous chondrocyte implantation and allogenic meniscus transplantation: A biological knee replacement. The Knee, Volume 14, Issue 5, October 2007, Pages 361-368.

[2] E. Peña, B. Calvo, M.A. Martínez, M. Doblaré. A three-dimensional finite element analysis of the combined behavior of ligaments and menisci in the healthy human knee joint. Journal of Biomechanics, Volume 39, Issue 9, 2006, Pages 1686-1701.

[3] J.F. Nishimuta, M.E. Levenston. Response of cartilage and meniscus tissue explants to in vitro compressive overload. Osteoarthritis and Cartilage, In Press, Uncorrected Proof, Available online 13 January 2012.

[4] Jochen G. Hofstaetter, Fawzy A. Saad, Raymond E. Samuel, Livius Wunderlich, Yeong-Hoon Choi, Melvin J. Glimcher. Differential expression of VEGF isoforms and receptors in knee joint menisci under systemic hypoxia. Biochemical and Biophysical Research Communications, Volume 324, Issue 2, 12 November 2004, Pages 667-672.

[5] Eleftherios A. Makris, Pasha Hadidi, Kyriacos A. Athanasiou. The knee meniscus: Structure–function, pathophysiology, current repair techniques, and prospects for regeneration. Biomaterials, Volume 32, Issue 30, October 2011, Pages 7411-7431.

[6] John D. Kisiday, Eric J. Vanderploeg, C. Wayne McIlwraith, Alan J. Grodzinsky, David D. Frisbie. Mechanical injury of explants from the articulating surface of the inner meniscus. Archives of Biochemistry and Biophysics, Volume 494, Issue 2, 15 February 2010, Pages 138-144.

[7] J. Richard Steadman, William G. Rodkey. Tissue-Engineered Collagen Meniscus Implants: 5- to 6-Year Feasibility Study Results. Arthroscopy: The Journal of Arthroscopic & Related Surgery, Volume 21, Issue 5, May 2005, Pages 515-525.

[8] K. Messner. The concept of a permanent sythetic meniscus prothesis: a critical discussion after 5 years of experimental investigation using Decron and Teflon implants. Biomaterials, Volume 15, Issue 4, March 1994, Pages 243-250.

[9] Rupert Meller, Frederike Schiborra, Gudrun Brandes, Karsten Knobloch, Thomas Tschernig, Stefan Hankemeier, Carl Haasper, Andreas Schmiedl, Michael Jagodzinski, Christian Krettek, Elmar Willbold. Postnatal maturation of tendon, cruciate ligament, meniscus and articular cartilage: A histological study in sheep. Annals of Anatomy - Anatomischer Anzeiger, Volume 191, Issue 6, 20 November 2009, Pages 575-585.

© (2012) Trans Tech Publications, Switzerland
doi:10.4028/www.scientific.net/AMM.164.132

Preparation Process of Antioxidation Coating of Prebaked Carbon Anode Steel Claw

Zhixiang Liu [1, a], ZheshengQiu[1], JikangYan[2], GuoyouGan [2] , RuijiaoJia [2], YongquanZhou [1], JianhongYi [2]

([1.]Yunnan Aluminium Co., Ltd Kunming,650502, P R China.)

([2.]Faculty of Materials Science and Engineering, Kunming University of Science and Technology, Kunming,650093, P R China.)

[a]email：liuzx@ylgf.com

Keywords:Inert coating SnO_2; Heat-treatment; Microstructure

Abstract. In this paper, the preparation and antioxidant properties of SnO_2 coating of steel claw of prebaked carbon used as electrolytic aluminium anode was investigated. A denser SnO_2 coating on steel claw was prepared by high temperature glaze method . Phase Analysis , microstructure and chemical composition of the steel claw antioxidant coating were by Japan Rigaku D/Max2200 type X-ray diffraction, the Philip XL30 ESEM and EDS. the Oxidation resistance experiments results showed that the better anti-oxidation coating has a optimal thickness size of about 0.4mm.

Introduction

In pre-baked aluminum production process the anodic Steel Claws is the conductor of Electrical which through a strong current ,at the same time play the role of supportting and joining the aluminum rod. Because the Anodic Steel Claws stays in the air and the environment of high concentrations of CO_2 , so the air and CO_2 leading to the oxidation of the anodic Steel Claws.the Oxidation of the anodic Steel Claws [1]. The oxidation of anodic Steel Claws consumes a lot of steel, reduces the cross-sectional area of the steel claws and increases energy consumption of the aluminum.

At present, there are two mainly reasons for the oxidation of the anodic Steel Claws: (1) The anodic Steel Claws are exposed to air for a long time . (2)At a high temperatures, the Steel Claws are easily oxidated by air and CO_2.In order to solve the oxidation of the anodic Steel Claws at a high tempertures,through continuous exploration and research, a technique which called SnO_2 inert coating was developed to prevent the oxidation of the anodic Steel Claws. The coating has good high temperature oxidation resistance on the surface of the Steel Talons, and benefit to the environment protection,which has a broad and bright future for application.

Experimental procedure

Sample Preparation.The material SnO_2 is the coating material,using the High-temperature glaze Method prepare a layer of dense SnO_2 coating on the surface of the substrate, then achieve the goal that let it be antioxidant.

The experimental process is: Steel Claws pretreatment → prepare the coating → heat-treatment → inert coating of steel substrate

(1)Steel Claws pretreatment:First, use metallographic sandpaper of different specifications to polish the surface of Steel Claws ,let it be rough, then immerse in 15% dilute hydrochloric acid for about 10min.

(2) prepare coating: Let the SnO_2, flux, and methyl cellulose mix equably then get the SnO_2 slurry, coating the SnO_2 slurry evenly on the pretreated Steel Claws.

(3) Heat-treatment: heat-treatment is the key process to determine the microstructure and overall performance of the coating products of the steel substrate, during the heat-treatment, the compacts have a series of physical and chemical changes, which makes the occurrence of bonding between the

sintered powder particles, the strength of sintered body increased, the density improved and the porosity reduced. At the beginning of the heat-treatment, the reactants particle diffuses , viscous flow and plastic flow, the particles reactions between itself and the grains grow up. During the heat-treatment, the heating rate, the heat-treatment temperature, the holding time and the cooling rate will affect the effect of heat-treatment.

Put the prepared inert coating SnO_2 of the Steel Claws into a tubular resistance furnace and heated it to 1250° C for 2 hours, then cooling it with the furnace.

Structure Detection. Scrape the coating SnO_2 which has been heat-treated off the Steel Claws and ground it into fine powder. Using Japan Rigaku D/Max2200 type X-ray diffraction to analyse the phase of the coating and test the oxidation of the Steel Claws. Use the Philip XL30 ESEM,the EDAX to test the microstructure and chemical composition of the sample.

Determine the high temperature oxidation resistance of the coating. Put the SnO_2 coating which have been heat-treated into a box resistance furnace. At 50 ° C insulation 30min, in the next 120 minutes, heated it to 150 ° C insulation 30 minutes then re-heating temperature to 400° C and insulation 30 minutes, heating from 400 ° C to 960° C, insulation 8 hours, and then furnace cooled. Observe and record the morphology changes of the Surface of the sample, measuring the weight and thickness of the sample to calculate the oxidation rat Put the coating SnO_2 which have been heat-treated into a box resistance furnace, heating curve as shown in Fig.1. At 50° C insulation 30min, in the next 120 minutes, heated it to 150℃ insulation 30 minutes then re-heating temperature to 400° C and insulation 30 minutes, heating from 400° C to 960 ° C, insulation 8 hours, and then furnace cooled. Observe and record the morphology changes of the Surface of the sample, measuring the weight and thickness of the sample to calculate the oxidation rate .

Results and Discussion

Phase analysis of the SnO_2 coating. Fig.1 is the XRD spectra of the SnO_2 coating, from it we can find that the mainly oxides on the the surface of substrate are Fe_2O_3 and Fe_3O_4。 At the interface of the coating and the Steel Claws it mainly generated Fe and Al phosphate, the SnO_2 also have a larger proportion. That's because first ,in the 1250 ° C heat-treatment process, the oxides on the surface of substrate mainly are Fe_2O_3 and Fe_3O_4, the content of FeO is very small ; second ,The coating can not prevent the oxidation of the substrate at a high temperatures, it can only reduce the oxidation rate of the matrix; third,iron phosphate generated in the interface of the coating and the substrate, which is the reaction of the flux and the substrate occurred, to ensure the bond strength of the coating and the substrate.

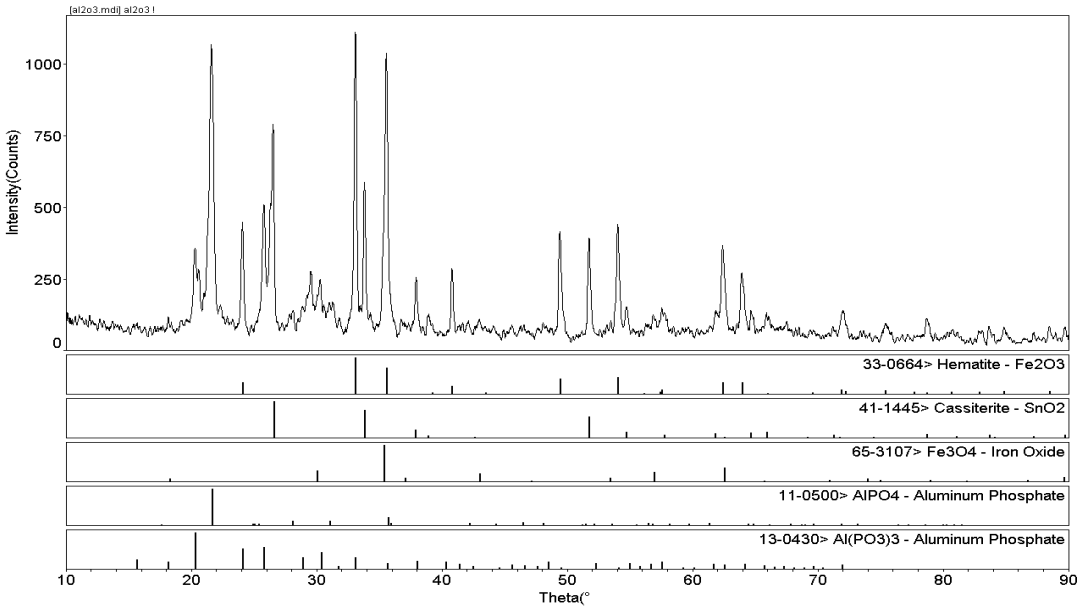


Fig.1. XRD spectrum of SnO2 coating

Analysis of the microstructure. The Fig.2 (a) and (b) are showing the scanning electron microscope images whose resolution is 5000 × and 2000 × ,the images are the SEM of the contact section of the heat-treated coating and the oxide layer on the surface of substrate. From Fig. 2 (a) we can draw that the oxide layer on the surface of substrate have a thickness of 10.8μm, the material at the bright areas is SnO_2.From Fig. 2 (b) we can draw that in the scan area,the oxide layer and the coating have a good contact, but the coatings and the oxides don't have enough density, both of them have a lot of porosity.

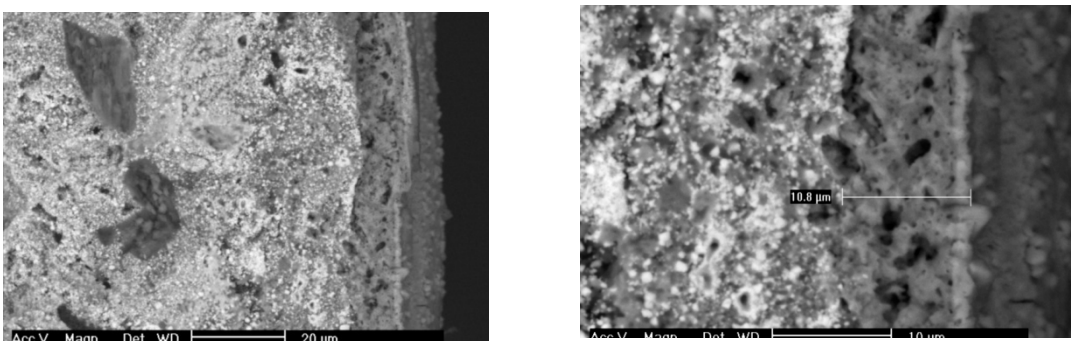
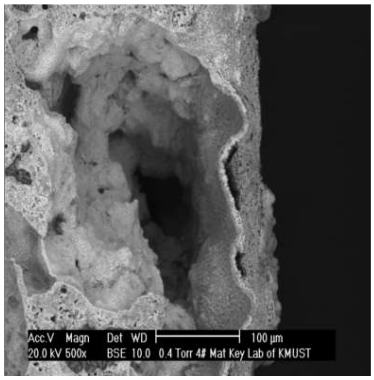
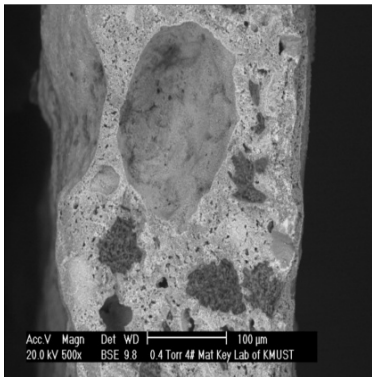


Fig. 2 The SEM of contact section of the heat-treated coating and the oxide layer of the the substrate surface

Fig. 3 (a) and (b) are showing the electron microscopy images in different contact sections of the heat-treated coating and the oxide layer on the surface of substrate, and the resolution of the images are 500x. From Fig.3 we can clearly see that there are a lot of large holes in the coating internal, voids also occurred in the contact surface of the oxide layer and the coating. In the high temperature heat-treatment process the organic matter in the SnO_2 slurry does not completely evaporate and exclude, the internal gas of the coating can't evaporate, then cause the expansion of the volume. And finally the large holes formed. This article improved the process of the heat-treatment, eventually get the interfacial structure of the coating that shown in Figure 4.The antioxidant experiments shows that the inert coating SnO_2 of the Steel Claws which improved heat-treatment has a good antioxidant performance.



(a)



(b)

Fig.3 After heat-treatment, the SEM of different contact section of coating and the oxide layer of the surface of substrate

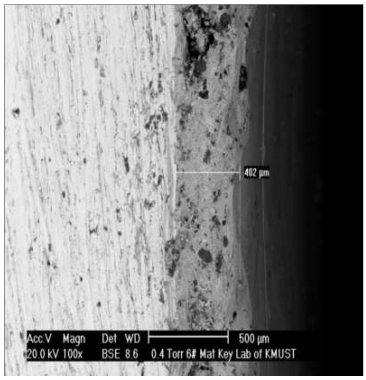


Fig.4 After the heat-treatment process improved, the SEM of the coating and the surface of substrate..

Fig.2 EDXS for Grains in samples sintered at different temperature for 2h in air: (a) 1250°C, (b) 1300°C, (c) 1350°C, (d) 1400°C.

The Fig.5 (a) and (b) are showing the scanning electron microscope images whose resolution is 2000 × and 100 × , the images are the surface of the heat-treated coating. It can be seen from fig.5(a) that the coating has a good density and the bright section is SnO_2,the regular substance is crystal Al2O3;Fig.5(b) shows that from the point of macroscopic view, the coating surface has some small holes.

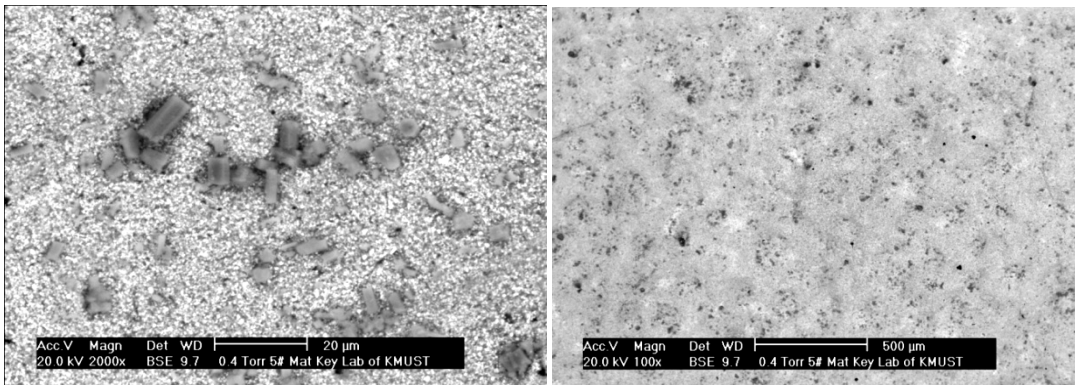


Fig.5 The microstructure of the surface of the coating after the antioxidant experiments, (a) 2000× (b) 100×

Analysis of the chemical composition.

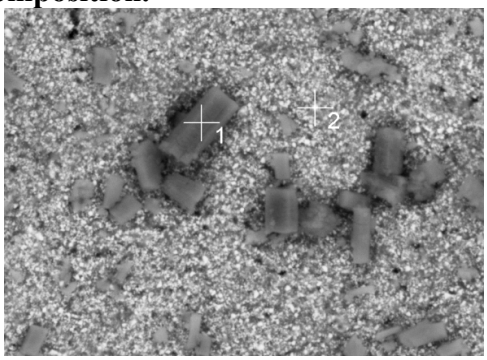


Fig.6 The EDS component analysis of the surface of the heat-treatment coating (Point 1 and point 2 are the location of schematic of the point scanning.)

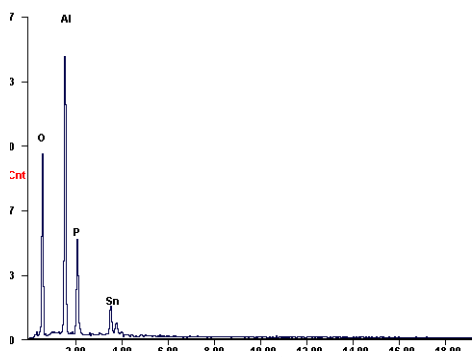


Fig.（a）

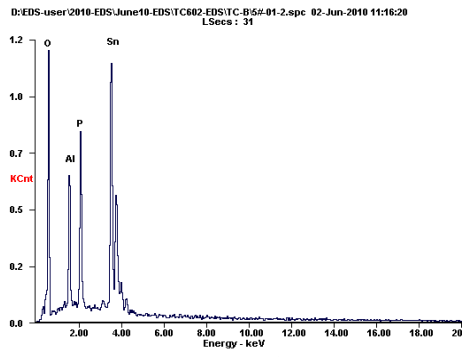


Fig.（b）

Fig.7 (a) the elementary map of mark 1 scanned by Fig.6. Fig.7(b) the elementary map of mark 2 scanned by Fig.6

From Fig.7(a) can infer that the regular crystal in the point 1 of Fig.6 is the oxide crystals of aluminum. From Fig.7(b) can infer that the Lighter material in the point 2 of Fig.6 is SnO_2.

Analysis of the anti-oxidation performance. Table 1 shows that the different thickness of the coating cause different oxidation rate, the average oxidation rate is 0.46%. To a certain extent, the coating on the surface of the substrate blocked the contact of air and the substrate, which makes the oxygen in the air difficult to react with the substrate, and that's the reason the coating has the anti-oxidation performance. But because the effect of the density of coating, the thickness of coating,

the pore at surface of coating and other factors, the air can still be in contact with the substrate and then cause a small amount of air at high temperatures react with the substrate. So the partial oxidation of the substrate happened. When the coating is thin, oxygen and CO_2 tend to spread to the surface of the substrate then the oxidation occurred, so lead to a larger oxidation rate. When the coating is thicker, all of the organic matter can not immediately removed, pores formed in the coating, cause the density of coating is low, while the oxidation occurred. The appropriate thickness of the coating is 0.4mm.

Table 1 Performance of anti-oxidation

thickness of coating [mm]	0.1	0.2	0.4	0.8
oxidation rate of the substrate[%]	0.61	0.56	0.20	0.46

Conclusion

1. Use the inert anodic materials SnO_2 as the coating material, prepared the antioxidant coating SnO_2 of the Steel Claws by the method of high-temperature glaze.

2. The analysis of XRD shows that the mainly oxides on the surface of the steel substrate coating are Fe_3O_4 and Fe_2O_3, the coating can not prevent substrate from oxidizing at a high temperatures, it can only reduce the oxidation rate of the substrate.

3. Analysis of the microstructure of SEM and EDS shows that the surface of the steel substrate coating has a high density, because between the coating and the substrate there exists the chemical bonding, the interface is compact and the strength of bond is high.

4. When the thickness of the coating is around 0.4mm, the oxidation resistance of the inert coating SnO_2 is much better.

References

[1] X.C. Guo,F.F. He. Encyclopedia of Chemical (Professional Volume)[M]. chemical industry publishers, 44-46(2003).

[2] N .Burks. metal high-temperature oxidation Introduction[M]. Beijing: Metallurgical Industry Press.(1989),P245～250.

[3] J.X.Qu,H.H.Wang. Surface Engineering Manual [M]. Beijing: Chemical Industry Press,(1998), p739～781.

[4] P.F.Wang,Aluminum electrolytic carbon anode technology [M].(2002),p125～136.

[5] N.Wang,X.Cao,L.Guo. Facile Cstruction of Qasi 1D Timanganese Ttraoxide Nnostructures Va Soft Templating. Physics[J]. Mechanics & Astronomy 54,11,(2011)1958-1962.

[6] S.F.Shao , X.M.Qiu , D.F.He , R.Koehn , N.J.Guan , X.H.Lu , N.Z.Bao. Grimes Low temperature crystallization of transparent, highly ordered nanoporous SnO_2 thin films,application to room-temperature hydrogen sensing[J]. Nanoscale3,3(2011)4283-4289.

[7] A.Janotti, Chris.G, V.Walle, LDA+U and hybrid functional calculations for defects in ZnO, SnO_2, and TiO_2[J]. physica status solidi (b) 248,4.(2011)799–804.

[8] L.J.Lu, F.L.Cheng, Z.L.Hong, Y.G.Wang, L.Zhang .$Ba0.25Sr0.75Al_2Si_2O_8$ Environmental barrier coating preparation and water resistance to corrosion [J]. Journal of Inorganic Materials ,26,3,(2011)701-706

[9] Z.L. Hong, L.T.hang, et al. Water vapor corrosion be-havior of scandium silicates at 1400℃. Journal of the American Ceramic Society,92,1(2009)193−196.

[10] Y.H.wu, L.F.cheng, Y.G. wang, , et al. $BaO-A1_2O_3-SiO_2$ Preparation of the environmental isolation coating and corrosion resistance characterization of silicate transaction ,Journal of the Chinese Ceramic Society, 37,8,(2009)1299−1305.

© (2012) Trans Tech Publications, Switzerland
doi:10.4028/www.scientific.net/AMM.164.137

Study on Pile-soil Interaction During Pile Sinking and Drivability of Pile in Offshore Platform

YuPeng Song [1,2], YongFu Sun [2], ChengLin Cao [2], ShuLing Li [2]

([1.] College of Marine Geosciences，Ocean University of China ，Qingdao 266071，China;
[2.] The First Institute of Oceanography, SOA. Qingdao, 266061，China)

Key words: jacket platform; pile foundation; pile driving; soil plug

Abstract: The main mode of pile-soil interaction and the influence factors of pile sinking in offshore platform construction were analyzed and discusses the reasons that penetration resistance increases after stop driving and then continue. To study the drivability of piles of specified driving hammer, taking a jacket platform of Bohai Sea for instance, the results showed that continuous driving will make the open-end steel piles be driven to the designed depth, and driven-on will cause soil plug and pile driving refusal. Based on the results, the paper gives some suggestions about pile driving.

Introduction

Platform with pile foundation and frame is a common structural style of platform for offshore oil exploitation [1] which is made up of deck, frame and pile foundation. To meet the bearing capacity requirement, piles are often driven to designed depth. Driving piles is a necessary process of platform construction . The piles driving process is often interrupted because of bad weather, changing ship or driving hammer and then re-driving will usually increase penetration resistance or even cause piles can't be driven to the designed depth which is called driving refusal. This problem appears frequently but has not been drown enough attention and less study right now, so it is worth to be researched.

Soil-pile interaction and soil reaction mechanics on the condition of continuous piles driving and paused then driving on were analyzed. The reasons why soil resistance around piles recovered or even increased after stopped driving were analyzed using the cavity expansion theory and effective stress principle. Soil plug arising mechanism, influence factor were discussed and drivability of piles with specified hammer taking a platform of the Bohai Sea oil and gas exploitation area for instance were analyzed. The drivability of piles in different soil plug effect and construction suggestions were talked about and some useful conclusions were got.

1 Excess static pore pressure caused from continuous driving piles process

Continues driving increases the total stress in soil which is undertaken by pore pressure instantaneously and causes excess pore pressure increasing. Pile driving is a very complicated process. Vesic[2]took the single pile driving process as cavity expansion in infinite earth mass, and deduced elastic-plasticity area and resolution of stress and displacement distribution around soil after cavity expansion in saturated clay and non-draining condition using elastic-plasticity theory. The theory was supposed that soil was homogeneous and isotropic ideal elastic-plasticity material, the cavity expanded in infinite soil in which has equal pressure p_0 and soil yielding is not influenced by static hydrostatic pressure. Fig 1 shows the cavity expansion phenomenon. There is a cavity in infinite earth mass, whose radius is a_0 and inter pressure is p_0。After the time of t, the cavity expands

the radius of which changed to be a and inter pressure changed to be p_u. A annular plasticity destruction region with radius of R forms outside which is elastic area in the influence of expanding pressure p_u , and the influence of expanding pressure is decreased with the distance increasing.

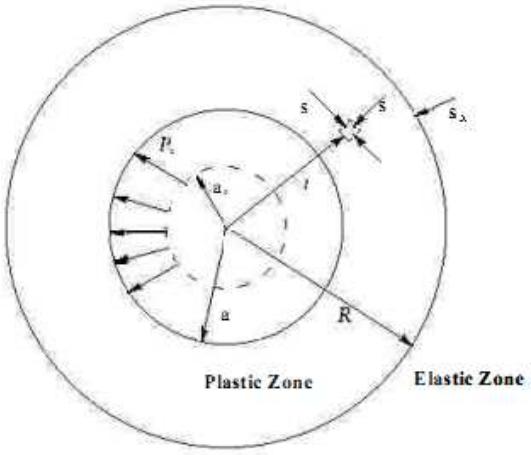


Fig.1 Sketch of cavity expansion

Combining cavity expansion theory and Henkel pore pressure equation, the excess pore pressure caused by cavity expansion is deduced [3,4]. Lots of studying results of researchers showed that most stress and pore pressure increment in soil of pile side can be approximately estimated by cavity expansion theory [5,6].

2 Effective stresses increasing after stop driving

The fact that soil strength recovers and increases after stop driving and re-driving can be explained using effective stress principle [7]. The total stress on any face of saturated soil can be divided into effective stress and pore pressure, Soil deformation and strength is dependent on effective stress changing and effective stress increasing while pore pressure decreasing and vise versa. .

During stop driving , excess static pore pressure caused by continues driving will dissipate. According to the soil effective stress principle, the dissipating pore pressure turn to effective stress, soil resistance around piles side and tip increases, and shaft resistance and tip resistance is influenced. The difficulty of piles driving were increased.

3 Factors influence soil strength increasing

The excess static pore pressure in the plastic area around pile dissipates mainly along three ways of pile boundary surface, ground surface and permeable stratum [8]. Piles of marine project are usually so long that ground surface drainage can be neglected and pile boundary surface and permeable stratum are main dissipating ways of excess static pressure. Draining time may be different resulting from different geological conditions. The long pile will pass through many soil stratums in foundation that consists of sand or silt with high permeability increasing soil drainage speed, and meanwhile high permeability of interlayer abbreviate drain path and increase consolidation speed of clay.

Soil skeleton around piles are vigorously extruded and disturbed by great energy of driving that result to soil structure destroyed and some crevices appeared. Hydraulic fracturing theory shows that [9] because of low intensity of tension, crevices phenomenon will appear in soil when pore pressure exceeds constraint pressure. It is the fact that crevices will appear in soil as long as

pore pressure cumulates to some point during continuous driving. The existing measured data and results [10,11] showed that crevices will appear below the sea floor surface of ten meters during driving. Those crevices increase drainage channel and accelerate soil consolidation speed much more faster than soil without crevices.

Extent excess static pore pressure turns to effective stress is closely related to stop driving duration, and soil consolidation degree is the function of time[7]. Excess static pore pressure dissipating process is related to consolidation coefficient, drainage distance and time. Soil consolidation degree is raised as drainage time increases under the same conditions.

After stop driving for a while, excess static pore pressure dissipated and effective stress increased lead to increasing of soil strength and friction between soil and piles inwall, and soil plug occurred and added the difficultly of piles driving . The soil plug was one of main reasons of pile driving refusal after stopped driving[12]. The duration of stop driving is several hours or days even weeks in construction work, so the long time of stop driving will cause the excess static pore pressure in soil around piles dissipating and soil strength recovering.

3 Related calculating case

Choosing a new jacket platform of Bohai Sea oil and gas exploitation, with three kinds of steel pipe pile whose wall thickness is 38.1mm, radiuses are 762mm, 1200mm and 1400mm, drivability of piles were analyzed. The type of hydraulic driving hammer is IHCS-500, whose Max Energy is 496.5KJ, ram weight is 398.2KN, stroke is 2.02m.The designed driving depth of piles are 50m, 70m and 70m. Table 1 shows physical mechanics parameters of foundation soil.

Table1. Physic mechanical properties of soil

Serial Number	Soil Description	Layer Thickness[m]	Unit friction [kPa]	Unit tip resistance [kPa]
1	Silt	6.5	12.0	393.9
2	Silty Clay	8.5	19.0	90.0
3	Silty Sand	2.7	72.0	3087.0
4	Silty Clay	1.1	40.0	360
5	Silty Clay	8.4	81.3	4162.9
6	Silty Clay	11.7	60.0	540.0
7	Silt	2.3	95.7	9600.0
8	Silty Sand	12.0	95.7	9600.0
9	Silt	5.9	95.7	9600.0
10	Silty Sand	3.6	95.7	9600.0
11	Silty Clay	3.5	80.0	720.0
12	Silty Sand	9.3	95.7	9600.0
13	Silt	3.4	95.7	9600.0
14	Silty Sand	11.8	95.7	9600.0

Drivability of piles analysis is that first estimating dynamic resistance during driving, second analyzing the overcome resistance by hammer- pile combination relationship using wave equation theory, and then forecasting the relationship of driving depth and stroke number.

In granular soil lateral friction of soil is the same , which equal to soil's static surface friction under the condition of "continuous driving" and "stopped then re-driving ". But in clay soil , dynamic surface friction of piles is much less than static surface friction for continuous driving and need long time to recover to the static level when stopped driving.

According to the platform field geology condition, soil plug will not occur during continuous driving .The dynamic surface friction in clay soil is 50 percent of static condition, which are 50 percent and 100 percent of static condition in sand. The unit dynamic tip resistance is same to static condition in both clay soil and granular soil, but it just act on the annular surface of pile's inwall.

Under the condition of stopped driving and re-driving, dynamic resistance in clay will increase when driving again resulted from the recovered bearing capacity and temporary soil plug during stopped driving. So it is supposed that full soil plug occurred, driving resistance equates to static bearing capacity when stopped driving and re-driving and tip resistance acts on the whole tip surface . Soil dynamic resistance of steel pipe piles with diameter of 762mm, 1200mm and 1400mm were estimated.

Soil resistance that can be overcome by pile-hammer-soil combination system is calculated by computer program designed according to Smith [13] wave equation theory. Driving stress of each point of pile and soil resistance overcome by different strike number were calculated by running the program.

Dividing the pile and soil into discrete unit and each strike into short time-interval, strike number of per unit of driving depth are calculated using recurrence method.

The relationship of overcome driving resistance and strike number was established by wave equation analysis of steel pipe pile with diameters of 762mm, 1200mm and 1400mm. It was generally supposed that strike number of pile driving refusal is more than 300 times / 0.3m, and the corresponding soil resistance is the greatest driving resistance the hammer can overcome. Table 2 shows the calculated driving refusal depth.

Table 2. The estimated depth of refused penetration

Serial Number	Diameter （mm）	estimated depth of refused penetration（m） Continuous penetration without plug	Intermittent penetration with plug
1	762	>50	>50
2	1200	>70	54.3
3	1400	>70	47.4

According to calculated results, under the condition of continuous driving, piles with diameter of 762mm can be driven to designed depth of 50m, and piles with diameter of 1200mm and 1400mm can be driven to 70m . Under the condition of stop driving and form soil plug, pile driving refusal will appear when piles with diameter of 1200mm and 1400mm be driven to 54.3m and 47.4m.

4 Conclusions

There are two reasons that pore pressure increases in soil around pile during continuous driving: first is pile's compressing soil effect; second is driving energy effect. Pore pressure caused by compressing soil effect can be calculated using cavity expansion theory, and pore pressure caused by driving energy effect can be calculated according to dynamic consolidation.

Soil skeleton was strongly extruded by great energy and long time driving which causes soil structure to be completely destroyed. Soil's consolidation speed of soil with crevices is much faster than that soil without crevices. With the time of stop driving lengthen, soil consolidating, excess static pore pressure dissipating, soil strength gradually recovering, increasing and even exceeding the initial strength that cause continuous driving difficult even driving refusal. Besides, foundation soil stratum distribution and soil plug in piles are also the reasons of pile driving refusal.

Taking a jacket platform of Bohai sea oil and gas exploitation as a case, drivability of open end steel pipe piles was analyzed using Smith wave equation theory and the results show that pile driving refusal of great diameter will occur because of stop driving causing soil plug. For the purpose of avoiding retard driving time, the necessary equipments should be prepared well on site. Clay soil stratum should be chosen if it is necessary to stop driving to joint pile. When pile driving refusal occur, it can be try to continuous driving on the basis of not increasing driving energy to cause sand liquefaction, soil plug disappearing and driving piles to designed depth

Acknowledgement: This paper was sponsored by Marine Specific Research for Public-"Forecast and appraisal for geologic hazard of inshore seafloor and study of key technology for protection"(project number:201005005) and State Oceanic Administration Youth Fund-"Study of soil stability of the Yellow River Delta seabed under wave action and pipe cable safety"(project number:2010306).

References：

[1] TingQuan Liu, Xing-Guo Wang, Jing Zhou, etc. Optimum design of earthquake-resistance for jacket platform based on pile-soil-structure interaction . Journal of Ship Mechanics, 2004，8（4）：80-81.
[2] Vesic A S．Expansion of cavities in infinite soil mass.ASCE-JSMFD, 1972,98（3）:265-290.
[3] YuXing Wang, Jun Sun. Influence of pipe driving on properties of soils around pile and pore water pressure. Chinese Journal of Rock Mechanics and Engineering,2004,23（1）:153-158.
[4] Shi-Dong Tang, LianSheng He, Zong Fu. Excess pore water pressure caused by an installing pile in soft foundation.Rock and Soil Mechanics, 2002, 23（6）:725-729.
[5] QingJun Zeng, Bo Zhou, XiaoNan Gong. The properties of pore water pressure in saturated clay soils under impact load.Rock and Soil Mechanics, 2001, 22（4）:427-431.
[6] QingShan Meng, Ren Wang, GuanShi Liu. Experimental study on pore water pressure and axial strain of saturated soft clay under impact load. Journal of Hydraulic Engineering, 2005,36 (4):467-472.
[7] JiaHuan Qiang, Zong-Ze Yin. Civil Engineering Principles and Calculation. Beijing:China Water Conservancy and Hydropower Press,1996.
[8] WenQin Yu. Discussion on interrupting period of squeezing earth piles in saturated soft soil［J］.Journal of Geological Hazards and Environment Preservation, 2002,13（4）:73-76.
[9] ShiDong Tang, YongXing Wang, ZhenHua Ye. Excess Pore Water Pressure Caused by Installing Pile Group in Saturated Soft Soil. Journal of Tongji University, 2003,31（11）:1290-1294.
[10] Bing Bai，JianPing Xu，Jian Zhou．Study on squeezing effect against soil and pore pressure by pile pushing in saturated soft clay foundation. Journal of Jiaotong Institute, 2000, 19（3）:3-7.
[11] LinQiang Lu. Change in pore water pressure and effecting to underground wall construction caused by driving a steel tubing.Underground Engineering and Tunnels.1993(4):101-106.
[12] Matsumoto Tatsunori, Michi Yuji, Hirano Tadao. Performance of axially loaded steel pipe piles driven in soft rock. Journal of Geotechnical Engineering, 1995,121（4）:305-315.
[13] Smith E A L. Pile-driving analysis by the wave equation. Journal of Soil Mechanics and Foundations Division, ASCE, 1960, 86（4）：35-61.

© (2012) Trans Tech Publications, Switzerland
doi:10.4028/www.scientific.net/AMM.164.142

Mechanical and thermal properties of kaolin/Natural rubber nanocomposites prepared by the conventional two-roll mill method

Qian zhang[1, a], Yude zhang[1] and Yan Wang[2]

[1] School of Materials Science and Engineering, Henan Polytechnic University, Jiaozuo 454000, China

[2] Center of quality inspection and testing, Jiaozuo Bureau of quality and technical supervision, Jiaozuo 454002

[a]zhangqian361@hotmail.coml

Keywords: Kaolinite, Natural rubber, Reinforcement, Mechanical property.

Abstract. Nanoomposites consisting of natural rubber (NR) reinforced with the modified kaolin were fabricated. The effect of modified kaolin loading on the mechanical properties of the vulcanizates was examined by varying its incorporation (20–50 phr). The NR-based nanocomposites were characterized using the transmission electron microscopy (TEM), Instron tensile machine and thermal analyser. These filled NR composites exhibit outstanding mechanical properties and much higher thermal stability compared to the pure NR. The hardness and tensile properties increased with increasing filler loading and an optimum of tensile strength was achieved at 50 phr of modified kaolin. The morphological studies by TEM revealed that kaolinite layers were finely dispersed into the natural rubber matrix and orientationally arranged in parallel.

Introduction

In recent years researches both in industry and in academia have focused their interest on polymeric nanocomposites since they frequently show unexpected hybrid properties [1, 2]. The phyllosilicate is one of the most common inorganic particles as dispersed phase in polymer matrix to fabricate such “hybrid organic-inorganic nanocomposites” [3]. Qureshi and Qammar prepared natural rubber nanocomposites with similar amounts of carbon black and organo–clay minerals by incorporating nanofillers into solid rubber using a conventional two–roll mill. The tensile strength of the rubber composite with 5 mass% organo–clay minerals increased by 20% compared to the rubber composite filled with carbon black [4]. The research of organo–clay minreal polymer nanocomposites has been extended into various polymer systems including epoxys, polyurethanes, polyimides, polyesters, polypropylene polystyrene, polysiloxanes, nitrile rubber, styrene-butadiene rubber, natural rubber and isobutylene–isoprene rubber.

Over the years montmorillonites have been used for the preparation of organomodified nanofillers. Recently, the use of kaolin in the preparation of organomodified filler for rubber has been reported [5]. In general, kaolinite minerals consist with hexagonal plate-like or disc-like particles with typical diameters of 2μm or less. They are available in a wide variety of chemistries, both naturally-occurring (mined) and synthesized. Kaolin is used in a wide-range of industrial and consumer applications and is thus of a great interest for study [6]. As filler in polymer, it provides improved physical mechanical properties, gas permeability and so on.

Natural rubber is an important elastomer material with excellent properties, which has been exploited in a wide range of applications [7]. However, raw natural rubber shows poor thermal and mechanical properties. A common practice to enhance the mechanical properties is compounding particulate fillers with the rubber matrix.

In this paper, a kind of natural rubber nanocomposite based on kaolin was prepared by melt blending and the mechanical and thermal properties of these composites were investigated.

2. Experimental

2.1 Materials. One of the saline-modified kaolinite particles was obtained as an industrial product from SanXing High-New Material Company of Zaozhuang, China. Natural rubber was supplied by Hainan Natural Rubber Industry Group, China. Sodium hydroxide, hydrazine hydrate, zinc oxide, stearic acid, sulphur and mercaptobenzothiazole were obtained from the open market.

2.2 Composites Preparation. The natural rubber formulations with varying loading of kaolinite particles were shown in Table 1. First, gum rubbers were laminated for 3-5 minutes in an open two-roll mill at the temperature of 30-40 °C. Thereafter, accelerants, activators, kaolin, softeners and sulfur were successively mixed with NR. The obtained mixtures were plasticized for about 12-15 minutes and thin-passed several times at 90 °C. The mixes were vulcanized and molded using a 400 mm×400 mm 25TQLB vulcanizer at 153 °C under 10 MPa pressure for the optimum cure time, which was determined by a C2000E non-rotor vulkameter.

Table 1 NR compound formulations.

Ingredients	NR	Zinc oxide	Stearic acid	Accelerator	Antioxidant	Sulfur	OMK
Amount(phr)	100	5	4	1	1.5	3	Variable

2.3 Characterization and measurement. The mechanical properties of samples were measured using a fully computerized INSTRON mechanical tester (T2000E) at an elongation rate of 20 mm/min at room temperature. The tensile properties values were obtained as averages of at least three measurements.TEM observations of natural rubber/kaolin composites were performed on an H-800-1 transmission electron microscope (Hitachi Co., Japan) with and acceleration voltage of 200 kV. The thermal stabilities of the rubber composites were measured by a TASC 414/4 thermogravimetric analyzer (NETZSCH Co., Germany). The samples were heated from 25 °C to 800 °C at a heating rate of 10 °C/min under the condition of nitrogen ambience.

3. Results and discussion

3.1. Mircostructure of NR Composites. The microstructure of NR filled with 50 phr OMK was observed by low and high magnification TEM images (Fig 1). The kaolinite particles are uniformly dispersed in NR matrix (Fig. 1a). There is no significant aggregation of kaolinite particles, which indicats the excellent dispersibility of the kaolinite particles even at a high loading. The kaolinite layers are around 20 to 50 nm in thickness and orientationally dispersed in the rubber matrix (Fig. 1b). The OMK particles were imbedded in the rubber matrix and formed evident interaction domination between the kaolinite particles and the rubber matrix. This showed that the OMK particles were compatible with the rubber matrix, and were attached to the rubber chains. The formation of parallel alignment of kaolinite layers may endow the NR composites with high thermal stability and enhanced tensile properties.

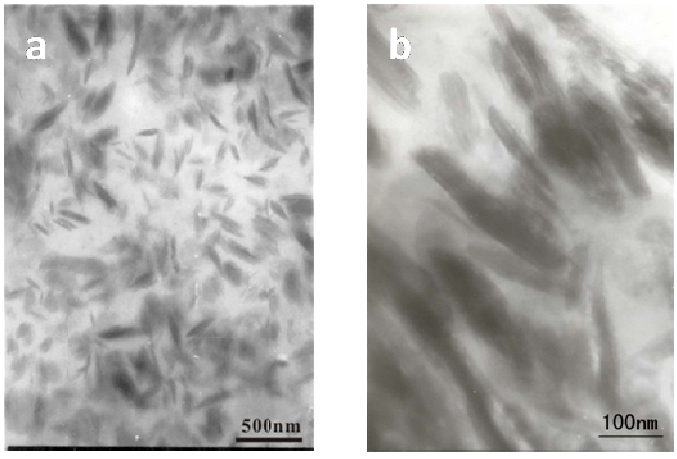


Figure1 TEM pictures of NR composites filled with 50 phr OMK

3.2. Mechanical properties of kaolin/NR Composites. The mechanical properties of the pure NR and the NR/OMK composites in various loading concentrations are presented in Table 2. The 300% and 500% stress of NR composites are strongly increased with the incorporation of OMK (50 phr) and reach to 3.8and 11.8 MPa respectively, which is more than a 2-fold increase compared to the pure rubber. The tensile strength and the elongation at break are sharply increased with the increasing OMK content and reach a maximum value of 27.1 MPa and 745 % at 30 phr filler content respectively, and then slowly decrease with the further increasing filler loading. From all the above results, particular interest is the observation that even very large filler loading (50phr), OMK gives significant reinforcement. The excellent reinforcement efficiency of the clay mineral may be attributed to the good compatibility and strong interaction between the modified kaolin and natural rubber [8].

Table 2 Mechanical properties of NR filled by OMK

Amount (phr)	Stress (MPa)		Tensile stress （MPa）	Elongation at break (%)
	300%	500%		
0	1.9	5.5	23.4	726
20	2.5	7.6	25.6	733
30	3.2	9.9	27.1	745
40	3.4	10.3	26.3	718
50	3.8	11.8	25.9	694

3.3 Thermal stability. The thermal stability of NR/OMK was greatly improved compared to that of pure NR. The degradation temperatures of NR/OMK composite at the loss weight of 5% and 50% were 325.6 and 413.5 °C respectively which were much higher than those of the unfiled NR (Fig. 2). The Residual mass of the NR/OMK composite at 550 °C was 35.0 % much higher than 2.9% of pure NR (Fig. 2). The peak mass loss rate of OMK filled rubber was 1.0 mg/min and dramatically decreased by 22.3% than pure NR (Fig. 3). This is mainly attributed to that plate-like kaolinite particles acting as a superior insulator and mass transport barrier to the volatile products generated during decomposition.

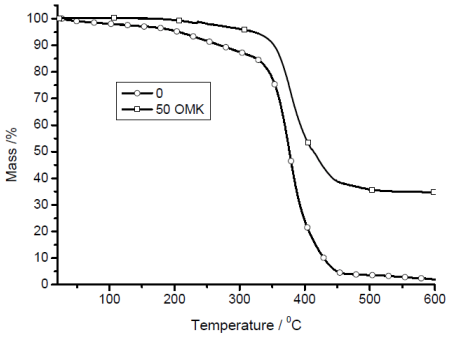


Figure 2 TG curves of NR composites filled with OMK

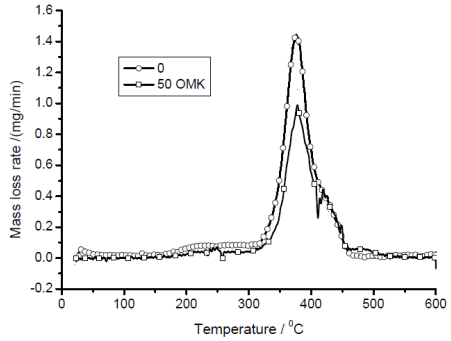


Figure 3 DTG curves of NR composites filled with OMK

Summary

The highly filled natural rubber/ kaolin composites were successfully prepared by melt blending. These filled NR composites exhibit outstanding mechanical properties and much higher thermal stability compared to the pure NR. The hardness and tensile properties increased with increasing filler loading and an optimum of tensile strength was achieved at 50 phr of modified kaolin. The Residual mass of the NR/OMK composite at 550 °C was 35.0 % much higher than 2.9% of pure NR. These dramatic improved properties were mainly attributed to the more finely dispersed SMKS nanoparticles into the polymer matrix.

Acknowledgements

The authors gratefully acknowledge the National 226 Natural Science Foundation of China (51034006) and the Ph.D. programs foundation of Henan Polytechnic University (648479).

References

[1] S.S. Ray and M. Okamoto: Progress in Polymer Science Vol. 28 (2003), p. 1539.

[2] S. Pavlidou, C.D. Papaspyrides: Progress in Polymer Science Vol. 33 (2008), p. 1119.

[3] B. Xu, Q. Zheng, Y.H. Song: Polymer Vol. 47 (2006) p. 2904.

[4] M.N. Qureshi, and H. Qammar: Materials Science and Engineering Vol. 30 (2010), p. 590.

[5] S. Rugmini, A.R.R. Menon: Joural of Applied Polymer Science Vol. 107 (2008), p. 3476.

[6] H.M. Haydn: Applied Clay Science Vol.17 (2000), p. 207.

[7] Y. Q. Wang, H. F. Zhang, Y. P. Wu: European Polymer Journal Vol. 41 (2005a), p. 2776.

[8] Q. Liu, Y. Zhang, and H. Xu: Applied Clay Science Vol. 43 (2008), p. 232.

© (2012) Trans Tech Publications, Switzerland
doi:10.4028/www.scientific.net/AMM.164.146

Study on Aggregation Behaviour of Mixture of Alkylbenzene Sulfonate Gemini Surfactant Ib and Nonionic Surfactant Triton X-100

Xigang Du[1,2,a] Changshui Zhang[1] Jun Zhang[1] Xuming Guo[1] Weiwei Lu[1] Zhenyu Yang[1]

[1] School of Chemical Engineering and Pharmaceutics, Henan University of Science and Technology, Luoyang, 471003, People's Republic of China

[2]College of Chemical Sciences, Qufu Normal University, Qufu, 273165, People's Republic of China

[a]yyduxigang@yahoo.com.cn

Key Words: Anionic Gemini surfactant; Nonionic surfactant; cmc; Aggregation number

Abstract. The interaction between the anionic Gemini surfactant Ib and the conventional nonionic surfactant Triton X-100 was investigated. The critical micelle concentrations (cmc) of different mixtures were measured by surface tension measurement at 298 K. The results showed that the cmc of different mixtures at any mole ratio was lower than that of either pure Ib or Triton X-100, indicating synergetic behavior. And the interaction parameter ß values for the mixed micelles were negative, showing attractive interaction between these surfactant molecules. Besides, the micelle aggregation number (N) was measured using a steady state fluorescence quenching method. The N values of the mixed surfactant system were larger than that of pure Ib but lower than pure Triton X-100 at any ratio.

Introduction

Gemini surfactants are at present attracting considerable interest in international colloid science and relative fields [1]. Gemini surfactants are made up of two amphiphilic moieties connected at the level of the head groups or very close to the head groups covalently linked through a spacer group. Owing to the different structures from conventional surfactants with one hydrophilic group and one hydrophobic group, Gemini surfactants have some more excellent properties. For example, their cmc values are generally 10 to 100 times lower than that of the corresponding conventional surfactants. They lower the surface tension of water more efficiently than the corresponding conventional surfactants. And the aqueous solutions of some quarternary ammonium gemini surfactants with short spacers have high viscosity in the absence of added salt whereas the solution of the corresponding monomer remain low viscous [1−4] . Owing to the widespread application of surfactant mixtures and the remarkable difference between mixed surfactants and individual components, the study of the properties of Gemini mixtures and single-chain surfactants are considered very important for both practical and fundamental aspects. However, there are few reports about the mixed system of anionic Gemini surfactants and conventional nonionic surfactants [5-6]. This article aims to investigate the molecular interaction in the mixed micellization of the anionic Gemini surfactant Ib and the nonionic surfactant Triton X-100.

Materials

Triton X-100 (>99.9％， Sigma); pyrene (99.9％, Aldrich) and benzophenone (99.9％, Aldrich) were recrystallized for three times in alcohol. All solvents were of analytical grade. Triply distilled water was used in all experiments. The anionic Gemini surfactant Ib was synthesized in the laboratory [6]. And its structure is shown in Fig.1.

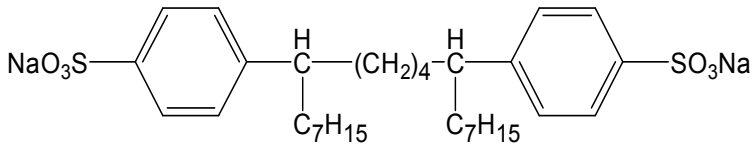


Fig.1 The chemical structure of the studied Gemini surfactant Ib

Determination of micelle aggregation number (N)

50 μL 2.00×10^{-3} mol·L^{-1} pyrene in ethanol was transferred into a 50mL pyknowmeter flask and ethanol was evaporated with nitrogen. 3.75 mmol·L^{-1} surfactant solution was added and the solution was stirred for 24 h. A different amount of benzophenone solution in methanol was added into a 5 mL pyknowmeter flask and methanol was evaporated with nitrogen. The surfactant solution containing pyrene was transferred into the pyknowmeter flask. The solution was stirred for 24 h, then shaken for 24 h in a water bath shaking incubator. The fluorescence emission spectrum of pyrene was determined using a HITACHI F-4500 fluorescent spectrophotometer at an excitation wavelength of 335 nm. EX: 2.5 nm, EM: 1.0 nm, Excitation voltage: 700 V.
The micellar aggregation number (N) was calculated from the equation [7].

$$\ln(I_0/I) = [Q]/[(c-cmc)/N] \quad (1)$$

where, [Q] and c are the concentrations of the quencher and the total surfactants, respectively. cmc is the critical micelle concentration of the total surfactants. I_0 and I are the fluorescence intensities in the absence and presence of the quencher at wavelength 372 nm.

RRSULT AND DISCUSSION

Critical micelle concentration

A series of mixed surfactant solutions were prepared at different ratio and at different concentrations. And the surface tensions of the surfactants solutions were measured at 298 K. The cmc values of the different mixed surfactants obtained by the drop-volume technique are listed in Table 1. The cmc value of pure Triton X-100 was 3.1×10^{-4} mol·L^{-1} in the previous article [8]. It can be seen from Table 1 that the cmc value determined in this article was in good agreement with that in the previous article. It is seen from table 1 that the cmc values of mixed surfactants at any rate were lower than that of the single surfactant, indicating synergetic behavior. The decrease in both electrostatic repulsion of headgroups for single Ia and steric repulsion of the oxyethylene headgroup for single Triton X-100 was caused by mixing the anionic Gemini surfactant and the nonionic surfactant, which was helpful for the formation of micelles. According to the theory of entropy increase, the more closed-packing surfactants reduced directional water molecules around hydrophilic groups and increased free water molecules, which resulted in the easier formation of micelles [9].

Molecular interaction

Table 1 Cmc for mixed Ib/Triton X-100 surfactant systems in aqueous solution at 298K

X_{Ib}	0.0	0.1	0.3	0.5	0.7	0.9	1.0
10^4cmc(mol·L^{-1})	3.32	0.42	0.35	0.33	0.41	0.37	0.43

X_{Ib} is the mole fraction of Ia in the mixed Ib/Triton X-100 surfactant solution.

β is the molecular interaction between two surfactants in mixed micelles; β values are negative, showing attractive interaction between two molecules. The larger negative β values indicate better synergism. β values are obtained from γ−c plots of individual surfactants and their mixtures. The β values are calculated from the equations [10].

$$\frac{x}{1-x}\frac{\ln(X\mathrm{cmc}_M / x\mathrm{cmc}_1)}{\ln[(1-X)\mathrm{cmc}_M/(1-x)\mathrm{cmc}_2]} = 1 \quad (2)$$

$$\beta = [\ln\frac{X\mathrm{cmc}_M}{x\mathrm{cmc}_1}]/(1-\mathrm{x})^2 \quad (3)$$

where, X and x are the mole fractions of surfactant 1 in the solution phases and in micelles, and cmc1 and $\mathrm{cmc_M}$ are the critical micelle concentrations of surfactant 1 and the total mixed surfactants, respectively. Equation (2) is solved iteratively for x, which is then substituted into equation (3) to calculate β. It is seen from Table 2 that the molecular interaction parameter β values between two surfactants in the mixed micelles are negative at any ratio. This indicates attractive interaction between two molecules during the formation of mixed micelles. The mole fractions of surfactants in the solution phases and in micelles are consistent.

Table 2 Characteristic parameters of mixed micellization in Ib/Triton X-100 system at 298K

X_{Ib}	x_{Ib}	β
0.1	0.10	-2.53
0.3	0.26	-3.85
0.5	0.34	-4.51
0.7	0.41	-4.41
0.9	0.51	-6.73

χ_{Ib} is the mole fraction of Ib in the mixed micelles. β is the interaction parameter in the mixed micelles.

Micelle aggregation number (N) of mixed surfactants

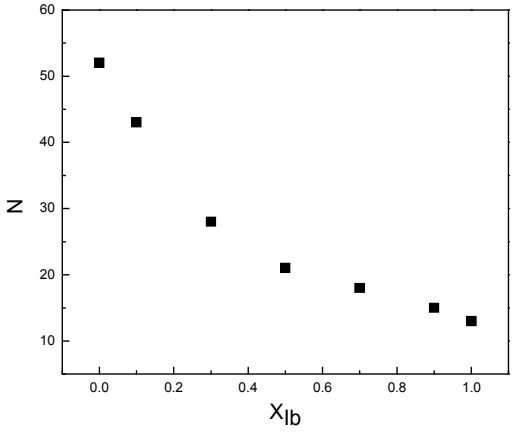


Fig. 2 Variation of *N* for Ib/ Triton X-100 with the mole fraction of Ib in the mixed surfactant system

The fluorescence method is a convenient method for determining aggregation number (N)[11]. N of the mixtures of anionic Gemini surfactant and conventional nonionic surfactant at any rate was determined using the fluorescence method. The concentration of total surfactants (3.75×10^{-3} $\mathrm{mol \cdot L^{-1}}$) is constant. The variation of the aggregation number for Ib/ Triton X-100 with the mole fraction of Ia in the mixed surfactant systems is shown in Fig.2. N of the mixtures was larger than that of Ib but smaller than that of Triton X-100. With the increment of Ib, N rapidly decreases. When the molar fraction of Ib was larger than 0.5, N decreased very slowly. The size of the mixed micelles was mainly determined by the electrostatic repulsion for headgroups and the steric repulsion for

oxyethylene head groups [12]. When Gemini surfactant was incorporated into nonionic micelles, the steric repulsion for oxyethylene head groups decreased with increasing Ib. However, the incorporation of sulfonate groups enhanced the electrostatic repulsion more obviously, i.e. the increase in the electrostatic repulsion was obviously larger than the decrease in the steric repulsion. Thus, N decreased quickly with increasing Ib. When the molar fraction of Ib was larger than 0.5, Ib was the predominant component. The electrostatic repulsion increased slowly, but the steric repulsion for oxyethylene head groups decreased obviously, and the increase in the electrostatic repulsion was slightly larger than the decrease in the steric repulsion. Thus, when the molar fraction of Ib was larger than 0.5, N decreased slowly.

Summary

The cmc values of mixed surfactants at any ratio were lower than that of single component, indicating synergetic behavior. And the molecular interaction parameter β values between two surfactants in the mixed micelles were negative at any ratio. This indicated attractive interaction between two molecules during the formation of mixed micelles. N of the mixtures was larger than that of Ib but smaller than that of Triton X-100.

Acknowledgments

This work was financially supported by the Doctor Fund Project of Shandong Province (BS2009SF019) and the National Natural Science Foundation of China (Grant No.21076063 and No.20963007).

References

[1] Zana, R. Advances in Colloid and Interface Science Vol. 97 (2002), p. 205.

[2] Espert, A., Klitzing,R. V., and Zana, R. Langmuir Vol. 14 (1998), p. 4251.

[3] Menger, F. M. and Littau, C. A. J. Am. Chem. Soc. Vol. 115 (1993), p. 10083.

[4] Zana, R. and Talmon, Y. Nature Vol. 362 (1993), p. 228.

[5] Durga, P. A., Hironobu, K. and Ken-ichi, A. J. Phys. Chem. B Vol. 108 (2004), p. 1790.

[6] Du, X., Lu, Y. and Wu, J. Z. Phys. Chem Vol. 223 (2009), p. 831.

[7] Turro, N. J. and Yekta,A. J. Am. Chem. Soc. Vol. 100 (1978), p. 5951.

[8] Zhao, J. and Brown, W. J. Phys. Chem. B, Vol. 100 (1996), p. 3775.

[9] Zhang, Z., Xu, G., Ye, F. and Luan, Y. Acta Phys -Chem. Sin., Vol. 17 (2001), p. 1122.

[10] Rosen, M. J. Surfactant and interfacial phenomenon. New York: Wiley, 1998.

[11] Ruiz,C. C. and Aguiar J. Mol. Phys. Vol. 97 (1999), p. 1095.

[12] Shiloach, A. and Blankschtein, D. Langmuir Vol.14 (1998), p. 7166.

© (2012) Trans Tech Publications, Switzerland
doi:10.4028/www.scientific.net/AMM.164.150

Synthesis and Properties of A Novel Material Chemistrty Unsymmetrical Material,Diarylethene with Cyano

Weiwei Geng, Congbin Fan, Shouzhi Pu*

Jiangxi Key Laboratory of Organic Chemistry Jiangxi Science and Technology Normal University Nanchang 330013, P. R. China

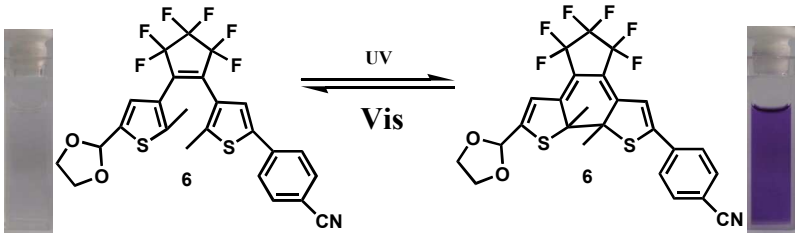
pushouzhi@tsinghua.org.cn

Keywords: Diarylethene; Photochromism; Fluorescence switching; Optical recording storage

Abstract. A unsymmetrical photochromic diarylethene, 1-{[2-methyl-5-(1,3-dioxolane)-3-thienyl]} -2-[2-methyl-5-(4-cyanophenyl)-3-thienyl]perfluorocyclopentene(1a),was synthesized, and its optoelectronic properties were also investigated in detail. The results showed that this compound exhibited reversible photochromism, changing from colorless to blue violet after irradiation with UV light both in solution and in PMMA amorphous film.The diarylethene exhibited a fluorescence switches along with the photochromism from open-ring isomers to closed-ring isomers. When irradiated by UV light, the photocyclization reaction was occurred and the emission intensity of the diarylethene decreased significantly, due to producing the non-fluorescence closed-ring isomers. The back irradiation by appropriate wavelength visible light regenerated its open-ring isomers and recovered the original emission intensity.

Introduction

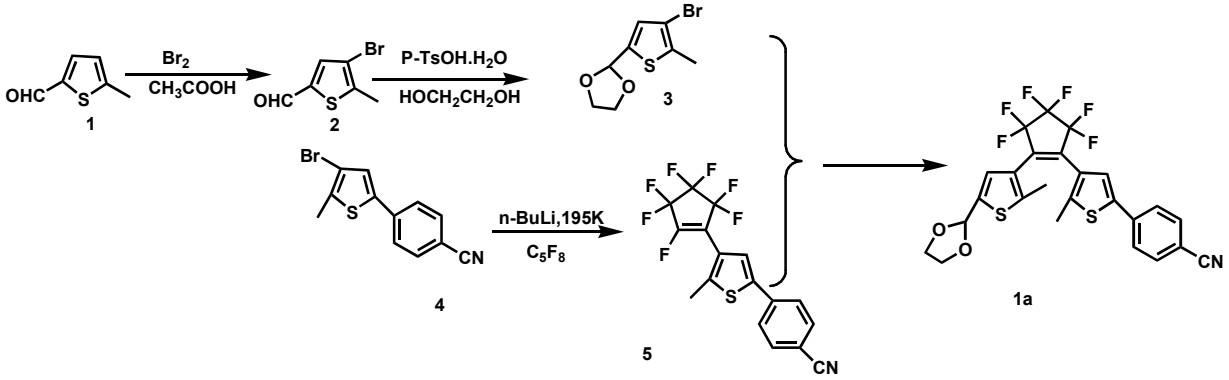
Various types of photochromic organic compounds, such as stilbene [1], azobenzenes [2], furylfulgides [3,4], spirooxazines [5] and diarylethenes [6,7] have been so far developed from the view points of fundamental organic photochemistry and practical applications such as light-modulating and optical recording materials. During the past several decades, there have been important achievements in the synthesis of new families of organic photochromic molecules [8,9]. Among the photochromic compounds, diarylethenes are regarded as the best candidates for such devices, because of their potential applications including optoelectronics such as optical recording, photo-switching, and full-color display devices [10-12]. Especially, dithienylethene is one of the most well-known and extensively investigated classes of photochromic molecules because of its good thermal stability and remarkable fatigue resistant performances required for optoelectronic applications [13]. The basic merit of diarylethene derivatives is that they can undergo a photo-induced reversible isomerization process between two isomers upon irradiation with light of appropriate wavelength. The two isomers of diarylethenes differ from each other not only in their absorption spectra, but in many physical and chemical properties including geometry, refractive index, as well as oxidation/reduction potential, etc. [14, 15]. This characteristic of diarylethene compounds makes them available in the field of photo-mode optical recording. The photochromic process of diarylethenes is based on a reversible transformation between the open-ring isomer with a hexatriene structure and the closed ring isomer with a cyclohexadiene structure, according to the Woodward–Hoffmann rule [16]. From the papers reported in this field, it can be easily concluded that most diarylethene derivatives show very large spectral shifts upon photoisomerization from the open-ring to closed-ring isomers [10]. The open-ring isomer is colorless in most cases, while closed-ring isomer shows some color depending on the molecular structures [17]. In this paper, we have designed and prepared a new asymmetrical diarylethene derivative, 1-{[2-methyl-5-(1,3-dioxolane)-3-thienyl]}-2-[2-methyl-5-(4-cyanophenyl)-3-thienyl]perfluorocyclo pentene(1a). Its photochromic，fluorescence property and optical recording were investigated. The photochromic reaction of diarylethene 1a is shown in Scheme 1.



Scheme 1. Photoisomerization of diarylethene 1a

Experiments

Synthsis of Diarylethene 1a. The synthetic route for diarylethene 1a is shown in Scheme 2. It was synthesized according to the similar procedure of Pu et al. [18]. The structure of compound 1a was confirmed by 1H NMR spectroscopy. 1H NMR (400 MHz, $CDCl_3$, ppm): δ1.94 (s, 3H, -CH_3), 4.07(t, 4H,-OCH_2-CH_2O-), 7.14(s, 1H, thiophene-H), 7.68 (d, 4H, benzene-H).



Scheme 1. Synthesis of diarylethene 1a.

Preparation of PMMA Film. First of all, one hundred milligram of PMMA was dissolved in 1mL chloroform, which was stirred ultrasonically to make it homogeneous. Samples were obtained by dissolving ultrasonically 10 mg of compounds 1a with 1mL of the PMMA solution, respectively, and the solution was spin-coated on a glass substrate with a spin rotation speed of 1500 rpm.

Results and Discussion

Photochromism in Hexane and in PMMA Film. Figure 1 shows the absorption spectral changes of diarylethene 1a in hexane (2.0×10^{-5} mol/L) by photoirradiation. It can be seen that diarylethene 1a has the absorption maximum at 310 nm (ε= 2.86×10^4 L mol^{-1} cm^{-1}). Upon irradiation with 297nm UV light, the colorless solution of 1a turned blue violet, in which absorption maximum was observed at 558 nm (ε= 1.16×10^4 L mol^{-1} cm^{-1},). The blue violet color is due to the formation of closed-ring isomer 1b. When the blue violet solution was irradiated with visible light (λ > 500 nm), the blue violet color returned colorless and its spectrum become the same as that of original one.

The further experiments revealed that the solution can keep similar absorption spectrum under several cycles irradiation with UV and visible light, indicated the high fatigue resistance property. Similar spectrum change of diarylethene 1a was observed in PMMA film (10% w/w). Upon irradiation with 297 nm UV light, the colorless PMMA film turned blue violet with new broad absorption band centered at 572 nm (Figure1), which assigned to the open-ring isomer 1a changed to the closed-ring isomer 1b. The colored PMMA film can also return to colorless upon irradiation with appropriate wavelength visible light.

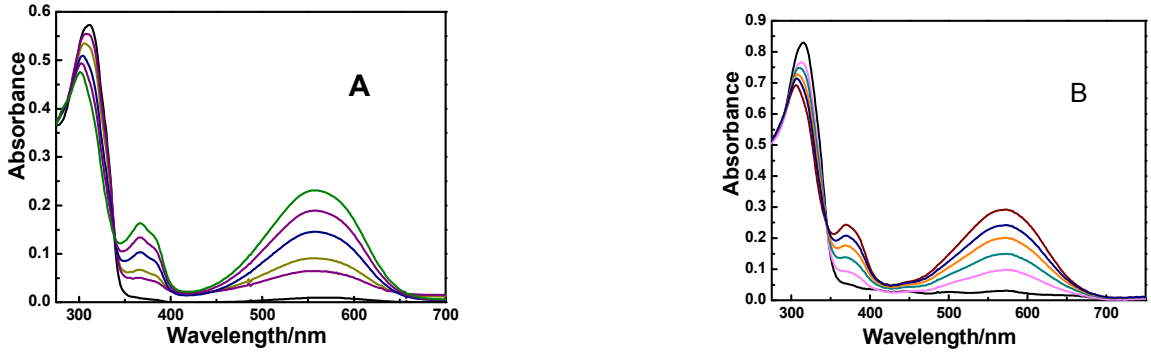


Fig. 1. Absorption spectral and colores changes of compound 1a in hexane (2.0×10^{-5} mol L^{-1}) (A) and in PMMA (B).

Fluorescence of Diarylethene 1a. Fluorescent properties can be useful not only in molecularscale optoelectronics, but for digital photoswitching of fluorescence [19].In this work,the fluorescence properties both in solution and in PMMA film were measured using a Hitachi F-4500 spectrophotometer, and the breadths of excitation and emission slit were selected 10.0 nm. The result showed that 1o exhibited good fluorescence both in hexane solution and in PMMA film, and the emission peaks are 376 nm and 419 nm, respectively. The fluorescence intensity of diarylethene 1a decreased dramatically along with the photochromism from open-ring isomer to closed-ring isomer upon irradiation with 297 nm light in hexane. As shown in Figure 2, when irradiated by light of 297 nm, the photocyclization reaction was carried out and the low fluorescent closed-ring form of the compound was produced. The back irradiation by appropriate wavelength visible light regenerated the open-ring forms of diarylethene 1a and recovered the original emission spectra. The phenomena are useful for application as the fluorescence switch [20, 21].

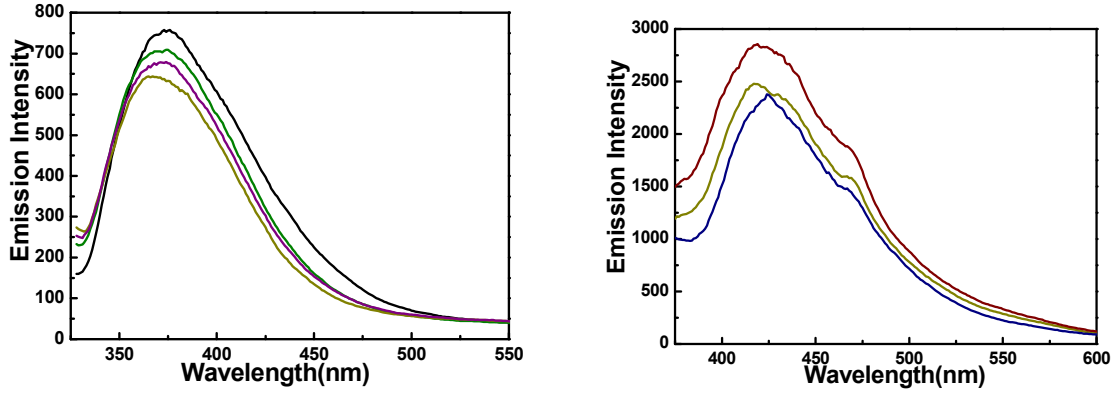


Fig. 2. Fluorescence spectral changes of diarylethene 1a in hexane (A) and PMMA (10%, w/w) upon irradiation with 297 nm UV light.

Summary

An unsymmetrical photochromic diarylethene 1a was synthesized and its optoelectronic properties were also investigated. The results showed that this compound had good thermal stability and exhibited photochromism both in solution and in PMMA amorphous film. The open-ring isomer of diarylethene 1a exhibited fluorescence. The fluorescence intensity decreased along with the photochromism upon irradiation with 297 nm light and its closed-ring isomer showed almost no fluorescence. The oxidation onset and the Eg of the open-ring isomer were higher than those of the closed-ring isomer. Furthermore, using diarylethene 1a as recording medium, polarization holographic optical recording was carried.

Acknowledgements

This work was financially supported by the Project of Jiangxi Academic and Technological leader (2009DD00100), the Natural Science Foundation of Jiangxi Province (2010GZH0040) and the Science Funds of the Education Office of Jiangxi, China (GJJ10241).

References

[1] D. H. Waldeck: Chem. Rev. Vol. 91 (1991), p. 415.

[2] G. S. Kumar and D. C. Neckers: Chem. Rev. Vol .89 (1989), p. 1915

[3] H. G. Heller and S. Oliver: J. Chem. Soc. Vol. 1 (1981), p. 197

[4] Y. Yokoyama: Chem. Rev. Vol.100 (2000), p. 1717

[5] M. V. Alfimov, O. A. Fedorova and S. P. Gromov: Journal of Photochemistry and Photobiology A: Chem. Vol. 158 (2003), p. 183

[6] M. Irie: Chem. Rev. Vol. 100 (2000), p. 1685

[7] H. Tian and S. J. Yang: Chem. Soc. Rev. Vol.33 (2004), p. 85

[8] F. M. Raymo and M. Tomasulo: Chem. Soc. Rev. Vol. 34 (2005), p. 327

[9] K. Matsuda and M. Irie: Chem. Lett. Vol. 35 (2006), p. 1204

[10] M. Iire: Chem. Rev. Vol. 100 (2000), p. 1685

[11] H. Tian and S. J.Yang: Chem. Soc. Rev. Vol. 33 (2004), p. 85

[12] K. Higashiguchi, K. Matsuda, N. Tanifuji and M. Irie: J. Am. Chem. Soc. Vol. 127 (2005), p. 8922

[13] J. Yin, X. Cao, F., Yu, G.-A. and S. H. Liu: Tetrahedron Lett. Vol. 49 (2008), p. 1582

[14] Y. Chen, C.M Wang, M.G. Fan, B.L Yao, and N. Menke: Opt. Mater. Vol. 26 (2004), p. 75

[15] H. Dürr, and H. Bouas-Laurent: *Photochromism, Molecules and Systems* (Elsevier, Amsterdam 2003).

[16] K. Matsuda and M. Irie: Journal of Photochemistry and Photobiology C: Photochemistry Rev. Vol. 5 (2004), p. 169

[17] M. Irie and K. Uchida: Chem. Soc. Vol. 71 (1998), p. 9852

[18] T. Fukaminato, T. Sasaki, T. Kawai, N. Tamai and M. Irie: J. Am. Chem. Soc. Vol. 126 (2004), p. 14843

[19] S. Z. Pu, G. Liu and J. K. Xu: Org. Lett. Vol. 9 (2007), p. 2139

[20] B. L. Yao, Y. L. Wang, M. Lei, N. Menke and G. F. Chen. Opt. Express. Vol. 13 (2005), p. 20

[21] B. Z. Chen, M. Z. Wang and H. Tian: Chem. Commun. Vol. 3 (2002), p. 1060

© (2012) Trans Tech Publications, Switzerland
doi:10.4028/www.scientific.net/AMM.164.154

Enhanced adsorption properties of poly(2-acrylamido-2-methyl-1-propansulfonic acid)/silica composite materials for heavy metal ion removal

JingJing Wang*[1, a] XianNing Li[2,b]

[1]School of Energy and Environment, Southeast university;
School of Material Engineering, Yancheng Institute of Technology, China
[2]School of Energy and Environment, Southeast university, China
[a]Email: jjwang1@hotmail.com
*Corresponding author: JingJing Wang, E-mail: jjwang1@hotmail.com

Keywords: Composite hydrogel; Heavy metal ion; Adsorption; Synergistic complexation

Abstract: Poly(2-acrylamido-2-methyl-1-propansulfonic acid)(PAMPS)/silica composite hydrogels have been prepared by in situ free-radical polymerization. The composite hydrogels were used to remove heavy metal ions from aqueous solution under the non-competitive condition. The results showed that the adsorption capacity of the hydrogels increased with the pH values and silica content in the formulation. Furthermore, the synergistic complexation of metal ions was found in the adsorption studies. Regeneration studies suggested that metal rebinding capacity of the hydrogels did not change significantly through repeated applications compared with the first run.

Introduction

As a result of industrialization and urbanization, the presence of heavy metal ions in water streams has readily increased. Traditional treatment techniques to remove the dissolved toxic metal ions from waste disposal by chemical treatment or ultrafiltration do not always provide a sufficient contaminant removal to meet pollution control limits. Recently, hydrogel adsorption has become one of the effective treatments [1]. Hydrogels are water-swollen network (crosslinked structure) of hydrophilic homopolymer or copolymers. They acquire a great interest due to the facility of the incorporation of different chelating groups into the polymeric networks. Hydrogels are promising materials in the field of water purification due to their chemical stability especially hydrolytic and thermal stability.

However, hydrogels prepared from either natural or synthetic sources usually exhibit poor mechanical properties. There are several ways to improve the mechanical properties of hydrogels, including copolymerization with hydrophobic monomers and formation of interpenetrating polymer network (IPN) [2,3]. Alternatively, the reinforcement of the mechanical properties can be achieved by the introduction of an inorganic phase inside the polymer matrix in the form of nanoparticles. Their formation yields significant improvement of mechanical properties in nanocomposites, when a very good dispersion of nanoparticles is succeeded at the nanoscale [4].

In the current research, poly(2-acrylamido-2-methyl-1-propansulfonic acid)(PAMPS)/silica composite hydrogels containing different contents of silica sol were prepared by in situ free-radical polymerization. Adsorption properties of the hydrogels were examined for the removal of Pb(II) ions from aqueous solutions under the non-competitive condition. Finally, the regeneration abilities of the hydrogels were evaluated.

Experimental section

Materials

2-acrylamido-2-methyl-1-propansulfonic acid (AMPS) was purchased from Sigma-Aldrich Chemicals. Silica sol (mean grain size: 8 nm) was obtained from Tianjin Guangfu Fine Chemical Research Institute, China. N,N'-methylene bisacrylamide (MBA) and ammonium persulfate (APS),

used as a crosslinking agent and an initiator, were purchased from Sigma-Aldrich Chemicals and used without further purification. Lead acetate [$Pb(CH_3COO)_2 \cdot 3H_2O$] used in adsorption experiments was purchased from Shanghai Chemical Reagents Co., China. In order to improve the metal ion adsorption capacity, silica was modified by the amination reaction using the method as described in the literature [5]. The structure of the modified silica is shown in Figure 1.



Fig. 1. The structure of the modified silica.

Preparation of PAMPS/silica composite hydrogels

A mixture of AMPS, silica sol and distilled water was stirred vigorously to produce a homogeneous and transparent solution. Then MBA (5% w/w based on AMPS) and APS (1% w/w based on AMPS) were added into the solution as the crosslinker and initiator. The solution was heated for 30 h in a constant temperature water bath at 65 °C until the monomer AMPS was completely polymerized.

Adsorption capability studies

Adsorption studies were carried out in magnetically stirred (160 rpm), thermostated (25ºC) cylindrical glass vessels in batch conditions. The sample was added into Pb(II) ion solutions to determine the metal ion adsorption capacity of the samples under non-competitive conditions. The pH of the metal feed solutions was adjusted before the hydrogels were applied for the adsorption process. Amount of the residual metal ion in the solution was determined using a Thermo Elemental-X Series Inductively Coupled Plasma-Mass Spectrometer (ICP-MS) after 24 h. Amount of adsorbed metal ion (Q, mmol/g), was calculated from the following equation:

$$Q = \frac{(C_0 - C)V}{m}$$

where C_0 (mmol/l) and C (mmol/l) were the metal ion concentrations in the initial solution and after the adsorption for different periods of time, respectively. V (l) was the volume of the solution added and m (g) was the amount of sample used.

Regeneration studies

The metal-complexed hydrogels were freed from metals by treating with 1 mol/l HCl. The acid-treated hydrogels were filtered and washed with distilled water and bicarbonate solution to remove HCl. The concentration of desorebed metals was determined as mentioned above. The desorption ratio was calculated as follows: desorption ratio = (Amount of metal ion desorbed into solution/Amount of metal ion bound to hydrogels)×100%. A second metal binding cycle was repeated with these regenerated hydrogels. Reuse of the composite hydrogels = (Amount of metal ion adsorpted in the second run/Amount of metal ion adsorpted in the first run)×100%.

Results and discussion

Adsorption studies

Metal ion adsorption capacity of silica and crosslinked PAMPS network at different pH values is listed in Table 1. Figures 2 illustrates the influence of silica content in the formulation and PH values of the feed solution on the adsorption capacity of the composite hydrogels. The theoretical adsorption values of composite hydrogels, which were used to reach certain conclusions about the incorporation of silica on the adsorption capacity, were also calculated. Briefly, theoretic values in Figures 2 were obtained as follows: Firstly, metal ion adsorption capacity of silica and crosslinked

PAMPS obtained from Table 1 was used in calculations. Then, the values of silica and PAMPS contents in the formulation were multiplied by adsorption values of each respective inorganic or polymer adsorbents. Finally, the both values were added to obtain theoretical results.

In order to investigate the relationship between adsorption capacity of the hydrogels and silica content in the formulation, the adsorption studies of the hydrogels for Pb(II) ions were conducted from single solutions (0.005 mol/L) fixing pH at 5. It was seen that the adsorption capacity increased with the silica content in the formulation. The results may be attributed to the fact that silica exhibited higher adsorption capacity compared with PAMPS. Therefore, the highest sorbing capacity for Pb(II) was observed for the hydrogel derived from the highest silica content in the formulation.

The influence of pH values on the metal ion absorption capacity was studied at various pH values with the hydrogel derived from silica content of 25% in the formulation. Seen from the results in Figure 2, the adsorption of metal ions was strongly dependent on the pH values. High adsorption at higher pH values showed that metal ions interacted with $–NH_2$ group by chelating.

Furthermore, it was found that the experimental value was larger than the corresponding theoretical value for the metal ion adsorption. The phenomena may be explained by synergistic complexation of metal ions with silica and PAMPS in the composites. Synergism is defined as the cooperative action of different ligands in producing an effect greater than the sum of the effects of all ligands acting separately. In the current research, $–NH_2$ groups in the silica and PAMPS, cooperated in the complexation of metal ions, leading to the enhanced amount of metal ion adsorption [6].

Table 1 Pb (II) adsorption capacity of silica and PAMPS at different pH values from the single metal ion solution (0.005 mol/L), [mmol/g]

pH value	Silica	PAMPS
pH=3	7.1	1.11
pH=4	12.4	1.22
pH=5	16.2	1.34

Table 2 Desorption and reuse ratio of composite hydrogel (CH)

Sample	Desorption ratio, %	Reuse ratio, %
CH 1 [a]	98.1	94.0
CH 2 [a]	98.5	94.3
CH 3 [a]	97.9	93.5
CH 4 [a]	98.0	93.7
CH 5 [a]	98.6	94.5

[a]Composite hydrogels 1, 2, 3, 4 and 5 were prepared with silica content of 5%, 10%, 15%, 20% and 25% in the formulation, respectively.

Regeneration studies

The composite hydrogels prepared with different silica content in the formulation were selected for the investigation of the desorption of metal ions using dilute HCl as desorbing agent. The data presented in Table 2 showed that the desorption ratio was higher than 97.5%, which meant that there was no difficulty in desorbing the metals from the composites, and both the strongly and weakly sorbed ions could be easily removed by the dilute acid. The dilute acid used for desorption leaded to breaking the coordination bonds between the metal ions and the ligands ($–NH_2$). Therefore, it leaded to the release of the metal ions from hydrogels into solution.

Easy removal of metal ions from the binding sites demonstrated that the composite hydrogels might be reused several times without significant loss of the metal ion adsorption capacity. The hydrogels which were regenerated with dilute HCl were used again in adsorption of metal ions to

observe the reuse properties. The results of Table 2 indicated that metal rebinding capacity of the hydrogels for Pb(II) ions did not change significantly through repeated applications compared with the first run. This character of the possibility for reusing the hydrogels several times made them economically suitable for use.

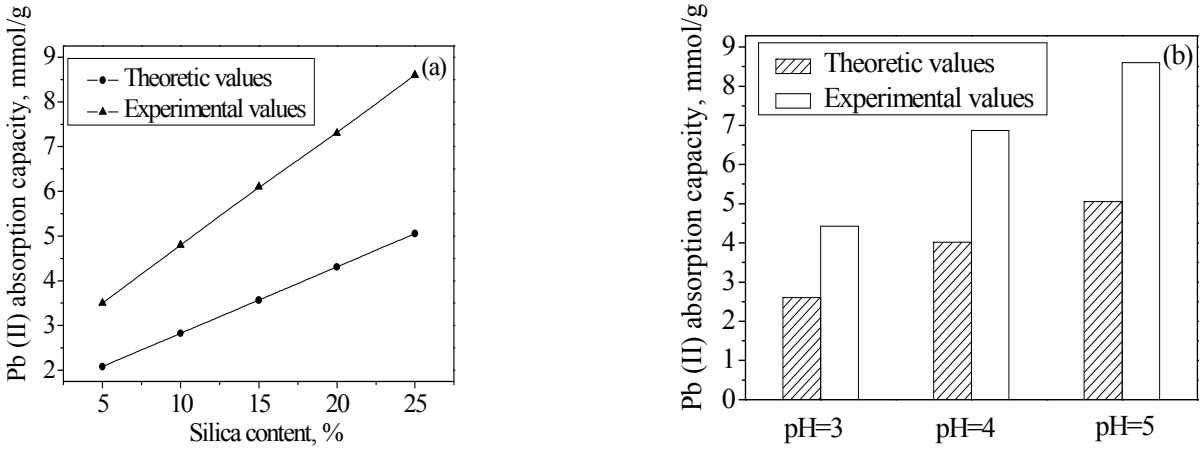


Fig.2 Influence of (a) silica content in the formulation on Pb(II) adsorption capacity fixing pH at 5, and (b) pH values on Pb(II) adsorption capacity of the composite hydrogel derived from silica content of 25% in the formulation

Conclusions

In the current research, PAMPS/silica composite hydrogels have been successfully prepared by in situ free-radical polymerization. The metal ion adsorption capacity of the composites increased with the pH values of the feed solution and silica content in the formulation. Furthermore, the synergistic complexation of metal ions was found in the adsorption studies. Regeneration studies suggested that the composite hydrogels may be reused several times without significant loss of its metal ion capacity.

ACKNOWLEDGMENT

We express our gratitude to the education department of Jiangsu Province (natural science fund for colleges and universities, NO: 11KJB430013) and the Yancheng Institute of Technology (natural research fund, NO: XKR2011010). The project was supported by research fund of Key Laboratory for Advanced Technology in Environmental Protection of Jiangsu Province (NO: AE201069).

References

[1] C. Selva and G. Gülten: Ind. Eng. Chem. Res. Vol. 48 (2009), p. 2652
[2] J.J. Wang and X.S. Li: J. Appl. Polym. Sci. Vol. 116 (2010), p. 2749
[3] J.J. Wang and X.S. Li: Polym. Adv. Technol. Vol. 22 (2011), p. 2091
[4] C. Sanchez, G.J.A.A. Soler-Illia, F. Ribot, T. Lalot, C.R. Mayer and V. Cabuil: Chem. Mater. 2001, 13, 3061
[5] K. Suzuki, S. Siddiqui, C. Chappell, J.A. Siddiqui and R.M. Ottenbrite: Polym. Adv. Technol. Vol. 11 (2000), p. 92
[6] A.A. Kriger, B.A. Moyer and S.D. Alexandraos: React. polym. Vol. 24 (1994), p. 35

© (2012) Trans Tech Publications, Switzerland
doi:10.4028/www.scientific.net/AMM.164.158

Effect of Interface States on the Properties of a-Si:H/c-Si Heterojunction Solar Cells based on Solar materials

C.L. Zhong[a], L.E. Luo, Y.Q. Xia

Hunan University of Technology, Zhuzhou, China

[a]Zhongcljust2007@163.com

Keywords: solar cells, a-Si:H/c-Si heterojunctions, interface states.

Abstract. The effect of the interface states on the properties of (p^+) a-Si:H/(n) c-Si heterojunction solar cells is studied by a set of simulations. The results show that there is almost no effect on the short-circuit current. At very low interface states, there is almost no effect on the open-circuit voltage V_{OC} and the fill factor *FF*, and then the conversion efficiency. Although, at high interface states, V_{OC} decreases due to the decrease of the excess minority carrier density at the c-Si neutral region and the increase of the effective interface recombination velocity at the heterojucntion interface, which also results in the decrease of *FF*. In particular, at very high interface states, the hole transport is limited by the interface potential barrier, which results in S-shaped *J–V* characteristics and low fill factors. As a result, the conversion efficiency decreases with interface states increasing at high interface states.

Introduction

Amorphous hydrogenated silicon and crystalline silicon (a-Si:H/c-Si) heterojunctions are of great interest for photovoltaic applications due to the high conversion efficiencies of solar cells achieved so far up to 22% and the possibility of complete fabrication at low temperature process [1]. The a-Si:H thin films with high bandgaps is taken as the window layer (namely the emitter) of a-Si:H/c-S heterojunction solar cells, and crystalline silicon is taken as the absorber. Heterojunction solar cells of a-Si:H and c-Si are promising candidates for low cost photovoltaic applications and highly efficient solar cells, because it combines the merits of c-Si solar cells and the a-Si:H production techniques.

In particular, the properties of the a-Si:H/c-Si interface are one of the critical issues for the photovoltaic application because the recombination at interface states may significantly decrease the solar cell efficiency. So the suppression of carrier recombination at the *a*-Si:H/*c*-Si heterojunction interface is crucial to improve the properties of a-Si:H/c-Si heterojunction solar cells. Surface passivation [2-3], such as using hydrofluoric acid-based solutions, was proposed to reduce interface recombination or interface states in the past two decades. In the recent decade, the use of a thin intrinsic a-Si:H ((i) a-Si:H) buffer layer between the emitter and the wafer was proposed to decrease interface states at the heterojunction interface [4-5]. The passivation of crystalline silicon surfaces by an intrinsic a-Si:H layer leads to very low effective surface recombination velocities [6]. Sanyo uses the passivation properties of (i) a-Si:H in their so-called HIT structure solar cell consisting of (p^+) a-Si:H/(i) a-Si:H/(n) c-Si/(i) a-Si:H/(n^+) a-Si:H. The passivation properties of (i) a-Si:H led to high conversion efficiencies of about 23.0% with V_{OC} higher than 700 mV [1].

In this paper, the effect of the interface States on the properties of a-Si:H/c-S heterojunction solar cells was performed by a set of simulations using AMPS, and then the mechanism is discussed.

Simulation details

The heterojunction solar cells of TCO/10 nm (p^+) a-Si:H /300 μm (n) c-Si/Al type structure are considered. The effect of the interface states on the properties of a-Si:H/c-Si heterojunction solar cells was performed by a set of simulations using AMPS [7]. The front and back contacts were assumed to be ohmic. The density of gap states (DOS) [8] adopted for a-Si:H is composed of two

exponential Urbach tail states distributions and two Gaussian midgap states distributions. The interface is described by introducing a very thin defective c-Si interface layer between a-Si:H and c-Si. For a-Si:H/c-Si heterojunction solar cells, we changed the interface defect density in the range of 10^9– 5×10^{13} cm^{-2}. The material parameters used in the numerical calculations for the c-Si and a-Si:H layers are shown in Table 1.

Table 1 Main parameters of heterojunction layers used in the simulations

Parameters	c-Si	a-Si:H
Thickness [nm]	3×10^5	10
Electron affinity [eV]	4.05	3.85
Band gap [eV]	1.12	1.8
Impurity concentration [cm^{-3}]	10^{16}	10^{19}

Reuslts and discussion

Fig. 1 shows the simulated effect of the interface states D_{it} on the properties of (p^+) a-Si:H/(n) c-Si heterojunction solar cells. There is almost no effect on the short-circuit current J_{sc} in the simulations. At very low interface states, there is almost no effect on the open-circuit voltage V_{OC} and the fill factor FF; although, at high interface states, V_{OC} and FF decrease with D_{it} increasing, which results in the decrease of the conversion efficiency. In particular, at very high interface states, the properties of heterojunction solar cells decrease dramatically. At very low interface states (D_{it} = 1×10^9 cm^{-2}), it achieves the conversion efficiency of about 23.54% with V_{OC} of 663 mV and FF of 0.824. At D_{it} =5×10^{13} cm^{-2}, V_{OC} and FF respectively decrease down to 0.445 V and 0.423 with the conversion efficiency of 7.238%.

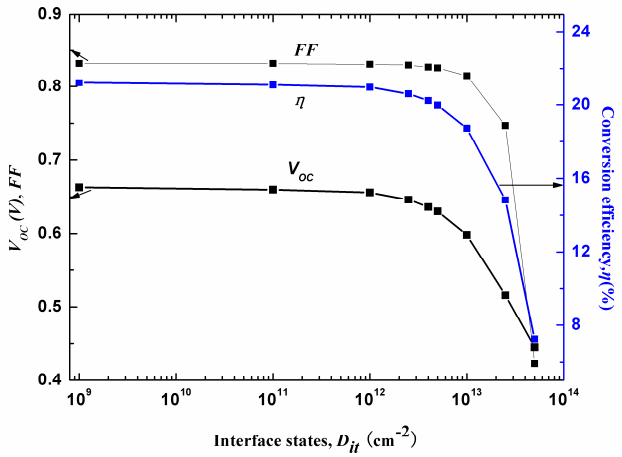


Fig.1. The properties of a-Si:H/c-Si heterojunction solar cells at various values of D_{it}.

The open-circuit voltage V_{OC} of (p^+) a-Si:H/(n) c-Si heterojunction solar cells is expressed as [9]

$$V_{OC} = E_{g1} - \delta_{n1} - \beta \ln \frac{N_{V1}}{\Delta p(1-\frac{S_n}{\frac{D_n}{L_n}+S_n})} = E_{g1} - \delta_{n1} - \beta \ln \frac{N_{V1}}{\Delta n} \cdot \frac{D_n/L_n+S_n}{D_n/L_n} \quad (1)$$

where $\beta = kT/q$, E_{g1} is the band gap of c-Si, δ_{n1} *is* the activation energy of n-type c-Si, S_n is the effective interface recombination velocity for electrons, N_{V1} is the effective density of states in the valence band edge of c-Si, Δn is the excess minority carrier density at the c-Si neutral region, D_n is the electron diffusion constant, L_n *is* the electron diffusion length, and β is the thermal voltage. At very low interface states, Δn is independent on D_{it} [10], and simultaneously S_n is small enough to

neglect compared to D_n/L_n, so they almost have no effect on V_{oc}. At non-negligible interface states, S_n increases with increasing D_{it} and is comparable with D_n/L_n, and furthermore the value of Δn decreases with D_{it} [10], which results in a decrease of V_{oc}.

Usually, an empirical expression for the fill factor is [11]

$$FF = \frac{qV_{OC}/nkT - \frac{kT}{q}\ln(V_{OC}+0.72)}{V_{OC}+1}\left(1-\frac{R_S J_{SC}}{V_{OC}}\right) \tag{2}$$

where $v_{OC} = qV_{OC}/nkT$, R_S is the series resistance, and n is the ideality factor of heterojunctions. Since V_{OC} decreases with D_{it} increasing at non-negligible interface states, deduced from Eq.(2), FF decreases with D_{it} increasing.

At very high interface states, the hole transport is influenced by the valence band discontinuity at the a-Si:H/c-Si interface, namely the potential barrier of the valence band offset. It results in the S-Shaped J-V characteristics as shown in Fig.2, and then the fill factor FF decreases dramatically. At very high values of D_{it}, the holes accumulate at the heterojunction interface, pushing the depletion region inside a-Si:H and resulting in a redistribution of the energy band diagram of silicon heterojunction. Fig. 3 shows the energy band diagram of silicon heterojunction solar cells at thermal equilibrium and at short circuit under illumination at D_{it}=10^9 cm^{-2} eV^{-1} and D_{it}=5×10^{13} cm^{-2} eV^{-1}. The valence band edge at the c-Si neutral region is close to or even higher than the potential barrier tine at short circuit under illumination. Photogenerated holes will have more difficulty in diffusing over the potential barrier. It results in the carrier transport limited by the potential barrier at the interface, and then S-shaped J–V characteristics and low fill factors.

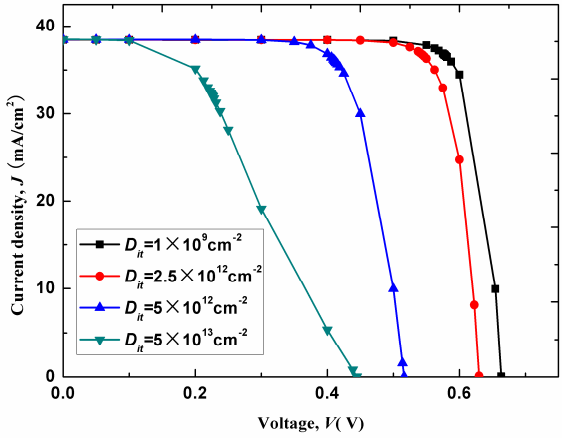


Fig. 2 J-V characteristics of (p^+) a-Si:H/(n) c-Si solar cells for various values of D_{it}

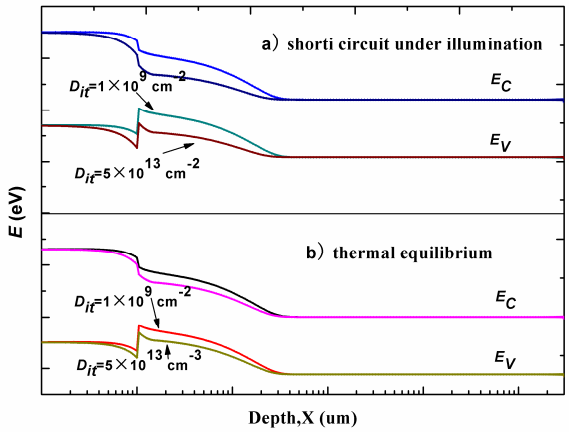


Fig. 3 Energy band diagram of (p^+) a-Si:H/(n) c-Si heterojunctions at thermal equilibrium and at short circuit under illumination for various value of D_{it}

As a results, the conversion efficiency of a-Si:H/c-Si heterojunction solar cells decreases with D_{it} increasing at non-negligible interface states, especially at very high interface states.

Summary

The effect of the interface states on the properties of a-Si:H/c-Si heterojunction solar cells has been studied by a set of simulations. The results show that there is almost no effect on the short-circuit current. At very low interface states, there is almost no effect on V_{OC} and FF, and then the conversion efficiency. Although, at high interface states, V_{OC} and FF decrease with D_{it} increasing, resulting in the decrease of the conversion efficiency. In particular, at very high interface states, the properties of heterojunction solar cells decrease dramatically.

References

[1] Y. Tsunomura, Yukihiro Yoshimine, Mikio Taguchi, et al : Sol. Energy Mater. Sol. Cells Vol. 93 (2009), p. 670-673

[2] E. Yablonovitch, D. L. Allara, C. C. Chang: Phys. Rev. Lett. 57(1986), p. 249

[3] Y.J. Song, W.A. Anderson: Sol. Energy Mater. Sol. Cells Vol. 64 (2000), p. 241-249

[4] T.H. Wang, E. Iwaniczko, M.R. Page, et al : Thin Solid Films Vol. 501 (2006), p. 284–287

[5] Sang-Kyun Kim, Jeong Chul Lee, Seong-Ju Park, et al: Sol. Energy Mater. Sol. Cells Vol. 92 (2008), p. 298–301

[6] K.V. Maydell, L. Korte, A. Laades, et al: J. Non-Cryst.Solids Vol. 352 (2006), p.1958

[7] For AMPS-1D please see :http ://www. emprl . psu. Edu/amps

[8] Madhumita Nath, P. Chatterjee, J. Damon-Lacoste, P. Roca i Cabarrocas: J. Non-Cryst. Solids Vol. 103(2008), p. 034506

[9] C. L. Zhong: A Dissertation for the Degree of Doctor of Philosophy [D] (2011)

[10] C. L. Zhong, R. H. Yao, K. W. Geng: J. Phys. D: Appl. Phys. Vol. 43 (2010), p. 495102

[11] P. J. Rostan, U. Rau, V. X. Nguyen, T. Kirchartz, M. B. Schubert, J. H. Werner: Sol. Energy Mater. Sol. Cells Vol.90 (2006), p. 1345

© (2012) Trans Tech Publications, Switzerland
doi:10.4028/www.scientific.net/AMM.164.162

Preparation and Charactorization of Superfine YAG Powder Materials via the Co-precipitation Methods

Jieguang Song[1 a], Aixia Chen[1 b], Qiang Li[1], Zhiwen Qiu[1], Jianfeng Zhou[1], Yongfeng Xiong[1], Ting Xu[1], Wei Wei[1] and Wentao Li[1]

[1] School of Mechanical and Materials Engineering, Jiujiang University, Jiujiang, Jiangxi, 332005, China

[a] songjieguang@163.com

[b] chenaixiao2001@126.com

Keywords: YAG powder materials, co-precipitation method, X-ray powder diffraction, differential analysis, micrograph analysis

Abstract. YAG is widely applied as the structure materials and the functional materials because of some excellent performances in the chemistry. The pure superfine YAG powder materials are prepared via the co-precipitation method after calcining the precursor of YAG at 1100℃. The superfine YAG powders has the better dispersion, the particle size distribution range is narrow bewteen 200 and 350nm. The superfine YAG mainly show near-spherical, and partly sintering behavior among the particles.

Introduction

Yttrium aluminium garnet (YAG or $Al_5Y_3O_{12}$) adopts the cubic garnet structure, it is of great interest as a high-temperature engineering materials, due to its high-temperature strength coupled with low creep rates. Also some of its properties render it of interest for nuclear iste management applications. In particular, its relatively high melting point (2243K) and the neutronic inertness of its constituent atoms have lead to its consideration as a matrix, into which minor actinides can be incorporated, and subsequently transmuted by neutron irradiation [1-2]. So $Y_3Al_5O_{12}$ is widely applied as the structure materials and the functional materials because of stable chemical performance [3-4].

However, the wider application of YAG is limited, because the manufacture of jumbo size YAG single crystal shows some disadvantage factors that special equipment, complicated technology, long production period, high cost and defective index. Be compare with single crystal, the mass manufacture of YAG polycrystal powder materials is easily realized [5], the performance of polycrystal materials is better than that of single crystal materials under the some specifically conditions, so it substitute for the single crystal materials to produce the structure materials and the functional materials [6-7].

The manufacture methods of YAG powder materials include the sol–gel processing, the metal-organic preceramic processing, the hydrothermal synthesis and the co-precipitation methods[8-9]. The co-precipitation methods is wide applied due to some advantages that sample methods and easy accuracy control.

In this paper, the preparation and charactorization of superfine YAG powder materials via the co-precipitation methods is researched, which lay a strong foundation for the preparation of high performance superfine YAG powders materials.

Experimental procedure

Analytical grade of aluminum nitrate, yttrium nitrateand ammonia are used. Aluminum nitrate solution (0.0126 mol/L) and yttrium nitrate solution (0.00756mol/L) were mixed to get the $A1(NO_3)_3$ and $Y(NO_3)_3$ composite solution, which are added slowly (3mL/min) into the deionized water to form the suspensions. The suspensions are further stired. The ammonia (NH_4OH) is added

into the suspension at various titration rates to certain final pH values for 9. Then the suspension is stirred further for 1h, filtered, washed the precipitation for four times (three times with deionized water and then one time with absolute ethyl alcohol) and dried at 100℃ to obtain the YAG precursor powders. The YAG precursor powders were calcined under different temperature for 1 hour to attain the superfine YAG powder materials. The preparing process flow diagram is shown in Fig.1.

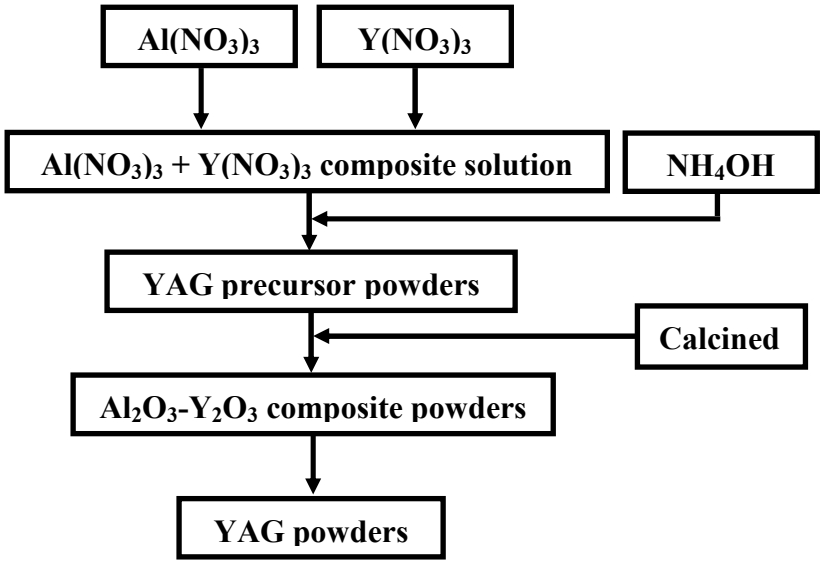


Fig.1 Process flow diagram of preparing superfine YAG powders

The phase analysis of the YAG precursor powders and the superfine YAG powder materials is identified by the X-ray powder diffraction (XRD) (Model: D/Max-RB, Japan). The differential analysis is performed by the differential thermal analyzer (TG-DSC) (Model: NETZSCH STA 449C, Germany). The microstructure analysis of the superfine YAG powders is performed by the scanning electron microscopy (SEM) (Model: TESCAN VEGA Ⅱ, Czech) and the transmission electron microscopy (TEM) (Model: FEI Tecnai G20, American).

Results and discussion

The phase analysis of calcined the YAG precursor powders under different temperature is shown in Fig.2, which indicate that the YAG precursor powders do not show the obvious characteristic diffraction peak of crystalling phase (Fig.2-a), because the YAG precursor powders is amorphous body. The obvious diffraction peak is shown as 2θ for 25-35° after calcined the YAG precursor powders under 600℃for 1 hour (Fig.2-b), which indicate the powders aways keep the amorphous state, but small quantities of crystalling phase already begin to produce. When the calcined temperature is increased, the characteristic diffraction peak of Y_2O_3 and Al_2O_3 are shown after calcined the YAG precursor powders under 800℃ for 1 hour (Fig.2-c), which indicate $Al(OH)_3$ and $Y(OH)_3$ both are decomposed. The characteristic diffraction peak of YAG are shown after calcined the YAG precursor powders under 1100℃ for 1 hour (Fig.2-d), which indicate that Y_2O_3 and Al_2O_3 both are reacted to produce the YAG crystalling phase [10]. The characteristic diffraction peak of YAG are strong, which indicate the YAG crystalling phase is integrated and pure.

The TG-DSC analysis of the YAG precursor powders is shown in Fig.3, which indicate that the TG curve show the continuous descended tendency, most of mass loss is produced under 800℃, because the absorbed water is evaporated, $Al(OH)_3$ and $Y(OH)_3$ both are decomposed. The mass loss is few above 800℃, which indicate the whole YAG precursor powders are transformed into Y_2O_3 and Al_2O_3. The DSC curve show the obvious thermopositive peak at 934.6℃, which indicate the YAG crystalling phase is produced [11], the result is in accordance with the XRD analysis of calcined the YAG precursor powders under different temperature.

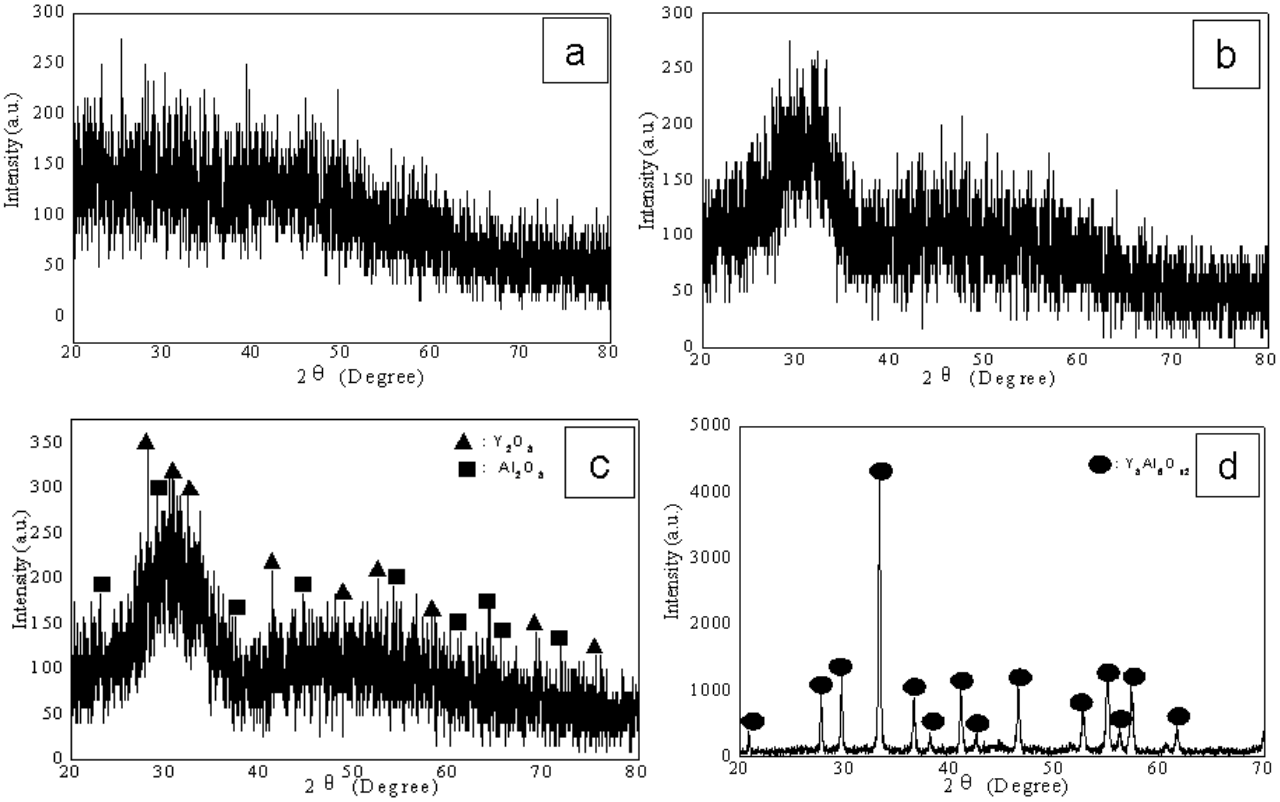


Fig.2 Phase analysis of calcined the YAG precursor powders under different temperature (a: YAG precursor powders, b: 600℃, c: 800℃, d: 1100℃)

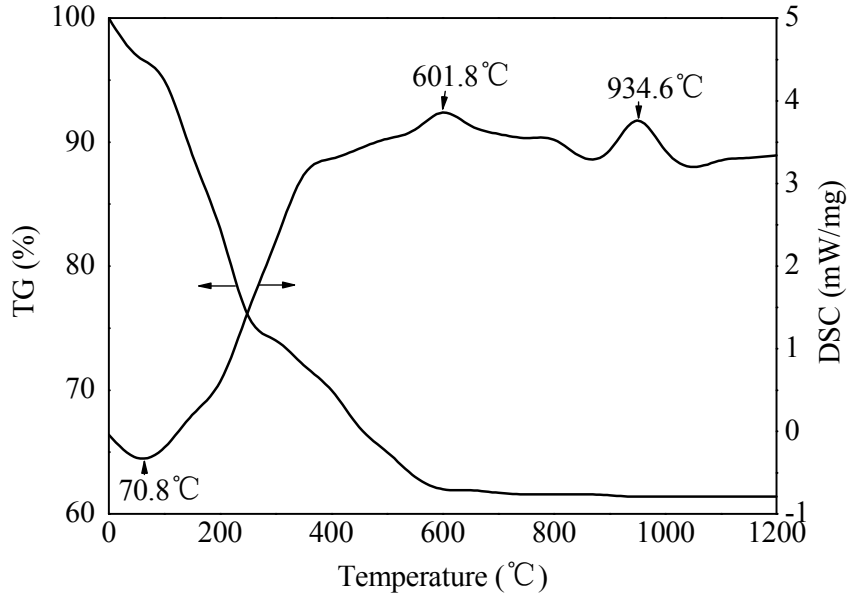


Fig.3 The TG-DSC analysis of the YAG precursor powders

The microscopic appearance analysis of prepared YAG powders by calcined the YAG precursor powders at 1100℃ for 1 hour are shown in Fig.4, which indicate YAG particles is dispersion and superfine, the particle size is fairly homogeneous, the particle size distribution range is narrow bewteen 200 and 350nm (Fig.4-a). The mainly superfine YAG particles show near-spherical, because YAG is cubic crystal structure [12].The partly sintering behavior among the particles is produced (Fig.4-b), because superfine YAG particles own the high surface energy, which show the high activation energy, the particles is easily sintered under the lower heat treating temperature, which indicate the sort of superfine YAG powder materials is easily prepared the mass materials under the lower sintering temperature, and help for the sintering behavior of other materials as sintering aid.

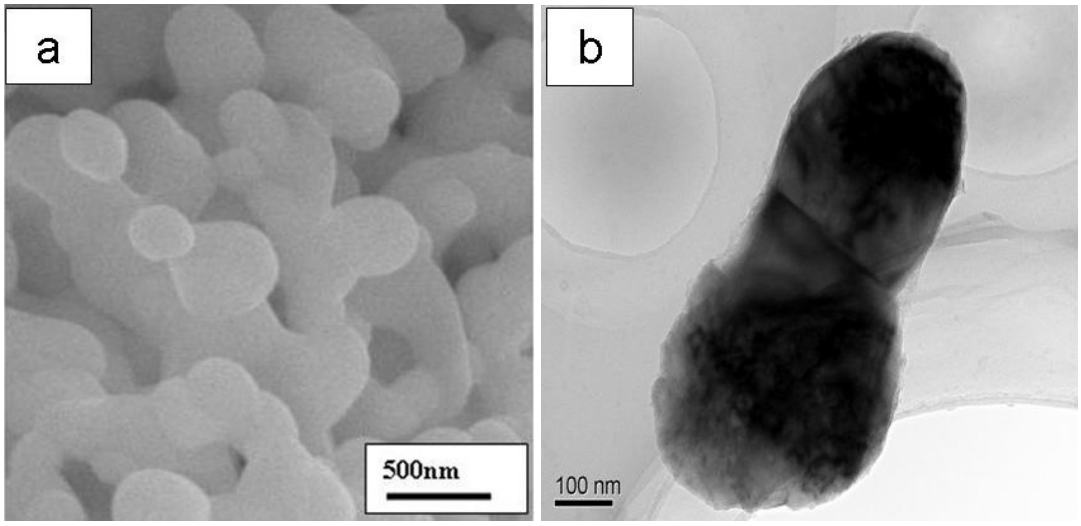


Fig.4 The microscopic appearance analysis of prepared YAG powders

(a: SEM, b: TEM)

Conclusion

The pure superfine YAG powder materials are prepared via the co-precipitation method after calcining the precursor of YAG at 1100℃. The superfine YAG powder materials has the better dispersion, the particle size distribution range is narrow bewteen 200 and 350nm. The superfine YAG mainly show near-spherical, and partly sintering behavior among the particles.

Acknowledgments

The authors are thankful for the financial support provide by the Natural Science Foundation of Jiangxi Province, China (Grant No. 20114BAB216023), The Science and Technique Foundation of the Educational Department of Jiangxi Province, China (Grant No.GJJ09595), and and The University Students' Independent Innovation Experiment Foundation of Jiujiang University (Grant No.11XSCXXSY06).

References

[1] N. Frage, S. Kalabukhov and N. Sverdlov: J. Eur. Ceram. Soc. Vol. 30 (2010), p. 3331
[2] S.J. Wang: Mater. Sci. Eng. B Vol. 127 (2006), p. 203
[3] J.G. Song, D.M. Du and Y.Y. Ju: J. Reinf. Plast. Comp. Vol. 29 (2010), p. 710
[4] A. Tarafder, A. R. Molla and B. Karmakarw: J. Am. Ceram. Soc. Vol. 93 (2010), p. 1
[5] A. Fernandez: J. Mater. Sci. Vol. 38 (2003), p. 2331
[6] A. Lukowiak, R.J. Wiglusz and M. Maczka: Chem. Phys. Lett. Vol. 494 (2010), p. 279
[7] M. Zarzecka: J. Eur. Ceram. Soc. Vol. 27 (2007), p. 593
[8] Y.H.Sanga, H. Liu and Y.H. Lv: J. Alloy. Compd. Vol. 490 (2010), p. 459
[9] Y.M. Zhang and H.M. Yu. Ceram. Int. Vol. 35 (2009), p. 2077
[10] L. Yang, T.C. Lu and H. Xu: J. Alloy. Compd. Vol. 484 (2009), p. 449
[11] X.X. Li and W.J. Wang: Powder. Technol. Vol. 196 (2009), p. 26-29
[12] Q.X. Zheng, B. Li and H.D. Zhang: J. Supercrit. Fluid. Vol. 50 (2009), p. 77

© (2012) Trans Tech Publications, Switzerland
doi:10.4028/www.scientific.net/AMM.164.166

Synthesis of a photochromic diarylethene material bearing fluorine atoms for rewritable holographic optical storage

Shanghua He, Weijun Liu, Gang Liu *

Jiangxi Key Laboratory of Organic Chemistry, Jiangxi Science and Technology Normal University, Nanchang 330013, P. R. China

liugang0926@163.com

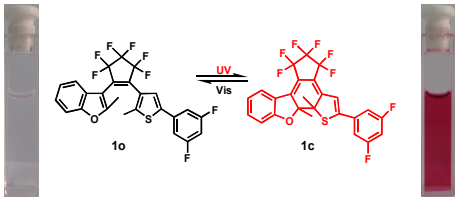
Keywords: Diarylethene, photochromism, fluorescence switches, optical storage.

Abstract. Photochromism is referred to as a photoinduced reversible transformation reaction between two isomers, open and closed, with different absorption spectra upon irradiation with light of an appropriate wavelength. A new photochromic diarylethene, 1-[2-methyl-5-(3, 5-difluorophenyl)-3-thienyl]-2-(2-methyl-3-benzofuran)perfluorocyclopentene(**1o**), has ben synthesized. The compound showed good phtochromism both in solution and in solid states. Diarylethene **1o** changed the color from colorless to magenta upon irradiation with 313 nm UV light, in which absorption maxima were observed at 523 nm in hexane and at 529 nm in PMMA film, respectively. Especially, the diarylethene exhibited a relatively strong fluorescence switches along with the phtochromism from open-ring isomers to closed-ring isomers in solid states. Using diarylethene **1c**/PMMA film as recording medium, optical recording was performed successfully. This new photochromic system also exhibited remarkable optical storage character.

Intorduction

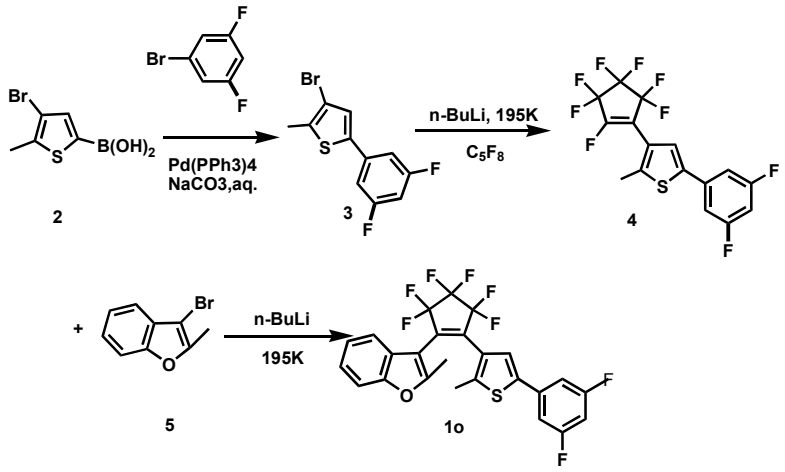
Photochromism is defined as a light-triggered reversible reaction between two isomers. The first published observation of what is known today as photochromism dates back to 1867, when Fritzsche found that an orange-colored solution of tetracene tends to bleach in the day light, regenerating its color in the dark [1]. Photochromic molecules have been attracted much attention from both fundamental as well as practical points of view because of their potential applications for optical devices, such as optical memories and switches [2-4]. To date, various types of photochromic compounds have thus far been synthesized. Among the various types of photochromic compounds, diarylethenes are regarded as the most promising candidates, Because of diarylethene derivatives have excellent thermal stability of the respective isomers, notable fatigue resistance, rapid response, and high reactivity in solid state, diarylethene with heterocyclic aryl rings are the most promising candidates for photoelectronic applications among various types of photochromic compounds [5-7]. Most of the heteroaryl moieties have been thiophene or benzothiophene rings, with just a few reports concerning other heteroaryl moieties, such as furan, [8] indole, [9, 10] benzofuran, [11] indene, [12] pyrazole, [13, 14] etc. There are also a few reports on diarylethene derivatives bearing thiazole rings with special properties [15-18], such as diarylethenes bearing thiazole rings could significantly shift the λ_{max} of the closed-ring isomer to shorter wavelengths and have good thermal stability.

Based on the above aspects, in this paper, we have developed a new photochromic diarylethene bearing a benzofuran unit and investigated its various properties. The synthesized diarylethenes is 1-[2-methyl-5-(3,5-difluorophenyl)-3-thienyl]-2-(2-methyl-3-benzofuran)perfluorocyclopentene(**1o**), Its photochromic scheme is shown in Scheme 1.



Scheme1. Photochromism of diarylethene **1o**.

Experiments. The synthetic route for the diarylethene 1 is shown in Scheme 2. 1-[2-methyl-5-(3,5-difluorophenyl)-3-thienyl]-2-(2-methyl-3-benzofuran)perfluorocyclopentene(**1o**) was synthesized according to the same procedures reported by Pu et al. Compound 5 was n-Butyl lithiated and then coupled with compound 4 to give diarylethene **1o**.The structure of **1o** was characterized by ^{1}H NMR spectroscopy. ^{1}H NMR (400 MHz, $CDCl_3$): δ 1.89 (m, 3H, -CH_3), 2.13 (s, 3H, -CH_3), 6.75 (s, 1H, thiophene-H), 7.03 (t, 2H, J = 8.0 Hz, phenyl -H), 7.20 (d, 1H, J = 8.0 Hz, phenyl -H), 7.24 (t, 1H, J = 8.0 Hz, benzofuran-H), 7.26 (m, 1H, benzofuran-H), 7.47 (d, 2H, J = 8.0 Hz, benzofuran-H).



Scheme2. Synthetic route for the compound **1o**.

Photochromism of Diarylethene. Photochromic reactivity of diarylethene 1 was examined both in hexane solution and in PMMA amorphous film at room temperature. The diarylethene **1o** exhibits good photochromic properties and can be toggled between its colorless ring-open and colored ring-closed forms by alternate irradiation with appropriate wavelengths of light. As shown in Fig.1 a, compound **1o** exhibited an absorption peak at 523 nm (ε, 2.5 × 10^4 mol^{-1} dm^3 cm^{-1}), in hexane. Upon irradiation with 313 nm light, a new visible absorption band centered at 529 nm (ε, 8.1 × 10^3 mol^{-1} dm^3 cm^{-1}) emerged while the original peak at 254 nm decreased, indicating the formation of the closed-ring isomer **1c**. Correspondingly, the colorless solution of **1o** turned magenta owing to produce the closed-ring isomer **1c**. The magenta colored solution turned colorless by irradiation with visible light (λ > 500 nm), indicating that **1c** returned to the initial state **1o** and a clear isosbestic point was observed at 314 nm.

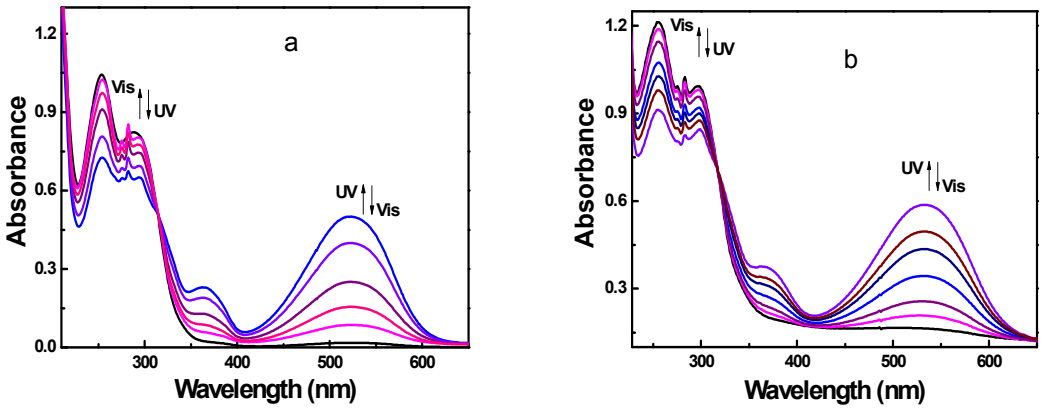


Fig. 1 Absorption spectral and color changes of compound 1 in hexane (2.0 × 10^{-5} mol dm^{-3}) (a) and in PMMA film (10%, w/w) (b).

Fluorescence of Diarylethene 1. The fluorescence properties in the solution of the title compound were measured using a Hitachi F-4500 spectrophotometer, and the breadths of emission slit were selected 10.0 nm. As shown in Fig. 2, the fluorescence intensity of diarylethene 1 decreased dramatically along with the photochromism from open-ring isomer to closed-ring isomer upon irradiation with 313 nm light in hexane. When irradiated by light of 313 nm, the photocyclization reaction was carried out and the non-fluorescent closed-ring form of the compound was produced. The back irradiation by appropriate wavelength visible light regenerated the open-ring form of diarylethene **1o** and recovered the original emission spectra. The phenomena are useful for application as the fluorescence switches.

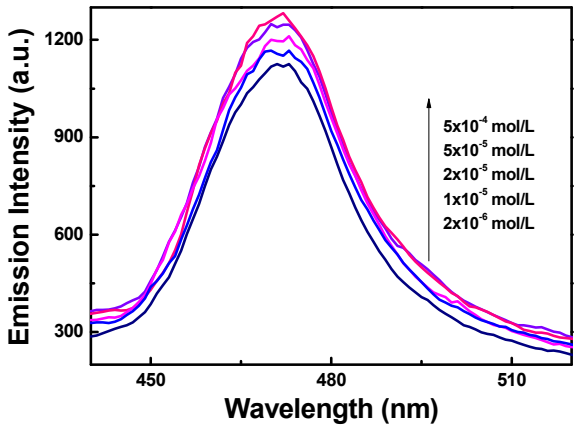


Fig. 2 The concentration effect on the fluorescent property of diarylethene 1 in hexane at room temperature.

Optical recording properties. Using dithienylethene **1c** as the recording medium, optical recording was performed. Dithienylethene **1c** was mixed with poly methyl methacrylate (PMMA) to coat the substrates by the spin-coating, and then applied to optical recording of 650 nm (105 mW) He-Ne laser beam by the solid immerse lens. The optical recording of the patterns recorded on the film are shown in Fig. 3. The size of recording marks was about 20 μm. The result demonstrated that the photochromic diarylethene can be used in high capacity optical storage.

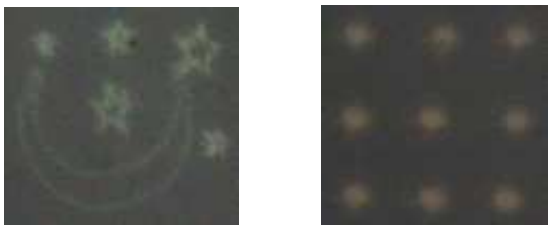


Fig. 3. Recording marks of diarylethene **1c** in polarization optical storage.

Summary

In summary, an unsymmetrical diarylethene was synthesized to investigate its photochromism, fluorescence and polarization optical recording. The results showed that diarylethene 1o showed good photochromism and a relatively strong fluorescence switches in solution. Polarization recording properties were performed successfully using diarylethene 1c as recording medium. The results illustrated that the diarylethene 1 had attractive properties for polarization holographic optical recording.

Acknowledgements

This work was supported by the Project of Natural Science Foundation of Jiangxi Province(2010DQ00200, 2010GQH0038) and the Science Funds of Jiangxi Education Office (GJJ1067).

References

[1] J. Fritzsche, Comptes Rendus Acad. Sci. Paris. Vol. 69 (1867), p. 1035

[2] Y. Chen, C.M. Wang, M.G. Fan, B.L. Yao and N. Menke: Opt. Mater. Vol. 26 (2005), p. 75

[3] T. Fukaminato, T. Sasaki, T. Kawai, N. Tamai and M. Irie: J. Am. Chem. Soc. Vol. 126 (2004), p. 14843

[4] S.Z. Pu, F.S. Zhang, J.K. Xu, L. Shen, Q. Xiao and B. Chen: Mater. Lett. Vol. 60 (2006), p. 485

[5] M. Irie: Chem. Rev. Vol. 100 (2000), p. 1685

[6] K. Matsuda and M. Irie: J. Photoch. Photobiol. C. Vol. 5 (2004), p. 169

[7] M. Morimoto and M. Irie: Chem. Commun. Vol. 36 (2006), p. 3895

[8] X.D. Deng and L.S. Liebeskind: J. Am. Chem. Soc. Vol. 123 (2001), p. 7703

[9] K. Yagi and M. Irie: Bull. Chem. Soc. Jpn. Vol. 76 (2003), p. 1625

[10] K. Yagi, C.F. Soong and M. Irie: J. Org. Chem. Vol. 66 (2001), p. 5419

[11] T. Yamaguchi and M. Irie: J. Org. Chem. Vol. 70 (2005), p. 10323

[12] Yamaguchi and M. Irie: Tetrahedron Lett. Vol. 47 (2006), p. 1267

[13] S.Z. Pu, T.S. Yang, J.K. Xu and B. Chen: Tetrahedron Lett. Vol. 47 (2006), p. 6473

[14] T.S. Yang, S.Z. Pu, B. Chen and J.K. Xu: Canadian J. of Chem. Vol. 85 (2007), p. 12

[15] K. Uchida, T. Ishikawa, M. Takeshita and M. Irie: Tetrahedron. Vol. 54 (1998), p. 6627

[16] S. Takami and M. Irie: Tetrahedron. Vol. 60 (2004), p. 6155

[17] H. Nakagawa, S. Kawai, T. Nakashima and T. Kawai: Org. Lett. Vol. 11 (2009), p. 1475

[18] S.Z. Pu, H. Li, G. Liu, W.J. Liu: Tetrahedron Lett. Vol. 51 (2010), p. 3575

© (2012) Trans Tech Publications, Switzerland
doi:10.4028/www.scientific.net/AMM.164.170

Sintering Temperature Establishment of Quartz Sand Heat Insulating Porous Materials

Jieguang Song[1 a], Fang Wang[1], Wenbin Li[1], Zhiwen Wang[1], Xiaodong Ma[1], Guanghua Cao[1], Qiang Li[1], Wei Li[1], Jun Zhang1 and Yonghua Liu[1]

[1] School of Mechanical and Materials Engineering, Jiujiang University, Jiujiang, Jiangxi, 332005, China

[a] songjieguang@163.com

Keywords: Low-grade quartz sands; heat insulating materials; sintering temperature; porous structure; differential analysis.

Abstract. The sintering temperature of the quartz sand heat insulating materials were researched thtough the differential analysis of the mixture in this paper. The conclusion show the density of the quartz sand heat insulating brick is increased with increasing sintering temperature, but the porosity of the quartz sand heat insulating materials is opposite discipline curve. The outside shape of the brick body is regular at 1100℃, however, the outside shape of the brick body is irregular at 1150℃, but the porosity of the quartz sand heat insulating materials at 1130℃ is lower than that of the quartz sand heat insulating materials at 1100℃. The sintering temperature is higher, the more energy will be consumed. So the better sintering temperature of the quartz sand heat insulating materials is decided at 1100℃ through analyzing the performance price ratio of the quartz sand heat insulating materials.

Introduction

With the development of modern industry, the demand of industrial raw material is increasing, it makes the high-grade raw material resources will be entirely consumed [1]. The industrial waste and the low-grade raw materials are being used to manufacture the high cost performance products in the some infant industries [2]. The high-grade quartz sands as non-metallic minerals raw materials are extensively used for the foundry industry, glass making industry and munitions industry [3]. However, the low-grade quartz sands are used as the mortar mixture in the construction industry, the low-grade quartz sands show the low cost performance [4].

With the development of town construction industry, the walling materials industry is fleetly developing at home and abroad, the consumption of fired clay brick is very high massive, it makes a mass of clay resources be consumed. Some countries propose to save the land resources for the sustainable development of the human society [5]. The quartz sand fired brick are prepared with the river sands as the low-grade natural raw materials, it makes the clay fired brick be replaced [6], the purpose of the work is to save the land resources, and use the low-grade natural resources to realize the high cost performance product.

The heat insulating materials is studied with the river sands of the Yangtze River, the pore microstructure and the outside shape must be controled suitably for the high-performance heat insulating brick. In this paper, the sintering temperature of quartz sand heat insulating brick is discussed and established throug the TG-DSC results and the properities of the quartz sand heat insulating brick, which is the foundation for preparing the high-performance quartz sand heat insulating brick.

Experimental procedure

The low-grade quartz sands along the Yangtze River in China as the main raw materials were dried under the sun because of containing the amounts of water, the weeds and the root of the dired sands is picked, and then the dired sands is sieved with the 50 mesh sieve. The sands are poured into the jar of

the planetary ball mill machine (Model: QM-BP, China), ball milled for 1 hour, the fine quartz sand powders were abtained. The component analysis of the river sands is shown in Tab.1. The mixture that the quartz sands for 80wt%, the kaolin for 15wt% and the sintering addative for 5 wt% is composed, the water is added into the mixture, ball mill mix to form the sizing agent, the Φ80×80mm volume green body is formed via the absorption methods with the sponge. The green brick is dried and sintered under the suitable temperature, the pore microstructure and the outside shape of the sintered heat insulating brick is tested. The process flow diagram of preparing the heat insulating materials is shown in Fig.1. The microstructure analysis of materials is tested by the scanning electron microscopy (SEM) (Model: TESCAN VEGA Ⅱ, Czech).

Tab.1 Chemical composition of the quartz sands

Chemical composition	SiO_2	Al_2O_3	CaO	MgO	K_2O+Na_2O	Ignition loss	Other	Total
Contents（wt%）	84.21	6.69	1.47	1.01	2.04	2.77	1.81	100

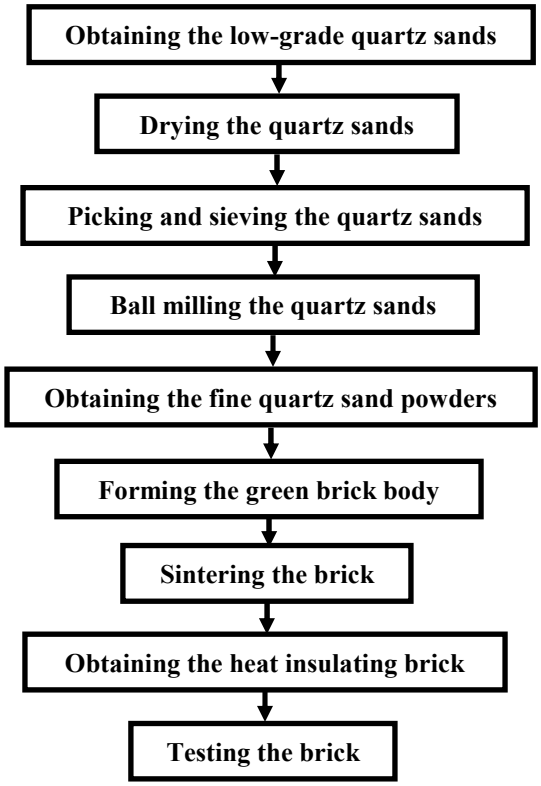


Fig.1 Process flow diagram of preparing the heat insulating materials

Results and discussion

The TG-DSC analysis of the mixture of the heat insulating materials is performed with the thermal analyser (Model: Q-600, American), the results is shown in Fig.2, which is indicated that the weightlessness of the mixture is about 9.5% after heating from room temperature to 1200℃, but the 9% weightlessness is producted under 700℃, because the weightlessness of the water, the sintering addative and the organic matter of the mixture are mainly factor. The crystal transfer of the carbonate produces a spiculate endothermal valley at 400℃. The crystal transfer of the quartz from alpha phase to beta phase produces the endothermal valley at 570℃. The decomposition of the carbonate produces the endothermal valley at 710℃. The smooth and broad endothermal valley from 1000℃ to 1200℃ is shown, because the liquid phase in the green brick appears under the high sintering temperature, which is the foundation for the sintering temperature establishment of the quartz sand heat insulating materials, the sintering temperature of the low-grade quartz sand heat insulating materials is decided from 1000℃ to 1200℃.

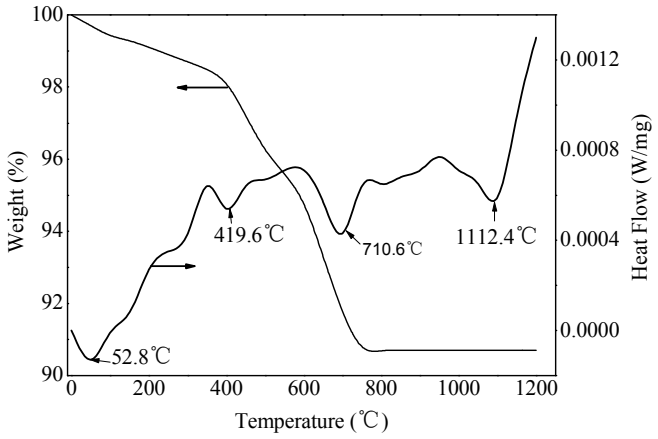


Fig.2 TG-DSC of the raw materials of the quartz sand heat insulating materials

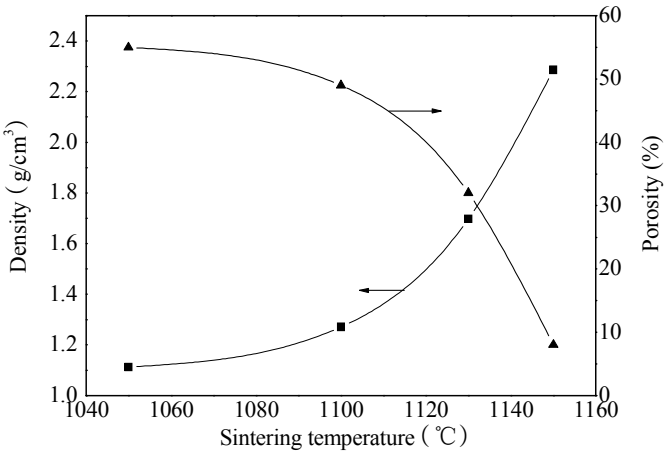


Fig.3 Effect of sintering temperature on the density and porosity of the heat insulating materials

The density of the heat insulating materials is increased with increasing the sintering temperature, but the porosity is opposity, it is show in Fig.3. Because the raw materials of the brick body is melten to form the liquid phase matter with increasing the sintering temperature, the viscosity of the liquid phase matter is high due to the low sintering temperature during the sintering initial stage, the liquid phase matter can not flow into the pores of the brick body. From the results of the Fig.4-a, the liquid phase matter only adhere on the surface of the pore of the brick body due to the surface tension action, which make the pore diameter be decreased and show the undercalcined macropore and micropore [7], the porous structure analysis of the brick body is accord with the performance results of the brick body. The Fig.4-b respectively is the macroporous stucture and the microporous structure, the quantity of the liquid phase matter is increased with increasing the sintering temperature through anakysising the porous structure. When the sintering temperature is further increased, the inside porous structure of the brick body are shown respectively in Fig.4-c, and Fig.4-d at 1130℃ and 1150 ℃, because the flow ability of the liquid phase matter can gradually overcome the surface tension action of the liquid phase matter during increasing the sintering temperature, the liquid matter will flow into the pore of the brick body to reach the densification action of the brick body, the results show that the porosity of the brick body is decreased, the density of the brick body is increased. The plentiful liquid phase matter is appeared in the brick body with increasing futher the sintering temperature, the plentiful pore of the brick body is filled by the plentiful liquid phase matter, which makes the density of the brick body be increased, and the porosity of the brick body is decreased [8]. The better sintering temperature of the quartz sand heat insulating brick is decided at 1100℃ through analyzing the performance price ratio of the quartz sand heat insulating materials.

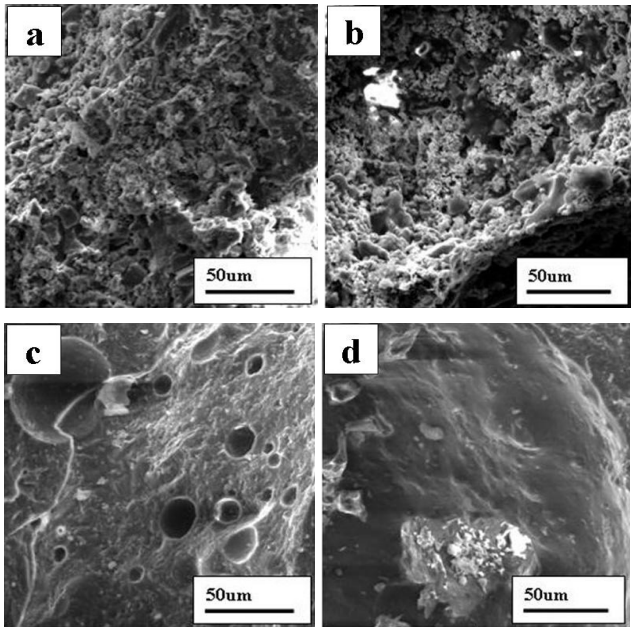


Fig.4 The micropore structure of sintered the quartz sand heat insulating materials at a) 1050℃, b) 1100℃, c) 1130℃ and d) 1150℃

Conclusion

The sintering temperature of the quartz sand heat insulating materials were researched thtough the differential analysis of the mixture, and the effect of sintering temperature on the density, the porosity, the microstructure and the outside measurement of the quartz sand heat insulating materials in this paper. The conclusion show the density of the quartz sand heat insulating materials is increased with increasing sintering temperature, but the porosity of the quartz sand heat insulating brick is opposite discipline curve. The outside shape of the brick body is regular at 1100℃, however, the outside shape of the brick body is irregular at 1150℃, but the porosity of the quartz sand heat insulating materials at 1130℃ is lower than that of the quartz sand heat insulating materials at 1100℃. The sintering temperature is higher, the more energy will be consumed. So the better sintering temperature of the quartz sand heat insulating brick is decided at 1100℃ through analyzing the performance price ratio of the quartz sand heat insulating materials.

Acknowledgments

The authors are grateful for financial support from The Science and Technique Foundation of the Educational Department of Jiangxi Province, China (Grant No.GJJ11624), and The Industry Science and Technique Foundation of Jiujiang, China (Grant No. JST2009-86-06).

References

[1] K. Koseoglu, M. Polat and H. Polat: J. Hazard. Mater. Vol. 176 (2010), p. 957
[2] X.R Tian, B.L. Wu and J. Li: J. Hazard. Mater. Vol. 160 (2008), p. 589
[3] K.B. Tynyshtykbaev K.T. Igibaev, and D.K. Suleev: Mater. Sci. Eng. B Vol. 134 (2006), p. 296
[4] M. Sahmaran, H.A. Christianto and I.O. Yaman: Cement Concrete Comp. Vol. 28 (2006), p. 432
[5] A. Christogerou, T. Kavas and Y. Pontikes: Ceram. Int. Vol. 35 (2009), p. 447
[6] J.G. Song and F.Wang: J. Ceram. Process. Res. Vol. 12 (2011), p. 357
[7] C.N.Djangang, A. Elimbi and U.C. Melo: Ceram. Int. Vol. 34 (2008), p. 1207
[8] S.J. Wang, Z.Q. Chen and Y.C. Jean: Mater. Sci. Forum Vol. 607 (2008), p. 204

© (2012) Trans Tech Publications, Switzerland
doi:10.4028/www.scientific.net/AMM.164.174

Wear morphology and mechanism analysis of plasma spraying Nanometer Al_2O_3-13%wtTiO_2 coating material

Zhifang Cheng[1, a] , Fuchi Wang[2,b] and Zhuang Ma[3,c]

[1]5 South Zhongguancun Street, Haidian District, Beijing 100081, P. R. China
[2]5 South Zhongguancun Street, Haidian District, Beijing 100081, P. R. China
[3]5 South Zhongguancun Street, Haidian District, Beijing 100081, P. R. China
[a]chengzhifang@hotmail, [b]fch@bit.edu, [c]mzh@bit.edu.cn

Keywords: Plasma spraying; Coatings; Nanometer Al_2O_3-13%wtTiO_2 ; Wear resistance

Abstract. Nanometer Al_2O_3-13%wtTiO_2 wear-resistant coating was prepared by The plasma spraying process , and the coating was tested through a SRV friction and wear testing machine, the worn surface and wear debris were observed by scanning electron microscopy, and the wear mechanism was analyzed. The friction coefficient of Nanometer Al_2O_3-13%wtTiO_2 decreases with the increase of the load. The main wear mechanism is adhesive wear, accompanied by a small amount of abrasive wear.

1. Introduction

Wear is one of the most important surface failure in Aerospace, metallurgy, chemicals, and machinery and other industrial fields. The wear of spare parts and equipment failure would cause huge economic losses. Ceramic materials with superior strength and chemical stability is widely used in a variety of wear resist occasions, including as coating material to increase the overall surface properties of materials.

the wear and tear of spare parts and equipment failure may cause huge economic losses. To study the wear characteristics of materials has great significance. ceramic materials prevalent brittleness and thermal shock resistance low the two major drawbacks limit the use of ceramic materials. However, the brittleness of ceramic materials limit the use of that materials. We also should think the bond strength between the ceramic coating and the substrate material, as well as the compactness of the coating itself.

Nanometer Al_2O_3-13%wtTiO_2 coating has good abrasion resistance, corrosion resistance and high resistance to temperature oxidation. Nanometer Al_2O_3-13%wtTiO_2 coating is widely used in the aerospace, gas, power generation, chemical, metallurgy, machinery, textile, paper and other industries. The study on wear mechanism of this Nanometer -coating could be barely seen.

2. Experimental

2.1. Preparation of coatings

The coatings were Prepared by Praxair TAFA 5500-2000 air plasma spraying equipment. The gun model is SG-100. The thickness of bond coat prepared by NiCrCoAlY powder is 0.1mm,That of wear resistant coatings with Nanometer structured Al_2O_3-13%wtTiO_2 powder is about 0.5mm. The spraying process parameter is shown in Table 1.

2.2 Wear test

Wear test was conducted on the coated layers using a SRV wear tester made by OPTIMOL company. The test coating which is Polished to a lower, more uniform roughness Ra0.4um was placed in the down platform. The wear of friction pairs was Gr15 ball which roughness was Ra0.28um, Test stroke was 1.3mm.The frequency was 20Hz.The loads were 20,30,40 and 50 N, and wear time was 20min.

Table 1:Plasma spray process parameter

coating	Spray distance/ mm	Current /A	The main gas/SCFH	Non-major gas/SCFH	The carrier gas/SCFH	The powder feed rate/kg/h	Coating thickness/mm
NiCrCoAlY	75	700	120	0	11	3	0.1
Al_2O_3-13%TiO_2	75	780	80	25	10	2	0.5

3. Results and disscussion

3.1 Friction coefficient

From Fig1 we can see that the relative motion of two paired surface from the "run" phase into the stable wear stage after one minute,. The friction coefficient of the coating has a slow upward trend with time increasing, but the change is relatively flat. The friction coefficient decreases with the increase of the load. This kind of trend is related with the size of the actual contact area.

The contact surface is in elastic state When the load is very small. The actual contact area is proportional to 2/3 power in the load. Friction is proportional to real contact area .So friction coefficient is proportional to 1/3 power in the load. The surface contact is in elastic-plastic state when the load is high. The change of actual contact area is relatively flat, so the friction coefficient decreases as the load increases.

3.2 wear debris

Fig.2 is SEM micrographs of wear debris remained on the worn surface under 30N. From it we can see a large number of small debris. The presence of this size debris makes wear resistance of nanometer-coating greatly improved. Small debris will fill the pits on the coating and Gr15steel. That makes the worn surface smoother so that reduce the friction coefficient. These small particles on the friction surface can also play the role of "micro-needle". That can change part of the sliding friction into rolling friction.

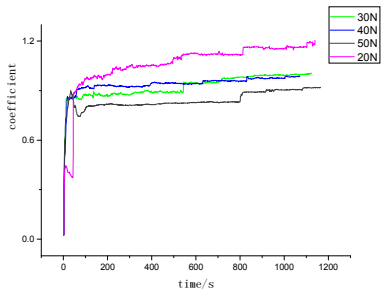


Fig 1 Friction coefficient

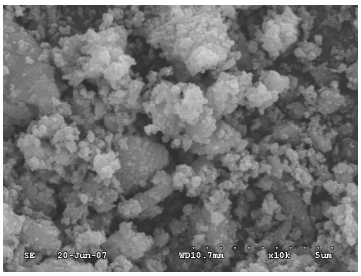
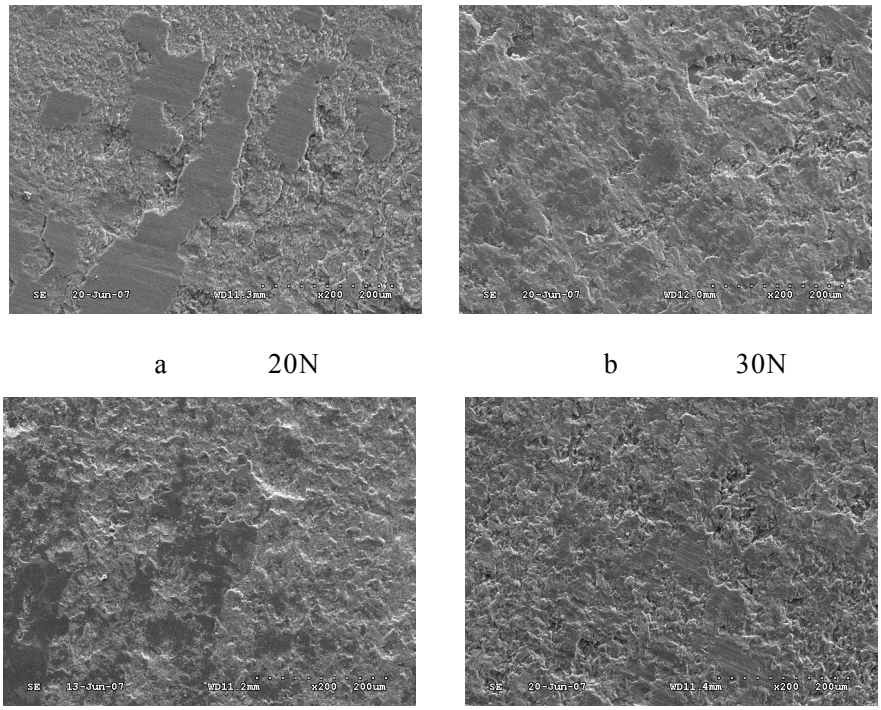


Fig.2 SEM micrographs of wear debris remained on the worn surface under 30N

3.3 Worn morphology

There are two kind morphologies in the worn coating surface .One is smooth area the other is rough area. Plastic deformation and brittle fracture occur in the coating surface at the same time. The coating has high toughness so micro-cracks can hardly be observed in the worn surface .One

reason is that there are so many plats which play a role in skeleton in the coating that improve the wear resistance of the coating greatly. The other is that there are a large number of nanometer particles to enhance the toughness of the coating. The nanometer particles can absorb propagation energy of micro crack decrease crack growth speed. From Fig.3 we can see the smooth area reduce while the rough area increase with the load increase. This indicates there are more deformation of coating lamellar structure along the wear direction than perpendicular to it with the increase of the load.



a 20N b 30N

c 40N d 50N

Fig.3 Wear surface morphology under different load

4 Conclusions

1) The friction coefficient decreases with the increase of the load.

2) There are two kind morphologies in the worn coating surface .One is smooth area the other is rough area. Plastic deformation and brittle fracture occur in the coating surface at the same time. The coating has high toughness so micro-cracks can hardly be observed lin the worn surface

3) The presence of this size debris makes wear resistance of nanometer-coating improved greatly.

References

[1] Balog M, Sajgalik P, Lences Z, etal. Influence of α and β SiC seeds on microstructural development and mechanical properties of liquid phases intered SiC with RE_2O_3 and AlN additives[J]. Diffusion and Defect Data Pt.B：Solid State Phenomena, 2003, 90/91：273

[2] Mitsuoka, Takeshi, Yamamoto, etal. Improvement in high temperature properties of Al_2O_3 ceramics by microstructure and grain boundary control[J]. Key Engineering Materials, 2003, 247：349

[3] K.Vijayakumar, ApurbbaKr.Sharma, M.M.Mayuram,R.Krishnamurthy. Response of plasma sprayed alumina–titania ceramic composite to high frequency impact loading[J]. Materials Letters, 2002, 56：252–262

[4] B. Normand, V. Fervel , C. Coddet, V. Nikitine．Tribological properties of plasma sprayed alumina–titania coatings: role and control of the microstructure[J]．Surface and Coatings Technology, 2000, 123：278–287

[5]P.V.Ananthapadmanabhan ,T.K.Thiyagarajan ,K.P.Sreekumar ,R.U.Satpute ,N.Venkatramani , K. Ramachandran．Co-spraying of alumina–titania: correlation of coating composition and properties with particle behaviour in the plasma jet[J]．Surface and Coatings Technology, 2003, 168：231–240

[6] S. Steinhauser , B. Wielage, U. Hofmann, Th. Schnick, A. Ilyuschenko, T. Azarova．Plasma-sprayed wear-resistant coatings with respect to ecological aspects[J]．Surface and Coatings Technology, 2000, 131：65-371

[7] Sofiane Guessasma, Ghislain Montavon, Christian Coddet．Velocity and temperature distributions of alumina–titania in-flight particles in the atmospheric plasma spray process[J]．Surface & Coatings Technology, 2005, 192：70– 75

[8] Balog M, Sajgalik P, Lences Z, etal．Influence of α and β SiC seeds on microstructural development and mechanical properties of liquid phases intered SiC with RE_2O_3 and AlN additives[J]．Diffusion and Defect Data Pt.B：Solid State Phenomena, 2003, 90/91：273

[9] Mitsuoka, Takeshi, Yamamoto, etal．Improvement in high temperature properties of Al_2O_3 ceramics by microstructure and grain boundary control[J]．Key Engineering Materials, 2003, 247：349

[10] D. Goberman , Y.H. Sohn, L. Shaw, E. Jordan, M. Gell．Microstructure development of Al_2O_3–13wt.%TiO_2 plasma sprayed coatings derived from nanocrystalline powders [J]．Acta Materialia , 2002 , 50 ： 1141–1152

© (2012) Trans Tech Publications, Switzerland
doi:10.4028/www.scientific.net/AMM.164.178

Synthesis and Properties of a New Photochromic Material Based on Isoxazole Unit for Optical Storage Recording

Taofeng Wang, Yanhua Yang, Shiqiang Cui, Gang Liu*

Jiangxi Key Laboratory of Organic Chemistry, Jiangxi Science and Technology Normal University, Nanchang 330013, P. R. China

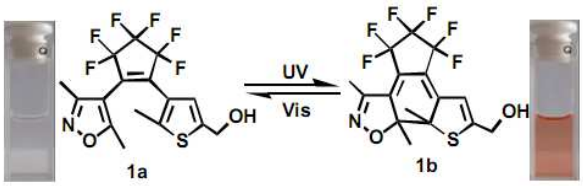
liugang0926@163.com

Keywords: Diarylethene, Photochromic, Fluorescence, Optical storage recording.

Abstract. A novel photochromic diarylethene compound containing isoxazole unit, 1-(3,5-dimethyl-4-isoxazolyl)-2-[2-methyl-5-hydroxymethyl-3-thienyl]perfluoroyclopentene have been synthesized. Its photochromic, fluorescent and optical storage properties were investigated. The compound exhibited remarkable photochromism both in solution and in PMMA film. In addition, the open-ring isomer of the diarylethene **1a** exhibited relatively clear fluorescent switches in hexane solution and PMMA film when excited at 300 nm. This new photochromic system also exhibited remarkable optical storage character.

Introduction

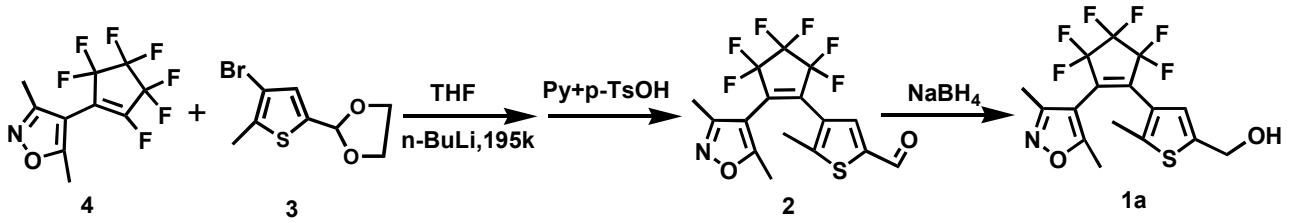
Photochromism is the reversible transformation between two isomers with different absorption spectra caused by alternating irradiation with UV and visible light. The design and synthesis of novel photochromic molecules has attracted interest due to their potential application in photonic devices such as memory media and optical switching [1,2]. Among these compounds, diarylethenes with heterocyclic aryl groups, especially those bearing two thiophene or benzothiophene rings, are considered the most promising candidates for technological applications because of their excellent thermal stability, remarkable fatigue resistance, and high sensitivity [3-6]. However, up to date, there are a few examples of photochromic diarylethenes bearing ioxazole rings [7-9]. The diarylethene derivatives exhibit good photochromism in hexane and are very useful materials for full-color imaging because they provide one of the three primary colors. The results give us valuable insight and encourage us to develop a new class of hybrid photochromic diarylethene derivatives bearing an isoxazole moiety. Therefore, introduction of isoxazole ring into the heteroaryl moieties of diarylethene derivatives can be expected to undergo excellent photochromic reactions. As far as we are aware, photochromic diarylethenes bearing both isoxazole and thiophene moieties have rarely been reported [10]. On the basis of these considerations, we have designed to investigate the reversible molecule fluorescence switching properties and optical storage of a new asymmetrical photochromic diarylethene 1a based on isoxazole and thiophene units. Its photochromic reactivity and fluorescent properties were investigated in detail. Using this dithienylethene as recording medium, optical recording storage was performed successfully. Scheme 1 showed the molecular structure and photoisomerization of photochromic diarylethene, which was discussed in this paper.



Scheme 1. Photochromism of diarylethene **1a**.

Experiments

Diarylethene **1a** was prepared according to the method described in scheme 2. First, the mono-substituted (3,5-dimethyl-4-isoxazolyl)perfluorocyclopentene (**4**) was synthesized by the similar method reported by Pu et al [11]. 3-Bromo-2-methyl-5-(1,3-dioxolane)thiophene (**3**) was lithiated and coupled with **4**, the crude product was directly hydrolyzed in the presence of pyridine and *p*-toluenesulfonic acid in acetone/water to give diarylethene **2**. Finally, compound 2 was deoxidized by $NaBH_4$, and the mixture was extracted with ether. The organic layer was collected and dried over $MgSO_4$, filtered and evaporated. The crude compound was purified by column chromatography on silica gel using petroleum/ethyl acetate (2:1) as the eluent to give diarylethene **1a**. The structures of diarylethene **1a** were confirmed by NMR spectra were recorded on Bruker AV400 (400 MHz) spectrometer with $CDCl_3$ as the solvent and tetramethylsilane as an internal standard. 5 mg diarylethene sample and 50 mg PMMA were dissolved ultrasonically into 0.5 ml chloroform. The PMMA film was prepared by spin-coated on a glass substrate with a spin rotation. The structure of **1a** was characterized by ^{1}H NMR (400 MHz, $CDCl_3$, TMS): δ2.09 (t, 1H, -OH), 2.31 (s, 3H, -CH_3), 2.35 (s, 3H, -CH_3), 4.79 (d, 2H, J = 8.0 Hz, -CH_2), 6.48 (s, 1H, thiophene-H); ^{13}C NMR (100 MHz, $CDCl_3$, TMS): δ 9.09, 11.12, 12.03, 60.23, 101.89, 103.80, 111.70, 118.29, 124.40, 126.65, 127.61, 134.95, 136.43, 158.08, 172.24.



Scheme 2. Synthetic route for the compound **1a**.

Results and discussion

Photochromic behaviours. The photochromic behaviors of diarylethene **1a** induced by photoirradiation at room temperature were measured both in hexane and in PMMA amorphous film. In hexane, the compound **1a** exhibited an absorption peak at 237 nm (ε, 3.42 × 10^4 L mol^{-1} cm^{-1}) in hexane, as showed in Fig. 1A. Upon irradiation with 297 nm light, a new visible absorption band at 490 nm (ε, 3.54 × 10^3 L mol^{-1} cm^{-1}) appeared while the original peak at 237 nm decreased, indicating the new formation **1b** produced. Correspondingly, the colourless solution of **1a** in hexane solution turned pink. The pink solution turned colourless by irradiation with visible light (λ > 500 nm), indicating that **1b** returned to the initial state **1a**.

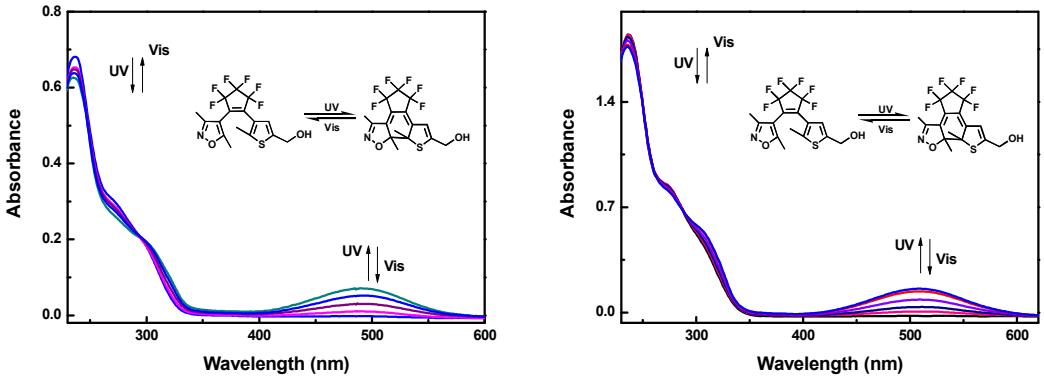


Fig. 1. Absorption spectral and color change of compound 1a in hexane (A) (2 × 10^{-5} mol/L) and in PMMA (B).

In PMMA amorphous film, as showed in Fig. 1B, diarylethene **1a** also showed good photochromism as similar to that in solution (Fig. 1A). The absorption maximum of compound **1a** was observed at 236 nm. Upon irradiation with 297 nm light, the color of the PMMA film turned pink too, in which the absorption maximum was observed at 508 nm. The pink film turned colorless, too, upon irradiation with visible light ($\lambda > 500$ nm).

Fluorescence of diarylethene. Generally, diarylethene derivatives undergo a reversible transformation from the open-ring isomer to the close-ring isomer upon irradiation with UV light and are accompanied by a decrease of fluorescent emission intensity; the inverse process from the closed-ring isomer to the open-ring isomer can be accomplished by the irradiation of visible light with appropriate wavelength and the fluorescent intensity recovers to the initial state. This characteristic is usually used to design the fluorescent controllable switch. Therefore, the fluorescent properties of the diarylethene **1a** both in hexane solution and PMMA film were measured using a Hitachi F-4500 spectrophotometer and the breadths of excitation and emission slit were selected 10.0 nm and 10.0 nm, respectively. Fig. 2 shows the fluorescence spectral changes of **1** in hexane (A) (2.0×10^{-5} mol/L) and PMMA film (B) (10%, w/w) upon irradiation with 297 nm light at room temperature. It could be clearly seen that the compound in hexane solution and PMMA film exhibited good fluorescence switches when excited at 300 nm, as shown in Fig. 2. The fluorescence intensity decreased along with the photochromism from open-ring isomers to closed-ring isomers upon irradiation with 297 nm UV light, due to producing the non-fluorescence closed-ring isomer [12]. The emission intensity of the diarylethene in a photostationary state was quenched to ca. 55.6% and 56.3%, respectively. The incomplete cyclization reaction and the existence of parallel conformations may be the main cause for the moderate change in fluorescence induced by photoirradiation [13]. The back irradiation by appropriate wavelength visible light regenerated its open-ring isomer and recovered the original emission intensity.

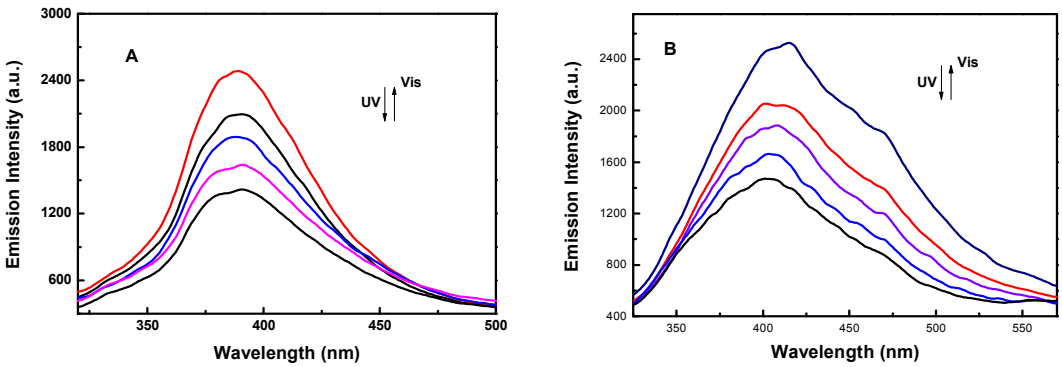


Fig. 2. Fluorescence spectral of the diarylethene in solution (A) and PMMA (10%, w/w) film change by irradiation with UV and visible light.

Optical recording properties. With a He-Ne laser (wavelength: 650 nm, 105mW) in the experimental setup. The evaluation of potential of photochromic diarylethene as a polarization medium by recording and reading in a real-time operation was investigated. Using diarylethene **1b**/PMMA film as recording medium, the polarization patterns were recorded and read on the film under the microscope, the polarizations of the patterns recorded on the film are shown in Fig. 3. The exposure time for each spot was 0.04 s and the patterns were about 20 μm. The result indicated that the new diarylethene compound can be applied in high capacity optical storage.

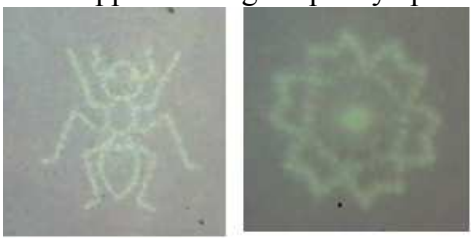


Fig. 3. Recording marks of diarylethene **1b** in polarization optical storage.

Summary

A new unsymmetrical diarylethene **1a** were synthesized and its photochromic and fluorescent properties were also investigated. The results showed that the new compound exhibited remarkable photochromism and acted as a notable fluorescent switch. The fluorescence intensity decreased along with the photochromism upon irradiation with 297 nm light. Using diarylethene 1b as recording medium, optical recording was carried out successfully. The result indicated that the new photochromic diarylethene **1b** can be applied in high capacity optical storage.

Acknowledgments

This work was supported by the Project of Natural Science Foundation of Jiangxi Province(2010DQ00200) and the Science Funds of Jiangxi Education Office (GJJ1067).

References

[1] G.H. Brown: *Photochromism： molecules and systems* (Wiley-Interscience, New York 1971).

[2] M. Irie: *PhotoReactive Materials for Ultrahigh-Density Optical Memory* (Elsevier, Amsterdam 1997).

[3] H. Tian, S. Wang: Chem. Commun. (2007), p. 781

[4] O. Miyatake, T. Fukaminato and M. Irie: Chem. Commun. (2005), p. 3921

[5] Q.F. Luo, H. Tian, B.Z. Chen and W. Huang: Dyes Pigm. Vol. 73 (2007), p. 118

[6] B.Z. Chen, M.Z. Wang, Q.F. Luo and H. Tian: Synth. Met. Vol. 137 (2003), p. 985

[7] L. Kuroki, S. Takami, K. Shibata and M. Irie: Chem. Commun. (2005), p. 6005

[8] S. Takami, L. Kuroki and M. Irie: J. Am. Chem. Soc. Vol. 129 (2007), p. 7319

[9] T. Yamaguchi, W. Taniguchi, T. Ozeki, S. Irie and M. Irie: J. Photochem. Photobiol. A. Vol. 207 (2009), p. 282

[10] S.Z. Pu, H. Li, G. Liu, W.J. Liu, S.Q. Cui, C.B. Fan: Tetrahedron. Vol. 67 (2011), p. 1438

[11] C.H. Zheng, S.Z. Pu, J.K. Xu, M.B. Luo, D.C. Huang and L. Shen: Tetrahedron. Vol. 63 (2007), p. 5437

[12] H.B. Guo, F.S. Zhang, G.S. Wu, S.Z. Pu and G.S. Qi: Opt. Mater. Vol. 22 (2003), p. 269

[13] S.Z. Pu, F.S. Zhang, J.K. Xu, L. Shen, Q. Xiao and B. Chen: Mater. Lett. Vol. 60 (2006), p. 485

© (2012) Trans Tech Publications, Switzerland
doi:10.4028/www.scientific.net/AMM.164.182

Transport of a Thermophilic *Geobacillus* sp. in Sandpack Core as an Enhanced Oil Recovery Material

XiangPing Kong

College of Chemistry and Pharmacy, Qingdao Agricultural University, Qingdao 266109, Shandong, PR China

email: kxp2004@163.com

Keywords: *Geobacillus* sp.; bacterial transport; thermophilic bacteria; sandpack core

Abstract: The effects of temperature, permeability and the presence of a residual oil phase on the transport of the bacterium *Geobacillus* sp. were investigated experimentally in sandpack cores. A lower reduction in permeability and a higher effluent bacterial concentration were obtained in the higher permeability sandpacks, or at a higher temperature. The bacterial transport could be enhanced by the pulse injection, but reduced with the presence of residual oil. When the injected cell concentration is relatively high (>10^8 cells/mL), log-jam effect or pore bridging may be the primary mechanism, and the surface adhesion may act as the secondary mechanism of bacteria retention and permeability reduction.

Introduction

Microbial enhanced oil recovery (MEOR) is a tertiary recovery technology utilizing the microorganisms and/or their metabolic products for recovery of residual oil, strewn with both successes and failures [1]. The continued appeal of MEOR, however, is that it is an environmentally benign, low-cost means of oil recovery with relatively simple operation. The ability to transport the target bacteria through porous rock is crucial to the implementation of MEOR processes or to the removal of environmental pollutants in groundwater through bioaugmentation. Certain thermophilic and halophilic *Geobacillus* spp. have been proposed as candidates for MEOR and oil-waste bioremediation technology owing to their good performances of taking crude oil as the sole carbon source, reducing the viscosity of crude oil and producing active biosurfactants [2, 3]. However, there has been no report about their transport in the porous rock yet. Here, the effects of temperature, permeability and the presence of a residual oil phase on the transport of the bacterium *Geobacillus* sp. were investigated experimentally in sandpack cores.

1. Materials and methods

1.1 Bacterium and medium

Geobacillus sp. used in this study was isolated and characterized as a hydrocarbon degrading strain by Liu et al. [3]. The cell shape was 0.5-0.7 × 1.5-4.0 μm. The basic nutrients and their concentrations (g/L) of the culture medium were sucrose 30, NaCl 5, KNO_3 2, KH_2PO_4 1.35, $Na_2HPO_4 \cdot 12H_2O$ 3.65, $FeSO_4 \cdot 7H_2O$ 0.01, $MgSO_4 \cdot 7H_2O$ 0.2, $CaCl_2$ 0.01 and yeast extract 0.5, pH 7.0-7.2. The concentration of cell suspension at the stationary phase was (4-7) × 10^8 cells/mL.

1.2 Methods

The core flooding equipment used has been reported earlier [4]. There were 3 sandpack cores, designated as S1, S2 and S3, respectively. The average measured porosity of the cores (length 16.00 cm, diameter 2.15 cm) were 38.2, 39.6 and 38.9%, and the permeability were 2500, 4600 and 2500

mD, respectively. The sandpacks of S1 and S2 were saturated with the crude oil, and the residual oil saturation were 29.5 and 28.3% with the effective brine permeability of 196 and 980 mD after the primary water flooding with sterile produced water, respectively.

All the experiments were carried out by injecting the cell suspension of the stationary phase into the cores, followed by the displacement with the sterile produced water continuously. The flow velocity was 0.5mL/min. 0.4 pore volume (PV) samples of effluent were collected at different time intervals from the core outlet for the cell density analysis, and the pressure across the core was monitored during the displacement process. The hemacytometer counting method was used for the bacteria counting. The bacterial concentration ratio of the effluent (effluent concentration divided by the injected concentration, C_e/C_i) and the permeability ratio (permeability at a given time divided by the initial effective brine permeability, K/K_i) were measured as functions of the dimensionless time, which was defined as the cumulative volume of fluid collected divided by the pore volume of the sandpack [5].

2. Results and discussion

2.1 Effect of temperature

The sandpack S1 was used all through the temperature experiments. The dry-heat sterilization was carried out to the sandpack at 150°C for 3 h after the 30°C investigation, and then it was washed with 10 PV of sterile produced water prior to the 60°C experiment.

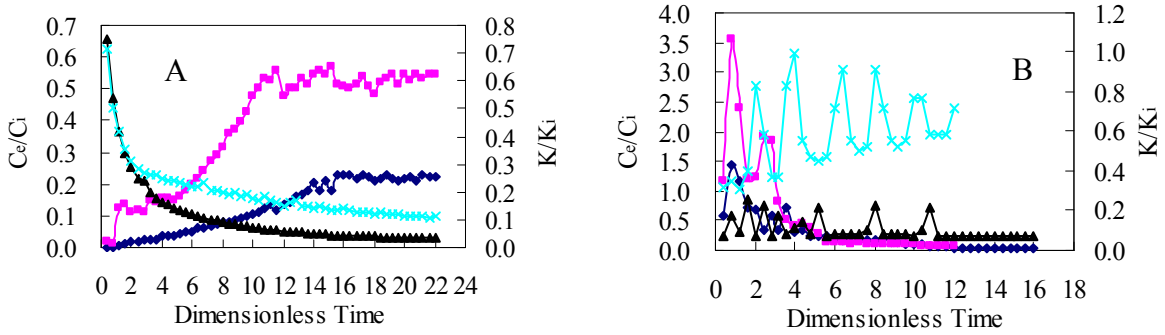


Fig. 1 The bacterial concentration ratio of effluent at 30°C (◆) and 60°C (■) and the permeability ratio at 30°C (▲) and 60°C (×) during the bacteria flooding (A) and the subsequent sterile water flooding (B).

Similar tendency about the permeability impairment at 30°C and 60°C was found. The permeability dropped sharply during the initial period of the bacteria flooding and then further decreased gradually in a linear fashion, and the permeability with the sterile water flooding fluctuated sharply at the initial period and then the fluctuating range reduced (Fig. 1). A lower permeability impairment was evident at 60°C compared to 30°C, consistent with the substantially higher bacterial concentration in effluent detected at 60°C during the whole bacteria flooding process and the initial stage of sterile water flooding. The relatively low temperature may lead to a decrease in the Brownian energy of bacteria, then the cell aggregation was more extensive and larger cell clusters even filter cakes may formed, resulting in a lower permeability.

Interesting, both the C_e/C_i and K/K_i at the initial stage of the sterile water flooding were higher than those at the end of bacteria flooding. There was 20 to 30 min interval between the two displacements. Some bacterial coagulation became loose, improving the bacterial transport capacity

and leading to a higher permeability. Subsequently, the bacteria repeated the aggregation-disaggregation process until the balance had been achieved. This could be proved by the fluctuations of C_e/C_i and K/K_i at the initial stage of the sterile water flooding (Fig. 1 B). The results suggested that log-jam effect or pore bridging was the primary mechanism of the bacteria retention, and the pulse injection (repeatedly starting and stopping injection) could enhance the transport of bacteria. In addition, the bacteria could still be detected after the 16 PV and 12 PV of sterile water flooding at 30°C and 60°C, respectively, indicating that there was attachment-detachment process of bacteria at the surface of sandstone or oil. So the surface adhesion may serve as the secondary bacteria retention mechanism.

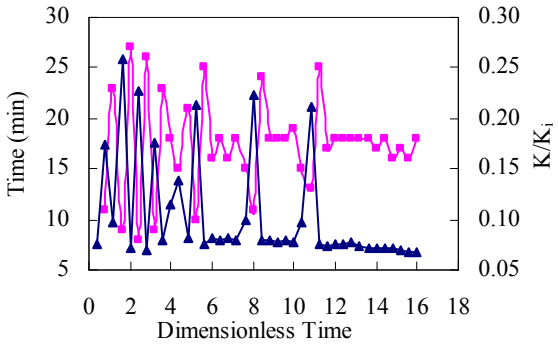


Fig. 2 The time consumed by 0.4 PV of sample collecting (■) and the permeability ratio (▲) during the subsequent sterile water flooding at 30°C.

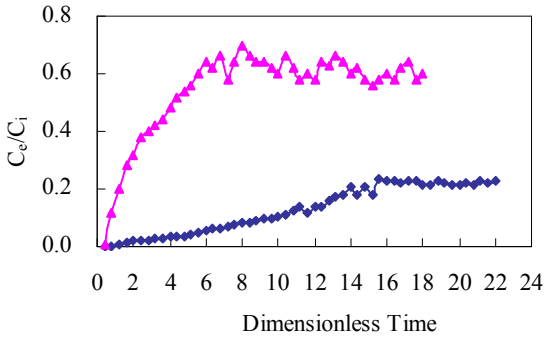


Fig. 3 The bacterial concentration ratio of effluent in the presence (◆) or absence (▲) of residual oil during the bacteria flooding at 30°C.

Particularly, the time consumed by 0.4 PV of sample collecting fluctuated around the value from the pump (18 min) before the dimensionless time of 12 during the sterile water flooding at 30°C (Fig. 2). It could be explained that the bacteria repeated the blockage and blockage-relieving process until the formation of stable blockage under the effect of water dynamics. However, the fluctuation was not found in the displacement of 60°C, further indicating that the higher temperature facilitated the bacterial transport due to a lower degree of blockage.

2.2 Effect of residual oil

The displacements were conducted with sandpacks of S2 and S3 at 30°C. The maximum bacterial concentration of effluent reduced significantly due to the presence of residual oil (Fig. 3), in agreement with what Sarkar et al. reported [5]. In addition, the bacterial concentration of effluent with the residual oil was also found to have reached the balance slower, which may be caused by the reduction of effective brine permeability or the cell adsorption at the oil-water interface.

2.3 Effect of permeability

The maximum bacterial concentration of effluent was higher and achieved the balance faster under the effective brine permeability of 980 mD (S2) than 196 mD (S1), but the values of K/K_i were almost the same (Fig. 4 C). The injection pressure changed from 0.020 to 0.306 MPa (S1) and 0.004 to 0.048 MPa (S2) with the injected bacterial volume of 0.4 to 14 PV, respectively. It indicated that the permeability impairment in the sandpack of S2 was lower compared to S1, consistent with the result of subsequent sterile water flooding (Fig. 4 D). Additionally, no

fluctuation of C_e/C_i or K/K_i was found at the initial stage of sterile water flooding of S2. It may be explained by the reduced bacteria retention and blockage in sandpacks known from the high effluent cell concentration.

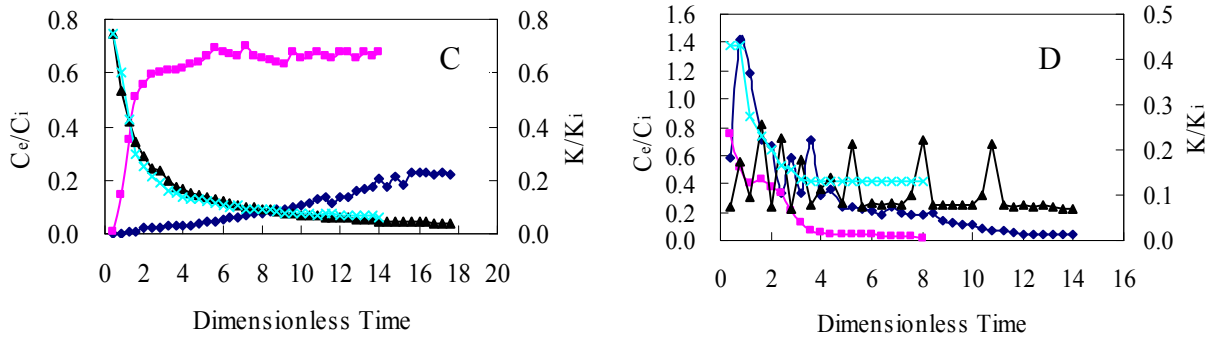


Fig. 4 The bacterial concentration ratio of effluent at the effective brine permeability of 196 mD (◆) and 980 mD (■) and the permeability ratio at 196 mD (▲) and 980 mD (×) during the bacteria flooding (C) and the subsequent sterile water flooding (D) at 30°C.

3. Conclusions

The increases in temperature or permeability resulted in the enhanced bacterial transport and a lower permeability impairment of sandpack core. The pulse injection facilitated the transport of bacteria, while the presence of a residual oil phase reduced the efficiency of bacterial transport. As a bacterial transport of high injected cell concentrations (>10^8 cells/mL), log-jam effect or pore bridging may be the primary mechanism, and the surface adhesion may act as the secondary mechanism of bacteria retention.

Acknowledgements

The author is grateful to the Research Institute of Oil Production Technology, Shengli Oilfield Ltd. Co. for the experimental samples provision and technical support, and also thanks their staff for the assistance with the experiments.

References

[1] L.R. Brown: Curr. Opin. M. Vol. 13 (2010), P. 316-320
[2] L. Feng, W. Wang, J.S. Cheng, Y. Ren, G. Zhao, C.X. Gao, Y. Tang, X.Q. Liu, W.Q. Han, X. Peng, R.L. Liu, and L. Wang: P. NAS US Vol. 104 (2007), P. 5602-5607
[3] Q.K. Liu, J. Wang, G.Q. Li, T. Ma, F.L. Liang and R.L. Liu: Env. Sci. Vol. 29 (2008), P. 3554-3560 (in Chinese)
[4] X.P. Kong, Y.D. He, H.S. Zhang, X.L. Geng, P. Xu, X.L. Wang: J. Xi'an Shiyou University Vol. 21(6) (2006), P. 44-48 (in Chinese)
[5] A.K. Sarkar, G. Georgiou, M.M. Sharma: Biotech. Bio. Vol. 44(4) (1994), P. 489-497

© (2012) Trans Tech Publications, Switzerland
doi:10.4028/www.scientific.net/AMM.164.186

Effect of placement pattern and quantity of iron shavings in reactor on Biological Nutrient Removal from Domestic Wastewater

Zi Wang [a], Zhe Chen [b], Hongwu Wang [c], Luming Ma [d]

National Engineering Research Center for Urban Pollution Control, State Key Laboratory of Pollution Control and Resources Reuse, Tongji University, Shanghai 200092, China
[a]wangziandllp@gmail.com, [b]chenzhedb@163.com,
[c]wanghongwu@tongji.edu.cn, [d]lumingma0708@yahoo.com.cn

Keywords: iron shavings; enhancement; biological treatment; placement pattern

Abstract. Effect of placement pattern and quantity of iron shavings in reactor on biological nutrient Removal from domestic wastewater was conducted. The results indicate that: different placement pattern had obvious effect on TP removal, but had no distinct effect on TN removal; when iron was placed beside aerator, the highest TP removal can be obtained. Adding more iron can just slightly enhance TP and TN removal when iron shaving quantity increased from 5 g to 20 g per 900 ml wastewater; iron adding restrained transfer of ammonia to nitrate by microbe and this defect should be overcome in practice; 5 g iron per 900 mL is the best choice to balance good nutrient removal and low cost.

Introduction

Zero-Valent Iron (ZVI), serving as a reducing agent, has been utilized in permeable reactive barriers (PRBs) for in situ remediation of contaminated groundwater for a long time [1]. In PRBs system many researchers found that some microbial community would co-exist with ZVI and therefore enhance the removal efficiency of many contaminants [2, 3]. So the combination of ZVI and microbe for contaminants removal enhancement was given great interesting. Till et al. reported that grain ZVI could support autotrophic denitrification [4]. Yamashita et al. found that three processes (wood degradation by heterotrophic denitrification, iron oxidation by hydrogen trophic denitrification and phosphorus removal) could occur simultaneously in a denitrification reactor packed with iron and wood as electron donors [5]. These research results indicate that ZVI pre-treatment can be coupled with biological process and the removal of nutrient can be enhanced by combination of ZVI and microbe. However, using ZVI to enhance nutrient removal from municipal wastewater has not been reported. Based on this, the main objective of this paper is to find the practice feasibility of iron enhancing nutrient removal and the emphasis focused on iron placement pattern and their effectiveness on nutrient removal.

Methods and materials

Batch tests were carried out in 1000 ml wide-mouth bottles containing 900ml wastewater inoculated with about 4000 mg MLSS L^{-1}. 900ml wastewater consists of 600 ml effluent and 300ml influent, which made fill to reaction ratio be 1:3. Wastewater and activated sludge used in experiment were all taken from a municipal sewage treatment plant in China. Operation mode was as follows: anoxic 30 min, aeration 90 min and settling 30 min. Dissolved oxygen (DO) in each bottle was kept at 2~4 mg L^{-1} when aerating. Three different placement patterns, in which iron shavings (10 g) were placed above, under and beside aerator, respectively (as shown in Fig. 1), were evaluated to determine optimal placement. Based on results of this test, different quantity (2.5g, 5 g, 10 g and 20 g) of iron shavings were placed beside aerator for reaction in next experiment to

observe and determine proper iron quantity of adding in practice. Samples were taken from supernatant at beginning and end time of reaction. All bottles are placed in a shaking 25℃ water bath at 60 rpm. Iron shavings (with 95.20-96.95% iron content) used in this experiment were purchased from machinery factory and have a specific surface area of 26.34 cm^2 g^{-1}. The whole experiments were replicated 3 times.

COD, NH_3-N, NO_3^--N, NO_2^--N, TP, TN were tested immediately after sampling. All chemicals used in analysis were of analytical grade. Purkinje General UV spectrophotometer (TU1810) was used for measurements of light absorption. The test items and process were carried out following standard methods.

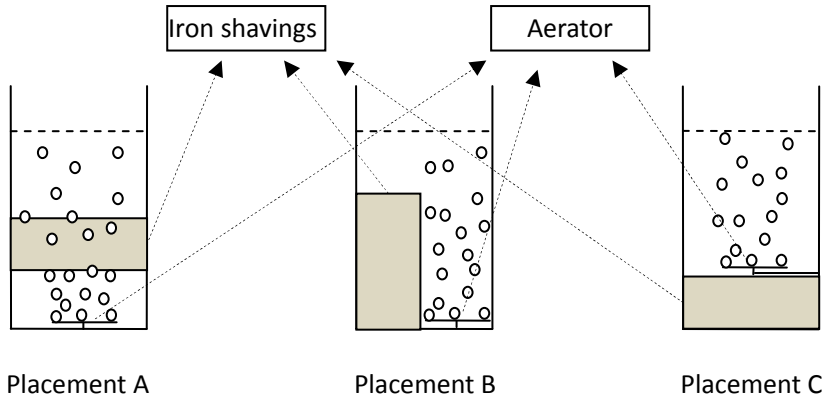


Fig. 1 Placement pattern of iron shavings in batch test

Results and discussions

Effect of iron placement pattern on biological treatment is shown in Table 1. As can be seen, different placement pattern had obvious effect on TP removal, but had no distinct effect on TN removal, COD removal and pH change. And adding iron shavings in biological reactor cause obvious concentration change of nitrate, nitrite and ammonia.

Table 1 Effect of iron placement pattern on biological treatment

item	Unit	Initial value	Final value			
			Control	Placement A	Placement B	Placement C
TN	mg L^{-1}	19.72	14.67±1.03	15.21±1.25	14.08±1.19	14.29±1.01
TP	mg L^{-1}	1.79	1.12±0.12	1.38±0.22	0.19±0.04	0.58±0.09
Total iron	mg L^{-1}	1.15	0.18±0.03	9.57±0.85	0.58±0.11	0.46±0.08
NH_3-N	mg L^{-1}	9.13	1.66±0.51	8.98±1.21	7.26±1.02	7.05±0.98
NO_2^--N	mg L^{-1}	0.25	0.58±0.11	2.18±0.43	1.38±0.33	1.47±0.26
NO_3^--N	mg L^{-1}	9.56	11.69±0.92	6.18±1.17	4.97±0.91	5.13±0.89
COD	mg L^{-1}	65	26±5	46±12	38±9	32±7
pH	-	7.57	7.78±0.17	7.43±0.32	7.48±0.28	7.51±0.19

TP removal was enhanced obviously in placement B and C compared to control test. But effluent TP concentration (1.38±0.22 mg L^{-1}) in placement A was higher than that in control test (1.12±0.12 mg L^{-1}). Compared to placement B and C, iron shavings were placed above aerator in placement A, which made oxygen contact directly with iron when aerating. Oxygen corrosion of iron would happen in this condition[6]. So an iron oxide layer would formed on iron surface and just a very little free ferrous may be released to solution. Besides this, it should be noticed that effluent total iron concentration in placement A was 9.57±0.85 mg L^{-1} which was much higher than

that in placement B (1.14±0.11 mg L^{-1}) and C (0.46±0.08 mg L^{-1}). Based on these facts, it can be deduced that the main phosphorus removal mechanism in this process may be adsorption of phosphate on iron oxide layer. Iron-based sorbents can achieve high levels of phosphorus removal due to the strong affinity of the phosphate anion for positively charged ferric iron[7, 8]. Parts of iron oxygen corrosion products formed on iron surface were stripped by aerating and so these products suspended in effluent. Therefor the phosphorus which adsorbed on these products increased effluent TP concentration.

Some researchers [4],[9] have proven that the hydrogen generated by the reaction of ZVI and water can serve as electron donor to support autotrophic denitrification, which can enhance TN removal. However, enhancement of TN removal by iron addition was not observed in this experiment no matter how the placement pattern was. There may be two reasons for this: one is the lower specific surface area (26.34 cm^2 g^{-1}) of iron shavings used in this experiment than Nano-ZVI[10] and so iron may just cause low-level hydrogen production rate; another is due to the shorter HRT (3~4 h) than that used by Till et al. (0.67~2.33 days) [4] and Biswas et al. (2~13 days) [9]. Iron shaving was chosen as main material in this experiment because of their low cost which is much lower than Nano-iron particles. HRT of 3~4 h used in this experiment may be too short to enhance TN removal obviously. However, it is unpractical to prolong HRT in most municipal sewage plant because of many limitations. So these facts may indicate that enhancing TN removal by using iron shavings is infeasible. This conclusion will be confirmed according to long-term operation results.

It can be observed that adding of iron restrained transfer of ammonia to nitrate by microbe. When ZVI was used as reducer, the reduction from nitrate to ammonium was mainly observed only at low pH, as reported by Huang et al.[11] and Rocca et al.[12]. Considering that pH in reaction is 7.43 ~ 7.78 and nitrite increasing after adding iron was observed, it can be inferred that iron may restrain the metabolism activity of ammonia-oxidizing bacterias, as mentioned by Oikonomidis [13]. This defect may impair the use-value of iron shavings and should be observed more in practice.

In addition, it should be noticed that 1-A level of TP in Chinese national discharge standard is 0.5 mg L^{-1} and 1-B level is 1.0 mg L^{-1}. With the increasing demands for wastewater treatment level in nowadays china, many sewage plants face the problem of improving emissions standards from 1-B to 1-A. That means effluent TP concentration should be reduce to < 0.5 mg L^{-1}, so only placement B can meet this requirement.

Table 2 Effect of iron quantity on biological treatment when iron was placed beside aerator

Item	Unit	Initial value	control	Final value (g iron per 900 mL)			
				2.5	5	10	20
TN	mg L^{-1}	19.33	14.31±1.18	14.29±1.06	14.17±1.23	13.95±1.31	13.71±1.42
TP	mg L^{-1}	1.71	1.01±0.03	0.85±0.05	0.25±0.04	0.19±0.04	0.07±0.02
Total iron	mg L^{-1}	1.08	0.17±0.08	0.25±0.12	0.85±0.15	1.01±0.21	1.56±0.25
COD	mg L^{-1}	61	22±6	27±7	31±7	39±7	49±9

Effect of iron quantity on nutrient removal when iron was placed beside aerator (placement B) is shown in Table 2. As can be seen, 20 g iron in 900ml wastewater did not show much better (or just a little higher) enhancement of nutrient removal than 10 g and 5 g iron. Effluent TP concentration was 0.25±0.04 mg L^{-1}, 0.19±0.04 mg L^{-1} and 0.07±0.02 mg L^{-1} in addition of 5 g, 10 g and 20 g iron shavings in 900 ml water, respectively. Effluent concentrations of TN, total iron and COD are close among three different quantities. To decrease treatment cost, adding lower iron quantity (5 g iron per 900 mL) may be the best choice in practice.

Summary

Effect of iron placement pattern and iron quantity on TN and TP removal by biological treatment were studied in this experiment. Some conclusion can be obtained from the Results of batch test. First, different placement pattern had obvious effect on TP removal, but had no distinct effect on TN removal. When iron was placed beside aerator, the highest TP removal can be obtained. Adding more iron can just slightly enhance TP and TN removal when iron shaving quantity increased from 5 g to 20 g per 900 ml wastewater. Second, adding of iron restrained transfer of ammonia to nitrate by microbe. This defect should be overcame in practice. Third, to decrease treatment cost, adding iron quantity (5g per 900 mL) would be the best choice in practice.

Acknowledgement: This study has been financially supported by the funds of National 863 plans (2009AA063902, 2008AA06Z310) and Shanghai Science and Technology Base Project (09dz2202300)

References

[1] Henderson, A.D. and A.H. Demond, *Long-term performance of zero-valent iron permeable reactive barriers: A critical review.* Environmental Engineering Science, 2007. **24**(4): p. 401-423.

[2] Della Rocca, C., V. Belgiorno, and S. Meric, *Overview of in-situ applicable nitrate removal processes.* Desalination, 2007. **204**(1-3): p. 46-62.

[3] Liang, L.Y., et al., *Geochemical and microbial reactions affecting the long-term performance of in situ 'iron barriers'.* Advances in Environmental Research, 2000. **4**(4): p. 273-286.

[4] Till, B.A., L.J. Weathers, and P.J.J. Alvarez, *Fe(0)-supported autotrophic denitrification.* Environmental Science & Technology, 1998. **32**(5): p. 634-639.

[5] Yamashita, T. and R. Yamamoto-Ikemoto, *Phosphate removal and sulfate reduction in a denitrification reactor packed with iron and wood as electron donors.* Water Science and Technology, 2008. **58**(7): p. 1405-1413.

[6] Cornell, R.M. and U. Schwertmann, *The iron oxides : structure, properties, reactions, occurrences, and uses*. 2nd, completely rev. and extended ed. 2003, Weinheim: Wiley-VCH. xxxix, 664 p.

[7] Rittmann, B.E., et al., *Capturing the lost phosphorus.* Chemosphere, 2011. **84**(6): p. 846-853.

[8] Rentz, J.A., I.P. Turner, and J.L. Ullman, *Removal of phosphorus from solution using biogenic iron oxides.* Water Research, 2009. **43**(7): p. 2029-2035.

[9] Biswas, S. and P. Bose, *Zero-valent iron-assisted autotrophic denitrification.* Journal of Environmental Engineering-Asce, 2005. **131**(8): p. 1212-1220.

[10] Shin, K.H. and D.K. Cha, *Microbial reduction of nitrate in the presence of nanoscale zero-valent iron.* Chemosphere, 2008. **72**(2): p. 257-262.

[11] Huang, C.P., H.W. Wang, and P.C. Chiu, *Nitrate reduction by metallic iron.* Water Research, 1998. **32**(8): p. 2257-2264.

[12] Della Rocca, C., V. Belgiorno, and S. Meric, *An heterotrophic/autotrophic denitrification (HAD) approach for nitrate removal from drinking water.* Process Biochemistry, 2006. **41**(5): p. 1022-1028.

[13] Oikonomidis, I., L.J. Burrows, and C.M. Carliell-Marquet, *Mode of action of ferric and ferrous iron salts in activated sludge.* Journal of Chemical Technology and Biotechnology, 2010. **85**(8): p. 1067-1076.

© (2012) Trans Tech Publications, Switzerland
doi:10.4028/www.scientific.net/AMM.164.190

Study of Rapid Synthesis on $LiFePOB_{4B}$ and $LiFePOB_{4B}$/C by Molten Salt Method and Its Electrochemical Properties as Cathode Material

Ningyu GU[1,a], Xinghua HE[1] and Chao LI[2]

[1],Department of Chemistry, Nanchang University, Nanchang 330031, China

[a]nygu@ncu.edu.cn

[2], Jiangxi Meiya Energy Co., Ltd. Nanchang 330500, China

Keywords: Lithium ion batteries; Cathode materials; $LiFePO_4$; Molten salt method

Abstract. The $LiFePOB_{4B}$ and $LiFePOB_{4B}$/C cathode materials were rapidly synthesized by molten salt method, where a KCl-$MgClB_{2B}$ eutectic salt was used as reaction media of the formation of $LiFePOB_{4B}$ and a relatively low synthesis temperature was adopted. X-ray diffraction (XRD) patterns of both samples were identified to orthorhombic olivine $LiFePOB_{4B}$ without obvious impurities. The $LiFePOB_{4B}$ was observed to micron-sized cuboid structure and the $LiFePOB_{4B}$/C with nano-carbon layers had particle size distribution from nanometers to 3 μm by morphological characterization. The electrochemical results showed that the $LiFePOB_{4B}$/C deliverd a larger discharge capacity than the $LiFePOB_{4B}$ did due to the conductive carbon improving the electrchemical activities of the materials and providing a high LiP^{+P} transfer kinetics.

Introduction

Initially studied by Padhi et al. in 1997, olivine-type $LiFePOB_{4B}$ has been considered as a suitable cathode material for lithium-ion batteries, for it exhibits a high theoretical capacity of 170 mAh/g, a flat voltage plateau around 3.4 V versus Li/LiP^{+P}, and an excellent cycling stability [1]. However, attempts to overcome the intrinsic disadvantages of low electron conductivity and lithium ion diffusion had been mainly focused on before its application for power lithium ion batteries, because they prevent electrochemical activities of $LiFePOB_{4B}$ [2]. As an obviously effective technique, carbon coating has apparently been regarded as quite proper and employed widely to strengthen rate performance of $LiFePOB_{4B}$ due to conductive carbon produced by carbon sources deposits on the surface of individual particles at high temperature under inert gas, in despite of lowering the tap density. Many synthesis routes to prepare $LiFePOB_{4B}$ materials have been reported, such as solid-state reaction, hydrothermal, and sol-gel methods [3-5]. Recently, a kind of new means, namely molten salt method, has been an effective approach to synthesize $LiFePOB_{4B}$ materials [6]. Above the melting point, the molten salt acting as reaction media can form a liquid system, where ions diffuse rapidly between reaction components. In this paper, a composite KCl-$MgClB_{2B}$ salt was used as eutectic molten salt to prepare $LiFePOB_{4B}$ sample and its carbon-coated $LiFePOB_{4B}$/C sample.

Experimental

The $LiFePOB_{4B}$ samples were synthesized by molten salt method using KCl-$MgClB_{2\,B}$(molar ratio of 1:1) eutectic salt. Stoichiometric amounts of raw materials LiCl, $FeCB_{2B}OB_{4B}{\cdot}2HB_{2B}O$, and $NHB_{4B}HB_{2B}POB_{4B}$ in the molar ratio of 1:1:1 were weighed and mixed. The mixture was ground by ball-milling and then pre-sintered at 400 °C for 3 h under argon. After the pre-sintered precursor cooling to ambient temperature, a certain amount of KCl-$MgClB_{2B}$ mixture as molten salt medium was added. The molar ratio of KCl-$MgClB_{2B}$/$LiFePOB_{4B}$ was 2. Then the precursor was calcined at a temperature above the eutectic point for 4 h, which was 550 °C in this work. Finally, naturally cooling to ambient temperature, the products were washed for times with de-ionized water, filtered and then dried in vacuum. To prepare $LiFePOB_{4B}$/C composite, a certain amount of glucose (25g per mol of $LiFePOB_{4B}$) as carbon source was added in above-mentioned mixture precursor. By molten salt method, $LiFePOB_{4B}$ and $LiFePO_4$/C cathode materials could be synthesized rapidly under rather low calcination temperature compared with normally solid-state reaction.

Bruker D8 Focus X-ray diffractometer (Germany) with monochromatized Cu Kα radiation was used to identify the crystalline structure of the materials. Morphological characterizations were performed by scanning electron microscope (SEM, FEI XL30 ESEM-FEG) and transmission electron microscope (TEM, FEI TECNAI F20). The carbon content was detected by a HCS-140 elemental analyzer (China). The electrochemical properties of the as-obtained cathode electrodes prepared by mixing the obtained $LiFePOB_{4B}$/C composites with super P carbon black, and polyvinylidene fluoride in the weight ratio of 85:10:5 were evaluated in CR2025 coin-type cells assembled in a MBRAUM LAB Master130 argon-filled glove box (Germany) using lithium foil as the counter electrode. The cells were charged and discharged between 2.0 and 4.2 V on a LAND CT2001A battery test instrument (China). Cyclic voltammetry (CV) from 2.0 to 4.2 V at a scan rate of 0.1 mV sP^{-1P} and electrochemical impedance spectrum (EIS) with a vibration of 5 mV in a frequency range of $10P^{-1P}$-$10P^{5P}$ Hz were carried out on a Zahner Zennium electrochemical workstation (Germany).

Results and discussion

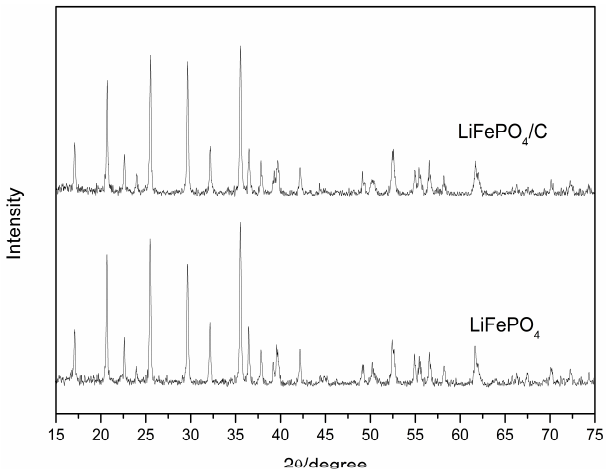


Fig. 1 X-ray diffraction pattern of $LiFePO_4$ and $LiFePO_4$/C

X-ray diffraction (XRD) patterns of samples $LiFePO_4$ and $LiFePO_4$/C are shown in Fig. 1, from which a series diffraction peaks identified to be orthorhombic olivine *Pnmb* structure (JCPDS card No. 40-1499) were observed without obvious impurities. The results indicate that pure and well-crystallized $LiFePO_4$ can be prepared by molten salt method. We detected the carbon content of the $LiFePO_4$/C composite and it was found that 3.22 wt.% carbon remained. No diffraction peaks of the residual carbon in $LiFePO_4$/C sample were found due to its amorphous phase.

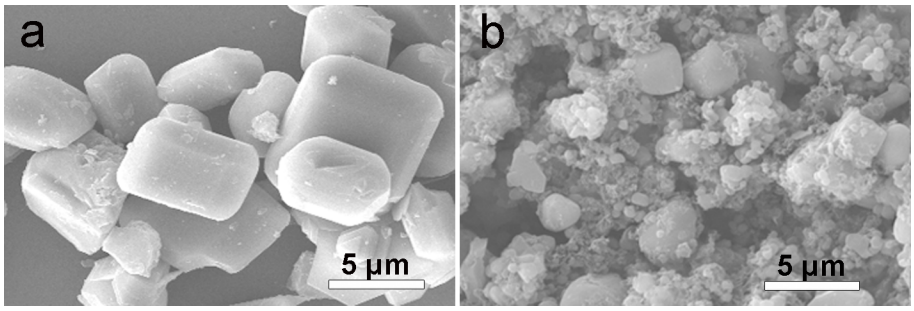


Fig. 2 SEM images of $LiFePO_4$ (a) and $LiFePO_4$/C (b)

The microstructure of samples $LiFePOB_{4B}$ and $LiFePOB_{4B}$/C are presented in SEM images shown in Fig. 2. The SEM image suggests that $LiFePOB_{4B}$ sample (Fig. 2a) has the micron-sized cuboid structure, the particle size of which is around 5 μm. Whereas particle size distribution of

$LiFePOB_{4B}$/C sample is from nanometers to 3 μm, seen in Fig. 2b. The results could be ascribed to the adding of glucose, which was a carbon source generating carbon layer and limiting particle growth during calcinations. The TEM images of $LiFePOB_{4B}$/C is shown in Fig. 3. From Fig. 3a we can see that the surfaces of $LiFePOB_{4B}$ particles were coated by carbon layers, which enhanced the conductivity of the final product. The thickness of such carbon layers is of several nanometers by the observation on surface morphology of the $LiFePOB_{4B}$/C sample, which is shown in Fig. 3b.

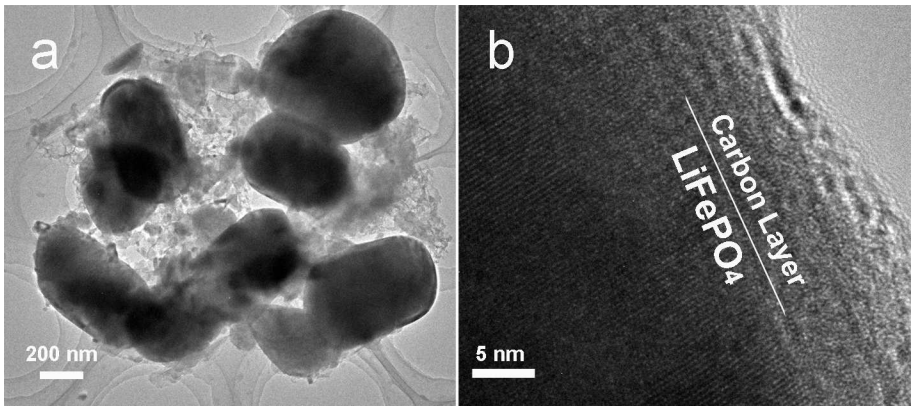


Fig. 3 TEM images of the $LiFePO_4$/C sample

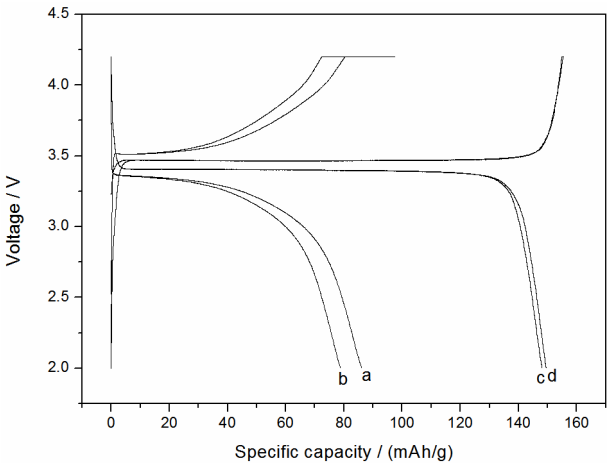


Fig. 4 Initial (a) and second (b) charge/discharge cures of samples $LiFePO_4$ at a rate of 0.1 C; Initial (c) and second (d) charge/discharge cures of $LiFePO_4$/C at 0.1C rate

The electrochemical performances of the prepared samples as cathode for lithium ion batteries were tested. Fig. 4 illustrates the initial and second charge/discharge cures of samples $LiFePOB_{4B}$ and $LiFePOB_{4B}$/C at a rate of 0.1 C. The results showed that $LiFePOB_{4B}$ sample delivered a initial discharge capacity of 86.3 mAh/g and it decreased to 78.8 mA/g after second discharge because of its poor electron transport. However, the $LiFePOB_{4B}$/C deliverd a discharge capacity of 148.0 and 149.5 mA/g for the first and the second cycle, respectively, and both charge and discharge voltage plateaus were flat. It was carbon that increased the conductivity of $LiFePOB_{4B}$/C sample and improved its electrochemical performance.

Fig. 5 is the EIS spectra of the cells assembled with samples $LiFePOB_{4B}$ and $LiFePOB_{4B}$/C. In all Nyquist plots there is a semicircle in the high-middle frequency region and an inclined line in low frequency region, representing the charge transfer resistance (RB_{ctB}) and the Warburg impedance (ZB_{wB}), respectively. By fitting the cures with an equivalent circuit model, the Rct value of samples $LiFePOB_{4B}$ and $LiFePOB_{4B}$/C was about 563 and 128 Ohm, respectively. The results imply that $LiFePOB_{4B}$/C had a good kinetics for LiP^{+P} transfer between $LiFePOB_{4B}$/C paricles and the electrolyte due to its higher conductivity. CV measures of samples $LiFePOB_{4B}$ and $LiFePOB_{4B}$/C

shown in Fig. 6 were performed on work electrode to characterize the chemical reactions in half cell. There was only one peak pair corresponding to the phase transition between $LiFePOB_{4B}$ and $FePOB_{4B}$ in each sample. The oxidation and reduction peaks are approximately symmetric to each other, and the ratios of IB_{paB}/IB_{pcB} are close to 1, which indicate good reversibility for lithium ion intercalation/de-intercalation. Obtained from Fig. 6, the oxidation peak position of samples $LiFePOB_{4B}$ and $LiFePOB_{4B}/C$ was located on 3.55 and 3.69 V, and the reduction peak position was 3.31 and 3.18 V, respectively, indicating the gap between the oxidation peak potential and the reduction peak potential of sample $LiFePOB_{4B}/C$ was smaller, which was beneficial to lithium ion intercalation/de-intercalation.

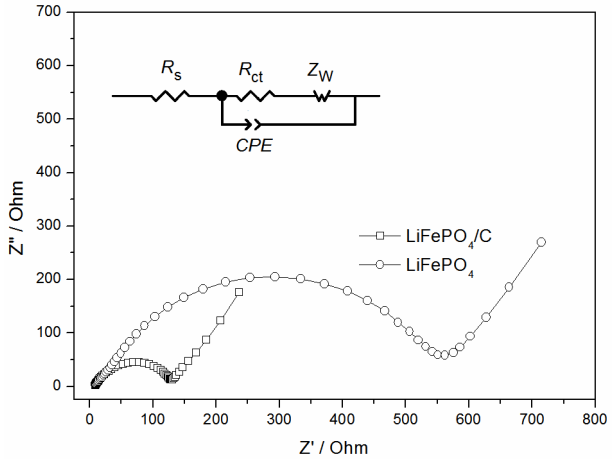


Fig. 5 EIS spectra of the cells assembled with samples $LiFePO_4$ and $LiFePO_4/C$

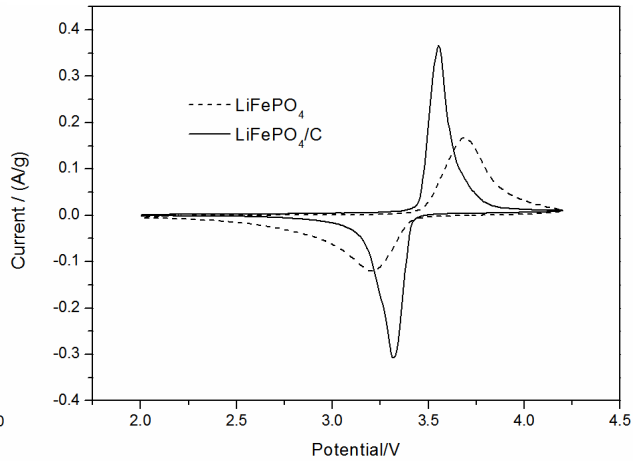


Fig. 6 CV profiles of samples $LiFePO_4$ and $LiFePO_4/C$

Conclusions

In this paper, pure and well-crystallized $LiFePOB_{4B}$ and $LiFePOB_{4B}/C$ were successfully prepared by molten salt method using $KCl\text{-}MgClB_{2B}$ eutectic salt at a relatively low synthesis temperature. The physical results show that the $LiFePOB_{4B}$ has the micron-sized cuboid structure (around 5 μm), but the $LiFePOB_{4B}/C$ has paricles between nanometers and 3 μm, the surfaces of which were surrounded by carbon layers of several nanometrs. The electrochemical results shows that the $LiFePOB_{4B}/C$ deliverd a larger discharge capacity than the $LiFePOB_{4B}$ did due to the conductive carbon's improving the electrchemical activities of the materials and providing a high LiP^{+P} transfer kinetics.

References

[1] A.K. Padhi, K.S. Nanjundaswamy, J.B. Goodenough: J. Electrochem. Soc. Vol. 144 (1997), p.1188

[2] A.S. Andersson, J.O. Thomas: J. Power Sources Vol. 97-98 (2001), p.498

[3] S.F. Yang, P.Y. Zavalij, M.S. Whittingham: Electrochem. Comm. Vol. 3 (2001), p.505

[4] M.A.E. Sancheza, G.E.S. Britoa, M.C.A. Fantinia, et al.: Solid State Ionics Vol. 177 (2006), p.497

[5] H.C. Kanga, D.K. Juna, B. Jin, et al.: J. Power Sources Vol. 179 (2008), p.304

[6] Z.Y. Chen, W. Zhu, H.L. Zhu, et al.: Trans. Nonferrous Met. Soc. China Vol. 20 (2010), p.809

© (2012) Trans Tech Publications, Switzerland
doi:10.4028/www.scientific.net/AMM.164.194

Synthesis and properties of the ESA/AMPS copolymer

Zhan Liu[1,2,a], Xin Wang[1,2,b], Zhenfa Liu[2,c]

[1]College of Chemical Engineering, Hebei University of Technolog, Tianjin, China

[2]Hebei Engineering Research Center for Water Saving in Industry, Institute of Energy Resources, Hebei Academy of Science, Shijiazhuang, China

[a]liuzhan1216@126.com, [b]hbsjzwx10@163.com, [c]lzf63@sohu.com

Keywords: ESA/AMPS copolymer; polyepoxysuccinic acid; scale inhibition and dispersion; biodegradation performance

Abstract： A copolymer was prepared from epoxy succinic acid (ESA) and 2-acrylamido-2-methyl propane sulfonic acid (AMPS). The structure of the ESA/AMPS copolymer was characterized by means of FTIR. The performances of scale inhibition, dispersion and biodegradability of the ESA/AMPS copolymer were studied. The results showed that the scale inhibition performance of the ESA/AMPS copolymer on calcium phosphate and dispersing performance on ferric oxide were much better than PESA. The scale inhibition rate on calcium carbonate was 85% when the ESA/AMPS copolymer was 8mg·L^{-1}. The scale inhibition rate on calcium phosphate was 65% when the ESA/AMPS copolymer was 30mg·L^{-1}. The ESA/AMPS copolymer had good biodegradation performance and biodegradation rate could reach 65% after 28 days.

1. Introduction

With the development of industrial water treatment technology, the awareness of inhibitor's requirement has been from the pursuit of a single high inhibition rate to biodegradable and environmental friendly performance. The biodegradable environmentally friendly water treatment chemicals has become an important field of water treatment agents development. Polyepoxysuccinic acid (PESA) is a environmental friendly water treatment agent that has been reported at home and abroad. Zhifang Lv [1] reported that polyepoxysuccinic acid (PESA) had both corrosion and scale inhibition function. It was a biodegradable water-soluble polymer[2]. However, the scale inhibition performance of polyepoxysuccinic acid on calcium phosphate needs to be improved and its dispersion is limited[3-4]. A ESA/AMPS copolymer was prepared from epoxy succinic acid (ESA) and 2-acrylamido-2-methyl propane sulfonic acid (AMPS) by introducing sulfonic acid group to the molecular structure, in order to improve copolymer's scale inhibition on calcium phosphate and dispersion.

In this paper, a ESA/AMPS copolymer and polyepoxysuccinic acid (PESA) were synthesised, the structures of ESA/AMPS and PESA were characterized by means of FTIR. Their scale inhibition and dispersion performance were compared.

2. Experimental

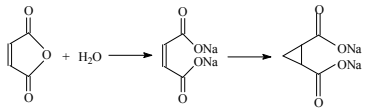
2.1. Experiment apparatus and chemicals

constant temperature water bath (Hebei Aerospace Instrument Factory, DZKW-D), FT-IR (USA Perkin-Elmer Spectrum 100), UV spectrophotometer (Beijing Purkinje General Instrument Co., Ltd., 721), spectrophotometer (Shanghai Optical Instrument Factory, 724).

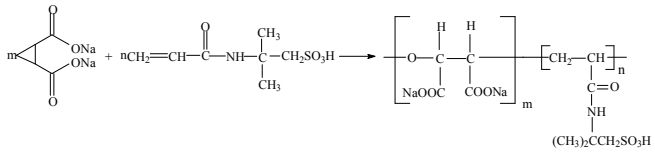
maleic anhydride, 2-acrylamido-2-methyl propane sulfonic acid (AMPS), sodium hydroxide (mass fraction of 50%), hydrogen peroxide (mass fraction of 30%), sodium tungstate, ammonium persulfate, calcium chloride hexahydrate, sodium bicarbonate.(All chemical reagents are A.R. grade)

2.2. Synthesis of the ESA/AMPS copolymer

A given amount of maleic anhydride was added into deionized water and stirred at room temperature till completely transparent. 50% NaOH solution was dropped slowly into the solution below 25 ℃ and the solution was heated to 55℃ in water bath, then Na_2WO_4 and hydrogen peroxide were added to the above solution slowly in 0.5 h. The value of pH was kept at 8~9 by adding 50% NaOH solution. Then the solution was heated to 65 ℃ and maintained for 2 h, then the intermediate product ESA[5] was achieved. The ESA and AMPS were polymerized for 3 h. The light brown ESA/AMPS copolymer[6] was achieved.



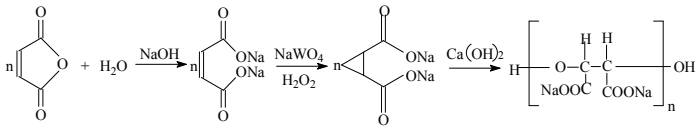
Scheme1. The synthetic route of epoxy succinic acid(ESA).



Scheme2. The synthetic route of the copolymer ESA/AMPS.

2.3. Synthesis of polyepoxysuccinic acid[7]

The value of pH of ESA solution was adjusted above 12 with 50 % NaOH solution. The ESA solution was heated to a certain temperature. The initiator $Ca(OH)_2$ was added in batches at certain reaction time and temperature, the colorless viscous liquid PESA solution was achieved.



Scheme3. The synthetic route of PESA.

2.4. Purification of products

2.4.1. Purification of the ESA /AMPS copolymer

The ESA/AMPS copolymer solution and alcohol was mixed and stirred. The precipitation of ESA/AMPS copolymer was filtered by suction, the residue was dried at 60 ℃ in a drying cabinet. The light yellow solid was ESA/AMPS copolymer.

2.4.2. Purification of PESA[8]

The value of pH of methanol was adjusted to 2.5 with hydrochloric acid, then PESA solution was poured into the methanol. After filtering by suction, the residue was dried at 60 ℃ in a drying cabinet. Then the white powdery solid was PESA.

2.5. Measurement of performance of products

2.5.1. Measurement of the rate of static scale inhibition on $CaCO_3$

Water sample was confecting water(containing calcium carbonate 400mg·L^{-1}). 500mL confecting water with an amount of pharmacy was heated to 80 ℃ and then kept 80 ℃ for 10 hours. Using EDTA titration to detect the content of calcium ion in the cooling and filtrating water.

2.5.2. Measurement of the rate of static scale inhibition on $Ca_3(PO_4)_2$

Water sample was confecting water ($C(Ca^{2+})$=250 mg·L^{-1}, $C(PO_4^{3-})$=150 mg·L^{-1}, pH=9.0 (regulated by 25 g·L^{-1} sodium borate solution)). 500 mL confecting water with an amount of pharmacy was heated to 80 ℃ and then kept 80 ℃ for 10 hours. The content of PO_4^{3-} in the cooling and filtrating water was determined by 721 spectrophotometer.

2.5.3. Evaluation of dispersing ferric oxide performance

Water samples were prepared by dissolving $CaCl_2$ and $(NH_4)_2Fe(SO_4)_2·6H_2O$(A.R. grade) with deionized water, $C(Ca^{2+})$=150 mg·L^{-1}, $C(Fe^{2+})$=10 mg·L^{-1}, pH=9(regulated by 25 g·L^{-1} sodium borate solution). The experiment conditions were as follows: 500mL water sample with and without the measured agents was placed in flasks, put the flasks in constant temperature water bath at 50 ℃ for 5 h. The transmittance of the water samples were mensurated by 724 spectrophotometer. Distilled water was as reference and its transmittance was 100%.

2.5.4. Biodegradability of copolymers

The biodegradability of ESA/AMPS was estimated by shaking-bottle incubating test. The main method was as follows: a 500 mL solution with 1.0 mL inoculum was prepared in a conical flask and the content of a certain amount of polymer. Put the conical flask on a shaking-bottle incubating device and kept the temperature at 25 ℃. The chemical oxygen demand (COD) was detected at the first day, the seventh day, the fourteenth day, the twenty-first day and the twenty-eighth day respectively. The preparation method of inoculum was putting 100 g nutritious soil into 1000mL distilled water and filtrating.

2.5.5. Calculation of scale inhibition and biodegradability

The rate of scale inhibition is calculated by formular (1).

$$\text{Rate of scale inhibition}=\left(\frac{C_1-C_0}{C_2-C_0}\right)\times 100\% \quad (1)$$

Where C_0, C_1 and C_2 represent the mass concentrations of Ca^{2+} or PO_4^{3-} in the blank water sample after heated, the water sample with the inhibitor after heated and the blank water sample before heated, respectively.

The rate of biodegradability is calculated by formular (2).

$$\text{Rate of biodegradation}=\left(1-\frac{C_t-C_{bt}}{C_0-C_{b0}}\right)\times 100\% \quad (2)$$

Where C_0 is the initial numerical value of COD in the inoculated solution with chemical reagent; C_t is the time numerical value of COD in the inoculated solution with chemical reagent; C_{b0} is the initial numerical value of COD in the blank solution; C_{bt} is the time numerical value of COD in the blank solution.

2.5.6. Characterization of products

Using USA PerkinElmer Spectrum 100 FT-IR to analyse structure of PESA and ESA/AMPS, the experiment condition was resolution 400 cm^{-1}, scanning rate 0.20 cm·s^{-1} and scanning scope 500~4000 cm^{-1}.

3. Results and Discussion

3.1. Infrared spectra analysis of products

3.1.1. Characterization of PESA

Fig.1 was the same as the standard spectra of PESA, so the product was preliminary estimated as PESA.

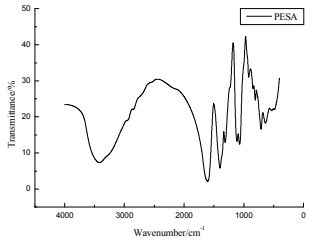


Fig.1. FT-IR spectrum of PESA.

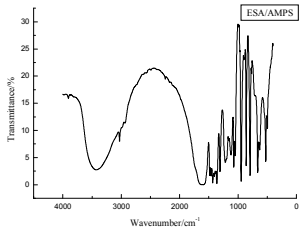


Fig.2. FT-IR spectrum of ESA/AMPS.

3.1.2. Characterization of the ESA/AMPS copolymers

From Fig.2, the strong absorption peak at 3429.13 cm^{-1} was characteristic absorption peak of amino, methyl groups' peak were observed at 3028.57 cm^{-1}, the peak at 1595 cm^{-1} was stretching vibration absorption peak of carboxylic acid group, stretching vibration absorption peak of sulfonic acid group was at 1217.47 cm^{-1} and 1049.37 cm^{-1},the peak at 1120.31 cm^{-1} was -COC- after open-loop, absorption peak at 946.49 cm^{-1} was -CH, stretching vibration absorption peak of C-S accoured at 662.10 cm^{-1}, there's no peaks of -C=C- at 1635 cm^{-1}-1620 cm^{-1}, this indicated that monomers had copolymerized fully. The characteristic groups of ESA/AMPS copolymer were all present in the infrared spectrum of product and the preliminary view that the product was ESA/AMPS copolymer.

3.2. Results of static scale inhibition

3.2.1. Scale inhibition rate on $CaCO_3$

It can be seen from Fig.3 that the scale inhibition rate of ESA/AMPS copolymer on $CaCO_3$ was less than PESA when dosage was low, however, when the concentration of ESA/AMPS copolymer was above 10 $mg \cdot L^{-1}$, the scale inhibition rate was good.

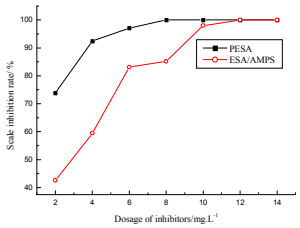


Fig.3. Scale inhibition on $CaCO_3$

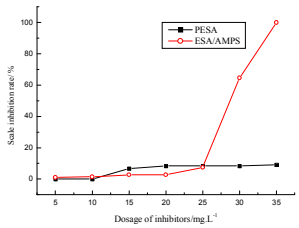


Fig.4. Scale inhibition on $Ca_3 (PO_4)_2$.

3.2.2. Scale inhibition rate on $Ca_3(PO_4)_2$

As shown in Fig.4, to both PESA and ESA/AMPS, there was no scale inhibition on $Ca_3(PO_4)_2$ when dosage was in the low concentration, the effect of the ESA/AMPS copolymer could up to 100% when in high concentrations, but PESA basically had no effect.

3.3. Results of dispersin g ferric oxide experiment

From Fig.5, the dispersing performance of ESA/AMPS was much better than PESA.

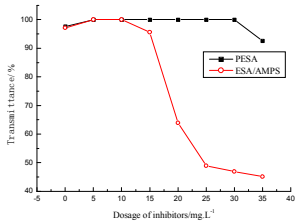


Fig.5. Dispersion performance on Fe_2O_3.

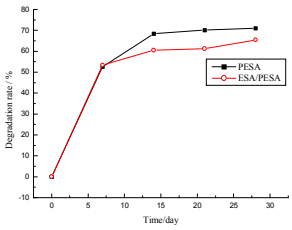


Fig.6. Biodegradation.

3.4. Biodegradation Performance

It was found from Fig.6 that ESA/AMPS copolymer possessed better biodegradation performance, although its biodegradability was slightly lower than PESA, it's biodegradation rate could reach 65% after 28 days, so the ESA/AMPS copolymer was easily biodegradable.

4. Conclusions

Scale inhibition and dispersion test showed that the scale inhibition rate of the ESA/AMPS copolymer on $Ca_3(PO_4)_2$ and dispersion performance of the ESA/AMPS copolymer was better than PESA. The experiments indicated that the introduction of sulfonic acid group could improve the function of scale inhibition on $Ca_3(PO_4)_2$ and dispersing performance. The experiment on biodegradation showed us that the ESA/AMPS copolymer was easily biodegradable.

Acknowledgements

This work was financially supported by the Natural Science Foundation of Hebei Province（B2011302001）and（B2010001558）.

References

[1] Lv ZF, Dong W and Xia MZ. Scale and corrosion inhibition properties of polyepoxysuccinic acid, Industrial Water Treatment, 21(3): 23-25, 2001.

[2] Wei G, Xu YN and Xiong RC. Study on biodegradation of scale inhibitors, Beijing University of Chemical Technology, 28(1): 35-37, 2001.

[3] Betz Laboratories , Inc. Method of inhibiting corrosion in aqueous systems :US ,5256332. 1993.

[4] Zhang BR and Li FT. Multi-scale inhibition performance of polyepoxysuccinic acid, Industrial Water Treatment, 22(9): 21-24, 2002.

[5] Du JJ, Bo ZL and Li SH. Synthesis of epoxysuccinate by using mesoporous molecular sieve catalysts, Guangdong Chemical, 25(3): 11-13, 2008.

[6] Sun M, Liao HX. Scale inhibition performance of ESA / AMPS copolymer, Journal of Yangtze University, 8(1): 27-29, 2011.

[7] Wang LM, Liu ZF. Scale inhibition properties of polyepoxysuccinic acid, Newspaper of Hebei Provincial Academy of Sciences, 24(3) : 64-67, 2007.

[8] Cai SJ. Properties and characterization of green water treatment agent polyepoxysuccinic acid, graduate thesis Beijing University of Chemical Technology, 61, 2004.

© (2012) Trans Tech Publications, Switzerland
doi:10.4028/www.scientific.net/AMM.164.199

Advanced Landfill Leachate Treatment using the Tubular Membrane Bio-electro Reactor

Enhua Liu [a], Li Yang [b], Heying Xu [c]

Key Laboratory of Hollow Fiber Membrane Material and Membrane Process of Ministry of Education, Tianjin Polytechnic University, Tianjin 300160, China

[a] liu-enhua@sohu.com, [b] yangli0903_2001@sina.com, [c] xuheying999@sina.com

Keywords: landfill leachate, membrane bio-electro reactor, tubular membrane

Abstract. The paper studied advanced landfill leachate treatment with tubular membrane bio-electro reactor. The results showed that the tubular membrane flux be stability, COD of effluent be 350～650 mg L^{-1}, while COD of feed water is 500～800 mgL^{-1}, and the removal of COD reached 25%～45%.

1. Introduction

Landfill Leachate produced from the process of landfilling, which contains a large amount of soluble or suspended organic matters, $NH4^{+}$-N and inorganic ions, may cause nuisance to adjacent communities and contribute severe environmental hazards when it is not properly collected, treated and safely disposed. But the conventional landfill leachate treatment is difficult to removal non-biodegradable matters in the flow of landfill leachate, COD of effluent still reached up to hundreds of mg/L and was much higher than Chinese effluent standard.

In recent years, Membrane Bioreactor (MBR) was used to treat Landfill Leachate and improved the effluent water, but some mater in Leachate wasn't decomposed. Electro-catalysis method is a kind of advanced oxidation style, it is fit to treat high toxicity or non-biodegradable organic waste water. If combined MBR and Electro-catalysis method (that be MBER) to treat Landfill Leachate, How will the results? The paper studied treatment effect using MBER to treat Landfill Leachate that had be treated by MBR.

2. Materials and methods

2.1 MBER

The MBER was composed of a bioreactor with 30L working volume, one membrane modules and two plate electrodes (Fig. 1). The membrane module was made of 0.1 μm tubular membrane of polyvinylidene fluoride (PVDF). The membrane module with the area of 0.03 m^2 was placed in the bioreactor, and the aerator in the bioreactor located just below the module. Air was supplied from the bottom of the modules by an air pump. Aeration in this MBER had three functions: transferring oxygen to microorganisms, mixing the liquor and cleaning the membrane. Two plate electrodes, positive plate is carbon plate(25cm*20cm) while negative plate is galvanized sheet(22cm*20cm), were front to front at the membrane module sides and the distance between them was 20cm. They were are connected with a direct-current source through the wires. The influent was fed intermittently into the bioreactor. The permeation was driven by 30-40kPa of the hydraulic pressure head between the level of mixed liquor in the bioreactor and the permeation outlet.

Active sludge in the MBER was taken from the aerobic reactor of some landfill in Tianjin, the feed water was the MBR effluent of the landfill leachate treatment system, its COD is 500-800mg/l, its BOD_5 is 0, its PH is 8.3-8.7.

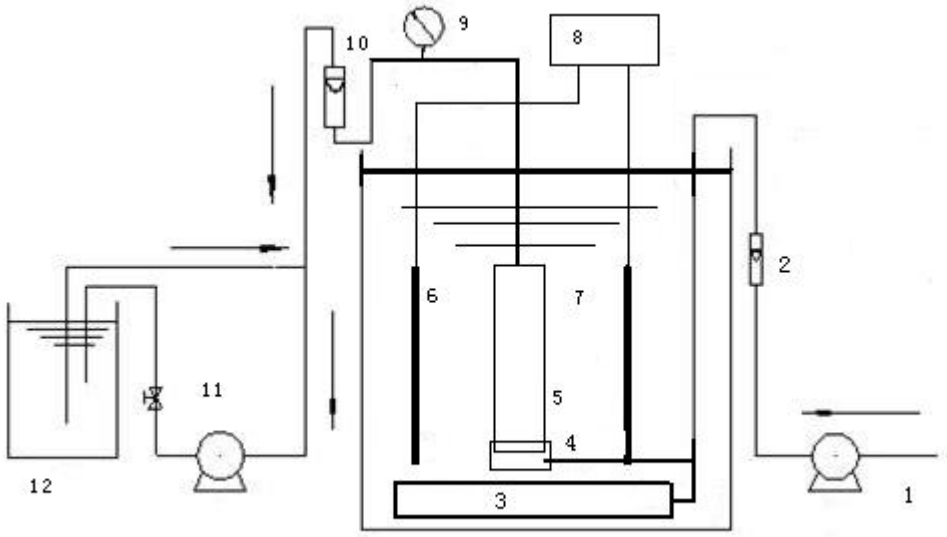
2.2 Running test

MBER run 7-9 hours every day during test. Air pump supplied air for special aerator below membrane module, air flow is 1.2-1.5 m^3/h. Water was discharged through the negative pressure supplied by discharging pump. After discharged water every day, fed equal original water into MBER.

The current between two electrodes maintained 40-70mA. Test running over every day, changed air supply for aerator pipe. The room temperature was 17-21.5°C in the whole process of test.

Under above conditions, tested pH, water temperature, DO(Dissolved Oxygen) and MLSS of MBER, and measured membrane flux, effluent COD and conductivity for studying MBER treated effect.

PH was tested with type25 pH meter, DO was tested with WTW series Dissolved Oxygen Analyzer(OXi-330i), MLSS was measured by gravimetric method(see GB11901-89), COD was measured by dichromatemethod(see GB11914-89).



1.air pump 2 .gas meter 3. aerator pipe 4. aerator 5. Tubular membrane module 6. negative plate 7. positive plate 8. direct-current source 9.pressure meter 10. Liquid meter 11.pump 12.tank

Fig.1 Schematic diagram of the MBER for landfill leachate treatment

3. Results and discussion

3.1 pH change with time

As can be seen from Fig.2, pH in MBER was steady in 8.9-9.16, higher than original water and slightly alkaline. This illustrated some acidic substances in original water were decomposed to make pH increasing.

3.2 DO changed with time

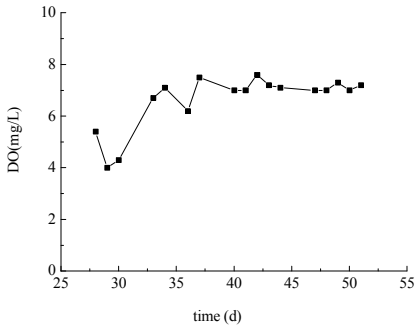


Fig.2 pH in MBER changed with time

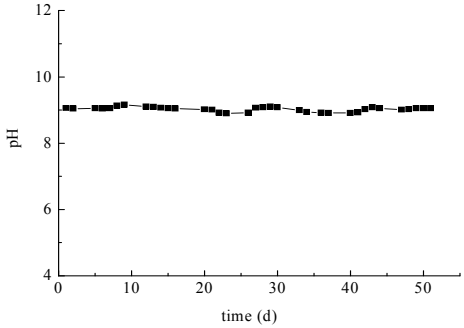


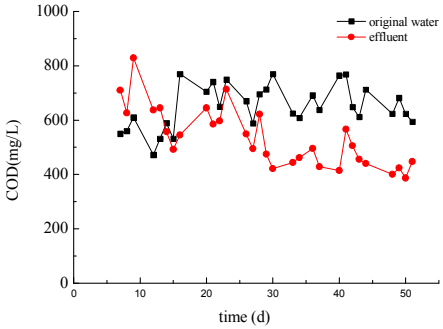
Fig.3 DO changed with time

Fig.3 can be seen that DO in MBER is stable in 6-8mg/l but it was lower in early days. That's due to the test point and test time is not fixed at initial phase. After we fixed them, DO is stable.

3.3 COD of original water and effluent changed with time

We can see from Fig.5 that COD of effluent is lower than COD of original but at early days. That's due to much water was evaporated with aerated air, COD in MBER was concentrated at initial phase. Later, refilled tap water into MBER to maintained its water level stable. During process of test,

original water COD changed from 500mg/l to 800mg/l, while effluent COD did from 350mg/l to 650mg/l. Although BOD of original water is 0, the removal ratio of MBER to COD was 25-45%, the results see Fig.5.



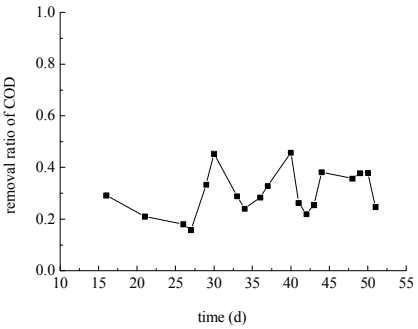


Fig.4 COD of original water and effluent changed with time Fig.5 Removal ratio of COD with time

3.4 Conductivity of original water and effluent changed with time

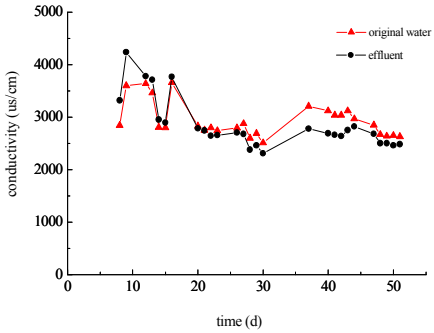
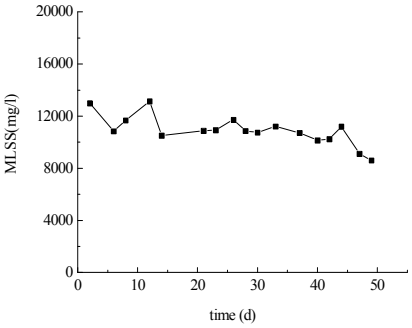


Fig.6 Conductivity of original water and effluent changed with time

We can see from Fig.6 that conductivity of effluent is lower than conductivity of original but at early days. This illustrated some matters were decomposed in process of test to reduce the concentration of dissolved matter in original water.

3.5 MLSS and membrane flux changed with time



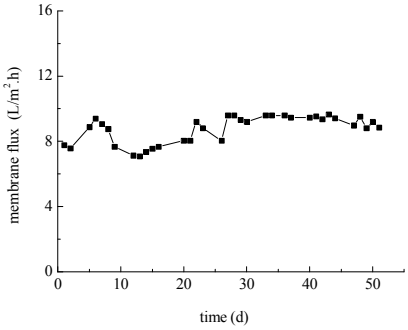


Fig.7 MLSS changed with time Fig.8 Membrane flux changed with time

From Fig.7 and Fig.8, we can see that at early days of test technological conditions of membrane module running, such as air flow, pumping pressure, were not stable, it resulted in membrane flux changed greatly. Later, the technological conditions were fixed, membrane flux kept stable. Due to the influence of activated sludge, the more MLSS was, the less membrane flux was. When MLSS reduced, the membrane flux increased.

4. Conclusions

Landfill leachate treated by MBR contains hundreds of mg/l COD, but not BOD5, its biodegradability was weak. But with MBER to treat this kind of landfill leachate, that had certain effect. The results listed as following: PH of effluent rise up than original water. COD of effluent reduced from original water 500-800mg/l to 350-650, the removal ratio of COD is 25-45%. Membrane flux is stable when MLSS is 10000-12000mg/l.

References

[1] Lou Ziyang, Zhao Yucai, Chai Xiaoli, et al. The research trend of the leachate in waste landfill, Environmental Pollution & Control. Vol.27(5)(2005), p. 358-362.

[2] Wang Min, Yang Xiaomin. Electrocataly Technology of Landfill Leachate from SBR Method. Environmental Sanitation Engineering. Vol.10(2)(2002), p. 68～71.

[3] Li Tinggang, Chen Jian. Study on Treatment of High Concentrated Landfill Leachate by ElectrochemicaI Oxidation Process. Shanghai Environmental Science. Vol. 22(12) (2003), p. 892—897.

[4] Wang Tao, Li Xingang, Sun Jinsheng, et al. Biodegradation of high strength phenol wastewater containing Cr^{6+} and Zn^{2+} by electrobiological reactor. Technology of Water Treatment. Vol. 32(11)(2006), p. 54-57.

[5] Wang Tao, Du Qiyun. Study on kinetics of treating high concentration phenol waste water by MBER method. Journal of Tianjin Polytechnic University. Vol. 27 (3)(2008), p.19-21.

© (2012) Trans Tech Publications, Switzerland
doi:10.4028/www.scientific.net/AMM.164.203

Effects of Organic Solvent Treated on the Performance and Structure of Polysulfone Tubular Ultrafiltration Membrane

Enhua Liu[a], Heying Xu[b] and Xuchen Zhao[c]

Key Laboratory of Hollow Fiber Membrane Material and Membrane Process of Ministry of Education, Tianjin Polytechnic University, Tianjin 300160, China

[a]liu-enhua@sohu.com, [b]xuheying999@sina.com, [c]125144414@qq.com

Keywords: polysulfone membrane, organic solvent, tubular membrane.

Abstract. The paper studied the effect of different kinds of organic solvents treated polysulfone tubular ultrafiltration membrane on its performances and structure. The results show that the surface of membrane treaded with n-hexane are smoother and less hydrophily, the content of carbon element increased at the same time. On the other hand, the water flux of membrane treated with alkane decrease, but the rejections to $MgSO_4$ and egg protein increase. While the surface of membrane treated with ethanol are rougher and more hydrophily, the contents of carbon and oxygen increase too. The water flux of membrane treated with alcohols increase obviously, but the rejection to egg protein decrease slightly.

Introduction

Membrane separation technology is widely applicated in water treatment, desalination of sea water, chemical separation, pharmaceuticals and so on, for its high efficiency and energy saving, easy operation and no secondary pollution. At present, composed membranes are the main, such as reverse osmosis, nanofiltration and small porous ultrafiltration composed membrane. Composed membrane is manufactured by interfacial polymerization on the surface of the porous ultrafiltration base membrane. They usually include an ultra-thin separating layer to improve properties of the membrane. The composed membranes have to contact with the organic phase in interfacial polymerization process, so the solvent of organic phase will affect the properties of composed membrane by its effect to base membrane. In this paper, for preparing high properties composed membrane, polysulfone tubular ultrafiltration membrane was treated with different kinds of organic solvents for studying the effect of solvents on its performances and structure.

1 Experimental

1.1 Main materials and instruments. Polysulfone tubular ultrafiltration membranes are made by ourselves. n-hexane is supplied by Tianjin Yingda Chemical Reagent Factory. 1-octane is purchased from Tianjin Bodi Chemical Incorporated Company. n-decyl hydride and dodecane are brought from Tianjin Kemiou Chemical Reagent Incorporated Company. Ethanol is supplied by Tianjin Linanlong Bohua Medicine Chemical Incorporated Company. Butyl alcohol and magnesium sulphate are purchased from Tianjin Chemical Reagent Two Factory.

Tubular membrane testing equipment is made by ourselves. Quanta 200 scanning electron microscopy is supplied by Dutch Philips Company. YH-168A contact angle meter is brought from Beijing Hake Experiment Instrument Factory. DDB-303A conductivity meter is purchased from Shanghai Precision Scientific Instrument Incorporated Company. UV2450 ultraviolet spectrophotometer is supplied by Japanese SHZMADZU Company.

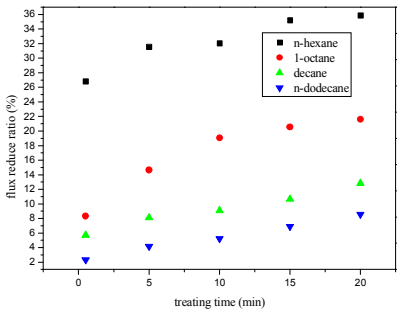
1.2 Experimental method. Polysulfone tubular membranes are immersed in n-hexane, 1-octane, n-decyl hydride, dodecane, ethanol and butyl alcohol for different time at room temperature, then washed excrescent solvents on the surface of membrane with pure water. At last, test properties of the membranes.

1.3 Test analysis. Scanning electron microscopy and energy dispersive spectrometer are used to analysis surface morphology and components of membranes. Contact angle is tested by contact angle meter at 20°C and 30~50%.relative humidity. The water flux and rejection to $MgSO_4$ and egg protein of membranes treated by organic solvents are tested under 0.1Mpa pressure.

2 Results and discussions

2.1 Effects of alkanes on the properties of polysulfone membrane

2.1.1 Effects of alkanes on the water flux of membrane.The water flux change of membrane treated with different alkanes is shown in figure 1. We can see that the water flux decreased after treating with alkanes and the decreasing is more serious with the extending of treating time. On the other hand, effects of alkanes on water flux reduced with the increasing of molecular weight of alkane, that is because the longer molecular chain alkane is the weaker interaction between it and polysulfone membrane is.



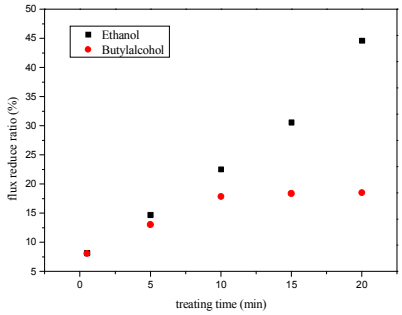


Fig.1 Flux of membrane treated with alkanes Fig.2 Flux of membrane treated with alcohols

2.1.2 Effects of n-hexane on different membranes. Table 1 is the water flux change of membrane treated with n-hexane for 30s. It shows that the membranes with higher water flux lost more water flux at the same treated conditions, that demonstrates membranes with higher porosity and larger pore diameter are effected more easily by n-hexane, so that they have the more loss of water flux.

Tab.1 The water flux change of membrane treated with n-hexane for 30s

Membrane number	1	2	3	4	5
Warer flux of original membrane($L\cdot m^{-2}\cdot h^{-1}$)	30	50	100	200	300
The rest of water flux($L\cdot m^{-2}\cdot h^{-1}$)	16.00	26.41	51.85	97.88	134.49
The loss of water flux(%)	46.66	47.18	48.15	51.06	55.17

2.1.3 Effects of alkanes on the rejection of membrane. Rejections of membranes treated with alkanes to $MgSO_4$ and egg protein are shown in Tab.2. The rejections of original membrane to $MgSO_4$ and egg protein are 6.46% and 83.90% respectively. After treating with alkanes, the rejections of membrane to $MgSO_4$ and protein increased, it demonstrates that alkanes make the pore diameter of membrane smaller.

Tab.2 The rejection of membrane treated with alkanes to $MgSO_4$ and egg protein

Membrane	treated with n-hexane	treated with 1-octane	treated with N-decyl hydride	treated with dodecane
Rejection to $MgSO_4$(%)	9.12	11.36	7.82	12.18
Rejection to protein(%)	86.42	87.98	87.89	88.06

2.2 Effects of alcohols on the properties of polysulfone membrane

2.2.1 Effects of alcohols on the water flux of membrane. The water flux change of polysulfone membrane treated with alcohols is shown in Fig.2. From it we can see that the water flux of membrane treated with alcohols increased and the more water flux is the longer treating time is. Effects of ethanol on the water flux is greater than butylalcohol.

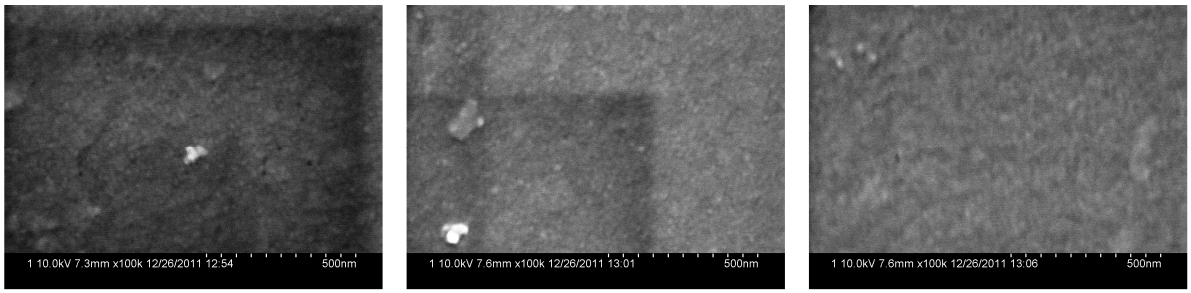
2.2.2 Effects of alcohols on the rejection of membrane. Table 3 shows the rejection of membrane treated with alcohols to $MgSO_4$ and egg protein. The rejection of original membrane to $MgSO_4$ and protein are 6.46% and 83.90% respectively. After treating with alcohols, the rejection of membrane to $MgSO_4$ increased, but the rejection to egg protein decreased slightly.

Tab.3 The rejection of membrane treated with alcohols to $MgSO_4$ and egg protein

Membrane	Membrane treated with ethanol	Membrane treated with butylalcohol
Rejection to $MgSO_4$(%)	11.61	8.76
Rejection to protein(%)	70.96	81.58

2.3 Effects of organic solvents on the structure of membrane

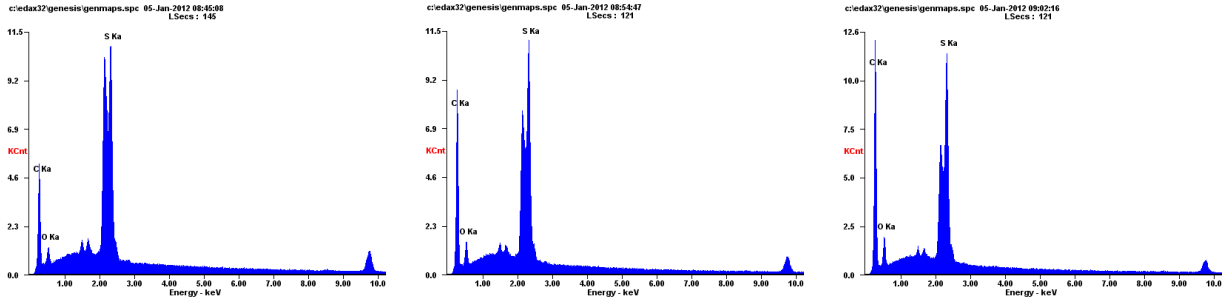
2.3.1 Effects on surface structure of membrane. The SEM photographs of polysulfone membrane surface are shown in Fig.3. It shows that the surface of membranes treaded with n-hexane are smoother than original membrane, while the surface of membranes treated with ethanol are rougher. It could explain that the surface structure of polysulfone membrane has been changed by n-hexane and ethanol. n-hexane made the pore diameter of original membrane smaller, but ethanol enlarged the pore. That is the reasons of water flux change of membranes.



(a) (b) (c)

Fig.3 The SEM photographs of polysulfone membane surface
(a) original membrane (b) treated with n-hexane (c) treated with ethanol

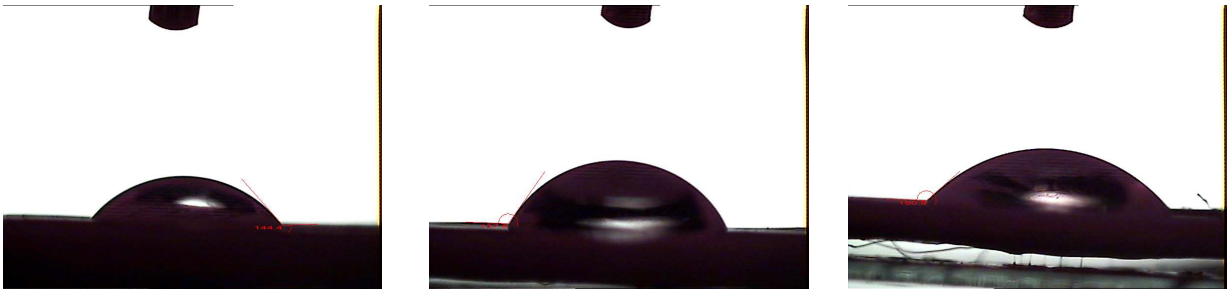
2.3.2 Effects on surface composition. Fig.4 are the energy spectrum diagrams of polysulfone membrane. The content of carbon element at surface of membrane treated with n-hexane increased, but the contents of sulfur and oxygen decreased at the same time. We can infer that the conformation of polysulfone has changed as the effect of n-hexane so that influencing the membrane properties and structure. In comparison, the contents of carbon and oxygen of membrane treated with ethanol increased, while the content of sulfur decreased obviously. Similarly, the conformation of polysulfone has changed by ethanol, and oxygen element gathering on the surface, that strengthening the surface polarity of membrane and changed the structure.



(a) (b) (c)

Fig.4 The energy spectrum diagram of polysulfone membrane
(a) original membrane (b) treated with n-hexane (c) treated with ethanol

2.3.3 Effects on surface contact angle of membrane. Fig.5 are the contact angle photographs of polysulfone membrane. We can see from the photos that the contact angles of original membrane, membrane treated with n-hexane and membrane treated with ethanol are 35.6º, 42.4º and 29.1º respectively. It could explain that the interaction between hydrophobic n-hexane molecules and polysulfone molecules weakened its hydrophily of polysulfone membrane, so the contact angle of membrane treated with n-hexane increased. The interaction between hydrophilic ethanol molecules and polysulfone molecules strengthening the hydrophily of polysulfone membrane, so that the water flux of membrane treated with ethanol increased.



(a) (b) (c)

Fig.5 The contact angle photographs of polysulfone membrane
(a) original membrane (b) treated with n-hexane (c) treated with ethanol

3 Conclusions

The polysulfone tubular ultrafiltration membranes treated with n-hexane, 1-octane, N-decyl hydride and dodecane have a lower water flux than original membrane, but rejection to MgSO4 and protein increases, membrane pore diameter is smaller and the surface of membrane is smoother. While the water flux of polysulfone tubular ultrafiltration membranes treated with ehtanol and butylalcohol increases and the rejection to protein decreases slightly, and the membrane pore diameter is lager and the surface is rougher and more hydrophily than original membrane.

References

[1] Qi Lihuan, An Shulin, Lu Jianan. Study on polyamide/polysulfone hollow fiber composite membrane. Journal of Tianjin Polytechnic University, Vol. 27(3) (2008), p. 60-63.

[2] Chen Hao, Zhang Haoqin, Liu Jindun. Research of interaction between polysulphone ultrafiltration membrane and low molecule organic matter. Applied Chemical Industry, Vol.37 (6) (2008), p. 673-676.

[3] Cao Yanxia, Zheng Guodong, Xu Jiping. Effects of internal interface modification on the performance of composite RO membranes-(I) property and characterization. Polymer Materials Science and Engineering,Vol.20(6) (2004), p. 138-140.

[4] Song Yanqiu, Yuan Xubo, Sheng Jing. Study on Modification of Hydrophobic Polysulfone Membrane. Chemical Industry and Engineering,Vol.19(2) (2002), p. 32-36.

[5] Cao Yanxia, Zheng Guodong, Xu Jiping. Effects of internal interface modification on the performance of composite RO membranes-(II) theoretical analysis. Polymer Materials Science and Engineering,Vol.20(11) (2004), p. 142-145.

[6] Cao Yanxia, Li Guangji, Zheng Guodong. Relationship between performances of reverse osmosis composite membrane(ROCM) and properties of its internal interface. Natural Science Journal of Xiangtan University, Vol. 29(6) (2007), p. 95-99.

[7] Cao Yanxia, Zheng Guodong, Wu Jicheng. Interfacial controls and the performance of composite membrane. Journal of Functional Polymers, Vol.12(3) (1999), p. 97-100.

© (2012) Trans Tech Publications, Switzerland
doi:10.4028/www.scientific.net/AMM.164.207

Germanium doping and impurities analysis on industrial scale mc-silicon ingot

Shuai Li [1,a], Peng Wu [2,c], Baitong Zhao[3,b], Wenxiu Gao[1,d]

[1] Shanghai Institute of Technical Physics of The Academy of Sciences, Shanghai 200083, Republic of China

[2] Xiamen University, Fujian Province, China, 361005

[3] University of Science and Technology Beijing ,30 Xueyuan Road, Haidian District, Beijing 100083 P. R.China

[a]ldsadmission123@gmail.com,[b]zbt100888@163.com,[c]fnaticwp@gmail.com ,
[d]gaowx@mail.sitp.ac.cn

Key words: mc-silicon, germanium, solar cell, carbon, oxygen, isostatic pressing method

Abstract. With mc-silicon (multi-crystalline silicon) being the most favorable feedstock for solar cell, germanium was reported to be a promising dopant to improve the quality of silicon crystal growth. In this paper, we investigated the feasibility of germanium doping for industrial scale production. A homogeneously distribution of germanium across usable section is presented, and subsequently we optimized our recipe for better controlling it. Sopori etched pits were utilized to reveal dislocations in silicon wafers, and we found a reduced dislocations density in germanium doped samples. Carbon and oxygen are two inevitable significant impurities during silicon ingot casting. In this paper, experimental results showed the impact of carbon on minority charge carrier lifetime and on interstitial oxygen. In addition, Isostatic pressing method is proved to be very prospective for recycling quartz crucibles.

Introduction

Multi-crystalline silicon ingot produced by directional solidification has been most extensively employed in photovoltaic industry. Mc-silicon ingot casting attracted worldwide attention due to its low production cost and high throughout. Heat exchange method or Bridgman method are widely used in multi-crystalline silicon directional solidification. But since last year, the price of solar cell module was successive lowing until this month. So it is pressing to optimize the ingot casting process. Industrial solidification silicon ingots only yield about 65% with respect to current technology, thus still we can try to improve the quality of ingot to increase the yield, eventually to reduce the cost of production.

Germanium is an emerging dopant in silicon to improve device performance. Germanium induced strain field which is due to its lattice mismatch can retard dislocation mobility for pinning effect. It is believed that germanium is not a detrimental dopant, meanwhile it is electrical inactive in silicon. Previous studies have proved that germanium doping can enhance the mechanical strength[1], suppress the formation of TDs (thermal donors)[2], reduce the light-induced degradation (LID) effect[1]. It is also reported that germanium doped silicon ingot have lower dislocation density, and dislocations are more homogeneously distributed[3].

Although the impact of germanium doping on the dislocation distribution has been investigated, it is only a pilot-scale experiment[4]. In this paper, a series of bulk ingots with height above 22cm was casted during a dynamical solidification process in industrial equipment initially for 450kg ingot.

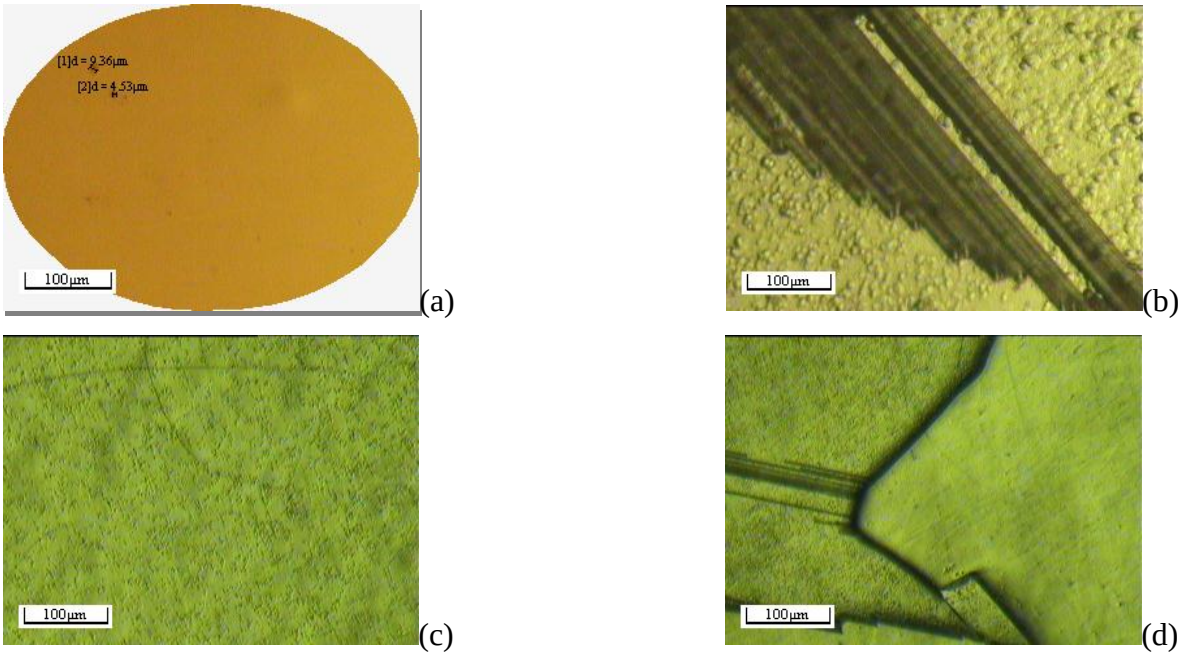
We focused on the controlling of distribution in real industrial production process. Sopori[5] etched pits were counted to reveal the dislocation density level, and we found a reduced tendency of dislocation density in germanium doped samples. Carbon and oxygen are two significant impurities in mc-silicon ingot, both their respective and relative content are essential to the quality of silicon ingot, especially minority carrier lifetime. Isostatic pressing method is proved to be very prospective for recycling quartz crucibles and our experiment gives a prospective future for casting high quality silicon ingot in current mc-silicon casting equipment.

Experimental

The experiments are conducted in industrial production furnace based on vertical-gradient-freeze which is equivalent to heat exchange method (HEM). Solar grade silicon (SOG silicon) with a purity of 6-N which is made by metallurgical process and selective purified by physical method is solidified in a quartz crucible coated with Si_3N_4 powder. The quartz crucible used here was fabricated by means of isostatic pressing with recycling granular particles made from crucible fragment. The industrial furnace is initially designed for up to 450kg ingot, thus we produced four ingots in one batch, and we named them as Si, Ge1, Ge2, Ge3. Every ingot produced is cylindrical with a diameter of 21 cm and a height of about 23 cm. Germanium doped in poly-silicon is 6N powder, intentionally placed right at the bottom of quartz crucible. The doping levels are listed in Table 1. Two similar experiments were undertaken with the same doping level but a slight difference on thermal condition following regular production receipt e.g. melting, homogenization, crystallization, block homogenization and tempering. Ingots were solidified with argon blowing from top to the melt surface, subsequently tempered at 1250℃ and 640℃.

Table 1. Initial germanium concentrations in every sample.

Ingots	Si	Ge1	Ge2	Ge3
Ge(ppma)	<1	60	200	600
Ge(PPmw)	<1	154	518	1555



(a) (b) (c) (d)

Fig.1 Samples observed by optical microscope (a) mechanically and chemically polished samples (b) bundles of Iron related precipitation (c) Sopori etched pits (d) chemically polished and etched grain boundaries

The distribution of impurity in silicon such as phosphorus, boron and germanium is determined by Inductively Coupled Plasma Optical Emission Spectrometer（ICP-OES）. Sopori etched pits were employed to reveal defect density. At first, slices were mechanically and chemically polished to remove saw damage, then cleaned in deionized water, finally etched in Sopori solution for 5 min. Metallurgical microscope is a convenient tool for observing and counting etched pits , even grain boundary, twins and Iron precipitation were observed on certain etched samples e.g. Figure 1. Minority carrier lifetime is mapped on center slices using microwave/laser photoconductance decay(μ-PCD) method(semilab,WT-2000). The concentrations of interstitial oxygen and substitutional carbon are measured by Fourier-transmission infrared spectroscopy (FTIR, nicolet6700), in addition that all samples are mechanically and chemically polished and checked by metallurgical microscope. The thickness of every slice is about 2mm. There are less than 5 five defects within eye sight with 40x aperture as pictured in Figure 1.

Results and discussion

Quartz crucible technology. Common quartz crucibles for multi-crystalline silicon casting are fabricated by slip casting which is complicated and has a long production cycle. Isostatic pressing method is a prospective alternative, and it is easier to make various shaped quartz crucibles. We firstly made the quartz crucible cylindrical, with regard to a better strength, easiness to fulfill the isothermal condition compared to square shaped crucibles. We optimized the relative positions of crucibles in hot zone with respect to our previous computer simulations. The lateral temperature gap around one crucible is confined not more than 1 k at 1650K of radiated temperature in our simulations. Cylindrical crucibles we used have been proved that it has a uniform stress effect on silicon ingot, thereafter it will be less likely to induce cracks in silicon ingot. This facilitate to produce high quality ingot, even quasi-monocrystalline silicon ingot when it is seeded.

The ingots casting cycle time is about 70 hours, and crucibles were used in argon gas atmosphere with pressure of 60 kPa. Crucibles were cracked into several parts during the tempering process ,and a cross section of used crucibles is showed in Figure 2. It is observed that a thin layer of crystalline precipitation is formed in areas adjacent to silicon melt. Some small cracks and silicon penetrations also existed, but no leaks were found. This is also one advantage of this method over slip casting quartz crucibles in which a small crack may lead to melt leak. Although subsequent investigation shows oxygen contamination in silicon ingot, we can improve our coating technology preventing it. The success of silicon ingot casting has proved that isostatic pressing technology using recycling crucibles is very prospective.


(a)

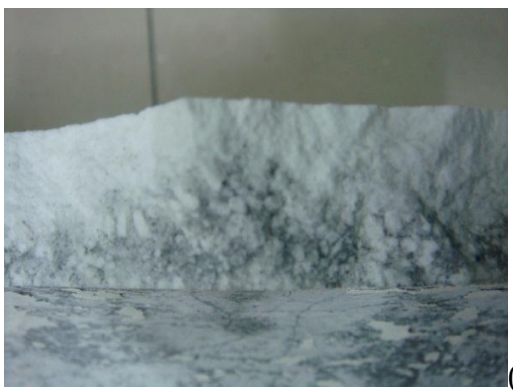

(b)

Fig. 2 Cross section of used quartz crucibles fragment. (a)bad phenomenon with deep penetration. (b) better phenomenon with less penetration with crystalline precipitation.

Germanium distribution and influence. It is well known that there is a significant difference between silicon and germanium melt in density (2.53g/cm^3 for silicon, 5.51g/cm^3 for germanium),and melting temperature of silicon is higher than germanium(1211K for germanium, 1687K for silicon). Germanium melted first and flowed uniformly at the bottom of crucibles. As previous studies reported, germanium tends to diffuse from the bottom to the top silicon melt. The diffusion process is not standard diffusion dominated[6]. Gravity force will apparently retard the germanium dissolving into silicon melt, in addition free surface effect and convection flow also affect a lot especially for large diameter industrial scale ingot casting. The distribution of germanium in silicon melt before solidification may presents a wavy curve with very high ratio of germanium at the bottom. Segregation efficient of germanium in silicon is reported to be 0.5[1]. According to equation below[7], the distribution of germanium in silicon solid has a relation to growing velocity.

$$k_{eff} = \frac{k_0}{k_0 + (1 - k_0)\exp(-v\delta/D)} \quad (1)$$

Where k_{eff} and v is effective segregation coefficient and velocity of growing interface, respectively.

In the crystallization process, the growing velocity is not fixed constant and it is not very convenient to define it. Nevertheless, in this paper, we made a large number of measurements to investigate the distribution of germanium in silicon ingot after a dynamic process of industrial ingot casting. In our forthcoming paper we will try to simulate the dynamic growing process and give some precise predictions.

As Figure 3 depicted, the distribution of germanium in silicon ingot is homogenous in a large diameter region. It shows a linear trend and the ratio of concentrations and initial doping concentrations is apparently independent of doping level with respective to the range of 60-600ppma. Thereafter we can easily estimate the doping levels versus height of ingot. In the second batch, we tried some methods (e.g. lowering the temperature of top heater, increase the blowing of argon gas) to control the segregation of Ge, and it revealed a more smoothly distribution as showed in Figure 4. The very low temperature of the top lead to greater sized grains but bad crystallization on the top. The inhomogenous temperature around one crucible shows its own effect with higher concentration of Ge for higher temperature region and conversely worked as Figure 5 suggested. This may be explained by effective segregation coefficient change.

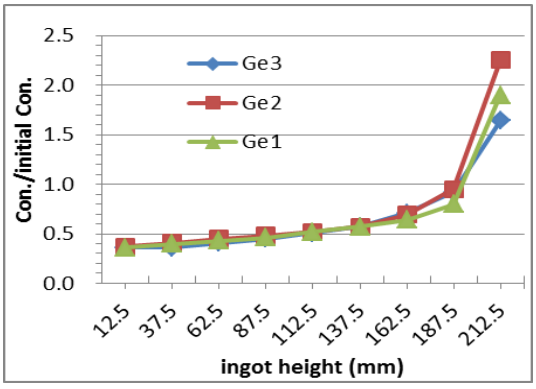


Fig.3 Ge distribution for three doped ingots in the first batch. An even distribution can be observed until the end.

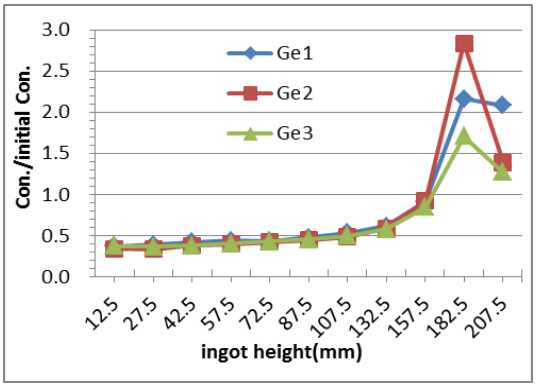


Fig.4 Ge distribution for three doped ingots in the second batch. It shows a more even distribution than the first batch until the end. The processing recipe had changed such as lower temperature of top heater.

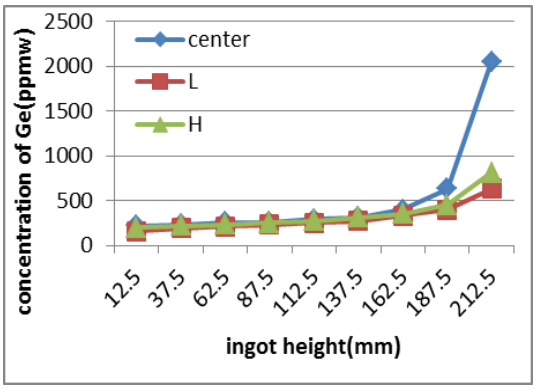


Fig.5 Vertical distribution of germanium, curve line named center is for ingot center line; curve line named L is for ingot with lower temperature; curve line named H is for ingot with higher temperature. Initial doping concentration is 518 ppmw.

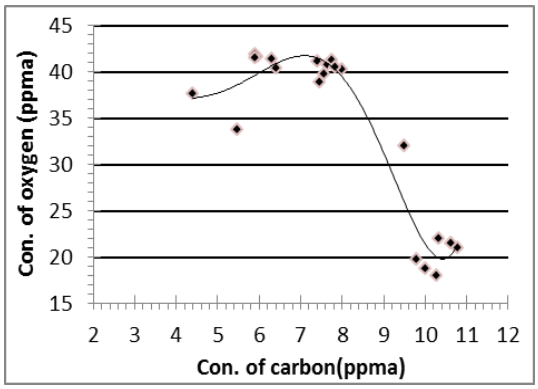


Fig.6 Concentration of substitutional carbon versus interstitial oxygen measured by FTIR on specimens from ingots. There is a drastically decrease of interstitial oxygen concentration when the substitutional carbon concentration is in the range of 8-10 ppma carbon corresponding to wavenumber 1107 cm^{-1} and 605 cm^{-1} respectively.

The energy conversion efficiency of solar cells based on multi-crystalline silicon now is not as high as that of mono-crystalline silicon. Some defects such as grain boundaries, dislocations, metallic and other impurities induced precipitation etc. act as active recombination centers of carriers in silicon wafers. For multi-crystalline silicon ingot casted using SOG-silicon feedstock, dislocation is key factor that influence the quality of silicon wafer. Dislocations nucleated at the bottom of ingot will be the origin of dislocations above. Especially, dislocation clusters grow in size with height. The number of dislocations in a given dislocation cluster also increase upwards in the ingot#. Germanium can suppress the mobility of dislocations due to pinning effect by induced strain field. Dislocations in Germanium doped samples also distributed more homogenously but accumulated in clusters. Sopori etched pits density (EPD) is employed to reveal the dislocation distribution. The samples were prepared from the bottom of the ingot and parallel to the growth direction which was reported to have lower EPD than samples cut perpendicular to growth direction. The etched pits were counted by metallurgical microscope, and the EPD results are listed in Table 2. Obviously that germanium doped samples have lower EPD, and EPD for doped Ge2, Ge3 is very similar. Thus it is indicated that doping level of 200ppma is sufficient to reduce dislocations for our experiment.

Table 2. List of etch pit density(EPD) for samples with unit of $1 \times 10^5 cm^{-2}$

Samples	Si	Ge1	Ge2	Ge3
EPD	1.8	0.9	0.25	0.20

Oxygen and carbon investigation. Oxygen concentration in multi-crystalline silicon ingot decreases from bottom to the top of the ingot. Reversely carbon concentration increases with the height of the ingot. Samples were sectioned in size of $6cm \times 2cm \times 2mm$ from ingots with 5mm above the bottom. Interstitial oxygen and substitutional carbon are both electrical inactive, but oxygen plays an important role in thermal donors, decorated dislocations and grain boundaries

which are effectively deleterious to minority charge carrier lifetime[8]. Previous studies have reported that oxygen precipitates are known to getter metal impurities and oxygen precipitates could enhance the precipitation of metals at dislocations and grain boundaries[8]. Silicon grains initially nucleate at the bottom of the quartz crucibles and a large number of grain boundaries and dislocations existed. Therefore, the reduction of the oxygen precipitation is a key factor to improve the performance of solar cells. In the IR spectrum interstitial oxygen and substitutional carbon content are associated with wavenumber bands 1107 cm^{-1} and 605 cm^{-1} respectively[9] depicted in Figure 7. Carbon has the effect to enhance nucleate and growth of oxygen precipitation, and it is demonstrated in Figure 5 which implied that substitutional carbon with concentration above 8 ppma can drastically reduce the interstitial oxygen concentration (the oxygen concentration is a little higher than commercial available feedstock, which is due to bad coating of the quartz crucible). Based on above analysis, oxygen in silicon is likely to precipitate under the assumption that initial oxygen concentration in silicon for one batch is similar. However, the wavenumber 1224 cm^{-1} band corresponding to SiO_2 precipitation are not observed[9], thus SiO_2 precipitation is not formed. This is not agreed with the results reported by M. Di Sabatino[9], in addition the behavior of oxygen in silicon is mostly dependent on the thermal history post solidification. Moreover, the minority charge carrier lifetime increases as the substitutional carbon concentration increases depicted in Figure 8. This may be explained by the formation of C_sO_i(i=1,2 or 3…),which is believed to suppress the thermal donors production[10]. More investigations are needed to clarify the mechanism with regarding to our casting process followed by two steps annealing at 1240℃ and 650℃.

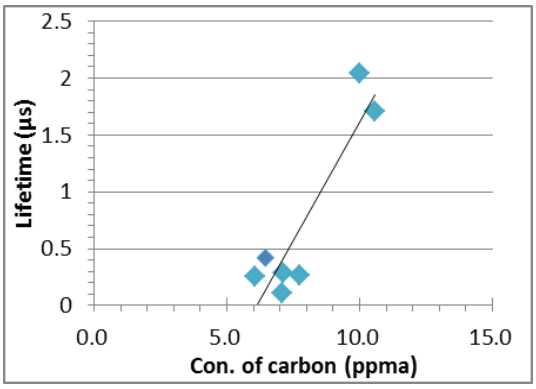


Fig.7 Average substitutional carbon concentration versus average lifetime which is measured by microwave photoconductance decay (μ-PCD).

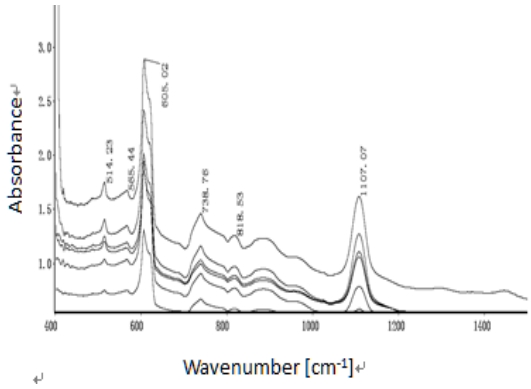


Fig.8 IR spectrum of interstitial oxygen and substitutional carbon.

Conclusion

It has been demonstrated that the incorporation of germanium with level above 200ppma is sufficient to suppress the growth of dislocations from the bottom of silicon ingot. We achieved more homogeneous distribution of germanium versus the height of ingot in dynamical industrial production process. Isostatic pressing method is proved to be a prospective method for recycling quartz crucible fragment. Cylindrical ingots tend to be less stressed adjacent to crucibles, thus it can be utilized to produce high quality mono-crystalline silicon ingot when it is seeded. This method is easy to integrate to current multi-crystalline and quasi-monocrystalline silicon ingot casting for higher yield and better quality. In addition, we can better control the concentration of carbon and oxygen to further improve the quality of wafers. All these factors are key parameters for reducing the cost, and facilitate the widespread use of solar cells.

Acknowledgement
The research is carried out in Nanyang Green Silicon Company, technical assistant and financial support provided by them are gratefully acknowledged.

References

[1] Peng Wang, Xuegong Yu, Peng Chen, Xiaoqiang Li, Deren Yang, Xue Chen, and Zhenfei Huang, Solar Energy Materials and Solar Cells **In Press, Corrected Proof**.
[2] C. Cui, D. R. Yang, X. Y. Ma, M. Li, and D. L. Que, Materials Science in Semiconductor Processing **9** (1-3), 110 (2006).
[3] C. A. Londos, A. Andrianakis, V. V. Emtsev, G. A. Oganesyan, and H. Ohyama, Mater Sci Eng B-Adv **154**, 133 (2008).
[4] M. P. Bellmann, T. Kaden, D. Kressner-Kiel, J. Friedl, H. J. Moller, and L. Arnberg, Journal of Crystal Growth **325** (1), 1 (2011).
[5] Sopori B, J Electrochem Soc (131), 667 (1984).
[6] N. Armour, S. Dost, and B. Lent, Journal of Crystal Growth **299** (1), 227 (2007).
[7] J. A. Burton, R. C. Prim, and W. P. Slichter, J Chem Phys **21** (11), 1987 (1953).
[8] H. J. Moller, L. Long, M. Werner, and D. Yang, Phys Status Solidi A **171** (1), 175 (1999).
[9] M. Di Sabatino, S. Binetti, J. Libal, M. Acciarri, H. Nordmark, and E. J. Ovrelid, Solar Energy Materials and Solar Cells **95** (2), 529 (2011).
[10] R. C. Newman and R. Jones, Curr Opin Solid St M **2** (1), 40 (1997).

© (2012) Trans Tech Publications, Switzerland
doi:10.4028/www.scientific.net/AMM.164.214

Research on the Mathematical Model of the Plastic Profile Cooling Analysis

XiangShan Huang[a], LiDan Chen[b]

(Zhejiang Technology Institute of Economy，Hangzhou 310018，China)

[a]hxshan98@163.com, [b]cld1121@126.com

Keywords: plastic profile, cooling, mathematical model

Abstract. According to the assumption of the plastic profile cooling analysis, Prandtl number P_r and Reynolds number R_e can be derived from the fluid parameters. The paper judge and analyze the movement of flow state, further study the formula of heat transfer coefficient α, thermal analysis and boundary conditions in Reynolds number R_e. The experimental results show mathematical model, which provides a theoretical basis for the cooling and forming of function blocks, it has certain guiding significance.

1 Foreword

Complex plastic profile shapes can be seen as the combinations of main body of profile and a variety of specific structure. The main body of profile is relatively simple geometry shapes of the thin-walled profiles, and those particular structures are referred to function blocks, which play an important role in the installation, destruction and usage of profiles.

The quality of the designed block affects the accuracy of extrusion die block molding and functional block's required function, and the quality of functional block molding has a direct impact on product quality profiles [1].

Given the characteristics of function blocks, it is difficult to analysis all the function blocks, but some type of function blocks are analyzed to arrive at a universal conclusions. Through cooling analysis for functional blocks, it can be predicted the deformation trend of function blocks, which solves the difficult problems of forming blocks in a certain extent.

2 Cooling analysis assumes that the plastic profile

As the extrusion profiles have the same cross-section characteristics, and cooling process in the shape of cross-section are exactly the same. Therefore, in the process of profile shape cooling in the wet and dry hybrid cooling units, make the following assumptions for further analysis of the simulation。

2.1There is no heat transfer in stereotypes set and vertical profiles.

2.2 Material boundaries replace the boundaries of mold and plastic parts, instead of using the geometric boundaries, we use physical boundary, ignoring contact resistance between stereotypes set and profiles, also ignoring the presence of air between them and the cooling effect generated by air flow [2].

2.3Assuming the temperature of cooling water is a constant, the heat release by profiles all covered by stereotypes set.

2.4The flow pattern of viscous parison into the shape sets out immediately after adsorption by the vacuum close to the cavity shape sets to shape to form the shape of cavity dwelling shape, and heat conduction by the shaping sets of cooling (ignoring heat radiation), the glass transition, in the process and setting dwelling Parison cavity shape is always consistent. Into the tank, the vacuum adsorption of the fixed effect disappeared, the parison in the freedom from external conditions continue to bear the cooling thermal stress and deformation, deformation of the final results are two states of linear superposition of thermal stress results

2.5 Profiles and stereotypes set in the cooling process maintain fit.

Structure modeled on the country setting sets the wind's low fan setting 80 sets of general assembly drawings, as shown in Fig. 1, Figure profiles (black line) of the Omo (top and bottom) are used "S" waterway for cooling, the smaller DC cooling water surface is used for cooling.

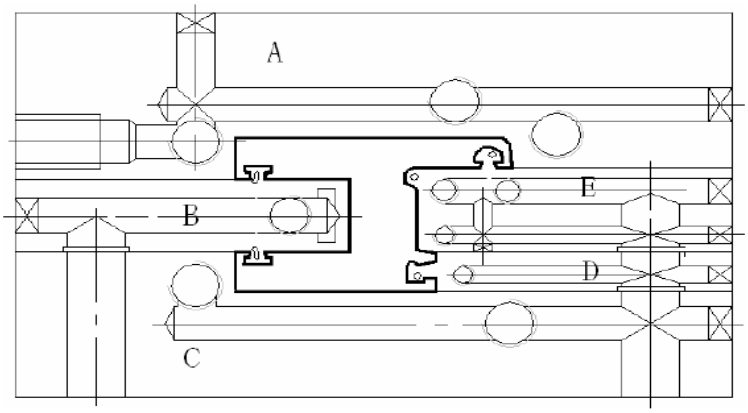


Fig.1 Stereotypes set of sections

3 Mathematical Model

3.1 Convective heat transfer coefficient and the formula

1) Convective heat transfer coefficient α

Convective heat transfer depends on the motion state of fluid: laminar or turbulent. Fully developed flow, ie $L / d > 50$, without considering the impact of the import segment, usually $Re < 2100$, the flow is laminar flow, it shall be calculated according to the experience of laminar flow; $Re > 10$, it should be formula according to turbulent flow; when $2100 < Re < 10$, it is transition zone that the flow from the layer into a turbulent flow. Reynolds number Re is the proportional relation between the inertial force Fg. and viscous force Fm. fluid flow when fluid flows.

When Turbulent flow (R e> 10), the convective heat transfer coefficient is calculated by the following formula:

$$\alpha = 0.023\frac{\lambda}{d}(Re)^{0.8}(Pr)^{0.4} \tag{1}$$

Where:

α is the convective heat transfer coefficient / W • (m^2 • K) $^{-1}$;

λ is the fluid thermal conductivity / W • (m • K) $^{-1}$;

d is pipe diameter / m;

Re is the Reynolds number;

Pr is Prandtl number.

When Re is between 2100 and 10^4, it belongs to a transitional zone. In the area where the fluid flow and heat transfer with the flow varies. If laminar flow to turbulent flow transition is abrupt, then the formula from the laminar and turbulent intersection formula to determine the turning point. Actually, it is not so simple, the flow is gradual transition to turbulence in a range of Re [3]. At present, empirical formula reflecting the current situation accurately in the transition zone heat is much few, it can use the following formula

$$\alpha = 0.012(Re^{0.87} - 280)(Pr)^{0.4}[1 + (\frac{d}{l})^{\frac{2}{3}}](\frac{P_r}{P_{rw}})^{0.11} \tag{2}$$

Where:

α is the convective heat transfer coefficient / W • (m^2 • K) $^{-1}$;

Re is Reynolds number;

Pr is Prandtl number;

d is the diameter / m;

l is the tube length / m;

P_{rw} is the thermal parameters of water.

The value of P_{rw} can be obtained by looking up table, $P_{rw} = 8.02$,when the water's temperature is 15 ℃

When in transition zone (10> Re> 2100), range of experimental verification formula for convective heat transfer coefficient is:

$$1.5 < P_r < 500 \qquad 0.05 < \frac{P_r}{P_{rw}} < 20 \qquad 2100 < R_e < 10^6$$

After analyzing and calculating, the flow motion state in stereotype set is not laminar flow stste (*Re* <2100), and here we don't give the formula of laminar flow convective heat transfer coefficient.

2) The Reynolds number *Re*

The fluid movement is the result of fluid micro-groups under a variety the action. In forced movement, the movement of fluid particles mainly depends on the mutual relations between inertia force and viscous force. *Re* number reflects the ratio between inertial force and viscous, so *Re* is called movement similarity criteria. Fluid Reynolds number is calculated as follows:

$$R_e = \frac{dv\rho}{\mu} \tag{3}$$

Where:

d is the pipe diameter / m;

v is the fluid velocity / m / s;

ρ is the fluid density / kg • m^{-3};

μ is the fluid dynamic viscosity / Pa • S

3) The Prandtl number P_r

Prandtl number can be used as similar scale in velocity and temperature field, it is calculated as follows:

$$P_r = \frac{Cp \times \mu}{\lambda} \tag{4}$$

Where:

Cp is the fluid specific heat / J • (kg • K) $^{-1}$;

μ is fluid dynamic viscosity / Pa • S;

λ is the fluid's thermal conductivity / W • (m • K) $^{-1}$.

3.2 Convection heat transfer coefficient determination

After fluid analysis:

Diameter of 8mm "S"-shaped waterway whose average flow rate of 1.39m / s,

Fluid Reynolds number: $R_e = \frac{dv\rho}{\mu} = \frac{0.008 \times 1.39 \times 999}{1.14 \times 10^{-3}} = 9744.6 > 2320$ the turbulence.

Turbulence Prandtl number: $P_r = \frac{Cp \times \mu}{\lambda} = \frac{4183 \times 1.14 \times 10^{-3}}{0.587} = 8.12$

Convective heat transfer coefficient:

$$\alpha = 0.023 \frac{\lambda}{d} (R_e)^{0.8} (P_r)^{0.4} = 0.023 \times \frac{0.587}{0.008} \times (9744.6)^{0.8} \times (8.12)^{0.4} = 6055 W/(m^2 \cdot K)$$

As the model is plane model, the heat taken away by cooling water is certain, and the cooling area of finite element model is not the same with that of the practical "S" type watercourse, so it needs to calculate the heat transfer coefficient of finite element model required.

$$\alpha = 0.012 \frac{\lambda}{d} (R_e^{0.87} - 280)(P_r)^{0.4} [1 + (\frac{d}{l})^{\frac{2}{3}}] (\frac{P_r}{P_{rw}})^{0.11} = 7144 W/(m^2 \cdot K)$$

Straight hole whose diameter is 5mm and its average flow rate is 2.52m / s

Fluid Reynolds number $R_e = \frac{dv\rho}{\mu} = \frac{0.005 \times 2.52 \times 999}{1.14 \times 10^{-3}} = 11041 > 10000$ the turbulence

Turbulence Prandtl number $P_r = \frac{Cp \times \mu}{\lambda} = \frac{4183 \times 1.14 \times 10^{-3}}{0.587} = 8.12$

Convective heat transfer coefficient:

$$\alpha = 0.012 \frac{\lambda}{d} (R_e^{0.87} - 280)(P_r)^{0.4} [1 + (\frac{d}{l})^{\frac{2}{3}}](\frac{P_r}{P_{rw}})^{0.11} = 7144W/(m^2 \cdot K)$$

Straight hole whose diameter is 2mm and its average flow rate is 1.82m / s

Fluid Reynolds number $R_e = \frac{dv\rho}{\mu} = \frac{0.002 \times 1.82 \times 999}{1.14 \times 10^{-3}} = 3190 > 2100$ transition zone

Turbulence Prandtl number: $P_r = \frac{Cp \times \mu}{\lambda} = \frac{4183 \times 1.14 \times 10^{-3}}{0.587} = 8.12$, $P_{rw} = 8.02$

Convective heat transfer coefficient:

$$\alpha = 0.012 \frac{\lambda}{d} (R_e^{0.87} - 280)(P_r)^{0.4} [1 + (\frac{d}{l})^{\frac{2}{3}}](\frac{P_r}{P_{rw}})^{0.11} = 7144W/(m^2 \cdot K)$$

3.3 thermal analysis and boundary conditions

The initial temperature for profile is 190 ℃;

Heat conduction equation $\rho C^p T' = k(\frac{\partial^2 T}{\partial x^2} + \frac{\partial^2 T}{\partial y^2})$

Third boundary condition (Convective boundary conditions thermal boundary conditions)

$Q = \alpha A(Tw - Tf)$;

The heat transfer coefficient to determined the formula for formula(1) ～(4).

4 Analysis

From Fig.2, we can be see that, on the right side of the profile there exist four cooling holes, the bottom side uses an "S"-shaped waterway to cool, the average flow rate of four cooling holes are 2.52m / s, after calculation, the out water of four cooling holes is three times of "S"-shaped waterways, and temperature difference is about 6 ℃, so it should promote the use of "S"-shaped channel when some parts can used "S"-shaped waterway cooling parts, which makes full use of water resources.

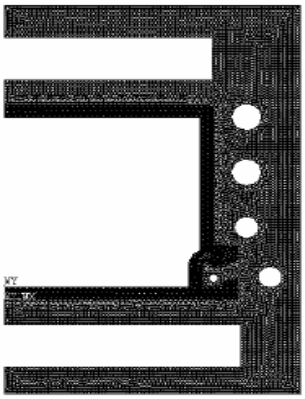


Fig.2 Use symmetry while functional block with a hole cooling profiles

References

[1] Wang fang.Research on extrusion die head for plastic on ANSYS[D]. Hefei:Hefei University of Techonology, 2004.

[2] Liu Zhigang, Songgang, Li Haimei, Shen Changyu. Numerical Simulation of the Extrusion Tenperature on the Material Boundary [J]. China Plastics, 2005, 19（3）52-55.

[3] Yang Shiming, Tao Wenquan. Heat Transfer (the third edition) [M]. Beijing: Higher Education Press 1998: 56-63.

© (2012) Trans Tech Publications, Switzerland
doi:10.4028/www.scientific.net/AMM.164.218

The Technology Analysis and Development Trend of Biological materials Energy

Shandan Zhou[a], Liming Hu [b], Xiaodong OuYang[c]

Air Force Service College, Xuzhou, 221000, China

[a] jack1975@126.com, [b] huliming@126.com, [c] ouyangxiaodong@126.com

Keywords: Biological materials energy, Energy, Technology analysis, Development trend

Abstract. The 21st century is the period of the rapid growth and development of renewable energy, which refers to fuel and raw materials that replaces the oil and can be recycled and required by people's living and production activities, and Biological materials energy resides in the first of renewable energy. This paper carries on a analysis and study mainly on the three basic technologies of Biological materials energy, analyzes the meaning and future development trend of Biological materials energy and proposes measures of the development.

Introduction

How long could people use the oil on the planet? This is a controversial issue. It is only more than a century for oil as a major energy source of the human beings, but after the development of more than a century, low and enough cheap oil era will end up and the post-oil era will be approaching, so renewable energy development of the 21st century will be subject for the whole humans.[1]

Renewable energy refers to non- fossil energy sources such as wind energy, solar energy, water energy, Biological materials energy, geothermal energy and ocean energy and so on. It emphasizes the use of modern science and technology for the development of natural energy, or shows that the development of renewable resources should establish on the basis of high-technology to achieve efficient, safe and practical purposes.

The Biological materials energy stays at the top of renewable resources. Biomass is a sustainable resource produced by the organic collaboration of air, water, earth and sun. If the biomass is not used by energy or materials, it will be broken down by microorganisms into water, carbon dioxide and heat and then dissipated. Biomass is the energy with carrier of biomass, that is, a form of energy storing solar energy in biomass through photosynthesis in the form of chemical energy. Carbohydrates are the storage of luminous energy; biomass is the carrier of light cycle conversion and the only renewable carbon source, which can be converted into a number of solid, liquid and gaseous fuels or energy of other forms, so it is known as the Biological materials energy. Coal, oil, gas and other traditional energy are also transformed under the influence of the geological process of the biomass. Therefore, biomass is the source of energy.

Technology Analysis of Biological materials Energy

Development and utilization of Biological materials energy have already caused the concern of world's governments and scientists and many countries have enacted appropriate development and research program. The United States has made the plan that the bio-based products in 2010 should add to 12% from the 5% of the total amount of product in 2001 and fuel ethanol should add to4% from the 0.5% of the total transportation fuels; Japan and India have developed the plan of "Sunshine" and "green energy projects" respectively. Other countries, such as Denmark, the Netherlands, Germany, France, Canada and Finland have been conducting their own research and development for many years and formed unique research and development systems of Biological materials energy with the respective technical advantages.

The Chinese Government and relevant departments attach great importance to the use of Biological materials energy and the National Science and Technology Commission has taken the research and application of Biological materials energy technology as a key research project in continuous three national five-year plans. In the next 15 years, the development of Biological materials resources in China will reach 1.5 billion tons of standard coal per year.

Development of Biological materials energy mainly uses the biogas technology, Biological materials pyrolysis gasification technology and biomass liquid fuel technology and so on.

Biogas Technology

Biogas technology mainly uses anaerobic method for the treatment livestock feces and high concentration and organic waste and is the older biomass utilization technology. It is the Biological materials energy utilization technology that develops earliest and more commonly in China. In the 1970s, China has been vigorously promoting the development and use of biogas technology for farmers to solve the problem of rural energy shortage. So far, China has built more than 30,000 medium-sized biogas pits with the total volume of over 1.37 million square meters, annual output of 55 million square meters of biogas, and the biogas projects with size of more than only 100 square meters reaches 630. Internationally, the developed countries have been developing the anaerobic technology mainly to deal with livestock manure, garbage and high concentrations organic wastewater.[2] At present, India, Philippines, Thailand and other developing countries have also built large or medium-sized biogas demonstration project for the treatment of livestock manure.

Biomass pyrolysis gasification technology

Since the 1970s, the United States, Japan, Canada, EU and other developed countries began the research and development of biomass pyrolysis gasification technology. Among them, the fluidized bed gasification technology has been the focus of attention of scientists since 1975 with uniform gas-solid contact, the big reaction area, the uniform reaction temperature and the big gasification intensity. The United States has 19 companies and research institutions engaged in the research and development of biomass pyrolysis gasification technology to the 1980s; 12 universities laboratories of Canada carry out the research of biomass pyrolysis gasification technology; the Philippines, Malaysia, India, Indonesia and other developing countries have also carried out the research in this area successively.

Biomass gasification technology in China has made great progress in recent years. Our nation has built more than 200 rural gasification stations currently and 100 sets of rice husk gasification generators, and the impact of the use of gasification technologies is gradually expanding.

Liquid fuel technology

Development of biomass liquid fuel technology attracts more concern, because the biomass liquid fuels include fuel ethanol, biomass liquefaction oil and biodiesel which can directly replace gasoline and other petroleum fuels as a clean fuel. In the aspect of the application of liquefied oil, the United States, New Zealand, Japan, Germany and Canada have carried out the research and development work successively. EU funds three projects, takes biomass as raw material, makes the liquid oil with the use of fast pyrolysis technology, has been completed 100kg/h pilot scale and intends to further expand the production and application. As for fuel ethanol, Brazil is the world's largest ethanol producer with production of 130 billion liters to keep the world leader in production and use of ethanol fuel. 90% ethanol in Brazil is used as fuel, and nearly 4 million cars use pure ethanol among 980 million vehicles, and ethanol fuel accounts for more than 50% of consumption of motor fuel. [3] In the bio- diesel, Germany develops relatively fast with the existing 23 biodiesel producers and 1717 biodiesel stations. The production capacity had reached 1.097 million tons in 2004. also, Germany will build the largest biodiesel plant device in the world.

In recent years, China's biomass fuel has made great achievements, especially the fuel ethanol production taking grain as raw material has basically formed the scale. In the tenth five years, our nation established the fuel ethanol factories with rotten rice as the raw material respectively in Henan, Anhui, Jilin and Heilongjiang with total 1.02 million tons each year. Now we have developed the

ethanol gasoline sales for vehicles in nine provinces (5 whole provinces and 27 cities of four provinces). By 2005, these places had realized the vehicle ethanol gasoline to replace gasoline except the army needs and national special reserve.

Compression technology

Compression technology of biomass could compress the solid agriculture and forestry waste into molding and make a briquetting fuel that can replace coal. For example, the United States has developed a biomass pellet fuel, Thailand, the Philippines and Malaysia and other the Third World countries have developed a rod-like fuel. Briquette fuel is mainly used in two aspects: First, further carbonized process into charcoal sticks or charcoal block as the civil grill charcoal or raw materials for industrial charcoal; Second, for the direct combustion as fuel for home heating fuel.

The significance of the development of Biological materials energy

The significance of the development of Biological materials energy is concentrated in four aspects:

- Reducing greenhouse gas emissions to improve the ecological environment.
- Reducing the energy import dependency to ensure the energy supply security.
- Stimulating economic development to increase employment.
- Developing new markets for agricultural products to promote rural development.

The use prospects and measures of Biological materials energy

The use prospects of Biological materials energy

Development of Biological materials energy is a systematic project , is essential for China to achieve sustainable development, construction , according to the characteristics of China's economic and social development , development and utilization of Biological materials energy is necessary to learn the advanced experience of foreign countries , but also with their own characteristics.[4]

- We should strengthen industrial applications of biomass and carry on scale production, increase the proportion of the use of Biological materials energy, improve the status of biomass in the energy field, expand the impact of biomass and create conditions for large-scale application of Biological materials energy in the future.
- We should make full use of the role of biomass as complement energy in rural areas. We should provide clean energy for rural areas, improve rural living environment and improve their quality of life which includes the use of biogas, small-scale gasification power generation and other practical skills.
- We should study the technology of biomass transferring into high-grade energy products, improve the value of biomass with the use of advanced technology and make a foundation for future multi-channel use of biomass to play the role of biomass better.
- We should develop new energy resources, base on existing resources, use marginal lands such as mountain, wasteland and desert, develop new biomass resources, research, cultivate and develop fast and high-yield plant varieties, develop the energy farms and forest in the area that the current conditions allow, establish Biological materials energy base and product scale wood, vegetable oil and other energy resources.

Development measures of Biological materials energy

Based on the prospects for the development of Biological materials energy, we put forward the following measures.

- We should provide policy support. Taking into account that the cost of Biological materials energy development is hard to compete with petroleum-based products, the state must have to support the development of a group of new energy backbone enterprises with plan and step, give policy subsidies on investment, pricing and taxation. Also, we should develop international

cooperation, introduce international advanced technology and capital; establish a dedicated display area of Biological materials energy resources to increase public cognition and awareness of energy conservation.

- We should promote industrialization, develop overall R&D plan and start industrialization projects. Relevant departments should strengthen the commercialization of Biological materials energy utilization technologies, develop strict technical standards, strengthen technical supervision and market management, regulate market activities and create a favorable market environment for the promotion of biomass technology. Biological materials energy enterprises should rely on scientific and technological progress and the enhancement of the management level to enhance the utilization of Biological materials energy and product diversification, unify the coordination layout from different parts and carry on the system optimization to maximize output and efficiency.
- We should Expand the industrial production, enhance the connection of biomass technologies and industrial production, solve critical technology in the demonstration and application, make a breakthrough for technical problems in the extending and application, improve and test the reliability and economy of Biological materials energy technologies in practice and create conditions for the large-scale application of Biological materials energy. We could take fuel ethanol, biodiesel, bio- ethylene, bio- plastics, methane power generation and curing fuel as leading products for industrial production currently and in the future.
- We should accelerate technology research, promote the biomass science and research step by step by level and category, adhere to the principles of combination of point and the entire area and overall progress with combination of near, middle and long-term goals. We should support the prospecting basic research, such as the use of straw energy, organic waste and energy technology, industrial organic waste and wastewater treatment and energy and so on, but also we should promote the project with the relatively mature technology into the pilot test phase or industry, such as efficient biomass gasification power generation technology, organic waste IGCC power generation technology, high-rate anaerobic treatment and biogas recovery technology, cellulose preparation of ethanol technology, biomass pyrolysis liquefaction technology, energy, plant breeding and use technology, biomass oxygen and other advanced technologies so as to make the "points" breakthrough in a short time.

Conclusion

Biological materials energy attracts the favor and attention of many countries around the world as a renewable energy source that could carry on material production, so the development of Biological materials energy has an important significance for the mitigation of energy crisis and protecting national security. Chinese fossil energy resources are limited, but China is vast in territory with rich biomass resources and a good technical basis and development condition, so the development and utilization of Biological materials energy has a unique advantage.

Meanwhile, China's Biological materials energy industry and technology development have a certain gap with the United States, the European Union and other developed countries. Therefore, we should understand the situation, identify the weaknesses, make full use of advantages, catch up, strive to reach the world advanced level within the shortest time and form solid Biological materials energy industry accumulate energy to protect China's national security and economic security and to play the heat for the construction of socialist new countryside and building a socialist harmonious society.

References

[1] Qian Bozhang. New Energy —an inevitable choice for the post-petroleum era [M]. Beijing: Chemical Industry Press. P15 2007

[2] Venkataraman C,Thomas S,Kulkarni P. Size distributions of polycyclic aromatic hydrocarbons-gas/particle Partitioning to urban aerosols[J].Journal of Aerosol Science,1999,30:759～770.

[3] Kusdiana D, Saka S. Kinetics of transesterification in rape seed oil to biodiesel fuel as treated in supercritical methanol [J]. Fuel, 2001, 80: 693-698.

[4] Asif, M., Muneer, T., 2007. Energy supply, its demand and security issues for developed and emerging economies. Renewable and Sustainable Energy Reviews 11 (7), 1388–1413.

© (2012) Trans Tech Publications, Switzerland
doi:10.4028/www.scientific.net/AMM.164.223

Effect of Preparation Conditions on the Performance of Anodic Aluminum Oxide Films

Xiaozhen LIU[1,a], Junhua YANG[1,b], Gang WANG[1,c], Lingling SONG[2,d] and Geshi ZHUANG[1,e]

[1]School of Chemical and Environmental Engineering, Shanghai Institute of Technology Shanghai, China 201418

[2]GanNan Normal University, Ganzhou, Jiangxi, China 341000

[a]liuxiaozhen1958@yahoo.com, [b]yangjunhua@sit.edu.cn, [c]wanggang@sit.edu.cn, [d]linglingsong@yahoo.com, [e]xlzhang@sit.edu.cn,

Keywords: Anodic aluminum oxide, Film, Neodymium, Microhardness, Thickness

Abstract. Neodymium salt was used as additives in preparing anodic aluminum oxide (AAO) films to improve its performance. AAO films were prepared by anodization method from a 15 vol. % sulphuric acid solution containing neodymium salt. The effects of anodization voltage, anodization temperature and anodization time on microhardness and thickness of AAO films were researched, respectively. The thickness of AAO film increases with the increase of anodization voltage, the microhardness of AAO film decreases with the increase of anodization voltage in 19 V～23 V. The thickness of AAO film increases with the increase of anodization temperature, the microhardness of AAO film decreases with the increase of anodization temperature in 11 ℃～19℃. The thickness of AAO film increases with the increase of anodization time, the microhardness of AAO film decreases with the increase of anodization time in 30 min～3 h. When the anodizing parameters: anodization voltage: 22 V, temperature: 15℃, anodization time: 2 h, the thickness and microhardness of AAO film is as high as 135μm and 305.4 HV.

Introduction

Anodic oxidation of aluminum can produce porous oxide film possessing these qualities, which has a highly oriented porous structure with very uniform and nearly parallel pores. Anodization is always carried in one of several acid electrolytes, such as oxalic acid, sulfuric acid, phosphate acid, tartaric acid, or their mixtures. Anodic aluminum oxide (AAO) films with uniform parallel nanochannels are widely used as templates for the growth of low-dimensional nano-materials and as a three-dimensional micro / nanostructure itself, and have recently been proposed in medical and biological, electrical, optical and micro-mechanical fields [1-4]. These include nanopores [5], nanowires [6], nanotubes [7], and nanodots [8], which are all functional materials for solar energy conversion, catalysis, sensors and separation filters. Rare earth compounds have been widely used in optics, electronics, metallurgy, chemical and materials engineering, due to their special physical and chemical characteristics [9]. The microhardness and thickness of AAO film were increased respectively by anodization method from a 15 vol. % sulphuric acid solution containing neodymium salt, praseodymium salt and erbium salt, respectively [10-12]. In this paper, AAO films were prepared by anodization method from a 15 vol. % sulphuric acid solution containing neodymium salt, and the effects of anodization voltage, anodization temperature and anodization time on microhardness and thickness of AAO film were researched, respectively.

Experimental

AAO films were prepared by according to [11]. High purity aluminum foils (99.99% purity, 35 mm×25 mm×0.3 mm) were used to grow anodic porous layers. High purity metal was preferred in order to minimize the influences of alloying elements. Before anodization the aluminum was degreased in acetone by using ultrasonic cleaner and annealed at 500℃ for 2 h to remove mechanical

stresses and recrystallize the aluminum, and then electropolished in a mixed solution of perchloric acid and ethanol (1:4 in volume) under a constant voltage of 18 V for 1 min below 5℃, followed by ultrasonic rinsing in a cold distilled water for 5 min. An electrochemical reactor was designed and built to carry out anodizing experiments. The electrolytes were 15 vol. % sulphuric acid solution containing neodymium nitrates (concentration of neodymium: 0.28g neodymium/L). The anodizing parameters: temperature: 11～19℃, voltage: 19～23 V, time: 30 min～3 h. After anodizing, each sample was washed thoroughly with distilled water and dried with an air jet.

Microhardness of AAO films were determined on a 401MVD^{TM} microhardness tester. The load and load time were 50gf and 15s, respectively.

Thicknesses of AAO films were determined on a MPORL thickness tester.

Results and discussion

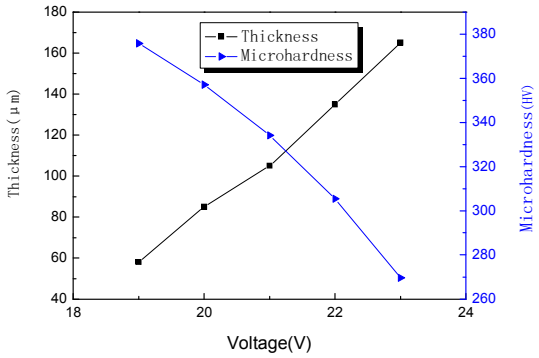


Fig.1 The effect of anodization voltage on the thickness and microhardness of the AAO film

The anodizing parameters: temperature: 15℃, time: 2 h. The relationship between the thickness of AAO film and anodization voltage, and the relationship between the microhardness of AAO film and anodization voltage are shown in Fig.1. As can be seen in Fig.1, in the range of anodization voltage from 19 V to 23 V, the thickness of AAO film increases with the increase of anodization voltage; the microhardness of AAO film decreases with the increase of anodization voltage. When anodization voltage is 23 V, the thickness of AAO film is as high as 165μm. When anodization voltage is 19V, the microhardness of AAO film is as high as 375.8 HV. When anodization voltage is 22 V, the thickness and microhardness of AAO film is as high as 135μm and 305.4 HV.

The anodizing parameters: anodization voltage: 22 V, time: 2 h. The relationship between the thickness of AAO film and anodization temperature, and the relationship between the microhardness of AAO film and anodization temperature are shown in Fig.2. As can be seen in Fig.2, in the range of anodization temperature from 11 ℃ to 19℃, the thickness of AAO film increases with the increase of anodization temperature; the microhardness of AAO film decreases with the increase of anodization temperature. When anodization temperature is 19 ℃, the thickness of AAO film is as high as 170 μm. When anodization temperature is 11℃, the microhardness of AAO film is as high as 351.0 HV. When anodization temperature is 15 ℃, the thickness and microhardness of AAO film is as high as 135μm and 305.4 HV.

The anodizing parameters: anodization voltage: 22 V, temperature: 15℃. The relationship between the thickness of AAO film and anodization time, and the relationship between the microhardness of AAO film and anodization time are shown in Fig.3. As can be seen in Fig.3a, in the range of anodization time from 4 min to 12 min, the thickness of AAO film increases with the increase of anodization time; the microhardness of AAO film increases with the increase of anodization time at the beginning, when anodization time is 8 min, the microhardness of AAO film is as high as 487.8 HV, and then, it decreases with increase of anodization time in 8 min～12 min. When anodization time is 12 min,, the thickness of AAO film is as high as 24μm.

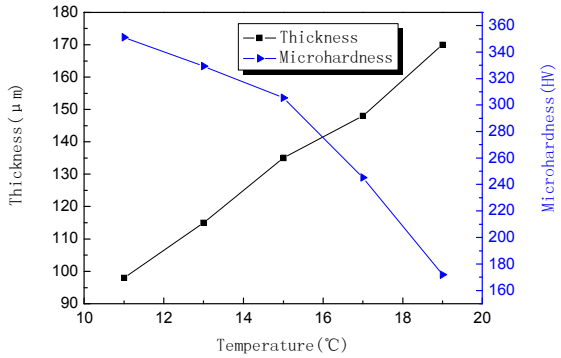


Fig.2 The effect of anodization temperature on the thickness and microhardness of the AAO film

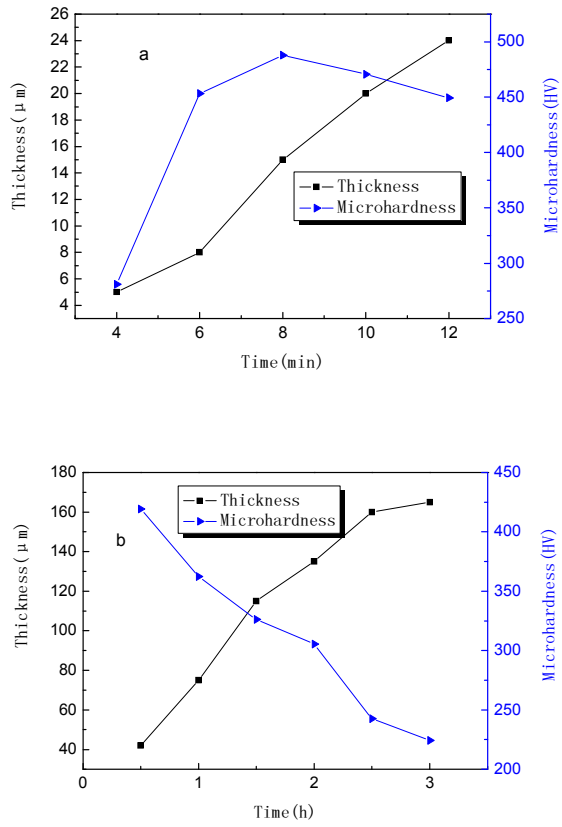


Fig.3 The effect of anodization time on the thickness and microhardness of the AAO film

As can be seen in Fig.3b, in the range of anodization time from 30 min to 3 h, the thickness of AAO film increases with the increase of anodization time; the microhardness of AAO film decreases with the increase of anodization time. When anodization time is 3 h, the thickness of AAO film is as high as 175 μm. When anodization time is 30 min, the microhardness of AAO film is as high as 419.1HV. When anodization time is 2 h, the thickness and microhardness of AAO film is as high as 135μm and 305.4 HV.

Conclusions

The thickness of AAO film increases with the increase of anodization voltage, the microhardness of AAO film decreases with the increase of anodization voltage in 19 V～23 V. The thickness of AAO film increases with the increase of anodization temperature, the microhardness of AAO film

decreases with the increase of anodization temperature in 11 ℃～19℃. The thickness of AAO film increases with the increase of anodization time, the microhardness of AAO film decreases with the increase of anodization time in 30 min～3 h. When the anodizing parameters: anodization voltage: 22 V, temperature: 15℃, anodization time: 2 h, the thickness and microhardness of AAO film is as high as 135μm and 305.4 HV.

Acknowledgements

This work was financially supported by the project supported by the National Natural Science Foundation of China(50972094), Leading Academic Discipline Project of Shanghai Municipal Education Commission(J51503), Science Technology Foundation of shanghai (10410703000) and the Program for Professor of Special Appointment(Eastern Scholar) at Shanghai Institutions of Higher Learning.

References

[1] S. Stojadinovic, Z. Nedic, I. Belca, R. Vasilic, B. Kasalica, M. Petkovic, Lj. Zekovic: Applied Surface Science Vol.256 (2009), p.763

[2] H.S. Kim, D.H. Kim, W. Lee, S.J. Cho, J.H. Hahn, H.S. Ahn: Surface & Coatings Technology Vol.205 (2010), p.1431

[3] S. Stojadinovic, R. Vasilic, Z. Nedic, B. Kasalica, I. Belca, Lj. Zekovic: Thin Solid Films Vol.519 (2011), p.3516

[4] X.Y. Han, W.Z. Shen: Journal of Electroanalytical Chemistry Vol.655 (2011), p.56

[5] C.R. Martin: Science Vol.266 (1994), p.1961

[6] J.P. O'Sullivan, G.C. Wood: Proc. R. Soc. Lond. A Vol.317 (1970), p.511

[7] H. Masuda, M. Ohya, H. Asoh, M. Nakao, M. Nohtomi, T. Tamamura: Jpn. J. Appl. Phys. Part 2: Lett. Vol.38 (1999), p.1403

[8] H. Masuda, K. Fukuda: Science Vol.268 (1995), p.1466

[9] X.Z. Liu, X. Li, A.B. Yu, W.J. Huang: Journal of Rare Earths Vol.27 (2009), p.480

[10] X.Y. Han, W.Z. Shen: Journal of Electroanalytical Chemistry Vol.655 (2011), p.56

[11] X.Z. Liu, J.Q. Gen, A.B. Yu, et al.: Advanced Materials Research Vol. 415-417 (2012), p.1895

[12] X.Z. Liu, Z.X. Liu, A.B. Yu, et al.: Advanced Materials Research Vol. 399-401 (2012), p.847

© (2012) Trans Tech Publications, Switzerland
doi:10.4028/www.scientific.net/AMM.164.227

Noise Reduction of Elastic Structure Paste Viscoelastic Material Based on Complex Radius Vector of Virtual Source

YuMing Wang[1, a], YuanAn He[2, b], DeJiang Shang[1, c]

[1]National Laboratory of Underwater Acoustic Technique

Harbin Engineering University, Harbin, China

[2]Systems Engineering Research Institute, Beijing, China

[a]email: wangyuming518@163.com, [b]email: heyuanan@sina.com

[c]email: shangdejiang@hrbeu.edu.cn

Keywords: Distributed virtual source; Complex radius vector; Viscoelastic material; Underwater noise reduction; Acoustic impedance transfer

Abstract. It is hard to theoretically calculate the noise reduction characteristics for underwater complex structure of paste viscoelastic material. This paper introduces complex radius vector inside radiator based on the advantages of singular integral provided by traditional virtual source superposition method to calculate the radiated sound field from finite cylindrical shells. This method adapts truncation regularization filter to overcome the effect of background noise to enhance the calculation accuracy and then use impedance transmission theory to calculate the noise reduction characteristics of the cylindrical shells paste viscoelastic material. Numerical simulations show the calculation accuracy is greatly dependent on the size and position of the distributed virtual sources. There exists an optimal complex radius to minimize the error.

1. Introduction

Traditionally, people use analytical method, finite element method and boundary element method to solve the problem of underwater radiation sound field of underwater structure. Recently, the virtual source superposition method based on the classical Helmholtz integral formula has been widely used, which originated in 1989 by Koopmann [1] based on the concept of solving elastic superposition method by Burgess and Mahajerin [2]. He proposed an indirect integral equation method for solving acoustic radiation and scattering problems. In this method, a series of virtual source are placed on a virtual closed surface of the vibration within the structure as a virtual boundary, then the external sound field is predicted by the intensity value of the virtual sources estimated by collocation method or the least squares method using the normal velocity on the surface of the vibrational structure. The virtual source intensity meets the Helmholtz equation and the Sommerfeld radiation conditions. Since the virtual source surface and the actual vibrational structure surface are different, this method can avoid the singular integral, and independent of the shape of vibrational structure.

2. Theoretical analysis

Traditional virtual source superposition method. As shown in Fig. 1, any three-dimensional space can be divided into internal domain V and the outer domain E by a boundary of S. A virtual surface S' within the closed boundary S is selected and configured with virtual sources.

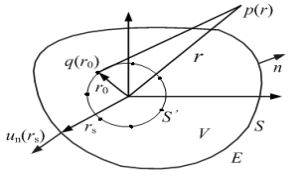


Figure 1 Illustration of virtual source superposition

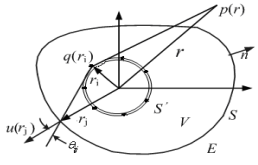


Figure 2 The virtual source distribution

For now, there are three commonly used method to configure the virtual source in S' [3]: single-layer potential, double-layer potential, Burton-Mille combination of single- and double-potential. Where single-layer potential can be expressed by

$$\Phi(p)=\int_{S'} q(r_0)G(p,q)\mathrm{d}S',\ p\in E \tag{1}$$

Where $G(p,q)$ is the Green function in free space, $\Phi(p)$ is velocity potential function, $q(r_0)$ is the intensity of the virtual source at r_0 inside V. According to the relationship between velocity potential function and pressure, and the linearization form of Euler equation, one can get normal direction velocity: $u_n(r_0)$. To solve the equation, we discrete $u_n(r_0)$, and suppose virtual source distribute in a virtual spherical shell with a thickness of δ. As shown in Fig. 2, we further divide the virtual source spherical surface S' into N segments, each area is indicted by σ_i. If σ_i is small enough, then $u_n(r_0)$ can be approximated as matrix format $U_n=DQ$. Q is the virtual intensity matrix, D is acoustic dipole matrix with dimensions of $N\times N$. The acoustic filed of other points can be calculated by Q, where ρ_0 is the density, ω is the harmonic vibration angular frequency.

$$p(r)=\sum_{i=1}^{N} j\omega\rho_0 G(r_i,r_j)Q_i \tag{2}$$

Complex radius vector virtual source superposition method. Similar with that of structural dynamics in solving the system response, the system damping is introduced to overcome the non-uniqueness of the characteristic frequencies of the virtual source solution. Based on this idea, the distance between the virtual source surface to the radiator center is treated as a complex vector. Set the parameter equation of vibrational structure surface S in spherical coordinates $R=f(\phi,\theta)$, where R is the module of the vector between coordinates origins with a point of S, ϕ and θ are respectively polar angles in spherical coordinates. The relationship between S' and S can be written as: $R'=\bar{\alpha}f(\phi,\theta)$, $|\bar{\alpha}|<1$, where $\bar{\alpha}$ is the contraction coefficient of the virtual source surface, for traditionally virtual source superposition method, $\bar{\alpha}$ is real. In this paper, it is a complex coefficient in order to add the effect of damping: $\bar{\alpha}=a(1+b\mathrm{i})$, $|a|<1$.

Singular value truncation regularization filter. In virtual source superposition method, one needs the singular value decomposition (SVD) when calculating the inverse of D, and σ_i is the singular value of D that statisfies $\sigma_1\geq\sigma_2\geq\ldots\geq\sigma_n\geq 0$. Truncation filtering method of singular value assign zeros to the corresponding filter coefficients of smaller singular value [4], to reduce background noise on the calculation accuracy by ignoring the very small singular value. When $\sigma_i<\alpha\sigma_1$, the filter coefficient f_i is set to: if $\sigma_i\geq\alpha\sigma_1$, $f_i=1$; if $\sigma_i<\alpha\sigma_1$, $f_i=0$. The selection of truncated coefficient ratio selected is more critical than the selection of α. If it is too small you'll lose a lot of useful information, if it is too large, there is no filter effect. The selection is generally based on the signal to noise ratio (SNR) of the sound field.

Impedance transmission theory of viscoelastic materials. For plane wave under normal incidence conditions, according to continuous conditions of the sound pressure and particle velocity in the boundary [5], we can get the acoustic transfer impedance matrix A, as in Eq. 3, p_1, u_1 and p_2, u_2 are the pressure and velocity on both sides of the viscoelastic material layer respectively.

$$\begin{Bmatrix} p_1 \\ u_1 \end{Bmatrix}=\begin{bmatrix} a_{11} & a_{12} \\ a_{21} & a_{22} \end{bmatrix}\begin{Bmatrix} p_2 \\ u_2 \end{Bmatrix}=[A]\begin{Bmatrix} p_2 \\ u_2 \end{Bmatrix} \tag{3}$$

Similarly, under spherical wave incident conditions [6], one can get

$$a_{11}=\left[(-1+jkr_2)e^{j2k(r_2-r_1)}+(1+jkr_2)\right]\Big/\left[j2kr_1e^{jk(r_2-r_1)}\right],\ a_{12}=\left[\rho cr_2\left(e^{j2k(r_2-r_1)}-1\right)\right]\Big/\left[2r_1e^{jk(r_2-r_1)}\right] \tag{4}$$

$$a_{21}=\left[(jkr_2-1)(1+jkr_1)e^{j2k(r_2-r_1)}+(1+jkr_2)(1-jkr_1)\right]\Big/\left[-2k^2\rho c r_1^2 e^{jk(r_2-r_1)}\right],\ a_{22}=\left[r_2(1+jkr_1)e^{j2k(r_2-r_1)}-r_2(1-jkr_1)\right]\Big/\left[j2kr_1^2e^{jk(r_2-r_1)}\right] \quad (5)$$

Where k is wave number, c is longitudinal wave of the material, r is the distance from the center of spherical wave. Similarity, under cylindrical wave incident conditions, then one can finally get:

$$a_{11}=\frac{H_0^{(2)}(kr_1)H_1^{(1)}(kr_2)-H_0^{(1)}(kr_1)H_1^{(2)}(kr_2)}{H_0^{(2)}(kr_2)H_1^{(1)}(kr_2)-H_1^{(2)}(kr_2)H_0^{(1)}(kr_2)}\ a_{12}=\frac{j\rho c\left[-H_0^{(2)}(kr_1)H_0^{(1)}(kr_2)+H_0^{(1)}(kr_1)H_0^{(2)}(kr_2)\right]}{H_0^{(2)}(kr_2)H_1^{(1)}(kr_2)-H_1^{(2)}(kr_2)H_0^{(1)}(kr_2)} \quad (6)$$

$$a_{21}=\frac{H_1^{(2)}(kr_1)H_1^{(1)}(kr_2)-H_1^{(1)}(kr_1)H_1^{(2)}(kr_2)}{j\rho c\left[H_0^{(2)}(kr_2)H_1^{(1)}(kr_2)-H_1^{(2)}(kr_2)H_0^{(1)}(kr_2)\right]},\ a_{22}=\frac{-H_1^{(2)}(kr_1)H_0^{(1)}(kr_2)+H_1^{(1)}(kr_1)H_0^{(2)}(kr_2)}{H_0^{(2)}(kr_2)H_1^{(1)}(kr_2)-H_1^{(2)}(kr_2)H_0^{(1)}(kr_2)} \quad (7)$$

3. Numerical simulation

Algorithm verification. The classical pulsating ball of sound radiation, for example, its radius is 1m, its surface is divided into a total of 114 nodes, and the surface normal velocity is 1m/s. Setting the same shape of virtual sources, pulsating sphere radiated sound field can be expressed by an analytical expression: $p(r)=j\rho_0 c_0 u_0 a^2 k e^{-jk(r-a)}/r(1+jka)$. Where a is the radius of the pulsating sphere ball, ρ_0 and c_0 are respectively the density and sound speed of the water. We calculated the radiated sound field at $r=2$ m using the above equation.

When there exists noise interference, the complex radius vector virtual source superposition method is introduced and combined with singular value truncation regularization filter to reduce the effect of background noise. Under a SNR of 20dB, the calculated position is at (0, 0, 2), the optimal complex radius vector is $0.1\times(1\text{-i}\times 0.15)$, the coefficient for singular value truncation regularization filter is 0.01, to minimize the calculated error. From Fig. 3 and Fig. 4, the errors of the sound field are both lower than 4% compared to that of analytical solution.

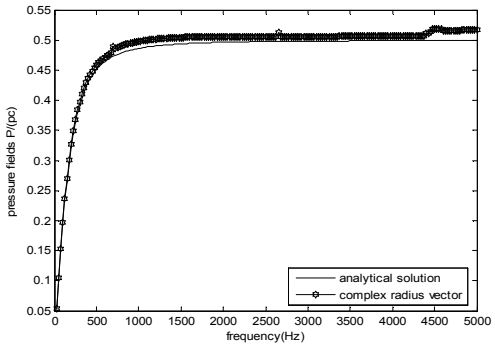


Figure 3 The sound field of a pulsating ball

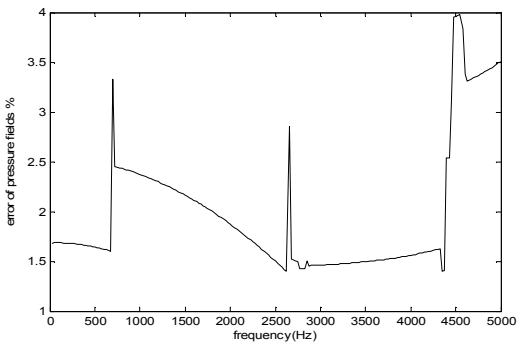


Figure 4 The error of sound field of a pulsating ball

Cylindrical shell viscoelastic materials noise reduction characteristics analysis. Cylindrical shell has a length of 2m, both closed ends with a diameter of 1.5m. The cylindrical shell circumferential surface is divided into 264 nodes, the surface radial vibration velocity is 1m/s. Inside the cylindrical shell, the conformal virtual cylinder source and non-conformal virtual spherical source were configured. Under a SNR of 20dB, the radiated sound field of 2m from the cylindrical shell was calculated by complex radius vector virtual source superposition method. When the cylindrical shell only vibrates along the circumferential surface with two ends non-vibrate, the radiated sound field can be approximated as uniform cylindrical wave radiated sound field, its analytical expression can written as: $p(r)=j\rho_0 c_0 u_0 H_0^{(2)}(kr)/H_1^{(2)}(ka)$, a is the cylindrical shell radius.

Figure 5 gives the calculated pressure fields of 2m from the cylindrical shell for conformal virtual cylinder source, non-conformal virtual single ball source and non-conformal virtual two ball sources calculated by our proposed method. As can be seen, the result of virtual two sources are much close to the analytical solution of the cylindrical shell, because the use of virtual two sources not only can adjust the complex radius vector of the spherical source but also can adjust the distance between the two sources, which can increase the calculation accuracy. For the calculation, the virtual source complex radius vector is taken as $0.2\times(1\text{-i}\times 0.2)$, the centers of the two ball sources are located in

(0,0,0.45), (0,0,-0.45), the error of pressure amplitude is less than 3.5%. Using cylindrical wave acoustic impedance transfer theory, the noise reduction characteristics can be expressed: $\Delta=20\log_{10}\left(p_n/p_y\right)$. Where p_y and p_n are the radiated sound fields for the radiator with and without viscoelastic material. The noise reduction characteristics is calculated and shown in Fig. 6.

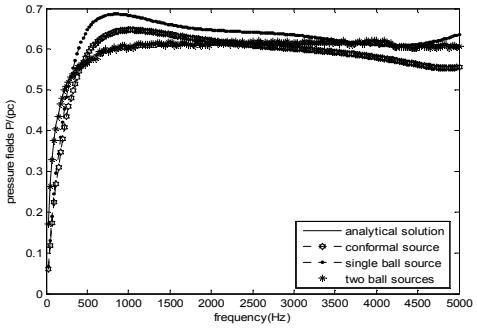


Figure 5 The amplitude-frequency characteristics with different virtual sources

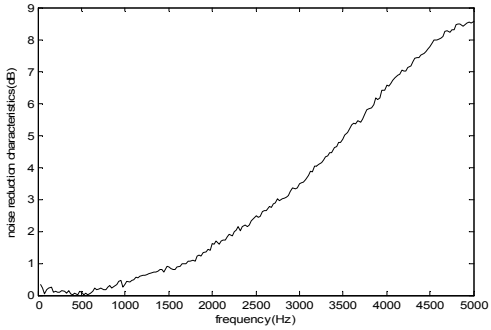


Figure 6 The noise reduction characteristics of cylindrical shell covered with viscoelastic materials

4. Conclusions

This paper uses complex radius vector virtual source, singular value truncation regularization filter and viscoelastic material impedance transfer theory to calculate the underwater structure radiated sound field and viscoelastic material noise reduction characteristics. By this method, the noise reduction of a cylindrical shell covered with surface viscoelastic material is numerically predicted. The results show that the radiated sound field error is very small if one uses double-ball virtual sources, the proposed method can also effectively overcome the noise interference.

References

[1] Koopmann G H, Song L M, Fahnline J B. A method for computing acoustic fields based on the principle of wave superposition. J. Acoust Soc Am., 86 (6), 1989, pp. 2433-2438

[2] Burgess G J, Mahajerin E A. A comparison of the boundary element and superposition methods. Computers & Structures, 19(5-6), 1984, pp. 697-705

[3] Xiang Yu, Huang Yuying. Wave superposition method based on virtual source boundary with complex radius vector for solving acoustic radiation problems. Acta Mechanica Solida Sinica, 25(1), 2004, pp. 35-41

[4] Bi Chuanxing. Theoretical and experimental study on nearfield acoustic holography based the distributed source boundary point method. Hefei University of Technology Doctoral Dissertation, 2004

[5] L M Brekhovskikh. Waves in layered media. Beijing, Academic Press, 1985, pp. 10-16

[6] He Zuoyong, Zhao Yufang. Fundamentals of Theoretical acoustics. Beijing, National Defense Industry Press, 1981

© (2012) Trans Tech Publications, Switzerland
doi:10.4028/www.scientific.net/AMM.164.231

Transport of Bacteria in Natural Core as Enhanced Oil Recovery Material

XiangPing Kong

College of Chemistry and Pharmacy, Qingdao Agricultural University, Qingdao 266109, Shandong, PR China
email: kxp2004@163.com

Keywords: *Geobacillus* sp.; bacterial transport; natural core

Abstract: The effects of the bacterial cell size and flow velocity on the transport of concentrated suspensions of bacteria were experimentally investigated, and the bacteria retention mechanism was studied by observing bacterial distribution in natural cores. A lower reduction in permeability and a higher effluent bacterial concentration were obtained in the core flooding with the smaller cell size bacteria or at a higher flow velocity. The bacteria were easier to migrate through the porous rock directionally compared to the rigid solid particles owing to their organic flexibility. Bacteria retention occurred primarily at the inlet section of the natural core, and log-jam effect or pore bridging may be the dominant mechanism.

Introduction

The ability to transport bacteria through porous rock to the target zone is crucial to the implementation of microbial enhanced oil recovery process [1] or to the removal of environmental pollutants in groundwater through bioaugmentation. Some researches about the parameters that determine the transport of bacteria in porous rock have been reported, but there is little information available on the bacteria retention mechanism. The purpose of this study was to evaluate the effects of bacterial cell size and flow velocity on the transport of concentrated suspensions of bacteria. Particularly, the bacteria retention mechanism was studied by observing the bacterial distribution in natural cores.

1. Materials and methods

1.1 Bacterial Strains and media

The cell shape of *Geobacillus* sp. DM-2 [2] is 0.5-0.7 × 1.5-4.0 μm. The incubation was carried out at 60 °C in the medium containing (g/L) sucrose 30, NaCl 5.0, KNO_3 2.0, KH_2PO_4 1.35, $Na_2HPO_4 \cdot 12H_2O$ 3.65, $FeSO_4 \cdot 7H_2O$ 0.01, $MgSO_4 \cdot 7H_2O$ 0.2, $CaCl_2$ 0.01 and yeast extract 0.5, pH 7.0-7.2. The diameter of streptococcus F2 is 0.8-1.1μm, and 3-6 cocci form a long chain. It was cultured at 37°C in the medium containing (g/L) glucose 3.0, peptone 3.0, KH_2PO_4 2.7, NaCl 5.0 and yeast extract 3.0, pH 7.0.

1.2 Methods

The earlier reported core flooding equipment [3] was used with slight modifications. The sandpack core was replaced by a core holder with the confining pressure of 6.5MPa during the experiments. There were 3 natural cores, designated as C1, C2 and C3, with the length (cm) × diameter (cm) of 6.796 × 2.504, 6.394 × 2.502 and 4.862 × 2.480, respectively. The average measured porosity of the cores were 19.8, 21.8 and 15.4%, and the permeability were 81.5, 20.9 and

15.8 mD, respectively. All the experiments were carried out by injecting the cell suspension of the stationary phase into the cores, followed by the displacement with the sterile produced water continuously. 0.5 pore volume (PV) samples of effluent were collected at different intervals from the core outlet for the cell density analysis, and the pressure across the core was monitored during the displacement process. The hemacytometer counting method was used for the bacteria counting. Effluent concentration divided by the injected concentration (C_e/C_i) and the permeability at a given time divided by the initial effective brine permeability (K/K_i) were measured.

The bacterial distribution in natural cores was observed using a Quanta 200 environmental scanning electron microscope (Philips, Holland). The sample pre-treatment was conducted as follows. The core was first flooded with 15 PV of the cell suspension at the stationary phase, followed by 3 PV of 2.5% glutaraldehyde (pH 6.86 phosphate buffer as solvent) to immobilize bacteria. Subsequently, the core was dehydrated by flowing 3 PV of 50%, 70%, 80%, 90% and 100% gradient ethanol, respectively. Then the core was placed in a desiccator for 12h.

2. Results and discussion

2.1 Effect of bacterial cell size

The cores of C2 and C3 were flooded by the cell suspensions of bacteria DM-2 and F2, respectively. The cell concentration in suspensions of DM-2 or F2 at the stationary phase was (6-9) $\times 10^8$ cells/mL. The flow velocity was 0.5mL/min, and the experiments were conducted at 30°C.

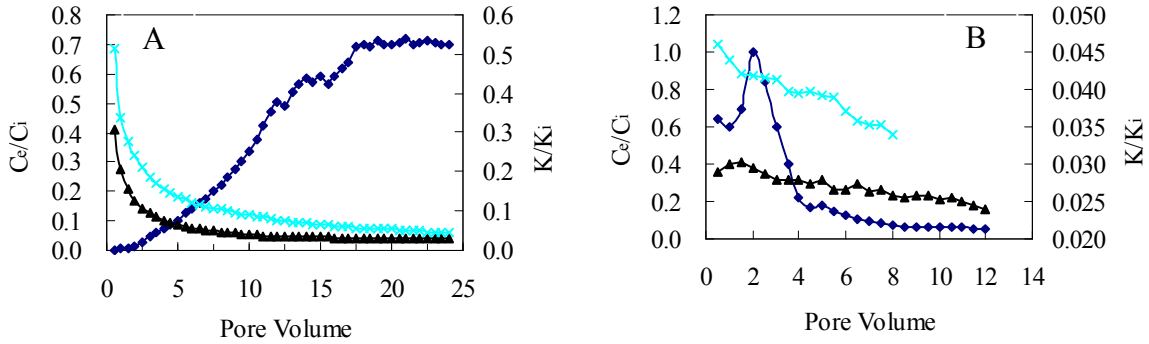


Fig. 1 The effluent bacterial concentration ratio of DM-2 (◆) and the permeability ratio of DM-2 (▲) and F2 (×) during the bacteria flooding (A) and the subsequent sterile water flooding (B).

Studies in filtration suggest that the ratio of particle to pore size must be no more than approximately 1/5 if the formation of an external filter cake is to be minimized [4]. The average pore diameter of core C2 is about 1.8 μm, and the width of five DM-2 bacteria is 2.5-3.5μm. However, there was no formation of an external filter cake in the core C2 during the bacteria flooding, and the bacterium DM-2 could migrate through the core with C_e/C_i of about 0.7 after 17 PV of bacteria flooding (Fig. 1 A). Moreover, DM-2 could only migrate through the core directionally under the effect of water dynamics since the length of bacteria was close to even greater than the pore diameter. The results indicated that the bacteria are easier to migrate through the core directionally compared to the rigid solid particles owing to their organic flexibility.

In the C3 core flooding experiments, the actual cell size of bacterium F2 is 0.8-1.1 × 2.4-6.6 μm given that 3-6 cocci form a long chain, close to even greater than the average pore diameter of C3 (about 1.8 μm). Because of the larger cell size and the higher cell aggregation tendency, F2 may be more difficult to migrate through the natural core than DM-2, consistent with the fact as follows.

The effluent bacterial concentration of F2 was about 10^6 cells/mL during the former 5 PV of bacteria flooding, and then the effluent became clear with C_e/C_i close to zero. However, the values of K/K_i of F2 flooding were higher than those of DM-2 flooding (Fig. 1). The results indicated that fewer bacteria had entered the core C3, proved by the fact that an obvious external filter cake of bacteria has been found at the inlet face of the core. Meanwhile, more internal cakes were also found in the core C3 than the core C2 (Fig. 2 and Fig. 3), indicating that the retention of F2 may be caused by the physical clogging at the pore throats by the individual cells. In addition, the bacteria F2 looks like bacilli rather than the streptococcus from Fig 3, indicating that the cell shape may be changed under the squeeze of pores when the bacterial cell size is much larger than the pore diameter of the core.

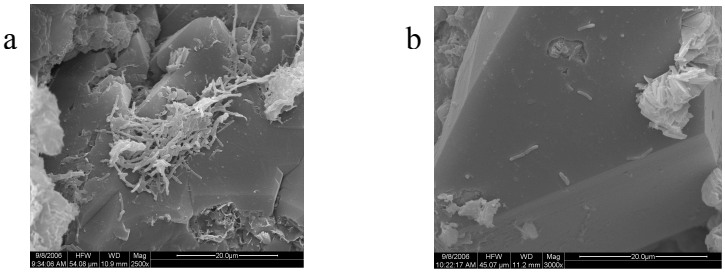


Fig. 2 The environmental scanning electron microscope images of bacteria DM-2 at the inlet section (a) and outlet section (b) of the core C2.

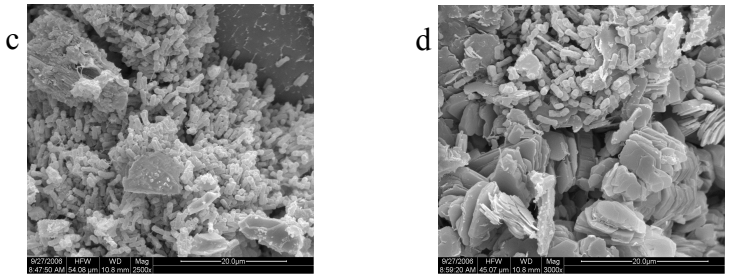


Fig. 3 The environmental scanning electron microscope images of bacteria F2 at the inlet section (c) and the middle section (d) of the core C3.

As shown in Fig. 2 and Fig. 3, the bacteria retention at the inlet section was substantially more than that at the middle or the outlet section, in agreement with what Sarkar et al. reported [4]. It indicated that log-jam effect or pore bridging may be the dominant mechanism of the bacteria retention. Thus, the increased applied pressure gradients may result in an increase in permeability as the deformable log-jams may be broken and the bacteria may be pushed deeper into the porous rock. It was proved by the fact that both the bacteria DM-2 and F2 could always be detected (plate count method) with the increasing injection pressure. In addition, the bacteria DM-2 could still be detected after the 12 PV of sterile water flooding (Fig. 1 B), indicating that there may be attachment-detachment process of bacteria at the surface of sandstone or oil.

2.2 Effect of flow velocity

The displacements were carried out with the core C1 and the bacteria DM-2 at 30°C. The concentration of cell suspension at the stationary phase was (3-6) × 10^8 cells/mL. The dry-heat sterilization was carried out to the core at 150°C for 3 h after the investigation at the flow velocity of 0.5mL/min, and then it was washed with 10 PV of sterile produced water prior to the experiment at the flow velocity of 0.2mL/min.

The values of C_e/C_i and K/K_i were both higher under the flow velocity of 0.5mL/min than those under 0.2mL/min (Fig. 4 C), indicating that the higher flow velocity facilitated the bacterial transport with a lower permeability impairment. Interesting, both the C_e/C_i and K/K_i at the initial stage of the sterile water flooding were higher than those at the end of bacteria flooding (Fig. 4). There was 20 to 30 min interval between the two displacements. Some bacterial coagulations or particle bridges that caused plugging of pores were relaxed and then may be partially disrupted by the subsequent flow. It further indicated that log-jam effect or pore bridging was the dominant mechanism of the bacteria retention, and the pulse injection (repeatedly starting and stopping injection) could enhance the transport of bacteria.

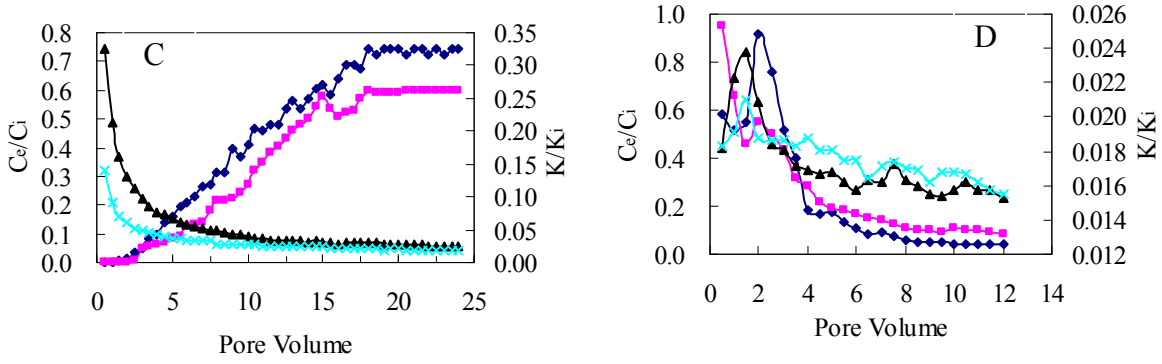


Fig. 4 The bacterial concentration ratio of effluent under the flow velocity of 0.5mL/min (◆) and 0.2mL/min (■) and the permeability ratio at 0.5mL/min (▲) and 0.2mL/min (×) during the bacteria flooding (C) and the subsequent sterile water flooding (D) at 30°C.

3. Conclusions

The increases in the bacterial cell size or flow velocity resulted in the enhanced bacterial transport and a lower permeability impairment of natural core. The bacteria are easier to migrate through the porous rock directionally compared to rigid solid particles owing to their organic flexibility. Bacteria retention occurred primarily at the inlet section of the natural core, and log-jam effect or pore bridging may be the dominant mechanism.

Acknowledgements

The author is grateful to the Research Institute of Oil Production Technology, Shengli Oilfield Ltd. Co. for the experimental samples provision and technical support, and also thanks their staff for the assistance with the experiments.

References

[1] L.R. Brown: Curr. Opin. M. Vol. 13 (2010), P. 316-320

[2] Q.K. Liu, J. Wang, G.Q. Li, T. Ma, F.L. Liang and R.L. Liu: Env. Sci. Vol. 29 (2008), P. 3554-3560 (in Chinese)

[3] X.P. Kong, Y.D. He, H.S. Zhang, X.L. Geng, P. Xu, X.L. Wang: J. Xi'an Shiyou University Vol. 21(6) (2006), P. 44-48 (in Chinese)

[4] A.K. Sarkar, G. Georgiou, M.M. Sharma: Biotech. Bio. Vol. 44(4) (1994), P. 489-497

© (2012) Trans Tech Publications, Switzerland
doi:10.4028/www.scientific.net/AMM.164.235

Properties and Application of a Novel Diarylethene Photochromism Material with a Naphthyl Ring

Liqin Wang[1, 2], Shouzhi Pu[1,*], Liushui Yan[2]

[1]Jiangxi Key Lab of Organic Chemistry, Jiangxi Science & Technology Normal University 330013, P.R. China.

[2]College of Environmental & Chemical Engineering, Applied Chemistry, Nanchang Hangkong University 330034, P.R. China.

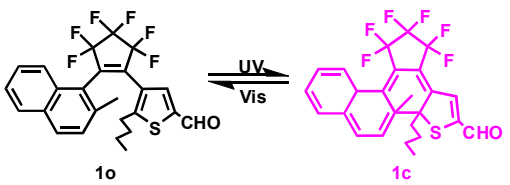
pushouzhi@tsinghua.org.cn

Keywords: Diarylethene, Fluorescence, Holographic optical recording.

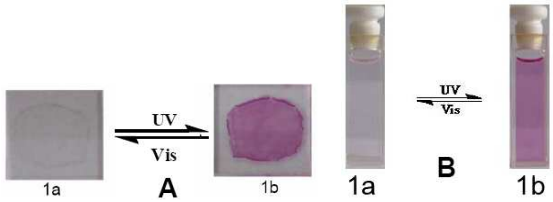
Abstract. A new unsymmetrical photochromic diarylethene 1-(2-methylnaphthyl)-2-(2-n-butyl-5-formyl-3-thienyl) perfluorocyclopentene (**1o**), was synthesized and its optoelectronic properties, such as photochromism in solution as well as in poly-methylmethacrylate (PMMA) amorphous films, and the fluorescence spectra of diarylethene **1o** were investigated. The diarylethene can be potentially used as holographic optical recording medium.

Introduction

Photochromism is of great interest in a variety of practical fields, including the development of optoelectronic devices, memories, and switches [1]. Among the photochromic compounds, diarylethenes are regarded as the best candidates for such devices, because of their advantages such as a high efficiency of photoisomerizations, sufficient thermal stability of both the open and the close forms, a very high resistance to photofatigue, and the ease with which the reaction can be monitored by UV-vis spectroscopy [2]. Diarylethene derivatives so far synthesized have hetero-aryl moieties such as thiophene, benzothiophene, thiazole, crysothiophene, and indole rings [3]. Their photochromic performance is strongly dependent on the aryl moieties. The diarylethene bearing naphthyl rings possesses excellent thermal stability, where the absorption intensity of its closed-ring isomer remains relatively constant for more than 500 h even at 343 K [4]. The majority of the research work has been devoted to the development of new molecules and investigative studies into their fundamental properties, and the results obtained have contributed to a broad understanding of the effects of substituents on the photochromism of diarylethenes [5]. Up to date, design and synthesis of new Photochromic compounds which is an active area of research [6]. In this Letter, we have investigated one asymmetrical photochromic diarylethene derivative bearing both naphthalene and thiophene moieties. The synthesized diarylethene is 1-(2-methylnaphthyl)-2-(2-n-butyl-5-formyl-3-thienyl)perfluorocyclopentene (**1o**). Its photochromic reactivity, fluorescence and photoinduced anisotropy and polarization multiplexed image recording are investigated in detail.



Scheme 1. Photochromism of 1o.

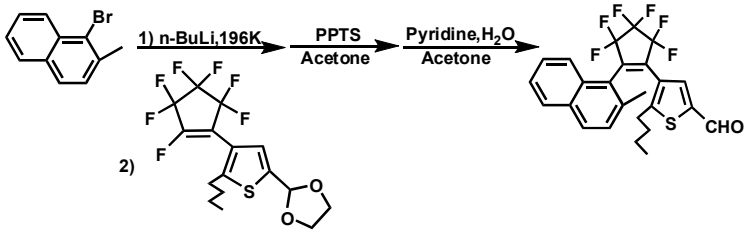


Scheme 2. Color changes for **1o** in PMMA (A) and in hexane (B).

Expriments

Synthsis of diarylethene 1a. The synthetic route for diarylethene **1o** was shown in Scheme 3 and its synthetic steps based on the similar procedure of Pu et al [7]. It optoelectronic properties, such as UV–Vis absorption spectra and fluorescence spectra were investigated in detail. Diarylethene **1o** was characterized by ^{1}H NMR spectroscopy. NMR spectra were recorded on Bruker AV400 (400MHz) spectrometer with $CDCl_3$ as the solvent. ^{1}H NMR ($CDCl_3$, 400 MHz, TMS): δ 0.95 (t, 3H, *J* = 7.5 Hz, $-CH_3$), 1.81 (s, 1H, -OH), 2.05 (t, 1H, $-CH_2$), 2.20 (s, 3H, $-CH_3$), 2.52 (m, 1H, $-CH_2$), 2.87 (m, 1H, $-CH_2$), 4.63 (d, 2H, J = 7.5 Hz, $-CH_2$-), 6.92 (s, 1H, thienyl-H), 7.41 (d, 1H, *J* = 7.5 Hz, naphthalene-H), 7.45 (m, 2H, naphthalene-H), 7.78 (t, 2H, *J* = 7.2 Hz, naphthalene-H).

Preparation of PMMA film. First of all, one hundred milligram of PMMA was dissolved in 10 ml chloroform, which was stirred ultrasonically to make it homogeneous. Samples were obtained by dissolving ultrasonically 10 mg of compounds **1o** with 1 ml of the PMMA solution, respectively, and the solution was spin-coated on a glass substrate with a spin rotation speed of 1500 rpm.



Scheme 3. Synthetic route for the compound **1o**.

Results and discussion

Photochromic behaviours. The absorption behavior of diarylethene **1o** induced by photoirradiation was examined at room temperature in hexane ($C = 2.0 \times 10^{-5}$ mol·L^{-1}) and in PMMA (10%, w/w). The absorption spectra of diarylethene **1o** in hexane and in PMMA were shown in Fig. 1. Irradiated with 297 nm UV light, the absorption peak of the open-ring isomer **1o** in hexane was observed at 271 nm ($\varepsilon_{max} = 2.45 \times 10^4$ L·mol^{-1}·cm^{-1}), the colorless solution changed to purple due to the decrease of the ring-open isomer, and a new absorption peak at visible region centered at 540 nm ($\varepsilon_{max} = 2.67 \times 10^3$ L mol^{-1}· cm^{-1}) was detected, which due to the formation of colored state **1c** [8]. When the purple solution was irradiated with visible light (λ > 500 nm), the purple color returned colorless and its spectrum became the same as that of original one. The quantum yields of cyclization and cycloreversion reaction of diarylethene **1o** were 0.13 and 0.11 at room temperature. Similar spectrum change of diarylethene **1o** was observed in PMMA film (Fig. 1B). Upon irradiation with 297 nm UV light, the colorless PMMA film turned purple with new broad absorption band centered at 544 nm for diarylethene **1o**, which assigned to the open-ring isomer changed to the closed-ring isomer. The absorption maximum of 1o was longer than those in solvent; it can be ascribed to the stabilization of molecular arrangement in solid state. The colored PMMA film can also return to colorless upon irradiation with appropriate wavelength visible light [9]. The colored PMMA film can also return to colorless upon irradiation with appropriate wavelength visible light.

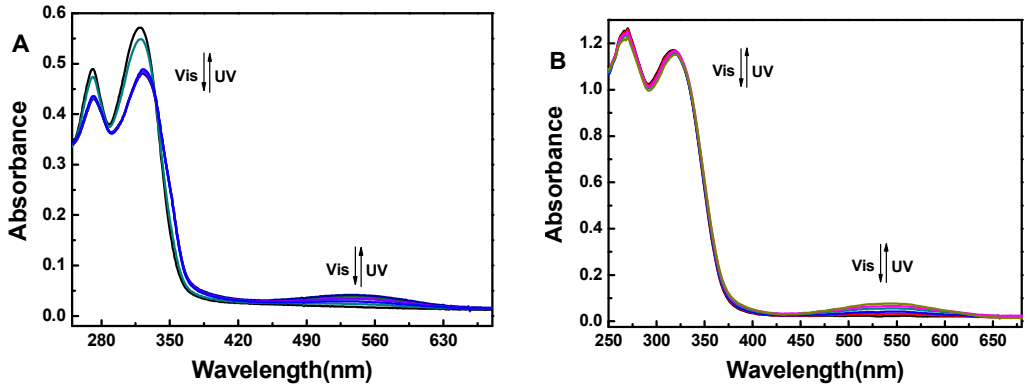


Fig.1. Absorption spectral and color changes of compound **1o** in hexane (A) and in PMMA (B).

Fluorescence of diarylethene. The fluorescence properties in the solution of the title compound were measured using a Hitachi F-4500 spectrophotometer, and the breadths of excitation and emission slit were selected 10.0 nm. The fluorescence excitation and emission spectra of **1o** in hexane at room temperature was illustrated. The results showed that diarylethene **1o** exhibited relatively weak fluorescence both in hexane solution and in PMMA film. The fluorescence spectras of diarylethenes **1o** were illustrated in Fig.2. We could clearly see that the fluorescent emissions of **1o** were at 393 nm in hexane and 445 nm in PMMA film. When it arrived at photostationary state, the emission intensities of diarylethenes **1o** were quenched to ca. 7.9% in hexane and ca. 25.2% in PMMA film. The fluorescence was efficiently quenched when the diarylethene unit converts from the open-ring to closed-ring form. The fluorescence intensity gradually decreased in proportion to the conversion from **1o** to **1c** [10]. The back irradiation with visible light of wavelength longer than 500 nm regenerated the open-ring forms and recovered the original emission spectra. Otherwise, the average times of "on" and "off" state shortened in proportion to the reciprocal power of radiated light by changing the power of the UV and visible light [11], indicating that the switching effect is perfect in hexane solution and in PMMA film.

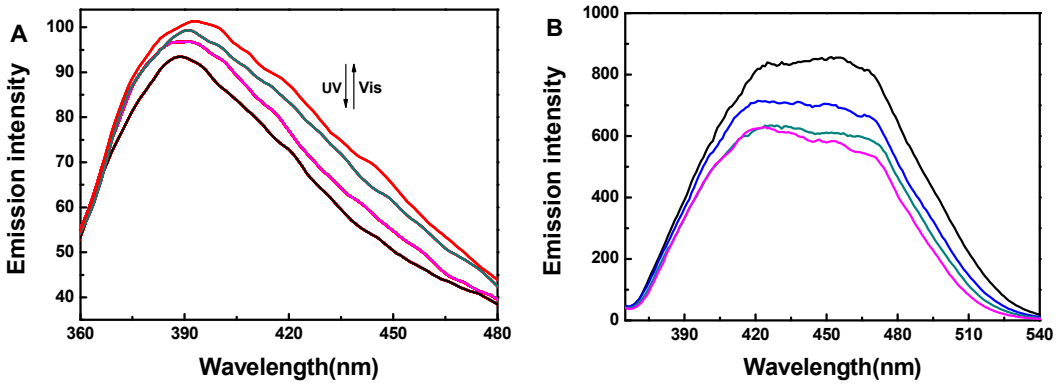
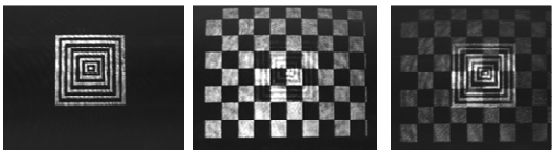


Fig. 2. Fluorescence intensity changes of **1o** in hexane(A) and in PMMA(B) .

Photoinduced anisotropy and polarization multiplexed image recording. Based on the photochromic and photo-induced anisotropic properties of diarylethene **1o**, we proposed an application as polarization pattern display. Readout patterns with the three types of polarization holographic optical recording are shown in Fig. 3. As shown in Fig. 3(a), we can see that the copolarization holographic recording obtains high diffraction efficiency as well as high scattering noise when the intensities of the recording wave and the readout wave are fixed. Fig. 3(b) shows the observed pattern by just using cross-polarization light for readout. Under the experimental condition, the angle between the polarization direction of P and the horizontal direction is 0 °. The result indicated that cross-polarization holographic recording obtains low diffraction efficiency as well as low scattering noise when the intensities of the recording wave and the readout wave are fixed. If the

polarization of P is 45 °, from the horizontal direction, only the vertical polarization light patterns can pass through the A-diarylethene-P system. Thus, the readout pattern is like Fig. 3(c). By this way, two polarization patterns can be hidden in the pattern and recorded in the diarylethene **1c**/PMMA film based on its photochromic and photoinduced anisotropic properties, and only readout with two orthogonal polarizers at certain polarization angles can pick up the patterns separately [12,13].



(a) (b) (c)

Fig. 3. Readout patterns from the film.

Conclusion

In conclusion, diarylethene **1o** changed the color from colorless to purple upon irradiation with 297 nm UV light, in which absorption maxima were observed at 540 nm in hexane and at 544 nm in PMMA. Diarylethene **1o** showed weak fluorescence intensity in hexane solution and in PMMA, the emission intensities of diarylethenes **1o** were quenched to ca. 7.9% in hexane and ca. 25.2% in PMMA film. Polarization multiplexed images was performed successfully in diarylethene **1c**/PMMA film, which illustrated that the diarylethene can be potentially used as holographic optical recording medium.

Acknowledgment

This work was supported by Program for the NSFC of China (20962008), the Project of Jiangxi Academic and Technological leader (2009DD00100) and the Science Funds of the Education Office of Jiangxi, China (GJJ09646).

References

[1] T.I. Maria, C. Stefano, G. Marco, C. Claudio, R. Marcella and S. Franco: J. Am. Chen. Soc Vol. 130 (2008), p. 7286.

[2] J.J. Liu, Y. Xu, X.C. Li and H. Tian: Dyes Pigments Vol. 76 (2008), p. 294.

[3] T.S.Yang, S.Z.Pu, C.B.Fan and G.Liu: Spectrochimica Acta Part A Vol. 70 (2008), p. 1065.

[4] K. Uchida, S. Nakamura and M. Irie: Res. Chem. Intermed Vol. 21 (1995), p. 861.

[5] S.Z. Pu, C.B. Fan, W.J. Miao and G. Liu: Dyes Pigments Vol. 84 (2009), p. 25.

[6]S.Z. Pu, C.B. Fan, W.J. Miao and G. Liu: Tetrahedron Vol. 64 (2008), p. 9464.

[7] R.J. Wang, S.Z. Pu, G. Liu, W. J.Liu and H.Y.Xia: Tetrahedron Lett Vol. 52 (2011), p. 3306.

[8] K. Kasatani, S.Kambe and M.Irie: J. Photochem. Photobiol. A: Chem Vol. 122 (1999), p. 11.

[9] K. Morimitsu, K. Shibata, S. Kobatake and M. Irie: J. Org. Chem Vol. 16 (2002), p. 4574.

[10] S.Z. Pu, W.J. Liu and W.J. Miao: J. Phys. Org. Chem Vol. 22 (2009), p. 954.

[11] S.Z. Pu, M. Li, C.B. Fan, G.Liu and L. Shen: J. Mol. Struc Vol. 919 (2009), p. 100.

[12] B.L. Yao, Y.L. Wang, M.Lei, N. Menke and G.F. Chen: Opt. Soc. of Am. Vol. 17 (2005), p. 20.

[13] S.Z. Pu, B.L. Yao, G. Liu, and Y.L. Wang: Opt. Eng. Vol. 57 (2008), p. 030502-1.

© (2012) Trans Tech Publications, Switzerland
doi:10.4028/www.scientific.net/AMM.164.239

Photochromism material of new unsymmetrical isomeric diarylethenes bearing a thiophene and pyridine unit

Ming Liu, Gang Liu*, Shiqiang Cui

Jiangxi Key Laboratory of Organic Chemistry Jiangxi Science and Technology Normal University Nanchang 330013, P. R. China

Liugang0926@163.com

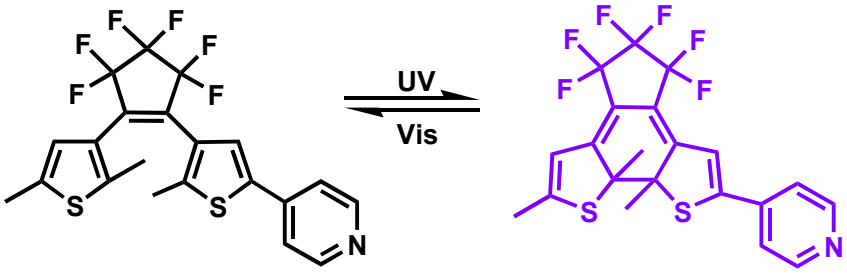
Keywords: Diarylethene; Photochromism; Fluorescence; Optical recording

Abstract. A new photochromic diarylethene compound, 1-(2,5-dimethyl-3-thiophene)-2-[5-(4-pyridine)-2-methyl-3-thienyl]perfluorocyclopentene(1a) was synthesized. its photochromic and fluorescent properties have been investigated in detail. The results of the research showed that it has shown good photochromic behavior and fluorescence switch in solution and PMMA film. Finally, photo-mode rewritable optical storage using 1b was performed. The images demonstrated that the compound can be used as optical storage material.

Introduction

Photochromic molecules attract much attention from fundamental as well as practical points of view because of their potential for applications to optical devices, such as optical memories and switches [1-3]. Among the photochromic compounds, diarylethenes are regarded as the best candidates for such devices, owing to its excellent thermal stability, fatigue resistance, and easy monitoring using UVevis spectroscopy [4,5]. As components of molecular electronics, it is desirable to develop various types of molecular switch devices with diarylethene compounds. During the past decades, there have been important achievements in the synthesis of new families of organic photochromic molecules [3,6,7].

In the present work, we synthesized a photochromic diraylethene 1-(2,5-dimethyl-3-thiophene)-2-[5-(4-pyridine)-2-methyl-3-thienyl]perfluorocyclopentene(1a). Its photochromic reactivity, fluorescence property and application for optical recording were investigated in detail. The photochromic reaction of diarylethene 1a is shown in Scheme 1.



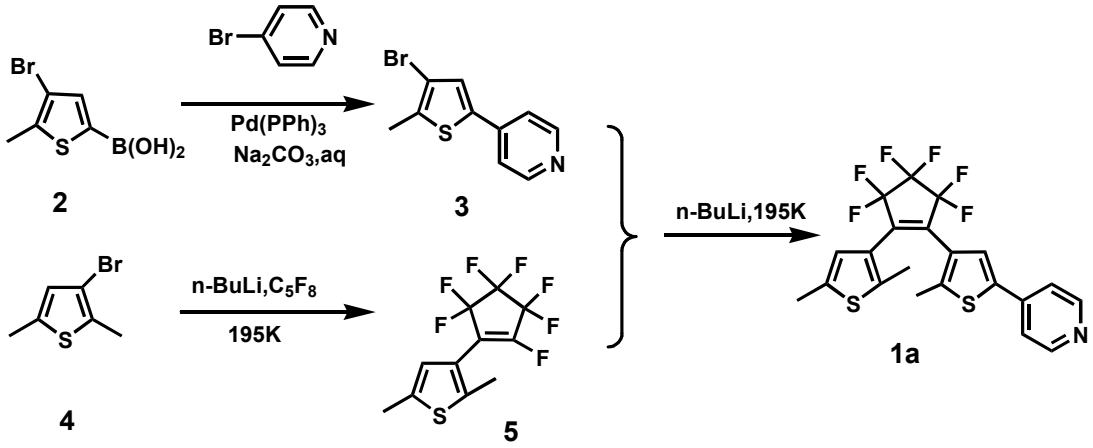
Scheme 1. Photochromism of diarylethene 1.

Experimental

The diarylethene 1a of synthetic route is shown in Scheme 2. It was synthesized according to the similar procedure of Pu et al. [8]. Firstly, compound 3 was prepared by reacting compound 2 with 4-bromopyridine in the presence of tetrakis(triphenylpho-sphine)palladium(0) and Na_2CO_3 in THF for 16h at 343K. Secondly, under an argon gas atmosphere, compound 4 was dissolved in THF and n-butyl lithium hexane solution was added at 195K. Stirring was continued for 30 min at this low temperature; octafluorocyclopentene was added and the mixture was stirred for 2h at this temperature. he reaction mixture was extracted with diethyl ether, dried with anhydrous $MgSO_4$, filtered, and evaporated in vacuo, then purified by column chromatography to give compound 5

(2,5-dimethylthiophene-3-perfluorocyclopenten) colorless transparent liquid. Finally, To a stirred THF solution of compounds 3 was slowly added a 2.5M n-BuLi/hexane solution at 195K under an argon atmosphere. After 30 min, compound 5 was added and the mixture was stirred for 2h at this temperature. The reaction mixture was extracted with diethyl ether, dried with anhydrous $MgSO_4$, filtered, and evaporated in vacuo, then purified by column chromatography to give 1a solid in 38% yield. The structure of 1a was characterized by ^1H NMR, ^{13}C NMR.

The structure of 1a was characterized by ^1H NMR. ^1H NMR (400 MHz, $CDCl_3$, ppm): δ 1.84 (s, 3H, -CH_3), 1.94 (s, 3H, -CH_3), 2.44 (s, 3H, -CH_3), 6.73 (s, 1H, thiophene-H), 7.40 (t, 1H, pyridine-H), 7.47 (s, 2H, thiophene-H), 8.59 (d, 2H, pyridine-H). ^{13}C NMR (400 MHz, CDCl3): δ 14.3, 14.8, 15.1, 119.5, 124.3, 124.5, 124.9, 126.6, 138.1, 138.7, 139.8, 140.4, 143.6, 150.4.



Scheme 2. Synthetic route for the compound 1a

Result and Discussion

Photochromism of diarylethene. The photochromic behaviours of diarylethenes 1 induced by photoirradiation at room temperature were measured both in hexane (2.0×10^{-5} mol/L) and in PMMA amorphous film (10%, w/w). In hexane, the absorption spectral changes of diarylethene 1 induced by alternating irradiation with UV light and visible light with appropriate wavelength are shown in Fig. 1. The absorption maximum of diarylethene 1o was observed at 294 nm in hexane (ε, 1.21×10^4 L mol^{-1} cm^{-1}), which arose from π–π* transition [9]. Upon irradiation with 297 nm light, the colorless solution of 1a turned purple, in which the absorption maximum was observed at 545 nm (ε, 5.75×10^3 L mol^{-1} cm^{-1}). The purple color was due to the formation of the closed-ring isomer 1b.

In PMMA amorphous film, diarylethene 1a has also shown good photochromism. Upon irradiation with 313 nm UV light, the colorless PMMA film changed to purple, and a new absorption band appeared at 567 nm, which was assigned to the formation of the closed-ring isomer 1b, the colored PMMA film can invert to colorless on irradiation of appropriate wavelength visible light (λ>500 nm). The red shift of the maximum absorption of 1b in PMMA film in comparison with those in hexane solution could be mainly ascribed to the molecular arrangement in solid state is more stable than in solution [10]. In addition, it was also found that both open-ring isomer and closed-ring isomer of diarylethene 1 were stable at room temperature in darkness.

Fluorescence of diarylethene. The fluorescence intensity of diarylethene 1a decreased dramatically along with the photochromism from open-ring isomer to closed-ring isomer upon irradiation with 305 nm light in hexane ($C = 5.0\times10^{-5}$ mol·L^{-1}) and in PMMA. As shown in Fig. 2, when irradiated by light of 297 nm, the photocyclization reaction was carried out and the non-fluorescent closed-ring form of the compound were produced. The back irradiation by appropriate wavelength visible light (λ > 500 nm) regenerated the open-ring forms of diarylethene 1a and recovered the original emission spectra. The incomplete cyclization reaction and the existence of parallel conformations may be the main cause for the moderate change in fluorescence induced by photoirradiation [11]. The back irradiation by appropriate wavelength visible light regenerated its

open-ring isomer and recovered the original emission intensity. This merit can be potentially applied to optical memory with fluorescence readout method [12]. In Fig. 2, we can know that the maximum emission intensity was observed at 362 nm in hexane and at 392 nm in PMMA.

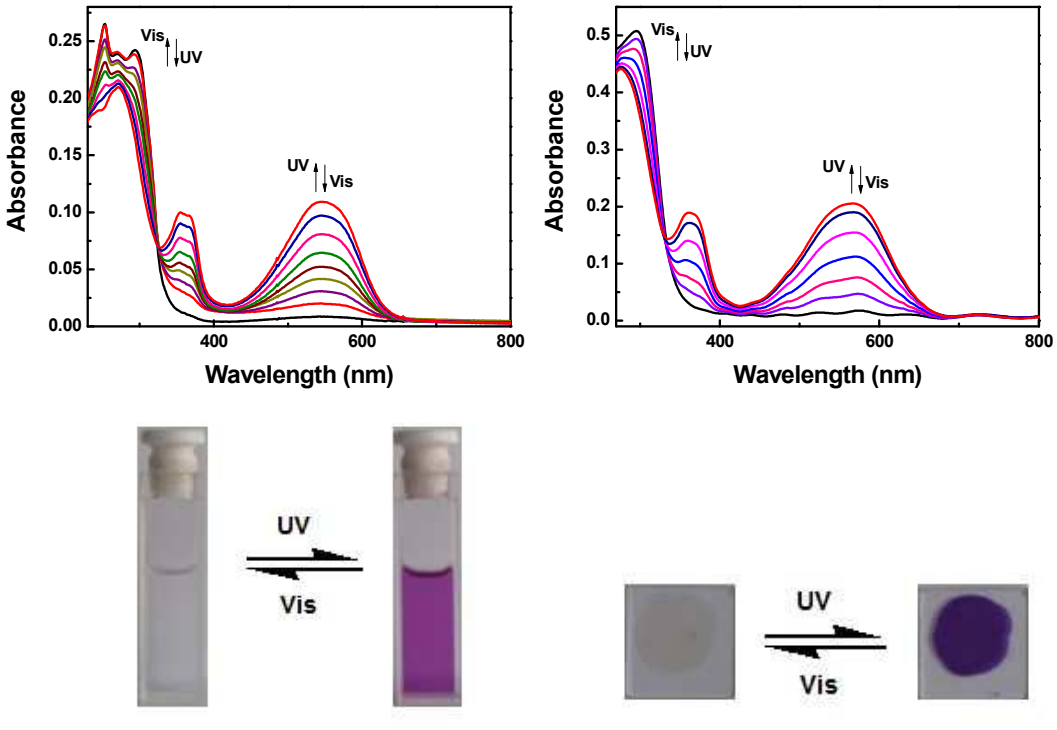


Figure 1. Absorption spectral changes of compound 1a in hexane (2.0×10^{-5} mol/L) and (B) in PMMA film (10%, w/w)

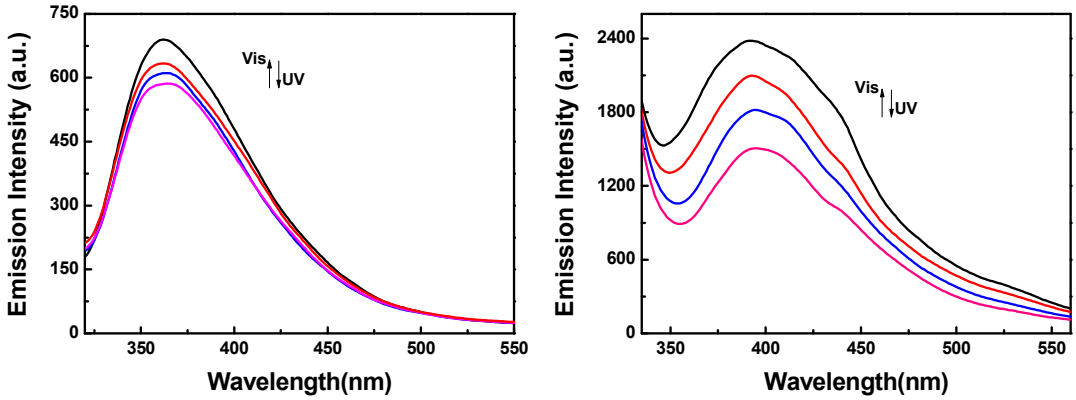


Figure 2. Emission intensity changes of diarylethene 1a in hexane (A) and in PMMA (10%, w/w)(B) upon irradiation with 297 nm UV light.

Rewritable Optical Storage. He-Ne laser beam by the solid immerse lens. As shown in Fig. 3, the quality of images recorded in 1b/PMMA film showed a clear contrast and without cross talk, which are important in rewritalbe data storage. With UV light, the recorded images can be erased completely, and no marked degradation in resolution of reconstructed image after 10 write/erase cycles was detected.

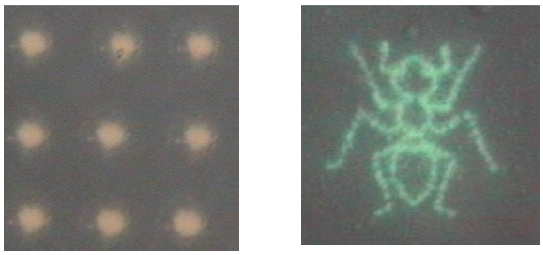


Figure 3. Rewritable optical images on diarylethene 1b/PMMA film.

Summary

A new symmetrical photochromic diarylethene was synthesized and its photochromic properties were investigated. And fluorescent properties were also investigated. The results showed that this compound exhibited reversible photochromism both in solution and in PMMA amorphous film. The fluorescence intensity decreased along with the photochromism upon irradiation with 297 nm light. Rewritable holographic optical storage was performed successfully using 1b as recording medium. This technique is useful for realizing high-density rewritable optical recording with photochromic diarylethene materials.

Acknowledgment

This work was supported by the Project of Natural Science Foundation of Jiangxi Province(2010DQ00200) and the Science Funds of Jiangxi Education Office (GJJ1067).

References

[1] M. Irie: Chem. Rev. Vol. 100 (2000), p. 1685

[2] C. Yun, J. You, J. Kim, J. Huh and E. Kim: J. Photochem. Photobiol., C Vol. 10 (2009), p. 111

[3] H. Tian and S.J. Yang: Chem. Soc. Rev. Vol. 33 (2004), p. 85

[4] H. Tian, B. Chen, H. Tu and K. Müllen: Adv. Mater. Vol. 14 (2002), p. 918

[5] F.M. Raymo and M. Tomasulo: Chem. Soc. Rev. Vol. 34 (2005), p. 327

[6] K. Matsuda and M. Irie: Chem. Lett. Vol. 35 (2006), p. 1204

[7] H. Tian and S. Wang: Chem. Commun. (2007), p. 781

[8] G.Z. Li, T. Zheng, S.Z. Pu and J.K. Xu: Acta Cryst. Vol. 62 (2006), p. 2877

[9] Z.X. Li, L.Y. Liao, W. Sun, C.H. Xu, C. Zhang, C.J. Fang and C.H. Yan: J. Phys.Chem. C Vol. 112 (2008), p. 5190

[10] K. Kasatani, S. Kambe and M. Irie: J. Photoch. Photobiol. A. Chem. Vol. 122 (1999), p. 11

[11] C.B. Fan, S.Z. Pu, G. Liu, and T.S. Yang: J. Photoch. Photobiol. A. Vol. 194 (2008), p. 333

[12] T.B. Norsten and N.R. Branda: J. Am. Chem. Soc. Vol. 123 (2001), p. 1784

© (2012) Trans Tech Publications, Switzerland
doi:10.4028/www.scientific.net/AMM.164.243

Synthesis a New Function Materials and Photochromic Properties of Diarylethene Bearing a Naphthalene and Isoxazole Moiety

Renjie Wang, Shiqiang Cui, Shouzhi Pu*

Jiangxi Key Laboratory of Organic Chemistry, Jiangxi Science and Technology Normal University, Nanchang 330013, P. R. China

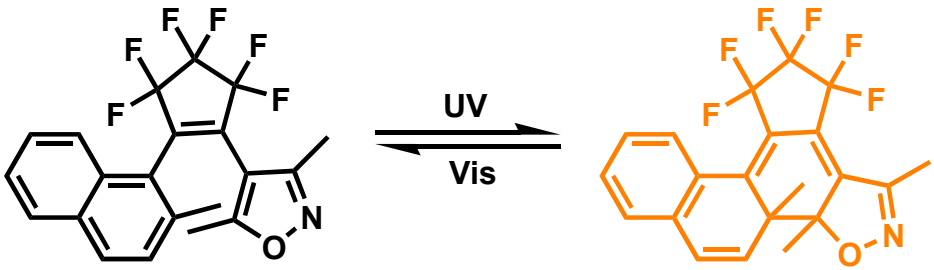
pushouzhi@tsinghua.org.cn

Keywords: Diarylethene; Photochromism; Fluorescence; naphthalene, isoxazole.

Abstract. A new photochromic diarylethene compound 1-(2-methylnaphthyl)-2-(3, 5-dimethyl-4-isoxazolyl)perfluorocyclopentene (**1o**), was synthesized and its photochromic and fluorescent properties were investigated. Diarylethene 1o changed the color from colorless to yellow upon irraditation with 297 nm UV light, which the absorption maxima were observed at 446 nm in hexane solution. The kinetic experiments indicated that the cyclization/cycloreversion process of the compound was determined to be the zeroth/first order reaction in hexane solution. The fluorescence intensity decreased along with the photochromism upon irradiation with 297 nm light and its closed-ring isomer showed weak fluorescence.

Intorduction

Currently, organic photochromic materials have received considerable attention because of their potential for photonic applications such as optical storage materials, photoswitches, and organic semiconductor devices [1-3]. To date, various types of photochromic compounds such as diarylethenes [4], fulgides [5], and phenoxynaphthacenequinines [6, 7], have been developed in an attempt to satisfy the requirements of these optoelectric devices. Among the reported photochromic systems, photochromic diarylethenes are the most promising candidates for such applications because of their good thermal stability, excellent fatigue resistance, rapid response, and high reactivity in the solid state [1, 8-10]. In order to research the diarylethene with excellent properties, a larger number of diarylethenes molecules were designed and synthesized. Previously, design and synthesize new diarylethenes which have new different aryl moieties is very important and significant.



Scheme 1. Photochromism of dithienylethene **1o**.

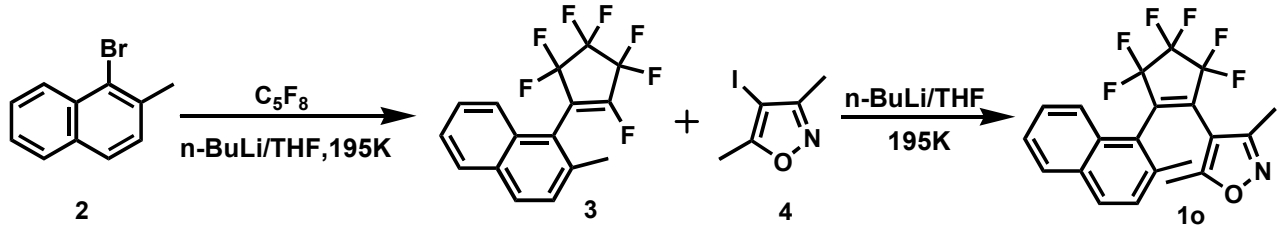
Generally, the photochromic performance of each kind of diarylethene is strongly dependent on the aryl moieties. The nature of the heteroaryl moieties greatly influences the photo-reactivity and the distinguishable features of diarylethenes. For example, diarylethenes with thiophene/benzothiophene moieties have good thermal stability and remarkable fatigue-resistance [4,11,12], whereas diarylethenes bearing two pyrrole groups is thermally unstable and returns to the open-ring isomers even in the dark [13]. In addition, the relationship between the thermally irreversible photochromic reaction and aryl groups aromatic stabilization energy are much closed, when the aryl groups have low aromatic stabilization energy the diarylethene derivatives can undergo thermally irreversible photochromic reactions [14]. However, in our previous paper, we reported diarylethene derivatives having naphthalene, thiophene and unsymmetrical six-membered at the heteroaryl moieties, and all of them are exhibited good photochromic, obvious fluoresce and notable fatigue resistance [15-17].

Especially, naphthalene is a particular aryl because it own high aromatic stabilization energy, but diarythenes who bearing naphthyl have good thermal stability even at 343 K [18]. Therefore, explore and further study photochromic diarylethenes base on naphthalene is very attractive and necessary. In this study, we explore a new asymmetrical diarylethene bearing both naphthalene and isoxazole moieties. The synthesized diarylethenes are 1-(2-methylnaphthyl)-2-(3, 5-dimethyl-4-isoxazolyl)perfluorocyclopentene **1o**, which photochromic and fluorescence properties were studied detail. The photochromic reaction of diarylethenes **1o** is shown in Scheme 1.

Experiment

Synthesis of diarylethene 1o. The synthetic route for diarylethenes **1o** is shown in Scheme 2. Firstly, 2-methyl-1-bromonaphthalene **2** was lithated and coupled with octaperfluorocyclopentene to give 2-methyl-1-naphthyl-perfluorocyclopentene **3** [17]. Thencompounds **4** were separately lithiated and then coupled with compound **3** to give diarylethenes **1o**. The structures of diarylethenes **1o** were were confirmed by elemental analysis, NMR, and IR. ^{1}H NMR (400 MHz, $CDCl_3$, TMS): Mp 145–146℃, Calcd for $C_{21}H_{15}F_6NO$ (%): Calcd C, 61.32; H, 3.68. Found C, 61.32; H, 3.68; ^{1}H NMR (400 MHz, $CDCl_3$, TMS): δ 1.85 (s, 3H, $-CH_3$), 2.11 (s, 3H, $-CH_3$), 2.38 (s, 3H, $-CH_3$), 7.12 (d, 1H, naphthalene–H, J = 8.0 Hz), 7.21 (t, 1H, naphthalene–H, J = 8.0 Hz), 7.30 (d, 2H, naphthalene–H, J = 8.0 Hz), 7.42 (d, 1H, naphthalene–H, J = 8.0 Hz), 7.46 (d, 1H, naphthalene–H, J = 8.0 Hz); ^{13}C NMR (100 MHz, $CDCl_3$, TMS): δ = 11.08, 12.36, 20.67, 103.74, 122.11, 124.11, 125.89, 126.97, 128.47, 128.52, 130.50, 131.40, 131.90, 135.25, 158.64, 169.16; IR (KBr, ν, cm^{-1}): 472, 518, 576, 599, 646, 747, 766, 811, 848, 874, 985, 1056, 1097, 1144, 1193, 1278, 1343, 1400, 1510, 1630, 3235, 3436.

Preparation of PMMA film. One hundred milligram of PMMA was first dissolved in 1 mL chloroform, which was stirred ultrasonically to make it homogeneous. Samples were obtained by dissolving ultrasonically 10 mg of compounds **1** with 1 mL of the PMMA solution, respectively, and the solution was spincoated on a glass substrate with a spin rotation speed of 1500 rpm.



Scheme 2. Synthetic route for diarylethene **1o**.

Results and discussion

Photochromismof diarylethene 1o. The photochromic behaviors of diarylethene **1o** in hexane (5.0×10^{-5} mol/L) induced by photo-irradiation at room temperature are shown in Figure 1. Figure 1A shows absorption spectral changes of **1** in hexane solution (5.0×10^{-5} mol · L^{-1}). The hexane solution of the open-ring isomer **1o** was colorless without absorption in the visible region and the maximum absorption of its colorless open-ring isomer **1o** was observed at 266 nm ($\varepsilon = 6.58 \times 10^3$ mol · L^{-1} · cm^{-1}). The color of the hexane solution turned yellow when irradiation with 297 nm UV light, in which the absorption maximum was observed at 446 nm (ε, 5.9×10^3 mol^{-1} dm^3 cm^{-1}). When the yellow solution was irradiated with visible light ($\lambda > 500$ nm), the yellow color returned colorless and its spectrum become the same as that of original state. Additionally, the photoconversion ratios from open-ring to closed-ring isomers of the five derivatives were analyzed by HPLC in hexane in photostationary state, and with the values were 26% are shown in Figure 1B.

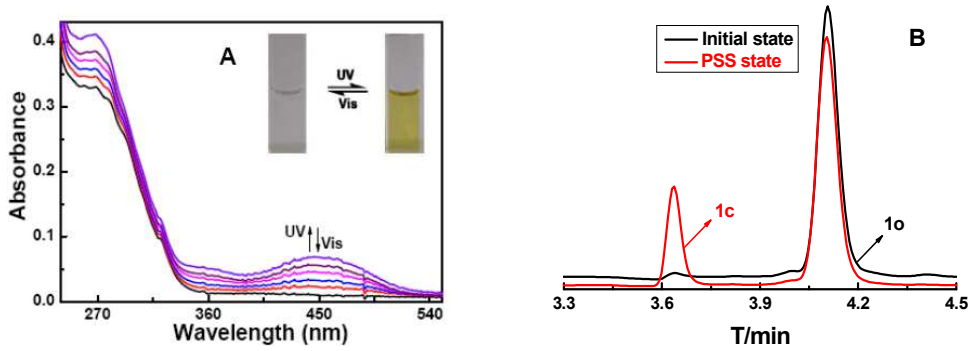


Figure 1. Absorption spectral and color changes of compound **1** in hexane (A) and the photoconversion ratios of diarylethenes **1** in photostationary state (B).

Photochromic reaction kinetics in hexane solution. The photochromic cyclization/cycloreversion kinetics of **1o** in hexane were determined by UV-Vis spectra upon alternating irradiation with UV and appropriate wavelength visible light at room temperature. The cyclization and cycloreversion curves of **1o** were shown in Figure 2. It can be seen that the relationships between the absorbance and exposal time have good linearity upon irradiation with 297 nm UV light. It is demonstrating that the cyclization processes of 1o belong to the zeroth order reaction when open-ring isomer changed to closed-ring isomer. The slope of every line in Figure 2(A) and Figure 2(B) represents the reaction rate constant (k) of diarylethene 1o in hexane. So all k of cyclization/cycloreversion process ($k_{o\text{-}c}$, 10^{-3}) of diarylethene 1o can be easily obtained, which are 4.8 s^{-1} and 5.28 s^{-1} in solution, respectively. As shown in Figure 2(B), during the cycloreversion of **1c**, the relationship between –log(Abs) and exposal time also behave perfect linearity, indicating that the cycloreversion process belong to the first order reaction.

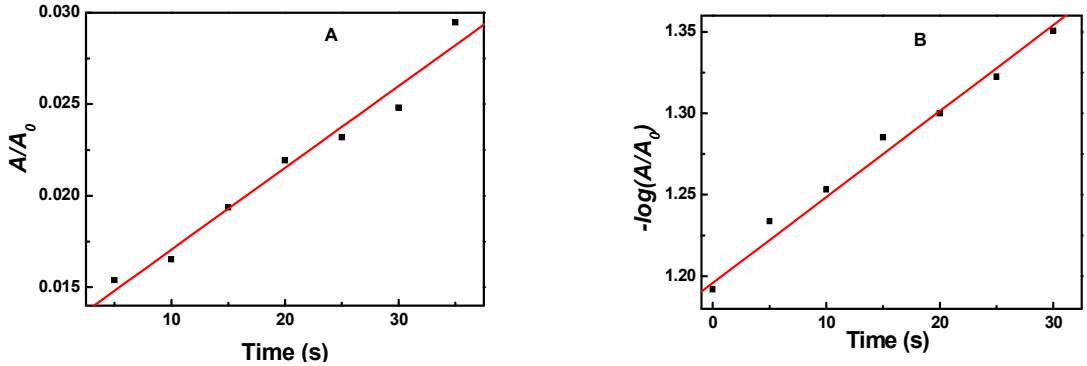


Figure 2. The kinetics of compound **1o** in hexane: (A) cyclization; (B) cycloreversion.

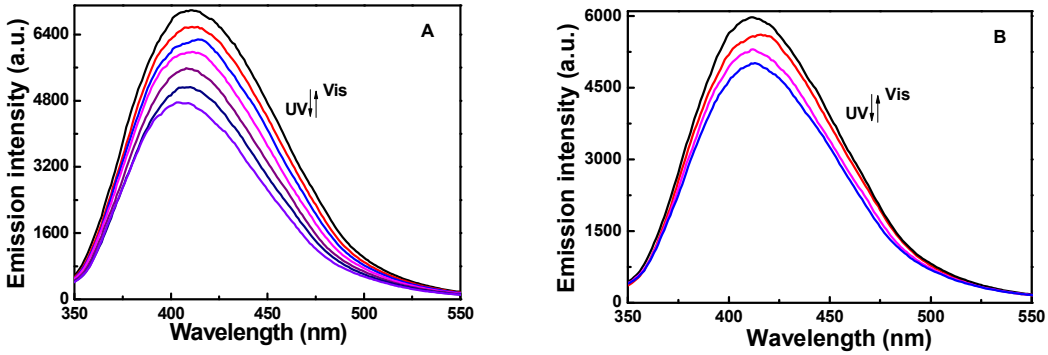


Figure 3. Fluorescence spectra of diarylethene **1o** in hexane (A) and in PMMA film (B) excited at 300 and 307 nm, respectively.

Fluorescence of diarylethene 1o. The fluorescence spectra of diarylethenes **1o** in hexane and PMMA film at room temperature are illustrated in Figure 3. It could be clearly seen that the fluorescence intensity of diarylethene **1** decreased dramatically with the photochromism from

open-ring isomer to closed-ring isomer both in hexane solution and in PMMA film along when irradiation with 297 nm light. The fluorescence emission of **1o** was observed at 411 nm in solution and 412 nm in PMMA film. The back irradiation by appropriate wavelength visible light regenerated its open-ring isomer and recovered the original emission intensity. When arrived at the photostationary state, the emission intensity of diarylethene **1o** was quenched to ca. 32% and 16% in solution and PMMA film, respectively. The phenomenon indicated that cyclization reaction is incomplete and the existence of parallel conformation may be the main cause for the change in fluorescence intensity [19].

Summary

A new photochromic diarylethene with naphthalene and isoxazole skeleton was synthesized and the results indicated that the diarylethene has good photochromic properties and fluorescent switch behavior. In addition, the photochromic reaction kinetics was also studied, and the results demonstrated that the cyclization processes of **1** belong to the zeroth order reaction and the cycloreversion process belongs to the first order reaction. The compound exhibited fluorescence switches accompany the cyclization reaction occurs when excited at 300 nm in hexane solution and 307 nm in PMMA film.

Acknowledgment

This work was supported by Program of New Century Excellent Talents in University (NCET-08-0702), the Project of Jiangxi Academic and Technological leader (2009DD00100), and the Project of the Science Funds of Jiangxi Education Office (GJJ09646 and GJJ11026).

References

[1] H. Tian and S.J.Yang: Chem. Rev. Vol. 33 (2004), p. 85
[2] C. Yun, J. You, J. Kim, J. Huh and E. Kim: J. Photochem. Photobiol. C Vol.10 (2009), p. 111
[3] T. Tsujioka and M. Irie: J. Photochem. Photobiol. C Vol. 11 (2010), p. 1
[4] M. Irie: Chem. Rev. Vol. 100 (2000), p. 1685
[5] Y. Yokoyama: Chem. Rev. Vol. 100 (2000), p. 1717
[6] F. Buchholtz, A. Zelichenok and V. Krongauz: Macromolecules, Vol. 26 (1993), p. 906
[7] A.J. Myles and N.R. Branda: J. Am. Chem. Soc. Vol. 123 (2001), p. 177
[8] M. Morimoto and M. Irie: Chem. Commun. 2005, p. 3895
[9] X.C. Li and H. Tian: Tetrahedron Lett. Vol. 46 (2005), p. 5409
[10] L. Giordano, T.M. Jovin, M. Irie and E.A. Jares-Erijman: J. Am. Chem. Soc. Vol. 124 (2002), p. 7481
[11] S. Kobatake, K. Shibata, K. Uchida and M. Irie: J. Am. Chem. Soc. Vol. 122 (2000), p. 12135
[12] S. Kobatake, M. Yamada, T. Yamada and M. Irie: J. Am. Chem. Soc. Vol. 121 (1999), p. 8450
[13] K. Uchida, T. Matsuoka, K. Sayo, M. Iwamoto, S. Hayashi and M. Irie: Chem. Lett. Vol. 8 (1999), p. 835
[14] T. Yamaguchi and M. Irie: Tetrahedron Lett. Vol. 47 (2006), p. 1267
[15] R.J. Wang, S.Z. Pu, G. Liu, S.Q. Cui and W.J. Liu: Tetra. Lett. Vol. 53 (2012), p. 320
[16] K. Uchida, S. Nakamura and M. Irie: Res. Chem. Intermed. Vol. 21 (1995), p. 861
[17] R.J. Wang, S.Z. Pu, G. Liu, W.J. Liu and H.Y. Xia: Tetra. Lett. Vol. 52 (2011), p. 3306
[18] S.Z. Pu, M. Li, G. Liu and Z.G. Le: Aust. J. Chem. Vol. 62 (2009), p. 464
[19] C.B. Fan, S.Z. Pu, G. Liu and T.S. Yang: J. Photoch. Photobiol. A Vol. 194 (2008), p. 333

© (2012) Trans Tech Publications, Switzerland
doi:10.4028/www.scientific.net/AMM.164.247

Synthesis and Properties of A Novel Photochromic Diarylethene Material Bearing Two Five-membered Aryl Unit

Xiaoting Li, Hui Li, Shouzhi Pu*

Jiangxi Key Laboratory of Organic Chemistry, Jiangxi Science and Technology Normal University

Nanchang 330013, P.R. China.

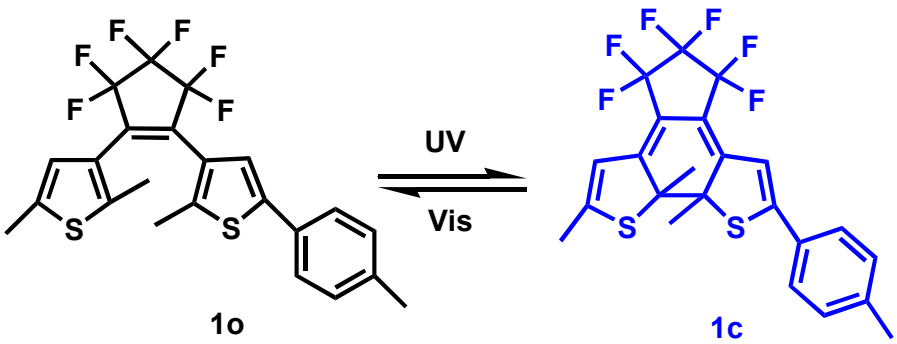
pushouzhi@tsinghua.org.cn

Keywords: Diarylethene, Photochromism, Fluorescence, Optical recording.

Abstract. A new unsymmetrical photochromic diarylethene, 1-(2,5-dimethyl-3-thienyl)-2-(2 -methyl-5-p-tolyl-3-thienyl)perfluorocyclopentene (1) was synthesized, and its photochromic and fluorescence properties were investigated. The results showed the compound exhibited good photochromism in hexane solution and in PMMA amorphous film with alternating irradiation by UV/Vis light, the maxima absorption of its closed-ring isomer 1c are 541 nm and 551 nm respectively. The open-ring isomer of the diarylethene 1 exhibited relatively strong fluorescence at 360 nm in hexane solution (5×10^{-5} mol/L) when excited at 305 nm. The fluorescence intensity decreased along with the photochromism upon irradiation with 297 nm light. The fluorescence intensity of diarylethene 1o also depended on the concentration. When the concentration of diarylethene 1 in hexane increase from 1×10^{-6} mol/L to 1×10^{-3} mol/L, the fluorescence intensity of the open-ring isomer become strong first, then become weak.

Intorduction

Holographic optical recording has attracted much attention in recent years because of its advantages of large capacity and high data transfer rate [1]. To a great extent, the performance of holographic system depends on the properties of the recording media, and the lack of suitable recording materials has long been an obstacle to the development of holographic recording [2,3]. To date, various types of photochromic compounds have been synthesized. Among these compounds, photochromic diarylethenes have attracted much attention as highly promising candidates for these applications because of the excellent properties, such as thermal stability of the respective isomers, notable fatigue resistance, and high reactivity in the solid state [4-8]. These diarylethenes derivatives bearing two thiophene or benzothiophene rings are regarded as the best candidates for photonics application such as optical memory [9] and switch [10]. In this study, a new unsymmetrical photochromic diarylethene compound, 1-(2,5-dimethyl-3-thienyl)-2-(2-methyl-5-p-tolyl-3-thienyl)perfluorocyclopentene(1), was synthesized and its photochemical and fluorescence properties, such as photochromism in solution as well as in PMMA amorphous film, and concentration effection properties were investigated in detail.

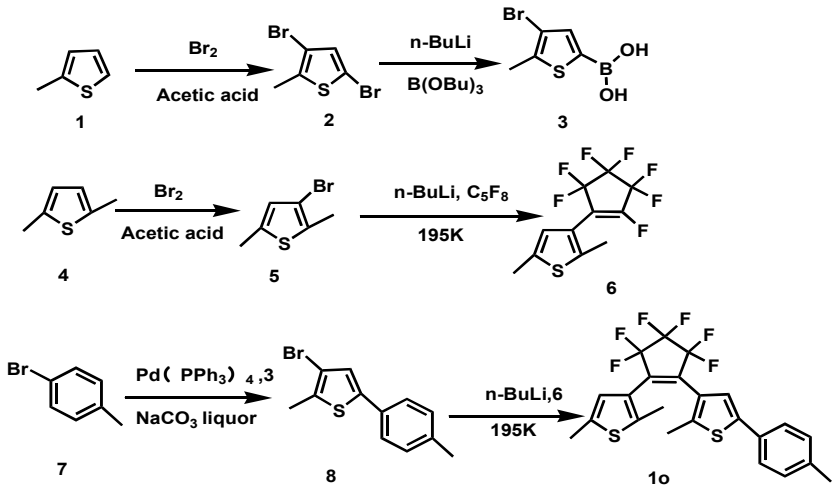


Scheme 1. Photochromism of diarylethenes 1o.

Experiment

Synthesis of Diarylethene 1o. The synthetic route of the photochromic compound was shown in Scheme 2.Diarylethene 1 was characterized by ^{1}H NMR spectroscopy. ^{1}H NMR (400 MHz, CDC1$_3$, TMS): δ 1.84 (s, 3H, -CH$_3$),1.89 (s, 3H, -CH$_3$), 2.36 (s, 3H, -CH$_3$), 2.42 (s, 3H, -CH$_3$), 6.73 (s, 1H, thiophene-H), 7.18 (s, 1H, thiophene-H),7.20-7.22 (d, 2H, J = 7.6 Hz, Ar-H),7.42-7.44(d, 2H, J = 8.0 Hz, Ar-H).

Preparation of PMMA Film. One hundred milligram of PMMA was first dissolved in 1 mL chloroform, which was stirred ultrasonically to make it homogeneous. Samples were obtained by dissolving ultrasonically 10 mg of compounds 1 with 1 mL of the PMMA solution, respectively, and the solution was spin-coated on a glass substrate with a spin rotation speed of 1500 rpm.



Scheme 2. Synthetic route for the compound 1o.

Result and Discussion

Photochromism of Diarylethene 1. The photochromic behaviors of diarylethene 1 induced by photoirradiation at room temperature were measured both in hexane and in PMMA amorphous film. In hexane(2×10^{-5} mol/L), the compound 1 exhibited an absorption peak at 288 nm, as showed in Fig. 1. Upon irradiation with 297 nm light, a new visible absorption band at 541 nm appeared while the original peak at 288 nm decreased, indicating the new formation 1c produced. Correspondingly, the colorless solution of 1 turned darkred. The darkred colored solution turned colorless by irradiation with visible light ($\lambda > 500$ nm), indicating that 1c returned to the initial state 1o.

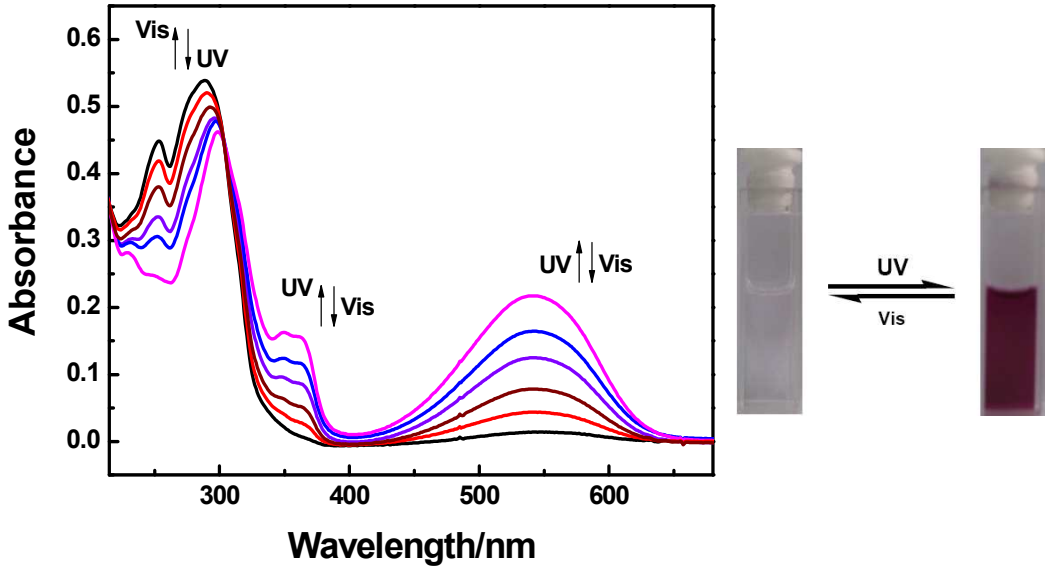


Fig. 1. Absorption spectra upon irradiation with 297 nm UV light and color change upon alternating irradiation with UV-Vis light of compound 1 in hexane (2.0×10^{-5} mol/L).

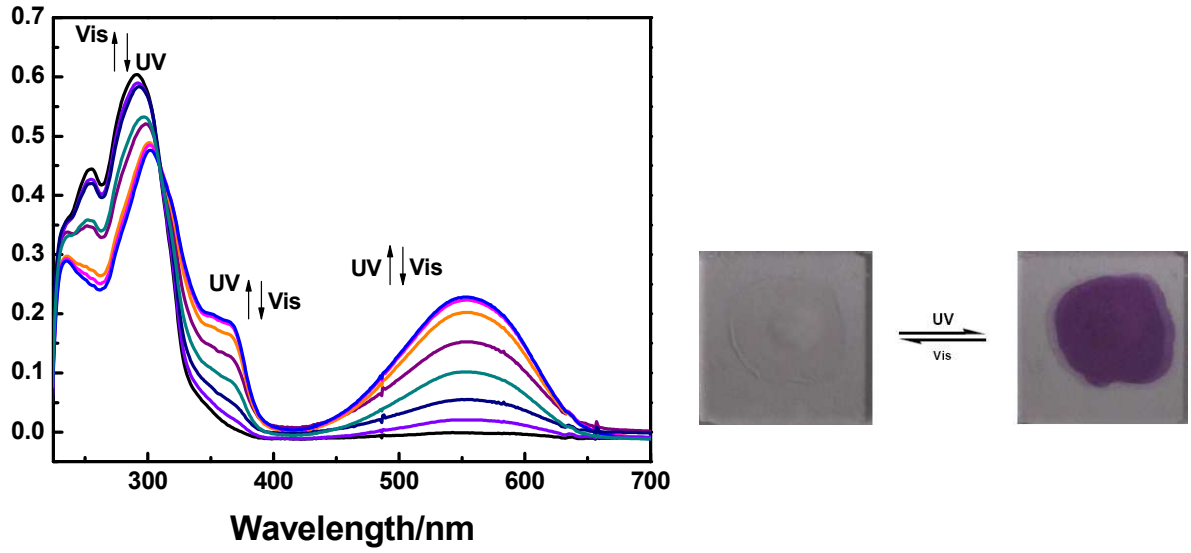


Fig. 2. Absorption spectra upon irradiation with 297 nm UV light and color change upon alternating irradiation with UV-Vis light of compound 1 in PMMA amorphous film.

In PMMA amorphous film, as showed in Fig. 2, diarylethene 1 also showed good photochromism as similar to that in solution (Fig. 1). The absorption maxunum of compound 1o was observed at 290 nm. Upon irradiation with 297 nm light, the color of the PMMA film turned darkred too, in which the absorption maximum was observed at 551 nm. The darkred film turned colorless, too, upon irradiation with visible light ($\lambda > 500$ nm).

Fluorescence of Diarylethene 1. The fluorescence properties in the hexane of the title compound (5.0×10^{-5} mol/L) were measured using a Hitachi F-4500 spectrophotometer, and the breadths of excitation and emission slit were selected 10.0 nm. The fluorescence emission spectra of 1o in hexane at room temperature was illustrated in Fig. 3. From this figure, we can see that the hexane solution of diarylethene 1 exhibited relatively strong fluorescence at 360 nm when excited at 305 nm. The fluorescence intensity of diarylethene 1 decreased dramatically along with the photochromism from open-ring isomer to closed-ring isomer upon irradiation with 297 nm light in hexane. As shown in Fig. 3, when irradiated by light of 297 nm, the photocyclization reaction was carried out and the low fluorescent closed-ring form of the compound was produced. The emission intensity of diarylethene 1 in a photostationary state was quenched to ca. 40%. The back irradiation by appropriate wavelength visible light regenerated the open-ring forms of diarylethene 1 and recovered the original emission spectra.

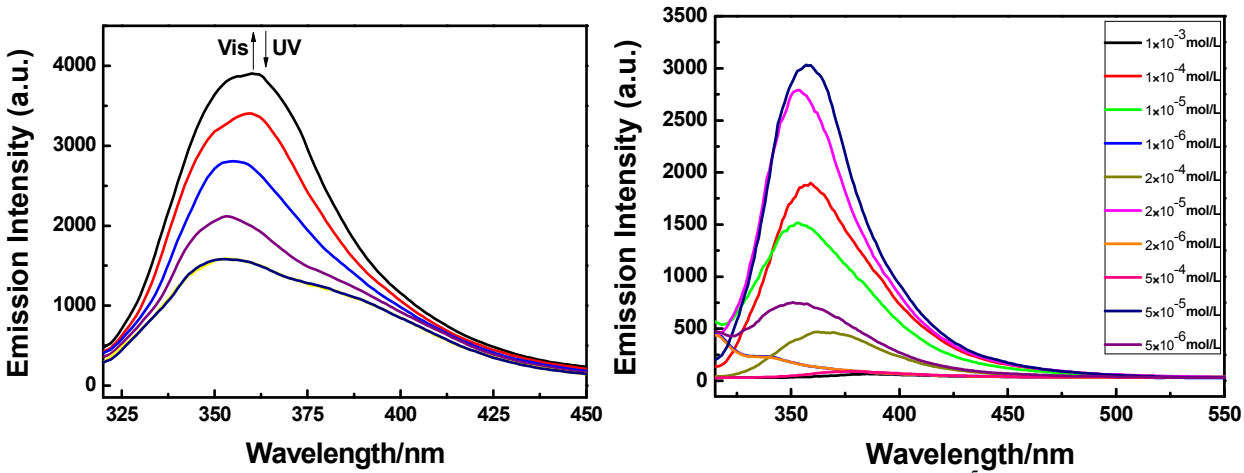


Fig. 3.Fluorescence spectral changes of diarylethene 1 in hexane(5.0×10^{-5} mol/L) excited at 305 nm upon irradiation with 297 nm UV light and emission spectral change of diarylethene 1 in different concentrations in hexane at room temperature (excited at 305 nm).

The concentration dependence on the fluorescence spectrum of diarylethene 1o was measured in hexane at room temperature. As shown in Fig. 3, when the concentration from 1.0×10^{-6} mol/L to 5.0×10^{-5} mol/L, the relative fluorescence intensity increased with increasing concentration. Especially, when the concentration increased from 1.0×10^{-5} mol/L to 2.0×10^{-5} mol/L, the relative fluorescence intensity increased remarkably. But when the concentration increased to 5.0×10^{-4} mol/L, the hexane solution showed relatively weak fluorescence. This self-quench phenomenon maybe resulted from the formation of excimers and of exciplexes in high concentration solutions so that deactivation effect can occur during the excited-state lifetime [11].

Summary

A new unsymmetrical diarylethene was synthesized and its photochromic and fluorescent properties were also investigated. The results showed that the new compound exhibited remarkable photochromism and acted as a notable fluorescent switch. The fluorescence intensity decreased along with the photochromism upon irradiation with 297 nm light. When the concentration changed, the fluorescence intensity also changed.

Acknowledgment

This work was supported by Program for the NSFC of China (20962008, 21162011), New Century Excellent Talents in University (NCET-08-0702), the Project of Jiangxi Academic and Technological leader (2009DD00100), and the Project of the Science Funds of Jiangxi Education Office (GJJ09646 and GJJ11026), and the Project of Education Reform of jiangxi Science and Technology Normal University(JGYB-11-21-21).

References

[1] Y. Chen, C.M. Wang, M.G. Fan, B.L. Yao and N. Menke: Opt. Mater. Vol. 26 (2004), p. 75
[2] S.J. Luo, K.X. Chen, L.C. Cao, G.D. Liu, Q.S. He, G.F. Jin, D.X. Zeng and Y. Chen: Opt. Express. Vol. 13 (2005), p. 3123
[3] S.Z. Pu, T.S. Yang, B.L. Yao, Y.L. Wang, M. Lei and J.K. Xu: Mater. Lett. Vol. 61 (2007), p. 855
[4] M. Irie: Chem. Rev. Vol. 100 (2000), p. 1685
[5] H. Tian and S.J. Yang: Chem. Soc. Rev. Vol. 33 (2004), p. 85
[6] K. Matsuda and M. Irie: J. Photochem. Photobiol. C. Vol. 5 (2004), p. 169
[7] S. Kawata and Y. Kawata: Chem. Rev. Vol. 100 (2000), p. 1777
[8] F.M. Raymo and M. Tomasulo: Chem. Soc. Rev. Vol. 34 (2005), p. 327
[9] S.Z. Pu, F.S. Zhang, J.K. Xu, L. Shen, Q. Xiao and B. Chen: Mater. Lett. Vol. 60 (2006), p. 485
[10] S.Z. Pu, L.S. Yan, Z.D. Wen, G. Liu and L. Shen: J. Photochem. Photobiol. A: Chem. Vol. 196 (2008), p. 84
[11] T. Fukaminato, T. Kawai, S. Kobatake and M. Irie: J. Phys. Chem. B. Vol. 107 (2003), p. 8372

© (2012) Trans Tech Publications, Switzerland
doi:10.4028/www.scientific.net/AMM.164.251

Photochromism and fluorescence of a Novel unsymmetrical Diarylethene Material Bearing benzene and thiophene ring

Shuhong Jing, Shouzhi Pu*, Hui Li

Jiangxi Key Laboratory of Organic Chemistry, Jiangxi Science and Technology Normal University, Nanchang 330013, P. R. China

pushouzhi@tsinghua.org.cn

Keywords: diarylethene, benzothiophene, Photochromic, Fluorescence.

Abstract. A new photochromic diarylethene compound, 1-[2-methyl-(5-(4- dioxolane) phenyl)-3-thienyl]-2-(2-methyl-3-benzothiophene)perfluorocyclopentene (1o)was synthesized. Its properties, including photochromism and fluorescence were investigated in detail both in solution and PMMA amorphous film. It underwent reversible cyclization and cycloreversion reactions upon alternating irradiation with UV and visible light in hexane.

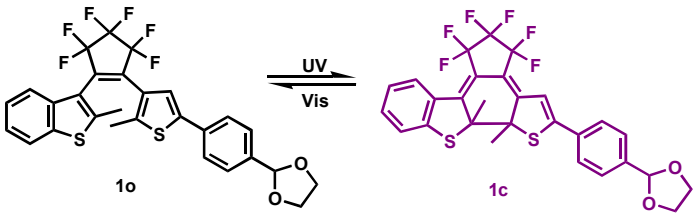
The compound showed good phtochromism both in solution and in solid states. Diarylethene 1o changed the color from colorless to purple upon irradiation with 297 nm UV light, in which absorption maxima were observed at 539 nm in hexane and at 547nm in PMMA film, respectively. Using diarylethene 1c/PMMA film as recording medium, optical recording was performed successfully. This new photochromic system also exhibited remarkable optical storage character.

Introduction

Photochromic diarylethenes have been extensively studied for optoelectronic applications because of their notable thermally irreversible photochromic behavior and remarkable fatigue resistance.Photochromism is a light-triggered reversible reaction between two isomers. During the past decades, there have been important achievements in the synthesis of new families of organic photochromic molecules [1, 2] .These molecules can play a key role in materials for photonic switches, memories, sensors, or actuators.

Photo-induced anisotropy is referred as a polarized-light anisotropic change for isotropic materials or anisotropic materials. To date,photo-induced anisotropy of some materials, such as photochromic glass, color crystal, and dye-polymer, was investigated extensively. The photo-induced anisotropy of photochromic pyrrylfulgide has also been reported by Yao [3] et al. In order to explore photo-induced anisotropy optical recording, the molecular scaffold of diarylethenes bearing six-membered aryl moieties has been designed. This asymmetrical diarylethenes bearing phenyl groups on the end are the most promising, because the end group can be substituted by electron donating group or electron withdrawing group [4-6].

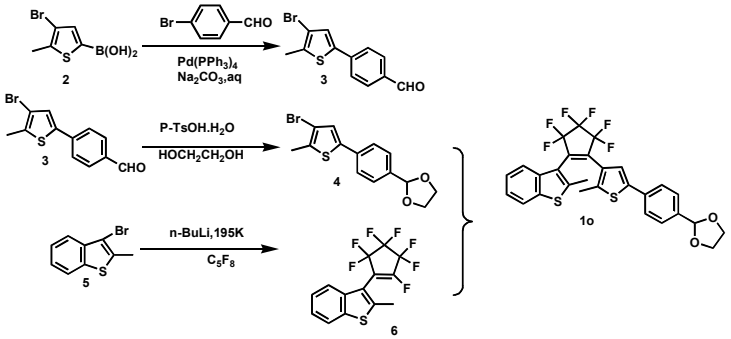
We report herein on a new diarylethene, 1-[2-methyl-(5-(4- dioxolane) phenyl)-3-thienyl]-2-(2-methyl-3-benzothiophene)perfluorocyclopentene, which presents photochromism both in solution and in solid. Thus, this molecule appeared to us as a good candidate to investigate photochromism on nanometer-sized materials. Its photochromic reactivity, and fluorescence property were investigated in detail. The photochromic reaction of diarylethene 1a is shown in Scheme 1.



Scheme 1. Photochromism of diarylethene 1o

Experiments

Synthesis of diarylethene 1o. The diarylethene 1o of synthetic route is shown in Scheme 2. It was synthesized according to the similar procedure of Pu [7]et al. Firstly, compound 3 was prepared by reacting compound 2 with 4-bromobenzaldehyde in the presence of tetrakis(triphenylpho-sphine)palladium(0) and Na_2CO_3 in THF for 16 h at 343K. Secondly, To a stirred THF solution of compound 5 was added dropwise a 2.5M n-BuLi/hexane solution at 195 K under nitrogen atmosphere. Stirring was continued for 30 min at 195 K, octafluorocyclopentene (C_5F_8) was slowly added and the reaction mixturewas stirred for 2.0 h at this low temperature. The reaction was quenched by water. The product was extracted with diethyl ether. The organic layer was washed with 1Maqueous HCl and water, and then dried over anhydrous $MgSO_4$, filtrated and evaporated in vacuo. he reaction mixture was extracted with diethyl ether, dried with anhydrous $MgSO_4$, filtered, and evaporated in vacuo, then purified by column chromatography to give compound 6 (2, -methyl-3- benzothiophene -perfluorocyclopentene) crimson liquid. Finally, To a stirred THF solution of compounds 4 was slowly added a 2.5M n-BuLi/hexane solution at 195K under an argon atmosphere. After 30 min, compound 6 was added and the mixture was stirred for 2h at this temperature. The reaction mixture was extracted with diethyl ether, dried with anhydrous $MgSO_4$, filtered, and evaporated in vacuo, then purified by column chromatography to give 1o.
The structure of 1a was characterized by ^{1}H NMR. ^{1}H NMR (400 MHz, $CDCl_3$, ppm): δ 1.94(s, 3H, $-CH_3$), 2.29 (s, 3H, $-CH_3$), 4.02 (t, 2H, dioxolane-H), 4.08(t, 2H, dioxolane-H), 5.81(s, 1H, dioxolane-H),7.17 (s, 1H, thiophene-H), 7.31 (d, 2H, benzene-H), 7.44 (d, 2H, benzene-H), 7.43 (t, 2H, benzothiophene-H), 7.56 (d, 1H, benzothiophene-H), 7.74(d, 1H, benzothiophene-H).



Scheme 2. Synthetic route for the compound 1o

Preparation of PMMA film. First of all, one hundred milligram of PMMA was dissolved in 1mL chloroform, which was stirred ultrasonically to make it homogeneous. Samples were obtained by dissolving ultrasonically 10 mg of compounds 1 with 1mL of the PMMA solution, respectively, and the solution was spin-coated on a glass substrate with a spin rotation speed of 1500 rpm.

Photochromism of Diarylethene. Photochromic reactivity of diarylethene 1 was examined both in hexane solution and in PMMA amorphous film at room temperature. The diarylethene 1o exhibits good photochromic properties and can be toggled between its colorless ring-open and colored ring-closed forms by alternate irradiation with appropriate wavelengths of light. As shown in Fig.1 a, compound 1o exhibited an absorption peak at 300 nm (ε, 1.5×10^4 mol^{-1} dm^3 cm^{-1}), in hexane. Upon irradiation with 297 nm light, a new visible absorption band centered at 539 nm (ε, 7.7×10^3 mol^{-1} dm^3 cm^{-1}) emerged while the original peak at 300 nm decreased, indicating the formation of the closed-ring isomer 1c. Correspondingly, the colorless solution of 1o turned magenta owing to produce the closed-ring isomer 1c. The magenta colored solution turned colorless by irradiation with visible light (λ > 500 nm), indicating that 1c returned to the initial state 1o .

The further experiments revealed that the solution can keep similar absorption spectrum under several cycles irradiation with UV and visible light, indicated the high fatigue resistance property. Similar spectrum change of diarylethene 1a was observed in PMMA film (10% w/w). Upon irradiation with 297 nm UV light, the colorless PMMA film turned purple with new broad absorption band centered at 547 nm (Figure 2), which assigned to the open-ring isomer 1a changed to the closed-ring isomer 1b. The colored PMMA film can also return to colorless upon irradiation with

appropriate wavelength visible light. Figure. 2 showed the color changes of diarylethene 1o both in hexane and in PMMA film. From Figure. 2, it can be easily seen that the two isomers have distinguishable color attributed to different π-conjugation and they can be reversible changed each other by alternating irradiation with UV and visible light. Therefore, there exists enough high contrast between the two isomers, which are promising candidates for rewritable photon-mode optical memory media.

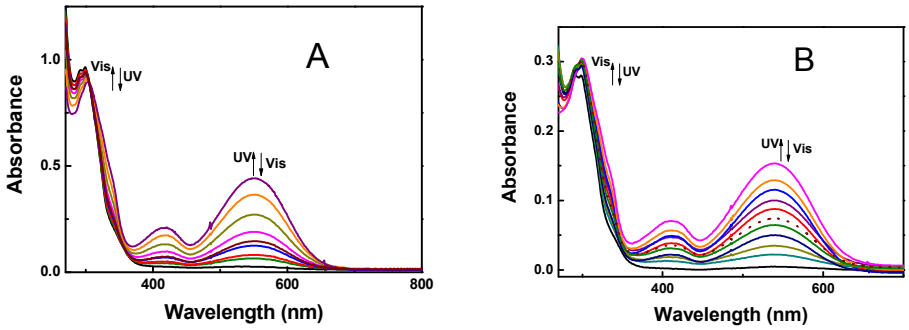


Figure. 1 Absorption spectral changes of compound 1o (A) in hexane (2.0×10^{-5} mol/L) and (B) in PMMA film (10%, w/w)

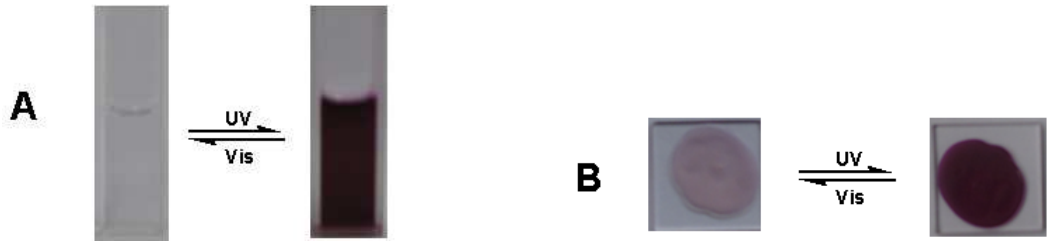


Figure. 2 Color changes of 1 (A) in hexane and (B) in PMMA film.

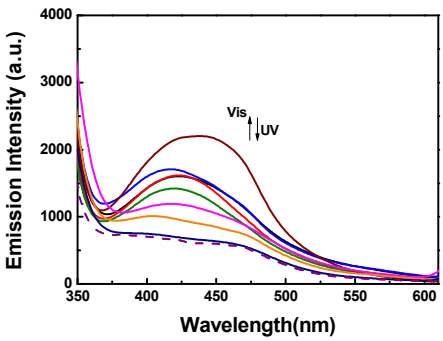


Figure. 3 Emission intensity changes of diarylethene 1a in PMMA film (10%, w/w) upon irradiation with 297 nm UV light.

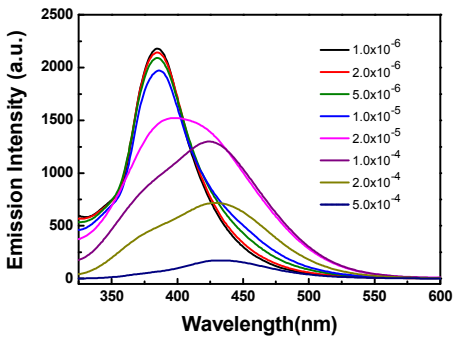


Figure. 4 Emission spectral change of 1a in different concentrations in hexane at room temperature (excited at 311nm)

Fluorescence of Diarylethene 1. The fluorescence intensity of diarylethene 1o decreased along with the photochromism from open-ring isomer to closed-ring isomer upon irradiation with 297 nm light in PMMA film. As shown in Fig. 3, when irradiated by light of 297nm, the photocyclization reaction was carriedout and the non-fluorescent closed-ring form of the compound were produced. The back irradiation by appropriate wavelength visible light (λ > 500 nm)regenerated the open-ring forms of diarylethene 1a and recovered the original emission spectra. The incomplete cyclization reaction and the existence of parallel conformations may be the main cause for the moderate change in fluorescence induced by photoirradiation. The reversible changes of the emission intensity of diarylethene 1o are useful for application as thefluorescence switches. The result showed that 1o exhibited good fluorescence both in hexane solution and in PMMA film, and the emission peaks are

385 nm and 438nm, respectively. As shown in Figure 3,4, when irradiated by light of 297 nm, the photocyclization reaction was carried out and the low fluorescent closed-ring form of the compound was produced. The back irradiation by appropriate wavelength visible light regenerated the open-ring forms of diarylethene 1o and recovered the original emission spectra. The phenomena are useful for application as the fluorescence switch [8, 9].

Polarization recording properties. Using dithienylethene 1c as the recording medium, Polarization recording was performed. Dithienylethene 1c was mixed with poly methyl methacrylate (PMMA) to coat the substrates by the spin-coating, and then applied to Polarization optical recording of 650 nm (105mW) He-Ne laser beam by the solid immerse lens. The polarizations of the patterns recorded on the film are shown in Fig. 5. The size of recording marks was about 20 μm. The result demonstrated that the photochromic diarylethene can be used in high capacity optical storage.Using diarylethene 1b/PMMA as recording medium, the results demonstrated that the diarylethene compound had attractive properties for high capacity optical storage.

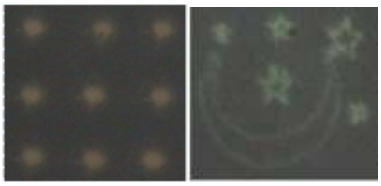


Figure. 5 Readout patterns from the diarylethene 1b/PMMA film

Summary

A new photochromic diarylethene was synthesized, the photochromic properties were studied, the results indicated that the diarylethene has excellent photochromic and fluorescence properties both in solution and in PMMA film. Using diarylethene 1b/PMMA as recording medium, the results demonstrated that the diarylethene compound had attractive properties for high capacity optical storage.

Acknowledgment

This work was supported by Program for the NSFC of China (20962008, 21162011), New Century Excellent Talents in University (NCET-08-0702), the Project of Jiangxi Academic and Technological leader (2009DD00100), and the Project of the Science Funds of Jiangxi Education Office (GJJ09646 and GJJ11026).

Reference

[1] M. Irie: Chem. Rev. Vol. 100 (2000), p. 1685

[2] H. Tian and S.J. Yang: Chem. Soc. Rev. Vol. 33 (2004), p. 85

[3] Y. Chen, C.M. Wang, M.G. Fan, B.L. Yao and N. Menke: Opt. Mater. Vol. 26 (2004), p. 75

[4] S.Z. Pu, L.S. Yan, Z.D. Wen, G. Liu and L. Shen: J. Photoch. Photobiol. A: Chem. Vol.196 (2008), p. 84

[5] S.Z. Pu, J.K. Xu, L. Shen, Q. Xiao, T.S. Yang and G. Liu: Tetrahedron Lett. Vol. 46(2005), p. 871

[6] S.Z. Pu, H.H. Tang, B. Chen, J.K. Xu and W. H. Huang: Mater. Lett. Vol. 60(2006), p. 3553

[7] G. Li, T. Zheng, S.Z. Pu and J.K. Xu: Acta Cryst. E. Vol. 62 (2006), p. 2877

[8] B.L. Yao, Y.L. Wang, M. Lei, N. Menke and G. F. Chen: Opt. Express Vol. 13(2005), p. 20

[9] B.Z. Chen, M.Z. Wang and H. Tian: Chem. Commun. Vol.3 (2002), p. 1060

© (2012) Trans Tech Publications, Switzerland
doi:10.4028/www.scientific.net/AMM.164.255

Photochromic properties of 1-[2-methyl-5-(4-chlorophenyl)-3-thienyl]-2-[2-methyl-5-(phenanthren-10-yl)-3-thienyl]perfluorocyclopentene

Xue Li, Congbin Fan, Gang Liu*

Jiangxi Key Lab of Organic Chemistry, Jiangxi Science & Technology Normal University, Nanchang 330013, China

liugang0926@163.com

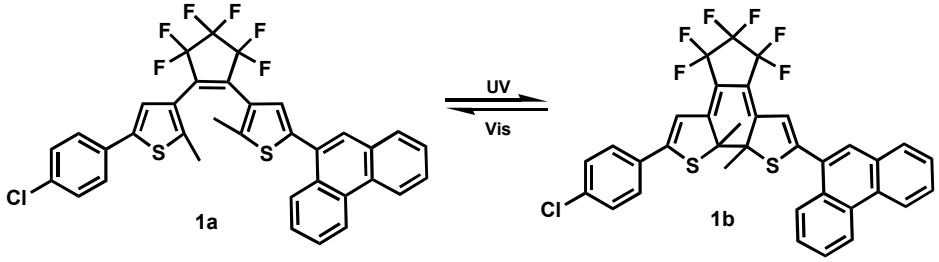
Keywords: Diarylethene; Photochromism; Fluorescence; Synthesis.

Abstract. A novel photochromic diarylethene, 1-[2-methyl-5-(4-chlorophenyl)-3-thienyl]-2-[2-methyl-5-(phenanthren-10-yl)-3-thienyl]perfluorocyclopentene was synthesized and its photochromic and fluorescent properties were also investigated. The compound exhibited remarkable photochromic, changing from colorless to blue after irradiation with UV light both in solution and in PMMA film.

Introduction

Diarylethene derivatives are a family of photochromic compounds that have been extensively studied because of their potential for fabricating photonic devices such as all-optical memories and switches [1,2], as well as nano- and microactuators [3,4]. Photochromism is defined as a light-induced reversible transformation between two isomers having a distinguishable absorption spectral change [5]. Photochromic compounds are classified into two categories, i.e., thermally reversible compounds and thermally irreversible compounds [6,7]. Among these photochromic stable compounds, diarylethene derivatives bearing two thiophene-derived groups are the most promising because of their excellent thermal stability in isomers, remarkable fatigue resistance, and rapid response and high reactivity in the solid state [1,8-10].

To date, a large number of publications concerning diarylethene derivatives with different aryl moieties, such as thiazole [11-13], indole [14], benzofuran [15], crysothiophene [16], pyrrole [17] and indene [18], etc, have been reported. Among these compounds, diarylethenes bearing two thiophene or benzothiphene-derived groups have received the most attention since they are particularly well suited as switching units. In fact, they have been considered as the most promising photochromic compounds due to these outstanding photochromic performances. So, we synthesized a novel photochromic diarylethenes 1-[2-methyl-5-(4-chlorophenyl)-3-thienyl]-2-[2-methyl-5-(phenanthren-10-yl)-3-thienyl]perfluorocyclopentene(1a). Its photochromic reactivity, fluorescence property were investigated in detail. The photochromic reaction of diarylethene 1 is shown in Scheme 1.

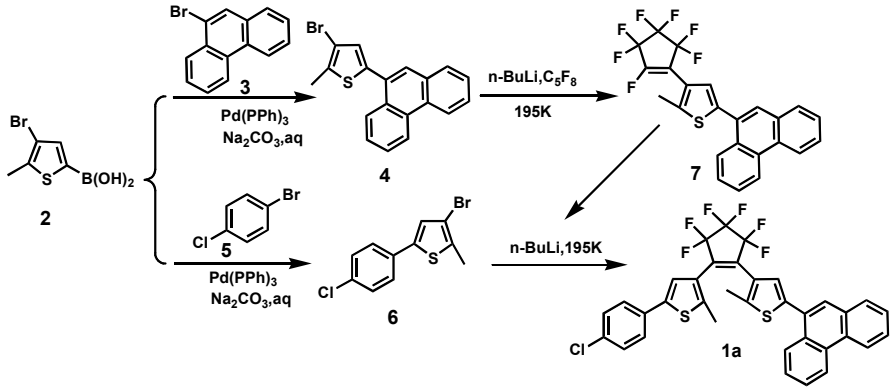


Scheme 1. Photochromism of dithienylethene 1a.

Experimental

The diarylethene 1a of synthetic route is shown in Scheme 2. It was synthesized according to the similar procedure of Pu et al.[19]. Firstly, compound 4 and 6 was prepared by reacting compound 2 with 1-brom-4-chlorophenyl and 9-bromophenanthrene in the presence of tetrakis(triphenylphosphine)palladium(0) and Na_2CO_3 in THF for 16h at 343K. Secondly, under an argon gas atmosphere, compound 4 was dissolved in THF and n-butyl lithium hexane solution was added at 195K. Stirring was continued for 30 min at this low temperature; octafluorocyclopentene was added and the mixture was stirred for 1h at this temperature. The reaction mixture was extracted with diethylether, dried with anhydrous $MgSO_4$, filtered, and evaporated in vacuo, then purified by column chromatography to give compound 7 (2-methyl-5-(phenanthren-10-yl)-3-thienyl -perfluorocyclopenten) white solid. Finally, to a stirred THF solution of compounds 6 was slowly added a 2.4M n-BuLi/hexane solution at 195K under an argon atmosphere. After 30 min, compound 7 was added and the mixture was stirred for 1h at this temperature. The reaction mixture was extracted with diethylether, dried with anhydrous $MgSO_4$, filtered, and evaporated in vacuo, then purified by column chromatography to give 1a blue oil liquid in 30% yield. The structure of 1a was characterized by ^{1}H NMR.

The structure of 1a was characterized by ^{1}H NMR. ^{1}H NMR (400 MHz, $CDCl_3$, TMS): δ 2.08 (s, 6H, $-CH_3$), 6.84 (s, 2H, thiophene-H), 7.59 (d, 2H, benzene-H), 7.42 (d, 2H, benzene-H), 7.79 (s, 1H, phenanthrene-H), 7.62-7.65 (t, 2H, phenanthrene-H), 7.69-7.71 (t, 2H, phenanthrene-H), 8.69-8.71 (d, 2H, J = 8, phenanthrene-H), 8.76-8.78 (d, 2H, J = 8, phenanthrene-H).



Scheme 2. Synthetic route for the compound 1a.

Results and discussion

Photochromism of diarylethene. The unsymmetric diarylethene 1a exhibits good photochromic properties and can be toggled between its colorless ring-open and colored ring-closed forms by alternate irradiation with appropriate wavelengths of light. The absorption spectral changes in hexane are shown in Fig. 1.The open ring isomer has an absorption maximum at 301 nm (ε, 2.5×10^4 mol^{-1} dm^3 cm^{-1}) which was arisen from π→π* transition. Upon irradiation with 297 nm UV light, the colorless hexane solution of compound 1a turned blue, in which absorption maximum was observed at 569 nm (ε, 1.0 × 104 mol^{-1} dm^3 cm^{-1}). The blue color is due to the formation of the closed ring isomer. When the blue solution was irradiated with visible light (λ > 450 nm), the blue color could return back to colorless and its spectrum became the same as that of original one, indicating compound 1a returned to the initial open ring isomer. The coloration/discoloration cycle could be repeated more than 50 times and a clear isosbestic point was observed at 323 nm even after 50 cycles, and the photostationary spectrum was almost the same as that of the colored isomer. This indicates a high conversion from the colorless to the colored isomers by irradiation with 254 nm light.

For practical applications in optical devices, it is very important that photochromic materials can keep good photochromic in a polymer film, such as the PMMA film. Dissolved ultrasonically 5 mg diarylethene sample and 50 mg PMMA into 0.5 mL chloroform, the film was prepared by spin-coating method. In PMMA amorphous film, diarylethene 1a also showed good photochromic (Fig. 1b) as similar to that in solution. Upon irradiation with 297 nm light, the colorless diarylethene

1a/PMMA film turned blue for which the absorption maxima were observed at 581 nm, as the closed-ring isomer 1b was generated. The colored diarylethene/PMMA films can revert to colorless upon irradiation with visible light (λ > 450 nm). The color changes of diarylethene upon photoirradiation in hexane and in PMMA are also shown in Fig. 1a and Fig. 1b respectively. The maximum absorption peaks of both the open-ring and the closed-ring isomers in PMMA film are longer than those in hexane solution. The red shift phenomenon is consistent with those of the majority of the reported diarylethenes [20].

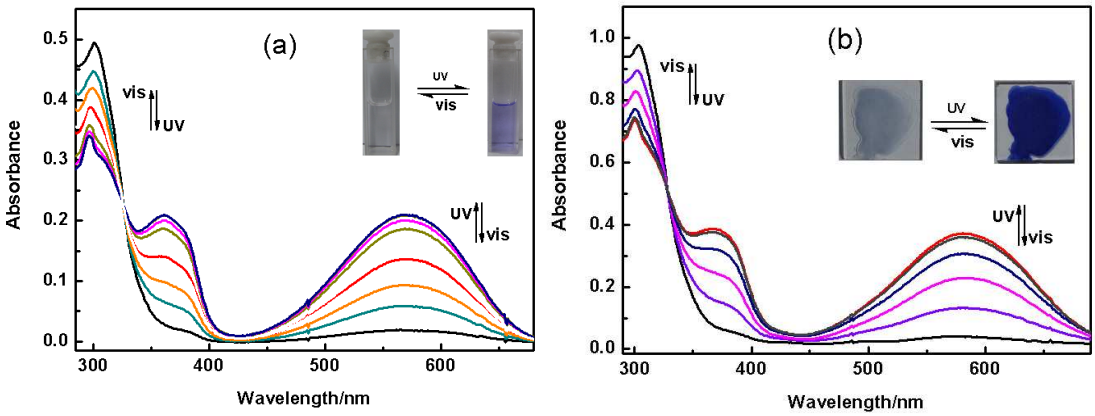


Fig. 1 Absorption spectral and color changes of compound 1 in hexane (2.0 × 10-5 mol dm-3) (a) and in PMMA film (10%, w/w) (b).

Fluorescence of Diarylethene. Fluorescent properties can be useful not only in molecularscale optoelectronics, but for digital photoswitching of fluorescence. In this work, the fluorescence properties of the diarylethene both in solution (2×10^{-5} mol/L) and in PMMA film (10% w/w) were measured using a Hitachi F-4500 spectrophotometer. Just like most of the diarylethenes [21]，the fluorescence of closed-ring isomers of diarylethenes is inactive. When the pohoisomerization reaction of diarylethene 1 occurs, the notable fluorescent switches were observed both in hexane and in PMMA film, and the emission peaks are 389 and 445 nm, respectively.The fluorescence intensity of diarylethene 1 decreased dramatically along with the photochromism from open-ring isomer to closed-ring isomer upon irradiation with 297 nm light. As shown in Fig. 2, when irradiated by light of 297 nm, the photocyclization reaction was carried out and the closed-ring form of the compound was produced. The back irradiation by appropriate wavelength visible light regenerated the open-ring forms of diarylethene 1a and recovered the original emission spectra. The incomplete cyclization reaction and the existence of parallel conformations may be the main cause for the moderate change in fluorescence induced by photoirradiation. The reversible changes of the emission intensity of diarylethene 1 are useful for application as the fluorescence switches [21, 22].

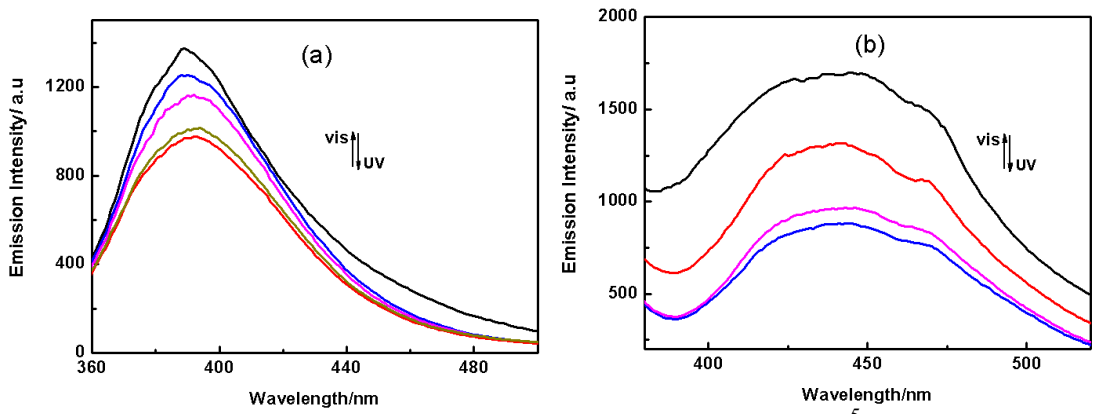


Fig. 2 Fluorescence spectral changes of compound 1 in hexane (2.0×10^{-5} mol/L) (a) and in PMMA (10%, w/w) (b) with 297 nm UV light.

Summary

In summary, an unsymmetrical diarylethene was synthesized to investigate its photochromism, fluorescence. The results showed that diarylethene 1a showed good photochromism and a relatively strong fluorescence switches in solution and in PMMA. The results illustrated that the diarylethene 1 had attractive properties for polarization holographic optical recording.

Acknowledgements

This work was supported by the Project of Natural Science Foundation of Jiangxi Province (2010DQ00200, 2010GZH0040) and the Science Funds of Jiangxi Education Office (GJJ1067).

References

[1] M. Irie: Chem. Rev. Vol. 100 (2000)，p. 1685.

[2] H. Tian, S. Yang: J. Chem. Soc. Rev. Vol. 33 (2004), p. 85.

[3] M. Irie, S. Kobatake and M. Horichi: Science. Vol. 291 (2001), p. 1769.

[4] S. Kobatake, S. Takami, H. Muto, T. Ishikawa and M. Irie: Nature. Vol. 446 (2007), p. 778.

[5] H. Dürr, H. Bouas-Laurent: Elsevier. 1990.

[6] M. Irie, M. Mohri: J. Org. Chem. Vol. 53 (1988), p. 803.

[7] T. Kaieda, S. Kobatake, H. Miyasaka, M. Murakami, N. Iwai, Y.I. Nagata,A. Itaya and M. Irie: J. Am. Chem. Soc. Vol. 124 (2002), p. 2015.

[8] N. Tamai, T. Saika, T. Shimidzu and M. Irie: J. Phys. Chem. Vol. 100 (1996), p. 4689

[9] S. Kobatake, K. Uchida, E. Tsuchida and M. Irie: Chem. Commun. Vol. 23 (2002), p. 2804.

[10] K. Matsuda, M. Irie, J. Photochem. Photobiol. C: Photochem. Rev. Vol. 5 (2004), p.169.

[11] S. Takami, M. Irie: Elsevier B. V. Vol. 60 (2004), p. 6155.

[12] K. Uchida, T. Ishikawa, M. Takeshita, and M. Irie: Elsevier B. V. Vol. 54 (1998), p. 6627.

[13] G. Liu, S. Z. Pu and X. M. Wang: Elsevier B. V. Vol. 66 (2010), p. 8862.

[14] K. Yagi, M. Irie: Bull. Chem. Soc. Jpn. Vol. 76 (2003), p. 1625.

[15] T. Yamaguchi, M. Irie: J. Org. Chem. Vol. 70 (2005), p. 10323.

[16] T. Yamaguchi, Y. Fujita, H. Nakazumi, S. Kobatake and M. Irie, Elsevier B. V. Vol. 60 (2004), p. 9863.

[17] S. Z. Pu, G. Liu, Q. Shen and J. K. Xu: Org. Lett. Vol. 9 (2007), p. 2139.

[18] T. Yamaguchi, M. Irie: Elsevier B. V. Vol. 47 (2006), p. 1267.

[19] G. Li, T. Zheng, S.Z. Pu and J.K. Xu: Acta Cryst. E. Vol. 62 (2006), p. o2877.

[20] S.Z. Pu, H.H. Tang, B. Chen, J.K. Xu and W.H. Huang: Mater. Lett. Vol. 60 (2002), p. 3553.

[21] H. Tian, B.Z. Chen, H.Y. Tu and K. Müllen, Adv. Mater. Vol. 17 (2002), p. 915.

[22] B. Chen, M. Wang, Y. Wu and H. Tian, Chem. Commun. Vol. 21 (2002), p. 1060.

© (2012) Trans Tech Publications, Switzerland
doi:10.4028/www.scientific.net/AMM.164.259

Properties and Synthesis of a Novel Unsymmetrical Photochromic Diarylethene Functional Material

Haichang Ding, Chunhong Zheng, Shouzhi Pu*

Jiangxi Key Lab of Organic Chemistry, Jiangxi Science & Technology Normal University

330013, P.R. China

pushouzhi@tsinghua.org.cn

Keywords: diarylethene, property, photochromism, fluorescence,

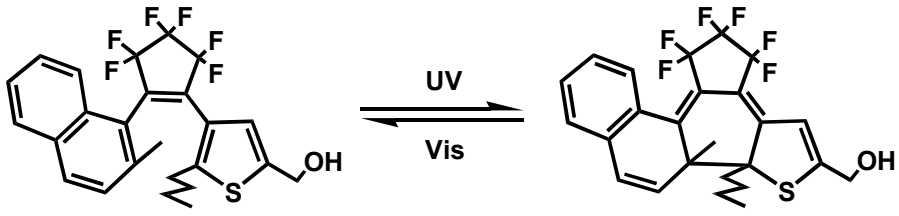
Abstract. A new unsymmetrical photochromic diarylethene, 1-(3-thienyl)-2-(2-n-butyl-5-hydroxymethyl-3-thienyl) perfluoroncyclopentene (1a), was synthesized and its optoelectronic properties, such as photochromism and fluorescence in solution and in PMMA film were investigated. This compound exhibited remarkable photochromism, changing from colorless to pink after irradiation with UV light in hexane solution. The new diarylethene also exhibited relatively strong fluorescence by photoirradiation in solution and in PMMA film, and the fluorescence intensity decreased along with the photochromism upon irradiation 297 nm light and its closed-ring isomer showed almost no fluorescence.

Introduction

Photochromism is referred to as a reversible photoisomerization process induced at least in one direction by an electromagnetic radiation between two isomers having different absorption spectra [1]. During the past decades, Photochromic compounds have been extensively investigated for their optoelectronic properties, for example as materials for optical recording, full-color displays, photoswitches etc [2 ~ 4]. Among the various types of photochromic compounds, diarylethenes are regarded as the most promising candidates for these applications because of their excellent thermal stability, fatigue-resistant character, rapid response and high reactivity in the solid state [5, 6]. Among these photochromic compounds, diarylethene derivatives bearing two thiophene or benzothiophene rings are the most promising candidates for optoelectronic devices [7]. Up to date, design and synthesis of new photochromic compounds is an active area of research. The majority of the research work reported has been devoted to the development of these molecules and investigative studies of their fundamental properties, and the results obtained have contributed to a broad understanding of the photochromism of diarylethene [8~10].

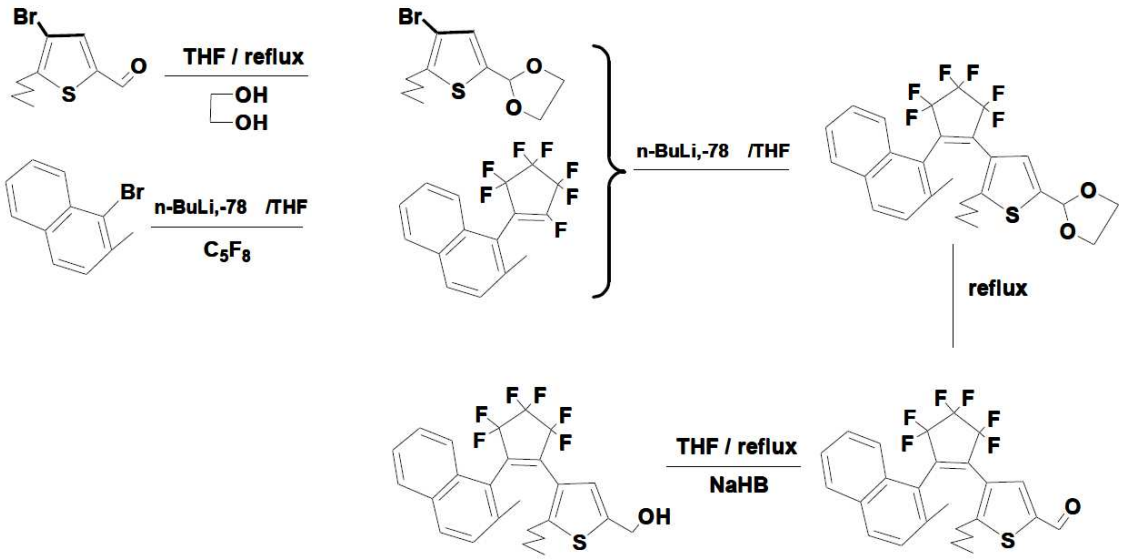
Experiment

In this paper, we synthesized a new unsymmetrical photochromic diarylethene 1-(3-thienyl)-2-(2-nbutyl-5- hydroxymethyl -3-thiopheneyl) perfluoroncyclopentene (1a). Its photochromic reactivity and fluorescence were investigated in detail. The photochromism of diarylethene 1a is shown in Scheme 1.



1 a 1 b

Scheme 1. Photochromism of diarylethene 1a.



Scheme 2. Reagents and conditions

The synthetic route for diarylethene 1a was shown in Scheme 2 and its synthetic steps based onthe similar procedure of Pu et al [11]. described in scheme 2. NMR spectra were recorded on Bruker AV400 (400 MHz) spectrometer with CDCl3 as the solvent and tetramethylsilane as an internal standard. The absorption spectra were measured using Agilent 8453 UV/VIS spectrometer. Photoirradiation was carried out using SHG-200 UV lamp, CX-21 ultraviolet fluorescence analysis cabinet, and BMH-250 Visible lamp. Light of appropriate wavelengths was isolated by different light filters. The fluorescent property was measured using a Hitachi F-4500 spectrophotometer.

The recording film was prepared as follows: diarylethene 1a (10 mg) was dissolved ultrasonically in PMMA chloroform solution (10%, w/w, 1ml). The mixture solution was then spin coated on a glass substrate (20 mm × 20 mm × 1 mm) which was then dried in air at room temperature. The thickness of the film was about 12 μm.

Results and Discussions

Photochromism of diarylethene 1a. The diarylethene 1a displays photochromism both in hexane solution (2×10-5 mol • L-1) and in PMMA amorphous film (10% w/w). Fig. 1 shows their absorption spectral changes upon photoirradiation. Compound 1a displayed an absorption peak at 262 nm (ε, 8.85×104 mol-1 • dm3 • cm-1), which was arisen from π→π* transition. Irradiation of hexane solution of compound 1a at 297 nm results in an immediate increase in the absorption in the visible spectral region where a new visible absorption band centered at 520 nm emerged and a visual change in color from colorless to pink due to the appearance of the ring-closed isomer. Upon irradiation with visible light (λ >500 nm), the colored solutions returned to their original colorless forms. Similarly, the color of dithienylethene 1a in PMMA film (λmax = 263nm) changed from colorless to pink with the appearance of a new broad absorption band at λmax = 532 nm upon irradiation 297 nm light, which was attribute to the formation of the closed form 1b. The colored PMMA film can invert to colorless, upon irradiation appropriate visible light (λ>500nm). The distortion of the spectra in the UV region is attributed to UV light being absorbed by the glass substrate and high concentration of diarylethene sample in the PMMA films leading to a non-linear absorption response. As has been observed for most of the reported diarylethenes, the maximum absorption peaks of both the open-ring and the closed-ring isomers in PMMA film incomparison with those in hexane solution can be ascribed to the stabilization of molecular arrangement in solid state [12].

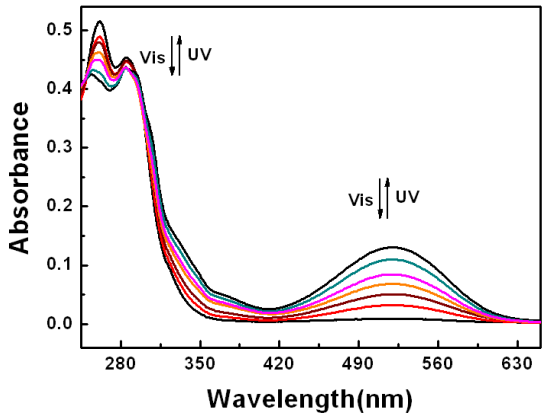


Fig 1.Absorption spectral changes in solution

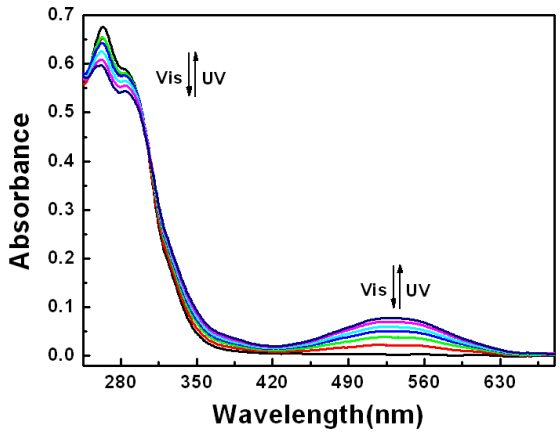


Fig 2. Absorption spectral changes in PMMA

Fluorescence of diarylethene. The fluorescence properties in the hexane solution and in PMMA film of the compound were measured using a Hitachi F-4500 spectrophotometer, and the breadths of excitation and emission slit were selected 10.0 nm. The fluorescence spectra of diarylethenes 1a in hexane solution and in PMMA film at room temperature is illustrated in Fig 3 and Fig 4 respectively. We could clearly see that the fluorescent emissions of 1a was at 433 nm and 436nm when excited at 300 nm. When it arrived at photostationary state, the emission intensities of diarylethenes 1a was quenched to ca 38% and 37%. The fluorescence was efficiently quenched when the diarylethene unit converts from the open- to closed-ring form. The fluorescence intensity gradually decreased in proportion to the conversion from 1a to 1b. The back irradiation with visible light of wavelength longer than 450 nm regenerated the open-ring forms and recovered the original emission spectra. Otherwise, the average times of "on" and "off" state shortened in proportion to the reciprocal power of radiated light by changing the power of the UV and visible light, indicating that the switching effect is perfect in hexane solution and in PMMA film [13, 14].

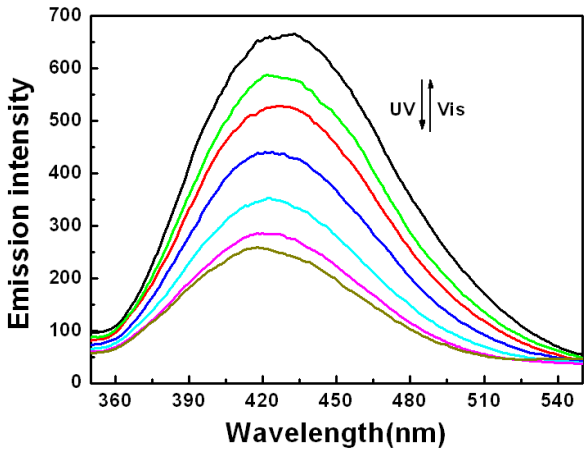


Fig. 3 Fluorescence spectra changes in solution

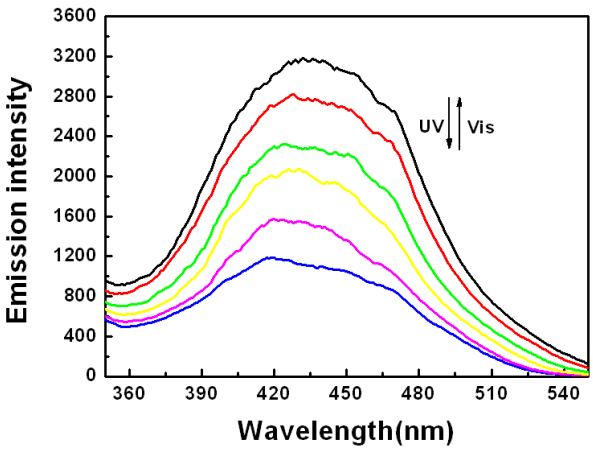


Fig. 4 Fluorescence spectra changes in PMMA film

Summary

A new unsymmetrical photochromic diarylethene 1a was synthesized and its photochromic, fluorescence properties were investigated. The results showed that this compound exhibited reversible photochromism, undergoing reversible cyclization and cycloreversion reactions upon alternating irradiation with UV and visible light both in solution and in PMMA film, and its absorption maxima were observed at 520 nm in hexane and at 532 nm in PMMA amorphous film, respectively, upon irradiation with 297 nm UV light. The fluorescence intensity of diarylethene decreased dramatically along with the photochromism from open-ring isomer to closed-ring isomer upon irradiation with 297 nm UV light in hexane solution and in PMMA film, and its closed-ring isomer showed almost no fluorescence.

Acknowledgement

This work was supported by Program for the NSFC of China (20962008, 21162011), New Century Excellent Talents in University (NCET-08-0702), the Project of Jiangxi Academic and Technological leader (2009DD00100), and the Project of the Science Funds of Jiangxi Education Office (GJJ09646 and GJJ11026).

References

[1] S. Kobatake and M. Irie: Chem. Lett., Vol. 32(2003), p. 1078

[2] F. Stellacci, C. Bertarelli, F. Toscano, M. C. Gallazzi, and G. Zerbi: Chem. Phy. Lett. , Vol. 302(1999), p. 563

[3] S. Z. Pu, J. K. Xu, L. Shen, Q. Xiao, T. Yang, and G. Liu: Tetrahedron Lett., Vol. 46(2005), p. 873

[4] W. Yuan, L. Sun, W. Huang, H. Tang, Y. Wen, and G. Jing, et al.: Adv Mater., Vol. 17(2005), p. 156

[5] M. Irie: Chemical Reviews. , Vol. 100(2000), p. 1685

[6] H. Tian and S.J. Yang: Chemical Society Reviews, Vol. 33(2004), p. 85

[7] N. Tanifuji, K. Matsuda, and M. Irie: Org. Lett., Vol. 7(2005), p. 3777

[8] S. Z. Pu, G. Liu, L. Shen and J.K. Xu: Org. Lett., Vol. 9(2007), p. 213

[9] J. K.W. Lee, C. C. Ko, K. M. C. Wong, N. Y. Zhu and V. W. W. Yam: Am. Chem. Soc, Vol. 26(2007), p. 12

[10] Y.L. Feng, Y.L. Yan, S. Wang, W.H. Zhu, S. X. Qian and H. Tian: J. Mathe. Chem., Vol. 16(2006), p. 3685

[11] C. B. Fan, S. Z. Pu, G. Liu and T. S. Yang: J. Photoch. Photobiol. A: Chemistry, Vol. 194(2008), p. 333

[12] S. Z. Pu , C. B. Fan, W. J. Miao and G. Liu: Tetrahedron, Vol. 64(2008), p. 9464

[13] K. Matsuda and M. Irie: J. Photoch. Photobiol. C , Vol. 5(2004), p. 169

[14] T. Norsten and N. Branda: Chem. Soc.Vol. 123 (2001), p. 1784.

© (2012) Trans Tech Publications, Switzerland
doi:10.4028/www.scientific.net/AMM.164.263

Recovery of precious metal material Ni from nickel containing wastewater using electrolysis

Ruijie Jin[a], Changsheng Peng [b,*] , Ahmed Abou-Shady[c] and Kedong Zhang[d]

The Key Lab of Marine Environmental Science and Ecology, Ministry of Education, Ocean University of China, Qingdao, 266100, China

[a]ruijiejin@126.com, [b]cspeng@ouc.edu.cn, [c]shady_desert@yahoo.com, [d]mail4dong@gmail.com

[*] Corresponding author. Tel.: +86 532 66782011; fax: +86 532 66782011.

E-mail address: cspeng@ouc.edu.cn (C. Peng).

Keywords: Nickel recovery; Precious metal material; Electrolysis; Taguchi approach; Efficiency

Abstract. The recovery of Ni^{2+} from nickel containing solution is a worthwhile work, owing to its precious value. In the present work, the optimal values of electrolysis (EL) operating parameters were elaborately investigated using Taguchi approach. The effect of Ni^{2+} initial concentration, boric acid, pH, and voltage were investigated in terms of nickel recovery and energy consumption. The results obtained showed that the influential factors on nickel recovery were voltage > boric acid > pH > concentration. However, in terms of energy consumption the following order of concentration > boric acid > pH > voltage was obtained. A confirmation experiment was carried out with the optimized parameters (boric acid 18g/L, nickel concentration 1000 mg/L, voltage applied 4.0 V, and pH 4). The recovery of Ni^{2+} yielded about 88%, and the outlet Ni^{2+} was as low as 119 mg/L. The electrolysis dynamic mode was investagated with flow rate 20 mL/min. The results showed that the outlet nickel concentration was 350 mg/L equal to 65% of Ni^{2+} recovery and energy consumption of 25.7 kW h/kg. Electrolysis could effectively recover nickel, however the Ni^{2+} concentration of the residual electrolyte was much higher than the restriction of 1 mg/L, so we used electrodialysis to further treat the residual electrolyte and the nickel concentration has been reduced below 1 mg/L , which will be discussed in other paper.

Introduction

Ni^{2+} is considered as a strategic metal owing to the main contribution in electroplating scale, as well as production of stainless steel and other alloys [1]. High concentration of Ni^{2+} in wastewater might be found in various industrial raw. This kind of wastewater can cause serious harm to environment and human. The outlet discharge raw must comply with the restrictions level of 1 mg/L.

Various methods could be employed to treat Ni^{2+} containing wastewater, such as chemical precipitation [2], adsorption method [3,4], electrodialysis (ED) [5], electrocoagulation [6], and ion-exchange[7]. However, these methods have showed various shortcomings owing to the need to chemical additives and high costs.

Electrodeposition is a method commonly used for metal refining. During electrodeposition, a direct current is passed from an inert anode through electrolyte containing metal ions. So, metal ions is extracted and deposited onto cathode surface. High quality Cu[8] and Pb[9] have been succefully extracted from heavy metal wastewater by electrodeposition in our previously work. Electrodeposition is known as a clean and environment friendly technology to recover nickel from nickel-containing wastewater [10].

The aim of our work was to study and determine the optimal electrodeposition conditions for Ni^{2+} recovery. The influence of the initial Ni^{2+} concentration, boric acid, pH, and voltage applied were investigated in terms of Ni^{2+} recovery and energy consumption. Taguchi approach was utilized as a statistical procedure to evaluate the overall process.

Experimental

Reagent and apparatus. Chemical reagent include Nickel sulfate ($NiSO_4 \cdot 5H_2O$) , boric acid(H_3BO_3), 0.1 M H_2SO_4 and 0.1 M NaOH ,which were analtical grad bought from (Sinopharm Chemical Reagent Co., Ltd, China. A power supply (PS-303D, Hongkong Longwei Ltd. China) was used to generate stable volatge, AAS (Solar M6, Thermo Elemental, USA) was used to detect the outlet Ni^{2+}, pH meter (pH-3D, Shanghai Leici Ltd, China) and conductivity meter (DDS-307, Shanghai Leici Ltd, China) were used to determine the pH and conductivtiy, respectively.

Electrodeposition unit. The effective volume of the acrylic electrolyser cell provided with four anodes and three cathodes was 3.7 L. The anode-cathode gap was set to be 1 cm. The anode was made of titanium grid covered with iridium and ruthenium oxides with surface area of 294 cm^2. The cathode was graphite plates with an effective surface area of 315 cm^2.

Experimental design (Taguchi method)**.** In this study, the evaluation of nickel recovery and energy consumption was carried out by Taguchi approach [9]. Orthogonal array (L_{16}OA) was applied to study the effect of influential parameters (Table 1).

Table 1 Orthogonal array (L_{16}OA) and the experimental results for each run

experimental plan					results			
Trails	Boric acid[g/L]	Concentration[mg/L]	Voltage[V]	pH	R [%]	S/N	EC [kW h/kg]	S/N
1	0	500	3.0	3	31.62	30.01	156.11	43.87
2	0	1000	2.5	6	41.52	32.38	21.47	26.64
3	0	1500	4.0	4	78.69	37.92	64.43	36.18
4	0	2000	3.5	5	45.79	33.22	41.87	32.44
5	6	500	2.5	5	9.56	19.61	104.23	40.36
6	6	1000	3.0	4	49.97	33.97	34.88	30.85
7	6	1500	3.5	6	38.47	31.7	51.98	34.32
8	6	2000	4.0	3	71.69	37.11	38.09	31.62
9	12	500	4.0	6	97.17	39.75	77.64	37.8
10	12	1000	3.5	3	51.01	34.15	51.77	34.28
11	12	1500	3.0	5	34.91	30.86	29.10	29.28
12	12	2000	2.5	4	42.61	32.59	7.04	16.95
13	18	500	3.5	4	80.16	38.08	52.01	34.32
14	18	1000	4.0	5	80.17	38.08	41.18	32.29
15	18	1500	2.5	3	57.16	35.14	6.56	16.34
16	18	2000	3.0	6	55.37	34.87	13.30	22.48

The recovery of Ni^{2+} and energy consumption were calculated as follows:

$$R = \frac{C_0 - C_t}{C_0} \times 100\ \% \tag{1}$$

$$EC = \frac{\sum UIt}{(C_0 - C_t)V} \tag{2}$$

where R is Ni^{2+} recovery %, C_0 is the initial Ni^{2+} concentration, C_t is the Ni^{2+} concentration after t hours of running, EC is the energy consumption of EL(kW h/kg), U is the voltage (V), I is the current (A); t is the time(h), and V is the electrolytic cell volume (L).

Results and discussion

Effect of parameters on Ni^{2+} recovery and energy consumption. Sixteen trials were performed to evaluate the experimental response as it listed in Table 1. The outlet samples were collected after 8 h of intial operation.

Boric acid was added as a buffer solution to maintain the electrolyte pH in a small range that appropriates nickel deposit. Besides, boric acid and Ni^{2+} may form nickel borate that can increase the overpotential of H^+ and reduce H_2 evolution [11]. Different doses of boric acid (0, 6, 12, and 18g/L) were investigated. Fig. 1(a) shows that Ni^{2+} recovery gradually increased with increasing the concentration of boric acid. Boric acid additives have significant influence on reducing the total energy consumption. Accordingly, the high concentration of boric acid (18 mg/L) was chosen to optimize the recovery.

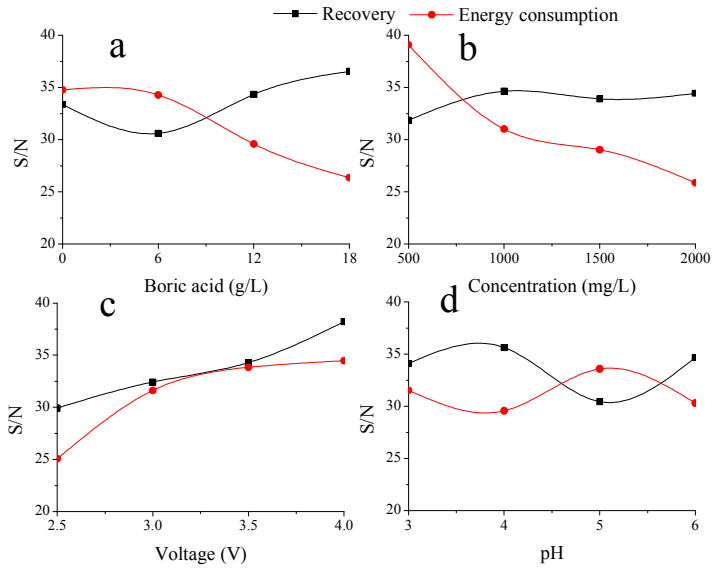


Fig. 1. Effect of Ni^{2+} influential parameters on S/N values of nickel recovery and energy consumption (EC)

Effect of different initial Ni^{2+} concentrations (500, 1000, 1500, and 2000 mg/L) on Ni^{2+} recovery and energy consumption are depicted in Fig. 1 (b). Ni^{2+} recovery increased rapidly with Ni^{2+} concentration from 500 to 1000 mg/L and then tended to be stable. The energy consumption decreased with increasing Ni^{2+} concentration. Therefore, Ni^{2+} concentration of 1000 mg/L was chosen to increase the total recovery.

Voltage is considered as one of the most important parameters, because it is considered the driving force for metal deposit. Four levels of voltages (2.5, 3.0, 3.5, and 4.0 V) were investigated. The high voltage can provide more electrons for Ni^{2+} reduction. In addition, the side reaction of H_2 evolution that can stay on cathode surface owing to a bad impact of wetting property of sulfate electrolyte on cathode [12]. Fig. 1 (c) reveals that the higher voltage increased both Ni^{2+} recovery and energy consumption. To gain high recovery, cell voltage 4 was chosen to carry out the confirmation experiment.

The effect of pH was reflected in the evolution of H_2 adjacent to cathodes, which leads to an increase of OH^- concentration near the cathode, and then resulted in metal hydroxide formation. It may precipitate in the cathode surrounding and eventually reducing the current efficiency [10]. Different electrolyte pH values (3, 4, 5, and 6) were investigated (Fig. (1d)). Ni^{2+} recovery increased slightly when pH was varied from 3 to 4. The lowest recovery was achieved when pH was 5. Then, the recovery increased when the electrolyte pH increased from 5 to 6. The energy consumption changed in the opposite direction compared with Ni^{2+} recovery. The maximum S/N value for Ni^{2+} recovery (minimum for energy consumption) was observed at pH 4.

ANOVA analysis [9]. Analysis of variance derived from Taguchi approach include the number of degrees of freedom (DOF), sum of squares (SS), variance (V), variance ratio (F factor), and contribution percentage (P), which are summarized in Tables 2.

The effect of voltage was significant at α (risk) levels of 0.05 and 0.01; however the other parameters were not significant. The effect of initial Ni^{2+} concentration on energy consumption was significant at α (risk) level of 0.05. However, boric acid, voltage, and initial pH were not significant. The most influential factor affected Ni^{2+} recovery were voltage (61.21%) > boric acid (19.04%) > pH (11.88%) > concentration (0.31%). The most influential factors for energy consumption were concentration (57.76%) > boric acid (18.86%) > pH (5.96%)> voltage (6.82%).

Table 2 ANOVA analysis of nickel recovery

	Nickel recovery					Energy consumption				
Factors	DOF	SS	V	F	P [%]	DOF	SS	V	F	P [%]
Boric acid	3	1452.18	484.06	2.52	19.04	3	4154.26	1384.75	1.78	18.86
Concentration	3	24.01	8.00	0.04	0.31	3	12721.67	4240.56	5.45	57.76
pH	3	906.18	302.06	1.57	11.88	3	1310.75	436.92	0.56	5.95
Voltage	3	4668.2	1556.07	8.11	61.21	3	1503.07	501.02	0.64	6.82
Error	3	575.93	191.98	-	-	3	2334.02	778.01	-	-
Total	15	7626.49	2542.16	-	-	15	22023.77	7341.26	-	-

Confirmation experiment. The confirmation experiment was performed under the optimal operation parameters (boric acid 18g/L, concentration 1000 mg/L, voltage 4 V, and pH 4). Fig.2 shows the variation of Ni^{2+} concentration versus time. The recovery rate was almost stable after 6 hours. The final concentration of Ni^{2+} in the electrolyser box after 8 hours was 119 .66 mg /L, which yielded recovery rate 88%.

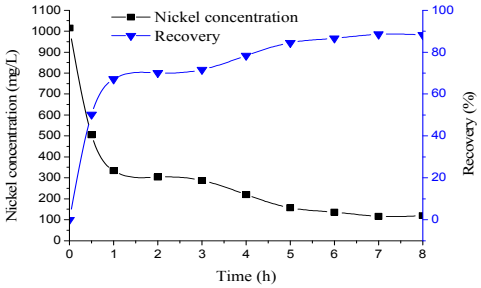


Fig. 2. The variation of outlet Ni^{2+} at the optimal levels (confirmation experiment).

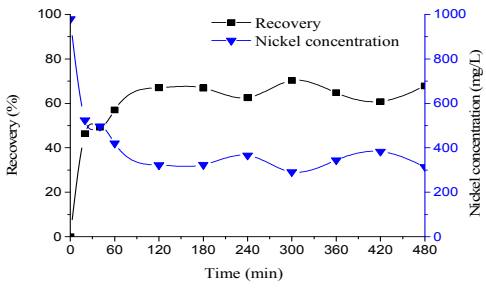


Fig. 3 The variation of outlet Ni^{2+} at the optimal levels (dynamic electrodeposition)

Fig. 3 shows the recovery of Ni^{2+} in the dynamic mode with flow rate 20 mL/min, under the optimal operation parameters. After 90 min of initial operating, the finial Ni^{2+} concentration was about 350 mg/L that yielded nickel recovery about 65%. The energy consumption was 25.70 kW h/kg. In view of high market price nickel (about 130 yuan /kg), the recovery of Ni^{2+} from Ni^{2+}-containing wastewater by electrodeposition is a worthwhile work.

Conclusions

Based on the results obtained, some conclusions could be summarized as follows:

(1) The most influential factors affected Ni^{2+} recovery were voltage (61.21%) > boric acid (19.04%) > pH (11.88%) > concentration (0.31%). However, the most influential factors of energy consumption were concentration (57.76%) > boric acid (18.86%) > pH (5.96%)> voltage (6.82%).

(2) Under the optimal parameters (boric acid 18 g/L, initial Ni^{2+} concentration 1000 mg/L, voltage applied 4 V, and pH 4), the finial Ni^{2+} concentration was 119 mg/L that represented recovery rate 88%. Dynamic mode of electrolysis was carried out with flow rate 20 mL/min. The results showed that the outlet Ni^{2+} concentration was about 350 mg/L that represented recovery rate (65%), and energy consumption (25.70 kW h/kg).

(3) Electrolysis could effectively recover nickel, however the Ni^{2+} concentration of the residual electrolyte was much higher than the restriction of 1 mg/L, so we used electrodialysis to further treat the residual electrolyte and the nickel concentration has been reduced below 1 mg/L, which will be discussed in other paper.

Acknowledgements

This work was supported by the Cultivation Fund of the Key Scientific and Technical Innovation Project, Ministry of Education of China (708060), the Program for New Century Excellent Talents in University, SEM, China (NCET-08-0508) and Special Funds for Environmental Nonprofit Research Project (200809095).

References

[1] Archana Agrawal , D. Bagchi, S. Kumari and V. Kumar, B.D. Pandey: Powder Technology, Vol. 177 (2007), p.133-139.

[2] I. Giannopoulou and D. Panias:Minerals Engineering,Vol. 20 (2007), p.753-760.

[3] M. Helen Kalavathy and Lima Rose Miranda: Chemical Engineering Journal, Vol.158 (2010), p.188-199.

[4] P. Senthil Kumar, S. Ramalingam, S. Dinesh Kirupha, A. Murugesan, T. Vidhyadevi and S.Sivanesan: Chemical Engineering Journal, Vol.167 (2011), p.122-131.

[5] K.Dermentzis: Journal of Hazardous Materials, Vol.173 (2010), p.647-652.

[6] F. Akbal and S. Camc: Desalination, Vol.269 (2011), p.214-222.

[7] A.H. Elshazly and A.H. Konsowa: Desalination , Vol.158(2003), p.189-193.

[8] C.S. Peng , Y.Y. Liu, J. J.Bi, H.Z. Xu and A. Abou-Shady: Journal of Hazardous Materials, Vol.189 (2011) , p.814-820.

[9] A. Abou-Shady, C.S. Peng, J.J. Bi, H.Z.Xu and J. Almeria O: Desalination, Vol.286 (2012), p.304-315.

[10] R. Idhayachander and K. Palanivelu: E-Journal of Chemistry, Vol.7（2010）, p.1412-1420.

[11] J.Lu, Q.H.Yang and Z.Zhang: Nonferrous Met. Soc. China , Vol.20(2010) , p.s97-s101.

[12]Y.D.Shu, R.R.Zhao, B.Z.Chen, Q.Y.Fu and H.Y.Jiang: Nonferrous Metals, Vol.3(1983), p.47-50. (in Chinese)

© (2012) Trans Tech Publications, Switzerland
doi:10.4028/www.scientific.net/AMM.164.268

Preparation and performance of Si/Al/C composites anode material prepared by glucose-modified

Xu Ma[1,a], Linglong Kong[1,b] Yuling Liu[1,c],Yanhong Ding[2], Jie Zhao[1], Lei Li[3], Ning Xu[3]

[1]School of Materials Science & Engineering, Key Lab of Display Materials & Photoelectric Devices Ministry of Education,Tianjin University of Technology, Tianjin 300384, China

[2]Tianjin Key Laboratory of Film Electronic and Communication Devices, School of Electronics Information Engineering, Tianjin University of Technology, Tianjin 300384, China

[3]Tianjin B&M Science and Technology, Tianjin 300384, China

[a]maxumax_cn@sina.com, [b]linglongkong@163.com, [c]liuyuling126@126.com

Keywords: Lithium-ion battery, ball milling, Aluminum, glucose, Si/Al/C composites

Abstract. Si/Al/C composites were synthesized by the method of doping aluminum and glucose-modified. The samples were characterized by XRD, SEM, and the capacity and cycling stability of the composites were tested by electrochemical charge/discharge test system. After glucose was pyrolyzed, the first discharge and charge capacity of Si/Al/C composites were 1312 and 956.7mAh/g, and the first coulombic efficiency was 72.9%. After 50 cycles, the capacity of Si/Al/C composites was 440mAh /g and the coulombic efficiency remained over 98.1%.

Introduction

Now Lithium-ion batteries are widely applied in nearly all electronic products, such as mobile phones, cameras, laptops and electric motor cars. Lithium-ion batteries have more advantages, such as lower self-discharge, higher voltage, higher energy and no memory [1].

The reason why silicon as anode materials is becoming more attractive for the Lithium-ion battery is that it has high theoretical specific capacity. It can reach 4200mAh/g when $Li_{4.4}Si$ alloys [2] are formed, which is more than 11 times that of carbon anodes. But a large volume change emerges during the process of alloying and de-alloying which leads to a large irreversible capacity and losing capacity rapidly [3,4,5].

Experimental

Silicon (~2μm) powders and aluminum (~2μm) were transferred to a nylon container with some agate balls and the weight ratio of balls and silicon was 12:1. Then the mixed powders were milled in an ethanol liquid media for a certain time. Then a certain amount of graphite powders were transferred to the nylon container, and the milling time was 5h. Then the mixture should be dried in vacuum drying oven. Glucose was dissolved in the water in a beaker, and then a certain amount of the prepared composites were added into the beaker. The beaker was put on a magnetic stirrer to make the water completely volatilize. The obtained powders should be calcined for 5h in the tubular furnace with a flowing argon atmosphere at 600°C. The composites were marked as SAC.

The samples were tested by X-ray diffractometer(XRD)with D/MAX- 2500X.The goniometrical precision was 0.02°and Cu target scanning velocity was 8°/min, the pipe flow was 150mA, the pipe pressure was 40KV. The morphology and particle size of the samples were observed with field emission scanning electron microscope (JEOL, JSM-6700F).

Electrodes containing active material, polyvinglidence fluoride (PVDF), binder in N-methyl-2 pyrolidinone (NMP) and carbon black (8:1:1)were made by coating the slurry onto copper foil and drying at 120°C in vacuum drying oven for 10h. The lithium foil negative electrode and positive electrode were separated by Celgard 2400 separator, and 1 mol/L LiPF6/ EC+DMC (1:1 by volume) was got as the electrolyte. Then the electrode was assembled into a half cell in a glove box filled with pure argon.

Results and discussion

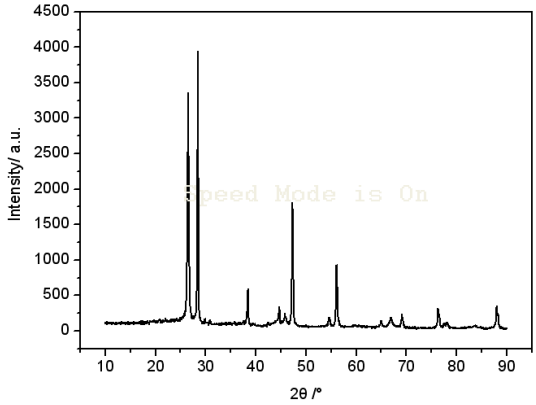


Fig.1 XRD patterns for Si/Al/C composites material

Fig.1 was the XRD pattern of Si/Al/C after thermal treatment. The diffraction peak of sample at 2θ=28.4, 47.1, 56.1° were assigned to the Si phase, while the diffraction peak position of the carbon phase was at 2θ=26.5°. There was no peak was assigned to the Si/C phase, so it was very important to the activity of the material.

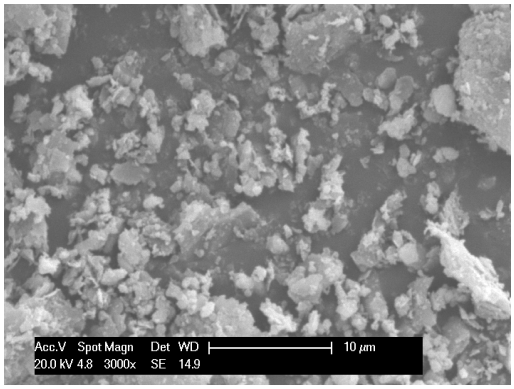


Fig.2 SEM patterns of Si/Al/C composites material

Fig.2 showed SEM patterns of Si/Al/C composites material. As we could see, the sample had disordered carbon, silicon and graphite particles could come into internal of disordered carbon which could keep the structure stable. A porous carbon matrix was formed and surrounded the Si particles, as a result of glucose's thermal decomposition during the firing process.

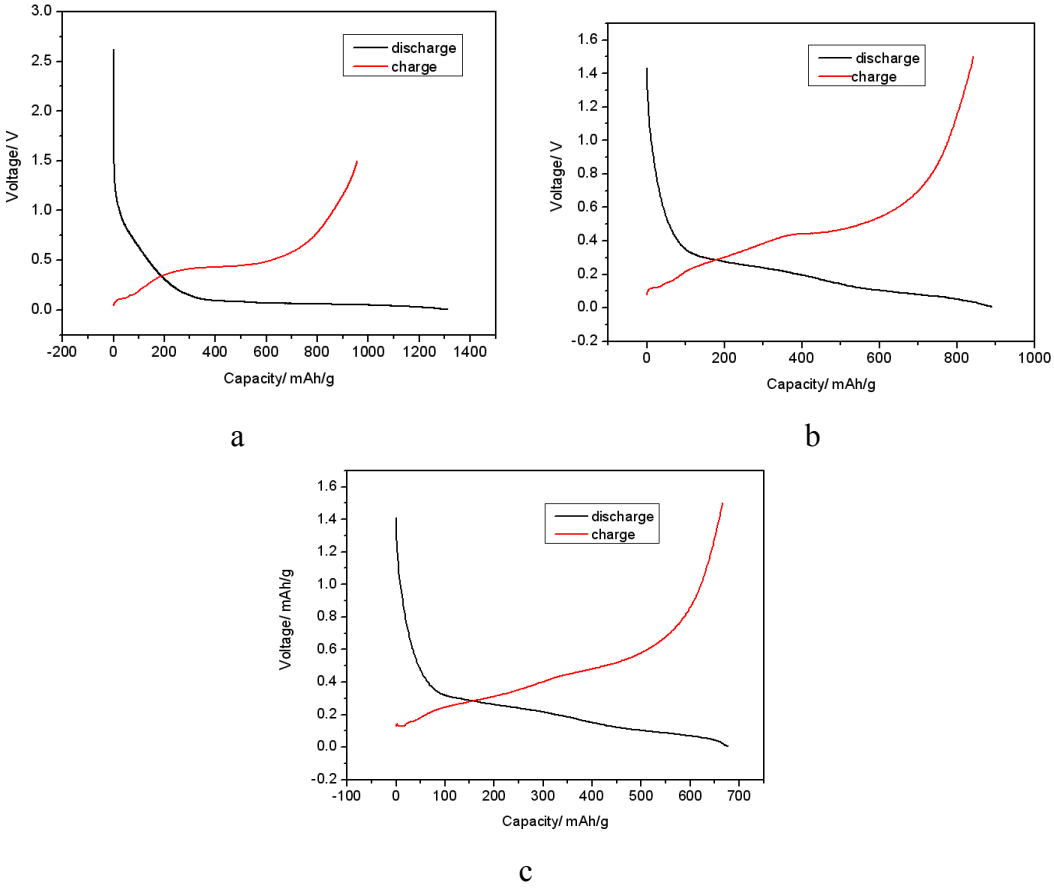


Fig.3 The 1st (a), 2nd (b), 12th (c) charge/discharge curve of SAC composites

Fig.3 showed the 1st, 2nd, 12th charge/discharge curve of SAC composites. Figure (a) showed that the first discharge/charge capacity was 1312/956.7mAh/g, and the first coulombic efficiency reached to 72.9%. The discharge voltage was at about 0.1V, and the charge voltage was at 0.4V.After the second cycle, the discharge/charge capacity reduced to 889.6/842.2mAh/g, but the coulombic efficiency increased to 94.7%. The irreversible capacity significantly reduced. After the twelfth cycle, the charge/discharge capacity maintained at about 660mAh/g, and the coulombic efficiency significantly increased to 98.1%.But the charge/discharge curves slopped gradually and the charge/discharge plateau curves also disappeared, that was because the activity of materials was changing in the cycling. It indicated that the disordered carbon after pyrolyzing the glucose and conductive graphite in or around silicon contributed to avoiding large irreversible capacity, and rapid capacity losing, and increasing coulombic efficiencies.

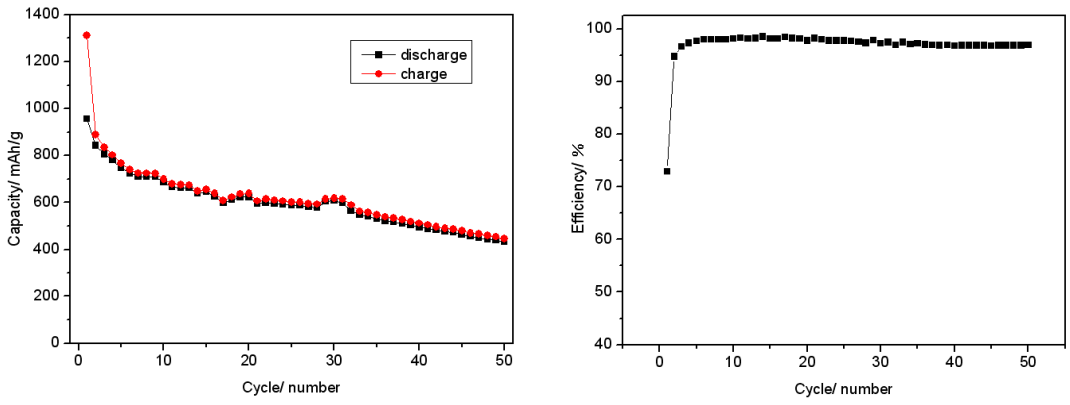


Fig.4 The cycle performance curve of SAC composites

What was shown in Fig.4 was the cycle performance curve of SAC composites. The capacity of SAC composites reduced fast between the first cycle and the fifth cycle, but after 5 cycles the capacity kept at about 780mAh/g and reduced less slowly. At last it almost kept at 440mAh/g after 50 cycles. The disordered carbon could provide continuous electrical contact networks around silicon particles, and the volume changed slightly during lithium insertion or extraction process. In the process of cycling, the coulombic efficiency of SAC composites changed form72.9% to 98.1%. From the fifth cycle on, the coulombic efficiencies became stable.

Conclusions

After glucose-coated and being pyrolyzed, the first discharge and charge capacity of Si/Al/C composites were 1312 and 956.7mAh/g, and the first coulombic efficiency was 72.9%. After 50 cycles, the capacity of Si/Al/C composite was above 440mAh/g and the coulombic efficiency remained over 98.1%. It indicated that carbon which was formed after glucose was pyrolyzed played a decisive role in improving the cycling performance of the Si/Al/C composites.

Acknowledgements

This work was supported by National Natural Science Foundation of China (No. 51101113), Key Technology Support Program of Tianjin China (11ZCKFGX03900), Tianjin Colleges and Universities Science &Technology Development Fund Projects (No. 20080310), the Foundation of State Key Laboratory of Rolling and Automation, Northeastern University (Grant No.2009011).

References

[1] S. Hossain, Y.K. Kim, Y. Saleh, R. Loutfy, J. Power Sources Vol. 161 (2006), p. 640.

[2] M.-S. Park, Y.-J. Lee, S. Rajendran, M.-S. Song, H.-S. Kim, J.-Y. Lee, Electrochim. Acta Vol. 50 (2005), p. 5561.

[3] K.-M. Lee, Y.-S. Lee, Y.-W. Kim, Y.-K. Sun, S.-M. Lee, J. Alloys Compd. Vol. 472 (2009), p.461.

[4] K. Wang, X.M. He, L. Wang, J.G. Ren, C.Y. Jiang, C.R. Wan, Solid State Ionics Vol. 178(2007), p. 115.

[5] M. Holzapfel, H. Buqa, L.J. Hardwick, M. Hahn, A. Würsig, W. Scheifele, P. Novák,R. Kotz, C. Veit, F.M. Petrat, Electrochim. Acta Vol. 52 (2006), p. 973.

© (2012) Trans Tech Publications, Switzerland
doi:10.4028/www.scientific.net/AMM.164.272

Toxic Effect of Cadmium Material on *Eisenia fetida*

Minyi Huang[a], Renyan Duan[b],Ruijuan Hao[c] and Liping Ren[d]

School of Life Science, Anqing Teacher College, Anqing An hui, 246011, China

[a]huangmiyi@yahoo.com, [b]renyanduan@aqtc.edu.cn, [c]ruijuanhao@yahoo.cn, [d]lipingren@yahoo.cn

Keywords: Cadmium material; *Eisenia fetida*; Avoidance; Trial and error learning; Memory duration

Abstract. Utilizing international standards organization published the earthworm avoid behavioral responses to evaluate the quality of the soil experimental method standardization, we test the effect of six different concentrations of cadmium on the behavior of response of the earthworms (*Eisenia fetida*). After 24 hour and 48 hour respectively, the number of earthworms in the different quantity of the soil was counted. And at the same time, the earthworms were used to do a try-wrong learning behavior experiment, to research the relation between the earthworms treated with different concentrations of cadmium and memory time. The results showed that the earthworms like to stay in 50 mg/kg concentration in the soil.

Introduction

Along with the development of industry and agriculture, a large number of pollutants run by various ways into the environment, and cause the deterioration of the environment [1], Cadmium is one of the environmental hazards. Cadmium is not the essential elements in the human body, and cadmium exposure is a risk factor associated with early arteriosclerosis and hypertension, which can lead to cardiovascular disease. Cadmium has the toxicity of the mutation and deformed, belong to environmental endocrine disruptions, the research of cadmium is mainly about the reproduction and endocrine in mammals [2,3]. The earthworm is one of the important instruct creatures for evaluation of soil environmental quality, the earthworm avoid behavior test is considered to be a strong and practical toxicity assessment tool in contaminated soil on the ecological risk assessment [4]. Recently, international standard organization ISO made use of the test method of earthworm avoid behavior effect draft to inspect the soil quality, and Earthworm's behavior choice reaction is looked as a test end point for 48 h, to evaluate the soil ecological function and the behavior of earthworms affected by pollutants.

Eisenia fetida are widely distributed, an important indicator creature to evaluate the soil environmental quality. We research the exact impact of cadmium pollution on the earthworm in the six room behavior instrument and maze of try-wrong learning behavior and to observe the learning ability of earthworms under the influence of cadmium.

Materials and Methods

Materials. *Eisenia fetida* were obtained from surrounding farmland in Anqing, Anhui China, and raised with cow muck soil (dry cow muck: peat soil = 1:1), and loess as a breeding matrix. They were put under the natural light and the temperature is 20 ~ 25℃. Before used, the muck soil was dried under the natural air indoor, and plant roots and the big particles were removed through 2 mm screen. Then, the medium was baked in the oven in 80℃ for 24 h to kill small animals or microorganisms which soil could contain. The color bright and sexual maturity *Eisenia fetida* were chosen for experimentation. And the weight was 300-500 mg. Chemicals were CdCl2·2.5H2O, the relative molecular mass is 228.35, the purity is 99%.

Avoidance behavior experiment. Choose six room behavior observers to test the behavior of *Eisenia fetida i*n the cadmium polluted soil. The reaction observer is made by the stainless steel material (2 mm thick), like dual cylinder structure. The diameter of the outer cylinder is 230 mm in diameter, the inner is 54 mm, and the high is 87 mm. There are six small equal rooms in the area between the inner and outer cylinders which are distributed by six pieces of stainless steel

clapboard. Each clapboard has three holes in the bottom (the diameter is 10 mm), which makes the room to connect with each other, and they can move freely among the different room. There are two holes (10 mm in diameter) in the inner cylinder, which allow *Eisenia fetida* release from the inner cylinder to the small room. The observers have stainless steel cover, which can prevent water in the soil from evaporate and avoid them escape during the experiment (Fig.1).

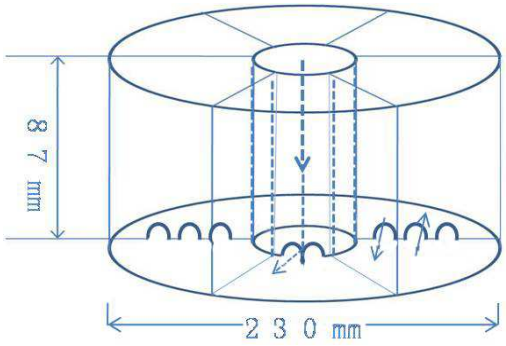


Fig. 1 The six room behavior observers

Cadmium was diluted by 500 ml distilled water in the beaker, and the concentration was 50, 100, 200, 400 and 800 mg/kg respectively, and 1 kg soil was put into the different concentration of cadmium separately (control group contained the corresponding distilled water) and mixed fully. The soil was adjusted to its biggest is water holding capacity of 60%, and stirred well. And 300 g wet soil containing a different concentration of cadmium was taken into the different room of the observers randomly. We took 10 *Eisenia fetida* which had been domesticated in the soil for 24 h, used water to wash clean, and sucked them dry by filter paper, then put them in the inner cylinder, observed and recorded the number in each outer cylinder after 5 min in the light condition. The time which they chose to enter firstly was recorded as tested starting time (t_0), that is to say, how many *Eisenia fetida* were like to move into the different cadmium concentration treatment of the soil). After they had moved into the soil in outer cylinder, the top of the observers were covered by the air vents and header, and then the observers were move into the artificial climate instrument, where temperature was tuned to (20 ± 1) ℃, light was about 500 lx (L: D = 12 h: 12 h), and they were under the condition for 48 h. The plastic clapboard without holes inserted among the channels in the observers was used to prevent them from free migration after 48 h. They were taken out smoothly from each room and the number was counted. The time was noted for the testing end time (t_{48}), and then the observers were taken out from the climate instrument. If Eisenia fetida was cut off by two part by the inserted plastic board, no matter how length was, they were all be marked as 0.5 individual. The number of *Eisenia fetida* was counted. At the same time, the parallel control group was set, and the experimental repeat.

Maze experiments. The maze difficulty coefficient (n) refers to the path numbers which experimental animals choose when they enter a maze, climb to a bifurcation point. If a maze has many bifurcation points, then the difficulty coefficient is equal to the accumulation of coefficient of each point. We designed "Y" maze with different difficulty coefficient, difficult coefficients were n = 2, n = 3 and n = 4 separately. Memory of *Eisenia fetida* for different difficulty maze was observed. (Fig. 2) The cultural condition in the maze experiment is the same with the avoidance behavior experiment, 120 *Eisenia fetida* with little difference were selected to do error behavior in the maze. They were raised respectively in 0, 50, 100 and 200 mg/Kg for 72 h, and were dividedly randomly to 3 groups, and every group had 10 individual in each cadmium concentration. At the same time, the parallel control group was set.

The material for making a maze is common plastic foam, its advantage is based on low price, rough surface, suitable for *Eisenia fetida* to climb, but it has many pores which *Eisenia fetida* climb into. So we fill the molten paraffin wax into the gaps of the foam to avoid the escape of *Eisenia fetida*.

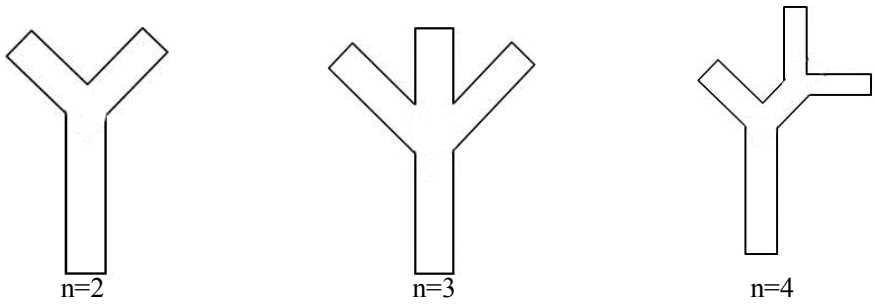


Fig.2 The difficult coefficients of maze

We use the head of forceps to stimulate *Eisenia fetida* in the vertical surface at a certain frequency and continuous appropriate dynamics, and then they can climb fast and arrive at a bifurcation point soon. From then, they will randomly choose to the left or right arm to continue walking, it will be to stimulate by Nacl solution at the end of the left arm of the maze or reward by the wet clay at the end of its right arm. The times which *Eisenia fetida* treated with different concentrations of cadmium climb rightly out of the different types of the maze is counted, and work out the accuracy rate. The data were subjected to analysis by SPSS.

Results and Discussion

There were no death and escape phenomenon in *Eisenia fetida* for 48h. In t0 and t48, they like to stay in the soil containing 50 and 100 mg/Kg cadmium (Fig.3), on the contrast, they showed obvious avoidance behavior in 400 ~ 800 mg/Kg cadmium, especially, the reaction of *Eisenia fetida* show intensely in 800 mg/Kg. The result show that they are not adapted to high levels of cadmium. The earthworm shows avoid reaction to cadmium pollution, which shows that it has the perception and the avoidance instinctive reaction. It is the similar research as the avoid behavior reaction of other earthworms to soil pollution [5, 6]. It is important that using animal avoidance test evaluation can examine the quality and the function of the soil.

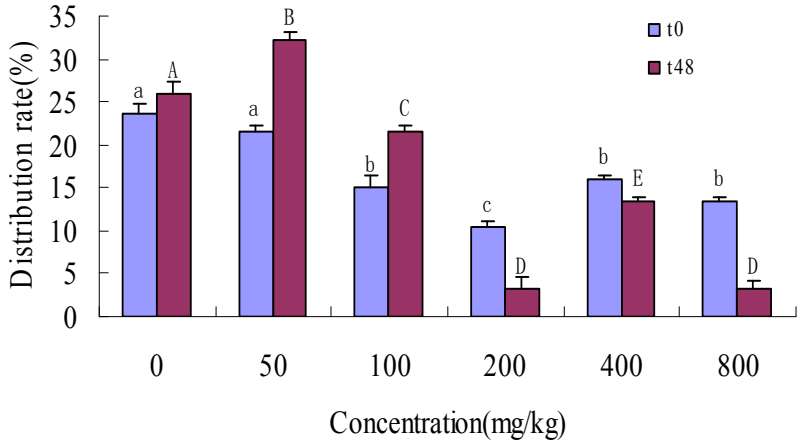


Fig. 3 The distribution rate of *Eisenia fetida* in different concentrations of cadmium

The values sharing the same letters mean different at $P > 0.05$, the values sharing the different letters mean different at $P < 0.05$.

With the cadmium concentration increasing, the correct rate of Eisenia fetida treated with different cadmium concentration into a different coefficient maze with wet mud decreased. There is no effect on the learning ability and memory of Eisenia fetida in 50 mg/Kg cadmium contrasting control group, but higher than and equal to 100 mg/Kg cadmium concentration, at the same maze, recognition capability in Eisenia fetida is worse($P<0.05$). Whatever cadmium concentration is, with

the complexity of the maze increase, the correct rate of Eisenia fetida decreased. The results show that it is safe for Eisenia fetida to live in 0 ~ 50 mg/Kg cadmium concentration, which has little influence on the nervous system and correct recognition ability. Along with the increase of cadmium concentration, the correct recognition in the maze decrease, cadmium can damage organ system, the brain barrier, enter the central nervous system, causing brain morphology change, influence the neurotransmitter content of the enzyme activity, cadmium may be harmful for the nervous system in terrestrial invertebrates [7].

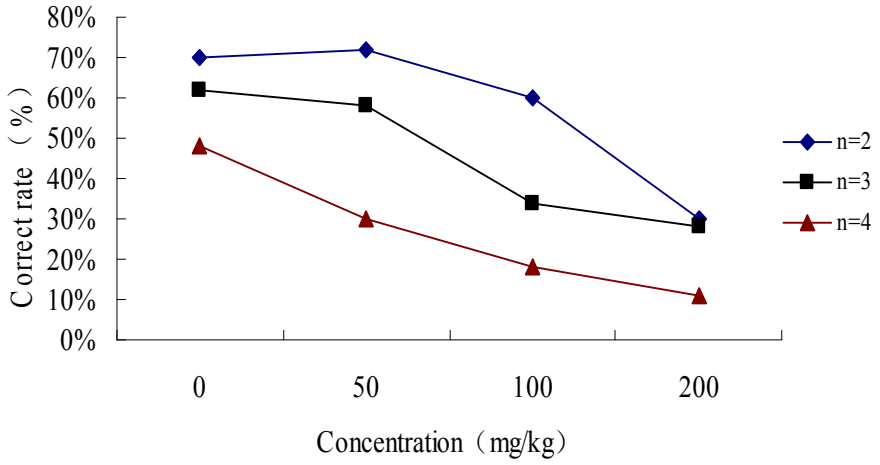


Fig.4 The correct rate of Eisenia fetida treated with different cadmium concentrations into a different coefficient maze with wet mud

These results show that it is reasonable and feasible that using the avoided earthworm's reaction to detect the high concentration of cadmium, and it is important to strengthen the work to detect pollutant concentration identification and research, and the mechanism of earthworms feeling chemical research should be studied further.

Acknowledgements

This work was funded by the Education Department of Anhui Province Natural Science Foundation of China (No. KJ2010B092), the Second Focus Technology Project of Anqing city Anhui Province (No. 20101005) and Anqing normal college youth natural science fund (No.KJ201118).

References

[1] R. K. Achazi and J. Soils: Sed. Vol. 2(2002), p.174

[2] C. Byrne, S. D. Divekar, G. B. Storchan, D. A. Parodi and M. B. Martin: Toxicol. Appl. Pharmacol. Vol. 238(2009) , p.266

[3] I. Iavicoli, L. Fontana and A. Bergamaschi: J. Toxicol. Environ. Health. B. Crit. Rev. Vol. 12(2009) , p.206

[4] M. Schaefer and J. Soils: Sed. Vol. 3(2003), p.79

[5] S. Loureiro, A. M. Soares and A. J. A. Nogueira: Environ. Pollut. Vol. 138(2005) , p. 121

[6] T. N. D. Luz, R. Ribeiro and J. P. Sousa: Environ. Toxicol. Chem. Vol. 23(2004) , p.2188

[7] K. Lock and C. R. Janssen: Ecotoxicology, Vol. 10(2001) , p.315

© (2012) Trans Tech Publications, Switzerland
doi:10.4028/www.scientific.net/AMM.164.276

The effects of the sputter-etching power on the formation of conical protrusions on the surface of SUS304 stainless steel

Tao Bai [1, a], Qinglian Zhang [2,b]

College of Mechanical Engineering, Donghua University, Engineering Research Center of Advanced Textile Machinery, Ministry of Education, Shanghai 201620
Tube, Pipe & Bar Technology Center, Research Institute, Baoshan Iron & Steel Co., Ltd., Shanghai 201900, China
[a]baitao@dhu.edu.cn, [b]zhangqinglian@baosteel.com

Key words: sputter-etching; radio frequency; SUS304 stainless steel; protrusion

Abstract. SUS304 stainless steel samples were sputter-etched by a radio frequency (RF) magnetron sputtering apparatus. Correlation between the formation of conical protrusions on the steel surface and sputter power was discussed. The results show that the conical protrusion precipitates both uniformly and densely on the surface with the power being 600W, the anode-to-substrate distance being 50mm, the argon gas flow ratio being 50sccm and the sputter-etching time being 6h. The roughness of the samples sputter-etched at various sputtering powers for 6h was analyzed. According to the results, sputter-etching brings about the development of surface roughness, which in turn may affect the sputter-etching process.

Introduction

Plasma-assisted surface modification is an important material process for modifying material surface properties [1-3]. Sputter-etching, an interesting ion-sputtering method, has been widely used not only for drawing ultra-fine patterns on semiconductor films like photo-etching to fabricate large scale integration, but also for obtaining a smooth surface on materials like the electrolytic-polishing of metals.

RF magnetron sputter-etching, which is an improved ion sputter-etching method, has been applied to modify material surfaces. In RF magnetron sputter-etching, an RF field generates plasma between the sputter-etching sample and the anode. In magnetron sputter-etching, a magnetic configuration is present under the sample, which traps electrons nearby the sample. The electrons cause ionization in the work gas. Part of the ions is accelerated towards the sample by the voltage drop that is present between the plasma and the sample. The bombarding ions cause material to move from the sample because of the energy that is transferred when energetic ions collide [4].

The research contained in this paper is focused on the use of argon RF plasma to form conical carbides on the surface of SUS304 stainless steel with low carbon content. The paper studied the effect of the plasma power on the formation behavior of conical carbides during sputter-etching. The relationship of the roughness of samples with the sputtering power was investigated. The surface hardness of the samples was also assessed to find the effect of the sputter-etching behavior on the surface hardness of the SUS304 stainless steel sample.

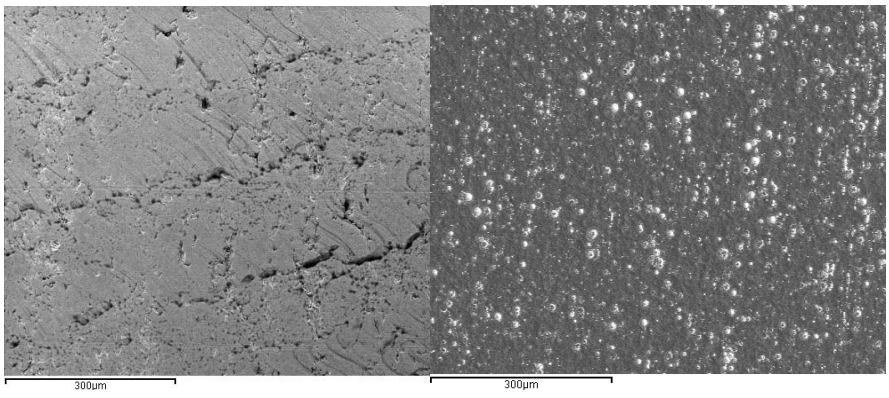
Experimental Details

The material used was SUS304 stainless steel with the main chemical composition being C: 0.06, Si: 0.63, Mn: 0.90, P: 0.032, S: 0.002, Cr: 0.29, Ni: 0.16 and Fe: Bal. The steel was processed into samples that were Φ75mm and 1mm thick. The surfaces of all the samples were degreased before being cleaned in deionized water.

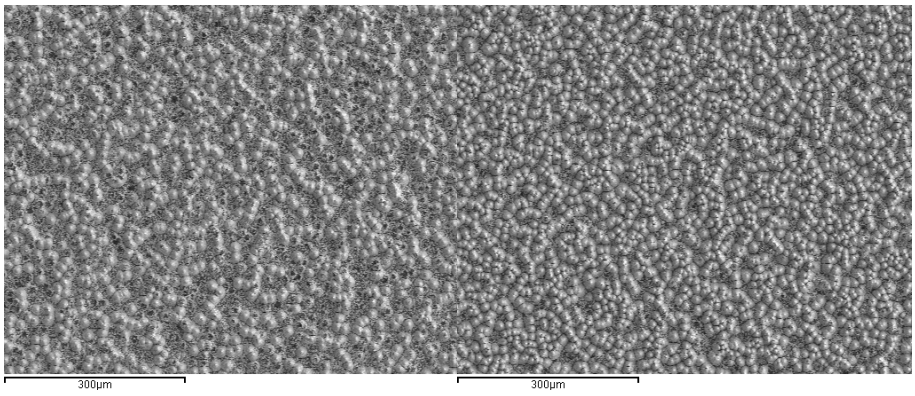
The samples were sputter-etched in an RF magnetron sputter apparatus. Each sample was placed on a 1mm thick stainless steel tray, which was placed on the sputter apparatus' sample platform. Under the sample platform, there was a cooling device which circulates water. It generated a temperature gradient between the surface and the back of the sample. Each sample surface was observed using a scanning electron microscope (SEM, FEI, QUANTA400). Roughness data were obtained using a surface roughness tester (Mahr, Perthometer), and the values from more than five indents were averaged for each sample. The surface hardness of the samples was assessed by means of a Vickers hardness tester (FUTURE-TECH, FV-700A). The applied load was gradually increased to 2N. An average was then produced using the data from ten positions.

Results and Discussion

In order to investigate the etching effect of various sputtering powers (P), experiments were carried out on SUS 304 stainless steel samples. The argon gas flow ratio R was 50sccm, the anode-to-substrate distance D was 50mm, and the sputter-etching time T was 6h. Fig.1 shows the SEM micrographs of the samples. In Fig.1 there are only a few conical protrusions on the surface of the sample etched at 200W. The number of conical protrusions on the surface of the sample increases following increases in the sputtering power. When the sputtering power is 400W, a lot of protrusions can be found on the sample surface. For the substrate etched at 600W, the protrusions precipitate both uniformly and densely on the surface.



(a) 0 W (b) 200W



(c) 400W (d) 600W

Note: *D*=50mm; *R*=50sccm; *t*=6h

Fig.1 The SEM images of sputter-etched SUS304 stainless steel

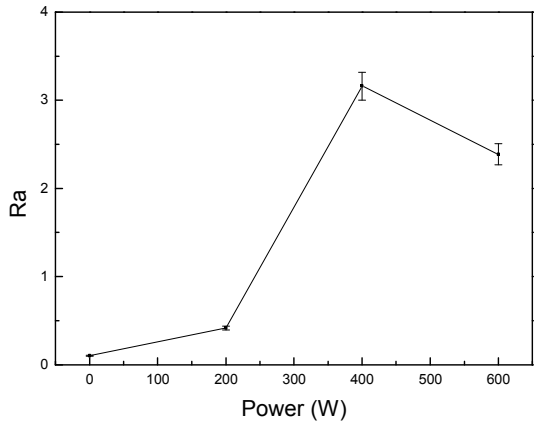
Sputter-etching is the removal of material from objects through the energy transfer that occurs when energetic atomic projectiles collide. The energy of incident ions and the energy transfer are important factors in the sputter-etching process. The RF power supply provides most of the incident ions' energy. In other words, the greater is the power, the higher is the energy of ions. In the sputter-etching process, the sputter-etching rates increase once the energy threshold is passed. Sputtering does not occur below this threshold. After the maximum is passed, the sputter-etching rates decrease at high energies. The threshold energy is not the surface binding energy but a substantially higher energy. Due to the differences in energy transfer between atomic masses and the differences in the binding energies of each component, it was found that different component atoms are removed at different rates. The sputter-etching rate of carbon atoms is lower than those of other elements in SUS304 stainless steel. When the argon ions collide with the sample surface, they transferred their energy and momentum to the sample atoms. Most of the transmitted energy was transferred into heat which caused the sample's temperature to rise. Following the increase in the sputtering power, the temperature of the sample rose. The circulated water then cooled the sample platform to generate a temperature gradient between the surface and the back of the sample. A large amount of carbon was diffused from the interior of the sample to the surface during sputter-etching. This brought about the segregation of the carbon elements at the surface because of the sharp temperature-gradient. The two reasons stated above supplied a sufficient amount of carbon atoms near the surface in sputter-etching to form a carbide layer.

The etched velocities of the micro-regions were different because of difference between the energy of the etching ions and the incident directions. The size and shape of the carbide protrusions differed following the changes in the sputter-etching conditions. The change in the surface topography also affected the etching velocity. When the sputtering power was increased within the limit, the difference between the energy of the etching ions energy was greater. From the above discussion, it can be seen that sputtering power is an important factor behind the formation of carbide protrusions on the surface of steel.

The roughness of the sputter-etched samples was analyzed using a surface roughness tester. Fig.2 shows the variation in the roughness of the surface of the samples as a function of the sputtering power. In Fig.2, it can be seen that the roughness values of the samples sputter-etched with the power being 0W, 200W, 400W and 600W were 0.103, 0.417, 3.161 and 2.387, respectively. The increase of the roughness indicates that the various amounts of carbide protrusions on the surface of the samples increased following the increase in the sputtering power. It can also be found that the roughness of the surface etched when the power was 200W only increased slightly compared with the SUS304 stainless steel sample. It implies that the number of carbide protrusions increased slowly, which can be observed in the SEM images. Roughness measurements present a rapid increase, corresponding to the sputtering power ranging from 200W to 400W. The formation of a lot of protrusions on the surface of the sample appears to be responsible for the increase in roughness. When the sputtering power increased to 600W, the roughness of surface of the sample decreased from 3.161 to 2.387. The decrease in roughness can be attributed to the increase in the density of protrusions and the uniformity of the protrusion height.

Under certain conditions, discharge carrier ionization and ion density will rise following an increase in the sputtering power. Therefore, high energy ions can easily etch the elements of the steel surface and precipitate conical protrusions, and the roughness of the surface increases. An increased roughness affects sputter-etching yields by locally varying the angle of incidence. The development of roughness alters the angular distribution of the ejecta as sputtered particles are trapped in the surfaces adjacent to the emission point. When argon ions occur at an oblique angle to

the normal surface, the sputter-etching yield increases with the angle. However, increasing the angle also means that more ions are reflected from the surface, thereby sputter-etching consumes substantially less energy. The competition of these two factors explains why the dependence of the sputter-etching yield on the angle of incidence peaks at a particular incidence angle. The slope of protrusions on the surface is different and the incidence angles of the ions are different, which leads to different sputter-etching yields on the steel surface. Sputter-etching therefore causes the development of surface roughness, which in turn may affect sputter-etching. The difference of sputter-etching yields in different local areas can lead to the uniformity of the protrusion height. This explains why the roughness of the surface sputter-etched at 600W is lower than that sputter-etched at 400W.



Note: *D*=50mm; *R*=50sccm; *T*=6h

Fig.2 The relationship between the roughness of the samples' surface and the sputtering power

Summary

When the sputtering power is 600W, the anode-to-substrate distance is 50mm, the argon gas flow ratio is 50sccm and the sputter-etching time is 6h, the conical protrusion precipitates are both uniform and dense on the surface of the sample. The surface roughness of the sample etched at high power is higher than that of the sample etched at low power.

Acknowledgment

The authors would like to acknowledge the financial support provided by"the Fundamental Research Funds for the Central Universities".

References

[1] D. Depla , R. De. Gryse: Surf.Coat.Technol Vol.183(2004), p.196.
[2] D. Chen, D. Xu, J. J.Wang, *et al*: Vacuum Vol.83(2009), p.282.
[3] Q. L. Zhang, R.G. Wang, M. Kato, *et al*: J. Jpn. Inst. Met Vol.69(2005), p.312.
[4] B. Feddes, J. G. C .Wolke:Jansen J A, *et al*. J. Appl. Phys Vol. 93(2003), p. 662.

© (2012) Trans Tech Publications, Switzerland
doi:10.4028/www.scientific.net/AMM.164.280

Efficient Synthesis and Properties of a Novel Unsymmetrical Photochromic Diarylethene Material Based on Pyrazolyl Group

Weijun Liu[1], Weiping Wang[2], Duohua Jiang[1], Gang Liu[1,*]

[1]Jiangxi Key Laboratory of Organic Chemistry, Jiangxi Science and Technology Normal University, Nanchang 330013, P.R.China

[2]Institute of Fishery in Jiangxi Province, Nanchang 330039, P.R.China

liugang0926@163.com

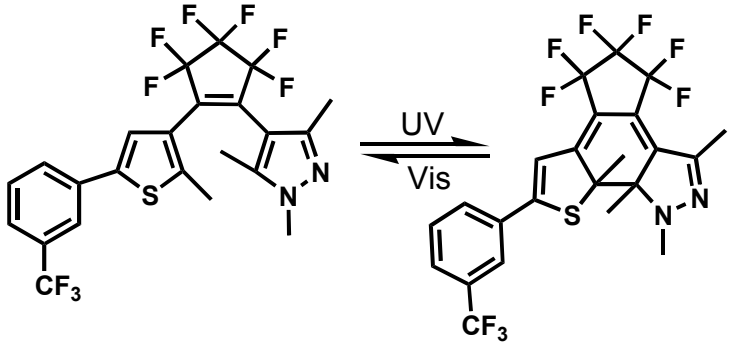
Keywords: Diarylethene; Photochromism; Fluorescence switching; Cyclization.

Abstract. An unsymmetrical diarylethene derivative was synthesized, and its photochromic properties and fluorescence switch were investigated in detail. The results showed that this compound exhibited reversible photochromism, undergoing reversible cyclization and cycloreversion reactions upon alternating irradiation with UV and visible light both in solution and in PMMA film, and its absorption maxima were observed at 574 nm in hexane and at 579 nm in PMMA amorphous film, respectively, upon irradiation with 297 nm UV light. The diarylethene 1a in hexane solution exhibited relatively strong fluorescence at 413 nm when excited at 322 nm. The fluorscence intensity is highest at the concentration of 1.0×10^{-4} mol/L when excited at 322 nm.

Intorduction

Organic photochromic compounds have obtained considerable interest due to their potential agree for photonic applications to optical data storage, optical memory and switching devices [1-6]. Up to date, among various photochromic compounds, diarylethenes derivatives have been investigated due to their excellent thermal stability, fatigue resistance, rapid response and high reactivity in the solid state [4,7]. Upon photo-irradiation, diarylethene materials happen to reversible photochromic reactions and photogenerated isomers go back the original isomers upon irradation with visible light in solution or in the solid state. Above all, diarylethenes bearing phenyl groups on the end are of special interest, because the end group substituted by electron donating group or electron withdrawing group, inevitably influence the optoelectronic properties of corresponding diarylethenes [8].

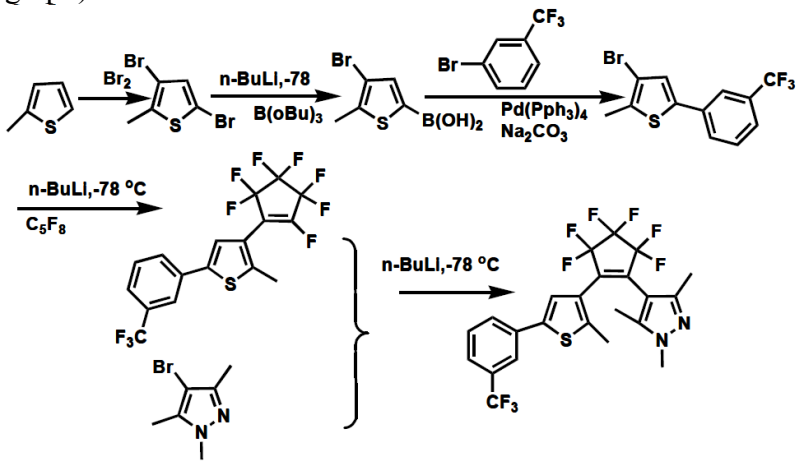
In the present study, we designed a photochromic diarylethene compound, 1-[2-methyl-5-(3-trifluoromethylphenyl)-3-thienyl]-2[1,3,5-trimethyl-4-pyrazolyl]-perfluorocyclopentene(1a). The results showed that this compound exhibited reversible photochromism, undergoing reversible cyclization and cycloreversion reactions upon alternating irradiation with UV and visible light in solution and PMMA film, respectively. The fluorescence intensity of diarylethene 1a decreased dramatically along with the photochromism from open-ring isomer to closed-ring isomer upon irradiation with 297 nm UV light in hexane. The photochromic reaction of diarylethene 1a is shown in Scheme 1.



Scheme 1. Photochromism of diarylethene **1**.

Experiments

Synthesis of a novel photochromic diarylethene. THF was distilled over lithium aluminium hydride under argon. All other solvents were used as received. The other reagents were purchased from Beijing Reagents Ltd. Diarylethene 1a was prepared according to the method described in scheme 2. The structure of compound 1a was confirmed by ^{1}H NMR. ^{1}H NMR ($CDCl_3$, 400 MHz, TMS): δ 1.98 (s, 3H, -CH_3), 1.99 (s, 3H, -CH_3), 2.02 (s, 3H, -CH_3), 3.70 (s, 3H, -CH_3), 7.32 (s, 1H, thienyl-H), 7.50 (t, J = 7.6 Hz, 1H, phenyl-H), 7.55 (d, 1H, J = 7.6 Hz, phenyl-H), 7.70 (d, 1H, J = 7.6 Hz, phenyl-H), 7.74 (s, 1H, phenyl-H).The section headings are in boldface capital and lowercase letters. Second level headings are typed as part of the succeeding paragraph (like the subsection heading of this paragraph).



Scheme 2. Synthetic route for the compound 1a.

Preparation of PMMA film. One hundred milligram of PMMA was first dissolved in 1mL chloroform, which was stirred ultrasonically to make it homogeneous. Samples were obtained by dissolving ultrasonically 10 mg of compounds 1 with 1mL of the PMMA solution, respectively, and the solution was spin-coated on a glass substrate with a spin rotation speed of 1500 rpm.

Result and Discussion

Photochromism in solution and in PMMA film. The changes in the absorption spectra of diarylethene 1 induced by photoirradiation at room temperature in hexane are shown in Fig. 1. Upon irradiation with 297 nm UV light, the colorless solution of 1a turned to blue with a new visible absorption band centered at 574 nm attributable to the closed-ring isomer 1b. The blue colored solution reverted to colorless upon irradiation with visible light (λ > 450 nm), indicating that 1b returned to the initial state 1a, and a clear isosbestic point was observed at 322 nm.

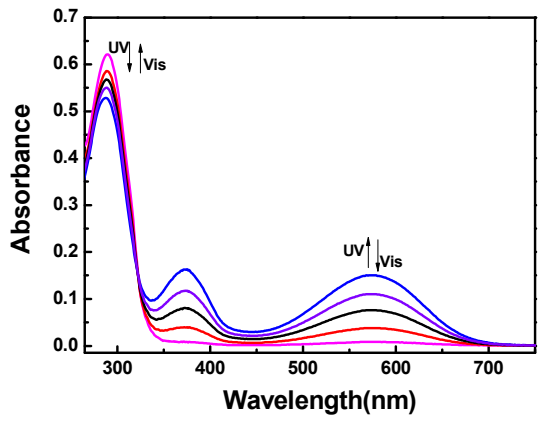


Fig. 1. Absorption spectral changes of 1a in hexane (2.0×10^{-5} mol/L).

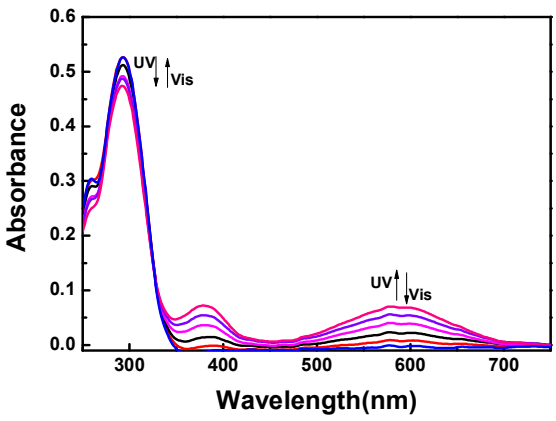


Fig. 2. Absorption spectra of compound 1a in PMMA amorphous film(10%w/w).

Similarly, diarylethene 1a also showed good photochromism in the PMMA amorphous film, as shown in Fig. 2. In PMMA film, upon irradiation 297 nm UV light, the color of 1a/PMMA flim (λ = 289 nm) changed from colorless to blue due to the appearance of a new broad absorption band at λ = 579 nm assigned to the formation of the closed-ring isomer 1b. Then, upon irradiaton of appropriate visible light (λ > 450 nm), the colored PMMA film can invert colorless. Form the above descripion, we can easily get a conclusion that the maximum absorption wavelengths of both the open-ring isomer and the closed-ring isomer in PMMA film are longer than those of them in hexane solution. In addition, it was found that both open-ring isomer and closed-ring isomer of this diarylethene 1a were stable both in solution and in PMMA film at room temperature in darkness.

Fluorescence spectral of diarylethene 1a in hexane solution. The fluorescence properties of the compound 1a in hexane were measured using a Hitachi F-4500 spectrophotometer, and the breadths of excitation and emission slit were selected 10.0 nm and 10.0 nm, respectively. Upon irradiation with 297 nm light, the fluorescence spectral changes of 1a in hexane at room temperature were demonstrated in Fig. 3. As shown in this figure, it could be clearly seen that 1a in hexane exhibited relatively strong fluorescence at 444 nm when excited at 322 nm. The fluorescence intensity decreased along with the photochromism from open-ring isomers to closed-ring isomers upon irradiation with 297 nm UV light, due to producing the weak fluorescence closed-ring isomer [10]. The emission intensity of diarylethene 1 in a photostationary state was quenched to ca. 77%. The incomplete cyclization reaction and the existence of parallel conformations may be the main cause for the moderate change in fluorescence induced by photo-irradiation [11]. The back irradiation by appropriate wavelength visible light regenerated its open-ring isomer and recovered the original emission intensity. This merit can be potentially applied to optical memory with fluorescence readout method [12].

Fig. 4 shows the concentration dependence of fluorescence emission spectra of 1a in hexane at room temperature. When the concentration of 1a in hexane excited at 322 nm increased from 1.0×10^{-6} to 1×10^{-3}mol/L, the fluorescence intensity increased with increasing concentration, but when the concentration increased enough high, the fluorescence intensity decreased rapidly. The fluorscence intensity is highest at the concentration of 2.0×10^{-4} mol/L. The result designated that molecular aggregation and fluorescence quench take place due to concentration increasing [12].

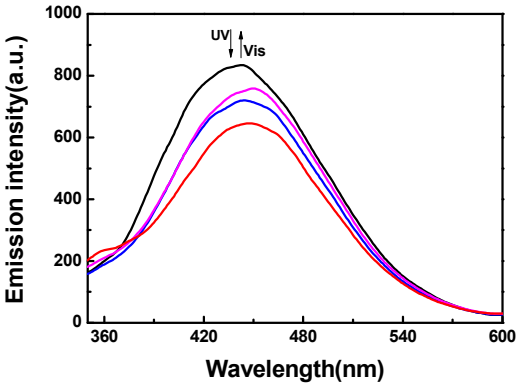


Fig. 3. Fluorescence spectra of diarylethene 1a in hexane excited at 322 nm upon irradiation with 297 nm UV light.

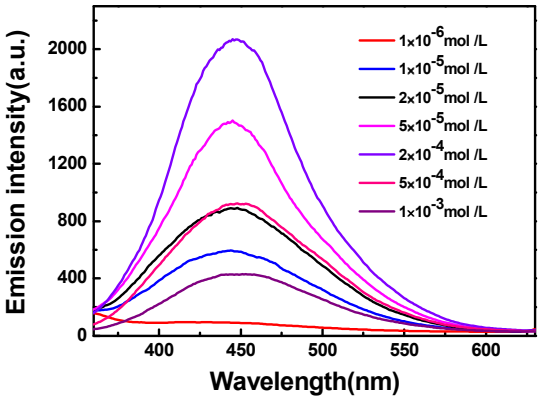


Fig. 4. Fluorescence spectra of diarylethene 1a in various concentrations in hexane excited at 322 nm at room temperature.

Conclusion

In a word, the new diarylethene with a benzothienyl aryl unit described here has been synthesized and it showed good photochromic behavior both in solution and in PMMA film. Diarylethene 1a showed relatively strong fluorescence in hexane solution, and its fluorescence intensity decreased along with the photochromism from open-ring isomers to closed-ring isomers upon irradiation with 297 nm UV light. In hexane, the fluorscence intensity is highest at the concentration of 2.0×10^{-4} mol/L at 446 nm when excited at 322 nm.

Acknowledgment

This work was supported by the Project of Natural Science Foundation of Jiangxi Province (2010GQH0038 and 2009GQH0036) and the Science Funds of Jiangxi Education Office (GJJ1067).

References

[1] M. Irie: *Photo-Reactive Materials for Ultrahigh-Density Optical Memory*(Elsevier, Amsterdam 1994).
[2] B.L. Feringa: *Molecular Switches* (Wiley-VCH Publication, Germany, 2001).
[3] M. Irie: Chem. Rev. Vol. 100 (2000), p. 1685.
[4] H. Tian and S.J. Yang: Chem. Soc. Rev. Vol. 33 (2004), p. 85.
[5] M. Irie, T. Fukaminato, T. Sasaki, N. Tamai and T. Kawai: Nature Vol. 420 (2002), p. 759.
[6] H. Durr and H. Bouus-Laurent: *Photochromism: Molecules and Systems* (Elsevier, Amsterdam, 2003).
[7] K. Matsuda and M. Irie: J. Photoch. Photobiol. C. Vol. 5 (2004), p.169.
[8] S.Z. Pu, T.S. Yang, J.K. Xu, L.Shen, G.Z. Li, Q. Xiao and B. Chen: Tetrahedron Lett. Vol. 61 (2005), p. 6623.
[9] S.Z. Pu, J.K. Xu, L. Shen, Q. Xiao, T.S. Yang and G. Liu: Tetrahedron Lett. Vol. 46 (2005), p. 871.
[10] C.B. Fan, S.Z. Pu, G. Liu and T.S. Yang: J. Photoch. Photobiol. A. Vol. 194 (2008), p. 333.
[11] T.B. Norsten and N.R. Branda: J. Am. Chem. Soc. Vol. 123 (2001), p.1784.
[12] F. Tuyoshi, K. Tsuyoshi, K. Seiya and M. Irie: J. Phys. Chem. B. Vol. 107 (2003), p. 8372.

© (2012) Trans Tech Publications, Switzerland
doi:10.4028/www.scientific.net/AMM.164.284

The effects of the self-assembly time on the preparation of lanthanum-based thin films on sulfonated 3-mercaptopropyl trimethoxysilane

Tao Bai [1, a], Xianhua Cheng [2,b]

College of Mechanical Engineering, Donghua University, Engineering Research Center of Advanced Textile Machinery, Ministry of Education, Shanghai 201620
College of Mechanical Engineering, Shanghai Jiao Tong University, Shanghai 200030, China

[a]baitao@dhu.edu.cn, [b]xhcheng@sjtu.edu.cn

Key Words: rare earth, self-assemble film, AFM, characterization of the films

Abstract. Lanthanum-based thin films are deposited on the oxidized 3-mercaptopropyl trimethoxysilane self-assembled monolayer (MPTS-SAM) based on the chemisorption of the sulfonic group. The surface energy, chemical composition, phase transformation and surface morphology of the films are analyzed by using contact angle measurements, X-ray photoelectron spectroscopy (XPS) and atomic force microscopy (AFM). The experimental results indicate that the lanthanum-based thin films are absorbed on oxidized MPTS-SAM and lanthanum element with different oxidation states exists in the thin films deposited on the surface of self-assembly monolayers. The content of lanthanum on the oxidized MPTS-SAM increases with the extension of the assembly time and the rare earth reached saturation when the time was 6h.

Introduction

SAMs are ordered molecular assemblies formed by the chemical adsorption of an active surfactant on a solid surface. The research of SAMs has become a focus in the field of material science in the last decade [1-2]. Du et al. [3] found that functionalized, siloxane-anchored, organic thin films can be spontaneously formed on the oxide layer of silicon substrates by immersion into solutions of alkyltrichlorosilanes, where terminal groups determines the exposed monolayer surface functionality and the trichlorosilane is the anchoring group. Usually, the terminal functionality can be chemically or photochemically modified so as to dramatically alter the monolayer's chemical composition, reactivity, and physical characteristics. Ordered molecular arrangements can be supplied by SAM adsorption even on solid surfaces of random atomic arrangements such as those of glass substrates, which provides a great potential for controlled inorganic crystal growth [4].This simple process makes SAMs inherently manufacturable and thus technologically attractive for engineering.

Numerous studies have been conducted to understand the applications of RE in many fields such as optics, medicine, magnetics, tribology and so on [5-8]. A lot of RE compounds have been used as lubricants and lubricating additives and some RE organic compounds such as rare earth dialkyldithiophosphate exhibit good friction -reducing and wear-resistant properties, excellent corrosion resistance and high anti-scuffing ability [9]. The self-assembled RE films is sequential compact structure which shows wide potential application in lubrication and wear protection. The RE multilayer films reacted with the substrate by chemical bond. This reaction was thought to be

helpful in increasing the bonding strength between the films and the substrates, which can avoid sever brittle fracture happening on the surface of the films in the friction and wear which led to the invalidation of the films.

In this study, RE films were prepared and the properties were investigated. Several means, such as X-ray photoelectron spectroscopy (XPS), atomic force microscopy (AFM), etc. were applied to characterize the structure and properties of the thin films.

Experimental Details

Firstly, the preparation of the MPTS SAM was performed according to the literature [10]. The Rare-earth solution was prepared as follows: 0.3 wt% lanthanum chloride (LaCl3) and 0.1 wt% ethylenediamine tetra-acetic acid were mixed with alcohol, followed by stirring at room temperature for 1 h. The PH was adjusted to 4-5 using nitric acid. Then the substrates coated with the sulfonated MPTS-SAM were immersed in the resulting mixed solution at 90 oC for different time, to allow the adherence of the lanthanum-based thin films on the sulfonated MPTS-SAM. Finally, the substrates were cleaned ultrasonically with deionised water to remove physisorbed ions or molecules and dried, then cooled in a desiccator.

In this study XPS analysis was conducted on a PHI-5702 XPS system, using Mg-Ka radiation operating at 250 W and a pass energy of 29.35 eV. The binding energy of C1s (284.6 eV) was used as the reference. Morphological properties of the RE films were performed with a NanoScope IIIa atomic force microscopy (Digital Instruments Inc.) using “constant force” mode. All measurements were performed in air at 23 oC and 37 % relative humidity (RH). Contact angles of water were measured by the sessile drop method using the OCA-20 measurement apparatus (DataPhysics Instruments GmbH) under ambient laboratory conditions (24 oC, 40 % RH).

Results and Discussion

Fig.1 shows the XPS spectra of La3d on the surface of sulfonated MPTS-SAM coated with RE. The La3d core level band of surface also decomposed into four peaks at binding energies of 835, 838.6, 851.8 and 855.2 eV, but, the characteristic binding energy of La3d is 834.8 eV [11]. That indicates that a lanthanum based film has been successfully obtained in our work. The existence of different oxidization states which can be seen at the binding energy side of the La3d band indicated that the chemical structure of La in the deposited films was complicated. The atomic relative concentrations of lanthanum element in the deposited films increase with self-assembled time, which indicates that the adsorption behaviour of rare earth is a gradual process. Fig.2 shows the trend of the lanthanum content on the surface with the assembly time. From Fig6, the content of lanthanum increases with the extension of the assembly time. The content of lanthanum no further increase when the time was 6h, indicated that the rare earth reached saruration.

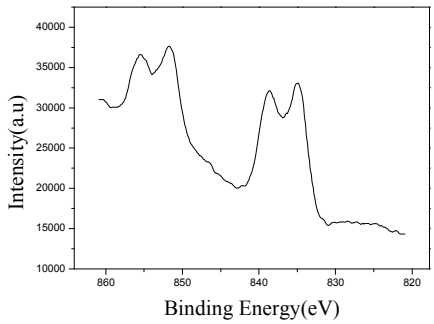


Fig.1 XPS spectra of La_{3d} in RE SAM

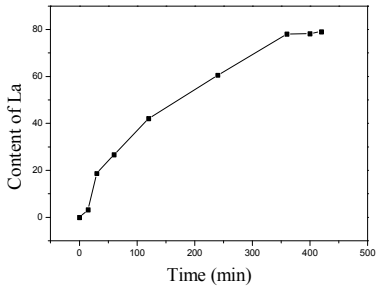
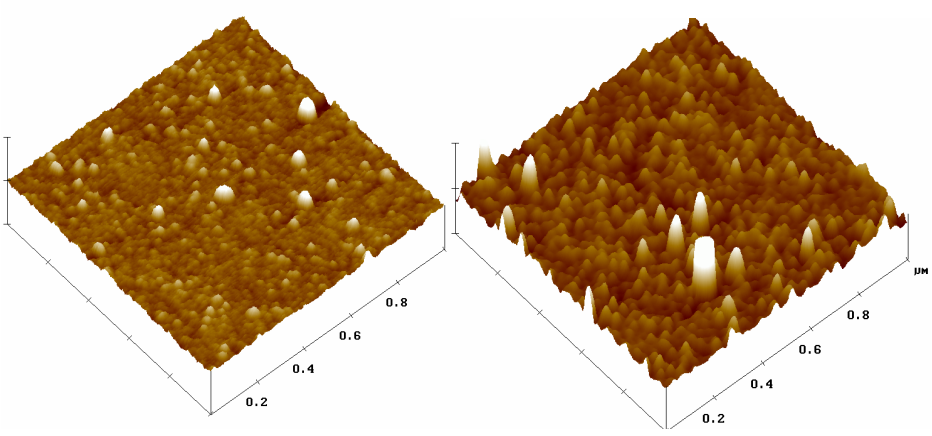
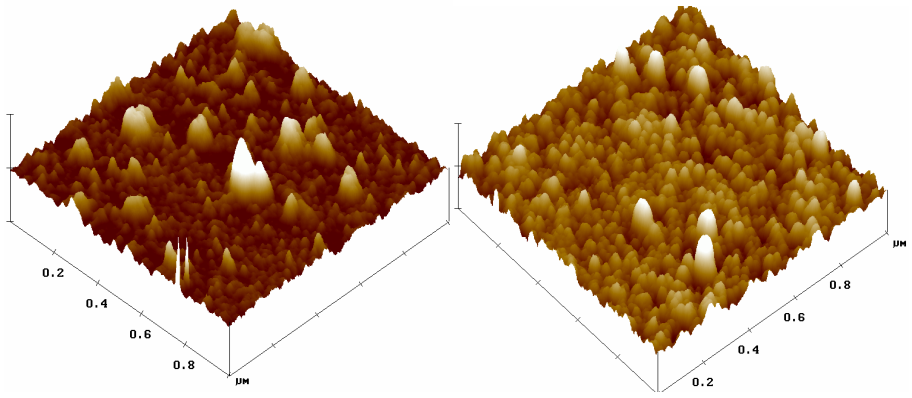


Fig.2 Content of La^{3+} in RE SAM acquired as a functional of immersion time

The effects of the self-assembled time on the formation of lanthanum films was analyzed with the deposition on the sample surface lasting for 0.5h,1h, 3h and 6h, respectively. The results are presented in Fig.3. Fig.3 shows a series of AFM images of Lanthanum-based thin film deposited in different time. From the AFM images presented in Fig.3 (a), only a few of globular islands are deposited on the MPTS-SAM. After the deposition of the Lanthanum-based thin film on the sulfonated MPTS-SAM, much difference is visible in the corresponding AFM images. Namely, the surface of the deposited film is rough and shows quadratically-looking features. From the Fig.3 (b)-(c), the globular islands on the deposition films increase with the increase of the deposition time. When the time was 6h, there were a large of protrusions on the surface and the size of the protrusions was smaller than that on the substrate for 3h.



(a) 30 min (b) 60 min

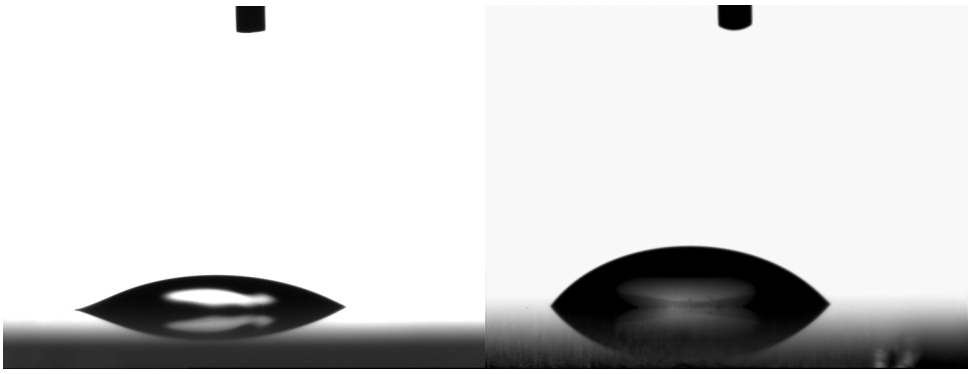


(c) 3h (d) 6h

Fig.3 AFM of RE SAM acquired as a functional of immersion time

Fig.4 shows a series of water contact angles of Lanthanum-based thin film deposited in different time. Fig.5 shows a typical plot of the variation of water contact angles as a function of time after deposition. The increase of contact angle from 30 to 64^{o} indicates that the various ratios of lanthanum-based thin film absorbed on oxidized MPTS-SAM increase with increasing times. Water contact angle measurements present a rapid increase, corresponding to deposition times ranging from 0 to 6h. Obviously, the increase of the number of molecules absorbed on the substrate is responsible for the increase in the contact angles. When deposition time is over 6 h, the contact angle remains constant, which implies that the adsorption becomes saturated.

The rare-earth elements belong to IIIB in the periodic table of elements. Rare-earth element's special electronic shell provides them a complicate mechanism to bond with other elements. Rare earth elements have outstanding chemical activity due to their special 4f electronic shell structure. Due to electrons on the 4f electronic shell do not screen the atomic nucleus completely, RE atom has a big effective nuclear charge [12].The oxidized MPTS-SAM provide net negative charge, thus promoting the process of self-assembly. In this process, the group in the sulfonated MPTS-SAM provides a high degree of surface acidity which can promote the adsorption of rare earth.



(a) 0 min (b) 6 h

Fig.4 Contact angle of water on RE SAM acquired as a functional of immersion time

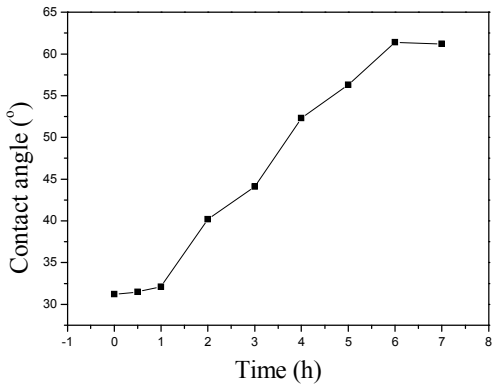


Fig.5 Contact angle of Lanthanum-based thin film acquired as a functional of time

Summary

Lanthanum-based thin films were formed on the oxidized MPTS-SAM, and different oxidation states of lanthanum element exist in the films as-deposited. From the experimental results, the adsorption behaviour of rare earth on the MPTS-SAM is a gradual process. On the basis of detailed shape analysis of the La3+ XPS peaks, the true chemical shift resulting from the La3+ chemical state variation indicates that the RE film almost reacted with the substrate by chemical bond.

Acknowledgement

The authors would like to acknowledge the financial support provided by “the Fundamental Research Funds for the Central Universities”

References

[1] H. Cheng, Y. A. Hu: Adv. Colloid Interface Sci Vol.171-172 (2012), p. 53.
[2] I. Y. Huang, M. C. Lee: Sens.Actuators, B Vol.132 (2008), p. 340.
[3] Y. Z. Du, L. L. Wood, S. S. Saavedra: Mater. Sci. Eng C Vol. 7 (2000), p. 161.
[4] Z. Xiao, J. Gu, D. Huang, Z. Lu, Y. Wei: Appl. Surf. Sci Vol.125 (1998), p. 85.
[5] T. Bai, X.H. Cheng: J. Rare Earth Vol. 1 (2007), p. 114.
[6] T. Bai, X.H. Cheng: J. Rare Earth Vol. 26 (2008), p. 93.
[7] J. Zhuang, Y. Y. Chi, J. N. Shi, D. H. Zhu, M. J. Tu: J. Rare Earth Vol.20 (2002), p.324.
[8] :Thin Solid Films Vol. 515(2006), p. 2262.
[9] X.H. Cheng, T. Bai: Wear Vol. 260 (2006), p. 745.
[10] Z. Xiao, L. Su, N. Gu, Z. Lu, Y. Wei:Thin Solid Films Vol. 333 (1998), p. 25.
[11] S. G. Yang, J. Y. Liu, Z. Y. Wu, Y. S. Lin, X. Y. Chen, M. X. Zhan: J. Xiamen University (Natural Science) Vol. 43 (2004), p. 423.
[12] T. Bell, Y. Sun, Z. Lui, M. Yan: Heat Treat Metal Vol.27 (2000), p. 1.

© (2012) Trans Tech Publications, Switzerland
doi:10.4028/www.scientific.net/AMM.164.289

Feasibility of Reutilizing Municipal Solid Waste Incineration residues as Construction Materials

Ruijing ZHANG, Yanjun HU

Institute of Energy and Power Engineering, Zhejiang University of Technology, Hangzhou, China,
E-mail: zjuthyj@163.com

Keywords: Municipal solid waste incineration (MSWI), incineration, bottom ash, reutilization, road base

Abstract: The presented study mainly focused on investigating detailed engineering properties of municipal solid waste incineration residues as road construction materials with different application classes. Also, the leachability of heavy metals and salts in the residues as a function of the ratio of liquid and solid was tested. The Chinese specifications about road construction materials were employed to evaluate the application capacity of the waste incineration residues. The obtained results indicate that bottom ash basically complies with the technical requirements for road base and sub-base materials with exception of the low compataclity and high organic content of the fine fraction. The toxicity test showed that bottom ash can satisfy the limit values of heavy metals and salts that was established by Chinese specification for hazard solid waste. For the application of the ash in road base, it should be mixed with other materials to improve the compataclity. Pretreatment of fine fraction of bottom ash to remove organic matter is necessary.

Introduction

In China, sustainable waste management policies are encouraging reutilization of municipal solid waste incineration residues, such as bottom ash and fly ash. One of the advantages is to avoid the possible environmental impact as a result of landfills of MSWI residues [1]. In addition, to make full use of bottom ash as a natural aggregate substitute is a promising way of managing solid waste and saving natural rock materials [2, 3]. The assessment of reusing MSWI residue and its toxicity has not been established in a generalized route yet in China, especially incineration bottom ash. Some studies have been conducted regarding physical, mineralogical, and chemical properties of fractions of MSWI bottom ash [4-5]. However, a detailed research work in the field of reutilizing bottom ash as road base materials is still in a starting and relatively blank stage. The ash is a highly heterogeneous burnt-out mixture of slag, ferrous and non-ferrous metal, ceramics, glass, other non-combustibles and residual organic matter. The extreme heterogeneity of bottom ash combined with the potential leachability of heavy metals and salt means that basic information concerning engineering properties is likely to be necessary to be assessed and investigated prior to its reutilization in most civil engineering applications. Therefore, a proper evaluation about the possibilities of recycling main components of bottom ash is significant and necessary.

This study was aimed to investigate the feasibility of recycling main components of MSWI bottom ash in road construction and assess its environmental hazard. The present work comprehensively focused on engineering properties, chemical characteristics and toxicity of MSWI bottom ash towards its eventual reutilization in road base and sub-base materials.

1 Experimental

1.1 Samples collection and preparation

Bottom ash was sampled from a MSW incineration facility located in Tianjin. The facility was started to operate in the year of 2006. It incinerated 1200 ton/day of household waste and produced approximately bottom ash of 300 ton/day and fly ash of 14 tons per day. Approximately 1 ton of bottom ash was sampled through quartering. The method of quartering for the sampling work was conducted to decrease the sample size from 100 tons to 1 ton. Metal and unburned materials contained in MSWI bottom ash will increase the damage and complexity of reutilization. A magnetic separator and an eddy current separator were therefore used to remove metals and organic matters from bottom ash.

1.2 Determination of engineering and chemical parameters

A typical road pavement consists of several layers, composed of different materials, chosen for their particular properties, such as wearing course, base course, road base, sub-base, capping layer and sub-grade. The specific engineering parameters defined by the Chinese Specification for road construction, were required on the materials in each layer [6-9]. To determine the feasible application of MSWI bottom ash as an aggregate substitute in road construction, some key engineering and chemical compositions were analyzed in this study. The toxicity of bottom ash was conducted following the identification standards for hazardous wastes-Identification of extraction toxicity [10]

2 Experimental Results

2.1 Study of the bottom ash leachates

The leaching tests focused on the reproduction of field conditions to yield information about the potential environmental impact. The results of the leaching tests of the tested bottom ash are shown in Table 1.

Table 1 Results of the leaching of MSWI bottom ash

Major leachates	Leaching limit value of solid waste in China (mg/l)	Fine fraction (mg/l) (<4.75mm)			Coarse fraction (mg/l) (>4.75mm)		
		S/L=1:2	S/L=1:5	S/L=1:10	S/L=1:2	S/L=1:5	S/L=1:10
PH value	-	11.8	11.4	11.6	11.8	11.7	11.6
Conductivity (mS/cm)	-	4.60	2.39	1.82	3.81	2.07	1.55
Temperature	-	25	25	25	25	25	25
Redox potential mV	-	49.6	75.1	72.5	51.3	74.9	63.6
Chlorides	-	978.9	459.9	233.8	791.5	303.4	161.6
Sulfates	-	575.6	378.8	199.8	267.2	196.4	154.9
Cu	50	0.55	0.55	0.15	1.30	0.21	0.30
Zn	50	0.12	1.9	0.08	9.45	0.71	3.06
Mo	-	0.15	0.6	0.04	0.10	0.05	<0.03
Hg	0.05	<0.03	<0.03	<0.03	<0.03	<0.03	0.03
Ni	25	<0.03	<0.03	<0.03	0.06	<0.03	<0.03
Pb	0.03	<0.05	<0.05	<0.05	<0.05	<0.05	<0.05
As	-	<0.03	<0.03	<0.03	0.06	<0.03	<0.03
Cd	-	<0.03	<0.03	<0.03	0.06	<0.03	<0.03
Cr	-	0.05	0.04	<0.03	0.08	<0.03	0.03

2.2 Reactivity with cement alkalis:

Results obtained from measurement of the potential reactivity with the cement alkalis showed that soluble silicon concentration was 7.5 mmol/l, and alkalinity reduction (R) was 277 mmol/l. The R parameter was compared with a predefined value, and the aggregate was would be reactive if: R>70 and the concentration SiO_2> R, or R < 70 and the concentration SiO_2>35+ 0, 5 R. Therefore, the bottom ash did not present reactivity with the cement alkalis.

2.3 Evaluation of utilizing bottom ash as road construction materials

The aggregates were classified as fine (< 4.75 mm) and coarse (> 4.75 mm) fractions. They were usually referred to as sand and gravel originating from different natural extraction sources. The obtained results of the main engineering properties of the fine and coarse fractions of MSIW bottom ash were compared with Chinese specification for road construction materials. The comparison between requirements and the tested incineration bottom ash were shown in Table 2, 3, 4 and 5.

Table 2 Summary of the results of the test required by Chinese specification for road construction: concrete: fine fraction

Test	Condition: fine fractions for making concrete	Bottom ash result	Fulfilled
Grain size distribution	The smaller than 0.08 mm particles should be less 5%.	0.05% of smaller than 0.075 mm particles	YES
Silicon percentage	In pavement, percentage of silicon particles not lower than 28%	50-55.8%	YES
Organic matter content	<2%	Fine fraction: 3.6%	NO
Reactivity	Does not present potential reactivity with cement alkalis	Without potential reactivity	Yes
Plasticity			

Table 3 Summary of the results of the test required by Chinese specification for road construction: coarse aggregate

Test	Condition: coarse fractions for making concrete	Bottom ash result	Fulfilled
Grain size distribution	The maximum size is smaller than 50 mm, the sizes. The fraction with size smaller than 0.08 mm will be lower than 1.1%	Sizes of all particles is bigger than 4.75 mm	YES
Wear coefficient	Lower than 52	53.5	No
Sand equivalent	Sub-base, heavy and medium traffic: higher than 30; For light traffic higher than 25.	31	YES
Organic matter content	<2%	1.9%	YES
Reactivity	Does not present potential reactivity with cement alkalis	Without potential reactivity	Yes

Table 4 Summary of the results of the test required by Chinese specification for road construction: heavy traffic way

Test	Condition of granular bases and sub-bases	Bottom ash result	Fulfilled
Grain size distribution	Maximum size is 37.5 mm, the smaller than 0.075mm particles should be less 7%.	Maximum size is 40mm 0.05% of smaller than 0.08 mm particles	YES
Bear capacity			NO
Standard density	2600-2700 kg.m^{-3}	Coarse fraction: 2800-2940 kg.m^{-3} Fine fraction:2460-2720 kg.m^{-3}	YES No
Wear coefficient	Lower than 52	Coarse fraction: 40 Fine fraction:34.4	Yes
Sand equivalent	Higher than 35	75	Yes
Bearing capacity	CBR index higher than 18	Average value: 63.5	YES
Plasticity	Index < 5	no plasticity	YES
Organic content	<2%	2.7%	No

Table 5 Summary of the results of the test required by Chinese specification for road construction: Medium and light way

Test	Condition of granular bases and sub-bases	Bottom ash result	Fulfilled
Grain size distribution	Maximum size is 37.5 mm, the smaller than 0.075mm particles should be less 7%.	Maximum size is 40mm 0.05% of smaller than 0.08 mm particles	YES
Bear capacity			NO
Standard density	2600-2700 kg.m^{-3}	Coarse fraction: 2800-2940 kg.m^{-3} Fine fraction:2460-2720 kg.m^{-3}	YES No
Wear coefficient	Lower than 52	Coarse fraction: 40 Fine fraction:34.4	Yes
Sand equivalent	Higher than 35	75	Yes
Bearing capacity	CBR index higher than 18	Average value: 63.5	YES
Plasticity	Index < 5	no plasticity	YES
Organic content	<2%	2.7%	No

4. Discussion and conclusions

From the results of the leaching tests, it can be found that the leaching contents of a few elements exceed the leaching limitation values in developed countries, such as the Netherlands and France. It can be expected that a more strict limitation of toxic elements leaching can generate a deep change in the application possibilities and the related management. So far, the toxicity test showed that bottom ash can satisfy the limit values of heavy metals and salts that was established by Chinese specification for hazard solid waste.

On the basis of the engineering properties analyses, the bottom ash shows a well-graded granular with a continuous grain size distribution and low proportions of non-plastic fractions. It happens to be a basically feasible material for base and sub-bases granular layers of the medium and light traffic road. However, it is not suitable to use in the high way and one-class road of the heavy traffic as results of its several deficiencies. Compared with the standard apparent particle density of natural aggregates ranged from 2600 to 2700 kg/m^3, the coarse fraction of bottom ash can be reutilized as natural aggregates and the fine fraction is suitable to be used as a material lighter than natural gravel. The water sorption of the coarse fractions are considered to be higher in comparison with those observed for normal natural aggregates (<3.5%). Therefore volume reduction during field compaction and possible damage because of frost action in cold areas should be taken into account. The results of wear resistance show that the fine fraction of MSWI bottom ash has a poorer resistance to abrasive wear. As required, the wear coefficient of the fine fraction did not fulfill the

standard of smaller than 30 when reutilizing it as road bases of heavy or medium traffic. Therefore, the fine fractions of MSWI bottom ash do not fulfill above standard, and the coarse fraction was very close the standard value for light traffic.

The obtained results indicate that bottom ash basically complies with the technical requirements for road base and sub-base materials with exception of the low compataclity and high organic content of the fine fraction. For the fine fraction, because of its high organic content, it is limited to use in the concrete pavement. Nevertheless, the use of the fine fraction of MSWI bottom ash in concrete pavement would be feasible if the organic content can be decreased through improving combustion technologies, or add pre-treatment of MSWI bottom ash prior to reutilization. However, the reutilization in concrete pavement, highway and first grade class road will be limited as results of the high organic content in the fine fraction, and the deficiencies of sand equivalent and compatibility of the bottom ash.

With the growth of incineration of MSW, the disposal of the increasing amount of bottom ash is becoming a new issue in the field of waste management. A societal goal towards bottom ash management is focusing on converting the ash into useful products without any negative impact on environment and human health. Feasible technologies of improving its engineering properties are necessary to up-cycle the ash as a higher class material. In addition, with the structure of the incinerated MSW changing, such as more and more small WEEE, plastics, parts of medical and industry wastes ending up into incinerator, the toxicity of the ash should be taken into account in future in case of pollution. A continuous control and monitor of the environmental quality of the ash has to be carried out.

5 Acknowledges

The authors want to appreciate the projects of National Natural Science Foundation (Grant No.51008279) and Zhejiang Provincial Natural Science Foundation (No. Y5100258) for providing financial support of this research work.

References

[1] Y. Q Pei, L. Wang, S. M Ding, et.al.. Leaching characteristics and impact factors of heavy metals on the flying ash due to the urban garbage incineration [J], Safety and Environment. 2008, 8(4): 23-26

[2] O Hjelmar, Disposal strategies for municipal solid waste incineration residues [J], *Hazardous Materials*, 1996, 47(1-3): 345-368

[3] R. A. Rashid, G. C. Frantz. MSW incinerator ash as aggregate in concrete and masonry [J], *Materials in Civil Engineering*, 1992, 4(4): 353-368

[4] C. Speiser, T. Baumann, R .Niessner, Characterization of municipal solid waste (MSWI) bottom ash by scanning electron microscopy and quantitative energy dispersive X-ray microanalysis (SEM/EDX), Fresenius J. Anal Chem, 2001, 370(6): 752-759

[5] S. Dugenest, H. Casabianca, M. F. Grenier-Loustalot, Municipal solid waste incineration bottom ash: Physicochemical characterization of organic matter [J]. *Analysis*, 1999, 27(1):75-81

[6] Technical Standard of Road Surface and Base materials (JTJO34-2000) [S]，Ministry of Transport of the People`s Republic of China, 2000.

[7] Technical Norm NLT 111, 1987, Geotechnical Laboratory Cedex (Centro de Estudiosy Experimentación deobras públicas）[S]. Ministry of Foment, Spain.

[8] Technical Norm NLT 108, 1991. Geotechnical Laboratory Cedex [S]. Ministry of Foment, Spain

[9] ASTM C1260 - 07, 2003, Standard Test Method for Potential Alkali Reactivity of Aggregates

[10] Identification standards for hazardous wastes-Identification of extraction toxicity [S]，GB5086.1-1997 [S], Ministry of Environmental Protection of the People's Republic of China，1997

© (2012) Trans Tech Publications, Switzerland
doi:10.4028/www.scientific.net/AMM.164.293

Preparation and electrochemical performance of $Li_4Ti_5O_{12}$ as anode material for Li-ion battery by solid state method

Fang Gu[1,a]

[1]Key Laboratory of Food Science and Engineering,College of Food Engineering, Harbin University of Commerce Harbin 150076

[a] gufangwell@126.com

Keywords: Lithium-ion battery . Anode material . $Li_4Ti_5O_{12}$. Solid state method

Abstract. Spinel compounds $Li_4Ti_5O_{12}$ were synthesized via solid state reaction in an Air atmosphere and electrochemical properties were investigated by means of X-ray diffraction, cyclic voltammetry, and charge–discharge tests. The results indicated that the compound was spinel structure, and the initial capacity could reach 162.28 $mAh \cdot g^{-1}$ and the cycling performance was good, implying the spinel structure of $Li_4Ti_5O_{12}$ was more stable when the material was tested by charging-discharging. The Li^+ could reversibly intercalate and deintercalate in the anode material. The material prepared by solid-state method showed a promising commercial application in lithium-ion batteries.

Introduction

Ohuzuku [1] et al reported the spinel $Li_4Ti_5O_{12}$ as lithium ion battery anode materials firstly at 1995. This material had gained more attention[2-5]. Traditional preparation methods of spinel $Li_4Ti_5O_{12}$ mainly had high temperature solid state method and sol-gel method[6]. Hsiao[7]et al prepared D- $Li_4Ti_5O_{12}$ and P- $Li_4Ti_5O_{12}$ by solid state method. The reversible capacity of D- $Li_4Ti_5O_{12}$ and P- $Li_4Ti_5O_{12}$ were 165 $mAh \cdot g^{-1}$ and 165 $mAh \cdot g^{-1}$ at 0.2C respectively. Nakahara [8] et al prepared $Li_4Ti_5O_{12}$ by the high temperature solid state method using TiO_2 and $LiOH \bullet H_2O$ as raw material, the material showed high rate and good cycle stability.Yao[9] prepared $Li_4Ti_5O_{12}$ by solid state method, specific capacity could reach 200 $mAh \cdot g^{-1}$ at the 0.2C discharge to 1V. Yuan[10] et al synthesized $Li_4Ti_5O_{12}$ at 800℃ by using cellulose as auxiliary fuel ,TiO_2 and Li_2CO_3 as raw materials. The reversible capacity could reach 100 $mAh \cdot g^{-1}$ at 10C..

With these considerations, in this work, we reported the electrochemical performances of $Li_4Ti_5O_{12}$ anode materials at 0.2*C* charge-discharge rate. This anode material was synthesized via solid state method to show a promising commercial application in lithium-ion batteries.

Experimental

Materials characterization The crystalline phase of $Li_4Ti_5O_{12}$ was identified with X-ray diffraction (XRD, Rigaku D/MAX-RC) with Cu Kα radiation (λ=1.5405Å, 45.0kV, 50mA). The cells were charged and discharged on a Neware Battery Testing System over a voltage range of 1.0-2.5V at 0.2C rate. Cyclic voltammetry was performed using a CHI604C electrochemical working station at a scanning rate of $0.2mV \cdot s^{-1}$.

Materials preparation $Li_4Ti_5O_{12}$ sample was prepared using a solid state method with stoichiometric mixture of TiO_2-anatase and Li_2CO_3 as precursors, then the reactants were mixed in ethanol solvent and milled in a ball mill for 6h. The dried mixture was placed in tubular furnace and heated in an Air atmosphere, sintered at 750℃ for 12h, then cooled down to room temperature.

Results and discussion

Structural characterization of $Li_4Ti_5O_{12}$

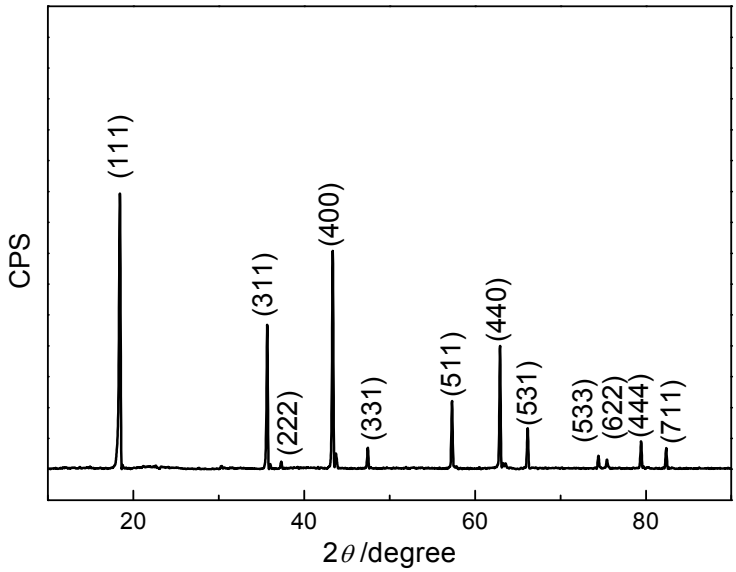


Fig.1XRD pattern of $Li_4Ti_5O_{12}$ powders

The XRD patterns of the $Li_4Ti_5O_{12}$ materials was shown in Fig.1. All the observed diffraction peaks were in good agreement with JCPDS card NO-26-1198. Any other phases such as TiO_2 or Li_2TiO_3, the most possible impurities, were not detected among the diffraction peaks. The well-defined and sharp peaks in the XRD patterns of the synthesized $Li_4Ti_5O_{12}$ sample suggested that it was both single-phase spinel compounds and well crystallized.

Electrochemical characterization of $Li_4Ti_5O_{12}$

Electrochemical performance of $Li_4Ti_5O_{12}$ was examined by charging and discharging. Fig.2 showed the initial charge/discharge voltage profiles of $Li_4Ti_5O_{12}$ at 0.2C rate. The initial discharge capacity reached 162.28 $mAh \cdot g^{-1}$.

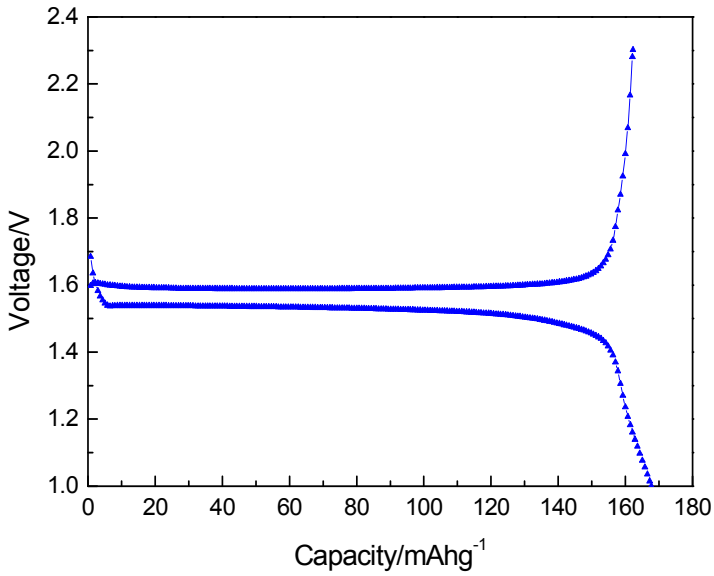


Fig.2 The initial charge and discharge curves of $Li_4Ti_5O_{12}$

The cycling performances were plotted in Fig.3. After 30 cycles the capacity was almost no decay. It was clear that $Li_4Ti_5O_{12}$ had a better cycling performance.

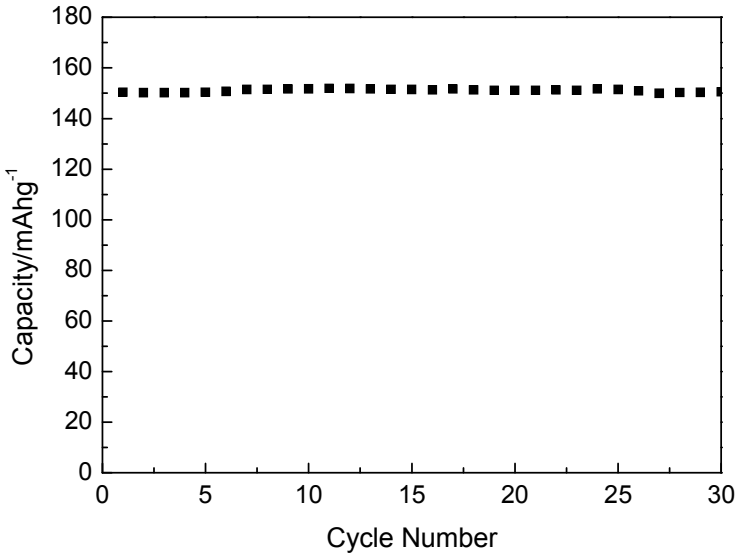


Fig 3 The cycle curves of $Li_4Ti_5O_{12}$ systhesised by solid state method

The electrochemical behaviors of both samples prepared in this work were characterized by cyclic voltammograms. As shown in Fig.4. the voltage was scanned form 1V to 3V at the rate of $0.2mV \cdot s^{-1}$. It can be clearly found that there was one pair of symmetric redox peaks for sample. The sharp and symmetrical peaks appeared at around 1.48V and 1.69V could be attributed to the redox of Ti^{4+}/Ti^{3+}. These phenomena confirmed that sample was beneficial to the reversible intercalation and de-intercalation of lithium-ion in this synthesized anode material.

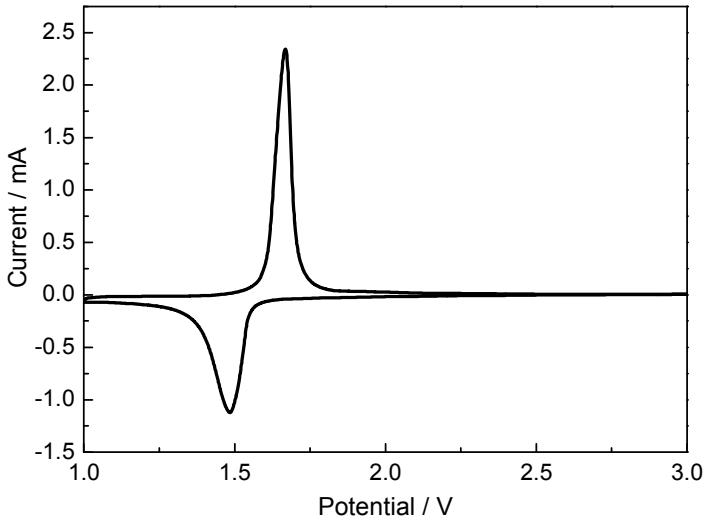


Fig. 4 Cyclic voltammetry profiles of $Li_4Ti_5O_{12}$

Summary

Well crystallized $Li_4Ti_5O_{12}$ compound with spinel structure were prepared by a simple, low cost solid state method. The initial discharge capacity reached 162.28 $mAh \cdot g^{-1}$. After 30 cycles the capacity was almost no decay. The synthesized $Li_4Ti_5O_{12}$ material may find promising applications in lithium-ion batteries due to its simple synthesis route, low cost and excellent electrochemical performance.

References:

[1] T.Ohuzuku, A.Ueda, N. Yamamoto: J. Electrochem Soc. Vol. 142 (1995), P. 1431

[2] P.P. Prosini, R. Mancini, L.Petrucci: Solid State Ionics Vol. 144 (2001), P. 185

[3] K.C. Hsiao, S.C. Liao, J.M. Chen: Electrochim. Acta. Vol. 53 (2008), P. 7242

[4] T. Yuan, R. Cai, P. Gu, Z.P. Shao: J. Power Sources. Vol: 195 (2010), P. 2883

[5] K. Kunimitsu, T. Yasuhiko, K. Norihito, A. Junji, K. Ohshima.: J. Physics and Chemistry of Solids Vol:69 (2008), P.1454

[6] M. Tabuchi, A. Nakashima, H. Shigemula: J. Materials Chemistry. Vol. 13 (2003), P. 1747

[7] K.C. Hsiao, S.C. Liao, J.M. Chen: Electrochim. Acta. Vol. 53 (2008), P. 7242

[8] K. Nakahara, R. Nakajima, T. Maysushima, H. Majima: J. Power Sources. Vol. 117 (2003), P. 131

[9] X. L. Yao, S. Xie, H. Q. Nian, C. H. Chen: J. Alloys Compd. Vol. 465 (2008), P. 375

[10] T. Yuan, R. Cai, P. Gu, Z.P. Shao: J. Power Sources. Vol. 195 (2010), P. 2883

© (2012) Trans Tech Publications, Switzerland
doi:10.4028/www.scientific.net/AMM.164.297

Application of carbonaceous materials to phenol removal from aqueous solution by adsorption

Weifang Dong[1a] Lihua Zang* [1b] Qingchao Gong [1c] Cuncun Chen[1d]
Caihong Zheng [1e] Xiangsen Meng[1f] and Tuantuan Liu[1g]

[1]Key Laboratory of Cleaner Production and Industrial Wastes Recycling and Resourcization in Universities of Shandong, Shandong Polytechnic University, Jinan250353, Shandong Province, P.R.China

*Corresponding author

[a]email: dwf@spu.edu.cn [b]email: lhz2010@yahoo.com.cn

Keywords: adsorption; granular activated carbon; powdered activated carbon; petroleum coke; multi-walled carbon nanotube

Abstract: Low cost carbonaceous materials were evaluated for their ability to remove phenol from wastewater. The effects of adsorbents dosage, contact time and maximum adsorption capacity were investigated for granular activated carbon, powdered activated carbon, petroleum coke and multi-walled carbon nanotube (MWNT). Equilibrium studies were conducted in 50mg/L initial phenol concentration, solution pH of 5 and at temperature of 23℃. The results showed the adsorption process was fast and it reached equilibrium in 3 h. Petroleum coke and MWNT had poor adsorption which could reach the removal efficiency of phenol with 43.18% and 36.64% respectively. The granular activated carbon possessed good adsorption ability to phenol with 96.40% at the optimum dosage 5g and optimum time 90min.The powdered activated carbon was an effective adsorbent with a maximum adsorption capacity of 42.32 mg/g.

Introduction

Phenols and its derivatives are classified as priority pollutants due to their high toxicity and poor biodegradability. They enter into environment through industrial applications such as the manufacturing of resins and plastics, petroleum refining, steel production, coal conversion, coal mines, dyestuff, textiles, tanning, fiberboard production, painting, pulp and paper, pesticides and pharmaceuticals. They are harmful to environment and human health at low concentrations[1-5].

Phenol is considered an environmental pollutant due to its toxicity and carcinogenic effect. Therefore, its elimination from industrial wastewater is of great importance[6].Various processes have been employed for the removal of phenols from aqueous media[7] .They include biological degradation[8], photocatalytic degradation[9], advanced oxidation[10-11], Nanofiltration membrane[12], electrochemical oxidation, [13-14], ozonation[15], ione xchange, precipitation, distillation, gas stripping, solvent extraction, complexation and adsorption[7].

Adsorption process is considered to be the cost effective method for the removal phenol contaminants of low concentration level from wastewater. In this work, Adsorption was used to eliminate phenol from aqueous solutions. The adsorptive property of the carbonaceous materials was tested and adsorption capacity revealed the potential use of carbonaceous materials as adsorbents.

2. Experimental

2.1. Chemicals and materials

Phenol was purchased from Jinan kaijun chemical Co.Ltd. The reagent was above analytical grade. Granular activated carbon was commercial made in Yantai universal activated carbon limited company . Activated carbon powder was purchased from the Kunshan ri er chemical production Co.Ltd. Multi-walled carbon nanotubes was purchased from Shenzhen Nanotech Port company. Petroleum coke was took from a city refinery. Deionized water was made by ourselves in laboratory.

2.2. Methods of the adsorption abilities of carbonaceous materials

The adsorption abilities of carbonaceous materials were evaluated as follows. An aqueous solution containing phenol in a concentration of 50mg/L was prepared by adding deionized water. The volume of 150mL phenol solution was added to the grinding mouth beaker flask. Then a certain amount of carbonaceous adsorbent was mixed to the solution by oscillation of the HY-5 cyclotron oscillator. The clear liquid was obtained by separation of the TDL-50B high-speed centrifuge. After 10 time intervals, a specific amount of solution (mg/L^{-1}) was taken for examination using a TU-1901 UV-vis Spectrophotometer at a wavelength of 270nm. The concentration of phenol in solution (mg/L^{-1}) was calculated according to the absorbance of the phenol.

The removal efficiency of phenol on the carbonaceous materials was calculated by the following equation:

$$\eta(\%) = \frac{(C_0 - C_t)}{C_0} \times 100 \quad (1)$$

Where η is the removal efficiency of phenol, C_0 is the initial phenol concentration (mg/L), C_t is the phenol concentration at time *t* (mg/L).

The phenol adsorption capacity (*q*e, mg/g) was determined as follows:

$$q_e = (C_0 - C_t)\frac{V}{m} \quad (2)$$

where q_e (mg/g) is the uptake (mg/g), C_0 is the initial phenol concentration (mg/L), C_t is the phenol concentration at time *t* (mg/L), V is the volume (L) of aqueous solution containing phenol, and m is the mass of adsorbent (g).

3. Results and discussion

3.1 The effect of optimum dosage for different carbonaceous adsorbents

In any adsorption process, the amount of adsorbents played an important role. In order to evaluate the effect of adsorbents dosage (in grams of adsorbents per 0.15 liter of solution) on phenol adsorption, wastewater samples had an initial phenol concentrations of 50 mg/L. Fig. 1 showed the removal of phenol as a function of dosage by carbonaceous materials at the solution pH of 5. It was found that the concentration of phenol decreased with an increase in adsorbent concentration. This was expected, as increasing the adsorbent concentration at a fixed phenol initial concentration provided more available adsorption sites for phenol and hence the removal was enhanced. Granular activated carbon dosage was varied from 1.0 to 9 .0g .It was evident that for the dosage of 5.0 g is required for 96.4% removal efficiency of phenol. The data clearly showed that the granular activated carbon was more effective than the powdered activated carbon, petroleum coke and MWNT for the removal of phenol. The results also indicated that the removal efficiency increased up to the optimum dosage beyond which the removal efficiency was negligible.

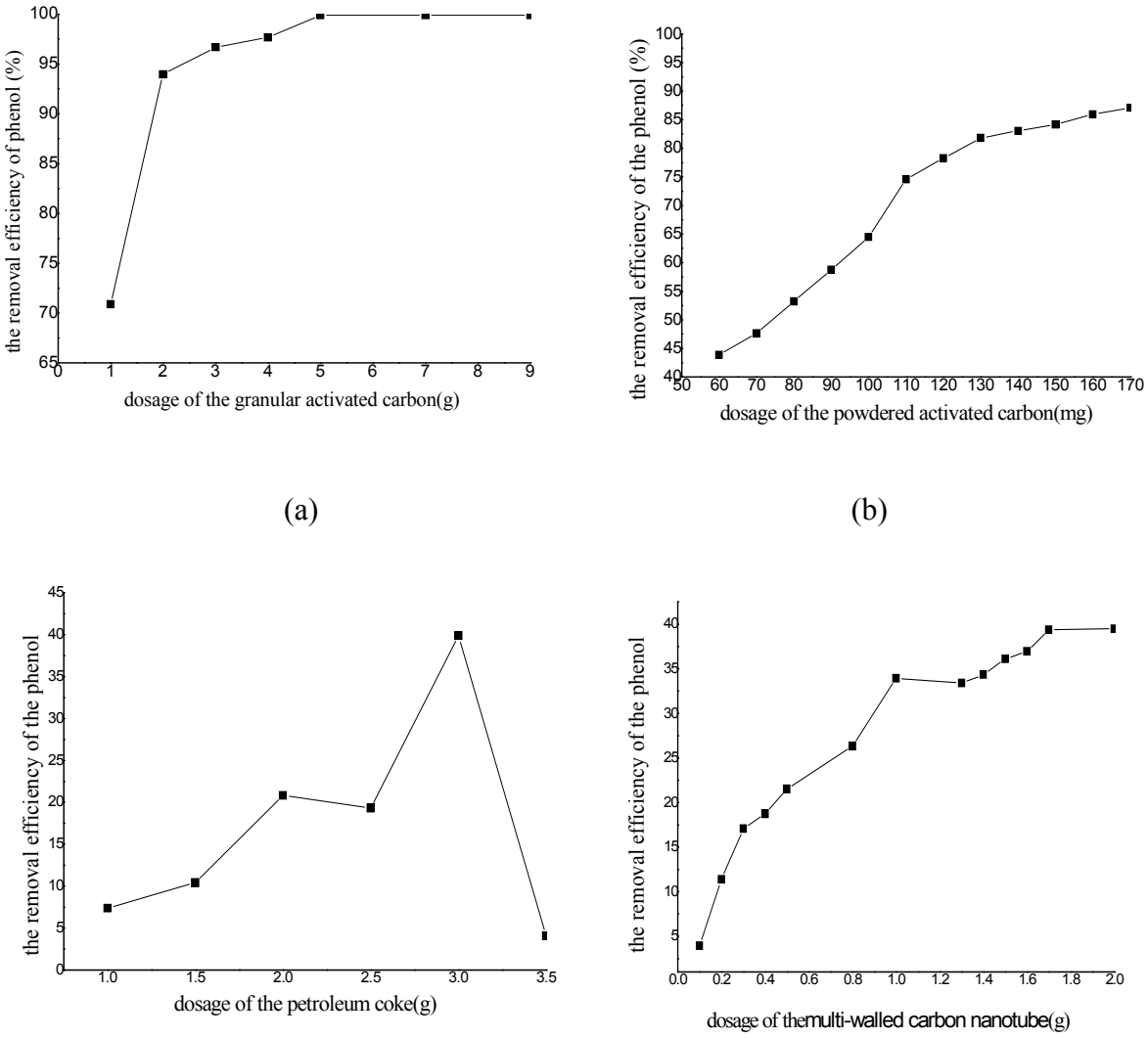


Fig. 1. Effect of carbonaceous materials dosage on the removal efficiency of phenol

(a) Effect of granular activated carbon dosage (pH=5.0, equilibration time=90min, phenol concentration=50 mg /L)

(b) Effect of powdered activated carbon dosage (pH=5.0, equilibration time=100min, phenol concentration=50 mg /L)

(c) Effect of Petroleum coke dosage (pH=5.0, equilibration time=120min, phenol concentration=50 mg /L)

(d)Effect of MWNT (pH=5.0, equilibration time=140min , phenol concentration=50 mg /L)

3.2 Effect of contact time for different carbonaceous adsorbents

The experimental condition: granular activated carbon dosage=5g, powdered activated carbon dosage =0.14 g, petroleum coke dosage=3g, MWNT dosage =1.7 g, phenol initial concentration=50 mg /L, the volume solution=150mL, pH=5.0)

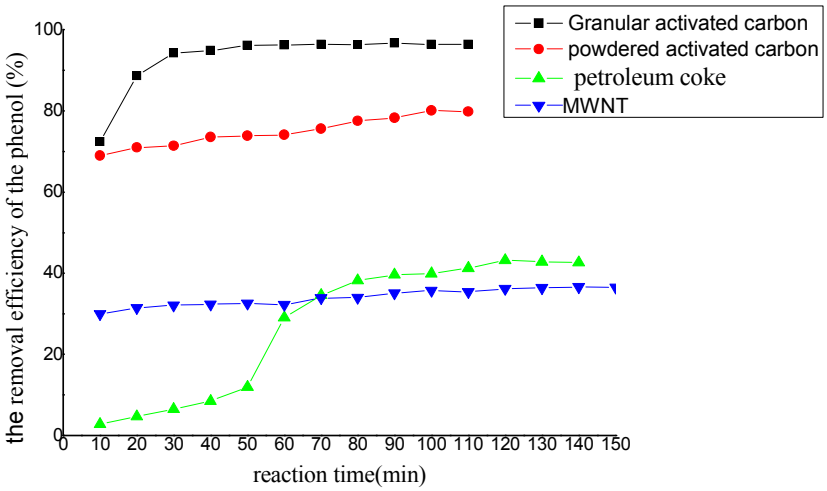


Fig. 2. Effect of contact time for the removal of phenol by carbonaceous adsorbents

150ml volume of phenol solution with optimum adsorbents dosage was kept in the HY-5 Cyclotron oscillator for the period ranging 0-3 h. The adsorption curve of carbonaceous material for phenol was shown in Fig2 .The removal increases with time and attains equilibrium in 90min, 100min, 120min, 140min for granular activated carbon, powdered activated carbon, petroleum coke and MWNT respectively. The result indicated that granular activated carbon would require less residence time for the complete removal of phenol compared to other adsorbents. The curves of the phenol removal versus time were single, smooth and continuous leading to saturation, suggesting the possible monolayer coverage of phenol on the surface of the adsorbents.

3.3 Contrast of adsorption capacity and removal efficiency to phenol

Under the optimum dosage and contact time, the adsorption capacities were shown in table1. Powdered activated carbon possessed the best adsorption capability to phenol with 42.32 mg/g, However, Petroleum coke had poor adsorption capability with 1.07 mg/g. This may be due to the presence of impurities present in petroleum coke which may interfere in the adsorption process.

Table1 The contrast of phenol adsorption capacity to different carbonaceous adsorbents

Carbonaceous adsorbents	Granular activated carbon	Powdered activated carbon	Petroleum coke	MWNT
q_e[mg/g]	1.43	42.32	1.07	1.61
Removal efficiency of phenol [%]	96.40	80.09	43.18	36.64
optimum dosage [g]	5.00	0.14	3.00	1.70
optimum time[min]	90	100	120	140

4. Conclusions

Granular activated carbon and powdered activated carbon were capable of removing phenol effectively from wastewater. Granular activated carbon can reached the removal efficiency of phenol with 96.40%. The adsorption capacity of the powdered activated carbon was 42.32mg/g. MWNT was not suitable for adsorbent to phenol with less removal efficiency 36.64%.Petroleum coke was a low-value byproduct of the petroleum industry and had 43.18% removal of phenol. In future study, it will be modified to improve the removal efficiency of phenol in wastewater for the purpose of waste into resources.

References

[1] L. A. Rodriguesa, M. L. C. P. Silva, M. O. Alvarez-Mendes, A. R. Coutinho, G. P. Thim, Phenol removal from aqueous solution by activated carbon produced from avocado kernel seeds, Chemical Engineering Journal Vol.174 (2011), p. 49-57

[2] A. C. Lua, Q. P. Jia, Adsorption of phenol by oil–palm-shell activated carbons in a fixed bed ,Chemical Engineering Journal Vol.150 (2009) , p. 455-461

[3] M.L. Leong, K.M. Lee , S.O. Lai, B.S. Ooi ,Sludge characteristics and performances of the sequencing batch reactor at different influent phenol concentrations, Desalination, Vol.270 (2011) p. 181-187

[4] R.M. Aghav, Sunil Kumar, S.N. Mukherjee, Artificial neural network modeling in competitive adsorption of phenol and resorcinol from water environment using some carbonaceous adsorbents, Journal of Hazardous Materials Vol.188 (2011) , p. 67-77

[5] Y. J. Wang, J. Song, W. Zhao, X.L. He, J. Chen, M. Xiao, In situ degradation of phenol and promotion of plant growth in contaminated environments by a single Pseudomonas aeruginosa strain, Journal of Hazardous Materials Vol.192 (2011) p. 354-360

[6] S. Nosrati, N.S. Jayakumar, M.A. Hashim, Performance evaluation of supported ionic liquid membrane for removal of phenol, Journal of Hazardous Materials Vol.192 (2011) p. 1283-1290

[7] Rushdi I, Yousef, Bassam El-Eswed, Ala H. Al-Muhtaseb, Adsorption characteristics of natural zeolites as solid adsorbents for phenol removal from aqueous solutions: Kinetics, mechanism, and thermodynamics studies,Chemical Engineering Journal Vol.171 (2011) p.1143-1149

[8] S. Kumar, M. Zafar, J. K. Prajapati, S. Kumar, S. Kannepalli, Modeling studies on simultaneous adsorption of phenol and resorcinol onto granular activated carbon from simulated aqueous solution, Journal of Hazardous Materials Vol.185 (2011) p.287-294

[9] T. Luenloi, B. Chalermsinsuwan, T. Sreethawong, N. Hinchiranan, Photodegradation of phenol catalyzed by TiO_2 coated on acrylic sheets: Kinetics and factorial design analysis, Desalination Vol.274 (2011) , p. 192-199

[10] P. R. Shukla, S. B. Wang, H. Q. Sun, H. Ming Ang, M. Tadé, Activated carbon supported cobalt catalysts for advanced oxidation of organic contaminants in aqueous solution, Applied Catalysis B: Environmental Vol.100 (2010) , p. 529-534

[11] R. Alnaizy, A. Akgerman, Advanced oxidation of phenolic compounds, Advances in Environmental Research Vol. 4 (2000) ,p.233-244

[12] A. Bódalo, E. Gómez, A.M. Hidalgo, M. Gómez, M.D. Murcia, I. López, Nanofiltration membranes to reduce phenol concentration in wastewater ,Desalination Vol. 245 (2009) , p.680-686

[13] T. A. Enache, A. M. Oliveira-Brett, Phenol and para-substituted phenols electrochemical oxidation pathways, Journal of Electroanalytical Chemistry Vol.655 (2011) , p.9–16

[14] J. J. Wei, X. P. Zhu, J.R. Ni，Electrochemical oxidation of phenol at boron-doped diamond electrode in pulse current mode, Electrochimica Acta Vol.56 (2011), p.5310–5315

[15] Z. L. Wu, M. Franke, B. Ondruschka, Y. C. Zhang, Y.L. Ren,P. Braeutigam, W.M Wang, Enhanced effect of suction-cavitation on the ozonation of phenol,Journal of Hazardous Materials Vol.190 (2011) , p.375-380

© (2012) Trans Tech Publications, Switzerland
doi:10.4028/www.scientific.net/AMM.164.302

The Study on Carbon Emission Influencing Factors of Industrial Energy Consumption of Changchun City

Zhuo Ma[1, a], Xiaogang He[2,b], Xunzhou Tong [3,c], Haiyan Duan[4,d], Xian'en Wang[5,e], and Deming Dong[6,f]

[1,2,4,5,6]Key Laboratory of Groundwater Resources and Environment, Ministry of Education, Jilin University, Changchun, China, 130012

[3] Economics School of Jilin University, Changchun, China, 130012

[a]110573667@qq.com, [b] 904742021@qq.com, [c] 49826070@qq.com, [d] petrel1980@126.com, [e]wxen@jlu.edu.cn, [f] dmdong@jlu.edu.cn

Corresponding author: Xian'en Wang

Key words: Industrial Energy Consumption, Carbon Emission, Changchun City, LMDI Mode.

Abstract: To make great efforts for energy saving and promote low-carbon transition of industrial development pattern have been the most crucial tasks for Changchun industrial developmen. Using Logarithmic Mean Divisia Index (LMDI) mode decomposes the carbon emission influencing factors of the industrial department in Changchun, and study on the effects of factors on the carbon emissions of industrial energy consumption. The result shows that the major factors for carbon emissions of industrial energy consumption in Changchun are economic development, the population size and the industrialization rate, and the key factors for the carbon emission changes in industrial department of Changchun are the energy consumption structure and the energy intensity.

Introduction

In "The People's Republic of China National Economy and Social Development in the Twelfth Five Year Plan"of the year 2011, it is proposed that energy consumption per unit of GDP and the carbon emission decrease by 16% and 17% respectively, which puts forward new requirements for the energy saving and emission reduction in the process of developing economic society in China in the new period. As a center city in the old industrial base of northeast China, Changchun is still facing critical tasks of economic development in this new period. The traditional economic structure which takes industry as the principal content is rather difficult to change, to enhance the intensity of energy saving and emission reduction and promote the low-carbon transition of industrial development mode has become one of the significant tasks for the industrial development of Changchun. By employing Logarithmic Mean Divisia Index (LMDI) mode, this article decomposes the carbon emission influencing factors of industrial department and provides policy suggestions for the low-carbon development of industrial department in Changchun based on analysis results.

Current Situations of Industrial Energy Consumption and Carbon Emission in Changchun

According to statistics, the industrial energy consumption of enterprises above designated size in Changchun is 11.1722 million tons of standard coal in the year 2010, which takes up 58.4% of the total energy consumption in the city. Wherein, the number of the industrial enterprises which consume more than 5000 tons of standard coal is 62, which accounts for 6% of the industrial enterprises above designated size. The energy consumption is 12.857 million tons of standard coal, which increases by 4.3% than that of the year 2009, taking up 97% of total energy consumption of the industrial enterprises above designated size in the whole city. Judging from the energy consumption situation of various industries, the energy consumption of heavy industry is 11.2667

million tons of standard coal, which accounts for 85.01% of the total energy consumption; energy consumption of light industry is 1.9861 million tons of standard coal, which accounts for 14.99% of the total energy consumption. The specific division is: the energy consumption of mining industry takes up 0.23% of industrial total energy consumption, manufacturing industry accounts for 37.89%, and the industry of fuel gas and water production takes up 61.88%.

Since the year 2000, the carbon dioxide emission of Changchun industrial department has presented a stable increasing trend. The increasing of the carbon emission from the year 2003 to 2007 is rather obvious; the growing speed of the period from 2007 to 2008 is relatively slowed down, but the incremental quantity is grossly evident. The carbon dioxide emission of Changchun industrial department in 2008 is 2.18 times than that of the year 2000.

Model Mode and Data Sources

LMDI Model Design. By employing the Logarithmic Mean Divisia Index (for short LMDI) mode, this article decomposes all the factors with no residual. The fundamental formula of the carbon emission of the energy consumption of Changchun industrial department can be decomposed:

$$C = \sum_i C_i = \sum_i \frac{C_i}{E_i} \times \frac{E_i}{E} \times \frac{E}{Q} \times \frac{Q}{G} \times \frac{G}{P} \times P = \sum_i F_i e_i ISYP \qquad \text{Formula (1)}$$

In this formula, C is the sum of all emissions of carbon dioxide, means the amount of carbon dioxide corresponding to the burning of fossil fuels (including coal, petroleum and natural gas) released heat, we use i to separate different types of energy, and C_i refers to the amount of carbon dioxide which comes from some industrial department consume the i kind of energy; E_i indicates energy consumption of the i kind of fuel of industrail department; E represents the total industrial energy consumption; Q shows total output value of industrial department; G means total output value of the region; P indicates population.

Data Description. All of the data we adopted in the calculation come from the *Statistical Yearbook of Changchun City*. There take the year 2005 as the constant price in GDP and gross industrial production.

Results Analysis

The calculation results of the contribution situation of each carbon dioxide emissions influencing factor in Changchun industrial department are listed in Table 1 (because of the little variation in unit energy emissions intensity coefficients, we only take the influences of the other five factors into consideration). Economic development has been the main contribution factors in the increase of carbon dioxide emissions in Changchun industrial department during the period of 2000 to 2008, the contribution values has presented a year-by-year rising trend, from the 1222.5 thousand tons in the period of 2000-2001 to the 4360.3 thousand tons of the period 2007-2008. Population scale factor has always presented a positive effect, but its contribution values to carbon dioxide emissions has been rather small, which always maintained in less than 300 thousand tons; industrialization rate factors also have brought about positive effects except the period of 2004-2005, with the acceleration of industrialization, the carbon dioxide emissions of the industrial department increased; energy intensity is the main factors to reduce the carbon dioxide emissions; the influence brought about by energy consumption structure fluctuated obviously.

Judging from the contribution rate of each affecting factor, economic development factors and population factors always present positive effects; other factors show different fluctuations, but the general trend is obvious; industrialization rate factors and energy consumption structure factors show overall positive effects; energy intensity factors indicate overall negative effects. In other

words, from the year 2000 to 2008, economic growth has been the main reason for the increase of carbon dioxide emissions in Changchun industrial department, and the reduction of the energy intensity is the main factor for the slowing down of carbon dioxide emissions.

Table 1 The Contribution Values of Carbon Emissions Influence Factors in Industrial Department

Year	Influence factors（ten thousand tons）					
	Emission Variation of CO_2	Population	Economic Development	Industrialization Rate	Energy Consumption Structure	Energy Intensity
2000-2001	100.91	13.23	122.25	38.58	34.26	-105.27
2001-2002	47.45	15.33	129.77	11.60	-25.48	-85.26
2002-2003	12.47	12.98	145.19	43.76	-2.50	-186.96
2003-2004	280.04	14.49	189.38	74.21	11.71	-9.57
2004-2005	280.04	20.86	213.47	-14.69	10.17	50.38
2005-2006	231.75	24.49	298.20	47.69	13.35	-151.57
2006-2007	613.13	24.19	382.12	143.81	0.68	62.65
2007-2008	173.17	27.51	436.03	53.41	-31.49	-312.29

Economic Development Factors. According to the data, economic development, as the main factor for the increase of carbon emissions in Changchun, whose the contribution values of the carbon emission increase in industrial department present a year-by-year rising trend. After analyzing the GDP growth rates of Changchun over the years, we found that the trend of GDP growth rates is similar to that of carbon dioxide emission contribution values of economic development factors. Relevant statistical data show that the economic development level of Changchun improves unceasingly in recent years, regional GDP has increased from 90.943 billion of the year 2000 to 233.648 billion of 2008, increased by nearly 2.6 times. The rapid development of economy inevitably leads to the increase of energy consumption and carbon emissions. Changchun, at present, is still at the economic developing stage of highly relying on energy, whose economic development needs the increase of energy consumption as a guarantee, which will inevitably lead to the constant increase of carbon emissions in the rapid developing process of economy.

Population Factors. The population of Changchun fluctuates rather slightly from the year 2000 to 2008, the variation rate is between 0.8% and 1.1%, and the contribution value of carbon emission initiated by population factors is relatively small. Normally, the population of Changchun fluctuates slightly in a short-term. Hence, the contribution value of carbon emission caused by population factors will remain relatively stable in a certain period.

Industrialization Rate. In recent years, the industrialization rate of Changchun keeps increasing, increased from 33.67% of 2000 to 40.50% of 2008. The model simulated data show that the contribution value trend of carbon dioxide emissions of the industrialization rate factor is similar to that of the variation rate of industrialization rates of different years, which presents a rising trend as a whole. This indicates that the improving of industrialization rate and industrial output have consumed a lot of energy, which has led to the constant increase of carbon emissions. Thus, adjusting the industrial structure and reducing the industrialization level will slow down the carbon emission trend effectively in the industrial department of Changchun.

Energy Consumption Structure. Judging from decomposition results of industrial influential factors in Changchun over the years, energy intensity factor is the principal factors to slow down the emissions of carbon dioxide in Changchun city. Except during the period of 2004-2005 and 2006-2007, in the rest of the object years, the effects of carbon dioxide emissions have presented negative. Reducing the energy intensity plays important role in the carbon dioxide emissions reduction in the industrial department of Changchun city. Changchun is the center city of the old

industrial base in northeast China, the equipment of industrial department of which is rather old and the technology level need to be improved. It has rather great potentials to improve energy efficiency and reduce energy intensity, with grossly large potential to reduce the carbon dioxide emissions. In the meantime, with speeding up of China's paces of "rejuvenating the northeast China", the development of Changchun's industrial scale will increase the demand for energy. Hence, reducing the energy intensity of Changchun will play an even greater part in slowing down the increasing speed of carbon dioxide emissions in the future.

Conclusion and Suggestions

The development of economy, the expansion of population scale and the improvement of industrialization rate are the main factors for the increase of carbon dioxide emissions in the industrial department of Changchun over the years. Moreover, the proportion changes of coal in the energy structure and the changes of energy intensity are the crucial factors which affect the changes of carbon dioxide emissions in the industrial department of Changchun. The population size of Changchun is difficult to change significantly in a short term. At present, Changchun is in the stage of industrialization, whose industrialization rate's keeping improving in a short time is an inevitable trend. Hence, under the premise of keeping economy developing fast and steady, in order to slow down the carbon emissions of industrial department, we should focus on making great efforts to grasp energy intensity factors and reduce energy intensity as far as possible; at the same time, we should optimize the energy structure and lower the proportion of coal in the energy structure.

Acknowledgements

This work was financially supported by National Social Science Foundation Youth Project (08CRK004), Jilin Province Science and Technology Development Plan Project (20110638), ilin Province Science and Technology Development Plan Project (20120606) and Jilin Province Development and Reform Commission project (Study on Low-carbon economic development strategic)

References

[1] Common M S.Sustainability and policy:limit to economics.Cambridge:Cambridge university Press,1995.

[2] Donald Hanson, John A, "skip" Lathery. 2004.An integrated analysis of policies that increase investments in advanced energy-efficient /Low 3/ Carbon technologies. Energy Economics,26:4.

[3] NiuWenYuan. A low carbon economy is an important breakthrough of implementing the scientific concept of development. March 19, 2009. China reports.

[4] ZhuangGuiYang. A low carbon economy: China's development way under the background of climate change. 2007. Beijing: China meteorological press.

[5] ZhouHongChun. The state council development research center. The countermeasures to realize our country's energy and emission reduction goals .2007. "the China science and technology achievement", 22.

[6] Ann P. Kinzig and Daniel M. Kammen. 1998. "National Trajectories of Carbon Emissions: analysis of proposals to foster the transition to low-carbon economies".Global Environmental Change, No.3:183-208.

© (2012) Trans Tech Publications, Switzerland
doi:10.4028/www.scientific.net/AMM.164.306

Anti-corrosion Materials and Spray Technology in the Coastal Wind Generating Set

HongMei Sun[1,a] XiGuo Feng[2,b]

[1].Beijing Polytechnic, Beijing, 100029; China

[2] Beijing JINGCHENG New Energy Co.,Ltd. Beijing 100040,China

[a]sunhongmei3412@sohu.com, [b] Feng.x.g@bzd.com

Keywords: Salt fog, Hot-dip zinc, Dacromet,Anti-corrosion Materials

Abstract: Through the depth introduction of the characteristics and the corrosion mechanism of the salt fog, analysis of the corrosion and hazards may be caused to the wind generating sets, from the epoxy zinc-rich primer, epoxy micaceous iron oxide intermediate paint, aliphatic polyurethane topcoat consisting of anti-corrosion material system, hot-dip zinc coating, zinc, chromium film coating material spraying technology, and other aspects to expound fan anti-corrosive means.

1. Introduction

With the rapid development of science and technology of the late 20th century, a number of new technological achievements into the use of new materials have been developed successfully, international and domestic wind power enterprises emerging blowout unit capacity from tens of kilowatts in the first few hundred kilowatts to the current of a few megawatts. Wind energy has become the most mature technology, with the best scale of development and conditions of the renewable clean energy. China has a vast and long coastline, abundant wind energy resources suitable for the open sea wind power. At present, China's first offshore wind power project has been run electric power generation, the project is the installation of 33 sets of 3MW wind turbine. However, offshore wind power wind turbine quality and reliability requirements are higher, especially high-power coastal wind turbine by the salt fog corrosion more serious than the inland wind turbine must be a reliable solution to protect the wind turbine the various components.

2. Salt fog and its hazards to wind generating set

2.1 The formation of salt fog

There is a certain amount of water vapor in the air, the higher the temperature the more water vapor in the air can hold, on the contrary, the less. When the air temperature is low to accommodate the water vapor contained in the original, the excess water vapor condenses into small droplets. Coastal areas where the air contains a lot of salt come from the evaporation of sea water, and the salt soluble in water droplets forming in high concentrations of salt fog.

2.2 The corrosion characteristics of the salt fog

2.2.1 Corrosion

Corrosion is the damage or deterioration of the material or performance caused by the environment, and is a common and most destructive phenomenon. Salt fog corrosion of metals in the atmosphere is based on electrochemical methods, electrochemical corrosion phenomena in nature is most common, the harm caused by the most serious.

2.2.2 The main component of salt fog

The main ingredient in the salt fog is NaCl, and NaCl in solution is as Na+ and Cl^- in the form of existence. Through the salt fog technology and IC reliability test, it was informed that the deposition rate of salt fog is proportional to the concentration of Cl^- :

$Sd=AV[Cl]^-/(S*t)$

Thereinto ,Sd——deposition rate of salt fog

$[Cl]^-$——the concentration of Cl^-

Therefore, salt fog deposition rate is also great at the offshore, salt fog with high concentrations naturally becomes the carrier of the NaCl solution.

2.2.3 The corrosion characteristics of salt fog[1]

Through test, the corrosion of salt fog to metals is affected by the temperature and salt concentration. by the following figure illustrates:

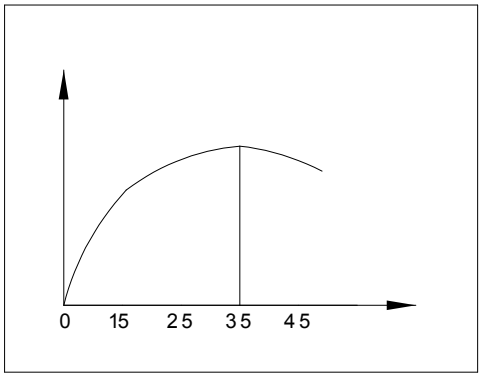


Figure 1: The abscissa is temperature (° C), the vertical axis is the corrosion rate

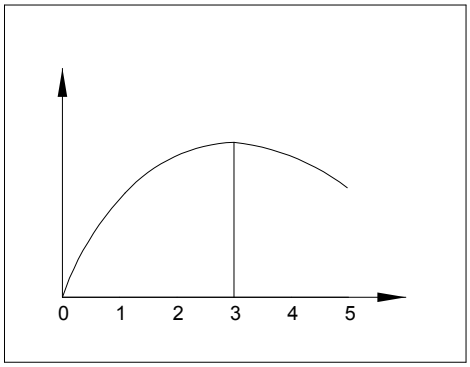


Figure 2: Abscissa for the salt concentration (%), the vertical axis is the corrosion rate

From the figure we can see that the maximum effect point of metal corrosion (chemical reaction) is temperature at35 ° C and the concentration of salt solution at 3%. High concentration NaCl in the salt fog is decomposed into Na+ and Cl^- rapidly, and taken chemical reaction with active metal materials. Metal ions in the resultant strong acidic metal salts are reduced to stable metal oxide in contact with oxygen.

In addition, any metal material in the medium has its own corrosion potential, in the same medium, the more positive potential the more backward metal activity, and the metal is not likely to corroded. Currently iron, aluminum and other active metal materials are used in the wind turbine.

Concluded from the above analysis, the main conditions of the salt fog to metal corrosion are concentration, temperature, oxygen content, corrosion potential.

2.3. The dangers of salt fog to the wind turbine[2]

The decorative layer or coating of salt fog corrosion of shell surface, causing the surface of the decorative layer or coating blistering, wrinkling, cracking or peeling, and thus corrosion of the bottom metal, the shell surface of Ma Hang, and even perforation, the leak. The salt fog will fasteners severe corrosion, causing difficult to remove, affect the maintenance of such products. Deposition of salt fog particles will lead to the blocking of the instrument moving parts, stuck. Salt fog on the internal electronic components and supporting the use of special equipment of, resulting in the eroded layer, decapitated and reduce the insulation properties or cause open; contacts of electronic components and also because the settlement of salt fog dry after crystallization, the increase in the parts of the impedance, resulting in the circuit barrier; connectors due to corrosion caused by the contact resistance increases, causing poor contact and affect the product work.

3. Anti salt fog measures of wind turbine

Structures in wind turbine including castings, forgings, weldments,

standard parts and other accessories, each components should have the appropriate anti-corrosion coating. Before the wind turbine assembly, in accordance with the requirements of the standard coating thickness, pretreatment measures and the quality of the manufacturing process, the protection against corrosion must be completed. Raised the following points with strong cost-effective corrosion protection measures for the actual operating environment of the wind turbine, combined with current technology trends, considering the economic factors:

3.1 Epoxy zinc-rich primer + intermediate coat of epoxy micaceous iron oxide + aliphatic polyurethane topcoat

Constitute a corrosion resistant zinc-rich paint, primer, intermediate coat epoxy anti-corrosion coatings, aliphatic polyurethane topcoat system. Contains large amounts of zinc powder primer is called a zinc-rich primer film of zinc powder contact with each other and in contact with the metal surface while the conductive sacrificial anode cathodic protection for steel from the corrosive environment. In the first corrosion resistant stage, the action of zinc-rich primer is cathodic protection to steel by the dissolution of zinc powder.

At a later stage, with the dissolution of the zinc powder, in the middle of the zinc dust particles deposited on a lot of corrosion products, these dense and slightly alkaline corrosion products are non-conductive, filling the pigment layer, blocking shield corrosion factor through, namely anti-corrosion effect by the shielding effect in the later stage. Intermediate coat of

epoxy micaceous iron oxide + aliphatic polyurethane finish coating system plays the role of isolation in the external environment, has excellent chemical stability, between which the paint has excellent resistance to solar radiation, that is excellent weathering performance, to prevent the destruction of the UV and visible light on the aging of the coating to protect the integrity of the coating.

3.2 Surface treatment of the hot-dip zinc coating technology on the structure[3]

Hot-dip zinc is soaked soaked in liquid zinc, stay a certain period of time between the two atom penetration and diffusion of each other, then dip the surface of zinc particles accumulation and the formation of a protective layer of zinc (zinc-iron alloy layer). The alloy layer has a dense, uniform, firm adhesion, light, resistant to rust corrosion and other features. Hot-dip zinc has been widely used in various industries of metal structure facilities.

3.3 Surface treatment of zinc and chromium coating (Dacromet) coating technology on the structure [4]

Its anti-corrosion mechanism is:

Controlled self-sacrifice to protect the role of zinc

Chromic acid in the processed workpiece surface to form a dense oxide film which can not easily be corrosion;

Layered canopy of the zinc tablets are superimposed coating forming a shielding effect, the intruder to reach the surface through the path of the Dacromet dry film chromate compounds do not contain crystallization water, its resistance to high temperature and heating after the corrosion resistance is also very good. Compared with hot-dip zinc, zinc-chromium coating anti-corrosion better, the drawback is that the coating thickness is not easy to control, adhesion not as good as the hot-dip zinc.

3.4 Other methods

Photocatalyst coating fog the surface of the leaves, which use sunlight, rain, air as a basic reaction medium, so that the pollutants attached after decomposition to achieve the antifogging and self- cleaning purpose [5].

The wind farm should be inspected regularly and found the equipment corrosion and timely use of new environmentally friendly metal surface coating pretreatment agent because it can quickly react with the metal substrate to form complexes, the metal surface to form a dense molecular protective film to prevent the erosion of chlorine and other substances to metals, and subsequently coated with a high-performance nanometer-coatings.

Sealing the electrical components concentrated areas against damp, and cooling protection in order to reduce the corrosion rate.

Built-in dehumidification system is needed in the design of the electrical components, and dehumidification devices are also set in the wind turbine.

With the rapidly development in science and technology, a lot of technical difficulties will be broken through, and there will be more new materials, new technologies into the wind power industry, which must bring new programs and tools for more effective anti-corrosion of the wind power generation equipment.

4. Prospect

With the increasing advances in science and technology, the metal process and heat treatment technology, continuous improvement and development is bound to gradually ease the problem of salt fog corrosion for fans looking for a light weight, performance, and corrosion resistance of new and improved materials for the future development of the inevitable trend.

References

[1] GUO Rui-feng, GE Hong-hua , YE Jun, FU Yang. Research on corrosion resistance of materials for wind power equipment by salt fog tests, East China Electric Power, Vol.8 (2009), p, 1400-1403

[2] Li Xin-jun. New Progress of salt fog protection technology. Fifth electronic product protection seminar. 2006

[3] Fan Wen-long. Hot Dipping Zinc Craft Research. Science & Technology Information. 2010(13),p,33

[4] Dong Jin-zhong. New coating process and equipment. R & D Information. Vol. 5 (2001), p,18-20

[5] Zhao Qingjun. Study on Coatings Applied on Fan Blade of Aerogenerator. Modern Paint and Finishing.Vol.4(2011),p, 38-40

CHAPTER 2:

Mechanics Study in Mechanical Engineering, Industry and Manufacturing Engineering

© (2012) Trans Tech Publications, Switzerland
doi:10.4028/www.scientific.net/AMM.164.313

Mechanics Analysis of Protective Casing and Splicing Sleeve

Jian Qin[a], Ya Ping Qiu[b]

China Electric Power Research Institute, Beijing, 100055, China

[a]mathmech@126.com, [b]qyp@epri.sgcc.com.cn

Keywords: splicing sleeve, protective casing, stringing sheave, finite element model

Abstract: The splicing sleeve is the important part in the transmission line construction. The stresses of the sleeve and its protective casing are analyzed by finite element method over the stringing sheave. Several important positions are investigated in the equipment. Typical situations are selected covering the entire stringing procedure, including horizontal position, 45-degree position and vertical position. Based upon the results, the safety assessment of the protective casing and splicing sleeve is conducted according schemes.

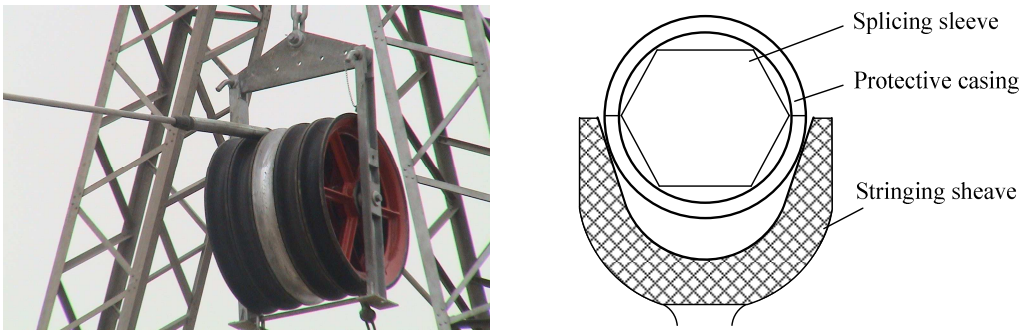
Introduction

The splicing sleeve is important for large-scale section transmission line in overhead transmission line construction, which connected the lines together. There is the protective casing which envelops the splicing sleeve to prevent wire drop or rupture accident during the construction[1,2].

The simulation of protective casing is a very complicated subject covered with the contacts between the shells and solid structures. The load distribution of the casing is uncertain, so the stresses of the casing and sleeve are difficult to be accurately calculated. To ensure the safety of the protective casing during stringing project and make new relational national design codes of our country, it is necessary to carry on the finite element analysis for the protective casing structure to obtain the loading capacity of the sleeve shells during design.

The protective casing, the splicing sleeve and stringing sheave, in Fig. 1 (a) has different sizes for different projects. The slot bottom size of the common stringing sheave in Fig. 1 (b) is 710mm, the load at the end of protective casing is 25kN, the width of sheave is 100mm, and the section area of the power line is 500 mm^2~630mm^2[3].

The protective casing of splicing sleeve is composed of two hemicycle pipes and two rubber ends. Its length is about 740mm, which includes 680mm of the main body and 30mm of the skirt. The outer diameter of the main body is 68mm. The thickness of pipe is 6mm. The material of sleeve and casing is mid steel.



(a) (b)

Fig.1. The photo and section of stringing structure

Numerical simulation model

From Fig. 1, one can clearly see that there are several contacts between different parts of the casing, sleeve and sheave which are complicated for finite element method.

It is necessary to simplify the whole stringing procedure firstly before analysis. During the stringing, the splicing sleeve and protective casing pass through the top of the sheave with three steps in Fig.2. The second stringing step in Fig.2 is typical status in which the change of the stresses in the structure is small and continuous if the transmission speed is slow. Therefore, this status is studied and the static analysis can satisfy the engineering precision.

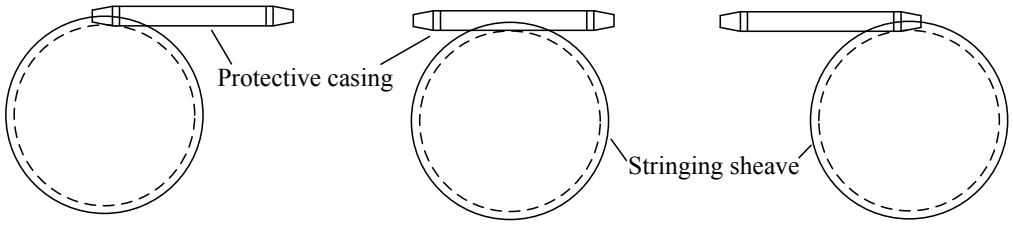


Fig.2. The process of casing overpass stringing sheave

In the following analysis, the 3D model of the stringing system is created by means of ANSYS software[4], which includes the several contacts of the parts. The effects of each part on others can be simulated.

Finite elements model. The splicing sleeve is a long hexagonal prism(Fig. 3) which contacts with the two protective casings at the vertices. Two protective casings (Fig. 4) are tied at the end by a solid ring which replaces the steel wire and are set above the splicing sleeve.

The stringing sheave is a wheel with slot whose size is much larger than the diameter of sleeve. The sheave deformation is very small compared with splicing sleeve, so considering the calculation time and the computer memory capacity, the sheave is simplified as rigid wheel here.

Since the whole system is symmetrical about the vertical axis, only half of the structure is included in the numerical model to simplify the simulation procedure. After symmetry simplification, the 3D model of half structures created and shown in Fig. 5.

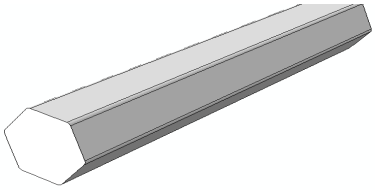


Fig. 3 The splicing sleeve

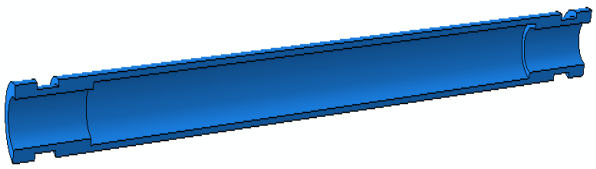


Fig.4 The protective casing

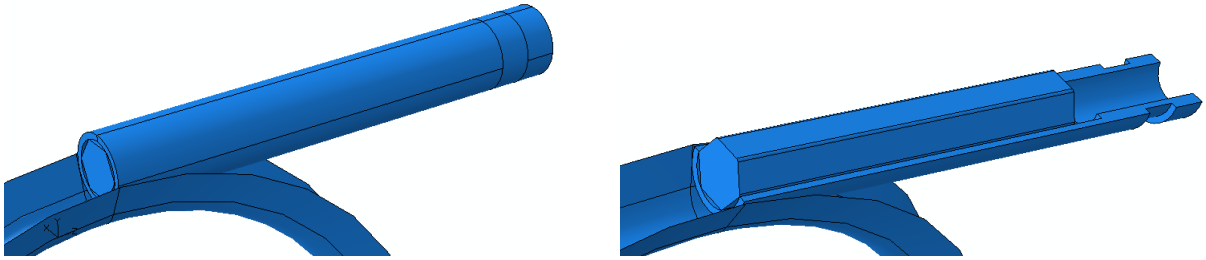


Fig. 5 The assembly of stringing system

In addition, only three typical stringing positions, horizontal stringing condition(β=0), 45 degree stringing condition(β=45) and vertical stringing condition(β=90), seen in Fig. 6, are considered and computed for describing the stringing procedure.

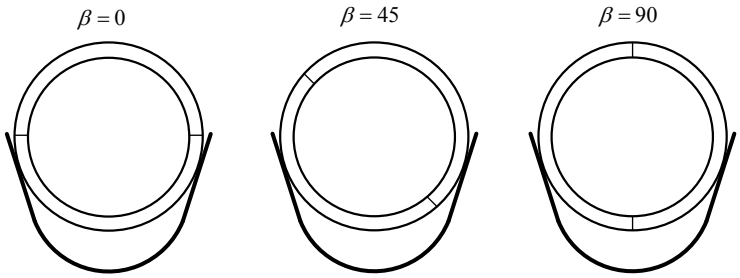


Fig. 6 The typical position of stringing system

Mesh of the structure. In order to obtain precise stress distribution, the brick element C3D8I is adopted for the structure, which is 8-node linear brick incompatible element and accurate enough for the current mesh in stresses analysis.

Here the structure mesh shown in Fig. 7 is used for the final simulation of the stringing system. The total number of element number is 6024.

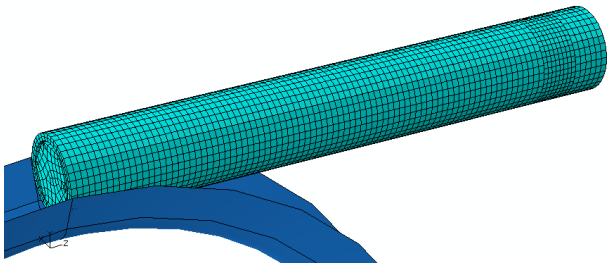


Fig. 7 The mesh of the splicing sleeve and protective casing

Contact constraint. The contact analysis of different parts is a nonlinear problem in FEM. In ANSYS a capability is included to model small-sliding contact of two bodies with respect to each other. With this formulation the contacting surfaces can undergo only relatively small sliding relative to each other, but arbitrary rotation of the bodies is permitted.

The small-sliding capability can be used to model the interaction between two deformable bodies. With this approach one surface definition provides the “master” surface and the other surface definition provides the “slave” surface. Small-sliding contact is computationally less expensive than finite-sliding contact, so all the contacting surfaces are set with small-sliding contact without frictional.

There are 16 contacts in the model, including 2 between two protective casings, 6 between splicing sleeve and casings, 6 between rope ring and two casings, 2 between casings and stringing sheave.

Load application. The reference nodes are set at the end of protective casings, the constraint distributes loading such that the resultants of the forces at the casings are equivalent to the loading at the reference node. The design value of load is 25kN.

Boundaries. In this model, the boundary constraints are set on the end of sleeve and casing and the surfaces of two end of segmental arc.

Numerical Results

The loading capacity of a structure is very important for the design of stringing sheave system. Therefore the influence of any change in the structure should be well studied to ensure the structure safety. From this point of view, the finite element analysis is conducted here to obtain the loading capacity of protective casing with different situations.

From the stress results of protective casing under the acting loads shown in Fig. 8(β=0), it is known that the maximal Von Mises stress appears at the node P1 caused by contact of rope ring and casings which is not concerned here. The node P2 is the contact vertex of sleeve and casing. The other important nodes are around the end of casing where is the main loading area, such as P-45 at the 45 degree of the circle and so on.

The stress results of these nodes in different positions are listed and discussed in the following.

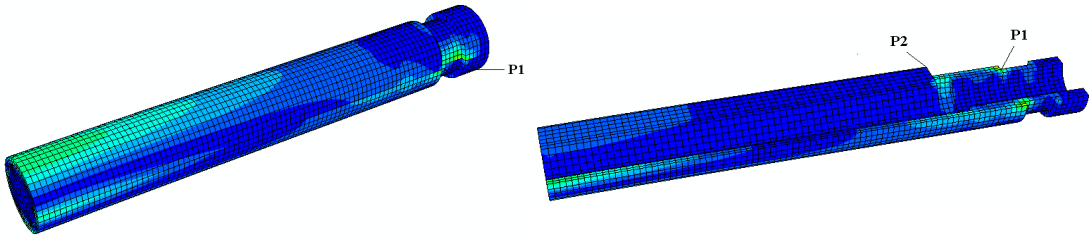


Fig. 8 Stress distribution of splicing sleeve and protective casing

Compared with the average stress around the end of casing in the Table 1, it can be concluded that the 45 degree condition is the unfavorable and critical position which has the largest stress. The stress in other part of casing is small. The contact force between sleeve and casing are always large, and the location of the node changes with the position of sleeve and casing.

Table 1 The Von Mises stress σ [N/mm^2]

Position	P-45	P-90	P-135	P-225	P-270	P-315	P1	P2
0	415.7	704.5	361.4	446.3	636.1	232.9	450.3	621.8
45	985.7	339.8	179.3	753.1	266.2	163.2	358.4	933.0
90	316.3	856.7	262.9	166.3	502.8	198.0	69.1	709.4

The high stress concentration (seen in Fig. 9) may result in collapse of the casing, but considering the splicing sleeve made by aluminum which deforms easily, the real stresses of the nodes can be accepted in the construction. If possibly the angle of the sleeve prism should be larger or smoother.

In the stringing procedure there is centrifugal force acting on the sleeve and casing when the sheave is rotational[5]. The centrifugal force increases with the revs, and the force acting on the protective casing decreases accordingly. So the results here is safe for the system through they are all larger than the allowable stress.

Summary

The stress results of splicing sleeve and its protective casing above the stringing sheave is made by finite element method with static analysis.

The contact forces between sleeve and casing have been obtained at different positions in stringing procedure. According to the results, the 45 degree stringing condition is the critical position and should be avoided in stringing procedure. And the reasonable design scheme of sleeve is proposed.

References

[1] H. P. Jiang: Electric Power Construction, Vol.30(2009), p.8

[2] S. Q. Xu, K. Liu, Z. M. Tan: Electric Power Construction, Vol. 31(2010), p.106

[3] Bureau of Energy of P. R. *China: Stringing blocks of overhead transmission lines (DL/T371-2010)* (China Electric Power Press, Beijing 2010).

[4] Structural Analysis Guide (ANSYS Release 5.7) on www.ANSYS.com

[5] J. H. Cao, S. R. Liu: Journal of Jiujiang University (natural sciences), Vol. 3(2011), p.32

© (2012) Trans Tech Publications, Switzerland
doi:10.4028/www.scientific.net/AMM.164.317

CAD/CAE on the mould plates of horizontal type high-pressure grouting machine

Zhicheng Huang

College of Mechanical and Electronic Engineering

Jingdezhen Ceramic Institute

Jingdezhen, China

Huangwu555@sina.com

Keywords: High-pressure grouting machine mould plate horizontal type ceramics for daily use CAD CAE

Abstract: In order to study the stress and strain of front and back mould plates of high pressure grouting machine, this paper took a type of ceramics for daily use horizontal type high pressure grouting machine as the object of study. Established its CAD model and analysed it with finite element analysis software. The analysis results can provide a reference for design, and have some engineering and practical value.

Introduction

At present, slip casting is the most important production process for sanitary ceramics. In high-pressure grouting process, high pressure is imposed on the mud, force the water in the mud to diffuse and penetrate toward the model, and then discharge out of the model. After draining the remaining mud, form adobes with a certain strength and thickness.

High-pressure grouting process requires the high-pressure grouting machine has large enough clamping force, and the mould plates with large sizes are the key component of high-pressure grouting machine, stiffness is the main design criteria. If the stiffness or strength of the mould plates of the high-pressure grouting machine is not enough, it may lead to leakage of slurry and the worst case may lead to a molding failure. Therefore, the static analysis of the mould plates is very necessary.

The finite element analysis on the mould plates

Technical conditions. The material of the mould plates is 45 steel, and its characteristic coefficients and mechanical properties are as follows: mass density: 7800kg/m^3; elastic modulus: 2 e +11 Pa; Poisson's ratio: 0.32; yield limit: 355MPa; limit strength: 600MPa. The maximum grouting pressure is 4MPa.

Molding. The three-dimensional (3D) models of the mould plates are established by using CAD software Pro / Engineer, and then import them into ANSYS program to analysis through the ANSYS data access module (DDA). Fig.1and Fig.2 are respectively the 3D model of the front mould plate and back mould plate.

Meshing. Solid92 unit is tetrahedron ten nodes unit with high-precision, and there are three degrees of freedom per node, respectively X, Y, and Z displacement.The internal displacement of the unit is according to the parabolic interpolation, while the internal stress of the unit is according to the linear law change. The unit is well suited to three-dimensional solid with irregular boundaries. Therefore, the Solid92 unit is selected to mesh the model of the front mould plate in this paper, and the method used is free mesh method. The size of the mesh is controlled by “Smart Sizing” command. Fig. 3 and Fig. 4 are respectively the mesh model of the front mould plate and back mould plate.

Imposing constraints. In the high-pressure grouting process, the back of the front mould plate is withstood by a slider-crank mechanism, and the back of the back mould plate is withstood by an adjustment device .Therefore, the all degrees of freedom of the concave on the back of the mould plates are all needed to be qualified.

Loading. In the high-pressure grouting process, 4MPa grouting pressure is applied to the front of the plates. Therefore, 4MPa surface loads are imposed on the facade of the both plates.

Solving. To obtain very accurate solutions, we select "the Frontal Solver" method.



Fig.1. 3D model of thefront mould plate



Fig.2. 3D model of the back mould plate



Fig.3. Mesh model of the front mould plate



Fig.4. Mesh model of theback mould plate

Analysis results

Deformation distribution. Fig.5 and Fig.6 are respectively showed the X direction displacement of the front and back mould plates; Fig.7 and Fig.8 are respectively showed the Y direction displacement of the front and back mould plates; Fig.9 and Fig.10 are respectively showed the Z direction displacement of the front and back mould plates; Fig.11 and Fig.12 are respectively showed the total displacement of the front and back mould plates.

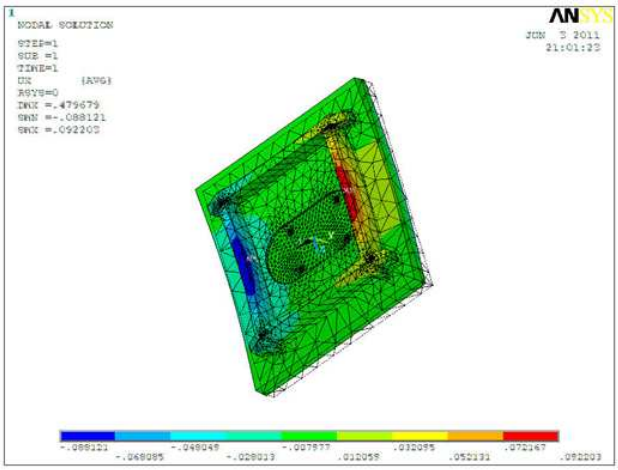


Fig.5.The X direction displacement of the front mould plates

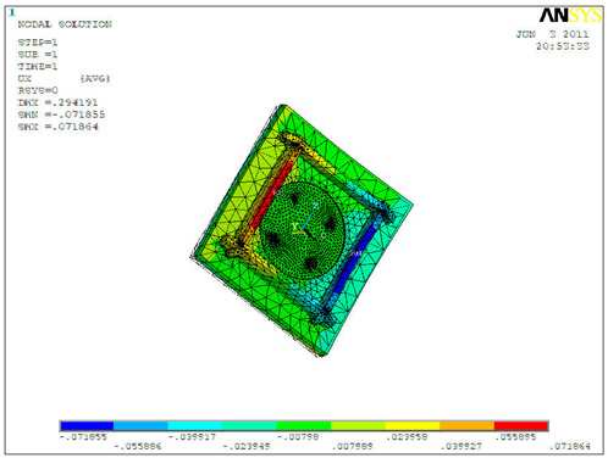


Fig.6.The X direction displacement of the back mould plates

Stress distribution. Fig.13 and Fig.14 are respectively showed the X direction stress nephogram of the front and back mould plates; Fig.15 and Fig.16 are respectively showed the Y direction stress nephogram of the front and back mould plates; Fig.17 and Fig.18 are respectively showed the Z direction stress nephogram of the front and back mould plates; Fig.19 and Fig.20 are respectively showed the Von-mises stress nephogram of the front and back mould plates.

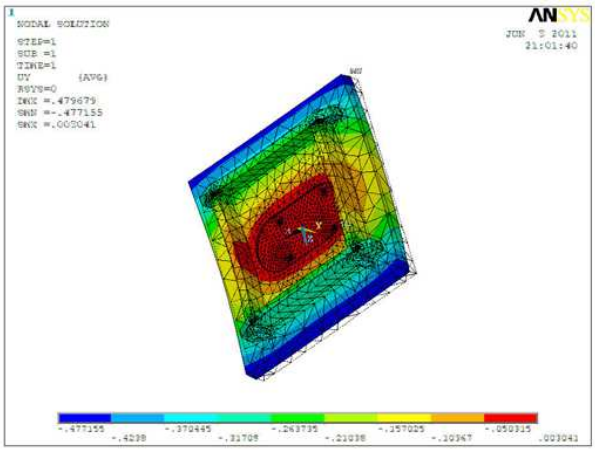


Fig.7.The Y direction displacement of the front mould plates

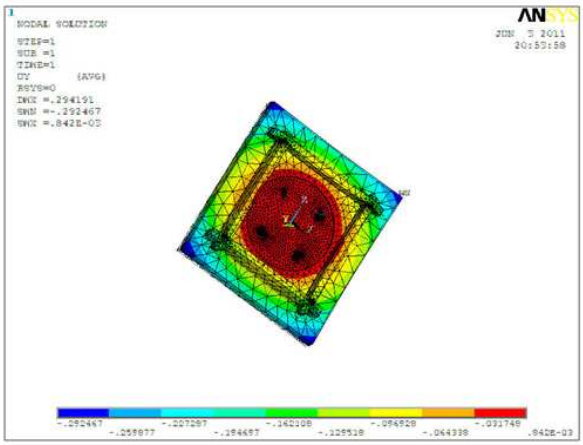


Fig.8.The Y direction displacement of the back mould plates

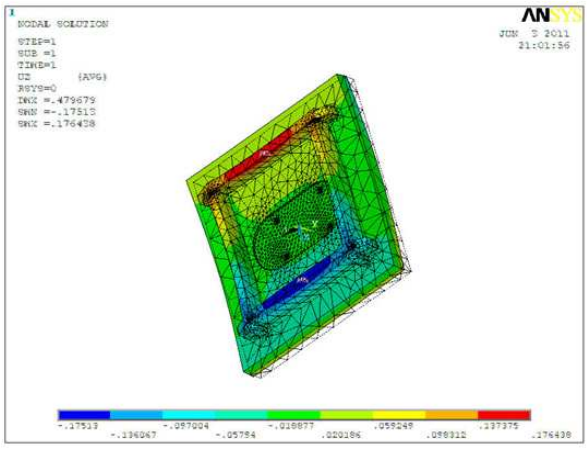


Fig.9.The Z direction displacement of the front mould plates

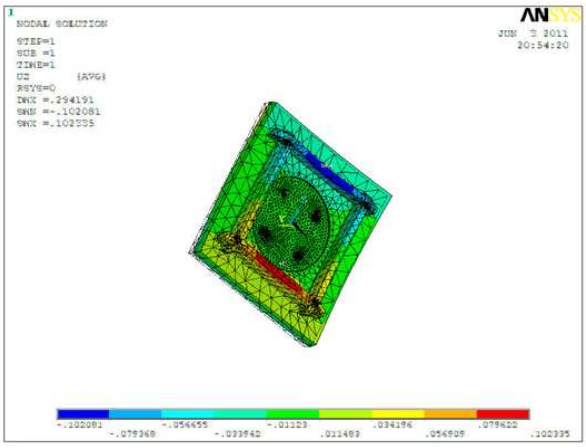


Fig.10.The Z direction displacement of the back mould plates

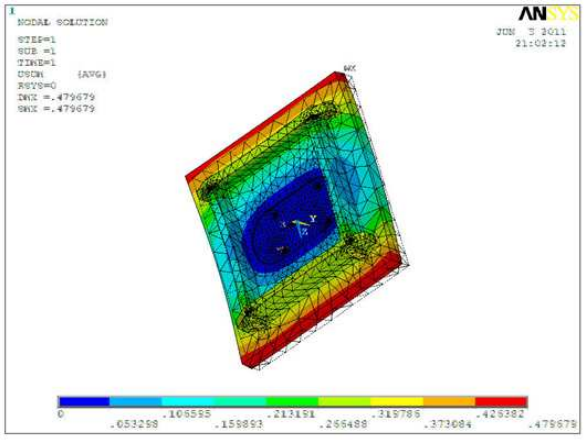


Fig.11.The total displacement of the front mould plates

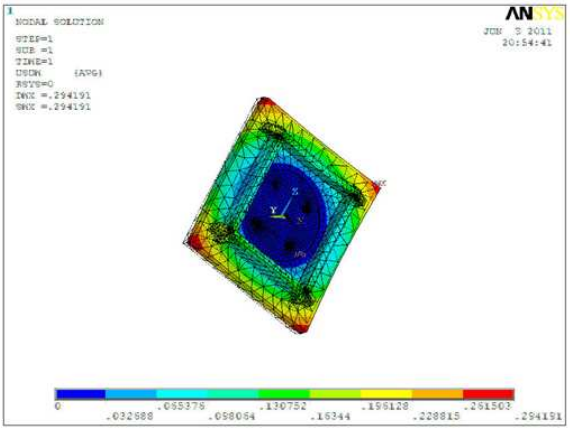


Fig.12.The total displacement of the back mould plates

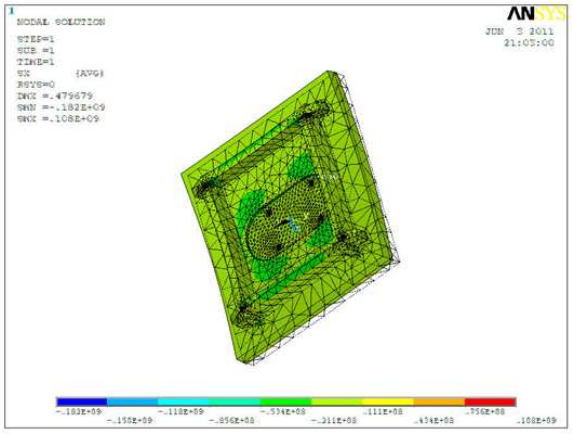


Fig.13.The X direction stress nephogram of the front mould plates

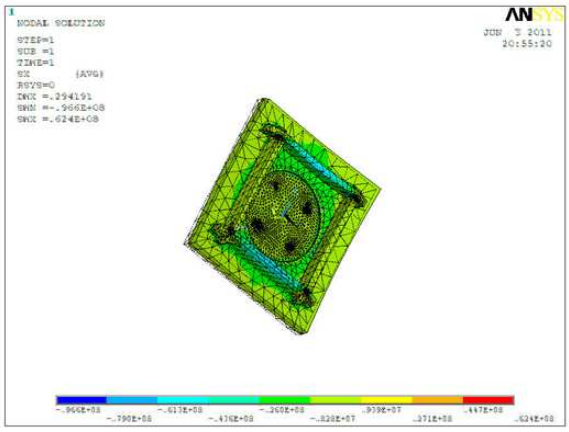


Fig.14.The X direction stress nephogram of the back mould plates

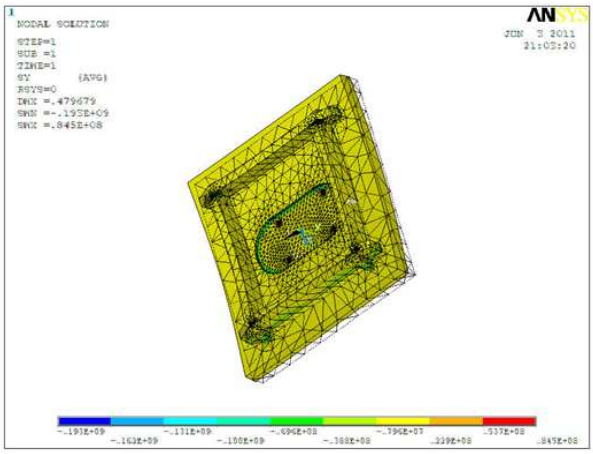


Fig.15.The Y direction stress nephogram of the front mould plates

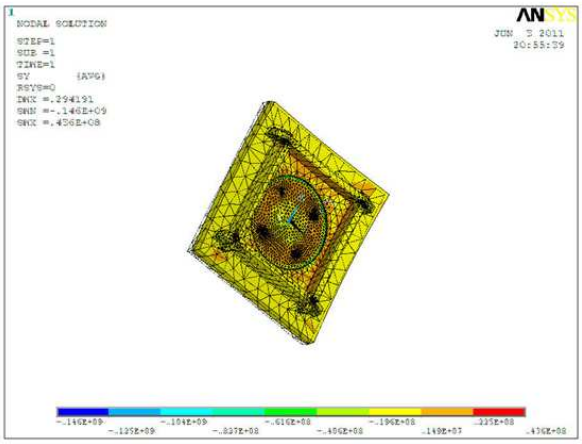


Fig.16.The Y direction stress nephogram of the back mould plates

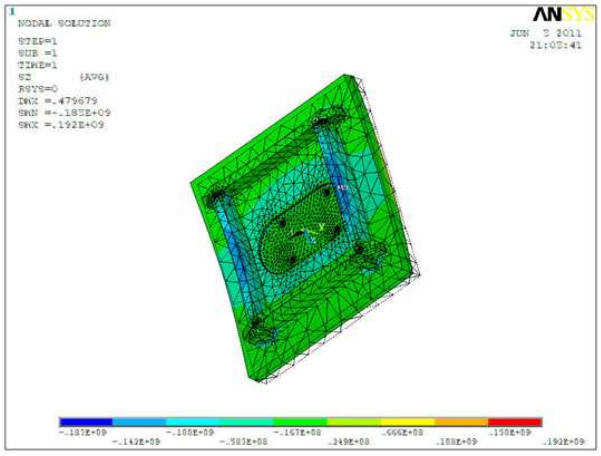


Fig.17.The Y direction stress nephogram of the front mould plates

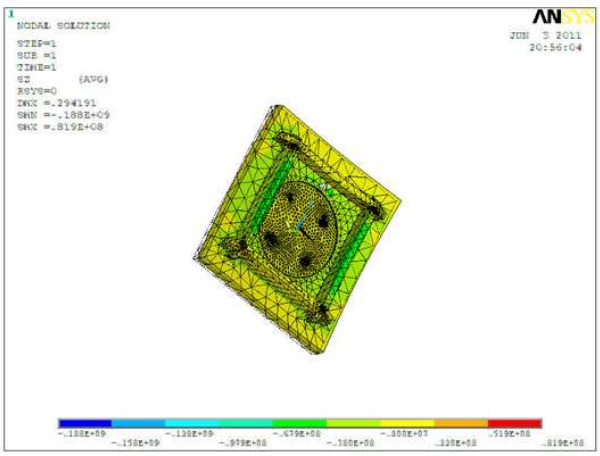


Fig.18.The Y direction stress nephogram of the back mould plates

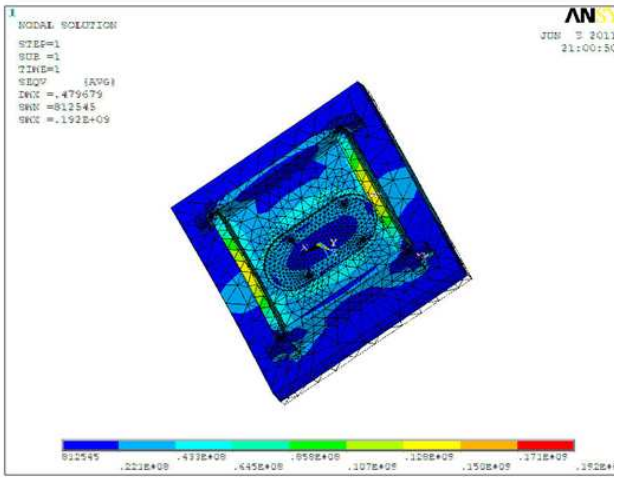


Fig.19.The Von-mises stress nephogram of the front mould plates

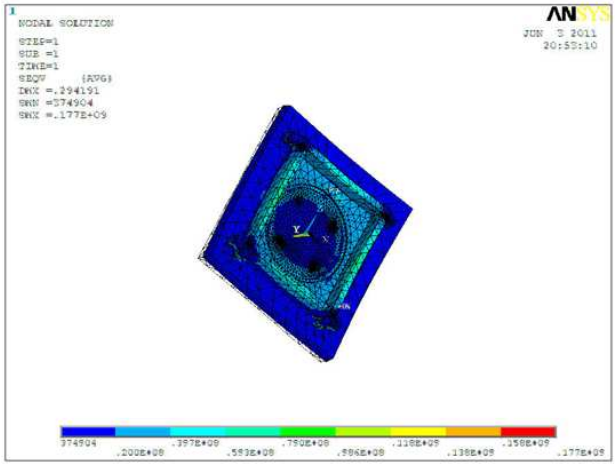


Fig.20.The Von-mises stress nephogram of the back mould plates

Conclusions

（1）The X direction maximum displacement values of the front and back mould plates are respectively 0.092mm and 0.072mm; Similarly, the Y direction values are 0.03mm and 0.042mm; the Z direction values are 0.176mm and 0.102mm; the total direction values are 0.479mm and 0.294mm.

（2）The X direction maximum stress values of the front and back mould plates are respectively 108MPa and 62.4 MPa; Similarly, the Y direction values are 84.5 Mpa and 43.6Mpa; the Z direction values are152 Mpa and 81.9Mpa; The von-mises stress values are 192 Mpa and 177Mpa.

（3）The maximum total displacement of both mould plates are all located in the four corners, and the values are all less than 0.5mm. Therefore, the stiffness of the both mould plates meets the design requirements.

（4）The von-mises stress of the both mould plates are all located in the middle of the ribs, and the values are all far less than 355 Mpa. Therefore, the strength of the both mould plates meets the design requirements.

（5）All the stress and strain are in the design range, so the design of the mould plates meets the work requirements

References

[1] Yuxin Xiao. Introduction of high-pressure grouting technology and equipment. Jingdezhen Ceramic Design Institute .1982

[2] Zhemin Shi. Development and Countermeasures of sanitary porcelain high-pressure grouting technology

[3] ANSYS.INC. Basic Analysis Procedures Guide. Release5.7

[4] ANSYS.INC. Modeling and Meshing Guide. Release5.7

[5] He, Y. N., Xu, J. C., and Zhou, A. H. Local and parallel finite element algorithms for the Navier-Stokes problem. J. Comput. Math. 24(3), 227–238 (2006)

[6] Ma, F. Y., Ma, Y. C., and Wo, W. F. Local and parallel finite element algorithms based on two-grid discretization for steady Navier-Stokes equations. Appl. Math. Mech. -Engl. Ed. 28(1), 27–35(2007)

© (2012) Trans Tech Publications, Switzerland
doi:10.4028/www.scientific.net/AMM.164.322

Analysis of Jib Strength and Broken Jib Accident of High Pedestal Jib Crane from the Perspective of Mechanics

Qing-dun Zeng[1,a] and Fang Liu[1,b]

[1]School of Civil Engineering and Transportation, South China University of Technology, Guangzhou 510640, China

[a]emqdzeng@scut.edu.cn, [b]659901748@qq.com

Keywords: High pedestal jib crane, Jib frame, Broken jib accident, FEM, Analysis of mechanics.

Abstract. According to an example of the broken jib accident of a high pedestal jib crane (HM2564) in a Shipyard Co., Ltd. in Guangdong province, this paper used a finite element software ANSYS to establish a solid model for the jib frame of the crane, calculated the stresses of jib system under various actual working conditions and checked the strengths. Simultaneously, the reasons of broken jib were quantitatively analyzed from the perspective of mechanics. The results show that the strengths of the jib system meet the requirements of safe use under all kinds of working conditions, but the related hoistman incorrectly operated the facility, cables can't be winded normally in pulleys, thus resulting in that the tensile force of a cable was directly applied on the main jib by pulley spindle and the failure of the jib frame occurred under heavy compressive force of lifting cables.

Introduction

High pedestal jib crane is a kind of important rail cranes and an indispensable facility to realize the mechanization of productive process [1]. Nearly 20-year, the study about cranes and engineering practices has achieved great progress in our country; new methods of calculation and computing technologies have continuously been applied to productive practices. At same time, the finite element method is a kind of numerical computation methods for structural analysis, and the availability is very good. The jib frame is one of the important bearing parts for crane, so the design of jib structure is therefore the key to project high pedestal jib cranes. However, because of harsh working conditions, intensive use and overload, the faults about jib structure hold a large proportion for cranes. Meanwhile, there are many security issues in the jib system, such as the rivet ecclasis, stress concentration, fatigue crack and rusting attenuation [2], which results in the reduction of preplanned functions, or even risks that can cause serious accidents and great financial losses. In order to improve the safety and reliability of cranes, we should take the strength test [3] for cranes, and absorb the lessons from the past for the sake of lowering accident rate.

The paper analyzes the broken jib accident on a high pedestal jib crane. With the help of ANSYS [4,5], we check the strength of the jib and try to find out the causes of broken jib accident, which has the important significance and practical value for the research of cranes and engineering practices.

Accident Summary

The base for repairing and building ships of a Shipyard Co., Ltd. is located at Dongjiang mouth near the Dasheng Village in Machong Town, Dongguan City, Guangdong province. On 5th April 2010 at about 10:00 am, a cable of 30mm-diameter for a high pedestal jib crane (HM2564), in no-load lifting process of the main hook, was slided off the main lifting pulley and stuck by a gap between pulleys, which was subsequently broken by the winding engine of the crane hoist. In this course, the jib frame first appeared multi-local bending deformations. Soon afterwards, the jib frame dropped**,** but the cables used to prevent jib frame from falling did not play a protective role. As a result, it fell on the deck of a ship with displacement of 57,000 tons which was being built. Then, the secondary accident occurred, which resulted in the bending failure and breakage of the jib frame, that is, the buckling of some member bars and the complete damage of integral structure, as shown in Fig. 1. Furthermore, the gate seat of the high pedestal jib crane subjected to torsion occurred local deformation, which led to running off the rail about 15cm on both sides of the crane.

Checking of Jib Strength

This paper uses a finite element software ANSYS to establish the solid model for the jib frame of the high pedestal jib crane. The stresses of the jib system under various actual working conditions are calculated, the strength of the jib system is checked.

All Kinds of Working Conditions for Crane. In working positions, according to the actual situation of the high pedestal jib crane, the main hook is divided into 4 working conditions, that is, when working range (radius) of crane respectively are 25m, 30mm, 40m and 55m, the correspondingly rated lifting weights of the main hook are 25t, 20t, 15t and 8t, respectively. Meanwhile, each condition is divided into two cases of the static and dynamic loads.

(1) Under the static load condition, the jib system is only subjected to the dead-weight, wind load and rated lifting weights of the main hook. At same time, the structural dead-weight is multiplied by 1.2 of partial safety factor, and the rated lifting load is multiplied by 1.25 [6]. Therefore, under the static load condition, the load combination is $1.2P_G$, $1.25P_Q$ and P_{WII}, where, P_G is the dead-weight of the jib frame of crane and is automatically applied in software ANSYS, P_Q is the rated lifting load, depended on different working conditions, and P_{WII}=14.34kN is the maximum wind load in working positions of crane.

(2) Under the dynamic load condition, the jib system is subjected to the comprehensive action of the dead-weight, wind load, rated lifting load of main hook and its inertia force. The structural vibration load induced by dead-weight is multiplied by 1.2 of partial safety factor. Therefore, under the case, the load combination is $1.2P_V$, P_E, P_{H1}, P_{H2} and P_{WII}, where P_V=$1.1P_G$ is the structural vibration load induced by dead-weight, P_E=$1.073P_Q$ is the lifting dynamic load, depended on different working conditions, P_{H1}=$1.5\times(m_G+m_Q)\times0.108$=$0.162(m_G+m_Q)$ is horizontal inertial force induced by starting and braking of crane at longitudinal and lateral movement in horizontal plane, and P_{H2}=$1\times(m_G+m_Q)\times0.6$=$0.6(m_G+m_Q)$ is the rotary centrifugal force of crane and horizontal inertial force induced by starting and braking of rotary and luffing movement of jib frame. Here, m_G and m_Q are the mass of jib structure and the rated lifting mass, respectively.

Under non-working condition, we just consider the influence of both the structural dead-weight and wind load. Therefore, the load combination is $1.2P_G$ and P_{WIII}, where P_{WIII}=65.39kN is the maximum wind load under the non-working condition.

Checking of Jib Strength. By used a finite element software ANSYS, the solid model for the jib frame is established in this paper, the stresses are calculated and the strengths are checked. According to the design drawings, Beam188 (beam element) is used to simulate the chord and web members of the jib frame, and the different beam sections are defined in the light of different size members. Shell63 (shell element) is used to simulate the steel plates which connect forepart and head of jib frame and Link10 is used to simulate cables. The spacial finite element solid model established for the jib frame is shown in Fig. 2.



Fig. 1 Broken jib picture of the crane

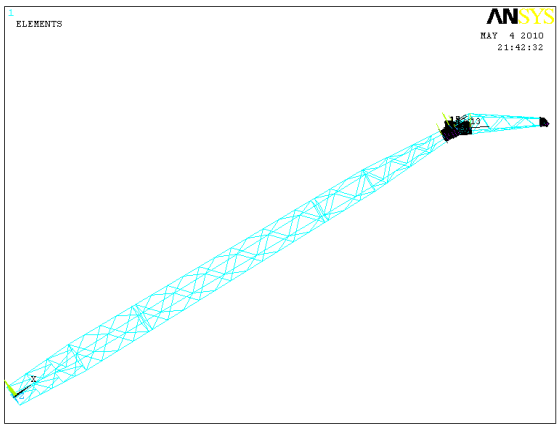


Fig. 2 Solid model for jib system

After meshing the solid model as the beam and shell elements, then the loading is performed. The tensile forces are applied in the cable ends to keep that the structure is statically determinate and the dead-weight of pulleys is applied to the pulley spindle when the pulley block is simplified as a pulley spindle. The different load combinations are applied in the model and the stress values of chord and web members are calculated. The maximum stresses of chord and web members under various working conditions are shown in Table 1. The chord and web members of the jib frame are respectively used to be Q345B and number 20 seamless steel tubes whose strengths are 345MPa and 245MPa, respectively. It can be seen from Table 1 that when the working radius of the jib frame is 25m, the stresses of chord and web members under static and dynamic loads respectively have the maximum values which are 343.39MPa and 161.88MPa. Therefore, the strengths of the jib system meet the requirements of the safe use.

Table 1 Maximum stresses of chord and web members under various working conditions

Working Conditions		Maximum stress (MPa) Chord member	Web member
Working radius: 25m	Static load	343.39	160.22
	Dynamic load	329.47	161.88
Working radius: 30m	Static load	234.34	122.65
	Dynamic load	226.91	127.62
Working radius: 40m	Static load	147.10	98.34
	Dynamic load	145.24	104.42
Working radius: 55m	Static load	96.29	86.74
	Dynamic load	101.86	93.37
Non-working Condition (Jib lies in 25m working radius)		125.06	108.29

Analysis of Accident Cause on Broken Jib Frame

Cause of Broken Jib Frame. The spacial finite element model of simulating the failure process of the jib frame in a no-load upgrade process of the main hook is the same as Fig. 2, and the working condition is selected as the working radius of 25m. According to the damage cases of the jib frame and luffing cables in the accident scene, it can be obtained from Ref. [7] that when the minimum tensile strength for ϕ30 cable is 1400N/mm^2, the broken tensile force of the cable is 478.20kN. In this case, the tensile force of the luffing cable twining in the pulley is acted on pulley spindle, and the ends of other luffing wire ropes are articulated in order to keep the structure statically determinate. The load combination acted on the finite element model for the jib frame is P_D, P_G and P_{WII}, where P_D =478.20kN is the broken force of luffing cable.

The loading of the finite element solid model is performed, and the stresses for chord and web members are calculated. Finally, the calculated results are checked by the general postprocessor. The axial force diagrams of chord and web members are shown in Figs. 3 and 4, respectively.

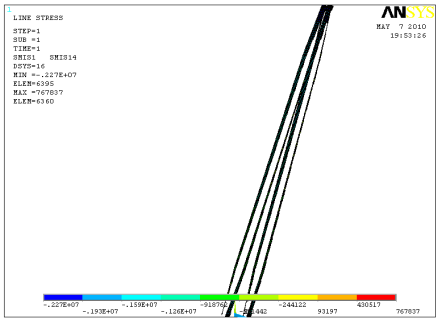


Fig. 3 Axial force diagram of chord members

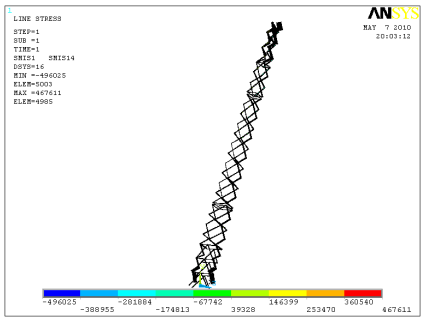


Fig. 4 Axial force diagram of web members

It can be known from Figs. 3 and 4 that under the working condition, the maximum compressive forces of chord and web members respectively are 2.27×10^7N and 4.96×10^5N. The chord and web members respectively areφ203×7 andφ102×6 seamless steel tubes whose cross sectional areas are 4.31×10^{-3}m^2 and 1.81×10^{-3}m^2, respectively. Therefore, we can calculate that the maximum compressive stresses of chord and web members are 526.68MPa and 274.03MPa, respectively, which all are larger than their strengths 345MPa and 245MPa, respectively, thus resulting in the failure of chord and web members.

The above calculated results show the reason of occurrence of broken jib accident for HM2564 crane. In operation process of the main lifting hook, because cables could't be winded normally on pulleys, the tensile force of luffing cable was putted on the main jib by pulley spindle. The main jib is a truss structure and its length is very long. Although the design strength of the jib frame met the requirements of the safe use, it was inevitable for the jib frame to occur a buckling under heavy compressive force, when a cable was slided off the main lifting pulley and stuck by a gap between pulleys. The jib structure first appeared the bending deformation and local instability. Soon afterwards, the jib frame dropped**,** but the cables used to prevent the jib frame from falling did not play a protective role. As a result, it fell on the deck of a ship which was being built. Then, the secondary accident occurred, which resulted in the bending failure and breakage of the jib frame. The complete damage of integral structure had taken place.

Failure of Cable. It can be known from the scene of accident that when the downward tensile force of cables of lifting weight is less than the torsional moment of side direction of cables, or the sway of cables occurs, the main lifting cables are easy to wrap together, resulting in that cables are slided off the main lifting pulley. The main reason of occurrence of abnormal twining of cables may be that in processing production molding of cables, certain turning force has to be applied to the cable, in order to twist into a cable from formed steel wire ropes of multistrand. Because the applied external force must overcome the surface tension and elastic force of cables, so the steel wire ropes of multistrand can be screwed together and the cables can be formed. Therefore, formed cables have relatively large elastic recovery stress after their processing is completed.

After cables are installed in crane, under no-load condition, because of their own elastic recovery stress and the bending stress induced by winding fall blocks and fixed pulleys, the superposition of two kinds of stresses will generate the torsional moment of side direction in opposite direction of turning direction of cables. Longer the cable length, larger the torsional moment in side direction.

Inadequate Operation by Workers. The occurrence of "broken jib" accident for the high pedestal jib crane at work was obviously related to the hoistman's improper operation. When the abnormal condition occurred, the hoistman didn't turn off the winding engine to check what happened, thus resulting in the occurrence of the broken jib accident for high pedestal jib crane.

Conclusions

The present analytical results indicate that, because the related hoistman incorrectly operated the facility, cables can't be winded normally in pulleys, thus resulting in that the tensile force of a cable is directly applied to the main jib by pulley spindle. Although the strength of the jib system met the requirements of the safe use, the jib frame occurred failure under heavy compressive force of lifting cables. By the analysis, the paper suggests that it is effective for protecting jib frame to install a load limiter with pulling ring or **(**SUC630H) high counter-force (RH) rubber fenders.

References

[1] X. J. Li: Strength and dynamics analysis for boom system of portal crane, M.S. thesis, Dalian Jiaotong University, 2008. (in Chinese)

[2] R. Ma: The research on structure security evaluation and reliability of gate crane jib system, M.S. thesis, Dalian Jiaotong University, 2008. (in Chinese)

[3] H. M. Zhang, S. L. Li and Z. B. Zhang: Mech. Manag. Dev., Vol. 25(1) (2001), p.1. (in Chinese)

[4] H. G. Jia, W. L. Li and S. William: J. Vibration and Shock, Vol. 29(12) (2010), p.136.

[5] S. G. Dong, J. X. Ge and Y.L. Wu: J. Zhejiang Univ. (Eng. Sci.), Vol. 43(11) (2009), p. 2085.

[6] L.Wai,G.L.Xu and D.M.Gu:*Crane design specification* (Standards Press of China, Beijing 2008).

[7] Z. R. Jiang: *Construction Engineer's Handbook* (China Building Industry Press, Beijing 2009).

© (2012) Trans Tech Publications, Switzerland
doi:10.4028/www.scientific.net/AMM.164.326

Analysis of Flanges Mechanics and Sealing on Horizontal Pipes Connector in Deep Sea

Zh. Wang, Y.J.LI, B. Zhang, W. Zhang and F. K. Liu

College of Mechanical and Electrical Engineering, Harbin Engineering University, Harbin 150001, China,

wangzhuo_heu@hrbeu.edu.cn

Keywords: Horizontal pipes connector, Flanges contact , Mechanics Analysis,Sealing ring

Abstract. The mechanism structure of horizontal pipes connector was designed in order to connect two pipes in deep sea. The contact property of mechanics and sealing ring between the two flanges was analyzed, which was used finite element method, and obtained permissible compressive force and displacement of the sealing ring to realize sealing. The result is that the metal sealing ring allows the largest compression displacement of the metal sealing ring is 2 mm. It is accurately required to control the displacement of the pistons of hydraulic cylinders that push the flange.

Introduction

Since 1960s, with the rapid development of the underwater engineering technology of the maritime powerful countries in the world, as a branch of it, Subsea Tie-in systems is no exception. Foreign companies have formed the design technology with the water depth about 3000m, which is bad maritime conditions, complex undersea geographical and geological conditions .Meanwhile, they have developed a series of Subsea Tie-in methods of construction technology, and all sorts of technology are formed in series abroad. The ancillary products are sold as well. As one of the Subsea Tie-in machinery，horizontal pipes connector is a quick connecting device which is widely used in deep-sea oil and gas pipeline system, the working environment of which is usually deep water, poor working conditions, uncertain elements, so workers can not work. Therefore, it is assisted by the implementation of ROV operations, which can connect two pipes rapidly and accurately. Its main work processes in sequence are composed of five parts：vertical coarse alignment, rotary and level of precise alignment, butt joint seals, locking and fixxing and auxiliary and recyclable targeting device. Among them, the butt joint seals is the key part of the steps, because it is required to be effectively sealed after the butt joint the two connecting pipes flanges to make sure that there is no leaky phenomenon. This article will focus on the horizontal pipe flange sealing problem and analyze the characteristics of sealing.

Design of Mechanism Structure of Horizontal Pipes Connector

The mechanism body structure of horizontal pipes connector is the most important part of connector. Other hydraulic control systems complete a variety of functions taking mechanism body as the actuator, which are the function of the product function. It is the specific implementers. Three-dimensional design of body structure of horizontal pipes connector is shown in Fig.1. The body structure is mainly composed of the fixed support plate 1, soft land hydraulic cylinder 2, propeller hydraulic cylinder 3, jumper pipe 4, upper alignment cone 5, lower alignment groove 6, connection plate 7, collet 8, upper flange 9, lower flange 10, actuator ring 11, fixed sleeve 12, propeller sleeve 13 and other components. The connection forms of two flanges in horizontal pipes connector is different from the ordinary bolt flange connection. propeller hydraulic cylinders drive the collet by which two flanges are connected and the metal sealing ring is installed in the middle of upper flange and lower flange. In the connection process, firstly, the upper flange surface receives the action of soft land hydraulic cylinder and levelly moves itself forward to be the connected position. Then lower flange surface ,namely, lower seal surface contacts and extrudes with sealing ring until the sealed position.

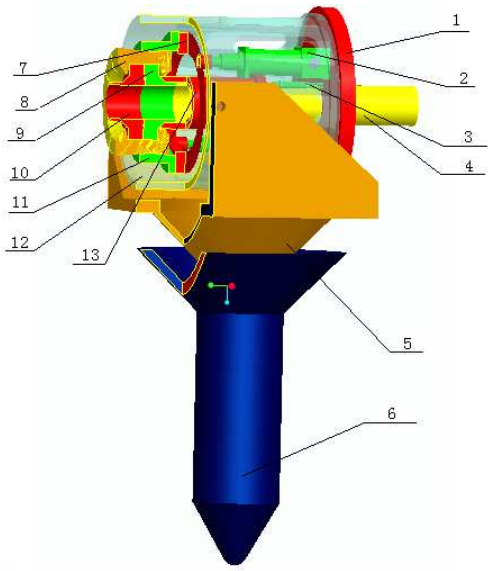


Fig.1 The body structure of horizontal pipes connector.

Analysis of Flanges Mechanics and Sealing Ring Characteristic

The choice of sealing ring references the Chemical Industry Standard of People's Republic of China HG20612-97. The sealing ring adopts the oval metal ring with model R58. 316L is selected the material of sealing ring(equivalent to 00Cr17Ni14Mo2). The highest working temperature is 600° . tensile strengthσb equals 480Mpa. yield limit $\sigma_s \geq 177$MPa . The test degree of hardness is 160HB. Since the metal sealing ring is allowed a small amount of compression, it is necessary to make a nonlinear contact analysis of metal sealing ring. within the limit of its effective sealing performance, the main analysis is the maximal amount of compression that the metal sealing ring can achieve. The results have a guiding significance for the seal grooves strength of flange, the strength of sealing ring, the sealing effect, and the determine of hydraulic cylinder effective travel.

The total axial force of sealing ring caused under the inner pressure is counted by the following formula:

$$F = 0.785D_G^2 p \tag{1}$$

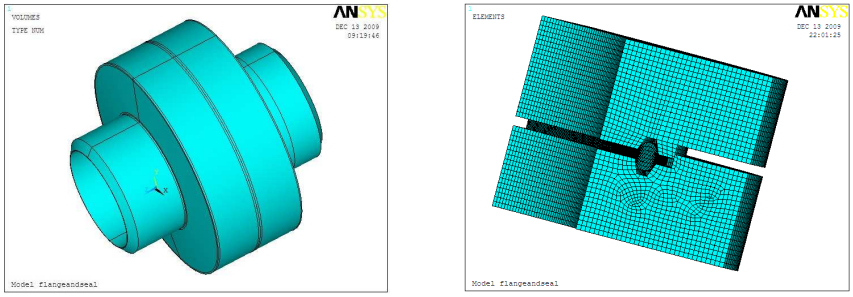
Where: D_G is diameter of the flange center circle，m；p is inner pressure of pipe，MPa。

The minimum packing force of gasket during the pre-tightening is counted by the following formula:

$$F_a = 3.14D_G by \tag{2}$$

Where: b is effective width of sealing ring，m； y is sealing specific pressure，MPa。

The modeling of two flanges and sealing ring is shown in Fig. 2(a).



(a) (b)

Fig.2 The model of contact stress analysis flanges and sealing ring and its meshing.

According to installation standards, the spacing of two flange facing is 5mm during the operation of the initial concavo-convex flange joint. The model is simplified and meshed as shown in Fig.2(b).

In the model, the connection process of flanges can be seen as a movement of the upper and lower flanges together with the same motion means but the opposite motion direction. The symmetrical contact analysises of model show as follows:

Contact pairs for the model are respectively established between the upper surface of sealing ring and the side of sealing groove of upper flange and between the lower surface of sealing ring and the side of sealing groove of lower flange. In the process of establishing contact pairs, the most important is to set the contact stiffness. In ANSYS, the setting of contact stiffness relates to the authenticity of the analysis. In principle , the contact stiffness depends on the permeability size between two surfaces. Generally speaking, the contact analysis bodies which occur the deformation through contact are not allowed to have the permeability. in the simulation analysis, not only can the two bodies contact occur the deformation, but also cause the osmosis. In general, the selection of contact stiffness should be large enough to ensure contact osmosis small to be acceptable, while, at the same time, the selection of contact stiffness should be small enough not to cause the ill-conditioned problem of the total stiffness matrix and to ensure the astringency. a real constant FKN can be used to specify a proportionality factor which is usually between 0.01~10 or a true value for the contact stiffness. When it is to avoid the excessive iterations, the osmosis should be the minimum as much as possible. Through several repeated experiments from small to large, the contact stiffness that is used in this analysis is 0.1, which can not only ensure contact analysis not affected, but also close to the actual situation.

A contact analysis was made to two pairs of contact pairs. The reasonable compression of sealing ring and the scope of the effective stroke of the hydraulic cylinder which can achieve this compression was obtained by loading the displacement to the upper surface of the model of flanges in different levels and analysing the displacement and changing of stress between the contact pairs

The upper flange and the lower flange relativing to the sealing ring respectively generate the displacement of 0.5mm in the first load. The result of the analysis is shown as Fig.3 below. From Fig.3, two flanges, each of which was condensed 0.5 mm, compress tightly to sealing ring, and the sum of the equivalent displacement vector of the sealing ringwas zero. It illustrates that the slopes of the flange seal groove slopes and the arc surface of sealing ring have not contacted to make sealing ring pressed and need to continue to be loaded.

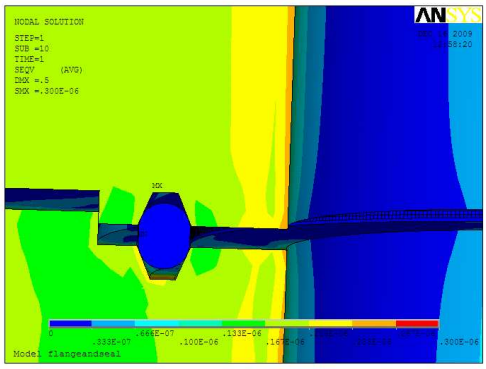


Fig.3 The sum of the equivalent displacement vector of the sealing ring when the displacement is 0.5 mm.

For the second load, firstly, two flanges are not affected by force and are turned to be the initial state. The upper flange and the lower flange relativing to the sealing ring respectively generate the displacement of 1 mm and its result was that the yield limit of the materials is 67.35MPa which shows that sealing ring has the feasibility to be compressed and loaded for the third time. The loading displacement is 1.5mm for the third load. The analysis of contact pairs is shown as Fig. 4. From this figure, the contact surfaces of flanges and sealing ring increase and exacerbate to deform. Accordingly the permeability of sealing ring increases simultaneously and the mutual pressure of flanges and

sealing ring also surge and the maximum measure up 200MPa whose amount has exceeded the yield piontof the materials. At this moment, the friction pairs is in the critical state, flanges and sealing ring are out of the elasticity deformation and they are not crushed and still belong to the plasticity deformation.

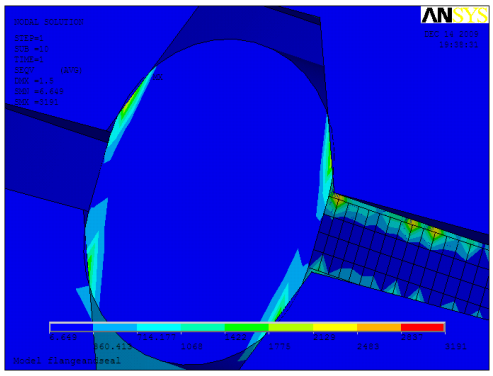


Fig.4 The sum of the equivalent displacement vector of the sealing ring when the displacement is 1.5 mm.

Sealing pairs is loaded for the last time. Flanges are restored to the initial state and loaded the displacement vector of 2mm from the position of z. The analysis of the force of sealing pairs is shown as Fig.5 below. Obviously, the biggest overwhelming force of contact pairs is 444.44MPa when it is loaded the displacement vector of 2mm. At this time sealing pairs has already been crushed and flanges and sealing ring have been destroyed. It illustrates that the sealing has been invalid at this moment.

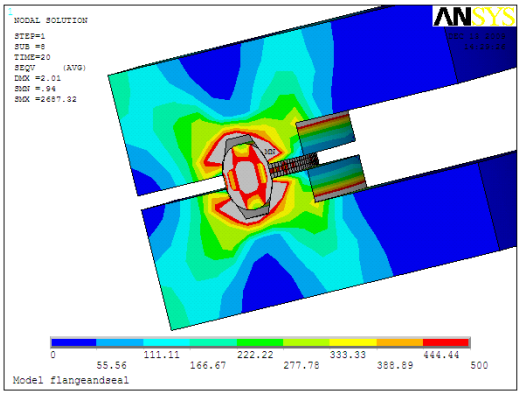


Fig.5 The sum of the equivalent displacement vector of the sealing ring when the displacement is 2 mm.

Summary

It can be obtained by the upper analysis that the metal sealing ring allows the minimum amount of compressed and the largest compression of the metal sealing ring is 2mm. So It is accurately required to control the displacement of the pistons of hydraulic cylinders that push the flange. The four hydraulic cylinders that are fixed on the same flange surface must be ensured to keep synchronous movement at the same time. Otherwise it will cause leak because the sealing ring local has the gap.

References

[1] Anon:Journal of Offshore Technology. Vol.28(2001),p.28-30

[2] Z.J.Huang : *Application of Modern Sealing Technology*(Machinery Industry Press, Chian,2008)

[3] Q.F. Wang ,L.D. He : Thermal power engineering. Vol.24(2009),p38-43

[4] D.B.Dong:*Critical Technology Research of The Subsea Oil & Gas Horizontal Pipe Collet Connection*(Master of Engineering, Harbin Engineering University,2010)

© (2012) Trans Tech Publications, Switzerland
doi:10.4028/www.scientific.net/AMM.164.330

Research on the Virtual Prototype of Grinding System for Wafer Precision Grinding Machine based on Mechanical System Mechanics

Zhihua Sha [a], Zongnan Zhang [b] and Shengfang Zhang [c]

School of Mechanical Engineering, Dalian Jiaotong University, Dalian China

[a]zhsha@djtu.edu.cn, [b]zhangzongnan1105@126.com, [c]zsf@djtu.edu.cn

Keywords: Wafer Precision grinding machine, Grinding system, Mechanics, Virtual prototype, Simulation.

Abstract. In order to decrease the development costs, shorten the developing cycle, improve the overall performance and reduce the environmental pollution of the wafer precision grinding machine, the structure, transmission, movement of grinding system for wafer precision grinding machine is analyzed based on mechanical system mechanics, the three-dimensional model of the grinding system is established, based on frame animation technology and via secondary development of Pro/E in the environment of VS 2008, the virtual prototype of grinding system for wafer precision grinding machine is developed, the kinematics and dynamics simulation of the grinding system is realized.

Introduction

Virtual prototyping technology [1, 2] is a digital design method based on computer simulation model of the product. By combining the models of several engineering field, virtual prototype can simulate the appearance, function and action of the real product. Virtual prototype can replace the physical prototype in creative design, test and estimation of the product, in turn, the developing time and cost can be reduced remarkably [3, 4].

In this paper, oriented to certain type of wafer precision grinding machine which is being researched and developed, based on mechanical system mechanics, the virtual prototype of grinding system is established, and the kinematics and dynamics simulation of the virtual prototype is realized. The simulation result can estimate the reasonableness of the design of the grinding system, so the developing time and cost of the wafer precision grinding machine can be reduced.

Design of Virtual Prototype System

Based on mechanical system mechanics, the establishing plan of virtual prototype system is shown is Fig. 1. First, all of the part of the physical prototype of the grinding system for wafer precision grinding machine is modeled into three-dimensional (3D) digital model using Pro/E; then, by analyzing the parameter of every part and the mutual constraints between parts in physical prototype, these parts are assembled into a complete 3D assembly model; based on 3D graphics transformations and frame animation technology, using secondary developing tool – Pro/Toolkit and VS2008 as developing tools, the virtual prototype of the grinding system for wafer precision grinding machine is developed, and the kinematics and dynamics simulation of the virtual prototype is realized finally.

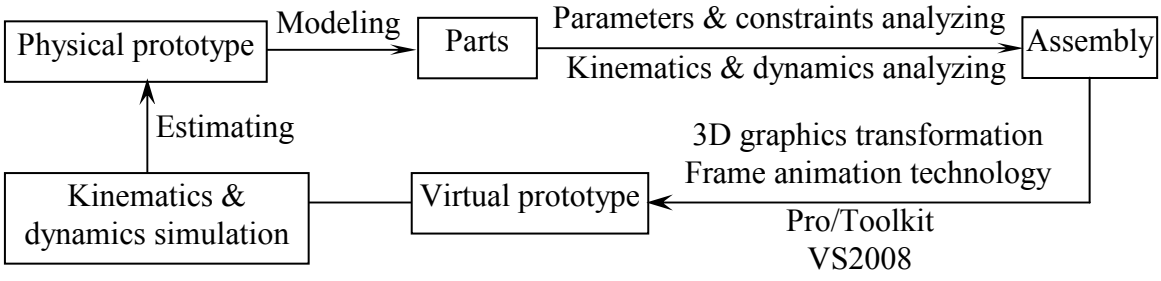


Fig.1 The establishing plan of virtual prototype system

The Structure and Motion Analysis of Grinding System

Wafer precision grinding machine is composed by grinding system, transmission system, cleaning system and electrical system. As a key component of the grinding machine, the grinding system is made up by indexing table, coarse and fine grinding spindle, as shown in Fig. 2.

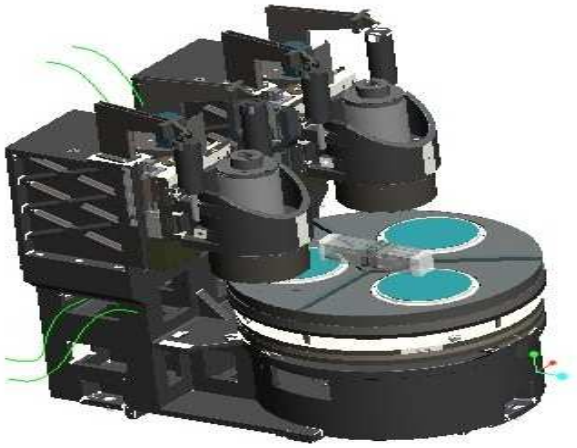


Fig. 2 The model of grinding system

As shown in Fig. 2, the indexing table is controlled by a servo motor and can rotated around the central axis in order to transform the wafer among the position of rough grinding, precision grinding or preparation. The structure of the rough grinding spindle and precision grinding spindle are similar and complex. They can realize two kinds of motion: principal motion and feed motion, and the principal motion is realized by electrical spindle, the feed motion is realized by server motor, during the processing of wafer machining, the wafer is transferred from the initial station to the coarse grinding system, where 90% allowance of the wafer is removed; then the wafer is transferred from the coarse grinding system to the fine grinding system to finish the wafer grinding finally. Servo motor is the active part of feed motion, which drives the ball screw that convert rotation into translation in order to complete feed motion. Grinding spindle is the electrical spindle.

The constraint relations, freedom, speed and connectivity in grinding spindle are shown in Fig.3.

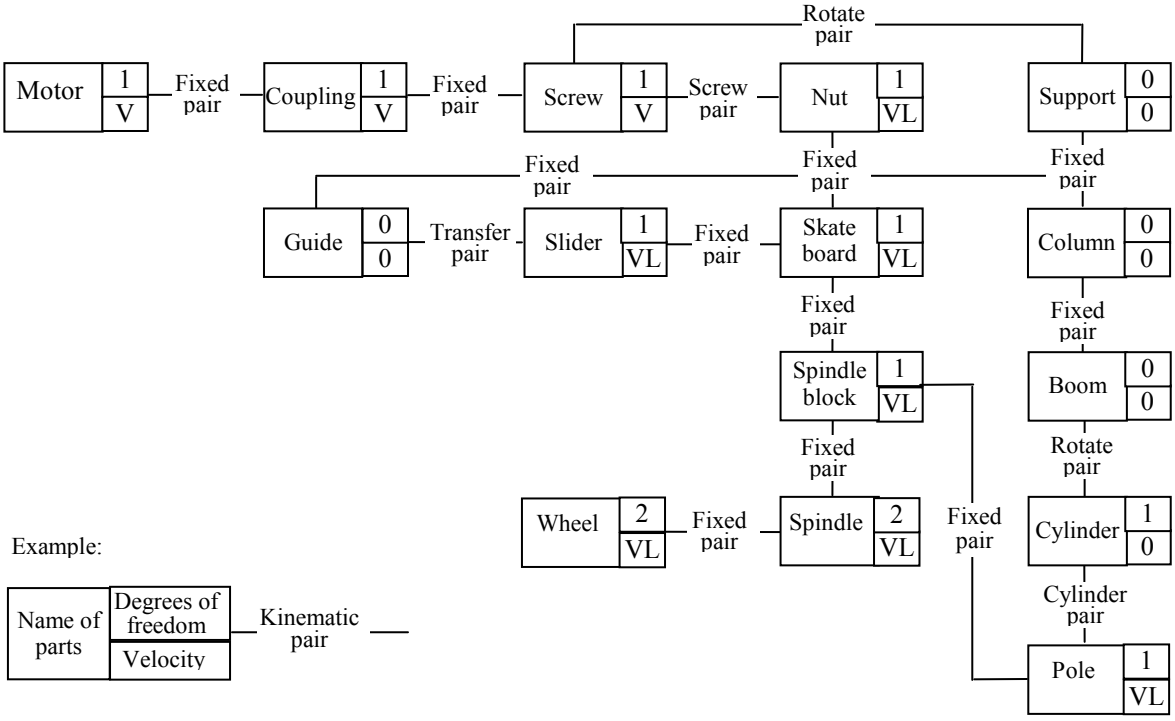


Fig. 3 Relationship among parts in grinding spindle

Realization principle of simulation

Building crucial prototype and dynamic simulation is realized by the combine of 3D graphics transforming [5] and frame animation technology [6]. The movement of parts is achieved by the location coordinates of each part multiplies with the corresponding transformation matrix. The non-continuous motion of the whole grinding system can be achieved by the 3D graphics transformation of each components, for a certain part, the transformation can be expressed as:

$$[x' \quad y' \quad z' \quad 1]=[x \quad y \quad z \quad 1]M \tag{1}$$

In which, M is a 4×4 transformation matrix, that is

$$M=\begin{bmatrix} A & B & C & P \\ D & E & F & Q \\ H & I & J & R \\ L & M & N & S \end{bmatrix} \tag{2}$$

This matrix can be decomposed into the upper left, lower left, upper right and lower right four parts, by adjustment of these four parts the 3D graphics transformations can be realized.

In order to realize the dynamic simulation of the virtual prototype continuously, the frame animation technology is used, which means drawing frame content in certain frame, according to the human eye's persistence of vision effect, the PAL standard used is 24 frames per second， in order to reduce the space occupied by the program 10 frames per second is carried which is still able to ensure the continuity of the animation. Certain animation is compiled with the increase of the number of frames and the key frames are defined in the movement of indexing table, and the movement of grinding spindle in order to achieve a coherent action.

Secondary Development Technology of Pro/E

In this paper, the Pro/Toolkit library is visited through VS 2008, which is named Pro/E secondary development [7, 8]. First, a series of Environment variable should be set, what's more, header files and libraries should be added in program so as to create main code, including the start Proe code ProEngineerStart, getting model code ProMdlDisplay, creating movement code ProAnimobjectCreate and so on. The entire wafer grinding machine uses top-down assembly approach, a general assembly composed by a number of levels, the level and the characteristics of ID should be found, After selecting the components by ID, 3D graphics transformation method is used, multiplying the matrix of the parts by the transformation matrix and make the location change with the change of frames, the specific movement of the parts can be achieved.

In order to get the continuous movement of the whole system, frame animation technology [6] should be taken to compile certain code. Some key codes are shown as follow:

Add header file code: include "ProAnimate.h"；

Movement sequence defination code: ProAnimObj anims[MAX_FRAMES_NUM]；

Movement frames defination code:static ProAnimFrame *frames；

Creating movement code: n_frames = 0，

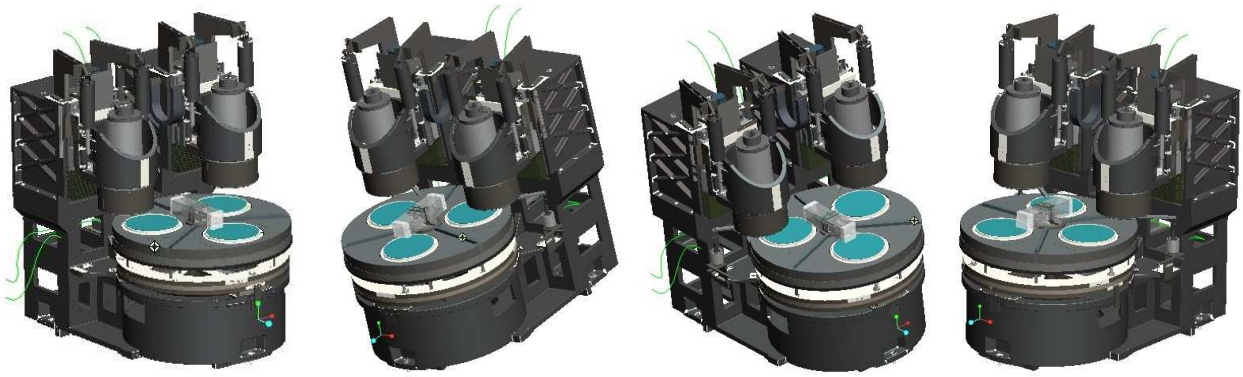
for(i=0; i<n_frames; i++)

{ProAnimframeCreate(m_frame_view, &(frames[i]));}

Establishment of Virtual Prototyping System of Grinding System

Based on 3D graphics transformations and frame animation technology, and using Pro/Engineer secondary developing technology, the virtual prototype of the grinding system for wafer precision grinding machine is developed finally, and the kinematics & dynamics simulation of the virtual

prototyping is realized, as shown in Fig. 4. Fig. 4 shows the four key step of the grinding system's movement, which are initial station, rough grinding, fine grinding and ending station in turn. By analyzing the kinematics & dynamics simulation of the virtual prototyping system of the grinding system, the defects of the designed can be fined, and consequently the optimization design of the grinding system can be conducted.



(a) Initial station (b) Rough grinding (c) Fine grinding (d) Ending station

Fig. 4 Virtual Prototyping System of Grinding System

Conclusion

In this paper, based on mechanical system machanics, by getting the relationship of the key parts in grinding system, analyzing the relationship between movement and time of each part, the virtual prototype of grinding system for wafer precision grinding machine is developed, the kinematics & dynamics simulation of grinding system is realized. Via simulation, the interference and design defects of the grinding system can be found. By this way, testing cost can be reduced and testing cycle can be shorten. What's more, for its convenience, flexibility and intuitivity, the virtual prototype can be used in virtual experiment for grinding grinding system, consequently lay a solid foundation for the optimization design of the grinding system and even the wafer precision grinding machine.

Acknowledgements

The research was supported by Natural Science Foundation of Liaoning Province (No. 20081082 and No.201102021).

References

[1] G. L. Xiong, B. H. Li and X. D. Chai: Journal of System Simulation, Vol.13 (2001), p. 114.

[2] X. Zhang and E. R. Mao: Journal Of China Agricultural University, Vol. 4 (1999), p. 94.

[3] T. Li, B. H. Li and X. D. Chai et. al: Computer Integrated Manufacturing Systems, Vol. 17 (2011), p. 1178.

[4] J. Y. Zhu: *Design of Feed System in Ultra-precision Grinding Machine based on Virtual Prototype Technology* (Master's degree thesis of Dalian University of Technology 2008).

[5] M. Chang: *Computer Graphics* (Huazhong Technology University Press, Wuhan China 2009).

[6] G. H. Chen: Computer Simulation, Vol. 24 (2007), p. 221.

[7] Parametric Technology Corporation: *Pro/Toolkit User's Guide* (PTC, USA 2001).

[8] J. C. Zhang: *A Practical Course-book* of *Pro/Engineer Secondary Development* (Peking University Press, Beijing China 2003).

© (2012) Trans Tech Publications, Switzerland
doi:10.4028/www.scientific.net/AMM.164.334

Faults Monitoring and Diagnosis of Air Compressor from Vibration Mechanics

Yujing Jia[1, a], Guangzhen Cheng[1, b] and Yanyan Han[1, c]

[1]Huzhou Teachers College, Huzhou, Zhejiang Province 313000, P.R. China

[a]jyjng@126.com, [b]chgzh169@126.com, [c]453363995@qq.com

Keywords: Vibration mechanics, Air compressor, Vibration analysis, State monitoring, Faults diagnosis

Abstract. This paper introduces vibration analysis, state monitoring, faults diagnosis, system compose, test scheme and measure point disposal of air compressor. This uses CDMS to do. Analyzing the mechanics vibration parameters in time domain and frequency chart in frequency domain. According to the results of information dispose finding out faults reasons and position, educing diagnosis conclusion, the motor-side bearings 3628 has more serious pitting and peeling off, recommended replacement，the horizontal chute and vertical chute of the air compressor has wear, exists insufficient lubrication. Lubrication management and monitoring should be strengthened.

Introduction

As progressive of the microelectronic technology, sensor technology and signal analysis technology, computer technology has been used widely in signal analysis, dynamic testing; equipments state monitoring and faults diagnosis technology has been developed rapidly, which becoming necessary technical measures to improve modern management and enhance safety of equipments. We carry out the research and application of the mechanical and electrical equipment state monitoring and faults diagnosis technology, carry on the detection and diagnosis of the mine hoist, air compressor, fan, water pump, coal mining, boring machines and other equipments. Here, use CDMS fault diagnosis system to detect the vibration of air compressor, determine the status of compressor. Analysis as follow[1].

Testing Program to Determine

The State Parameters of the Air Compressor. The measured air compressor is L-type crank-connecting rod air compressor, the crank-connecting rod organizations adopt the crosshead. One rotate shaft driven two crank-connecting rods, which drive the piston of high and low pressure cylinders respectively. Thus completing the suction, compressed air and pressurized. Maximum output pressure is 0.8Mpa of the air compressor. Use synchronous motor drive, the motor synchronous rotate speed is 450rpm. The motion of air compressor is reciprocating, vibration causes are quite more. Now the main oscillators are as follows.

Forced vibration. Rotation frequency of the compressor rotor. The motor rotor and the compressor rotor are connected together， constitute a compressor rotor system. If there is misalignment or imbalance in the rotor，that will generate additional dynamic reaction force, the characteristic frequency is shown in Eq.1.

$$f_r = 450/60 = 7.5Hz \tag{1}$$

The reciprocating movement frequency of the piston and the slide block. Each revolution of the rotor, the piston and the slide block pass through the upper and lower dead point one time, the characteristic frequency is shown in Eq.2[2].

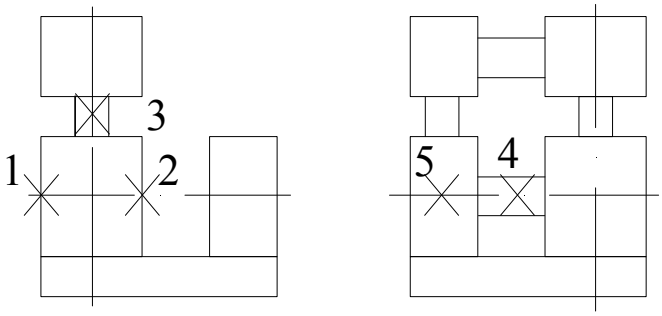
$$f_h = 2f_r = 15Hz \tag{2}$$

The passing frequency of the rolling bearing. The support at both ends of the compressor Crankshaft uses double row radial spherical roller bearings. The roller bearings model at motor side is 3630; the roller bearings model at oiler side is 3628. Related pass through frequency can calculate as follow[3].

3630 bearing inner ring pass through frequency: 46Hz
The outer ring pass through frequency: 67Hz
Balls pass through frequency: 19Hz
3628 bearing inner ring pass through frequency: 42Hz
The outer ring pass through frequency: 62Hz
Balls pass through frequency: 18Hz

Magnetic vibrations. The vibration characteristic frequency that the uneven motor magnetic gap caused is 7.5Hz. The vibration characteristic frequency that the electromagnetic frequency and high harmonic Caused is 50,100,150Hz, etc.

Sensor selection and arrangement of measuring points. According to the air compressor characteristic frequency, select the speed sensor to ensure that the test has high sensitivity. Because the compressor is rotating reciprocating machinery, detection radial, axial vibration of bearing and cylinder is more convenient and reliable. Location of measuring point distribution is shown in Fig. 1. measuring point 1and point 2 is at bearing, measuring point 3 is at vertical chute, measuring point 4 is at horizontal chute, measuring point 5 is at the high and low pressure cylinder. Each measurement point is furnished with two sensors and measured horizontal and vertical vibration velocity respectively[4].



1 Left bearing measure point, 2 Right bearing measure point, 3 Vertical chute measure point, 4 Horizontal chute measure point, 5 High and low pressure cylinders measure point

Fig. 1 Measure point layout

Measuring Point Vibration of Time-domain and Frequency-domain Analysis

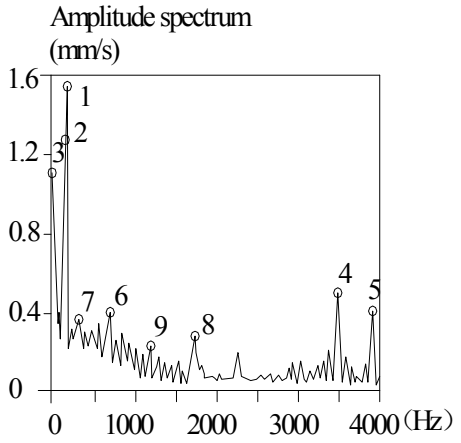
Time-domain analysis of vibration velocity. Through the vibration testing of each measuring point with CDMS system, the vibration velocity obtained is shown in Table 1.

Table 1 Vibration velocity virtual value(mm/s)

Measure Point	Horizontal Vibration Velocity	Vertical Vibration Velocity
1	2.40	2.92
2	5.07	3.69
3	4.08	3.69
4	0.43	0.43
5	4.88	4.02

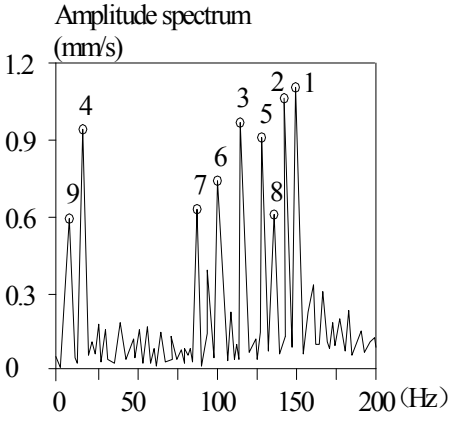
According to ISO2372 and ISO3954, there is higher vibration intensity at measuring point 2 and measuring point 5, which is in an unsatisfied condition. The vibration of the remaining points is in the allowable range, Hence, Focus on monitoring the vibration at measuring point 2 and measuring point 5, further carry through spectral analysis, identify the cause of the vibration.

Spectral analysis. In order to more clearly reveal the signal at each measuring point composition and properties. Understand the frequency composition and corresponding amplitude of the signal, use CDMS to do frequency domain analysis. Due to space limitations, here only analysis measuring point 2 and measuring point 5,because the measuring point 2 and measuring point 5 has larger vibration intensity. The spectrums of measuring point 2 and measuring point 5 are shown in Fig. 2, Fig. 3, Fig. 4 and Fig. 5.



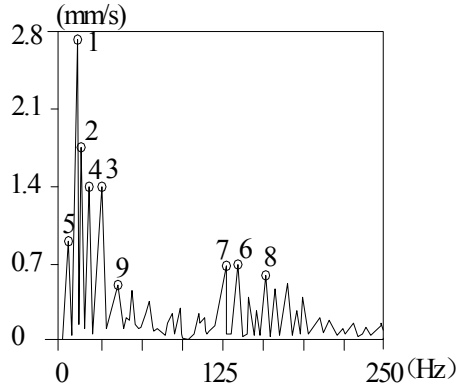
No.	Frequency	Amplitude
1	146.48	1.52
2	117.19	1.12
3	9.97	1.07
4	3359.38	0.53
5	3867.19	0.41
6	585.94	0.38
7	419.92	0.38
8	1751.25	0.36
9	1260.76	0.34

Fig. 2 Measuring point 2 horizontal direction spectrum



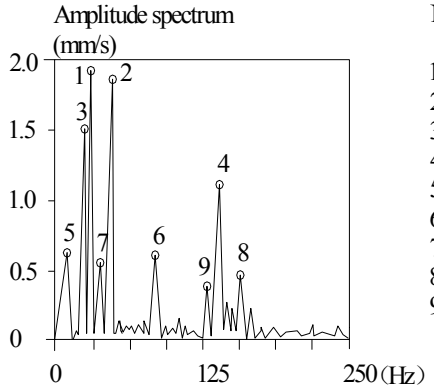
No.	Frequency	Amplitude
1	150.39	1.11
2	143.55	1.06
3	114.26	1.00
4	14.65	0.98
5	128.91	0.96
6	100.59	0.71
7	85.94	0.67
8	136.72	0.62
9	6.84	0.58

Fig. 3 Measure point 2 vertical direction spectrum



No.	Frequency	Amplitude
1	14.65	2.73
2	21.97	1.73
3	35.40	1.48
4	28.08	1.38
5	7.32	0.94
6	135.50	0.68
7	128.17	0.67
8	157.47	0.58
9	42.72	0.52

Fig. 4 Measuring point 5 horizontal direction spectrum



No.	Frequency	Amplitude
1	28.08	1.95
2	42.72	1.89
3	21.97	1.54
4	135.50	1.14
5	7.32	0.64
6	85.45	0.62
7	35.40	0.56
8	157.47	0.37
9	128.17	0.36

Fig. 5 Measure point 5 vertical direction spectrum

The measuring point 2 is located close to the motor side; uses double row radial spherical roller bearings. The model is 3630, From radial, axial vibration spectrums of the measuring point 2 can be seen, the main vibration frequency is 146.68, 117.19, 9.77, 150.39, 143.55, 114.26 Hz. These frequencies is close to the bearings pass through frequency or the pass through frequency multiplier, These instructions the bearings at measuring point 2 have a greater wear.

The measuring point 5 is located in the high and low pressure cylinder of the air compressor, the main vibration frequencies are 14.65, 21.97, 35.40, 28.08, 42.72, 21.97 and 135.50 Hz, we can see that these frequency components is equal to reciprocating frequency or Multiple of reciprocating frequency. It shows that two cylinders there are center offset, and imbalanced appearances in different degrees, and the two cylinders have 135.50HZ frequency vibration. it explanations that two cylinders are subject to the gas vibration. The difference is that high-pressure cylinder vibration amplitudes are larger in 135.50Hz, that illustrates the excitation caused by high-pressure cylinder is stronger, the gas excitation is often caused by the intake and exhaust valves, These can be drawn that valves loose or gaskets worn exists in the high-pressure cylinder.

In time-domain vibration intensity analyzes , the measuring point 2 and measuring point 5 has bigger vibration amplitude. that is directly related to the above factors.

Conclusion

Based on the above analysis can draw the following conclusions:

(1) The motor-side bearings 3628 has more serious pitting and peeling off, recommended replacement.

(2) The horizontal chute and vertical chute of the air compressor has wear, exists insufficient lubrication. Lubrication management and monitoring should be strengthened.

(3) The intake and exhaust valves of the high and low pressure cylinder have local loose. When examine and repair should check tighten.

(4) Recommend analysis lubricant quality, detect the moisture content, and pay attention to cooling.

(5) Recommended use the iron spectral analysis, to examine wear debris composition in lubricating oil, determines the wear parts.

References

[1] J.Y. Lei: *Machinery faults diagnosis based* (Xi'an Jiaotong University Press, China 1989)

[2] J.S. Mitchell: *Machine faults analysis and detection* (Mechanical Industry Press, China 1990)

[3] F.T. Lifu: *The method in equipment diagnostic on-site* (Mechanical Industry Press, China 1985).

[4] G.Z. Cheng, J.P. Tao and Y.Y. Wu: Coal Mine Automation Vols. 23 (2000) NO.2, pp.26-28.

[5]Y.J. Jia: Coal Mine Machinery Vols. 22 (2001) NO.11, pp.71-73.

© (2012) Trans Tech Publications, Switzerland
doi:10.4028/www.scientific.net/AMM.164.338

Coupling Analysis of Vibration and Fatigue Crack Propagation for a Breathing Cracked Beam

Wei Cui[1, a], Jianjun Wang[1,b]

[1] School of Jet Propulsion, Beihang University,
Xueyuan Street 37, Haidian District, 100191 Beijing, China

[a]cuiwei.buaa@gmail.com, [b]wangjianjun@buaa.edu.cn

Keywords: Coupling analysis, vibration, crack propagation, resonant response, breathing crack

Abstract. The coupling effect of vibration and fatigue crack propagation for a cracked cantilever beam is studied in this paper. The dynamic characteristics and fracture mechanics parameters are calculated by using 2D 8-nodes elements in FEM code. The nonlinear dynamic behavior of breathing crack is described by a frictionless contact FEM model. Linear fracture mechanics theory is used to calculate the stress intensity factor. At resonant state, coupling effect is significant between vibration and crack propagation. The response of beam under harmonic excitation is extremely sensitive to the structure natural frequency decrease which is caused by crack length growth. An approach of sweeping crack length analysis is proposed in resonant response evaluation of cracked beam. Two numerical tests are calculated to investigate coupling effects at resonant state: crack arrest problem and crack unstable propagation problem.

Introduction

The initiation and propagation of fatigue cracks are the main factors which can lead to engineering structure failures. Beam is a typical mechanics structure, and many engineering structures, such as gas turbine blades, rotor shafts, and helicopter rotor blades can be simplified as beams in some specific situations. Many studies have been carried out on the dynamic response of cracked beams in analytical [1] [2], numerical [3] [4], [5], [6] and experimental approaches [1][2].

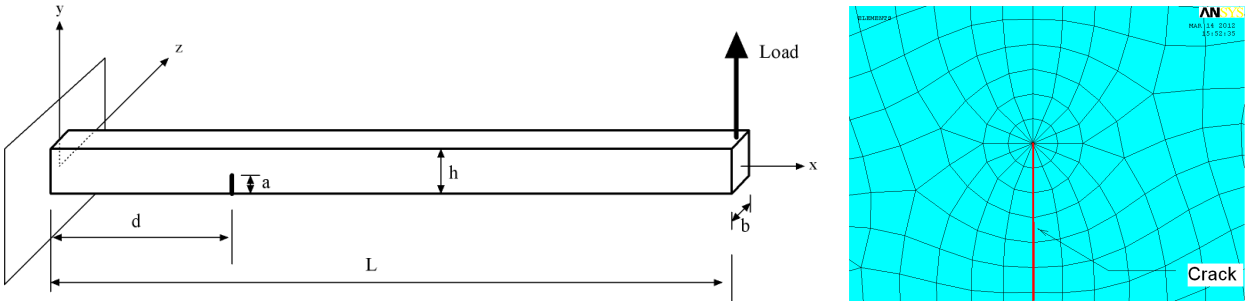
There are generally two kinds of crack stiffness models in cracked beam vibration researches: open crack model and breathing crack model. In the early studies, some researchers [1] assumed that the crack is always open under vibration load and the system is a linear vibration system. The open crack model ignores the stiffness increase of when crack is closed, which could not represent real characters of cracked structures in engineering. Later more researchers [2-8] used breathing crack models to investigate cracked beam vibration problems. Chondros and Dimarogonas [2] used a bilinear breathing crack model to investigate vibration of cracked beam in both analytical and experimental approaches. Andreaus [6] and Hu [7] investigated dynamic response of cracked beam by using contact finite element method. Contact FEM crack model shows more details of stiffness changes during crack open and closed, which is more similar to practical situation than bilinear breathing crack model.

Under vibration excitation, crack propagation will change the dynamic characteristic of cracked beam, and the behavior of fatigue crack propagating will change as well, which leads to “coupling phenomenon”. The coupling effects of vibration and fatigue is studied by some researchers [4][5][8] in recent years. Zhong [4] and Chen [5] studied the coupling effects of vibration and fatigue crack growth for connecting rod structures, and calculate the lifetime of the rod structure. Liu et al. [8] used a single freedom lumped parameter model to investigate crack growth life of a cracked beam under vibration excitation by considering coupling effects. All the above works considering the coupling effects are at non-resonant state and focus on lifetime calculation. In aircraft engine blades fatigue studies, resonant states are the most dangerous conditions, which usually lead to fatal failure in very short time. It is necessary to investigate the resonant response of cracked beam by considering coupling effects.

In this paper, a single cracked cantilever beam has been studied. The breathing crack model is described in contact FEM approach. The main goal is to investigate dynamic response and the coupling effects of vibration and fatigue crack propagation at resonant state.

Vibration analysis

System model. This problem represents a cantilever beam of length ***L***= 300 mm which has a single-side edge fatigue crack of depth ***a***. The crack is located at the bottom edge of the beam at a distance of ***d*** = 81mm, as Fig. 1 (a) shows. The beam has a rectangular uniform cross-section of $20 \times 20\ mm^2$. The material is structural steel 12CrNi3A which has Young's modulus 206.6GPa, Poisson ratio 0.3, and mass density $7850 kg/m^3$.



(a). (b).

Fig. 1 Cracked cantilever beam: (a) cracked beam model; (b) contact FEM crack model

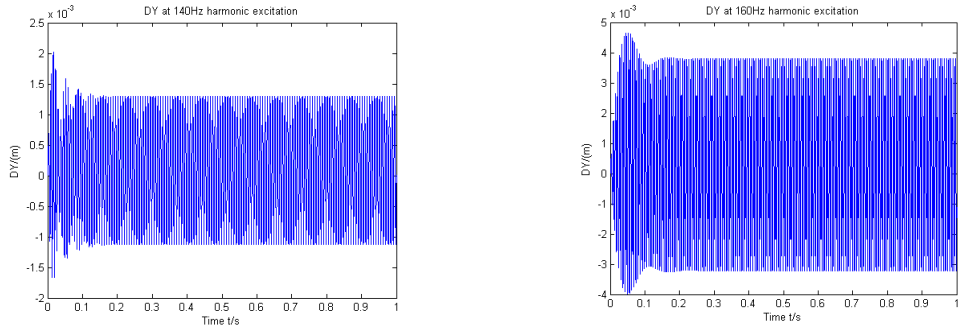
Contact crack FEM model. The breathing crack is described as a 2-D frictionless contact model. Finite element model is established in commercial FEM code ANSYS 12.0, as Fig.1 (b) showing.

Harmonically forced response. The forced response of the cracked beam is investigated by applying harmonic excitation load at the end of the beam, as Fig. 1(a) shows. In order to predict the first resonant frequency ω_{br} , a bilinear single freedom model is used to calculate the breathing cracked beam's resonant frequency. The bilinear system frequency ω_{br} is studied in literature [9] and can be calculated by the following equation,

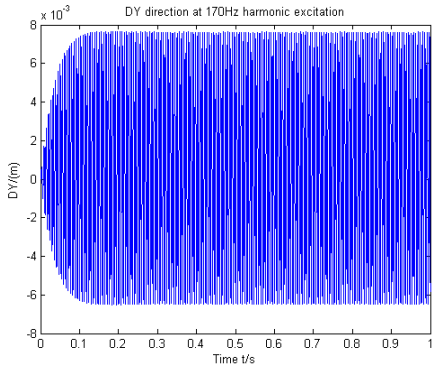
$$\omega_{br} = 2\omega_1\omega_2 /(\omega_1 + \omega_2) \tag{1}$$

ω_1 =156.86Hz represents the natural frequency of the open crack beam, ω_2 =183.75Hz represents the natural frequency of the closed crack beam. The bilinear cracked beam's first resonant frequency ω_{br} is 169.24Hz.

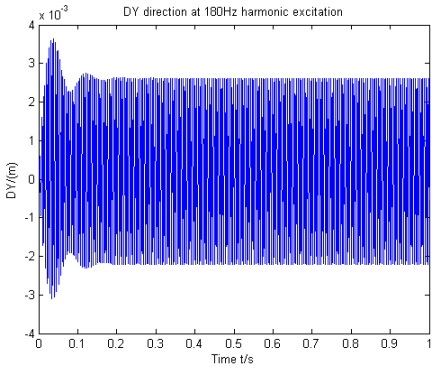
The forced response is calculated in ANSYS by using Newmark's method with Rayleigh damping α =50, β =0. The Y direction displacement of the load point (See Fig.1 (a)) is denoted as DY. DY is chosen as a representative parameter to measure the resonance degree in this paper. The harmonic excitation has a same magnitude of 100N and frequencies 100Hz, 140Hz, 160Hz, 170Hz, 180Hz, 200Hz and 240Hz. Some of the results are plotted, as can be seen in Fig. 2.



(a) 140Hz (b) 160Hz



(c) 170Hz



(d) 180Hz

Fig. 2 Y direction displacement of load point: (a) 140Hz, (b) 160Hz, (c) 170Hz, (d) 180Hz

Fig. 2 (c) shows that the resonant frequency is near 170Hz. Responses under more frequencies are calculated later. These steady state response results are plotted into two frequency response curves in Fig. 3. The blue color curve represents the maximum positive value of DY, which represents crack open status; the red color curve represents the absolute value of minimum DY, which represents crack close status. At 168 Hz harmonic excitation, both positive and negative displacements achieve to the maximum absolute magnitudes. We can conclude that the first resonant frequency of this cracked beam is about 168Hz at α=50, β=0 Rayleigh damping condition. The resonant frequency result (168Hz) of contact crack model is slight less than the bilinear model (169.24Hz).

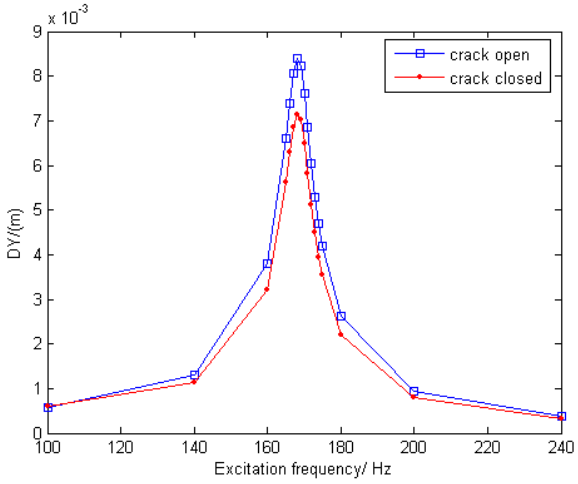


Fig. 3. Frequency response curves of DY: blue line represents the maximum response when crack opening (steady state); red line represents the absolute value of minimum response (steady state).

Fatigue crack propagation

The quarter point displacement method. In this study, the stress intensity factor is calculate by using quarter point displacement method in FEM. Henshell and Shaw [10] and Barsoum [11] proved that the theoretical $1/\sqrt{r}$ stress singularity at the corner of a 8-node plane element can be exactly achieved by moving the mid-side nodes of the elements to 1/4 point positions, as shown in Fig. 3. The stress intensity factor can be estimated from the crack-surface displacements at these 1/4 points, i.e.

$$K = \frac{E}{4(1-\nu^2)}\sqrt{\frac{2\pi}{r_{(1/4)}}}u_{z(1/4)} \tag{2}$$

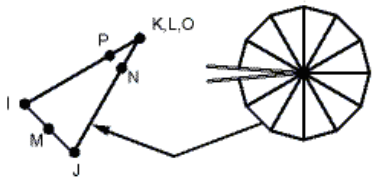


Fig. 4. Crack tip elements in quarter point displacement method

For example, a constant force of 100N is applied at the end of cracked beam in a static FEM analysis. Using above quarter point displacement method to calculate SIF in crack tip, we obtain: K_I=4.365$MPa\cdot\sqrt{m}$, K_{II}=0.06035$MPa\cdot\sqrt{m}$. K_{II} is insignificant compare to K_I . Based on linear fracture mechanics theory, the direction of crack propagation will be grows strait as a " quasi-type I " crack.

Fatigue crack propagation model. The cantilever beam material is low carbon alloy steel 12CrNi3A, the fracture mechanics parameters is: fracture threshold value ΔK_{th}=9.0 $MPa\cdot\sqrt{m}$, fracture toughness K_{IC}=135 $MPa\cdot\sqrt{m}$, and experimental frequency range is 150~180Hz. The full range crack propagation equation based on experimental data [12] is represented by:

$$\frac{da}{dN}=1.017\times10^{-6}\left[\frac{\Delta K^2-\Delta K_{th}^2}{(1-R)^2K_{Ic}^2-\Delta K^2}\right]^{1.26}+2.5\times10^{-10}(m/cycle) \tag{3}$$

Coupling analysis

At resonant state, dynamic response is sensitive to structure stiffness decrease due to crack propagating. Ideal approach for a coupling analysis is to calculate fracture mechanics parameter in every single load cycle and update calculating model every time when crack grows. This huge task of model updating is unacceptable in current hardware condition. This paper develops a coupling analysis approach using "sweep crack length" approach. The concept of sweeping crack lengths is from sweeping frequencies. Cracked beam model of different crack lengths are calculated to obtain the relationship between SIF and crack length at resonant state. Following sections will introduce this method by two numerical examples in the following sections.

Numerical example 1: crack arrest problem. This numerical example is to simulate the crack arrest problem at resonant state. The harmonic excitation has a force magnitude of 15N and frequency of 168Hz which will cause resonance. The stress intensity factors are calculated in different crack length from 10mm to 12mm, as shown in Fig. . The author named this analysis of resonant response "sweep crack length".

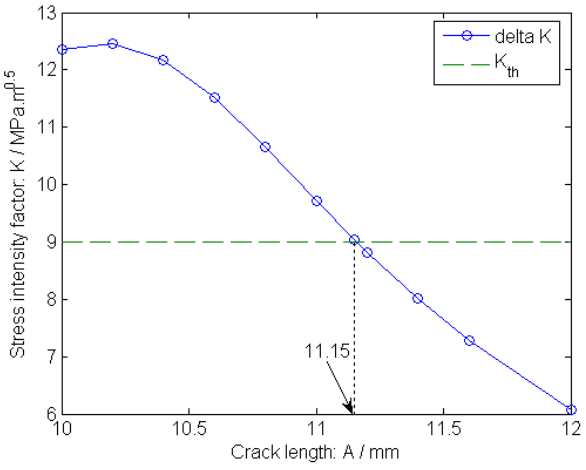


Fig. 5. SIF - crack length curve of crack arrest problem at resonant state: blue curve is ΔK , green line is ΔK_{th} . (15N, 168Hz harmonic excitation)

The first resonant frequency decreases during crack propagating. As Fig. 5 shows, at the beginning stage of the curve, SIF increases when crack grows from 10mm to 10.2mm model, which means that the exact resonance is slight lower than excitation frequency (168Hz). Then SIF monotonically declines as crack grows from 10.2mm to 12mm crack model, which means that cracked beam is leaving the resonant state. When the crack grows to 11.2mm, SIF achieve to the fracture threshold value $\Delta K_{th}=9.0MPa\cdot\sqrt{m}$, which means crack stops propagation. BY using full range equation in 3.2 section, updating crack model every increment, the number of cycles can be calculated as:

$$L_{total}=\sum_{i=1}^{n} L_i=\sum_{i=1}^{n}\frac{\Delta a_i}{1.017\times10^{-6}\left[\frac{\Delta K_i^2-\Delta K_{th}^2}{(1-R)^2K_{Ic}^2-\Delta K_i^2}\right]^{1.26}+2.5\times10^{-10}} \tag{4}$$

L_{total} is total cycles of crack propagation, Δa_i is the increment of crack length, ΔK_i is mean SIF amplitude in the *i*th calculation step. In this example, 0.2mm increment is used and total cycles L_{total} from 10.2mm to 11.15mm is calculated as 1.900143×10^6 cycles. Crack will stop growing after 1.900143×10^6 vibration cycles.

Numerical example 2: unstable crack propagation. This numerical example is to simulate the unstable crack propagation problem at resonant state. The harmonic excitation has a force magnitude of 160N and frequency of 166 Hz which is very close to resonant frequency. The stress intensity factors are calculated in different crack length from 10mm to 10.6mm, as shown in Fig. 6.

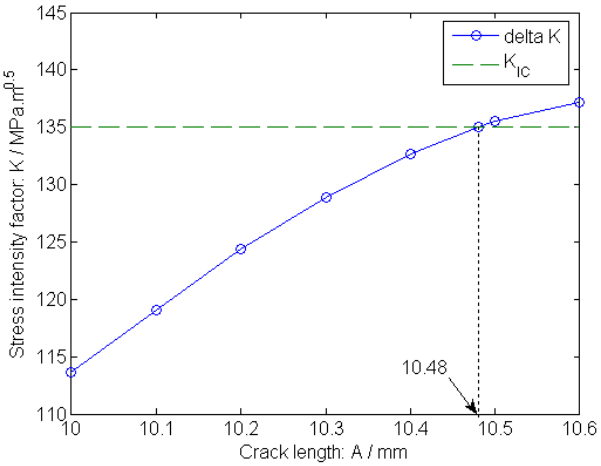


Fig. 6. SIF – crack length curve of unstable crack propagation at resonant state: blue curve is ΔK, green line is K_{IC}. (160N, 166Hz harmonic excitation)

As Fig.6 shows, SIF monotonically increases when crack grows from 10mm to 10.6mm model, which means that the exact resonance is higher than excitation frequency (166Hz). Cracked beam is approaching into resonant state in this example. When the crack grows to 10.48mm, SIF achieve to the fracture toughness value $K_{IC}=135.0MPa\cdot\sqrt{m}$, which means crack is in unstable propagation state. The structure will be failure. By using equation (4), updating crack model every 0.1mm of increment, lifetime before unstable propagation can be calculated as 53 cycles, which means the structure will achieve unstable state after 53 cycles.

Conclusions

The coupling analysis of vibration and fatigue crack propagation for a breathing cracked cantilever beam has been studied at resonant state. The sweep crack length approach is proposed in cracked structure vibration and crack propagation analysis. By using sweep crack length approach, crack arrest and crack unstable propagation problems are studied. The results can be concluded in the following:

1. The bending stiffness of breathing cracked beam declines while crack propagating. At resonant state, vibration responses are sensitive to stiffness changes, and coupling effect should be considered.

2. An approach of sweeping crack length analysis is proposed in resonant response evaluation of cracked beam. By calculating SIF responses of different crack lengths at specific excitation frequency, the sweeping crack length analysis result intuitively shows boundaries of crack arrest and unstable in resonant response evaluation.

3. At resonant/ quasi-resonant state, crack propagation will significantly change the response of cracked beam. When periodic excitation frequency is slightly lower than the resonance frequency of cracked structure, degree of resonance will decrease during crack length grows, and at specific cases crack could stop propagation. This is a relative safe situation of resonant state. When periodic excitation frequency is slightly higher than resonance frequency of cracked structure, degree of resonance will increase during crack length grows, ant at specific cases crack will unstable propagate. This condition is dangerous and should be avoided in structural designing.

Acknowledgements

This research is supported by National Basic Research Program of China.

References

[1] Chondros T. G., Dimarogonas A. D., Yao J.: A continuous cracked beam vibration theory [J]. Journal of Sound and Vibration, 215(1): 17-24 (1998)

[2] Chondros T. G., Dimarogonas A. D., Yao J.: Vibration of a beam with a breathing crack [J]. Journal of Sound and Vibration, 239(1): 57-67 (2001)

[3] Cheng S M, Wu X J, Wallace W: Vibrational response of a beam with a breathing crack [J] . Journal of Sound and Vibration, 225(1): 201-208 (1999)

[4] Zhong Z. Y.: Coupling Analysis of vibration and fatigue crack growth of a four-bar mechanism. Chung Yuan Christian University, Master thesis. (2002)

[5] Chen S. Z.: Coupling Analysis of vibration and fatigue crack growth for a crank-slider Mechanism. Chung Yuan Christian University, Master thesis. (2003)

[6] Andreaus U, Casini P, Vestroni F: Non-linear dynamics of a cracked cantilever beam under harmonic excitation. International Journal of Non-Linear Mechanics, Vol. 42(3): 566-575 (2007)

[7] Hu J S, Feng X, Zhou J: Study on the nonlinear dynamic response of a beam with a breathing crack. Journal of Vibration and Shock (in Chinese), 28 (1): 76-80, 87 (2009)

[8] Liu W G, Chen G P: Coupling analysis of vibration fatigue crack growth for breathing cracked beam, China Mechanical Engineering (in Chinese), 21(23): 2798-2802 (2010)

[9] Chu Y C, Shen M H H. Analysis of forced bilinear oscillators and the application to cracked beam dynamics [J]. AIAA Journal. 1992, Vol. 30 (10): 2512-2519

[10] Henshell RD, Shaw KG. Crack tip finite elements are unnecessary. International Journal for Numerical Methods in Engineering, Vol. 9: 495-507 (1975)

[11] Barsoum RS. On the use of isoparametric finite elements in linear fracture mechanics. International Journal for Numerical Methods in Engineering, Vol. 10: 25-37. (1976)

[12] Ma D L, Common ferrous metal materials fracture mechanics parameters handbook [M]. Weapon Industry Press. (1994). (in Chinese)

© (2012) Trans Tech Publications, Switzerland
doi:10.4028/www.scientific.net/AMM.164.344

Rotating Clamping Device of the Hydraulic Prop Disassemble Machine Based on Hydromechanics

Yujing Jia[1, a], Dayu Zhang[2, b], Guangzhen Cheng[1, c] and Yingjun Dai[1, d]

[1]Huzhou Teachers College, Huzhou, Zhejiang Province 313000, P.R. China

[2]Heilongjiang Bayi Agricultural University, Daqing, Heilongjiang Province 163319, P.R. China

[a]jyjng@126.com, [b]zdy214@163.com, [c]chgzh169@126.com, [d]616249581@qq.com

Keywords: Rotating clamp, Disassemble machine, Maintenance, Hydraulic prop,Hydromechanics

Abstract. This article introduces a rotating clamping device, using with the disassemblage machine of monomer hydraulic prop. It was used for clamping hydraulic prop, which was mainly comprised by the coupling mechanism, clamping mechanism and compressing mechanism. The coupling mechanism sleeve was bolted to the spindle. Clamping mechanism located at the end of sleeve, working with the spindle rotation. Compressing mechanism hang around the sleeve, not working with the spindle rotation. Compressing mechanism passed the clamping force through the thrust bearing, clamping the hydraulic prop. It was easy to operate. Clamping force is decentralized, the stress in cylinder was even, so the cylinders seldom distort, which reduced the impact, extending the life of the equipment.

Introduction

Hydraulic prop is an important supporter of mining enterprise, which is used wide. Maintenance is onerous, especially of demolition. Hydraulic prop disassemble machine is special equipment, which has the advantage of efficiency, less labor force and high quality of maintenance. When dealing to the rusting prop, clamping force is highly required. There are two existing ways. One is by the mechanical chuck, which is time-consuming and often needs the manual processing, even makes the cylinder scrap. The other is eccentric clamping. Although easy to operate, but the motor must reverses when releases, which cause a waste of time and the impact to the equipments. The clamping parts linear contact with the fuel tank, which is force-concentration, increased the friction of eccentric clamping and deformation of fuel tank. To restore the cylinder geometry and to avoid the scrapping of cylinder, we design the following hydraulic clamping device.

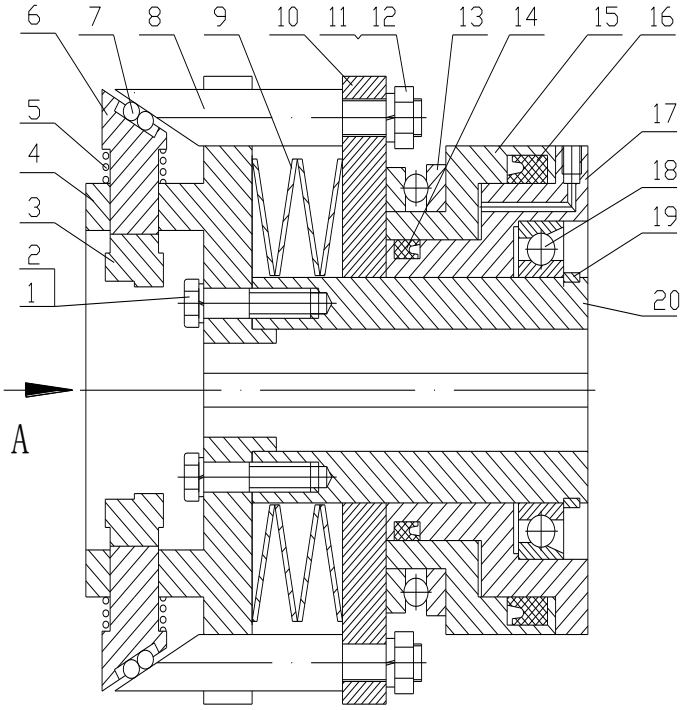
Structure Composition

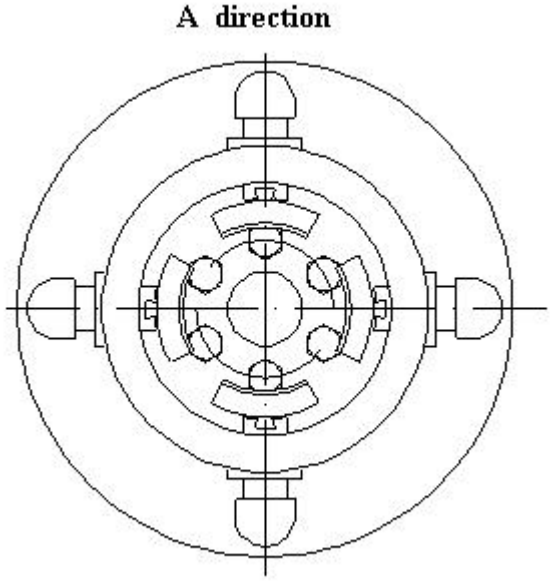
The structure of rotating clamping device is shown in Fig 1, composed of the clamping block, front panel, return spring, radial connecting rod, disc-type springs, push plate, thrust ball bearing, L-shape cylinder tube L-shape piston, angular contact ball bearings and so on. Hydraulic clamping device directly links to the output shaft of the main gear of the prop demolition, used to clamp the base of hydraulic prop or reduce the velocity of electric motor through V-belt, driving the main speed reducer.

Hydraulic clamping device includes coupling mechanism, clamping mechanism and compressing mechanism. The sleeve 20 and the output shaft send the torque by the parallel key. The front plate 4 is fixed on the sleeve 20 through bolt 1and small washer 2. Clamping mechanism is located at the end of sleeve 20, both rotating with the spindle. Compressing mechanism hangs around the sleeve 20, not rotating with the spindle. It passes on the clamping force to the clamping mechanism through the thrust bearing 13, clamping the monomer hydraulic prop.

Compressing mechanism consists of the L-shaped cylinder and its control devices. Control devices control the L-shaped cylinder, then control the clamping mechanism to clamp or release hydraulic prop. L-shaped cylinder is composed of L-type cylinder tube 15, L-shape piston 17, seal

ring 14 and seal ring 16. L-shape cylinder tube 15 included the size of two ladder-shaped bore. L-shape piston 17 included the size of two step-shaped shaft. Seal ring 14 located at the left Cylindrical of the L-shape piston 17. Seal ring 16 located at the right hole of the L-shape cylinder tube 15. L-shape cylinder tube 15 connects to the thrust bearing 13, transmit the clamping force to clamp hydraulic prop. L-shape piston 17 Installed in the sleeve 20. Angular contact ball bearing 18 Located between the sleeve 20 and L-shape piston 17. Angular contact ball bearing 18 positioned on the sleeve 20 through the axial thrust ring 19.





1 bolt, 2 washers, 3 clamping block, 4 front plate, 5. Reset spring, 6 radial connecting rod, 7 steel ball, 8 axial connecting rod, 9 disc- shape spring, 10 push plate, 11 nut, 12 washer, 13 thrust ball bearing, 14. seal ring, 15 L-shape cylinder tube, 16 seal ring, 17. L-shape piston, 18 angular contact ball bearing, 19 thrust ring, 20 Axle sleeve.

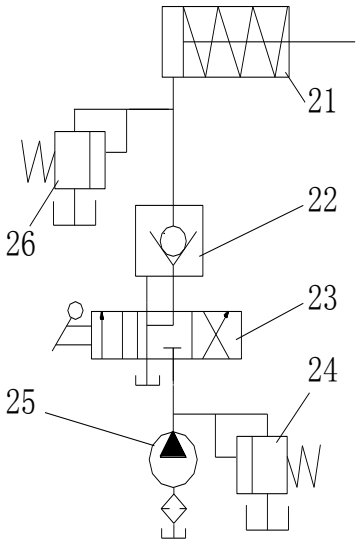
Fig. 1 The structure of rotating clamping device

Clamping mechanism include the front plate, the radial clamping mechanism, the axial clamping mechanism. The front plate 4 fixed to sleeve 20. There was a group of four axial holes at the front plate, used to assemble axial clamping mechanism. There was a group of four radial holes at the front plate, used to assemble radial clamping mechanism. The front end of the axial clamping mechanism and the radial clamping mechanism are equipped with s, compress mechanism transmit clamping force to the front of the radial clamping mechanism with ramp. Clamped hydraulic prop, Installs the steel ball 7 between the two ramps, instead of sliding friction to rolling friction, flexible movement, reducing the friction loss.

Radial clamping mechanism includes a group of clamping block 3 and the radial connecting rod 6, the end of the radial connecting rod 6 is the ramp, the other end of the radial connecting rod 6 connect the clamping block 3. The radial clamping mechanism also includes the spring 5 that reset the radial connecting rod 6. Axial clamping mechanism includes a set of axial connecting rod 8, push plate 10. The Push plate 10 is located behind the front plate 4, empty set in the sleeve 20. The axial connecting rod 8 located through a group of four axial holes in the front plate 4. Other end of the axial connecting rod 8 fixed on the plate 10 with nut 11 and washer 12. The axial clamping mechanism includes spring 9 that reset the axial connecting rod 8 through the plate 10.

Hydraulic System

The power source of the clamping mechanism is the hydraulic pump station that is supplied for the hydraulic prop disassemble machine. Hydraulic system is shown in Fig. 2. It is compose of cylinder, cone-way valve controlled by fluid, Manual direction valve , Overflow valve, hydraulic pump and Safety valve.



21 cylinder, 22 cone-way valve controlled by fluid, 23 Manual direction valve,
24 Overflow valve,25 hydraulic pump,26 Safety valve
Fig. 2 Hydraulic system diagram

When Clamping device work, manipulate the Manual direction valve 23 to the left position, the pressure oil from the hydraulic pump 25 through the valve 23, the cone-way valve controlled by fluid 22, go into the cylinders 21, L-shape piston 17 Move out, push the push plate 10, compress disc-shape spring 9, axial connecting rod 8 Move forward in the axial direction, promote the radial connecting rod 6 Move forward in the radial direction to clamp the workpiece. Manual direction valve 23 reset the middle position, the clamping mechanism maintain the clamped state.

When Need to release, manipulate the manual direction valve 23 to the right position, the pressure oil from the hydraulic pump 25 through the valve 23 go to the control port of the cone-way valve controlled by fluid 22, the cone-way valve 22 is opened, the compressed disc- shape spring 9 promote the push plate 10 Retracted loosen the clamping device, the clamping mechanism restore the original position. Overflow valve 24 is used to adjust the work pressure of the clamping device, Safety valve 26 is used to achieve Overload protection of the clamping device.

Work Process

When Clamping device work, manipulate the Manual direction valve 23 to the left position, the pressure oil from the hydraulic pump 25 through the valve 23 , the cone-way valve controlled by fluid 22,go into the cylinders 21, L-shape piston 17 Move out, push the push plate 10, compress disc- shape spring 9, axial connecting rod 8 Move to the left in the axial direction, through steel ball 7 promote the radial connecting rod 6 Move forward in the radial direction ,droved clamping block 3 to clamp the Hydraulic prop that would be disassembled. After clamping, the main motor starts, droved Axle sleeve 20, front plate 4, Reset spring 5, radial connecting rod 6, steel ball 7, axial connecting rod 8, disc- shape spring 9, push plate10 rotate. Other parts remain stationary.

When need to release, manipulate the manual direction valve 23 to the right position, the pressure oil from the hydraulic pump 25 through the valve 23 go to the control port of the cone-way valve controlled by fluid 22, the cone-way valve 22 is opened, the compressed disc- shape spring 9 promote the push plate 10 and the axial connecting rod 8 Retracted， the pressure oil Flow back into the pumping station from the cylinder 21. The Reset spring 5 promote the radial connecting rod 6 to restore the initial position. Release the hydraulic prop, the clamping mechanism restore.

Conclusion

In summary, the hydraulic clamping device used in hydraulic prop disassemble machine, It has the following advantages.

(1) Improved the mechanization level of disassembling hydraulic prop. Saving auxiliary time, Work efficiency higher.
(2) The force is even at the clamping parts, cylinder deformation is smaller.
(3) When working, manipulate the Manual direction valve can clamp workpiece, even without human clamp tight, significantly reduce labor intensity, Operation is very convenient.
(4) When need to release workpiece, without starts the main motor reverse, so that the starting numbers of the main motor and the main speed reducer reduces to original half. Extended equipment life.

References

[1] Y.J. Jia, G.Z. Cheng and X.R. Cao: Coal Mining Machinery Vols. 24 (2003) NO. 1, pp.65-66.

[2] L.G. Pu.: *Mechanical Design* (Higher Education Press, China 2006) (in Chinese).

[3] Y.J. Jia and G.Z. Cheng: Hydraulic and pneumatic, Vols. 33 (2009) NO.9, pp.4-6.

[4] Y.D. Yang: *Mechanical Design* (Chongqing University Press, China 1989) (in Chinese)

[5] G.Z. Cheng and Y.T.Zheng: Mechanical design and manufacturing Vols. 44 (2006) NO. 1, pp.152-153.

© (2012) Trans Tech Publications, Switzerland
doi:10.4028/www.scientific.net/AMM.164.348

Research on Energy Saving Mechanism of Optimal Regulation Voltage for Overhead or Gantry Crane Based on Mechanics Analysis

Bin Zhong[1,a], Wen-ming Cheng[2,b]

[1]School of Transportation and Logistics Southwest Jiaotong University Chendu, China

[2]Research Institute of Mechanical Engineering Southwest Jiaotong University Chengdu, China

[a]E-mail: zhongbinchina@163.com, [b]E-mail: wmcheng@home.swjtu.edu.cn

Keywords: crane; energy saving; asynchronous motor; electric total loss; optimal voltage; mechanics

Abstract: For overhead or gantry crane direct relationship between electric total loss and stator voltage or load torque is obtained based on the asynchronous motor's Γ-shape equivalent circuit because the stator's copper loss and iron loss are regarded as invariable loss that only relates to stator voltage and the rotor's copper loss is regarded as variable loss that is changed following load torque's changing. The optimal regulation voltage is obtained through mathematical calculation on the condition that make the asynchronous motor be stable running. The electric total loss will be minimum when the stator's voltage is the optimal regulation voltage. The research results showed: the electric total loss's error between the exact solution and the approximate solution obtained according to the approximate slip ratio while the asynchronous motor's stable running was bigger when the stator voltage was less than 200V, and the error was nearly zero when the stator voltage was more than 200V, but the optimal voltage error would not be more than 7V; the crane's effect of energy saving was prominent with optimal voltage regulation mode according to the load torque's changing.

Introduction

Asynchronous motor is main power plant of traveling mechanism and hoisting mechanism for the overhead and gantry crane (hereinafter referred to as crane), [1], [2] and [3]. In order to adapt to crane's wider range of hoisting load, at the same time, generally because crane is started with full load, power of the installed traveling motor or hoisting motor will be greater than actual power, especially during the hoisting mechanism's a working cycle, [4], the motor's working states is often under-load state, no-load state and state of generate electricity. But the motor is working with power supply of constant voltage, so there is electric energy's waste. The energy saving effect of speed regulation mode on variable frequency and changing pole is prominent for the fans and pump load. But the energy saving effect of speed regulation mode on variable frequency and changing pole is often but prominent for the crane with characteristics of constant torque load and variable working condition load. In order to realize crane's optimal regulation voltage control, generally the highest efficiency or minimum is selected as objective function, [5]. In this paper, aiming at crane's constant torque characteristic, according to asynchronous motor's Γ-type equivalent circuit; the optimal regulation was solved and the direct relation ship between electric total loss and voltage or torque was obtained after the stator's copper loss and iron loss were seen as invariant loss that was only related to stator's voltage and the rotor's copper loss was seen as variant loss that was changed with load's changing.

Analysis on electric total loss based on asynchronous motor's Γ-type equivalent circuit

In order to obtain the direct relationship between electric total loss and stator voltage or load torque and study on the part of invariant loss from the stator's copper loss, asynchronous motor's Γ-type equivalent circuit in figure 1 is considered, and the plural correction coefficient C_1 is introduced. For by-pass I, when the stator voltage is constant, the power loss on resistance R_1 and R_m can be expressed as

$$P_u = m_1 r U_1^2 \tag{1}$$

where: r is by-pass I's equivalent conductivity, and $r = (R_1 + R_m)/[(R_1 + R_m)^2 + (X_1 + X_m)^2]$.

According to figure 1, P_u shows the constant part of iron loss and stator's copper loss that result form excitation current I_0. From the expression (1), P_u is only connected with stator voltage. So P_u is called as asynchronous motor's invariant loss, correspondingly, by-pass I is called invariant loss by-pass and by-pass II is called variant loss by-pass. For by-pass II, corresponding loss on $C_1^2 R_2'$ is

$$m_1 I_2''^2 C_1^2 R_2' = m_1 I_2'^2 R_2' = P_{Cu2} \tag{2}$$

Equally, the power consumption on resistance $C_1^2 \dfrac{1-s}{s} R_2'$

$$m_1 I_2''^2 C_1^2 \frac{1-s}{s} R_2' = m_1 I_2'^2 \frac{1-s}{s} R_2' = P_{MEC} \tag{3}$$

According to expression (3), motor's electromagnetic power can be expressed as

$$P_{em} = P_{MEC} - P_{Cu2} = m_1 I_2''^2 C_1^2 \frac{R_2'}{s} \tag{4}$$

The electric power that is commonly consumed by resistance $C_1 R_1$ and $C_1^2 R_2'$ is variant loss P_v that changes with current I_2'' changing. Let $R_1'' = C_1 R_1$ and $R_2'' = C_1^2 R_2'$, and we have the following expression according to expression (4),

$$P_v = m_1 I_2''^2 (R_1'' + R_2'') \tag{5}$$

Then, according to the relationship among torque, power and rotor's angular velocity, the expression (5) is changed to

$$P_v = T_{em} \omega_1 \frac{R_1'' + R_2''}{R_2''/s} \tag{6}$$

where: T_{em} is motor's electromagnetic torque and it's unit is $\mathrm{N \cdot m}$; ω_1 is motor's synchronous machine angular velocity, and $\omega_1 = 2\pi n_1 / 60$ is motor's synchronous rotate speed, and $n_1 = 60 f_1 / p$. f_1 is supply frequency and p is motor's number of pole pairs.

When crane motor's rotor's rotate speed does not change, the motor will working at the stable state, namely, $T_L = T_{em}$. According to figure 1's divided power loss, the motor's electric total loss is the sum of invariant loss and variant,

$$\sum P = m_1 r U_1^2 + \omega_1 s \frac{R_1'' + R_2''}{R_2''} T_L \tag{7}$$

Calculation on energy saving of optimal regulation voltage

In figure 1, we let $X_1'' = C_1 X_1$ and $X_2'' = C_1^2 X_2'$, and the following expression can be obtained from the expression (4),

$$T_{em} = \frac{m_1 U_1^2}{(R_1'' + R_2''/s)^2 + (X_1'' + X_2'')^2} \cdot \frac{R_2''/s}{\omega_1} = \frac{m_1 U_1^2 \cdot s R_2''}{\omega_1 \{R_2''^2 + 2 s R_1'' R_2'' + s^2 [R_1''^2 + (X_1'' + X_2'')^2]\}} \tag{8}$$

When crane's motor stably works, $s^2 \approx 0.0001 \sim 0.0009$, the calculation error of electromagnetic torque often does not exceed $2\,\mathrm{N \cdot m}$ if expression (8)'s $s^2 [R_1''^2 + (X_1'' + X_2'')^2]$ in denominator. And the calculation error is permitted in engineering practice. At the same time, the computational process will be greatly conveniently and simplified. s's approximate expression showed by T_L is

$$s \approx \frac{\omega_1 R_2'' T_L}{m_1 U_1^2 - 2\omega_1 R_1'' T_L} \tag{9}$$

Take expression (9) into expression (7), and obtain the crane's electric total loss $\sum P$ showed by the stator voltage U_1 and load torque T_L,

$$\sum P = m_1 r U_1^2 + \frac{\omega_1^2 (R_1'' + R_2'')}{m_1 U_1^2 - 2\omega_1 R_1'' T_L} T_L^2 \tag{10}$$

According to expression (10), we have the following expression

$$\frac{\mathrm{d}\sum P}{\mathrm{d}U_1}=2m_1rU_1-\frac{2T_L^2\omega_1^2m_1(R_1''+R_2'')U_1}{(2T_L\omega_1R_1''-m_1U_1^2)^2} \tag{11}$$

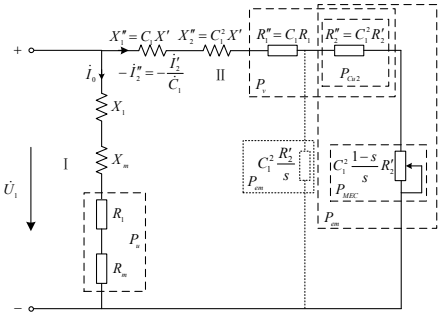


Fig. 1 Γ-type equivalent circuit of asynchronous motor

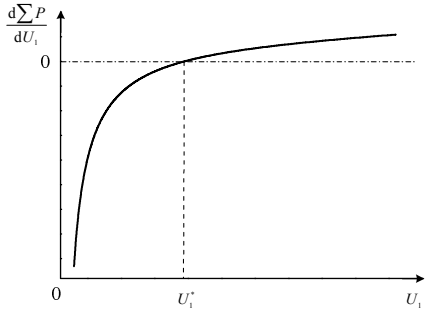


Fig. 2 Stator voltage's effect on electric total loss's change rate

Figure 2 is stator voltage's effect on change rate of electric total loss: total loss will decrease from decreasing quickly to decreasing slow with U_1's increasing when $U_1<U_1^*$ and total loss will increase slow with increasing when $U_1>U_1^*$, and U_1^* is optimal regulation voltage.

Let expression (11) be zero, we solve crane's energy saving of optimal regulation voltage U_1^*

$$U_1^*=\begin{cases}\sqrt{\dfrac{(2R_1''+\sqrt{\dfrac{R_1''+R_2''}{r}})\omega_1T_L}{m_1}} & T_L>0\\ \sqrt{\dfrac{(2R_1''-\sqrt{\dfrac{R_1''+R_2''}{r}})\omega_1T_L}{m_1}} & T_L<0\end{cases} \tag{12}$$

where: $T_L>0$ shows that motor works in power-driven condition or electromagnetic brake condition; $T_L<0$ shows that motor works in generator condition.

Generally, in order to make crane's motor work normally, let $U_1\neq 0$. So, we may take

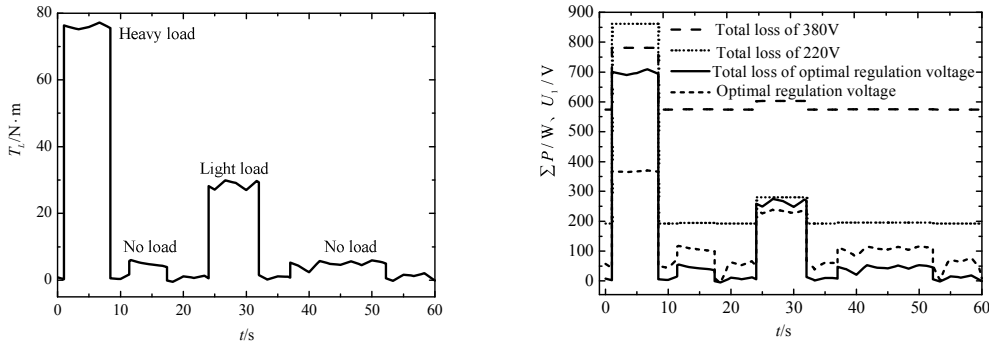
$$U_1^*=\alpha\sqrt{T_L} \tag{13}$$

where: $\alpha=\sqrt{(2R_1''+\sqrt{\dfrac{R_1''+R''}{r}})\omega_1/m_1}$, and α is called as optimal voltage coefficient of crane's energy saving. When supply frequency f_1 is determined, α is only connected with motor's structure parameters. Take expression (13) into expression (7), we obtain electric total loss's minimum value

$$\min\sum \mathrm{P}=[2rR_1''+\sqrt{r(R_1''+R_2'')}+\frac{R_1''+R_2''}{R_2''/s}]\omega_1T_L \tag{14}$$

Simulation research

Take cage induction motor with 3 phases and 6 poles as an example, let motor's parameters be: $R_1=1.375\Omega$, $X_1=2.430\Omega$, $R_2'=1.047\Omega$, $X_2'=4.400\Omega$, $R_m=8.340\Omega$, $X_m=82.600\Omega$. Rated slip is $s_N=0.0298$. In order to verify effectiveness of energy saving for optimal regulation voltage mode, the crane's load torque according to crane's working characteristic is taken as input in figure 3's (a), and there is certain fluctuation of load. The comparison of optimal voltage and total loss tracking load's changing is showing in figure 3's (b). From figure 3's (b), the total loss of drive with constant 220V is maximal when crane is working with heavy load. The total loss of drive with constant 380V is obviously maximal when crane is working with light load. The energy saving effectiveness is prominent for optimal voltage control according to load's changing.



(a) Load torque curve (b) Curves of total loss and optimal voltage

Fig. 3 Crane's load torque and energy saving of optimal regulation voltage

Conclusion

There is optimal voltage U_1^* that makes crane motor's electric total loss minimum when the load torque is determined. Total loss will decrease from decreasing quickly to decreasing slow with U_1's increasing when $U_1 < U_1^*$ and total loss will increase slow with increasing when $U_1 > U_1^*$. The total loss error is bigger when the stator voltage is under 200V, but the total loss error is almost zero when the stator voltage exceeds 200V. The optimal voltage error does not exceed 7V through calculating in crane's working voltage range. The total loss of drive with constant 220V is maximal when crane is working with heavy load. The total loss of drive with constant 380V is obviously maximal when crane is working with light load. The energy saving effectiveness is prominent for optimal voltage control according to load's changing.

Acknowledgement

This research is supported by the National Natural Science Foundation of China (51005246).

References

[1] B. ZHONG, "Research on Structure Parameter of Railway Container Crane's Hydraulic Anti-sway System", 2010, 31（3）:133-137.

[2] W. M. CHENG，B. ZHONG，Z. Q. ZHANG, "Dynamic Analysis for the Structure of Container Crane Hydraulic Anti-sway System", China Railway Science, 2007, 28（2）: 105-108.

[3] M. CHENG, R. W. CAO, G. W. HU, G. L. CAI, "Energy-saving Control Based on Stator Voltage-regulation of Asynchronous Motor", Electric Power Automation Equipment, 2008, 28（1）:6-11.

[4] X. S. CUI, Y. L. LUO, Y. L. YANG, "Energy Saving Theory and Approach for Asynchronous Motor under the Periodically Variable Running Condition", Proceedings of the CSEE, 2008, 28(18):90-97.

[5] C. Q. ZHU, X. H. WANG, N. SHEN, X ZHANG, "Variable-voltage Energy Saving Strategy for Three-phase Induction Motor in Oil Pumpjacks", Acta Automatica Sinica, 2007,33(7):749-752

© (2012) Trans Tech Publications, Switzerland
doi:10.4028/www.scientific.net/AMM.164.352

Hoist Lubricating Oil Pressure and Liquid Level Detection

GuangZhen Cheng[1, a] and Jin Lin[2, b],

[1]Huzhou Teachers College, Huzhou, Zhejiang Province 313000, P.R. China
[2]Beijing Forestry University, Beijing,100083, P.R.China

[a]chgzh169@126.com, [b]676786164@qq.com

Keywords: pressure measurement, liquid level measurement, display, mine hoist

Abstract. This article describes the structure, working principle and technical parameters of the lubricant oil pressure and liquid level indicating alarm system of the mine hoist. In order to send signals to the main control room displaying pressure and liquid level， the use of digital circuit-designed smart modular pressure transmitter, level transmitter, with the light beam warning indicator, display the fluid pressure and fluid level signal in the main control room, the limit alarm, and the upper and lower limit settings.

Introduction

Coal mine hoist is an important large fixed equipment, its duty is the transportation of people, coal, waste rock, material and equipment, it is the important transport equipment that links the ground and the underground. The reliability of the hoist is directly related to employee safety and business interests. For operation, maintenance and management of hoist, "coal Mine Safety Regulations" have put forward strict requirements. At present, China's coal mine equipment maintenance and management needs to be improved, for the general equipment maintenance, the repair is arranged until the equipment can not be used, and a serious lack of maintenance shortens the useful life of equipments. For mine hoist and other large key equipment, they should stop working for the maintenance on a regular basis. Regardless of how the status, repair should be a daily work and overhaul should be done for certain time. But too much downtime causes over-maintenance. Both cases above would cause the waste of human and finance resource, and the device status and the problems are not clear. To ensure facilities in good health and safe operation, it is essential in terms of safety, efficiency and accident-prevention to carry out the work of monitoring and diagnosis in mining equipment and make the reasonable arrangements according to the specific status of equipment.

To understand the status of mine hoists better and to make the operator observe the lubrication easier, we improve lubricant oil pressure and the display of liquid level display, the design Lubricant oil pressure and liquid level indicator alarm system, which sends the oil pressure and level signal to the main console display.

Work Principle Block Diagram

Pressure sensors, level sensors were used to detect the oil pressure and oil tank level signal, there are corresponding electrical signal translate by pressure transmitter and level transmitter. Input the actual pressure and level in the display device and shows the setting upper and lower limits of oil pressure and level. At the same time, compare the setting conversion circuit with the upper and lower limits. When the actual value exceeds the setting range, turn on the indicator and buzzer alarm and send audible and visual alarm signal. Block diagram is shown in Fig. 1[1].

Determination Sensor Transmitter

Pressure Sensor. Hoist machine oil pressure signal is from the oil pump discharge port. The pressure transmitter WP800B-2.5MPa-5G24Ek2i is chosen for convenience of displaying the signal in the main control room, which is shown in Fig. 2. This intelligent transmitter module use CPU-centric

digital circuit. The signal output by sensor go through the A / D converter into the CPU. Amended by the operation, the analog signal output by the interface circuit and the contact switch signal is for the use of display control. The advantage is Anti-interference ability, high stability, compact and practical and easy to install[2].

The main technical parameters:

Measuring range: 0 ~ 2.5Mpa
Output Type: 4 ~ 20mADC
Power supply: +24 VDC
Accuracy: 0.5
Operating temperature: -20 ~ 70 ℃
Relay load capacity: 220VAC/3A; 30VDC/5A
Over Pressure: 150% FS

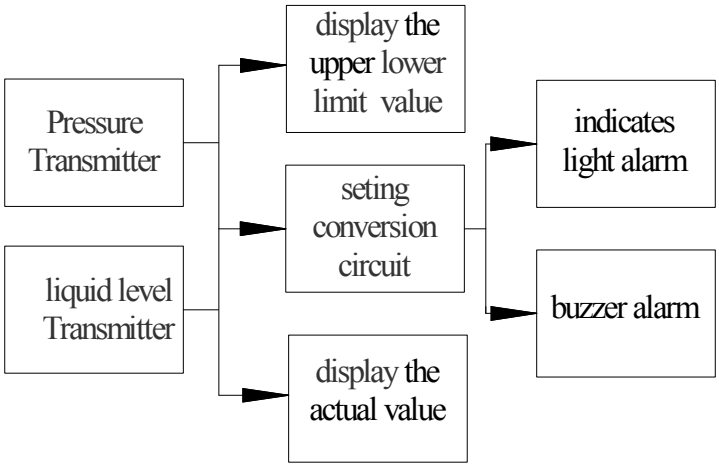


Fig. 1 Block diagram of the pressure and liquid level detection

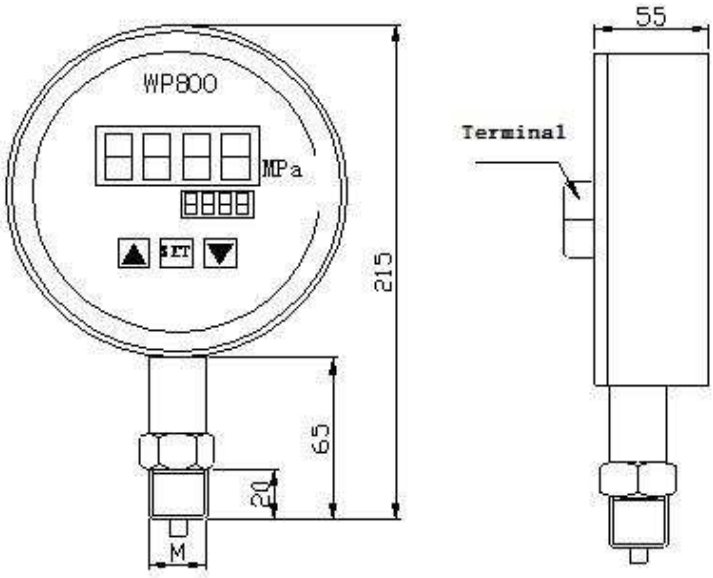


Fig. 2 Pressure transmitter

Liquid Level Sensor. Oil level sensor is installed in the tank. Based on the principle that the liquid static pressure is proportion with liquid level height in tank, the liquid static pressure acts on the semiconductor sensor. Using the piezoresistive effect of sensitive components, the hydrostatic is converted to the corresponding resistance value, measure the circuit through unbalanced bridge, then the level signals is turned into the standard electrical signals through temperature compensation and

linearity correction. Considering the installation conditions, long-distance signal transmission and the convenience of setting upper and lower alarm value limit, the model KYB19-02M1F1Z2C1i level transmitter is chosen, shown in Fig. 3[2].

The main technical parameters:

Measuring range: 0 ~ 3.5m
Output Type: 4 ~ 20mADC
Power supply: +24 VDC
Accuracy: ± 0.25% FS
Medium temperature: 0 ~ 70 ℃
Load capacity: ≤ 600Ω
Over Pressure: 200% FS

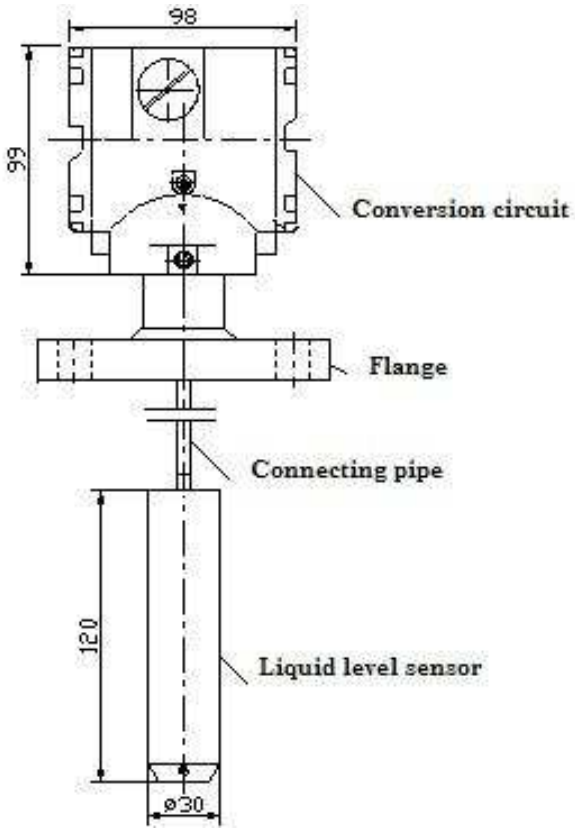


Fig. 3 Liquid level sensor and transmitter

Alarm and Display Device in Sound and Light

Alarm indicating device is shown in Fig. 4, which is composed by 24V DC power supply, the upper and lower limit device, beam monitors, alarm, Comparison and control device, control relays, lights, alarm buzzer and so on.

Changing the contact position of potentiometer R1, the maximum voltage U2 is changed. Then changing the contact position of potentiometer R2, the minimum voltage U3 is changed. Through this way the upper and lower limit value are set. The upper limit value U2 was display by the light beam monitor Z1 from top to bottom. The lower limit U3 was display by the light beam monitor Z1 from bottom to top. The upper limit must be greater than the lower limit, the dark band at middle is safe operating area. The actual measurement value U1 is displayed by the beam monitor Z2.

When working normally, the actual measurement value U1 is greater than the lower limit U3, and less than the setting upper limit U2, comparator A1and A2 does not change, relay KV1, KV2 stay power-off, normally closed contact KV1, KV2 are closed, the green light H1 shows the normal parameters. When U1 is greater than the upper limit U2, the comparator A1 makes contacts K1, relay

coil KV1 is energized, normally closed contact KV1 is off, the green indicator light H1 power off, normally open contacts KV1 close, the red indication light H2 turned on, indicating that the actual measurement value exceeds the upper limit, at the meantime the upper limit buzzer B1 alarms. When U1 is less than the lower limit U3, the comparator A2 makes contacts K2, relay coil KV2 is energized, normally closed contact KV2 is off, the green indicator light H1 powers off, normally open contacts KV2 is closed, yellow indicates light H3 turns on, indicating that the actual measurement value is less than the lower limit, while the lower limit buzzer B2 alarms[3].

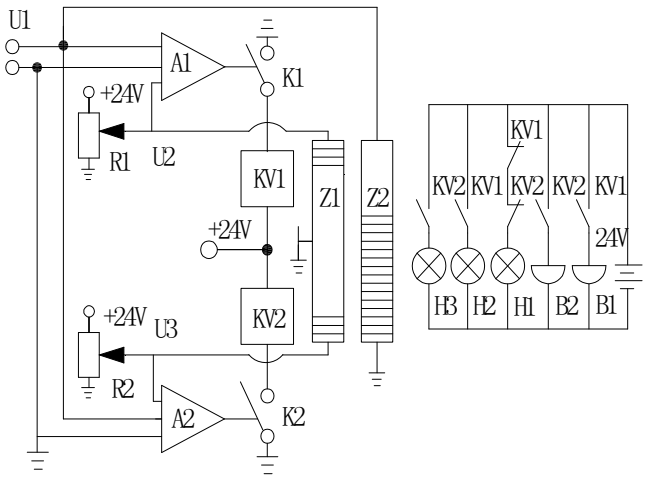


Fig. 4 Alarm and indicating devices

Conclusion

(1) Dual light beam monitor indicates pressure and liquid level signal, which is clear to understand with sound and light alarm, the system can detect anomalies, more securely and reliably.
(2) Using Potentiometer to set the upper limits and lower limits of pressure and liquid level is simple, reliable, economical and practical.
(3) Pressure and liquid level signal are turned into standard electrical signals and transmitted to the control room. The indicating instrument of display lubrication oil pressure and liquid level are shown in the control room, which solves the problem of long-distance transmission signal

References

[1] H. Zhang: *Thermal measurement and instrumentation* (China Metallurgical Industry Press, China 2006) (in Chinese).

[2] Y.M. Li: *Chemical meter and automation* (Chemical industry Press, China 1999) (in Chinese).

[3] G.Z. Cheng: Coal Mining Machinery Vols. 29 (2008) NO.11, pp.115-117.

[4] Y.J. Jia, Y.B. Cheng and Y.Y. Han: Advanced Materials Research Vols. 228-229 (2011) pp. 744-748.

[5] D.S. Feng: *Frequency Conversion application and maintenance* (South China University of Technology Press, China 2001) (in Chinese).

[6] G.Z. Cheng and Y.B. Cheng: Applied Mechanics and Materials Vols. 34-35 (2010) pp. 1573-1577.

© (2012) Trans Tech Publications, Switzerland
doi:10.4028/www.scientific.net/AMM.164.356

Study on Mechanics of Special Materials against Oil Volatility Risk

Tian Li

School of Finance, Harbin University of Commerce, China

Key words: Oil volatility; Hedging; Dynamic waves

Abstract: Crude oil is the most important material for the modern industry, while its volatility risk's threatening to the industry developments is increasing stronger and stronger. In 2008 and 2009, some Chinese corporations have suffered from huge losses from their earlier hedging operations on crude oil prices. These incidents reflected the shortage of management methods and experiences on risks. In fact, those corporations might hedge their short positions on the crude oil puts by longing the US Treasury Bonds puts so as to avoid the huge losses.

1. Introduction

In 2008, to avoid the risk of fluctuations in international oil prices, some domestic businesses (especially airlines) have been hedging on oil prices. However, by the middle of 2009, these hedging companies began to suffer huge losses due to the decline in international oil prices.

These companies adopted a "self-financing" means access to hedge funds. Specifically as follows: when the international crude oil prices rise over $120, the hedging company set to buy European call options with $ 140 as exercise price (referred to as C140). In order to pay the costs of C140, these companies sold the European put options with the exercise price of $60 (referred to as P60). As the international oil prices are much lower than U.S. $ 60(Figure 1) (this case lasted until mid-2009), so these hedging companies' puts bring them huge losses.

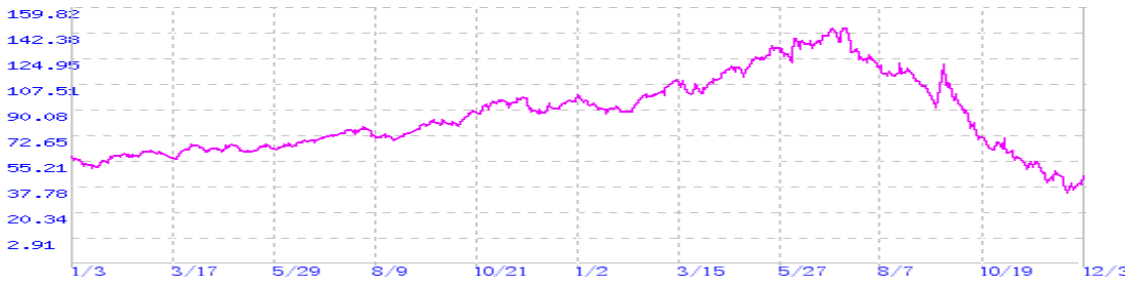


Figure 1
New York crude oil futures prices (January 2007-December 2008) Unit: USD / barrel
Source: International Petroleum Network http://www.in-en.com/oil/

Based on the study on the relationships between the oil price volatilities and the U.S. bond yields, this paper shows the possibility of replicating oil puts by T-bond calls, which can solve the problem of insufficient supplies of P60 when the price of oil is about fall below $ 60, and the problem of oil options price distortion caused by the imbalance between supply and demand.

2. The empirical correlation tests on the U.S. bond yields and oil prices

2.1 Variable selection and data description

Table 1 Shows indicators

Variable code	Variable meaning	Source
P	WTI Spot oil price	International Petroleum Network
R20	20-year T-bond yield	U.S. Treasury Official Website

U.S. West Texas Intermediate crude oil spot price of WTI is the representative of the crude oil data in the international oil pricing system. After the preliminary data treatment and tests, this paper selects U.S. West Texas Intermediate crude oil spot price (P) and its relevance to U.S. Treasury 20 year bond yields (R20) as a variable of indicators.

2.2 Correlation test

Negative correlation between the oil spot prices and the 20-year T-bond yields based on the 0.01 significance level can be found through by the PERSON correlation analysis on the samples, with the correlation coefficient of -0.490.

Table-2 Correlation test

		20-year-T-bond -yield	Spot price of oil
20-year-T-bond-yield	Pearson Correlation	1	-.490**
	Sig. (2-tailed)		.000
	N	117	117
Spot price of oil	Pearson Correlation	-.490**	1
	Sig. (2-tailed)	.000	
	N	117	117

**. represents significantly correlated at the level of 0.01 confidence.

2.3 Unit root test

To avoid the possible fallacy of regression caused by the use of non-stationary variables when regress, we first use the ADF (Augmented Dickey-Fuller) to test all the stationary time series variables. The test sequence is subject to unit root process. Test results are as follows.

Table-3 ADF Unit root test

The original sequence	ADF Value	(C,t,p)	1% Threshold	Conclusion	Difference sequence	ADF value	1% Threshold	Conclusion
R20	-2.1319	(c,0,1)	-3.4891	unstable	ΔP	-11.066	-4.0412	stable
p	-2.2754	(c,0,1)	-3.4891	unstable	ΔR20	-7.5900	-3.4886	stable

From the test results, R20 and P at the 5% are stable at the significance level, therefore their cointegration relationship may exist.

2.4 Cointegration test

From the result of stability test on R20 and P, R20 ~ I (1), P ~ I (1)meet the prerequisite of cointegration tests. So we can continue to use the method of Johnsen Cointegration test to analysis the cointegration of the two variables. This method is based on vector auto regression (VAR) model to carry out, so between the two variables need to determine the structural VAR model.

Eviews6.0 gives a wide selection of criteria for the best lag VAR model. Generally, the principle of the application is to select the best lag according to the criteria of AIC and SC. However, while the lags determined by the two are inconsistent, the final lag determined by LR criteria should be primarily chosen. From the table below, the lags determined by criteria are all 3.

Table 4 The best lag tests

Lag	LogL	LR	FPE	AIC	SC	HQ
0	-580.0335	NA	164.4564	10.77840	10.82807	10.79854
1	-358.4392	430.8779	2.924573	6.748874	6.897881	6.809291
2	-350.1621	15.78775	2.702149	6.669669	6.918015	6.770364
3	-337.8211	23.08223*	2.315941*	6.515206*	6.862890*	6.656179*
4	-336.1410	3.080207	2.418597	6.558167	7.005189	6.739418
5	-334.1292	3.613868	2.510918	6.594985	7.141345	6.816514
6	-332.7568	2.414435	2.638566	6.643644	7.289342	6.905451
7	-328.8757	6.684082	2.647739	6.645846	7.390882	6.947931
8	-326.6396	3.768264	2.740212	6.678511	7.522885	7.020874

Note: * indicates the best lag selected by the corresponding criteria

VAR model based on the AR root map and AR root table are used to judge the stability of the VAR model. The following figure clearly shows: the reciprocals of all the roots of the characteristic equation are within the unit circle. Thus, VAR model is stable.

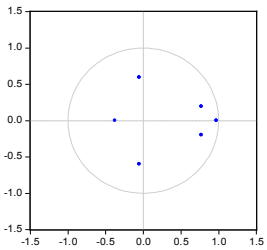


Figure -2 AR roots graph of VAR model stability test

The optimal lag of Johansen Cointegration Test is one less than that of VAR model. Since the optimal lag of VAR model is 3, so the lag of Johansen Cointegration Test is 2. Test results are as follows.

Table -5 Johansen cointegration test on P and R20

Variable group	Eigenvalue	Trace statistic	5% Threshold	λ Statistics	5% Threshold	The number of cointegration equations
P and R20	0.124941	17.52497	15.49471	15.08144	14.2646	None *
	0.021392	2.443526	3.841466	2.443526	3.841466	One at most
Project		R20		P		
Standardized cointegration coefficient		1		0.023104 (0.00580)		

The above table shows the empirical results at the 5% confidence level refuse the original hypothesis that the cointegration equation is not existed, and accept the hypothesis about the existence of the cointegration equation. This means there is a long-term stable equilibrium relationship between the spot oil price and the 20-year yield. And the cointegration coefficients shows the negative relationship between them.

As the two variables are I (1) sequence, and there is a cointegration between them, according to the Granger theorem, a vector error correction model is assure to be established. Based on the vector error correction model, the short-term dynamic relationship between these variables can be learnt more. This relationship can be expressed as the error correction form:

$$\Delta R20 = \underset{[-1.3247]}{-0.0299} - \underset{[-2.5952]}{0.1023} \times ECT_{t-1} - \underset{[-0.5748]}{0.0505} \times \Delta R20_{t-1} - \underset{[-3.9762]}{0.3467} \times \Delta R20_{t-2} + \underset{[0.7491]}{0.0028} \times \Delta P_{t-1} + \underset{[2.7127]}{0.0105} \times \Delta P_{t-2} \quad (1)$$

Among them, the ECT_{t-1} is the error correction term which can be expressed as $ECT_{t-1} = -6.1880 + R20_{t-1} + \underset{[4.03746]}{0.0231} \times P_{t-1}$

The equation (1) shows the error correction term coefficient is -0.0676, which is significant at the 5% significance level. This indicates that there is a reverse-adjustment-mechanism when the equilibrium deviates from the long-term equilibrium within a short-term, the 6.76% of the deviation between the real oil prices and long-term equilibrium is amended.

3. Design of the hedging application of U.S. Treasury-bond options on the oil puts

The empirical tests show that the price of oil and the 20-year U.S. Treasury-bond yields were negatively correlated, while the oil prices were positively correlated with the 20-year U.S. Treasury-bond prices. Based on this conclusion, we can design the following hedging program to hedge the risk of short position of oil puts by using U.S. Treasury bonds options.

According to the obtained correlation coefficient between the U.S. Treasury-bond yields and the oil prices, we can figure out the 20-year U.S. Treasury yield to maturity (R20) when the oil spot price of is $ 60. Assuming the par value of these bonds is $ 1,000 with coupon rate of 2%, the present value of the corresponding bonds is: $NPV(60) = \sum_{i=1}^{20} \frac{20}{(1+R20)^i} + \frac{1000}{(1+R20)^{20}}$

Since the oil spot price and bond price changed in the same direction, when the oil prices are expected to below the exercise price of $ 60, we may buy the 20-year T-bond puts with the exercise price of $X = NPV(60)$ to hedge those oil puts.

3.1 Static hedge ratio design

We assume that the hedge ratio of this hedging program (ratio of U.S. T-bond puts and the oil puts) is a linear function of oil prices. When the spot oil price P = 59 dollars, according to the standard cointegration equation R20 =- 0.023104 × P, the standard cointegration coefficient is 0.023104. At this time, the corresponding 20-year T-bond yields is: $R20' = R20 \times (1 + \frac{60-59}{60} \times 2.31\%)$, Where $R20'$ is the 20-year U.S. Treasury-bond yield to maturity when oil price is at $ 59. At this point, the bond price is: $NPV(59) = \sum_{i=1}^{20} \frac{20}{(1+R20')^i} + \frac{1000}{(1+R20')^{20}}$

The value of put corresponding to the Bonds is $NPV(60) - NPV(59)$. At this time, the value of P60 is $ 1, meaning a short of P60losses $ 1. So, when oil prices fell to $ 59 from $ 60, the hedging ratio between the oil put and the government bonds is $1 / [NPV(60) - NPV(59)]$. When oil prices fell to P (<60) from $ 60, according to the assumption of the linear relationship, the hedging ratio should be $(60-p) / [NPV(60) - NPV(p)]$.

Specifically, if the oil price is $ 60, 20-year U.S. Treasury-bond yield to maturity is 4.38%, then, $NPV(60) = \sum_{i=1}^{20} \frac{20}{(1+4.38\%)^i} + \frac{1000}{(1+4.38\%)^{20}} = 687.16$;

According to the standard cointegration equation R20 =- 0.023104 × P, the standard cointegration coefficient is 0.023104, so when oil price fell to $ 59, the 20-year U.S. Treasury yield is: $R20' = 4.38\% \times (1 + \frac{60-59}{60} \times 2.31\%) = 4.3817\%$ The corresponding bond price: $NPV(59) = \sum_{i=1}^{20} \frac{20}{(1+4.3817\%)^i} + \frac{1000}{(1+4.3817\%)^{20}} = 686.98$,

At this point the value of bonds put is $ 0.18 and the value of oil P60 puts $ 1, indicating a short of P60 will loss $ 1 and the hedging ratio is 5.5.

3.2 Dynamic hedge ratio

In practice, the hedging ratio will change with changes in oil prices and the value of the U.S. Treasury options. According to the previous discussion, the proportion of available hedging function $\Delta(P) = \frac{60-P}{NPV(60) - NPV(p)}$, $NPV(p) = \sum_{i=1}^{20} \frac{20}{(1+R_{20}')^i} + \frac{1000}{(1+R_{20}')^{20}}$

$R_{20}' = R20 \times (1 + \frac{60-P}{60} \times 2.31\%) = R20(2 - 0.3805\%P)$。The dynamic hedging ratio function is $\Delta'(P)$.

Reference:

[1] Fisher Black,Emanuel Derman,William Toy. A One-Factor Model of Interest Rates and Its Application to Treasury Bond Options.Financial Analysts Journal[J].1990

[2] I.A. Moosa. Price Discovery and Risk Transfer in the Crude Oil Futures Market: Some Structural Time Series Evidence. Economic Notes Issue[J]. 2002

© (2012) Trans Tech Publications, Switzerland
doi:10.4028/www.scientific.net/AMM.164.362

Research on Constant Pressure of Air Supplying and Energy Saving for the Air Conditioning System

GuangZhen Cheng[1, a], ZuoQing Liu[2, b] and HongFei Lin[3, c]

[1]Huzhou Teachers College,Huzhou, Zhejiang Province 313000, P.R. China

[2]Cet Pinggao Group Co., Ltd, Pingdingshan, Henan Province 467000, P.R. China

[3]Pingdingshan Industrial College of Technology, Pingdingshan, Henan Province 467000, P.R.China

[a]chgzh169@126.com, [b]Liuzq@pinggao.com, [c]lhfwhw@126.com

Keywords: Velocity modulation, Constant pressure control, Saving energy

Abstract. This paper provides a method of supply constant pressure air for air conditioning system. It analysis the energy consumption betwwen the damper adjuste air flow with variable frequency speed regulation adjuste air flow. The paper Introduce the Energy conservation principle of the frequency control blower. The supplying air Pipeline subject to a uniform force, the equipments mechanical properties was improved.The results show that Uses the frequency conversion velocity modulation to carry on supply constant pressure air, obviously reduces the energy consumption.The electrical motor starting characteristic is improved, realizes the electrical motor soft start.

Introduction

In the central air conditioning control system with changing the supply wind amount ,the blast static pressure should maintain constant, removes various disturbance that static pressure fluctuation brings for. The traditional constant pressure adjustment method, uses the back plate throttle control. According to back plate's installment position in air flue, may divide into the outlet damper control, the entrance back plate control. When the outlet damper controls, with back plate close the wind resistance increases, cannot adjust the wind amount in the wide scope. Moreover, in the small amount of wind sector, the shaft power change is small, the energy conservation effect is not obvious. Compareing The entrance back plate controls with the outlet damper control, the amount of wind control area is broad, turns small entrance back plate, the shaft power roughly is proportion to drop with wind amount. the static pressure automatic control example showed in Fig. 1, the pressure transmitting instrument 5 change the static pressure to 4~20mA DC signal, this signal delivers to the monitor 4 demonstrate static pressures, at the same time delivers to the controller 3 takes the control signal. The controller 3 input signals are the 4~20mA DC standard signals, its output is the 0~10V DC PI control signal, the implementing agency is the electric operator 2, it has the valve locator witch electrically operated, the electric operator control air blower entrance opening, carries on the wind amount regulation, keep the static pressure constantly. This control method, the air blower actuates and the electrical motor constant rotate, uses the entrance back plate control to replace the outlet damper control, the performance has the improvement, but the energy consumption is still big, The efficiency is low. Along with frequency conversion velocity modulation technology mature day by day, equipment performance price compared to the enhancement, uses the frequency conversion velocity modulation to carry on the blast constant pressure control, the system performance is stable, the energy conservation effect is very remarkable [1].

Frequency Conversion Velocity Modulation Energy Conservation principle

Air blower, water pump equipment, when movement its flows Q, , shaft power N and rotational speed n has the following relations [2]. The relationship between flows Q and rotational speed n is as Eq.1.

$$\frac{Q}{Q_0} = \frac{n}{n_0} \tag{1}$$

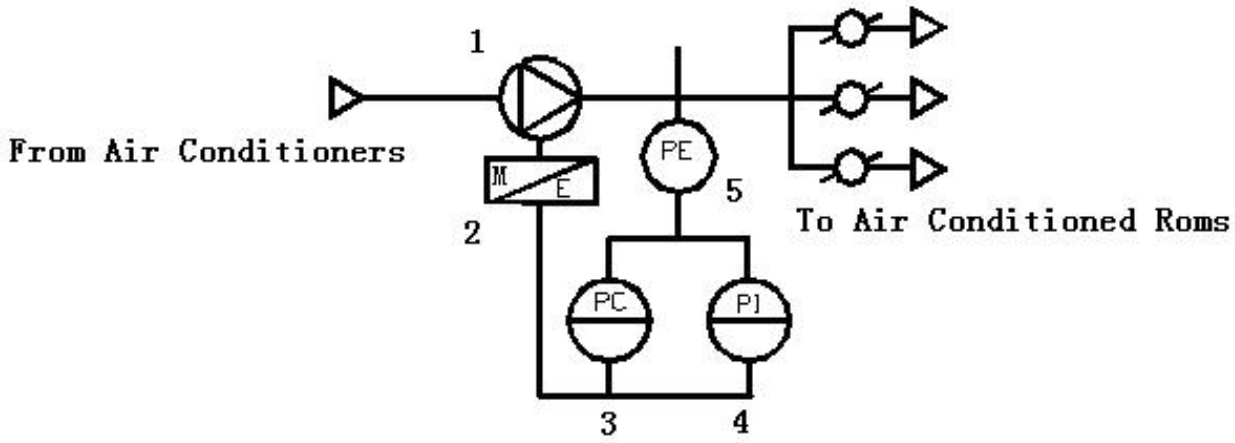
The relationship between pressure P and rotational speed n is as Eq.2.

$$\frac{P}{P_0} = \left(\frac{n}{n_0}\right)^2 \tag{2}$$

The relationship between shaft power N and rotational speed n is as Eq.3.

$$\frac{N}{N_0} = \left(\frac{n}{n_0}\right)^3 \tag{3}$$

Here: n_0 is the rated rotation;
Q_0 is the rated flow when the rotation is n_0;
P_0 is the rated pressure when the rotation is n_0;
N_0 is the rated shaft power. when the rotation is n_0.



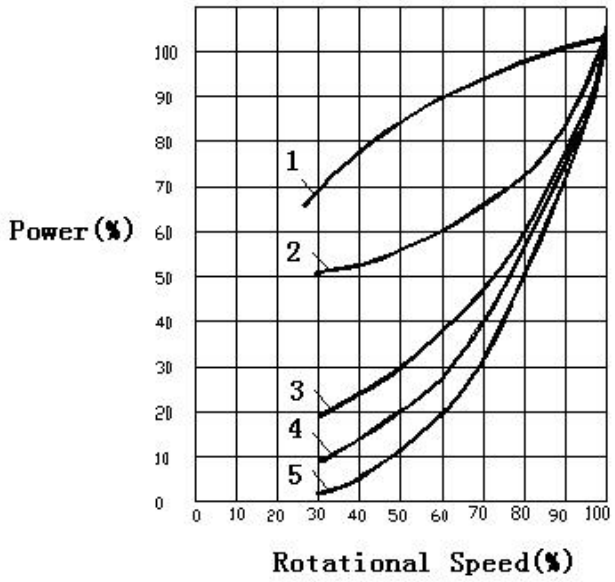
1.fan, 2. electric valve positioner, 3.pressure controller, 4.pressure monitor, 5.pressure transmitter
Fig. 1 Press automatic control using damper

The air blower, the water pump equipment's characteristic is that its load torque is proportional with the rotational speed square, its shaft power is proportional with the rotational speed cube. compare With uses the electrical motor constant speed revolution, the entrance back plate control amount of wind to maintains the constant pressure, when the load is smaller than the rated load, according to the wind amount need, adjusts electrical motor's rotational speed, maintains the wind pressure constant, may obtain the electricity saving effect. when uses the different control method,the air blower power dissipation curve shown in Fig. 2. Obviously, uses the frequency conversion velocity modulation control,the power dissipation to be closest the ideal curve [3].

The Frequency Inverter Choice

Air blower and Pumping equipment is the reduce torque load, that is, when the speed is reduced, the output torque reduce, Torque is proportional to the square of the rotate speed .Therore, for the reduce torque load, the best selection is U/f mode that is the reduce torque load, the voltage compensation value is big, causing the motor input current decreases, compares with the permanent torque loading's U/f pattern, may improve electric motor's efficiency. At the same time the U/f mode control is simple, the cost is low, suits the air blower, the water pump, this kind of equipment's control precision request is not high, serves purpose which the energy conservation falls consumes

Through a comprehensive comparison of different brands Frequency Conversion, the Frequency Inverter witch model is FRNVG7S-4 is selectted, the Frequency Conversion manufactured by the Japanese Fuji Electrical Company, Is suitable electrical motor capacity 15KW, three-phase supply voltage 380~480V, frequency 50/60Hz [4].



1.export damper control, 2.entrance damper control,
3.hydraulic transmission, 4. inverter control, 5.ideal curve
Fig. 2 Power consume of differ adjust method for fan

Frequency Conversion Exterior Wiring Diagram

Frequency inverter exterior wiring diagram is shown in Fig. 3. Frequency Conversion's R, S and T end connect with the three-phase power source, in order to change the motor rotation direction, usually change the motor terminals U, V and W of power. R0 and T0 are the auxiliary input terminal of control power source, takes as the antijamming filter power source and the external potentiometer, to set work frequency, their input impedance is 22KΩ; A1 and M is the input terminal analog simulation electric current signal, the flows transducer turn flows signal to the 4-20mA direct electric current signal, from this port inputs, compares with the frequency hypothesis signal, the differential value use as the control signal that control electrical motor rotational speed; FWD, REV and CM are the witch-on switch-off input terminal, FWD is the forward rotation start and stops, REV is the reversing rotation start and stop, CM is the public connection port.

Conclusion

1) Uses the frequency conversion velocity modulation to carry on constant pressure blast, obviously reduces the energy consumption, saving electricity 30%~40%.
2) Chooses U/f the pattern frequency Conversion, It is a typical AC - DC - AC voltage general purpose inverter, it is suitable for the air blower, the water pump, the technology is mature, the control is simple, economical and reliable.
3) The electrical motor starting characteristic is improved, realizes the electrical motor soft start.
4) The protecting function is complete, improves the control quality, the energy conservation has been remarkable, the revolution was reliable.
5) The frequency Conversion has fault display, that is advantageous for analysis and Solve the problem.

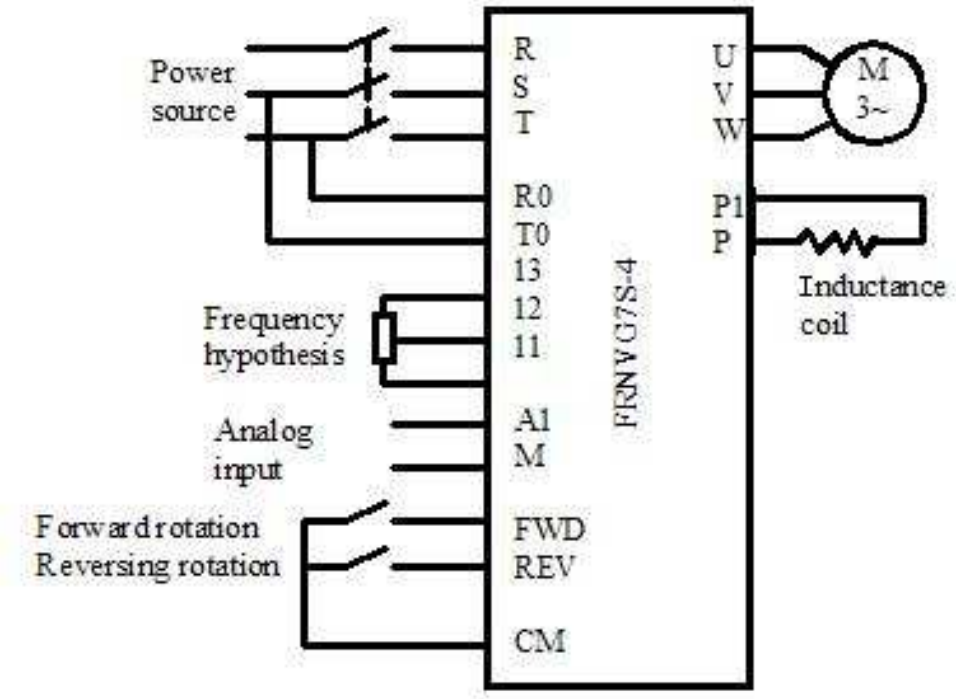


Fig. 3 Frequency inverter outer wiring diagram

References

[1] Y.M. Li: *Chemical meter and automation*(Chemical industry Press, China 2006) (in Chinese).

[2] D.S. Feng: *Frequency Conversion application and maintenance* (South China University of Technology Press, China 2001), (in Chinese).

[3] Y.S. Fan: *Electrical Control and PLC applications*(China Electric Power Press, China 2006) (in Chinese).

[4] Z.Q. Qi. *Machine Electrical Control Technology*(Machinery Industry Press, China 2002) (in Chinese).

[5] G. Z.Cheng and Y. B. Cheng: J. Applied Mechanics and Materials Vols. 34-35 (2010) pp 1573-1577.

[6] H.J. Zhang: Hydraulic metal cutting machine tools(Jiangsu Science and Technology Press, China 2009) (in Chinese).

[7] G.Z. Cheng and Y.B. Cheng: Advanced Materials Research Vols. 201-203 (2011) pp 2338-2342.

© (2012) Trans Tech Publications, Switzerland
doi:10.4028/www.scientific.net/AMM.164.366

Calculating Method of Assembly Clearance Magnitude of Centrifugal Pump Impeller with Mechanics Analysis

Lihong LI [1,a] Qianjin GUO[2,b]

[1]College of Vehicle and Motive Power Engineering, HUST, Luoyang

[2]Institute of Chemistry, CAS, Beijing

[a]Lyh_5204@163.com, [b]guojiauu@163.com;

Keywords: Impeller assembly clearance, Boundary-layer theory, calculating clearance magnitude method, mass flux

Abstract: When designing the centrifugal cooling pump, the people have been accustomed to design the normal clearance of the impeller shroud by mechanical assembly principle only for preventing parts from interference. But in the practice, the shroud clearance magnitude of the cooling pump is very difficult to be confirmed because of either serious leakage or high power consumption. As so far, it hasn't been specific theory about its magnitude which was designed only by a large of experiment. The boundary-layer thickness theory can be introduced to calculate the impeller clearance magnitude. This method first breached conventional experiment way in determine the shroud clearance magnitude and applied scientific theory to the engineering design. As a result, this method can save a great deal of industrial resources such as manpower, materials and funds, and give the more precise scientific reference to relative research about pump.

Introduction

The Normal shroud clearance magnitude of the centrifugal cooling pump impeller influences greatly on the performance of the pump. As yet there has been no any appropriate theory on it. The dimension of the clearance is traditionally designed depending on plentiful experiments which may consume a great deal of manpower, materials and funds. The boundary-layers in shroud clearance of impeller can be considered as 3D symmetrical and rotational boundary layers which can be converted into 2D boundary layers by coordinate conversion. The Boundary-layers thickness in clearance can be calculated by the more mature method computing 2D boundary-layers thickness. Most studies have been done by the exploited departments of the enterprise, which spent little time on it because of the influence of profit. So, the normal shroud clearance of impeller was designed by engineer greatly depending on their experiences and technical level. In this paper the method of calculating clearance magnitude was firstly put forward based on the theory of boundary layer thickness, which will greatly economize enterprise resources and supply more precise scientific basement for deciding the shroud clearance magnitude.

The Mathematic study of Boundary Layer in the Clearance of the Impeller

On the surface of the pump shell, the fluid speed is zero, and gradually increases along the normal till to the mainstream speed. This lamella is called as boundary layer. The boundary layer thickness is the distance from the surface of shell to the point where the velocity gets to 99% magnitude of mainstream speed along normal. The boundary layer on the shroud of impeller can be considered as that on the three dimension (3D) axial-symmetry rotating surface. The flow state of fluid in boundary layer has two kinds: laminar flow and turbulent flow. The fluid doesn't only produce

pulsatory flow but also turbulently diffuse in landscape orientation. With a view to that the boundary layer on two dimension（2D） axial-symmetry rotating surface was detailed and the approximatively solved method was introduced respectively by Liu huizhi and Wu yulin[1] in the theory of boundary layer and viscous hydromechanics. So, supposed that the blade of impeller were spread to a plane, in which the orthogonal curves coordinate system can be established shown in Fig.1, the intersect points of the shell and the blade would be a curve, the point corresponding to the start point of shell is origin, the arc length *x* along the curve is one coordinate, the distance *y* from surface along the normal of curve is the other coordinate, the third coordinate is rotating angle θ. Then, the boundary layer on 3D axial- symmetry rotating surface would be considered as the boundary layer on 2D axial- symmetry rotating surface. The liquid flows at relative speed *W* along the intersect curve.

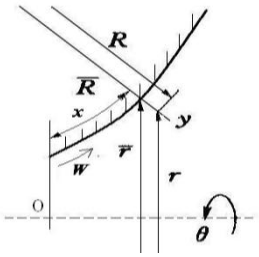


Fig. 1 2D axial- symmetry boundary layer

In the boundary layers theories, these are movement thickness δ_1, momentum loss thickness δ_2 and energy loss thickness δ_3. Corresponding boundary layer thickness is also called boundary layer nominal thickness δ.According to the coordinate equations of orthogonal curves, the flow momentum equation and continuous equation in boundary layer were built and were simplified with scalar grade as:

$$\delta_2^2 = \frac{0.45\nu}{\bar{r}^2 W^6}\int_0^x W^5 \bar{r}^2 dx \tag{1}$$

Where: as long as relative speed *W* and radius $\bar{r}$ were given, δ_2 can be calculated and then δ_1.

The streamline equation of blade bone line in centrifugal pump impeller is:

$$dx = rd\vartheta = Ce^{-k\frac{q}{2\pi r_0}\vartheta} d\vartheta \tag{2}$$

Substitute the Eq.2 into Eq.1:

$$\delta_2^2 = \frac{0.45\nu}{\bar{r}^2 W^6}\int_0^{\vartheta} W^5 \bar{r}^2 Ce^{-k\frac{q}{2\pi r_0}\vartheta} d\vartheta \tag{3}$$

According to flow velocity triangles in impeller, *U* is circumferential velocity and *W* is relative velocity along the tangential line at certain point which radius is *r*, then the relative velocity at the point is:

$$W = \frac{C_m}{\sin\theta} = \frac{Q}{2\pi r b \sin\theta} \tag{4}$$

$$b = -\left(\frac{150}{r-10} - \frac{450}{r}\right) \tag{5}$$

Substituting the Eq.4 andEq.5 intoEq.3, the momentum loss thickness in boundary layer can be gained as:

$$\delta_2^2 = \frac{0.45\nu}{(Ce^{\frac{q}{r}\vartheta})^2(\frac{Q}{2\pi r b\sin\theta})^6}\int_0^{\vartheta}(\frac{Q}{2\pi r b\sin\theta})^5(Ce^{\frac{q}{2\pi r_0}\vartheta})^3 d\vartheta \tag{6}$$

$$\delta_1 = H(\lambda)\delta_2 \tag{7}$$

$$\lambda = \frac{\delta_2^2}{\nu}\frac{dW}{dx} = -\frac{\delta_2^2}{\nu}\frac{Q}{2\pi \sin\theta (r-15)^2} \quad (8)$$

$H(\lambda)$ expresses the shape factor. After λ is calculated and $H(\lambda)$ can be gained by Thwaites[1] as Table 1

Table 1 $H(\lambda)$ value and boundary layer thickness

r [mm]	θ [°]	ϑ [°]	b [mm]	δ_2 [mm]	λ	$H(\lambda)$	δ_1 [mm]
38	38.8	21	11.78	0.2576	-0.064	3.04	0.783
50	39.4	39	8.23	0.2563	-0.068	3.09	0.792
56	39.7	47	7.08	0.2546	-0.072	3.15	0.802
61	39.9	54	6.25	0.2978	-0.076	3.22	0.959

From Table 1, when the impeller radium is 61mm, the movement thickness is 0.959mm which is close to the shroud normal clearance 0.86mm from plentiful experiments in certain factory. This shows that the method of calculate the shroud clearance by boundary layer theory is feasible.

Experimental analysis

The Fig.2 is a pump sample, which speed rating is 2600 rpm, power rating is 95kW, and the impeller radium is 61mm. This sample was designed by cooperating tractor academy, and made in Henan Province Xixia Automobile Water Pump Co.,Ltd. The experimental device was furnished as Fig.3.To validate the method veracity of calculating normal clearance magnitude between impeller shroud and shell, set five clearance magnitudes respectively: 0.65mm，0.85mm，0.96mm，1.2mm，2.5mm. The compared results were shown in Fig.4, Fig.5, Fig.6.

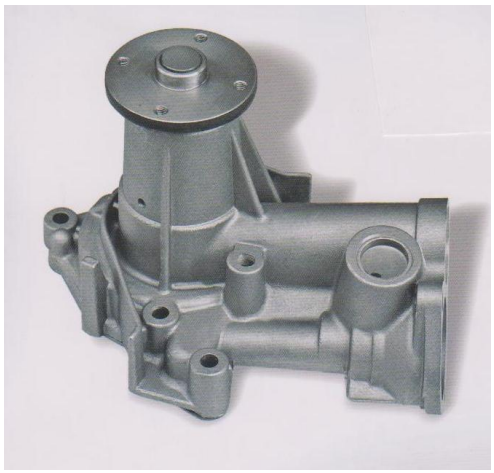


Fig.2 Cooling pump assembly



Fig.3 Experimental device

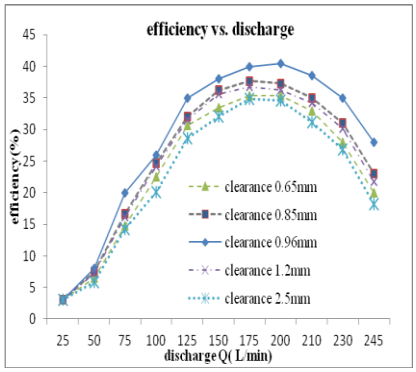


Fig.4 Efficiency vs.discharge

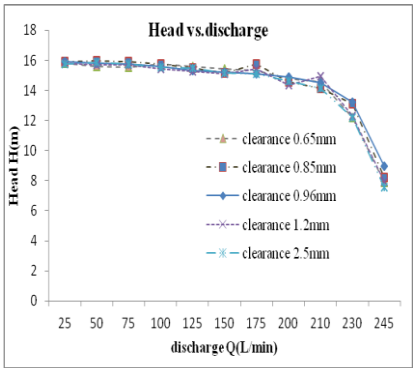


Fig.5 Head vs.discharge

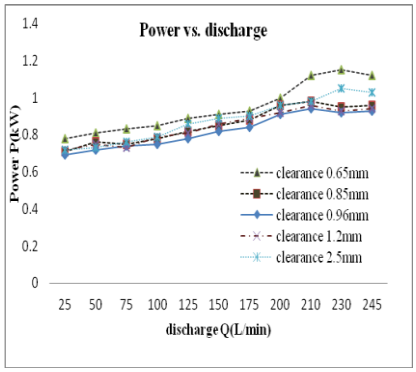


Fig.6 Power vs.discharge

In diagram Fig.4, the efficiency hadn't almost changed in low discharge field. When discharge increases, the difference comes into being. The highest efficiency takes place at the clearance 0.96mm. When the clearance is smaller the efficiency can declined because of overcoming the viscous resistance, reversely, when the clearance is bigger the leakage can influence on the efficiency. Fig.5 shows the five heads have little difference. Five Power diagrams is shown in Fig.6, with the clearance magnitude increasing, the shaft power decreases gradually, the lowest value is in the clearance 0.96mm curve. Because the viscous resistance is bigger immediately close to the wall, the bigger power must get over the resistance. When clearance magnitude is bigger than 0.96mm the turbulent energy can consume more energy and the shaft power increases.

Summary

For the shaft power, when the normal clearance between the impeller shroud and shell would be small, the viscous resistance acting on impeller would be large, the torque and shaft power would be large too. Where the boundary layer thickness would be smaller than the movement thickness, the viscous resistance would decline with increasing clearance and decreasing velocity grads. But due to the influence of the wall and the shape of blade surface, the turbulent flow take increasing action against liquid with increasing distance from the wall. So, where the boundary layer thickness would be larger than the movement thickness, the magnitude of clearance influence a little on the efficiency of the water pump, but the turbulence need to be taken into account. For volume efficiency, where it is close to the wall, leakage isn't severe because of fluid viscosity. But with increasing clearance the leakage become serious. If big the clearance is too much, tne leakage will greatly influence on the efficiency of the water pump.

That the boundary layer theory was applied to the normal clearance of impeller shroud can't only explain the reason that the normal clearance magnitude of impeller shroud directly influence on the performance and efficiency of water pump, but also deduce the method of calculating clearance magnitude by boundary layer thickness theory which will promote the development of corresponding clearance theory in engine water pump or liquid pump, and also greatly economize manpower, material, funds and so on.

Reference

[1] Liu Huizhi, Wu Yulin. The theory of the boundary layer.China machine press, p.35-120

[2]Chen X.L., Zhang W.G., Huang Z.. Relationship of the performance of centrifugal oil pump and its similarity. Journal of Shanghai Jiaotong University， Vol 37(2003),p. 686-689.

[3]Cong X.Q., Jia Z.Q., Zhang J, et al. Flow calculation and experiment of photovoltaic centrifugal pump under weak radiation, Journal of Drainage and Irrigation Machinery Engineering, V28(2010), p.305-309

[4] Numerical simulation of internal flow through the spiral casing of centrifugal pump,Journal of Jiangsu University, V25（2004）, p.185-188

[5]Cui Baoling.Numerical simulation and theoretical analysis of high-speed centrifugal pump with inducer. Hangzhou: Zhejiang University(2006)

[6]Chen naixiang. Centrifugal pump.China machine press,(2003),p.68-76

[7] Fan Zheng-xiang. Test unit for protector's performances of electric submersible centrifugal pump[J]. Journal of Xi'an Petroleum Institute, V12(1997), p.37-38

[8] Daniel B. Blanchard. Macroscale and microscale fluid mechanics in rotary pumps. Utah.:University of Utah(2007)

[9] Daniel baun. Hydrodynamic forces in centrifugal pump and compressor impellers in volute casings:measurements using magnetic bearings and CFD simulations. Virginia: The university of Virginia(2002)

[10] Eng J. Fluids Effect of Surfactant Additives on Centrifugal Pump Performance[J]. Journal of Fluids Engineering,, V128(2006), p.794-799

© (2012) Trans Tech Publications, Switzerland
doi:10.4028/www.scientific.net/AMM.164.371

Pumping underground extended-range application practice and process analysis with mechanics

LiJun Qiu [1, a] Jia Yang [2,b]

Liaodong University Mechanical and Electrical College, Dandong 118003, liaoning,China

[a]qlj7710@163.com, [b]Onlyyangjia@163.com

Keywords: pumping unit, extended range, underground installation, oil pump

Abstract. The extended range device for hanging above the pump to increase the pump piston stroke.The diameter of the extended range is greater than the diameter of the tubing. The extended range and pump tube connection transition tubing and excessive sucker rod. Transition tubing and excessive sucker rod length is accurate. The limit position pump piston stroke is not from the pump body and not collide with the pump with the pump. The extended-range device installation location is away from two pumping tubing length.The output rod of extended-range device does not bear the weight of the sucker rod.

Introduction

Oil extraction production improve pumping efficiency, save energy, increase efficiency and pump suction force and stroke is to study the underground extended-range motivation. Underground extended-range, namely in pumping wells pump top hanging distance increasing device. To add a distance increasing device is designed in order to increase the pump stroke. The realization of short long stroke pumping unit work.

Extended-range device is a method of increasing pump stroke device. Extended-range device in use when the extended-range device placed in the underground. It is in the oil pumping underground installation position is closely located above the pump. The general situation and pump relative distance in two to three of root sucker rod distance. As a result of extended-range device is installed in the wells, so the extended-range device above the oil pumping rod movement unchanged original. Which does not increase the original sucker rod load [1]. Underground installation of extended-range device is another advantage can reduce the distance increasing device by the pulling force. The increasing range of the output rod load of sucker rod weight. Extended-range device can improve the pump piston stroke. Particularly suitable for short stroke pumping unit. Short stroke of the pumping unit can realize long stroke work. No change in pumping unit stroke condition can improve the unit time of extraction fluid volume. Reducing the unit output power consumption [2].

Sucker rod with extended-range device is the increasing range of the outer working barrel connected with an oil pumping pipe. Extended-range device power input rod of the upper pull rod and at the top of the sucker rod connection. Increasing range of stroke increasing mechanism will be input to the motor speed by the power output rod moves and stroke output. Power output rod and pump piston connecting pull pump piston movement. Implement pump piston stroke to increase.

Mechanical extended-range device generally adopts the gear rack transmission mechanism. Gear rack transmission mechanism has the advantages of compact structure, easy to realize. Gear rack composed of stroke increasing mechanism of extended range ratio of 2 times [3]. As a result of extended-range device in downhole applications make the gear rack working space is limited. Underground working medium is different. Gear and the rack gear transmission ratio, there must be sufficient fatigue strength and wear resistance. Therefore, special attention should be paid to the gear of the material and the processing requirements. Gear bearing requirements and the rotation frequency and gear are made of the same. Bear gear force and rotating friction. In addition to having a foreign body and bearing high pressure resistant performance. In order to ensure the service life of the device is increased.

Sucker rod hanging extended-range device and method

Sucker rod hanging extended-range device in pump wells simultaneously into the distance increasing device. To add a range-extended is nowadays well order of subsurface pump barrel, tubing, the transition pump plunger, connected with the sucker rod string, extended-range device.

Due to increasing range output rod in the assembly distance increasing device and a gear rack mechanism of the movable rack. Use of short rod connected at the output end of the movable rack. Extended length greater than a sucker rod joint length value. Extended-range device lifting alignment wellhead when first output rod joint and the lower end of the sucker rod connection. The extended-range device outer tube joint and the oil pumping pipe connection. Extended range for pipe joint connected with an oil pumping pipe after the extended-range device into the wells. Extended-range device into the outer tube joints after upper end connected with an oil pumping pipe and tubing all into the oil well. In the oil pumping pipe column under well operation is completed under the joint bolt and a sucker rod string. When docking anchor head and extended-range device in the docking docking completed. Sucker rod string operations under the well completion.

For the butt joint of anchor head and extended-range device in the docking docking, taking repeated pulling rod method, in the extended range for maximum range of travel up and down to put the oil pumping rod, observe the hook load change and sucker rod falling position, to judge the docking and extended-range device if the normal work..

To lift a sucker rod length, changing the optical lever down sucker rod to its original position.Tubing and sucker rod string operations under the well completion. Wellhead impingement distance, distance increasing device in BDC 100mm---200mm anti-collision distance. The pumping unit stroke is less than or equal to the maximum travel distance increasing, prevent the gear and the fixed rack and connection. In accordance with the normal lifting anticollision distance method for setting anticollision spacing. The connecting polished rod and sealing wellhead. Installation of rope suspension device, optical rod clamp, operations under the well completion.

Extended-range device in the completion of wells after. Try to draw the process should pay attention to the following several aspects. Hang the extended-range device of oil pumping method and normal oil pumping method for the same. Just start pumping before should pay attention to oil pumping rod with extended-range device docking docking status. Repetitive lifting sucker rod look well out of gas to determine the size of the sucker rod and the increasing range of docking status. In the setting of the sucker rod and the extended-range device docking docking right after work.

Extended-range device using related content

According to the pumping unit stroke selection using extended-range device. Extended-range device power input end of maximum travel of at least 300mm anti-collision stroke as a sucker rod on off connector in BDC anti-collision distance and in the upper dead point of the anti-loosing clamping safety distance. When the pumping unit output stroke is small anti-collision travel will increase accordingly.

According to the dynamic liquid level depth of pump diameter selection. In the casing connected oil wells extended-range device load and dynamic liquid level depth and the area of the piston. In accordance with the needs of dynamic liquid level depth checking pump load [4]. Extended range is approximately equal to the load of pump load.

Pump length selection. In a known method for the calculation of pumping unit stroke press pump length. In two a pumping piston pump barrel pump length calculation. The effective length of the pump cylinder according to the following formula:

$$L = 2S_0 + L_1 + L_2 \tag{1}$$

Type : L - pump barrel of the effective length m; S_0 - pumping unit output maximum stroke m; (as shown in Fig.1)

L_1 - Oil pumping piston length m; L_2 -the piston maximum anti-collision distance m. (about 0.1m)

In order to release in the removal of cards is 1 / 3 around the piston out of the pump barrel pump length calculation. Pump barrel length according to the following formula:

$$L = 2S_1 + 1/3\, L_1 \tag{2}$$

Type : L - pump barrel of the effective length m; S_1 - extended range output maximum stroke m; L_1 - piston length m;

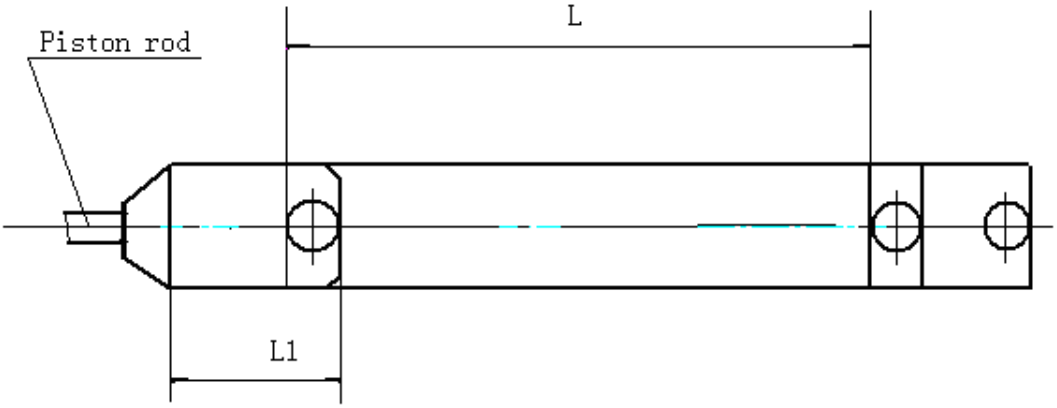


Fig 1 Schematic diagram of pump

L1 - The piston length,L - The effective length of the pump cylinder

In accordance with Eq.1 and the Eq.2 two kinds of method to get the length of the pump cylinder value larger selection as the pump. The actual selection of pump selection and calculation values close to the length [5].

In accordance with the piston does not touch the bottom valve principle with extended range to pump transition tubing and sucker rod string. Extended-range device and pump of indirect 1-2 pipes, in order to facilitate the matching of sucker rod string matching method, as shown in figure 2. Piston anti-collision distance control in general about 100mm [1].

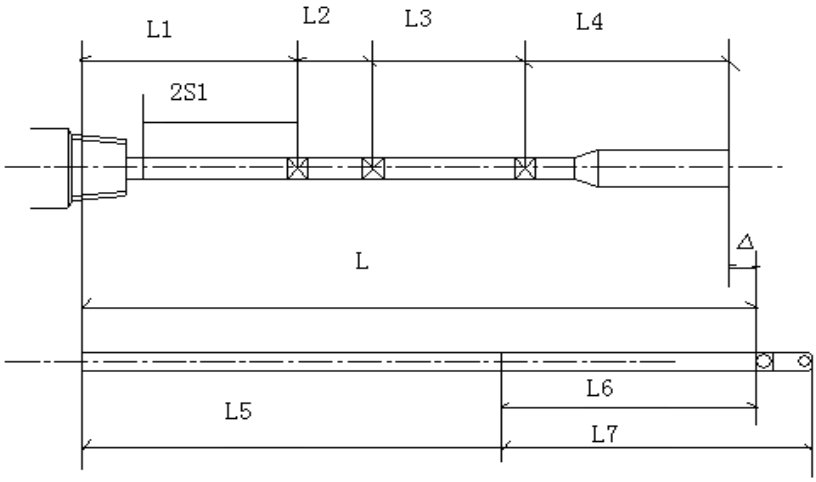


Fig 2 Tubing and sucker rod connection diagram

$2S_1$ - output maximum stroke; L_7 - pump barrel length

The pumping rod string length

$$L_0 = L_1 + L_2 + L_3 + L_4 \tag{3}$$

Type: L_1 - output maximum elongation L_2 - short length; L_3 - sucker rod length; L_4 - length of piston. -

The tubing string length

$$L = L_5 + L_6 \tag{4}$$

Type: L_5 -length of tubing; L_6 - pump barrel length.

According to (3) and (4) pump rod length should be less than the total length of about 100mm tubing string. The piston of the anticollision distance of.

According to the path is greater than the outer diameter of docking anchor other down hole tool. When the well in a drain and other downhole tools, the path must be greater than the distance increasing device for butt anchor diameter. Ensure butt-joint device to pass.

Conclusion

Pumping unit well coupled extended-range device to increase the pump stroke. In the application of extended-range device in practice we should do the work of the following respects. We must first understand the extended-range device type. Mechanical gear rack mechanism of extended range for extended range rate is 2 times. Other computation is based on the extended range rate calculation.

Underground coupled extended-range device, pump length selection should be based on the sucker two piston pump barrel pump can not calculate the length and releaser in off the card is 1 / 3 around the piston out of the pump barrel pump length calculation. Calculated length of oil-well pump. To take a larger value as the selection of pump length.

In the distance increasing device and the oil pump is arranged between the tubing and sucker rod string, the extended-range device output lever in BDC, the anticollision distance control in 100mm.

Underground coupled extended-range device of sucker rod joint anchor head and the increasing range of docking docking to multiple pulling rod ensure docking. Wellhead extraction anticollision spacing when taken with normal impingement from the same method of operation. But it should be adopted to reduce the distance of each extracted in order to ensure the normal gear rack and pinion.

Reference.

[1] Yumen Petroleum Administrative Bureau" sucker" compilation group. Oil pumping. Beijing: petroleum chemical industry press. 1976

[2] Qiu Lijun, the oil well pumping unit distance increasing device application and effect analysis. Jiangxi: Nanchang Hangkong University press. 1998.12

[3] Yi Su-jun, QIU Li-Jun . Pumping downhole extended-range device design and analysis. Nanchang : East China Jiaotong University. 2002, 4: 68-70 (in Chinese)

[4] Qiu Lijun, Yang Jia, Liu Ying, elongated rack processing method and practice, Advanced Materials Research v.146-147p650

[5] Yang Jia, Qiu Lijun, pumping underground extended-range research and practice of Advanced Materials Research v.146-147p687

© (2012) Trans Tech Publications, Switzerland
doi:10.4028/www.scientific.net/AMM.164.375

Fit Clearance of Impeller to Turbocharger Performance Influence with Mechanics Properties

Suying Xu [1, a] Lijun Qiu [2,b]

[1] Liaodong University Mechanical and Electrical College, Dandong 118003, liaoning,China

[a]Xusuying0002@163.com, [b]qlj7710@163.com,

Keywords: Impeller shaft structure, impeller. gap, sports performance

Abstract: The fit clearance between the impeller and the impeller shell directly affect the characteristics of the turbocharger. Assembly dimension chain is the basis of the design and analysis of workpiece size.Reducing the fit clearance of the impeller and the impeller shell can improve the booster effect. The impeller of the small inertia is beneficial to increase the rotation speed of the impeller and the impeller rotation stability requirements.The turbocharger of installation small inertia impeller is characterized by small size. Followed by its supercharged performance.

Introduction

Exhaust gas turbocharger as an energy-saving, environmental protection, efficiency of engine auxiliary air intake device has been a great attention. Turbocharger engine in various applications are obtained the remarkable effect. Turbocharger application practice shows, engine turbocharger after installation. Raise power of engine, mechanical efficiency, emission of engine exhaust gas concentration reduced. In engine output high power while improving the combustion rate of fuel.
Exhaust gas turbine supercharger power input is completely using the exhaust discharged from the engine as the power source. It is not attached to any other sources of energy. Turbocharger is the best example of engine exhaust utilization. Turbocharger is the biggest characteristic of high speed. That is to say in the turbocharger in the working process, the impeller shaft and the impeller of high speed is its working characteristic. Change and control of turbocharger power input is further improving turbocharger performance and adaptability of efficient way [1].

Turbocharger impeller structure and analysis

Figure 1 is the turbocharger impeller assembly drawing. Exhaust gas as the active impeller impeller. It and the turbine casing exhaust machine work unit. It works in high temperature environment. The impeller is directly in contact with the exhaust gas of the engine [2]. So the impeller is heat resistant alloy for casting. After forming the impeller on the blade outer contour processing. Impeller hub, leaf surface and leaf are not processing. The impeller and shaft prior to welding impeller processing and coaxial precision of welding and subsequent finishing can produce an effect. Impeller is machined in the impeller and shaft welding after. Due to the turbine shaft assembly is in the turbocharger rotor. Turbine shaft rotation speed is little criterion tens of thousands to hundreds of thousands of more than 10 million turn, turn. For a small moment of inertia of the rotor, impeller speed can reach over 300000 turns per minute. Impeller of high speed, rotational balancing requirements. The impeller shaft component can be seen the impeller is the main factor affecting shaft dynamic balance.

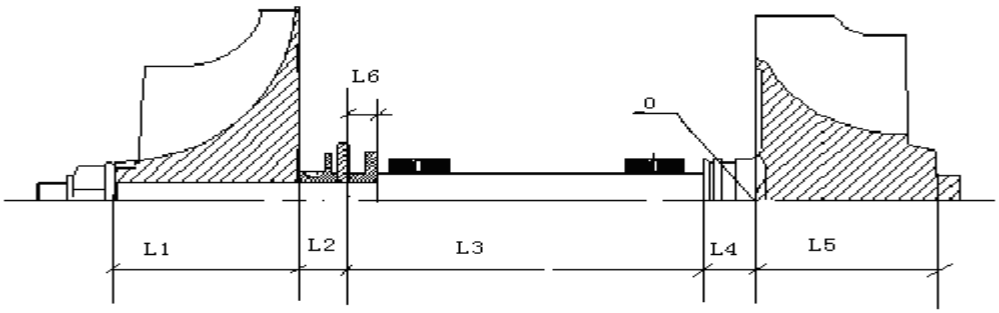


Fig .1. Turbochargers are axle assembly drawing

The impeller shaft is in accordance with the flexible shaft working condition design. Shaft speed should be greater than and close to the first order critical speed. The general and the rotational speed of the shaft is 1.4 times higher than the first critical speed. At the same time, do not close to the second critical speed. Typically taking the shaft speed is less than 0.7 times the second critical speed [3].

In the flexible shaft in the process of starting, speed from 0.8 to 1.4 times the first order critical speed. Because the transition time is short, so the shaft at the instant of resonance is tending to rotate smoothly. The shaft material damping characteristics for the elimination of the adverse effects of instantaneous resonance plays a very important role.

The impeller shaft comprises two portions of the impeller and shaft. From the end of the starting shaft diameter decrease gradually. Maximum diameter of the shaft in the welding interface. Minimum diameter of impeller to install office. The shaft intermediate section is bearing mounting section. The smallest diameter of axis and the middle section diameter is larger. Shaft fracture easily occur during this transition. Measures should be taken to reduce the stress concentration.

For variable cross section control input power booster. Attention should be paid to in the regulation of input air intake do not let the shaft speed of long residence time in the resonance region.

The impeller assembly gap analysis

Turbocharger impeller assembly clearance affects the shaft two impeller and housing clearance. The fit clearance of turbocharger performance will have a direct impact. The turbocharger has two separate assembly relationship. A shaft assembly of parts size relation. A body casing assembly dimensional relation. The two assembly is interconnected. Formation of axial size determines the impeller and the shell of the gap. Bearing radial clearance determines the impeller to rotate smoothly.

The impeller and the shell space is determined the main factors affecting the efficiency of turbine supercharger. At the same time influence turbocharger performance. As the heat balance and boost efficiency. Bearing clearance determines the impeller rotation stability. As the shaft rotates in the radial runout and axial transmission. Figure 2 shows the turbocharger assembly drawing. The shaft is composed of two radial sliding bearing and a thrust bearing. These two types of bearings are mounted on the intermediate casing. And the intermediate connecting only one thrust bearing fixing support base. Therefore, the impeller axial size and intermediate position can be defined. This size can also determine the exhaust impeller position. Exhaust gas turbine from the location of the thrust bearing and a radial bearing location determination. Exhaust casing and the intermediate body after installation will determine the impeller and the casing clearance.

Another way of assembly relationship is the compressor impeller and the shell of the fit clearance of assembly loop. The direction of the parts are mounted on the other end of the shaft. Parts of shaft end sealing ring and an impeller. Effect of impeller and casing clearance is thrust bearing axial size and the sealing ring size, the impeller machining dimension and shape precision.

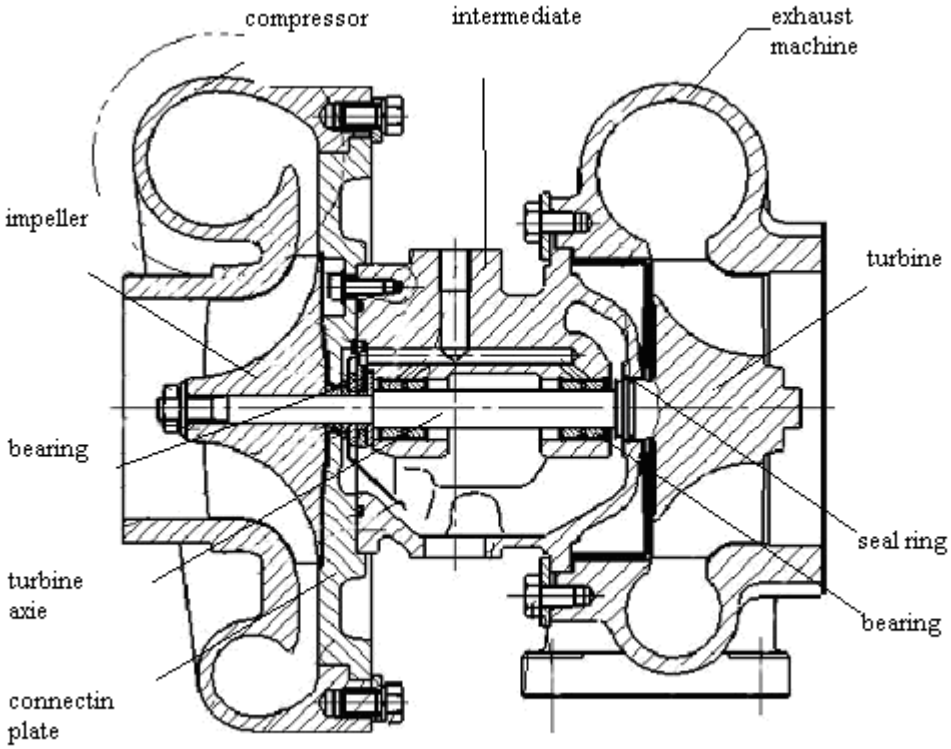


Fig .2. Turbocharger assembly drawing

Turbine casing and impeller mounting assembly dimension chain [4]. As shown in figure 3. Turbocharger parts are made from various parts manufacturers to provide. Especially in the turbocharger production of relatively concentrated areas have formed a specialized parts manufacturing and production. Parts and components production has been formed by the various specialized manufacturing plant pattern. Have the production license of whole plants no longer depends on the overall processing mode of production but the professional collaborative approach to production. The machining quality of the parts can completely meet the requirement completely interchangeable assembly method.

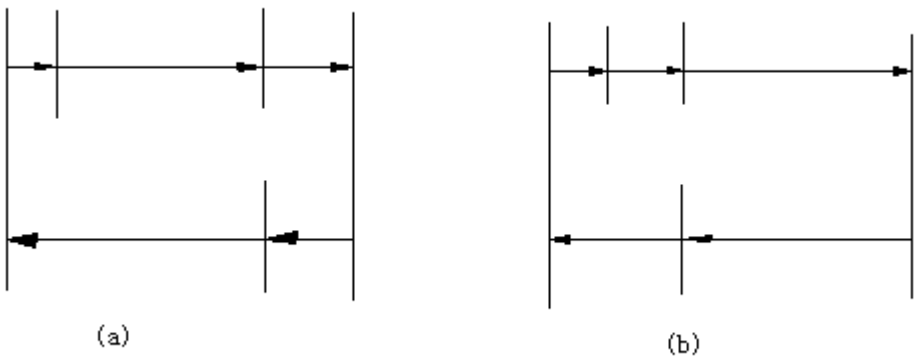


Fig. 3 .Diagram of assembly dimension chain

From the turbocharger impeller assembly consisting of two dimensional relationship analysis. The impeller assembly and housing clearance is basic requirement. According to the impeller axial positioning analysis. The two wheel assembly dimension chain can be discussed separately. Fig. 3 (a) is the compressor end of assembly dimension chain. Fig. 3 (b) gas terminal assembly dimension chain. As can be seen through the assembly dimension chain. Turbocharger impeller and casing assembly relation is simple. In a small number of workpiece. Theory of assembly dimension is easy to control. Reduce the fit clearance between impeller and the casing is helpful to improve the turbocharger performance.

The impeller and the shell of the clearance between the impeller shape determination and improvement

The impeller and the shell clearance selection has control over a relatively large range of values. With the gap value selection is not matching shell collision as the premise. The assembly relationship can be calculated from the assembly after the impeller and the casing with the upper and lower deviation. Design of the minimum size is larger than the shell processing and the impeller with dimension deviation on. It can guarantee that the impeller in the process of rotation does not contact the shell. Small impeller end can control the gap is the original gap value of 1 / 4. That the small end contour and the shell of the gap is maintained in 0.05-0.1mm. Impeller end is positioned within the housing. From the working drawings can be processed into a small impeller end face contour and the shell with the same required shape. The control section of the clearance can reach the intake requirements [5]. Impeller outer contour and the shell of the gap should be used in large space. In order to facilitate the turbocharger inhaled gas out of.

By reducing the diameter of impeller and reduces the hub quality design method. With small inertia, reducing impeller impeller rotational resistance. Small inertia wheel small moment of inertia balance sensitive coefficient. Therefore the small inertia can be used to improve the impeller impeller speed method to improve the performance of turbocharger.

Conclusion

Exhaust gas turbocharger impeller structure of a direct impact on the shaft bearing, shaft parts installation and assembly clearance. The contour and the shell of the clearance decreased properly can reduce the diameter of the impeller. The purpose of reducing impeller inertia.

Turbocharger exhaust gas engine and compressor impeller and the shell of the mounting clearance through parts of the processing requirements are effectively reduced.

The impeller assembly dimension chain through the intermediate shell thrust bearing on determining respective assembly relationship. A simplified assembly dimension chain of interconnected size relation of clear. The calculation results show that the gap between the impeller and the shell can be reduced.

In reducing impeller and housing gap state. By decreasing the small impeller end and the shell of the gap. Improving turbocharger efficiency.

Reference

[1]Lijun Qiu, Restruction of Turbosupercharger's design exploration,Advanced Materials Research Vols(2010)102-104p60-63

[2] Northwestern Polytechnical University, mechanical principles and teaching and research compiled mechanical parts, Mechanical design, People's Education Press ,1979.9,491-492 (in chinese)

[3] Urbocharger Co., Ltd. of Liaoning. Supercharger instruction manual, 2000.5

[4] Chen LongDe,Interchangeability and Measurement Technology, Dalian University of Technology Press.1993.12(in chinese)

[5] Lijun Qiu, Jia Yang,SuYing Xu,The Analysis and Design of Tutbocharger Thrust Bearing ,Advanced Materials Research Vols(2011)308-310p1333

© (2012) Trans Tech Publications, Switzerland
doi:10.4028/www.scientific.net/AMM.164.379

Finite Element Modeling and Stress Analysis for Planetary Gear with Thin Rim

Jiafeng Huo[1,a], Jun Zhang*[2,b] and Yimin Song[1,c]

[1]School of Mechanical Engineering, Tianjin University, Tianjin, China

[2]School of Mechanical Engineering, Anhui University of Technology, Ma'an'shan, China

[a]huojiafeng1988@163.com, [b]junzhang@ahut.edu.cn, [c]ymsong@tju.edu.cn
*Corresponding Author: Jun Zhang E-mail: junzhang@ahut.edu.cn

Keywords: finite element, stress, planetary gear, thin rim

Abstract: In this paper, a sophisticated and a simplified parametric 3-D finite element model for helical planetary gearing were developed sequentially with the help of ANSYS APDL. Based on the proposed two models, the meshing characteristics of planetary gear were analyzed and the simulation results were then compared. The comparison indicates that the simplified finite element model is capable of evaluating the gear stress with satisfactory accuracy. Therefore, an investigation on effects of primary design variables on gear stress and strain was conducted on the basis of proposed simplified finite element model. The investigation reveals that the tooth width affects the meshing characteristics mostly, followed by the factors of rim thickness, helix angle successively.

Introduction

Planetary gearing with thin rims are widely used in aeronautic and marine industries with the purpose of achieving more compact volume and lighter overall weight. Numerous investigations mentioned that reducing the rim thickness of gear may arise the rise of bending stress and premature fatigue of the transmission [1-5]. However, fewer of present researchers have explored the effects of rim thickness on gear strength. Among them, Tengjiao Lin[6] analyzed the effects of gear rim on stress and strain by using a 3D finite element model, respectively. The photoelastic experiments validated that the tooth root bending stress increased dramatically when the rim thickness reducing to a certain value. Shen and Liu [7, 8] also presented a finite element model to study the stress and strain in thin-rimmed gears. Similar investigation can be found in the publications of Kahraman[9,10].

Considering the analytical method cannot figure out the stress distribution of gear mesh, a finite element model has to be proposed to evaluate the stress and strain of planetary gear with thin rim as an alternative way.

In this paper, a parametric 3-D finite element modeling method for helical planetary transmission is proposed with the aid of ANSYS APDL. With the proposed method, a sophisticated and a simplified FE model are developed, based on which the stress analysis is conducted and the effects of rim thickness as well as other structure parameters on planetary gear stress/strain are further analyzed.

Finite Element Modeling

The process of finite element modeling for a helical gear and planetary transmission can be described as followings:

(1) The profile of a helical gear tooth is divided into several segments: the involute, the tooth root fillet, transition curve of tooth root, fillet of tooth top. Then, each curve segment is discretized into key points with corresponding coordinates and represented by a B-spline curve drawn with BSPLIN code.

(2) By mirroring the above B-spline, the profiles of single tooth can be generated.

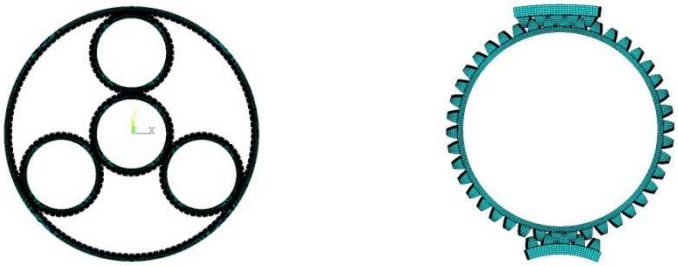
(3) By precisely controlling node location and number, middle nodes can be filled among the tooth profile on each side.

(4) With coordinate transformation, the nodes along the gear axis can be generated.

(5) Generate hexahedral elements with above nodes according to their spatial positions.

(6) Array the finite element model of single tooth along the circumferential direction and merges coincident nodes.

Following above steps, a 3-D finite element model for helical gear is obtained. And with the same method, a finite element model for helical planetary gearing can be developed according to the kinematic relationships between each individual gear. The parametric finite element model for a helical planetary transmission is shown in Fig.1 (a).



(a) sophisticated model (b) simplified model

Figure 1. Finite element model of helical planetary gearing

The above sophisticated model for the planetary transmission claims a large number of nodes and elements. Thus, it is time-consuming when conducting a loaded tooth contact analysis (LTCA). Considering the above problem, a simplified finite element model is further developed on the basis of sophisticated model. The simplified model is shown as Fig. 1(b), which only includes teeth in meshing zone of sun gear.

Finite Element Analysis

A. Comparison between two different models

By adding corresponding boundary conditions to the developed finite element models, the stress and strain of each gear can be obtained. Table 1 demonstrates the stress and strain distribution of planetary gear in each model.

Table 1. Calculation results of two finite element models

	σ_{rmax}	λ_{rmax}	σ'_{rmax}	λ'_{rmax}
sophisticated model	87.1[Mpa]	0.011336[mm]	13.600[Mpa]	0.08952[mm]
simplified model	95.9[Mpa]	0.011278[mm]	13.601[Mpa]	0.08 864[mm]

Herein, σ_{rmax} and λ_{rmax} denote the maximum Von Mises stress and the maximum displacement of planetary gear, while σ'_{rmax} and λ'_{rmax} denote the maximum Von Mises stress and the maximum displacement of planetary gear rim, respectively.

From Table 1, it can be observed that the calculation error between two models are 10.2%, 0.5%, 0.022%, 1% accordingly. Obviously, the calculation results are very close except a slight difference in the maximum stresses of planetary gear. This confirms the thought of using simplified finite element model to investigate the effects of design variables on meshing characteristics with the aim of shortening computation time.

In addition, Table 1 indicates that the distribution of stress in gear rim is much smaller than that of gear mating zone. However, attention should be paid to the deformation of gear rim because it is very close to that of gear mating zone.

B. Influence of parameters and orthogonal test

Further investigation reveals that the rim thickness δ, the gear width b and the helix angle β have the most distinct effects on meshing characteristics in planetary gear transmission. Therefore, an orthogonal test is conducted to figure out the effects of above parameters on gear stress and deformations of planet gear with thin rim.

Before conducting an orthogonal test, design variables and their levels must be designated. Here, we choose three design variables and each of them has three levels. The variables and their levels are shown in Table 2.

Table 2. Variables and their levels

Levels	Variables		
	δ (rim thickness)	b (width)	β (helix angle)
1	5mm	10mm	15°
2	10mm	15mm	20°
3	15mm	20mm	25°

According to the test number, we select table $L_9(3^3)$ to do the orthogonal test. With the proposed simplified finite element model, the stress and strain distribution can be determined. The analysis results are listed in Table 3.

Table 3. Analysis results

Test index	Parameters	Variables		
		δ	b	β
σ_{rmax}	Range	21.131	110.031	17.829
	Best combination		$\delta_3 b_3 \beta_3$	
λ_{rmax}	Range	0.005239	0.010172	0.000765
	Best combination		$\delta_3 b_3 \beta_3$	
σ'_{rmax}	Range	0.860	15.767	0.429
	Best combination		$\delta_1 b_3 \beta_1$	
λ'_{rmax}	Range	0.004941	0.008246	0.000684
	Best combination		$\delta_3 b_3 \beta_2$	

From Table 3, it can be conclude that when maximum Von Mises stress is chosen as a test index, the gear width b has the strongest influence on σ_{rmax}. By sorting ranges of three design variables, we can conclude that the sequence order is $b > \delta > \beta$.

Similarly, according to the value of ranges of other test indexes, the sequence orders are as follows: $\lambda_{rmax}: b > \delta > \beta$, $\sigma'_{rmax}: b > \delta > \beta$, $\lambda'_{rmax}: b > \delta > \beta$.

The smaller the values of stress and deformation are, the better the level combination is, so that according to the order σ_{rmax}, λ_{rmax}, σ'_{rmax}, λ'_{rmax}, the best level combinations are respectively $\delta_3 b_3 \beta_3$, $\delta_3 b_3 \beta_3$, $\delta_1 b_3 \beta_1$, $\delta_3 b_3 \beta_2$. Levels of each variable are not all the same, so by comprehensive consideration, we choose $\delta_3 b_3 \beta_3$ as the best level combination.

Conclusions:

1. A parametric finite element method for helical planetary gear transmission is proposed with the help of ANSYS APDL, which can evaluate the stress and strain distribution of gear with thin rim in a quick and precise manner.

2. The calculation difference between the proposed sophisticated and simplified finite element model are quite small, thus the simplified one can be used to analyze meshing characteristics of planet gear with higher efficiency.

3. According to the orthogonal test, influence sequence of design variables on stress and strain of tooth and rim are gear width, rim thickness, helix angle.

Sponsored by NSFC Grant No. 50905122

REFERENCES

[1] Bodas A, Kahraman A. Influence of carrier and gear manufacturing errors on the static load sharing behavior of planetary gear sets [J]. International Journal of JSME. 2004, 47, 47:908-915.

[2] Baud S, Velex P. Static and dynamic tooth loading in spur and helical geared systems: Experiments and model validation [J]. ASME Journal of Mechanical Design. 2002,124, 124:334-346.

[3] KIMDuck-Hoi, KIMJae-Hoon, KIMGi-Gwang. Random fatigue analysis of automotive bevel gear .Key Eng Materials, 2006, 326-328, 326-328: 987-990.

[4] Li S. Gear contact model and loaded tooth contact analysis of a three-dimensional thin-rimmed gear [J]. ASME Journal of Mechanical Design, 2002, 124(9): 511-517.

[5] Li S. Centrifugal load and its effects on bending strength and contact strength of a high speed thin-walled spur gear with offset web [J]. Mechanism and Machine Theory, 2008, 43: 217-239.

[6] Tengjiao Lin, H Ou, Runfang Li. A finite element method for 3D static and dynamic contact/impact analysis of gear drives. Computer Methods in Applied Mechanics and Engineering, 2007,196, 196 (9-12):1716-1728.

[7] Liu Geng, Shen Yunwen, Lin Tiancun. The modal experiment of cylindrical gears with thin rim and different arrangements of web plate [J]. Mechanical science and technology,1995,(4):89-93.

[8] Zhan Yongcai, Liu Geng, Lin Tiancun. The experimental study of dynamic stress of helical gear structure with thin rim. [J]. Journal of Aerospace Power, 1995, 10 (4): 391-395.

[9] Kahraman A, Kharazi A A, Umrani M. A deformable body dynamic analysis of planetary gears with thin rims [J]. Journal of Sound and Vibration, 2003, 262: 752-768.

[10] Kahraman A, Vijayakar S. Effect of internal gear flexibility on the quasi-static behavior of a planetary gear set [J]. ASME Journal of Mechanical Design, 2001, 123: 408–415.

© (2012) Trans Tech Publications, Switzerland
doi:10.4028/www.scientific.net/AMM.164.383

Research on Pre-slip Gait Mechanical Contributions and Gait Self-balancing Mechanics during Walking

HaiLong Su[1, 2a]*, DaWei Zhang[1,b]

[1]School of Mechanical Engineering, Tianjin University, Tianjin, China

[2]School of Mechanical Engineering, Tianjin University of Science & Technology, Tianjin, China

[a]suhailong@tust.edu.cn, [b]medzhang@tju.edu. cn, *corresponding author

Keywords: slip and fall, gait self-balancing, biomechanics, balance, locomotion, perturbation

Abstract. Walking is a complex dynamic task that requires the regulation of the whole-body angular momentum to maintain dynamic balance while performing walking subtasks such as propelling the body forward and accelerating the leg into swing. To investigate the characteristic of slips and falls during gait self-balancing, a method was proposed that could better understand the effects of pre-slip gait response biomechanics on the risk for falls. A new segmental model of the human body was developed and this model would be used continuously measured locations from nearly 85 points on the body to produce a dynamic postural record of human movement. The muscles surrounding the hip were found to be most important in maintaining control of the trunk and preventing collapse in response to the forward perturbations (FP).

Introduction

Gait is one of the most common forms of human movement, yet the underlying neurological and biomechanical processes by which this movement occurs are complex and individualistic. Nowadays, falls are one of the largest public health problems among elderly people due to the high morbidity, mortality and costs for the family and society. The fact that we as humans are bipeds and locomote over the ground with one foot in contact(walking), no feet in contact(running), or both feet in contact(standing) creates a major challenge to our balance control system. Proactive control of truck verticality in sagittal and frontal palnes is important because it stabilizes the head, which contanis visual and vestibular sensory references. The main risk factors for slips and falls in the population are related to functional limitations, increasing age, muscle weakness, history of falls, use of psychotropic drugs, the female gender, environmental risks and visual deficits. Quantitative study of sudden off-balance conditions is relevant for understanding the events preceding falling and the functioning of short-latency postural restabilization mechanisms.

The inherent instability involved in human locomotion results from a relatively small base of support, long single support phase, and the observation that 2/3 of the body's mass is located in the head_/arm_/trunk (HAT) segments [1]. Successful locomotion requires three essential elements, (a) the ability to generate and maintain fundamental locomotor patterns appropriate for moving toward an intended destination; (b) maintenance of basic dynamic equilibrium between a shifting center of mass (COM) and a constantly changing base of support; and (c) the ability to change locomotor patterns in response to external or internal inertial changes that threaten dynamic equilibrium [2].

Much research has been done on gait and balance control in the older adult population. Under summary of done work, the dynamic model of the lower limb with Kane equation was proposed and gave the calculation method of the amendment maximum slipping friction coefficient during the process of the body balance adjustment, slip and fall response factors.

Methods

The lower limb are composed of hipbone, thighbone, patella, shankbone, fibula and foot bones, including the three largest joints of human body(hip, knee and ankle joints). The human hip joint is the largest and one of the most stable joints and also is a typical ball mortar joints. During walking the

inverted pendulum model explained the dynamics of the balance of HAT in both the A/P and M/L directions. Here the model includes the couple due to the acceleration of the weight-bearing hip as well as gravitational perturbations. The exclusive control of A/P balance and posture are the hip extensors and flexors, while in the M/L direction the dominant control is with the hip abductors with very minor adductor involvement. At the ankle the inverted pendulum model sees the COM passing forward along the medial border to the weight-bearing foot. The critical importance of the hip abductors/adductors in balance during all phases of standing and walking is evident. The separate mechanism is important from a neural control perspective and clinically it forcus major attention on therapy and potential problems with some surgical procedures. On the other hand the minuscule role of the ankle invertors/evertors is important to note.

The standard formulation for the equation of motion is,

$$\boldsymbol{\tau} = \boldsymbol{M(q)\ddot{q} + C(q,\dot{q}) + G(q)} \tag{1}$$

For n degrees of freedom: $\boldsymbol{\tau}$ is the nx1vector of generalized torques, $\boldsymbol{M}$ is the nxn inertia matrix, C is the nxl vector of coriolis and centrifugal terms, $\boldsymbol{G}$ is the nxl vector of gravity terms, and $\boldsymbol{q}$ is the nxl vector of configuration variables.

Relocating markers present in the static trial but removed for dynamic trials may have introduced error as well, especially when the remaining markers either may have moved relative to each other or when the underlying segment was not truly rigid. The errors that these discrepancies might introduce to the kinematic and kinetic measures (as well as COM determination) were assumed to be small. Another potential source of error for this model is related to segment definition vectors that are orthogonal to a plane. This planar sensitivity was particularly troublesome for the toe segments. Finally, static maker relocations that are based on noisy or otherwise unreliable trajectories have the potential to greatly impact segment definitions.

Experiment

The experimental protocol was designed to produce unexpected slip perturbations. Previous research performed using the same protocol has shown that subjects do not alter their gait from their preceding dry trials for the unexpected slip trial. Supporting this contention, the contact angle for the leading foot at heel strike was not significantly different from dry to slip ($p = 0.515$).

A laboratory study was conducted to examine gait changes associated with aging and the effect of these changes on initiation of slips and frequency of falls utilizing newly defined biomechanical parameters of slips and falls. At the beginning of the experiment, the subjects were told that they would be walking for three blocks of trials at each of their preferred slow and fast speeds, and that they might be slipped. They were told to try and recover their balance upon any slip occurrence and continue walking. Forty-eight participants(27 male and 21 female, average age 62.5 and min 60, max 72) from two groups(non-faller and five or more minor slips at least in the past year) walked around a straight track at a comfortable pace wearing a safety harness. These old people are retirees and can take care of themselves, moreover they have no other organic diseases that affect their daily walking activity.

The subjects walked at a self-selected comfortable pace that was maintained throughout data collection via a metronome. Each subject began walking at a sufficient distance from the force plate so that the self-selected pace was attained prior to the foot of the test limb making contact with the center of the force plate[6].

Table 1: Participant characteristics

	Female	Male	Age	Height(cm)	Weight(kg)
Younger	15	12	21.8(2.5)	169.5(7.5)	53.6(11.2)
Older	12	9	62.5(3.9)	162.2(6.4)	73.3(9.9)

The research included 21 older individuals aged 55 to 66 years old and 27 younger individuals aged 19 to 26 years old (Table 1). Written informed consent, approved by the University of Pittsburgh Institutional Review Board, was obtained prior to participation. Exclusionary criteria included a

clinically significant history of neurological, orthopedic, cardiovascular and pulmonary 70 abnormalities as well as any other difficulties hindering normal gait. As well as, subjects were excluded if a clinical neurological examination revealed abnormalities that might affect balance.

Subjects were first allowed to practice walking along the gait path while the starting position was adjusted such that the participant appropriately (right foot on first plate, left foot on second plate) hit each force plate with one and only one foot [7]. Room lighting were then dimmed to conceal the eventual application of contaminant onto the floor and additional practice trials were conducted. Participants were instructed to walk as naturally as possible at a self-selected comfortable pace throughout the experiment.The COM velocity in the direction of progression as reported in Winter was normalized to mean stride velocity. However, the overall shape of that graph is similar to the unnormalized, unfiltered velocity resulting from our model. In addition, the range of anteriorposterior (AP) velocity from Winter was approximately 0.35 m/s while the current model resulted in a mean AP velocity of about 0.25 m/s, well within the standard deviations from Winter's data.

Results and discussion

During initiation and termination of gait these two separate mechanisms control the trajectory of the COP to ensure the desired acceleration and deceleration of the COM. During initiation the initial acceleration of the COM forward towards the stance limb is achieved by a posterior and lateral movement of the COP towards the swing limb. Previous experimental efforts demonstrated that slip outcomes can include falls and recoveris, as expected, for lager slips. However, additonal outcomes were also observed. These additional outcomes included non-slips (slip distance<0.01 m), mini-slilps (slip distance<0.03 m), and lager slips with indeterminate outcomes where participants either sipped beyond the contaminated area but did not fall or relied on the safety support harness to an unknown degree to prevent falls. Finally, these standing posture studies have examined the effects of aging and support the hypothesis that older individuals likely respond to perturbations differently[3-5].

Therefore, a new classification for fall risk was devised based on the motion of the slipping foot. Longer and faster slips were classified as hazardous, implying an increased risk for falls, while shorter and slower slips were classified as non-hazardous. Severity classification using a 1.0 m/s peak slip velocity threshold for hazardous slips allowed all observed outcomes to be included in analyses relating pre-slip gait parameters to slip severity(hazardous or non-hazardous). Because the (COP-COM) signal is directly related to the horizontal acceleration of the COM it can be considered the error signal that the balance control system is sensing. The 'gain' of the feedback control system would alter both the magnitude and frequency of the error signal. Thus an increased gain would not only increase the amplitude of the error signal but also the frequency of the oscillations.

Six kinematic reflective markers were placed on the skin overlying the base of the fifth metatarsal, lateral malleolus, lateral condyle of the femur, greater trochanter of the femur, and acromion process of the scapula. A reflective marker was also placed on the force plate to register plate movement and serve as the point of reference for transformation of local center of pressure (COP) coordinates to global kinematic coordinates. The digitized position data for all markers were then low-pass filtered between 5 and 9 Hz using a 4th order dual-pass Butterworth filter. Kinematic data were collected at 120 Hz for a 6s duration with each of the four cameras synchronized with the MATLAB system. Each marker was then digitized for the entire collection period including the stride before and after the stance phase on the force plate. Optimal filter frequencies were determined for each force signal based on power spectral analyses wherein 79.6% of the raw signal was retained after the filtering process. Linear and angular position, velocity and acceleration data were then calculated and exported for further analysis.

One research group has questioned the validity of a inverted pendulum model. Unfortunately their rationale was flawed: they compared the full-wave-rectified shear force with a range of anthropometric measures on their subjects and found no correlation. They gave no mathematical reason that these passive anthropometric measures should be correlated with the shear force magnitude.

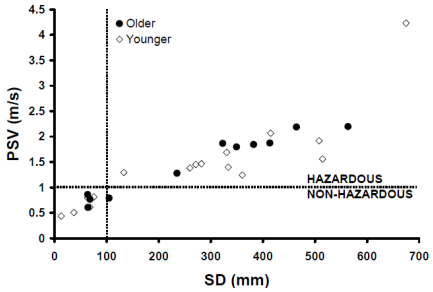


Figure 1: Relationship between peak slip velocity (PSV) and slip distance (SD)

In Figure 1, the vertical dotted line indicates a potential SD slip severity threshold of 100 mm proposed in the literature while the horizontal dotted line illustrates the actual PSV slip severity threshold of 1.0 m/s used for this report. Only one trial would have been classified differently using the two different thresholds. As the nervous system there is a big delay from the feedback received (0.15 ~ 0.25s), the human foot center of pressure (COP, Center of plantar) and COM control coordination between the joint stiffness is accomplished, with the stiffness control joint angle changing start immediately.

Conclusion

In addition to the effect that slips have on the sliding foot, slips also cause changes to the dynamic posture of the entire body. Thus, responses to slips combine, in a coordinated fashion, passive, reflexive, and active components of response across many body segments. An effective strategy for maintaining the postural stability of bipeds involves two phases: a reflex phase and a recovery phase. During a disturbance, the biped induces an increasing angular momentum $\boldsymbol{H}$ to fall along the direction of the disturbance force to maintain controllability. Although a primary goal could also be objectives. Clearly, these smaller slips are often not perceived nor do they appear to require active response: passive or reflexive responses correctly compensate for these slips and gait continues naturally.

Acknowledgements

Funding for this project by Natural Science Foundation of Tianjin(No. 11JCYBJC05700) and the National Natural Science Foundation (No. 50975204).

References

[1] D.A. Winter, Human balance and posture control during standing and walking, Gait and Posture. 3(1995) 193-213.
[2] E.T. Hsiao, S.N. Robinovitch, Biomechanical influences on balance recovery by stepping, Journal of Biomechanics.32(1999) 1099-1106.
[3] A.N. Droegemeier, K.A. Ensz， D.M. Hildebrand, et al, The relationship of plantar flexor strength to functional balance in older adults, in Proceeding of the 5th annual GRASP symposium ， Wichita State University, America, 2009, pp.90-91.
[4] M.A. Rongfei, Biomechanics-based responsive balance recovery animation, Journal of Computational Information System. 6(2011) 2087-2095.
[5] T. Bhatt, J.D. Wening, Y.-C. Pai, Adaptive control of gait stability in reducing slip-related backward loss of balance, Exp Brain Res.170(2006) 61-73.
[6] R. Ferber, L.R. Osternig, M.H. Woollacott, et al, Reactive balance adjustments to unexpected perturbations during human walking, Gait and Posture.16(2002) 238-248.
[7] B.E. Maki, W.E. Mcllroy, Control of rapid limb movements for balance recovery: age-related changes and implications for fall prevention, Age and Ageing.35-S2(2006) iil2-iil8.

© (2012) Trans Tech Publications, Switzerland
doi:10.4028/www.scientific.net/AMM.164.387

Oscillatory Behavior in a Nonlinear Gyroscopic System with Mechanics

Chunhua Feng[1, a], Yuanhua Lin[2,b]

[1] Guangxi Normal University, Guilin, China, 541004

[2]Hechi Institute, Yizhou, Guangxi, China, 546300

[a]chfeng@mailbox.gxnu.edu.cn, [b]lyh4773@163.com

*Corresponding author
Email addresses: chfeng@mailbox.gxnu.edu.cn (Chunhua Feng),
lyh4773@163.com (Yuanhua Lin).

Keyworks: nonlinear gyroscopic system, instability, oscillation

Abstract. In this paper, a nonlinear gyroscopic system is investigated. Two sufficient conditions to ensure the existence of oscillations for the system are proposed. Simulations are demonstrated for the provided results. In the study, the authors has researched the nonlinear gyroscopic system from the mechanics perspective, which will be useful in dynamic mechanical system, especially for parametric vibration. In fact, the nonlinear gyroscopic system is closely connected with mechanics, and they also influences each other during study.

Introduction

In a dynamic mechanical system, damping or stiffness can lead to parametric vibration. Therefore, parametric stability of the system is an important research topic in engineering. Liew et al. have investigated the dynamic stability of rotating cylindrical shells subjected to periodic axial loads[1].Yu and Cleghorn have discussed the dynamic instability problem of high-speed flexible four-bar mechanisms with parametric resonance induced by periodically varying mass, gyroscopic and stiffness matrices in the formulation [2]. Lin and Chen have studied the dynamic stability of spinning pre-twisted sandwich beamswith a constrained damping layer [3]. Kirillov discussed gyroscopic stabilization of a linear second order with the matrix coefficients conservative system, which is statically unstable and can be either improved or destroyed by weak damping and circulatory forces [4]. Lancasteret al. studied the strong stability of gyroscopic system. It is shown that stability is retained under a considerably weaker condition formulated in terms of the spectral radius [5]. For the case of linear potential gyroscopic systems with a degenerate matrix of gyroscopic forces is investigated by Salnikova [6]. Recently, Agafonov has discussed the possibility of stabilizing for a gyroscopic system with two degrees of freedom using non-linear dissipative and positional non-conservative forces. The stability conditions are obtained in terms of the system parameters [7]. This gyroscopic system is the following:

$$x1''+gx2'-vx1+\beta1x12x1'+\gamma1x1'3+\alpha1x12+\alpha3x1x2+\alpha2x22x2=0,x2''-gx1'-1-vx2+\beta2x22x2'+\gamma2x2'3-\alpha1x12+\alpha3x1x2+\alpha2x22x1=0. \quad (1)$$

where parameters . Terms with the factors , 0 (i=1,2) represent non-linear dissipative forces, while the factors 0 (i = 1, 2, 3) are non-conservative forces. By constructing suitable Lyapunov's functions some criteria have been given to guarantee the asymptotic stability of the solutions for system (1). Comparison with stability of gyroscopic systems, a few works deal with the oscillatory behavior analysis [8-11]. In this paper, we discuss the oscillatory behavior for system (1). By means of simplified mathematical analysis method, some sufficient conditions to ensure the oscillations of the system (1) are obtained.

Preliminaries

It is convenient to write system (1) as an equivalent four dimensional first order system as follows:

$$x1'=x2,x2'=vx1-gx4-\beta1x12x2-\gamma1x23-\alpha1x12+\alpha3x1x3+\alpha2x32x3,x3'=x4,x4'=1-vx3+gx2-\beta2x32x4-\gamma2x43+\alpha1x12+\alpha3x1x3+\alpha2x32x1. \quad (2)$$

System (2) can be expressed in the following matrix form:

$$(t)=AX(t)+B(X(t)) \quad (3)$$

where ,,
B(X(t))=.
The linearization of system (3) at origin is

$$(t)=AX(t) \quad (4)$$

Definition 1 A solution of system (2) (or (3)) is called oscillatory if the solution is neither eventually positive nor eventually negative.
Lemma 1 For , system (2) (or (3) has a unique real equilibrium point.
Proof An equilibrium point =is a constant solution of the following algebraic equation

$$x2^*=0,vx1^* -gx4^* -\beta1x1^*2\,x2^* -\gamma1x2^*3 -\alpha1\,x1^*2 +\alpha3\;\; x1^*\,x3^* +\alpha2x3^*2x3^*=0,x4^*$$
$$=0,x4^*=0,1-vx3^* +gx2^* -\beta2x3^*2x4^* -\gamma2x4^*3 +\alpha1x1^*2+\alpha3\;\; x1^*\,x3^* +\alpha2x3^*2x1^*=0. \quad (5)$$

Since 0, from (5) we hav

$$vx1^* -\alpha1\,x1^*2 +\alpha3\;\; x1^*\,x3^* +\alpha2x3^*2x3^*=0,1-vx3^* +\alpha1x1^*2+\alpha3\;\; x1^*\,x3^* +\alpha2x3^*2x1^*=0 \quad (6)$$

From (6) one can easy to get

$$vx1^*\,x3^* = \quad (v-1)x3^*\,x1^*, \text{ or } x1^*2 = v-1vx3^*2. \quad (7)$$

Noting that , then from (7) we only have 0. Hence system (2) only has a real equilibrium point .

Main result

For system (3), one can think of B(X(t)) as a disturbed team of homogeneous system (4). Noting that not only is an equilibrium point of homogeneous system (4) but also is an equilibrium point of disturbed system (3). Generally speaking, if the trivial solution of homogeneous system (4) is stable, then this stability of the trivial solution may change to instability for disturbed system (3). However, if the trivial solution of homogeneous system (4) is unstable, then this instability of the trivial solution would maintain in disturbed system (3). In other words, it does not change the instability of the trivial solution of homogeneous system (4) to stability of itself disturbed system (3). Therefore, in order to discuss the oscillatory behavior of the trivial solution of disturbed system (3), we only need to investigate the instability of the trivial solution of the homogeneous system (4). First we have

Theorem 1 If parameters ,) such that there exists at least one positive real part of the following eigenvalues

$$\lambda1,22=12(1-g2 \pm g2-12-4v1-v) \quad (8)$$

Then the equilibrium point of system (3) is unstable, and there exists an oscillatory solution of system (3). Indeed, this oscillatory solution is periodic solution if equation (8) only has two pairs pure imaginary roots .

Proof Consider the homogeneous system (4):

$$x1'=x2,x2'=vx1-gx4,x3'=x4,x4'=1-vx3+gx2. \tag{9}$$

The characteristic equation of system (9) is the following:

$$\lambda 4 + (g2-1)\lambda 2 + v1-v = 0 \tag{10}$$

The four eigenvalues of equation (10) is (8). Since there exists at least one eigenvalue has real positive part or there are two pairs of pure imaginary roots, the equilibrium point of system (4) is unstable according to the theory of differential equation, implying that the trivial solution of system (4) is oscillatory. Based on the above analysis, it means that the trivial solution of system (3) is also oscillatory.

Theorem 2 Suppose that system (1) has a unique equilibrium point. For given parameters, denoted

$$\omega 12 = 121-g2+g2-12-4v1-v,\ \omega 22 = 121-g2-g2-12-4v1-v.\ \text{Let}$$

$$A11= -12(\omega 12 -\omega 22)\omega 12 +v-12g22\omega 12 +v3\omega 12\ \beta 2+3\omega 12\ \gamma 2+\omega 12\ v\omega 22 +vg2\beta 1+3\omega 12\ \gamma 1-4g\omega 12\ (g2\omega 12\ \alpha 1+\omega 12 +v2\alpha 2), \tag{11}$$

$$A22=12(\omega 12 -\omega 22)\omega 22 +v-12g22\omega 22 +v3\omega 22\ \beta 2+3\omega 22\ \gamma 2+\omega 22\ v\omega 12 +vg2\beta 1+3\omega 22\ \gamma 1-4g\omega 22\ (g2\omega 22\ \alpha 1+\omega 22 +v2\alpha 2). \tag{2}$$

Proof The proof is based on [7]. For system (1), make the change of variables:
+ where ,
Introduce complex-conjugate variables by the formulae as follows:
, , k=1,2.
Again let , k=1,2. where is a third-order homogeneous form and
. Thus, we will have

$$u1' =i\omega 1u1+A11u12\ u1+A12u1u2u2,u2' =i\omega 2u1+A22u22\ u2+A21u1u2u1. \tag{14}$$

whereand are complex numbers. Since there is at least one, implying that the equilibrium point is unstable, and system (1) generates permanent oscillations. The proof is completed.

Computer simulation

We first fix parameters Then equation (8) only has two pairs pure imaginary roots: . Figure 1 provided three cases of the periodic oscillations for system (1) about parameters In Fig.1a,; . In Fig.1b,; . In Fig.1c,; . By Theorem 1, system generates periodic oscillation. From Fig.1a to Fig.1c, we see that the oscillatory amplitudes change very clear, while the oscillatory frequency just a slightly change. Then we fix parameters; . Let then equation (8) has positive real part roots:Let then equation (8) has positive real part roots: 0.57890.5789. Let then equation (8) has positive real part roots: 0.53400.5340. In those three cases, equation (8) has positive real part roots, the solutions of gyroscopic system are oscillatory. The more time t that passes, the amplitude gets higher (see Fig. 2a-2c).

Conclusion

This paper discusses the oscillatory behavior of the gyroscopic system. The parameters g and v play an important rule to ensure the oscillations of the system. If g>1, the oscillation indeed is periodic. If g<1, the greater the time, the higher the amplitude.

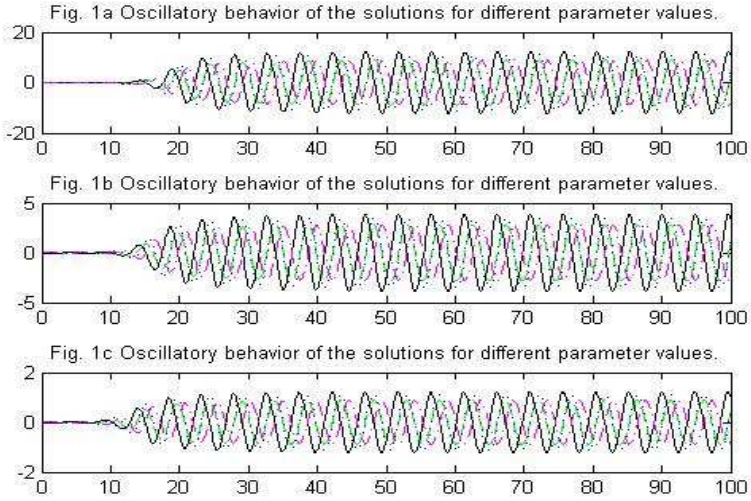


Fig.1 Fixing g=1.4, v=0.2, In Fig.1a we select ; . In Fig.1b,; . In Fig.1c,; .

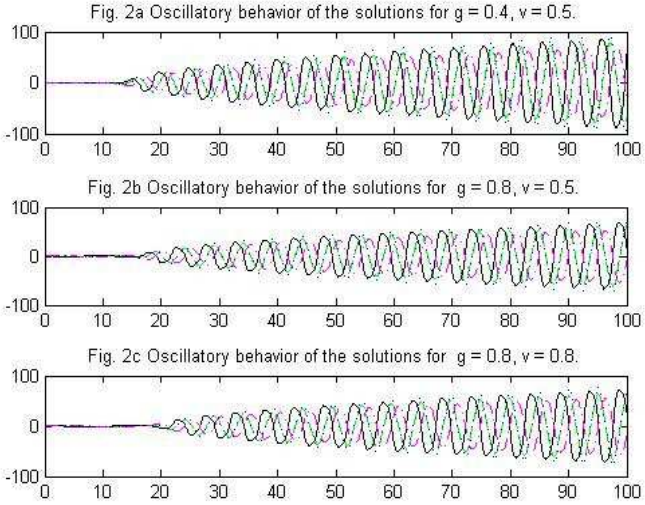


Fig.2 Fixing; . In Fig.2a the parameters g=0.4, v=0.5, In Fig.2b the parameters g=0.8, v=0.5, while in Fig.2c the parameters g=0.8, v=0.8. Where dashed line: (t), solid line: (t), dashdotted line: (t), dotted line: (t).

Acknowledgement: Supported by NNSF of China (10961005) .

References

[1] K.M. Liew, Y.G. Hu, X. Zhao, Dynamic stability of rotating cylindrical shells subjected to periodic axial loads, Int. J. Solids and Structures, Vol. 43 (2006), 7553–7570.
[2] S.D. Yu, W.L. Cleghorn, Dynamic instability analysis of high-speed flexible four-bar mechanisms, Mech. Machine Theory, Vol. 37 (2002), 1261–1285.
[3] C.Y. Lin, L.W. Chen, Dynamic stability of spinning pre-twisted sandwichbeams with a constrained damping layer subjected to periodic axial loads, Composite and Structures Vol. 70 (2005), 275–286.
[4] O.N. Kirillov, Gyroscopic stabilization of non-conservative systems, Physics Letters A, Vol. 359 (2006), 204–210.
[5] P. Lancaster, A.S. Markus, F. Zhou, A wider class of stable gyroscopic systems, Linear Algebra Appl. Vol. 370 (2003), 257–267
[6] T.V. Salnikova, The stability of linear potential gyroscopic systems, J. Appl. Math. Mech.,Vol. 70 (2006), 32–35.

[7]S.A. Agafonov, The stability and stabilization of the motion of non-conservative mechanical Systems, J. Appl. Math. Mech.,Vol. 74 (2010), 401–405.
[8] V.V. Voronin, V.V. Sazonov, Periodic motions of gyroscopic systems, J. Appl. Math. Mech.,Vol. 52 (1988) 560-569.
[9] R.J. Mcdonald, N.S. Namachchivaya, Global bifurcations in periodically perturbed gyroscopic systems with application to rotating shafts, Chaos, Solitons & Fractals, Vol. 8 (1997), 613-636.
[10] B. Herve, J.J. Sinoub, H. Mahe, L. Jezequel, Extension of the destabilization paradox to limit cycle amplitudes for a nonlinear self-excited system subject to gyroscopic and circulatory actions, J. Sound Vibration, Vol. 323 (2009), 944-973.
[11] D.N. Vadiraja, A.D. Sahasrabudhe, Vibration analysis and optimal control of rotating pre-twisted thin-walled beams using MFC actuators and sensors, Thin-Walled Structures, Vol. 47 (2009), 555-567.

© (2012) Trans Tech Publications, Switzerland
doi:10.4028/www.scientific.net/AMM.164.392

Hydraulic Cylinder Cold Pulling Processing and Mechanics Analysis

XiXi Zhang[1, a], YuJing Jia[1, b] and GuangZhen Cheng[1, c]

[1]Huzhou Teachers College, Huzhou, Zhejiang Province 313000, P.R. China

[a]646562332@qq.com, [b]jyjng@126.com, [c]chgzh169@126.com

Keywords: Hydraulic Cylinder, Cold Pulling, Cold Hardening, Mechanics Analysis

Abstract. This paper describes a method about hydraulic cylinder cold pulling processing. Take seamless steel tubes as raw materials, they are acidified and phosphates before the cold pulling to guarantee that mold and pipe have a good lubrication and have a high temperature stability during the cold pulling processing, thus the cold pulling process can be stable . When the seamless steel tubes are brought into the drawing processing, a process provides with a Hydraulic pulling machine, matches special cold pulling die, then they occur plastic deformation uniformly and satisfy the dimension requirements ,whose accuracy can reach IT7~IT8 and the surface roughness is Ra0.4 ~ 0.6. At the same time, it causes producing cold hardening, which makes the material strengthened. Compared with the traditional processing methods, drawing processing can remarkably improve the production efficiency, ensure product quality and improve the qualification rate of finished products.

Introduction

Hydraulic cylinder is a part, which has a high processing precision and with a great amount of processes. The traditional processing method is that seamless steel pipe brought into the process includes the rough, finishing, quenching and tempering treatment, chrome, honing. There exist some problems, such as the complex process, a large of workload, low material utilization and high processing cost. Therefore, there is no denying that adopting the advanced scientific technological method to reduce production cost. At present, the cylinder processing usually assume the following two processes, one is boring and rolling process at traditional hardening and tempering, the other is advanced drawing and honing process in recent years. The former has some disadvantages, reasons for it includes the low usage of material, the low production efficiency, and the high processing cost. However, the latter makes great difference on improving the quality of the fluid pressure cylinder and making the production efficiency go up, which improves the whole efficiency and realizes a processing without scraps [1]. It is widely used because of the high production efficiency, good surface quality, the high strength, no chips and high utilization ratio of material. Such as cold-drawn seamless steel pipe, cold pulling stainless steel tubes, cold-drawn round steel, cold-drawing tube, all kinds of these have a broad market , especially hydraulic cylinder processing. Consider the former process ,which is complex , low efficiency and high energy consumption, so drawing process replace of the original method can improve production efficiency, ensure product quality, improve the qualification rate of finished products [2] Mechanical properties.

Cylinder Cold Pulling Process

Cold pulling machine is the main equipment of production line, which is mainly composed of a main oil cylinder, a rack, a clamping mechanism, a feeding mechanism, a discharging mechanism, the core rod, mold, pumping component and so on. The main spare parts, such as pumps, valves, seals should be used in domestic or imported brands that are more appropriate, in order to improve the service life of equipment and stability. The best selection to choose frame is prestressed structure, ensuring that the frame integral stiffness and stability to avoid increasing stroke blindly ,then make pressure bar instable in that case [2]. When the seamless steel tubes are brought into the drawing processing, a process provides with a Hydraulic pulling machine, matches special cold pulling die, then they occur

plastic deformation uniformly and satisfy the dimension requirements, whose accuracy can reach IT7~IT8 and the surface roughness is Ra0.4~0.6. At the same time, it causes producing cold hardening, which makes the material strengthened. The schematic diagram of cold pulling deformation was shown in Fig. 1.

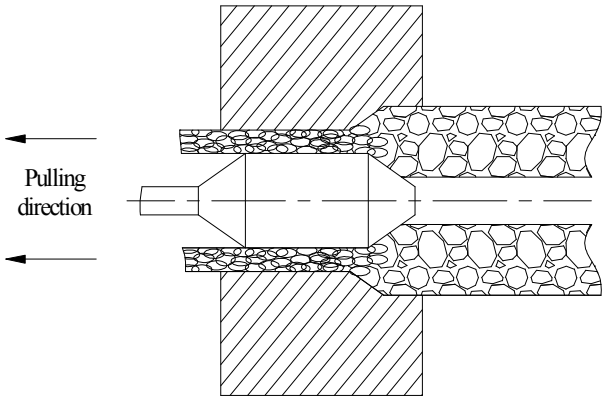


Fig. 1 The cold pulling deformation diagram

Cold Pulling Pretreatment. In order to improve the plasticity of materials and reduce deformation resistance, cold pulling materials shall be in annealed state so that can prevent the cold pulling changing shape unequally, even cracking to be scrapped. Material is generally 35 steel or alloy steel 27SiMn, cold-drawn before, their hardness is HB140~160. Preprocessing consists of pickling, neutralizing tank, water tank, phosphates slot, saponification bath, heating system and so on, in addition, flushing the work piece is an important step as well. To this issue, the pickling tank can be inlaid with marble or simple resin treatment. Concerned about the problem of corrosion of acid tank, preferably configured mist processing system, besides, can also consider air curtain isolation or drainage with lime water absorption. Neutralizing tank can use lime water or alkaline water, which can reduce pollution and conserve water. For lubrication and anti-corrosion phosphates, saponification bath should be provided with a heating device, the general heating temperature was 65 ~ 80°C [3].

Lubricating. During the process of cold pulling, mold and pipe must be maintained with good lubrication. Lubricant has high temperature and high pressure stability that guarantees the stability of cold pulling process. Therefore, the raw material should be deal with phosphates process. Phosphates solution is the ratio of ZnO: 23~26 g/L, H3PO4: 40g/L, HNO3: 22~24 g/L, and temperature of itself is 75 degrees during phosphates process for about 30 ~ 40 min. Based on it, pipe's surface forms with a strong adsorption capacity of the phosphates film. Further with concentration of 5~ 8 g/L hard acid sodium solution or the concentration of 80~100 g/L soap water soaking for 10 min at 60~70 °C, the pipe surface will form a stable lubricating film**.**

Allowable Deformation. Cold pulling pipe section size was shown in Fig. 2. Before cold pulling, the pipe internal diameters was d1, the pipe external diameters was D1. After cold pulling, the pipe internal diameters was d, the pipe external diameters was D. Thus the contraction ratio of section of allowable deformation refers to a deformed cross section shrinkage limitation in cold pulling process .Low /Medium carbon content is about 70%~90%, with higher phosphorus content, that reduces the amount of allowable deformation. In the actual operation, the section shrinkage deformation must be less than the allowable deformation, otherwise may cause cracking or breaking. In addition, drawing speed, precision molds, drawing machine assembly precision, precision, material uniformity and the size shape precision all is the factors of the pipe quality after drawing, which should be combined all together to consider throughly. The Formula of cold pulling pipe contraction ratio of section is as Eq. 1[4].

$$W = \frac{\pi(D1^2 - d1^2) - \pi(D^2 - d^2)}{\pi(D1^2 - d1^2)} = \frac{(D1^2 - d1^2) - (D^2 - d^2)}{D1^2 - d1^2} \tag{1}$$

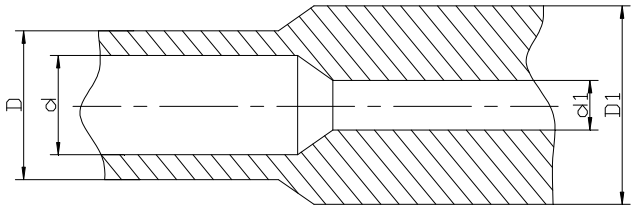


Fig. 2 Cold pulling pipe section size

Cold Pulling Cylinder Structure and Properties

Cold plastic deformation not only makes the pipe dimensions satisfy the design requirements, but also makes the metal organization and performance have a great change.

The Metal Grains Elongated at Axially along. In the cold plastic deformation, the inner metal grain shape is flattened to be elongated . Along with the deformation increasing, the grain is pulled into thin strips to form a fibrous tissue, this was shown in Fig. 1. So that its axial tensile strength increase, which benefits to axial force.

Hardening. Dislocation deformation have grain elongated ,and appear dislocation accumulation in the vicinity of grain boundary at the same time. Within grain is formed the tangled dislocation, as a result, grain crushes into the sub grains. The larger deformation is, the more dislocation accumulation and grain crusher produce, the stronger plastic deformation resist, which makes the material strengthened, hardness and wear resistance increase, plasticity and toughness decrease, work hardening and without quenching and tempering treatment can also reach the requirements of the mechanical properties of cylinder. The low carbon steel hardening curve was shown in Fig. 3 [3].

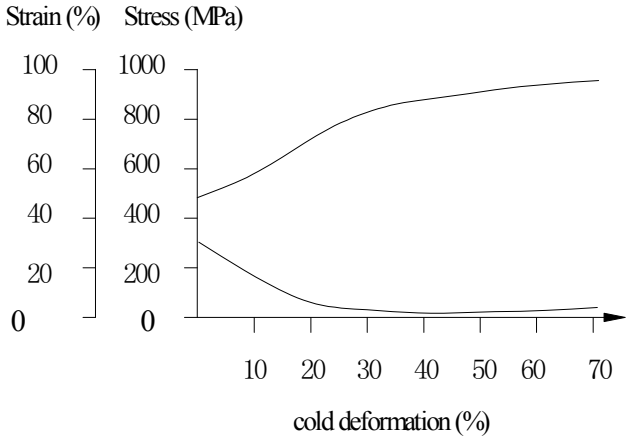


Fig. 3 The low carbon steel hardening curve

Plastic Deformation and Residual Stress. Different parts of the deformation inhomogeneous causes macro internal stress, and within grain or inner grain of different areas having the uneven deformation will generate microscopic stress.These two kinds of stress will decrease the strength of metal and influence the corrosion resistance, in general,it should be eliminated by annealing. The low carbon steel Performance curve was shown in Fig. 4. The plastic deformation of metal performance and stress will vary with temperature while in the heating, therefore annealing should be conducted below the re-crystallization temperature in order to retain the advantages of work hardening to the mechanical strength and eliminate most of the residual internal stress. All kinds of metal recrystallization temperature is as Eq. 2.

$$T_z \approx 0.4T_r . \quad (2)$$

T r: melting temperature

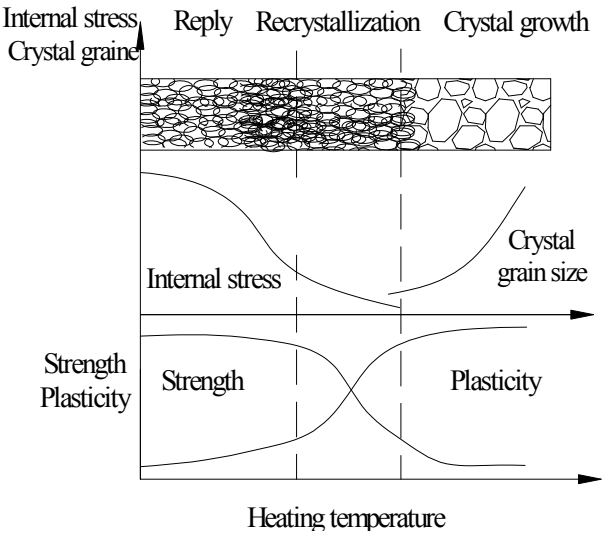


Fig. 4 Internal stress, intensity and plasticity curve with temperature

The key of bulk annealing is to control the annealing temperature below but close to that of reconstruction . The high temperature will cause microstructure recrystallized, meanwhile ,the strength will decrease dramatically. On the contrary ,the low temperature is not enough to eliminate the internal stress.

Conclusion

(1) Take seamless steel tubes as raw materials, they are acidified and phosphatized before the cold pulling to guarantee that mold and pipe have a good lubrication and have a high temperature stability during the cold pulling processing, thus the cold pulling process can be stable.
(2) When the seamless steel tubes are brought into the drawing processing,a process provides with a Hydraulic pulling machine, matches special cold pulling die, then they occur plastic deformation uniformly, satisfy the dimension requirements, realize machining without chips and high material utilization rate.
(3) Go with plastic deformation causing cold hardening, in that case allowing the material to be strengthened..
(4) Compared with traditional processing methods, drawing processing can remarkably improve the production efficiency, ensure product quality and improve the qualification rate of finished products.

References

[1] R.F. Huang: Mechanical Research & Application Vols. 114 (2009) NO.1, pp.125-126.

[2] J. Cong: Technology Wind Vols. 170 (2008) NO.14, pp.42.

[3] Y.J. Jia: Coal Mine Machinery Vols. 22 (2001) NO.11, pp.71-73.

[4] C. Zhang: *Mechanical Principle* (China Machinery Industry Press, China 2011 (in Chinese).

[5] H.W. Liu: *Material Mechanics* (China Higher education Press, China 2004 (in Chinese)..

[6] G.Z. Cheng and X.Q. Chen: Applied Mechanics and Materials Vols. 101-102 (2012) pp 33-36.

[7] G.Z. Cheng and Y.B. Cheng: Applied Mechanics and Materials Vols. 34-35 (2010) pp 1573-1577

© (2012) Trans Tech Publications, Switzerland
doi:10.4028/www.scientific.net/AMM.164.396

Calculating the Quasi-static Pressures of Confined Explosions Considering Chemical Reactions under the Constant Entropy Assumption

Wei Zhong[1,a], Zhou Tian[1,b]

[1]Northwest Institute of Nuclear Technology, Xi'an, China
[a]lengshui222@163.com,[b]tianzh2003@163.com

Keywords: confined explosions; chemical reactions; constant entropy assumption; quasi-static pressures; explosive charge volume ratio

Abstract. On the basis of the energy conservation and the state equation of the ideal gas, a formula of quasi-static pressures of the confined explosions calculating was derived under the constant entropy assumption of the detonation products expansion and the constant volume assumption of the chemical reactions. Taking the TNT explosive as an example, the quasi-static pressures of the confined explosion either considering the influence of the chemical reactions or not were calculated and the quasi-static pressures of the confined space were obtained.

Introduction

The so called "confined explosion" is explosion that happens under constrained conditions, such as explosions happen in the sealed blast chambers or the underground closed blast chambers. The environment of high-temperature and high-pressure produced by confined explosions, would result in chemical reactions between the detonation products and oxygen of the confined space and change the energy distribution.

Ornellas, a scientist at Lawrence Livermore National Laboratory in the USA, was the first person to research this problem. Ornellas [1] measured the amount of energy respectively for 25g TNT explosives exploding either in a 5.3L spherical chamber filled with oxygen or in a 5.3L vacuum spherical chamber. The measurement showed that the amount of energy in the chamber filled with oxygen was bigger than the amount of energy in the vacuum chamber. This result indicated that the chemical reactions of the detonation products were very important to the total energy of the whole system. A.L. Kuhl et al [2~4] carried on this work, and they had made systemic research about the confined explosions with chemical reactions of the detonation products. A.L. Kuhl et al considered that the detonation products of the confined explosions contained high amounts of carbon (C) and carbon monoxide (CO). As vast amounts of oxygen was contained in the high-temperature and high-pressure confined space after explosions, there were chemical reactions of the carbon and carbon monoxide with oxygen which resulted in a marked increase in quasi-static pressures of the confined systems.

In this paper, based on the constant entropy assumption of the detonation products expansion and the constant volume assumption of the chemical reactions, a theoretical analysis of the confined explosions quasi-static pressures taking consideration of the chemical reactions was presented and a formula of the quasi-static pressures was derived. At last we validate the correctness of the formula by carrying out the experimental research of TNT.

Formula Derivation of Calculating the Quasi-static Pressures

The Influence of Explosions on the Quasi-static Pressures

On the basic assumption of the detonation products expansion with constant entropy, for the instantaneous explosion, the state equation was given as follows [5]:

$$p = Av^{-\gamma} + f(v)T$$

As the charge density ρ_0 usually greater than 1g/cm^3 for common explosives, the influence of the pressure caused by the molecular motion of the detonation products was negligible. Therefore, we got a simplified state equation:

$$p = Av^{-\gamma} = A\rho^{\gamma} \tag{1}$$

Where A and γ were constants determined by the physical characteristics of explosives. Assuming the detonation products expansion to be an isentropic process, then γ could be seen as local isentropic index, which changed during the detonation products expansion.

Describing the state of the expansion at the start by equation (1):

$$p_{\text{start state}} = A_{\text{start state}} v_{\text{start state}}^{-\gamma_{\text{start state}}} = A_{\text{start state}} \rho_{\text{start state}}^{\gamma_{\text{start state}}} \tag{2}$$

Taking air as part of the detonation products, the isentropic expansion formula of the ideal gas was:

$$p_{\text{final state}} = A' v_{\text{final state}}^{-\gamma'} = A' \rho_{\text{final state}}^{\gamma'} \tag{3}$$

Where A' and γ' were constants relating to the assumed expansion.

From equation (2) and equation (3), we had:

$$p_{\text{final state}} = \frac{A' \rho_{\text{final state}}^{\gamma'}}{A_{\text{start state}} \rho_{\text{start state}}^{\gamma_{\text{start state}}}} p_{\text{start state}}$$

Considering A_s and A' were both constants, and $\gamma_{\text{start state}}, \gamma'$ both took on the character of isentropic adiabatic index, we could reduce above equation to equation (4):

$$p_{\text{final state}} = \left(\frac{\rho_{\text{final state}}}{\rho_{\text{start state}}}\right)^{\gamma} p_{\text{start state}} \tag{4}$$

Where γ was a constant which should be determined by experience or experiments. $p_{\text{start state}}$ was pressure calculated from JWL isentropic equation, and $\rho_{\text{start state}}$ was the corresponding density.

The Influence of Chemical Reactions on the Quasi-static Pressures

Assuming the gas in the confined space was ideal gas, the state equation of the ideal gas was [6]:

$$p_{\text{chemical}} V = nRT \tag{5}$$

Where p_{chemical} was the quasi-static pressure caused by the chemical reactions of the detonation products, V was the volume of the confined space, n was the detonation product amount of substance, T was the thermodynamical temperature, and R was the gas constant whose value was 8.314 J • mol^{-1} • K^{-1}.

According to thermodynamics [7]:

$$\begin{cases} C_p - C_V = nR \\ C_{p,m} / C_{V,m} = k \end{cases} \tag{6}$$

Where C_p was the specific heat capacity at constant pressure, C_V was the specific heat capacity at constant volume, $C_{p,\text{m}}, C_{V,\text{m}}$ were the values of C_p and C_V for 1mol ideal gas, and k was the specific heat ratio.

Assuming the chemical reactions of the detonation products happened in a constant volume, taking the chemical reaction of $i (i = 1, 2, \cdots, N)$ as an example, from equation (5) and equation (6), we obtained:

$$(p_{\text{chemical}})_i = \frac{n_i RT}{V} = (k-1) \cdot \frac{C_{Vi} \cdot T}{V} \tag{7}$$

According to thermodynamics [7], making U the internal energy of the system:

$$(\mathrm{d}U)_V = C_V \mathrm{d}T \tag{8}$$

Then,

$$U_V - U_0 = C_V T - C_V T_0$$

According to thermodynamics, when the absolute zero of temperature [7]:

$$U_0 = C_V T_0 = 0$$

And here:

$$Q_i = U_{V1} = C_{Vi} \cdot T \tag{9}$$

Where Q_i was the heat released by chemical reaction of $i(i = 1, 2, \cdots, N)$.

Replacing $C_{Vi} \cdot T$ of equation (7) by equation (9), we got:

$$(p_{\text{chemical}})_i = (k-1) \cdot \frac{Q_i}{V}$$

Considering all chemical reactions:

$$p_{\text{chemical}} = \sum_{i=1}^{N} (p_{\text{chemical}})_i = \sum_{i=1}^{N} [(k-1) \cdot \frac{Q_i}{V}] \tag{10}$$

Formula of Calculating the Quasi-static Pressures

It was easy to get the formula of calculating the quasi-static pressures of the confined explosions by equation (4) and equation (10):

$$P = P_{\text{start state}} \cdot (\frac{\rho}{\rho_{\text{start state}}})^{\gamma} + (k-1) \cdot \frac{1}{V} \sum_{i=1}^{n} Q_i$$

In this paper, we got continuous values of isentropic adiabatic index γ and specific heat ratio k by Langrange interpolation using some experimental data.

Example

The explosion equation of TNT was:

$$C_7H_5O_6N_3 = 2.5H_2O + 3.5CO + 3.5C + 1.5N_2 \tag{11}$$

The explosion happened in a sealed chamber which was filled with air (O_2~21%, N_2~78%, Noble Gases ~0.96%, CO2~0.03%, H_2O and other~0.03%), and the probable reactions for different explosive charge volume ratios were shown in Table 1.

Table 1 Reactions after the confined explosion

explosive charge volume ratio Q/V (kg/m^3)	the probable reactions
[0,0.3713)	$C+O_2 \rightarrow CO_2$, $CO+0.5O_2 \rightarrow CO_2$
[0.377,0.4874)	$C+O_2 \rightarrow CO_2$, $CO+0.5O_2 \rightarrow CO_2$, $CO+H_2O \rightarrow CO_2+H_2$
[0.4874,0.5570)	$C+O_2 \rightarrow CO_2$, $CO+0.5O_2 \rightarrow CO_2$, $CO+H_2O \rightarrow CO_2+H_2$
[0.5570,1.1140)	$C+0.5O_2 \rightarrow CO$, $CO+0.5O_2 \rightarrow CO_2$, $CO+H_2O \rightarrow CO_2+H_2$
[1.1140,3.8991)	$C+0.5O_2 \rightarrow CO_2$, $C+H_2O \rightarrow CO+H_2$, $CO+H_2O \rightarrow CO_2+H_2$
[3.8991,+∞)	$C+0.5O_2 \rightarrow CO_2$, $C+H_2O \rightarrow CO+H_2$, $C+2H_2 \rightarrow CH_4$

The expression of the specific heat ratio k was [5]:

$$k = \frac{\sum_{i=1}^{N} n_i (C_{p,\mathrm{m}})_i}{\sum_{i=1}^{N} n_i (C_{V,\mathrm{m}})_i} = \frac{\sum_{i=1}^{N} n_i (a_i + b_i T + c_i T^2 + \frac{c_i^{'}}{T^2})}{\sum_{i=1}^{N} n_i (a_i + b_i T + c_i T^2 + \frac{c_i^{'}}{T^2}) - R\sum_{i=1}^{N} n_i} \tag{12}$$

Where N was the number of the components, n_i was the amount of substance of component i. As equation (12) was complex, values of γ and k were obtained by Langrange interpolation in this paper, whose results were shown in Fig. 1.

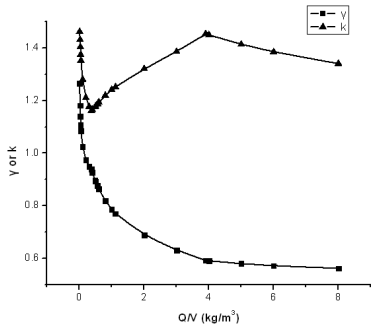


Fig.1 Plot of γ or *k* with explosive charge volume ratio *Q*/*V*

According to the method provided in this paper, the quasi-static pressures of confined explosion of TNT were obtained, and the plots of quasi-static pressures p with explosive charge volume ratio Q/V for considering chemical reactions and not considering chemical reactions compared with the experimental data were shown in Fig. 2.

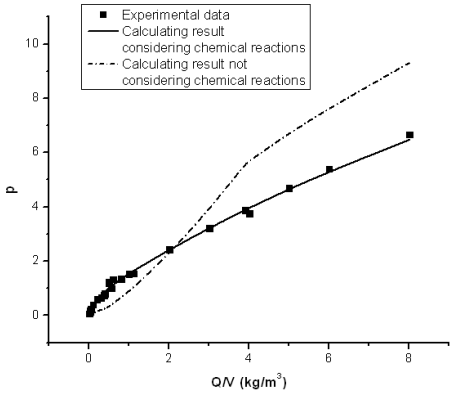


Fig.2 Plot of quasi-static pressures *p* with explosive charge volume ratio *Q*/*V*

Fig. 2 indicated that the calculating results considering the chemical reactions agreed well with the experimental data, but the results not considering the chemical reactions were very different from the experimental data.

Conclusions

In this paper, a formula of calculating the quasi-static pressures of confined explosions considering the chemical reactions of the detonation products was proposed. Taking the explosion in a sealed chamber of TNT as an example, this formula was proved to be correct. By comparing the calculating results of quasi-static pressures considering the chemical reactions and not considering the chemical reactions with experimental data, we confirmed that the chemical reactions of the detonation products had evident effects for the quasi-static pressures.

References

[1] D.L. Ornellas: Technical Report UCRL-52821, Lawrence Livermore National Laboratory, CA. 1984.

[2] A.L. Kuhl and H. Reichenbach: Proceedings of the Combustion Institute. Vol.32 (2009), p. 2291-2298.

[3] A.L. Kuhl, J.W. Forbes and J.B. Chandler: 34th Int. Annual Conf. of ICT. 2003.

[4] A.L. Kuhl and B. Khasainov: 38th Int. Annual Conf. of ICT. 2007.

[5] B.P. Zhang, Q.M. Zhang and F.L. Huang: *Detonation physics*(Weapon Industry Press, Beijing.2000).

[6] S.H. Zhang: *College Physics Book Two-Thermal Physics* (Tsinghua University Press, Beijing.2002).

[7] Y.J. Yin, Z.K. Xi and S.Y. Zhang: *The concise Course of Physical Chemistry* (*4th Edition*) (Higher Education Press, Beijing.2009).

© (2012) Trans Tech Publications, Switzerland
doi:10.4028/www.scientific.net/AMM.164.401

Failure Analysis of Rolling Bearing Based on Oil Monitoring Techniques with Mechanics Basis

Xufeng Jiang[1, a], Fang Liu[2, b], Pengcheng Zhao[1, c]

[1]Air Force Servece College of PLA, Xuzhou, Jiangsu, 221000, China

[2]Air Force Shanghai Logistics Training Base, Shanghai, 200120, China

[a]jiangziya@163.com (corresponding author), [b]15162167853@163.com, [c]jiangziya70@163.com

Keywords: rolling bearings, failure, oil monitoring

Abstract. To determine the failure cause of rolling bearing of a factory heating device, oil samples extracted from the recovery of lubricant oil and were tested by comprehensive oil monitoring techniques (including physico-chemical properties analysis, pollution degree detection and ferrography wear particle analysis). The results show that root cause of failure is the operating temperature of the bearing is too high. Failure form is burning. Therefore, the application of oil monitoring techniques to analyze the mechanical failure mechanism, to prevent mechanical failure and extend machine life is very helpful.

Introduction

Dozens of rolling bearings of a large factory heating device were lubricated by oil mist. The type of lubricating oil was steam turbine mineral oil ESSO T68. The working temperature of some bearings is very high, up to 240℃. Since the operation, the life of rolling bearings has been lower. The average value was only 2 years.

Bearing failure surfaces accompanied by large amounts of viscous brown residue, sludge; some failure bearing was severely burned, after serious high-temperature oxidation as blue and black (refer with: Fig. 1); burning of black carbon sintered bearing surface to remain solid, rigid sheet (refer with: Fig. 2).



Fig. 1 Failure bearings (bearings inner and outer rings oxidized under high temperature)

The shaft neck connected with the bearing appears excessive wear, shaft diameter from Φ 65mm wear to Φ 63mm, and accompanied by overheating (refer with: Fig. 3).



Fig. 2 The black carbon sheet residue on the surface of failure bearing



Fig. 3 The shaft neck after excessive wear

In order to analyze the causes of bearing failure, propose solutions, and determine the lubricating oil recovered will continue to be used or not, engineers arrived on site to survey equipment and parts failure, and sampled the recovery lubricating oil from the oil-mist device.

Oil monitoring

Oil monitoring consists of three parts:

Physico-chemical properties test. The viscosity of 40 degrees. Testing lubricant viscosity change degree after using, know whether the failure associated with the lubricant viscosity-temperature properties, as well as judge the recovery oil is suitable for continued use or not; Acid value. Characterization of the oxidation degree of the oil; Resistance of emulsion. Confirming whether the lubricating oil lubrication is suitable for continued use; Emission spectroscopy. Detecting of the concentration levels of additives, contaminants and wear metals in lubricating oil, distinguishing lubricating oil pollution, additive consumption level and the degree of wear.

Lubricating oil pollution determination. Water and particulate contamination. Detecting of recovered oil pollution degree to determine whether to continue to use.

Ferrography wear particle analysis. By microscopic observation of separating wear particles in lubricating oil samples to understand the bearing wear and failure mechanisms, and analyze the reasons for bearing failure.

Results and discussion

Usability evaluation of recycled lubricating oil. To confirm whether the recovery of lubricating oil can be reused, the physico-chemical properties, performance and lubricating oil pollution must be tested (refer with: Table 1).

The test results indicate that particle pollution of the recovered oil is largely because of the dust in the air. But after filtering oil can achieve the required cleanliness and continue to be used. The acid value and anti-emulsifying properties of oil are in the normal range. However, the reduced viscosity of lubricating oil sample is more than 10%. Therefore, the recovery oil is not suitable for continued use. If synthetic lubricating oil with excellent performance of resistance of high temperature

performance has been chosen, the viscosity of recycled lubricating oil probably won't drop or drop no more than 10%. If other indicators are in the qualified range, after filtering, the recovery lubricating oil can be suitable for continued use.

Table 1 Test results of recovery lubricating oil sample from oil mist device

Test item	Result	Instruction
Viscosity [40 degrees change]	58%	Viscosity decreased more than 10%, and is not suitable for continued use
Acid value [mg KOH/g]	0.038	Normal
Resistance to emulsion	40-38-2	Normal
Water [%]	＜0.05%	Normal
Pollution degree, ISO	22/21/19	Severely exceed the standard, after filtration, up to cleanliness standards
PQ index	2	Can be reduced to zero after filtering
Zn	1	Close to the new oil level
P	6	Close to the new oil level
Si	2	Close to the new oil level
Fe	0	
Cu	0	
Pb	2	
Al	1	

Failure analysis of rolling bearings. The failure of rolling bearings of the heating device has three characteristics: (1) rolling bearings work in high temperature, up to 240° c; (2) failure bearings attached on a large number of brown sludge residues; (3) surface has black coke products.
Lubricating oil analysis results has two characteristics: (1) oil acid value of lubricating oil did not change basically, indicating that the oil antioxidant additive consumption is not obvious; (2) the oil viscosity is not increased, but declined. These two features further indicated oil sludge and coke in failure bearings mainly related to the effects of high temperature pyrolysis and / or bubble crush induced microdieseling effect, instead of the usual lubricating oil oxidation and aging. An understanding of this point is very important for recommending lubricating oil.
These features reveal the high temperature is the root cause of bearing failure and high temperature related primarily to the cooling effect of the device. High temperature and / or microdieseling effect causes the lubricating oil deposit formation, and residue within the raceways, obstructs the bearing element to rotate, so that the friction force increases, turning difficult, thus the bearing internal temperature increase. When the bearing surface temperature reaches a very high, sticky clay is heat-hardening and high surface temperature (＞500~600℃) can also directly result in oil coking, the formation of black hard sheet material (refer with: Fig. 2).
In this state, the bearing will occur burning, rather than wear failure. Comprehensive analysis of wear results coincides with this conclusion match. Emission spectroscopy and PQ index analysis showed that the oil sample almost had no small wear particles generated by normal wear.
Ferrography wear particle analysis clearly demonstrated, in oil samples normal wear particles were hardly seen, wear particles are big ball-shaped particles, black oxide and very few hard scratching particles formed by wear surface material after burn (refer with: Fig. 4).Therefore, the cause of bearing failure is not contact fatigue wear, also not abrasive wear of the contaminant and sliding abrasion, but burning and melt caused by high temperature.

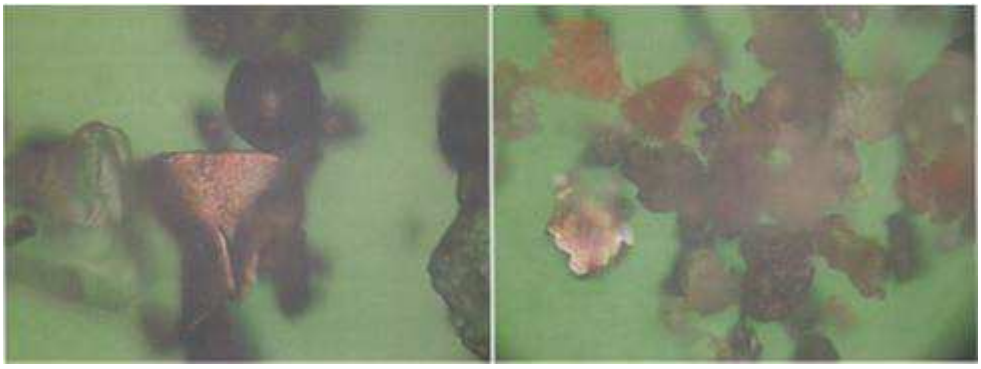


Fig. 4 Wear particles generated by rolling bearing burning failure

It is due to the rotation difficultly even sintering of bearing internal rolling component, resulting in the relative rotation between the bearing inner ring and the shaft neck, making the shaft neck appeared excessive wear (refer with: Fig. 3).

Summary

The monitoring results show that failure of rolling bearing of the heating device is mainly due to poor cooling effect of the bearing system, causes the bearing temperature is too high, beyond the working temperature range of the ordinary mineral turbine lubricating oil, resulting in severe thermal cracking, sludge and coke of lubricating oil, but this is not a lubricating oil quality problems, but the using lubricating oil can not meet working conditions. High temperature leads to the degradation of lubricating oil which produced deposit adhesion in the bearing, so that the gap is reduced, resulting in the frictional resistance and bearing temperature increases, eventually bearing burning failure.

In order to extend bearing life and preventing bearing failure, we can start from the following two aspects, on the one hand, to take measures to reduce the temperature of the bearing, such as the use of more effective cooling method, reducing the external high-temperature steam for bearing; on the other hand, to use synthetic lubricating oil with high temperature performance, reduce or avoid the generation of thermal cracking, sludge and coking.

References

[1] Zhang Yingtang, Ren Guoquan, The Present Condition and Development of Oil Monitoring Technique, J. Lubrication Engineering. 2 (2000) 65-66.

[2] Li Qiongwei, Mao Meijuan, Chen Yong, Research on State-of-the-Art and Trends of Oil Analysis for Equipment, J. China Mechanical Engineering. 15 (2004) 272-275.

[3] Xu Bin,Yu Xuejun, The Application and study of oil analysis in equipment maintenance, J. Lubricating Oil. 21 (2006) 61-64.

[4] Huang Zongping, Application of inductively coupled plasma-atomic emission spectrometry for analysis of impurity elements in lubricating oil, J. Metallurgical Analysis. 2 (2006) 43-46.

[5] Xiao Hanliang, Ferrography and its application in machine monitoring and diagnosis, Beijing People Communication Press, Beijing, 1993.

© (2012) Trans Tech Publications, Switzerland
doi:10.4028/www.scientific.net/AMM.164.405

Study of Thermodynamics of Alkali-free Glass Reaction

Shan Liu [1, 2] , Yaochun Yao [1, 2, *], Yanli Liu [1, 2], Yongnian Dai[1, 2]

[1]Faculty of Metallurgical and Energy Engineering, Kunming University of Science and Technology, Kunming 650093, China

[2]National Engineering Laboratory of Vacuum Metallurgy, Kunming University of Science and Technology, Kunming 650093，China

[*] Corresponding author: yaochunyao@gmail.com

Keywords: Alkali-free glass；Thermodynamics；TG-DSC.

Abstract: Thermal learn calculation was used on the process of glass melting of alkali-free glass, the relationship type between free enthalpy and temperature was obtained. Results show that B_2O_3 begin to melt at T=700 K, this reaction contained more step reactions. Carbonate barium ($BaCO_3$) decomposed to generated BaO and CO_2 around 1300 K, BaO began reaction with small amounts SiO_2 to generate silicate. BaO and SiO_2 were easy to react in low temperature because of their high reactivity. Reaction between SiO_2 and Al_2O_3 was a reversible reactions, the turning point was T=1700 K. Combined with the calculation results, each reaction in different temperature range was discussed. In addition, the mechanism of reaction in the glass melting process was studied and discussed by use of thermogravimetric-differential scanning calorimetry.

Introduction

The current glass melting technology has been using the Siemens furnace developed in the 1860s [1]. The conventional method used for glass melting is the air-fuel firing technology in the Siemens furnace, it is inefficient, time-intensive and energy-consuming, especially in the melting and refining process. In addition, the usage of fossil fuel with the traditional technology involves more environmental responsibility due to the emissions of greenhouse gases like CO_2 and NO_x. With the rapid growth of glass usage and the increased energy and environmental issues, it is time to develop a new glass melting technology with small energy consumption and emissions.

Alkali-free glass is employed as a transparent glass substrate for a liquid crystal display or the like. The alkali-free glass is melted at a higher temperature in comparison with glass containing an alkali melted component, because of a higher viscosity of the molten glass. In melting the alkali-free glass, a vitrifying reaction usually takes place at from 1200 to 1400^{o}C, and bubble reduction and homogenization are executed at a high temperature of 1500^{o}C or higher. The conventional method used for alkali-free glass melting is difficulty. Among various kinds of thermal plasma reactors, a multi-phase arc is more effective due to the following advantages, namely low equipment investment, feasible mass production, and high energy efficiency [2, 3].

The process of glass melting system of alkali-free glass involves a lot of chemical reactions, regardless employ any melting technology, it is fatal to study the reaction mechanism and thermodynamics. Therefore, in this paper thermal learn calculation was used on those reactions, also combined with differential thermal analyzer preliminary analysis and discuss some of the heat parameters and phase change involved in glass melting process.

Thermomechanical Analysis

The most of the thermodynamics parameters in this paper were quoted from the book [4].

Table 1 Chemical reaction equations

Reaction equations	No.
$2H_3BO_3(s) = B_2O_3(S)+3H_2O(s)$	**(1)**
$BaCO_3(s)+SiO_2(s) = BaSiO_3(s)+CO_2(g)$	**(2)**
$BaO(s)+SiO_2(s) = BaSiO_3(s)$	**(3)**
$3Al_2O_3(s)+2SiO_2(s) = 3Al_2O_3\cdot 2SiO_2(s)$	**(4)**
$BaO(s)+Al_2O_3(s) = BaO\cdot Al_2O_3(s)$	**(5)**

Table 2 The relationship of standard free enthalpy (ΔG^o) and temperature (T)

No.	The relationship of ΔG_T^o and T
(1)	$\Delta G_T^o = -30.099InT + 26.385\times10^{-3}T^2 + 11.686\times10^5T^{-1} - 243.608T + 173529.5$
(2)	$\Delta G_T^o = -13.598InT + 20.021\times10^{-3}T^2 + 3.243\times10^5T^{-1} - 89.3861T + 108727.6$
(3)	$\Delta G_T^o = -3.055InT + 2.239\times10^{-3}T^2 + 0.816\times10^5T^{-1} + 19.667T - 157322$
(4)	$\Delta G_T^o = -289.143InT + 22.958\times10^{-3}T^2 - 75.142\times10^5T^{-1} + 1664.617T - 2819819$
(5)	$\Delta G_T^o = -2.757InT + 4.243\times10^{-3}T^2 - 0.278\times10^5T^{-1} - 11.6557T - 99000.3$

For simplicity, we often simplify the Gibbs energy into $\Delta G_T^o = AT + B$, thus the relationship of standard free enthalpy and temperature, involved in chemical reactions **Table 2**, can be simplified as follows:

$$\Delta G_T^o = -243.608T + 17352 \quad (6)$$

$$\Delta G_T^o = -89.386T + 10872 \quad (7)$$

$$\Delta G_T^o = 19.667T - 157 \quad (8)$$

$$\Delta G_T^o = 1664.617T - 2819 \quad (9)$$

$$\Delta G_T^o = -116557T - 9900 \quad (10)$$

According to the equations (6)-(10), we obtain the free enthalpy under different temperature of the reactions, calculation results are as **Table 3**.

Table 3 Free enthalpy of each reaction under different temperature $\Delta_r G_m$ (kJ/mol)

No.	$\Delta_r G_m$						
	500K	**600K**	**700K**	**800K**	**900K**	**1000K**	**1100K**
(1)	51	27	3	-21	-45	-70	-94
(2)	108	64	55	46	37	28	19
(3)	-147	-145	-143	-141	-139	-137	-135
(4)	-1987	-1821	-1654	-1488	-1311	-1155	-988
(5)	-104	-106	-107	-108	-109	-110	-111

No.	$\Delta_r G_m$						
	1200K	**1300K**	**1400K**	**1500K**	**1600K**	**1700K**	**1800K**
(1)	-118	-143	-167	-191	-216	-240	-264
(2)	10	1	7	-16	-25	-34	-43
(3)	-133	-131	-129	-127	-125	-123	-121
(4)	-822	-655	-489	-322	-156	10	176
(5)	-113	-114	-115	-116	-117	-118	-120

Table 3 indicates reaction (1) starting near 700 K, according to the relevant documents [5~7], boric acid heat to 353~373 K begin to lose water, decompose and turn into HBO_2, converte to $H_2B_4O_7$ at 413~433 K, form molten B_2O_3 at 572~843 K, which can be expressed as follows:

$$4H_3BO_3 \overset{353K}{\rightleftharpoons} 4\ HBO_2 \overset{393K}{\rightleftharpoons} H_2B_4O_7 \overset{600K}{\rightleftharpoons} 2B_2O_3 \tag{11}$$

Reaction (2) begin to start near 1300K. First, $BaCO_3$ decompose to BaO and CO_2, meanwhile, BaO start to reaction with SiO_2 to form silicates. In reaction (3), BaO as strong basic oxide and SiO_2 as strong acid oxide, they were easy to react in low temperature because of their high reactivity. From the equation (8), reaction can happen even at low temperatures. From the above calculation, reaction (4) turn to reverse reaction with the temperature increasing, it illustrates the exothermic reaction. The reverse reaction becomes dominant reaction around 1700 K. From the calculation reaction (5), as temperature increases, the reaction freedom enthalpy has not a significant change.

Reaction mechanism analysis

First, five kinds of materials were taken according to a proportion of $49SiO_2$ -$15B_2O_3$-$10Al_2O_3$ -25BaO-$1Sb_2O_3$ in an agate container, add a little deionized water to grind 3 hours then take ball milled material into drying box for 2 hours. And then respectively weight 10g H_3BO_3, $BaCO_3$ and Sb_2O_3, with the same treat process. Finally take the material to do differential thermal analysis, by rate of 20 ^oC/min heat to 1600 ^oC.

Figure 1 (a) shows the DG-DSC result of $BaCO_3$. There is a clear endothermic peak at 1085 ^oC, which corresponding $BaCO_3$ decomposition temperature. First, $BaCO_3$ decomposes to CO_2, then to CO 1000 ^oC [8].

From Fig.1 (b), boric acid has an evident weight loss between 100 and 200 ^oC, two obvious endothermic peaks appear at the 125 ^oC and 160 ^oC. It is consistent with above analysis results like reaction (11). Weight losses around 1300^oC~1400^oC, corresponding with generation temperature of B_2O_3. In the stage of borosilicate and glass forming, highly reactive carbonate and silicate minerals react with B_2O_3 to generate high-melting-point compounds, their saturated steam pressure is lower, volatile of boron reduces [6]. Around 1000~1550 ^oC, boron volatile actually takes place in fluctuation surface only due to the existence of liquid glass,.

Figure 1 (c), Sb_2O_3 has an obvious absorption peaks at 650 ^oC, meanwhile, Sb_2O_3 melt to fluid, Sb_2O_3 stem molecules is Sb_4O_6, then begin to decompose to Sb_2O_3 over 800 ^oC.

Figure 1 (d) shows the G-DSC curve of 49 SiO_2 -15B_2O_3-10Al_2O_3-25BaO-1Sb_2O_3 glass system. Boric acid decomposes and water molecules of components evaporates at 180.6~414.9^oC. The decomposition of boric acid is a multistep reaction, first decomposition to metaboric acid, then teraboric acid, final boric anhydride. Boric anhydride all becomes molten liquid near 500 ^oC. Sb_2O_3 melts at 600^oC, then turns to molten at 663.2^oCe. When the temperature reaches up to 800 ^oC, $BaCO_3$ starts to decompose and react with SiO_2 to form silicates.

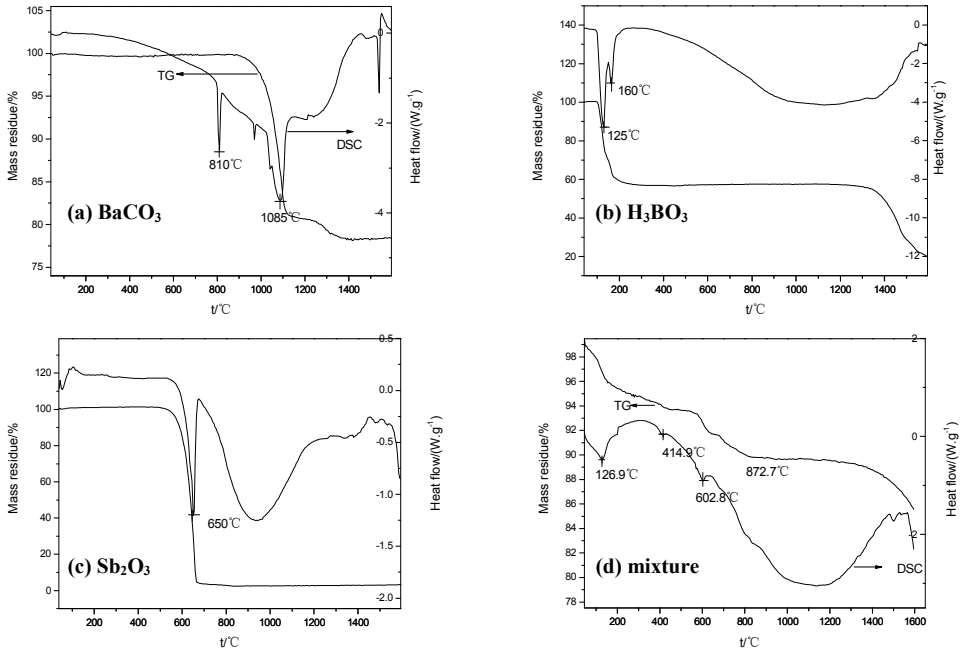


Fig.1 DG-DSC curves: (a) $BaCO_3$, (b) H_3BO_3, (c) Sb_2O_3 and (d)mixture

Conclusions

The relationship of standard free enthalpy and temperature of five main reactions in the glass melting process was obtained though thermodynamics calculation, and the free enthalpy of reactions was calculated standard respectively in a range of 500K~1300K. BaO and SiO_2 were easy to react in low temperature because of their high reactivity. The free enthalpy of reaction between BaO and Al_2O_3 had no obvious change with the increase of temperature.

Acknowledgments

This work is financially supported by NSFC (No: 51002067), SRF for ROCS, SEM, Natural Science Foundation of Yunnan Province of China (No: 200927049)

References

[1] C. P. Ross, Am. Ceram. Soc. Bull., Vol. 83 (2004), p. 18
[2] Y. Yao, T. Watanabe, T. Yano, et al., Sci. Technol. Adv. Mater., Vol. 9 (2008). p. 025013
[3] Y. Yao, K. Yatsuda, T. Watanabe, T. Yano, Plasma Science and technology, Vol. 11 (2009), p. 699
[4] D. Ye, J. Hu. Handbook of Thermodynamics Date for Practical Inorganic Matters (in Chinese), Beijing: Metallurgical IndustryPress (2002)
[5] Y. Ma, The Process of Glass Production, Northwestern Polytechnical University press (2008)
[6] S. Yu, Glass Fiber, Vol. 2 (2003), p.18
[7] Y. Wang, Z. Fu, H. Wang, J. Zhang, Q. Zhang, J. Chin. Ceram. Soc., Vol. 30, (2002), p. 340
[8] Z. Hu, China Glass, Vol. 4 (2005), p. 25

© (2012) Trans Tech Publications, Switzerland
doi:10.4028/www.scientific.net/AMM.164.409

Research on Magnetic Fluid Based Optical Deformable Mirrors with Fluid Mechanics

Zhizheng Wu[1], Mei Liu[1, 2]

[1]Department of Precision Mechanical Engineering, Shanghai University,
#149 Yanchang Road, Shanghai, China, 200072
[2]State Key Laboratory of Transducer Technology, Shanghai Institute of Microsystem and Information Technology, Chinese Academy of Sciences, 200050

zhizhengwu@shu.edu.cn, mliu@shu.edu.cn

Keywords: Magnetic fluid, fluid mechanics, deformable mirror, adaptive optics

Abstract. Magnetic fluid based liquid mirrors represent a promising technology. Compared with the conventional solid mirrors, magnetic fluid deformable mirrors (MFDMs) have the advantages of large strokes, low cost and easy scalability. In this paper, the brief history of the development of MFDMs was first introduced, the working principle of MFDMs with fluid mechanics and electromagnetic field was presented next and then the advantages of MFDMs as well as their challenges are discussed.

Introduction

The quality of images provided by an imaging system is affected by imperfections (aberrations) in the optical path of light traveling from the object being imaged to the location of the image. The effects of these imperfections on the light rays or waves, and consequently on the resulting image can be corrected using adaptive optics (AO) technology, which has been successfully used in astronomical seeing, free space laser communication and retinal imaging, etc. Adaptive optics system utilizes adaptive optical elements called wavefront correctors to compensate for aberrations, and the most important type of wavefront correctors is the deformable mirrors, which are normaly built from solid materials.

The common drawbacks of these solid thin plate or membrane based mirrors are the high cost of per actuator channel and the relatively low stroke deflection. However, the recent soaring number of new adaptive applications has exhibited the need for deformable mirrors with low cost, high stroke and a large number of actuators for scalability. Under such conditions, magnetic fluid deformable mirrors (MFDMs) were proposed a few years ago as an alternative to the conventional solid wavefront correctors in AO systems. Though the idea of MFDMs is quite new, they have been appraised by a number of preliminary studies as a promising future technology [1-7].

In this paper, the operating principle and properties of MFDMs are briefly presented based on our previous work [5-7]. The advantages, limitations and challenges of this new type of deformable mirrors are also discussed.

Magnetic Fluids

Magnetic fluids - also called ferrofluids - were originally discovered in the 1960s at NASA Research Center, where scientists were investigating different possible methods of controlling liquids in space as the basis for a spacecraft's attitude control system. The benefits of using a magnetic fluid include that the location of the fluid could be precisely controlled through the application of a magnetic field, and by varying the strength of the field, the fluid could be forced to flow, thus change the angular momentum and influence the rotation of the spacecraft.

Magnetic fluids are stable colloidal suspensions of nano-sized, single-domain ferri- or ferro-magnetic particles. When subjected to a magnetic field, the suspended particles affect the flow properties of the carrier fluid. One of these effects is the variation of shape of the fluid free surface, which has been exploited to develop deformable mirrors.

Depending on the type of the carrier fluid used, the magnetic fluids can be broadly categorized as water-based and oil-based systems. In most technological applications of magnetic fluids, the magnetic particles are obtained from one of a number of different ferrites. Researchers have prepared ferrofluids containing small particles of ferromagnetic metals, such as cobalt and iron, as well as magnetic compounds, such as manganese zinc ferrite. But by far, the most commonly used ferrites are magnetite (Fe_3O_4) and maghemite ($\gamma - Fe_2O_3$). The typical size of these particles is 10 nm in diameter, which is small enough for thermal agitation to disperse them evenly within a carrier fluid, and for them to contribute to the overall magnetic response of the fluid.

Since the individual magnetic particles are in a permanent state of saturation magnetization, there exists a strong magneto-static attraction between the particles and, as a result, the particles tend to agglomerate in the carrier fluid. To avoid the agglomeration, the magnetic particles are coated with surfactants, which introduce an entropic repulsion between the particles resulting in stable suspensions of the particles. The magnetic attraction of nanoparticles is weak enough that the surfactant's Van der Waals force is sufficient to prevent magnetic clumping or agglomeration. Ferrofluids usually do not retain magnetization in the absence of an externally applied field and thus are often classified as superparamagnets rather than ferromagnets. In some applications, the repulsive mechanism is achieved by charging the surface of the particles, which produces an electrostatic repulsion.

Since their introduction in early 1960s, magnetic fluids have seen applications ranging from sink-float systems to drug delivery systems. Some of the well-known applications include liquid seals, dampers for audio speakers and heat-transfer agents. Recently, ferrofluids are also being investigated for applications in biomedical applications, MEMS and nano-technology [8,9]. Their use as MFDMs particularly in AO systems, remains one of the most advanced emerging optical applications, such as their potential use in ophthalmology imaging and extremely large telescopes, etc.

Magnetic Fluid Deformable Mirror

The free surface of a liquid follows an equipotential surface to a very high degree of precision. This characteristic of liquids can be exploited to deform their surface to any desired shape. The process of shaping the free surface may be controlled by varying one or more of the force fields that contribute toward the potential level. Magnetic fluids are a class of liquids which respond to variations in magnetic field and hence their surface shape can be controlled by controlling the magnetic field they are exposed to. If a beam of light incident on the free surface of a magnetic fluid can be adequately reflected, the surface of the fluid can be utilized to control the shape of the wavefront of the incident light, i.e., the magnetic fluid surface can be used as a deformable mirror.

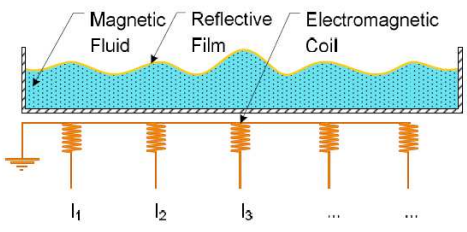


Figure 1: The basic principle of a magnetic fluid deformable mirror.

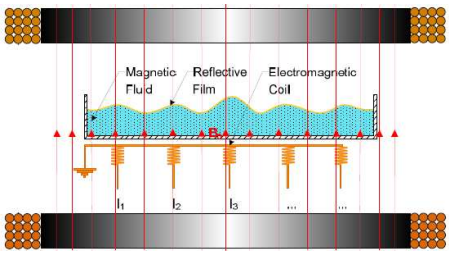


Figure 2: Modified magnetic fluid deformable mirror.

Figure 1 shows the working principle of a MFDM in its simplest form. The device comprises a thin layer of a magnetic fluid which, under the effect of gravity alone, features a planar free surface. When exposed to a magnetic field, such as the one created by a small magnet, the surface deforms to

a new equipotential surface supported by both gravity and the magnetic field. A more practical device is obtained by using electromagnetic coils to generate the magnetic field shown in Figure 1, which can be locally varied by controlling the currents applied to the individual coils. The varying magnetic field in turn affects the equipotential surface thus providing means to control the shape of the magnetic fluid surface. The deformation of a ferrofluid in a static magnetic field is determined by the equilibrium between gravity and the force from the magnetic field. The deformation amplitude can be approximated by the following equation:

$$h = \frac{(\mu_r - 1)}{2\mu_r \mu_0 \rho g}\left(\left|B \cdot n\right|^2 + \mu_r \left|B \times n\right|^2\right),$$

where ρ and μ_r are the density and the relative permeability of the ferrofluid, n is a unit vector normal to the surface of the liquid, B is the applied magnetic field, The source of the external magnetic field B can come from permanent magnets or currents carrying wires and is the sum of all the individual magnetic fields produced by the actuators.

It can be seen that the above equation is nonlinear with respect to the external magnetic field and depends on the vectorial addition of each magnetic field component produce by the corresponding actuators, which means the linear control algorithms in conventional AO systems is not applicable to the magnetic fluid deformable mirrors. The overall shape generated by the sum of each actuator cannot be simply obtained by summing scalar deformations from individual actuators, since the surface obtained with several actuators is shaped by the sum of the magnetic vectors instead of the sum of surfaces generated from each actuator.

Furthermore, the equation shows that the surface deformations are proportional to the square of the applied magnetic field, therefore, only unidirectional deformations can be produced on the mirror surface, which means the actuators only can push not pull the mirror surface. A modified design of a MFDM, which superimposes a uniform vertical magnetic field on the magnetic field of the array of electromagnetic coils, was proposed in [5]. The schematic diagram of the modified system is shown in Figure 2. The design modification allows for the linearization of the response of the MFDM to the applied magnetic field generated by the actuators. It follows that linear control algorithms can be developed and used to control the surface shape of the MFDM. Such control algorithms, which can be used to compensate for static and dynamic high-order wavefront aberrations, were recently reported by Wu, etc. in [6,7].

Typically the magnetic fluids have poor reflectivity and hence cannot be used as a functional mirror. This limitation can be successfully overcome by films of reflective particles thin enough - abbreviately called MELLFs - that they pose no significant change to the deformation of the fluid but greatly enhance the reflectance of the deformable surface [4].

Since the introduction of the idea of a MFDM as an alternative to existing wavefront correctors [1], a number of studies characterizing various features of the mirrors have been reported. Important features and challenges of the MFDMs found by the studies so far are reviewed and discussed as follows:

- *Stroke.* The most promising aspect of the MFDMs is their ability to provide large deflections of their deformable surface. They are reported to have surface deflections easily exceeding $20\mu m$ [2]. Recently MFDM offering hundreds of microns surface deflections have been discussed for their application in large astronomical telescopes [4]. This feature - referred to as stroke in conventional deformable mirrors – shows an unparalleled advantage over the conventional micro-machined solid deformable mirrors which feature stroke lengths of only a few microns.

- *Cost.* The simple design and expendable nature of MFDMs render them remarkably more economical than any other known type of wavefront correctors. Based on similar components used in the electronic industry, Laird *et al.* [1] projected a cost of only per channel of $2 − $5. For large mirror telescopes, it is estimated that for a given diameter, the cost of the magnetic liquid mirror is only about two orders of magnitude less than a solid glass mirror.
- *Speed.* Initial studies reported the magnetic fluid wavefront correction speeds between 10-50 Hz only and shows the main disadvantage of their significantly lower bandwidth compared to solid deformable mirrors. However, recently Brousseau *et al.* [2,3] have disclosed some unintuitive features, which allow the correction speed to be enhanced beyond 900 Hz. By increasing the viscosity of the magnetic fluids, along with an overdrive technique, the response time of MFDMs can be improved dramatically. Experiments have shown a bandwidth of the order of 1KHz with a 494 cP-viscous ferrofluid. However, the current results are limited to small amplitudes of the order of a few microns and need to be further improved for large amplitudes.
- *Vibrations.* The susceptibility of the magnetic fluid volume to mechanical vibrations is one of the most obvious concerns associated with use of MFDMs. For applications that require the AO setup to be positioned on a moving platform, the mechanical vibrations as well the strict requirement of keeping the MFDM surface horizontal remain the prohibiting factors. However, for applications such as ophthalmic AO systems which can afford static installation of the mirror, the effects of mechanical vibrations can be minimized. Like any other precision system, the optical setup should be mounted on vibration isolators. It has been found that the amplitudes of disturbances are less than 1/10 of a wave when a low-viscosity magnetic fluid layer (about 6 cP) with thickness of 2 mm is put on an optical table. Beyond that, Borra *et al.* [4] assert that the effect of mechanical vibrations on a fluid mirror is minimal if the thickness of the fluid layer is limited to less than one millimeter. Increasing viscosity of the magnetic fluid is also reported to have minimizing impact on the mirror surface vibrations resulting from the ambient noise. Nonetheless, the most effective remedy is presented by the applied magnetic field itself. The magnetic field applied to control the surface profile of the mirror dampens the vibrations significantly [4-6]..
- *Stability and Compatibility of Reflective Film.* A significant part of the research efforts expended thus far in the area of MFDMs has been directed at the development of appropriate magnetic fluids and compatible MELLFs. As mentioned earlier, the previously known types of MELLFs were incompatible with the oil-based magnetic fluids. On the other hand, water-based magnetic fluids, which showed compatibility with the MELLFs, suffered from the drawback of evaporation over time. The recent introduction of a new type of oil-based magnetic fluid [10], which are compatible with the silver MELLFs, is a significant advancement, which increased the likelihood of their practical application in near future. However, the effects of the reflective film on the dynamics and control of the mirror need to be further studied and experimentally validated.
- *Control.* Difficulties in the control of the MFDM surface were first highlighted in [1], which revealed that the deflections of the MFDM surface could not be obtained as a linear superposition of the influence of the individual actuator coils - a method routinely used in the existing solid deformable mirrors. This unique feature of the MFDM has had serious implications in the control of these mirrors. A breakthrough was made recently by Iqbal, Wu and Ben Amara [5-7], where a modified MFDM was proposed by superimposing a uniform vertical magnetic field on the magnetic field of the array of electromagnetic coils. The strong uniform magnetic field helps linearize the response of MFDMs and allows the conventional linear control algorithm to be used

[6,7]. However, a final look at the strengths and the challenges of MFDMs still brings forward the control of the mirror as the most pressing requirement that needs to be met before they can be considered for a practical application.

Achievement of the unique features has certainly brought the MFDMs much closer to their deployment in practical AO systems. However, the challenges of other aspects of MFDMs will have to be addressed before they can be finally used practically in clinical or astronomic applications.

Acknowledgment

This work was supported by the National Natural Science Foundation of China (51075254), the Shanghai Pujiang Program (11PJ1404000), the Innovation Program of Shanghai Municipal Education Commission (11YZ16), and the 211 Leading Academic Discipline Project of Shanghai University (A004-1-yi-1002).

References

[1] Laird P., etc., *Ferrofluid-based deformable mirrors: A new approach to AO using liquid mirrors,* In Proceedings of SPIE Volume 4839, Adaptive Optical System Technologies II, Edited by Peter L. Wizinowich and Domenico Bonaccini, SPIE - The International Society of Optical Engineering, 2003.

[2] Brousseau D., Borra E. F., Rochette M. and Landry D. B., *Linearization of the response of a 91-actuator magnetic liquid deformable mirror*, Optics Express, vol.18, no.8, pp.8239-8250, 2010.

[3] Brousseau D., Borra E. F., Ruel H. J., and Parent J., *A magnetic liquid deformable mirror for high stroke and low order axially symmetrical aberrations,* Optics Express, vol.14, pp.11486-11493, 2006.

[4] Borra E. F., *Liquid Mirrors in Engineering*, Optics & Photonics News, pp.14-17, September 2009.

[5] Iqbal A. and Ben Amara F., *Modeling and experimental evaluation of a circular magnetic-fluid deformable mirror*, International Journal of Optomechatronics, vol. 2, no.2, pp. 126–143, 2008.

[6] Iqbal A., Wu Z. and Ben Amara F., *Closed-loop control of magnetic fluid deformable mirrors,* Optics Express, vol.17, no.21, pp. 18957-18970, 2009.

[7] Wu Z., Azhar I. and Ben Amara F., *LMI-based multivariable PID controller design and its application to the control of the surface shape of magnetic fluid deformable mirrors,* IEEE Transaction on Control System Technology, vol.19, no.4, pp.717-729, 2011.

[8] Zahn M., *Magnetic fluid and nanoparticle applications to nanotechnology,* Journal of Nanoparticle Research, vol.3, pp.73-78, 2001.

[9] Nakano M., etc., *Drug delivery system using nano-magnetic fluid,* ICICIC ’08, 3rd International Conference on Innovative Computing Information and Control, pp.338, June 18-20, 2008.

[10] Dery J. P., Borra E. F., and Ritcey A. M., *Ethylene glycol based ferrofluid for the fabrication of magnetically deformable liquid mirrors,* Chemistry of Materials, vol.20, no.20, pp.6420-6426, 2008.

© (2012) Trans Tech Publications, Switzerland
doi:10.4028/www.scientific.net/AMM.164.414

Mechanics Analysis of Grade V Surrounding Rock Primary Support in Maanziliang Tunnel

Jiaming Han[1, a]

[1] School of Architecture and Civil Engineering, Xi'an University of Science and Technology, No.58 Yanta Zhonglu, Xi'an, Shannxi, 710054, China

[a]jiaminghan@163.com

Key words: Finite Element Method; Tunnel; Primary Support; Mechanics

Abstract: Commonly used finite element strength reduction to calculate the safety factor of slope, to analyze the stability of the slope[1~ 3]. Recently it also proposed the methods to evaluate the safety factor for the stability of surrounding rock of underground chambers and supporting structural mechanics[4~ 6]. For Qinling Mountains of the complex geological conditions in the Maanziliang highway tunnel, this article use the finite element method from the bolt resist tension, bolt length, the force of sprayed layer of concrete to computing grade V surrounding rock section of primary support safety factor, to give evaluation to support mechanics of the Maanziliang tunnel.

Introduction of Maanziliang tunnel

Maanziliang highway tunnel is typical separation long in Shaanxi section from Shiyan to Tianshui highway. The range of right line stake is YK34+614~ YK39+539. Full-length is 4925m. The Stake of grade V surrounding rock section is YK34+625~ YK34+728(103m), YK38+467~ YK38+693(226m), YK39+372~ YK39+533(161m).

Wall rock lithology and depth

Elastic modulus of surrounding rock is 1×10^9Pa, Poisson's ratio of surrounding rock is 0.35, Rock bulk density is 20×10^3N/m^3, Rock lateral pressure coefficient is 0.5, Cohesion of surrounding rock is 0.05×10^6Pa.

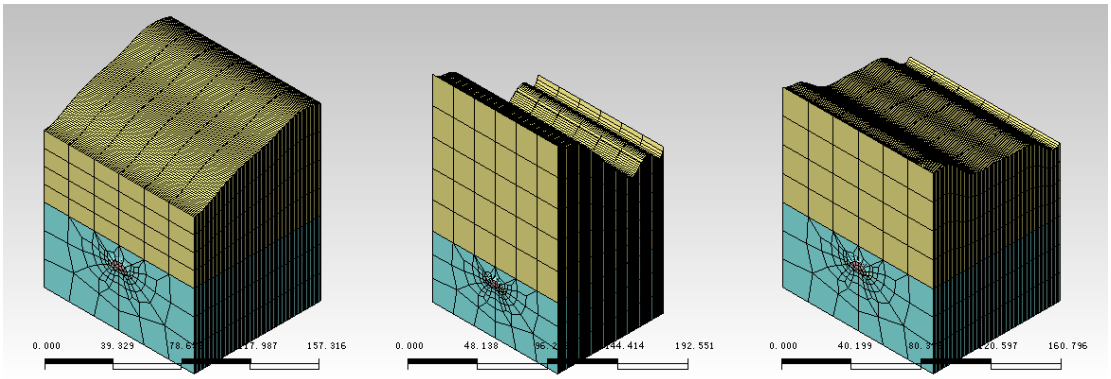
The YK34+625~ YK34+728 section tunnel depth 20.98m~ 49.28m, and the YK38+467~ YK38+693 section tunnel depth 103.26m~ 51.31m, and the YK39+372~ YK39+533 section tunnel depth 52.12m~ 22.09m.

Grade Ⅴ surrounding rock section support parameters

It adopted advanced support of φ50 Ultra-catheter, which the length 5m, wall thickness 4mm, round spacing 40cm, row spacing 3.6m. Primary support use I20b steel arching, spacing 60cm, and arching design radius is R1=7.415m, R2=6.290m. φ22 vertical connection spacing is 1m. φ22 early-strength mortar bolt length is 4m, spacing 100cm×60cm (loop × vertical) which the upper part has 20 or 21, the lower part 2,3 on each side. φ8 reinforced mesh size is 20cm×20cm, mesh size 180cm×80cm. C20 spray concrete is thickness 26cm.

Finite element method of analysis

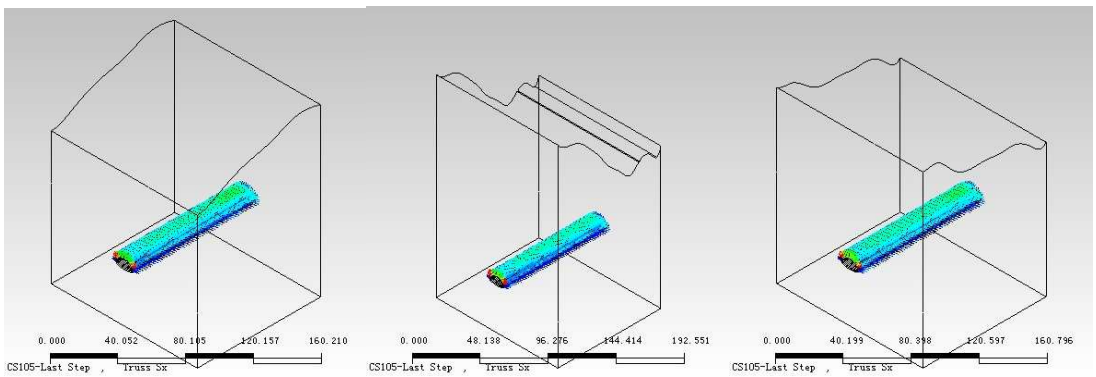
Model and mesh. YK34+625~ YK34+728 section has 2111 embedded bolt units, 2266 shotcrete board units, surrounding rock 12978 entity units and 18574 nodes. The construction phase can be divided 103 1m-segments according to footage. YK38+467~ YK38+693 section has 2111 embedded bolt units, 2258 shotcrete board units, surrounding rock 13596 entity units and 54388 nodes. The construction phase can be divided 226 1m-segments according to footage. YK39+372~ YK39+533 section has 2111 embedded bolt units, 2266 shotcrete board units, surrounding rock 12978 entity units and 51916 nodes. The construction phase can be divided 161 1m-segments according to footage, shown in Fig.1.



(a) (b) (c)

Fig.1 Model and mesh (a) YK34+625~ YK34+728 section (b) 2YK38+467~ YK38+693 section (c)YK39+372~ YK39+533 section

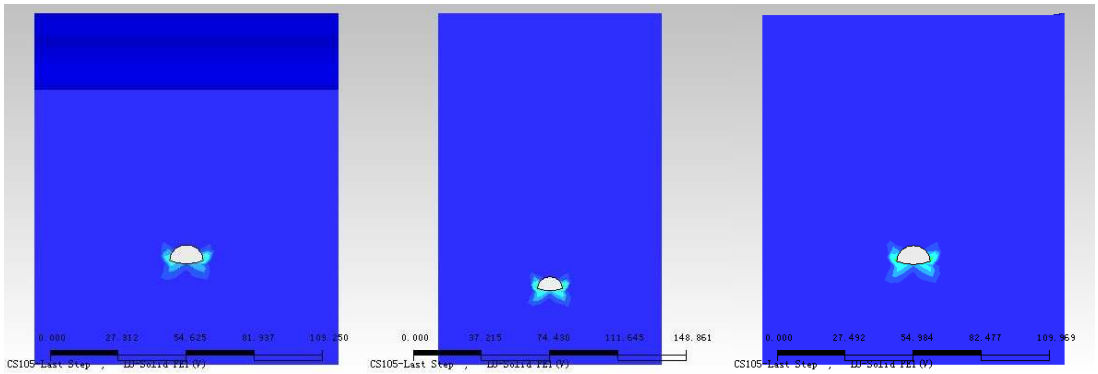
Bolt tension analysis. All bolt units plastic strains are 0 and not destruction that the bolt is in the elastic state.YK34+625~ YK34+728 section the maximum bolt stress is 1.49133 × 10^8N/m^2, bolt tension safety factor is $\frac{418\times10^6}{1.49133\times10^8}=2.8029$. YK38+467~ YK38+693 section the maximum bolt stress is 2.05219×108N/m^2, bolt tension safety factor is $\frac{418\times10^6}{2.05219\times10^8}=2.0368$. YK39+372~ YK39+533 section the maximum bolt stress is 1.37837×108N/m^2, bolt tension safety factor is $\frac{418\times10^6}{1.37837\times10^8}=3.0326$, shown in Fig.2.



(a) (b) (c)

Fig.2 Bolt Stress (a) YK34+625~ YK34+728 section (b) 2YK38+467~ YK38+693 section (c)YK39+372~ YK39+533 section

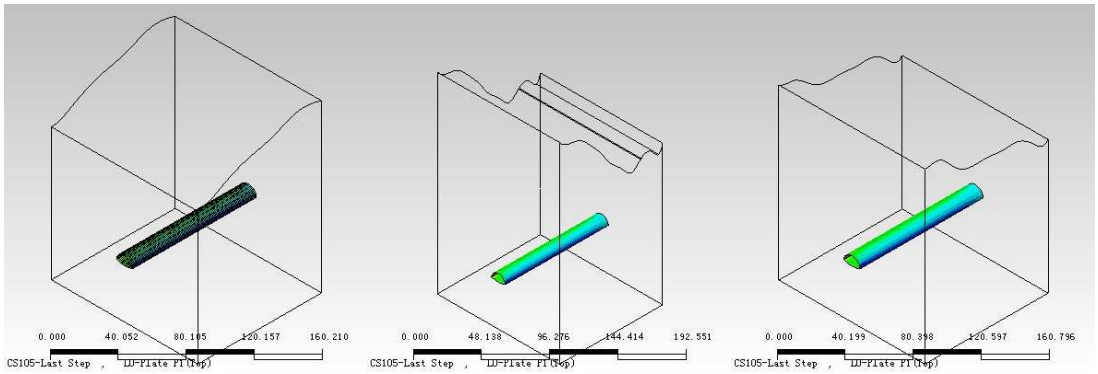
Bolt length analysis. Bolt length is 4m. YK34+625~ YK34+728 section plastic zone maximum distance is 5.6m, and the length of rock bolt safety factor is $\frac{4}{5.6}=0.714$. YK38+467~ YK38+693 section plastic zone maximum distance is 6.8m, and the length of rock bolt safety factor $\frac{4}{6.8}=0.588$ .YK39+372~ YK39+533 section plastic zone maximum distance is 6.3m, so the length of rock bolt safety factor is $\frac{4}{6.3}=0.635$, shown in Fig.3.



(a) (b) (c)

Fig.3 Surrounding rock plastic strain (a) YK34+625~ YK34+728 section (b) 2YK38+467~ YK38+693 section (c) YK39+372~ YK39+533 section

Spray layer stress analysis.YK34+625~ YK34+728 section shotcrete maximum stress is 6.42698×107N/m^2, Considering the spray thickness effects of spray concrete safety factor is $\frac{20\times10^6}{6.42698\times10^7}\times\frac{0.81}{0.1}=2.521$ .YK38+467~ YK38+693 section shotcrete maximum stress is 9.75225×107N/m^2, Considering the spray thickness effects of spray concrete safety factor is $\frac{20\times10^6}{9.75225\times10^7}\times\frac{0.81}{0.1}=1.661$. YK39+372~ YK39+533 section shotcrete maximum stress is 6.74805×107N/m^2, Considering the spray thickness effects of spray concrete safety factor is $\frac{20\times10^6}{6.74805\times10^7}\times\frac{0.81}{0.1}=2.4007$, shown in Fig.4.



(a) (b) (c)

Fig.4 Spray spindle stress of the concrete top level (a) YK34+625~ YK34+728 section (b)2YK38+467~ YK38+693 section (c) YK39+372~ YK39+533 section

Rock section of the initial support safety factor of Maanziliang highway tunnel of grade V

According to the Maanziliang highway tunnel in YK34+625~ YK34+728 section, YK38+467~ YK38+693 section, YK39+372~ YK39+533, it is analysised of primary support grade V surrounding rock section by finite element method. the initial support safety factor of grade V should be taken as the minimum bolt tension, bolt length, sprayed concrete layer safety factor, being0.588.

Acknowledgements

This work was financially supported by the Scientific Research Program Funded by Shaanxi Provincial Education Department (Program No. 08JK363, 09JK570) and the Culture Foundation of Xi'an University of Science and Technology (Program No. 2010033).

References

[1] Xi Chen, Chun-jie Liu. 'FEM strength safety factor in the subtraction search algorithm' [J]. Journal of Geotechnical Engineering,2010,32(9):1443-1447. In Chinese.

[2] Lin-chao Lin, Bo Liang Ji Diao. etc.. 'Reduction request based on ANSYS finite element strength safety factor of slope '[J]. Chongqing Jiaotong University.2009,28 (5): 889- 910. In Chinese.

[3] Hong Zheng, Bin Tian, De-fu Liu, etc.. 'The definition of safety factor on the finite element slope stability analysis '[J]. Rock Mechanics and Engineering ,2005,24 (13): 2225-2230. In Chinese.

[4] J. M. Han, S. Q. Su. Analysis of Pitted Courtyard Cave Dwellings Stability in Baishe Village when Rainfall Infiltration [J]. Advanced Materials Research, 2011, (250-253): 2468-2472.

[5] J. M. Han, S. Q. Su. Effect of Rainfall Infiltration on Loess Pitted Courtyard Cave Dwellings Stability [J]. Advanced Materials Research, 2012, (430-432): 1992-1995.

[6] J. M. Han. Study on Safety Factor of Loess Cave Dwellings with Pitted Courtyard in Different Rainfall Infiltration [J]. Advanced Materials Research, 2012, (446-449): 1555-1558.

CHAPTER 3:

Industry, Mechanical Engineering, Manufacturing Engineering Based on Dynamic Systems

© (2012) Trans Tech Publications, Switzerland
doi:10.4028/www.scientific.net/AMM.164.421

Research of Hydraulic Cylinders Dynamic Characteristic and Synchrocontrol on Horizontal Pipes Connector in Deep Sea

Zh. Wang, Y.J.LI,B. Zhang, W.Zhang and Y.Z.Zhang

College of Mechanical and Electrical Engineering, Harbin Engineering University, Harbin 150001, China,

wangzhuo_heu@hrbeu.edu.cn

Keywords: Horizontal pipes connector, Hydraulic cylinder, Dynamic characteristic ,Synchrocontrol

Abstract. The electro-hydraulic position-servo synchronization system of horizontal pipes connector was designed in order to connect two pipes in deep sea and make sure the journey of synchronization hydro-cylinders in the hydraulic system is less than 2 mm.Its transfer function of symmetric servo controlling oil-cylinder electro-hydraulic servo system were derived . Simulation analysis of its dynamic characteristic was done, and PID controller was applied on the system to regulate two hydraulic cylinder synchronization controls. In the end ,when the proportionality coefficient is K_p=0.55,integral coefficient is K_i=60,differential coefficient is K_d=0,the error of synchronic displacement was less than 0.5 mm, that achieved the request of the control system.

Introduction

As one of the Subsea Tie-in machinery, horizontal pipes connector is a quick connecting device which is widely used in deep-sea oil and gas pipeline system, the working environment of which is usually deep water, poor working conditions, uncertain elements, so workers can not work. Therefore, it is assisted by the implementation of ROV operations, which can connect two pipes rapidly and accurately. Its main work processes in sequence are composed of five parts: vertical coarse alignment, rotary and level of precise alignment, butt joint seals, locking and fixxing and auxiliary and recyclable targeting device. This article will focus on the horizontal pipe flange sealing problem and adopt the synchrocontrol way to control the precise displacement of the flange to achieve the unmanned underwater work.

Analysis of Two Cylinders Synchronization and its Dynamic Characteristic

The Mathematical Model of the Electro-Hydraulic Position-Servo Dynamic System. The principle of the hydraulic synchronization system of the horizontal pipes connector is shown as Fig.1.

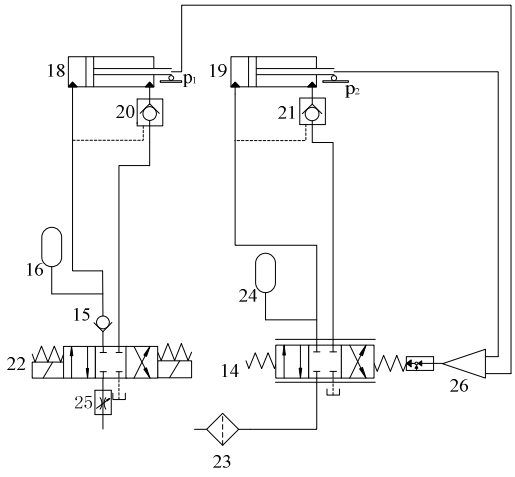


Fig.1 The hydraulic loop of the connect mechanism.

The benchmark of this system is hydraulic cylinder 18, the piston of which is acting followed by the piston of the hydraulic cylinder 19 in order to keep them at the same pace. the displacement sensor p1 and p2 produce the displacement signals of two pistons constantly when they are working, and two signals are compared and then a deviation signal is obtained. The deviation signal is entered into the amplifier and then the electro-hydraulic position-servo valve to be controlled in order to make the piston of hydraulic cylinder 19 and the piston of hydraulic cylinder 18 in a same pace. This system is composed of two Synchronous circuits and controls the error of synchronic displacement to be no more than 0.5mm

The system mathematical model is established by the force feedback displacement synchronization servo control hydraulic system. The block diagram as Fig.2 is obtained on the basis of the three basic equations the dynamic characteristics of the valve controlling hydraulic cylinders.

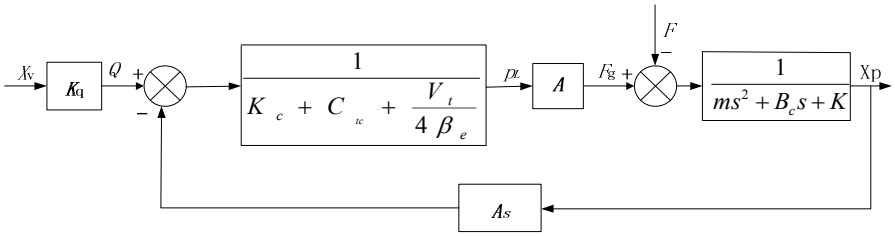


Fig.2 The block diagram of the valve controlling hydraulic cylinders.

Combining the mathematical model of open-loop system and mathematical model of closed-loop system can obtain the results for a total hydraulic system mathematical model as shown in Fig.3 and the transfer function of system as formula (1).

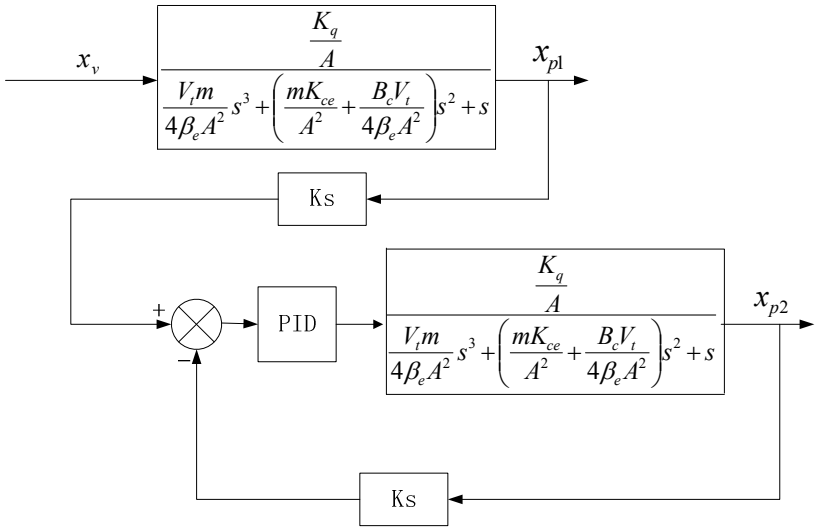


Fig.3 The mathematical model of total hydraulic system.

$$\varphi(s)=\varphi_1(s)\cdot\varphi_2(s)=\frac{\frac{K_q}{A}}{\frac{V_t m}{4\beta_e A^2}s^3+\left(\frac{mK_{ce}}{A^2}+\frac{B_c V_t}{4\beta_e A^2}\right)s^2+s}\bullet\frac{\frac{K_q}{A}PK_s}{\frac{V_t m}{4\beta_e A^2}s^3+\left(\frac{mK_{ce}}{A^2}+\frac{B_c V_t}{4\beta_e A^2}\right)s^2+s+\frac{K_q}{A}PK_s} \quad (1)$$

$$=\frac{\frac{K_q}{A}}{s\left(\frac{s^2}{w_n^2}+\frac{2\xi_n}{w_n}+1\right)}\bullet\frac{\frac{K_q}{A}PK_s}{s\left(\frac{s^2}{w_n^2}+\frac{2\xi_n}{w_n}+1\right)+\frac{K_q}{A}PK_s}$$

Setting the Dynamic Simulation Parameters. On the basis of the mathematical model, the simulation parameters are determined as follows: the elastic modulus of effective volume is β_e , $\beta_e = 800\text{MPa}$; the density of oil is ρ , $\rho = 900$ Kg/m; the pressure of fuel feeding

is p_s , $p_s = 16$ Mpa; the pressure of load is p_L , $p_L = 15$ Mpa; the coefficient of flow ia C_d , $C_d = 0.62$; the coefficients of internal and external leaks are roughly the same and can be neglected to be zero, i.e., C_{ic}=0, C_{ec}=0.

Because the load of this system is not elastic， the spring stiffness of the load is 0, i.e., K=0; The viscous damping coefficient of the piston and the load is very small and can be neglected， i.e., B_c=0; the sectional area of the piaton is A, A=$\pi D^2/4$=0.0177 m^2， the cavity volume is Vt , Vt=$\pi(D^2-d^2)L/4$ =0.0144 m^3; The area gradient of the piston valve core is w, w=πd_1=0.2669m; The glow gain is Kq, $K_q = Cdw\sqrt{(p_s - p_L)/\rho} = 5.5159$. Because of the application of linear simulation， the value of K_c is calculated in the condition of the balance point when it is that X_v=0.0003 m; the total divulging coefficient is C_{tc} , $C_{tc} = C_{ic} + C_{ec}/2 = 0$;

Total flow—pressure coefficient: $K_{ce} = K_c + C_{tc} = 8.27 \times 10^{-10}$;

Damping ratio: $\xi_n = \frac{K_{ce}}{A}\sqrt{\frac{\beta_e m}{V_t}} + \frac{B_c}{4A}\sqrt{\frac{V_t}{\beta_e m}} = 0.348$

Hydraulic inherent frequency: $w_n = \sqrt{4\beta_e A^2/(V_t m)} = 263.86$

Feedback ratio coefficient: K_s=1.

Dynamic Simulation Analysis of Two Hydraulic Cylinders Synchronization Control

After the mathematical model and the parameter setting of the electro-hydraulic servo system of horizontal pipes connector are finished, the model of the electro-hydraulic servo system is established and the simulation analysis is made in MATLAB/ Simulink software. This analysis is made into two steps: firstly, synchronization system without PID controller is simulated and its function is analyzed. Secondly, PID controller that is applied on the system is simulated and each link's effect to sychronization function is analyzed in order to determine the optimal PID controller.

The Dynamic Simulation Analysis without PID Controller. According to the transfer function of system and the block diagram, the hydraulic system model is established in MATLAB/ Simulink and it is shown as Fig.4. The simulation parameters are formed into file.m which is made a simulation analysis. The result of the dynamic analysis is illustrated in Fig.5.

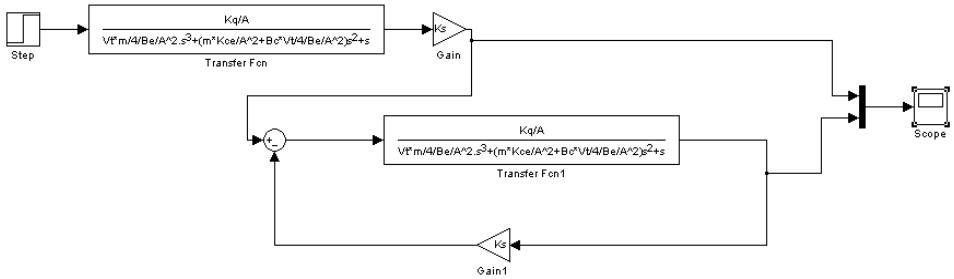


Fig.4 The simulated model of the electro-hydraulic servo system.

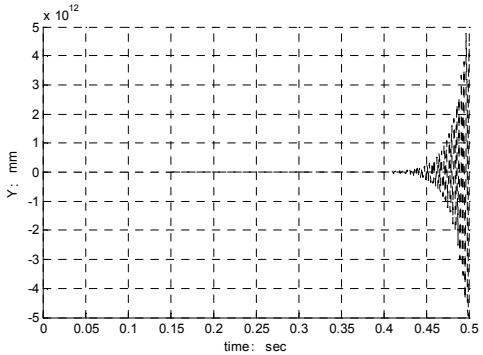


Fig.5 The synchronization dynamic analysis without PID controller for two hydraulic cylinders.

On the basis of the result, the curve of the following hydraulic cylinder has diffused after starting 0.4 seconds and the system cannot achieve synchronization. So the correction link must be added to and PID controller is chosen to adjust it.

The Dynamic Simulation Analysis with PID Controller. As for The loop following links of the systematical model in Fig.4, PID controller is added before the transfer function. A group of the optimal values of PID is obtained according to the stimulation analysis of each link of PID controller. The measurement error of two hydraulic cylinder synchronization is the minimum. The coefficients of proportion, integral and differential are adjusted respectively and series of simulation curves are gotten. At last after the comprehensive analysis and comparison, the control requirements of the system are achieved. That is, when the coefficient of proportion is K_p, K_p=0.55, the coefficient of is K_i, K_i=60, and the coefficient of is K_d, K_d=0. The following hydraulic cylinder can follow the position of active hydraulic cylinder in 0.02 seconds and the system has no vibration. Synchronous effect displacement error is not more than 0.5mm. the result of the stimulation is shown as Fig.6.

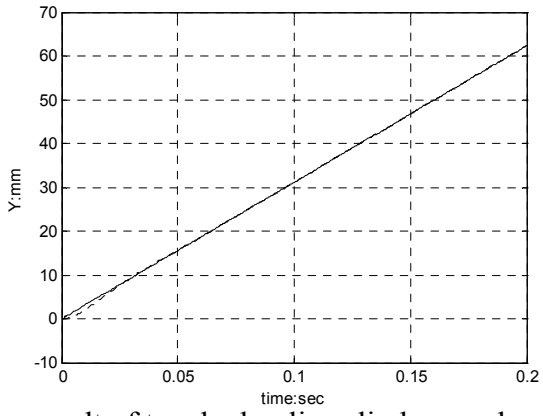


Fig.6 The dynamic simulation result of two hydraulic cylinder synchronization after PID controller being ensured.

From Fig.6, the following hydraulic cylinder and the active hydraulic cylinder exist the displacement error before 0.02s. The displacement line of following hydraulic cylinder and active hydraulic cylinder overlaps and the displacement error disappears after 0.02s.

Summary

The following three points are abstained by the synchronous control research of flange displacement of the horizontal pipe connector. The first, the largest compression of the displacement of flange is controlled for 2 mm.The second, the displacements of the pistons of hydraulic cylinder which push the flange need be ensured for the synchronization movement and the end, two cylinders displacement synchronous accuracy can be controlled in the scope of system errors by PID controller.

References

[1] Q.F.Wang,L.D.He.:Thermal power engineering.Vol.24(2009),p.38-43

[2] Y.M.Gong: *The Study on Electrohydraulic Digital Servo Synchronization System*(Master of Engineering, ZHE JIANG industry university, 2007)

[3] D.B.Dong: *Critical Technology Research of The Subsea Oil & Gas Horizontal Pipe Collet Connection*(Master of Engineering, Harbin Engineering University,2010)

[4] Y.X.Chen,Q. He,C. CH.Zhan etc: Hydraulic and pneumatic,Vol.32(2008),p36-42

[5] O.Keles, Y. Ercan: Control Engineering Practice. Vol 10(2002),p.645-654.

[6] G.Bartolini: Journal of Dynamic Systems, Measurement, and Control.Vol.122(2000),p.604-610

© (2012) Trans Tech Publications, Switzerland
doi:10.4028/www.scientific.net/AMM.164.425

Analysis of 3D Dynamic Response for TC4 Blades by the FEM

YingWu Fang[a], YingHong Li[b] and WeiFeng He[c]

Air Force Engineering University, Xi'an China

[a]fangyw72@126.com, [b]yinghli@126.com, [c]wfenghe@163.com
Corresponding author: Yingwu Fang, Email: fangyw72@126.com, fywwy123@yahoo.com.cn
Address: 1st East Fenghao Road No.117, Xi'an 710077, Shaanxi, China

Keywords: 3D FEM; Dynamics behaviors; TC4 blades

Abstract. TC4 blades are one of the major parts of the aero engine, and the examples of engine invalid and even wrecked are common. In this paper, a 3D analysis system of the vibration behaviors of the TC4 blades is given. The 3D analysis model of blade was described using 20 nodes elements. The finite element procedure was worked out using the blade vibration behaviors analysis of the aero engine. At last, the modal shapes and stress nephograms of the first six frequencies are gotten which influenced the blade vibration characteristics. Results show that the program has offered an effective, flexible research means for analyzing dynamic response of TC4 blades.

Introduction

Fan/compressor is the main parts of aeroengine. At present, titanium alloy blades of high specific strength are applied widely in the fan/compressor[1]. Owing to the accident of blades vibration is one-third of the engine structure approximately, vibration performance of blades can influence the security of blades operating directly. Thereby, it is one of the very complex and important issue during development for analyzing blades vibrational strength of aeroengine[2,3]. As a kind of important aviation parts, it has very important meaning for analyzing dynamic behaviors of TC4(Ti-6Al-4V).

Based on present research, super-parametric shell element of 8 nodes can be adopted to disperse thin blades of compressor usually. The computing is simple, but computational precision cannot meet the design requirement[4]. In this study, tetrahedral elements of 20 nodes is applied to intelligent grid division on the base of static analysis and fore- post processor of 3D finite element method (FEM), and dynamic behaviors of TC4 blade will be simulated by analyzing 3D dynamic responses.

The FEM model of TC4 blade

TC4 blade has complicated structure, and establishing entity model is very difficult by ANSYS. Firstly, the TC4 blade is scanned by laser scanner, data information of TC4 blade are gotten, and the corresponding entity model are established by CAD/CAM. Whereafter, the data information of TC4 blade are led to ANSYS by seamless interface of ANSYS and PRO/E.

In order to improve computational precision of dynamic response, tetrahedral elements of 20 nodes are applied to the whole compressor blade include margin plate and rabbet. At last, the number of 6326 elements and 12553 nodes is given to establish the FEM model of TC4 blade by intelligent grid, and the corresponding model was shown in Fig.1.

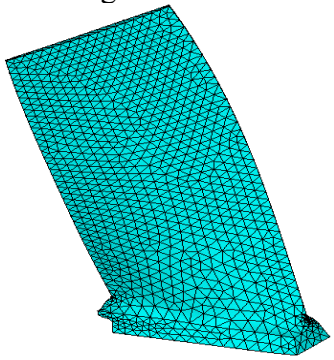


Fig.1 The FEM model of TC4 blade

Dynamic rsponse equations of TC4 model

Damping force is one kind of dissipative force of influence vibrational behaviors, and it can reduce amplitude and dynamic stress nearby resonance region, especially. So, providing blade damp is a main measure of reducing dynamic stress. It is very diffcult for precise analyzing damp, and the linear combination of $[M]$ and $[K]$ is assumed as $[C]$[5], the following equation was obtained:

$$[C]=\alpha[M]+\beta[K]. \tag{1}$$

Considering the influence of damp, the following differential equation was given:

$$\sum_e\left([M]^e\{\ddot{\delta}\}^e+[M_G]^e\{\dot{\delta}\}^e+[C]^e\{\dot{\delta}\}^e-[K_c]^e\{\delta\}^e+[K_0]^e\{\delta\}^e+[K_\sigma]^e\{\delta\}^e\right)=\sum_e\{Q_c\}^e+\sum_e\{Q_p\}^e. \tag{2}$$

Where $[M]^e$ is the mass matrix, $[M_G]^e$ is the Coriolis force matrix, $[C]^e$ is the damp stiffness matrix, $[K_c]^e$ is the centrifugal force stiffness matrix, $[K_0]$ is the linear stiffness matrix, $[K_\sigma]$ is the stiffness matrix of initial stress, $[Q_c]^e$ is the vector of centrifugal force, $\{Q_p\}^e$ is the vector of aerodynamic force, $\{\delta\}^e$ is the vector of nodal displacement.

The differential equation of whole blade could be written:

$$M\ddot{\delta}+[C+M_G]\dot{\delta}+(K_0+K_\sigma-K_C)\delta=Q_c+Q_P. \tag{3}$$

Because of the value of $[K_c]$ is less, it could be ignored. Thereby, the dynamic response equation was given when blade is static and dynamic:

$$([K_0]+[K_\sigma])\{\varphi\}=[M]\{\varphi\}[\lambda]. \tag{4}$$

Where $\{\varphi\}$ is the eigenvector matrix, $[\lambda]$ is the eigenvalue matrix, $[M]$ is the mass matrix of discrete system, $[K]$ is the stiffness matrix of discrete system.

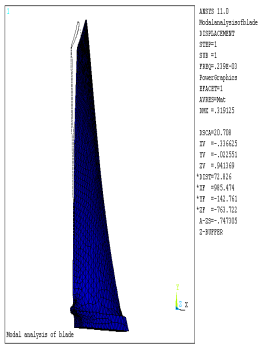
Based on the Lanczos method, the frequency behaviors of TC4 blade could be gotten by solving Eq.(4), and the corresponding static and dynamic natural frequencies could be obtained effectively.

Example computation

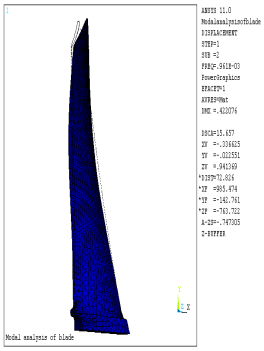
A case of TC4 blade dynamic response was analyzed by FEM simulating, and the constraint was applied to bottom of blade rabbet. ρ=4500kg·m^{-3}, υ=0.342, E=110GPa. In the process of computing, tetrahedral elements of 20 nodes were selected, and the number of 6326 elements and 12553 nodes were given to analyze the dynamic response of TC4 blade. At last, first six natural frequencies of TC4 blade were given in Table 1. The corresponding modal shapes and stress nephograms of first six natural frequencies were shown in Fig.2 and Fig.3, respectively.

Table 1 Comparison of the computed and experimental values for TC4 blade (f/Hz)

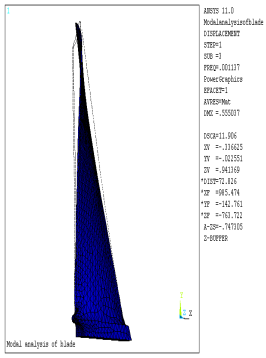
Orders	1	2	3	4	5	6
Computed results(Hz)	239	961	1137	2229	2755	3329
Measured results(Hz)	245	973	1184	2352	3019	3666
Relative errors(%)	2.45	4.61	3.97	5.23	8.75	9.19



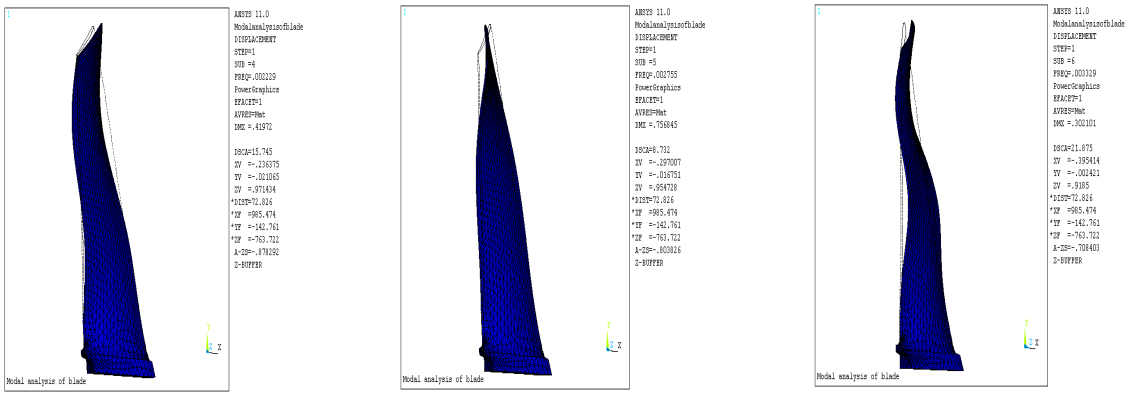
f=239Hz



f=961Hz

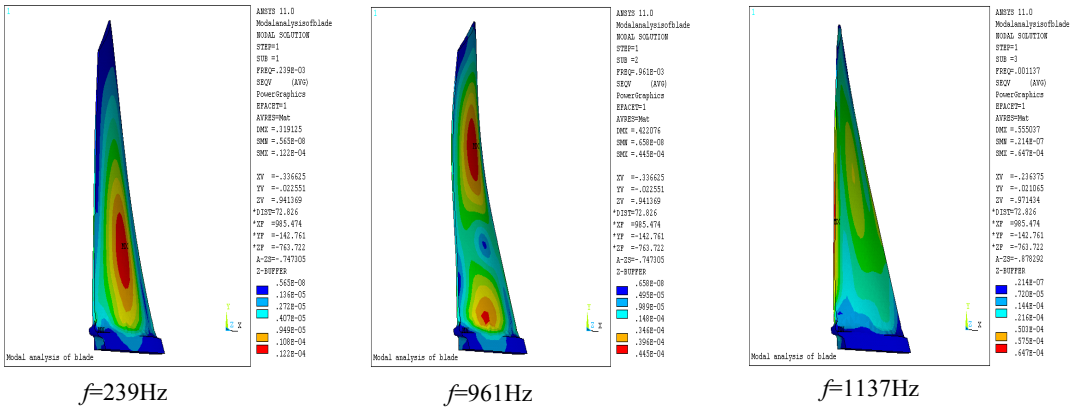


f=1137Hz

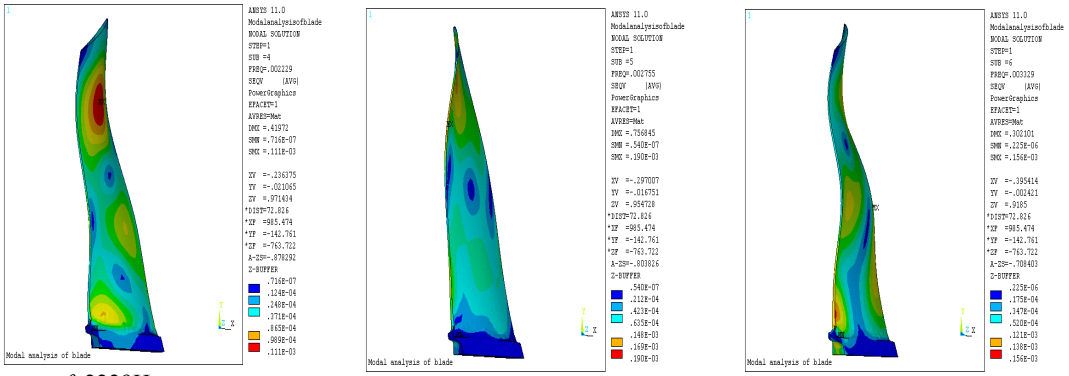


f=2229Hz *f*=2755Hz *f*=3329Hz

Fig.2 Modal shapes of first six natural frequencies



f=239Hz *f*=961Hz *f*=1137Hz



f=2229Hz *f*=2755Hz *f*=3329Hz

Fig.3 Stress nephograms of first six natural frequencies

The modal shapes and stress nephograms of first six natural frequencies were given in Fig.2 and Fig.3 by calculating. The following will discuss the influence of resonance vibration for TC4 blade. Through analyzing the modal data of 239Hz, 961HZ, 2229Hz, 3329Hz, the first order and second order frequencies belong to bending vibration, and the forth order and sixth order frequencies belong to twisting vibration by the modal shapes and stress nephograms of TC4 blade. So, the geometry of blade was already deformed when resonance state was kept. With the increase of resonance frequency, the deforming of blade will be severe.

In order to verify the validity of the blade model, the dynamic behaviors of the TC4 blade were measured by exciting test through the HP3562A dynamic signal analyzer. Experimental apparatus and flow were shown in Fig.4. In order to reduce experimental error, the average values of ten times self-excited vibration was taken out in the process of dynamic experiments, and the measured results were given in Table 1. The maximum relative error of the natural frequencies between calculating and measuring is 9.19%, which showed that the simulated model can be used to analyze the dynamic

response of TC4 blade. Fig.5 is the error analysis of the computed and experimental results for TC4 blade. Here errors of calculating are mainly aroused in calculated modeling, and boundary conditions were simplified. At the same time, measure instruments itself can also bring some errors, etc.

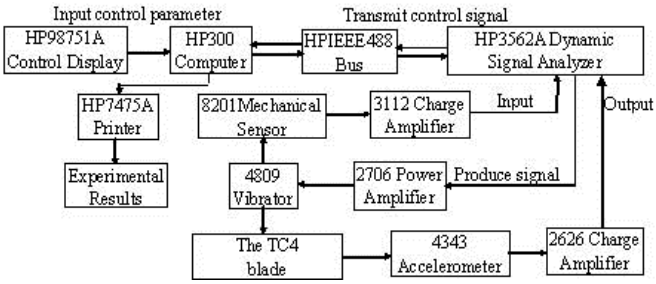


Fig.4 The flow chart of TC4 blade dynamic experiments

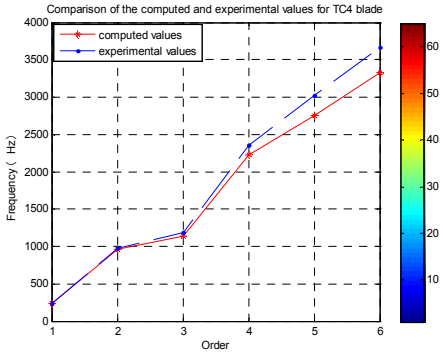


Fig.5 Error analysis of the computed and experimental values

Conclusions

This paper investigates the dynamic response of TC4 blade. The computation is based on FEM, which is used on compute the dynamic behaviors of TC4 blade, and the analysis and discusses which influenced the blade vibration characteristic of the aeroengine were given. The computation results showed that the simulated model and computed results is effective. The finite element analysis using ANSYS was employed for result verification, and the result comparison show that the maximum difference between the results from the two methods is less than 10%. Thereby, this program has offered an effective, flexible research means for blades of aeroengine fatigue damage and dependability. A fast calculated method of analyzing blade dynamic response can be provided by this study. At the same time, the simulated results will provide theoretical guide for analyzing laser shocking process of TC4 blade at its design stage deep.

Acknowledgements

The authors would like to express their sincere gratitude to the support from the natural science foundation of shaanxi province, China (No. 2010JM6012), China postdoctor (No. 20100471835) and the national defence key project of AATR program.

References

[1] A.C. Lavender, S.T. Hong and M.T. Smith, et al: The effect of laser shock peening on the life and failure mode of a cold pilger die. J. Materials Processing Technology Vol. 204 (2008), p. 486-491.

[2] C.S. Lei, A. Davis and E.W. Lee. Effect of BSTOA and mill anneal on the mechanical properties of Ti6Al4V casting. Advanced Materials & Processes Vol. 2 (2000), p. 75-80.

[3] D. Lee and S.Kim: Effects of micro structural morphology on quasistatic and dynamic deformation behavior of Ti-6Al-4V alloy. Metal Trans A. Vol. 32A (2001), p. 315-318.

[4] W. He and B.Z. Huang: Analysis of 3D vibration characteristics for rotor blades of aero engine by the finite element method. Journal of Shenyang Agricultural University Vol. 37 (2006), p. 754-757.

[5] J.H. Griffin: Friction damping of resonant stress in gas turbine engine airfoils. ASME Journal of Engineer for Power Vol. 102 (1980), p. 329-333.

© (2012) Trans Tech Publications, Switzerland
doi:10.4028/www.scientific.net/AMM.164.429

Engine valve motion simulated with Mechanical dynamics

Zongzheng Ma[1, a], Xinli Wang[1,b]

[1]Department of Mechanical Engineering, Henan Institute of Engineering, Zhengzhou, China

[a]zongzhengma@163.com, [b]wangxingli01@sina.com

Keywords: Engine; valve; simulation; Pro/E

Abstract. One of the important methods for studying the valve train system is simulation. So the feasibility of valve motion simulation by Pro/E is discussed in this paper. After model establishing and connection completing, the valve motion is simulated and some results are reached. It can be seen from the results that valve motion can be simulated based on Pro/E environment. It also be seen that the valve acceleration varied at high frequency and the impact between the valve and seat is existed for the studied valve system. For studied valve it meets the demand of the engine.

Introduction

The train valve is one of the most important parts of the engine, and it is function is fresh charge inlet and exhaust exit according the order of the engine based on the intake and exhaust valve. Therefore the valve is the heart of the train valve which plays an important role in gas exchange system and it affects the shock, vibration, noise, durability and reliability directly. Especially, it is plays a more important role in the train valve of modern gasoline engine [1-3].

Today an important method for studying the valve train system is code simulation. The valve cam quality is equivalent to the concentrated mass and the system stiffness is replaced by cam follower overall stiffness for traditional method for valve train simulation. Meanwhile the system parameters can be determined by experiment or the empirical formula [1, 2].

Since the first version of Pro/E is released in 1988 by the United States Parametric Technology Corporation (Parametric Technology Corporation, referred to as PTC), it has become one of the most important CAE tools [4]. The Pro/E includes the part design, surface design, 2D drawing, product assembly, mold development, NC machining, pipeline design, circuit design, sheet metal design, casting design, model design, reverse engineering, concurrent engineering, automatic measurement, mechanism simulation, stress analysis, finite element analysis, and product data management. Among them, the mechanism motion analysis module (the Mechanism module) is integrated the motion simulation and mechanism analysis function which can do motion simulation and mechanism analysis after assembling all body parts [5].

Fundamental of engine valve mechanical dynamics

The various components of the actual train valve in the process of high-speed operation have a certain degree of deformation because of the great stiffness. So an important reason for studying the dynamic characteristics of train valve is the deflection of the valve trajectory in the process of high-speed movement.

At the beginning the valve train is simplified as concentrated mass-spring vibration model for dynamic characteristics research. And the common models are single degree of freedom model and multi-degree of freedom model. In order to simulate the valve train more accurately the flexible dynamic model is developed which is analyze the impact of valve train components elastic kinematic modeling assumes that the various components of movement is very simple. With the development of the theory based on simulation technology much commercial simulation software, such as Solid Works, UG, the Pro/E and other software are developed which has interactive user interface, modeling, assembly and post-processing process.

So the connection between the frame and composition of the parts or components of the kinematic part is defined according the design intent firstly. Then define the servo motor whose function is to impose a force or torque and to provide the specified movement. Finally the movement is running and the results can be got.

Process of motion simulation

The general process of motion simulation is as follows:

(1)Motion connection is establishment in the assembly environment.

In order to ensure the body movement, the part should be connected. The difference between the general assembly constraints and Pro/E constraints is the assembly of moving parts to keep the required degree of freedom for Pro /E connection.

(2)Inter the analysis environment.

(3)Set the drive to define the servo motor.

(4)Set the analytical conditions and run.

(5)Obtain the results of the analysis.

Motion simulation can use the playback and measurement functions to further understand the process and results of the analysis, such as interference checking for motion analysis, measurement trajectory. And the simulation process is shown in figure1.

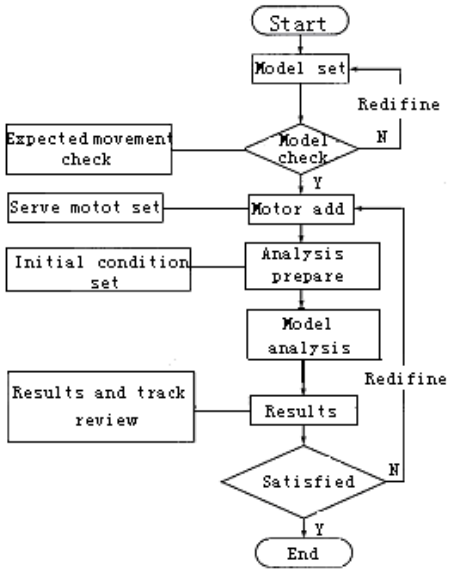


Fig.1 Diagram of mechanism simulation

1) Establishment of motion connection

Mechanical simulation technology must rely on the realistic parts of three-dimensional model, Pro/E as the flagship product of the three-dimensional modeling software, accurate modeling of complex parts of any shape can be achieved and it can also realize parametric modeling based on secondary development tools combined with Pro/E [5].

At the beginning, the three-dimensional model of valve, rocker arm, cam and camshaft is established in the Pro/E platform, and the model is shown in figure2.



(a)Valve (b)Rock arm (c)Crank and crankshaft

Fig.2 Three-dimensional model of different parts

2) Assemble of the motion simulation model

There are bottom-up design methods and top down design method for parts assemble design and the later is more traditional. For the bottom up design way all parts are designed firstly and then individually transferred to the assembly environment, and finally add a constraint tie between the various parts according to the assembly of functional and design requirements. So the bottom up way is selected in this paper. The complete simulation model can be seen in figure 3.



Fig.3 Simulation model

3) Definition of connection parts

In general, the connection assembly, the choice will directly affect the movement of the organization and the correct connection of components is the key for successful simulation. So in order to do motion simulation, the assembly model should be created by user-defined constraints and the connection constraints. User-defined

constraints are used to create the assembly does not require moving parts such as rack, base, etc.. The connection constraints are used to create moving assembly such as the rotation axis, the slider. Based on above analysis, the rotational movement is defined by connection constraints and the rack is defined by user-defined constraints.

4) Driver added

In order to active the model the driver should be added which should be an accurate definition of the connection relationship between the joints and geometric primitives, such as rotation or translation. Click the button to open the [servo motor definition] dialog box, and to create a new drive for motion simulation of gasoline inlet and outlet valve. Meanwhile the cam rotation axis is selected as the drive shaft and an appropriate speed should be set.

Results and discussion

1) Valve lift and velocity

During the operation of valve train, detachment of the valve and other components can occur because of inertia on high-speed reciprocating motion. In this case, the valve is only controlled by valve spring and the impact speed of valve is too high to destroy the valve set. Also it can result valve rebound phenomenon. Practice has proved that when the impact velocity is more than 500-800mm/s, valve and valve seat of common material can be quickly damaged [6]. So the analysis of the speed of the valve lift and impact speed for considering whether it meets the design requirements is needed firstly.

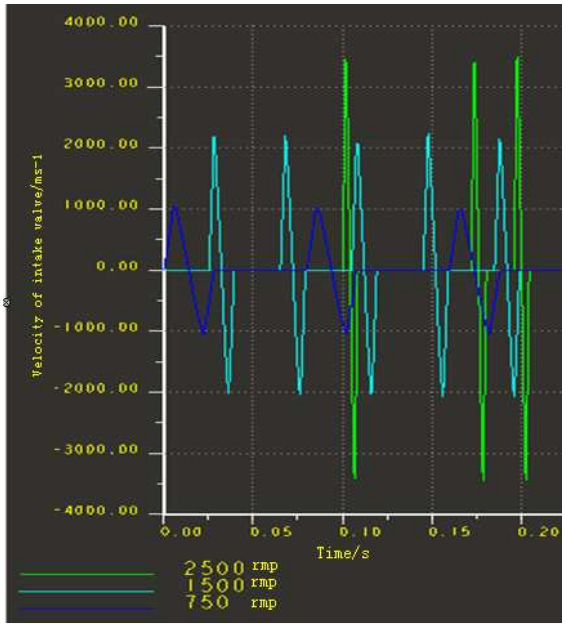


Fig.4 Valve velocity at different speed

Therefore, three camshaft speed 750r/min, the 1500r/min 2500r/min of the intake valve are discussed. The vale lift and velocity can be seen in figure 4. It can be seen from the figure that maximum valve speed is 1000mm/s, 2250mm/s, and 3458mm/s at camshaft speed 750r/min, the 1500r/min 2500r/min respectively. And there is no rebound phenomenon at all camshaft speed. And although the valve open and seated processes are accompanied by large amplitude vibration of the valve speed, it can be seen that the valve opening speed and seated speed are all less than 300mm/s which can meet valve design requirements. However, when the cam speed is 2500r/min, the greatly speed varies cause the valve acceleration shock which can be seen from acceleration.

2) Valve acceleration

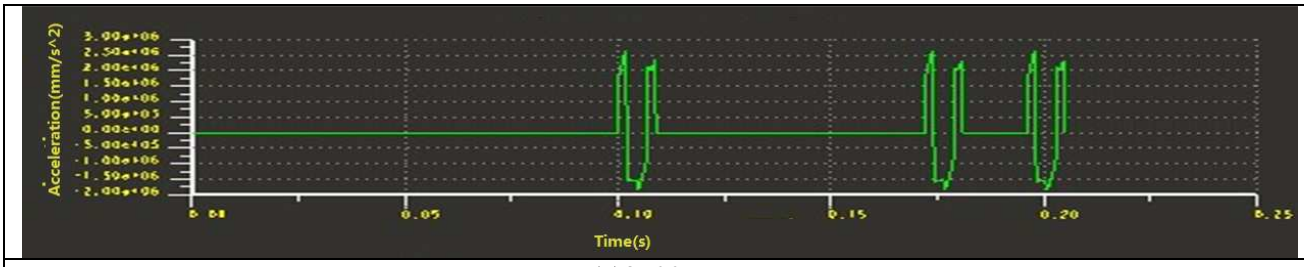
With the increase of engine speed, the cam curve with high acceleration values may cause damage to valve seat. So it is very important to learn valve acceleration. The valve acceleration can be seen in figure 5. From the figure it can be seen that:

(1)Valve acceleration varied at high frequency and the amplitude is large which is increased with the increase of the camshaft speed.

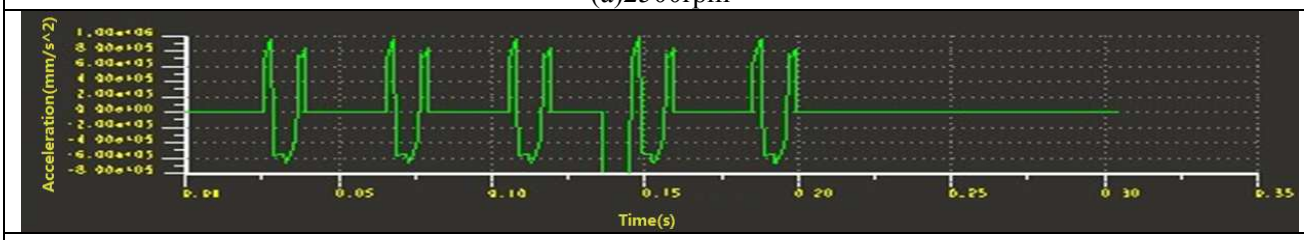
(2)The value of valve acceleration is very large in the open and seated stage and the impact between the valve and seat is existed.

(3)There is oscillation of the valve acceleration curve when the acceleration at maximum value.

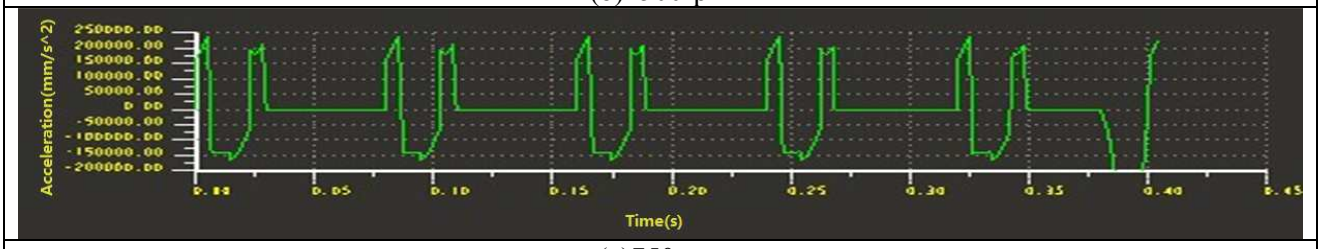
(4)The high-frequency oscillation of valve acceleration resulting in variable inertia force to the valve seat and the impact caused high-frequency noise.



(a)2500rpm



(b)1500rpm



(c)750rpm

Fig.5 Valve acceleration at different cam speed

Summary

Based on Pro/E environment, the valve motion is simulated. Some conclusion can be reached as follows:

(1)The engine valve motion can be simulated based on Pro/E environment.

(2)The velocity meets design for research cam and valve system.

(3)Valve acceleration varied at high frequency and the impact between the valve and seat is existed.

References

[1] Xu Yan-dao, Ding Xian-hua, in: High speed diesel engine concept design and application.Beijing: China Machine Press, 2004

[2] Guo Lei, Chu Chao-mei, Chen Jia-qi, in: Study of Effects of Characteristic Parameters of Cam Profile With High-Order Polynomial on Valve Train Performance, Chinese Internal Combustion Engine Engineering , 2005 26:20-23

[3] Yao Hai-rong. in: Plane cam design and motion simulation system. Beijing: China agriculture university,2004

[4] Sun xiao-lao, Qi he-yi, in: Tutorial of Pro/ENGINGGR Wildfire 4.0 in Chinese. Beijing: Tinghua university press, 2008

[5] Second-generation Long shock studio, in: Movement, structure, thermal analysis based on Pro/E wildfire2.0. Beijing: Electronic Industry Press, 2006

[6] Fu guang-qi, Kang xiu-ling,in: Dynamic Calculation on OHC Valve Train in High-Speed Diesel Engines. Transactions of Csice, 2000(2):113-116

© (2012) Trans Tech Publications, Switzerland
doi:10.4028/www.scientific.net/AMM.164.433

Power Spectral Density Model of Torsional Dynamic Wind Loads on Tall Buildings

Tianyin Xiao

College of Civil Engineering and Architecture, Hainan University, Haikou, 570228, P.R. China

xiaotianyin@163.com

Keywords: fluctuating pressure; power spectral density; dynamic wind loads

Abstract. 9 models of tall buildings with different rectangular cross-sections are tested in a wind tunnel. After processing and analyzing the measured data of fluctuating pressure on the models, the effects of models'height, aspect ratio, side ratio on the power spectra of torsional wind loads are studied. New formulas of power spectral density of torsional wind loads are proposed by curve fitting method. The applicability of the formulas has been verified by the results from the wind tunnel test.

Introduction

The horizontal stiffness of tall buildings with high aspect ratio is low. The lateral load occupies a great proportion in the total loads. Aside from earthquake load, the main lateral load is the wind load which acts on buildings frequently. As for tall buildings, the wind load is an important design load, sometimes plays a crucial role. The torsional wind vibration of high-rise buildings can enlarge the displacement and acceleration near the section boundary. A great deal of tests and measured data show that the torsional wind induced-response plays the main role in the total responses of the section boundary points when the building's aspect ratio is over 3 and with an irregular body shape.

Habitants in tall buildings are susceptible to perceive torsional movement than translational motion. Hence, it is very important to evaluate torsional wind loads and responses in the design of tall buildings[1]. The mechanism of tall buildings' torsional vibrations is rather complicated. At present, computational wind engineering is not perfect enough to be used in practical engineering, and wind tunnel test is still a primary and reliable means to investigate and describe torsional wind loads on tall buildings[2].

This paper researches on 9 models with various geometric parameters. We obtained wind pressure data on building models through a series of wind tunnel test and used FFT method to process the data, and analyzed characteristics of the power spectra of torsional wind loads. New formulas of power spectral density of torsional wind loads are proposed by curve fitting method. The formulas are based on several parameters such as wind velocity, intensity of turbulence, side ratios, etc. And the formulas have been verified by the results from the wind tunnel test.

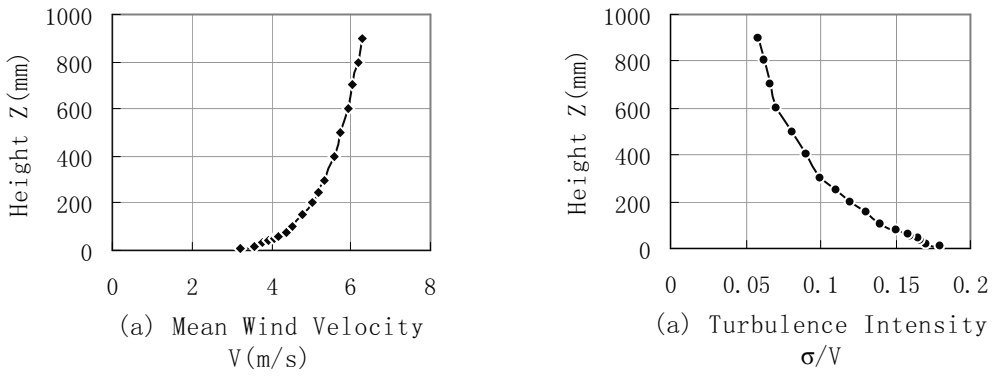


Figure 1. Wind Current Characteristics in Test

Wind Tunnel Tests

Wind Current Characteristics. Wind tunnel tests were carried out in a 3.1m×2.0m wind tunnel with a 16m boundary layer in length. The measured mean wind speeds and turbulence intensities at the test sections are illustrated in Fig 1.

Test Models. The cross sections of the building models for tests are rectangular. All models are 1:500 of the scale to the real buildings. All models have the same sectional area, denoted as BD=0.01m^2. The models have various geometric parameters as shown in Table 1.

Tabel 1 Test Models' Geometric Parameters

Model No.	Breadth B (mm)	Depth D (mm)	Height H (mm)	Side ratio D/B	Aspect ratio $H/\sqrt{BD}$
M1	100	100	300	1.0	3
M2	100	100	400	1.0	4
M3	100	100	500	1.0	5
M4	79	126	400	1.6	4
M5	71	142	400	2.0	4
M6	58	173	400	3.0	4
M7	126	79	400	0.6	4
M8	142	71	400	0.5	4
M9	173	58	400	0.3	4

Wind Test. Fluctuating wind pressures on the model's surface were measured by pressure transducers placed at ten elevations throughout the model height as shown in Fig 2. Each level of a building model has 8 lateral force test points and 8 torque test points on each side. The wind direction is perpendicular to the windward side. The time interval of sampling is 1.6 milliseconds. The total number of samples is 16992 and the whole time span is about 27.2 seconds.

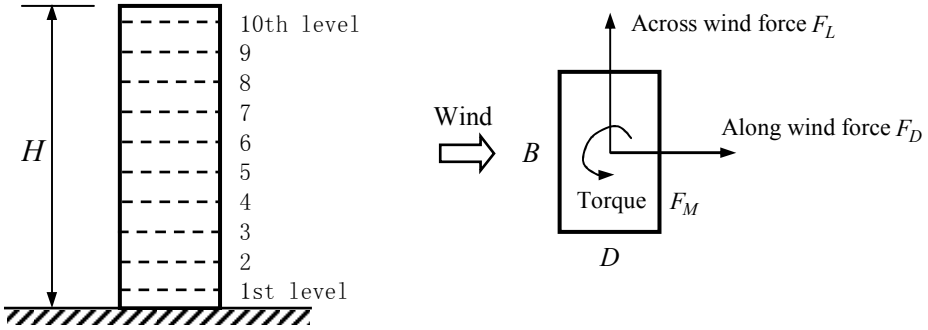


Figure 2. The Feature of the Model's Section

Analysis of the Test Results

After the time histories of torsional wind force of each level are measured, the power spectra of torsional wind force can be obtained by data-processing software using FFT method. Frequency n is expressed as nB/U, in which, B is the breadth of windward side, U is the wind velocity. The power spectral density is expressed as $nS(n)/\sigma^2$. Thus the frequency and the power spectra are both dimensionless. Generally, we consider the conditions when nB/U<1.0.

Generally speaking, the magnitude of torque acting on models changes along with the side ratios of the cross section. There are obvious differences between power spectra of torque with side ratio D/B≥1 and those with side ratio D/B<1 as shown in Fig 3. Their features are discussed as follows:

When D/B<1, there is an obvious peak on the curve of torque spectra. Because the windward side is broader, the pressure changes due to vortex shedding on the leeward side are the main contribution to dynamic torque.

When D/B>1, there are two peaks on the curve of torque spectra, where the first peak is primarily caused by the asymmetric pressure due to vortex shedding on the two sides, and the second peak is caused by reattachment of separated flow. The two peaks on the spectrum curve are not sharp, and thus the spectrum curve has a broad bandwidth, which changes along with the side ratios, respect ratios and turbulence intensity.

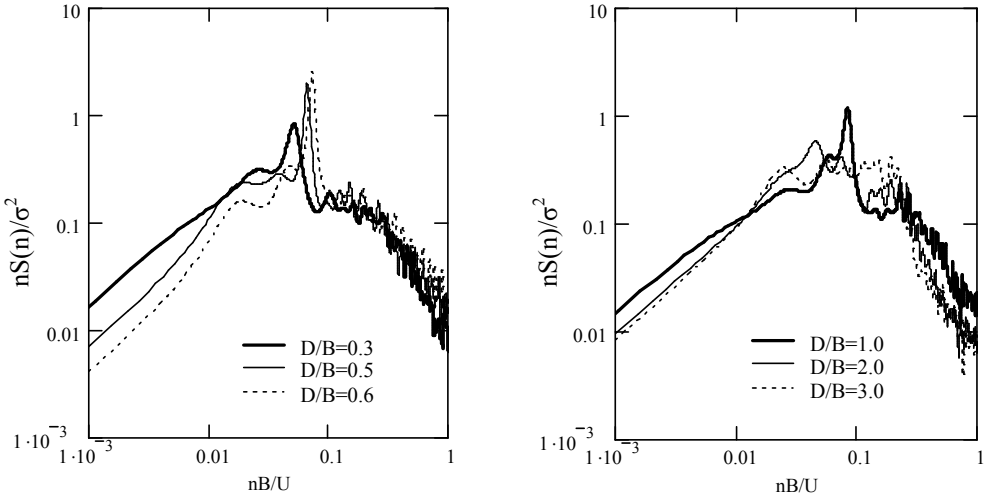


Figure 3. Influence of Side Ratios (D/B) on the Torque Spectra

Curve Fitting of Power Spectral Density

Some papers proposed analytical functions of torsional wind loads power spectral density based on wind tunnel tests which are not well fitted with test results, especially in high frequency range.

The power spectral density of torsional wind loads should be regarded as a function of three variables: side ratio, aspect ratio and turbulence intensity. This paper proposes the following normalized formula fitted to the test results:

$$\frac{nS(n)}{\sigma^2}=\frac{1.2}{1+1.5\sin\dfrac{\pi}{1+\left(\dfrac{\overline{n}}{1.5}\right)^3}}\left[M_1(\overline{n})+M_2(\overline{n})\left(\beta\cdot F(\overline{n})+\frac{1}{10}\cdot\ln\left(\frac{2D}{B}\right)\right)\right] \tag{1}$$

the parameters can be calculated as follows:

$$M_1(\overline{n})=\frac{1.2\,\overline{n}/k}{\left(1+(\overline{n}/k)^2\right)^{2.5}},\quad k=\begin{cases}1.6/\sqrt{D/B} & D/B<1\\ 1.6 & \mathrm{D}/B\geq 1\end{cases} \tag{2}$$

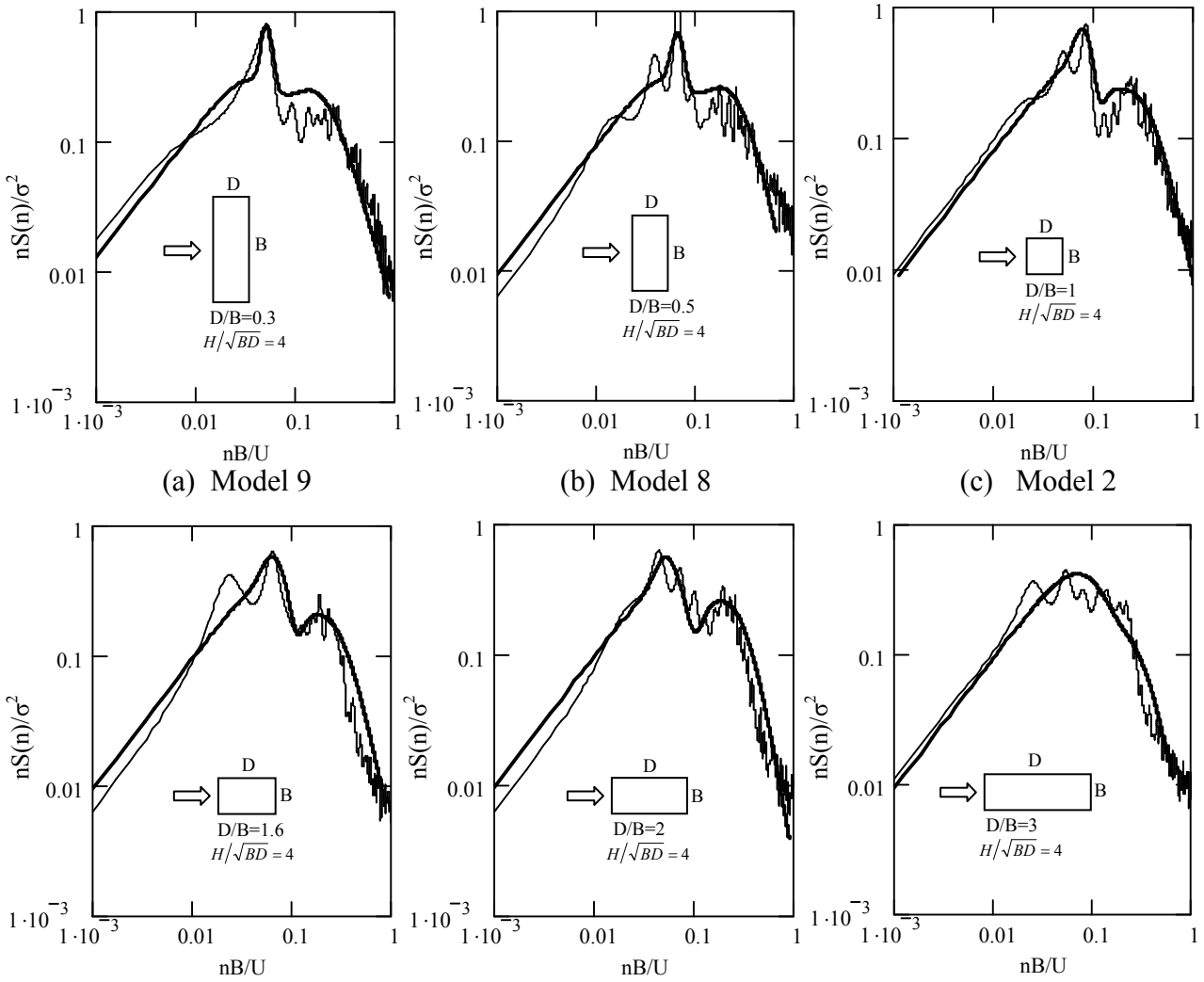
$$M_2(\overline{n})=\frac{1}{\sqrt{2\pi}\delta}\exp\left(-\frac{1}{2}\left(\frac{\ln(\overline{n})+\delta^2/2}{\delta}\right)^2\right),\quad \delta=\begin{cases}I(H/3) & \mathrm{D/B}<1\\ 1.6\cdot\mathrm{I}(H/3) & \mathrm{D/B}\geq 1\end{cases} \tag{3}$$

$$F(\overline{n})=\exp\left(-\frac{\overline{n}}{\gamma}\right)\cdot\cos\left(\pi-\frac{\pi}{1+(\overline{n}/\gamma)^{1.5}}\right),\quad \gamma=1.0-0.37\ln(D/B) \tag{4}$$

$$\beta=\begin{cases}1.0 & \mathrm{D}/B<0.5\\ 1.45\ln(4D/\mathrm{B}) & 0.5\leq D/B\leq 2.0\end{cases} \tag{5}$$

$$\overline{n}=n/n_s\ ,\quad n_s=S_t\cdot\overline{U}(z)/B \tag{6}$$

In which, S_t is Strouhal number, n_s is the vortex shedding frequency, $I(H/3)$ is the turbulence intensity at 1/3 height of the model, $\overline{U}(z)$ is mean wind speed. The comparison between the proposed formula and test results is shown as Fig 4.



(a) Model 9 (b) Model 8 (c) Model 2

(d) Model 4 (e) Model 5 (f) Model 6

Figure 4. Comparison Between Proposed Formulas and Test Results of Models
(thin line is the test result curve，thick line is the proposed formulas curve)

From Fig 4, we can see that the proposed formula not only provides good agreement with test results within the peak range, but also has little error in high frequency range.

Summary

After processing and analyzing the measured data of fluctuating pressure on rectangular rigid models with various side ratios and aspect ratios in a boundary layer wind tunnel, this paper researches on the influence of models' geometric parameters on the power spectra of torsional wind loads and proposes new formulas of power spectral density of torsional wind loads.

The mathematical model presented in this paper is in good agreement with the test results obtained by wind tunnel tests. It is reliable and applicable to the design of isolated tall buildings with rectangular cross section. A calculation method based on this mathematical model can be established to evaluate wind-induced torsional responses of rectangular tall buildings at preliminary design stage.

References

[1] Shuguo Liang, Shengchun Liu, Liangliang Zhang, Ming Gu. Mathematical model of acrosswind dynamic loads on rectangular tall buildings[J]. J of Wind Engineering, 2001, No.89(2):81~84

[2] LIN Ning, Letchford C, Tamura Y. Characteristics of wind forces acting on tall buildings[J]. Journal of Wind Engineering and Industrial Aerodynamics, 2005, 93: 217.

© (2012) Trans Tech Publications, Switzerland
doi:10.4028/www.scientific.net/AMM.164.437

Structure and Motion Analysis of a Tire Building Drum Based on Parallel Mechanism

Xuehai Pan

Zibo Vocational Institute, Zibo, Shandong Province 255314, P.R. China

panxuehai2001@sina.com

Keywords: tire building drum,parallel mechanism,position analysis,motion track

Abstract. A new type of tire building drum based on parallel mechanism was presented and the analysis of the structure was carried out.The calculation of dof and the output motion type analysis and positive solution and inverse solution were included. Solid model of the mechanism was set up and the trajectory analysis was conducted using software of UG and MATLAB, which provided theoretical base for optimal design application of the mechanism.

Introduction

Since the parallel mechanism has high rigidity, compact structure, strong bearing capacity and good dynamic performance, which has become a hot research now and is widely used in industrial robots, micro robots, parallel virtual axis machine tools and other fields. Over the past six degrees of freedom parallel robot has been extensive research on many occasions, however, less-DOF parallel robot driven by fewer components, low-cost, compact and has a higher practical value[1,2,3,4]. Because of the tire building drum are flat organizations in the past, which has stiffness, poor load-bearing capacity disadvantages. In this paper, a less degree of freedom parallel mechanism was used in tire building drum mechanism, which can effectively make up for the traditional mechanism of the tire building drum of the shortcomings. The structure was analysed and the direct and inverse dis-placement equations were given. Solid model of the mechanism was set up and the trajectory analysis was conducted using software of UG and MATLAB, which provided theoretical base for theoretical analysis application of the mechanism.

Institutional structure

Fig.1 shows a tire building drum in parallel mechanism, it consists of moving platform 14, moving platform 11, fixed platform 1, two symmetrical mixed branched-chains for connecting the static and dynamic platform and a simple branched-chain, the branched-chain2,3,8,9 have the same length, platforms 14 and 11 connected by a revolute pair. One of a mixture of branched-chain is spatial mechanism which is composed of revolute pairs R4, R5, R7, R9, a prismatic pair P1 and components of 1,3,5,7,9,11 , the four revolving shafts are parallel, both sides of the prismatic pair P1 connects with revolute pair R4, R7.The simple branched chain is a mechanism which is composed of revolute pairs R1, R11, a prismatic pair P3 and components of 1,10,13,14, one end is connected with moving platform 14 by revolute pair R11, the other end is connected with fixed platform by revolute pair R1, drive P1, P3 two prismatic pair, moving platform 14 would realize rotation around the z-axis and along the y-axis movement.

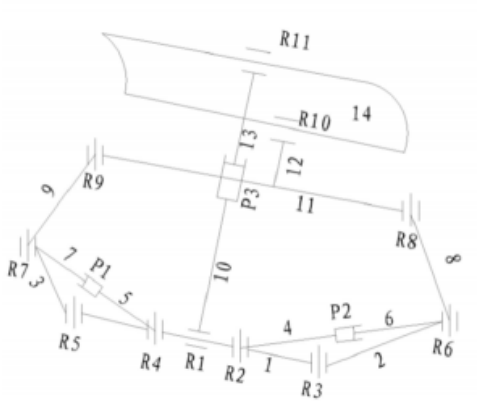


Fig.1 Institutions diagram of tires building drum

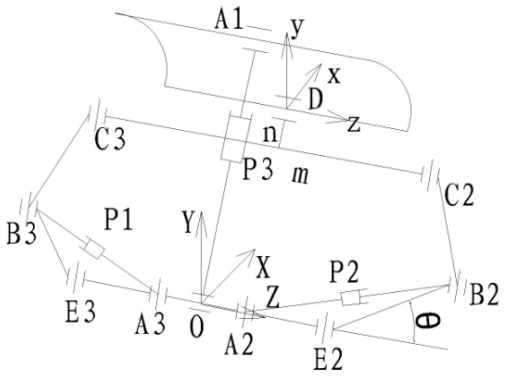


Fig.2 Computing model of tire building drum

Movement determinism analysis. Determinism analysis of the mechanism movement is the degree of freedom computation and initiative vice-selection. Regarding Fig.1 mechanism, which has movement vice-number m=14, component number n=14, the basic circuit counts is v=m-n+1, taking R1-R4-R5-R7-R9-R10-R11-P3-P1 branched chain construct the basic circuit. The formula of calculating a degree of freedom is:

$$F = \sum_{i=1}^{m} f_i - \varepsilon = (9+3+2) - 12 = 2$$

f_i —degree of freedom of the i kinematic pair;

ε —the number of independent displacement equation.

Known from the formula, the degree of freedom is 2, therefore, the mechanism needs 2 initiative pairs, Selected P1, P3 mobile sides as the active side and stiffness, after stiffening degree-of-freedom of the mechanism is F= (9+3) - 12=0,which satisfies the initiative pair-existence criterion, therefore P1, P3 two sliding pairs are designated as initiative pair.

Analysis of output characteristics of moving platform. Known from the literature [5], the leg number is the N parallel mechanism. Each single open-chain (Single-Opened Chain, SOC) branched-chain components of the rack and output is part of dynamic and static platform of parallel robot mechanism, Moving platform can only realize all branched-chain movement of the common elements of the output moment under the SOC branched common constraints, the parallel line from the spiral theorem shows:

$$S_{pa} = \bigcap_{i=1}^{N} S_{1i}$$

S_{pa} corresponding parallel organization speed output matrix M_{pa}, S_{1i} corresponding in the i leg's speed output matrix M_{1i}, the mechanism movement output equation is:

$$M_{pa} = \bigcap_{i=1}^{N} M_{1i} = \bigcap_{i=1}^{N} \begin{bmatrix} x_i & y_i & z_i \\ \alpha_i & \beta_i & \gamma_i \end{bmatrix}_{1i}$$

x_i, y_i, z_i —the origin of moving coordinate system in static coordinates of coordinate system;

α_i, β_i , γ_i —moving coordinate system relatives to static coordinate system axes x, y, z of the three Euler angle.

Example of the 14 moving platform:

$$\begin{bmatrix} \bullet & y & \bullet \\ \bullet & \bullet & \gamma \end{bmatrix}_{SOC_1} \bigcap \begin{bmatrix} x & y & z \\ \alpha & \beta & \gamma \end{bmatrix}_{SOC_2} = \begin{bmatrix} \bullet & y & \bullet \\ \bullet & \bullet & \gamma \end{bmatrix}$$

"$\bullet$"—is a constant.

So the moving platform 14 can achieve along the y-axis direction of the movement and rotation around the z-axis.

Position Analysis

Fig.2 is the calculation model. O spot is the zero point of O-XYZ which fixed on static coordinate frame. Z-axis along the direction of static platform to the right spindle, Y-axis is perpendicular to the static platform the up， X-axis determined by the right hand rule. Taking D spot as the zero point of D-xyz, each coordinate axis parallel to the fixed axis, γ is shaft angle which the moving coordinate system around Z axis of fixed coordinate system O-XYZ, θ is shown in Fig.2.The distance between D and the center of waiwa is a and the distance between D and the edge of waiwa is b. The coordinates of A_1 in moving platform is $\left(A_{1x}, A_{1y}, 0\right)$, the coordinates of C_2 in static coordinate is $\left(-a, C_y, b\right)$, The coordinates of B_2, A_2 and E_2 are $\left(0, l\sin\theta, l\cos\theta + E_z\right)$, $\left(0, 0, A_z\right)$, $\left(0, 0, E_z\right)$.

$B_2C_2 = B_2E_2 = l$, $A_1O = L_1$, $A_2B_2 = L_2$.

Inverse kinematics. Inverse kinematics is solving the output quantity of mechanism through position of moving platform. The method is coordinate transformation of space analytic geometry[6].

Transformation matrix are:

$$R = \begin{bmatrix} \cos\gamma & -\sin\gamma & 0 \\ \sin\gamma & \cos\gamma & 0 \\ 0 & 0 & 1 \end{bmatrix} \tag{1}$$

$$P = (a \quad D_y \quad 0)^T$$

$$A_{10} = RA_1 + P$$

$$= \begin{bmatrix} \cos\gamma & -\sin\gamma & 0 \\ \sin\gamma & \cos\gamma & 0 \\ 0 & 0 & 1 \end{bmatrix} \begin{pmatrix} A_{1x} \\ A_{1y} \\ 0 \end{pmatrix} + \begin{pmatrix} a \\ D_y \\ 0 \end{pmatrix} \tag{2}$$

$$= \begin{bmatrix} A_{1x}\cos\gamma - A_{1y}\sin\gamma + a \\ A_{1x}\sin\gamma + A_{1y}\cos\gamma + D_y \\ 0 \end{bmatrix}$$

Variable rod length $L_1 = \sqrt{(A_{1x}\cos\gamma - A_{1y}\sin\gamma + a)^2 + (A_{1x}\sin\gamma + A_{1y}\cos\gamma + D_y)^2}$ (3)

Variable rod length $L_2 = \sqrt{l^2 + 2(E_z - A_z)l\sin\theta + (E_z - A_z)^2}$ (4)

Here $\theta = 2\arctan\left[\left(A - \sqrt{A^2 + B^2 + C^2}\right) \Big/ (B - C)\right]$

$A = -2l\left(C_y + D_y\right), B = -2\left(b - E_z\right)l, C = \left(C_y + D_y\right)^2 + \left(b - E_z\right)^2$

Formula(3),(4) is expression of active pole length variation.

Forward kinematics. The position D_y and angle γ of moving platform can be obtained by the active lever leg's length. The unknown equations about D_y and γ can be obtained from the formula(3) and (4).

$$f_i\left(D_y, \gamma = 0\right) \quad (i = 1,2) \tag{5}$$

$$f_1 = L_1^2 - A_{1x}^2 - A_{1y}^2 - a^2 - D_y^2 - 2\left(aA_{1x} + D_yA_{1y}\right)\cos\gamma - 2\left(D_yA_{1x} - aA_{1y}\right)\sin\gamma$$

$$f_2 = L_2^2 - l^2 - 2\left(E_z - A_z\right)l\sin\theta - \left(E_z - A_z\right)^2$$

Using m and n to represent $\sin\gamma$ and $\cos\gamma$ respectively. Taking into account

$$m^2 + n^2 = 1 \tag{6}$$

Linear equations about D_y and γ can get from formula(5)and(6),the method is Newton-Raphson [7].

Trajectory planning of tire building drum

Because of the limit of the structure, the parallel mechanism is not flexible working space. This paper uses space trajectory of the reference point of moving platform to describe the working space of mechanism[8]. Therefore, reference point occupied space in the process of movement reflect the size of the moving platform workspace.

There are several factors that influence the parallel mechanism motion trajectory:

a) The movement of active pole.The rod length must meet $L_{\min} \le L_i \le L_{\max}$,Telescopic trip of each rod directly effects the motion trajectory shape.

b) Rotation range of revolute pair.In fact, the rotation range of revolute pair in PM is limited.

c) Mutual interference between the connecting rod. Because each rod has certain the section size,the two adjacent rod may interference in the process of movement.

As the movement of neiwa is related to the output of waiwa, a control curve fitting and optimization strategy of drum is easier to get from formula (3) and (4). Trajectory curve of neiwa and waiwa is shown in Fig.3 and Fig.4.

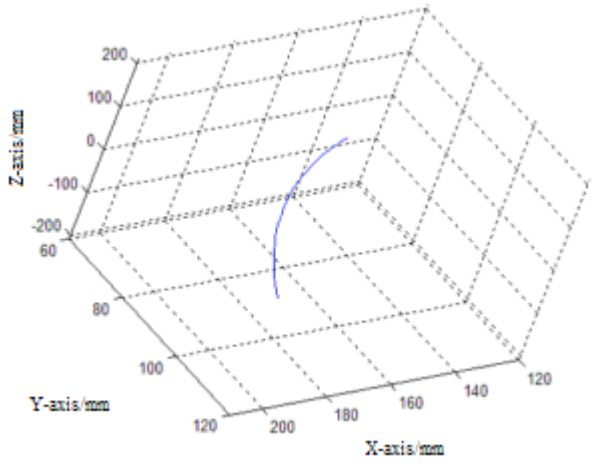


Fig.3 The trajectory of neiwa

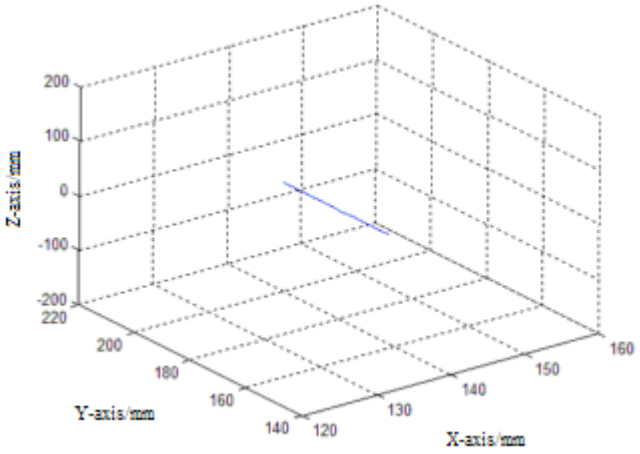


Fig.4 The trajectory of waiwa

Conclusions

A new type of tire building drum based on parallel mechanism was presented and the positive solutions and inverse solution of position was established. Solid model of the mechanism was set up by UG and the trajectory analysis was conducted by MATLAB, which provided theoretical base for practical application.

References

[1] Zhao T S,Dai J S and Huang Z:International Journal of Mechanical Engineering Science,Vol.216(2002)No.1, pp.1175-1185.

[2] Huang Xiguang,He Guangping,Tan Xiaolan,et al:Journal of North China University of Technology, Vol.21(2009)No.3,pp.25-30.

[3] Zhu J G:Science & Technology Association Forum, Vol.09(2010)pp.94-95.

[4] Duan J G,Guo Z H and Wang K J:Journal of Shandong University of Technology (Natural Science Edition), Vol.22(2008)No.1,pp.23-27.

[5] Yang T L:Topology structure design of robot mechanisms(Beijin Mechanical Industry Press, china 2004).

[6] WANG Hai-dong, BI Yu-quan, YANG Bing-heng et al:Science Technology and Engineering,Vol.10(2010)No.35,pp.8826~8830.

[7] CHEN W J,ZHAO M Y,CHEN S H,et al:Proc IEEE Conf on Rob Auto,(2001),pp.3350-3355.

[8] Peng Kai,Wang Jian-ping,Li Xiao-feng,et al:Mechanical Research & Application. Vol. 05(2010),pp.25-28.

© (2012) Trans Tech Publications, Switzerland
doi:10.4028/www.scientific.net/AMM.164.441

Research on Energy Harvesting Behaviors of Different Shapes of Piezoelectric Vibrator

WeiDong Chen [1,a], HongSheng Hu [1, b], SuXiang Qian [1,2, c], DingKun Zhu [1,2]

[1]Department of Mechanical and Electrical, University of Jiaxing, Zhejiang Province, China

[2]School of Mechanical and Electrical, University of Changzhou, Jiangsu Province, China

[a]hhs999@mail.zjxu.edu.cn, [b]wjhhs@126.com, [c]jjqsx@126.com

Keywords: Piezoelectric vibrator, energy harvest, triangular cantilever, cylindrical vibrator.

Abstract. Shapes and geometry parameters of piezoelectric vibrator have a greatly influences on its energy harvesting ability. In this paper, both of static and modal characteristics of piezoelectric vibrators were respectively simulated by using the finite element analysis software Ansys, where influences from stress and the exciting force's frequency on the outputting voltage of a cylindrical piezoelectric vibrator and a triangular cantilever piezoelectric vibrator were analyzed. The numerical simulation results show that its geometry sizes of triangular cantilever piezoelectric vibrator could result in its outputting voltage and first-order natural frequency's shift, however, the exciting frequency of the external force has no any influences on its outputting voltage of the cylindrical vibrator. Besides, an optimized design was researched in order to improve its power generation capacity per unit volume for the triangular cantilever piezoelectric vibrator.

Introduction

In recent years, energy harvesting equipment has been a hot issue in engineering fields [1, 2]. There are four ways to transfer vibration energy into electrical energy, including thermoelectric power conversion, piezoelectric power conversion, electromagnetic power conversion and electrostatic power conversion. Compared with the other transferring ways, there are several merits for the piezoelectric power conversion way, such as easy to realize in its structure, high efficiency in harvesting vibration. Therefore, most of researches on energy harvesting technology are based on the piezoelectric power conversion way.

Piezoelectric ceramics has a unique mechanical-electrical coupling characteristic. It has been a new kind of power generation technology to apply piezoelectric effects of piezoelectric ceramic making mechanical vibration energy changed into electric energy. Piezoelectric energy technology has begin 80-90 times of the twentieth century, nowadays piezoelectric vibration power generation technology has been a hot researching topic in engineering field at home and abroad because of its simple structure, no heat, no electromagnetic interference. ARDEC has harvested the vibration energy weapons launch produces and transferred it into electrical energy by applying the piezoelectric power conversion way. Theses harvesting energy could be used to provide other electric equipment operation or be stored into super capacitor. Shad Roundy from California University had analyzed the piezoelectric cantilever beam's vibration-to-electrical theory model, and designed a micro piezoelectric structure to harvest vibration energy. The designed harvesting equipment maximum output power could be reached 125~975 μW.

The most kernel part of piezoelectric generator is piezoelectric vibrator. There are many references about its optimal design. For example, References 2 concluded that a cantilever beam piezoelectric vibrator has lower frequency and higher efficiency than other structures at the same condition. References 3, 4 and 5 compared different shapes of piezoelectric vibrators' generating capacity and solved frequency's matching problem by changing piezoelectric vibrator's geometry shapes. Experimental results have proved that the triangular piezoelectric vibrator has a maximum outputting power compared with other shape's structures. For example, its power generation of triangular

piezoelectric vibrator has been 3.3 times of rectangular piezoelectric vibrator in the same volume of piezoelectric materials. Compared to the rectangular and trapezoidal piezoelectric vibrator, the triangular piezoelectric vibrator has a more power generation capacity and could effectively improve its output characteristics in the finite volume. However, there are only few references about its structure and parameter's optimization of triangular piezoelectric vibrator and its energy harvesting characteristic [6]. In this paper, based on reference 4, a triangular cantilever beam piezoelectric vibrator is chosen and its finite element model is built. Using the finite element analysis software Ansys, its static and modal analysis is finished. The numerical simulation results show that its outputting voltage and natural frequency have a greatly influences by its geometry shape of triangular piezoelectric vibrator, in which an optimal design is also finished.

Modeling of Piezoelectric Vibrator

When load is acted on piezoelectric structure, charges piezoelectric vibrator harvests are proportion to its deformation. The greater the deformation is, the more the harvesting charges are. The piezoelectric cantilever structure has been a dominant position harvesting device because it could provides more deformations than other structures under a certain force conditions. However, piezoelectric cantilever structure is difficult to be integrated into some applied objects, cylindrical piezoelectric structure is widely applied into some engineering equipments.

When the external force is acted on the piezoelectric energy harvesting equipment, its physical model of the cylindrical piezoelectric vibrator could be expressed as Figure 1. From Figure 1, there exists in several piezoelectric ceramics between the above and down pressing block. When the external force is actuated on the pressing block, the cylindrical piezoelectric ceramic patches could produce charges and the energy harvesting circuit could collect charges.

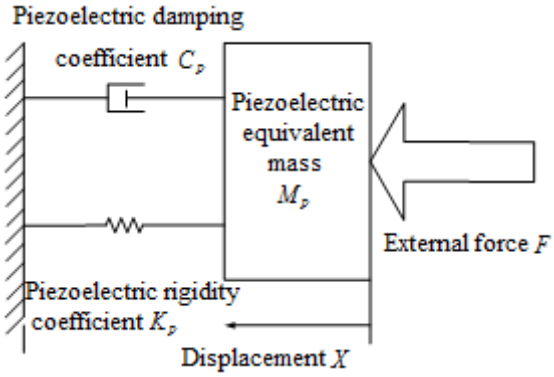


Figure .1 Physical model of piezoelectric vibrator

From Figure 1, its movement equation of the cylindrical piezoelectric vibrator under the external force action could be expressed as followers:

$$M_P \ddot{X} + C_P \dot{X} + K_P X = F \tag{1}$$

In Equation (1), M_P for piezoelectric ceramic's equivalent mass, C_P for piezoelectric ceramic's equivalent damping coefficient, K_P for piezoelectric ceramic's equivalent rigidity coefficient, X for displacement, F for the equivalent acting force the external vibration environment produces.

The mechanical energy from external vibration during the eternal force's action could be expressed as followers:

$$W_{\text{mech}} = F \cdot X_P \tag{2}$$

Substitution Young's modulus Y of piezoelectric material, Equation (2) could be re-expressed as followers:

$$W_{\text{mech}} = \frac{1}{2}\frac{F^2 h_P}{YA} \tag{3}$$

In Equation (3), h_p is for high of cylindrical piezoelectric vibrator, A for bottom area of cylindrical piezoelectric vibrator.

It's above and down surface of cylindrical piezoelectric vibrator under the external force's action would produce charges, and then charges would be formed into current by the transmission circuit. Finally, the produced electrical energy could be stored or directly used.

Finite Element Analyzing of Piezoelectric Vibrator

According to the above mentioned finite element theory and analysis software ANSYS, Solid 98 is selected as the unit type of piezoelectric element's multi field coupling analysis [7]. The designed cylindrical piezoelectric vibrator size is Φ80mm*Φ20mm*15mm, its material kind is PZT-5H and its material density is $7.6*10^3 kg/m^3$. When the piezoelectric vibrator is only considered the polarization direction of applied force, it could be simplified as a d_{33} type vibrator, where it could be equivalent to a fixed bottom surface model, and its above surface is acted by external applied force F. The build finite element model is expressed as Figure 2.

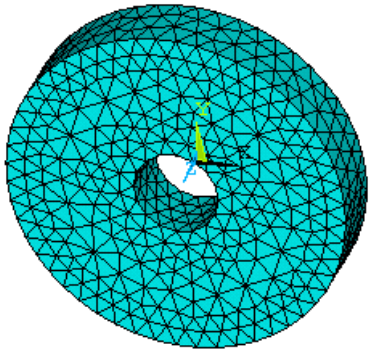


Figure 2. Finite element model of cylindrical piezoelectric vibrator

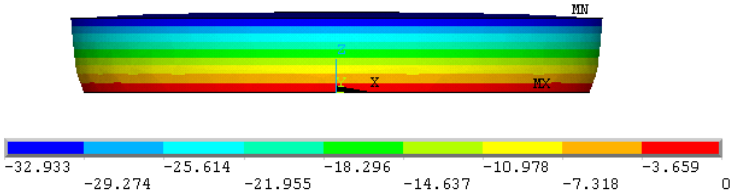


Figure 3. Voltage distribution cloud chart of vibrator

Based on the above build finite element model's static analysis, Figure 3 shows its voltage distribution cloud chart of the cylindrical piezoelectric vibrator. From Figure 3, it could be seen that its stress distribution of piezoelectric vibrator gradually reduced from top to bottom along axial, and its voltage distribution's piezoelectric vibrator is also gradually reduced along the axial direction with stress's reduction. The produced voltage of piezoelectric vibrator is proportion to its stress. In the above mentioned Figure 3, the top surface bears a pressure $10^5 N/m^2$, its bottom surface is fixed. When the pressure $10^4 N/m^2$, $3\times10^4 N/m^2$, $5\times10^4 N/m^2$, $8\times10^4 N/m^2$ and $10^5 N/m^2$ is respectively applied into its top surface, Figure 5 shows a relationship between stress and voltage.

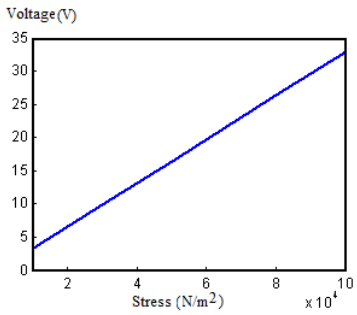


Figure 4. Stress versus voltage

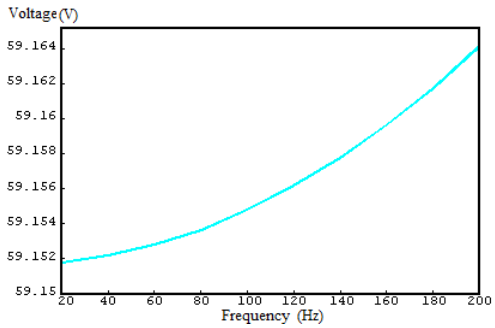
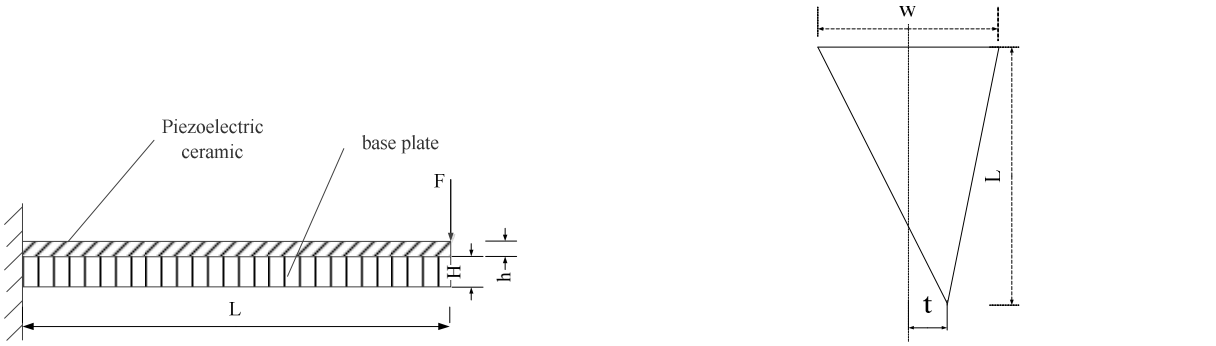


Figure 5. The outputting voltage versus frequency

From Figure 4, it could be seen that its outputting voltage of piezoelectric vibrator is proportional to stress. From Figure 5, the outputting voltage is slowly increased with the external force frequency. When the external force frequency increases from 0Hz to 200Hz, its outputting voltage only increases 0.014V. Therefore, when its bottom surface of the cylindrical piezoelectric vibrator is fixed, it would

be difficult to achieve a resonant state along the axial direction because its natural frequency is great and its main vibration mode doesn't exist in the axial vibration. When the piezoelectric vibrator is in a low frequency vibration environment, frequency has no any influences on its outputting voltage of cylindrical piezoelectric vibrator.



a Cantilever piezoelectric vibrator beam structure b The geometric size of triangle beam

Figure 6. Cantilever piezoelectric vibrator structure scheme diagram

Further, its energy harvesting behavior of a square-ring cantilever vibrator is also analyzed. One end of the cantilever beam is fixed in bearing, the other end with the vibration environment. According to the piezoelectric theory, when a cantilever beam was loading, beam bended deformation and then caused oscillator stress and strain, vibrator surfaces will have charge generation. Cantilever piezoelectric resonators structure is expressed as Figure 6a. The triangle piezoelectric vibrators scheme is expressed as Figure 6b, where L is vibrator length; w is the length of constraint end side; h is piezoelectric ceramic thickness; H is base plate thickness; t is the triangle vertex to perpendicular line distance. Because of symmetry principle, value interval of t is selected as $[0, \frac{w}{2}]$. The smaller t is, the better symmetry of vibrator is. Figure 7 shows the output voltage influenced the changed geometry size of piezoelectric vibrator.

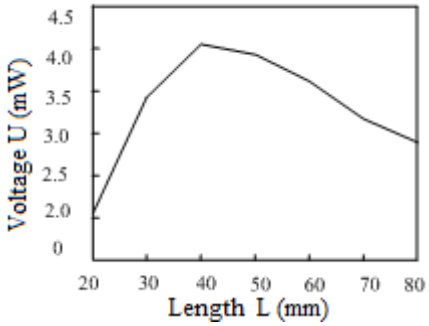


Figure 7. Chart of L versus voltage

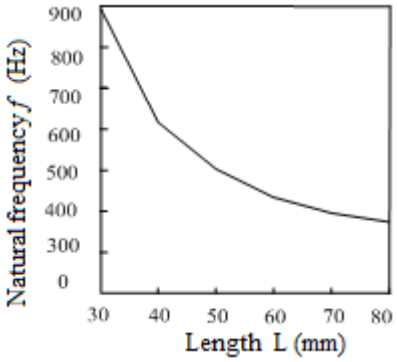


Figure 8. Chart of L versus natural frequency

Based Figure 7, when the triangular piezoelectric vibrator was deformation, the output voltage increased with the length increased. Once the length increased to certain value, the output voltage reduced with the length increased. In addition, the output voltage increased with the length of the constraint end increased. When the triangular piezoelectric vibrator was deformation, it could be concluded that the voltage value increased with the distance of the triangle vertex and the perpendicular bisector increased. In other words, under certain conditions, the better the triangular piezoelectric vibrators symmetry is, the worse the power generation capacity is. Besides, using the finite element software ANSYS to model and analyze the triangular piezoelectric vibrator. The boundary condition of piezoelectric cantilever beam is that the end all DOF and the other end mechanical freedom. Figure 8 shows the first-order natural frequency influenced the changed piezoelectric vibrator geometry size. It could be seen from Figure 8 that the first-order natural

frequency reduced with the length and the length of the constraint end increased when the triangular piezoelectric vibrator was auto oscillation. It explains the smaller the triangular piezoelectric vibrator geometry size is, the better the auto oscillation is. It could also be concluded that the first-order natural frequency reduced with the distance of the triangle vertex and the perpendicular bisector increased. It explains the better the triangular piezoelectric vibrators symmetry is, the better the auto oscillation is, the greater frequency drive source resonate with vibrator is.

Summary

By using the piezoelectric direct coupling method in Ansys software, energy harvesting behaviors of different shapes and sizes piezoelectric vibrator were simulated. The finite element numerical simulated results show that its outputting voltage of the cylindrical piezoelectric vibrator is proportional to stress, and slowly increased with the external force frequency. Besides, a triangular piezoelectric vibrator is also modeled and simulated in this paper, where influences of length of constraint end and symmetry of a piezoelectric vibrator on the outputting voltage and the first-order natural frequency are also analyzed. The numerical simulation results show its outputting voltage of the triangular piezoelectric vibrator is also proportional to stress. When its exciting frequency of the external force is the same with its natural frequency of the triangular piezoelectric vibrator, the outputting voltage would achieve the most value; however, considering its natural frequency of the cylindrical piezoelectric vibrator is high, its exciting frequency of the external force has no any influences on its outputting voltage in low-frequency environment. Further, an optimized design is finished in order to improve its power generation capacity per unit volume for the triangular cantilever piezoelectric vibrator. The numerical simulation results show that its volume of the optimized size is 0.94 times of the original size and its output voltage of the optimized size is 1.03 times of the original size considering the same boundary conditions and external force.

Acknowledgements

The research work is supported by natural science foundation of Zhejiang Province (Y1110313), Science & Technology foundation of Jiaxing City (2010AY1086) and New Talents Project of Zhejiang Province (2011R417006, 2010R417033). The first author wishes to thank Song Hongwei /NUST for a good previously research work basis, especially contribution to theory derivation and numerical simulation.

Author Biography

Hongsheng Hu was born in Shucheng County, Anhui Province, China in 1976. He received PhD from Nanjing University of Science and Technology, China in 2005. Now he is an associate professor in department of Mechanical and Electrical, Jiaxing University. His research interests include vibration control, signal processing and fault diagnosis.

References

[1] Juan Pu, Xiaojun Yan, Yadong Jiang, et al. Sensors and Actuators: Vol. 164 (2010), pp. 131-136.

[2] Deng Guanqian, Chen Zhongsheng, Tao Limin. Piezoelectric & Acoustooptics: Vol.32 (2010), pp.440-446.

[3] Shan Xiaobiao, Yuan Jiangbo, Xie Tao, et al. Journal of vibration and shock: Vol.29 (2010), pp.177-180.

[4] U Gabbert, J Lefevre, F Laugwitz, et al. International Journal of applied electromagnetics and mechanics: Vol.31 (2009), pp.29-39.

[5] Jimenez R, Calzada M.L, Gonzalez A, et al. Journal of the European ceramic society: Vol.24 (2004), pp.319-323.

[6] Poulin G, Sarraute E, Costa F. Sensors and Actuators: Vol. 114 (2004), pp.461~471.

[7] Hongwei Song. Nanjing: Nanjing University of Science and Technology, 2012.

© (2012) Trans Tech Publications, Switzerland
doi:10.4028/www.scientific.net/AMM.164.446

Research on improving the test effectiveness of rock dynamic fracture toughness

Sheng Zhang , Xin-wen Li , Xiang-hao Yang

Henan Polytechnic University, School of Energy Science and Engineering, Jiaozuo, 454001

82468775@qq.com

Key words: dynamic fracture toughness; fracture time; dynamic load; pulse shaper

Abstract: Some problems of testing rock dynamic parameters in the SHPB experiment were analyzed and the relevant measures were proposed, which included how to determining the fracture time and the dynamic load etc. Based on the dynamic fracture experiment in the SHPB system with flattened Brazilian disc made of marble, the strain gauge technique to get the accurate fracture time was applied, and the different pulse shaper were adopted to get more precise wave data. The effective test methods of determining rock dynamic fracture toughness were discussed.

1 Introduction

As a natural product, rock is a typical quasi-brittle material. The failure process of rock is a process of crack incubation, initiation propagation and coalescence. Rock dynamic fracture toughness is one of the main characteristic parameters [1,2]. Lots of research work of testing method has been done.

However, due to instantaneity of dynamic failure, it is very complicated for the material performance change caused by dynamic impact under different strain rate and stress wave propagation in the materials[1,3]. So far, none of a national or general situation has promulgated the test standard of rock dynamic fracture toughness in the world [1]. Disc specimens are gradually applied to the test of dynamic fracture toughness because of small volume and simple structural. For example, Lambert [2] used Brazilian disc samples in the dynamic split tests. Zhang [4] put forward a method to determine the rock fracture toughness with the hold-cracker flattened Brazilian disc. Literatures [5] adopted the edge notched disc. There are many problems in the test effectiveness.

Due to the particularity of rock material and complexity of dynamic testing method, it is difficult to get the rock dynamic mechanical properties accurately. Combining with disc specimen apply to SHPB system, specification experimental test and data post process method would be studied in this paper.

2 The problems in SHPB dynamic test with the disc specimen

In 1949, Kolsky improved the pressure bar system which was presented by Hopkinson to test the transient pulse stress and developed it to be the SHPB equipment. The SHPB equipment can product high strain rate (10^2~10^4/s) and the stress pulse keep short duration time (10^{-6}~10^{-4} s). It has been used to test the rock dynamic mechanical parameters widely. SHPB system is shown in Fig.2. The mode-Ⅰ loading is done on a disc specimen in this paper, that is to say, the load angle between the pre-crack and the elastic compression bar is 0° .

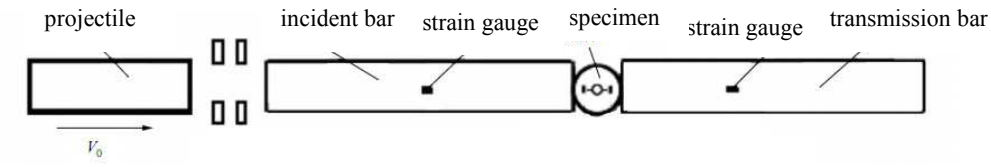


Fig.1 SHPB device

Guo ect.[4,7] determined the dynamic fracture toughness of marble by experiment-numerical analysis. The dynamic loads and fracture time were gotten by post-processing, and the dynamic fracture toughness K_{Id} was determined by the corresponding fracture time and the dynamic stress intensity factor history was calculated using the loading as input for the finite element analysis. This method has been widely used because the effect of the inertia effect has been considered.

In order to improve the test effectiveness of determining the rock dynamic fracture toughness in the SHPB system, some key problems should be solved in the experiment-numerical analysis. First, which kind of disc specimen should be selected in SHPB experiment to get better application? Second, how to get elongate rising time to reduce concussion of the tip. Third, how to make accurate fracture time. At last, how to determine the dynamic loads according to the strain curve.

3 Some suggestions to improve test effectiveness

3.1 Specimen configuration selected

The contrastive analysis of the mechanical response on the Brazil disc specimen and flattened Brazil disc specimen under dynamic impact was taken by Song Xiao-lin, Li-Wei and others. They found that the flattened Brazilian disc has important significance for dynamic impact by eliminating the stress concentration of loading end. Moreover, the flattened Brazil disc may shorten the balance time [3,8].

The experimental results are inaccurate because of the frictional effect, inertia effect and the dispersion effect between the specimens and loading end. The effect of the flattened Brazilian disc's parallelism is particularly outstanding to the experimental results. When the parallelism of the platform is poor, we can't completely guarantee the specimen platform contacting with the elastic compression bar, and the effectiveness of the experimental results may be affected when the failure occurs in the end firstly. Choosing the suitable parallelism of the flattened Brazilian disc is particularly urgent to improve the test precision in the SHPB experiment. So, the disc specimen on the double side surface should be grinded. Using the dial indicator to check precision of the platform to ensure the parallelism's deviation of the platform disc specimens is less than 0.02mm [9]. We should avoid the comminuted failure happening at the end, and decrease the effect of the experiment result which is caused by the end friction as possible.

3.2 Determining fracture time

In the impact process, the strain-time and the fracture time of the elastic pressure bar can be ensured by strain gauge method. The correct paste position and number of the strain gauge affect the real effectiveness of the experimental data. It is so important to ensure accurately the dynamic fracture toughness of the brittle materials. Because the crack initiation maybe not at the same time along the thickness direction, the fracture time of the left and right crack tips is different. Therefore, strain gauges are attached crack front 3mm above extended line of crack and near the tip of the notch in order to detect the time of crack initiation. The strain gauges are pasted at two ends of the both sides. The time which is the earliest crack initiation at the crack tip is named t_c. The strain gauge pasted on the specimen is shown in fig.2.

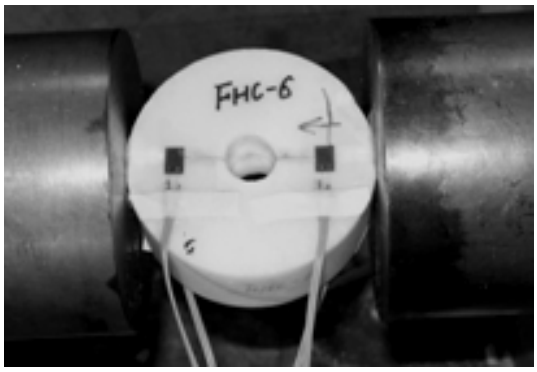


Fig.2 The strain gauge pasted on the specimen

The distance of the crack initiation beginning from the center of the crack tip and the thickness direction must be considered [10]. Formula (1) would be used to decrease the error effect caused by the strain gauge test.

$$t_f = t_c - \sqrt{3^2 + (B/2)^2}/C \tag{1}$$

Among them, B is the thickness of the disc specimen, C is the elastic wave velocity of the rock. The time t_c tested by the strain gauge subtract the time which is extended from the crack tip to the strain gauge, neglecting or making the t_c as the fracture time t_f of the specimen all affect the test precision of the dynamic fracture time, furthermore the result of the dynamic fracture toughness test.

3.3 Wave-shaping technique

In 1972, Christensen R.J.[11] put forward wave-shaping technique and incident wave can be reformed to triangle stress pulse. How to use wave-shaping technique to get high quality, good reproducibility, and nearly constant strain rate waves, which will be helpful to the further study on loading specimen.

Fig.3 show that air gun directly impacts incident bar where measured pulse waveform. There is obvious oscillation in the original elastic wave. Wave pulse shaper have many advantages, such as, it can increase the rising time of incident bar, reduce the concussion of the whole wave. Pulse shaper does not change wave of amplitude and time history, but can reform of waveform configuration.

When a thin aluminum circular plate as pulse shaper pasted the end of incident bar, the wave will firstly impact the aluminum plate. Because of severe plastic deformation, high frequency signal produced by collision between the air gun and incident bar filtered, which can reduce the geometric dispersion effect due to radical inertia very obvious. At the same time, the incident wave can prolong the rising time, which is beneficial to lengthen loading time to obtain uniform stress distribution within specimen through enough reflections before its failure. The strain rate of specimen is reduced. Shortening the distance between incident bar and transmission bar in order to fixed specimen. The interface between compression bar and specimen can reduce the friction force by lubricating oil [4].

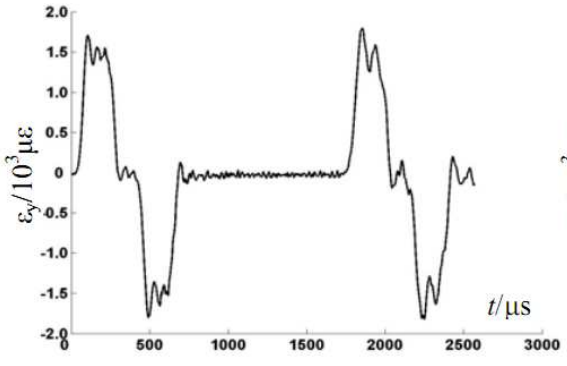


Fig.3 Elastic wave

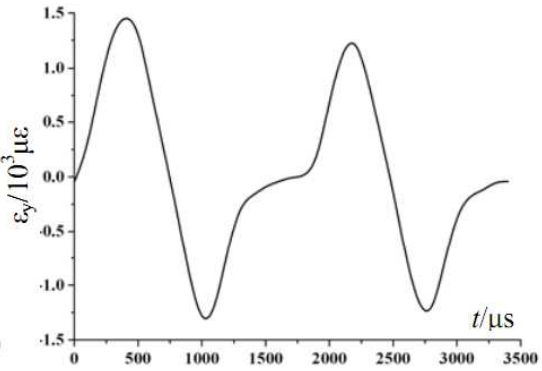


Fig.4 Wave of pulse shaper

3.4 Determining dynamic loading

There are three methods to determine the loads between the specimen loading end, one method is that the load calculated by strain signal on the transmission bar is used[12]; the second is than the load calculated by the strain signal on the incident bar is used; the third is that the calculated average load of the strain signals on the transmission bar and the incident bar are used[4]. We called one-wave method, two-wave method and three-wave method. Which method should be selected to get the dynamic load should base on the post-processing of the experimental state.

One-wave method reflects force condition of transmission bar. Direct utilization of stress curve has less oscillation in the beginning by transmission bar. Literature [5] show that transmitted wave of quasi-brittle materials and noise signals are an order of magnitude, which lead to distortion of transmission wave. The loading which can be determined by two-wave method on the specimen was got from the strain gauge on the incident bar. It has a lot of higher-frequency vibration signal which lead to oscillation. Three-wave method is obtained by strain signal of incident bar and transmission bar. It does not reach stress equilibrium, especially incident wave is higher than transmitted wave when specimen is failure suddenly. How to ensure the dynamic load will be researched in the future.

5 Summary

In order to improve the test effectiveness of determining the rock dynamic fracture toughness in the SHPB system, some suggestion method and the measures were put forward. The parallelism of the disc specimens should be less than 0.02mm. The strain gauge method can ensure the fracture time of the rock accurately. The wave-shaping technique can get high quality stress wave. There are three methods to determine the loads, we must select one method according to the post-processing of the experimental state. How to evaluate the dispersion effect in the specimen which has influence on dynamic fracture toughness needs further study.

Acknowledgement

This work was financially supported by National youth fund （51004043) and Henan university of technology fund. Dr（B2008-66648270) and Henan university of technology young teachers aid（649105）.

References

[1] Hong Fan, Sheng Zhang, Qizhi Wang. Determination of dynamic initiate toughness of concrete using cracked straight-through flattened Brazilian disc,2010,41(10):1234-1240.(in Chinese)

[2] Lambert DE, Ross CA. Strain rate effects on dynamic fracture and strength. International Journal of Impact Engineering, 2000, 24: 985-998.

[3] Xiao-lin Song. Dynamic split tension strength of marble and the properties of crack initiation and crack propagation under dynamic split tests. Chengdu: Sichuan University, 2005, 4-6. (in Chinese)

[4] Sheng Zhang, Wang Qi-zhi, Ya-lei Liang. Method for determination of dynamic fracture toughness of rock using holed-cracked flattened disc specimen,2006,28(8):723-728.(in Chinese)

[5] Zhan-lu Li. Qi-zhi Wang. Wei Li. Experiment on dynamic rock facture toughness using e dge-notched disc specimen,2006,23(2):54-57.(in Chinese)

[6] Bi-jun Su, Qi-zhi Wang. Experimental study of dynamic mechanical properties for Quasi-brittle materials using the split Hopkinson pressure bar,2003,10(24):580-584.(in Chinese)

[7] Guo WG, Li YL, Liu YY. Analytical and experimental determination of dynamic impact stress intensity factor for 40Cr steel. Theoretical and Applied Fracture Mechanics. 1997, 26: 29-34.

[8] Wei Li. Experimental study for dynamic mechanical properties of marble using split Hopkinson pressure bar. Chengdu: Sichuan University, 2005, 19-23. (in Chinese)

[9] Shi-sheng Hu, Dao-rong Wang, Jian-fei Liu. Experimental study of dynamic mechanical behavior of concrete. 2001,18(5):115-118. (in Chinese)

[10] Jing-rui Luo. Study on Damage,Fracture and Constitutive Relation of PBX. Mianyang: China Academy of Engineering Physics, 2001. 95-98. (in Chinese)

[11] Christensen R.J., Swanson S.R, Brown W.S. Split Hopkinson bar tests on rocks under confining pressure. Experimental Mechanics，1972, 12:508-513.

[12] Shan Ren-liang, Yu-sheng Jiang, Bao-qiang Li. Obtaining dynamic complete stress－strain curves for rock using the Split Hopkinson Pressure Bar technique. International Journal of Rock Mechanics and Mining Sciences. 2000,37:983-992.

[13] Grote D.L, Park S.W, Zhou M. Dynamic behavior of concrete at high strain rates and pressures: I. experimental characterization. International Journal of Impact Engineering. 2001, 25:869-886.

© (2012) Trans Tech Publications, Switzerland
doi:10.4028/www.scientific.net/AMM.164.451

Design and Analysis on the Dynamic System of an Oil-well Pump Lifting Test System

Biao Li

Drilling & Production Technology Research Institute of Liaohe Oilfield Company,

Panjin, Liaoning Prov., P.R.China, 124010

lea-13@163.com

Keywords: Dynamic System. Design and Analysis. Oil-well Pump Lifting Test System. Strength Check.

Abstract. In order to meet the demand of the oil-well pump lifting test, designed a set of dynamic system, which can do long stroke reciprocating motion rapidly. On the use of composite liquid cylinder can effectively solve the problem of the load force is not the average when the cylinder moves reciprocally. The maximum lifting force of dynamic system is 120kN; maximum speed is 0.8m/s, reached the design index. At the same time, this set of dynamic system combined electro-hydraulic proportional control method and the oil production, provides a new exploring space.

Introduction

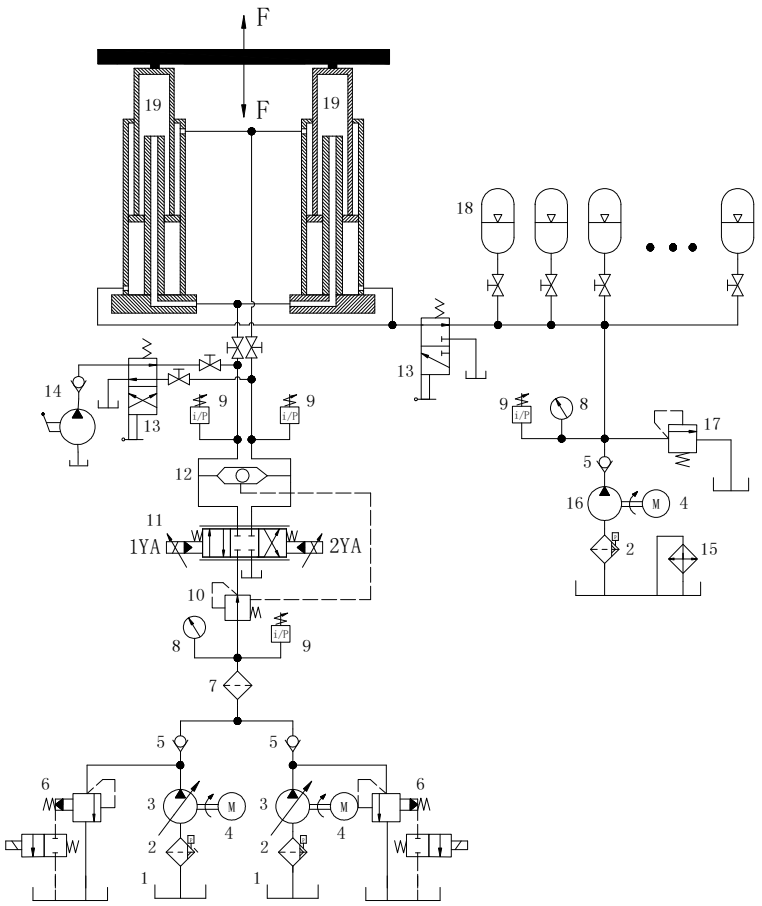
The properties of well oil pump influence the oilfield capacity and economic benefit directly as important oilfield lifting device [1]. According to how the oil-well pump is fixed, it's classified into tubular pump and rod pump. Most of the oil pumps in China are tubular pump [2]. At present, with the oil well conditions worsening, such as sand, high water oil ratio, severely corrosive, less liquid, the domestic and foreign enterprise are producing new type of oil pump for special well conditions hardly.

Compared with the development of the technology of pump, the oil well pump test technology is much more backward relatively. More and more scientists began to carry out the oil well pump the experimental research. Liaohe oilfield as China's largest base of heavy oil production carried out the oil well lifting test technology research actively. In order to meet the needs of Liaohe special oil pump, the dynamic system must meets that the push force is not less than 120kN, the pull force is not less than 15kN, and the speed should be about 0.8m/s.

After a lot of previous studies, we find that electro-hydraulic proportional control method has the characteristic of that compact structure, conveying high velocity, starting fast, slow down smoothly and position precision higher[3], it's very suitable to be the dynamic system of this oil-well pump lifting test system

Overall design of the dynamic system

This dynamic system is mainly achieved through the electro-hydraulic proportional control method. According to the principle, the lifting system and the hydraulic counterweigh system are controlled by the main valve system [4]. To reach the best effect, we did several principle system designs after much calculation rounds. Finally, following the principle of lower assembly power, lower operation power, more smooth pressure and flow, lower cost, easier to maintain, the overall design of the system is that, two compound cylindes is controlled by main valve control system, as shown in Fig. 1.



1 Tank
2 Income filter
3 Plunger pump
4 Motor
5 One-way valve
6 Pilot overflow valve
7 Pipe filter
8 Pressure gage
9 Pressure sensor
10 Reducing valve
11 Proportional change valve
12 Shuttle valve
13 Manual change valve
14 Manual pump
15 Cooler
16 Slippage pump
17 Direct overflow valve
18 Accumulator
19 Hydraulic cylinder

Fig. 1 The principle of the dynamic system

Design and strength check of the compound hydraulic cylinder

The hydraulic cylinder is the critical executive part in this system, the structure must be reasonable, and the strength must meet the requirements. Through convention design calculation, the structure of this hydraulic cylinder is shown in Fig.2. And the parameters are shown in Tab.1.

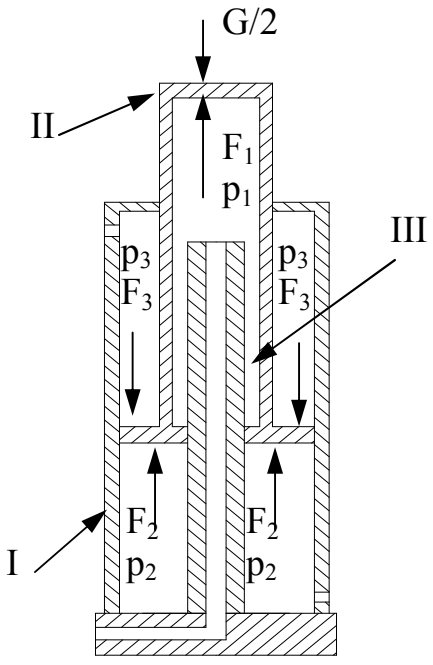


Fig. 2 The structure of the compound hydraulic cylinder

Tab. 1 The parameters of the compound hydraulic cylinde

Components	Outer Diameters （mm）	Inner Diameters （mm）	Thickness （mm）
Cylinder I	169	150	9.5
Plunger II	125	93	16
Plunger III	80	60	10

(1) Strength check for plunger II:

$$F_H = G/2 = 6\times10^4 N \text{。} \tag{1}$$

$$\alpha = d_2 / D_2 \tag{2}$$

$$A = \frac{\pi}{4} D_2^2 (1-\alpha^2) \tag{3}$$

$$J = \frac{\pi}{64} D_2^4 (1-\alpha^4) \tag{4}$$

$$r_k = \sqrt{\frac{J}{A}} = \frac{D_2}{4}\sqrt{1+\alpha^2} \tag{5}$$

When the slenderne ratio of plunger II $\lambda=l_2/r_k>90$， calculate the critical force F_k with Euler's formula, we got:

$$D_2 < \frac{4l_2}{\phi_1\sqrt{\phi_2}\sqrt{1+\alpha^2}} = \frac{0.2222}{\sqrt{1+\alpha^2}} \tag{6}$$

Where, F_H: the equivalent force, **α**: ratio of inner diameter to outer diameter, A: sectional area, J: moment of inertia, r_k: inertia radius. When $l>>10D$， should check the stability of plunger II. The material is mild steel, flexibility factor ϕ_1=90, modulus of elasticity E=2.06×10^{11}N/㎡.

(a) When both of the ends is fixed, $\phi_2 = 1$, calculate the critical force F_k with Euler's formula:

$$F_k = \frac{\pi^2 EJ}{(\phi_2 l_2)^2} = \frac{\pi^3 E(D_2^4 - d_2^4)}{64(\phi_2 l_2)^2} = 4.3\times10^5 N \tag{7}$$

So the safety factor:

$$n_k = \frac{F_k}{F_H} = 7 \tag{8}$$

(b) When only one end fixed， $\phi_2 = 2$, calculate the critical force F_k with Euler's formula:

$$F_k = \frac{\pi^2 EJ}{(\phi_2 l_2)^2} = \frac{\pi^3 E(D_2^4 - d_2^4)}{64(\phi_2 l_2)^2} = 1.1\times10^5 N \tag{9}$$

So the safety factor:

$$n_k = \frac{F_k}{F_H} = 1.75 \tag{10}$$

(2) Strength check for plunger III:

$$\beta = d_3 / D_3 = 0.75 \tag{11}$$

$$F_H = p_1(A_3 - A_3') = F_1(1-\beta^2) = 1.48\times10^4 N \tag{12}$$

Where, F_H: the equivalent force, β: ratio of inner diameter to outer diameter, the same argument, we can get calculate the critical force F_k with Euler's formula:

$$F_k = \frac{\pi^2 EJ}{(\phi_2 l_2)^2} = \frac{\pi^3 E(D_3^4 - d_3^4)}{64(\phi_2 l_3)^2} = 1.12 \times 10^5 N \tag{13}$$

So the safety factor:

$$n_k = \frac{F_k}{F_H} = 7.5 \tag{14}$$

According to the calculation above, we can get that the strength of this compound hydraulic cylinder is enough.

Selection and checking of some chief components

(1) Plunger pump

The maximum stream flow is 499 *L*/*min*, when the plunger moves down, if the volumetric efficiency of the pump is $\eta_v = 0.95$, the rotate speed of the motor is 1480*r*/*min*, the output volume is:

$$q = \frac{Q}{n \cdot \eta_v} = \frac{499 \times 1000}{1480 \times 0.95} = 355ml/r \tag{15}$$

So, we selected two plunger pumps work together:

$$Q_1 = \frac{qn\eta_v}{1000} = \frac{125 \times 1480 \times 0.95}{1000} = 176L/\min \tag{16}$$

$$Q_2 = \frac{qn\eta_v}{1000} = \frac{250 \times 1480 \times 0.95}{1000} = 352L/\min \tag{17}$$

(2) Accumulator

The pressure of the accumulator:

$$p_2 = \frac{F_3}{A_1' - A_3} = \frac{F_3}{\frac{\pi}{4}(d_1^2 - D_3^2)} = \frac{5.25 \times 10^4 / 2}{\frac{3.14}{4} \times (0.145^2 - 0.08^2)} = 2.29Mpa \tag{18}$$

As the working pressure range is ±15%, set the minimum working pressure is $p_{\min} = 0.85 p_2$, inflation pressure $p_0 = 0.8 p_{\min}$.

Suppose that the Accumulator is adiabatic, the volume of the accumulator is:

$$V = \frac{\Delta V}{(\frac{p_0}{p_{\min}})^{0.715} - (\frac{p_0}{p_{\max}})^{0.715}} = \frac{2 \times \frac{\pi}{4}(d_1^2 - D_3^2)l}{(\frac{0.8 p_{\min}}{p_{\min}})^{0.715} - (\frac{0.8 \times 0.85 p}{1.15 p})^{0.715}} = \frac{115}{0.8^{0.715} - 0.59^{0.715}} = 689L \tag{19}$$

So we set 10 accumulators parallel connected, the volume of each accumulators is 7L.

(3)Main oil way motor

According to the features of the compound hydraulic cylinder, when the plunger stay at the upper point, the pressure is 7.5MPa, and at the under point, the pressure is 7.25MPa, the power of the motor is:

$$P_1 = \frac{(p + \Delta p_1 + \Delta p_2)Q_1}{60 \times 0.9 \times 0.95 \times 0.95 \times 0.9} = \frac{(7.5 + 1 + 0.2) \times 176}{60 \times 0.9 \times 0.95 \times 0.95 \times 0.9} = 35\text{kW} \tag{20}$$

$$P_2 = \frac{(p + \Delta p_1 + \Delta p_2)Q_2}{60 \times 0.9 \times 0.95 \times 0.95 \times 0.9} = \frac{(7.5 + 1 + 0.2) \times 352}{60 \times 0.9 \times 0.95 \times 0.95 \times 0.9} = 70\text{kW} \tag{21}$$

Velocity response test

After the installation and debugging of system, a velocity response test was carried out, the load force is 120kN. we got the velocity diagram of this system, shown in Fig.3. As the diagram shows, system runs smoothly.

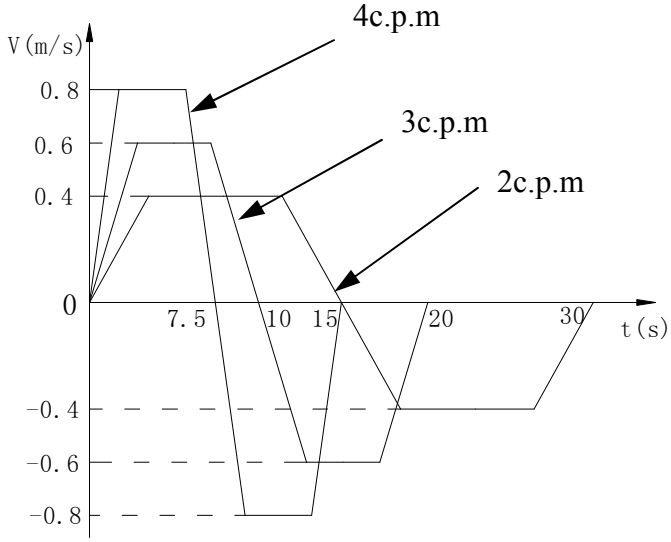


Fig.3 The velocity diagram of the system

Summary

Through the research, calculation and the checking on this lifting test system, some features of this system is that:

(1) Combined electro-hydraulic proportional control principle and oil producing technology, satisfied the needs of oil pump action of the test, it's an attempt of oil lifting technology.

(2) Though the use of the compound liquid cylinder to do a hydraulic balance, solve the problem of the load force is not the average when the cylinder moves reciprocally, make the system more stable, and at the same time and reduce the cost.

(3) Through the simulation test founds that the system's velocity is smooth, achieve the design index.

References

[1] Juan He, Yang Sui: Domestic Special Pump Type and Performance Analysis. Journal of Henan Science and Technology. Vol.07 (2011), p.63.

[2] Zhanyu Ge, Qing Liu: Research on the movement rules of the plunger and cylinder of underground oil pump. Journal of the University of Petroleum. Vol.17,No.6(1993), p.56.

[3] Meiquan Li: Application of Electro-hydraulic Proportional Control Technology in Combination Mchine Atomatic Line. No.09(1992).

[4] Xin Wei, Jun Sun, ect.: Design of New Hydraulic Pumping Unitwith Electro-hydraulic Proportional Control. MACHINE TOOL & HYDRAULICS. Vol. 37, No.2(2009), P.39.

[5] Genyi Li, Jinxi Zhang, ect.: Dynamic Design and Simulation of Proportional Directional Valve with Displacement Feedback Based on the Moving Valve Sleeve, MACHINE TOOL & HYDRAULICS. Vol.37, No.4(2009), p.(69~71).

© (2012) Trans Tech Publications, Switzerland
doi:10.4028/www.scientific.net/AMM.164.456

Modal Finite Element Analysis of Reconstructive Structure for Gantry Crane on the Basis of ANSYS and Dynamic Stiffness

Qing-dun Zeng[1,a] and Bao-hua Guan[1,b]

[1]School of Civil Engineering and Transportation, South China University of Technology, Guangzhou 510640, China

[a]emqdzeng@scut.edu.cn, [b]baohua_guan1988@sina.com

Keywords: Gantry crane, Principal mode, Laterodeviation, Modal analysis, Finite element method.

Abstract. Due to business development, a Shipyard Co., Ltd. in Guangdong planned to remould a double girder gantry crane of MG32/10-37A5 (32t-37m) into a type of 20t-37m and to heighten 6m lifting height of structure. A Cranes Machinery Co., LTD. in Guangzhou undertook this job. After the completion of transformation for the crane, the serious laterodeviations of the crane were found in operational process, which affected its safety use. This paper used a finite ANSYS to perform the modal analysis of the crane before and after reconstruction. The results show that the dynamic stiffness of the remoulded crane was reduced obviously. For the reason, the four reinforcement schemes of the crane were put forward by the Cranes Machinery Co., LTD.. This study again performed the model analysis for the schemes and selected an optimal one by calculation, analysis and contrast, which has successfully solved the above problem. The present results can provide a reference for solving similar problems in the future.

Introduction

The application of crane is more and more universal with the development of modern industry. The newly manufactured cranes are usually designed as the stereotypes products by crane design unit. Namely, if various parameters of cranes can all meet the requirements of the relevant specifications [1~3], the cranes can be used safely.

In engineering practice, due to the change of production requirements at times, the transformation of structure or function of original cranes is inevitable. The remoulded cranes are the non-stereotypes products, while for such cranes the indexes in the specifications cannot be simply applied mechanically. Even if every index of remoulded cranes can meet the requirements of the relevent codes, they may not be assured to operate safely.

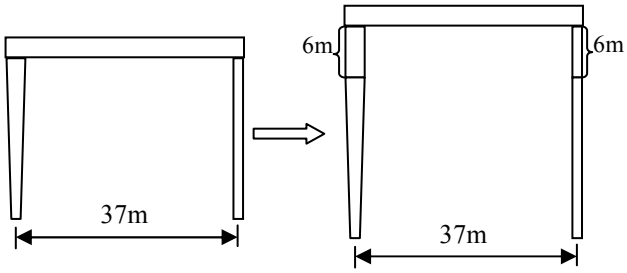
Due to business development, a Shipyard Co., Ltd. in Guangdong planned to remould a double girder gantry crane of MG32/10-37A5 (32t-37m) into a type of 20t-37m, that is, heightening 6m lifting height of structure. A Cranes Machinary Co., LTD. in Guangzhou undertook this job. After the completion of transformation, the serious laterodeviations of the crane were found in use process and affected its normal safety operation.

A finite ANSYS was used to research the static stiffness of the crane before and after transformation (see another paper by the present authors). The research results indicate that the static stiffness of the crane before and after transformation can meet the requirements of the relevant specifications. However, the inharmonious stiffness between the rigid and flexible legs caused the serious laterodeviations of the crane. Therefore, the dynamic stiffness of crane is involved. But there is not a specific regulation on the crane's dynamic stiffness in the relevant specifications. At present, the researches on the modal analysis of cranes mostly focuse on the stereotype products [4, 5] and rarely touch upon the remoulded cranes.

In this paper, a finite ANSYS is used to research the modal performance of integral structure of the crane before and after transformation. The results show that the dynamic stiffness of the remoulded crane is obviously reduced, thus affecting its normal use. After contrasting the change of the static stiffness and dynamic stiffness of original and remoulded cranes, the four reinforcement schemes were put forward by the Cranes Machinary Co., LTD.. By carrying out modal analysis on the crane reinforced by the four reinforcement schemes, one of the schemes is identified as the most reasonable one on the basis of the modal analysis results for the original crane as the basic standard.

Structural Style of Crane before and after Transformation

The span and lifting height of a gantry crane of MG32/10-37A5 (32t-37m) is 37m and 22m, respectively. Its one side is rigid legs while the other is flexible legs. Due to production needs, the crane will be remoulded as a type of 20t-37m, that is, its rated hoisting weight is reduced from 32t to 20t, and the lifting height of structure is heightened to be 6m. Thus the lifting height of the remoulded crane now is 28m and the sketch map of remoulded crane is shown in Fig.1.



(a) MG32/10-37 A5 (b) MG20/10-37 A5

Fig.1 The sketch map of remoulded crane

The relevant specifications [1~3] of crane design have the specific rules for the static stiffness of cranes. However, the requirements of dynamic stiffness of cranes have been mentioned only in *Design rules for cranes* (GB3811-1983) which specifies that the natural vibration frequency of gantry cranes under full load should not be less than 1Hz.

FEM Model and Four Reinforcement Schemes

In this paper, a finite ANSYS is used to establish the solid models based on the design drawings of the original crane (MG32/10-37 A5) and the remoulded crane (MG20/10-37 A5) shown in Fig. 1. In modeling process, based on the actual situation and considered the convenience of modeling, the influence of the local details of bolted connection and the peripheral auxiliary facilities (such as handrail, staircase, etc.) on the structure will be ignored, and the thin shell elements of SHELL 163 will be use on all construction members and stiffening ribs. The connections between construction members will all be rigid; they come true by coupling linear displacement of nodes. The finite element solid models established for the original and remoulded cranes are shown in Fig. 2 and Fig. 3, respectively.



Fig.2 Whole model diagram of crane MG32/10-37A5



Fig.3 Whole model diagram of remoulded crane

By contrusting the change of static stiffness and dynamic stiffness of the crane before and after transformation, the four reinforcement schemes put forward by the Cranes Machinary Co., LTD. are as follows:

Scheme 1: Plan to add a crossbeam in the middle of rigid legs and supports on the top of rigid legs.

Scheme 2: Plan to add supports on the top of flexible legs and each with a crossbeam in the middle of rigid legs and flexible legs.

Scheme 3: Plan to add each with a support on the top of flexible legs and rigid legs and each with a crossbeam in the middle of rigid legs and flexible legs.

Scheme 4: On the basis of Scheme 3, the outer side of the rigid legs is strengthened and the self weight of trolley is reduced from 14.8t to 6.5t.

Modal Analysis of Gantry Crane on the Basis of ANSYS

The modal analysis is also called as the extraction of feature eigenvalues. It is used to solve the natural frequency and corresponding mode of free vibration of multiple-degree-of-freedom system. The inherent characteristic of structural vibration is only related to its own mass and stiffness. Therefore, it is also called as the natural characteristic [6]. The dynamic response behavior of structure under dynamic load will be determined by it. It is a very common problem that the phenomena of structure's dynamics resonance will appear when the frequency of the loads which are applied on the structure is close to the frequency of the structure itself. One important aspect of structural dynamic design is to avoid structure's dynamics resonance on external excitation function by adjusting the distributions of structure's stiffness and mass reasonably. Certainly, the modal analysis on the gantry cranes is aimed at searching the basis of adjusting the distributions of cranes' stiffness and mass.

According to the vibration theory, for a multi-degrees-of-freedom vibration system, the natural frequencies of lower order make greater contribution to the system's dynamic response while the natural frequencies of higher order make less [7]. Therefore, for the multiple-degree-of-freedom system, only need to extract the natural frequencies of lower order can the dynamics characteristics been well reflected. So, only the first five-order modalities of crane are extracted during the modal analysis. In this way, it can not only get the natural frequencies which make greater contribution to gantry crane, but also accelerate the velocity of model-solving. In the process of analysis, the block Lanczos method will be chosen to extract the modalities of crane. The calculated natural frequencies of first five orders for original, remoulded and reinforced cranes are listed in Table 1, and vibration modes of their first two orders are shown in Fig. 4~Fig. 9.

Table 1 Natural frequencies of first five orders for original, remoulded and reinforced cranes (Hz)

Order number	MG32t-37m	Remoulded crane	Scheme 1	Scheme 2	Scheme 3	Scheme 4
1	1.0292	0.6394	0.7049	0.7470	0.7207	1.1735
2	1.1956	0.9328	0.9942	1.0300	1.0990	1.1902
3	1.2565	1.3176	1.3212	1.4942	1.4873	1.5410
4	2.1145	2.4480	2.5475	2.6360	2.6311	2.8304
5	2.2473	2.5215	2.7502	2.9608	2.9418	3.3759

It can be seen from Fig. 4~Fig. 9 that the laterodeviations of the crane nearly are the same as the natural vibration modes of first two orders. This is because the frequencies of the loads which are applied on the crane are the same as or close to the frequencies of first two orders for the crane, thus resulting in resonance. The data in Table 1 shows that each order frequency of the reinforced cranes has increased to some extent. This indicates that the reinforcement schemes are useful for improving the integral stiffness of the crane. Among all the four reinforcement schemes, each order frequency of the crane reinforced by Scheme 4 is higher than that of the other five cases, except for that the second order frequency of Scheme 4 is slightly below that of the original crane. This can indicate that the laterodeviations of the crane will be reduced if the crane is reinforced by Scheme 4. This conclusion has been proved by the final reinforcement result.



Fig.4 The first order vibration mode of original crane



Fig.5 The second order vibration mode of original crane



Fig.6 The first order vibration mode of remoulded crane



Fig.7 The second order vibration mode of remoulded crane

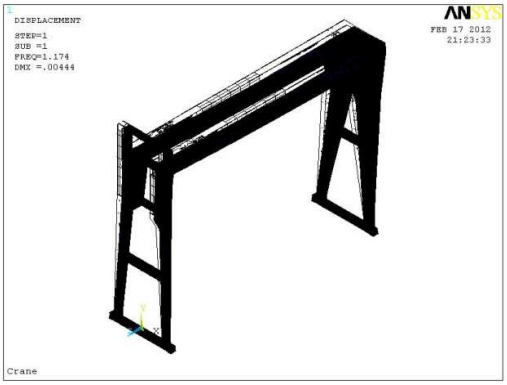


Fig.8 The first order vibration mode of crane reinforced by Scheme 4

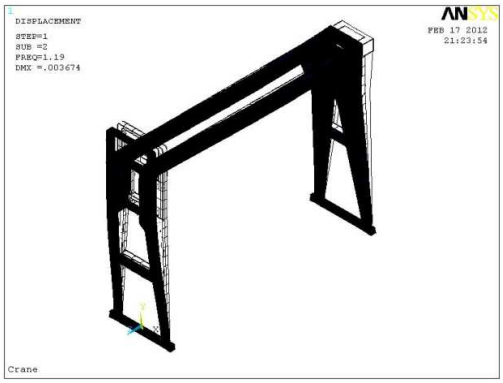


Fig.9 The second order vibration mode of crane reinforced by Scheme 4

Conclusions

In this paper, a finite element ANSYS is used to research the integral structure of a double girder gantry crane remoulded by a company. The reason why the remoulded crane could not be operated safely (serious laterodeviations of the crane occur in using process) is found by analyzing the research results. This is because the remoulded crane's stiffness distribution is inharmonious; the frequencies of the loads which are applied on the crane nearly are the same as the first 2 order frequencies of the crane, thus resulting in resonance. Scheme 4 is chosen as the best reinforcement scheme to solve the above problem by comparing the four reinforcement schemes.

We can conclude from this case that in the remoulded process of crane, not only the static analysis should be carried out to ensure that all the parameters of crane can meet the requirements of the relevant specifications, but also the modal analysis should be performed. So the unstable condition of structure vibration can be known and the structure resonance may be avoided. The modal analysis is of great value for ensuring the safe operation of cranes.

References

[1] *Gantry crane for general purpose* (GB/T14406-2011) (Standards Press of China, Beijing 2011).

[2] *Code for design of steel structures* (GB50017-2003) (China Planning Press, Beijing 2003).

[3] *Crane design specification* (GB/T3811-2008) (Standards Press of China, Beijing 2008).

[4] Y. Q. Zheng, J. L. Huang and S. Z. Zhang: Min. Proce. Equip., Vol. 38 (17) (2010), p.54.

[5] S. C. Wang, et al.: Mech. Sci. Tech. for Aero. Eng., Vol. 29 (7) (2010), p. 912. (in Chinese)

[6] F. Ju and Y. S. Choo: ASCE J. Eng. Mech., Vol. 131(1) (2010), p. 88.

[7] F. Ju, Y. S. Choo and F. S. Cui: Int. J. Solids Struc., Vol. 43 (2) (2006), p. 376.

© (2012) Trans Tech Publications, Switzerland
doi:10.4028/www.scientific.net/AMM.164.460

Analysis on the Characteristics of Scale Wave Energy dynamic system during Extended Period of the Massive Drought in Southwestern Region

Tiangui Xiao [1] Yao Wu [1] Ronghua Jin [2]

[1.] Department of Atmospheric Science, Chengdu University of Information Technology, Chengdu 610225;
[2.] National Meteorological Center, Beijing 100008

Keywords: Southwestern Region, Drought, Wave-Packet Propagation Diagnosis (WPD), Characteristics of Wave Energy

Abstract. Through the wave-packet propagation diagnosis (WPD), the essay discusses and analyzes the characteristics of wave packet distribution and wave energy propagation during the extended period of the massive drought in southwestern region in the country by using the reanalysis grid data of the daily NCEP/NCAR geopotential height field and $1^0 \times 1^0$ horizontal resolution from September 2009 to April 2010. The results show that: the characteristics of wave energy propagation at the middle and high height fields can better reflect the stage features of this drought during the period. The wave energy time-variation chart shows that the wave disturbance during the drought is weak and the wave packet value is small. However, the wave packet value during the drought still has some changes, reflecting the characteristics of the drought change in weakness. At the maintenance period of the wave packet value, the drought is often severe, and when the wave packet value changes greatly, the magnitude of the drought will change. Seen from the characteristics of longitudinal and altitudinal propagation of the wave energy, when the wav packet strength increases, the energy will accumulate and the drought tends to be weakened; on the contrary, when the wave packet strength decreases, energy will discharge and the drought will become more severe—particularly when the wave packet weakens quickly, the drought will become more drastic. This study provides a meaningful idea for discussing the forecast of the scale weather process during the extended period.

1. Introduction

Since September 2009, the five provinces and municipalities in southwestern region, Yunnan, Guizhou, Guangxi, Sichuan and Chongqing have encountered a wide range of persistent drought. In some areas, the rainfall is seven to nine times less than previous years, and the water flowing into the main rivers is unprecedentedly low. The continuous drought from autumn to spring brought a 100-year extra-massive drought to some areas of the five provinces and municipalities, and the arid scope and magnitude created a record high. This essay is to analyze and study the accumulation of the disturbed energy and propagation characteristics of the scale during the 10-30d extended period of this long drought from the perspective of the wave energy.

2 Data and Methods

2.1 Data

The data adopted for the study in this essay is the daily $1^0 \times 1^0$ grid reanalysis data of the NCEP/NCAR geopotential height field from September 2009 to April 2010 as well as the CI data of the integrated meteorological drought index from 723 station around the country.

2.2 Calculation Method

The changes in the wave energy can be realized by wave packet propagation calculation[1-6]. In theory, wave energy is spread along the wave envelope, and the movement of the maximum wave amplitude refers to the movement of a wave packet, which also implies the energy propagation of

this wave. Therefore, through computing the variations of time and space of all wave amplitudes, the movement of the wave packet and the wave energy propagation can be identified. Since this essay mainly focuses on the trend of the weather of the extended period scale (10-30d), the 10-30d band-pass filter shall be selected. After obtaining the narrowband signal with the extension scale characteristics, the wave packet value of all space points shall be re-gained. Through the analysis of the wave packet value, it discusses the characteristics of the wave energy of the extended period scale during the drought. According to the literature, the specific calculation steps for the wave packet propagation diagnosis are as follows:

(1) The 10-30d band-pass filter for the geopotential height field to get the low frequency wave narrowband signal $P(x,y,z,t)$ of the height field

(2) Hilbert transform of the known narrowband signal $\hat{P}(x,y,z,t)$, i.e.:

$$\hat{P}(x,y,z,t)=\mathrm{A}(x,y,z,t)\cdot\sin\left[kx+ly+mz+\omega_0 t+\varphi(x,y,z,t)\right]$$

(3) Calculate the amplitude $A_i(x,y,z,t)$ of analytic signal $P_c(x,y,z,t)$; that is to calculate the wave packet value of the narrowband signal by the following formula:

$$P_c(x,y,z,t)=\mathrm{A}(x,y,z,t)\cdot\cos\left[kx+ly+mz+\omega_0 t+\varphi(x,y,z,t)\right]+i\mathrm{A}(x,y,z,t)\cdot$$
$$\sin\left[kx+ly+mz+\omega_0 t+\varphi(x,y,z,t)\right]=\tilde{\mathrm{A}}(x,y,z,t)e^{i(kx+ly+mz+\omega_0 t)}$$

i.e.:

$$P_c(x,y,z,t)=P(x,y,z,t)+i\hat{P}(x,y,z,t)$$

Wherein:

$$A(x,y,z,t)=\sqrt{P^2(x,y,z,t)+\hat{P}^2(x,y,z,t)}$$

(4) Based on the wave packet data of various spatial points, draw the wave packet distribution diagrams, and then calculate the continuous changes of the wave packet distribution diagrams and discuss the wave packet propagation characteristics.

3 Classification of the Drought and Drought Process Stages

3.1 Drought

From September 2009 to April 2010, the five provinces and cities encountered a long time drought from autumn to spring which affected wide areas. The drought occurred mainly in most part of Yunnan, southern Sichuan, most part of Guizhou, western Guangxi and Chongqing, spanning the latitude and longitude range of 97-110° E, 21-34° N.

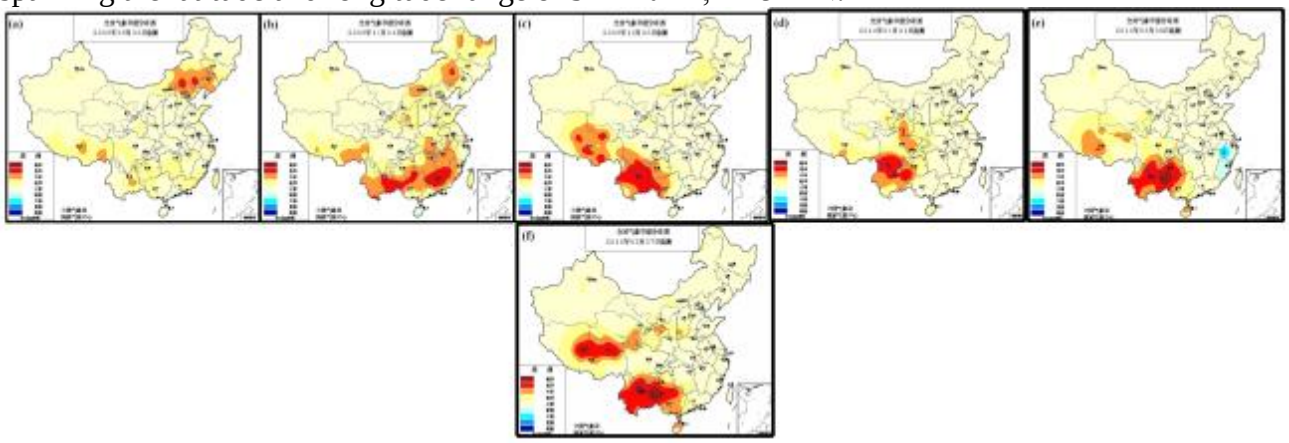


Fig. 1 National Meteorological Drought Distribution Map from September 2009 to April 2010. (a) Sep.23, 2009 (b) Nov.1, 2009 (c) Dec.5, 2009(d) Jan.31, 2010 (e) Mar.8, 2009 (f) Mar.31, 2010

The pre-drought stage started from mid-September 2009. Fig. 1(a) provides the distribution of national meteorological drought on September 23, 2009. In October, Yunnan, southern Guizhou and other areas suffered constant droughts, mainly the moderate meteorological droughts. From December, the drought in southwestern region broke out massively, signifying the start of the early

stage of the drought eruption, and southern Sichuan and most part of Yunnan recoded moderate to severe drought weather. In early January 2010, the arid middle stage started, during which most part of Yunnan, most part of Sichuan, southern Gansu and western Guizhou had continuous meteorological droughts, recording the meteorological drought above the moderate level. From February to early March, most part of Yunnan, most part of Guizhou, west and north Guangxi, south Sichuan and southwestern Hunan recorded the meteorological drought above the moderate level. From March to early April, most part of Yunnan, western and southern Guizhou, northern Guangxi, southern West Sichuan Plateau etc. recorded the meteorological drought above the moderate level, and the central, northern and eastern part of Yunnan, western and southern Guizhou, northwest Guangxi, southern West Sichuan Plateau recoded severe drought weather. After the mid April, arid areas were gradually smaller, the drought intensity weakened gradually, and the drought in southwestern region was gradually alleviated. This essay mainly focuses the extended scale disturbance energy characteristics since September 2009 when the drought broke out.

3.2 Classification of Drought Process Stages

According to the integrated meteorological drought index CI value for four representative stations in southwest region (Mianyang, Kunming, Shapingba and Guiyang) from September 2009 to April 2010, and the time variation diagram is drawn as shown in Fig. 2:

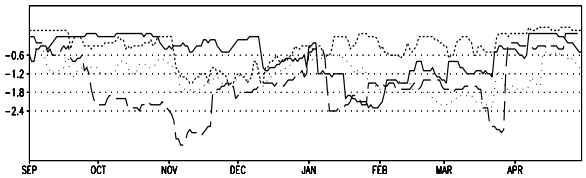


Fig. 2 CI index series of Four representative stations in southwest region (Mianyang, solid line), Kunming (long broken line), Shapingba (short broken line) and Guiyang (dot line) from September 2009 - April 2010

According to the CI index value for the drought in Fig. 2, we divide the drought process into 7 stages, namely, no drought before September 21, 2009, slight drought from September 21 - November 5, 2009, moderate drought from November 6 - December 15, 2009, slight drought from December 16, 2009 to January 10, 2010, moderate drought from January 11 to February 22, 2010, heavy drought from February 22 to March 20, 2010 as well as no drought after March 21, 2010. See Table 1 for details:

Table 1 Drought Process Stages

Early stage	No drought	Before September 21, 2009
	Light drought	September 21, 2009 - November 5, 2009
Mid-stage	Moderate drought	November 6, 2009 - December 15, 2009
	Light drought	December 16, 2009 – January 10, 2010
	Moderate drought	January 11, 2010 - February 22, 2010
	Heavy drought	February 22, 2010-March 20, 2010
Late stage	No drought	After March 21, 2010

4 Average Wave Energy Change at the 500hPa Height Field During the Drought in Southwestern Region

Wave energy propagation theory suggests that, the size of the wave packet represents the intensity of disturbance energy, and the increase and decrease in wave packet value that accumulation of the disturbance energy and release weakening. According to the analysis of the drought, the studies of this paper mainly includes 97-110 E, 21-34 N.

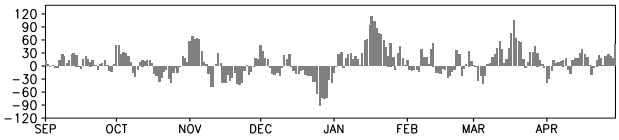


Fig. 3 500hPa height field anomaly from September 2009 - April 2010

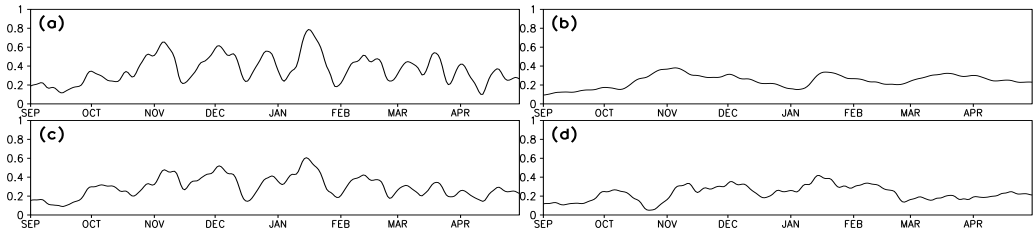


Fig. 4 500hPa height field wave packet from September 2009 to April 2010.
(a)10-30d, (b)20-30d, (c)10-20d, (d)10-15d

Fig 3 shows the 500hPa height field anomaly in the above range of the arid area from September 2009 to April 2010. From the chart we can see before November, the 500hPa height field was slightly high, with small change; at the early stage of November, there was a peak period of 10 days, and the drought became severe quickly. From the mid-November to December, the 500hPa height field anomaly was extraordinarily low, and drought became less drastic; after January until April, the 500hPa height field was high, especially for mid-January and mid-March, corresponding to the two drastic droughts in Fig. 2 respectively.

Fig 4 shows the change curve for the extended period multi-scale wave packet average value in the selected area from September 2009 to April 2010. As shown in the figure, the extended period wave packet values of all scales do not exceed 0.8, and it indicates that during the entire period of drought, the disturbance in the southwestern region was weak. In the wave packet theory, weak disturbance contributes to the development and maintenance of drought.

The change in height field at the early stage of drought is small, and the wave packet value is also small. From the late October, the wave packet value began to grow. On the 10-30d wave packet curve, from November to December, 500hPa height field wave packets change hugely, the wave packet values of other scales at this stage also increased to various extents. Figure 3 shows that this stage is the negative anomaly, and the drought eased. In mid-January, an extreme large wave packet value occurred under the joint effects of the 10-20d and 20-30d wave packets, the disturbance intensified, significantly positive anomaly occurred and drought intensified. After that, the wave packet value was below 0.5 at a low level, and drought continued. After March, the wave packet has been very low, which is obvious on the 10-15d wave packet chart, and the drought is serious.

According to the drought intensity, 10-30d wave packet average drawings from September 1 to September 30, October 1 to October 31, November 1 to November 20, November 21 to January 10, January 11 to February 28 and March 1 to - March 31 as well as April 1 to April 30 are drawn, in order to analyze the characteristics of wave packet distribution at different periods of heavy drought, slight drought, etc.

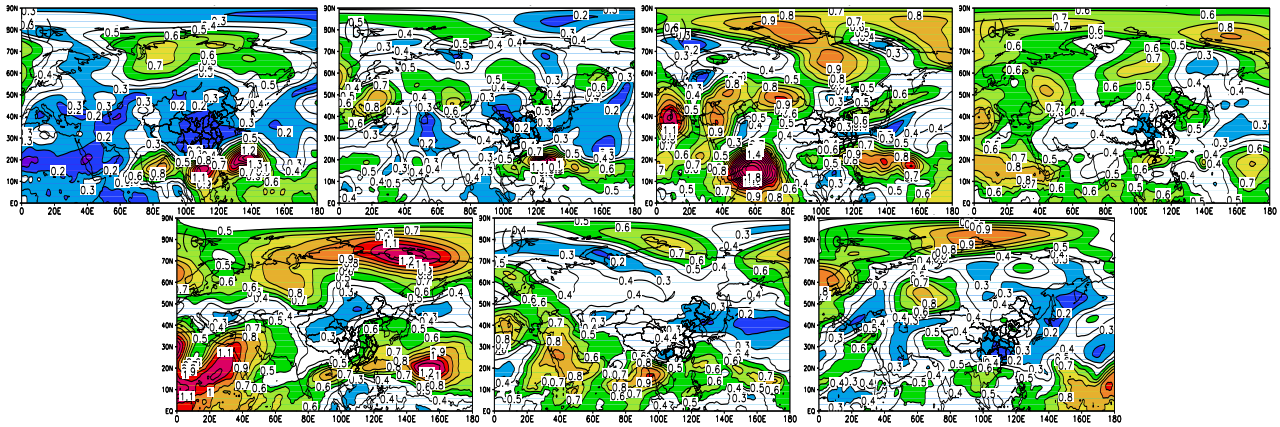


Fig 5 500hPa wave packet distribution of drought process
(a) Sep.1, 2009 –Sep.30, 2009 (b) Oct.1, 2009 – Oct.31, 2009.(c) Nov.1, 2009 – Nov.20, 2009
(d) Nov.21, 2009 – Jan.10, 2010.(e) Jan.11, 2010 – Feb.28, 2010(f) Mar.1, 2010 – Mar.31, 2010
(g) Apr.1, 2010 – Apr.30, 2010

Fig. 5 shows the average wave value of 500hPa geopotential height field in the different periods. At the early stage of the drought (Fig. 5 (a)), China was controlled by the weak wave packet, and wave packet value of the whole area was less than 0.3. The lager wave packet areas of more than 0.5 are distributed from the India Peninsula to the east of Philippines: there are three strong wave packet centers, with the strength of 0.9, 1.2 and 1.4 respectively; from October 1 to October 31 (Fig. 5 (b)), the Yangtze River Basin and the north area in China still had small wave packet value. The strong wave packet centers on the southern sea combined and enhanced, distributed in a strip shape, and tended to raise northward. The value at the center reached 1.5, and large amounts of energy released in the South China Sea. From November 1st to November 20 (Figure 5(c)), the strong wave packet center weakened round 20 N, but it still continued to influence the southern region of China, and wave energy continued to release. Since December until April, the wave packet value in southwest region of China was weaker. Because of the abnormal energy release in southwestern region, this region maintained an abnormal drought condition under weak disturbance.

5 Distubrance Wave Energy Accumulation and Propagation Characteristics During the Drought

In order to further study the disturbance energy propagation characteristics during the drought in southwestern region from September 2009 to April 2010, the 30°E - 120°W time-longitude profile and 20°S - 60°N time-longitude profile of the 500hPa height field during this period were given to analyze the disturbance energy propagation path and the energy change of the height field during the drought.

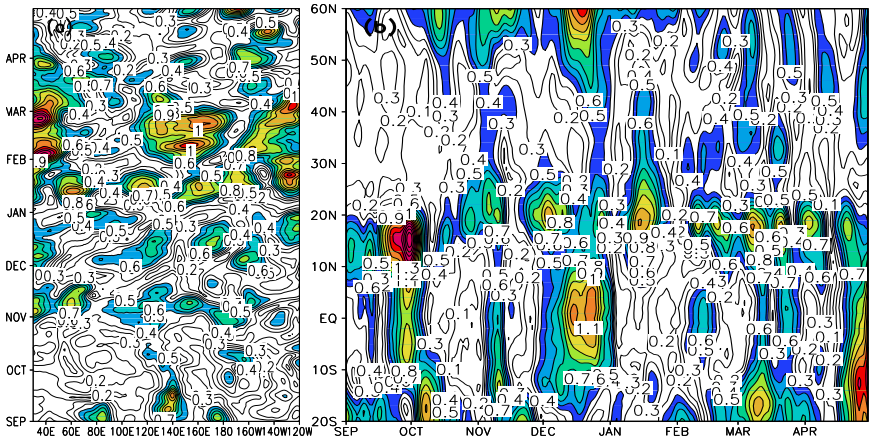


Fig.6 Time profile of 500hPa geopotential height wave packet from September 2009 to April 2010.
(a) 21-34°N average time-longitude profile.(b)97-110°E average time - latitude profile.

Fig. 6(a) shows that there are 3 strong wave packet value periods in the EW direction of 500hPa, i.e. early stage of drought in early September, early November and continuous period in February. However, in October and March, the wave packet is relatively small, below 0.5. At the end of September, the strong wave packet center is located at 80°E and 120°E the Asian areas near China, when the drought disaster is slight. After that, the wave packet value weakened, disturbance energy was released, and drought became drastic. In November strong wave packet center are located in the 40-60°E in Arabia Peninsula and 110-160°E Southern China, the disturbance developed, and the central intensity was 0.9 and 0.8 respectively, and it spread eastward, and the drought became drastic. In December; wave packet value was slightly weakened, the drought continued but alleviated; In Mid-January, the wave packet enhanced in the southwest region, and in early February, the strong wave packet center was moved to 140-160°E West Pacific, and the central intensity enhanced to 1.2; In March, the wave packet weakened, and the weak wave packet could not be continued, and the drought became drastic again. After March, the wave packet had been smaller, drought was severe. Fig. 6 (b) showed that the southern region of China in the northern hemisphere at 500hPa of 10-20°N has an obvious strong wave packet. At the end of September, the wave packet is stronger, when the drought is lighter but also in the continuous accumulation. Subsequently, the wave packet values weakened, energy was still accumulated, and the drought gradually began to develop. In November strong wave packet center was located at 25°N southwest, wave packet slightly developed; In February wave packet slightly moved southward, and the southwestern was still in drought under weak disturbance.

Through the summary of strength and propagation characteristics of wave packets, we found that in the period when the wave packet intensifies, the energy accumulated, and often the drought development will follow; in the period when the wave packet weakens, the energy is released, at the same time the weakened disturbance will disable the early abnormal condition to quickly spread, leading to the exacerbation of drought in the regio

6 Conclusion

(1) The wave packet of 500hPa height field can better reflect the phase characteristics of the in this period.

(2) From the wave packet time diagram, when the wave packet value is small, the drought process continues, and the drought is more serious.

(3) Through the altitudinal and longitudinal propagation of wave energy, we found that in the period when the wave packet intensifies, the energy accumulated, and often the drought development will follow; in the period when the wave packet weakens, the energy is released, at the same time the weakened disturbance will disable the early abnormal condition to quickly spread, leading to the exacerbation of drought in the region.

Acknowledgements: This thesis is funded by the National Science and Technology Support Program (Project No.: 2009BAC51B03).

References

[1] CHANG E K M, YU D B. Characteristics of wave packets in the upper troposphere part I: northern hemisphere winter[J]. J Atmos Sci, 1999,56(11): 1708-1728.

[2] CHANG E K M. Characteristics of wave packets in the upper troposphere part II: Seasonal and hemispheric variations[J]. J Atmos Sci, 1999,56(11): 1729-1747.

[3] CHANG E K M. Wave packets and life cycles of troughs in the upper troposphere: Examples from the southern hemisphere summer season of 1984/85[J]. Mon Wea Rev, 2000, 128(1): 25-50.

[4] CHANG E K M. The structure of baroclinic wave packets[J]. J Atmos Sci, 2001, 58(13): 1694-1713.

[5] Miao Jinhai, Xiao Tiangui, Liu Zhiyuan. The oretic foundation and computational method about the wave- packet propagation diagnosis[J]. Acta Meteorologica Sinica, 2002, 60(4): 461-467.

[6] ZENG Qingcun. The evolution and structure of a Rossby-wave packet in forced mean flow[J]. Scientia Sinica, 1983, 25(8): 872-881.

© (2012) Trans Tech Publications, Switzerland
doi:10.4028/www.scientific.net/AMM.164.467

Dynamic Modeling for a Non-linear System Based on the MOESP Algorithm

Qin Teng[a], JianBo Zhang[b], Peng An[c]

School of Mechanical and Automobile Engineering, Hefei University of Technology, Hefei, China

[a]Tengqin_7348@163.com, [b]zhangjianbo120@126.com, [c]anpeng620@163.com

Keywords: Exhaust gas oxygen sensor; Dynamic modelling; Hammerstein model; MOESP model; AIC criterion; MDL criterion

Abstract. In order to measure accurately air fuel ratio in the engine exhaust gas, the Hammerstein model of the exhaust gas oxygen (EGO) sensor was identified using the multivariable output error state space (MOESP) algorithm. Firstly, a static model of the EGO sensor was identified based on engine experiment data as a static nonlinear part of the Hammerstein model. Then, the MOESP algorithm was used to build a state space model (SSM) of dynamic linear part of the Hammerstein model. To estimate model order, the Akaike Information Criterion (AIC) and the Minimum Description Length (MDL) criterion were computed, and validity of structure identification was verified by residual analysis. Then, the auto-regressive model with exogenous input (ARX) was compared with a subspace model. The result shows that a two-order SSM using MOESP algorithm is suitable to dynamic part of the Hammerstein model for EGO sensors.

Introduction

Usually, an exhaust gas oxygen sensor (EGO) is used for controlling air fuel ratio (AFR) in the engine tail-gas as a key component of the feedback signal to maintain excess air factor λ around 1. A precise mathematical model of the EGO plays an important role in the modern control methods in engine applications. This sensor is a typical non-linear system, because the relation between output voltage sensor and operating temperature of the EGO and oxygen partial pressure comply with the Nernst equation, leading to sensor characteristics showing highly nonlinear (the curve changes sharply at $\lambda = 1$).

The establishment of the state space model (SSM) suitable to modern control methods has been a difficult part for a long time. In recent years, the subspace identification method as one of the two main stream techniques of system identification (the other is prediction error method) attracts much attention due to its unique advantages. Firstly, the parameterization of the subspace identification algorithm is very simple, and the order is the only structural index needed to be decided, totally avoiding demand for the normalized parameterization. Secondly, the subspace identification method based on singular value decomposition of QR, has a higher numerical stability and reliability as it doesn't use the optimization algorithm such as iteration, nonlinear parameter estimation, and the results obtained by the non-iterative subspace identification method no longer needs to use the iterative parameter optimization method for further improvement. Moreover, the subspace identification method is convenient for estimation, filtering and prediction of the modern control systems as its expression formula of state space.

Verhaegen et al [1, 2] first tried to extend the subspace identification algorithm to the nonlinear model with block connection, the Hammerstein and Wiener. In this paper, aiming at a switching type EGO sensor of ZrO_2 in most common use, based on a typical subspace identification algorithm, multivariable output error state space (MOESP) algorithm[3,4], the MOESP model is applied to the Hammerstein models with block connection as its dynamic linear part. Construction selection and experiment verification for the MOESP model is presented.

Modelling principle

Hammerstein model. Hammerstein model consists of a static nonlinear function and a linear dynamic model in series, as shown in Fig.1.

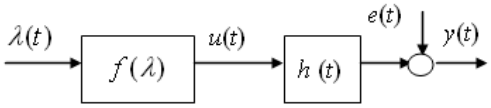


Figure.1 Hammerstein model block diagram

Where, $\lambda(t)$ is the input signal and $u(t)$ is the intermediate variable obtained through a static nonlinear function $f(\lambda(t))$. And $h(t)$ is impulse response function, $y(t)$ is the output of the system, $e(t)$ is the additive noise of the output.

The static nonlinear function is

$$u(t) = F[\lambda(t)] = f(\lambda(t),T) + r_1\lambda(t) + r_2\lambda^2(t) + \cdots r_p\lambda^p(t) \tag{1}$$

Where, r_1, r_2, …, r_p are regression coefficients, while $f(\lambda(t),T)$ is the arc tangent function of the coefficient of excess air λ and temperature T.

Considering the dynamic linear part as a linear time-invariant system, the state space expression is:

$$\begin{cases} x(t+1) = Ax(t) + Bu(t) + w(t) \\ y(t) = Cx(t) + Du(t) + v(t) \end{cases} \tag{2}$$

And,

$$E\left[\begin{pmatrix} w(t) \\ v(t) \end{pmatrix}\begin{pmatrix} w(s)^T & v(s)^T \end{pmatrix}\right] = \begin{bmatrix} Q & S \\ S^T & R \end{bmatrix}\delta_{ts} \tag{3}$$

Where, A, B, C and D are the matrixes of the system. Q, R and S are the noise covariance matrixes. u is the input signal, and y is the output signal. w is the process disturbance, and v is the output disturbance. E is the expectation operator, and δ is the Kronecker delta.

Now the modified expression of the system is given：

$$\begin{cases} x(t+1) = Ax(t) + Bu(t) + Ke(t) \\ y(t) = Cx(t) + Du(t) + e(t) \end{cases} \tag{4}$$

Where, K is the Kalman gain and $e(t)$ is the zero mean white noise.

$$\mathrm{Cov}\{e(t)\} = P \tag{5}$$

Then the parameters in Eq.4 will be identified using subspace method.

Realization of a deterministic system. For identifying system matrixes of the SSM –A, B, C and D, MOESP algorithm proposed by Verhaegen et al[3,4,5] is used. The basic steps are as follows:

- Constructing the Hankel matrix and defining related variables. The Hankel matrix for defining "past" input and output of the system are:

$$U_{0|i-1} = \begin{bmatrix} u_0 & u_1 & \cdots & u_{j-1} \\ u_1 & u_2 & \cdots & u_j \\ \vdots & \vdots & \vdots & \vdots \\ u_{i-1} & u_i & \cdots & u_{i+j-2} \end{bmatrix}, \quad Y_{0|i-1} = \begin{bmatrix} y_0 & y_1 & \cdots & y_{j-1} \\ y_1 & y_2 & \cdots & y_j \\ \vdots & \vdots & \vdots & \vdots \\ y_{i-1} & y_i & \cdots & y_{i+j-2} \end{bmatrix} \tag{6}$$

Similarly, the Hankel matrix of "future" input and output is $U_{i|2i-1}$ and $Y_{i|2i-1}$ .The augmented observable matrix and the augmented controllable matrix are:

$$\Gamma_i = \begin{bmatrix} C & CA & CA^2 & \cdots & CA^{i-1} \end{bmatrix}^T, \quad \Omega_i = \begin{bmatrix} B & AB & \cdots & A^{i-1}B & A^{i-2}B \end{bmatrix} \tag{7}$$

The state matrix is:

$$X_i = \begin{bmatrix} x_i & x_{i+1} & x_{i+2} & \cdots & x_{i+j-1} \end{bmatrix} \tag{8}$$

The lower triangular Toeplitz matrix is:

$$H_i = \begin{bmatrix} D & 0 & 0 & \cdots & 0 \\ CB & D & 0 & \cdots & 0 \\ CAB & CB & D & \cdots & 0 \\ \vdots & \vdots & \vdots & \ddots & \vdots \\ CA^{i-2}B & CA^{i-3}B & CA^{i-4}B & \cdots & D \end{bmatrix} \tag{9}$$

- LQ decomposition of the 'past' input and output Hankel matrix.

$$\begin{bmatrix} U_{0|i-1} \\ Y_{0|i-1} \end{bmatrix} = \begin{bmatrix} L_{11} & 0 \\ L_{21} & L_{22} \end{bmatrix} \begin{bmatrix} Q_1^T \\ Q_2^T \end{bmatrix} \tag{10}$$

- The singular value decomposition of L_{22}.

$$L_{22} = \begin{bmatrix} U_1 & U_2 \end{bmatrix} \begin{bmatrix} \Sigma_1 & 0 \\ 0 & 0 \end{bmatrix} \begin{bmatrix} V_1^T \\ V_2^T \end{bmatrix} = U_1 \Sigma_1 V_1^T \tag{11}$$

The number of the decomposed singular value is equal to the order of the system, i.e. $n = \dim \Sigma_1$. Then the augmented observable matrix Γ_i can be determined:

$$\Gamma_i = U_1 \Sigma_1^{1/2} \tag{12}$$

- Determining the system matrixes A, B, C and D. The coefficient matrix satisfying linear equations can be obtained through simple derivation.

$$\begin{cases} C = \Gamma_i(1:p, 1:n) \\ \Gamma_i(1:p(k-1), 1:n) A = \Gamma_i(p+1:kp, 1:n) \end{cases} \tag{13}$$

$$U_2^T H_i = U_2^T L_{21} L_{11}^{-1} \tag{14}$$

According to Eq.13, the parameter matrixes A and C can be determined. Then the transcendental linear equations Eq.14 is solved using the least square (LS) to determine parameter matrix B and D. This method for determining system matrix is named as realization approach by Tohru Katayama[6].

Realization of a random system. The noise covariance matrix P and the Kalman gain K are estimated[7, 8].

- Substituting the identification matrix of the system into Eq.1.

$$\begin{bmatrix} \varepsilon_w \\ \varepsilon_v \end{bmatrix} = \begin{bmatrix} \hat{X}(t+1) \\ Y(t) \end{bmatrix} - \begin{bmatrix} A & B \\ C & D \end{bmatrix} \begin{bmatrix} \hat{X}(t) \\ U(t) \end{bmatrix} \tag{15}$$

Thus, the noise covariance matrix in Eq.2 can be estimated, i.e.

$$\begin{bmatrix} Q & S \\ S^T & R \end{bmatrix} = \frac{1}{j} E\left[\begin{pmatrix} \varepsilon_w \\ \varepsilon_v \end{pmatrix} \begin{pmatrix} \varepsilon_w^T & \varepsilon_v^T \end{pmatrix} \right] \tag{16}$$

- Solving the algebraic Riccati equation (ARE) determined by A, C, Q, S and R, the Kalman gain K and the noise covariance matrix P can be attained.

Structure identification of the Hammerstien model

Determination of the static nonlinear model. The static calibration experiment and estimation of the static model parameters will be performed.

Static calibration experiments are on the basis of Xiali 376 engine bench test. Both an EGO sensor and an UEGO sensor are installed in parallel on the exhaust pipe. The output voltages of the two sensors are measured by a MS8050 digital multi-meter, and changes of the excess air coefficient are measured by HORIBA MEXA-700λ air fuel ratio meter. The temperature of the exhaust gas is recorded by a DAS-1B temperature data logging devices.

Based on the static calibration experimental data, iteration is performed using the LS method until the residual square sum (RSS) is 0.07267, so a static nonlinear regression model of the EGO sensor is established.

$$f(\lambda) = -2.5223 - 0.2366\arctan((\lambda - 0.9998) \times 423.8964) + 0.0005(\lambda - 1)T + 11.0764\lambda - 12.3662\lambda^2 + 4.2669\lambda^3 \quad (17)$$

Where, $f(\lambda)$ is the output voltage of the sensor. λ is the excess air coefficient. T is the temperature of the exhaust gas.

Determination of the dynamic linear model. The dynamic calibration experiment and estimation of the model order will be performed.

Dynamic calibration experiment is conducted on a 4GA1 intake port fuel injection engine. The power supply of electromagnetic fuel injectors is suddenly switched off and switched on in a short period of time, leading to a step change of the air-fuel ratio from thin to thick. The steady-state amplitude before and after the engine AFR changes is measured by the AFR meter. The dynamic response signal and trigger signal (injector voltage switch signal) are collected by a digital storage oscilloscope TDS3014B, and sampling frequency is 10 kHz with sampling points of 10000.

In subspace identification, the determination of the order n is arbitrary. Generally, the model order is determined through calculating singular value of the Hankel matrix for the model impulse response. However, in many cases, the input signal may be 'polluted' by noise. Also, the singular value spectral gap of the system is disturbed by noise, causing that abrupt changing of the order is not obvious. Now the model is establish by selecting the dynamic data of the step change of excess air factor λ from 1.092 to 0.865 when the temperature is 694℃. The changing of the singular value of the Hankel matrix resulted from impulse response of the SSM with different orders is shown in Fig.2.

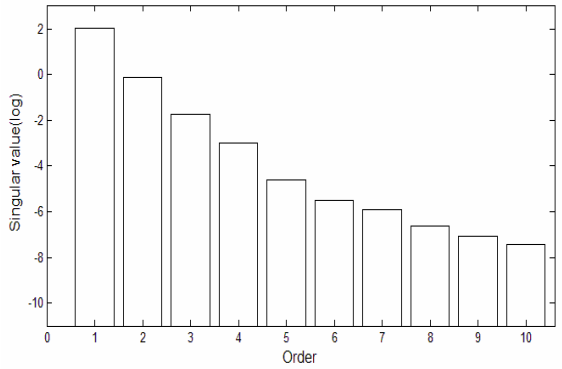


Figure.2 Singular value of MOESP

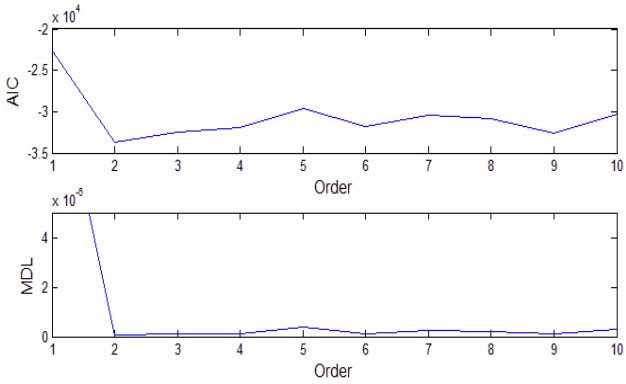


Figure.3 Change of AIC and MDL criterion

It is very difficult to find the mutation point of singular value from the diagram above, and thus the model order can't be decided. To solve this problem, T. Bastogne et al [9] have once estimated the order of the SSM by simulation error criterion, and the minimum error corresponds to the correct model order. Here, the order of the SSM is determined using both the Akaike information criterion (AIC) proposed by Akaike[10] and the minimum description length (MDL) criterion proposed by Rissanen[11].

$$\mathrm{AIC} = N(\log(V(\hat{\theta}_N))) + 2d, \quad \mathrm{MDL} = V(\hat{\theta}_N)\left[1 + \frac{d\ln N}{N}\right] \quad (18)$$

Where, $V(\hat{\theta}_N)$ is the prediction error loss function, d is the number of the parameters, and N is the data length.

The change tendency of AIC and MDL criterion with the model orders is shown in Fig.3. It can be seen that in the simulation of the model order, the AIC and the DML value reach minimum essentially when the model order is 2, accordingly the determined order of the SSM is 2.

Residual analysis of the model. The independence tests for a residual sequence are usually conducted in order to check validity of model structure identification. Especially when the disturbance is coloured noise, the correlation between the residuals and the past inputs also has to be checked. The estimated autocorrelation function $\hat{R}_{\varepsilon}(\tau)$ of model residuals and the estimated cross-correlation function $\hat{R}_{\varepsilon u}(\tau)$ between the residuals and the past inputs u_i as follows:

$$\hat{R}_{\varepsilon}(\tau)=\frac{1}{N-\tau}\sum_{k=1}^{N}\varepsilon(k)\varepsilon(k-\tau)\,,\quad \hat{R}_{\varepsilon u}(\tau)=\frac{1}{N-\tau}\sum_{k=1}^{N}\varepsilon(k)u(k-\tau) \tag{19}$$

A curve of the model verification for the Hammerstein model based on MOESP algorithm is shown in Fig.4. The dashed line in the figure represents a confidence interval whose confidence probability is 99%. When $\tau\to\infty$, the residual autocorrelation function tends to zero, which means there is non-obvious dependence between the current residual value and the future value, also the residuals can be nearly regarded as white noises. While when $\tau>0$, the cross-correlation function is approximately zero, indicating that the residuals are un-correlation to the past inputs, and the model "pick ups" all information from the past inputs. Results of residual analysis reflect rationality of the selected model order from another aspect.

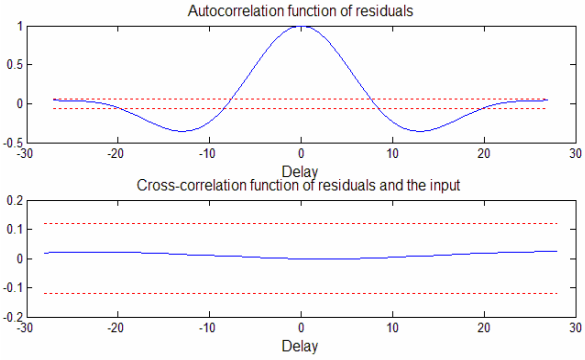


Figure.4 Residuals correlation analysis

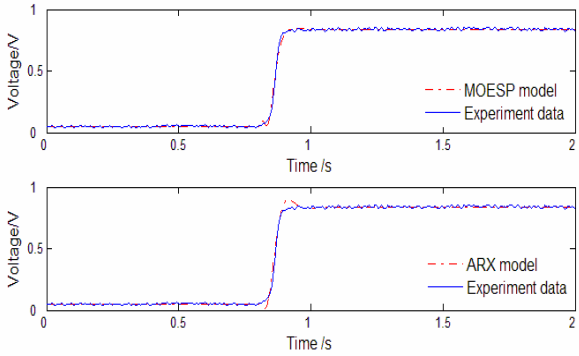


Figure.5 Comparison of the MOESP model with the ARX model

Cross-validation

To determine the robustness of the SSM established in terms of the MOESP algorithm in the Hammerstein model, a two-order ARX model is compared with the SSM by simulation. The test data of the engine tail-gas temperature 496℃ and the excess air factor from 1.21 to 0.86 are used as validation data. The fitting case of the Hammerstein model based on both algorithms is shown in Fig.5. Apparently, the identification output and simulation output of both the MOESP model and ARX model match fairy well with true output of the sensor. But overshoot of the ARX model is larger. To describe quantitatively accuracy of the model simulation, a typical method is to calculate the goodness of fit (η) and mean square error (MSE).

$$\eta=1-\sqrt{\sum_{j=1}^{N}(y_j-\hat{y}_j)^2/\sum_{j=1}^{N}(y_j-\bar{y}_j)^2}\quad,\quad \mathrm{MSE}=\frac{1}{N}\sum_{j=1}^{N}(y_j-\hat{y}_j)^2 \tag{20}$$

Where, y_j and $\hat{y}_j$ represent actual output and calculated model output at the j-th point, respectively. The simulation results of the model based on both algorithms is shown in Table 1 and the estimation accuracy is given for comparison.

Table 1 Comparison of identification and simulation performance index for two algorithms

Algorithm	Goodness of fit (%)		MSE (10^{-4})	
	identification	simulation	identification	simulation
ARX	95.33	93.79	3.28	4.95
MOESP	97.53	95.80	1.84	2.27

It can be seen that fitting effects containing MOESP model, either the identification or the simulation, are better than ARX model. Thus the SSM established on MOESP algorithm reflects more truly dynamic characteristics of the EGO sensor; and it has a strong robustness to some extent.

Identification result of dynamic linear part

Based on MOESP algorithm, final parameters of the SSM in dynamic linear part of the Hammerstein model of the EGO sensor are determined as follows:

$$A=\begin{bmatrix}-29.82 & 1225.7\\ -1.617 & -37.98\end{bmatrix},\quad B=\begin{bmatrix}96.27\\ -6.17\end{bmatrix},\quad C=\begin{bmatrix}-0.5943 & 0.7007\end{bmatrix},\quad D=\begin{bmatrix}0.3259\end{bmatrix}$$

$$K=\begin{bmatrix}-4891.5\\ -1993.4\end{bmatrix},\quad X(0)=\begin{bmatrix}-0.0041\\ 0.00072\end{bmatrix}$$

Summary

1) The AIC and MDL criterion for linear state subspace is used to estimate order of MOESP model, which make up for the shortage of determining model order by singular values of the Hankel matrix. Through the residuals auto-correlation analysis, cross-correlation analysis between the residuals and the inputs, the accuracy of the model structure identification is verified.

2) The identified state space model with two orders based on MOESP algorithm can be extended to nonlinear models like the Hammerstein model in practice. In addition, compared with the ARX model, it more suitable for dynamic linear part of the Hammerstein model of the EGO sensor.

References

[1] M. Verhaegen and D. Westwick: *Identifying MIMO Hammerstein systems in the context of subspace model identification methods*, Internal. J. Control, Vol. 63(1996), p. 331-349.

[2] D. Westwick and M. Verhaegen: *Identification MIMO Wiener systems using subspace model identification methods*, Signal Processing, Vol. 52(1996), p. 235–258.

[3] M. Verhaegen and P. Dewilde: *Subspace model Identification, Part 1: The output-error state-space model identification class of algorithms*, Internal. J. Control, Vol. 56(1992), p. 1187-1210.

[4] M. Verhaegen and P. Dewilde, *Subspace model Identification, Part 2*, J. Control, Vol. 56(1992), p. 1211-1241.

[5] M. Verhaegen: *Identification of the deterministic part of MIMO state space models given in innovation form from input-output data*, Automatica, Vol. 30(1994), p. 61-74.

[6] Tohru Katayama, Giorgio Picci: *Realization of stochastic systems with exogenous inputs and subspace identification methods*, Automatica, Vol. 35(1999), p. 1635-1652.

[7] P. Van Overschee, B. De Moor: *Subspace algorithms for the stochastic identification problem*, Automatica, Vol. 29(1993), p. 649-660.

[8] P. Van Overschee, B. De Moor: *N4SID: Subspace algorithms for the identification of combined deterministic stochastic systems*, Automatica, Vol. 30(1994), p. 75-93.

[9] T. Bastogne, H. Noura, P. Sibille, A. Pichard: *Multivariable identification of a winding process by subspace methods of tension control*, Control Engineering Practice, Vol. 6(1998), p. 1077-1088.

[10] Hirotugu Akaike: *A new look at the statistical model identification*, IEEE Transaction on Automatic Control, Vol. 19(1974), p. 716-723.

[11] A. Barron, J. Rissanen, Bin Yu: *The minimum description length principle in coding and modeling*, IEEE Transactions on Information Theory, Vol. 44(1998), p. 2743- 2746.

© (2012) Trans Tech Publications, Switzerland
doi:10.4028/www.scientific.net/AMM.164.473

Dynamic model of the knife rollers in the spiral cutting machines

Ling-song WANG，Ji-li CHENG ，Dong-ai WANG，Hui-na NI，Yu-chen HAN

Tianjin University of Commerce, Tianjin 300134, China
lswang1023@yahoo.com.cn

Key words: The spiral corrugate cardboard cutting machine，Dynamic simulation，Mathematical modal，Matlab

Abstract： Nowadays, the spiral cutting machines have been widely used in many areas, such as packaging materials. However, the theoretical researches of that are very rare in academia. On the one hand, the machines' technological principles are the commercial secrets. On the other hand, developing manufacturing of the machines has no theoretical basis. So, in a word, it's blank in academia about the spiral cutting machines. In this article, we did quantitative analysis on the part of spiral knife roller and blade, and also set up a modal by describing that in a mathematical way. In addition, we analyzed spiral knife dynamically establishing equations of blade, ground point, roller as well, and finally realized dynamic simulation of the spiral knife by matlab tool. What's the most special feature of this simulation is that it can do simulations for different parameters. The simulation is convenient for deepening theoretical researches, optimizing parameter selections and being auxiliary tools of design.

Introduction

The spiral corrugate cardboard cutting machine is the key cutting equipment appearing in recent years, and it is widely used in the corrugate cardboard product line. Because of the advantages ,such as significantly reducing the shear force, more flexible starting/braking for the knife roller size is relatively small , substantially improving the quality of shear, the equipment gets fast application.

Recently years, rapid economic growth leads to a high requirement of corrugate cardboard packages. As the production speed, width and wrapping paper plate weight of the high speed corrugate cardboard product line are constantly refreshing, the traditional straight blade cutting machine has to increase the size of the knife roller to improve the shear force, but it will make the starting/braking inflexible and consume a lot of power.[1] These dramatically disadvantages cannot meet the production needs and suffer to be eliminated. But to a certain extant the spiral cutting machine can overcome the shortages above. So it get widely application.

1.Principle and advantage of spiral cutting machine

Corrugate cardboard cutting machine is the special equipment used on corrugate cutting machine product line. It cuts the Corrugate cardboard into certain length single cardboard which can used to assemble the product box.

The traditional straight blade cutting machine principle is: use a pair of upper and lower knife roller surface cutting edge which parallel with the mother line relative-rotation cut the cardboard into a certain length. So when cutting the board, the entire blade contact with the board at the same time, that is the "line contact", which needs a large shear force. Since the cardboard is in the state of moving forward continuously and there is an immediate relative movement between tape and cutting edge, the quality of the board edge can't be guaranteed. So the traditional cutting machine can't adjust to the high speed product any longer.

Show as fig.1. The principle of spiral cutting machine is:
Change the straight blade edge of upper and lower knife rollers into a pair of left and right oblique spiral blade edge. When the cardboard moves through the blade edges with high speed, under the cooperation control of velocity measurement device and PLC, according to the prior input

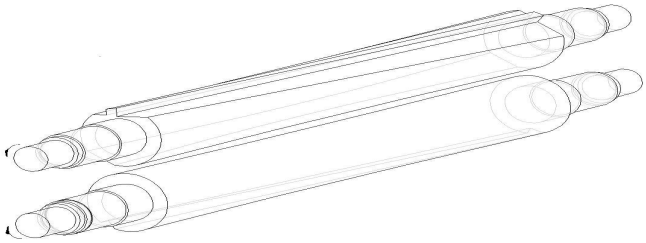


Fig.1: Diagram of the spiral cutting drum

requirement of cutting length, we control system to start the knife drum servo motor timely, making a pair of blade edge of the helical blade with small spiral angle θ reverse rotation (θ is the angle between the knife roller blade spiral direction and bus of the point direction). After nearly half-circle acceleration, in the center plane of the upper and lower knife rollers, the upper and lower knife roller blade will enter the cross-cutting state with equal angular velocity and constitute a hinge shear force on exactly position where cardboard requires to cut. The point always moves along the axis of the knife roller center plane, cutting the cardboard from one side to the other side in the minute. The motor enters the braking state immediately under the control of servo after the board was cut. Nearly a half-circle braking process of the knife roller makes the blade first plunge edge stop at the exactly position of upper and lower tip, waiting for next shear. Repeat as above process. 【2】【3】

From above principle we can see, this kind of cutting machine cuts the cardboard with *point contact* way. There is no doubt it can significantly reduce the cutting resistance. Due to the smaller cutting resistance, the size of knife roller can be reduced, and the shaft can be made into a holly type. Besides, as a result of the obviously reduction of inertia, start/braking becomes flexible , also the torque reduces significantly . Compared with the same breathed size straight blade, the spiral cutting machine motor can save nearly 40% power. Being suitable for large breadth cardboard cutting is another advantage of the spiral cutting machine. According to above principle. We can see that the technology can meet the energy-saving and emission reduction production requirement in today's society.

under the spiral cutting mode, in order to realize the dynamic cutting state, the value of velocity component in board movement direction must equal to the value of speed in forward direction, but their directions are opposite. This will cut the edge vertical to the cardboard edge.(show as fig.2 Composition of velocities). The accomplished method is: when we install the cutting machine, let the knife roller axis direction remain (90-θ)degree with the cardboard edge, the rotation direction can be decided according to the fig.2.

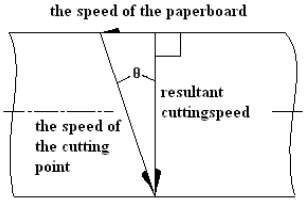


Fig.2: Composition of velocities

2.Spiral cutting machine knife roller dynamic simulation mathematical modeling

These operating principles described above have shown many advantages and promotion value of the cutting way. But many machinery manufacturing enterprises usually import drawings from foreign countries. The depth of the study on the theory is not enough. For example, what size spiral angel should be taken? How to optimize the diameter parameter of the outside and internal circle? So many problems lack researches. Taking into account the above factors, the author conducted a study on the theory of spiral cutting, and do the dynamic simulation depending on mathematical theories. This paper describes the theory to conduct industry designers to do theoretical study , understand and design parameters . 【4】【5】

2.1 Knife roller static mathematical model

There are four parameters for spiral knife roller certain system: roller length *L*, roller radius *R*, blade spiral angel θ, rotation angular velocity ω. If analyze static model first, we can ignore the rotation angular velocity temporally. So there are only their parameter in the static system L,R,θ . 【6】

According to the actual situation, we regard the roller length direction as the spatial coordinate system X orientation. Regard the output and input direction as the spatial coordinate system Y orientation. Setting the zero point on the center plane of the two knife roller. Show as the fig.3：

Under the space and parameters described above ,the study on the model of knife roller can be divided into two parts: the static model of the roller

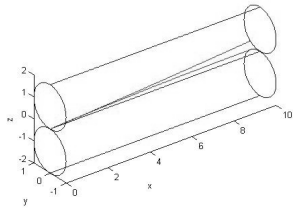


Fig.3

$$\begin{cases} upper\begin{cases} x = L\cdot k \\ y_1^{\,2}+(z_1-R)^2=R^2 \end{cases} \\ lower\begin{cases} x = L\cdot k \\ y_2^{\,2}+(z_2+R)^2=R^2 \end{cases} \end{cases} \quad k\in[0,1]$$

If *k* belongs to the system ,the independent variable ranges from 0 to 1. L, R, a are system parameters. Upper roller is described by (x, y_1, z_1). Lower roller is described by (x, y_2, z_2).

Spiral blade mathematical model is described as follow:

k belongs to the system variable range from 0 to 1. L, R, a are system parameters. Upper roller is described by (x, y_1, z_1). Lower roller is described by (x, y_2, z_2)

$$blade\begin{cases} upper\begin{cases} x = L\cdot k \\ y1 = \sin\left(\frac{\tan(a)\cdot L\cdot k}{2\cdot\pi\cdot R}\right)\cdot R \\ z1 = R-\cos\left(\frac{\tan(a)\cdot L\cdot k}{2\cdot\pi\cdot R}\right)\cdot R \end{cases} \\ lower\begin{cases} x = L\cdot k \\ y2 = y1 = \sin\left(\frac{\tan(a)\cdot L\cdot k}{2\cdot\pi\cdot R}\right)\cdot R \\ z2 = -z1 = \cos\left(\frac{\tan(a)\cdot L\cdot k}{2\cdot\pi\cdot R}\right)\cdot R - R \end{cases} \end{cases}$$
$$k\in[0,1]$$

Basing on the above model, the author used *matlab* program generating two views from two different perspectives . Show as fig.4

2.2Knife roller dynamic mathematical model

There are four parameters for spiral knife roller certain system: roller length L, roller radius R, blade spiral angel θ, rotation angular velocity ω. Dynamic parameters are L, R, a, ω, t . t is the time of movement. The motion equation of spiral blade is below:

If researchers only want to study the static state of roller, they could use the model of knife roller and blade as above. If they need to study the dynamic situation or combine the hinge point movement situation, they could use the latter model. [7] [8]

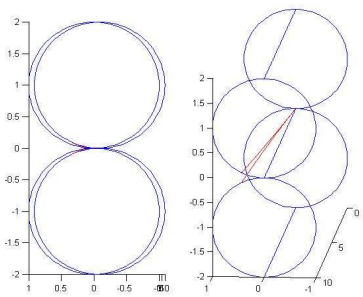


Fig.4: Simulation tip view

$$\begin{cases} upper \begin{cases} x = L \cdot k \\ y1 = \sin\left(\frac{\tan(a) \cdot L \cdot k}{2 \cdot \pi \cdot R} - \omega \cdot t\right) \cdot R \\ z1 = R - \cos\left(\frac{\tan(a) \cdot L \cdot k}{2 \cdot \pi \cdot R} - \omega \cdot t\right) \cdot R \end{cases} \\ lower \begin{cases} x = L \cdot k \\ y2 = y1 = \sin\left(\frac{\tan(a) \cdot L \cdot k}{2 \cdot \pi \cdot R} - \omega \cdot t\right) \cdot R \\ z2 = -z1 = \cos\left(\frac{\tan(a) \cdot L \cdot k}{2 \cdot \pi \cdot R} - \omega \cdot t\right) \cdot R - R \end{cases} \end{cases}$$

$$k \in [0,1],\ t \in [0,+\infty]$$

Motion equation of hinge point:

$$hinge \begin{cases} x = \frac{1}{\omega} \cdot \frac{L \cdot \tan(a)}{2 \cdot \pi \cdot R} \cdot t \\ y = 0 \cdot t \\ z = 0 \cdot t \end{cases}$$

2.3 Simulation model

Apply the matlab software to design the program. Use the matlab gui to conduct the interface design of graphic simulation control, and ultimately realize the simulation presentation. The length and radius of spiral blade, spiral angel of blade ,as well as shear velocity are the input parameters for demonstrating. Designers can use the options of drop-box to control the presentation. When checking the static state, you can chose static spiral item and input parameters. After you clicking presentation, it will show the drawings automatically. When you want to see working state of the spiral blade, you need to chose the spiral knife first, and input the parameters, then click presentation, it will perform directly. Show as fig.5

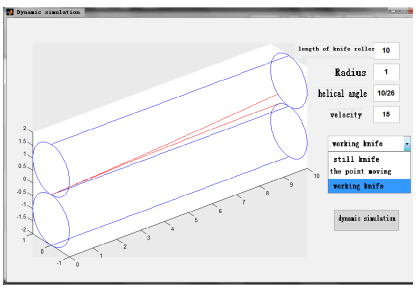


Fig.5: Simulation animation parameter

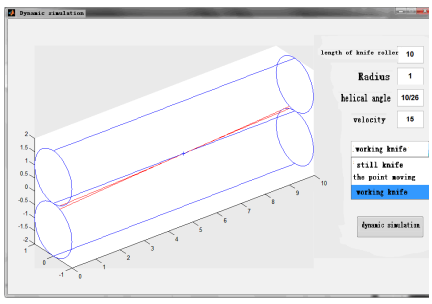


Fig.6: Simulation animation interface

When you want to check the dynamic state of the shear point, you can chose the hinge point dynamic first, and input parameter, then click the simulation. After that, it carries out easily. Show as fig.6

3.Conclusion

Based on the model above, the author not only founded the static model graphic of knife roller, but also simulated the rotation of knife roller and dynamic regulation of hinge point, in a way of matlab programming . This method can simulate rotation of knife roller and dynamic of hinge point. At the same time, it can perform presentation. So it can be the important secondary efficient simulation tools for studying the spiral corrugate cardboard cutting machine and make the dynamic research more intuitive.

Tianjin natural science fund projects (0JCYBJC06100)

Brief introduction of the author

WANG Ling-song：male, associate professor of the Department of Mechanical Engineering ,Tianjin University of Commerce，born in Octobor,1955，Major research areas: structure design of mechanical engineering，optimizing structure design of machines and packages ,and so on.

Telephone: 13132008603, Postcode：300134, E-mail: lswang1023@yahoo.com.cn

References

[1] Tang Shanhua，Corrugated cardboard cutting machine without the key link design[J],packaging engineering, 2007, 28（03）. 93-94

[2] Wang Zetian，Corrugated line in the design of the cutting machine and discussion, paper making in Shanghai, 1989：Z1. 113-115

[3] Ge Fei，Xie Xiaoxin，Hou Xifang，Corrugated production line LXDNHQ-1800 Spiral knife cutting machine development [J]， Zhengzhou university journal (Engineering version) 2004：25，

[4] Xin Shoumin，Wang Shi，Wu Shengmin, 1500 Cutting machine of gilead and commissioning of the development [J]，Non-ferrous equipment, 1988：S1.14-17

[5] He Hongse，Li Mian，Direct transmission corrugated cardboard cutting machine [J]，China packaging industry, 1997, 02, 26-26

[6] Han Tiwen，Wei Zeding，Corrugated paper cutting machine control system modeling[J],package engineering, 2009, 06 , 27-28

[7] Liu Weicheng, Corrugated cardboard cutting machine realization of computer transformation an efficient way [J], Hunan packaging , 1996,04,17-18

[8] Huang Mi, Wu Shufang, Du Qixiang , EBE stare blankly corrugated cardboard cushioning curve research [J], packaging engineering, 2011, 13, 19-20

© (2012) Trans Tech Publications, Switzerland
doi:10.4028/www.scientific.net/AMM.164.478

Photochromism,Fluorescence and Dynamic system of a Novel Unsymmetrical Diarylethene Material Based on Naphthyl rings

Panpan Ren, Min Deng, Shiqiang Cui, Gang Liu*

Jiangxi Key Laboratory of Organic Chemistry, Jiangxi Science and Technology Normal University, Nanchang 330013, P. R. China

liugang0926@163.com

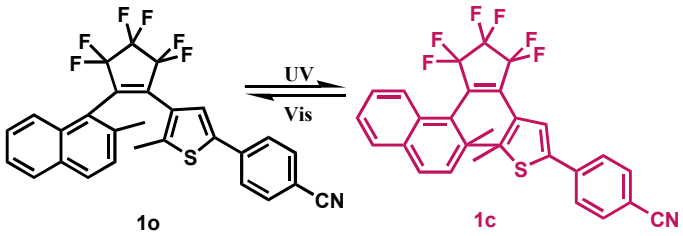
Keywords: diarylethene, cyclization, cyanophenyl, Photochromic, Fluorescence

Abstract. A new photochromic diarylethene compound, 1-[(2-methyl-5-(4-cyanophenyl)-3-thienyl)] -2- (2-methylnaphthlen-1-ly) perfluorocyclopentene (1o), was synthesized. Its properties, including photochromism, fluorescence and kinetics properties optical storage propertieswere investigated in detail both in solution and PMMA amorphous film. It underwent reversible cyclization and cycloreversion reactions upon alternating irradiation with UV and visible light in hexane.

Introduction

Photochromism is referred to as a photoinduced reversible transformation between two isomers having different absorption spectra [1]. Photochromic compounds have attracted much attention because of their potential applicability to photonics devices, such as rewritable optical memory media [2]and optical switches. Up to date, photochromic compounds, such as spirobenzopyrans, azobenzene [3], fulgides [4], and diarylethenes, have been extensively investigated for their potential applications in erasable optical recording, color displays, and photoswitches. Diarylethenes bearing terminal phenyl groups have raised considerable interest in the last few years because the properties of the phenyl-substituted diarylethene derivatives can be further modified by suitable functionalization of the aromatic rings with electron-donating groups or electron-withdrawing groups [5-7]. The diarylethene bearing naphthyl rings possesses excellent thermal stability, where the absorption intensity of its closed-ring isomer remains relatively constant for more than 500 h even at 343 K [8].

In this study, we synthesized a new unsymmetrical photochromic diraylethene 1-[(2-methyl-5-(4-cyanophenyl)-3-thienyl)]-2-(2-methylnaphthlen-1-ly)perfluorocyclopentene (1o), Its photochromic reactivity , fluorescence were investigated in detail. The photochromic reaction of diarylethene 1o is shown in Scheme 1.

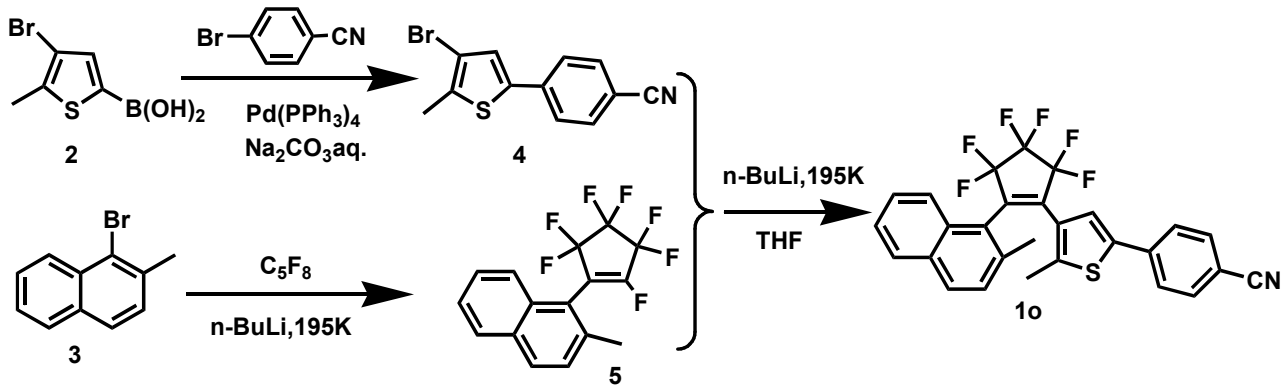


Scheme 1. Photochromism of diarylethene 1o.

Experiments

Synthesis of diarylethene 1o. The diarylethene 1o of synthetic route is shown in Scheme 2. It was synthesized according to the similar procedure of Pu [9]et al. Suzuki coupling of the bromobenzene derivative with a thiophene boronic acid 2 gave the compounds 4. Then, compound 3 was lithiated and coupled with perfluorocyclopentene to give mono-substituted perfluorocyclopentene derivatives 5. Finally, 1-bromo-2-methylnaphthalene was lithiated and then coupled with compounds 4 to give the unsymmetrical diarylethene derivative 1o. The structures of diarylethenes 1o were confirmed by

^{1}H NMR. ^{1}H NMR (400 MHz, $CDCl_3$, TMS):δ 2.22 (s, 3H, -CH_3), 2.38 (s, 3H, -CH_3), 6.95 (s, 1H, thienyl-H),7.47(t,1H,nathphy-H),7.49(t,1H,nathphy-H),7.52(t,1H,nathphy-H),7.54(t,1H,nathphy-H) ,7.55(t,1H,nathphy-H),7.60(t,1H,nathphy-H),7.69 (d, 1H, phenyl-H, J=8.0Hz), 7.72 (d,1H,phenyl-H, J = 8.0Hz), 7.77 (d, 1H, phenyl-H). 7.80 (d, 1H, phenyl-H).



Scheme 2. Synthetic route for the compound 1o.

Results and discussion

Photochromism of diarylethene 1o. Fig. 1 shows the absorption spectral changes of 1o in hexane (C =2.0 × 10^{-5} mol/L, Fig. 1A) and in poly methyl methacrylate (PMMA) film (10% w/w, Fig. 1B) by photoirradiation. In hexane, as shown in Fig.1a, diarylethene 1o has the absorption maximum at 311 nm (ε =2.9 × 10^4 L mol^{-1} cm^{-1}). Upon irradiation with 297 nm light, the colorless solution of 1o turned Crimson, in which absorption band was observed at 518 nm (ε = 7.4× 10^3 L mol^{-1} cm^{-1}). The Crimson color is due to the closed ring form 1c. The color disappeared by irradiation with visible light. Similar spectrum change of diarylethene 1o was observed in PMMA film (Fig. 1B). Upon irradiation with 297 nm UV light, the colorless PMMA film turned Crimson with new broad absorption band centered at 527 nm for diarylethene 1o, which assigned to the open-ring isomer 1o changed to the closed-ring isomer 1c. The red shift of the ring-closed form of diarylethene 1o in PMMA film in comparison with that in hexane solution can be ascribed to the stabilization of molecular arrangement in solid state.

Fig. 2 showed the color changes of diarylethene 1o both in solution and PMMA amorphous film. From Fig. 2, it can be easily seen that the two isomers have distinguishable colors attributed to different-conjugation and they can be reversible changed each other by alternating irradiation with UV and visible light. Therefore, there exists enough high contrast between the two isomers, which are promising candidates for rewritable photon-mode optical memory media.

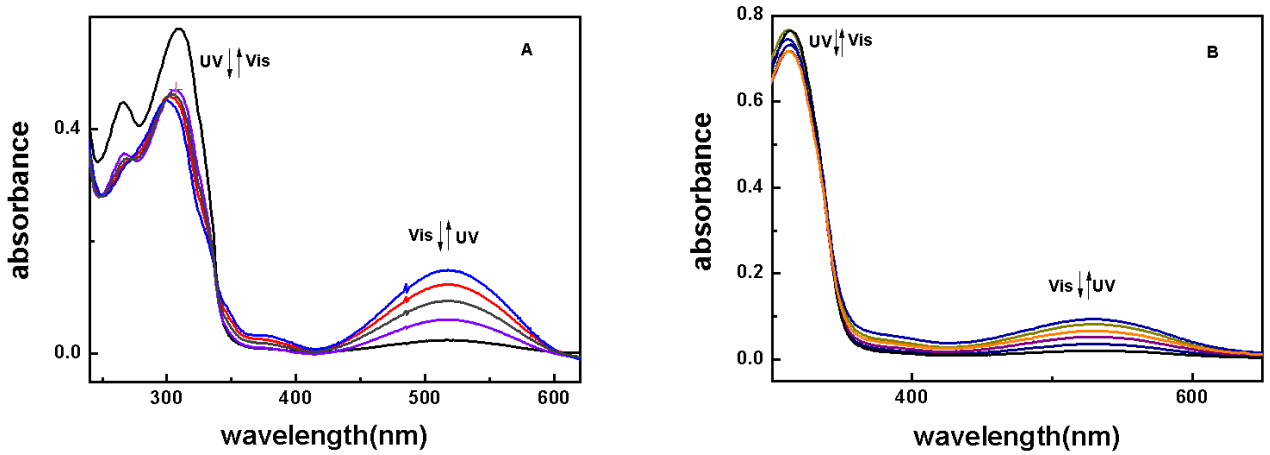


Fig. 1 Absorption spectral changes of diarylethene 1o both in hexane and in PMMA film at room temperature: (A) in hexane (c=2.0×10^{-5} mol L^{-1}); (B) in PMMA film (10%, w/w).



Fig.2 Colour changes of compound 1o in hexane (2.0×10^{-5} mol L^{-1}) and in PMMA

Fluorescence of diarylethene 1o The fluorescence properties in the hexane of the title compound ($C = 1.0 \times 10^{-4}$ mol/L) were measured using a Hitachi F-4500 spectrophotometer, and the breadths of excitation and emission slit were selected 10.0 nm. The hexane of diarylethene 1o exhibited relatively strong fluorescence at 391 nm when excited at 314 nm. The Stokes shift of the fluorescence was relatively large and the fluorescence spectral edge showed a blue-shift in comparison with the absorption edge. Fig. 3 shows the emission intensity changes of diarylethene 1o during the process of photoisomerization in PMMA film. Upon irradiation with 314 nm light at room temperature, the emission intensity of compound 1o decreased remarkably along with the photoisomerization from open-ring isomers to closed-ring isomers when excited at 300 nm. The incomplete cyclization reaction and the existence of parallel conformation of diarylethenes 1o may be the main cause for the moderate change in fluorescence induced by photoirradiation [10]. The back irradiation by appropriate wavelength visible light regenerated its open-ring isomer and recovered the original emission intensity. This merit can be potentially applied to optical memory with fluorescence readout method [11].

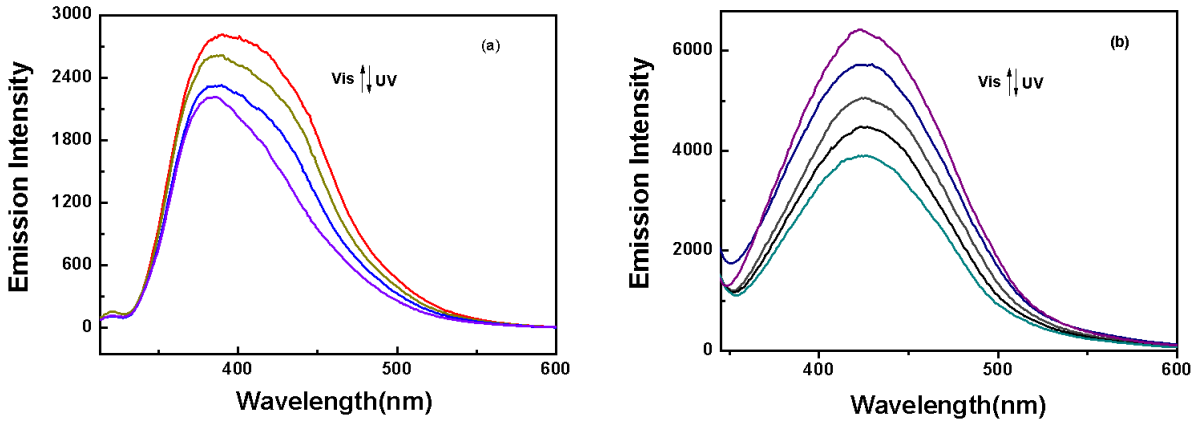


Fig. 3 Emission intensity changes of diarylethenes 1 both in hexane (2.0×10^{-5}mol L^{-1}) and in PMMA film (10%, w/w)

Photochromic reaction kinetics in hexane solution. The photochromic cyclization/ cycloreversion kinetics of 1o in hexane were determined by UV-Vis spectra upon alternating irradiation with appropriate wavelength UV and visible light at room temperature. The cyclization and cycloreversion curves of 1o were shown in Fig. 4, respectively. It can be seen that the relationships between the absorbance and exposal time have good linearity upon irradiation with 297 nm UV light suggesting that the cyclization processes of 1o belong to the zeroth order reaction when open-ring isomers changed to closed-ring isomers. The slope of the line in Fig. 4 represents the reaction rate constant (k) of diarylethenes 1o in hexane. So the k of cyclization process (ko-c, 10^{-3}) of diarylethenes 1o can be easily obtained, which is $2.4s^{-1}$.The cyclization (A) and cycloreversion (B) kinetics of compound 1o in hexane. As shown in Fig. 4, during the cycloreversion of 1o, the relationship between –log(Abs) and exposal time also behave perfect linearity, indicating that the cycloreversion process belong to the first order reaction. The k of cycloreversion (kc-o, 10^{-3}) process of diarylethenes 1c can be easily obtained, which is 14.3 s^{-1}.

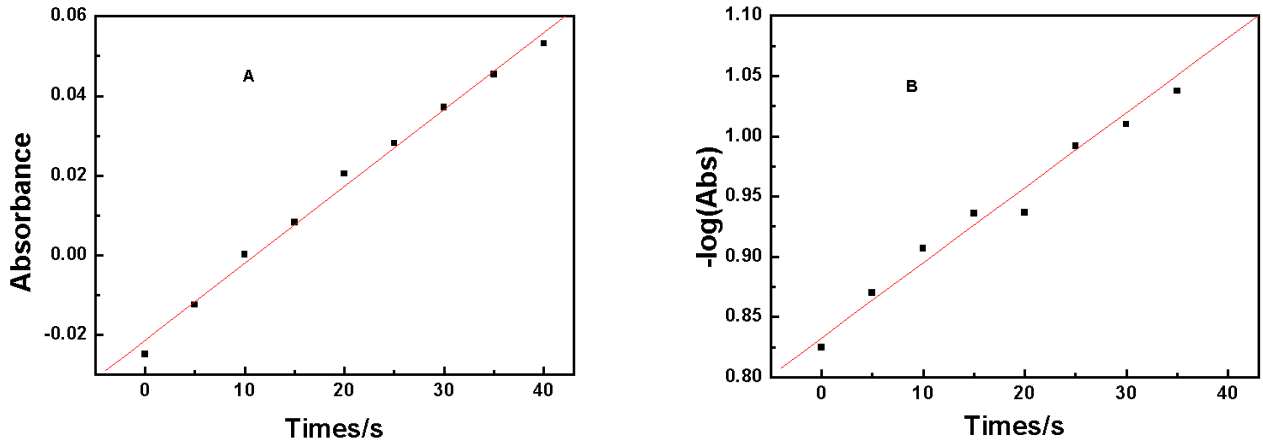


Fig. 4 The kinetics of compound 1o in hexane: (A) cyclization; (B) cycloreversion..

Summary

A new photochromic diarylethene 1o was developed and its photochromic and fluorescent properties were investigated. The compound exhibited good reversible photochromism both in solution and in PMMA amorphous film. Moreover, it also exhibited remarkable fluorescence switching in the solid state. When diarylethene 1o/PMMA used as recording medium, optical recording experiment was carried out successfully and the results demonstrated that it had attractive properties for high capacity data storage.

Acknowledgment

This work was supported by the Project of Natural Science Foundation of Jiangxi Province(2010DQ00200) and the Science Funds of Jiangxi Education Office (GJJ1067).

References

[1] M. Irie: Chem. Rev Vol. 100(2000), p. 1685–1716
[2] M. Morimoto and M. Irie: Chem. Commun Vol. 2005(2005), p. 3895–3905
[3] N. Tanifuji, K. Matsuda and M. Irie: Org. Lett Vol. 7(2005), p. 3777–3780
[4] S.Z. Pu,W.J. Miao, S.Q. Cui, G. Liu and W.J. Liu: Dyes and Pigments Vol. 87(2010), p. 257-67
[5] S.Z. Pu, J.K. Xu, L. Shen, Q. Xiao, T.S. Yang and G. Liu: Tetrahedron Lett Vol. 46(2005), p. 871–875
[6] A. J. Myles and N. R. Branda: J. Am. Chem. Soc. Vol.123(2001), p. 177–178
[7] K. Uchida , T. Matsuoka , S. Kobatake , T. Yamaguchi and M. Irie: Tetrahedron Vol. 57(2001) p. 4559-65
[8] N. Tanaka, C. Okabe, K. Sakota and M. Irie: J. Mol. Struct Vol. 616(2002), p. 113–118
[9] G. Li, T. Zheng, S. Z. Pu, and J. K. Xu: Acta Cryst. E Vol. 62 (2006) p. o2877
[10] C. B. Fan, S. Z. Pu, G. Liu and T. S. Yang: J. Photoch. Photobiol. A: Chemistry Vol. 194(2008), p. 333–343
[11] Tyler B. Norsten and Neil R. Branda: J. Am. Chem. Soc. Vol. 123(2001), p. 1784–1785

© (2012) Trans Tech Publications, Switzerland
doi:10.4028/www.scientific.net/AMM.164.482

Study on optimal circulation dynamic system and feasibility analysis for a solar biogas digester

You Zhang[a], Changsheng Peng[b,*] and Fengmin Li[c]

The Key Lab of Marine Environmental Science and Ecology, Ministry of Education, Ocean University of China, Qingdao, 266100, China

[a]zhangyou417@163.com, [b]cspeng@ouc.edu.cn, [c]lfm01@ouc.edu.cn

[*] Corresponding author. Tel.: +86 532 66782011; fax: +86 532 66782011.
E-mail address: cspeng@ouc.edu.cn (C. Peng).

Keywords: Solar biogas digester; Circulation dynamic system; Dissipation model; Feasibility analysis

Abstract. According to biogas digester heated by circulation of water heated by solar cell, three modes of hot water circulation dynamic system (one-stage cycle, multi-stage cycle, and continuous cycle) were proposed to reduce operating costs and optimize the operation. The results obtained showed that multi-stage cycle had a clear advantage in improving operating efficiency, the heat transfer of which was 41.57KJ, much higher than 7.21KJ of one-stage cycle and 2.20KJ of continuous cycle. A model was built to simulate the overall process of heat dissipation in comparison with what was obtained from the conventional experiments. Both the simulation and the experimental measurement data showed that multi-stage circulation dynamic system operated well.

Introduction

Biogas is known as a clean energy source that provides an effective way to solve energy crisis. During the biogas production, fermenting materials will be transformed into biogas manure, which is a new way for harmless and resourceful realization. Although biogas is commercially considered as competitive energy source, the utilizing of such technology is not common in north of china. This is mainly because of the low temperature in winter that can't meet the requirement of biogas fermentation. It was shown that biogas fermentation could be better operated when digester temperature is higher than 15℃, at which the gas production rate is 0.1-0.2 $m^3/(m^3 \cdot d)$ [1].

Due to the advantages of renewable and environmental protection, solar has been introduced in biogas engineering. Aiming at improving the fermentation efficiency in winter, some solar heating methods have been proposed. Among them, warming by heated water circulating is considered a mature technology [2-4]. For high operation cost and expensive investment, this technology developed slowly though it is feasible. The aim of this work was to evaluate the performance of biogas digester working under three modes of heated water circulation dynamic system.

Materials and methods

Experimental working ambient. This present test was carried out in Nansihu Lake Water Special Project (Xiwan Village, Shandong Province, China) during October, 2011. The mean temperature was 15.1℃ under total sunshine time of 219.6h and solar radiation intensity of 8.696kcal/cm^2 [5]. The measurements of the daily mean temperatures are showed in Fig. 1. Notice that, the 1st, 2nd, 3rd, 15th, 16th, 17th, 18th, 19th, 25th, 29th, and 30th are clear days. However, the 10th, 11th, 12th, 13th, 22nd, 23rd, and 28th are rainy days, the rest are cloudy days. From the presented map it can be seen that the efficiency of solar water heater was significantly affected by the weather and long-term rainy weather would result in a lower circulating water temperature than the expected value.

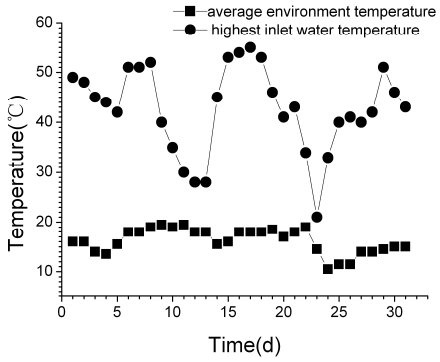


Fig. 1. Daily average temperature and highest inlet water temperature during Oct.

Digest unit. Digest equipment is showed in Fig. 2. Haier solar water heater was used. The properties of solar cell were as follows (length 1.8m, pipe diameter 58mm, pipe number 16, aperture area 2.07m^2, and volume of storage tank 200L). Circulating pump (Qunxiang JET35-1.1 single-way jet self-priming pump) was selected with suction force 1.5m^3/h, power 1.1kw. Temperature controlled meter used Jinghui XMTD-2002 digital display regulator, ranging form -50 to 150 °C. The biogas digester was ellipsoidal hydraulic organic-fiberglass biogas digester (2.4m×2.3m) provided with heat exchanger made of aluminum alloy radiator about 5L.

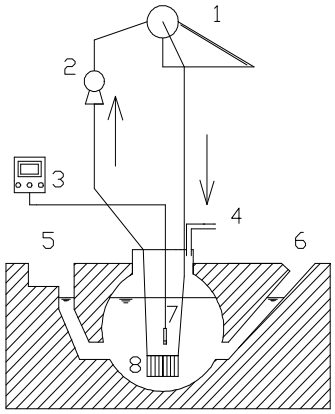


Fig. 2. Schematic diagram of the biogas digester (1) Solar water heater, (2) Pump, (3) Temperature-controlled meter, (4) Air outlet pipe, (5) Hydraulic pool, (6) Feed inlet, (7) Temperature sensor, and (8) Heat exchanger.

Circulation dynamic system. Three different water circulating modes were proposed for improving the performance including (a) one-stage cycle, before sunset (18:00 pm) water was heated by solar to the hottest, then all the water was continuously circulated to heat the biogas digester, (b) multi-stage cycle in which the heated water was circulated with 5 minute intervals about 5L water each time, and (c) continuous cycle in which the water circulated as soon as the solar cell operated in the morning. Every day at 9:00 AM, new water was injected into solar water heater to be heated. The circulation flow rate was controlled at 7L/min, while initial pool temperature was set to be 20 °C. Some parameters of the three modes are list in Table 1.

Table 1. Daily parameters of three different modes

	Solar-warming duration	Water-flowing duration	Pump-working duration	Circulating water flow	Transfering duration
One-stage cycle	9h	26m20s	8min	200L	26m20s
Multi-stage cycle	9h	26m20s	8min	200L	200min
Continuous cycle	9h	9h	151min12s	3780L	9h

Evaluation method. The heat dissipation between inlet and outlet pipe can be ignored, as they are both immersed in the biogas digester. According the conservation of energy law, the total heat absorbed by biogas digester will be calculated through the following equations:

$$Q = Cm\Delta T \quad (1)$$

Where C is the specific heat capacity of water, m the mass of circulating water, ΔT the different value between average temperature of inlet and outlet pipe each day.

The operating efficiency was evaluated through heat absorption by the biogas digester when pump consumed one unit of energy.

Results and discussion

The variation of inlet and outlet temperature. Figure 3 shows the daily average inflow-outflow temperature of three circulation modes. It can be seen that the outlet water temperature fluctuates with the inlet water. Notice that, the inlet water temperature was affected by the weather and air temperatures. when the inlet water temperature was low and differed slightly with the ambient temperature, the difference value between inflow-outflow temperatures was not significant, and the biogas digester got a less amounts of heat. It can be concluded that rainy weather restricts the operating efficiency. Through paralleling contrast, it can be also seen that the temperature difference between mode (a) and mode (c) was very small. Most of the heat was lost in water recycling tank or in external ambient, which resulted in low transfer efficiency. While in mode (b), temperature difference was obviously higher. According to the conservation of energy law, through mode (b) the biogas digester can obtain more heat.

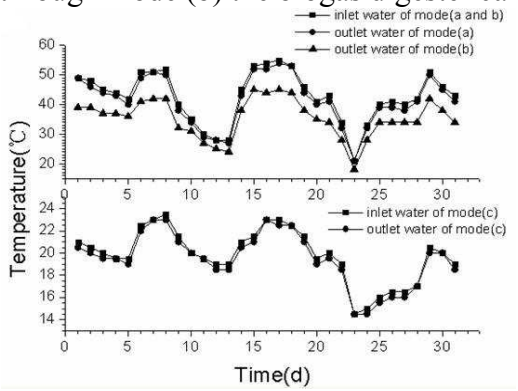


Fig. 3. The daily average inlet and outlet water temperature for the three modes

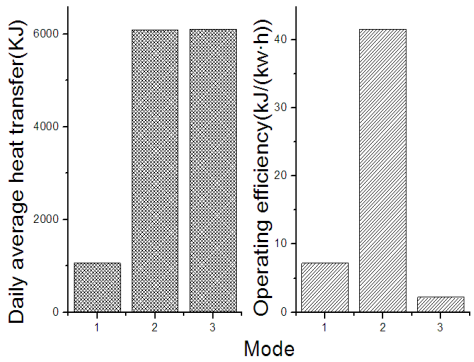


Fig. 4. The daily average heat transfer and the efficiency for the three modes

The capacity of heat transmission and operating efficiency. As seen in Figure 4, the total daily heat transfer quantities for the three modes are 1057kJ, 6097kJ, and 6112kJ respectively. Mode (b and c) transmitted an equivalent heat, whereas in mode (a) the heat transmit was more less. This is may be due to the period of heat transfer in mode (b and c) are longer than mode (a), where the biogas digester can absorb more. However, mode (c) consumed more energy. Daily pump energy consumption for the three modes are 0.147kw·h, 0.147kw·h and 2.772kw·h respectively. If the heat absorption when pump consumed one unit of energy can be represented for operating efficiency, the operating efficiency of the three modes are 7.21kJ/(kw·h), 41.57kJ/(kw·h) and 2.20kJ/(kw·h). Mode (b) has an obvious advantage in economically and effectively operating.

Dissipation model and feasibility analysis. Due to the biogas digester using the same fermenting materials and the microorganism living in the same growth environment, the biological heat of anaerobic fermentation was the same. This part can be ignored to simulate the process conveniently, according to the actual situation which suggested as follows:

(1) In general, the daily change of soil temperature become very small about 0.8-1.0 m beneath the surface, so the heat dissipation model of biogas digester can be seen as a hemisphere, radius of which is 1.175m (the temperature of the hyposphere is constant, so only the episphere dissipated heat), thickness of which is 0.007m. Accordingly, we can suppose the main part of the digester encapsulated by soil which thickness is 1.175m.

(2) The fomenter temperature is uniform and stable, it can be seen as a global.

The total thermal conductivity of multilayer even wall can be calculated from the equations:

$$K = \frac{1}{\frac{1}{h_1} + \sum_{i=1}^{n} \frac{\delta_i}{\lambda_i} + \frac{1}{h_2}} = \frac{1}{\frac{1}{h_1} + \frac{\delta_1}{\lambda_1} + \frac{\delta_2}{\lambda_2} + \frac{1}{h_2}} \quad (2)$$

Where K is total thermal conductivity of multilayer even wall, h_1 heat transfer coefficient of internal convection in biogas digester, h_1=1800w/(m^2·℃) [6], h_2 heat transfer coefficient between soil and surroundings, h_2=11.63w/(m^2·℃) [7], λ_i thermal conductivity (In general, thermal conductivity of soil varies from 1.0 to 2.4w/(m·℃), here taking value of 1.7w/(m·℃), thermal conductivity of fiberglass is 0.4w/(m·℃)), δ_i thickness of each layer.

Through the obtained calculating, K=1.258 w/ (m·℃). The optimum biogas fermentation temperature is over 20℃, which can be set as simulation value, while the mean temperature is 15℃ in October. So that, the heat loss power of biogas digester is $Q_0=KS\Delta T/\delta_2$=46.4w. The daily energy consumed for keeping the main part of digester 20℃ is $Q_1=3600\times24\times Q_0=4.0\times10^6$J, this value is less than the power that obtained in mode (b) 6.1×10^6J. So the multi-stage circulation dynamic system is able to work in October.

Figure 5 shows the comparison of biogas digester temperature in mode (b) and in the blank. The mean monthly temperature of test group was 20.4℃, whereas the parallel blank was 17.1℃. It can be seen that, the temperature was affected by weather and air temperature. Also, the test group shows more obvious advantage and fits well with the simulation data. Both the simulation and practical operation show that multi-stage circulation dynamic system (mode b) is an economic effective method.

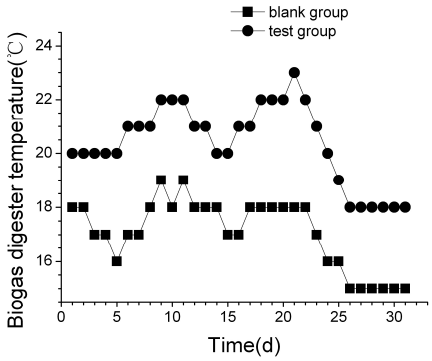


Fig. 5. Biogas digester temperature of blank and optimized test (mode b)

Conclusions

Three different heated water circulation dynamic systems (a) one-stage cycle, (b) multi-stage cycle, and (c) continuous cycle for biogas digester were proposed. The water was heated using a solar cell. Based on results obtained from the practical and simulation tests, the following conclusions can be drawn:

(1) Long-term rainy weather markedly affected the efficiency of solar water heating system. Low temperature can decrease the efficiency of heat transfer and the biogas digester can not receive the expected heat.

(2) Based on the efficiency of heat transfer and total costs, multi-stage circulation dynamic system has a comparatively much more advantage.

(3) According to the results obtained from the practical experiments and heat dissipation model for the biogas digester, the multi-stage circulation dynamic system was found to be more efficient.

Acknowledgements

This work was supported by the Cultivation Fund of the Key Scientific and Technical Innovation Project, Ministry of Education of China (708060), National water pollution control and management technology major projects (2009ZX07210-008, 2009ZX07210-009) and Special Funds for Environmental Nonprofit Research Project (200809095).

References

[1] J. Sun, M.Y. Zheng and F. Wu: Renewable Energy Resources, Vol. 26 (2008), p. 46-49

[2] C.F. Li and X.M. Xu: Agricultural Mechanization Research, Vol. 32 (2010), p. 170-172

[3] Lei Wu: Journal of Gansu Science, Vol. 21 (2009), p. 146-149

[4] A.P. Zheng and X. Zhang: Construction Conserves Energy, Vol. 36 (2008), p. 58-60

[5] Information on http://hi.baidu.com/wawsh2/blog/item/7a8740e7cbc3562cb93820e4.html

[6] H.M. Yu, L. Zhou and Y. Ding: Heilongjiang August First Land Reclamation University, Vol. 18 (2006), p. 53-56

[7] Z.X. Miu and M.Z. Song: Jiangsu Biogas, Vol. 6 (1988), p. 11-14

© (2012) Trans Tech Publications, Switzerland
doi:10.4028/www.scientific.net/AMM.164.487

Helicid-loaded zein microparticles prepared using electrohydrodynamic atomization

Deng-Guang YU*, Xia WANG*, Yao-Zu LIAO, Ying LI, Wei QIAN, Xiao-Yan LI

School of Materials Science & Engineering, University of Shanghai for Science and Technology, Shanghai 200093, China

ydg017@usst.edu.cn (DG YU), wangxia@usst.edu.cn (X Wang)

Keywords: Electrohydrodynamic atomization, Microparticles, Zein, Helicid, sustained release

Abstract. An electrohydrodynamic atomization (EHDA) process was exploited to prepare helicid-loaded zein microparticles. SEM observations showed that all the particles prepared under varied voltages were round and solid with their sizes gradually decreased from 3.4 ± 1.7 to 1.1 ± 0.5 μm as the applied voltages rose from 6 to 18 kV. Wide-angle X-ray diffraction analyses demonstrated that helicid had been totally converted into an amorphous state in the zein matrix microparticles. Attenuated total reflectance Fourier transform infrared analysis disclosed that the hydrogen bonding presented between helicid and zein molecules. *In vitro* dissolution tests verified that the microparticles were able to provide a fine sustained drug release profile. The present study provides an easy way to develop novel biomaterials for drug delivery and for providing sustained drug release profiles.

Introduction

Zein is a mixture of proteins with different molecular weights in corn gluten meal. Apart from favorable biodegradability and biocompatibility, it has low hydrophilicity, good elasticity and film forming capabilities. Zein is used in the manufacture of a wide variety of commercial products, including coatings for food, excipient in pharmaceutics and clothing. Recently, it has drawn increasing attentions that zein is electrospun into nanofiber mats for various applications, particularly in biomedical field such as scaffold and matrix of novel drug delivery systems [1].

Drug-loaded micro/nanoparticles are often defined as particulate dispersions or solid particles with the drug is dissolved, entrapped, encapsulated or attached to a particle matrix. They have been used as a physical approach to alter and improve the pharmacokinetic and pharmacodynamic properties of various types of drug molecules [2].

Micro/nanoparticles have been prepared most frequency by the following methods: 1) dispersion of preformed polymers; 2) polymerization of monomers; and 3) ionic gelation or coacervation of hydrophilic polymers; 4) supercritical fluid technologyand 5) particle replication in non-wetting templates. Because of many advantages of using micro/nanoparticles as a drug delivery system, new methods for preparing drug-loaded nanoparticles are highly sought after. Especially those that can overcome some limitations associated with traditional preparation methods, such as particle aggregation, difficulty of physical handling of micro/nanoparticles, limited drug loading and burst release.

Electrohydrodynamic atomization (EHDA), a simple and straightforward process for the preparation of particulate polymeric micro- and nano- particles, fibers and thin films, is now becoming more and more popular recently. A significant feature of this technique is its ability to generate particles and fibers with a mean diameter that can be varied between hundreds of micrometers and tens of nanometers by varying the processing parameters for a particular system such as flow rate, needle diameter, applied voltage, as well as the chemical composition and concentration of the polymer solution [3-10].

Helicid, the therapeutic ingredient that is the focus of this study, was originally isolated as one of the main active constituents from *Helicid nilgrinica Bedd*, a plant indigenous to western China that has been used for thousands of years for curing headache and insomnia, and no obvious side effects have been reported. Helicid is a poorly water-soluble drug. A formulation that allows rapid dissolution and absorption for fast onset of therapeutic action is highly desirable [11].

With zein as the drug-loaded matrix and helicid as the model drug, EHDA process was exploited to prepare helicid-loaded microparticles, which exhibited good drug sustained release profiles *in vitro*.

Experimental

Materials Zein was obtained from Aldrich (a purity of 98%, Milwaukee, WI, USA). Helicid was obtained from Yunnan Yuxi Wanfang Natural Medicine Co., Ltd. (Production batch No. 070702) (Yunnan, China). Anhydrous ethanol was provided by Sinopharm Chemical Reagent Co., Ltd (Shanghai, China). Water was double distilled just before use.

Preparation of EDHA solutions A co-dissolving solution of zein and helicid was prepared for EDHA. The solution consisted of 10:2% of zein and helicid, meaning 16.7% content of helicid in the prepared zein microparticles.

The feeding rate was fixed at 1.0 mL/h by a syringe pump (KDS100, Cole-Parmer®, USA). A high power supply (Shanghai Sute Electrical Co., Ltd., China) was applied to the metallic capillary (with 0.7 and 0.5 mm outer and inner diameter respectively), and a piece of aluminum foil was used to collect the microparticles with a distance of 15 cm from the needle tip.

Characterization The surface morphologies of microparticles were assessed using a a Quanta FEG450 scanning electron microscope (SEM, FEI Corporation, Netherlands). The average size was determined by measuring diameters of over 100 particles from SEM images using Image J software (National Institutes of Health, USA).

Wide-angle X-ray diffraction analyses (XRD) were obtained on a D/Max-BR diffractometer (RigaKu, Japan) with Cu Kα radiation in the 2θ range of 5-60º at 40 mV and 300 mA. Attenuated total reflectance Fourier transform infrared (ATR-FTIR) analysis was carried out on a Nicolet-Nexus 670 FTIR spectrometer (Nicolet Instrument Corporation, Madison, USA) over the range 500-4000 cm^{-1} and at a resolution of 2 cm^{-1}.

The *in vitro* dissolution of microparticles was performed according to the Chinese Pharmacopoeia (2005 Edn.), a paddle method using a RCZ-8A dissolution apparatus (Tianjin University Radio Factory, China). All experiments were conducted at 37 ˚C and 50 rpm in 900 mL physiological saline. At pre-determined time intervals, aliquots of 5 mL were withdrawn for sampling and replaced by an equal volume of physiological saline to maintain a constant volume. After filtration through a 0.22 μm membrane (Millipore, USA) and appropriate dilution, the sample solutions were analyzed at 270 nm by a UV spectrophotometer (Unico Instrument Co., Ltd., Shanghai, China). Helicid dissolved at specified time periods was plotted as percentage released versus time. All measurements were conducted in triplicate and results are reported as average values.

Results and discussion

As shown in Fig. 1a and b, a common EHDA system comprises four major components: a high-voltage power supply, a grounded collector, a fluid driving device-syringe pump, and a capillary for introducing the fluid. In a typical EHAD process, a liquid is fed to a metal capillary at the end of which a droplet is formed. When the droplet is exposed to a strong electric field, a charge is induced on its surface. Provided the liquid has sufficient electrical conductivity, there will be a range of combinations of the liquid flow rate and the applied voltage for which the drop will assume a conical shape (the Taylor cone). At the apex of this cone, a narrow jet is formed (cone-jet mode) which subsequently breaks up into fine droplets (Fig. 1 c and d).

The applied voltage is a key parameter in EHDA process. Four different voltages were taken for the preparation of helicid-loaded zein microparticles. SEM images of the the microparticles are depicted in Fig. 2. As the applied voltages rose from 6 to 10, 12 and 18 kV, SEM observations showed that the microparticles' diameter decreased from 3.4 ± 1.7 to 2.3 ± 0.8, to 1.8 ±0.8 and 1.1 ± 0.5 μm. At a voltage of 6 kV, the microparticles could not be totally dried and thus resulted in aggregation of them in the collector.

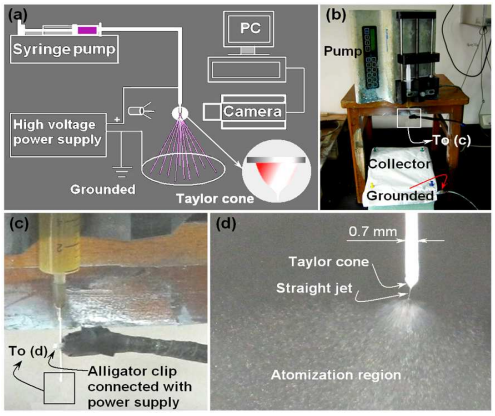


Fig. 1 EHDA process: (a) A schematic diagram of the EHDA process; (b) A digital picture of the apparatus; (c) The connection of the spraying head with syringe and high power supply; (d) The atomization process (taken by a canon camera PowerShot A490 under a magnifications of 12×, 18kV)

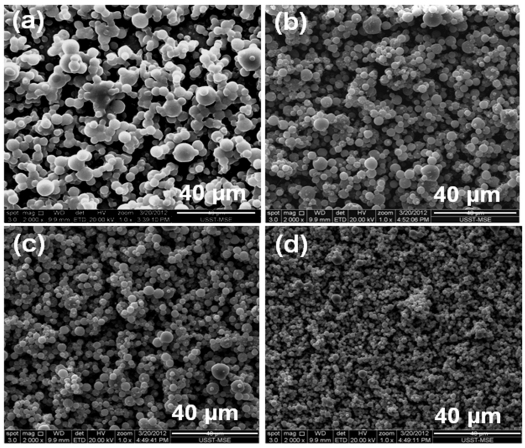


Fig. 2 SEM images of the microparticles prepared under varied voltages (kV): (a) 6, (b) 10, (c) 12, (d)18

It is desirable if the process can alter the physical status of drug to the favorable nanocrystalline, amorphous or solid solution phases for effective drug delivery. To investigate the physical status of helicid in the EHAD zein microparticles, XRD analyses were conducted. The presence of distinct peaks in the XRD patterns of the helicid raw particles indicated that helicid was present as crystalline material with characteristic diffraction peaks (Fig. 3). Zein exhibits only two hump characteristic of amorphous forms. There are no any speculate peaks of crystalline helicid detectable in the XRD patterns of the microparticles, indicating that all the helicid loaded in the particles was no longer present as crystalline material, but had been totally converted into an amorphous state.

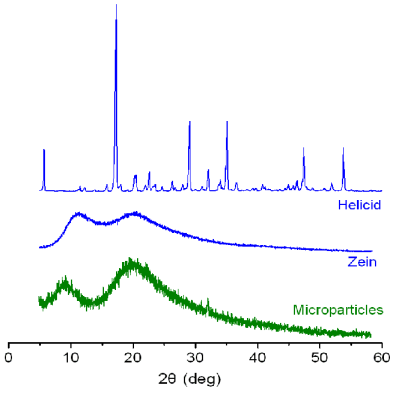


Fig. 3 X-ray patterns of helicid, zein and their EHAD microparticles

Compared to the spectra of pure helicid and zein, there are significant changes in the spectra of the microparticles (Fig. 4), including (1) the characteristic peaks of the carbonyl groups (C=O stretch vibration) at 1663 cm^{-1} in zein spectra shifting to 1651 cm^{-1}; (2) the disappearance of the numerous peaks in the finger region of helicid; (3) the characteristic peaks of the carbonyl groups (C=O stretch vibration) at 1668 and 1606 cm^{-1} of helicid melting into the 1651 cm^{-1}. All these changes can be attributed to hydrogen bonding between helicid and zein, including (1) between C=O of helicid and O-H of zein, and (2) between the C=O of zein and the O-H of helicid. All these secondary interactions would avail to the formation of helicid-zein composites in the form of microparticles, meaning that helicid would distribute in the zein matrix molecularly.

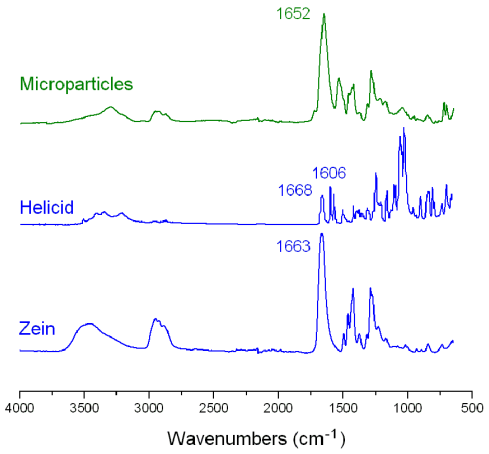


Fig. 4 ATR-FTIR spectra of helicid, zein and their EHAD microparticles

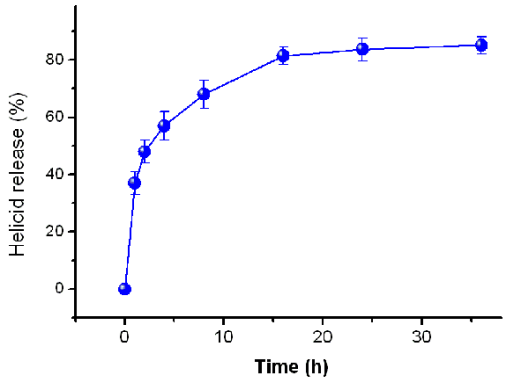


Fig. 5 *In vitro* drug release profiles of the microparticles

To evaluate helicid release profiles from the drug-loaded microparticles, *in vitro* dissolution tests were carried out and the drug release profiles of microparticles prepared under a voltage of 18 kV are shown in Fig.5. The microparticles showed fine sustained drug release profiles, which was over a time period of 16 h and released 81.2% of the contained helicid.

Conclusion

EHDA process was successfully exploited to prepare helicid-loaded zein microparticles. SEM results showed that all the particles were round and solid with their sizes gradually decreased when the applied voltages increased. XRD analyses demonstrated that helicid had been totally converted into an amorphous state in the EHDA zein microparticles. ATR-FTIR spectra disclosed that the secondary interaction-hydrogen bonding presented between helicid and zein molecules took their role in promoting the formation of helicid-zein composites. *In vitro* dissolution tests verified that the microparticles had a fine sustained drug release profile. The present study demonstrated an easy way to develop novel drug delivery systems using zein as drug carrier and through EHDA process.

Acknowledgement

This work was supported by the scientific starting funds for young teachers of University of Shanghai for Science and Technology (No.10-00-310-001), Grant 10JC1411700 from the Science and Technology Commission of Shanghai Municipality and National Science Foundation of China (No. 51173107).

References

[1] W. Nie, D.G. Yu, C. Branford-White, X.X. Shen and L.M. Zhu: Mater. Res. Innov. Vol.14 (2012), p.16

[2] O.C. Farokhzad and R. Langer: ACS Nano: Vol.16 (2009), p.3

[3] D.G. Yu, J.H. Yang, X. Wang and F Tian: Nanotechnology Vol.23 (2012), p.105606.

[4] D.G. Yu, G.R. Williams, J.H. Yang, X. Wang, J.M. Yang and X.Y. Li: J. Mater. Chem**.** Vol.21 (2011), p.15957.

[5] D.G. Yu, G.R. Williams, L.D. Gao, S.W.A. Bligh, J.H. Yang and X. Wang: Colloid Surface A Vol.396 (2012), p.161

[6] D.G. Yu, C. Branford-White, S.W.A. Bligh, K. White, N.P. Chatterton and L.M. Zhu: Macromol. Rapid Commun. Vol.32 (2011), p.744

[7] D.G. Yu, L.M. Zhu, C. Branford-White, S.W.A. Bligh and K. White: Chem. Commun. Vol.47 (2011), p.1216

[8] D.G. Yu, C. Branford-White, N.P. Chatterton, K. White, L.M. Zhu, X.X. Shen and W. Nie, Macromolecules Vol.43(2010), p.10743

[9] D.G. Yu, K. White, J.H. Yang, X. Wang, W. Qian and Y. Li: Mater. Lett. Vol. 67 (2012), p.78

[10] D.G. Yu, N.P. Chatterton, J.H. Yang, X. Wang, Y.Z. Liao: Macromol. Mater. Eng. DOI: 10.1002/mame.201100258 (2012).

[11] D.G. Yu, D.G. Yu, L.D. Gao, K. White, C. Brandford-White, W.Y. Lu and L. M. Zhu: Pharm. Res. Vol.27 (2010), p.2466

© (2012) Trans Tech Publications, Switzerland
doi:10.4028/www.scientific.net/AMM.164.492

Research on mechanical properties of geopolymer concrete under early stage curing system

Qing Wang[a], Kun Ran[b],Zhaoyang Ding[c], Linge Qiu[d]

School of Materials Science and Engineering, Shenyang Jianzhu University, Shenyang, 110168, China

[a]wangqingmxy@126.com, [b]rankun1@126.com, [c]smallnew69@126.com, [d]qiuchen_888@sina.com

Keywords: Slag; Metakaolinite; Geopolymer concrete; Curing system; Compressive strength

Abstract. Mechanical properties of geopolymer concrete under early stage curing system were studied. The results showed that at the early stage of curing time, compressive strength was improved significantly with the increasing of curing temperature and curing time. The compressive strength decreased and was close to that of standard curing condition at the age of 28d as the curing age increased. In addition, prolonging the storage time at room temperature before the step of high temperature curing could increase the long-term strength.

Introduction

Geopolymer is a new type of ceramic-like cementitious materical, which is produced through chemical reactions in alkaline condition. Geopolymer has the advantage of ceramic, cement and polymer. Moreover, it is an environmentally friendly material, which is rich in resource, easy to prepared, low cost and less in energy consumption.[1] With the advantage of "energy saving" and " environmental protection", geopolymer has good social and economic benefit and receives a lots of attention from scholars both domestic and abroad.[2]

Rrecently, more and more researches have been conducted on the chemical, mechanical and microstructural aspects of geopolymer, but there is very little work has been done to the curing system, which is very important to the mechanical properties of geopolymer. In this study, Slag and metakaolinite were used as raw materials and water-glass was used as alkali activator, G40 geopolymer concrete was prepared, in which cement was replaced by geopolymer as binder. The effect of early stage curing system on compressive strength of geopolymer concrete was researched by changing the curing temperature, curing time and the storage time.

Test

Raw materials

(1) Slag: granular blast fumace slag is obtained from Anshan Iron and Steel Company; its chemical composition is shown in table 1.

Table 1 Chemical composition of granular blast furnace slag (mass %)

CaO	SiO_2	TiO_2	Al_2O_3	MgO	V_2O_5
26.54	24.37	23.83	13.76	8.48	0.34

(2) Metakaolinite: metakaolinite is obtained from Inner Mongolia, and the chemical composition of metakaolinite is shown in table 2.

Table2 Chemical components of metakaolinite (mass %)

SiO_2	Al_2O_3	Fe_2O_3	TiO_2	CaO	MgO	Na_2O	Ignition Loss
52.65	43.2	0.25	0.56	0.004	0.013	0.086	0.135

(3) Alkali activator: liquid water glass (modulus 3.4) used in the experiment is obtained from Shenyang Fangda Chemical Plant, in which the mass content of Na_2O is 8.06%, and the mass content of SiO_2 is 25.90%. Analytically pure agent NaOH, granular or flaky, with a mass fraction greater than 96.0% is obtained from Sinopharm Chemical Reagent Co. Ltd.

(4) Sand: bank sand, the modulus is 2.8.

(5) Gravel: the specification of continuous gradation is 5~31.5.

Experimental Method. First, slag, metakaolinite, sand and gravel were put into the oven and dried for 6h (drying temperature was 120℃). Those were then put into the pot with alkali activator and stired for 5min. The prepared mix was placed into the mode (size: 100mm×100mm×100mm), the fresh geopolymer concrete was prepared after the vibration process.Finally, the compressive strength of geopolymer concrete under different curing condition were tested.

Results and Analysises

Contrast test. Geopolymer which is cured under standard curing condition was prepared as the blank test, the compressive strength of concrete is shown in Tab.3.

Table 3 Compressive strength of geopolymer concrete on normal curing

Curing age (d)	1	3	7	28
Compressive strength (MPa)	22.7	30.1	48.5	62.4

Influence of temperature of warm water on the compressive strength of geopolymer concrete. After curing 24h under normal temperature, the moulds were removed and geopolymer concrete specimens were cured 4h in the water bath at constant temperature whose temperature was 20℃, 40℃, 60℃, 80℃ and 100℃respectively. The samples were then took out and cured at standard condition till the end of the curing age. The influence of water temperature on the compressive strength of geopolymer concrete is shown in Fig.1

Fig. 1 shows that the 7d compressive strength of concrete reaches the top as the curing temperature is 60℃ in the different curing system. The compressive strength is relaxation shrinkage with the prolonging of the curing age. This phenomenon indicates that the early age compressive strength enhances with the increasing of the temperatue in the process of polymerization, because of quicker reactions. The latter compressive strength is influenced at the same time, since the activationenergy can be offered to the depolymerization and polymerizaton reacation of aluminosilicate. The low temperature can lead to the slower reacation rate. During this process, the content of aluminosilicate and silicate which are dissolved in the system and are connected by the bridging oxygen atom are low. The temperature is so low that the rate of reactions is slow and the materials are jointed by the physical cementing. As a result, the chemical bonds do not form and the compressive strength of concrete is very low. Increasing temperature, the speed of polymerization reactions is rapider, while the over temperature is a adverse factor. The reason is that the water as transfer medium and recation media is transformed to gas when the temperature is over high, the consequent thermal force can generate certain comperssive stress and expansion in the internal concretnal. The internal cracks which lead the adverse effect to growth strength are formed. Therefore, in preparing geopolymer concrete, the curing temperature can be reasonably set at 60℃. On this condition, the early strength of concrete is high and the 28d strength is preferably.

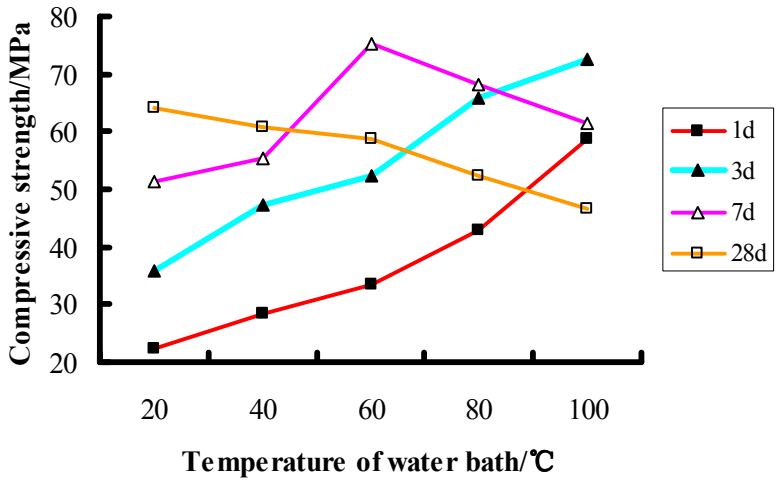


Fig. 1 Influence of temperature of warm water on strengh of geopolymer concrete

. **Influence of curing time of warm water on strength of geopolymer concrete.** After curing 24h under normal temperature , the moulds were removed, and geopolymer concrete samples were cured in the water bath at 60℃, the curing time were respectively 2h, 4h, 6h, 8h and10h. The concrete specimens were took out and put into the curing room until the specified age. The compressive strength of geopolymer concrete is shown in Fig. 2.

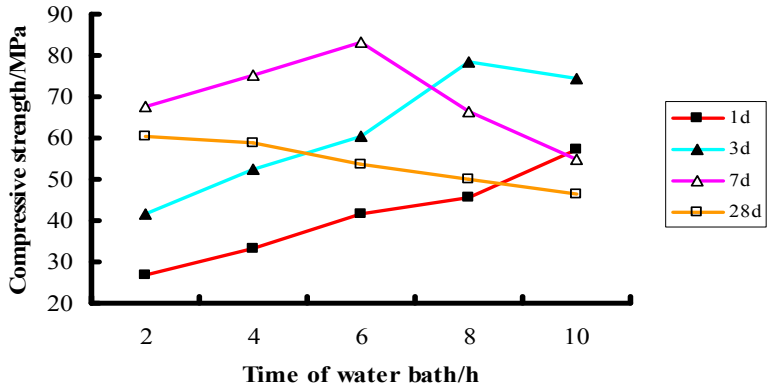


Fig. 2 Influence of curing time of warm water on strength of geopolymer concrete

Fig. 2 shows that at the water bath condition of 60℃, the early age compressive strength of geopolymer concrete constantly increases when the curing time prolonged. The top of compressive strength in curing age of 1d, 3d and 7d respectively appears 10h, 8h, and 6h. As a result, the curing system that high temperature and long time can improve the early age strength, but when the time prolongs the effect is opposite. The rate of polymerization reactions is quicker, the content of aluminum silicon tetrahedron is getting more and the strength is growing more rapidly when the curing time is reasonably prolonged. On the other hand, when the cuing time is excessive, the shortage of alkali goes against the long-term strength of concrete.

Influence of standing curing time on strength of geopolymer concrete. Standing curing time was the time that the specimen was set at normal temperature after shaped. Standing curing 0h, 4h, 6h, 8h and 10h respectively, the specimens were set at the 60℃ water bath for 6h and then the specimens were put into the curing room until the defined age. The compressive strength of geopolymer concrete is shown in Fig. 3.

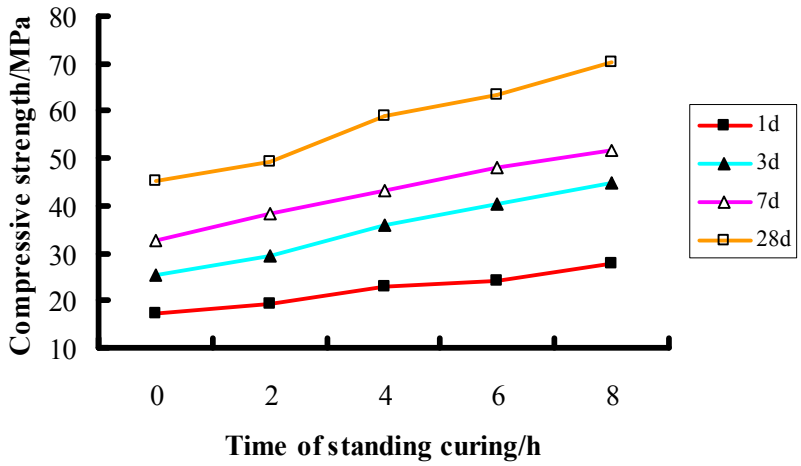
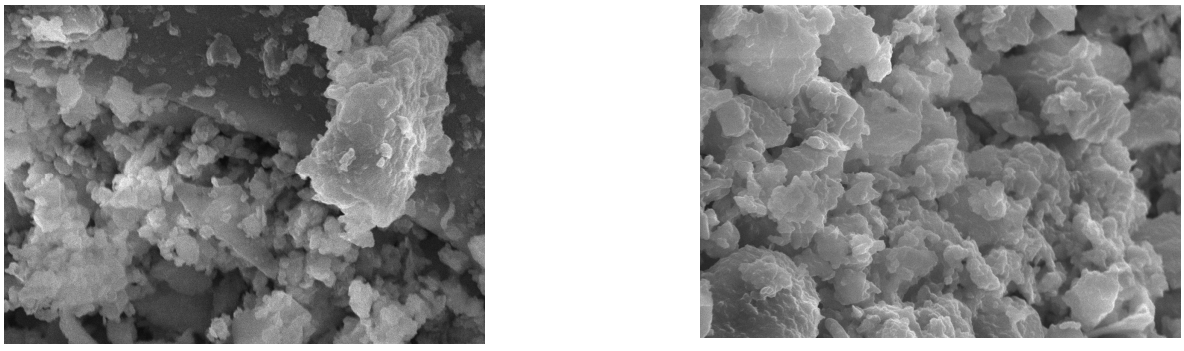


Fig. 3 Influence of standing curing time on strength of geopolymer concrete

The Fig. 3 shows that the more standing curing time, the more growing of compressive strength. It indicates that the adverse factor of high temperature curing to long-term strength is weakened when the standing curing time is prolonged. In the high temperature curing process, the thermal force that is generated through the water which is changed to gas can produce the compressive stress to internal structure. If the cementing specimens do not have enough strength, the internal cracks can be occurred. The prolonging time changed the structure of internal hole ,so the adverse factor can be weaken by prolonging curing time under high temperature. The average aperture fall down and concrete get enough strength for resisting the thermal expansion. Prolonging time should improve the long-term strength, but this factor will reduce the production efficiency as well. Thus, the curing time should be chosen reasonably. According to the test, 4h of the standing curing time is appropriate and economical.

SEM analysis of geopolymer concrete. The SEM images of geopolymer concrete which are set at the 60℃ water bath for 6h and cured standard condition until the defined age are shown in Fig. 4. The specimen of contrast test is geopolymer concrete cured under normal temperature .



(a) (b)

Fig. 4 The SEM images of geopolymer concrete

Fig.4 (a) is the SEM image of geopolymer concrete which is cured at 60℃ water bath for 6h and then normal curing system for 7d. The magnification is 5000.

Fig.4 (b) is the SEM image of geopolymer concrete which is cured under normal curing system for 7d. The magnification is 5000.

Fig.4 (a) shows that the specimens cured in 60℃ water bath for 6h and then under normal temperature curing system can generate more aluminum silicon tetrahedron, resulting in complete polymerization reaction and total compact degree of structure ,so the strength is higher On the contrary, the amount of aluminum silicon tetrahedron is a little and the speed of reaction is slower without warm water curing, so the strength is weakened ,shown as Fig. 4 (b). Appropriate early curing for promoting the strength is necessity.

Conclusions

a. At the early stage of curing time, compressive strength is enhanced significantly with the increasing of curing temperature and curing time, and higher than normal temperature curing. But with the prolonging of curing time, there is a tendency of descent in compressive strength and 28d strength is close to the level of normal temperature curing. Therefore, the early strength of concrete is high and the 28d strength is preferably when the curing temperature is set at 60℃.
b. Prolonging of standing time in normal temperature properly and then aging at high temperature could reduce adverse effect of later strength under high temperature. According to the test, 4h of the standing curing time is appropriate and economical.

References

[1]Yunsheng Zhang，Wei Sun，Jianfang Sha，Zhijian Liu．Preparation, Property and Mechanism of Fly Ash Based Geopolymer Concrete[J]．China Concrete and Cement Products: 2003，2：13~15.

[2] Hongling Wang，Haihong Li，Zhizhong Feng，Nong Tian，Fengyuan Yan．Study of Geopolymer Based on Kaolinite with Different Activation [J]．Journal of Materials Science&Engineering2004，22(4)：550~553

[3] Qing wang，Lei Liu，Changpeng Wu，Zhitong Sui．Study on the Mechanical Properties of Slag-based Inorganic Geopolymer．Journal of Shenyang Jianzhu University (Natural Science)：2007，1：73~76

[4] Djwantoro Hardjito, Steenie E. Wallah．Fly Ash-Based Geopolymer Concrete, Construction Material for Sustainable Development. Concrete World: Engineering &Materials, American Concrete Institute, India Chapter,Mumbai, India, December 9-12, 2004

[5] Djwantoro Hardjito, Steenie E. Wallah．On the development of fly ash-based geopolymer concrete. ACI Materials Journal,2004,11-12:467~472

[6] Gang Wang，Hongwen Ma，Yufeng Ren，Wuwei Feng，Qiuxia Ding．Preparation of Mineral Polymer Based on Flyash:An Experimental Study．IM&P：2004，5：24~27

© (2012) Trans Tech Publications, Switzerland
doi:10.4028/www.scientific.net/AMM.164.497

Water Storage Bucket Chain Convey-Cleaning Machine for Cleaning up Coal Mine Water Storage

Yujing Jia[1, a], Dayu Zhang[2, b], Guangzhen Cheng[1, c] and Yingjun Dai[1, d]

[1]Huzhou Teachers College, Huzhou, Zhejiang Province 313000, P.R. China

[2]Heilongjiang Bayi Agricultural University, Daqing, Heilongjiang Province 163319, P.R. China

[a]jyjng@126.com, [b]zdy214@163.com, [c]chgzh169@126.com, [d]616249581@qq.com

Keywords: Coal mine water storage, Electrical control, Cleaning machine, Bucket chain conveyor

Abstract. This Paper introduced a water storage bucket chain conveyor cleaning machine used in coal mine to clean up the underground water storage, which was mainly made up of the mechanical structure and electrical control system. The mechanical structure consists of walking flatbed, walking drives, chain bucket conveyor. Here focuses on the special structure, the working principle, the work process, the electrical control system, the working condition, the main features and the purpose of the chain bucket convey-cleaning machine. The machine structure was reasonable, the stress was even, the vibration was small, the movement was steady. It can not only adapted to a large water content of coal slime, but also adapted to dry coal slime. It overcomes the low efficiency of spiral roller clearance dealing with the large water content of the slime and the weakness when vacuum suction-type pneumatic conveyor is to clean the dry slime.

Introduction

Coal mine water storage is the important facility to prevent the flood in mine. For the groundwater-rich mine, as the expansion of mining area, water inflow would increase, as a result, the water can not be discharged out by drain pump in time. It accumulates in underground water storage and playing the role of cushion. Due to a large number of solid particles are carried into the gushing water storage, the effective capacity of underground water storage is limited, so it is necessary to clean up the water storage regularly, especially with the large number of water inflow when the storage can not be used in time. In this situation, the use of mechanized equipment cleaning water storage is very important. At present there are two types of common sump cleaning equipments, which are spiral roller and vacuum suction pneumatic conveyor. With the application of these two Cleaning machines, production efficiency is increased significantly. however, limited by the principle of the device structure, the spiral roller clearance is less efficient in dealing with the coal slime which contains a large number of water. On the opposite, the vacuum suction-type pneumatic conveyor is inefficient when the water content of the coal slime is low. So the design of the bucket chain convey-cleaning machine is designed to overcome those weaknesses [1].

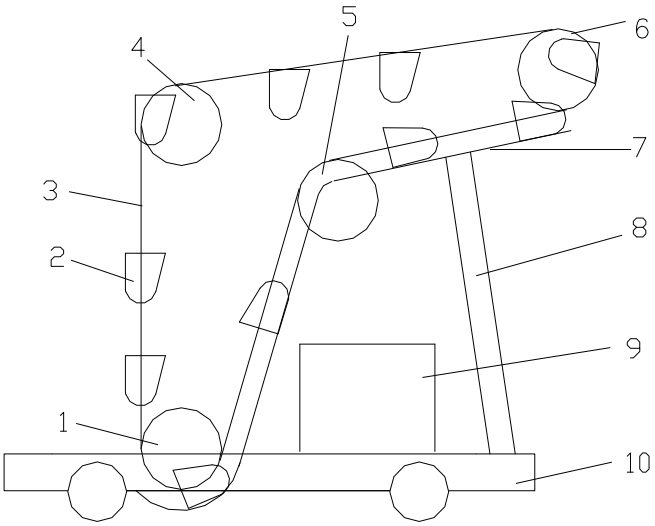
Composition and Working Principle

The structure of the bucket chain convey-cleaning machine is shown in Fig. 1. Body frame and walking driver 9 are installed on the flatbed 10, sprocket driver 1 and oriented sprocket 4, 5, 6 are installed on the frame body, bucket chain 2 is hinged with chain 3 solidly, the pallets 7 solid joint with the frame body. When working, firstly start the motor, chain bucket convey-cleaning machine reach the working position with a tramcar, start the drive sprocket 1st motor, the chain roll in a clockwise way, walking driver drive the whole machine move forward, bucket chain move to the bottom, automatically loading the material, the machine tip when moving to bucket chain sprocket 6, pour the material into the tramcar. Since bucket 2 hinged solidly in the chain 3, the loading section of bucket chain keeps upright and open-upward by gravity, mandatory unloading agencies on sprocket 6 forced bucket chain to tip to achieve the uninstall, then the state of bucket chain is maintained by the pallet 7,

to drive a sprocket loading the material when reach sprocket driver 1. The tramcar was towed by motor vehicle to transport tunnel when it is full, another empty tramcar is ready to start the next loading cycle.

Electrical Control Principle

The electrical control schematic of chain bucket convey-sump cleaning machine is shown in Fig. 2, which is the main circuit. The control circuit is shown in Fig. 3 [2].



1. Bucket drive, 2. Bucket, 3. chain, 4.5.6. Sprockets,
7. Pallets, 8. Support, 9. Travel drive device, 10. Flatbe.
Fig. 1 Structure diagram

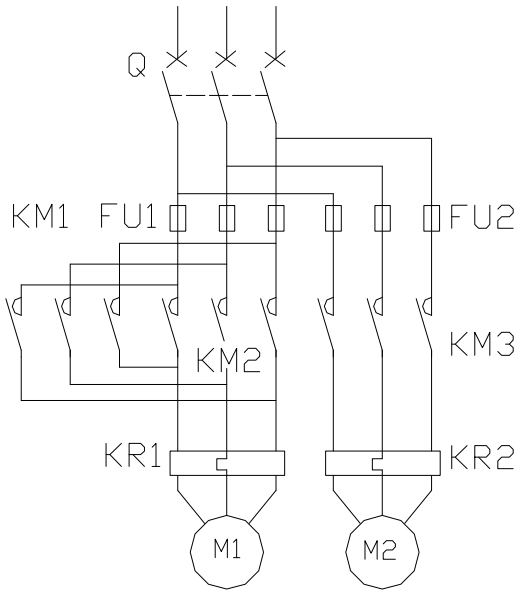


Fig. 2 Main electrical circuit

Press the start button SB2, contactor KM1 line package is electric, KM1 main contacts are closed, normally open contact closure and self-lock at the same time, drive motor M1 moves forward. When getting to back, press the button SB1, contacts KM1 line package is power-off, contactors KM2 energize and self-lock, M1 reverse, walking device moves backward. Pressing the button SB5 can

stop the walking device at any time, whether it is forward or backward. To prevent short circuit of the contactor KM1, KM2 when energized at the same time, the normally closed contact of KM1 and KM2 should be in series in each others' control circuit respectively, forming an interlock. Press the start button SB3, line contactor KM3 package was electric, main contacts of KM3 are closed, normally open contact closure and self-lock at the meantime, chain bucket conveyor motor M2 is electric and start, chain bucket conveyor system start to work, press the stop button SB4 , contactor KM3 line package is power-off, chain bucket conveyor system stop functioning. SB5 is used to control the stop of both moving forward and backward, it is also the start-stop switch to the whole. FU1, KR1 are to prevent over current and over temperature of the walking drive motor, FU2, KR2 are for the protection of chain bucket conveyor motor M2 from over current and overt emperature [3].

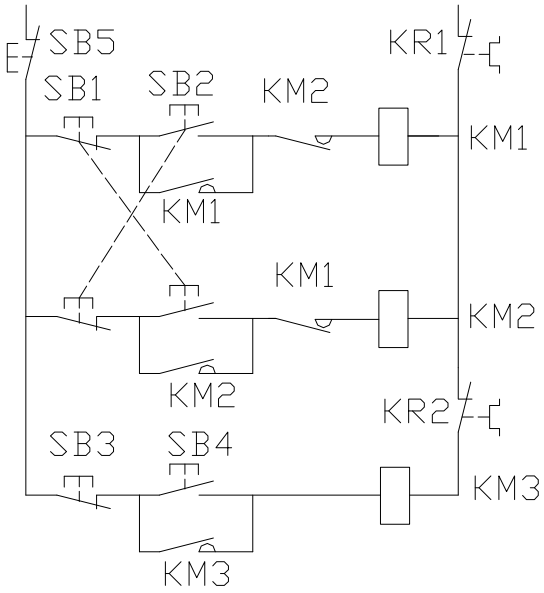


Fig. 3 Electrical control principle diagram

The electrical control components I / O allocation table is shown in table 1 [4].

Table 1 The electrical control components I / O allocation table

Component	Signal Defined
SB1	walking device forward button
SB2	walking device back button
SB3	chain bucket conveyor stop button
SB4	chain bucket conveyor start button
SB5	the machine stop button
KM1	walking device electric motor forward contactors
KM2	walking device electric motor reverse contactors
KM3	chain bucket conveyor electric motor contactors
KR1	walking device electric motor thermal relay
KR2	chain bucket conveyor electric motor thermal relay
M1	walking device electric motor
M2	chain bucket conveyor electric motor

The Main Technical Parameters

Rated walking speed: 1 m/s
Chain bucket conveyor rated speed: 20 rpm
Rated capacity: 30 m^3/h
Walk drive motor rated power: 4 kW
Chain bucket conveyor motor rated power: 5.5 kw

Conclusion

(1) Chain bucket convey-sump cleaning machine can not only adapt to a large water content of coal slime, but also adapt to dry slime.
(2) It overcomes the low efficiency of spiral roller clearance dealing with the large water content of the slime and the weakness when vacuum suction-type pneumatic conveyor is to clean the dry slime.
(3) Water storage bucket chain convey-cleaning machine is flexible and easy to use with a self-walking driver.
(4) Convenient operation, greatly reducing the labor intensity of clearance, clearance efficiency increases double due to the reasonable structure.

References

[1] Y.T. Zheng and G.Y. Wang: Coal Mining Machinery Vols. 27 (2006) No.5, pp.127-128. (in Chinese)

[2] Y.S. Fan: *The electric control and PLC apply* (China Electric Power Press, China 2004) (in Chinese)

[3] G.Z. Cheng and Y.J. Jia: Coal Mining Machinery Vols. 23 (2002) No.8, pp 46-47.

[4] S.H. Chen: *Mechanical device electric control* (South China University of Technology Press, China 2002) (in Chinese).

[5] Y.J. Jia, Y.B. Cheng and Y.Y. Han: dvanced Materials Research Vols. 228-229 (2011) pp. 744-748.

[6] G.Z. Cheng and Y.B. Cheng: Applied Mechanics and Materials Vols. 34-35 (2010) pp. 1573-157

[7] D.S. Feng: *Frequency Conversion application and maintenance* (South China University of Technology Press, China 2001), (in Chinese). 7.

© (2012) Trans Tech Publications, Switzerland
doi:10.4028/www.scientific.net/AMM.164.501

Features of Jianshanchong Klippe and Its Control to Gas Geology at Qingshan Coal Mine, Jiangxi Province

Zhigen Zhao [1, a], Jia Chen [2, b], Jiaping Yan [3, c]

[1]School of Earth and Environment, Anhui University of Science and Technology, Huainan, China

[2]School of Earth and Environment, Anhui University of Science and Technology, Huainan, China

[3]School of Surveying, Anhui University of Science and Technology, Huainan, China

[a]zhgzhao@aust.edu.cn, [b]chenj1a@126.com, [c]jpyan@aust.edu.cn

Keywords: Qingshan Coal Mine; Jianshanchong klippe; coal and gas outburst; prediction of gas geology in deep area.

Abstract: The coal and gas outburst is serious at Qingshan Coal Mine of Jiangxi Province, so it is of significance to research the features of Jianshanchong klippe and its control to gas geology. The research reveals that: Jianshanchong klippe is distributed from the east boundary of Qingshan Coal Mine to No. 45 Exploration Line, its transverse profile is like a funnel while its longitudinal profile is like a wedge, northwest side of the klippe is thicker and deeper while southeast side is thinner and more shallow. Because of the cover and insert of Jianshanchong klippe, the structure of coal-bearing strata is more complex, some secondary folds are formed, and also, the coal seam is changed greatly, the tectonic coal is well developed and the coal seam is suddenly thickening or thinning. Due to the effect of Jianshanchong klippe, the coal and gas outbursts occur in the area of secondary folds, thicker coal seams or tectonic coals. Concerning the prediction of gas geology in deep area, in view of the facts including simpler structure, stable coal seam and decreased thickness, the gas emission rate and the coal and gas outburst will decrease in Fifth and Sixth Mining Level than that in Second and Third Mining Level.

Introduction

Qingshan Coal Mine is located in Pingxiang City of Jiangxi Province, 6 km to the west of Pingxiang City. The First, Second and Third Mining Level have been finished their mining, and at present, the Fourth Mining Level is mining while the Fifth Mining Level is opening the tunnels. The Geological Report of Sixth Mining Level was submitted in 2010, and provides the basis for mining design. Qingshan Coal Mine is a high gas mine, and is serious in coal and gas outburst [1-2], so it is of significance to research the the features of Jianshanchong klippe and its control to gas geology.

General Geology of Qingshan Coal Mine

The geological structure of Qingshan Coal Mine is an asymmetric compound syncline in the direction of N50-60°E. The southeast limb is comparatively gentle with the dip angle about 35-45° while the northwest limb is considerably steep with the dip angle about 70-85°. The main geological features of Qingshan Coal Mine and its surrounding include: Luexiachong syncline, Xianfengyan anticline and Xintangchong syncline are distributed in turn from northwest to southeast, and the small secondary folds are well developed. Pengjiayuan reverse fault is located to the northwest edge of Qingshan Coal Mine, Dishuiyan reverse fault, Shilongwo reverse fault and Zhangshupo normal fault are located to the southeast edge, Tianzishan reverse fault is located in the area of No. 45 Exploration Line, and, Jianshanchong klippe is in the northeast of Qingshan Coal Mine. Fig. 1 is the structure outline map of Qingshan Coal Mine and its surroundings.

The coal seams of Anyuan coal-bearing strata are developed at Qingshan Coal Mine. From bottom to top, the strata in the studied area include: Zijiachong Stage (T_3a^1), Sanjiachong Stage (T_3a^2) and

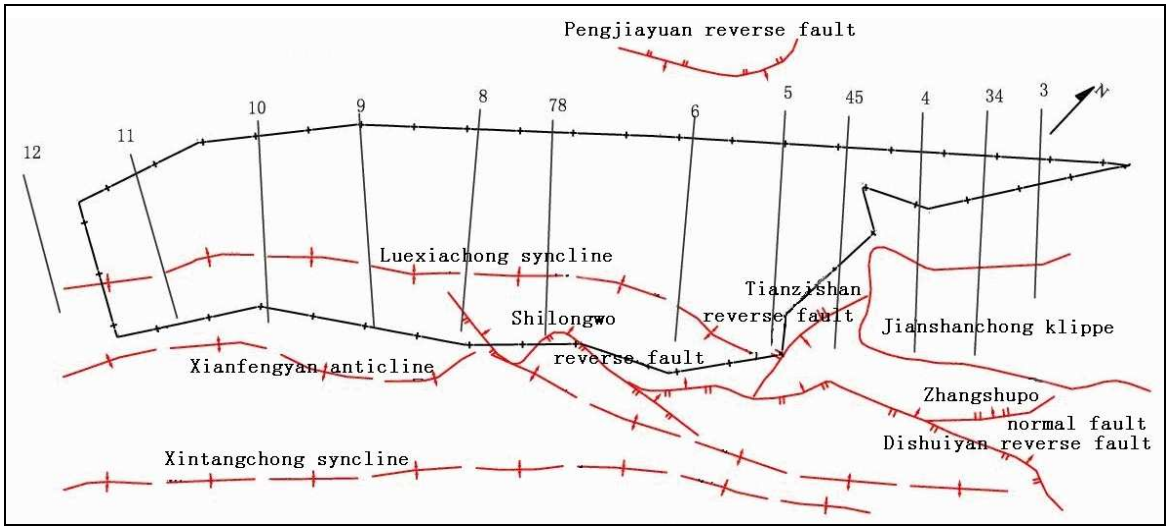


Fig. 1 Structure outline map of Qingshan Coal Mine

Sanqiutian Stage (T_3a^3) . Within the strata, Zijiachong Stage is well developed, and include several minable coal seams, while Sanjiachong Stage is the sediment with no coal seam, and, Sanqiutian Stage is the sediment with no minable coal seam [3]. There are 9 coal seams of Zijiachong Stage at Qingshan Coal Mine, the total thickness of coal seams is 20.65m, and the coal-bearing ratio is 3.39%. There are 5 coal seams are minable within these 9 coal seams, from bottom to top, these 5 minable coal seams are: Dacao coal seam (No. 1 coal seam), Guanzicao coal seam (No. 5 coal seam), Dahuacao coal seam (No. 6 coal seam), Zhuzicao coal seam (No. 7 coal seam) and Yingzicao coal seam (No. 8 coal seam). Dacao coal seam is minable in the whole area of coal mine, and is the main mining object, while Guanzicao, Dahuacao, Zhuzicao and Yingzicao coal seams are partially minable. The coal quality is from high rank bituminous coal to anthracite, and most of them are anthracite.

Features of Jianshanchong Klippe

Jianshanchong nappe structure is a klippe, distributed from the east boundary of Qingshan Coal Mine to No. 45 Exploration Line. The exposed area on the ground of Jianshanchong klippe is 0.2km^2, and its lithology is Xiaojiangbian limestone. The transverse profile of Jianshanchong klippe is like a funnel while the longitudinal profile is like a wedge, northwest side of the klippe is thicker and deeper while southeast side is thinner and more shallow. Fig. 1, 2 display the shape of Jianshanchong klippe.

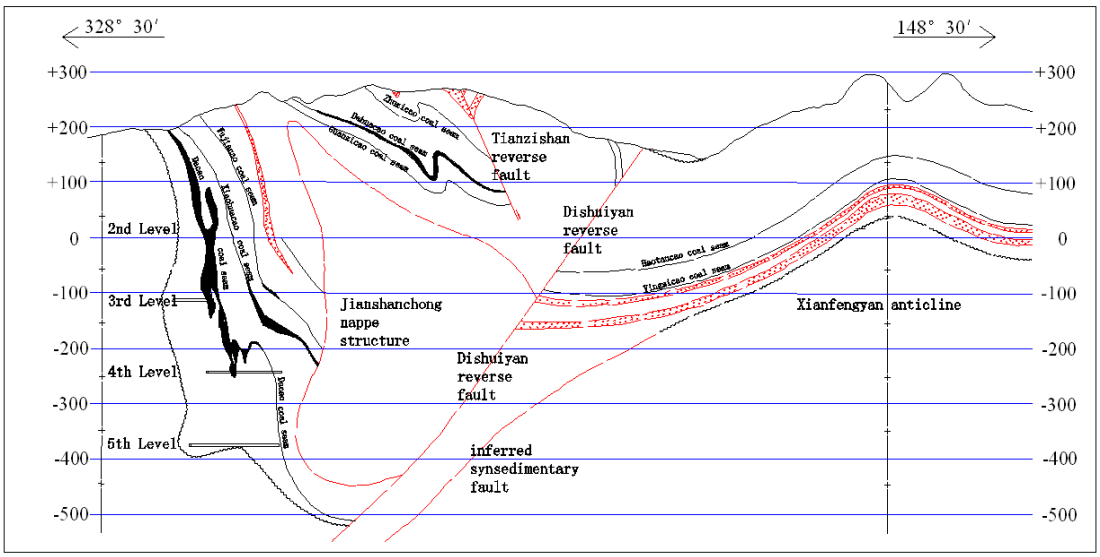


Fig.2 Geological section map of No. 45 Exploration Line at Qingshan Coal Mine

Control of Jianshanchong Klippe to Gas Geology

The coal-bearing strata in northwest limb of Luexiachong syncline is well developed, the thickness of Zijiachong Stage is more than 480 m, while the strata in southeast limb is not well developed, the thickness of Zijiachong Stage is only 180 m, Fig. 2, so, the coal seams of northwest limb are mainly mined. And thus, the control of Jianshanchong klippe to gas geology is discussed mainly about northwest limb instead of southeast limb.

Effect of Jianshanchong Klippe to Structure and Coal Seams

Because of the cover and insert of Jianshanchong klippe, the structure of coal-bearing strata is more complex. The synclinal axis is raised in the area of No.3, No.4 and No.45 Exploration Lines, which leads to that some coal seams are exposed to the surface so as to be partial eroded. In the area of No.5 and No.56 Exploration Lines, the effect of Jianshanchong klippe is reduced, more secondary folds are formed, while in the area of No.67 Exploration Line, Jianshanchong klippe is almost no effect to the structure. And also, the influence of Jianshanchong klippe to coal seam is significant. The tectonic coal is well developed, many mylonitic coal and granulated coal for Dacao coal seam, and many granulated coal and cataclastic coal for Yingzicao coal seam. And, the continuity of coal-bearing strata is destroyed, the dip angles of coal-bearing strata are considerably steep, more than 60°, and, the thickness of coal seams is greatly changed, the imbricated structure and thick areas of coal seam are formed. Taking the Dacao coal seam as an example, as the result of Jianshanchong klippe's insert into coal-bearing strata, the secondary structure of Dacao coal seam is more complex, and the thickness of coal seam is changed greatly, suddenly thickening or thinning.

Features of Coal and Gas Outburst of Dacao Coal Seam

Altogether, there are 33 coal and gas outbursts at Qingshan Coal Mine. And 22 outbursts occur in Dacao coal seam. There are two features about coal and gas outburst of Dacao coal seam. One is: the coal and gas outbursts occur in or is adjacent to geological tectonic belts including secondary syncline, secondary anticline and faults [4], Fig. 3. The other is: the coal and gas outbursts concentrate in Second and Third Mining Level, while no outburst is happened in First Mining Level, and only 1 outburst is happened in Fourth Mining Level [4], Fig. 4.

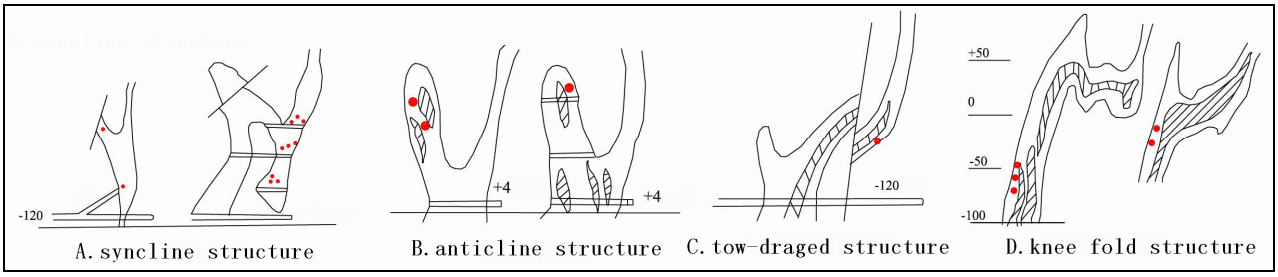


Fig.3 Relation between coal and gas outburst and geological structure at Qingshan Coal Mine

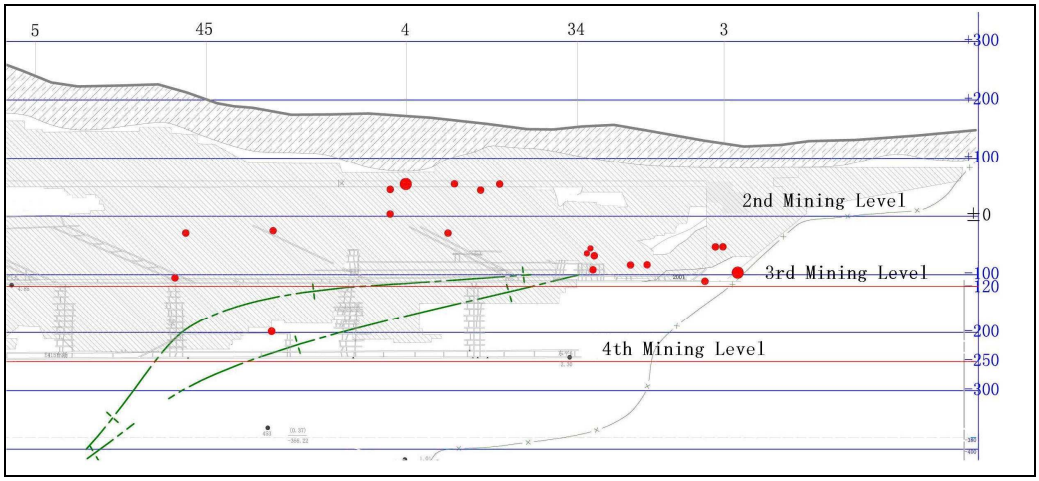


Fig.4 Distribution of coal and gas outburst about Dacao coal seam at Qingshan coal mine

Prediction of Gas Geology in Deep Area of Dacao Coal Seam

Usually, with the increase of coal seam's buried depth, the gas content, gas pressure and gas emission rate increase, and the risks of coal and gas outburst also increase, which is the universal law [5-6]. It is based on this law to predict gas content, gas pressure and gas emission rate in deep mining area or in new mining level [6-7]. But this law is not absolute, but conditional. This condition is that the other geological factors are the same or similar, except the factor of buried depth of coal seam.

In this paper, because of the cover and insert of Jianshanchong klippe, the structure of coal-bearing strata and the shape and thickness of coal seams are changed significantly, which become the major factor controlling the gas emission and outburst. The risk area of coal and gas outburst is the high gas area, and is consistent with the area of secondary folds, thicker coal seams or tectonic coals. Thus, the coal and gas outbursts of Dacao coal seam are closely related to geological tectonic belts include secondary syncline, secondary anticline and faults, the outbursts concentrate in Second and Third Mining Level while no outburst in First Mining Level and only 1 outburst in Fourth Mining Level. As far as the research in this paper, the buried depth is not the major factor controlling the gas emission and outburst, so the statistical predicted method can not be accepted here using buried depth to predict the gas emission and outburst in deep mining area or in new mining level. The gas data collected from coal mining also provide some helpful information. From the angle of gas content, the gas contents in Second Mining Level and in Third Mining Level are high while the gas contents in Fourth Mining Level have no obvious increase. From the angle of gas pressure, the determination of gas pressure reveals that: the gas pressure in Third Mining Level is maximum, and the gas pressure tend to decrease in deeper mining area. In addition, Fig. 2 shows that: the Dacao coal seam in deep area intersect with Dishuiyan fault, and, the Dacao coal seam in deep area contact with Maokou limestone caused by synsedimentary fault, these two are favorable to gas migration and emission [8], which probably leads to the decrease of degrees of gas emission and coal and gas outburst.

Based on the above analysis, in view of the facts including simpler structure, more stable coal seam and decreased thickness in deep mining area, the gas emission rate and the risk of coal and gas outburst will decrease in Fifth and Sixth Mining Level than that in Second and Third Mining Level.

Conclusion

1. Jianshanchong klippe is distributed from the east boundary of Qingshan Coal Mine to No. 45 Exploration Line, its transverse profile is like a funnel while its longitudinal profile is like a wedge, northwest side of klippe is thicker and deeper while southeast side is thinner and more shallow.

2. Because of the cover and insert of Jianshanchong klippe, the structure of coal-bearing strata is more complex, some secondary folds are formed, and also, the coal seam is changed greatly, the tectonic coal is well developed and the coal seam is suddenly thickening or thinning.

3. Due to the effect of Jianshanchong klippe, the coal and gas outbursts occur in the area of secondary folds, thicker coal seams or tectonic coals. The buried depth is not the major factor controlling the gas emission and outburst.

4. Concerning the prediction of gas geology in deep area, in view of the facts including simpler structure, more stable coal seam and decreased thickness, the gas emission rate and the risk of coal and gas outburst will decrease in Fifth and Sixth Mining Level than that in Second and Third Mining Level.

Acknowledgments

The research is financially supported by the National Natural Science Foundation of China (No. 41172138) and by the special fund project of Jiangxi Energy Bureau (No. 20100730). The authors wish to thank professor Xiuyi Tang from Anhui University of Science and Technology for his constructive advice. The authors also express our gratitude to the technical personnels from Jiangxi Exploration Institute of Coalfield Geology, Qingshan Coal Mine for their kind help.

References

[1] J Z Xie, C X Peng, Q Shuai, D H Ouyang, Discussion about gas occurrence regularity and their main effecting factors in Pingxiang Mining Area, in: Z X Zhang, Z M Zhang, K S Luo, New progress of gas geology, Henan Science and Technology Press, Zhengzhou, 2001, pp. 10-15

[2] X P Zhang, G C Peng, Y Z Zhu, Gas pressure determination of W482 Working Area at Qingshan Coal Mine, Jiangxi Coal Science and Technology, 32(2010):(3)57-58

[3] X D Tan, R F Yang, S X Mo, X H Liu, Study of coal-controlled structures in Pingxiang Mining Area of Jiangxi province, Hunan Geology, 20(2009):(3)168-171

[4] J Chen, Research on the features of gas geology of Dacao Coal Seam at Qingshan Coal Mine in Pingxiang Mining Area, Anhui University of Science and Technology's Master degree thesis, 2011

[5] R S Long, Mine Geology, Coal Industry Press, Beijing, 1991, pp. 115-135

[6] Z M Zhang, Gas Geology, China University of Mining and Technology Press, Xuzhou, 2009, pp. 119-165

[7] State Administration of Work Safety, The predicted method of mine gas emission rate (The people's Republic of China safety standards (AQ1018-2006)), Coal Industry Press, Beijing, 2006

[8] J Chen, S Wang, M M Zhang, Analysis of factors effecting gas content of main mining coal seams at Qingshan Coal Mine in Jiangxi Province, in: M X Zhang, W Li, The technology and development of modern mine geology, China University of Mining and Technology Press, Xuzhou, 2010, pp. 399-404

© (2012) Trans Tech Publications, Switzerland
doi:10.4028/www.scientific.net/AMM.164.506

Effect of anode size, membrane and membrane size on power generation and wastewater treatment in Microbial Fuel Cells

Guangyu Zhou [a], Yuichiro Yoshino [b], Takahiro Yamashita [c], Takahiro Sato [d] and Yasunori Kawagoshi [e]

Graduate school of science and technology, Kumamoto university, 2-39-1, Kurokami, Kumamoto, 860-8555, Japan

[a]syuukouu@gmail.com, [b]yuichiro.0708@softbank.ne.jp, [c]yamazi.3219@i.softbank.jp, [d]sato@tech.eng.kumamoto-u.ac.jp, [e]goshi@kumamoto-u.ac.jp

Keywords: MFCs, biomass energy, abiotic factor, wastewater treatment, orthogonal experiment

Abstract. Using wastewater as substrate, taking anaerobic sludge as inoculant, microbial fuel cells (MFCs) have emerged in recent years, which can generate electricity and accomplish wastewater treatment simultaneously. Based on the evaluation indexes of output voltage, coulombic efficiency, power density and TOC removal rate, three abiotic factors, anode size, membrane and membrane size, affecting MFC performance were investigated with an orthogonal experiment (L_4 (2^3)). The results show that the impact order of factors through analyzing the value "R" was "anode size > membrane > membrane size". The optimal set with these three factors for the performance of MFCs was big size anode, Naf-117 and big size membrane. Meanwhile, the high TOC removal rate (more than 90%) and high acetates consumed rate (100%) show the MFCs have strong ability of wastewater treatment. Cation exchange membrane Yumi-28 has compared ability of wastewater treatment and energy-production potential in MFC work.

Introduction

Microbial fuel cells (MFCs) have emerged in recent years as a promising yet challenging technology. MFC is considered to be a promising sustainable technology to meet increasing energy needs, especially using wastewater as substrate, which can generate electricity and accomplish wastewater treatment simultaneously, thus may offset the operational costs of wastewater treatment plant [1]. In MFCs studies the capacities of electricity generation and wastewater treatment are the primary focuses by researchers [2]. Recently, many efforts for improving the power generation were on the aspects of biotic factor and abiotic factor [3]. Compare with biotic factors, abiotic factors as reactor conduction, material of electrode, temperature, PH and so on are easy to control. But most of the investigations are not systematic. These factors always were considered individually in recently studies. There have been very few investigations into the interaction of various factors.

Orthogonal experimental design is one way to qualitatively analyze the correlations among the relevant variables at different levels through designing orthogonal table and statistic analysis. In this study, two-chamber MFCs reactors, which inoculated with digestion sludge, were set at 28 °C. Effects of anode size, membrane and membrane size on the MFCs performance were studied. The orthogonal table L_4 (2^3) was used in the experiment, anode size, membrane and membrane size were set as the investigation targets. Two levels were set for each factor [4]. Power density, coulombic efficiency (CE) and total organic carbon (TOC) removal rate were compared and analyzed to find out the optimum level and the optimum combination.

Materials and Methods

Reactor configuration. Two-chamber MFC reactors made with acrylic resin, which consist of two cuboids (volume 144ml, 40 mm (L) × 40 mm (W) × 90 mm (H)) for anode- and cathode- chambers, were used in this study. There were two kinds of apertures (8.04 cm^2, 15.39 cm^2) between the cuboids to install membranes. Plain carbon clothes (30 mm × 30 mm × 4 mm, 30 mm × 30 mm × 4 mm × 3) were boiled in 10% nitric acid for 1 hour and used as an anode electrode, and a platinum sheet (20 mm

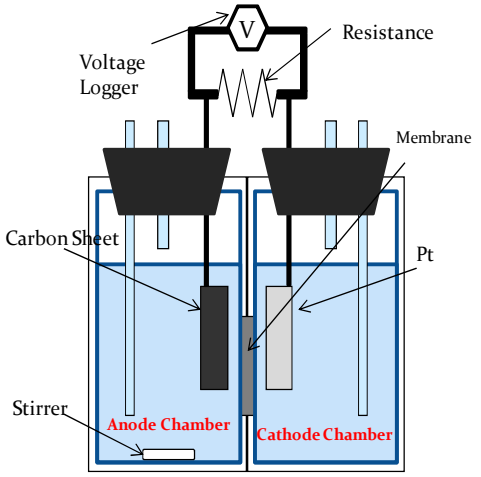


Figure 1. Schematic diagram of two-chambers MFC

× 20 mm × 0.1 mm) was used as a cathode electrode (Figure 1). The two kinds of membranes were used as follows: 1) Nafion 117 (Naf-117, proton exchange membrane (PEM), DuPont Co. Ltd., USA), 2) Yumigraftor BA28DGZ (Yumi-28, cation exchange membrane (CEM), Yuasa Membrane Systems Co. Ltd., Japan). Two chambers were connected by copper wire with 1 kΩ resistance. The reactors are operated at 28 °C. All reactors were operated in duplicate and more than 10 consecutive batch experiments were conducted.

Medium and MFC Operation. A synthetic medium for the anode chamber was prepared according to table 1 [5]. The pH of the medium was maintained by phosphate buffer. The medium was sterilized at 120 °C for 15 minutes before being filled into the anode chamber. The cathode chamber contained phosphate buffer [6]. There was an air pump (e-air 1000SB, GEX Co., Ltd., Japan) to supply oxygen (atmosphere, about 0.4 L/min) into the cathode chamber continually.

Table 1. Formula of synthetic wastewater

Media	CH_3COONa	Yeast extract	$(NH_4)_2 \cdot SO_4$	$MgCl_2 \cdot 6H_2O$	NaCl	$CaCl_2 \cdot 2H_2O$	vitamin solution	mineral solution
	0.82 g/L	0.5 g/L	1 g/L	0.2 g/L	0.2 g/L	0.045 g/L	1 mL/L	1 mL/L
Phosphate buffer	$NaH_2PO_4 \cdot 2H_2O$	$NaH_2 \cdot PO_4$						
	5.62 g/L	2.44 g/L						
Vitamin solution	Vitamin H	Pyridoxine HCl	Thiamine HCl	Nicotinic acid	Vitamin B_{12}	p-aminobenzoic acid		
	0.05 mg mg/L	0.3 mg/L	0.5 mg/L	0.5 mg/L	0.05 mg/L	0.3 mg/L		
Mineral solution	Na_2SeO_4	EDTA-2Na	$MnCl_2 \cdot 4H_2O$	$NiCl_2 \cdot 6H_2O$	$FeSO_4 \cdot 7H_2O$	$CoCl_2 \cdot 6H_2O$		
	0.001 mg/L	3.0 mg/L	0.1 mg/L	0.02 g/L	2 mg/L	0.1 mg/L		
	$ZnCl_2$	$CuCl_2 \cdot 2H_2O$	KI	$AlK(SO_4)_2$	H_3BO_3	$Na_2MoO_4 \cdot 2H_2O$		
	0.1 mg/L	0.01 mg/L	0.2 mg/L	0.1 mg/L	0.1 mg/L	0.02 mg/L		

The anode chamber was inoculated with 0.5 g digestion sludge and sparged by pure nitrogen gas for 10 min to get anaerobic condition. At the beginning of experiments, the circuit of MFC reactors were applied with a 500 mV in order to accelerate the start-up of MFC [7] and operated in batch mode. An electric voltage was continuously monitored by multiple data logger (midi LOGGER GL200A, GRAPHTEC Corp., Japan). When the voltage value decreased to below 50 mV in each batch, the contents of the both chambers were replaced with fresh ones to start next batch. The reactors were exposed to air for 10 minutes to restrain methane bacteria after the end of every batch [8]. The reactors were maintained in the incubators at 28 °C.

Orthogonal Experiments Designing. The quantitative evaluation and statistic analysis of the effects were investigated through orthogonal experiments designing [4]. Three relevant factors were investigated: anode size, membrane and membrane size. The orthogonal table L_4 (2^3) was designed. Two levels were set for each factor, anode sizes were 9 cm^2 and 27 cm^2, two kinds of membranes were Naf-117 (PEM) and Yumi-28 (CEM), and two levels of 8.04 cm^2 and 15.39 cm^2 were set for membrane sizes. The orthogonal experimental table is shown in Table 2.

Table 2. The factors and their levels in orthogonal experiments design

Level	Anode size [cm^2]	Membrane	Membrane size [cm^2]
a	9	Naf-117	8.04
b	27	Yumi-28	15.39

Analyses and MFC Performance Evaluation. The current-voltage characteristics were investigated by applying a constant voltage to the circuit using potentiostat (HAB-151A, Hokuto Denko Corp., Japan). The TOC and acetate concentrations were measured by TOC meter (TOC-V, Shimadzu Corp., Japan) and high performance liquid chromatograph (LC-10 AD, Shimadzu Corp., Japan), respectively.

In order to evaluate the MFC performance, power density (P_D) and *CE* were calculated as follows [9]:

$$P_D = I \times U / A \tag{1}$$

$$CE = (C_M / C_T) \times 100 \tag{2}$$

$$C_M = \int_{t=0}^{t} Idt \tag{3}$$

$$CT = (F \times n \times S \times V) / M \tag{4}$$

Where, P_D: power density (mW/m^2), I: electric current (A), U: electric voltage (mV), A: electrode area (m^2), *CE*: coulombic efficiency (%), C_M: measured coulomb value (C), C_T: theoretical coulomb value (C), F: Faraday constant (96485 C/mol), n: number of moles of electrons produced per mole of substrate ($n = 8$ for acetate in this study), S: substrate concentration (g/L), V: substrate volume (L), M: molecular weight of substrate (g/mol).

Results and Discussion

The MFCs voltage across a 1000 Ω resistor was automatically collected every 10 min using a data acquisition program and reached stable within 3 batches in all experiments. The results of maximum output voltage, CE and maximum power density with orthogonal design experiments were shown in table 3.

Table 3. Orthogonal design experiment result

Group		Factors			Maximum voltage	Culombic efficiency (%)	Power density (mW/m^2)
		Anode size	Membrane	Membrane size			
1		Small	Naf-117	Small	157.6	9.2	16.5
2		Small	Yumi-28	Big	131.7	7.6	22.2
3		Big	Naf-117	Big	189.1	10.2	5.4
4		Big	Yumi-28	Small	173.2	5.4	2.2
Maximum voltage	k1	144.65	173.35		165.4	Impact order	A>B>C
	k2	181.15	152.45		160.4	Optimum set	big:Naf-117:small
	R	36.5	20.9		5		
Culombic efficiency	k1	8.4	9.7		7.3	Impact order	B>C>A
	k2	7.8	6.5		8.9	Optimum set	small:Naf-117:big
	R	0.6	3.2		1.6		
Power density	k1	19.35	10.95		9.35	Impact order	A>C>B
	k2	3.8	12.2		13.8	Optimum set	small:Yumi-28:big
	R	15.55	1.25		4.45		

The results indicated that there was not evident relevance among the maximum voltage, CE and maximum power density. For instance the power density with reactor 2 was the highest but the maximum voltage and CE were lower than other reactors. It was because that there were many factors influence the performance of MFCs. We should analyze every result individually rather than using single result to deduce other results of MFCs performance.

Base on the range (R) reckoning, the impact order of factors for maximum voltage was as follows: anode size > membrane > membrane size. The performance with big size anode was better than with small size, with Naf-117 was better than with Yumi-28, and with small size membrane was slight better than with big size membrane but almost the same.

The impact order of factors for maximum CE was as follows: membrane > membrane size > anode size. The performance with small size anode was better than with big size anode that may because not only exoelectrogens bacteria [10] accumulated more on the big size anode but also other anaerobic digestion bacteria did. The anaerobic digestion bacteria, which also consumed the substrate, decreased the CE. With membrane Naf-117 was better than with Yumi-28, and with big size membrane was better than with small size.

The impact order of factors for maximum power density was as follows: anode size > membrane size > membrane. The performance with small size anode was better than with big size anode. That's because anode size is a denominator in power density calculation. Although the "density" of output power was lower with big size anode, the "totally" output power was not lower than with small size anode. With membrane Yumi-28 was a bit better than with Naf-117, and with big size membrane was better than with small size.

In our studies, TOC removal rates with these reactors are almost 90%. And the acid consume rates are 100% (data not shown).

The two of key points of MFCs are output voltage and the ability of wastewater treatment. Big size anode can attach more bacteria than small size anode. It means higher biological activity, smaller internal resistance, and more electronic transfer. Membrane type also affects the performance of MFCs. In previous studies CEMs had similar internal resistances with PEMs but the performance were about 6% lower than PEMs [11, 12]. We therefore presumed that different results would be obtained between the reactors with Yumi-28 and Naf-117 before beginning of experiments. However, there was no significant difference between them, the performance with Yumi-28 even a little higher than Naf-117. The CEMs such as Yumi-28 are conventional membrane widely used for electrodialysis, they have low thickness and good mechanical strength. The low thickness CEMs can reduce the internal resistance of MFCs reactor [12]. Thus the availability of other common cation-exchange membrane to MFC would be expected.

The bigger size membrane can reduce the internal resistance. Though the influence was smaller than anode size and the type of membrane, it is also an improvement factor in MFCs studies.

In conclusion the impact order of factors for the performance of MFCs was: anode size > membrane > membrane size. The optimal set with these three factors of their levels was: big size anode; Naf-117; big size membrane.

Acknowledgements

We thank Kedong Song and Wenzhong Liu for their insightful advice and valuable suggestions, Kato Michelle and Yuanzhi Liu for their helpful advice.

References

[1] N. Lu, S.G. Zhou, L. Zhuang, J.T. Zhnag, J.R. Ni, Electricity generation from starch processing wastewater using microbial fuel cell technology, Biochem. Eng. J. 43 (2009) 246–251.

[2] Z. He, S.D. Minteer, L.T. Angenent, Electricity generation from artificial wastewater using an upflow microbial fuel cell, Environ. Sci. Technol. 39 (2005) 5262–5267.

[3] T. Zhang, Y.L. Zeng, S.L. Chen, Improved performances of E. coli-catalyzed microbial fuel cells with composite graphite/PTFE anodes, Electrochemistry Communications. 9 (2007) 349-353.

[4] D.Y. Fan, Y.H. Chen, Probability theory and mathematical statistics, Zhejiang University Press, Zhejiang China, 1996, pp. 215.
[5] W.E. Balch, G.E. Fox, L.J. Magrum, C.R. Woese, R.S. Wolfe, Methanogens: Reevaluation of a unique biological group, Microbiology and Molecular Biology Reviews. 43 (1979) 260-296.
[6] H. Liu, B.E. Logan, Electricity generation using an air-cathode single chamber microbial fuel cell in the presence and absence of a proton exchange membrane, Environ. Sci. Technol. 38 (2004) 4040-4046.
[7] K. Shinogi, H. Ikeda, T. Ito, T. Watanabe, Effect of preparation for anodic biofilm by electrolytic stimulation on performance of microbial fuel cell, Japan Society on Water Environment. 43 (2009) 165, Japanese.
[8] Y. Ahn, B.E. Logan, Effectiveness of domestic wastewater treatment using microbial fuel cells at ambient and mesophilic temperatures, Bioresource Technology. 101 (2010) 469–475.
[9] K. Rabaey, G. Lissens, S. Siciliano, W. Verstraete, A microbial fuel cell capable of converting glucose to electricity at high rate and efficiency, Biotechnol. Lett. 25 (2003) 1531–1535.
[10] B.E. Logan, D. Call, S. Cheng, H.V.M. Hamelers, T.H.J.A. Sleutels, A. Jeremiasse, R.A. Rozendal, Microbial electrolysis cells for high yield hydrogen gas production from organic matter, Environ. Sci. Technol. 42 (2008) 8630–8640.
[11] J.R. Kim, S. Cheng, S. Oh, B.E. Logan, Power generation using different cation, anion, and ultrafiltration membranes in microbial fuel cells, Environ. Sci. Technol. 41 (2007) 1004-1009.
[12] R.Y. Hamid, S.M. Carverb, A.D. Christya, O.H. Tuovinenb, Cathodic limitations in microbial fuel cells: An overview, Journal of Power Sources. 180 (2008) 683-694.

© (2012) Trans Tech Publications, Switzerland
doi:10.4028/www.scientific.net/AMM.164.511

Research on the characteristics of gas geology in Yongshanqiao Mining Area, Jiangxi Province

Zhigen Zhao [1, a], Mingming Zhang [2, b], Jiaping Yan [3, c]

[1]School of Earth and Environment, Anhui University of Science and Technology, Huainan, China

[2]School of Earth and Environment, Anhui University of Science and Technology, Huainan, China

[3]School of Surveying, Anhui University of Science and Technology, Huainan, China

[a]zhgzhao@aust.edu.cn, [b]397146766@qq.com, [c]jpyan@aust.edu.cn

Keywords: Yongshanqiao Mining Area; gas emission; coal and gas outburst; tectonic control; metamorphism degree of coal.

Abstract: The coal and gas outburst is very serious in Yongshanqiao Mining Area of Jiangxi province, so it is of significance to research the characteristics of gas geology and their controlling factors. Based on the statistical analysis of gas data during coal exploration and coal mining, the regularity is revealed of the characteristics of gas geology in Yongshanqiao Mining Area. From east to west and from south to north, the relative gas emission rate and the absolute gas emission rate tend to increase, the frequency and intensity of coal and gas outbursts rise, the gas contents also tend to increase. The controlling factors of characteristics of gas geology in Yongshanqiao Mining Area are researched in this paper. The work reveals that: corresponding to characteristics of gas geology, the distribution characteristics of coal quality, the characteristics of geological structure and the lithology characteristics of the roof and the floor of the coal seams in Yongshanqiao Mining Area present regular changes, and are all favorable to gas generation and gas preservation. So, the characteristics of gas geology in Yongshanqiao Mining Area are the result of comprehensive effects by geological factors.

Introduction

Yongshanqiao Mining Area is located in the northeast of Jiangxi Province, 15 km to the south of Jingdezhen City. In this Mining Area, three major coal mines from east to west are Xiancha Coal Mine, Yangou Coal Mine and Yongshan Coal Mine [1]. These three coal mines are all high gas mines, and are highly coal and gas outburst-prone, so it is of significance to research the characteristics of gas geology and their controlling factors.

General Geology of the Mining Area

The geological structure of the studied area is an incomplete syncline. The north limb is incomplete because of the intersection by F8 thrust fault while the south limb is completely preserved. The synclinal axis is in the direction of N50-60°E and is tilted in the east. The secondary folds are not well developed [2-3] (Fig. 1). The dip angles of coal bearing strata are considerably steep, about 45-75°, including even partial strata which are inverted.

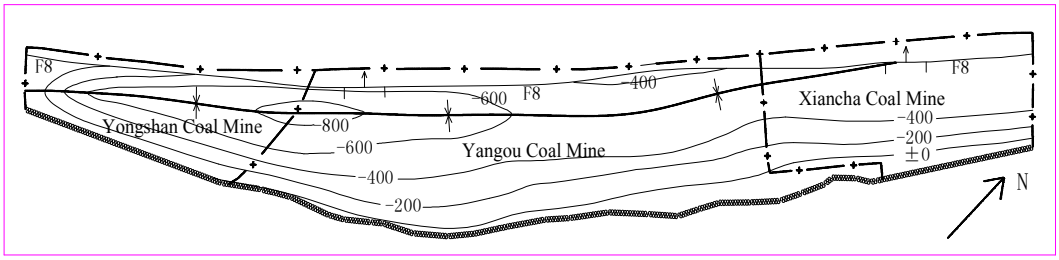


Fig. 1 Sketch map of geological characteristics in Yongshanqiao Mining Area

From bottom to top, the strata of the studied area include: Shuangqiaoshan Group (Pt_2sh) of the Middle Proterozoic; Yanguan Formation (C_1y) of the Lower Carboniferous and Huanglong Formation (C_2h) of the Upper Carboniferous; Chuanshan Formation (P_1c) of the Lower Permian, Qixia Formation (P_2q) and Maokou Formation (P_2m) of the Middle Permian, Longtan Formation (P_3l) and Changxing Formation (P_3c) of the Upper Permian; Daye Formation (T_1d) of the Lower Triassic, Anyuan Formation (T_3a) of the Upper Triassic; Menkoushan Formation (J_1m) of the Lower Jurassic; Shixi Formation (K_1s) of the Lower Cretaceous; Quaternary (Q). Within these strata, the Longtan Formation of the Upper Permian and the Anyuan Formation of the Upper Triassic are the coal-bearing strata, and the coal seams in Anyuan Formation are the major mining objects [3-4]. Anyuan Formation is unconform above the Daye Formation (T_1d). The total thickness of coal bearing strata of Anyuan Formation is 300-1000m, in which the No. 1 to No. 15 coal seams are developed, most coal seams being minable, and some being partially minable. Based on the mark layers, the Anyuan Formation (T_3a) is sub-divided into Baiyichong Stage (T_3a^1), Xiakou Stage (T_3a^2), Jingkenshan Stage (T_3a^3) and Malashan Stage (T_3a^4) [5].

Characteristics of Gas Geology

The statistical analysis of such gas data during coal exploration and coal mining as gas emission, coal and gas outburst and gas content shows the regular changes of the characteristics of gas geology in Yongshanqiao Mining Area from east to west and from south to north.

Characteristics of gas emission

Along the strike of coal seam, the statistical results about gas emission of Xiancha Coal Mine, Yangou Coal Mine, Yongshan Coal Mine are shown in Table 1. The data in Table 1 show the noticeable increase of gas emission from east to west.

Table 1. Characteristics of gas emission in Yongshanqiao Mining Area

Coal Mine	Yongshan	Yangou	Xiancha
Number of samples	79	21	33
Average elevation (m)	-257	-231	-294
Mean value of Q (m^3/min)	3.452	2.271	2.213
Mean value of q (m^3/t)	26.509	14.312	14.644
Trend value (-250m elevation) of Q (m^3/min)	3.243	2.550	1.840
Trend value (-250m elevation) of q (m^3/t)	25.532	16.170	12.707

Note: Q: Absolute Gas Emission Rate; q: Relative Gas Emission Rate

Along the dip of coal seam, Fig. 2, 3, 4 are the statistical information about gas emission of representative mining districts at Xiancha Coal Mine, Yangou Coal Mine and Yongshan Coal Mine. From these figures, the absolute gas emission and the relative gas emission increase with the increase of depth along the dip of coal seam.

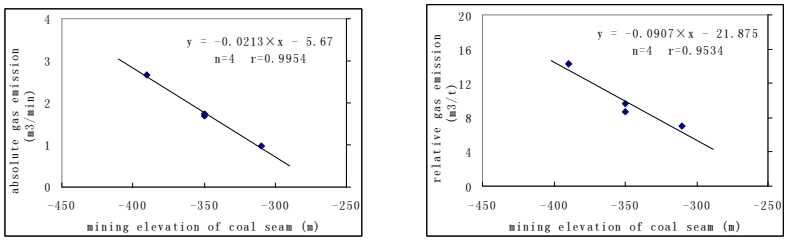


Fig. 2 Gas emission of No. 6 Coal Seam at Xiancha Coal Mine's No. 30 Mining District

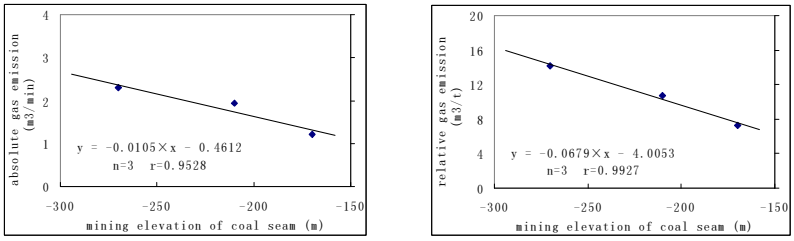


Fig. 3 Gas emission of No. 5 Coal Seam at Yangou Coal Mine's No. 25 Mining District

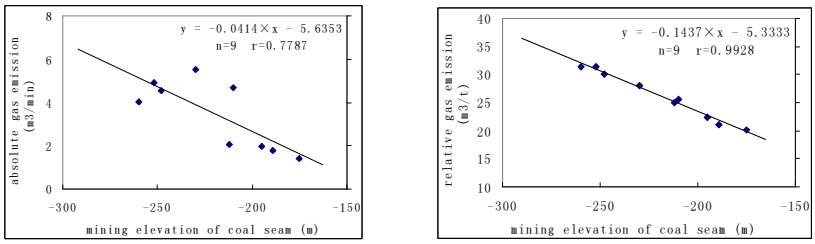


Fig. 4 Gas emission of No. 3 Coal Seam at Yongshan Coal Mine's No. 26 Mining District

Characteristics of coal and gas outburst

The statistical results about coal and gas outburst of Xiancha Coal Mine, Yangou Coal Mine, Yongshan Coal Mine are shown in Table 2. Table 2 shows the noticeably increased likelihood of coal and gas outburst from east to west according to the data of the increased outburst number, the increased maximum value of outburst coal and gas, and the increased number of super large outburst.

Table 2. Characteristics of coal and gas outburst in Yongshanqiao Mining Area

Coal Mine	Yongshan	Yangou	Xiancha
Number of outburst	98	47	13
Mean value of outburst coal (t)	206	248	91
Maximum value of outburst coal (t)	3988	2400	587
Maximum value of outburst gas (1×10^4 m^3)	16.7	15	1.5
Maximum elevation of outburst (m)	+60	-60	-35
Number of super large outburst	4	1	0

Table 3, 4 are the statistical information about coal and gas outburst of Xiancha Coal Mine and Yongshan Coal Mine in different mining depths. From these tables, the intensity of coal and gas outburst increases as the mining depth of coal seam increases.

Table 3. Comparison of coal and gas outburst in different mining depth at Xiancha Coal Mine

mining depth (m)	Mean value of outburst coal (t)	Maximum value of outburst coal (t)	Maximum value of outburst gas (m^3)
＜300	30	100	806
＞300	162	587	15000

Table 4. Comparison of coal and gas outburst in different mining depth at Yongshan Coal Mine

mining depth (m)	100~200	200~300	300~400	400~500
Mean value of outburst coal (t)	135.1	209.6	292.0	608.6

Characteristics of gas content

Comprehensive and detailed analysis about gas content in Yongshanqiao Mining Area is not available due to the few data of gas content collected from exploration and development of Yongshanqiao Mining Area. Thus, only the relationships between gas content and buried depth of No. 7 coal seam group at Yangou Coal Mine and at Yongshan Coal Mine are established (Fig. 5, 6). Based on the regression analysis of Fig. 5, 6, the gas content increases as the buried depth of coal seam increases.

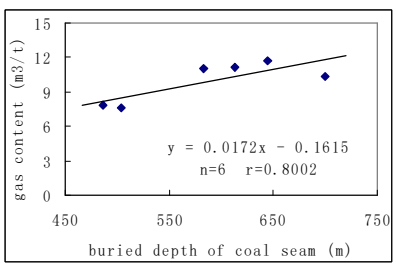


Fig. 5 Relation between gas content and buried depth of No. 7 coal seam group at Yangou Coal Mine

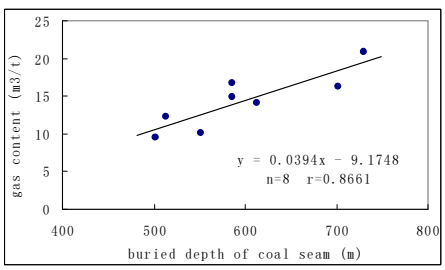


Fig. 6 Relation between gas content and buried depth of No. 7 coal seam group at Yongshan Coal Mine

And also, based on the regression analysis of Fig. 5, 6, it is revealed that: within the scope of statistical data and at the same buried depth of coal seam group, the gas content of Yangou Coal Mine is lower than that of Yongshan Coal Mine (Table 5). Furthermore, the incremental gradient of gas content at Yangou Coal Mine (1.72 m^3/t / 100m) is lower than that of Yongshan Coal Mine (3.94 m^3/t / 100m).

Table 5 Trend value of gas content of No. 7 coal seam group

Buried depth (m)	500	600	700
Trend value of gas content at Yangou Coal Mine (m^3/t)	8.44	10.16	11.88
Trend value of gas content at Yongshan Coal Mine (m^3/t)	10.53	14.47	18.41

Discussion

From the analysis above, the characteristics of gas geology display regularity of change in Yongshanqiao Mining Area. And, the geological factors controlling the regularity of gas geology shall be analyzed in the following part.

From the angle of gas generation

Taking No. 8-1 coal seam as an examples, the volatile matter (V_{daf}) is obviously decreased from east to west and from south to north in Yongshanqiao Mining Area (Fig. 7). Corresponding to the change of V_{daf}, the coal types are regularly changed. There are coking coal or slim coal at Xiancha Coal Mine, slim coal, lean coal or anthracite at Yangou Coal Mine, and anthracite at Yongshan Coal Mine [6].

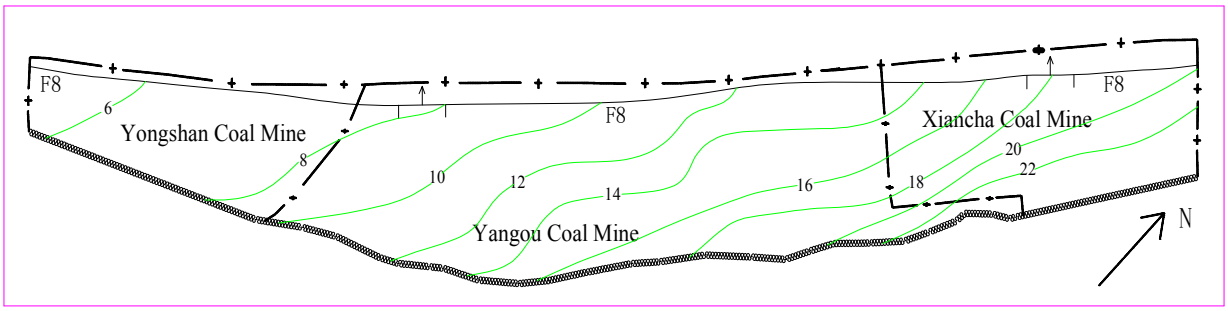


Fig. 7 V_{daf} distribution trend of No. 8-1 coal seam in Yongshanqiao Mining Area

The metamorphism degree of coal and gas storage are closely related. The higher the metamorphism degree of coal is, the more the coal's gas productivity is [7]. The trend of decreasing V_{daf} of coal from east to west and from south to north in Yongshanqiao Mining Area, that is to say, the trend of increasing metamorphism degree of coal, reflects the trend of increasing gas that is produced.

From the angle of gas preservation

Firstly, about the structure of the whole Mining Area of Yongshanqiao, it is an incomplete syncline extending in the direction of NE-SW. The north limb is incomplete because of the intersection by F8 thrust fault while the south limb is completely preserved, and the F8 thrust fault is roughly parallel to the synclinal axis [2, 4]. So, the closed structure in Yongshanqiao Mining Area is formed including the F8 thrust fault and the incomplete syncline. In this closed structure, a large amount of gas is easily preserved [8].

In terms of the internal structure characteristics of Yongshanqiao Mining Area, the complexity of structure increases from east to west [6]. Compared with Xiancha Coal Mine in the east, the Yongshan Coal Mine in the west is more complex concerning in geological structure. According to the report [9], averagely, there is a fault in every 2830 m^2 of mining area in Yongshan Coal Mine while one fault in every 71400 m^2 mining area in Xiancha Coal Mine. The increasing complexity of geological structure from east to west is favorable to the preservation of gas and is prone to the coal and gas outburst [10].

Secondly, about the surrounding rock of coal seams, in Yongshanqiao Mining Area, the roof and floor of the main coal seams consist of multilayer of mudstone and siltstone. These rocks are tight, so the permeability of the roof and floor is low, which provides the favorable conditions for gas storage [9]. On the other hand, the thickness of main coal bearing stages (Baiyichong Stage and Xiakou Stage) at Xiancha Coal Mine is less than that at Yangou Coal Mine, and also, the thickness at Yangou Coal Mine is less than that at Yongshan Coal Mine. At the same time, the grain size of rock in the coal bearing stages tend to be smaller from east to west. The trend of thicker coal bearing stages and smaller grain size of rock is more conducive to the preservation of gas [5].

Finally, about coal quality, the metamorphic degree of coal has considerable influence on coal's gas adsorption capacity. The coal's gas adsorption capacity increases from medium rank bituminous to anthracite [7]. The statistics based on the data from more than 160 mining area in China reveal the enveloping line relationship between the coal rank and gas content in coal reservoir [11], that is, with the increase of coal rank from brown coal to the early stage of anthracite, the maximum gas content of coal seam increases, the area with high gas content corresponds to the area with high rank coal. However, with the increase of coal rank from middle stage to later stage of anthracite, the methane adsorption capacity of coal seam decreases, and correspondingly, the maximum gas content of coal seam sharply decreases. As far as the Yongshanqiao Mining Area is concerned, the coal rank is from coking coal to anthracite, increasing from east to west and from south to north. And based on the characteristics of distribution and variation of coal rank, the increase of coal rank means more gas may be absorbed according to the coal's adsorption capacity.

In Yongshanqiao Mining Area, most of the coal body structures are destroyed and tectonic coals are widely distributed. The coals are soft and fragile, most of them are in the form of powder while some are broken into fragments [6]. Usually, the consistent coefficient of coal and the index of coal's Initial Speed of Diffusion are used to reflect the risk of coal and gas outburst [12-13]. Due to the coal's breakage, the consistent coefficient of coal (f value) is small, usually in the range of 0.15 to 0.50, and index of coal's Initial Speed of Diffusion (ΔP) usually larger than 10. The characteristic of coal quality is favorable to the preservation of gas and is conducive to the coal and gas outburst [14-15].

Conclusion

Based on the above analysis and discussion, some conclusions about the characteristics of gas geology and their controlling factors are drawn as follows:

The characteristics of gas geology display regularity of change in Yongshanqiao Mining Area. From east to west and from south to north, the gas emissions increase noticeably, the frequency and intensity of coal and gas outburst increase, and the gas contents also increase.

The characteristics of gas geology in Yongshanqiao Mining Area are the result of comprehensive effects by geological factors. In terms of gas generation of the studied area, from east to west and from south to north, the metamorphism degree of coal tends to increase, which reveals that more gases are generated. In terms of gas preservation, corresponding to characteristics of gas geology, the tectonic characteristics, rock property of roof and floor of coal seams, the coal qualities of coal seams in Yongshanqiao Mining Area present regular changes, and are all favorable to gas generation and gas preservation.

Acknowledgments

The research is financially supported by the National Natural Science Foundation of China (No. 41172138) and by the special fund project of Jiangxi Energy Bureau (No. 20100730). The authors wish to thank Xiuyi Tang and Xing Liu from Anhui University of Science and Technology for their advice. The authors also express our gratitude to the the technical personnels from Jiangxi Exploration Institute of Coalfield Geology, Jiangxi Leping Coal Mining Bureau for their kind help.

References

[1] G Guang, Existing Problems in the compilation and usage of Gas Geologic Map and its countermeasures, Jiangxi Coal Science and Technology, 32(2010):(3)49-50

[2] Y Y Wang, Opinions on the reformation of mining method in Leping Yongshanqiao Coal Mining Area, Coal Mining Technology, 8(2003):(3):36-37

[3] E Y Kuang, Y L He, X Q Zhang, Discussion about surface subsidence and treatment of water disaster in Yongshanqiao Mining Area, Jiangxi Coal Science and Technology, 26(2004):(1):36-37

[4] H Zou, Discussion about gas drainage and utilization in Yongshanqiao Mining Area, Modernization of Coal Mine, 17(2008):(3)82-83

[5] J P Yan, Palaeogeographic evolution and coal accumulation of Late Triassic in Northeast Jiangxi Province, Journal of Huainan Mining Institute, 14(1994):(2)1-5

[6] C X Peng, M Wang, H Chen, H Y Luo, Research on the $\Delta h2$ working face prediction limit of coal and gas outburst in Yongshanqiao Mining Area, Jiangxi Coal Science and Technology, 29(1997): (4)41-44

[7] Z M Zhang, Gas Geology, China University of Mining and Technology Press, Xuzhou, 2009, pp. 21-28, 121-134

[8] B Jiang, Z H Qu, G G X Wang, M Li, Effects of structural deformation on formation of coalbed methane reservoirs in Huaibei coalfield, China, International Journal of Coal Geology, 82(2010): 175-183

[9] W X Wu, Y D Chen, H B Zhu, Regularity of gas distribution in Leping Mining Area, Coal, 19(2010):(12)60-62

[10] T J Zhang, S X Ren, S G Li, T C Zhang, H J Xu, Application of the catastrophe progression method in predicting coal and gas outburst, Mining Science and Technology, 19(2009):(4)430–434

[11] Y Qin, X H Fu, J P Ye, D Y Lin, S H Tang, G Z Li, Geological controls and their mechanisms of coal-reservoir petrography and physics of coalbed methane occurrence in China, Journal of China University of Mining and Technology, 28(1999):(1)14-19

[12] D J Lei, C W Li, Z M Zhang, Y G Zhang, Coal and gas outburst mechanism of the "Three Soft" coal seam in western Henan, Mining Science and Technology, 20(2010):(5)712–717

[13] D Charrière, Z Pokryszka, P Behra, Effect of pressure and temperature on diffusion of CO2 and CH4 into coal from the Lorraine basin (France), International Journal of Coal Geology, 81(2010):373-380

[14] The State Administration of Work Safety, Regulations of coal and gas outburst prevention, Coal Industry Press, Beijing, 2009, pp. 4-18

[15] D M Wu, Y M Zhao, Y P Cheng, F H An, ΔP index with different gas compositions for instantaneous outburst prediction in coal mines, Mining Science and Technology, 20(2010):(5)723–726

© (2012) Trans Tech Publications, Switzerland
doi:10.4028/www.scientific.net/AMM.164.517

Enhancing Biological Nutrient Removal from Real Domestic Wastewater by Using Iron Shavings

Zi Wang [a], Zhe Chen [b], Hongwu Wang [c], Luming Ma [d]

National Engineering Research Center for Urban Pollution Control, State Key Laboratory of Pollution Control and Resources Reuse, Tongji University, Shanghai 200092, China
[a]wangziandllp@gmail.com, [b]chenzhedb@163.com,
[c]wanghongwu@tongji.edu.cn, [d]lumingma0708@yahoo.com.cn

Keywords: iron shavings; enhancement; biological treatment; real domestic wastewater

Abstract. Feasibility of enhancing nutrient removal in municipal sewage plant by using iron shavings in conventional biological treatment reactor was evaluated. Results of 209-days bench-scale test indicate that this method is feasible in practice. Compared to control test, TN and TP removal was increased 8.72 % and 57.83 %, respectively，by adding 400 g iron shavings in 75 L biological reactor. Effluent TP concentration could attain level 1A (0.5 mg L^{-1}) of China's urban sewage treatment plants discharge standards; Total iron concentration in effluent was 0.249 mg L^{-1} and iron consumption rate was 762.7 mg d^{-1} during stable period. The enhancing effect of iron shaving on nutrient removal is easy to achieve and low-cost. It is worth investigating in a deep-going way.

Introduction

Nowadays, influent water quality of many sewage treatment plants in south China has the characteristic of low C/N ratio and relatively high TP concentration and it is difficult to treat TN and TP to meet the Chinese national discharge standard of pollutants for municipal wastewater treatment plant (GB 18918-2002). Many enhanced technology were developed to solve this problem, such as A_2O/BAF process[1], UCT-type MBR process[2], modified step feed process [3],etc. But most of these technologies need complicated operation and precise control, which limited their application. ZVI pre-treatment, especially iron turnings or shavings of 38CrMoAl steel, have been successfully used for enhancing biological treatment of industrial wastewater by our research group [4, 5]. This study addresses the feasibility of enhancing the nutrient removal of municipal sewage plant by putting iron shavings (with iron content of 95.20-96.95%) directly in conventional biological reactor. Because HRT used in conventional municipal sewage plant is usually short (3~4 h) and fixed, the main emphasis of this research was focused on long-term effectiveness of iron on nutrient removal. Bench-scale Test of 209 days was conducted to evaluate long-term effectiveness.

Methods and materials

The experimental set-up is shown in Fig. 1. There were two cuboid rectors made of glass reinforced plastic with 75L available volume. 25 L wastewater was filled in each cycle. A plastic frame (20×20×20 cm and full of small holes with Demeter of 2 cm in all faces) including 400 g iron shavings was placed in reactor A. Reactor B was control reactor. The frame rested between the two aerator pipes so that air bubble did not contact with iron shavings directly, but the aeration turbulence would make the iron shavings and microbe contact frequently. The operation of the reactor was automatically controlled by three automatic clock switches through electromagnetic valve. Operation mode was same as that used in the sewage treatment plant (30 min for filling, 45 min for anoxic, 100min for aeration, 45min for settling and 30 min for decanting).

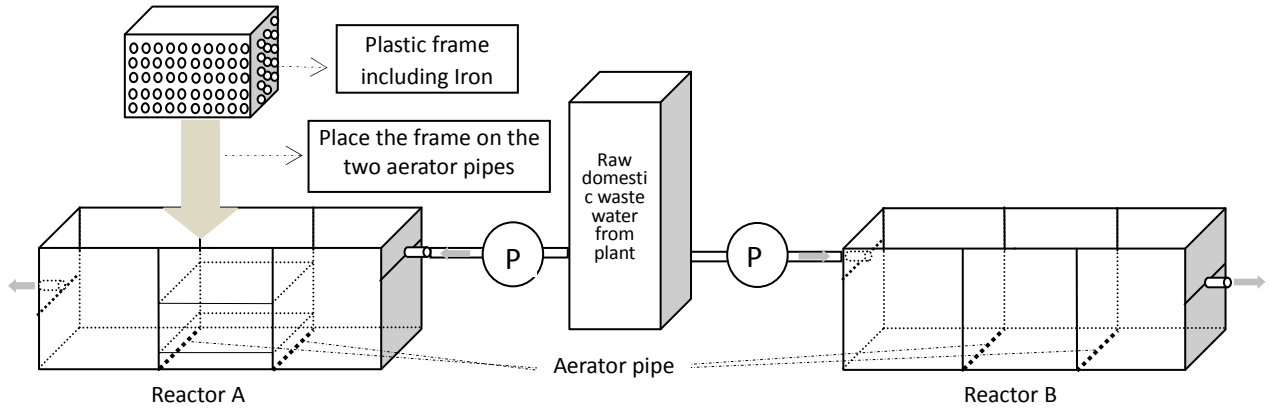


Fig. 1 Bench-scale experimental set-up

The feed-water was real domestic wastewater directly taken from catchment tank of the sewage plant and its characteristics were shown in Table 1. DO was 2~4 mg L^{-1} when aerating. SRT was 20 d. Initial activated sludge was taken from thickened sludge tank in the sewage plant mentioned above and initial MLVSS concentration in both reactors were both kept at 2800±200 mg L^{-1}. Plastic frame containing iron shavings was added in reactor A after two rectors had been operated parallelly for 20 days. Samples were taken at set time each day for quantitative analysis of COD, NH_3-N, NO_3^--N, NO_2^--N, TP, TN and PH. MLVSS concentration was tested once a week.

Table 1 Characteristics of feed-water (mg L^{-1}**)**

Index	NO_3^--N	NO_2^--N	NH_3-N	TN	TP	Total iron	COD	PH
Range	0.37-2.34	0.18-0.35	13.38-36.92	12.63-42.64	0.57-6.17	0.45-1.94	31-271	6.26-7.62
average	1.22	0.21	25.35	28.18	2.25	1.20	105	7.44

COD, NH_3-N, NO_3^--N, NO_2^--N, TP, TN and MLVSS were tested immediately after sampling. All chemicals used in analysis were of analytical grade. Purkinje General UV spectrophotometer (TU1810) was used for measurements of light absorption. The test items and process were carried out following standard methods.

Results and discussions

In first 20 days of running, parallel operation in the two reactors was kept. Iron shavings were added in reactor A at day 21. HRT was 4 h in first 60 days and then be shortened to 3 h in next 149 days because the temperature was higher than 20 ℃,which mode was the same as that used by the sewage plant. Although the temperature rose from 17 ℃ to 30 ℃ during experimental period, no significant change of effluent quality was observed. Therefore effect of temperature was not discussed in this paper. Iron shavings would be consumed slowly during operation, but it was not observed that iron shavings were exhausted during actual 209 days running-time.

TN concentration profiles during the whole experimental period are shown in Fig. 2. As can be seen, when influent TN concentration was 12.63~42.64 mg L^{-1} (30.32 mg L^{-1} in average), effluent TN concentration was 11.15~25.16 mg L^{-1} (17.21 mg L^{-1} in average) in reactor A and 10.51~25.62 mg L^{-1} (17.66 mg L^{-1} in average) in reactor B, respectively. However, it was observed that a difference between the two reactors gradually became distinct after 140 days, although the operation condition kept the same as before. Effluent TN concentration in reactor A was 1.54 mg L^{-1} (8.72%) lower in average than that in reactor B during the period from 140 to 209 day. The result indicates that adding iron can enhance TN removal after long time running. This enhancement effect may attribute to adaptability of microbes [6].

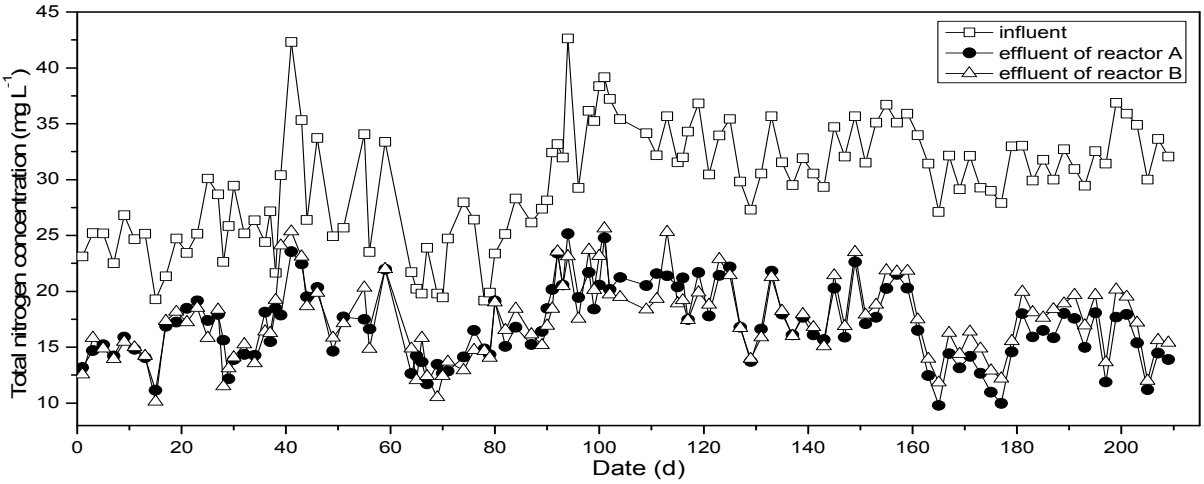


Fig. 2 TN concentrations in influent and effluent

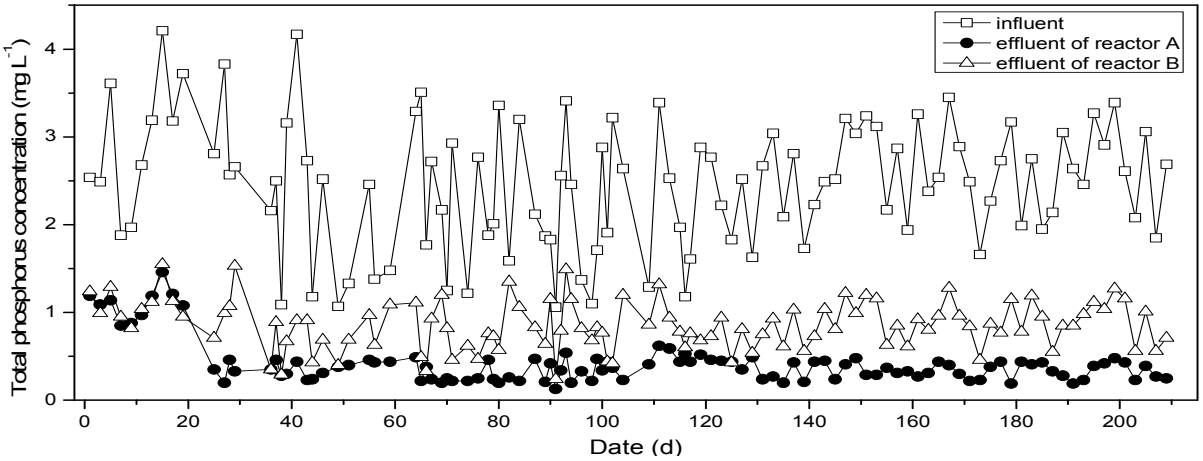


Fig. 3 TP concentrations in influent and effluent

TP concentration profiles are shown in Fig. 3. As can be seen, after putting iron shavings in reactor A, effluent TP concentration of reactor A was 0.35 mg L^{-1} (in average) which had attained level 1 A (0.5 mg L^{-1}) of China's urban sewage treatment plants discharge standards and was 57.83 % lower than that of reactor B which was 0.83 mg L^{-1} (in average). Furthermore, effluent TP concentration fluctuation of reactor A was smaller than that in reactor B during running, which indicates that adding iron is helpful for stabilization of effluent TP concentration. The enhancement effect of iron on TP removal is always stable during experimental period. So conclusion may be drawn that iron enhancing TP removal in biological process is feasible and stable in the long term.

Total Iron Concentration (TIC) in reactors had different change with running. When influent TIC was average 1.200 mg L^{-1}, effluent TIC was average 0.249 mg L^{-1} and 0.181 mg L^{-1} for reactor A and B, respectively. They were both lower than that in influent. It means that iron corrosion products would gradually accumulate in reactor. Concentration of total iron that suspended in reactor A increased quickly to 1052.5 mg L^{-1} (average) in 40 days and then it became stable. If iron corrosion products adsorbed to cell surfaces, formation of crusts would potentially limit the diffusion of substrates and nutrients to cell, which may lead to stagnation of cell metabolism [7]. But it was not observed that TP or TN removal efficiency decreased in the long term, so 1052.5 mg iron L^{-1} in biological reactor with 3800 mg MLVSS L^{-1} may be safe for biological treatment process.

Table 2 The overall Balance of Total Iron during stable operation period

Iron balance	Reactor A		Reactor B		Volume ($L\ d^{-1}$)
	Concentration ($mg\ L^{-1}$)	Total ($mg\ d^{-1}$)	Concentration ($mg\ L^{-1}$)	Total ($mg\ d^{-1}$)	
In from influent	1.2	240	1.2	240	200
Out from effluent	0.249	49.8	0.181	36.2	200
Out from sludge	1052.5	1052.5	202.9	202.9	1
Iron consumption	-	762.7	-	0.9	-

The overall balance of total iron during last 150 days was calculated (Table 6). As can be seen, the iron consumption was 762.7 mg d^{-1} in stable operation. On the fact that 200 L wastewater was treated each day, iron consumption rate was described as 3.81 mg iron L^{-1} water, too. Compared to total ZVI quantity (400 g), this iron consumption rate was low. Microbe can restrain iron corrosion [8], so iron corrosion rate was not fast. It means that iron shavings did not need to be replaced frequently in practical applications.

Summary

Iron shavings enhancing TN and TP removal in biological reactor is feasible in a long term. Effluent TN concentration was 1.54 mg L^{-1} (8.72 %) lower in average than that in control reactor during the period from 140 to 209 day. Effluent TP concentration during experiment was 0.35 mg L^{-1} (in average) which had attained level 1 A (0.5 mg L^{-1}) of China's urban sewage treatment plants discharge standards and was 57.83 % lower than that of control reactor. Iron consumption rate was 762.7 mg d^{-1}, which was very low. Concentration of iron released to reactor from iron corrosion increased quickly to 1052.5 mg L^{-1} (average) in 40 days and then became stable, which did not affect effluent quality. This method is practicable is worth investigating in a deep-going way.

Acknowledgement: This study has been financially supported by the funds of National 863 plans (2009AA063902) and Shanghai Science and Technology Base Project (09dz2202300)

References

[1] Ding, Y.W., et al., Removal of nitrogen and phosphorus in a combined A(2)/O-BAF system with a short aerobic SRT. Journal of Environmental Sciences-China, 2006. **18**(6): p. 1082-1087.
[2] Lee, H., J. Han, and Z. Yun, Biological nitrogen and phosphorus removal in UCT-type MBR process. Water Science and Technology, 2009. **59**(11): p. 2093-2099.
[3] Ge, S.J., et al., Enhanced nutrient removal in a modified step feed process treating municipal wastewater with different inflow distribution ratios and nutrient ratios. Bioresource Technology, 2010. **101**(23): p. 9012-9019.
[4] Ma, L.M. and W.X. Zhang, Enhanced biological treatment of industrial wastewater with bimetallic zero-valent iron. Environmental Science & Technology, 2008. **42**(15): p. 5384-5389.
[5] Fan, J.H. and L.M. Ma, The pretreatment by the Fe-Cu process for enhancing biological degradability of the mixed wastewater. Journal of Hazardous Materials, 2009. **164**(2-3): p. 1392-1397.
[6] Rawlings, D.E., Characteristics and adaptability of iron- and sulfur-oxidizing microorganisms used for the recovery of metals from minerals and their concentrates. Microbial Cell Factories, 2005. **4**.
[7] De Windt, W., et al., Cell density related H-2 consumption in relation to anoxic Fe(0) corrosion and precipitation of corrosion products by Shewanella oneidensis MR-1. Environmental Microbiology, 2003. **5**(11): p. 1192-1202.
[8] Potekhina, J.S., et al., Role of microorganisms in corrosion inhibition of metals in aquatic habitats. Applied Microbiology and Biotechnology, 1999. **52**(5): p. 639-646.

Keywords Index

3D FEM 425

A

a-Si:H/c-Si Heterojunctions 158
Abiotic Factor 506
Acoustic Impedance Transfer 227
Adaptive Optics 409
Add-On Bioenergy 52
Adsorption 154, 297
AFM 284
Aggregation Number 146
AIC Criterion 467
Air Compressor 334
Alkali-Free Glass 405
Aluminum 268
Aluminum Isopropoxide 21
Analysis 451
Analysis of Mechanics 322
Analytic Hierarchy Process (AHP) 7
Anionic Gemini Surfactant 146
Anode Material 293
Anodic Aluminum Oxide 223
ANSYS/LS-DYNA 3
Anti-Corrosion Materials 306
Application 128
Asynchronous Motor 348
Avoidance 272

B

Bacterial 103
Bacterial Transport 182, 231
Balance 383
Ball Milling 65, 268
Bamboo Products 89
Benzothiophene 251
$BiFeO_3$ 115
Bio-Deposition 103
Biodegradation Performance 194
Biodeposition 107
Biological Materials 128
Biological Materials Energy 218
Biological Treatment 186, 517
Biomass Energy 30, 506
Biomaterial 487
Biomechanics 383
Bottom Ash 289
Boundary-Layer Theory 366
Breathing Crack 338
Broken Jib Accident 322
BST 47
Bucket Chain Conveyor 497
Building Energy 77
Building Shading Materials 85
Building Shape Coefficient 93
Burning Time 52
BZT 47

C

CAD/CAE 317
Cadmium Material 272
Calculating Clearance Magnitude Method 366
Carbon 17, 207
Carbon Coated Nanoparticles 17
Carbon Emission 302
Carbon Nanotubes (CNT) 69
Carbon Steel 33
Case-Based Reasoning (CBR) 7
Catalytic Mechanism 21
Cathode Material 190
Ceramics for Daily Use 317
Changchun City 302
Characteristics of Wave Energy 460
Characterization of the Films 284
Chemical Reactions 396
Chloride Diffusion 107
Circulation Dynamic System 482
Cleaning Machine 497
CMC 146
Co-Precipitation Method 162
Coal Mine Water Storage 497
Coal Outburst 501, 511
Coating 174
Cold Hardening 392
Cold Pulling 392
Complex Radius Vector 227
Composite Asphalt Pavement 26
Composite Hydrogel 154
Compressive Strength 492
Concrete 107

Condition Monitoring 73
Conditional Experiment 111
Confined Explosions 396
Constant Entropy Assumption 396
Constant Pressure Control 362
Continuously Reinforced Concrete 26
Cooling 214
Corrsion Inhibition 33
Coupling Analysis 338
Crack Propagation 338
Cracked Concrete 103
Cracking Analysis 26
Crane 348
Critical Load Position 26
Curing System 492
Cyanophenyl 478
Cyclization 280, 478
Cylindrical Vibrator 441

D

Dacromet 306
DD6 3
Deformable Mirror 409
Design 451
Development Trend 218
Diarylethene 150, 166, 178, 235, 239, 243, 247, 251, 255, 259, 280, 478
Dielectric Property 47
Differential Analysis 162, 170
Disassemble Machine 344
Dispersion 194
Display 352
Dissipation Model 482
Distributed Virtual Source 227
Drought 460
Dynamic Characteristics 421
Dynamic Fracture Toughness 446
Dynamic Load 446
Dynamic Modelling 467
Dynamic Simulation 473
Dynamic System 451
Dynamic System of Wave Energy 460
Dynamic Waves 356
Dynamic Wind Loads 433
Dynamics Behaviors 425

E

Efficiency 263
Eisenia fetida 272
Electric Total Loss 348
Electrical Control 497
Electrohydrodynamic Atomization 487
Electroless Copper Deposition 59
Electrolysis 263
Electron Transport Properties 120
Energy 218
Energy Consumption 85
Energy Efficiency 85
Energy Harvest 441
Energy Saving 348
Energy-Saving Materials 93
Energy-Saving Rate 93
Engine 429
Enhancement 186, 517
Error Learning 272
ESA/AMPS Copolymer 194
ESR 69
Ether/Acetone Extractives 30
Eucalyptus urophydis 30
Exhaust Gas Oxygen Sensor 467
Explosive Charge Volume Ratio 396
Extended Range 371

F

Failure 401
Fall 383
Faults Diagnosis 334
Feasibility Analysis 482
FEM 322
Ferroelectric Properties 47
Film 223
Finite Difference Analysis 107
Finite Element (FE) 379
Finite Element Method (FEM) 414, 456
Finite Element Model (FEM) 313
Flanges Contact 326
Fluctuating Pressure 433
Fluid Flow Analysis 124
Fluid Mechanics 409
Fluorescence 178, 235, 239, 243, 247, 251, 255, 259, 478
Fluorescence Switches 166
Fluorescence Switching 150, 280

Fluorescent 97
Fracture Time 446
Fuel 52

G

Gait Self-Balancing 383
Gantry Crane 456
Gap 375
Gas Emission 511
Gas Outburst 501, 511
Gearbox 73
Geobacillus sp. 182, 231
Geopolymer Concrete 492
Germanium 207
Glucose 268
Graded Crushed Stone 81
Granite Materials 42
Granular Activated Carbon (GAC) 297
Green's Function 120
Grinding 42
Grinding System 330

H

Hammerstein Model 467
Hardness 55
Healing 103
Heat Insulating Materials 170
Heat Treatment 132
Heavy Metal Ion 154
Hedging 356
Helicid 487
Hexagonal Boron Nitride Nanoribbons 120
High Pedestal Jib Crane 322
High Pressure Grouting Machine 317
Holographic Optical Recording 235
Horizontal Pipes Connector 326, 421
Horizontal Type 317
Hot-Dip Zinc 306
HVOF 55
Hydraulic Cylinder 392, 421
Hydraulic Prop 344
Hydromechanics 344

I

Image Processor 97
Impeller 375
Impeller Assembly Clearance 366
Impeller Shaft Structure 375
Incineration 289
Industrial Energy Consumption 302
Inert Coating SnO_2 132
Infrared Imaging 42
Injury 128
Instability 387
Interface States 158
Iron Shavings 186, 517
Isostatic Pressing Method 207
Isoxazole 243

J

Jacket Platform 137
Jianshanchong Klippe 501
Jib Frame 322

K

Kaolinite 142

L

Landfill Leachate 199
Laser Processing 59
Laser Shock Processing 3
Laterodeviation 456
Lead Recycling 111
Leakage Ratio 97
$Li_4Ti_5O_{12}$ 293
$LiFePO_4$ 190
Liquid Level Measurement 352
Lithium-Ion Batteries 190, 268, 293
LMDI Mode 302
Locomotion 383
Louver Shading Materials 77
Low-Grade Quartz Sands 170

M

Magnetic Fluid 409
Magnetic Propriety 17
Maintenance 344
Mass Flux 366
Material 81
Material Selection Standard 81
Mathematical Model 214, 473
Matlab 473
Mc-Silicon 207
MDL Criterion 467
Mechanic 330, 348, 414

Mechanic Performance 37
Mechanical Property 142
Mechanics Analysis 326, 392
Membrane Bio-Electro Reactor 199
Memory Duration 272
Meniscus 128
Metakaolinite 492
Metamorphism Degree of Coal 511
MFCs 506
Micrograph Analysis 162
Microhardness 223
Microparticles 487
Microstructure 132
Mine Hoist 352
Mineralizer 65
Modal Analysis 456
Modeling 107
Modified Plastic 59
MOESP Model 467
Molding Technology 37
Molten Salt Method 190
Molten Steel 7
Motion Track 437
Mould Plate 317
Multi-Walled Carbon Nanotube 297
Municipal Road 81
Municipal Solid Waste Incineration 289

N

Nano-Crystallites 115
Nanometer Al_2O_3-13%wtTiO_2 174
Naphthalene 243
Natural Core 231
Natural Rubber (NR) 142
Neodymium 223
New Structure 124
Nickel Recovery 263
Nonionic Surfactant 146
Nonlinear Gyroscopic System 387

O

Oil Analysis 73
Oil Monitoring 401
Oil Pump 371
Oil Volatility 356
Oil-Well Pump Lifting Test System 451
Optical Property 47
Optical Recording 239, 247
Optical Recording Storage 150
Optical Storage 166
Optical Storage Recording 178
Optimal Voltage 348
Organic Coating Modification 12
Organic Solvent 203
Orthogonal Analysis 55
Orthogonal Experiment 506
Oscillation 387
Oxygen 207

P

Parallel Mechanism 437
PASP 33
Perturbation 383
Petroleum Coke 297
Photochromic 178, 251, 478
Photochromism 150, 166, 239, 243, 247, 255, 259, 280
Piezoelectric Vibrator 441
Pile Driving 137
Pile Foundation 137
Placement Pattern 186
Planetary Gear 379
Plasma Spraying 174
Plastic Profiles 214
Polyepoxysuccinic Acid 194
Polysulfone Membrane 203
Porous Structure 170
Position Analysis 437
Powder 65
Powdered Activated Carbon 297
Power Generation Method 111
Power Spectral Density (PSD) 433
Precious Metal Material 263
Prediction of Gas Geology in Deep Area 501
Pressure Measurement 352
Primary Support 414
Principal Mode 456
Pro/E 429
Propagation Characteristics 3
Property Analysis 259
Protective Casing 313
Protective Clothing 97
Protrusion 276
Pulse Shaper 446
Pumping Unit 371

Q

Qingshan Coal Mine 501
Quality 89
Quasi-Static Pressures 396

R

Radio Frequency 276
Rare Earth 284
Reaction Kinetics 21
Reaction Rate Constant 21
Real Domestic Wastewater 517
Reinforcement 142
Resonant Response 338
Reutilization 289
Road Base 289
Road Engineering 26
Rolling Bearings 401
Rotating Clamp 344

S

Safety Indexes 89
Salt Fog 306
Sandpack Core 182
Sandwich Structure 47
Saving Energy 362
Scale Inhibition 194
Sealing Coating 55
Sealing Ring 326
Seawater 33
Self-Assemble Film 284
Si/Al/C Composites 268
Silicon Nitride 12
Silicon Nitride Nanowires 69
Simulation 330, 429
Single-Phase 115
Sintering Temperature 170
Slag 492
Slip 383
Soil Plug 137
Solar Biogas Digester 482
Solar Cell 158, 207
Solar Shading Performance 77
Solid-State Method 293
Solid-State Reaction 65
Southwestern Region 460
Special-Shaped Surface 42
Spiral Corrugate Cardboard Cutting Machine 473
Splicing Sleeve 313
Sporosarcina pasteurii 103
Sports Performance 375
Sputter-Etching 276
State Monitoring 334
Static Mixer 124
Steady Polarization 33
Strength Check 451
Stress 379
Stringing Sheave 313
Surface Modification 12
SUS304 Stainless Steel 276
Synchrocontrol 421
Synergistic Complexation 154
Synthesis 115, 255

T

Taguchi Approach 263
TC4 Blades 425
Technology Analysis 218
Tectonic Control 511
Temperature 7
Temperature Field 42
TG-DSC 405
Thermodynamics 405
Thermophilic Bacteria 182
Thickness 223
Thin Film 47
Thin Rim 379
Tire Building Drum 437
Trial Learning 272
Triangular Cantilever 441
Tubular Membrane 199, 203
Tunnel 414

U

Underground Installation 371
Underwater Noise Reduction 227

V

Valve 429
Velocity Modulation 362
Vibration 338
Vibration Analysis (VA) 334
Vibration Mechanics 334
Virtual Prototype 330

Viscoelastic Material 227

W

Wafer Precision Grinding Machine 330
Wastewater Treatment 506
Water Lubricated 37
Wave-Packet Propagation Diagnosis (WPD) 460
Wear Resistance 174
Wood 30
Wood Extractives 52
Wood Products 89

X

X-Ray Powder Diffraction 162

Y

YAG Powder Materials 162
Yongshanqiao Mining Area 511
Yttrium Aluminum Garnet 65

Z

Zein 487

Authors Index

A

Abou-Shady, A. 263
An, P. 467

B

Bai, T. 276, 284
Bao, Z.G. 120

C

Cao, C.L. 137
Cao, G.H. 170
Cao, Y. 21, 65
Chen, A.X. 162
Chen, C.C. 297
Chen, H.Z. 97
Chen, J. 12, 17, 69, 501
Chen, L.D. 214
Chen, W.D. 441
Chen, Z. 186, 517
Cheng, G.Z. 334, 344, 352, 362, 392, 497
Cheng, J.L. 473
Cheng, W.M. 348
Cheng, X.H. 284
Cheng, Z.F. 174
Cui, L. 52
Cui, S.Q. 178, 239, 243, 478
Cui, W. 338

D

Dai, Y.J. 344, 497
Dai, Y.N. 405
Deng, M. 478
Ding, H.C. 259
Ding, Y.H. 268
Ding, Z.Y. 492
Dong, D.M. 302
Dong, J.T. 65
Dong, W.F. 297
Du, X.G. 146
Duan, H.Y. 302
Duan, R.Y. 272

F

Fan, C.B. 150, 255
Fang, Y.W. 3, 425
Feng, C.H. 387
Feng, X.G. 306

G

Gan, G.Y. 132
Gao, H. 21, 65
Gao, W.X. 207
Geng, W.W. 150
Gong, Q.C. 297
Gu, F. 293
Gu, N.Y. 190
Guan, B.H. 456
Guo, C. 93
Guo, H.F. 115
Guo, H.Y. 89
Guo, Q.J. 366
Guo, S.X. 115
Guo, X.M. 146

H

Han, B.A. 124
Han, J.M. 414
Han, Y.C. 473
Han, Y.Y. 334
Hao, R.J. 272
He, S.H. 166
He, W.F. 425
He, X.G. 302
He, X.H. 190
He, Y.A. 227
Hu, H.S. 441
Hu, L.M. 218
Hu, Y.J. 289
Huang, B. 42
Huang, M.Y. 272
Huang, X.S. 214
Huang, Y.C. 97
Huang, Z.C. 317
Huo, J.F. 379
Huo, P.F. 128

J

Ji, Z.H. 55
Jia, R.J. 132
Jia, Y.J. 334, 344, 392, 497
Jiang, D.H. 280
Jiang, K.Y. 59
Jiang, X.F. 73, 401
Jiang, Y.P. 47
Jin, B. 103, 107
Jin, R.H. 460
Jin, R.J. 263
Jing, S.H. 251

K

Kawagoshi, Y. 506
Kong, L.L. 268
Kong, X.P. 182, 231

L

Li, B. 451
Li, C. 55, 190
Li, F.M. 482
Li, G. 21
Li, H. 247, 251
Li, L. 268
Li, L.B. 115
Li, L.H. 366
Li, P.H. 103, 107
Li, Q. 162, 170
Li, Q.L. 124
Li, S. 26
Li, S.A. 207
Li, S.L. 137
Li, T. 356
Li, W. 170
Li, W.B. 170
Li, W.T. 162
Li, X. 255
Li, X.N. 154
Li, X.T. 247
Li, X.W. 446
Li, X.Y. 487
Li, Y. 487
Li, Y.H. 3, 425
Li, Y.J. 326, 421
Li, Y.Z. 26
Li, Z.K. 77
Liao, Y.Z. 487
Lin, H.F. 362
Lin, J. 352
Lin, Y.H. 387
Liu, D.B. 42
Liu, D.H. 7
Liu, E.H. 199, 203
Liu, F. 73, 322, 401
Liu, F.K. 326
Liu, G. 166, 178, 239, 255, 280, 478
Liu, K. 81
Liu, M. 239, 409
Liu, Q.X. 47
Liu, S. 405
Liu, T.T. 297
Liu, W.J. 166, 280
Liu, X.Z. 223
Liu, Y.H. 170
Liu, Y.L. 268, 405
Liu, Z. 33, 194
Liu, Z.F. 33, 194
Liu, Z.H. 26
Liu, Z.Q. 362
Liu, Z.X. 132
Lu, W.W. 146
Luo, C.H. 97
Luo, L.E. 158

M

Ma, C.B. 47
Ma, L.M. 186, 517
Ma, X. 268
Ma, X.D. 170
Ma, Z. 174, 302
Ma, Z.Z. 429
Meng, X.S. 297

N

Ni, H.H. 21
Ni, H.N. 473

O

Ouyang, X.D. 218

P

Pan, X.H. 437

Peng, C.S. 263, 482
Peng, J.M. 37
Peng, W.X. 30, 52
Peng, X. 59
Pu, S.Z. 150, 235, 243, 247, 251, 259

Q

Qian, S.X. 441
Qian, W. 487
Qin, J. 313
Qiu, L.G. 492
Qiu, L.J. 371, 375
Qiu, Y.P. 313
Qiu, Z.S. 132
Qiu, Z.W. 162

R

Ran, K. 492
Ren, L.P. 272
Ren, P.P. 478

S

Sato, T. 506
Sha, Z.H. 330
Shang, D.J. 227
Shi, Y.B. 42
Song, J.G. 162, 170
Song, J.J. 111
Song, L.L. 223
Song, S.P. 55
Song, Y.M. 379
Song, Y.P. 137
Su, H.L. 383
Sun, H.M. 306
Sun, Y.F. 137

T

Tang, X.G. 47
Teng, Q. 467
Tian, Z. 396
Tong, X.Z. 302

W

Wang, D.A. 473
Wang, D.Q. 120
Wang, F. 81, 170
Wang, F.C. 174
Wang, G. 223
Wang, H. 3
Wang, H.B. 7
Wang, H.W. 186, 517
Wang, J.J. 154, 338
Wang, L.Q. 235
Wang, L.S. 30, 473
Wang, Q. 492
Wang, R.J. 243
Wang, S.H. 97
Wang, T.F. 178
Wang, W.P. 280
Wang, X. 33, 194, 487
Wang, X.E. 302
Wang, X.G. 12, 69
Wang, X.H. 21, 65
Wang, X.L. 429
Wang, Y. 142
Wang, Y.M. 227
Wang, Y.R. 81
Wang, Z. 186, 326, 421, 517
Wang, Z.W. 170
Wei, W. 162
Wu, P. 207
Wu, Q. 124
Wu, Y. 460
Wu, Z.Z. 409

X

Xia, Y.Q. 158
Xiao, T.G. 460
Xiao, T.Y. 433
Xiong, D.P. 47
Xiong, Y.F. 162
Xu, A.J. 7
Xu, H.Y. 199, 203
Xu, N. 268
Xu, S.Y. 375
Xu, T. 162

Y

Yamashita, T. 506
Yan, J.K. 132
Yan, J.P. 501, 511
Yan, L.S. 235
Yang, C.Y. 37
Yang, H.Q. 120
Yang, J. 371

Yang, J.H. 223
Yang, J.L. 21, 65
Yang, L. 199
Yang, S.H. 97
Yang, X.C. 85
Yang, X.H. 446
Yang, Y.H. 178
Yang, Z.Y. 146
Yao, J. 77, 85, 93
Yao, Y.C. 405
Yi, J.H. 132
Yoshino, Y. 506
Yu, D.G. 487

Z

Zang, L.H. 297
Zeng, Q.D. 322, 456
Zhang, B. 326, 421
Zhang, C.S. 146
Zhang, D.M. 120
Zhang, D.W. 383
Zhang, D.Y. 344, 497
Zhang, H.Y. 17, 69
Zhang, J. 146, 170, 379
Zhang, J.B. 467
Zhang, K.D. 263
Zhang, M.M. 511
Zhang, Q. 142
Zhang, Q.L. 276
Zhang, R.J. 289
Zhang, S. 446
Zhang, S.F. 330
Zhang, W. 326, 421
Zhang, W.H. 81
Zhang, X.X. 392
Zhang, Y. 482
Zhang, Y.D. 142
Zhang, Y.S. 120
Zhang, Y.X. 26
Zhang, Y.Z. 421
Zhang, Z.N. 330
Zhao, B.T. 207
Zhao, G.Q. 65
Zhao, J. 268
Zhao, P.C. 73, 401
Zhao, X.C. 203
Zhao, Z.G. 501, 511
Zheng, C.H. 259, 297
Zheng, Z.Z. 89
Zhong, B. 348
Zhong, C.L. 158
Zhong, W. 396
Zhou, G.Y. 506
Zhou, J.F. 162
Zhou, S.D. 218
Zhou, Y.Q. 132
Zhu, D.K. 441
Zhuang, G.S. 223